Talanta

The International Journal of Pure and Applied Analytical Chemistry

FTIR—Multivariate curve resolution monitoring of photo-Fenton degradation of phenolic aqueous solutions
Comparison with HPLC as a reference method

O. Abbas, C. Rebufa *, N. Dupuy, J. Kister

*ISM2, UMR CNRS 6263, Equipe AD2EM, Groupe Systèmes Chimiques Complexes, Université Paul Cézanne, Case 451,
+ Avenue Normandie Niemen, 13397 Marseille Cedex 20, France*

ARTICLE INFO

ABSTRACT

A new analytical method based on Fourier transformed infrared spectroscopy (FTIR) using chemometric tools to treat spectral data is proposed to study the degradation of aqueous phenolic solutions by photo-Fenton process. Obtained results were validated by high-performance liquid chromatography (HPLC) taken as a reference method. First a discrimination of the different steps of phenol degradation was possible by applying a principal component analysis (PCA). Then a description of the reaction evolution was successfully made using MCR-ALS, a multivariate curve resolution method which has permitted to obtain the concentration profiles of phenol and its photoproducts. Kinetics of their formation and disappearance described with this new approach are in agreement with HPLC results. This methodology may be a good alternative to classical analyses for monitoring of the degradation reactions because a lot of data are recorded and treated simultaneously. It shows how species concentration varies over time, informing thus on the reaction mechanism because a structural identification of products is possible through pure extracted spectra.

1. Introduction

In parallel to the development of industry, pollutants and the industrial waste are increasingly present in the environment. Among these pollutants, phenol and its derivatives occupy a predominant place. A lot of processes have been developed to optimize its elimination by biological [1], physical (adsorption [2] or wet oxidation by activated carbon [3]), electrochemical [4] or chemical ways such as chlorination disinfection [5,6] or with advanced oxidation processes (AOPs). AOPs are particularly adapted for effluent treatment and usually operate at or near ambient temperature and pressure. They propose a degradation of organic pollutants with H_2O_2, O_3 or O_2 as oxidant to generate hydroxyl radical ($OH^\bullet$), in homogenous or heterogeneous phase (with metal ions [7,8] or semiconductors as TiO_2 [9,10]), powered in some cases by irradiations (UV, UV–visible, solar light) allowing a photocatalytic oxidation [11–13]. Among the most commonly used and attractive systems for industrial applications, we can find Fenton or photo-Fenton [14–16] processes which are based on the decomposition of H_2O_2 catalysed by Fe^{2+} at acid pH. They are characterized

by a high-oxidation power, simplicity of operation and low costs.

For these reasons, we have chosen the photo-Fenton process to degrade aqueous phenolic solutions. The originality of our work is the use of spectroscopic technique (FTIR-ATR) coupled to chemometric treatment to follow the evolution of reaction mixture and to identify the oxidation intermediates, their lifetime and their toxicity. In our knowledge, this approach has not been published yet for this type of applications.

Although infrared spectroscopy is commonly employed for qualitative and quantitative analysis, the identification of each component from FTIR mixture spectra is not evident when reactions take place in aqueous solution and when the photoproducts concentration is low because it prevents to obtain a good intensity of IR bands. Other difficulties occur when photoproducts have a very similar structure with widely overlapped absorption bands. Araña et al. [9,17] have already recorded FTIR measurements to follow the degradation of highly concentrated phenolic solutions by TiO_2 photocatalysis and photo-Fenton process. In the first one [9], identification of intermediates was done by the examination of TiO_2 surface and comparison of chemisorbed compounds IR bands with reference spectra of photoproducts, identified previously by HPLC. In the second process [17] photoproducts have been identified by the subtraction of the initial spectrum of phenol

---

and reference spectra of pure intermediate species from mixture spectrum.

In our case, a lot of FTIR measurements have been recorded in time but their direct interpretation has been difficult for the reasons exposed above which make it necessary to apply chemometric treatments on spectral data to prevent problems encountered with classical method of spectra analysis. These mathematic tools, efficient to extract relevant information from complex systems in various domains, permitted to analyse multicomponent mixtures without using a separative method. The majority of published studies [18,19] concern the use of calibration model such as partial least square regression (PLS) in order to predict the final concentrations of products after an oxidative stress.

Nevertheless, monitoring chemical reactions of evolutionary processes remains very interesting because real time information on the system is obtained by a simple sampling of mixture without perturbation of the reaction. Spectra measured at each time-point provide information about the chemical composition of the system and the progress of the chemical reaction.

For chemometric treatment of the collected spectra, we applied principal component analysis (PCA) and a multivariate curve resolution-alternating least squares (MCR-ALS).

While PCA permits to observe how samples taken at different times will be gathered, MCR-ALS associated to SIMPLISMA procedure resolves FTIR-ATR data into pure spectra of species produced during the reaction and their associated concentration profiles, without *a priori* information. Extracted pure spectra led us to identify the photoproducts and the concentration matrix allowed us to compare their kinetic of appearance and disappearance and to know if they are formed simultaneous or not, in the same or different proportions.

The aim of the present paper is to access the validity of the concentration profiles obtained from our spectroscopic interpretations by comparing them with the results obtained by HPLC technique.

2. Experimental

2.1. Chemicals

Phenol (Prolabo), catechol (or 1,2-dihydroxybenzene, Acros), hydroquinone (or 1,4-dihydroxybenzene, Acros), *p*-benzoquinone (Acros), resorcinol (or 1,3-dihydroxybenzene, Acros), pyrogallol (Acros), acetic, acrylic, formic, fumaric, maleic, malonic and oxalic acids (Fluka) were all of high purity (>99%) and were used as standards. Iron(II) sulphate heptahydrate p.a. ($FeSO_4$, $7H_2O$) was purchased from Acros Organics, hydrogen peroxide (30%, w/w, unstabilized) from Prolabo. All solutions were prepared in ultra-pure water and kept in the dark.

Methanol (Chromasolv for HPLC, Sigma–Aldrich), acetonitrile (Lichrosolv, Merk) were solvents used for HPLC technique. Water is also of HPLC grade.

2.2. Experimental setup

Experiments were performed in a glass reactor equipped with a cooling water jacket system keeping a constant temperature (18 °C in solution) and avoiding loss of volatile products. Irradiation was achieved by using UV lamp (Mercury arc lamp ORIEL, model 6286, 350 W), equipped with a water filter and with a reflecting mirror (200–30,000 nm) which allows a vertical lighting above the reactor. All irradiations were performed with a light intensity (UV-A) equal to 200 W/m². Ozone production was eliminated by an aspiration system on the level of the lamp's body. The reactor solution was stirred magnetically and irradiated for 60 min.

2.3. Oxidative processes

2.3.1. Photo-Fenton reactions

The principal reactions with Fenton reagent are well known [20] (reactions (1) and (2)). They generate ferric ion which catalyze the complete decomposition of H_2O_2 (Eqs. (3) and (4)):

$$Fe^{2+} + H_2O_2 \rightarrow Fe^{3+} + OH^\bullet + OH^- \tag{1}$$

$$RH + OH^\bullet \rightarrow photoproducts + H_2O \tag{2}$$

$$Fe^{3+} + H_2O_2 \rightarrow [Fe^{3+} \cdots O_2H]^{2+} + H^+ \rightarrow Fe^{2+} + HO_2^\bullet + H^+ \tag{3}$$

$$Fe^{3+} + HO_2^\bullet \rightarrow Fe^{2+} + H^+ + O_2 \tag{4}$$
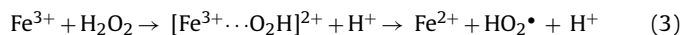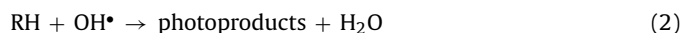
Unfortunately, parallel reactions can consume $OH^\bullet$ radicals [21] as described in Eqs. (5) and (6) allowing reduction of Fenton reagent efficacity over time:

$$OH^\bullet + Fe^{2+} \rightarrow Fe^{3+} + OH^- \tag{5}$$

$$OH^\bullet + H_2O_2 \rightarrow H_2O + HO_2^\bullet \tag{6}$$

UV irradiation leads to the photo-reduction of Fe^{3+} to Fe^{2+} (regeneration of Fe^{2+}) with production of $OH^\bullet$ radicals [22] (Eq. (7)), to the photolysis of hydrogen peroxide (Eq. (8)) and photo-reduce Fe^{3+} complexes formed during the reaction [23]:

$$Fe^{3+} + H_2O + h\nu \rightarrow OH^\bullet + Fe^{2+} + H^+ \tag{7}$$

$$H_2O_2 + h\nu \rightarrow 2OH^\bullet \quad (if \quad \lambda < 400\,nm) \tag{8}$$
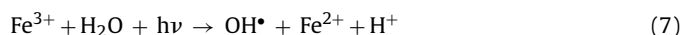
2.3.2. Photolysis process

To check UV stability of our substrate, 20 mL of phenol aqueous solution (5×10^{-3} mol/L) were irradiated in the conditions described previously. The solution was acidified (pH 2) with H_2SO_4.

2.3.3. Photo-Fenton process

20 mL of acidified phenol aqueous solution (0.25 mol/L) were stirred in dark with an appropriate weight of iron(II) salt (to have a final concentration of Fe(II) equal to 3.5×10^{-3} mol/L). After illumination of solution by UV radiations, 0.5 mL of H_2O_2 (0.3 mol/L) were added at time "T0" and after the times 30 and 45 min. Last additions have been undertaken to attempt the total degradation of phenol.

Phenol degradation's monitoring has been done by FTIR-ATR and by HPLC as a reference method.

After the addition of H_2O_2, the last compound introduced in the mixture, a modification of solution colour has been noted with the appearance of a brown precipitate.

2.4. Kinetic study

For HPLC analysis, aliquots (600 μL of irradiated solution) were withdrawn with an automatic pipette and mixed immediately, in HPLC vials, with 400 μL of methanol to inhibit oxidation of products by hydroxyl radicals $OH^\bullet$ and to avoid further reaction. To obtain a final concentration near 5×10^{-3} mol/L, solutions are diluted with water and then are filtered to eliminate the brown precipitate formed after the first addition of H_2O_2. All the vials were analyzed in the same run.

For the reactions monitoring by FTIR-ATR, some drops of mixture were pipetted and immediately deposited on ATR cell in order to be analyzed.

Four kinetics (A, B, C and D) were pursued and treated in the same conditions to check the reproducibility.

Time intervals were specific to each type of analysis and were more numerous when using spectroscopic techniques. This is essential for chemometric treatment.

2.5. Analytical equipments

2.5.1. HPLC

Samples were analyzed by an HPLC system equipped with a pump Waters 2695 separations module "Alliance", a sample injector and an UV–Visible Waters 2996 Photodiode Array Detector. System was controlled by Milleniumv®32 Chromatography Manager (version 3.20).

A Reverse-Phase Column (RP18, 22 cm × 4 mm, Purospher® STAR) was used. A guard column was fitted before the analytical one. The mobile phase was constituted by acetonitrile/water in the volumetric proportion of 30:70 with a flow rate equal to 1 mL/min. Detection wavelength for each product was fixed after examination of 3D plot (time, intensity, wavelength).

2.5.2. FTIR-ATR

Aqueous solutions are directly deposited on the "Golden Gate" cell (from Brucker), attenuated total reflectance (ATR) accessory composed by a diamond crystal prism (brazed in only one tungsten carbide part), four mirrors and two lenses of focusing in ZnSe to reflect optical way. The acquisition of FTIR-ATR spectra was made with a Thermo Nicolet Avatar 370 spectrometer equipped with a DTGS detector, an Ever-Glo source and a KBr/Germanium beamsplitter, at room temperature.

Data acquisition, made with an absorbance scale, was done from 4000 to 700 cm^{-1} with a 4 cm^{-1} nominal resolution. For each spectrum, 100 scans were co-added.

A background on pure water (in the same resolution and scanning conditions that it was for samples) was carried out before each record of spectra at different times during kinetics.

2.6. Mathematic treatments

Today, multivariate analysis is an essential tool to study data came from many observations made on several variables. Its aim is to resume information contained in data with a reduced number of dimensions to characterize as well as possible the differences or similarities between observations and variables. For that, information must be organized in a matrix. In your case, the data matrix ($m \times n$) is composed by m rows which are spectra measured at regular time intervals, and by n columns representing different wavenumbers.

2.6.1. PCA

PCA [24] is a multivariate technique acting in unsupervised manner and it is used to analyse inherent structure of data. It involves a mathematical procedure that transforms a matrix of correlated variables (measurements) into a new matrix of mutually uncorrelated variables called *principal components* which contain the quasi-totality of information and have the advantage to be not correlated or orthogonal between them. These variables are defined by a set of orthogonal loading vectors of the data covariance matrix. The first principal component accounts for as much of the variability in the data as possible, and each succeeding component accounts for as much of the remaining variability as possible. Objectives are to discover or reduce the dimensionality of data set without much loss of information and identify new meaningful underlying variables.

2.6.2. MCR-ALS

MCR-ALS is an effective and efficient multivariate self-modeling curve resolution method developed by Tauler and co-workers [25]. The quality of the relative contributions given by MCR-ALS was evaluated in order to develop a rapid procedure that can be applied to resolve highly overlapped spectra.

For the analyzed samples, one matrix $\mathbf{R}(\mathbf{n}, \mathbf{m})$ made up n row and m columns is obtained. Each row "n" is made up of a spectrum. Each column "m" gives the intensity at a wavenumber. $\mathbf{R}$ is the data matrix of n spectra and p wavenumbers. The $\mathbf{R}$ matrix is mathematically decomposed into the product of two-factor matrix:

$$\mathbf{R} = \mathbf{C} * \mathbf{S}^T + \mathbf{E} \tag{9}$$

Matrix $\mathbf{C}(\mathbf{n}, \mathbf{q})$ is the concentration matrix describing the evolution of the q chemical components in the samples. Matrix $\mathbf{S}^T(\boldsymbol{q}, \boldsymbol{p})$ is the spectroscopic matrix describing the pure infrared spectra of these components. $\mathbf{E}(\mathbf{n}, \mathbf{p})$ is the error matrix that provides the data variation not explained by the proposed p contributions. Eq. (9) assumes that data matrix $\mathbf{R}$ is bilinear, i.e. that the infrared signal can be decomposed into the sum of individual contributions, each described by a concentration profile in the matrix $\mathbf{C}$ and by a pure matrix spectra in matrix $\mathbf{S}^T$. The number of components or contributions q, to be considered in the mathematical decomposition of Eq. (9), can be estimated by singular value decomposition (SVD) analysis [26].

Eq. (9) is solved iteratively using an ALS procedure based on the two following matrix equations:

$$\mathbf{C} = \mathbf{R} * (\mathbf{S}^T)^+ \tag{10}$$

and

$$\mathbf{S}^T = \mathbf{C}^+ * \mathbf{R} \tag{11}$$

where $(\mathbf{S}^T)^+$ and $\mathbf{C}^+$ are the pseudo-inverse matrix of $\mathbf{S}^T$ and $\mathbf{C}$ [27]. Initial estimate, which are needed to start the ALS procedure described by these two equations, can be obtained by algorithms, such as *simpl*e-to-use *i*nteractive *s*elf-*m*odeling *a*nalysis (SIMPLISMA), which is described elsewhere [28–31]. SIMPLISMA searches for the pure variables where the selectivity of a given component is maximized. In order to obtain proper resolution of the mixture data, user interaction is necessary. Once, the pure variables were determined, they were used to calculate the corresponding pure species spectra because the intensity changes in the pure variables are proportional to the concentration evolutions and, if they are aligned in separated columns, they form the matrix $\mathbf{C}$.

The resolution was improved by applying several constraints during optimization. Some of the possible constraints are

- Non-negativity on the concentration profiles: this is a general constraint used in curve resolution methods [32]. It is applied to the concentration profiles, due to the fact that the concentrations of the chemical species are always positive values or zero.
- Non-negativity on the spectra: the application of this constraint depends on what instrumental technique is used for detection. In the case of FTIR spectra, the intensity of the radiation absorbed or reflected by the sample never takes negative values.

The computed solutions of the algorithms will be presented in terms of the lack-of-fit in percentage plus the resolved spectral and concentration profiles. The lack of fit relates to the difference between the squared sum of the input data and the squared sum of the modeled variation with the resolved MCR-ALS profiles. For one sample it is computed according to the following expression:

$$\mathrm{lof} = \sqrt{\frac{\sum_{i,j}(r_{ij} - \hat{r}_{ij})^2}{\sum_{ij} r_{ij}^2}} \tag{12}$$

where r_{ij} is the experimental absorbance at the jth wavenumber in the ith spectrum and $\hat{r}_{ij}$ is the corresponding value calculated by ALS. A low lack of fit percentage indicates that a model fits the data well [33,34].
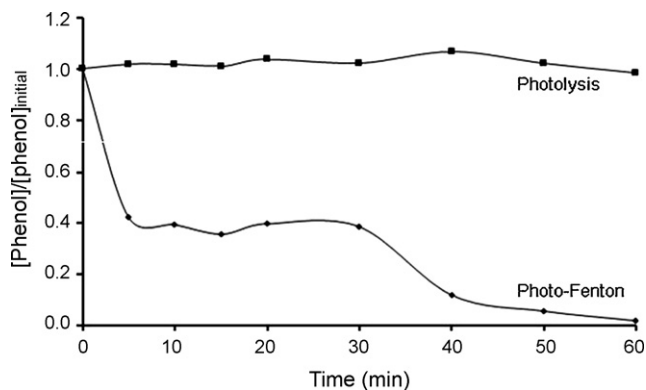
Fig. 1. Relative concentration of phenol vs. irradiation time ([phenol]$_{initial}$ = 5×10^{-3} M and $\lambda_{detection}$ = 270 nm).

2.7. Software

HPLC chromatograms are visualized and integrated on Millenium software (version 3.2).

FTIR-ATR spectra are recorded with OMNIC 7.2 (Thermo Nicolet) software.

PCA application and baseline correction of spectra were performed by the UNSCRAMBLER software version 9.6 from CAMO (Computer Aided Modelling, Trondheim, Norway).

MCR-ALS procedure, implemented on MATLAB code, was obtained from http://www.ub.es/gesp/mcr/ndownload. The SIMPLISMA routines were obtained by W. Windig. These programs were used under MATLAB 2007a.

All data injected in SIMPLISMA came from Unscrambler application. Second derivative spectra have been used in SIMPLISMA approach but original spectral data and SIMPLISMA concentration profiles have been the starting point for MCR-ALS algorithm.

3. Results and discussion

3.1. HPLC results

Comparative results between photolysis and photo-Fenton degradation of aqueous phenolic solution have been interpreted in terms of residual phenol relative concentration ([phenol]/

[phenol]$_{initial}$) which has been determined from calibration standards (Fig. 1).

We have noticed that for our photo-oxidation system (apparatus and conditions), the phenol is photo-stable by direct illumination, because UV lamp does not cover the domain of weak wavelengths. Chun et al. [10] showed also that no significant photolysis was observed when the phenol solution was irradiated at $\lambda > 300$ nm. The intensity of the irradiation and the initial concentration of the compound are key factors in the effectiveness of the direct photolysis.

In photo-Fenton process, phenol concentration drops very fast in the first minutes and practically vanishes after 60 min because UV provided photons to stimulate the regeneration of ferrous ion as shown in Eq. (7), but free formed hydroxyl radicals are instantaneously consumed by substrates that the reason why photo-Fenton curve shows a plate, meaning that the phenol degradation is practically stopped because of the interruption of OH• production. To obtain a complete disappearance of phenol, we had to make two supplementary additions of H_2O_2 at different times (after 30 and 45 min of UV irradiation).

HPLC results (Fig. 2) validated with standards for the identification of compounds show that the main photoproducts of phenol degradation are hydroquinone (T_R = 3.8 min at λ = 280 nm) and catechol (T_R = 5.5 min at λ = 280 nm). Traces of resorcinol (T_R = 4.5 min at λ = 280 nm) and p-benzoquinone (T_R = 6.1 min at λ = 250 nm) have been found. The p-benzoquinone has not been detected at every manipulation because of its very weak solubility in water and its disappearance during the filtration of the mixture before HPLC injections. The concentration profiles (Fig. 3) have been determined for these five compounds through standards calibration. The disappearance curve of phenol and those of appearance for photoproducts form a plate between 10 and 30 min because of the Fenton reagent exhaustion due to the formation of Fe^{3+} complexes [35] which give sharp solution darkness and inhibit iron regeneration cycle thus indirectly causing lack of OH radicals. The compounds evolution continues after the first re-injection of H_2O_2 (30 min) allowing their degradation, very advanced after the second addition. Araña et al. [17] have observed the same effects which have been surmounted with filtration treatment or when the H_2O_2 dose has been increased. After photo-Fenton reaction, the formation of hydroquinone and catechol, as main primary oxidation intermediates, has been always evoked but other transient species have been identified, by several authors [8,14,17,36] like
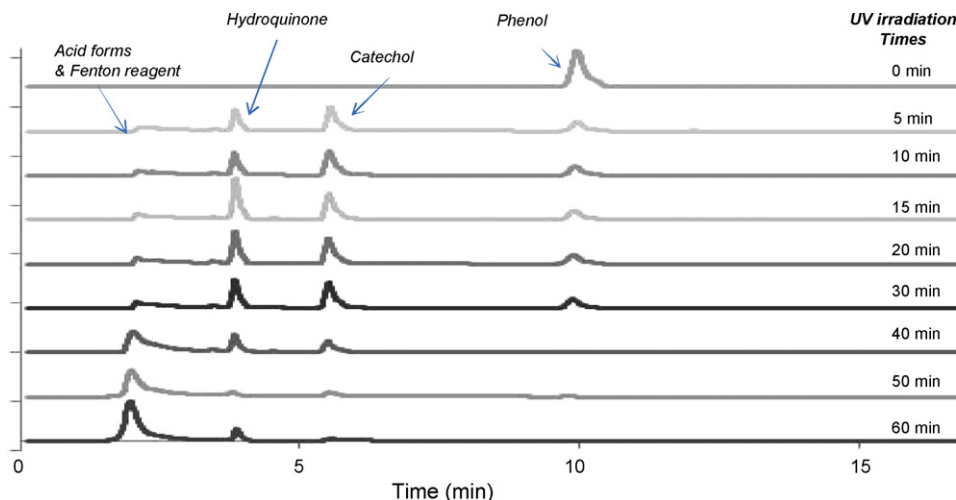
Fig. 2. HPLC chromatograms obtained at different times of UV irradiation ([phenol]$_{initial}$ = 5×10^{-3} M, $\lambda_{detection}$ = 280 nm).
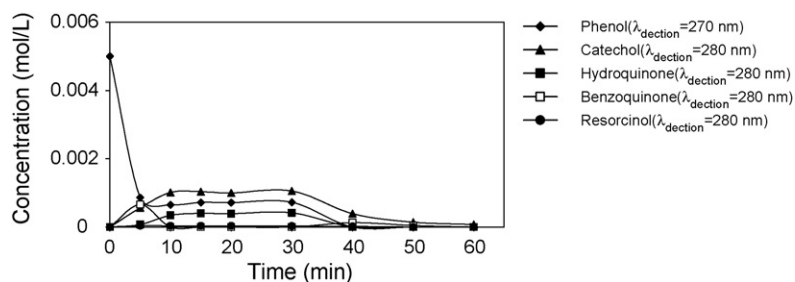
Fig. 3. Kinetic evolution of main products based on HPLC analysis.

pyrogallol, 1,2,3-benzenetriol or 1,2,4-benzenetriol, resorcinol, benzoquinone in redox equilibrium with dihydroxybenzenes (that explain the presence of *p*-benzoquinone and *o*-benzoquinone, unstable compound in aqueous solution) and several products of acid formation stage (maleic, oxalic, formic, acetic, muconic, malonic, fumaric acid). In our case, acid forms appear under a

large peak centred at $T_R = 2$ min that the intensity is constant in the first times because of the presence of sulphuric acid and increase when hydroquinone, catechol and resorcinol begin to disappear, after near 20 min of UV irradiation. This lets to us suppose that the organic acids formation is due to a degradation of primary photoproducts by a ring-opening of these aromatic intermediates.
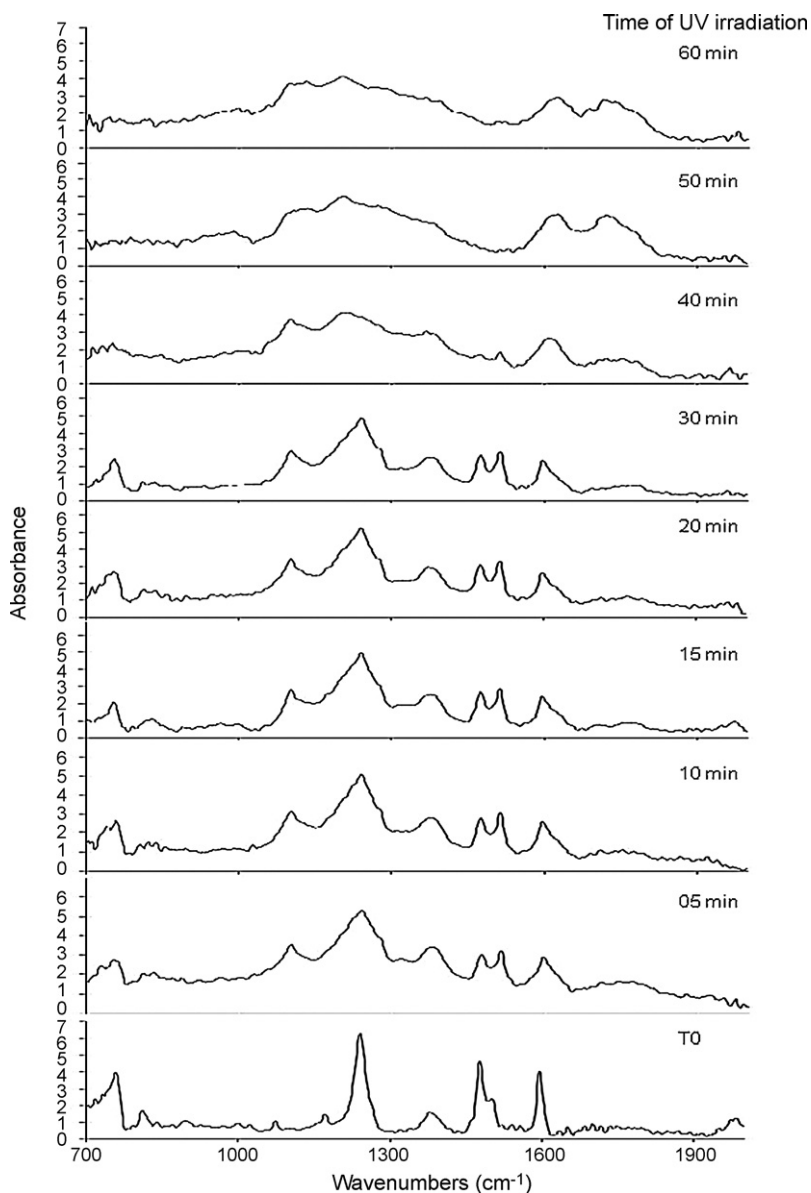
Fig. 4. FTIR-ATR spectra recorded during phenol photo-Fenton degradation in aqueous solution. T0: time just before the addition of H_2O_2 in the mixture (containing phenol, H_2SO_4 and Fe(II)).

Some of these carboxylic acids like oxalic and acetic acids are accumulated because they are recalcitrant to Fenton and photo-Fenton processes [37,38]. Standard solutions of organic acids cited before have been analysed by HPLC to verify that their retention time was resolved under the large peak centred at $T_R = 2$ min.

3.2. FTIR-ATR results with chemometric treatments

After examination of the infrared spectra (Fig. 4) recorded between 0 and 60 min of irradiation, only some variations could be detected in the spectral region where water does not interfere (i.e. between 700 and 2000 cm^{-1}) but these spectral modifications do not permit to apprehend clearly the apparition of new chemical species. Because of their low concentration in the mixture, the intensity of their characteristic bands is very weak. After recording spectra of phenol and photoproducts supposed present in aqueous solution (Fig. 5), many overlapped bands appear and only few vibrational bands (assigned in Table 1) permit their distinction. Despite the water problem and the similarity of the compounds, the interpretation of mixture spectra (recorded during the four kinetics of degradation by photo-Fenton process) has been realized with the help of mathematical algorithms in the spectral zone ranging between 700 and 2000 cm^{-1}.

3.2.1. PCA treatment

PCA treatment (Fig. 6) of FTIR-ATR data regroup samples in clusters defining four states for the reaction which takes place under our experimental conditions: the initial state, described by the aqueous solution of phenol, is isolated from the others, the second step includes samples of times between 5 and 30 min, a third part and a fourth one distinguish respectively samples collected after the first and the second re-injection of H_2O_2 done after 30 and 45 min of UV irradiation. The first component expresses 81% of variations; the second one corresponds to 10%. The last percents (9%) traduce not significant variations and noise.

PC1 axis regroups the first times (between 0 and 30 min of UV irradiation) in the negative part while the last ones are presented in the positive part. Its associated loading (Fig. 7a) shows that the specific bands of phenol, identified negatively (at 1594, 1498, 1477, 1379, 1241, 1170, 1074, 812, and 756 cm^{-1}) characterize the first irradiation times where this compound is still majority while band at 1722 cm^{-1} describes the final reaction products which can be acid compounds formed, by an open ring of phenol and its aro-
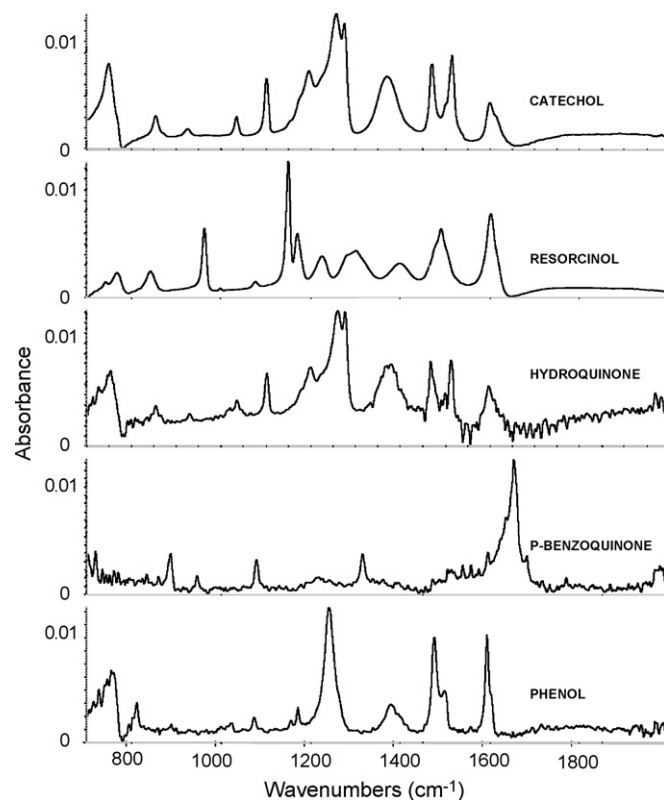
Fig. 5. FTIR-ATR spectra of pure products in aqueous solution.

matic photoproducts, after the second re-injection of H_2O_2. On the PC2 loading (Fig. 7b), the IR bands at 1512, 1472, 1371, 1276, 1259, 1219, 1101, 831, and 756 cm^{-1} describe two compounds: catechol and hydroquinone. Their contribution to the mixture composition is different following the photo-Fenton reaction evolution as PCA graph shows it by differentiating the times between 5 and 60 min with three captions distributed differently on PC2 axis. Another way to do PCA has been to remove the initial points "T0" of the kinetics to differentiate the photoproducts. But a same repartition of spectra has been obtained with 76% of variance for PC1 and 6% for PC2. Their associated loadings were also relative to the phenol or a mix-

Table 1
Characteristic of infrared assignments of phenolic compounds

Wavenumber (cm^{-1})					Type of vibration	Functional group
Phenol	Resorcinol	Catechol	p-Benzoquinone	Hydroquinone		
		1653			ν C=O	Quinones
1594	1602	1600				
1498	1490	1514		1514	ν C=C	−C=C− cycle
1477		1472		1473		
1378	1399	1375	1315	1371	O–H def	O–H def and ν C–O (phenol)
	1301	1277			ν C–O	−O-Aryl
1240		1260		1240		
1172	1225	1200		1220	ν C–O	O–H def and ν C–O (phenol)
	1170					
1074	1150	1103	1079	1100	δ =C–H	=C–H aromatic
		1034				
	965					
892	842	856	886	837	γ =C–H	=C–H aromatic
814		754	719	759		
754	767					

γ: deformation out-of-plane; ν: stretching; def: deformation; δ: deformation in plan.
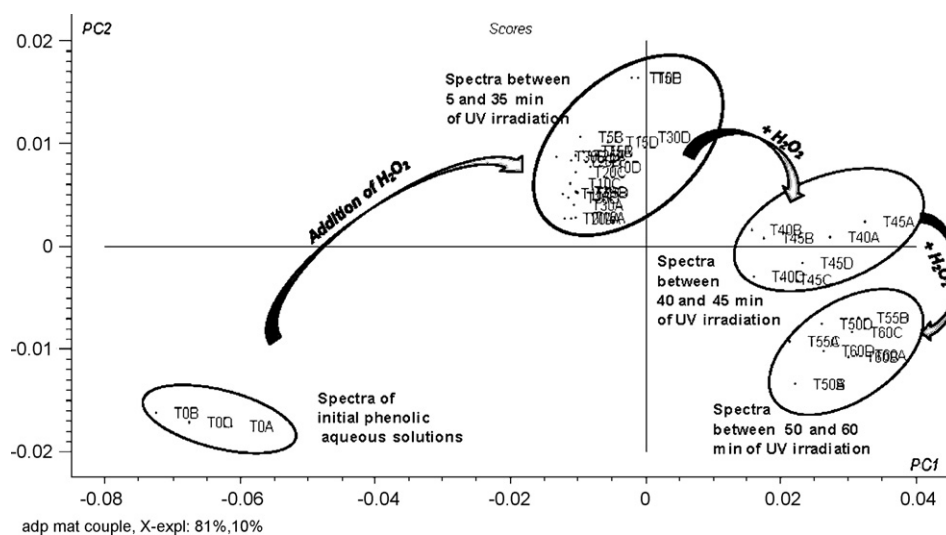
Fig. 6. PCA of FTIR-ATR spectra recorded during phenol photo-Fenton degradation in aqueous solution. *Significance of the notations in the clusters*: The letters A, B, C and D differentiate the four kinetics. The letter "T" followed by a number included between 5 and 60 corresponds at the spectrum recorded after different times of UV irradiation. "T0" is associated to the spectrum of initial mixture before hydrogen peroxide addition and UV illumination.

ture of photoproducts. A new addition of H_2O_2 in the mixture after 60 min of UV irradiation does not conduce to the mineralization of these carboxylic acids even if irradiation time is prolonged until 180 min.

3.2.2. MCR-ALS treatment from mixture spectra

Initially, SIMPLISMA treatment was applied to a series of 48 infrared spectra for the region between 700 and 2000 cm^{-1} using a second derivative mode (with Savitzky-Golay algorithm) to obtain a

Fig. 7. PC1 (a) and PC2 (b) loadings.

Fig. 9. Comparison of photoproducts FTIR-ATR spectra with extracted pure spectrum (a) mixture of catechol and hydroquinone (extracted pure spectrum); (b) catechol (recorded spectrum); (c) hydroquinone (recorded spectrum).

For the last extracted spectrum "c" of Fig. 8, we can suppose that it is representative of residual species like Fenton reagent ($FeSO_4$, H_2O_2 in H_2SO_4 acid conditions), acid forms produced after degradation of photoproducts and brown solid which has precipitated during the reaction. To confirm this hypothesis, we have recorded spectra of Fenton reagent and the brown solid obtained after evaporation of the mixture irradiated for 1 h. The spectral profile of brown solid presents large bands where the maxima are pointed at 1704, 1616, 1155, and 1043 cm^{-1}. Some authors [39,40] assimilate it to by-product complexes between iron and aromatic species. Araňa et al. [17] associate it to phenolic polymers because the spectrum acquired from their precipitate has been quite similar to the tannic acid one. For spectrum of Fenton reagent, absorption band at 1027 ± 4 cm^{-1} may be attributed to the function (S=O) due to the use of sulphate iron, source of Fe^{2+}. It was also the explanation given by Zazo et al. [36] who have found a percentage of sulphur after a microanalysis of the brown precipitate.

In parallel, aqueous solutions (0.25 M) of acid forms (acetic, acrylic, formic, fumaric, maleic, malonic, and oxalic acids) have been analyzed by FTIR in order to explain the presence of large spectral bands at 1620, 1708, and 1724 cm^{-1} on the extracted pure spectrum "c" of Fig. 8. Their spectra (Fig. 10) show also large and specific bands between 1620 and 1730 cm^{-1} that it let us to suppose that some of these compounds may be present in the mixture and participate to describe the profile of extracted spectrum "c".

To clarify the concentration profiles of these extracted pure spectra (Fig. 11), an average value of concentrations (determined for the kinetics A–D) has been calculated for each irradiation time. Results lead to the identical evolution as HPLC analysis for the disappearance of phenol (curve "a"). Catechol and p-hydroquinone described by the same curve "b" have been formed at the start of the reaction and then consumed after the first re-injection of H_2O_2 (after 30 min of UV light) to generate in parallel acids forms as shows the last concentration profile "c".

3.2.3. MCR-ALS treatment from mixture and pure photoproducts spectra

As separated spectra of catechol and hydroquinone could not be obtained mathematically, we have modified our data matrix by including supplementary information like spectra of standards recorded in aqueous solution at a concentration equal to 0.25 M. First SIMPLISMA procedure was applied on the 48 data used in the previous study and on 2 pure spectra relative to catechol and hydroquinone. Four concentration profiles were obtained. Then MCR-ALS

Fig. 8. Extracted pure spectra obtained from the first matrix: (a) phenol; (b) mixture of catechol and hydroquinone; (c) residual species.

better resolve of pure variables because the photoproducts present overlapped peaks. Then MCR-ALS procedure was applied using the 48 infrared spectra as data and the SIMPLISMA extracted profiles as concentration profiles. The best results are obtained with non-negativity constraints on spectra and concentration data. The statistical data characterizing this mathematical procedure are: $\sigma = 0.0003$, lof in % (PCA) = 1.87, lof in % (EXP) = 9.97, percent of variance explained = 99.00.

After treatment of four kinetics (A–D), three pure spectra (noted "a", "b" and "c") have been extracted (Fig. 8).

Extracted spectrum "a" describes the structure of phenol with characteristic IR bands cited above. In spectrum "b", absorption bands at 1612, 1278, and 858 cm^{-1} are attributed to catechol and those at 1244, 1228, and 837 cm^{-1} characterize hydroquinone, respectively. The remainder ones are common to both compounds. But none specific bands of resorcinol have been identified. We supposed that resorcinol has not been extracted because of its very low concentration in the mixture below the sensitivity threshold of our ATR accessory. A comparison of extracted spectrum "b" with those of standard products is presented in Fig. 9.

Fig. 10. FTIR-ATR spectra of organic acids solutions.
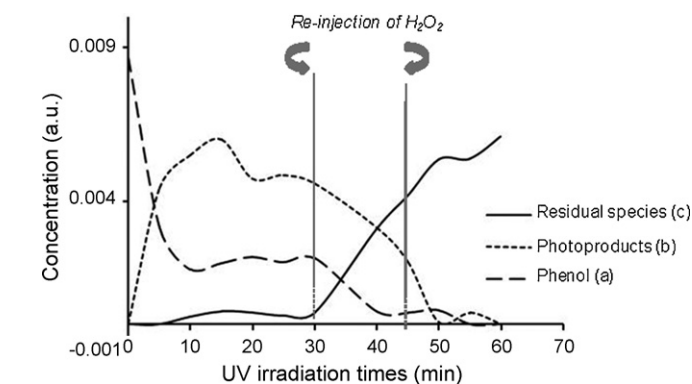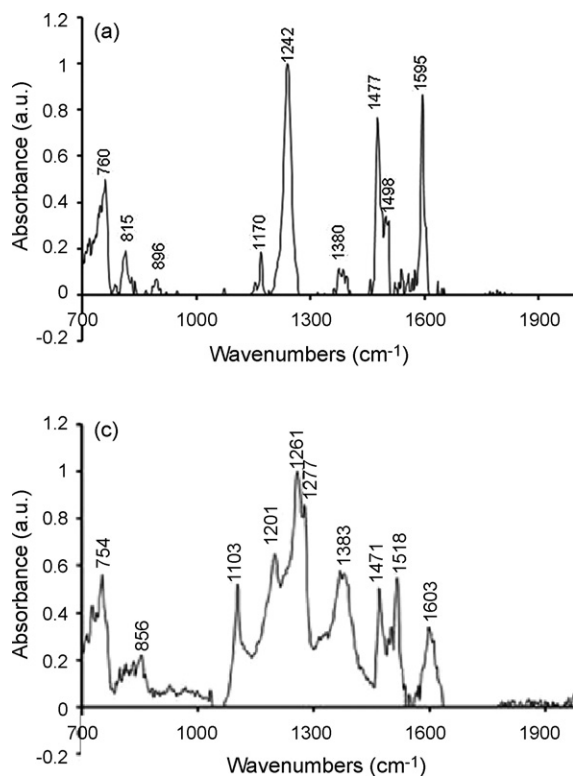
Fig. 11. (a–c) Concentration profiles of extracted pure spectra obtained from the first matrix.

treatment was applied on the 50 spectra and 4 concentration profiles. The best results have been obtained with non negativity constraint on spectra and concentration with the following statistical data: $\sigma = 0.0004$, lof in % (PCA) = 5.55, lof in % (EXP) = 10.08, percent of variance explained = 98.27. We can note that the addition of standards spectra in the data matrix decreases the performance of the MCR–ALS calculation but increases the chemical interpretation of the kinetic.

In this case, we success to extract four spectra (Fig. 12) which, after a comparative study of absorption maxima, are attributed respectively to phenol (spectrum "a"), hydroquinone (spectrum "b"), catechol (spectrum "c") and residual species (spectrum "d").

Their associated concentration profiles are presented in Fig. 13. The profile "d" describing the acid forms, iron complexes and Fenton reagent has the same evolution. We always notice that while catechol and hydroquinone are formed, phenol disappears. The quantity of catechol is most significant than the one of hydro-
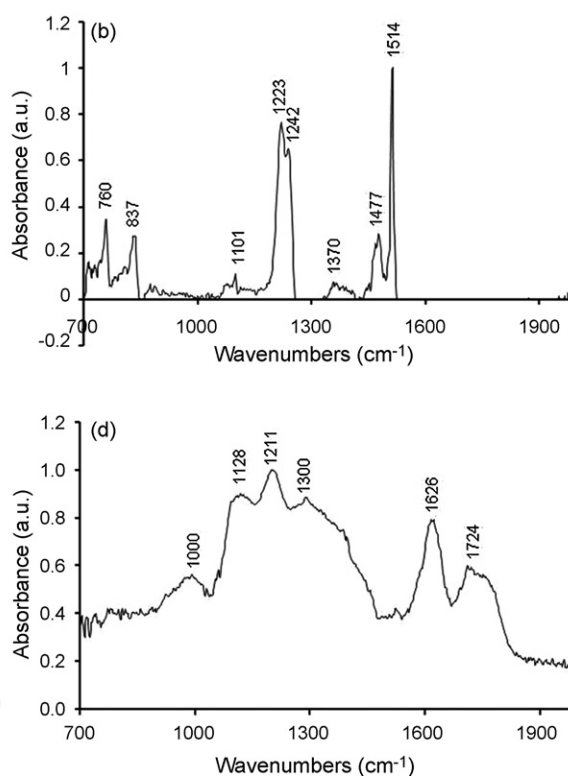
Fig. 12. Extracted pure spectra obtained from the second matrix: (a) phenol; (b) hydroquinone; (c) catechol; (d) residual species.

Fig. 13. (a–d) Concentration profiles of extracted pure spectra obtained from the second matrix.

quinone as the chromatography analysis has shown. The only difference remains in the detection of resorcinol which was not possible by FTIR measurements because of the low sensitivity of Diamond ATR accessory. Further measurements will be carried out with a specific liquid accessory for dilute aqueous solutions to show the goodness of this methodology in comparison with HPLC method.
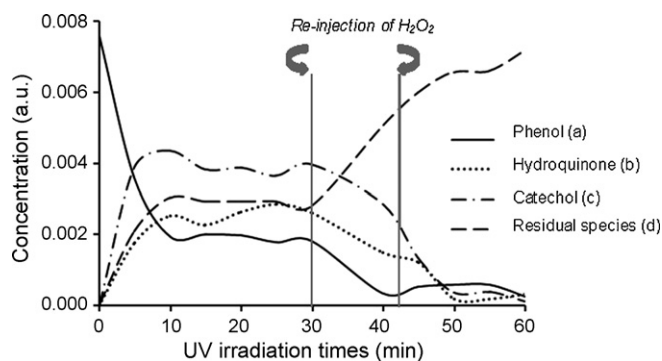
4. Conclusion

FTIR results are in good agreement with those obtained by chromatography analysis, even when it concerns photoproducts identification or the evolution of their concentration during a degradation reaction. Simplicity and facility of IR measurements lead to consider this technique as a rapid screening for monitoring of pollutants decrease and testing the effectiveness of one degradation process, before HPLC measurements which need a considerable analysis time to record, to choose the optimal experiment conditions for elution or to treat collected data.

Spectrum recording is fast but when a control on line is made, the classical exploitation time of IR spectra becomes very important and incompatible with the fixed goal which requires a mathematical treatment to extract rapidly the significant information. It is what chemometric tools propose like PCA and SIMPLISMA–MCR-ALS method. They have been validated in this study to acquire information about the evolution of all species. The advantage of SIMPLISMA–MCR-ALS chemometric treatment is its interactivity in the selection of pure variables. In combination with the high level of performance of this algorithm, it is not absurd to think that it would be possible to create automated systems on its basis to control the efficacy of different processes to cleanse water from FTIR data.

Acknowledgement

References

[1] J.C. Camposa, R.M.H. Borgesa, A.M. Oliveira Filhob, R. Nobregaa, G.L. Sant'Anna Jr., Water Res. 36 (2002) 95–104.
[2] A. Dabrowski, P. Podkoscielny, Z. Hubicki, M. Barczak, Chemosphere 58 (2005) 1049–1070.
[3] A. Santos, P. Yustos, S. Gomis, G. Ruiz, F. García-Ochoa, Chem. Eng. Sci. 61 (2006) 2457–2467.
[4] L.S. Andrade, E.A. Laurindo, R.V. de Oliveira, R.C. Rocha-Filho, Q.B. Cass, J. Brazil. Chem. Soc. 17 (2) (2006) 369–373.
[5] V.L. Heasley, A.M. Fisher, E.E. Herman, F.E. Jacobsen, E.W. Miller, A.M. Ramirez, N.R. Royer, J.M. Whisenand, D.L. Zoetewey, D.F. Shellhamer, Environ. Sci. Technol. 38 (2004) 5022–5029.
[6] F. Ge, L. Zhua, H. Chen, J. Hazard. Mater. B133 (2006) 99–105.
[7] D.H. Bremner, A.E. Burgess, D. Houllemare, K.C. Namkung, Appl. Catal.: Environ. 63 (2006) 15–19.
[8] A. Santos, P. Yusos, A. Qintanilla, S. Rodríguez, F. García-Ochoa, Appl. Catal. B: Environ. 39 (2002) 97–113.
[9] J. Araña, E. Tello Rendón, J.M. Doña Rodríguez, J.A. Herrera Melián, O. González Díaz, J. Pérez Peña, Appl. Catal. B: Environ. 30 (2001) 1–10.
[10] H. Chun, W. Yizhong, T. Hongxiao, Chemosphere 41 (2000) 1205–1209.
[11] N. Negishi, F. He, S. Matsuzawa, K. Takeuchi, K. Ohno, C.R. Chim. 9 (2006) 822–828.
[12] S.G. Poulopoulos, F. Arvanitakis, C.J. Philippopoulos, J. Hazard. Mater. B129 (2006) 64–68.
[13] M. Rodriguez, S. Malato, C. Pulgari, S. Contreras, D. Curcó, J. Gimenez, C. Pulgarin, Solar Energy 79 (2005) 360–368.
[14] H. Kušić, N. Koprivanac, A.L. Božić, I. Selanec, J. Hazard. Mater. B136 (2006) 632–644.
[15] R. Maciel, G.L. Sant'Anna Jr., M. Dezotti, Chemosphere 57 (2004) 711–719.
[16] W. Gernjak, J. Krutzler, A. Glaser, S. Malato, J. Caceres, R. Bauer, A.R. Fernandez-Alba, Chemosphere 50 (2003) 71–78.
[17] J. Araña, E. Tello Rendón, J.M. Doña Rodríguez, J.A. Herrera Melián, O. González Díaz, J. Pérez Peña, Chemosphere 44 (2001) 1017–1023.
[18] K.V. De Souza, P. Peralta-Zamora, Ann. Acad. Bras. Ciênc. 73 (2001) 4, 519–524, ISSN 0001-3765.
[19] M.S. Di Nezio, M.F. Pistonesi, W.D. Fragoso, M.J.C. Pontes, H.C. Goicoechea, M.C.U. Araujo, B.S.F. Band, Microchem. J. 85 (2007) 194–200.
[20] E. Oliveros, E. Legrini, M. Hohl, T. Muller, A.M. Braun, Water Sci. Technol. 35 (4) (1997) 223–230.
[21] R. Chen, J. Pignatello, Environ. Sci. Technol. 31 (8) (1997) 2399–2406.
[22] W. Spacek, R. Bauer, Chemosphere 30 (3) (1995) 477–484.
[23] E. Balanosky, F. Herrera, A. Lopez, J. Kiwi, Water Res. 34 (2) (2000) 582–596.
[24] S. Wold, K. Esbensen, P. Geladi, Chemometr. Intell. Lab. Syst. 2 (1987) 37–52.
[25] A. De Juan, S.C. Rutan, R. Tauler, D.L. Massart, Chemometr. Intell. Lab. Syst. 40 (1) (1998) 19–32.
[26] E.R. Malinowski, Factor Analysis in Chemistry, 2nd ed., Wiley, New York, 1991.
[27] R. Tauler, A.K. Smilde, B.R. Kowalski, J. Chemometr. 9 (1) (1995) 31–58.
[28] W. Windig, D.A. Stephenson, Anal. Chem. 64 (22) (1992) 2735–2742.
[29] W. Windig, S. Markel, J. Mol. Struct. 292 (1993) 161–170.
[30] P.J. Gemperline, J. Chemometr. 3 (4) (1989) 549–568.
[31] W. Windig, Chemometr. Intell. Lab. Syst. 4 (3) (1988) 201–213.
[32] O.S. Borgen, B.R. Kowalski, Anal. Chim. Acta 174 (1985) 1–26.
[33] C.B. Zachariassen, J. Larsen, F. van den Berg, R. Bro, A. de Juan c, R. Tauler, Chemometr. Intell. Lab. Syst. 83 (2006) 13–25.
[34] T. Azzouz, R. Tauler, Talanta 74 (5) (2008) 1201–1210.
[35] E. Balanosky, F. Herrera, A. Lopez, J. Kiwi, Water Res. 34 (2) (2004) 711–719.
[36] J.A. Zazo, J.A. Casas, A.F. Mohedano, M.A. Gilarranz, J.J. Rodríguez, Environ. Sci. Technol. 39 (2005) 9295–9302.
[37] S. Wold, K. Esbensen, P. Geladi, Chemometr. Intell. Lab. Syst. 2 (1987) 37–52.
[38] R. Alnaizy, A. Akgerman, Adv. Environ. Res. 4 (2000) 233–244.
[39] H.R. Eisenhauer, Water Pollut. Control Fed. 36 (1964) 1116–1128.
[40] D.H. Bremner, A.E. Burgess, D. Houllemare, K.C. Namkung, Appl. Catal. B: Environ. 63 (2006) 15–19.

Extraction and high performance liquid chromatographic determination of 3-indole butyric acid in pea plants by using imidazolium-based ionic liquids as extractant

Godratollah Absalan*, Morteza Akhond, Leila Sheikhian

Department of Chemistry, Faculty of Sciences, Shiraz University, Shiraz 71457, Iran

ABSTRACT

In this paper, imidazolium-based ionic liquids $[C_4mim][PF_6]$, $[C_6mim][PF_6]$, $[C_8mim][PF_6]$, $[C_6mim][BF_4]$ and $[C_8mim][BF_4]$ were tested as extracting solvents for removal of 3-indole butyric acid (IBA) from aqueous media with subsequent determination using HPLC. Percent extraction of IBA was strongly affected by pH of aqueous phases and the chemical structures of ionic liquids (ILs). Extraction of IBA was quantitative in the pH values lower than pK_a of IBA. Considering both extraction and stripping efficiencies of IBA, $[C_4mim][PF_6]$ was found to act more efficient than other studied ILs. Capacity of $[C_4mim][PF_6]$ was 17.6×10^{-4} mmol IBA per 1.0 mL of IL. Ionic strength of aqueous phase and temperature had shown no serious effects on extraction efficiency of IBA. A preconcentration factor of 100 and a relative standard deviation of 1.16% were obtained. It was found that ionic liquid phase was reusable almost five times for extraction/stripping purposes. 3-Indole acetic acid showed interferential effect in the extraction step. In order to assess the applicability of the method, extraction and stripping of IBA from pea plants and some other samples were studied.

© 2008 Elsevier B.V. All rights reserved.

1. Introduction

Auxins are well-known plant growth hormones that are actually involved in a variety of plant activities [1,2]. The auxin 3-indole acetic acid (IAA) was the first plant hormone that was used to stimulate rooting of cuttings [3]. It was discovered that a second, 'synthetic' auxin 3-indole-butyric acid (IBA) also promoted rooting and was even more effective than IAA [4–6]. IBA is now used commercially worldwide to root many plant species [7]. The greater ability of IBA to promote adventitious root formation compared with IAA has been attributed to the higher stability of IBA versus IAA both in solution and in plant tissue [8].

It has been found that IBA also occurs naturally in a number of plant species from maize (*zea mays*) and pea (*pisum sativum*) to arabidopsis [8–10]. Likewise, Bayer [11] found that nicotiana tumors have more IBA than normal tissues. Furthermore some microorganisms such as azospirillum brasilense UAP 154 found in the soil are able to produce IBA [12].

IBA has been identified by modern techniques such as GCMS in a wide variety of plants [8,10,12,13]. Applying other chromatographic methods, e.g. HPLC [10,12,14] are also frequently described in the literature. Furthermore capillary electrophoresis has been used as a tool for the determination of IAA, 3-indole-acetylaspartic acid (IAAsp) and IBA in pea plants [15]. However, disadvantages with most of these methods are the high demands placed on many sample purity steps. In the case of GC–MS, the derivatisation requirements have made the use of several preparation steps inevitable. Besides being time consuming, these steps introduce errors and discrimination in the analysis and cause considerable loss in analyte quantities.

Room temperature ionic liquids (RTILs) or ILs are ionic media resulting from combinations of organic cations and various anions that are viewed as a novel class of green benign media alternative to the conventionally used organic solvents [16–19]. ILs have many unique properties such as negligible vapor pressures, wide liquid temperature ranges, high specific solvent abilities, chemical and thermal stability, nonflammability, high ionic conductivity, and a wide electrochemical potential window [18–20]. Therefore, RTILs are regarded to be used as solvent in chemical reactions [19,21,22], multiphase bioprocess operation [23], batteries and fuel cells investigations [24]. In recent years, ILs have also aroused increasing applications in liquid–liquid extractions of metal ions and organic compounds [25]. ILs can be hydrophilic and hydrophobic depending on the structures of cations and anions [26,27]. The anion seems more important in determining the water miscibility

Cations	Abbreviation	Anions
1-butyl-3-methylimidazolium	$[C_4mim]^+$	PF_6^-, BF_4^-
1-hexyl-3-methylimidazolium	$[C_6mim]^+$	
1-octyl-3-methylimidazolium	$[C_8mim]^+$	

Fig. 1. Chemical structures of studied ionic liquids.

of ILs [28]. Those ILs based on hexafluorophosphate ($[PF_6]^-$), bis [(trifluoromethyl)sulfonyl] amide ($[Tf_2N]^-$) and tetrafluoroborate ($[BF_4]^-$) are normally water immiscible, therefore, they are the solvents of choice for forming biphasic systems in most IL extraction applications [29–31]. While this property is largely conveyed by the hydrophobicity of the anion, the water miscibility of the RTILs depend on the length of the alkyl chain or the temperature of the system [26,27].

The unique extraction ability of ionic liquids as environment-friendly solvents urged us to use them for extraction of plant-growth hormones. To the best of our knowledge other reported techniques are time-consuming and/or used toxic chemicals. In this study we used some imidazolium-based ionic liquids: $[C_4mim][PF_6]$, $[C_6mim][PF_6]$, $[C_8mim][PF_6]$, $[C_6mim][BF_4]$ and $[C_8mim][BF_4]$ (see Fig. 1) to extract 3-indole-butyric acid from real samples followed by stripping into aqueous phase for quantitative determination by HPLC method.

2. Experimental

2.1. Apparatus

UV absorption spectra were recorded against the solvent blank at room temperature, using Ultrospec 4000 spectrophotometer (Pharmacia Biotech) operated in double-beam mode. The HPLC apparatus (Jacso, Japan) consists of PU-2080 plus delivery system equipped with a UV-2070 plus detector set at 280 nm and connected to LC-Net II/ADC interface. Analysis was carried out at room temperature on a Finepak SIL C18, 100 Å pore size, 10-μm particle size and (250 mm × 4.6 mm) i.d. column. Injections were made by a RHEODYNE 7725i sample injector equipped with a 5-μL loop. The pH measurements were made with a Metrohm 780 pH meter using a combined glass electrode. NMR spectra were recorded on a Brucker-Advanced DPX/250 (^{1}H NMR 250 MHZ and ^{13}C NMR 62.9 MHZ) spectrophotometer.

2.2. Reagents

1-Bromobutane, 1-bromohexane, 1-bromooctane, 1-methylimidazolium, ammonium hexafluorophosphate, sodium tetrafluoroborate, 3-indole butyric acid, 3-indole acetic acid, gibberellic acid, and other reagents used in this study were of the highest purity available from either Merck or Fluka Chemical Companies and were used without further purification. Ionic liquids: $[C_4mim][PF_6]$, $[C_6mim][PF_6]$, $[C_8mim][PF_6]$, $[C_6mim][BF_4]$ and $[C_8mim][BF_4]$ were synthesized as described by Bonhote et al. [32] and their chemical structures were testified by using NMR spectroscopy. Doubly distilled deionized water was used throughout the work.

3. Results and discussion

3.1. Preliminary experiments

Preliminary experiments showed that IBA can easily be extracted into the imidazolium-based ILs, i.e. $[C_nmim][PF_6]$ and $[C_nmim][BF_4]$. As 3-indole butyric acid has strong absorbance in UV region (Fig. 2), thus extraction procedure was optimized by using spectrophotometric method at 280 nm as discussed below.

3.2. Recommended procedure

Aqueous solutions containing IBA (1.0 mL) were brought into contact with 100 μL of IL at room temperature for extraction purpose. For back extraction into aqueous phase, 1 mL of 2 M NaOH solution was used. The phase-contacting experiments were carried out in a carefully stoppered glass test tube. In both steps, system was vigorously stirred with magnetic stirrer (500 rpm) during the optimum times and then two phases were carefully separated using a centrifuge device.

For HPLC analysis of real samples, separated aqueous solutions containing IBA, without any further sample pretreatment, were vacuum dried at 37 °C, dissolved in 50 μL methanol, injected into the column, and eluted with %1 water–acetic acid/methanol as the mobile phase at a flow rate of 1.0 mL min^{-1}.

3.3. pH of the sample solution

The effect of the feed pH on the percent extraction of IBA into the imidazolium-based IL's i.e. $[C_nmim][PF_6]$ and $[C_nmim][BF_4]$ was studied (Fig. 3). Phosphate buffer (5 mM) was used for adjusting
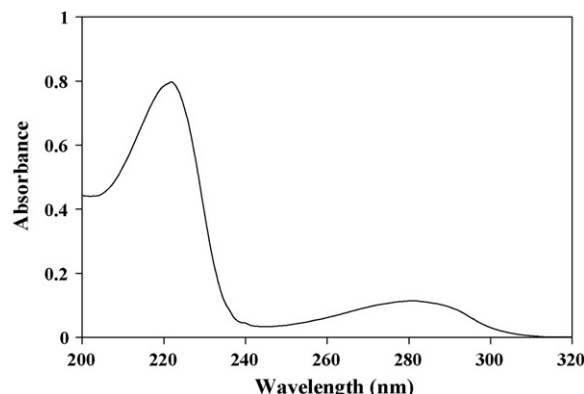
Fig. 2. UV spectra of 3-Indol butyric acid (2.0×10^{-5} mol L^{-1}).
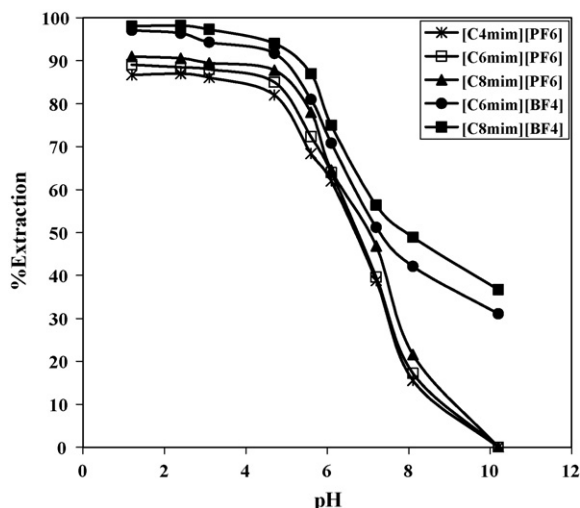
Fig. 3. Effect of pH of aqueous sample solution on percent extraction of IBA (1.0 mL, 1.0×10^{-4} mol L^{-1}) into different ILs (500 μL) with an extraction period of 30 min at room temperature.
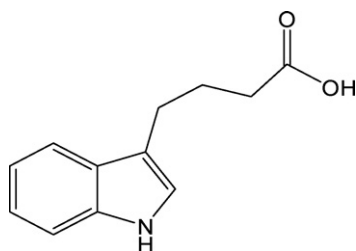
Fig. 4. Chemical structure of 3-Indol butyric acid (IBA).

pH values. It was found that percent extraction of IBA decreased steeply for pH > pK_a (where pK_a = 4.8 for IBA) and almost a plateau was observed for pH < pK_a. This behavior that was observed for all the studied ILs can be explained by electrostatic and/or hydrophobic interactions as well as H-bond formation between analyte and IL. If at pH < pK_a, NH group in the pyrrol ring of IBA (Fig. 4) could be protonated to $-NH_2^+$, electrostatic force between $-NH_2^+$ and anionic part of ionic liquid, i.e. PF$_6^-$ or BF$_4^-$ would be a driving force for IBA extraction into IL phase. But NH group has acidic property and cannot be protonated, because its lone-pair electrons participates in aromaticity of the pyrrol heterocyclic ring and then most of the IBA molecules remain neutral at pH < pK_a. Thus hydrophobic affinity of neutral IBA molecule to IL phase and also H-bonding of its hydroxyl group to PF$_6^-$ or BF$_4^-$ [33], dominate as driving forces for IBA extraction into IL phase. At pH > pK_a, the carboxyl group of IBA molecule is hydrolyzed, thus most of the IBA molecules gain negative charges due to their carboxylate groups. Because of the repulsion force between anionic site of IL and anionic form of IBA, percent extraction of IBA into IL phase was steeply decreased. It should be mentioned that at pH > pK_a, H-bonding formation between IBA and IL is not possible so a decrease in extraction

efficiency was observed. A pH of 2.4 was selected as the optimum pH to prevent any abrupt change in percent extraction of IBA.

3.4. Effect of chemical structures of ILs on percent extraction of IBA

The influence of variation in 1-alkyl group of [C$_n$mim][PF$_6$] and [C$_n$mim][BF$_4$] on percent extraction of IBA was investigated. As it is shown in Fig. 3, percent extraction of IBA is high for long chain of 1-alkyl group. This effect is consistent with affinity of IBA to more hydrophobic ILs. The effect of anionic part of ILs on percent extraction of IBA was also studied. Percent extraction of IBA into [C$_n$mim][BF$_4$] was found to be higher than [C$_n$mim][PF$_6$] where the cationic part of the ILs was similar and the same experimental conditions were performed. This is because a stronger H-bonding of hydroxyl groups of IBA molecules with [BF$_4$]$^-$ anion is provided that has been reported to have a much higher effective negative charge than [PF$_6$]$^-$ anion [34]. As a result, percent extraction of IBA was highest into [C$_8$mim][BF$_4$] than other studied ILs. The results in Fig. 3 also show that the effect of anionic part of the IL on percent extraction of IBA was more effective than its cationic part.

3.5. Time dependency of IBA extraction

Percent extraction of IBA into [C$_8$mim][BF$_4$] phase under the optimal experimental conditions for different extraction periods of time was studied. The IBA extraction was quantitative over a period of 45 min. A period of 50 min was selected as the optimum extraction time for more certainty to prevent any abrupt change in the percent extraction of IBA into [C$_8$mim][BF$_4$]. It should be mentioned that extraction of IBA into other studied ILs was also quantitative when the extraction time was increased from 50 to 90 min. It means that the extraction rate was high when [C$_8$mim][BF$_4$] was used as IL phase, the reason of which was discussed in previous paragraph.

3.6. Stripping of IBA molecules from IL phase

It is known that IBA molecule can be in its anionic form in the basic solution thus IBA can be removed from IL phase when it was brought into the contact with basic aqueous solutions. Thus NaOH solution was used to strip IBA molecules from [C$_8$mim][BF$_4$] phase. As it is seen in Table 1, IBA stripping even in the high concentrations of NaOH solution was not quantitative when [C$_8$mim][BF$_4$] was used. Therefore other ILs were used for extraction purpose. It was found that after 90 min. IBA molecules were completely extracted into [C$_4$mim][PF$_6$] phase and in a time period of 120 min were completely stripped into basic aqueous solution. Although percent extraction of IBA from aqueous solutions into [C$_8$mim][BF$_4$] was high during an extraction period of 50 min, but percent stripping of the analyte from this IL phase into basic solutions was low. Thus, extraction and stripping of IBA by using [C$_4$mim][PF$_6$] was found to be both less time consuming and efficient than other ILs. Although percent extraction of IBA by using [C$_8$mim][BF$_4$] was quantitative in the extraction step but generally [C$_4$mim][PF$_6$] was more suitable considering both extraction and stripping processes.

Table 1
Percent stripping of IBA molecules (1.0 mL of 1.0×10^{-4} mol L^{-1}) from different ILs (500 μL) by using 1.0 mL NaOH solution at different concentrations as stripping phase.

NaOH (mol L^{-1})	[C$_8$mim][BF]	[C$_6$mim][BF$_4$]	[C$_8$mim][PF$_6$]	[C$_6$mim][PF$_6$]	[C$_4$mim][PF$_6$]
0.01	32.0	55.4	63.2	68	73.2
0.1	47.0	60.0	70.5	72.0	83.3
1	52.6	69.8	79.0	84.3	92.5
2	61.6	75.0	85.5	91.0	~100
Extraction/stripping period (min)	50/120	60/120	65/120	75/120	90/120

Table 2
Percent extraction and stripping of 3-indol butyric acid (IBA) in the presence of 3-indol acetic acid (IAA), Gibberllic acid (GA) and Aspartic acid (Asp) as common coexistiong molecules.

Mixture	Extraction (%)	Stripping (%)
IBA and IAA	98.0 and 85.0	78.0 and 32.0
IBA and GA	~100 and none	~100 and none
IBA and Asp.	99.5 and 1.2	99.0 and none

Experimental conditions: IBA, IAA, GA, and Asp. 1.0×10^{-4} mol L^{-1}; sample solution: 1.0 mL, pH: 2.4, [C$_4$mim][PF$_6$]: 100 μL; extraction period: 90 min; room temperature; stripping phase: 1.0 mL of 2 mol L^{-1} NaOH; stripping period: 120 min.

3.7. IL volume

In order to find optimum [C$_4$mim][PF$_6$] volume for IBA extraction, 1.0 mL of 1.0×10^{-4} mol L^{-1} IBA was brought into contact with different volumes of [C$_4$mim][PF$_6$] in the optimum experimental conditions. It was found that extraction was efficient with IL volume of 100 μL.

3.8. IL capacity for IBA

In order to find the capacity of [C$_4$mim][PF$_6$] for IBA extraction, 1.0 mL of 1.0×10^{-3} mol L^{-1} IBA solution was brought into contact with 100 μL of [C$_4$mim][PF$_6$]. Percent IBA remained in solution after extraction was measured. It was found that the capacity of the [C$_4$mim][PF$_6$] was 17.6×10^{-4} mmol IBA per 1.0 mL of IL.

3.9. Temperature effect

In order to study the effect of temperature, extraction from aqueous solution into [C$_4$mim][PF$_6$] phase was performed at 5, 15, 25, 35 and 45 °C in the optimum experimental conditions. It was found that the temperature effect was negligible; therefore extraction step was carried out at room temperature without worrying about the effect of temperature fluctuations.

3.10. Ionic strength of aqueous sample phase

For studying the effect of ionic strength of aqueous phase, IBA extraction/stripping procedures were performed in the optimum experimental conditions by using different concentrations of KCl in the range of 0–0.1 mol L^{-1} for adjusting the ionic strength of the sample solutions. It was found that ionic strength of aqueous phase has no serious effect on extraction and consequently on stripping of IBA. Therefore, it should be mentioned that the effect of NaOH on stripping efficiencies of IBA is due to its basic effect; in other words the effect of ionic strength is not significant in this regard.

3.11. Interferences study

The selectivity of the system was studied by performing extraction/stripping procedure on equimolar mixtures of IBA and some compounds that may found in pea plants. It was found (Table 2) that

Table 3
Breakthrough volume study

Source phase volume (mL)	Volume ratio of source phase to IL phase	Extraction (%)	Stripping (%)
1.0	10	~100	~100
3.0	30	~100	~100
5.0	50	~100	~100
7.0	70	89.0	86.2
10.0	100	67.0	66.7

Experimental conditions: IBA: 1.0 mL of 1.0×10^{-4} mol L^{-1} diluted into different volumes with water; pH: 2.4; [C$_4$mim][PF$_6$]: 100 μL; extraction period: 90 min; room temperature; stripping phase: 1.0 mL of 2 mol L^{-1} NaOH; stripping period: 120 min.

with the exception of 3-indole acetic acid (IAA), other compounds are not extracted into IL phase. Since UV absorption of IAA and IBA are almost the same, this technique cannot be used for analysis of IBA in the presence of IAA; therefore HPLC technique was selected for measurement of IBA. The retention times for IAA and IBA were 3.9 and 5.1 min, respectively, that are completely different from each other and this makes the measurement of IBA feasible in the presence of IAA. The procedure is introduced in experimental section of this paper

3.12. Breakthrough volume and preconcentration factor

In order to find breakthrough volume, aliquots of 1.0 mL of 1.0×10^{-4} mol L^{-1} IBA solution were diluted into different volumes with water to have a constant amount (1.0×10^{-4} mmol) of IBA in different volume of the aqueous solutions. Extraction procedure from aqueous samples into 100 μL of [C$_4$mim][PF$_6$] phase was performed for each solution. As it is seen in Table 3, up to a volume ratio of 50 (i.e. volume of source phase to volume of IL phase), percent extraction was quantitative and for the higher volume ratios, the percent extraction of IBA decreased. This decrease in IBA extraction could be due to IL dissolution in aqueous phase. Stripping step was carried out with 1.0 mL of 2.0 mol L^{-1} NaOH solution and for HPLC analysis, aqueous solutions containing IBA were separately vacuum dried and dissolved in 50.0 μL of pure methanol to achieve a preconcentration factor of 100.

3.13. Reproducibility and reusability of the system

Extraction/stripping procedure was repeated ten times under the optimum experimental conditions for HPLC analysis. A relative standard deviation of 1.16% was obtained. It was also found that any IL phase was reusable for almost five times as the extracting phase; this causes less cost for analysis.

3.14. Real samples analysis

In order to assess the applicability of the method to the analysis of real samples, extraction/stripping of IBA from pea plants and other samples were studied (Table 4).

Table 4
Replicate analysis of IBA in real samples

Aqueous Sample	Initial IBA (μg mL^{-1})[a]	Added IBA (μg mL^{-1})	Found IBA (μg mL^{-1})[a]	Recovery (%)[a]
Sample 1	0.005 (±0.0005)	0.1	0.101 (±0.004)	96.2 (±3.7)
Sample 2	0.097 (±0.006)	0.1	0.199 (±0.01)	101.0(±4.7)
Sample 3	3.95 (±0.11)	1.0	4.88 (±0.2)	98.6(±4.2)

Experimental conditions: sample volume: 5.0 mL; pH: 2.4; [C$_4$mim][PF$_6$]: 100 μL; extraction period: 5–7 h; room temperature; stripping phase: 1.0 mL of 2 mol L^{-1} NaOH; stripping period: 2 h; sample 1: shoots of pea plants which were not placed in IBA solution; sample 2: shoots apices of pea plants which placed in 100.0 mL of 2.0×10^{-5} mol L^{-1} IBA solution; sample 3: IBA solution with cuttings dipped in (for 2 days).

[a] Mean ± $(1.96 s/\sqrt{n})$ $(n = 3)$.

Seeds of pea (*p. sativum*) were soaked in tap water for 6 h and germinated in trays with garden soil. After 10 days, cuttings were taken and set in two sample groups. The first group was sampled for measurement of IBA that was naturally present in the cuttings. The second group was immersed in a foil-covered glassy pot containing 100.0 mL of 2.0×10^{-5} M IBA ($4.06\,\mu g\,mL^{-1}$) solution, for a period of two days, in order to measure the amounts of IBA both uptaken by the cuttings and remained in the solution. Shoots of both sample groups were separately homogenized in liquid nitrogen. The resulting powder (10 g) in each group was extracted in 10.0 mL of $5\,mmol\,L^{-1}$ phosphate buffer (pH 7.0) for 1 h at $4\,^{\circ}$C in darkness [15]. In pH 7.0 the IBA molecule is in its anionic form and could be easily extracted into buffer solution. The resulting extracts were filtered through a glass microfibre filter. For extraction of the filtered solution by [C$_4$mim][PF6], the pH of the sample solution was adjusted on the value of 2.4. HPLC measurement was performed, the procedure of which was already mentioned in experimental section. It was found that $52.0 \times 10^{-4}\,\mu g$ IBA existed in one gram of the shoots of the first group of the cuttings. Analysis of the second group of the cuttings showed that $10.3 \times 10^{-2}\,\mu g$ IBA existed in one gram of shoots and the concentration of unabsorbed IBA was $3.95\,\mu g\,mL^{-1}$ in the solution.

4. Conclusions

From the above-mentioned results and discussions, it can be concluded that extraction of IBA was quantitatively done by using only 100 μL of ionic liquid. Value of pH for the aqueous phase and chemical structure of ionic liquid were effective parameters in this system. Any ionic liquid phase was reusable for almost five times. Thus, in comparison with other extraction methods for IBA, this method is less time consuming and more efficient and cheaper. The procedure is applicable for extraction of IBA from pea plants and some other similar samples.

Acknowledgments

References

[1] K.V. Thimann, J.B. Koepfli, Nature 135 (1935) 101.
[2] B.E. Haissig, T.D. Davis, A historical evaluation of adventitious rooting research to 1993, in: T.D. Davis, B.E. Haissig (Eds.), Biology of Adventitious Root Formation, Plenum Press, New York, NY, 1994.
[3] W.C. Cooper, Plant Physiol. 10 (1935) 789.
[4] P.W. Zimmerman and F. Wilcoxon, Contributions of the Boyce Thompson Institute 7 (1935) 209.
[5] E. Epstein, J. Ludwig-Müller, Physiol. Plantarum 88 (1993) 382.
[6] J. Riov, S.F. Yang, Plant Growth Regul. 8 (1989) 131.
[7] H.T. Hartmann, D.E. Kester, F.T. Davies, Plant Propagation: Principles and Practices, Prentice-Hall, Englewood Cliffs, NJ, 1990, p. 246.
[8] A.C. Nordstrom, F.A. Jacobs, L. Eliasson, Plant Physiol. 96 (1991) 856.
[9] J. Ludwig-Muller, E. Epstein, J. Plant Growth Regul. 14 (1994) 7.
[10] J. Ludwig-Muller, J. Plant Growth Regul. 32 (2000) 219.
[11] H. Bayer, Plant Physiol. 60 (1969) 211.
[12] L.J. Martinez-Morales, L. Soto-Urzua, B.E. Baca, J.A. Sanchez-Ahedo, FEMS Microbiol. Lett. 228 (2003) 167.
[13] D. Fitze, A. Wiepning, M. Kaldorf, J. Ludwig-Müller, J. Plant Physiol. 162 (2005) 1210.
[14] J. Ludwig-Müller, J. Plant Physiol. 164 (2007) 47.
[15] J. Olsson, K. Claeson, B. Karlberg, A.C. Nordstrom, J. Chromatogr. A 824 (1998) 231.
[16] C.M. Gordon, Appl. Catal. A: Gen. 222 (2001) 101.
[17] N. Jain, A. Kumar, S. Chauhan, S.M.S. Chauhan, Tetrahedron 61 (2005) 1015.
[18] K.R. Seddon, J. Chem. Technol. Biotechnol. 68 (1997) 351.
[19] T. Welton, Chem. Rev. 99 (1999) 2071.
[20] M.C. Buzzeo, C. Hardacre, R.G. Compton, Chem. Phys. Chem. 7 (2006) 176.
[21] J. Dupont, F. de Souza, P.A.Z Suarez, Chem. Rev. 102 (2002) 3667.
[22] P. Wasserscheid, W. Keim, Angew. Chem. Int. Ed. 39 (2000) 3772.
[23] S.G. Cull, J.D. Holbrey, V. Vargas-Mora, K.R. Seddon, G.J. Lye, Biotechnol. Bioeng. 69 (2000) 227.
[24] J.F. Brennecke, E.J. Maginn, AIChE. J. 47 (2001) 2384.
[25] H. Zhao, Sh. Xia, P. Ma, J. Chem. Technol. Biotechnol. 80 (2005) 1089.
[26] P.A.Z. Suarez, S. Einloft, J.E.L. Dullius, R.F. de Souza, J. Dupont, J. Chim. Phys. 95 (1998) 1626.
[27] J.D. Holbrey, K.R. Seddon, J. Chem. Soc. Dalton Trans. (1999) 2133.
[28] J.G. Huddleston, A.E. Visser, W.M. Reichert, H.D. Willauer, G.A. Broker, R.D. Rogers, Green Chem. 3 (2001) 156.
[29] J. Wang, Y. Pei, Y. Zhao, Zhiguo Hu, Green Chem. 7 (2005) 196.
[30] A. Soto, A. Arce, M.K. Khoshkbarchi, Sep. Purif. Technol. 44 (2005) 242.
[31] T. Katase, K. Murase, T. Hirato, Y. Awakura, J. Appl. Electrochem. 37 (2007) 339.
[32] P. Bonhote, A.P. Dias, N. Papageorgion, K. Kalyanasundaram, M. Gratzel, Inorg. Chem. 35 (1996) 1168.
[33] C.G. Hanke, N.A. Atamas, R.M. Lynden-Bell, Green Chem. 4 (2002) 107.
[34] H. Tsunekawa, A. Narumi, M. Sano, A. Hiwara, M. Fujita, H. Yokoyama, J. Phys. Chem. B 107 (2003) 10962.

Laser-induced breakdown spectroscopy for simultaneous determination of Sm, Eu and Gd in aqueous solution

D. Alamelu, A. Sarkar, S.K. Aggarwal *

Fuel Chemistry Division, Bhabha Atomic Research Centre, Trombay, Mumbai 400085, India

ARTICLE INFO

ABSTRACT

This paper reports studies on the determination of trace levels of samarium, europium and gadolinium in aqueous samples by laser-induced breakdown spectroscopy (LIBS). In this work, a membrane-based filter paper was used as a sample support for the liquid samples. The laser-induced plasma was produced in air at atmospheric pressure, using a pulsed Nd:YAG laser. Calibration standards and synthetic mixtures of these lanthanides were prepared using solutions prepared from respective high purity oxides. Linear calibration was obtained for Sm, Eu and Gd by normalizing the intensities of lanthanides emission lines with respective to C(I) 193.029 nm emission line. The concentrations of Sm, Eu and Gd were then determined in a solution containing a mixture of these lanthanides. The concentrations of individual lanthanides were obtained within 5% of the expected values. Limits of detection were found to be 1.3 ppmw (Sm), 1.9 ppmw (Eu) and 2.3 ppmw (Gd).

1. Introduction

Suitable techniques for direct measurements in liquids in control processes and in the effluents of the nuclear industry are of great interest. The technique should allow measurements in a corrosive and hostile environment and it should have good limits of detection (μg/g to mg/g range) with a large dynamic range ($\sim$10^4). The technique should also be able to analyze various types of solutions such as aqueous nitric acid, complex organic solutions, slurry solutions, effluents, etc. Finally, there should be sufficient reproducibility of the results for process monitoring.

Laser-induced breakdown spectroscopy (LIBS) has been extensively used for a wide range of scientific and industrial applications for the determination of trace and bulk components. The principle of LIBS is well described elsewhere [1–4]. LIBS is highly useful for the analysis of solid samples without any sample preparation steps, and provides good sensitivity and reproducibility. Analysis of liquid samples by LIBS is less favored due to the inherent drawbacks of the method such as splashing, surface ripples, quenching of emitted intensity and a shorter plasma lifetime [5,6]. Different method-

ologies have been developed for liquids analysis, which include freezing the samples, laminar flows, liquid jets, double-pulse technique, liquid to solid conversion technique, droplets, etc. [7–12]. In all these methodologies, there is an increase in the experimental effort as well as the complexity of the equipment. A tradeoff is usually made between the detection limits and increasing the time of analysis by increasing number of laser shots in order to average a large number of spectra. Using a solid sample support for liquids analysis by LIBS exploits the strengths of the technique eliminating the problems inherent to liquids analysis [13]. Thus in this work, the liquid samples were evaporated over a commercially available filter paper (Whatman-42) substrate prior to LIBS analysis.

Lanthanides are important group of elements having interesting physico-chemical properties [14]. Determination of lanthanides is required as a part of the chemical quality assurance of nuclear fuels and fuel materials, and in various other fields such as geology, forensic sciences, etc. Some isotopes of these lanthanide elements have high thermal neutron absorption cross-section and hence stringent specification limits have been set for these elements in nuclear industry. Lanthanides are also planned to be used for tagging the inks used for sensitive documents [15]. The physico-chemical behavior of lanthanide elements is similar to that of actinides and are therefore, used as surrogates to study the behavior of actinides in the environment.

* Corresponding author. Tel.: +91 22 25593740.
  E-mail addresses: skaggr@barc.gov.in, skaggr2002@rediffmail.com (S.K. Aggarwal).

India has a vast reserve of monazite sand where the total concentration of lanthanide oxides is about 59%, and the ratios of Sm_2O_3, Eu_2O_3 and Gd_2O_3 to the total amount of rare earth oxides are 3.1%, 0.015% and 1.4%, respectively. Since the rare earth elements in their purest form are also useful for many industrial applications, it is imperative to separate these elements from the bulk as well as from one another. Usually solvent extraction is employed for the separation of individual lanthanides [16]. The distribution ratios of Sm, Eu and Gd are very similar and hence in the initial separation column, they elute together. For the complete separation of these lanthanides from one another, their quantification during the development of separation and purification processes is very essential. Determination of Sm, Eu and Gd in the concentrates is usually carried out by chemical analysis or by X-ray fluorescence spectrometry, which is either tedious or expensive, respectively. A fast analysis technique like LIBS is highly attractive in such industrial applications.

A number of analytical methodologies are reported for the determination of lanthanides. Techniques based on thermal neutron activation analysis have been reported since a few isotopes of these elements have high thermal neutron absorption cross-sections [17]. Mass spectrometric techniques such as inductively coupled plasma mass spectrometry (ICP-MS) are also reported for the determination of various lanthanides in a variety of matrices [18]. The main limitation of this methodology is the isobaric interferences from the oxides and hydroxides of lighter lanthanide elements at heavier lanthanides. Many other techniques have also been reported for the determination of lanthanides such as inductively coupled plasma emission spectrometry [17], fluorescence spectroscopy [19], and high performance liquid chromatography (HPLC) [20]. A few reports are also published where LIBS has been employed for the quantification of lanthanides [21–26].

In this paper, an experimental set-up is described for the determination of lanthanides from aqueous solutions using a Whatman filter paper as a substrate and employing LIBS. The methodology is simple and fast and can be directly applied in a rare earth plant or in a nuclear reprocessing plant, where minimal sample preparation is preferred.

2. Experimental

2.1. Instrumentation

The Spectrolaser 1000 M, from Laser Analysis Technologies (now known as XRF scientific), Victoria, Australia was used in this work. The instrument is an integrated analysis system comprising of an excitation laser, optical spectrograph, gated charge coupled devices (CCD) detectors, and is fully software controlled through a computer. A high power Q-switched Nd:YAG laser which yields up to 200 mJ of pulse energy at the fundamental IR wavelength (1064 nm), in a 7 ns pulse, at a repetition rate of 10 Hz is used. The laser is focused on to the sample by a plano-convex lens having a focal length of 5 cm. The sample is located on a fast translational stage, which moves the sample between the two laser pulses, exposing a new and fresh region of the sample for analysis. The emission output is 'focused to four separate fiber optic cables which carry the plasma light to the entrance slit of four separate spectrographs in Czerny–Turner (C–T) configuration with CCD as detectors. Each of the four spectrograph cover different spectral range: 180–320 nm, 320–455 nm, 455–610 nm and 610–850 nm, giving a total spectral range coverage of 180–850 nm with a resolution of 0.6 nm. The output from each of the four CCDs is digitized by an analog to digital convertor (ADC) circuitry. The plasma light in the entire spectral range is thus recorded simultaneously for each

Table 1
Characteristics of spectral lines employed for LIBS analysis of Sm, Eu and Gd

Element	λ_{ij} (nm)	A_{ij} ($\times 10^8$ s^{-1})	E_j (cm^{-1})	E_i (cm^{-1})	g_j	g_i
Sm(I)	471.706	0.38	0.00	21193.67	–	–
Eu(I)	462.772	1.3	0.00	21605.16	8	8
Gd(II)	336.223	0.94	633.27	30366.81	–	–

λ_{ij} is the transition wavelength, A_{ij} is the transition probability, E_i and E_j are the energies of the upper and lower level, respectively, g_i and g_j are statistical weights of upper and lower level, respectively.

laser pulse. The acquisition of the spectrum can be done after fixing required delay between plasma ignition and recording of the emission spectrum. The dependence of line intensities on element concentrations are then analyzed using non-linear and linear equations. The spectra resulting from the accumulation of 50 shots were used for analysis in the present work.

2.2. Sample preparation

Standard solutions of individual lanthanides (Sm, Eu and Gd) were prepared using high purity oxides of these lanthanides (purity >99.95%), procured from M/s Indian Rare Earths Ltd. The stock solutions of required concentrations were prepared on weight basis after converting the oxides into nitrates by digesting them initially with supra-pure HNO_3. The solutions were then evaporated to dryness and the dried residues were re-dissolved in 1 M HNO_3 prepared from supra-pure HNO_3 (diluted using de-ionized water having resistivity of 18.2 MΩ cm at 25 °C). Suitable dilutions were then made from these stock solutions. The calibration standards for individual lanthanides were prepared with concentrations ranging between 2000 µg/g and 50 µg/g. Synthetic mixtures of the three lanthanides were also prepared having different amount ratios to study the effect of one lanthanide on the determination of the other, since the emission line pattern of Sm and Eu are quite similar [27]. Three synthetic mixtures, containing Sm:Eu:Gd in the ratio of 1:1:1, 5:1:1 and 1:5:1 were prepared on weight basis and were analyzed under the conditions identical to those used for the standards. LIBS technique usually applicable with minimal or no sample preparation. However, in the present method one sample preparation step, namely the transfer of liquid sample on to the solid substrate (Whatman-42 membrane-based filter paper) is necessary. 40 µL of solution was transferred drop-wise to the filter paper and was evaporated to dryness using a hot air blower. Subsequently the paper was allowed to cool to room temperature and was then mounted in the sample holder. Three independent analyses using separate sample loadings were done for each of the standards as well as of the synthetic mixture.

2.3. Selection of emission line

The spectral region used for recording the emission lines was from 180 nm to 850 nm, which contains almost all the emission lines of the lanthanide elements under study. Typical spectra of the individual lanthanides obtained under the identical conditions of LIBS analysis (laser energy of 60 mJ and acquisition delay of 3.2 µs) are shown in Fig. 1. By comparison of the emission spectra, regions where the spectral interferences from either the substrate or the other two lanthanide elements were minimal were identified and the suitable lines were selected for Sm, Eu and Gd. The emission lines used and their spectroscopic data are listed in Table 1 [27]. At Gd(II) 336.223 nm line, potential spectral interferences from Fe and Ca is expected. But studies have shown insignificant contribution at that line [28]. For the other two emission line Sm(I) 471.706 nm and Eu(I) 462.772 nm has no spectral interference from
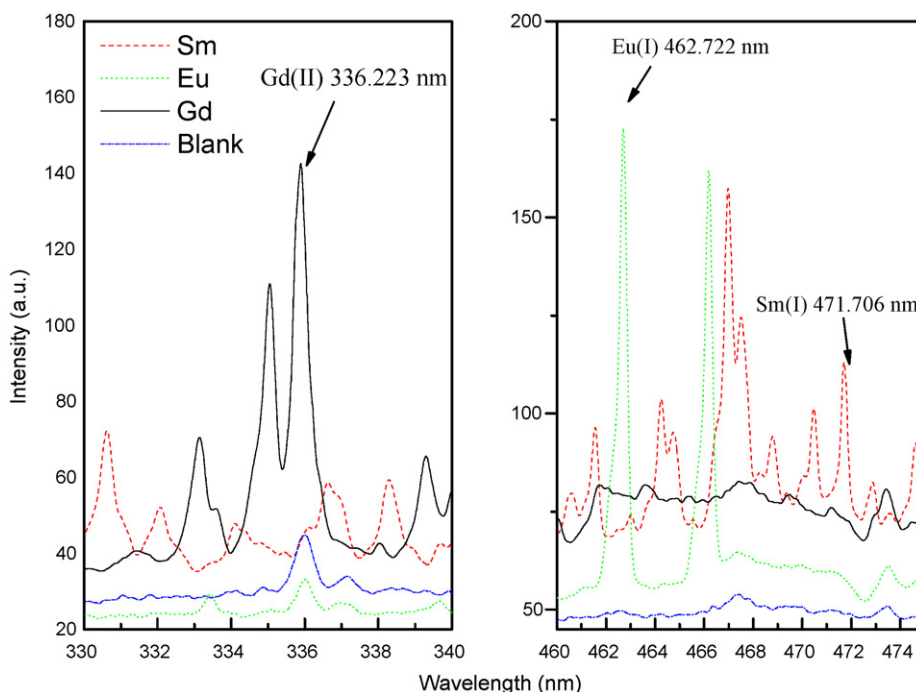
Fig. 1. Spectra of the individual lanthanides in solution under identical conditions.

Ca or Fe. Apart from these analytical lines, Gd(II) 348.127 nm, Gd(II) 343.998 nm, Gd(II) 367.12 nm, Eu(I) 466.187 nm, Eu(I) 459.403 nm, Sm(II) 477.783 nm and Sm(II) 470.44 nm emission lines also can be used for calibration, but the most sensitive lines (having the highest calibration slope) were chosen for analytical purpose in this work. The present system was basically developed to ascertain the Sm–Eu–Gd concentrate, where presence of other lanthanides is negligible. In case of a complicated system depending on the emission spectral pattern appropriate emission line need to be used.

The intensities of the selected emission lines of the lanthanides were normalized with respect to the intensity of C(I) 193.029 nm line. Carbon was chosen as internal standard since filter paper is made of cellulose. Among the two most intense C(I) lines at 193.029 nm and 247.856 nm, the latter was relatively intense, but the emission peak profile was much cleaner for the former line. Fe(I) at 249.064 nm present in the filter paper contributes to the background at the C(I) 247.856 nm line as shown in Fig. 2 and was thus not used for normalization.

3. Results and discussion

3.1. Temporal resolution for acquisition

The evolution of laser-induced plasma is divided into several transient phases. The spectrum from the early stage of the plasma is characterized by a continuum background emission due to bremsstrahlung and recombination of electrons with ions in the plasma. The continuum background decays rapidly as the plasma cools and expands. A properly selected detection window can improve the signal-to-noise ratio (SNR) of the data, which is very important for quantitative measurements. In general, the optimal acquisition delay time depends on the laser pulse energy, the kind of sample and the surrounding atmosphere. On the other hand, its dependence on the species is not significant and generally, a unique acquisition delay time can be chosen for all the elements [29]. In this work, an acquisition delay time of 3.2 μs was found to give the best

SNR corresponding to 60 mJ of laser energy. A typical plot of dependence of LIBS SNR for Gd(II) 336.223 nm emission line on delay time is depicted in Fig. 3. It is clear from the figure that the maximum SNR is recorded at around 3.2 μs of delay. The gate window of 10 μs is fixed and cannot be varied in the present instrument.

It is interesting to note that though the LIBS analysis was performed in ambient air, the emission lines of oxygen (777.195 nm) and nitrogen (746.86 nm) were not observed in the spectra. Filter paper being a carbonaceous material, nitrogen from air combines with carbon and forms cyanide and gives CN (0–0) emission due to B2X–X2Σ observed in the LIBS spectrum as shown in Fig. 4 [30]. This placed a limitation in using the most sensitive line at 385.925 nm Gd(I) for analysis. It would be interesting to perform these analyses in inert atmosphere such as argon, which would reduce the spectral background at 375–388 nm regions. But this
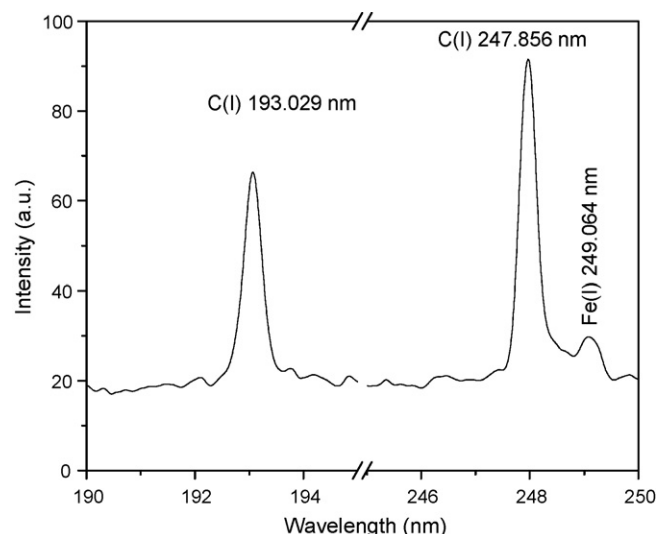
Fig. 2. Carbon emission line in the blank filter paper.
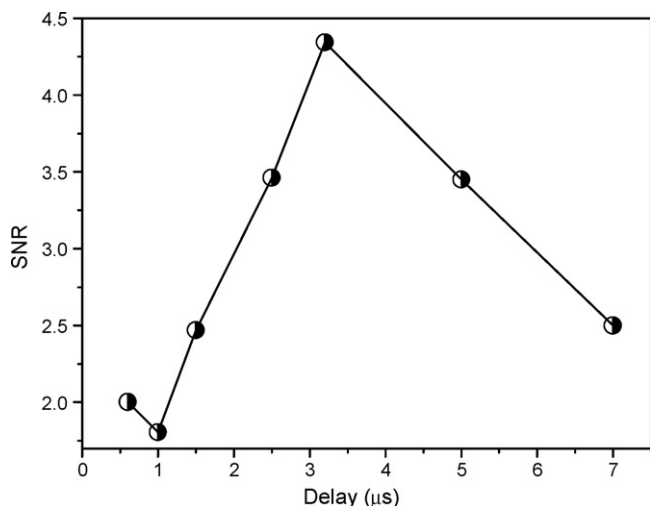
Fig. 3. Dependence of LIBS signal intensity on the delay time for Gd(II) 336.223 nm emission line, using 60 mJ of laser energy.

was not attempted for present experiments since the aim of the work was to develop a methodology for in-stream application.

3.2. Calibration curves

The data reported on the concentrations of different impurities in the Whatman-42 membrane filter paper are shown in Table 2. It can be seen that lanthanides are not present at detectable levels, and hence these filter papers were selected as sample supports for the determination of lanthanides in solutions. The calibration curves were obtained by normalizing the intensity of the selected emission line of lanthanide element with respect to the C(I) line (193.029 nm) versus the corresponding concentrations of Sm, Eu and Gd and are shown in Fig. 4. In these figures, each point corresponds to an average of three measurements performed using fresh filter paper and the error bars are the standard deviations ($\pm 1\sigma$).

The calibration curves for Eu and Gd were linear in the low concentration region and showed saturation at higher concentrations, due to self-absorption in the plasma. This is commonly observed in laser-produced plasmas at atmospheric pressure [32]. The presence of self-absorption is evidence from the variation in intensity ratio of

Table 2
Reported trace elements concentrations in the Whatman-42 membrane filter paper [31]

Element	ppmw
Al	2
Sb	<0.02
As	<0.02
Ba	<1
B	1
Br	1
Ca	13
Cl	80
Cr	0.3
Cu	0.3
F	0.2
Fe	6
Pb	0.2
Mg	1.8
Mn	0.05
Hg	<0.005
N	12
K	1.6
Si	<2
Na	33
S	<5
Zn	0.6

Eu(I) 462.772 nm to Eu(I) 459.403 nm for different concentrations of Eu in solution (Fig. 5). The theoretical value for the intensity ratio is 0.8, whereas in the higher concentration range, the ratio is in the range of 0.65 indication self-absorption of the resonant line Eu(I) 462.772 nm. The calibration curve for Sm showed a linear dependency over the entire concentration range used in the present work. For saturated calibration curves, a non-linear function, given below, was used to fit the experimental data.

$$y = a + bx + cx^2 \tag{1}$$

where x represents the element concentration and y the line intensity in arbitrary units (a.u.). For low concentrations, Eq. (1) is approximated by the straight line

$$y = a + bx \tag{2}$$

Calibration curves obtained by fitting experimental data to Eqs. (1) and (2) are shown in Fig. 6 and the corresponding values for the parameters a, b and c are listed in Table 3.

Fig. 4. Carbon monoxide and cyanide emission observed in the LIBS spectrum of a typical Whatmam-42 filter paper.
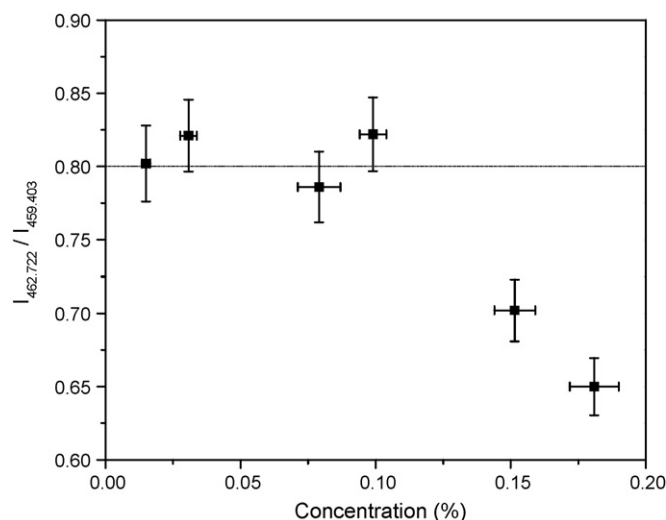
Fig. 5. Intensity ratios of Eu(I) 462.772 nm to Eu(I) 459.403 nm for different concentrations of Eu in solution. Dotted line indicates the theoretical intensity ratio of the lines.
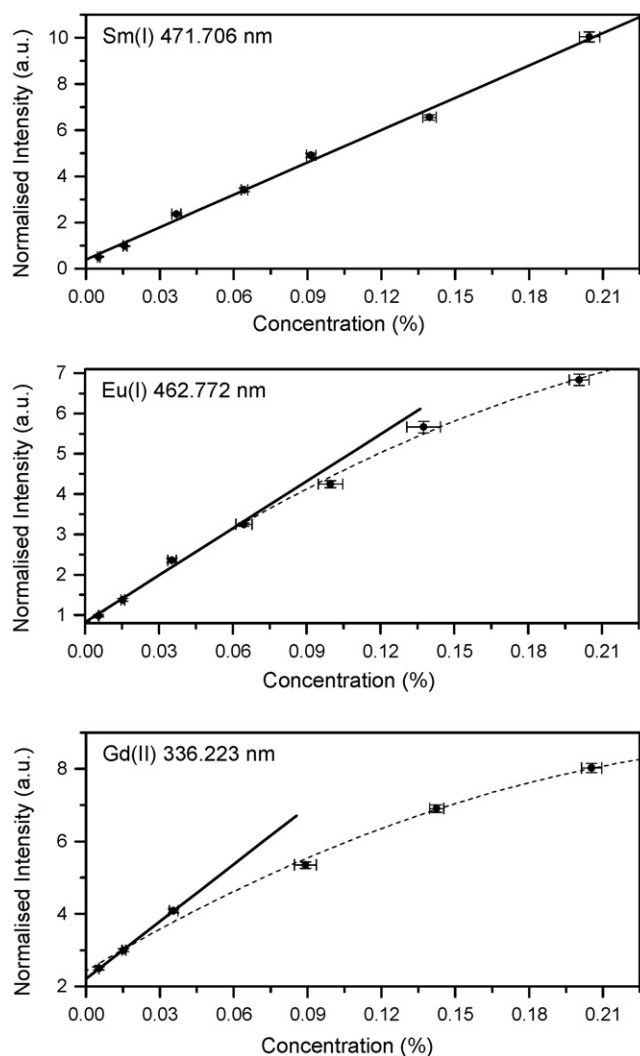
Fig. 6. Normalized elemental emissions from LIBS as a function of concentrations of Sm, Eu, and Gd.

Table 3
Parameters of Eqs. (1) and (2) obtained by fitting calibration curves and the correlation coefficients (R^2)

Element	Equation number	a	b	c	R^2
Sm	1	–	–	–	–
	2	0.389	46.738	–	0.996
Eu	1	0.771	43.049	−63.116	0.994
	2	0.820	38.889	–	0.987
Gd	1	2.425	40.529	−64.853	0.988
	2	2.214	52.571	–	0.999
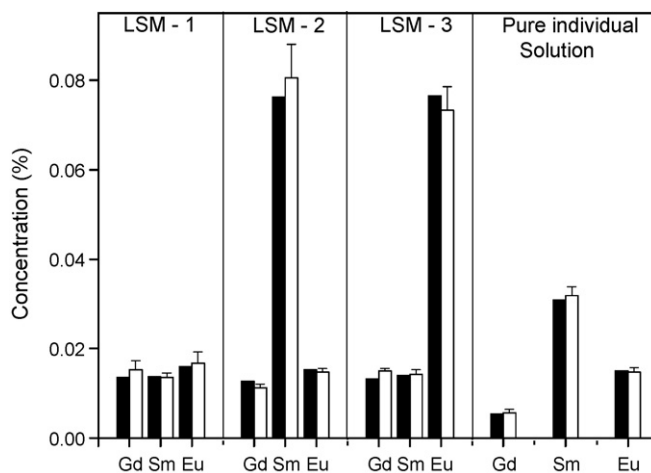
Fig. 7. Comparison of the expected values (filled bars) and LIBS (open bars) analysis results of the LSM and pure individual lanthanide solution samples.

3.3. Precision and detection limit

Solutions of pure lanthanides and three synthetic mixtures of the lanthanides (LSM) were then analyzed under the experimental conditions identical to those used for standards. The results presented in Fig. 7 show that the values obtained for the lanthanides in the mixture were in good agreement with the expected values and there is no systematic bias in the determination of Sm, Eu and Gd when they are present together in a mixture. To have a quality check on the spectral response of the system, a standard was always analyzed before analyzing the unknown samples.

The limit of detection (LOD) depends on the element and the emission line selected for the study. LODs were calculated as $3\sigma/m$, where m is the gradient of the line and σ is the uncertainty in the intensity for the calibration point with the lowest concentration. The detection limits calculated from the present work are given in Table 4 for the determination of lanthanides. LODs of Sm and Gd are much better than those reported by Ishizuka [26] in the solid NaCl matrix. The LOD of Eu is comparable with reported value in NaCl matrix.

Table 4
A comparison of the detection limits (ppmw) from present work with those reported in literature

Element	LOD		Remarks	Reference
	This work (ppmw)	Literature data		
Sm	1.3	40 ppm	NaCl matrix	[26]
		–	Polluted soil	[23]
Eu	1.9	5 ppm	NaCl matrix	[26]
		100 ppb	Quartz with Eu$_2$O$_3$	[21]
		3.3×10^{-5} mol/L	Aqueous suspension of Eu$_2$O$_3$(s) particles with Eu^{3+} ion present	[22]
Gd	2.3	200 ppm	NaCl matrix	[26]
		–	Gd plate and Gd coated on a stainless steel plate	[25]

ppmw: parts per million by weight; ppm: parts per million. Reported data are in ppm unit whereas the present work was carried out on weight basis, hence ppmw, i.e., µg/g unit was used.

4. Conclusions

LIBS has been applied for the determination of Sm, Eu and Gd in aqueous solutions. An accuracy of about 5% has been achieved in the determination of individual lanthanides from a mixture. LIBS technique is promising for the determination of lanthanides in different matrices, such as U/Th matrix with rich and complex emission spectra, after separation of the bulk of the matrix. LIBS provides an independent approach based on different physico-chemical principle for the determination of different trace constituents and hold potential for the development of trace element certified reference materials required for different matrices of interest in nuclear technology.

Acknowledgement

References

[1] D.A. Rusak, B.C. Castle, B.W. Smith, J.D. Winefordner, Crit. Rev. Anal. Chem. 27 (1997) 257.
[2] K. Song, Y.-I. Lee, J. Sneddon, Appl. Spectrosc. Rev. 32 (1997) 183.
[3] L.J. Radziemsky, Spectrochim. Acta Part B 57 (2002) 1109.
[4] E. Tognoni, V. Palleschi, M. Corsi, G. Cristoforetti, Spectrochim. Acta Part B 57 (2002) 1115.
[5] G. Arca, A. Ciucci, V. Palleschi, S. Rastelli, E. Tognoni, Appl. Spectrosc. 51 (1997) 1102.
[6] L. St-Onge, E. Kwong, M. Sabsabi, E.B. Vadas, J. Pharm. Biomed. Anal. 36 (2004) 277.
[7] J.O. Cáceres, J. Tornero López, H.H. Telle, A. González Ureña, Spectrochim. Acta Part B 56 (2001) 831.
[8] W.F. Ho, C.W. Ng, N.H. Cheung, Appl. Spectrosc. 51 (1997) 976.
[9] B.T. Fisher, H.A. Johnsen, S.G. Buckley, D.W. Hann, Appl. Spectrosc. 55 (2001) 1312.
[10] D.M. Díaz Pace, C.A. D'Angelo, D. Bertuccelli, G. Bertuccelli, Spectrochim. Acta Part B 61 (2006) 929.
[11] D.E. Poulain, D.R. Alexander, Appl. Spectrosc. 49 (1995) 569.
[12] H.A. Archontaki, S.R. Crouch, Appl. Spectrosc. 42 (1988) 741.
[13] R.L. Vander Wal, T.M. Ticich, H.R. West Jr., P.A. Householder, Appl. Spectrosc. 53 (1999) 1226.
[14] D.R. Lide, in: H.P.R. Frederikse (Ed.), Handbook of Chemistry and Physics, 76th ed., CRC Press, Boca Raton, FL, 1995.
[15] S.D. Maind, N. Chattopadhyay, A.K. Basu, C. Gandhi, M. Sudersanan, Proceedings of the XVII All India Forensic Science Conference, Raipur, India, 2005, p. 88.
[16] S. Sivasubramanian, V.R. Nair, Proceedings of the Emerging Trends on Separation Science and technology (SESTEC), BARC, 2006, p. 100.
[17] J.A. DÁngelo, L.D. Martinez, S. Resnizky, E. Periono, E.J. Marchevsky, J. Trace Microprobe Techn. 19 (2001) 79.
[18] A.R. Date, A.L. Gray, Spectrochim. Acta Part B 40 (1985) 115.
[19] T. Berthoud, P. Decambox, B. Kirsch, P. Mauchien, C. Moulin, Anal. Chim. Acta 220 (1989) 235.
[20] S. Rollin, Z. Kopatjtic, B. Wernli, B. Magyar, J. Chromatogr. A 739 (1996) 139.
[21] L.C. Jensen, S.C. Langford, J.T. Dickinson, R.S. Addleman, Spectrochim. Acta Part B 50 (1995) 1501.
[22] J.I. Yun, T. Bundschuh, V. Neck, J.I. Kim, Appl. Spectrosc. 55 (2001) 273.
[23] A. Ciucci, V. Palleschi, S. Rastelli, R. Barbini, F. Colao, R. Fantoni, A. Palucci, S. Ribezzo, H.J.L. Van der Steen, Appl. Phys. B 63 (1996) 185.
[24] K. Song, D. Kim, H.K. Cha, Y. Kim, E.C. Jung, I. Choi, H.S. Yoo, S. Oh, Microchem. J. 76 (2004) 95.
[25] G. Zikratov, R. Vasudev, F.Y. Yueh, J.P. Singh, J.C. Marra, Glass Technol. 40 (1999) 84.
[26] T. Ishizuka, Anal. Chem. 45 (1973) 538.
[27] http://physics.nist.gov/PhysRefData.
[28] E.M.S. Frame, E.E. Uzgiris, Analyst 123 (1998) 675.
[29] R. Wisbrun, I. Schechter, R. Niessner, H. Schroder, K.L. Kompa, Anal. Chem. 66 (1994) 2964.
[30] M. Baudelet, L. Guyon, J. Yu, J.P. Wolf, T. Amodeo, E. Fréjafon, P. Laloi, Appl. Phys. Lett. 88 (2006) 063901.
[31] www.whatman.com/CelluloseFilters.aspx.
[32] M. Sabsabi, P. Cielo, Appl. Spectrosc. 49 (1995) 499.

Simultaneous determination of cefotaxime and desacetylcefotaxime in real urine sample using voltammetric and high-performance liquid chromatographic methods

Mara M. Aleksić [a,*], Vera Kapetanović [b], Jasmina Atanacković [b],
Biljana Jocić [c], Mira Zečević [c]

[a] Institute of Physical Chemistry, Faculty of Pharmacy, University of Belgrade, Vojvode Stepe 450, 11000 Belgrade, Serbia
[b] Institute of Analytical Chemistry, Faculty of Pharmacy, University of Belgrade, Vojvode Stepe 450, 11000 Belgrade, Serbia
[c] Institute of Pharmaceutical Chemistry, Faculty of Pharmacy, University of Belgrade, Vojvode Stepe 450, 11000 Belgrade, Serbia

ARTICLE INFO

ABSTRACT

Two rapid, accurate and sensitive methods are developed and validated for the quantitative simultaneous determination of cefotaxime (CFX) and its active metabolite desacetylcefotaxime (DCFX) in urine.

Based on the previous results which showed the four electron reduction of CFX at ≈ -0.5 V, and the new findings that DCFX reduction occurred at more positive potential (-0.23 V), the new adsorptive stripping differential pulse voltammetric (AdSDPV) method was developed for determination of CFX in the presence of DCFX. Linear responses were observed over a wide concentration range (0.07–0.52 µg/ml for CFX and 0.22–1.3 µg/ml for DCFX) in urine.

The second assay involves subsequent separation on a reversed-phase HPLC column, with ultraviolet detection at 262 nm. Retention times were 4.057 and 1.960 min for CFX and DCFX, respectively. Linear responses were observed over a wide range, 0.55–6.60 µg/ml for CFX and 1.10–11.00 µg/ml for DCFX, in urine.

The statistical evaluation for both methods was examined by means of within-day repeatability ($n = 5$) and day-to-day precision ($n = 3$) and was found to be satisfactory with high accuracy and precision.

© 2008 Elsevier B.V. All rights reserved.

1. Introduction

Cefotaxime, (CFX), Fig. 1(A), is a semisynthetic third generation cephalosporin antibiotic used intravenously for the treatment of infections caused by a wide variety of Gram-negative and Gram-positive species of bacteria. In the human organism, it is metabolized by esterases to desacetylcefotaxime (DCFX), active metabolite, and several non-active metabolites Fig. 1(B). CFX and DCFX are primarily eliminated by the kidneys. The half-life of CFX and DCFX is approximately 1.1 and 1.5 h, respectively. The majority of the administered dose of CFX (50–60%) is being excreted unchanged in the urine [1].

The major routes of CFX degradation involve hydrolysis of the β-lactam ring and the acetoxy ester. At physiologically relevant pH (pH 6–7), temperature and concentration values the amide side-chain hydrolysis is negligible [2]. Deesterification proceeds more

rapidly than the β-lactam ring opening. At low pH, an internal ring closure can occur to form the lactone of the deesterified product [3]. Decomposition pathway is represented in the Scheme 1 where R represents the amide side chain, and R' represents sodium or hydrogen ion.

Among the various published methods concerning the determination of cephalosporins and its metabolites in biological matrices, HPLC methods have been primary described [4–6]. Derivatization process for cefotaxime determination has also been reported [7]. Only few of the reported methods in literature determine simultaneously CFX and DCFX in human plasma and cerebrospinal fluid (CSF) by high-performance liquid chromatography [1,4]. Literature data related to CFX/DCFX determination using HPLC method in urine sample [8,9] show that only spiked urine was studied. No literature data was found considering simultaneous voltammetric determination of CFX and DCFX neither in spiked nor in real urine sample.

Although the HPLC is dominantly applied technique for CFX/DCFX determination, the method is quite difficult, due to the polar nature of the analytes and their instability [4]. Also, the potential problem is the presence of unknown endogenous
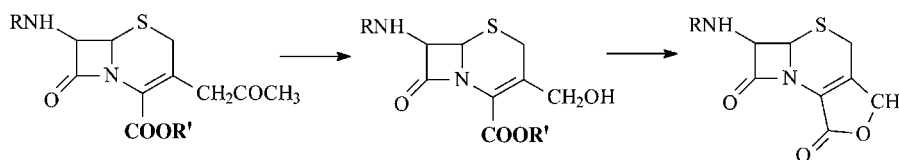
Scheme 1. Decomposition pathway of CFX.

components of human urine. Our previous investigations related to the cephalosporin reduction mechanism showed that the presence of different C-3 substituents influences the methoxyimino group reduction at 7-position [10–12], causing different peak position of the reduction of CFX and DCFX. Since both compounds contain the methoxyimino group, the different peak potential of CFX (≈ -0.5 V,) and its parent compound DCFX (-0.23 V), enables the simultaneous determination of both compounds. This paper demonstrates the application of HPLC and voltammetric techniques as tools for following and determination of CFX and its active metabolite as well, simultaneously in real urine sample having in mind the best separation conditions, the peak shape and the critical stability of analytes on different pH levels. Some extraction and detection methods have been employed to assay CFX and its metabolite in plasma, urine and CSF, but these methods were either not sensitive enough or required large volumes of matrix [8,9]. In bioanalytical methods it is important to minimize the sample preparation procedure, and solid phase extractions could sometimes compromise the stability and quantitativity of analytes. Therefore the simplest preparation procedure is always recommended.

For this reason in this study, a simple sample preparation method has been applied, including only protein precipitation and filtration through the membrane filter. This procedure has not influenced the quantitative assay of the investigated compounds and resulted in a good recovery values.

This paper describes two simple, rapid and specific methods for the simultaneous determination of CFX and DCFX in urine with good separation, sensitivity and linearity over a wide concentration range.

2. Experimental

2.1. Apparatus and conditions

2.1.1. Instrumentation

The Voltammetric measurements were performed with an Amel 433-A computerized polarographic analyzer. Three-electrode system was employed: hanging mercury dropping electrode (HMDE), Ag/AgCl reference electrode and a Pt-auxiliary electrode.
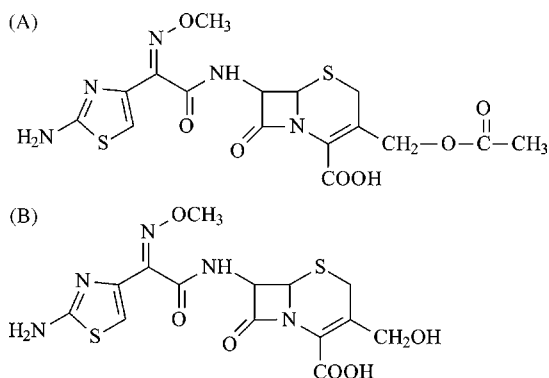
Fig. 1. Cefotaxime (A) and desacetylcefotaxime (B).

A Hewlett-Packard HP 1100 (Palo Alto, CA, USA) chromatographic system equiped with HP 1100 binary pump and HP 1100 UV–vis Detector was used. Sample injection was made through Rheodyne injector valve with a 20 µl sample loop. The isocratic chromatographic method used a C_{18} XTerra™ (150 mm × 3.9 mm, 5 µm) column (*Waters*, USA) maintained at 25 °C. Before use the mobile phase was degassed and vacuum filtered through 0.45 µm nylon membranes (*Alltech Associates Inc.*, Belgium), and then pumped at a flow rate of 1.0 ml/min. The detection of all analytes was performed at 262 nm. Data was acquired with ChemStation software from HP.

A centrifuge Tehtnica (Železniki) LC—320 was used.

A Radiometer pH meter, PHM 220, with appropriate standard buffer solutions was used.

2.1.2. Reagents and solutions

CFX was from Sigma and DCFX is kindly donated by Agency of Drugs and Medical Devices, Belgrade, Serbia. For checking the capabilities of the proposed methods in laboratory conditions the CFX/DCFX mixture was prepared by controlled alkaline hydrolysis of CFX [13]. The chromatographic internal standard was paracetamol (Carlo Erba, Milan, Italy).

Britton-Robinson buffer solution, used as supporting electrolyte for voltammetric measurements was prepared in the usual way [14].

All reagents were of analytical grade. Acetonitrile-HPLC grade (Lab Scan, Dublin, Ireland) and 85% ortophosphoric acid (Carlo Erba, Milan, Italy) were used. The mobile phase was prepared by mixing 85 ml 0.007 M solution of orthophosphoric acid and 15 ml of acetonitrile to 100 ml, then filtered and degassed before use.

A 50 µg ml^{-1} solution of paracetamol in the mobile phase was prepared as internal standard solution, and stock solutions of CFX and DCFX were made as 10 µg ml^{-1} water solutions.

Water was deionised using System Simplicity 185 (*Millipore*, USA).

The human urine samples were collected daily from at least six healthy individuals and a pool of these was used.

The real urine samples were obtained from the patients after the cefotaxime administration.

2.2. Procedures

2.2.1. Procedure for urine sample preparation

4.0 ml of concentrated urine sample was treated with 0.3 ml of methanol as urine protein precipitating agent. After the vortex during ∼30 s, the precipitated protein was separated out by centrifugation for 25 min at 3900 rpm. The clear supernatant layer was used in further procedure as protein-free human urine. This protein-free urine (1.0 ml) was diluted with redistilled water up to 10 ml (U_0) and filtered through the 0.2 µm membrane filters. The real urine samples were collected after 30, 60 and 120 min of administration of the drug to a patient, and the same preparation procedure was applied yielding the U_R solution.

2.2.2. Procedure for voltammetric determination

Cyclic voltammetry: In electrochemical cell 14 ml of BR buffer of different pHs was transferred, deaerated for 10 min with high purity nitrogen and 1 ml of stock solutions were added to make the final concentration of DCFX 7×10^{-5} M and CFX of 3×10^{-5} M. The solution was purged for another 3 min and cycle voltammograms were recorded with the scan speed of 100 mV s^{-1} and drop size 40 a.u.

DP voltammetry: An aliquot of 15 ml of supporting electrolyte (only BR or 0.15 ml of U_0 and 14.85 ml BR) solution was introduced into electrochemical cell and de-aerated with pure nitrogen for 10 min. A selected accumulation potential was then applied to a mercury drop, for a selected accumulation period, while the solution was stirred at 300 rpm. The stirring was then stopped, and after a 10 s rest period, an adsorptive stripping differential pulse voltammetry was applied in the negative direction over the range of −0.0 V to 1.2 V vs. Ag/AgCl. After the background voltammogram had been recorded, aliquots containing 60 and 120 μl of the stock solutions of DCFX and CFX were added to a cell and under the same conditions DP voltammogram was recorded at a new drop. The quantification was performed by standard addition method under the optimized conditions.

Quality control samples were prepared at three different concentration level for each drug (0.15, 0.30 and 0.45 μg ml^{-1} for CFX and 0.44, 0.87 and 1.29 μg ml^{-1} for DCFX), and were analyzed under the same conditions.

The same procedure was employed when the applicability of the proposed methods was checked, only the urine stock solution U_0, was replaced with real urine sample U_R, or with the CFX/DCFX mixture prepared by controlled alkaline hydrolysis of CFX [11].

2.2.3. Procedure for chromatographic determination

Urine drug-free samples were initially diluted with water at a volume 1:50 and filtered using 0.2-μm filter. For a blank urine sample a subsequent 1:1 dilution was performed with the mobile phase solution. Zero urine sample solution was prepared by mixing 5 ml of urine sample solution made in a 1:50 water dilution and 1 ml of internal standard solution in a 10-ml volumetric flask and by diluting this mixture to volume with the mobile phase solution. The concentration of internal standard in zero urine sample was 5 μg ml^{-1}. Spiked urine samples were prepared by adding the appropriate volumes of CFX stock solution, the internal standard stock solution and mobile phase solution to attain concentrations of 0.55, 1.10, 2.20, 3.30, 4.40, 5.50 and 6.60 μg ml^{-1} for CFX. The spiked urine samples containing DCFX were prepared in the same manner to attain concentrations of 1.10, 2.20, 3.30, 5.50, 7.70, 9.90 and 11.00 μg ml^{-1} for DCFX. In all non-zero solution of CFX and DCFX concentration of internal standard was 5 μg ml^{-1} and the final dilution of urine sample was 100-fold.

When the real urine samples were analyzed, 5 ml of the 50-fold diluted urine sample was transferred to 10-ml volumetric flask, 1 ml of the internal standard stock solution was added and the sample was further diluted to volume with the mobile phase solution.

Quality control samples were prepared at three different levels for each (low, medium and high QC samples). 5 ml of the 1:50 urine sample water dilution was transferred into 10-ml volumetric flask and appropriate amounts of internal standard, CFX and/or DCFX were added and diluted to volume with the mobile phase solution to produce the final concentrations equivalent to 5 μg ml^{-1} of internal standard and 1.10, 3.30 and 5.50 μg ml^{-1} for CFX and/or 2.20, 5.50 and 9.90 μg ml^{-1} for DCFX.

Chromatographic procedure: Three injections (20 μl) of each of these solutions were injected into the chromatographic system. The areas of the peaks were measured, and the ratios of the peak area of the CFX and DCFX to that of the internal standard were calculated for each injection. For calibration curve the average peak area ratio for each dilution was plotted against the quantity of CFX and DCFX in the solution.

3. Results and discussion

The presence of methoxyimino group in the molecules of CFX and DCFX is very important for its chemical and electrochemical behavior. Our previous studies [10–12] concerning the electrochemical behavior of Cefetamet, also the third generation cephalosporin resulted in the mechanistic scheme for the reduction of the O-methyloxime grouping of this antibiotic. It has been shown that its reduction occurred in two steps, corresponding to a reduction to the imine and amine, respectively. Those two two-electron processes are caused by differences in position and rate of establishment of acid–base equilibrium resulting in protonation of the oxime and imino grouping.

The reduction of the metoxyimino group in CFX molecule occurs in two step pathway [10,11]: the N-OCH$_3$ group is being protonated and than N–O bond is cleaved (1), yielding an imine which is subsequently protonated and reduced to an amine (2), as follows:

$$R_2C=NOCH_3 + 2H^+ + 2e^- \Leftrightarrow R_2C=NH + CH_3OH \quad (1)$$

$$R_2C=NH + 2e^- + 2H^+ \Rightarrow R_2CHNH_2 \quad (2)$$
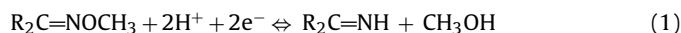
However, the absence of the COCH$_3$ group in DCFX molecule makes its methoxyimino group reduction easier. As a result the DCFX reduction occurs at about 200 mV positively relative to CFX, yielding only one reduction peak corresponding to the four electron reduction.

$$R_2C=NOCH_3 + 4H^+ + 4e^- \Leftrightarrow R_2CHNH_2 + CH_3OH \quad (3)$$

Occurrence of a single four-electron wave of DCFX is caused by the vicinity of the reduction potentials of oxime and intermediate imine. On contrary, splitting is occurring when the reduction of oxime happens at more positive potentials related to reduction potential of imine.

This difference in peak potential enables the CFX and its metabolite DCFX to be determined simultaneously in buffer solutions as well as in urine samples.

3.1. Influence of pH of the supporting electrolyte

The voltammetric behavior of DCFX:CFX (70%:30%) mixture has been examined in the pH range 2.0–12.0 by using CV and DPV. In acid medium, pH < 6, three peaks are present, one at −0.3 V (I) with much higher current intensity, and the other two smaller peaks (IIa and IIb) at more negative potentials (−0.45 and −0.6 V). The behavior of those negative peaks is similar to previously obtained for CFX standard solution and have been already reported [15,16]. According to above mentioned reduction pathway, it can be assumed that peaks IIa and IIb are due to the CFX reduction and peak I appears as a consequence of the DCFX reduction. The origin of the peaks was confirmed by standard addition method by adding an adequate volume of CFX or DCFX standard solution to DCFX/CFX mixture.

Some, representative, DP voltammograms of 7×10^{-5} M DCFX/3×10^{-5} M CFX in BR buffer solutions of pH 2–5 are presented in Fig. 2. Also, at the same Figure, the dependencies of the E_p vs. pH plots in the whole pH scale are attached.

The effect of the pH on the peak currents and peak potentials (I and II) was examined showing the peak current maximum at pH 2.8 and the involvement of the H$^+$ ions in the electron transfer process. The obtained dependencies of i_p vs. $\nu^{1/2}$ and i_p vs. ν for both peaks showed the irreversible, diffusion-controlled process which is strongly influenced by the adsorption of CFX and DCFX on the
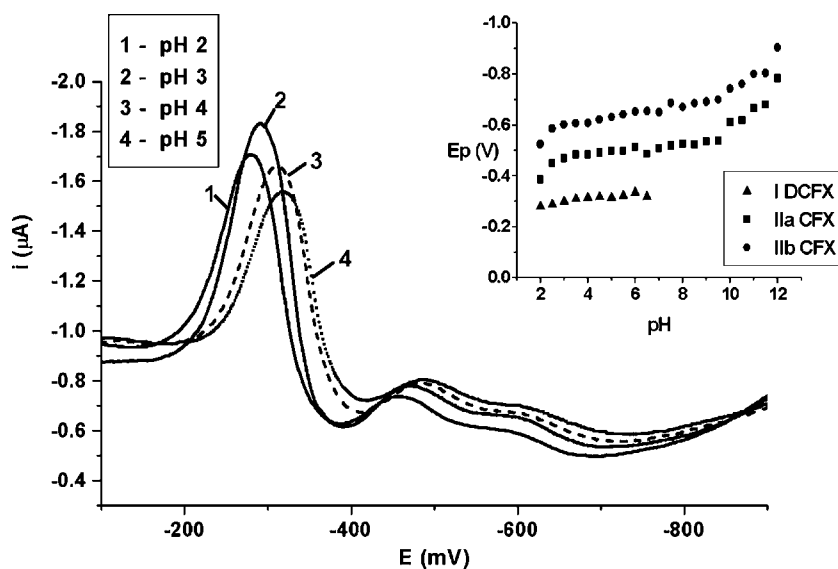
Fig. 2. The representative DP voltammograms of 7×10^{-5} M DCFX/3×10^{-5} M CFX in BR buffer solutions of pH 2–5; The influence of the pH on DPV peak potential response for 7×10^{-5} M DCFX/3×10^{-5} M CFX in BR buffer pH 2–12, $\nu = 20$ mV s^{-1} (attached).

mercury surface, the phenomena already established for the other cephalosporins [17].

The investigated pH dependence suggested the pH 2.8 as the optimal one for further analytical investigation.

3.2. Adsorptive character of the drug

After the preconcentration of 30 s of the mixture containing 1.4×10^{-6} M DCFX/6×10^{-7} M CFX (70:30) at pH 2.8 the higher peak current was obtained. The slope value of 0.958 of the logarithmic dependence of the peak currents vs. scan rate indicates the strong adsorption of the investigated specie on the mercury surface [18]. This phenomenon enabled the adsorptive stripping techniques to be preferable for the further analytical investigations. Among these techniques the square-wave adsorptive stripping voltammetry (SWAdSV) resulted in the highest signal intensity, but followed by the high background current in urine samples. For this reason, the adsorptive stripping differential pulse voltammetry (AdSDPV) was chosen due to the best signal/noise ratio.

3.3. Optimization of the DPV parameters

Several experimental parameters were examined in developing a suitable analytical procedure for the determination of DCFX/CFX mixture. The study was done with 7×10^{-7} M DCFX/3×10^{-7} M CFX in BR buffer (pH 2.8). The scan speed of 20 mV s^{-1}, the pulse amplitude of -50 mV, potential pulse width of 20 ms, and pulse repetition of 100 ms were further applied. Besides those four parameters, the influence of drop size, stirring rate and rest time on the peak current were also investigated. The chosen working conditions were: drop size of 60 au, stirring rate of 300 rpm and rest time of 10 s.

3.3.1. Effect of accumulation potential and time

To determine the optimal accumulation potential (E_{acc}) the potential range of 0.0 to -1.0 V was examined for 7×10^{-7} M DCFX/3×10^{-7} M CFX mixture in BR buffer in the pH range from 2.4 to 3.2, after the preconcentration period of 30 s. The best results for DCFX were recorded for $E_{acc} = -0.1$ V at pH 2.8. On the other hand, peak II corresponding to CFX reduction shows the highest

peak current at $E_{acc} = 0$ V. In order to achieve best selectivity and to determine DCFX in the CFX presence a deposition potential of $E_{acc} = -0.1$ V was selected.

The DPV adsorptive stripping voltammograms of 7×10^{-7} M DCFX/3×10^{-7} M CFX mixture were recorded under the chosen experimental conditions at increased accumulation time. The adsorptive saturation of the mercury surface was reached in short accumulation period and the accumulation time of 15 s was chosen for further determination.

3.4. Chromatographic method development

In bioanalytical method development it is always important to minimize the sample preparation procedure. Therefore, the use of solid-phase extraction (SPE) for isolating the analytes from the biological samples was considered and found to be not obligatory when dealing with urine. Therefore, urine samples were directly analyzed applying simple dilution and filtration through filter membranes porosity of 0.2 μm before analysis. The recovery rates that could be determined by comparing observed analyte concentrations in extracted sample and sample without SPE treatment are similar and there were no significant endogenous interference noticed also. Since the performing of SPE procedure could sometimes compromise the stability of analytes, the simplest preparation procedure was selected.

Various chromatographic conditions were investigated during the preliminary experiments including the use of acetate buffers solutions adjusted to different pH levels and use of methanol or acetonitrile as organic modifiers. On behalf of the known polarity characteristics of CFX and DCFX and the literature search, the stationary phase was selected to be a C_{18} column. Having in mind the best separation conditions, the peak shape and the critical stability of analytes on different pH levels, the possibility of using the composition of the mobile phase found in the literature considering the investigation of CFX and DCFX in human plasma and cerebrospinal fluid [1] was tested. The potential problems could be probably ascribed to the presence of unknown endogenous components of human urine. The performed chromatographic test runs proved that there were no critical interferences.

3.5. Validation of chromatographic and voltammetric methods

The chromatographic, and voltammetric methods were validated in accordance with FDA bioanalytical method validation guidance [19] in terms of specificity, sensitivity, linearity, intra-day and inter-day precision and accuracy short-term and freeze and thaw stability.

The method's specificity, as the ability of an analytical method to differentiate the analyte in the presence of other components in the sample, was tested for interference by observing the chromatograms and voltammograms of the blank urine samples and those obtained with the solutions of the urine spiked with CFX and DCFX at the lowest standard concentration on the calibration curves. All the unknown constituents of urine were eluted at different retention times of the analytes. CFX was eluted at about 4 min and its metabolite DCFX being a substance with greater polarity appeared at the chromatogram with the retention time of about 2 min. The proposed composition of the mobile phase appeared to be quite suitable to allow the appropriate retention of analytes in order to avoid all the interfering peaks or the co-elution of the complex urine matrix.

For sensitivity determination, the lowest standard concentrations on the calibration curves for CFX and DCFX were considered as the lower limits of quantification LLOQ. The LLOQ levels were expected to be at least five times the response compared to blank response and the analyte response to be reproducible with a precision of 20% and accuracy of 80–120%. The measured LLOQ levels for CFX and DCFX were 0.55 µg/ml and 1.10 µg/ml, and 0.07 µg/ml and 0.22 µg/ml for chromatography and voltammetry method, respectively. The linearity of the method was determined for each analyte in the sample by constructing the calibration curves consisting of a blank urine sample (matrix sample processed without internal sample), a zero sample (matrix sample processed with internal sample) and seven non-zero samples covering the expected range, including LLOQ. At least four of seven non-zero samples including LLOQ were expected to meet the acceptance criterion asking that there was not to be no more than 20% deviation at LLOQ from nominal concentration and no more than 15% deviation for samples above LLOQ. The acceptance criterion for the correlation coefficient was 0.998 or more. The proposed methods proved to be linear over a wide concentration ranges for both of the analytes. The concentration ranges were selected in accordance with the pharmacokinetic profile of CFX and could be appropriate even when dealing with the patients with impaired renal function since the most affected pharmacokinetic parameter by renal dysfunction is the half-life of CFX which increases while the amount of the drug recovered in the plasma decreases. The linearity was confirmed by calculating the important calibration curve parameters which were presented in Table 1. The intra-day precision and accuracy of the assay was tested by analyzing five spiked samples at three quality control levels (low, medium and high) for each analyte and by comparing the obtained results with those as calculated from regression equations. The inter-day precision and accuracy was determined over the period of three days by analyzing five spiked samples at each quality control (QC) level for both of the analytes in the sample. Nominal acceptance criteria for accuracy and precision were that the percent deviation of the mean concentration falls within ±15% of the nominal value and that relative standard deviation of each QC sample must be within 15%. The results for both, intra- and inter-day precision and accuracy, are within the acceptance criteria. Comparison of LLOQ levels for CFX and DCFX obtained with both methods showed that voltammetric method was much more sensitive, but at the same time less precise. It is obvious that R.S.D. values decrease with the concentration level increase (Table 2). These statements are valid in the case of voltammetric method for both intra and inter day examinations. However, the results obtained with HPLC method are in accordance with voltammetric ones in the case of intra-day investigations only. When inter-day precision and accuracy was tested, the results in HPLC method were not in accordance with the trend already mentioned. The explanation could be probably found in the difference of the sensitivities of the methods applied (Table 3).

During the short-term stability testing QC samples of both CFX and DCFX were kept at room temperature for 5 h based on the expected duration that samples will be maintained in the intended study during sample processing. The obtained results indicated reliable stability behavior of each QC sample at usual room temperature conditions for at least 5 h although the routine chromatographic and voltammetric analysis is expected to be even less time consuming.

Freeze and thaw stability was investigated over three freeze and thaw (room temperature) cycles conducted with QC samples of each analyte confirming that no stability-related problems would be expected during the samples routine analysis.

3.6. Applicability of the methods

For checking the capability of the proposed methods in laboratory conditions, the DCFX/CFX mixture was prepared by controlled alkaline hydrolysis. This means that after the certain time that CFX has been exposed to the sodium carbonate influence [13], pH was adjusted to 4.7 with the addition of glacial acetic acid, and the hydrolysis was stopped. After that a period of time is required to obtain the equilibrium mixture concentration. Voltammetric results confirmed that the DCFX peak intensity became constant after 1.5 h. Under these conditions the obtained ratio of DCFX:CFX was approximately 70%:30%, since the CFX is supposed not to be completely hydrolyzed. Therefore the appropriate standardization of this procedure was developed in order to obtain the constant components content.

In order to test the capability of the proposed methods (voltammetric and chromatographic ones) the sample of U_0 was spiked with adequate volume of DCFX/CFX mixture prepared by controlled alkaline hydrolysis. Two voltammetric and two chromatographic peaks at potentials of −0.28 V and −0.45 V, and retention times of 4.042 min and 1.951 min for CFX and DCFX, respectively, were

Table 1
Calibration curve parameters for HPLC and voltammetric methods

Calibration data	HPLC		AdSDPV	
	CFX	DCFX	CFX	DCFX
Concentration range (µg/ml)	0.55–6.60	1.10–11.00	0.07–0.52	0.22–1.3
$y = ax + b$	$y = 0.1719x + 0.0421$	$y = 0.1324x + 0.0595$	$y = 0.1860x + 0.0105$	$y = 0.2623x + 0.2031$
r	0.9984	0.9981	0.9994	0.9984
S_a	0.0043	0.0037	0.0075	0.0037
S_b	0.0173	0.0251	0.0173	0.00521

r = correlation coefficient; a = slope; b = intercept; S_a = standard deviation of slope; S_b = standard deviation of the intercept.

Table 2
Precision and accuracy of CFX and DCFX HPLC and voltammetric assay

Intra-day (n = 5)	HPLC				AdSDPV			
Analyte	Added (μg/ml)	Found ± S.D. (μg/ml)	R.S.D. (%)	Recovery (%)	Added (μg/ml)	Found ± S.D. (μg/ml)	R.S.D. (%)	Recovery (%)
CFX	1.10	1.077 ± 0.040	3.72	97.92	0.15	0.142 ± 0.009	6.52	94.67
	3.30	3.280 ± 0.077	2.35	99.41	0.30	0.321 ± 0.017	5.17	107.03
	5.50	5.718 ± 0.103	1.81	103.97	0.45	0.432 ± 0.014	3.21	96.11
DCFX	2.20	2.323 ± 0.066	2.83	105.58	0.44	0.431 ± 0.027	6.31	97.87
	5.50	5.189 ± 0.075	1.44	94.34	0.87	0.844 ± 0.042	4.95	96.96
	9.90	8.997 ± 0.101	1.12	90.88	1.29	1.234 ± 0.032	2.62	93.23
Inter-day (n = 3)	HPLC				AdSDPV			
Analyte	Added (μg/ml)	Found ± S.D. (μg/ml)	R.S.D. (%)	Recovery (%)	Added (μg/ml)	Found ± S.D. (μg/ml)	R.S.D. (%)	Recovery (%)
CFX	1.10	1.065 ± 0.050	4.70	96.83	0.15	0.143 ± 0.007	4.89	95.13
	3.30	3.187 ± 0.135	4.23	96.57	0.30	0.287 ± 0.011	3.66	95.67
	5.50	5.430 ± 0.376	6.93	98.72	0.45	0.438 ± 0.013	3.07	97.22
DCFX	2.20	2.227 ± 0.109	4.89	101.22	0.44	0.421 ± 0.019	4.52	95.78
	5.50	5.281 ± 0.115	2.18	96.02	0.87	0.846 ± 0.027	3.23	97.21
	9.90	9.011 ± 0.352	3.90	91.02	1.29	1.267 ± 0.033	2.63	98.20

S.D.: Standard deviation; R.S.D.: relative standard deviation.

obtained. The origin of these peaks was checked using standard addition method with DCFX and CFX stock solutions.

The concentrations of DCFX and CFX in obtained mixture were calculated from calibration graphs (Table 1) with R.S.D. of 5%.

The application of the proposed methods was also tested in real human urine. The real urine sample was obtained from the patient after the CFX administration, pretreated as mentioned above (Section 2.2.1). Adsorptive stripping differential pulse voltammograms were recorded and presented in Fig. 3. There are two voltammetric peaks present at reduction potentials of ≈ −0.23 V and −0.46 V. The origin of these peaks was checked using standard addition method with DCFX and CFX stock solutions.

These findings were confirmed by RP-HPLC method from the same solutions, simultaneously performed and shown in Fig. 4. The peaks of CFX and DCFX are well separated at retention times of t_R = 3.822 min and t_R = 1.915 min, respectively. The origin of these peaks was also proved after addition of CFX and DCFX. Besides, there are some components of the complex urine matrix, not influencing the main peaks of CFX and DCFX. The drug content in the real urine changes with the time of drug administration. With increasing time from 30 to 120 min concentration of CFX in the real
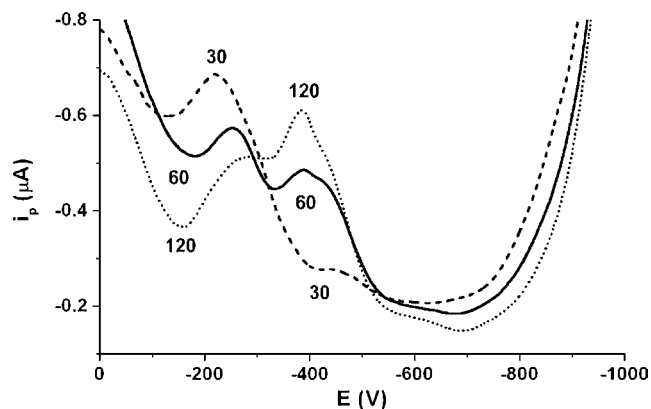
Fig. 3. Adsorptive stripping differential pulse voltammograms of real urine obtained 30, 60 and 120 min after intramuscular administration of CFX (v = 20 mV s^{-1}, E_{acc} = −100 mV, t_{acc} = 15 s).

Table 3
Data showing short-term and freeze and thaw stability of CFX and DCFX at all QC levels

Short-term stability	HPLC			AdSDPV		
Analyte	QC level (μg/ml)		Recovery (%)	QC level (μg/ml)		Recovery (%)
CFX	1.10		98.61	0.15		97.16
	3.30		96.68	0.30		98.61
	5.50		101.90	0.45		103.23
DCFX	2.20		107.64	0.44		95.24
	5.50		93.60	0.87		99.44
	9.90		101.04	1.29		94.33
Freeze and thaw stability	HPLC			AdSDPV		
Analyte	QC level (μg/ml)	Recovery (%)		QC level (μg/ml)	Recovery (%)	
		Cycle I	Cycle II	Cycle III		Cycle I	Cycle II	Cycle III
CFX	1.10	102.51	102.34	100.35	0.15	99.07	95.17	93.44
	3.30	101.08	100.13	100.56	0.30	98.24	96.04	92.70
	5.50	99.72	99.45	95.62	0.45	101.32	96.98	91.38
DCFX	2.20	105.01	104.39	103.19	0.44	98.86	92.92	90.52
	5.50	98.38	97.72	94.19	0.87	99.54	96.34	93.50
	9.90	101.48	101.18	99.85	1.29	99.48	97.16	89.97

centration began increasing. Later on, it reached almost a constant value. At the same time, the DCFX began decreasing, reaching a constant value-approximately 2–3 times smaller compared to CFX concentration. These findings are in a good agreement with literature data concerning the CFX and its active metabolite distrubution in serum.

4. Conclusion

The investigated drug CFX and its active metabolite DCFX can be simultaneously determined in urine after the drug administration using AdSDPV and RP-HPLC methods. The voltammetric method seemed to be much more sensitive related to the HPLC one. By applying these methods a good selectivity was achieved with quite satisfactory distinguished peaks of CFX and DCFX in human urine sample. These methods might be a good analytical tool for monitoring of the CFX/DCFX in clinical practice.

Acknowledgment

References

[1] K.B. Patel, D.P. Nicolau, C.H. Nightingale, R. Quintiliani, Pharmacol. 22 (1995) 49–55.
[2] S.M. Berge, N.L. Henderson, M.J. Frank, J. Pharm. Sci. 72 (1983) 59–63.
[3] K.A. Connors, Chemical Stability of Pharmaceuticals, A Wiley-Interscience Publication, John Wiley & Sons, New York, 1986, pp. 302–307.
[4] T. Scanes, A.F. Hundt, K.J. Swart, H.K.L. Hundt, J. Chromatogr. B 750 (2001) 171–176.
[5] E. Yun, A. Prince, J. McMillin, L. Welch, J. Chromatogr. B 712 (1998) 145.
[6] A. El-Gindy, A. El Walily, M. Bedair, J. Pharm. Biomed. Anal. 23 (2000) 341.
[7] L. Gallo-Martinez, P. Campins-Falco, A. Sevillano-Cabeza, Bosch-Reig, J. Chromatogr. B 718 (1998) 143.
[8] H. Fabre, G. Castaneda Penalvo, J. Liq. Chromatogr. 18 (18–19) (1995) 3877–3887.
[9] V.F. Samanidou, E.A. Hapeshi, I.N. Papadoyannis, J. Chromatogr. B 788 (2003) 147–158.
[10] V. Kapetanovic, M. Aleksic, P. Zuman, J. Electroanal. Chem. 507 (2001) 263–269.
[11] M. Aleksic, V. Kapetanovic, P. Zuman, Collect. Czech. Chem. Commun. 69 (2004) 1429–1442.
[12] P. Zuman, V. Kapetanovic, M. Aleksic, Anal. Lett. 33 (2000) 2821–2857.
[13] U.S. Pharmacopoeia 26-NF 21, 2002, pp. 369–370.
[14] D.D. Perrin, B. Dempsey, Buffers for pH and Metal Ion Control, Chapman and Hall, London, 1974, p. 155.
[15] M.M. Aleksic, V. Kapetanovic, J. Electroanal. Chem. 593 (2006) 258–266.
[16] P. Zuman, Sc. Pap. Univ. Pardubice Ser. A 5 (1999) 5–71.
[17] M. Erceg, V. Kapetanović, D. Sužnjević, D. Dumanović, Microchem. J. 57 (1997) 73–80.
[18] E. Laviron, J. Electroanal. Chem. 112 (1980) 1–9.
[19] Guidance for Industry: Boianalytical Method Validation, US Department of Health and Human Service, Food and Drug Administration, CDER, Rockville, MD, USA, 2001.

Fig. 4. Chromatograms of (A) CFX, DCFX and paracetamol as an internal standard in spiked urine sample, (B) blank urine sample and (C) real urine sample obtained from the patient 60 min after the administration of the drug.

urine sample increased, while the concentration of its metabolite DCFX decreased. The biggest change is observed in the first hour. According to literature [1], the maximal concentration of CFX in plasma was achieved after T_{max} of 0.78 h. In this period, CFX is intensively metabolised, and DCFX is predominantely present in excreated urine sample. After T_{max} being reached, the CFX con-

Comparison of direct solid sampling and slurry sampling for the determination of cadmium in wheat flour by electrothermal atomic absorption spectrometry

Rennan G.O. Araujo [a,b], Nédio Oleszczuk [c], Roger T. Rampazzo [c], Pedro A. Costa [c], Márcia M. Silva [c], Maria Goreti R. Vale [c,*], Bernhard Welz [b], Sérgio L.C. Ferreira [a]

[a] Universidade Federal da Bahia, Instituto de Química, Grupo de Pesquisa em Química Analítica, Campus Ondina, 40170-290 Salvador, BA, Brazil
[b] Universidade Federal de Santa Catarina, Departamento de Química, Campus Trindade, 88040-900 Florianópolis, SC, Brazil
[c] Universidade Federal do Rio Grande do Sul, Instituto de Química, Av. Bento Gonçalves 9500, 91501-970 Porto Alegre, RS, Brazil

ARTICLE INFO

ABSTRACT

Two analytical methods for the determination of cadmium in wheat flour by electrothermal atomic absorption spectrometry without prior sample digestion have been compared: direct solid sampling analysis (SS) and slurry sampling (SlS). Besides the conventional modifier mixture of palladium and magnesium nitrates ($10 \mu g$ Pd + $3 \mu g$ Mg), 0.05% (v/v) Triton X-100 has been added to improve the penetration of the modifier solution into the solid sample, and 0.1% H_2O_2 in order to promote an in situ digestion for SS. For SlS, $30 \mu g$ Pd, $12 \mu g$ Mg and 0.05% (v/v) Triton X-100 have been used as the modifier mixture. Under these conditions, and using a pyrolysis temperature of $800 °C$, essentially no background absorption was observed with an atomization temperature of $1600 °C$. About 2 mg of sample have been typically used for SS, although as much as 3–5 mg could have been introduced. In the case of SlS multiple injections had to be used to achieve the sensitivity required for this determination. Calibration against aqueous standards was feasible for both methods. The characteristic mass obtained with SS was 0.6 pg, and that with SlS was 1.0 pg. The limits of detection were 0.4 and 0.7 ng g^{-1}, the limits of quantification were 1.3 and 2.3 ng g^{-1} and the relative standard deviation ($n = 5$) was 6–16% and 9–23% for SS and SlS, respectively. The accuracy was confirmed by the analysis of certified reference materials. The two methods were applied for the determination of cadmium in six wheat flour samples acquired in supermarkets of different Brazilian cities. The cadmium content varied between 8.9 ± 0.5 and 13 ± 2 ng g^{-1} ($n = 5$). Direct SS gave results similar to those obtained with SlS using multi-injections; the values of both techniques showed no statistically significant difference at the 95% confidence level. Direct SS was finally adopted as the method of choice, due to its greater simplicity, the faster speed of analysis and the better figures of merit.

1. Introduction

Wheat is one of the basic foodstuffs in many parts of the world, and it is used to make bread, cakes, biscuits and farinaceous products in general. The cultivation of wheat has a strong contribution to the economy and the social structure of a country, influencing the trade balance and transferring income to other sectors of the economy. Among the greatest producers of wheat are China, the European Union, India, the United States of America [1,2].

Elemental food composition data are important to both consumers and health professionals, and recent food labeling legislation has highlighted this requirement. There has been a strongly increasing implement of food analysis of the past two decades to establish limits for human exposure from the diet. Moreover, different investigations have been carried out to measure constituents in food which are of interest because of their importance for human health, as a better knowledge of the nutritional quality of food products is clearly necessary [3–12].

The determination of trace elements and contaminants in complex matrices, such as food, often requires extensive sample preparation and/or extraction regimes prior to instrumental analysis. The traditional techniques for sample preparation are time-consuming and require large amounts of reagents, which are expensive, generate considerable hazardous waste, and might contaminate the sample with the analytes. Modern microwave-assisted acid digestion techniques have reduced these risks and disadvantages at least in part, however, they require specialized equipment, have only a limited sample throughput and are still

producing a significant amount of hazardous waste [6–9,13–15].

Electrothermal atomic absorption spectrometry (ET AAS) using a graphite tube atomizer is one of the most commonly used techniques for the determination of trace elements in complex matrices and in quality control. Although in this technique, samples are also often introduced in solution form, ET AAS greatly facilitates alternate sample introduction techniques, such as slurry sampling (SlS) and the direct analysis of solid samples (SS). Particularly the latter technique is characterized by several interesting advantages, such as a greatly reduced risk of contamination and analyte loss, high sample throughput and relatively moderate cost [16,17]. Both techniques have been extensively employed for the determination of volatile and medium volatile elements in environmental and biological samples mostly because of their toxicity importance [18,19]. However, for both techniques, problems resulting from high background absorption, calibration difficulties, weighing errors, sample inhomogeneity, etc. might become important, unless certain rules are strictly observed [18–22]. Direct SS and SlS ET AAS make possible the direct analysis of sub-mg masses of sample without previous preparation. However, the introduction of such small amounts of sample into the graphite furnace is a critical stage in the analytical process [16,17,23]. Particularly for SlS, the discontinuation of the only commercially available automatic slurry sampler [24] has brought back all the previously described problems associated with slurry stability and sedimentation.

Cadmium is a heavy metal with a high toxicity even at trace levels. The concentration of this element in food is therefore of world-wide concern for the sanitary authorities, who are trying to establish upper limits and to reduce the concentration of cadmium in food, which is considered the main source of intake of this contaminant for unexposed persons. In the United States a campaign of the food industries exists to acquire knowledge of the necessity to restrict this contamination and to preserve public health. In Brazil, the legislation allows a maximum concentration of $1.0 \, \mu g \, g^{-1}$ in foods [25]. Several papers have been published about the use of ET AAS for the determination of cadmium in wheat flour, rice flour and plant materials using complete digestion, slurry or solid sampling [26–33]. Official methods for the determination of cadmium, however, still involve the complete digestion and mineralization of the sample [6,28].

In this context, the present work considers the development and optimization of two analytical methods for the determination of cadmium in wheat flour, direct SS and SlS ET AAS. No direct comparison of the two techniques has been published yet, particularly not under the aspect of the availability of improved tools for direct SS and the discontinuation of the automatic slurry sampler for SlS. The goal of the work was to develop a faster, more reliable and more sensitive routine procedure for food control purposes, compared to conventional mineralization and solution analysis.

2. Experimental

2.1. Instrumentation and operation

All measurements were carried out using an AAS 5 EA atomic absorption spectrometer (Analytik Jena AG, Jena, Germany) with deuterium background correction, equipped with a transversely heated graphite tube atomizer. A cadmium hollow cathode lamp (GLE, Berlin, Germany) was used as the radiation source with a current of 4.0 mA. The main resonance line at 228.8 nm was used for all determinations with a spectral bandwidth of 0.8 nm. The spectrometer was interfaced to an IBM PC/AT-compatible computer. Argon with a purity of 99.996% (White Martins, São Paulo, Brazil) was the purge gas with a flow rate of 2.0 L min^{-1} during all stages,

Table 1
Graphite furnace temperature program for the determination of Cd in wheat flour samples by ET AAS using direct SS and SlS analysis

Program stage	Temperature (°C)	Ramp (°C s^{-1})	Hold time (s)	Gas flow rate (L min^{-1})
Drying 1[a]	90	15	10	2.0
Drying 2	120	5	15	2.0
Drying 3	150	10	21	2.0
Pyrolysis	800	100	80	2.0
Atomization[b]	1600	FP	6	0
Cleaning	2500	1000	5	2.0

[a] Drying 1 only used for SlS.
[b] Read in this stage.

except during atomization, where the flow was stopped. Integrated absorbance (peak area, A_{int}) was used exclusively for signal evaluation and quantification. All experiments with SS were carried out using solid sampling tubes without dosing hole (Analytik Jena Part No. 07-8130325) and solid sampling platforms (Analytik Jena Part No. 407-152.023). An SSA 5 manual solid sampling accessory (Analytik Jena) was installed in the sampling area of the spectrometer, and the pre-adjusted pair of tweezers, which is part of the SSA 5, was used to transfer the SS platforms into the atomizer. An M2P microbalance (Sartorius, Göttingen, Germany) was used for weighing the samples directly onto the SS platforms. Pyrolytic graphite-coated graphite tubes with integrated contacts and PIN platform (Analytik Jena, Part No. 407-A81.025) were used for the experiments with SlS. An MPE 5 furnace autosampler (Analytik Jena) was used for introduction of slurries and solutions. The optimized graphite furnace temperature program used for all determinations with is given in Table 1.

The medium particle size of the wheat flour samples was measured using a Superscan SS-550 scanning electron microscope (Shimadzu, Kioto, Japan).

A Unique-Thorton model USC-2850 ultrasonic bath (Thorton, São Paulo, Brazil) operated at a frequency of 37 ± 3 kHz, with temperature control up to 80 ± 5 °C, was used for preparation of the slurries.

2.2. Reagents and samples

Analytical grade reagents were used throughout. The nitric acid (Merck, Germany), used to prepare the slurries and aqueous calibration standards, was further purified by sub-boiling distillation in a quartz apparatus (Kürner Analysentechnik, Rosenheim, Germany). Distilled, deionized water with a resistivity of 18 MΩ cm from a Millipore water purification system (Millipore, Bedford, MA, USA) was used for the preparation of the samples and standards. All containers and glassware were soaked in 3 mol L^{-1} nitric acid for at least 24 h and rinsed three times with deionized water before use. The cadmium stock solution (1000 mg L^{-1} in 0.014 mol L^{-1} nitric acid) was prepared from cadmium nitrate (Merck). The working standards were prepared by serial dilution of the stock solution. Palladium modifier stock solution with ± 0.2 g L^{-1} Pd in 15% (v/v) nitric acid (Merck), magnesium modifier stock solution with 10 ± 0.2 g L^{-1} Mg in 17% (v/v) nitric acid (Merck), Triton X-100 (Union Carbide) and 30% (v/v) H$_2$O$_2$ (Merck) were used to prepare the mixed modifier solution.

The following certified reference materials (CRM) were used for validation of the method: NIST SRM 1567a Wheat Flour, NIST SRM 8433 Corn Bran and NIST SRM 1515 Apple Leaves (all from National Institute of Standards and Technology, Gaithersburg, MD, USA) and BCR no. 191 Brown Bread (European Commission, Community Bureau of Reference, Brussels, Belgium).

The wheat flour samples were collected in supermarkets of Salvador (SSA), Belém (BEL), São Paulo (SSP), Brasília (BSB), and Porto Alegre (POA), Brazil.

2.3. Sample preparation and methodology

2.3.1. Direct solid sample analysis

Approximately 2.0 mg of sample were weighed directly onto the SS platforms. Ten microliters of a modifier solution containing 10 μg Pd + 3 μg Mg + 0.05% Triton X-100 + 0.1% H_2O_2 were added with a micropipette and the SS platform was transferred to the graphite tube as described above. At least five replicates of each sample were weighed and analyzed. Calibration was performed using the standard calibration technique with aqueous standards that were pipetted manually onto the SS platform and analyzed under the same experimental conditions.

2.3.2. Slurry preparation

The slurries were prepared by placing 0.1 g of dried sample (medium particle size ~18 μm) and 10.0 μL of 30% (v/v) H_2O_2 into 10 mL volumetric glass flasks and completing to volume with 0.014 mol L^{-1} nitric acid. The slurries were homogenized for 15 min in an ultrasonic bath. They were shaken manually before they were introduced into the autosampler cups and homogenized by passing argon through the slurry just before it was delivered into the graphite tube for cadmium determination. Five aliquots of 20 μL were usually injected into the graphite tube, and each injection was followed by the first three stages of the graphite furnace temperature program shown in Table 1 in order to completely dry the injected sample. The last sample injection was followed by the injection of 10 μL of a modifier solution containing 30 μg Pd + 12 μg Mg + 0.05% Triton X-100, and the complete furnace temperature program was executed.

3. Results and discussion

All method development and optimization experiments were carried out using commercial wheat flour. The optimization experiments for direct SS and SIS analysis are presented in separate sections, as the methodology and the procedures are significantly different for the two approaches.

3.1. Direct analysis of solid samples

Firstly, the conditions for the determination of cadmium in wheat flour were optimized considering both the atomic and the background absorption as indicators. Fig. 1a shows the atomization signal of Cd and the background absorption for a wheat flour sam-
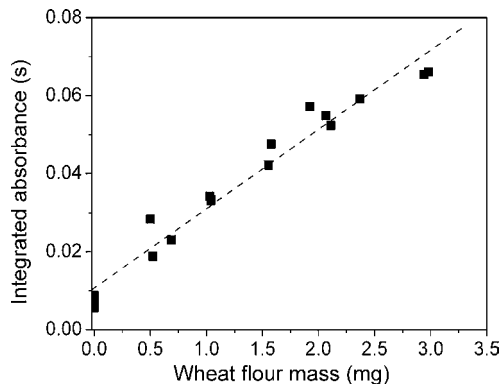
Fig. 2. Correlation between the wheat flour mass introduced into the graphite furnace and the integrated absorbance. T_{pyr} = 700 °C; T_{at} = 1600 °C; modifier: 10 μg Pd + 3 μg Mg + 0.05% Triton X-100 + 0.1% (v/v) H_2O_2.

ple with the addition of 10 μg Pd + 3 μg Mg + 0.05% Triton X-100 as the chemical modifier, a mixture that has been used successfully in previous applications of SS-ET AAS [34,35]. A relatively sharp background signal was observed early in the atomization stage under these conditions, causing a slight baseline distortion, which became more pronounced for higher sample masses. The addition of 0.1% (v/v) H_2O_2 to the modifier solution reduced the background absorption significantly and eliminated the associated baseline distortion, as can be seen in Fig. 1b. In addition, there was a clear increase in the cadmium absorption signal, both in height and in integrated absorbance. Gonzalez et al. [36] used a mixture of nitric acid and hydrogen peroxide in the determination of cobalt, chromium and nickel in wheat flour samples by SlS-ET AAS as oxidant modifier of the carbonaceous residues that are retained on the platform due incomplete destruction of the organic matrix. Cal-Prieto et al. [17] also encouraged the use of H_2O_2 to reduce the background and accumulation of carbonaceous residues of biological materials.

The mass of wheat flour that could be used for the direct SS determination of cadmium under the above established conditions has also been investigated. Fig. 2 shows a linear correlation between the integrated absorbance signal and the sample mass in the range from 0.5 to 3.0 mg. Each measurement point in Fig. 2 corresponds to an individual sample weighing and measurement, as it is almost impossible and also unnecessary to weigh and introduce repeatedly the same sample mass. Wheat flour masses >3 mg, however, required a longer pyrolysis time in order to be pyrolyzed efficiently; this approach has not been investigated systematically, as the volume capacity of the solid sampling platform also reached its limits, resulting in difficulties of sample transfer to the graphite furnace. In addition, the cadmium content in all samples was well above
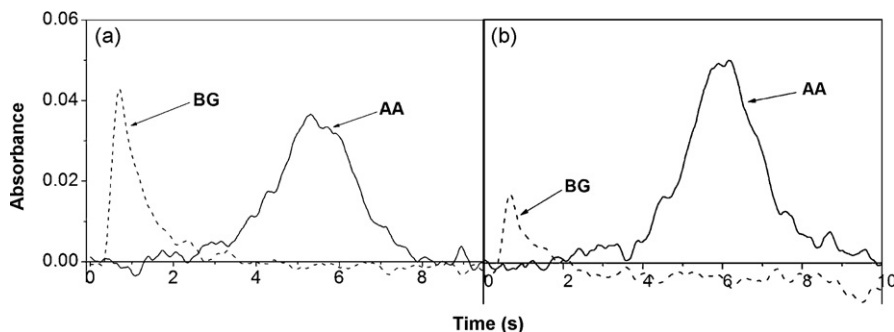
Fig. 1. Atomization pulses for Cd in approximately 1 mg of wheat flour, using SS with a pyrolysis temperature of 700 °C and an atomization temperature of 1600 °C: (a) with the addition of 10 μg Pd + 3 μg Mg + 0.05% (v/v) Triton X-100 as the modifier mixture; (b) same as (a) but with the additional use of 0.1% (v/v) H_2O_2; AA = atomic absorption; BG = background absorption.
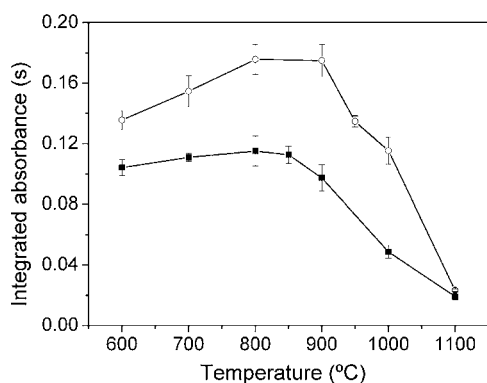
Fig. 3. Pyrolysis curves for cadmium in the presence of 10 μg Pd + 3 μg Mg + 0.05% (v/v) Triton X-100 + 0.1% (v/v) H_2O_2 as chemical modifier; (○) 0.02 ng Cd in 0.014 mol L^{-1} HNO$_3$; (■) integrated absorbance normalized for 2.0 mg wheat flour sample; atomization temperature 1600 °C; all points are average and standard deviation of n = 5 measurements.

Fig. 5. Atomization signals for Cd obtained for one, three and five 20-μL aliquots of 1% (m/v) wheat flour slurry into the graphite tube with 30 μg Pd + 12 μg Mg + 0.05% (v/v) Triton X-100 as chemical modifier. T_{pyr} = 800 °C; T_{at} = 1600 °C.

the limit of quantification, so that a further increase in sensitivity was not necessary. The positive intercept of the correlation curve of about A_{int} = 0.01 s with the integrated absorbance axis is due to the blank signal caused by the modifier mixture.

Pyrolysis curves have been established for a wheat flour sample and an aqueous solution using 10 μg Pd + 3 μg Mg + 0.05% Triton X-100 + 0.1% H_2O_2 as chemical modifier in both cases, and are shown in Fig. 3. The atomization temperature of 1600 °C has been optimized in previous work [37]; it is also in agreement with literature data for a transversely heated atomizer [38] and was not further investigated. The integrated absorbance values for the wheat flour sample in Fig. 3 have been 'normalized' for 2 mg of sample because of the above-discussed difficulties to weigh and introduce repeatedly the same sample mass into the graphite furnace. Hence, a sample mass close to 2 mg has been weighed accurately, and the integrated absorbance obtained for the actually introduced sample mass has been multiplied with the factor corresponding to the deviation of the actual sample mass from 2.00 mg. It is obvious that cadmium in aqueous solution is thermally stable up to 900 °C under the selected conditions, and no losses of cadmium are observed from wheat flour at least up to 800 °C. A pyrolysis temperature of 800 °C has therefore been chosen for all further investigations.

In addition to the similarity in the thermal behavior of cadmium in aqueous standards and the wheat flour sample, Fig. 4 shows that the atomization signals are not significantly different; indicating that calibration against aqueous standards might be feasible. Fig. 4b also shows the absence of any significant background signal, demonstrating the efficient removal of the wheat flour matrix in the pyrolysis stage.
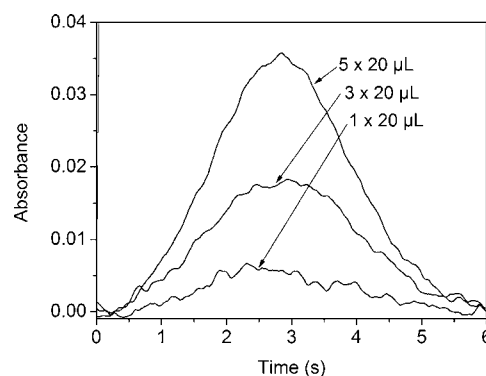
3.2. Method development for slurry sampling

Preliminary experiments have shown that injection of 20 μL of the wheat flour slurry (plus 10 μL of modifier solution) did not provide sufficient sensitivity for the determination of cadmium in the wheat flour samples. Significantly greater volumes of slurry could not be injected without the risk of an overflow because of the limited capacity of the platform. One possible solution of this problem would have been to prepare more concentrated slurry; however, difficulties have been encountered with the stability of the slurry in this case so that this approach was not further considered. A pre-concentration step using multiple injections was therefore investigated in order to reach an appropriate level of sensitivity. Twenty microliters of the slurry were injected into the graphite tube, followed by a thorough drying stage (steps 1–3 in Table 1) before the next aliquot was injected. After the last slurry injection, 10 μL of the chemical modifier solution (30 μg Pd + 12 μg Mg + 0.05% Triton X-100) was injected and the full temperature program shown in Table 1 was executed. Fig. 5 shows the absorption signals obtained for a wheat flour sample after the injection of one, three and five aliquots of 20 μL of slurry into the graphite tube. The increase in integrated absorbance was directly proportional to the number of aliquots injected into the graphite tube, i.e., to the sample mass.

The pyrolysis curves established with an aqueous standard solution and a wheat flour slurry, which are shown in Fig. 6, are quite similar to those in Fig. 3 obtained for direct SS. The minor

Fig. 4. Atomization signals for Cd, using a pyrolysis temperature of 800 °C and an atomization temperature of 1600 °C with the addition of 10 μg Pd + 3 μg Mg + 0.05% (v/v) Triton X-100 + 0.1% (v/v) H_2O_2 as chemical modifier: (a) 0.02 ng Cd in 0.014 mol L^{-1} HNO$_3$; (b) 2.0 mg of wheat flour.
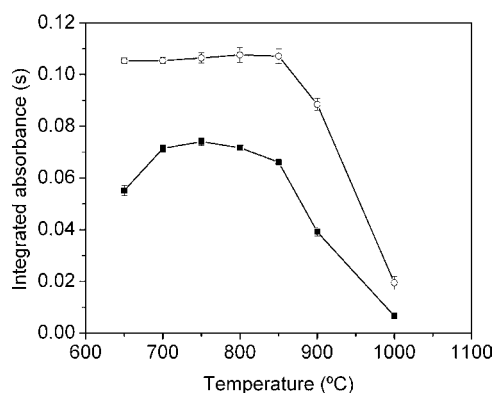
Fig. 6. Pyrolysis curves for (○) 0.02 ng Cd standard and (■) 1.0% (m/v) wheat flour slurry (5 × 20 μL), both with 30 μg Pd + 12 μg Mg + 0.05% (v/v) Triton X-100 as the chemical modifier. T_{at} = 1600 °C.

differences in the shape of the curves and in the maximum loss-free pyrolysis temperatures (850 °C for the aqueous standard solution compared to 900 °C in Fig. 3) are most likely due to the different tubes and platforms used for SS and SlS, respectively. The SS platform has a different mass and is inserted loosely into the SS tube, whereas the PIN platform is permanently fixed in the tube. This might result in a different heat transfer from the tube to the platform and slightly different apparent pyrolysis temperatures for the two platforms. The optimum pyrolysis temperature, however, was the same as for direct SS analysis, i.e., 800 °C, and the optimum atomization temperature was 1600 °C.

The atomization signals obtained under these conditions are shown in Fig. 7. Like in the case of direct SS, the signals for the aqueous standard and five injections of 20 μL aliquots of the wheat flour slurry are very similar in appearance time and peak shape, and there is essentially no background absorption visible. The significantly earlier appearance time and sharper peak shape compared to the signals obtained with SS (Fig. 4) are again due to the smaller mass of the PIN compared to the SS platform and the different heat transfer mechanisms. An additional factor that influences the peak shape is the absence of a dosing hole in case of the SS tube, which results in a longer residence time of the atoms in the absorption volume.

3.3. Figures of merit

The figures of merit for the determination of cadmium in wheat flour using SS-ET AAS and SlS-ET AAS with multiple injections are summarized in Table 2. The limits of detections (LOD) in both situations were calculated as three times the standard deviation of 10 measurements of a blank divided by the slope of the calibra-

Table 2
Figures of merit for the determination of Cd in wheat flour using SS-ET AAS and SlS-ET AAS

Parameter	SS-ET AAS[a]	SlS-ET AAS[b]
LOD (ng g^{-1})	0.4	0.7
LOQ (ng g^{-1})	1.3	2.3
m_0 (pg)	0.6	1.0

[a] Based on the introduction of 2.0 mg of solid sample into the graphite tube.
[b] Based on five consecutive injections of 20 μL of slurry, corresponding to 1.0 mg of sample introduced into the furnace.

tion curve; in SS-ET AAS the blank measurements were carried out according to the "zero mass response" technique [23], introducing repeatedly an SS platform containing the modifier mixture and running a full atomization cycle. The limit of quantification (LOQ) is based on the same measurements, using 10 times the standard deviation of the blank readings. The characteristic mass (m_0) is defined as the mass of analyte corresponding to an integrated absorbance of 0.0044 s.

A calibration curve established using a blank and eight calibration solutions in the concentration range 0.25–5.0 μg L^{-1} Cd (5–100 pg Cd) in 0.014 mol L^{-1} HNO$_3$, using the conditions described in Section 2 and a SS platform and tube gave the linear relationship:

$$A_{int} = 7.989m + 0.0059 \quad (R = 0.9997)$$

where m is the analyte mass. The same calibration solutions, using the PIN platform tube, which was used for SlS analysis, gave the linear relationship:

$$A_{int} = 4.096m + 0.015 \quad (R = 0.9998)$$

The lower sensitivity obtained in the latter case is due to the dosing hole in the PIN platform tube, which is absent in the SS tube, resulting in a longer residence time of the atoms in the absorption volume. The fact that a significant part of the analyte atoms are diffusing out of the dosing hole of a conventional graphite tube is well described in the literature [39–41].

3.4. Validation of the methods

The results obtained for cadmium in the CRM using the standard calibration technique with aqueous standard solutions are summarized in Table 3. There is no statistic difference between the results obtained by SS-ET AAS and SlS-ET AAS and the certified value for the wheat flour CRM, and between the results obtained by SS-ET AAS and the certified value for the other CRM on a 95% confidence level, based on a Student t-test. This result demonstrates that cadmium in wheat flour samples can be directly determined using the standard calibration technique. The other CRM have not
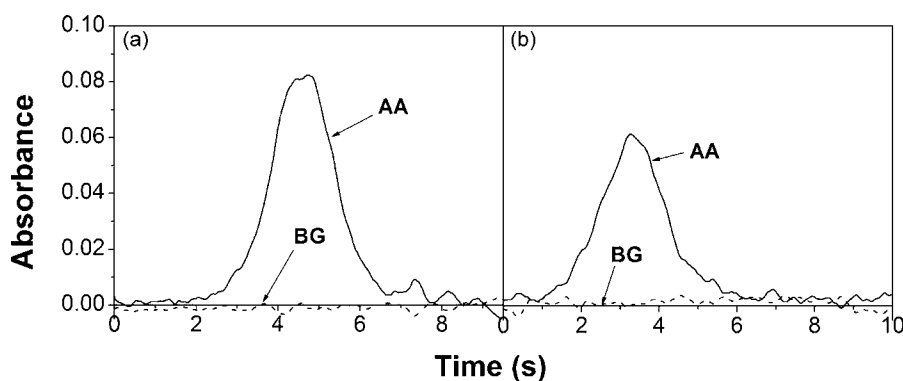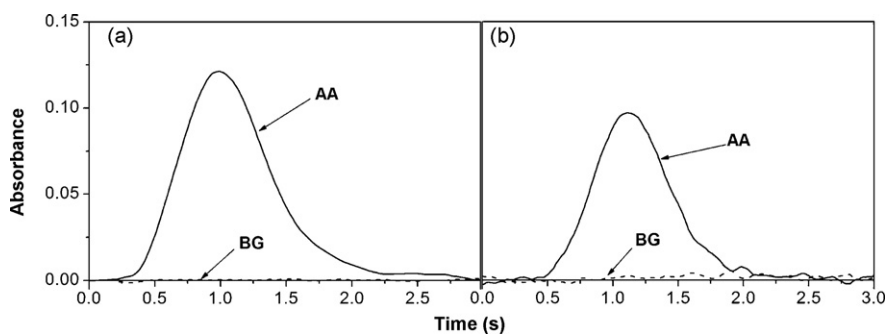

Fig. 7. Atomization signals for Cd, using a pyrolysis temperature of 800 °C and an atomization temperature of 1600 °C with addition of with 30 μg Pd + 12 μg Mg + 0.05% (v/v) Triton X-100 as chemical modifier: (a) 0.02 ng Cd in 0.014 mol L^{-1} HNO$_3$ + 0.1% (v/v) H$_2$O$_2$; (b) five aliquots of 20 μL of a 1% (m/v) wheat flour slurry.

Table 3
Cadmium determination in certified reference materials using SS-ET AAS and SlS-ET AAS and calibration against aqueous standards; all values are average and standard deviation of $n = 5$ measurements

Certified reference material	Certified ($\mu g\,g^{-1}$)	Found by SS ($\mu g\,g^{-1}$)[a]	Found by SlS ($\mu g\,g^{-1}$)[a]
Wheat flour NIST 1567a	0.026 ± 0.002	0.022 ± 0.006	0.023 ± 0.001
Corn bran NIST 8433	0.012 ± 0.005	0.016 ± 0.003	n.d.
Brown Bread BCR 191	0.0284 ± 0.002	0.031 ± 0.002	n.d.
Apple leaves NIST 1515	0.013 ± 0.002	0.016 ± 0.003	n.d.

n.d. = not determined.

[a] Average and standard deviation at the 95% confidence level.

been investigated using SlS-ET AAS because of their significantly different physical structure, which would have necessitated further optimization of the slurry preparation procedure. SS-ET AAS, in contrast, is not affected by these differences in the physical structure and can therefore be considered the more rugged technique.

3.5. Analysis of wheat flour samples

The proposed methods were applied for the determination of cadmium in six wheat flour samples, collected in supermarkets of Salvador/BA, Porto Alegre/RS, São Paulo/SP, Belem/PA and Brasilia/DF. The results expressed as confidence interval (at the 95% level) are summarized in Table 4. The cadmium content found in these samples was between 8.9 ± 0.5 and 13 ± 2 ng g^{-1} ($n = 5$). These values are about two orders of magnitude lower than the threshold value of 1.0 $\mu g\,g^{-1}$ established by the Brazilian Government for food products [25]. The t-test exhibited no significant difference between the cadmium values obtained with direct SS and SlS with multi-injections ($t_{calculated} = 1699$; $t_{value} = 2571$).

The precision calculated from $n = 5$ measurements of each wheat flour sample, expressed as relative standard deviation (R.S.D.), ranged between 6% and 16% for the direct SS method with an average of 10%, and between 9% and 23% for the SlS method with an average of 16%. The relatively high R.S.D. values found for both techniques can be attributed to the small sample mass introduced into the atomizer and the non-uniform distribution of the analyte in the analyzed samples [42]. However, it is obvious that direct SS provided better R.S.D. compared with SlS, which is in contrast to the widespread opinion about these two techniques [43]. This change in performance is without any doubt due to the fact that nowadays reliable tools for the introduction of solid samples into the graphite tube are available, whereas the autosampler for SlS, which has been used in most publications, is no longer available.

The R.S.D. of about 10% found in this work is typical for SS techniques, not only for ET AAS, but also for arc and spark emission or X-ray fluorescence spectrometry. A better R.S.D. could obviously be obtained after an acid digestion; however, as all values for Cd in the wheat flour samples investigated here were ≤10 × LOQ, an additional extraction and pre-concentration would have been necessary to bring the Cd concentration into a range where reliable determination is possible. Such a digestion/pre-concentration would make the whole procedure much more complex and time-consuming and

would also increase the risk of systematic errors due to contamination and/or analyte loss.

4. Conclusion

The analytical parameters obtained prove the viability of the proposed methods using direct SS- and SlS-ET AAS for the determination of Cd in wheat flour. Both methods are simpler, faster and more sensitive than wet digestion procedures and suitable for the routine screening of cadmium in wheat flour. Direct SS-ET AAS, however, is clearly the simplest, fastest and most sensitive technique, and it also provided the better precision compared to SlS-ET AAS. Another advantage of the direct SS analysis appears to be that it can apparently be applied to food and food products of significantly different physical structure, whereas the SlS technique is more dependent on the size and structure of the particles to be analyzed.

References

[1] Empresa Brasileira de Pesquisa Agropecuária, The National Research Centre for Wheat, 2008, http://www.cnpt.embrapa.br.
[2] Granotec do Brasil, 2008, http://www.granotec.com.br.
[3] E.E. Santos, D.C. Lauria, C.L.P. da Silveira, Sci. Total Environ. 327 (2004) 69.
[4] A. Pendergrass, D.J. Butcher, Microchem. J. 83 (2006) 14.
[5] A. Ikem, N. Egiebor, J. Food Compos. Anal. 18 (2005) 771.
[6] M. Rivero-Huguet, R. Huertas, L. Francini, L. Vila, E. Darre, Atom. Spectrosc. 27 (2006) 48.
[7] V.A. Lemos, E.M. Gama, A.D. Lima, Microchim. Acta 153 (2006) 179.
[8] U. Gottelt, K. Lusky, M. Stoyke, G. Henrion, Fleischwirtschaft 76 (1996) 1175.
[9] C. Almela, M.J. Clemente, D. Velez, R. Montoro, Food Chem. Toxicol. 11 (2006) 1901.
[10] G.Q. Shar, T.G. Kazi, M.A. Jakhrani, S.R. Sahito, M.A. Memon, J. Chem. Soc. Pakistan 24 (2002) 265.
[11] R.G.O. Araujo, F.D.S. Dias, S.M. Macedo, W.N.L. dos Santos, S.L.C. Ferreira, Food Chem. 101 (2007) 397.
[12] W.N.L. dos Santos, E.G.P. da Silva, M.S. Fernandes, R.G.O. Araújo, A.C.S. Costa, M.G.R. Vale, S.L.C. Ferreira, Anal. Bioanal. Chem. 382 (2005) 1099.
[13] M. Hoenig, A.M. de Kersabiec, Spectrochim. Acta Part B 51 (1996) 1297.
[14] F. Dolinsek, J. Stupar, V. Vrscaj, J. Anal. Atom. Spectrom. 6 (1991) 653.
[15] S. Bozhanov, I. Karadjova, S. Alexandrov, Microchem. J. 86 (2007) 119.
[16] M.G.R. Vale, N. Oleszczuk, W.N.L. dos Santos, Appl. Spectrosc. Rev. 41 (2006) 377.
[17] M.J. Cal-Prieto, M. Felipe-Sotelo, A. Carlosena, J.M. Andrade, P. López-Mahía, S. Muniategui, D. Prada, Talanta 56 (2002) 1.
[18] D. Baralkiewicz, H. Gramowska, Anal. Chim. Acta 510 (2004) 249.
[19] R. Nowka, I.L. Marr, T.M. Ansari, H. Muller, Fresen. J. Anal. Chem. 364 (1999) 533.
[20] N.J. Miller-Ihli, J. Anal. At. Spectrom. 3 (1988) 73.
[21] M.M. Silva, M.G.R. Vale, E.B. Caramão, Talanta 50 (1999) 1035.
[22] X. Chen, W.D. Marshall, J. Agric. Food Chem. 47 (1999) 3727.

Table 4
Results obtained for the determination cadmium in wheat flour samples by SS-ET AAS and SlS-ET AAS ($n = 5$)

Sample	SS-ET AAS[a] (ng g^{-1})	R.S.D. (%)	SlS-ET AAS[a] (ng g^{-1})	R.S.D. (%)
POA4	11 ± 1	6	10 ± 3	22
SSA3	8.9 ± 0.5	5	11 ± 2	14
BEL2	9.9 ± 1.8	14	14 ± 4	23
POA3	9.5 ± 1.0	8	11 ± 1	9
BSB1	13 ± 2	10	16 ± 3	16
SSP4	12 ± 2	17	11 ± 2	13

[a] Results expressed as average and confidence interval (at the 95% level).

[23] U. Kurfürst, in: U. Kurfürst (Ed.), Solid Sample Analysis, Springer, Heidelberg, 1988, pp. 21–127.
[24] G.R. Carnrick, W.B. Barnett, A. Fotinopoulos, At. Spectrosc. 10 (1989) 170.
[25] BRASIL, Leis, etc. Decreto no. 55.871 of 03/26/1965. Diário Oficial da União, Brasília, Section 1, pt. 1, 1965, p. 3611.
[26] E.J. Gawalko, T.W. Nowicki, J. Babb, R. Tkachuk, S.L. Wu, J. AOAC Int. 80 (1997) 379.
[27] P. Kalny, Z. Fijalek, A. Daszczuk, P. Ostapczuk, Sci. Total Environ. 381 (2007) 99.
[28] L. Jorhem, B. Sundstrom, J.N. Engman, J. AOAC Int. 84 (2001) 1984.
[29] J. Stupar, F. Dolinsek, Spectrochim. Acta Part B 51 (1996) 665.
[30] P. Vinas, N. Campillo, I.L. Gracia, M.H. Córdoba, Food Chem. 3 (1994) 317.
[31] P. Vinas, N. Campillo, I.L. Gracia, M.H. Córdoba, Fresen. J. Anal. Chem. 349 (1994) 306.
[32] E. Horner, U. Kurfurst, Fresen. Z. Anal. Chem. 328 (1987) 386.
[33] J. Štupar, F. Dolinšek, Acta Chim. Slov. 51 (2004) 641.
[34] I.C.F. Damin, M.M. Silva, M.G.R. Vale, B. Welz, Spectrochim. Acta Part B 62 (2007) 1037.
[35] N. Oleszczuk, J.T. Castro, M.M. da Silva, M.D.A. Korn, B. Welz, M.G.R. Vale, Talanta 73 (2007) 862.
[36] M. Gonzalez, M. Gallego, M. Valcarcel, Talanta 48 (1999) 1051.
[37] L. Bianchin, D. Nadvorny, A.F. da Silva, M.G.R. Vale, M.M. da Silva, W.N.L. dos Santos, S.L.C. Ferreira, B. Welz, U. Heitmann, Microchem. J. 82 (2006) 174.
[38] B. Welz, M. Sperling, Atomic Absorption Spectrometry, 3rd ed., Wiley–VCH, Weinheim, 1999, p. 941.
[39] O.A. Güell, J.A. Holcombe, Spectrochim. Acta Part B 43 (1988) 459.
[40] O.A. Güell, J.A. Holcombe, Spectrochim. Acta Part B 44 (1989) 185.
[41] O.A. Güell, J.A. Holcombe, Spectrochim. Acta Part B 47 (1992) 1535.
[42] M.A. Belarra, M. Resano, J.R. Castillo, J. Anal. At. Spectrom. 13 (1998) 489.
[43] C. Bendicho, M.T.C. de Loos Vollebregt, J. Anal. At. Spectrom. 6 (1991) 353.

Time-resolved fluoroimmunoassay for quantitative determination of ampicillin in cow milk samples with different fat contents

M.A. Bacigalupo [a,*], G. Meroni [a], F. Secundo [a], R. Lelli [b]

[a] Istituto di Chimica del Riconoscimento Molecolare, CNR, Via M. Bianco 9, Milan 20131, Italy
[b] Istituto Zooprofilattico Sperimentale dell'Abruzzo e del Molise "G. Caporale", Teramo, Italy

ARTICLE INFO

ABSTRACT

In this paper, we have reported an immunoassay with time-resolved revelation system for ampicillin in raw milk samples. Immunological methods appear to be a promising approach in the analysis of β-lactam compounds, because they do not need previous sample pre-treatments. In fact, β-lactam ring is not very stable in extensive sample pre-treatment procedures requested in conventional analytical techniques. Specimens were collected from lactating cows bred in various conditions and assayed for the fat contents. Ampicillin was assayed in samples with different fat concentrations. The assay was performed using ampicillin-specific polyclonal antibody raised in rabbit; the immunogen was synthesized using bovine thyroglobulin conjugated to ampicillin by glutaraldehyde reaction; as fluorescent marker we used goat anti-rabbit IgG conjugated with a chelating molecule complexed with Eu^{3+}. Bovine serum albumin (BSA) conjugated with ampicillin was synthesized and used to prepare a solid phase on polystyrene microtiter plates. The use of a lanthanide chelate as label allowed to achieve $1\,ng\,mL^{-1}$ sensitivity, which is four times more sensitive than limits requested from European Community. Fat contents did not affect the assay performance.

© 2008 Elsevier B.V. All rights reserved.

1. Introduction

Ampicillin is a semisynthetic antibiotic of the penicillin family. To extend the usefulness of penicillins to the treatment of infections caused by Gram-negative bacteria, the broad-spectrum penicillins (ampicillin, amoxicillin, carbenicillin, and ticarcillin) were developed. They are synthesized by attaching acid radicals to the central structure of 6-aminopenicillanic acid.

Ampicillin is widely used because it is similar in action to penicillin G, but is more stable in stomach acid pH, and therefore it may be given orally; it is also more active against certain strains of bacteria. The antibacterial effect is due to the interference in bacterial cell wall synthesis by interference with the transpeptidases. It is used regularly to treat common urinary tract pathogens, and gastrointestinal, respiratory and skin infections; in the dairy industry it is used as prophylactic drug to augment growth and yield and to combat mastitis causing bacteria, a frequent disease which causes large economic losses [1,2]. The presence of antibiotic in milk is relevant in public health risk and for impact on food technology. In the first case, antibiotic contamination can cause serious allergic reactions, modification of intestinal microflora and development of resistant strains of microrganisms [3,4]. On the other hand, the presence of antibiotics can also cause significant economic losses for producers and manufacturers of milk derivative products.

For protection of consumers, milk quality criteria have been established for the presence of antibiotics. Ampicillin is included on list of compounds to be controlled. European Union has established a maximum residue limit (MRL) for antibiotics in food. In particular MRL of ampicillin in bovine milk is set at $4\,\mu g\,L^{-1}$ [5]. On the other hand, analysis of β-lactam compounds is not easy. β-Lactam ring is stable in crystalline state, but it is not very stable in solution [6]. Ampicillin is the most stable of the commonly used β-lactam antibiotics, but the bulk solution must be preserved at $-20\,°C$ [7] Therefore, antibiotic assay can be affected by storage of milk samples [8]. Furthermore, conventional detection techniques need extensive sample pre-treatment procedures, with a risk of hydrolytic degradation and β-lactam ring opening. Several analytical approaches such as bioassays [9,10] liquid-chromatography and mass-spectrometry [11–16] capillary electrophoresis [17] and various immunological methods [18–23] have been described for detection of this compound. Conventional methods consist in separative techniques to isolate the target compound from other more concentrated compounds, because interferent peaks in the chromatograms and noisy base line must be removed to allow the required sensitivity. Therefore, immunoassays are useful because very low concentrations can be detected without the need for pre-

---

vious laborious and time-consuming sample pre-treatments. For instance, in the assay described in this paper, a single operator can analyze about 100 milk samples simultaneously within 2 h including the reading time. We used as fluorescent marker an europium chelate similar to the one we applied for detection of different analytes in various agricultural commodities [24,25]. In this paper, we described a time-resolved fluoroimmunoassay (TR-FIA) to determine ampicillin concentrations in raw cow milk.

2. Materials and methods

2.1. Chemicals

All of the chemicals, including standard ampicillin and the β-lactam cross-reacting compounds (amoxicillin; cloxacillin; dicloxacillin; oxacillin; penicillin G), thyroglobulin, BSA and goat anti-rabbit IgG were obtained from Sigma–Aldrich (Milan, Italy); ampicillin-specific polyclonal antibody raised in rabbit was obtained using ampicillin conjugated to thyroglobulin as immunogen.

2.2. Apparatus

Polystyrene micro-titer maxi-sorb wells were from Nunc (Pero, Milan, Italy).

Fluorescence was measured using a single-photon-counting time-resolved fluorometer (1232DELFIA Fluorometer; Wallac, Turku, Finland).

2.3. Specimen collection

The milk samples were collected from lactating cows bred with different diets in different geographical areas. Sampling was made in June and July from farms located in Po River basin and from alpine pasture in Aosta region. The samples were collected in glass vials, and stored at −20 °C until use. Pooled milk was obtained by mixing 100 mL of milk derived from the milking of 10 cows bred in farm with 100 mL of 10 cows bred at the mountain. The pool was fractioned in glass vials, stored at −20 °C, and treated in each experiment in the same way as samples.

The deep-freeze process does not affect the assay performance [26].

Samples were assayed for fat content by extractions according to the official method [27].

2.4. Syntheses

2.4.1. BCPDA and IgG-(BCPDA)$_n$

Europium chelator 4,7-bis(chlorosulfophenyl)-1,10-phenanthroline-2,9-dicarboxylic acid (BCPDA) was synthesized from 2,9-dimethyl-4,7-diphenyl-[1,10]-phenanthroline in three-step procedure as described in detail by Evangelista et al. [28]. Goat anti-rabbit IgG-(BCPDA)$_n$ conjugate was prepared using 2 mg of affinity purified IgG dissolved in 2 mL of 0.1 mol L^{-1} sodium carbonate buffer (pH 9). A solution of 500 μg of BCPDA in 100 μL of ethanol was then added and the mixture was incubated for 30 min at room temperature. The labeled IgG was separated on Sephadex G-50 column, eluting with 0.05 mol L^{-1} Tris–HCl buffer (pH 7.3). The value for n ($\cong$36) was assessed the absorbance of BCPDA at 325 nm; $\varepsilon = 1.52 \times 10^4$ M^{-1} cm^{-1}.

2.4.2. BSA–ampicillin

BSA–ampicillin derivative was prepared by glutaraldehyde reaction. Ampicillin sodium salt (370 mg) and BSA (80 mg) were dissolved in 3 mL of phosphate-buffered saline 0.15 mol L^{-1} pH 7.4;

glutaraldehyde solution (25%) was added in drops and the mixture was gently stirred at room temperature for 4 h before being eluted on Sephadex G-50 with 0.05 mol L^{-1} NH$_4$HCO$_3$ (adjusted to pH 7.4 with HCl 1 mol L^{-1}), lyophilized and stored at 4 °C. The ampicillin molar residues per mole of BSA were evaluated by matrix-assisted laser desorption/ionization (MALDI) mass spectrometry.

2.5. Preparation of solid phase

Polystyrene micro-titer wells were coated overnight at 27 °C with 200 μL of carbonate buffer 0.1 mol L^{-1}, pH 9.0, containing 5 μg mL^{-1} of BSA–ampicillin conjugate. The micro-titer wells were washed with carbonate buffer and a second coat was made with 250 μL of 2% BSA solution in the same buffer for 4 h at 27 °C. The wells were washed five times with 0.05 mol L^{-1} Tris–HCl buffer pH 7.5 containing 0.9% NaCl and stored dry at 4 °C until use.

2.6. Antibody production and characterization

Ampicillin–tyroglobulin conjugate was obtained by glutaraldehyde reaction as described above for BSA–ampicillin. Antiserum was produced in New Zealand white rabbits with 100 μg of conjugate for each immunization. The rabbits were subcutaneously injected monthly with the conjugate suspended in 1 mL of saline solution and Freund's complete adjuvant. The antisera were characterized by IEMA method. Antiserum with satisfactory characteristics was obtained 3–4 months after the first immunization. The anti-tyroglobulin present was eliminated by precipitation by adding 0.2% tyroglobulin to the rabbit serum. The affinity determined according to [29] was 1.7×10^9 L mol^{-1}. The antiserum was fractioned and stored at −20 °C in phosphate buffered saline 0.15 mol L^{-1} pH 7.4 containing 0.02% timerosal. The dilution giving 50% of fluorescence intensity in comparison with 100% of saturate solid phase fluorescence was chosen as working titer.

2.7. TR-FIA

All milk samples were briefly homogenized in a water bath at a temperature of 35 °C, mixed by repeated inversion and then quickly cooled to 20 °C. TR-FIA was performed either in buffer 0.05 mol L^{-1} Tris–HCl, pH 7.5 with 0.9% NaCl, or in pooled milk from untreated cows.

Ampicillin sodium salt was dissolved in distilled water. Fifty microliters of serial dilutions of standard between 1 ng mL^{-1} and 10^5 ng mL^{-1} of ampicillin were transferred in duplicate into polystyrene micro-wells coated with BSA–ampicillin conjugate. Specific antibody was diluted at a working titer of 1:60 000 in buffer 0.05 mol L^{-1} Tris–HCl solution, pH 7.5, containing 0.9% NaCl and 0.2% BSA; 100 μL of antibody solution was added to all of the wells other than that used for the blank evaluation, to which the same volume of buffer or pooled milk was added. Assay was performed directly in the milk by applying 50 μL of samples in duplicate instead of the standards. The wells were incubated for 30 min at 30 °C and washed three times with Tris–HCl buffer; then 150 μL of buffer containing an excess (1.8 nmol) of goat anti-rabbit IgG labeled with BCPDA were added and further incubation was carried at 30 °C for 30 min. After washing 150 μL of dissociation solution containing 4 mol L^{-1} urea, 1% sodium dodecylsulfate, and 10^{-6} mol L^{-1} Eu^{3+} were added to each well. Fluorescence was measured after 10 min, at the excitation wavelength of 345 nm. The delay time was 400 μs after excitation, the emitted light being read at 615 nm.

2.8. Matrix-effect evaluation

Matrix effect was evaluated by addition of standard ampicillin between 1 ng mL^{-1} and 10^5 ng mL^{-1} at three different milk samples with different fat concentrations and with undetectable ampicillin contents. The samples were equilibrated overnight at 4 °C and then assayed in comparison with calibration curve.

2.9. Recovery evaluation

Recovery was calculated at three different concentrations in five spiked samples as percent values of found ampicillin in comparison with 100% expected.

3. Results and discussion

3.1. Antibody specificity

Specificity of the polyclonal antibody was evaluated by assaying the cross-reactions of ampicillin-related compounds in buffer and in pooled milk, calculated at 50% of fluorescent signal reduction according to the formula:

$$\frac{IC_{50}\ (ng\,mL^{-1}) \text{of ampicillin}}{IC_{50}\,(ng\,mL^{-1}) \text{of competitor}}\%$$

All assayed compounds did not significantly interfere in the assay, as shown in Table 1.

3.2. Assessment of solid phase

The glutaraldehyde method was used to prepare BSA–ampicillin conjugate because this reaction could be performed in soft conditions, thus the β-lactam ring opening could be avoided. Ampicillin residues bound to the BSA, evaluated by MALDI mass spectrometry, resulted 8 mol/mol of BSA. Assay sensitivity was improved by reducing concentration of BSA–ampicillin onto the micro-well surface: coating micro-well concentration (5 μg mL^{-1}) was chosen consistently with fluorescent signal intensity. Stability of the coated plates stored dry at 4 °C was at least 6 months: during this time repeated calibration curves did not show any significant variations.

3.3. Assay performances

Dose–response curve carried out in a milk pool of untreated cows is shown in Fig. 1, in comparison with curve obtained with Tris–HCl buffer. The graphs were obtained by averaging eight individual curves normalized by reporting fluorescence values as % F/F_0 where F was the mean of cps for each standard and F_0 was the mean of cps for zero ampicillin concentration. F_0 values were 56800 ± 6189 cps and 58360 ± 6320 cps respectively, in milk and in buffer; blank values (3210 ± 295 cps and 2890 ± 288, respectively for assay in milk and in buffer) were subtracted.
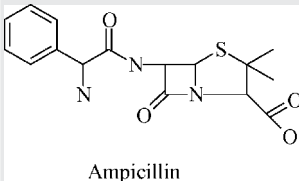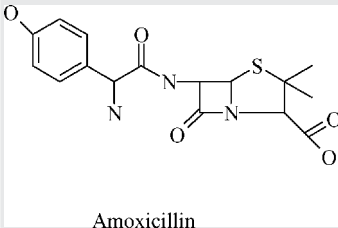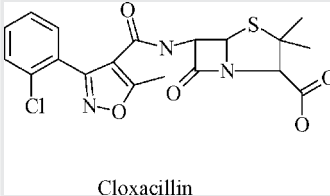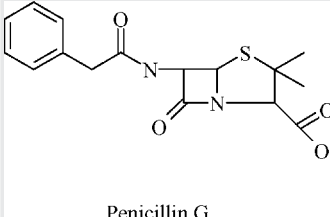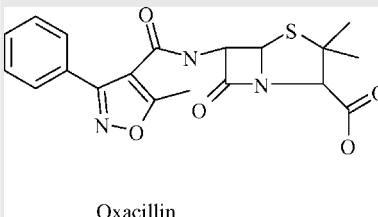
3.3.1. Sensitivity
The detection limit of the method (LOD) was determined by calculating the minimum amount of ampicillin that could be significantly distinguished from zero (mean binding at zero dose at three times the S.D.). LOD value, calculated from three curves prepared in duplicate was 1 ng mL^{-1}. The concentration of ampicillin at the IC$_{50}$ (50% inhibition of fluorescent signal) was 220 ng mL^{-1}.

3.3.2. Matrix effect
Twenty milk specimens collected from lactating cows bred in different conditions were assayed for the total fat concentration.

Table 1
Percentage of cross-reactivity of ampicillin-related compounds with ampicillin-specific antibody calculated in 0.05 M Tris–HCl buffer and in pooled milk, at 50% of fluorescence signal reduction

Compounds	% Cross-reactions	
	Buffer	Pooled milk
Ampicillin	100	100
Amoxicillin	2.1	2.8
Cloxacillin	1.0	0.9
Penicillin G	0.8	0.9
Oxacillin	0.08	0.1

The total fat amounts were in a range between 2.7% and 5.5% according to the variations of the diet and the breeding conditions (unpublished data). Three samples with high, medium and low fatty acid contents and undetectable ampicillin amount were assayed to evaluate matrix effect. Samples were spiked with 0.01 ng, 0.05 ng, 0.10 ng, 1 ng and 10 ng of ampicillin.

As shown the three curves resulted parallel to the standard curve obtained in pooled milk (Fig. 2) and therefore different fat concentrations did not affect the assay performance.

3.3.3. Accuracy evaluation
Accuracy was evaluated by recovery values of ampicillin concentrations in five milk samples spiked with low, medium and high concentrations of standard (Table 2).

Table 2
Ampicillin values in five milk samples spiked with low (1.5 ng mL^{-1}); medium (25 ng mL^{-1}) and high (500 ng mL^{-1}) standard concentrations assayed by TR-FIA (mean of 10 different assays; each sample was assayed in duplicate) concentrations of total fatty acids in each sample were reported

Spiked milk samples	% Fat content	Expected (ng)	Found (ng ± %CV)	% Recovery
Pooled milk	3.5	0.075	0.072 ± 0.007	96.5
		1.25	1.26 ± 0.110	101.0
		25	25.20 ± 2.208	100.8
Sample 1 (farm)	5.5	0.075	0.073 ± 0.005	97.3
		1.25	1.19 ± 0.110	95.2
		25	24.60 ± 2.330	98.4
Sample 2 (farm)	2.9	0.075	0.074 ± 0.008	98.5
		1.25	1.23 ± 0.130	98.4
		25	25.50 ± 1.800	102.0
Sample 3 (mountain)	3.9	0.075	0.072 ± 0.008	96.0
		1.25	1.30 ± 0.090	104.0
		25	25.6 ± 1.470	102.5
Sample 4 (mountain)	3.6	0.075	0.068 ± 0.006	90.8
		1.25	1.23 ± 0.108	98.3
		25	24.5 ± 2.080	98.0

The obtained values show a good recovery for all assays, independently of fat contents and analyte concentrations, allowing this method to be applied to real samples.

This study has a twofold advantage: it combines advantages of immunological methods and sensitivity of time-resolved fluorescent revelation system. Lanthanide chelates show narrow and strong emission bands around 600 nm and an exceptionally long decay time (up to a millisecond instead of nanoseconds of most molecules), which allow the elimination of the high background of the fluorescent labels. Furthermore, as the BCPDA chelate is fluorescent in aqueous solution, it is possible a direct fluorescence determination with a good sensitivity. It allows achieving 1 ng mL^{-1} sensitivity, which is four times higher than the limits requested from European Community. The antiserum used in this assay resulted highly specific for ampicillin. If antibody specific for β-lactam ring was available, this method should be applied also to the analysis of the β-lactam compounds family, as the enzyme-linked immunosorbent assay described in [23]. In comparison with previously published methods, the wider range of standard curve (over five orders of magnitude) allowed to measure high concentrations in samples without previous dilutions. Twenty milk samples obtained from different farms were assayed by the above-described method, using a calibration curve carried in pooled milk: in this case, ampicillin concentrations in all assayed specimens were below the fixed limits. In case a sample should result positive, a confirmatory assay with a chromatographic method is recommended: in fact, for high values of ampicillin the slope of calibration curve is lower and consequently the measures result less accurate and precise. This assay can be performed with raw milk, many samples can be analyzed simultaneously in a short incubation time and with a low cost, because the reagents can be easily obtained and their use does not need expert technicians. Therefore, it should thus provide a useful alternative to the conventional methods for a homemade control by milk-producing farms before mixing the milk bulks.
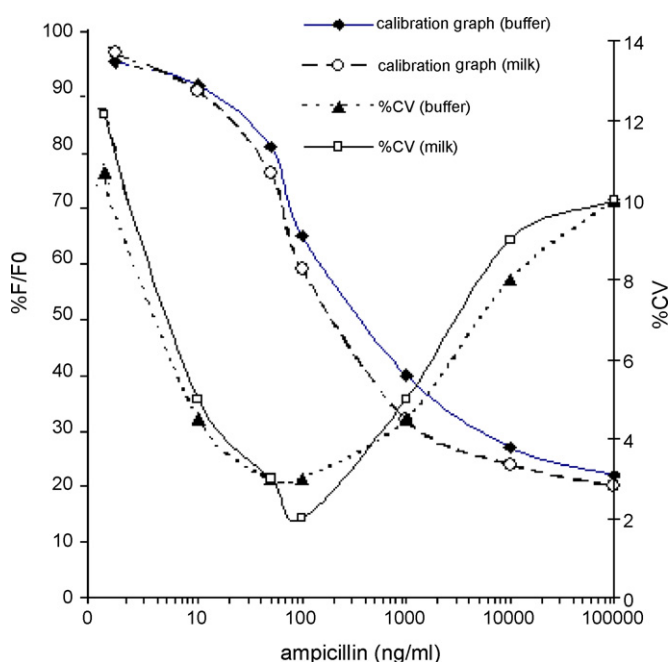
Fig. 1. Dose–response curve and precision profile (percent coefficient of variation) for TR-FIA of ampicillin. F and F_0 are expressed as cps. Each point represents the mean of eight determinations in duplicate.
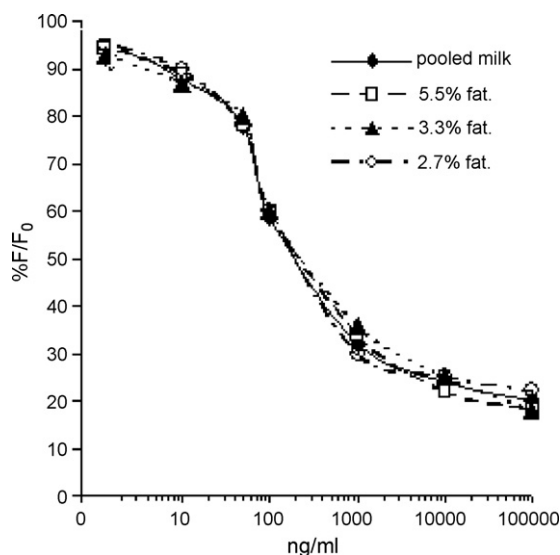
Fig. 2. Parallelism of the assays expressed as spline-smoothed function for milk samples with different fat contents. F and F_0 are expressed as cps (mean of three determinations run in duplicate).

Acknowledgements

References

[1] C. Hagnestam, U. Emanuelson, B. Berglund, J. Dairy Sci. 87 (2004) 3358.
[2] Y.T. Gröhn, D.J. Wilson, R.N. Gonzalez, J.A. Hertl, H. Schulte, G. Bennett, Y.H. Schukken, J. Dairy Sci. 90 (2007) 2260.
[3] Monograph on residues and contaminants in milk and milk products, International Dairy Federation, Brussel, 1997.
[4] C. Walsh, Antibiotics: Actions, Origins, Resistance, ASM Press, Washington, DC, 2003.
[5] EEC Council Regulation No. 2377/90, OJ No. L 224, June 26, 1990.
[6] M.B. Hickey, M.L. Peterson, E.S. Manas, J. Alvarez, F. Haeffner, O. Almarsson, J. Pharm. Sci. 96 (2007) 1090.
[7] L. Okerman, J. Van Hende, L. De Zutter, Anal. Chim. Acta 586 (2007) 284.
[8] F.J. Schenck, S.L. Friedman, Food Addit. Contam. 17 (2000) 675.
[9] T.J. Gilbertson, R.L. Mejeur, F.S. Yein, P.S. Jaglan, J. Dairy Sci. 78 (1994) 1032.
[10] K.L. Anderson, W.A. Moats, J.E. Rushing, D.P. Wesen, M.G. Papich, Am. J. Vet. Res. 57 (1996) 73.
[11] W. Luo, E.B. Hansen Jr., C.Y.W. Ang, J. Deck, J.P. Freeman, H.C. Thompson Jr., J. Agric. Food Chem. 45 (1997) 1264.
[12] S. Riediker, J.M. Diserens, R.H. Stadler, J. Agric. Food Chem. 49 (2001) 4171.
[13] S. Riediker, R.H. Stadler, Anal. Chem. 73 (2001) 1614.
[14] S. Ghidini, E. Zanardi, G. Varisco, R. Chizzolini, Food Addit. Contam. 20 (2003) 528.
[15] S. Bogialli, V. Capitolino, R. Curini, A. Di Corcia, M. Nazzari, M. Sergi, J. Agric. Food Chem. 52 (2004) 3286.
[16] W. Liu, Z. Zhang, Z. Liu, Anal. Chim. Acta 592 (2007) 187.
[17] S.M. Santos, M. Henriques, A.C. Duarte, V.I. Esteves, Talanta 71 (2007) 731.
[18] L. Okerman, K. De Wasch, J. Van Hoof, W. Smedts, J. AOAC Int. 86 (2003) 236.
[19] Z.V. Samsonova, O.S. Shchelokova, N.L. Ivanova, M.I. Rubtsova, A.M. Egorov, Appl. Biochem. Microbiol. 41 (2005) 589.
[20] E. Benito-Pena, M.C. Moreno-Bondi, G. Orellana, A. Maquieira, A. van Ameron-gen, J. Agric. Food Chem. 53 (2005) 6635.
[21] A. Sternesjo, E. Gustavsson, J. AOAC Int. 89 (2006) 832.
[22] S.P. Fitzgerald, N. O'Loan, R.I. Mcconnell, O. Benchikhel, N.E. Kane, J. AOAC Int. 90 (2007) 334.
[23] J. Lamar, M. Petz, Anal. Chim. Acta 586 (2007) 296.
[24] M.A. Bacigalupo, A. Ius, G. Meroni, M. Dovis, E. Petruzzelli, Analyst 119 (1994) 2813.
[25] M.A. Bacigalupo, A. Ius, R. Longhi, G. Meroni, Analyst 125 (2000) 1847.
[26] S.P. Huth, P.S. Warholic, J.M. Devou, L.K. Chaney, G.H. Clark, J. AOAC Int. 85 (2002) 355.
[27] ISO 14156 and International Dairy Federation 172, Geneva, 2001.
[28] P.A. Evangelista, A. Pollak, B. Allore, E.F. Templeton, R.C. Morton, E.P. Diamandis, Clin. Biochem. 21 (1988) 173.
[29] B. Friguet, A.F. Chaffotte, L. Djavadi-Ohaniance, M.E. Goldberg, J. Immunol. Methods 77 (1985) 305.

Multivariate near infrared spectroscopy models for predicting the iodine value, CFPP, kinematic viscosity at 40 °C and density at 15 °C of biodiesel

Patrícia Baptista [a], Pedro Felizardo [a], José C. Menezes [b], M. Joana Neiva Correia [a],*

[a] Centre of Chemical Processes, IST, Technical University of Lisbon, Av. Rovisco Pais, 1049-001 Lisbon, Portugal
[b] IBB, Centre for Biological and Chemical Engineering, IST, Technical University of Lisbon, Av. Rovisco Pais, 1049-001 Lisbon, Portugal

ARTICLE INFO

ABSTRACT

Biodiesel is one of the main alternatives to fossil diesel. It is a non-toxic renewable resource, which leads to lower emissions of polluting gases. In fact, European governments are targeting the incorporation of 20% of biofuels in the fossil fuels until 2020.

Chemically, biodiesel is a mixture of fatty acid methyl esters, derived from vegetable oils or animal fats, which is usually produced by a transesterification reaction, where the oils or fats react with an alcohol, in the presence of a catalyst. The European Standard (EN 14214) establishes 25 parameters that have to be analysed to certify biodiesel quality and the analytical methods that should be used to determine those properties.

This work reports the use of near infrared (NIR) spectroscopy to determine some important biodiesel properties: the iodine value, the cold filter plugging point, the kinematic viscosity at 40 °C and the density at 15 °C. Principal component analysis was used to perform a qualitative analysis of the spectra and partial least squares regression to develop the calibration models between analytical and spectral data. The results support that NIR spectroscopy, in combination with multivariate calibration, is a promising technique applied to biodiesel quality control, in both laboratory and industrial-scale samples.

1. Introduction

In the last decades, fuel needs have increased exponentially. In addition, there are several economical, political and environmental problems associated to the use of fossil fuels. Therefore, in the last years, general awareness about renewable energies, with lower environmental impact, has increased. Ideally, these alternatives should be economically competitive, technically achievable, environmentally acceptable and with high availability. As a result, in the near future, the use of renewable energies (such as biofuels, biomass, wave, hidric, wind and solar energies) will have to be widespread, in order to decrease the dependence on fossil fuels. Biodiesel appears as one of the main alternatives to diesel fuel [1,2].

Biodiesel production is commonly carried out through a transesterification reaction between a lipid source (vegetable oils or fats) and an alcohol (usually methanol) to produce an ester and a by-product, glycerol [3]. This reaction occurs stepwise, with mono- and diglycerides as intermediate products [4,5]. After the reaction period, the glycerol-rich phase is separated from the ester layer either by decantation or centrifugation. The resulting ester phase (crude biodiesel) contains contaminants such as methanol, glycerides, soaps, catalyst and glycerol, and has to be purified to comply with the European Standard EN 14214 [6]. In spite of the fact that there are several purification processes of biodiesel, usually these processes include one or more washing steps and a final drying step to remove the remaining water from the biodiesel [7]. The fact that refined biodiesel has similar properties to conventional fossil diesel allows its use as an alternative fuel. Additionally, biodiesel leads to the reduction of greenhouse gases, particle matter and sulphur emissions and, in case waste frying oils (WFO) are used as a raw material in biodiesel production, the treatment of an industrial or household waste [8–11].

According to geographic limitations and oil prices, biodiesel can be produced from different feedstocks [12–17]. Moreover, different technologies can be used in biodiesel production [5,18–23]. As a result, the final product can have different properties and, therefore, the quality control of biodiesel is very important. Actually, the EN 14214 establishes 25 parameters that have to be analysed

to certify biodiesel quality. These analyses are very expensive and time-consuming and near infrared spectroscopy (NIRS) appears as a cheaper and faster alternative to accomplish biodiesel quality control [24–29].

NIR spectroscopy is a well-known analytical technique based on the absorption of electromagnetic in the region from 780 to 2500 nm (12,820–4000 cm^{-1}). This technique allows multi-component analysis in a fast and non-destructive way, without requiring complex pre-treatments. In the NIR region, a component typically absorbs at more than one wavelength and, in chemically complex matrices, the absorbance at a given wavelength may have contributions from more than one analyte [30]. Therefore, well-established tools like principal component analysis (PCA) and partial least squares (PLS) were used for biodiesel classification and quantification purposes. To improve the correlation between the absorption of NIR radiation and the analytical reference data, specific spectra pre-processing and variable selection methods may be used [31–34]. The spectra pre-processing is used to reduce variations not directly related to the analyte concentration, such as random noise, baseline drift, light scattering, etc. Variable selection methods allow the determination of the spectral region(s) where variations are specifically related to changes in the analyte concentration, so that uninformative variables can be excluded, thus enabling the construction of simpler and more robust models for routine analysis with NIR.

Several recent papers describe the use of NIR, coupled with multivariate data analysis, for the analysis of biodiesel [24–29]. Knöthe [27–29] reports that there are two ranges in the NIR spectra of soybean oil and biodiesel, at 4430–4425 cm^{-1} and at 6005 cm^{-1}, which allow these products to be distinguished. In both regions, the methyl ester displays sharp peaks while the feedstock oil exhibits only shoulders. In addition, Felizardo et al. [24,25] report the development of calibration models for water and methanol in biodiesel, exploring the fact that the O–H group of water presents a peak at 5200 cm^{-1}, whereas the hydroxyl group of methanol shows a relatively broad peak at 4885–4480 cm^{-1}. These authors also report the use of NIRS to determine the methyl esters content of biodiesel, as well as the individual fatty acids methyl esters composition [26].

This work describes the use of NIRS to determine other important properties of biodiesel such as the iodine value, the cold filter plugging point (CFPP), the kinematic viscosity and the density. The iodine value of biodiesel is a measure of the degree of insaturation of the methyl ester molecules and an indicator of how easily these molecules polymerize. This value influences several important properties of biodiesel such as its CFPP and oxidative stability. In fact, it is known that oils and biodiesel with higher values of the iodine number have higher CFPP and a lower oxidative stability [4]. It is worth mentioning that the iodine value of biodiesel is similar to the iodine value of the oil used in its production and, therefore, to obey to the limits imposed by EN 14214, it is usually necessary to use mixtures of oils as raw materials (for example, soybean, rapeseed and palm oils).

The CFPP is also an important property of biodiesel that guarantees that it can be used at low temperatures. Actually, the CFPP is the highest temperature at which a given volume of biodiesel fails to pass through a standardized filtration device in a specified time, when cooled under standardized conditions. On the other hand, the knowledge of the kinematic viscosity of biodiesel is also important because it indicates its tendency to form engine deposits. It is known that the density and the kinematic viscosity of biodiesel are influenced by its methyl esters content [11], by the type of feedstock used in its production and by the presence of contaminants (namely, methanol).

2. Experimental

2.1. Materials and methods

Methanol, chromatographic grade (99.5%), was supplied by José M. Vaz Pereira (Lisbon, Portugal) and sodium methoxide, commercial grade (30% by weight of sodium methoxide in methanol) was purchased from BASF (Lisbon, Portugal).

2.1.1. Industrial samples

Soybean biodiesel samples and mixtures of palm, soybean and rapeseed biodiesel were supplied by *Iberol*, a Portuguese oil/biodiesel producing company. Biodiesel samples produced from WFO were supplied by *Space*, another Portuguese biodiesel producing company.

2.1.2. Laboratory-scale samples

Laboratory-scale samples were prepared by transesterification of soybean and WFO using the following procedure: 300 g of oil was transferred into a stirred tank reactor (1000 cm^3) immersed in a temperature-controlled water bath. For stirring, a single paddle round impeller (diameter = 6.5 cm) at 350 revolutions min^{-1} was used. The oil was heated until the desired temperature was reached (65 °C). At this point, a mixture of methanol and sodium methoxide was added to the oil and the transesterification reaction began. The reactor was kept at around 65 °C for 90 min.

At the end of the reaction period, the glycerol-rich phase was separated from the methyl esters layer in a decantation funnel. The esters phase (crude biodiesel) was washed with water, with a 0.5% HCl solution and again with water to provide a purified biodiesel. The washed methyl esters were then dried at 80–90 °C under vacuum (200 mbar) using a rotary evaporator (RE-111; Büchi, Flawil, Switzerland) or centrifuged (Sigma 4K10, Osterode am Harz, Germany).

Two types of strategies were used to produce biodiesel samples with a wide range of variation of the studied parameters (iodine value, CFPP, kinematic viscosity and density). On one hand, different oils (palm, soybean, rapeseed and waste frying) and mixtures of oils were used in the transesterification reaction because this led to differences, mainly, in the composition-related properties of biodiesel (for example, the iodine value and CFPP). On the other hand, different reaction conditions (molar ratio of methanol/oil and amount of catalyst) were used to produce biodiesel samples with a wide range of methyl esters content and, therefore, with an extended range of physical properties such as its density and viscosity [11]. For the development of the kinematic viscosity calibration, crude biodiesel samples were also used because biodiesel viscosity is greatly influenced by its methanol content.

2.1.3. Analyses

The standard methods were used as reference for the determination of the properties under study, except for the iodine value. In fact, the iodine value was determined using an alternative method to the Wijs method [35] presented in the EN 14214 [6], whereas the CFPP was determined by a filtration under standardized cooling conditions [36], the kinematic viscosity at 40 °C was determined using the viscometer method [37] and the hydrometer method was used to measure the density at 15 °C [38]. The errors of the analytical methods presented below are reproducibility errors, calculated using the data presented in the correspondent European Standard. The only exception is the iodine value method that, as mentioned above, was not determined using the reference method (the Wijs method), but using the alternative method presented in the EN 14214.

Table 1
Number and type of samples used in each calibration model

Parameter	No.	% Industrial samples	% Laboratory samples
Iodine value	311	50	50
CFPP	71	100	0
Kinematic viscosity	144	62	38
Density	91	69	31

The near infrared diffuse transmittance spectra of the biodiesel samples were acquired using an ABB BOMEM MB160 (Zurich, Switzerland) spectrometer equipped with an InGaAs detector and FTLA ACC131 liquid accessory with temperature control from ABB BOMEM but similar results were obtained when the spectra were acquired with a transflectance probe from SOLVIAS (Basel, Switzerland).

The spectra were recorded twice for each sample at room temperature ($25 \pm 1\,^{\circ}\text{C}$), with the aid of the Galactic Grams software package (Galactic Industries, Salem, NH, USA), in the wave number range of 12,000–4000 cm^{-1}, with a spectral resolution of 16 cm^{-1}. The average of the two measurements was used for model development.

2.1.4. Sample preparation

To obtain a stable NIR calibration model it is convenient to have calibration ranges wider than the ones allowed by the EN 14214. However, since most of the laboratory and industrial samples comply with the EN 14214, to extend the calibration ranges, several biodiesel samples were prepared at laboratory-scale. Therefore, different oils (palm, soybean and rapeseed) and mixtures of oils were used in the transesterification reaction and several biodiesel samples with different methyl esters and methanol contents were synthesized. In fact, the properties of the feedstock, as well as the degree of transesterification and the methanol content of biodiesel greatly influence the properties under investigation.

The number and type of samples used to develop the calibration models are presented in Table 1.

2.2. Data analysis and calibration development

All calculations were carried out using Matlab version 6.5 (MathWorks, Natick, MA, USA) and the PLS Toolbox version 4.0 (Eigenvector Research Inc., Manson, WA, USA). Only the region between 9000 and 4500 cm^{-1} was used for calibration because the noisy ($<4500\,\text{cm}^{-1}$) and non-informative ($>9000\,\text{cm}^{-1}$) ranges of the spectra were excluded.

Data analyses were performed using PCA for a qualitative analysis of the spectra, followed by the PLS regression to develop the calibration models between spectral and analytical data. Several pre-processing methods were applied to the spectra, prior to the models' development. These pre-processing methods are presented in Table 2.

In the PLS regressions, the optimal number of latent variables (LVs) needed in the calibration model was obtained by cross-validation (CV). The internal validation strategy used was the contiguous-block out method (block size equal to 10 samples) [31]. It is a recurring procedure, which sets aside 10 samples of the calibration set at a time, then builds a calibration model without the excluded samples and, finally, makes a prediction of the excluded samples using the calibration model developed.

The detection of outliers was performed based on the leverage values, Q-residuals, and Studentized y-residuals. As a result, a sample was considered to be an outlier if its leverage value was twice as large as the average leverage value (given by $2(1 + \text{LV})/N$, where LV is the number of latent variables and N the number of samples), or if its Q-residual falls above the 95% confidence limits for the considered model, or yet if y-residual of the sample was larger than twice the residual standard deviation [32].

The performance of the calibration models was analysed by calculating the root mean squares errors of cross-validation, RMSECV, and of external validation, RMSEP, and the respective determination coefficients, Q_y^2, between the predicted and the measured values [30,32]. The latter coefficient, which quantifies the variance in y being predicted by the model, was calculated as

$$Q_y^2 = \left(1 - \frac{(y - \hat{y})^{\text{T}}(y - \hat{y})}{y^{\text{T}}y} \right) \times 100 \tag{1}$$

Finally, the calibration models were developed using data sets randomly split using the *Shuffle* function of Matlab. Therefore, after the random reorder of the matrix rows, the complete data set was divided into the calibration (the first 2/3 of the matrix' rows) and the external validation sets (the last 1/3 of the matrix' rows). This procedure was repeated 10 times and the average errors obtained (RMSEC, RMSECV, . . .) are presented in the tables. The figures present the data split that allowed the calculation of the values of RMSECV and RMSEP to be equal to the mean values calculated from the results obtained after the several runs of the SHUFFLE function.

In order to identify the regions of the spectra that better capture the variance of each parameter, two "itoolbox" functions were used (iPLS and mwPLS). Both tools divide the spectra in a certain number or intervals, develop the calibration models for those intervals and validate them, given the correspondent model errors. The spectral regions chosen were the ones that gave the lowest errors.

3. Results and discussion

3.1. Development of calibration models for the iodine value

The possibility of using NIR spectroscopy to determine the iodine value is very interesting because its determination by the recommended analytical methods, gas-chromatography [6] or the Wijs method [35], is very expensive and time-consuming. Therefore, 311 industrial and laboratory-scale samples of biodiesel produced from soybean, palm and rapeseed oils, mixtures of oils

Table 2
Pre-processing methods used in each of the calibration models ($\sqrt{}$: used; ×: not used)

Parameter	Name	Pre-processing method			Mean centering	OSC[a]
		Savitsky–Golay derivative				
		Data points	Polynomial order	Derivative order		
Iodine value	PPM1			1st	$\sqrt{}$	×
CFPP	PPM2			2nd	$\sqrt{}$	×
Kinematic viscosity	PPM3	9	3rd	1st	$\sqrt{}$	$\sqrt{}$
Density	PPM4			1st	$\sqrt{}$	$\sqrt{}$

[a] Orthogonal signal correction.
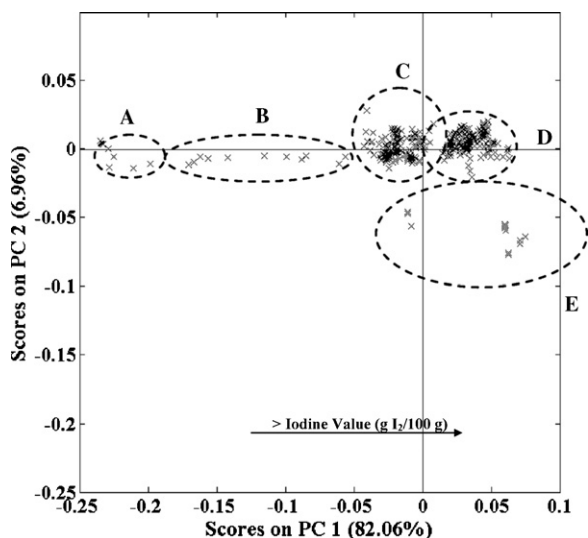
Fig. 1. Scores on PC1 versus scores on PC2 for PCA analysis for the calibration of the iodine value (9000–$4000\,cm^{-1}$). Group A: biodiesel produced from palm oil; group B: biodiesel produced from mixtures of oils; group C: biodiesel produced from rapeseed oil and mixtures of different oils; group D: biodiesel produced from soybean oil and WFO; group E: samples of crude biodiesel.

Fig. 2. Correlation between measured and predicted iodine value ($g\,I_2/100\,g$) of biodiesel (×: calibration set; ▲: validation set).

and waste frying oils were used for the development of the calibration model for the iodine value. The iodine value in the samples varied from 62 to $132\,g\,I_2/100\,g$ (the EN 14214 imposes and iodine value lower than $120\,g\,I_2/100\,g$).

The qualitative analysis of the data (between 9000 and $4000\,cm^{-1}$) was first performed by PCA, using as data pre-treatment a first-order Savitsky–Golay derivative with a filter width of 15 data points and a third-order polynomial fit followed by mean centering. The first four components captured 97.92% of the over-all variance of the original data (PC1 = 82.06% and PC2 = 6.96%) and Fig. 1 presents the scores of PC2 versus the scores of PC1.

As is presented in Fig. 1, the principal component analysis reveals the grouping of the samples according to the type of oil/mixture of oils used for biodiesel production. As was reported earlier [26], PC1 is capturing the type of oil used to produce the biodiesel, which influences its iodine value, whereas PC2 is related to the purification degree of the samples: from crude biodiesel (samples obtained after the transesterification reaction without further treatment and, therefore, contaminated with methanol, catalyst, glycerol, etc.) to washed and dried biodiesel. Therefore, the change in the iodine value can be easily observed from the samples' distribution: from the biodiesel produced using palm oil (64–$65\,g\,I_2/100\,g$; group A in Fig. 1) to the biodiesel produced from soybean oil (129–$135\,g\,I_2/100\,g$; group D on the right in Fig. 1).

For the PLS model's development, from the 311 samples, 210 were used for calibration and 101 for validation. After exclud-

ing 12 outliers (2 laboratory-scale samples produced from WFO and 10 industrial samples produced from mixtures of oils) using the above-mentioned procedure, the PLS model was developed by applying PPM1. Using the complete spectra, the lowest RMSECV was obtained with two latent variables, which allow capturing, 86.86% of the data variance in the spectra and 99.62% of the data variance concerning the iodine value of biodiesel. Table 3 presents the performance parameters of the models developed considering the spectral regions between 9000 and $4500\,cm^{-1}$.

The performance parameters presented in Table 3 demonstrate that these models allow the prediction of the iodine value with errors similar to the error associated with the analytical method used [6], but significantly lower than the errors of the reference method [35] ($3\,g\,I_2/100\,g$).

Furthermore, all models have a good predictive ability of the iodine value and the use of the spectral region between 5400 and $6300\,cm^{-1}$ led to the reduction of the number of latent variables (from 2 to 1) with a similar value of RMSEP. Furthermore, it is possible to conclude that these spectral regions describe the composition-related properties because both the iodine value and the linolenic acid methyl esters content [26] are calibrated in these spectral regions.

Fig. 2 shows the performance of the model developed considering the spectral region between 9000 and $4500\,cm^{-1}$ for both the calibration and validation sets. The results presented in Table 3 and Fig. 2 demonstrate that the calibration models developed to

Table 3
Cross-validation and external validation results for the prediction of the iodine value ($g\,I_2/100\,g$)

Model figures of merit	Spectral region (9000–$4500\,cm^{-1}$)	Spectral region (5400–$6300\,cm^{-1}$)	Spectral region (8100–$9000\,cm^{-1}$)
Latent variables	2	1	2
Filter width	9	9	9
R^2 calibration	0.996	0.994	0.996
R^2 validation	0.996	0.994	0.996
RMSEC ($g\,I_2/100\,g$)	0.7	0.9	0.7
RMSECV ($g\,I_2/100\,g$)	0.7	0.9	0.7
R^2 prediction	0.997	0.995	0.998
RMSEP ($g\,I_2/100\,g$)	0.8	1.0	0.7
Q_Y^2 external validation (%)	99.68	99.46	99.76
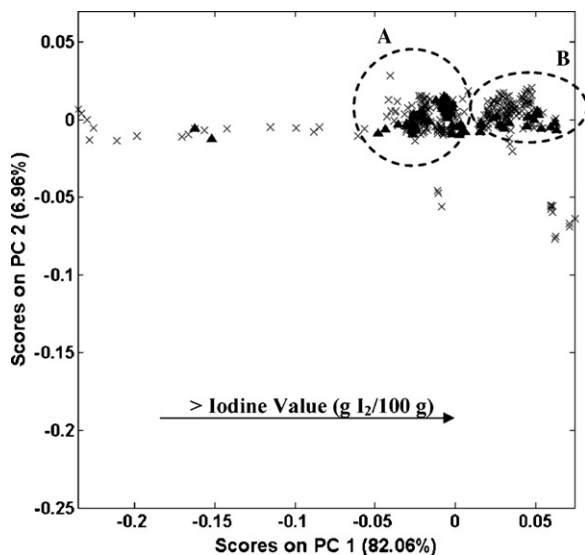
Fig. 3. Scores on PC1 versus scores on PC2 for the PCA analysis of the CFPP samples in the PCA model for the iodine value between 9000 and 4000 cm^{-1} (×: iodine value samples set; ▲: CFPP samples set). Group A: biodiesel produced from mixtures of oils; group B: biodiesel produced from soybean and waste frying oils.

Fig. 4. Correlation between measured and predicted CFPP (°C) (×: calibration set; ▲: validation set).

predict the iodine value of biodiesel perform very well not only in laboratory-scale samples but also in real industrial samples of biodiesel produced from different types of oils.

It is important to emphasize that no differences were detected between industrial and laboratory-scale samples of biodiesel, which anticipates the applicability of this model in an industrial environment.

3.2. Development of calibration models for the cold filter plugging point

As mentioned above, the cold filter plugging point is a measure of the behaviour of biodiesel at low temperatures and its ideal values change from winter to summer (the CFPP should be lower in winter). Since the reference method for CFPP may be troublesome, NIR spectroscopy may be a helpful alternative.

To obtain a calibration model for the biodiesel CFPP, 71 industrial samples of biodiesel produced from mixtures of soybean, palm and rapeseed oils and waste frying oils were used. The corresponding calibration range varied from −13 to +5 °C and, once more, only the region between 9000 and 4500 cm^{-1} was used for calibration.

Instead of developing a new PC analysis with the CFPP samples, the latter were tested in the above presented PCA model developed for the iodine value (Fig. 3).

Fig. 3 shows that the CFPP samples are spread along PC1, thus meaning that, as expected, these samples have different composi-

tions because they were prepared from rapeseed and soybean oils and mixtures of oils.

The calibration model for the CFPP was built using 49 samples for calibration and 22 samples for validation. The outliers were excluded (three industrial samples) and the PLS model was developed using PPM2 as the pre-processing method. Using the spectral region between 9000 and 4500 cm^{-1}, the obtained model needed three latent variables to capture 97.59% of the data variance in the spectra and 96.70% of the CFPP variance.

Table 4 and Fig. 4 show that the CFPP calibration model allows the prediction of this parameter with errors similar to the reference method error (1 °C). Additionally, the use of two narrower spectral regions for the CFPP calibration (4500–4960 and 8100–8560 cm^{-1}) allowed the results to be slightly improved. It is worth mentioning that the 8100–8560 cm^{-1} region also allowed the best model for the iodine value, which means that absorption in this spectral region should be related to the composition of the samples.

3.3. Development of calibration models for the kinematic viscosity

The kinematic viscosity of biodiesel is intrinsically related to its ester content [11]. To develop a calibration model for the kinematic viscosity of biodiesel, 144 samples of biodiesel were used. This set of samples contains biodiesel samples produced from different oils/mixtures of oils and samples from different production

Table 4
Cross-validation and external validation results for the prediction of CFPP (°C)

Model figures of merit	Spectral region (9000–4500 cm^{-1})	Spectral region (4500–4960 cm^{-1})	Spectral region (8100–8560 cm^{-1})
Latent variables	3	2	2
Filter width		9	
R^2 calibration	0.983	0.984	0.985
R^2 validation	0.958	0.964	0.966
RMSEC (°C)	0.9	0.8	0.8
RMSECV (°C)	1.0	0.9	0.9
R^2 prediction	0.936	0.953	0.951
RMSEP (°C)	1.1	1.0	1.0
Q_Y^2 external validation (%)	93.24	95.18	94.20
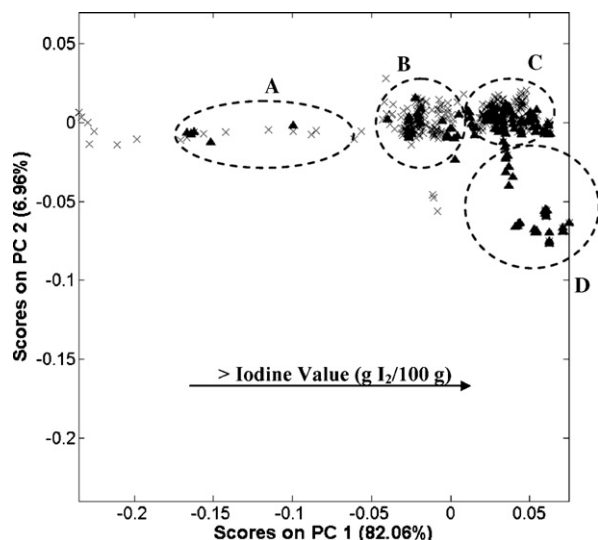
Fig. 5. Scores on PC1 versus scores on PC2 for the PCA test of the kinematic viscosity samples in the PCA model for the iodine value between 9000 and 4000 cm^{-1} (×: iodine value samples set; ▲: kinematic viscosity samples set). Groups A and B: biodiesel produced from mixtures of different oils; group C: biodiesel produced from soybean oil and WFO; group D: samples of crude biodiesel.

Fig. 6. Correlation between measured and predicted kinematic viscosity (mm^2 s^{-1}) (×: calibration set; ▲: validation set).

stages (from crude biodiesel, contaminated with methanol, glycerol, etc., to purified biodiesel—after the washing and drying steps). Therefore, it was possible to obtain a calibration range for the kinematic viscosity from 3.6 to 4.9 mm^2 s^{-1} (the EN 14214 acceptable range for this parameter is 3.5–5.0 mm^2 s^{-1}). As for the CFPP, these samples were tested in the above presented PCA model developed for the iodine value and the results are presented in Fig. 5.

Fig. 5 shows that the samples with different kinematic viscosities are spread not only along PC1, that is related to the type of oil used in biodiesel production, but also along PC2 that accounts for the purity of the samples/production stage.

After the PCA, the PLS model for the kinematic viscosity calibration model was built using 96 samples for calibration and 48 samples for validation. Four outliers were excluded (two industrial samples and two laboratory-scale sample) and the PLS model was developed using PPM 3 as pre-processing method. Using the complete spectral region (9000–4500 cm^{-1}), three latent variables are needed to capture 93.08% of the data variance in the spectra and 95.57% of the kinematic viscosity variance. The results are presented in Table 5 and Fig. 6.

The results obtained clearly indicate that NIRS may be used to determine the kinematic viscosity of biodiesel. Furthermore, Table 5 shows that this model allows the prediction of this parameter with an error around 0.1 mm^2 s^{-1}, which is an acceptable error when compared to the maximum error of the reference method (0.04 mm^2 s^{-1}). Moreover, the use of two narrower spectral regions

(5400–9000 and 5400–7700 cm^{-1}) allows reducing the number of latent variables, with slightly worse performance parameters of the model. Nonetheless, the fact that the number of latent variables is reduced means that these regions have crucial information about this parameter. It is also important to emphasize that these regions are not included in the most important methanol absorption band (4806–5060 cm^{-1}) [24,25], which means that the models presented above for the calibration of the kinematic viscosity were not negatively affected by the use of samples of crude biodiesel contaminated with methanol.

3.4. Development of calibration models for density

The set of samples used in density calibration contains 91 samples of biodiesel and oil (79 and 12, respectively), both industrial and laboratory, produced from soybean, palm, rapeseed and waste frying oils and from mixtures of these oils. Furthermore, oil samples were also used to extend the calibration range to higher density values. The calibration range goes from 877 to 922 kg m^{-3}, whereas the EN 14214 limits for the density are from 860 to 900 kg m^{-3}.

As shown in Fig. 7, the PCA analysis of the sample-set distinguishes the oil from biodiesel samples (group A versus group B) and a density variation pattern. In fact, as mentioned above for the other properties, the samples are distributed according to their matrix and, once again, the PCA analysis allowed to distinguish the palm oil and biodiesel samples (group C) from the soybean oils, WFO and biodiesel samples. It is also possible to conclude from Fig. 7 that the density difference between oils and biodiesel is higher than the one

Table 5
Cross-validation and external validation results for the prediction of kinematic viscosity (mm^2 s^{-1})

Model figures of merit	Spectral region (4500–9000 cm^{-1})	Spectral region (5400–9000 cm^{-1})	Spectral region (5400–7700 cm^{-1})
Latent variables	3	2	2
Filter width	9	9	9
R^2 calibration	0.956	0.936	0.928
R^2 validation	0.883	0.881	0.870
RMSEC (mm^2 s^{-1})	0.06	0.07	0.07
RMSECV (mm^2 s^{-1})	0.09	0.09	0.10
R^2 prediction	0.931	0.913	0.899
RMSEP (mm^2 s^{-1})	0.09	0.09	0.10
Q_Y^2 external validation (%)	87.94	86.52	83.75
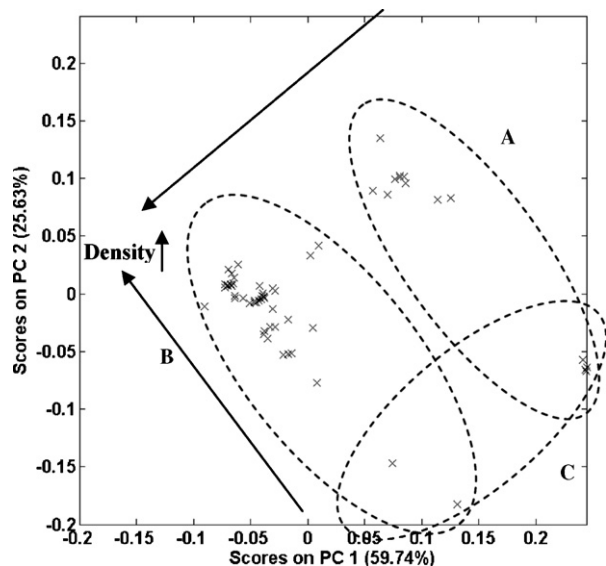
Fig. 7. Scores on PC1 versus scores on PC2 for PCA analysis for density calibration (between 9000 and 4000 cm^{-1}). Group A: biodiesel samples; group B: oil samples; group C: palm oils on the left and biodiesel samples on the right. The arrows indicate increasing density values.

observed between the samples of biodiesel produced from different raw materials.

To develop the density calibration model, 91 samples were used (62 in the calibration set and 29 in the validation set). Four outliers were excluded (from the set of industrial samples) and the PLS model was developed using PPM4 as the pre-processing method. Using the complete spectral region (9000–4500 cm^{-1}), six latent variables were necessary to describe the model, which captured 98.87% of the data variance in the spectra and 99.90% of the data variance concerning the density. It is worth mentioning that, as presented in Fig. 7, the differences between the oils and biodiesel density values are higher than those between the samples of biodiesel produced from different raw materials (Fig. 8).
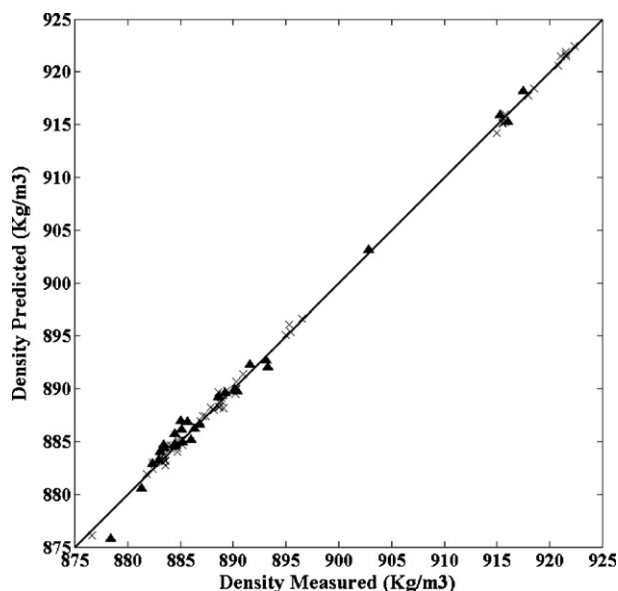
Fig. 8. Correlation between measured and predicted density (kg m^{-3}) (×: calibration set; ▲: validation set).

Table 6
Cross-validation and external validation results for the density's prediction (kg m^{-3})

Model figures of merit	Spectral region (4500–9000 cm^{-1})	Spectral region (5400–6310 cm^{-1})
Latent variables	6	5
Filter width	9	9
R^2 calibration	0.999	0.999
R^2 validation	0.998	0.996
RMSEC (kg m^{-3})	0.5	0.7
RMSECV (kg m^{-3})	0.9	1.2
R^2 prediction	0.999	0.997
RMSEP (kg m^{-3})	0.9	1.3
Q_Y^2 external validation (%)	99.19	98.31

As presented in Table 6, the density can be estimated with a prediction error of around 1 kg m^{-3}, which is comparable to the maximum error of the reference method (0.5 kg m^{-3}). Moreover, the use of a narrower region (5400–6300 cm^{-1}) allows similar results. Therefore, it is clear that the density of the vegetable oils and of biodiesel may be easily determined by NIRS.

4. Conclusions

The purpose of this work was to extend the use of NIR spectroscopy to calibrate several important biodiesel properties. Therefore, besides predicting the water and methanol [24,25] and the methyl ester contents in biodiesel [26], this work shows that NIRS may be used to predict the iodine value, the CFPP, the kinematic viscosity and the density of biodiesel. In fact, the derived models allow the prediction of the later properties with good statistical figures of merit with errors similar to the reference method.

As mentioned above, the iodine value is an indicator of several properties related to biodiesel composition (oxidative stability, CFPP, etc.) and its determination is expensive and time-consuming. On the other hand, the advantages of using NIRS to determine the CFPP, which is a measure of the behaviour of biodiesel at low temperatures, the kinematic viscosity and the density are of significance. In fact, besides the obvious advantages of allowing faster analyses, the NIR prediction of these parameters is a fast qualitative characterization tool, as well as an indicator of the transesterification degree of a biodiesel sample.

The proposed and validated NIR models were developed with industrial and laboratory-scale samples. Therefore, these calibrations can be used industrially, with the purpose of at-line and on-line monitoring of the process, as well as a simpler and more affordable alternative to carry out the quality control of the final product.

References

[1] A. Demirbas, Energy Policy 35 (2007) 4661–4670.
[2] A. Srivastava, R. Prasad, Renew. Sustain. Energy Rev. 4 (2000) 111–133.
[3] F. Ma, M.A. Hanna, Bioresour. Technol. 70 (1999) 1–15.
[4] G. Knöthe, J. VanGerpen, J. Krahl, The Biodiesel Handbook, AOCS Press, 2005.
[5] J. Marchetti, V. Miguel, A. Errazu, Renew. Sustain. Energy Rev. 11 (2007) 1300–1311.
[6] EN 14214, Automotive fuels – fatty acid methyl esters (FAME) for diesel engines – requirements and test methods, CEN—European Committee for Standardization, Brussels, Belgium, 2002.
[7] Y. Zhang, M. Dubé, D. McLean, M. Kates, Bioresour. Technol. 89 (2003) 1–16.

[8] Y. Ulusoy, Y. Tekin, M. Cetinkaya, F. Karaosmanoglu, Energy Sources 26 (2004) 927–932.

[9] K. Bozbas, Renew. Sustain. Energy Rev. 12 (2008) 542–552.

[10] J. Encinar, J. González, A. Rodríguez-Reinares, Fuel Process. Technol. 88 (2007) 513–522.

[11] P. Felizardo, M.J. Neiva Correia, I. Raposo, J.F. Mendes, R. Berkemeier, J.M. Bordado, Waste Manage. 26 (2006) 487–494.

[12] R. Sarin, M. Sharma, S. Sinharay, R. Malhotra, Fuel 86 (2007) 1365–1371.

[13] L. Oliveira, A. Franca, R. Camargos, V. Ferraz, Bioresour. Technol. 99 (2008) 3244–3250.

[14] H. Berchmans, S. Hirata, Bioresour. Technol. 99 (2008) 1716–1721.

[15] Y. Chisti, Biotechnol. Adv. 25 (2007) 294–306.

[16] U. Rashid, F. Anwar, Fuel 87 (2008) 265–273.

[17] X. Liu, X. Piao, Y. Wang, S. Zhu, H. He, Fuel 87 (2008) 1076–1082.

[18] L. Meher, D. Sagar, S. Naik, Renew. Sustain. Energy Rev. 10 (2006) 248–268.

[19] A. Demirbas, Energy Convers. Manage. 49 (2008) 125–130.

[20] M. Canakci, J. VanGerpen, Trans. ASAE 42 (5) (1999) 1203–1210.

[21] F. Abreu, D. Lima, E. Hamú, C. Wolf, P. Suarez, J. Mol. Catal. A: Chem. 209 (2004) 29–33.

[22] L. Bournay, D. Casanave, B. Delfort, G. Hillion, J.A. Chodorge, Catal. Today 106 (2005) 190–192.

[23] S.V. Ranganathan, S.L. Narasimhan, K. Muthukumar, Bioresour. Technol. 99 (2008) 3975–3981.

[24] P. Felizardo, P. Baptista, M. Uva, J.C. Menezes, J.N. Correia, J. Near Infrared Spectrosc. 15 (2) (2007) 97–105.

[25] P. Felizardo, P. Baptista, J.C. Menezes, J.N. Correia, Anal. Chim. Acta 595 (2007) 107–113.

[26] P. Baptista, P. Felizardo, J.C. Menezes, J.N. Correia, Anal. Chim. Acta 607 (2008) 153–159.

[27] G. Knöthe, J. Am. Oil Chem. Soc. 76 (7) (1999) 795–800.

[28] G. Knöthe, J. Am. Oil Chem. Soc. 77 (5) (2000) 489–493.

[29] G. Knöthe, Trans. ASAE 44 (2001) 193–200.

[30] Næs, T. Isaksson, T. Fearn, T. Davies, A User-friendly Guide to Multivariate Calibration and Classification, NIR Publications, Chichester, 2002.

[31] O. Preisner, J. Lopes, R. Guiomar, J. Machado, J. Menezes, Anal. Bioanal. Chem. 387 (2007) 1739–1748.

[32] H. Martens, T. Næs, Multivariate Calibration, John Wiley & Sons, New York, USA, 1991.

[33] M. Otto, Chemometrics: Statistics and Computer Application in Analytical Chemistry, Wiley–VCH, New York, 1999.

[34] T.A. Lestander, C. Rhén, Analyst 130 (2005) 1182–1189.

[35] European Standard EN 14111, CEN—European Committee for Standardization, Brussels, Belgium.

[36] European Standard EN 116, Diesel and domestic heating fuels—determination of cold filter plugging point, CEN—European Committee for Standardization, Brussels, Belgium, 1997.

[37] European Standard EN 3104, CEN—European Committee for Standardization, Brussels, Belgium.

[38] European Standard EN ISO 3675, Crude petroleum and liquid petroleum products – laboratory determination of density – hydrometer method, CEN—European Committee for Standardization, Brussels, Belgium, 1998.

Hydroxyl radical detection with a salicylate probe using modified CUPRAC spectrophotometry and HPLC

Burcu Bektaşoğlu, Mustafa Özyürek, Kubilay Güçlü, Reşat Apak*

Istanbul University, Faculty of Engineering, Department of Chemistry, Avcilar 34320, İstanbul, Turkey

ABSTRACT

Reactive oxygen species (ROS) may attack biological macromolecules giving rise to oxidative stress-originated diseases, so it is important to establish efficient methods to screen hydroxyl radical scavengers for antioxidant therapy. Since $^\bullet OH$ is very short-lived, secondary products resulting from $^\bullet OH$ attack to various probes are measured. As a low-cost measurement technique, we used a salicylate probe for detecting hydroxyl radicals generated from an equivalent mixture of Fe(II) + EDTA with hydrogen peroxide. The produced hydroxyl radicals attacked both the probe and the water-soluble antioxidants in 37 °C-incubated solutions for 2 h. The CUPRAC (cupric ion reducing antioxidant capacity) assay absorbance of the ethylacetate extract due to the reduction of Cu(II)–neocuproine reagent by the hydroxylated probe decreased in the presence of $^\bullet OH$ scavengers, the difference being proportional to the scavenging ability of the tested compound. Attack by $^\bullet OH$ radicals upon salicylate produced 2,3-dihydroxybenzoate, 2,4-dihydroxybenzoate, and 2,5-dihydroxybenzoate as major products. HPLC separation combined with CUPRAC spectrophotometry was used to identify and quantify hydroxylated salicylate derivatives in the presence of synthetic water-soluble antioxidants and green tea infusion. The developed spectrophotometric method for $^\bullet OH$ detection was validated with HPLC, i.e., the concentrations of dihydroxybenzoates produced by radical attack from the probe were determined by HPLC, and the sum of (concentration × absorptivity) products of these components approximately agreed with the experimentally found CUPRAC absorbances, confirming the validity of Beer's law for the selected system. Statistical comparison of the results found with the proposed methodology and HPLC was made with two-way ANOVA (analysis of variance) test. Under optimal conditions, about 53% of the probe (salicylate) was converted into dihydroxybenzoate isomers in the absence of $^\bullet OH$ scavengers, and these isomers were more specific markers of hydroxyl radicals than the non-specific malondialdehyde end-product of the TBARS test. Thus, the more costly and less speedy HPLC method could advantageously be substituted with the proposed spectrophotometric assay of $^\bullet OH$ detection, which was also of much higher yield than the TBARS colorimetric assay.

© 2008 Elsevier B.V. All rights reserved.

1. Introduction

When natural defenses of the organism (of enzymatic, non-enzymatic, or dietary origin) are overwhelmed by an excessive generation of reactive oxygen species (ROS), a situation of 'oxidative stress' occurs, in which cellular and extracellular macromolecules (proteins, lipids, and nucleic acids) can suffer oxidative damage, causing tissue injury [1,2]. The hydroxyl radical ($^\bullet OH$) is the most reactive product of ROS formed by successive 1-electron reductions of molecular oxygen (O_2) in cell metabolism, and is primarily responsible for the cytotoxic effects observed in aerobic organisms extending from bacteria to plants and animals [1,3,4].

It is generally assumed that $^\bullet OH$ is generated in biological systems [3,5] from H_2O_2 by the Fenton reaction:

$$Fe^{2+} + H_2O_2 \rightarrow Fe^{3+} + {}^\bullet OH + OH^-$$
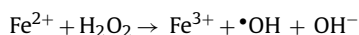
whereby Fe^{2+} required for the Fenton reaction is regenerated through reduction of Fe^{3+} by superoxide anion ($O_2{}^{\bullet -}$), giving rise to an overall Fe(II,III)-catalyzed Haber–Weiss reaction producing $^\bullet OH$ from H_2O_2 and $O_2{}^{\bullet -}$, potentially available in aerobic cells [6]. In laboratory simulations of the Fenton system, transition metal cations of the lower valency (e.g., Co(II) or Cu(I)) may be substituted for Fe(II).

* Corresponding author. Tel.: +90 212 4737028; fax: +90 212 4737180.
E-mail address: rapak@istanbul.edu.tr (R. Apak).

In the testing of potential •OH scavengers such as mannitol, glucose, metabisulfite, ascorbate, and many others [7], the use of naked (unligated) Fe^{2+} cation for •OH production by the Fenton reaction may cause site-specific damage to the tested scavenger or probe (detector) molecule, whereas the use of EDTA as the metal chelator (e.g., formation of $Fe^{(II)}$-EDTA) can remove iron from its attached ligating site and transfer damage elsewhere [7], enabling more objective measurement of the scavenging ability. Oxidative attack of hydroxyl radicals generated from such a Fenton reaction on deoxyribose produces malondialdehyde (MDA) and similar substances that are colorimetrically or fluorometrically reactive (i.e., that can form colored or fluorescent products) with thiobarbituric acid (TBA-reactive substances, or TBARS method, based on the formation of colored TBA-MDA adducts), forming the essence of •OH detection [7–10]. When •OH radicals generated by iron-EDTA + H_2O_2 in the presence of ascorbic acid oxidize deoxyribose and the reaction products yield a pink chromogen absorbing at 532 nm upon heating with thiobarbituric acid (TBA), hydroxyl radical scavengers added to the medium compete with the deoxyribose probe and diminish chromogen formation, enabling the calculation of second-order rate constants of •OH scavenging [11]. However, there are also criticisms to the classical TBARS method in which it is rather unspecific (e.g., also used for testing lipid peroxidation [12]), is of low efficiency (i.e., only a small percentage of deoxyribose is converted to TBA-reactive substances), and cannot properly assay the •OH scavenging power of phenolic antioxidants which may show pro-oxidant activity in the Fenton reaction system via iron recycling [13]. The TBARS method requiring acid heating at elevated temperature itself generates MDA, lacks specificity, and has other limitations [14,15]; therefore, it is questionable whether the TBARS test measuring MDA formation from various degradative pathways is a true indication of tissue oxidative stress in biological chemistry. Alternative instrumental technologies such as ESR and pulse radiolysis to detect and measure the scavenging of hydroxyl radicals are quite expensive and unavailable to many scientists interested in free radical biology and medicine [13]. It is also possible to use a benzoate [7,16] or salicylate [17] or N,N'-(5-nitro-1,3-phenylene) bisglutaramide [18] probe for •OH detection, separate the hydroxylation products of the probe by HPLC, and detect them electrochemically or fluorometrically as an indicator for hydroxyl radicals. Still, it may be better to stick to the 'test tube' assay proposed by Halliwell et al. [11] and to improve it in order to develop a simple and widely used assay for detecting hydroxyl radicals and assessing •OH scavenging antioxidant activity in vitro.

Our recently reported simple, low-cost, and widely applicable CUPRAC antioxidant capacity assay for dietary polyphenols, flavonoids, vitamins C and E [19], and plasma antioxidants [20] utilizes the copper(II)–neocuproine reagent as the chromogenic oxidant; phenolic hydroxyls are converted to the corresponding quinones in the CUPRAC redox reaction, producing a chromogen of Cu(I)–neocuproine absorbing at 450 nm [19]. In a recent work, we used three aromatic probes, namely p-aminobenzoate, 2,4-dimethoxybenzoate, and 3,5-dimethoxybenzoate for •OH radical scavenging assay of a number of important water-soluble compounds, made use of competition kinetics to simultaneously incubate the probe with the scavenger under the attack of hydroxyl radicals generated in a Fenton system, and measured the difference in CUPRAC absorbance of the probe (extracted into ethylacetate at the end of the incubation period) in the absence and presence of the scavenger (i.e., the hydroxylation product of the probe would show a higher CUPRAC absorbance when alone) [21]. Now, the idea here is to use the novel colorimetric 'test tube' assay of hydroxyl radical scavenging in conjunction with a salicylate probe that has been previously used for HPLC assay [17,22,23]
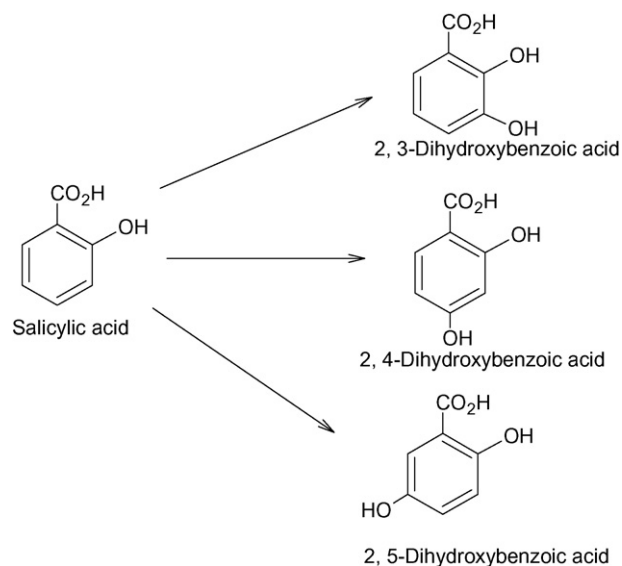
Fig. 1. Major hydroxylation products formed from a salicylic acid probe upon the attack of •OH radicals [23].

of •OH detection. Since it is possible to identify and quantify the hydroxylation products (dihydroxybenzoate isomers) of the salicylate probe with HPLC, Beer's law was applied to testing the additivity of absorbances of the hydroxybenzoates (i.e., to check whether the expected absorbances match with the experimentally found CUPRAC absorbances). The ultimate aim is to substitute the more sophisticated HPLC method requiring high cost and expertise with the simple modified CUPRAC colorimetric assay for hydroxyl radical detection in complex (food and biological) systems. Since one of the most effective and sensitive indicators of hydroxyl radical formation in biological fluids is a salicylate probe with separation of the dihydroxybenzoate (DHBA) isomers (major hydroxylation products: 2,3-; 2,4-; and 2,5-DHBA) formed from salicylate (Fig. 1) [23] with HPLC, followed by electrochemical detection [22,24], the proposed redox chromogen (copper(II)–neocuproine) is believed to play the part of an electrochemical detector in a simple colorimetric system even without requiring separation of the DHBA isomers. Salicylate was preferred as the •OH trapping agent in the developed colorimetric assay, because it had a very low CUPRAC absorbance and its definitely known and stable hydroxylation products had relatively high CUPRAC absorbances.

2. Experimental

2.1. Reagents and instrumentation

The following chemical substances of analytical reagent grade were supplied from the corresponding sources: neocuproine (2,9-dimethyl-1,10-phenanthroline), acetonitrile, and trichloroacetic acid (TCA): Sigma Chem. Co.; 2-thiobarbituric acid (TBA), 2,3-dihydroxybenzoic acid (2,3-DHBA), and ascorbic acid: Aldrich; copper(II) chloride dihydrate, ammonium acetate, iron(II) chloride tetrahydrate, hydrogen peroxide (30%, by mass), sodium metabisulfite ($Na_2S_2O_5$), mannitol, glucose, thiourea, ethylacetate, sodium hydroxide, dimethyl sulfoxide (DMSO), concentrated H_3PO_4, $Na_2HPO_4·2H_2O$, $NaH_2PO_4·2H_2O$ and concentrated HCl: E. Merck; disodium-EDTA, sodium salicylate, 2,4-dihydroxybenzoic acid (2,4-DHBA), 2,5-dihydroxybenzoic acid (2,5-DHBA), 2-deoxy-

D-ribose: Fluka; sodium thiosulfate pentahydrate ($Na_2S_2O_3 \cdot 5H_2O$), absolute ethanol: Riedel. Lipton green tea (*C. sinensis*) was purchased from Unilever San. Tic. Turk AS.

Either 1.0×10^{-2} or 1.0×10^{-3} M aqueous solutions of thiourea, mannitol, ascorbic acid, glucose, sodium metabisulfite, sodium thiosulfate pentahydrate, and DMSO were prepared in bidistilled water. The salicylate buffer (at 10 mM concentration) was prepared by dissolving 0.160 g of sodium salicylate in bidistilled water. Fe(II) at 20 mM concentration was prepared by dissolving 0.1988 g $FeCl_2 \cdot 4H_2O$ with 2 mL of 1 M HCl, and diluting to 50 mL with water. Na_2-EDTA at 20 mM concentration was prepared by dissolving 0.372 g of the salt in water and diluting to 50 mL. Hydrogen peroxide at 10 mM concentration was prepared from a 0.5 M intermediary stock solution (standardized by permanganate(VII) titrimetry) prepared from 30% H_2O_2, and then diluting this at a ratio of 1:50 with H_2O. 2,4-Dihydroxybenzoic acid, 2,5-dihydroxybenzoic acid, and 2,3-dihydroxybenzoic acid were prepared in bidistilled water at 1 mM (1.0×10^{-3} M) concentration. Copper(II) at 1.0×10^{-2} M was prepared by dissolving 0.4262 g of $CuCl_2 \cdot 2H_2O$ in water, and diluting to 250 mL. Ammonium acetate (NH_4Ac; 1.0 M) aqueous solution contained 19.27 g of the salt in 250 mL. Neocuproine (Nc) at 7.5×10^{-3} M was prepared by dissolving 0.078 g of the free base in 96% EtOH, and diluting to 50 mL with ethanol (preferably prepared fresh). Trichloroacetic acid (TCA) at 2.8% (by mass) was prepared in water, and thiobarbituric acid (TBA) at 1% in 50 mM aqueous NaOH. Deoxyribose at 10 mM was prepared in water.

Green tea bag (*Camellia sinensis*) supplied from the market was weighed as such to yield a mass of 2.0 g. The tea bag was dipped into and pulled out of beakers containing 500 mL of freshly boiled water for the first 2 min, and let to steep for the remaining 3 min in the covered beakers (total steeping time was 5 min) to prepare a tea infusion. The bag was removed, and the partly turbid solutions were filtered through a black band Whatman quantitative filter paper after cooling to room temperature. The clear extract was properly diluted for the CUPRAC and HPLC assays of hydroxyl radical scavenging activity (dilution ratio: 1:5). The dilution ratio of green tea infusion was selected so as not to give an initial CUPRAC absorbance (which would otherwise complicate the calculations). During the measurement of •OH scavenging activity of green tea infusion with the proposed procedure, 0.5 mL of the 1:5 diluted infusion was taken.

The spectra and absorption measurements were recorded in matched quartz cuvettes using a Varian CARY 100 Bio UV–vis spectrophotometer (Mulgrave, Victoria, Australia). Other related apparatus and accessories were a Clifton water bath, E521 Metrohm Herisau pH-meter equipped with glass electrodes, and Elektromag vortex stirrer.

The chromatograph was from PerkinElmer (Shelton, CT, USA), and consisted of a pump (PerkinElmer Series 200 HPLC pump), an injection valve (Model 7725i, Rheodyne, Cotati, CA, USA), a Hamilton 25 μL-syringe (Reno, NV, USA), an analytical stainless-steel column packed with Hamilton H × Sil C18 sorbent (250 mm × 4.6 mm, 5 μm) (Reno, NV, USA) and a variable-wavelength UV–vis detector (PerkinElmer Series 200). The mobile phase for HPLC analysis with gradient elution was prepared from phosphate ($H_2PO_4^-$) buffer and acetonitrile. This buffer was prepared by dissolving 0.78 g of sodium dihydrogen phosphate dihydrate in 500 mL of bidistilled water. The pH of the mobile phase thus prepared was adjusted to pH 2.5 with phosphoric acid. The elution program was run such that the initial composition of the mobile phase as 10% acetonitrile and 90% phosphoric acid aqueous buffer was linearly transformed into a final composition of 60% acetonitrile and 40% phosphoric acid buffer

mixture within the program period of 30 min. The flow rate was adjusted to 1.0 mL min⁻¹, and the UV detection wavelength was 280 nm.

2.2. Recommended procedure (modified CUPRAC method)

To a test tube were added fairly rapidly 3 mL of phosphate buffer (pH 7.0), 1 mL of 10 mM probe material (salicylate), 0.5 mL of 20 mM Na_2-EDTA, 0.5 mL of 20 mM $FeCl_2$ solution, $(4-x)$ mL H_2O, (x) mL scavenger sample solution (x varying between 0.5 and 2.5 mL, for constructing the calibration curves of scavengers) at a concentration of 1.0×10^{-2} or 1.0×10^{-3} M, and 1 mL of 10 mM H_2O_2 in this order, and the mixture in a total volume of 10 mL was incubated for 2 h in a water bath kept at 37 °C. At the end of this period, the reaction was stopped with adding 0.5 mL of 2 M HCl, vortexed, 4 mL of this acidified solution was taken, 4 mL of ethylacetate (EtAc) added, and mixed again. To 1 mL of the EtAc extract, the modified CUPRAC method [21] was applied in the following manner:

$$1 \, mL Cu(II) + 1 \, mL Nc + 1 \, mL \, NH_4Ac \, buffer + 1 \, mL \, EtAc \, extract$$
$$+ 1 \, mL \, EtOH$$

The absorbance at 450 nm of the final solution at 5 mL total volume was recorded 30 min later against a reagent blank.

The second-order rate constants of the scavengers were determined with competition kinetics by means of a linear plot of A_o/A as a function of [scavenger]/[probe], where A_o and A are the CUPRAC absorbances of the system in the absence and presence of scavenger, respectively [21]. The second-order rate constants found with the modified CUPRAC procedure with the use of competition kinetics [21] were then compared with those found with the conventional TBARS method [11].

During the validation of the modified CUPRAC method with HPLC, a salicylate probe as the hydroxyl radical trapping agent was used. As described in the 'recommended procedure', a salicylate buffer solution of initial concentration 10 mM was subjected to hydroxyl radical attack in the described Fenton system; the use of salicylate probe was either with ($x = 0.5$–1.5 mL of the tested solution) or without the addition of scavengers. After stopping the hydroxylation reaction with the addition of acid, 4 mL of EtAc was mixed with 4 mL of the incubated solution, vortexed, and the hydroxylation products together with the salicylic acid probe were extracted into the organic phase. A 2-mL aliquot of the organic phase was withdrawn into a test tube, and the solvent was evaporated under nitrogen flow. The evaporation residue remaining in the tube was dissolved with 2 mL of 1:3 (v/v) EtOH–H_2O mixture. This final solution was subjected to both CUPRAC colorimetric and HPLC analysis. The concentrations of the remaining salicylate and the converted hydroxylation products (DHBA isomers) were calculated from the chromatogram; the CUPRAC absorbance expected from each component was calculated (by means of the calibration curve drawn for each component), and these individual absorbances were summed up to find the expected CUPRAC absorbance of the mixture. This expected absorbance was compared to the experimentally found absorbance for different solutions of the Fenton hydroxylation system originally containing the probe and the scavenger.

To 0.25 mL of the 1:3 EtOH:H_2O extract, the modified CUPRAC method was applied in the following manner:

$$1 \, mL \, Cu(II) + 1 \, mL Nc + 1 \, mL \, NH_4Ac \, buffer$$
$$+ 0.25 \, mL \, EtOH : H_2O \, extract + 0.75 \, mL H_2O$$

2.3. HPLC method

After the dissolution of the evaporation residue of the EtAc extract (remaining in the test tube) with 2 mL of 1:3 (v/v) EtOH-H_2O mixture (see '*Recommended procedure*'), a suitable aliquot of this solution was injected into the HPLC column (5 μm ODS), and gradient elution was employed for separation of the hydroxylation products. The mobile phase consisted of acetonitrile and 10 mM of pH 2.5 phosphoric acid buffer in varying proportions. The retention times of the salicylic acid probe and the major hydroxylation products; namely 2,3-DHBA, 2,4-DHBA, and 2,5-DHBA [23] were compared with those of pure standards, and the method of standard additions was applied where necessary for complete identification of the reaction products.

2.4. Deoxyribose (TBARS: thiobarbituric acid-reactive substances) colorimetric method

The deoxyribose (TBARS) method was applied as the reference method of comparison for determining the rate constants [7–11]. To a test tube were rapidly added 3 mL of phosphate buffer (pH 7.0), 1 mL of 10 mM 2-deoxy-D-ribose (probe: pr), 0.5 mL of 20 mM Na_2-EDTA, 0.5 mL of 20 mM $FeCl_2$ solution, $(4–x)$ mL H_2O, (x) mL scavenger (sc) sample solution (x varying between 0.5 and 2.5 mL) at a concentration of 1.0×10^{-2} or 1.0×10^{-3} M, and 1 mL of 10 mM H_2O_2 in this order, and the mixture in a total volume of 10 mL was incubated for 4 h in a water bath kept at 37 °C. At the end of this period, the reaction was stopped with adding 5 mL of 2.8% TCA, 5 mL of 1% TBA was added, and the reaction mixture was kept in a 100 °C-water bath for 10 min. The test tube containing the final mix was cooled under a flow of running tap water, and the absorbance at 520 nm was recorded.

The second-order rate constants of the scavengers were determined with competition kinetics [11,25] by means of a linear plot of A_o/A as a function of [sc]/[pr], where A_o and A are the TBARS absorbances of the system in the absence and presence of scavenger, respectively.

2.5. Statistical analysis

Descriptive statistical analyses were performed using Excel software (Microsoft Office 2002) for calculating the means and the standard error of the mean. Results were expressed as the mean ± standard deviation (S.D.). Using SPSS software for Windows (version 13), the data were evaluated by two-way analysis of variance (ANOVA).

3. Results and discussion

3.1. Requirements for experimental design

Gutteridge has shown that the TBA-reactivity of deoxyribose (measured as the absorbance at 532 nm) was maximal when Fe^{2+} and EDTA were taken at equimolar concentrations (0.22 mM) for 1.1 mM deoxyribose in phosphate buffer at pH 7.4. In the absence of added EDTA, iron ions would bind to the detector or buffer molecules to produce 'site-specific' radical damage on the detector. In the presence of EDTA, however, iron is removed from these binding sites to produce •OH in 'free' solution [26].

At the time of the original TBARS assay development [8], carbohydrate (probe) degradation was brought about purely with Fe^{2+} (i.e., without EDTA). EDTA was later added to the system to prevent site-specific damage to the probe due to iron complexation. EDTA allows more •OH to escape into free solution to react with added scavengers [7] so as to enable investigating competitive kinetics of hydroxyl radical scavengers against the probe. EDTA has several other unique advantages such as reducing the redox potential of iron ions to enable easier oxidation of Fe(II) to Fe(III), solubilizing iron at physiological pH, and accelerating the autoxidation of Fe^{2+} ions [27]. Generation of thiobarbituric acid (TBA) reactivity from deoxyribose, however, was inhibited by EDTA when this exceeded the concentration of iron salt present [7]. Gutteridge has shown that when EDTA exceeds the concentration of iron salt present, it does not increase the formation of TBA-reactive material from deoxyribose [7]. There are reports in the literature where the researchers have used an excess of EDTA over Fe(II) in order to suppress the possible prooxidant effect of oxidized iron *via* binding to phenolic antioxidants [13], but usually, the solutions of iron ions and EDTA are taken equimolar in the assays [28,29] as we did in this work.

In the Fenton reaction system utilized, the absorbances due to the hydroxylation of the probe (salicylate probe of this work) almost reached saturation levels at the end of 1 h, and basically remained unchanged for a total period of 2.5 h. Naturally, salicylate was previously used as a probe for •OH detection in conjunction with HPLC [17,22,23], but not with colorimetry.

3.2. Mathematical treatment of data with competition kinetics

The basic equations used in competition kinetics for calculating •OH scavenging rate constants, as recommended by Halliwell and Gutteridge [11], can be summarized as follows:

$$\text{Probe (pr)} + {}^{\bullet}\text{OH} \rightarrow \text{Product}_1$$

$$\text{Scavenger (sc)} + {}^{\bullet}\text{OH} \rightarrow \text{Product}_2$$
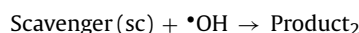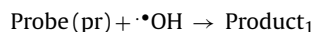
The rates of formation of the products, i.e., $(d[\text{Product}_i]/dt)$, are proportional to the corresponding CUPRAC absorbances:

$$\Delta A = A_o - A = K(k_{sc}[sc][{}^{\bullet}\text{OH}]) \tag{1}$$

$$A = K(k_{pr}[pr][{}^{\bullet}\text{OH}]) \tag{2}$$

where K is the instrumental constant, A is the absorbance in the presence of hydroxyl radical scavengers (sc) at concentration [sc] and A_o the absorbance in the absence of a scavenger; rate constants of reactions in the presence (k_{sc}) or absence of scavenger (k_{pr}), [pr] is the concentration of salicylate used in the experiment. CUPRAC absorbance arises from the reduction of the Cu(II)–neocuproine reagent to the Cu(I)–chelate [19] by the hydroxylated probe, while the salicylate probe had a negligible original CUPRAC absorbance, i.e., its molar absorptivity was $\varepsilon = 58$ L mol^{-1} cm^{-1}.

When Eq. (1) is divided by Eq. (2), we get

$$\frac{A_0 - A}{A} = \frac{K(k_{sc}[sc][rad])}{K(k_{pr}[pr][rad])}$$

$$\Rightarrow \frac{A_0}{A} - 1 = \frac{k_{sc}[sc]}{k_{pr}[pr]} \tag{3}$$

$$\Rightarrow \frac{A_0}{A} = 1 + \left(\frac{k_{sc}[sc]}{k_{pr}[pr]} \right)$$

Naturally Eq. (3) is applicable to cases where the concentrations of the probe and scavenger are greatly in excess of that of the transient radical, and remain effectively constant during the process.

A rate constant for the reaction of the scavenger with hydroxyl radical can be deduced from the inhibition of colour formation due to hydroxylation of the probe. Competition kinetics involving a probe and a scavenger for •OH reaction using various concentrations of the reactants should yield a straight line when A_o/A is plotted as a function of [sc]/[pr], where the slope would yield the ratio of the associated rate constants (the means for $N = 7$ data points regarding the slope

Table 1
The $^\bullet$OH scavenging activity of various antioxidant compounds using the modified CUPRAC method with a salicylate probe (linear equations with respect to Eq. (3), mean $\pm$ S.D., $N = 7$ data points)

$^\bullet$OH scavengers	Linear equation and correlation coefficient	Rate const. ($M^{-1} s^{-1}$)
$Na_2S_2O_5$ (10^{-3} M)	$y = 0.54x + 0.99$; r: 0.9872	$(1.27 \pm 0.13) \times 10^{10}$
Ascorbic acid (10^{-2} M)	$y = 0.05x + 0.98$; r: 0.9654	$(1.17 \pm 0.01) \times 10^{9}$
Mannitol (10^{-2} M)	$y = 0.04x + 0.99$; r: 0.9845	$(9.40 \pm 0.02) \times 10^{8}$
Glucose (10^{-2} M)	$y = 0.02x + 1.01$; r: 0.9864	$(4.70 \pm 0.02) \times 10^{8}$
DMSO (10^{-2} M)	$y = 0.50x + 1.15$; r: 0.9863	$(1.17 \pm 0.08) \times 10^{10}$
$Na_2S_2O_3$ (10^{-2} M)	$y = 0.63x + 1.09$; r: 0.9911	$(1.48 \pm 0.10) \times 10^{10}$

Note: $y = A_o/A$, $x = [sc]/[pr]$, as described in Eq. (3).

differed by $\leq \pm 6$–7%), and the intercept would be approximately equal to 1. The calculated rate constants of scavengers were proportional to the slopes of these lines, and the precision of data was associated with the linear correlation coefficients.

3.3. Comparative evaluation of hydroxyl radical scavenging rate constants

The rate constants of $^\bullet$OH scavenging of many aqueous metal ions is less than $3 \times 10^8 \, M^{-1} \, s^{-1}$, while for many reducing agents and organic molecules, it is at the order of 10^9–10^{10} [30]. We took thiourea as the reference compound, and using the second-order rate constant of thiourea for $^\bullet$OH reaction: $k \, (M^{-1} \, s^{-1}) = 4.7 \times 10^9$ as given by Halliwell [31], we measured the hydroxyl radical scavenging constant of the salicylate probe of this work as $2.35 \times 10^{10} \, M^{-1} \, s^{-1}$. With similar calculations, we found the k for 2-deoxy-D-ribose using the TBARS method as 2.97×10^9 against thiourea (the second-order rate constant of which is known), whereas its k is reported in the literature as $3.1 \times 10^9 \, M^{-1} \, s^{-1}$ [13]. With the use of Eq. (3), A_o/A plots as a function of [sc]/[pr] gave linear curves. The linear equations for $^\bullet$OH scavenger compounds in accord with Eq. (3), their linear correlation coefficients, and their calculated second-order rate constants are given in Table 1 with the tested probes using the CUPRAC method, and in Table 2 with the deoxyribose probe using the TBARS method. Naturally, since the competitive kinetic method of calculation is relative to certain reference compounds, no rate constant calculated with a given method should be expected to be identical to that with another, but their orders of magnitude should be comparable. The rate constants for metabisulfite, ascorbic acid, and mannitol calculated with the use of the salicylate probe (Table 1) were comparable to those found using the p-aminobenzoate as the reference probe [21]. Likewise, the values for mannitol and glucose using salicylate (Table 1) were in accord with those found with 2,4-dimethoxybenzoate [21]. The observation that glucose gave a higher $^\bullet$OH scavenging constant than ascorbic acid using the TBARS method with a deoxyribose probe (Table 2) pointed

Table 2
The $^\bullet$OH scavenging activity of various antioxidant compounds using the TBARS method with a 2-deoxy-D-ribose probe (linear equations with respect to Eq. (3), mean $\pm$ S.D., $N = 7$ data points)

$^\bullet$OH scavengers	Linear equation and correlation coefficient	Rate const. ($M^{-1} s^{-1}$)
$Na_2S_2O_5$ (10^{-3}M)	$y = 2.66x + 0.90$; r: 0.9965	$(8.25 \pm 0.17) \times 10^{9}$
Ascorbic Acid (10^{-2}M)	$y = 0.10x + 0.98$; r: 0.9380	$(3.10 \pm 0.04) \times 10^{8}$
Mannitol (10^{-2}M)	$y = 0.26x + 0.90$; r: 0.9781	$(8.10 \pm 0.02) \times 10^{8}$
Glucose (10^{-2}M)	$y = 0.41x + 1.05$; r: 0.9932	$(1.27 \pm 0.03) \times 10^{9}$
DMSO (10^{-3}M)	$y = 1.01x + 0.94$; r: 0.9943	$(3.13 \pm 0.08) \times 10^{9}$
$Na_2S_2O_3$ (10^{-2}M)	$y = 0.77x + 1.00$; r: 0.9857	$(2.39 \pm 0.19) \times 10^{9}$

Note: $y = A_o/A$, $x = [sc]/[pr]$, as described in Eq. (3).
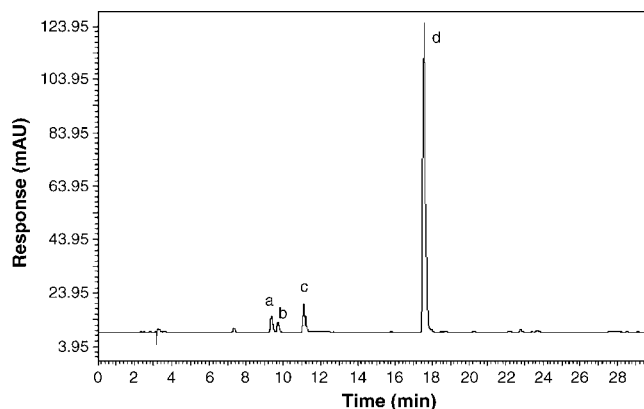
Fig. 2. The HPLC chromatogram for salicylate and its hydroxylation products in the absence of hydroxyl radical scavengers (HPLC separation of hydroxylation products extracted from salicylate (10 mM) incubated at pH 7 with a ferrous salt (20 mM) for 2 h at 37 °C and monitored at 280 nm). The retention times were (a) 2,5-DHBA 9.38 min; (b) 2,4-DHBA 9.78 min; (c) 2,3-DHBA 11.20 min; (d) salicylate 17.65 min.

out to possible errors inherent in this non-specific method. If the hydroxyl radicals were generated from an alternative system such as (Fe(III) + ascorbic acid + hydrogen peroxide) instead of the Fenton system used in this study [3], measurement of the scavenging rate constant of ascorbic acid would not be possible.

3.4. Comparison of the findings with modified CUPRAC and HPLC methods

During the development of salicylate as a hydroxylation probe [17,22,23], the basic products were identified as dihydroxybenzoic acid (DHBA) isomers (Fig. 1). For the salicylate probe without a scavenger, the HPLC chromatogram of the probe and its hydroxylation products is given in Fig. 2 (the conditions for the chromatogram are shown in the figure legend). The retention times of the identified peaks are very close to those recorded in the presence of $Na_2S_2O_3$ (Fig. 3) and DMSO (Fig. 4) as scavengers. As a result of the Fenton reaction, product conversion varied with respect to the nature of scavenger, e.g., the conversion ratio of the original probe to products in the presence of rapid scavengers (DMSO, $Na_2S_2O_5$, $Na_2S_2O_3$) was approximately 23–27%, whereas with slower scavengers (ascorbic acid, mannitol, glucose), this ratio increased to
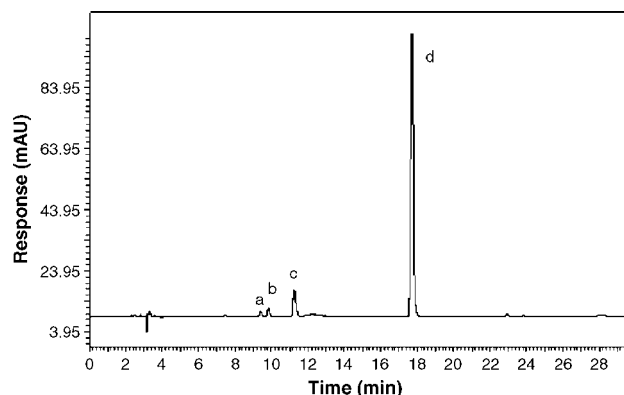
Fig. 3. The HPLC chromatogram for salicylate and its hydroxylation products in the presence of 1.0 mL 10^{-2} M $Na_2S_2O_3$ as hydroxyl radical scavenger (HPLC separation of hydroxylation products extracted from salicylate (10 mM) incubated at pH 7 with a ferrous salt (20 mM) for 2 h at 37 °C and monitored at 280 nm). The retention times were (a) 2,5-DHBA 9.41 min; (b) 2,4-DHBA 9.84 min; (c) 2,3-DHBA 11.25 min; (d) salicylate 17.71 min.

Table 3
The comparison of results with CUPRAC and HPLC assays using a salicylate probe

Sample	Composition of mixture	Concentration (M)	Expected absorbance (with respect to HPLC)	Yield % with respect to HPLC	Expected overall absorbance with respect to HPLC analysis	Experimentally found absorbance with respect to CUPRAC
Reference without scavengers	2,5-DHBA	1.35×10^{-4}	0.69	12.35	1.61 ± 0.02	1.70 ± 0.01
	2,4-DHBA	1.78×10^{-4}	0.10	16.28		
	2,3-DHBA	1.99×10^{-4}	0.82	18.21		
	SA	5.81×10^{-4}	0.005	53.15		
1.0 mL 1×10^{-2} M DMSO	2,5-DHBA	6.09×10^{-5}	0.31	4.68	0.84 ± 0.11	0.86 ± 0.03
	2,4-DHBA	1.74×10^{-4}	0.10	13.36		
	2,3-DHBA	1.03×10^{-4}	0.42	7.91		
	SA	9.65×10^{-4}	0.007	74.11		
1.0 mL 1×10^{-2} M Na$_2$S$_2$O$_3$	2,5-DHBA	1.38×10^{-6}	0.01	0.14	0.47 ± 0.06	0.62 ± 0.05
	2,4-DHBA	1.72×10^{-4}	0.10	17.22		
	2,3-DHBA	8.62×10^{-5}	0.35	8.63		
	SA	7.40×10^{-4}	0.006	74.07		
1.0 mL 1×10^{-2} M mannitol	2,5-DHBA	7.57×10^{-5}	0.39	7.14	1.05 ± 0.10	0.94 ± 0.04
	2,4-DHBA	1.76×10^{-4}	0.10	16.60		
	2,3-DHBA	1.36×10^{-4}	0.56	12.84		
	SA	6.72×10^{-4}	0.006	63.39		
1.0 mL 1×10^{-2} M glucose	2,5-DHBA	8.06×10^{-5}	0.41	8.15	1.03 ± 0.10	0.89 ± 0.02
	2,4-DHBA	1.75×10^{-4}	0.10	17.69		
	2,3-DHBA	1.24×10^{-4}	0.51	12.54		
	SA	6.10×10^{-4}	0.005	61.67		
1.0 mL 1×10^{-2} M Na$_2$S$_2$O$_5$	2,5-DHBA	2.62×10^{-5}	0.13	2.18	0.54 ± 0.01	0.53 ± 0.02
	2,4-DHBA	1.71×10^{-4}	0.10	14.25		
	2,3-DHBA	7.39×10^{-5}	0.30	6.16		
	SA	9.29×10^{-4}	0.007	77.42		
1.5 mL 1×10^{-2} M ascorbic acid	2,5-DHBA	1.17×10^{-4}	0.60	10.63	1.29 ± 0.09	1.31 ± 0.02
	2,4-DHBA	1.76×10^{-4}	0.10	16.00		
	2,3-DHBA	1.41×10^{-4}	0.58	12.82		
	SA	6.69×10^{-4}	0.006	60.82		
0.5 mL 1:5 diluted green tea infusion	2,5-DHBA	1.18×10^{-4}	0.60	9.17	1.29 ± 0.01	1.18 ± 0.08
	2,4-DHBA	1.76×10^{-4}	0.10	13.67		
	2,3-DHBA	1.41×10^{-4}	0.58	10.95		
	SA	8.52×10^{-4}	0.007	66.20		

37–40% due to less competition for $^\bullet$OH (Table 3). The linear calibration equations and correlation coefficients of hydroxylated salicylate products with respect to HPLC and CUPRAC methods are tabulated in Table 4.

3.5. Additivity of CUPRAC absorbances of dihydroxybenzoate products, and statistics

Among the hydroxylation products of salicylate, the DHBA isomers having the highest CUPRAC molar absorptivities were 2,5-DHBA ($\varepsilon = 4.2 \times 10^4$ L mol^{-1} cm^{-1}) and 2,3-DHBA ($\varepsilon = 3.4 \times 10^4$ L mol^{-1} cm^{-1}), and therefore these two isomers contributed with the highest share to the overall CUPRAC absorbance of the hydroxylation products after the Fenton reaction. As for the final form of analytes detected in the colour reaction of this

work, the limit of detection (LOD) of the two major chromophores produced from the salicylate probe upon $^\bullet$OH attack, i.e., 2,3-DHBA and 2,5-DHBA, were 1.3×10^{-7} and 2.2×10^{-7} M, respectively. Considering that the molar absorptivity of the TBA-MDA adduct was 1.53×10^5 L mol^{-1} cm^{-1}, it may be calculated that the detectable concentrations of MDA were roughly at the same order of magnitude. On the other hand, calculation of LOD in terms of hydroxyl radical attack on the initial probe gives a different picture: only a small percentage of the carbohydrate probe is converted to TBA-reactive substances in the deoxyribose assay [13,21], whereas in the proposed CUPRAC assay, probe conversion into colored products is definitely more efficient. Thus, detection limits in terms of initial analytes are lower for the proposed assay. The original probe almost showed no interference since its ε value was only 58, while 2,4-DHBA had $\varepsilon = 4.3 \times 10^3$ L mol^{-1} cm^{-1} because it

Table 4
Linear calibration equations and correlation coefficients of hydroxylated salicylate products with respect to HPLC and CUPRAC methods

Hydroxylated salicylate products	Linear equation and correlation coefficient (CUPRAC)	Linear equation and correlation coefficient (HPLC)
2,3-Dihydroxybenzoic acid	$y = 3.4 \times 10^4 x - 0.01$ $r = 0.9994$	$y = 5.9 \times 10^8 x + 12{,}107$ $r = 0.9998$
2,4-Dihydroxybenzoic acid	$y = 4.3 \times 10^3 x + 0.1$ $r = 0.9985$	$y = 3.4 \times 10^9 x - 569{,}039$ $r = 0.9957$
2,5-Dihydroxybenzoic acid	$y = 4.2 \times 10^4 x + 0.02$ $r = 0.9982$	$y = 3.3 \times 10^8 x + 5{,}969$ $r = 0.9999$
Sodium salicylate	$y = 58x + 0.007$ $r = 0.9943$	$y = 1.4 \times 10^9 x + 8{,}973$ $r = 0.9999$

Note: x = molar concentration of analyte (DHBA or salicylate), y = absorbance in the CUPRAC evaluation, y = peak area in the HPLC evaluation.
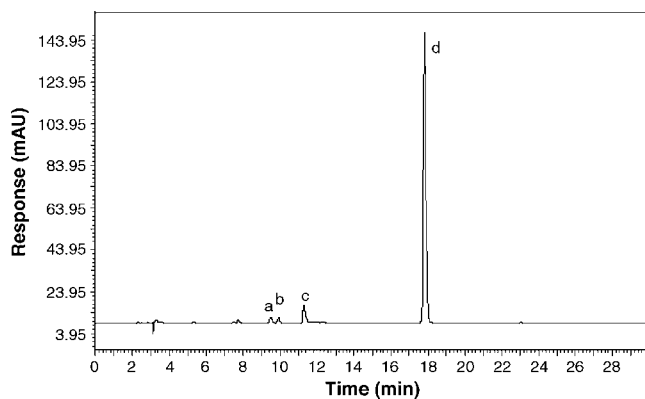
Fig. 4. The HPLC chromatogram for salicylate and its hydroxylation products in the presence of 1.0 mL 10^{-2} M DMSO as hydroxyl radical scavenger (HPLC separation of hydroxylation products extracted from salicylate (10 mM) incubated at pH 7 with a ferrous salt (20 mM) for 2 h at 37 °C and monitored at 280 nm). The retention times were (a) 2,5-DHBA 9.49 min; (b) 2,4-DHBA 9.90 min; (c) 2,3-DHBA 11.31 min; (d) salicylate 17.80 min.

lacked the *ortho-* and *para*-substituents for electron donation to stabilize the aryloxyl radical formed when the phenolic-OH lost an electron, i.e., a very important property of antioxidants [32]. By the use of calibration lines (or molar absorptivities) of individual DHBA isomers listed in Table 4, it was possible to calculate the overall CUPRAC absorbance of hydroxylation products (within ≤5–10% error) using the principle of additivity of absorbances of a mixture obeying Beer's law (Table 3). The concentrations of dihydroxybenzoates produced by radical attack from the probe were determined by HPLC, and the sum of (concentration x absorptivity) products of these components approximately agreed with the experimentally found CUPRAC absorbances, confirming the validity of Beer's law for the selected system. HPLC analysis of the Fenton reaction products showed that in the absence of hydroxyl radical scavengers, about half of the original probe (salicylate) remained intact whereas 2,3-; 2,4-; and 2,5-DHBA yields were $18.2 \pm 0.2\%$, $16.3 \pm 0.1\%$, and $12.4 \pm 0.6\%$, respectively. Using these conversion ratios, the CUPRAC absorbance of the final mixtures could be calculated by the equation [19]:

$$(\text{Total CUPRAC Absorbance})_{\text{expected}} = \sum \varepsilon_i C_i \qquad (4)$$

where ε_i and C_i were the molar absorptivity and concentration, respectively, of component (i) in the final mixture, using a 1-cm optical cell (*i* varied from 1 to 4, as shown in Table 3). Chromatographic calculation of the concentration of each species in the absence or presence of scavengers was made with the aid of calibration curves of salicylate and its hydroxylation products (DHBAs) drawn as peak area of analyte *versus* concentration (Table 4). The retention times of analytes in a real hydroxylated mixture were confirmed with the use of synthetic mixtures and the technique of standard additions. The HPLC-calculated concentrations were multiplied with the dilution ratio described in the CUPRAC method (i.e., 0.5/4.1), and these normalized concentrations were substituted in the corresponding CUPRAC calibration equations (Table 4) to find the theoretically expected absorbances. The accordance of expected and actually found absorbances was checked. Isomeric (DHBA) product ratio did not appreciably change under the selected reaction conditions in the absence of scavengers, but 2,3-DHBA/2,5-DHBA isomer ratio varied between 1.2 and 1.8 in the presence of scavengers not containing multivalent sulfur atoms (see Table 3). In these experiments, thiosulfate and metabisulfite exhibited anomalously high isomer ratios, possibly similar to the anomaly observed by ESR spectroscopy in the addition of S-containing intermediates

produced by •OH reaction with sulfide to a number of unsaturated compounds [33]. As the isomeric product ratio may show drastic changes with very fast scavengers, the reader is recommended to revert to another recent method published by the same authors [34] for measuring the •OH scavenging ability of extremely fast scavengers – such as phenolics and flavonoids – that are soluble in ethylacetate with •OH scavenging rate constants at the order of 10^{11}–10^{12} M^{-1} s^{-1}. Assuming that the 2,3-DHBA/2,5-DHBA product ratio is 1.47 for the reference sample (without scavengers) in Table 3, it could be easily calculated how a significant change in product ratio would affect the observed absorbance when the relative concentrations of the highest absorbing products, 2,3- and 2,5-DHBA, were to change within ±20% in a mixture of fixed total hydroxylated product concentration. Since the molar absorptivities of the two highly absorbing products are close, this calculation for the hypothetical extremes of product ratio (i.e., ±20%) showed that the overall expected absorbance would change by only ≤±2%, verifying the robustness of the proposed method for hydroxyl radical detection. Thus the more sophisticated but simultaneously more costly and lengthy HPLC procedure of hydroxyl radical detection could be completely substituted with the proposed colorimetric method.

The two-way ANOVA comparison by the aid of *F*-test of the mean-squares of 'between-treatments' (i.e., theoretically expected HPLC–CUPRAC absorbance and experimentally found CUPRAC absorbance of different samples in Table 3) and of residuals [35] for a number of real samples (consisting of a reference solution without scavenger, six standard water-soluble hydroxyl radical scavengers, and a green tea extract solution) enabled to conclude that there was no significant difference between treatments. In other words, the experimentally found CUPRAC results and theoretically expected HPLC–CUPRAC calculations were alike at 95% confidence level ($F_{\text{exp}} = 2.490$, $F_{\text{crit}} = 4.494$, $F_{\text{exp}} < F_{\text{crit}}$ at $P = 0.05$). Thus, the proposed methodology was validated against HPLC. On the other hand, there was significant difference between samples with respect to concentration of hydroxylated species (i.e., the 'residual' mean-square was much greater than 'between-sample' mean-square at 95% confidence level), indicating different extents of hydroxylation of the probe in the presence of different scavengers.

4. Conclusions

Aromatic hydroxylation – rather than the non-specific TBARS assay – is one of the most specific methods available for the detection of hydroxyl radicals [23], and this has been realized with the simple and inexpensive CUPRAC colorimetric method validated by HPLC analysis of hydroxylation products of salicylate. It is obvious that the proposed CUPRAC/salicylate assay of •OH detection is much more efficient than the conventional TBARS assay, because (i) approximately half of the salicylate probe is converted into hydroxylation products upon hydroxyl radical attack in the absence of a scavenger; (ii) about 30% of the probe is converted into two highly CUPRAC-absorbing species (i.e., 2,3-DHBA and 2,5-DHBA) in the absence of a scavenger; (iii) these two product DHBAs are responsible for ≥92% of the overall CUPRAC absorbance observed. On the other hand, the widely used TBARS assay is of low yield, because only a small percentage (at an order not exceeding a few %) of the deoxyribose probe is converted into TBA-reactive substances (such as malondialdehyde) yielding colored products [21,36]. At sufficiently low concentrations of food extracts, the proposed spectrophotometric method may be used specifically for hydroxyl radical scavenging measurement without interference from antioxidant vitamins and polyphenolics (that could normally respond to the CUPRAC assay).

Acknowledgements

References

[1] B. Halliwell, J.M.C. Gutteridge, Free Radicals in Biology and Medicine, Oxford University Press, Oxford, U.K., 1989.
[2] B. Halliwell, O.I. Aruoma, FEBS Lett. 281 (1991) 9.
[3] B. Halliwell, J.M.C. Gutteridge, FEBS Lett. 307 (1992) 108.
[4] B. Halliwell, J.M.C. Gutteridge, Biochem. J. 219 (1984) 1.
[5] B. Halliwell, J.M.C. Gutteridge, Arch. Biochem. Biophys. 246 (1986) 501.
[6] S.-X. Chen, P. Schopfer, Eur. J. Biochem. 260 (1999) 726.
[7] J.M.C. Gutteridge, Biochem. J. 243 (1987) 709.
[8] J.M.C. Gutteridge, FEBS Lett. 128 (1981) 343.
[9] B. Halliwell, J.M.C. Gutteridge, FEBS Lett. 128 (1981) 347.
[10] O.I. Aruoma, M. Grootveld, B. Halliwell, J. Inorg. Biochem. 29 (1987) 289.
[11] B. Halliwell, J.M.C. Gutteridge, O.I. Aruoma, Anal. Biochem. 165 (1987) 215.
[12] J.A. Buege, S.D. Aust, Methods Enzymol. 52 (1978) 302.
[13] Z. Cheng, Y. Li, W. Chang, Anal. Chim. Acta 478 (2003) 129.
[14] A. Valenzuela, Life Sci. 48 (1991) 301.
[15] H.H. Draper, M. Hadley, Methods Enzymol. 186 (1990) 421.
[16] B. Halliwell, M. Grootveld, J.M.C. Gutteridge, Methods Biochem. Anal. 33 (1988) 59.
[17] M. Grootveld, B. Halliwell, Biochem. J. 237 (1986) 499.
[18] S. Singh, R.C. Hider, Anal. Biochem. 171 (1988) 47.
[19] R. Apak, K. Güçlü, M. Özyürek, S.E. Karademir, J. Agric. Food Chem. 52 (2004) 7970.
[20] R. Apak, K. Güçlü, M. Özyürek, S.E. Karademir, M. Altun, Free Radic. Res. 39 (2005) 949.
[21] B. Bektasoglu, S.E. Çelik, M. Özyürek, K. Güçlü, R. Apak, Biochem. Biophys. Res. Commun. 345 (2006) 1194.
[22] H. Kaur, B. Halliwell, Methods Enzymol. 233 (1994) 67.
[23] A. Ghiselli, Methods in molecular biology, in: D. Armstrong (Ed.), Free Radical and Antioxidant Protocols, vol. 108, Humana Press, 1998, p. 89.
[24] A. Giovanni, L.P. Liang, T.G. Hastings, M.J. Zigmond, J. Neurochem. 54 (1995) 1819.
[25] O.I. Aruoma, B. Halliwell, B.M. Hoey, J. Butler, Biochem. J. 256 (1988) 251.
[26] J.M.C. Gutteridge, Biochem. J. 224 (1984) 761.
[27] M. Grootveld, B. Halliwell, Free Radic. Res. Commun. 1 (1986) 243.
[28] J.M. Joseph, C.T. Aravindakumar, J. Biochem. Biophys. Methods 42 (2000) 115.
[29] A.J. Gomes, C.N. Lunardi, S. Gonzales, A.C. Tedesco, Braz. J. Med. Biol. Res. 34 (2001) 1487.
[30] G.V. Buxton, C.L. Greenstock, W.P. Helman, A.B. Ross, J. Phys. Chem. Ref. Data 17 (1988) 513.
[31] B. Halliwell, FEBS Lett. 92 (1978) 321.
[32] R. Apak, K. Güçlü, B. Demirata, M. Özyürek, S.E. Çelik, B. Bektaşoğlu, K.I. Berker, D. Özyurt, Molecules 12 (2007) 1496.
[33] Y. Kirino, R.W. Fessenden, J. Phys. Chem. 79 (1975) 834.
[34] M. Özyürek, B. Bektaşoğlu, K. Güçlü, R. Apak, Anal. Chim. Acta 616 (2008) 196.
[35] J.C. Miller, J.N. Miller, Statistics for Analytical Chemists, third ed., Ellis Horwood/Prentice Hall, New York/London, 1993.
[36] N. Hogg, V.M. Darley-Usmar, M.T. Wilson, S. Moncada, Biochem. J. 281 (1992) 419.

Ligandless cloud point extraction of Cr(III), Pb(II), Cu(II), Ni(II), Bi(III), and Cd(II) ions in environmental samples with Tween 80 and flame atomic absorption spectrometric determination

Secil Candir [a,b], Ibrahim Narin [b,*], Mustafa Soylak [c]

[a] Erciyes University, Institute of Health Sciences, Department of Analytical Chemistry, 38039 Kayseri, Turkey
[b] Erciyes University, Faculty of Pharmacy, Department of Analytical Chemistry, 38039 Kayseri, Turkey
[c] Erciyes University, Faculty of Art and Science, Department of Chemistry, 38039 Kayseri, Turkey

ABSTRACT

A cloud point extraction (CPE) procedure has been developed for the determination trace amounts of Cr(III), Pb(II), Cu(II), Ni(II), Bi(III), and Cd(II) ions by using flame atomic absorption spectrometry. The proposed cloud point extraction method was based on cloud point extraction of analyte metal ions without ligand using Tween 80 as surfactant. The surfactant-rich phase was dissolved with 1.0 mL 1.0 mol L^{-1} HNO$_3$ in methanol to decrease the viscosity. The analytical parameters were investigated such as pH, surfactant concentration, incubation temperature, and sample volume, etc. Accuracy of method was checked analysis by reference material and spiked samples. Developed method was applied to several matrices such as water, food and pharmaceutical samples. The detection limits of proposed method were calculated 2.8, 7.2, 0.4, 1.1, 0.8 and 1.7 μg L^{-1} for Cr(III), Pb(II), Cu(II), Ni(II), Bi(III), and Cd(II), respectively.

© 2008 Elsevier B.V. All rights reserved.

1. Introduction

Inductively coupled plasma-atomic emission spectrometry (ICP-AES), inductively coupled plasma-mass spectrometry (ICP-MS), electrothermal atomic absorption spectrometry (ET-AAS), UV–vis Spectrometer, etc. have been used methods for determination of trace metals [1–5]. Flame atomic absorption spectrometry (FAAS) is most commonly used for the determination of trace metals [6]. In many cases the determination of trace metals in environmental samples by FAAS is notably difficult due to both the low levels of these metals in the samples and the high complexity of the sample matrices. It is usually necessary to carry out a separation step prior to the analysis. Some method for separation and preconcentration of trace metal ions has been included solid phase extraction, membrane filtration and coprecipitation, etc. [7–10].

Cloud point extraction (CPE) is a separation and preconcentration method [11]. This method has been some advantages such as low cost, rapidly procedure and widely application field. Cloud point extraction has been applied to determination of trace metal ions from different matrices recently years [12–16]. Cloud point

extraction was applied two different methods for separation of metal ions. In first method, metal ions are occurring complex with suitable ligand. Other method is based on direct application of cloud point extraction procedure without any ligand.

Polyethylene glycol sorbitan monooleate is known as Tween 80. It is a non-ionic detergent and emulsifier. Tween 80 was used for selective protein extraction and isolation of nuclei from mammalian cell lines [17]. According to our literature study, Tween 80 has not been used for trace metal extraction by cloud point extraction. This study described a cloud point extraction procedure used as surfactant of Tween 80 for separation/preconcentration of Cr(III), Pb(II), Cu(II), Ni(II), Bi(II), and Cd(II) ions in different matrices such as water, food samples and pharmaceutical sample.

2. Experimental

2.1. Instrumentation

A Varian AA240 model flame atomic absorption spectrometer was used for determination of metals. The operating parameters of elements were set according to the manufacturer recommendation. These conditions were presented in Table 1. For measuring pH values in the aqueous phase, WTW 330i model glass-electrode was employed. Pharmaceutical samples were decomposed by Bandelin model Sonorex Type RK52H ultrasonic bath.

* Corresponding author. Tel.: +90 352 4380486; fax: +90 352 4379169.
  E-mail address: narin@erciyes.edu.tr (I. Narin).

Table 1
Conditions for flame atomic absorption spectrometer

Elements	Wavelength, λ (nm)	Slit width (nm)	Lamp current (mA)
Cr(III)	357.9	0.2	40
Pb(II)	217.0	1.0	20
Cu(II)	224.8	0.5	100
Ni(II)	232.0	0.2	5
Bi(III)	223.1	0.2	15
Cd(II)	228.8	0.5	40

2.2. Reagents

All chemicals were at least of analytical grade. Deionised water (Millipore Elix® 5 UV resistant $14\,M\Omega\,cm^{-1}$) and high purity reagents were used for all preparations of the standard and sample solutions. The non-ionic surfactant Tween 80 (Sigma, St. Louis, MO, USA) was used without further purification. Stock standard solutions of ions at a concentration of $1000\,mg\,L^{-1}$ were prepared from nitrate salts of elements. Working standard solutions were prepared by dilution these stock solutions. All the plastic and glassware equipments were cleaned by soaking in dilute HNO_3 $(1+9)$ and were rinsed with deionised water prior to use. Phosphate buffers $(0.1\,mol\,L^{-1})$ for pH 7–8.5 and ammonium chloride buffer solutions $(0.1\,mol\,L^{-1})$ for pH 9–10 were used in the experiments.

2.3. Procedure for cloud point extraction

Proposed procedure of cloud point extraction was tested by using model solution. Ten micrograms of Cr(III), Pb(II) and 5 µg of Cu(II), Ni(II), Bi(III), Cd(II) were added to approximately 5–10 mL deionised water in a polyethylene centrifuged tube (capacity of 25 mL). Then, this model solution was adjusted to the pH 8.5 by 5 mL of phosphate buffer. Three millilitres of Tween 80 (4%, w/w) solution was added to the model solution. The tube was heated for 60 min in a thermostatic water bath at 60 °C. Then this turbid solution was cooled for 20 min at +4 °C in refrigerator. The solution was centrifuged for 10 min at 3500 rpm. Surfactant-rich phase was separated to aqua phase by simple decantation. The surfactant-rich phase was dissolved with 1.0 mL $1.0\,mol\,L^{-1}$ HNO_3 in methanol to decrease the viscosity. The final volume was completed to 5 mL with $1.0\,mol\,L^{-1}$ HNO_3 solution. Metal concentration of final solution was determined flame atomic absorption spectrometer in acetylene/air flame. The calibration curves were developed under the optimum conditions of the cloud point extraction procedure.

2.4. Sample preparation

About 100 mg of a reference material (SRM 07310) sample were treated with 15 mL aqua regia. Then this mixture heated to dryness. This process was repeated twice. The residue was solved wit approximately 10–15 mL with 10 mL of deionised water. The reference material was filtered through a blue band filter paper and the insoluble part was washed with distilled water. The chromium picolinate tablet (Solgar®, vegetable capsule) was decomposed with aqua regia. For the decomposition, about 100 mg of chromium picolinate tablet were treated with 15 mL aqua regia. This mixture was heated in approximately 60–70 °C by ultrasonic bath. This solution was clearly. Because of, this solution is not to be treatment. pH of this solutions were adjusted to 7–8 with $0.1\,mol\,L^{-1}$ NaOH solution. Then, proposed cloud point extraction given above was applied the final solutions. Proposed cloud point extraction method was applied to water samples without any treatment. Crushed wheat, hazelnut and tomato paste samples were digested with 15 mL aqua regia by ultrasonic bath at about 60–70 °C. This solu-
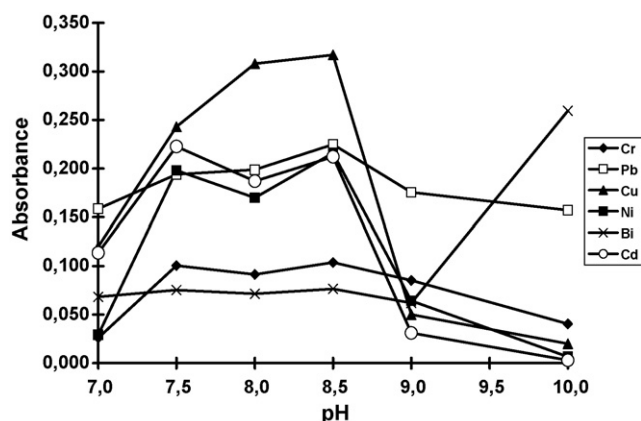
Fig. 1. pH–absorbance graph ($N = 7$).

tion was neutralized with $0.1\,mol\,L^{-1}$ NaOH solution. A proposed cloud point extraction method was applied to the solution.

3. Results and discussion

To determine the optimal condition for maximum extraction efficiencies for analytes, some analytical parameters including pH, surfactant concentrations, incubation temperature, sample volume, and interfering ions were examined.

3.1. Effect of pH

The effect of pH to the extraction systems was investigated in the range of 2–10. The micelles phase was not be occurring between pH 2 and 6.5. The results were depicted in Fig. 1. Optimum pH for proposed extraction system was preferred to 8.5.

3.2. Effect of Tween 80

The concentration of surfactant that is used in the CPE is a critical factor. Thus, amount of Tween 80 was investigated between 0.5 and 4.5 mL of Tween 80 (4%, v/v) for extraction performance. The results were given in Fig. 2. At point zero for concentration of Tween 80, absorbance of metals was 0. Absorbance values of analyte metal ions were approximately same value in the between 0.5 and 4.5 mL of surfactant. For all the other works, 3.0 mL of 4% (v/v) Tween 80 was used for not effect more sample volume.

3.3. Effect of temperature

In cloud point extraction system, temperature of extraction is very important parameter for micelleus occurring. The effect of
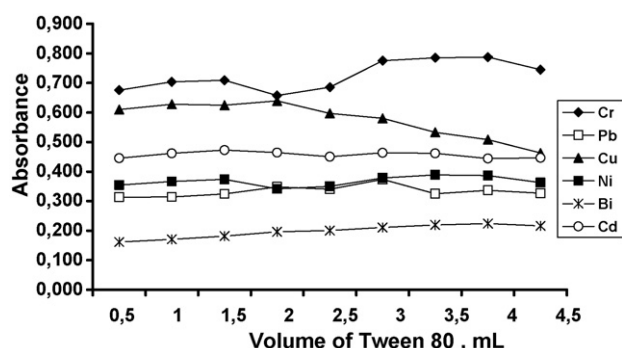
Fig. 2. Tween 80 volume–absorbance ($N = 7$).
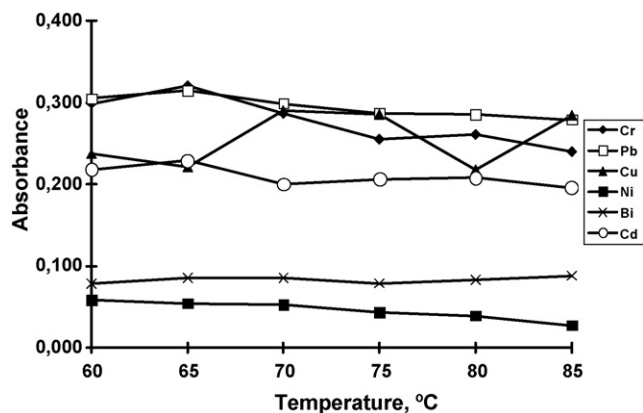
Fig. 3. Graph of temperature–absorbance ($N = 7$).

equilibration temperature was investigated from 60 to 85 °C. At lower temperatures than 60 °C the separation of the two phases was not complete. After 60 °C, the absorbance was approximately same value (Fig. 3). The incubation time was kept at 60 min which is sufficient for the completion of the physicochemical processes. Thus incubation temperature was to determine at 60 °C.

3.4. Effect of sample volume

In order to obtain high preconcentration factor, the sample volume is one of important analytical factor for preconcentration. The effect of sample volume was examined in the sample volume range of 10–50 mL. Investigated trace metal ions were recovered quantitatively in the all-working range (10–50 mL).

3.5. Interferences

The interferic effects of the some cation and anion were examined under optimized conditions. These results indicate that the metal recoveries are almost quantitative in the presence of investigated foreign ions (Table 2). The quantitative recover is accepted from 93% to 105% recoveries.

Table 2
Tolerable level of matrix ions, $\mu g\,mL^{-1}$ ($N = 7$)

Element	Matrix ion									
	Na^+	K^+	Mn^{2+}	Ca^{2+}	Mg^{2+}	Fe^{3+}	SO_4^{2-}	Cl^-	Co^{2+}	Zn^{2+}
Cr	1000	2500	50	5000	500	10	250	750	20	20
Pb	1000	1000	50	500	100	10	200	750	10	10
Cu	5000	5000	25	5000	500	50	500	750	7.5	7.5
Ni	5000	2500	50	5000	500	10	500	750	7.5	7.5
Bi	5000	5000	25	5000	500	10	500	5000	10	10
Cd	5000	1000	10	2500	250	50	500	1000	10	10

Table 3
Linear calibration range of elements

Ion	Linear calibration range of first calibration curve ($\mu g/mL$)	Linear calibration range of second calibration curve ($\mu g/mL$)
Cr(III)	0.5–1.5	2.0–10.0
Pb(II)	0.5–1.5	2.0–12.0
Cu(II)	0.2–0.6	1.0–6.0
Ni(II)	0.2–0.6	2.0–6.0
Bi(III)	0.5–1.5	1.0–6.5
Cd(II)	0.2–2.0	1.0–6.0

3.6. Calibration curves and detection limits

Calibration curves were obtained by preconcentration of standard solutions under optimized extraction conditions. Because of very narrow of the linear calibration range for the elements, two different calibration curves were obtained. The dynamic range of calibration curves for studied elements were in Table 3.

The detection limits (3σ) of Cr(III), Pb(II), Cu(II), Ni(II), Bi(III), and Cd(II) based on the tree times standard deviation of the blank were 2.8, 7.2, 0.4, 1.1, 0.8 and 1.7 $\mu g\,L^{-1}$, respectively [18].

3.7. Analysis of standard reference materials and chromium picolinate

The presented cloud point extraction procedure was applied to a sediment reference materials (SRM 07310) and a mineral tablet (chromium picolinate) for concentrations of Cr(III), Pb(II), Cu(II), Ni(II), Bi(III), and Cd(II) ions. The results were given in Table 4. The

Table 4
Analysis of standard reference materials and chromium picolinate tablet, $N = 4$

Element	SRM 07310			Chromium picalinate		
	Certificated value ($\mu g\,g^{-1}$)	Found value ($\mu g\,g^{-1}$)	Relative error (%)	Certificated value ($\mu g\,g^{-1}$)	Found value ($\mu g\,g^{-1}$)	Relative error (%)
Cr	136.0	127.3 ± 2.0	−6.0	200	194.6 ± 4.3	−2.7
Pb	27	25.8 ± 0.3	−4.4	–	53.6 ± 4.9	–
Cu	22.6	21.7 ± 4.4	−4.0	–	BDL	–
Ni	30.2	30.4 ± 3.1	0.6	–	18.2 ± 2.0	–
Bi	–	BDL	–	–	49.6 ± 7.8	–
Cd	1.12	5.9 ± 0.4	427	–	14.5 ± 1.6	–

BDL: below the detection limit.

Table 5
Trace metal levels of real samples, $N = 4$

Sample	Cr	Pb	Cu	Ni	Bi	Cd
Tap water 1*	13.4 ± 1.6	14.4 ± 0.8	BDL	BDL	33.8 ± 9.8	2.0 ± 0.3
Tap water 2*	13.8 ± 1.4	7.7 ± 0.4	BDL	1.9 ± 0.5	34.9 ± 8.6	2.0 ± 0.2
Mineral water 1*	236.3 ± 2.1	390.0 ± 38.8	BDL	94.0 ± 0.4	263.8 ± 43.2	69.8 ± 4.6
Mineral water 2*	230.5 ± 10.9	290.0 ± 10.3	BDL	109.6 ± 2.8	211.0 ± 19.2	71.9 ± 3.9
Mineral water 3*	242.5 ± 8.8	288.3 ± 10.4	BDL	91.8 ± 2.9	235.0 ± 15.4	84.5 ± 5.9
Crushed wheat**	12.5 ± 0.6	13.4 ± 0.6	BDL	4.0 ± 0.5	12.0 ± 1.8	3.5 ± 0.3
Hazelnut**	12.1 ± 0.2	16.3 ± 1.4	4.0 ± 0.3	4.6 ± 0.4	11.0 ± 0.6	16.3 ± 0.4
Tomato paste**	12.3 ± 0.6	14.6 ± 1.3	4.2 ± 0.1	4.0 ± 0.3	11.6 ± 1.3	14.6 ± 0.3

BDL: below the detection limit, mean ± S.D. *$\mu g\,L^{-1}$; **$\mu g\,g^{-1}$.

Table 6
Recovery of analytes from spiked natural water samples after application CPE, $N = 4$

Element	Added (μg L^{-1})	Tap water		Mineral water	
		Found (μg L^{-1})	Recovery (%)	Found (μg L^{-1})	Recovery (%)
Cr	–	13.8	–	25.7	–
	400	436.4	105.6	452.0	106.6
Pb	–	7.7	–	92.5	–
	400	378.9	92.8	509.9	104.4
Cu	–	BDL	–	34.8	–
	160	153.2	95.8	210.3	109.7
Ni	–	1.9	–	40.7	–
	160	149.8	92.4	203.5	101.8
Bi	–	34.9	–	235.0	–
	400	456.5	105.4	826.0	98.5
Cd	–	GSA	–	10.6	–
	160	158.8	98.0	172.9	101.4

BDL: below the detection limit.

Table 7
Recovery of trace element from spiked solid samples after application CPE, $N = 4$

Element	Added (μg g^{-1})	Crushed wheat		Hazelnut		Tomato paste	
		Found (μg g^{-1})	Recovery (%)	Found (μg g^{-1})	Recovery (%)	Found (μg g^{-1})	Recovery (%)
Cr	–	12.5	–	12.1	–	12.3	–
	20	36.5	120	34.0	114	35.7	117
Pb	–	13.4	–	16.3	–	14.6	–
	20	33.6	101	38.8	113	35.2	103
Cu	–	0.4	–	4.05	–	4.2	–
	8	5.42	63	4.36	4	9.5	67
Ni	–	GSA	–	4.6	–	4.0	–
	8	7.6	95	9.7	64	11.3	91
Bi	–	12.0	–	11.0	–	11.6	–
	20	34.3	112	32.8	109	35.3	118
Cd	–	3.5	–	16.3	–	14.6	–
	8	11.8	104	38.8	107	35.2	103

Table 8
Comparison of the characteristic data between recent published cloud point extraction methods and the developed method

Surfactant	Metals	Preconcentration factor	Limit of detection (μg L^{-1})	Method	References
Triton X-114	Bi	196	20	Electro thermal AAS	[19]
PONPE 7.5	Cd	62	0.560	Cold vapor AAS	[20]
Triton X-114	Cd	5	1.0	Flame AAS	[21]
Triton X-114	Cd.Ni	52/39	0.31/1.2	Flame AAS	[22]
Triton X-114	Cd/Cu/Pb/Zn	57.7/64.3/55.6/63.7	0.099/0.27/1.1/0.095	Flame AAS	[23]
Triton X-114	Co	5.8	0,021	Termospray flame AAS	[24]
Triton X-114	Co/Ni	57/65	0.24/0.44	Flame AAS	[25]
Triton X-114	Ge	200	0.59	Hydride generation AAS	[26]
Triton X-114	Cd/Pb	22/43	0.62/2.86	Flame AAS	[27]
Triton X-114	Co/Cu	15.9/16.3	0.12/0.26	Capillary electrophoresis	[28]
OP-10	Cu	10	10	Flame AAS	[29]
Tween 80	Cr/Pb/Cu/Ni/Bi/Cd	10	2.8/7.2/0.4/1.1/0.8/1.7	Flame AAS	Presented study

results are good agreement with the certificated values except cadmium. Relative errors of Cr(III), Pb(II), Cu(II), and Ni(II) are lower than 6.0%.

3.8. Analysis of real samples

The cloud point extraction procedure was applied to the separation and determination of Cr(III), Pb(II), Cu(II), Ni(II), Bi(III), and Cd(II) in two different tap water samples and tree different mineral water samples. The proposed procedure was applied to dried crushed wheat, a hazelnut and tomato paste samples. The results were given in Table 5.

For accuracy of the proposed method, the recovery of studied metals from water samples spiked with Cr(III), Pb(II), Cu(II), Ni(II), Bi(III), and Cd(II) and crushed wheat, hazelnut and tomato paste samples were also studied. The results tabulated in Tables 6 and 7. All elements in tap water samples and mineral water sample was quantitatively recovered (92.4–109.7%).

4. Conclusion

The proposed cloud point extraction method using surfactant as Tween 80 has shown to be an efficient, simple and rapidly separation and preconcentration methodology to deter-

mine for Cr(III), Pb(II), Cu(II), Ni(II), Bi(III), and Cd(II) in several matrices such as water, food samples and pharmaceutical sample. Effect of the extraction procedure was investigated analytical parameters such as pH, surfactant concentration, incubation temperature and foreign ions. The accuracy of method is assessed though recovery experiments and reference materials. Comparative data from recent papers on the cloud point extraction of some metal ions are summarized in Table 8. Preconcentration factor of developed method is generally more than small the other study. The detection limits of method are comparable level with the works in literature including cloud point extraction, solid-phase extraction and coprecipitation [28–32]. Simultaneous separation and preconcentration of six elements is one of the important advantages. The proposed method has been applied different matrices.

Acknowledgement

References

[1] S.L.C. Ferreira, J.B. de Andrade, M. das Graças, A. Korn, M. de, G. Pereira, V.A. Lemos, W.N.L. dos Santos, F. de Medeiros Rodrigues, A.S. Souza, H.S. Ferreira, E.G.P. da Silva, J. Hazard. Mater. 145 (2007) 358–367.
[2] H.C. dos Santos, M.G.A. Korn, S.L.C. Ferreira, Anal. Chim. Acta 426 (2001) 79–84.
[3] E.H. Evans, J.A. Day, A. Fisher, W.J. Price, C.M.M. Smith, J.F. Tyson, J. Anal. Atom. Spectrom. 19 (2004) 775–812.
[4] M. Kosanovic, M.Y. Hasan, D. Subramanian, A.A.F. Al Ahbabi, O.A.A. Al Kathiri, E.E.M.A. Aleassa, A. Adem, Food Chem. Toxicol. 45 (2007) 2261–2270.
[5] A. Sales, A. Alvarez, M.R. Areal, L. Maldonado, P. Marchisio, M. Rodriguez, E. Bedascarrasbure, J. Hazard. Mater. 137 (2006) 1352–1356.
[6] V.A. Lemos, L.S.G. Teixeira, M.A. Bezerra, A.C.S. Costa, J.T. Castro, L.A.M. Cardoso, D.S. de Jesus, E.S. Santos, P.X. Baliza, L.N. Santos, Appl. Spectrosc. Rev. 43 (2008) 303–334.
[7] S. Kartal, I. Ozdemir, S. Tokalioglu, V. Yılmaz, Sep. Sci. Technol. 42 (2007) 3199–3215.
[8] E. Kenduzler, Sep. Sci. Technol. 41 (2006) 1645–1659.
[9] I. Narin, M. Soylak, Anal. Chim. Acta 493 (2003) 205–212.
[10] A. Efendioglu, M. Yagan, B. Bati, J. Hazard. Mater. 149 (2007) 160–165.
[11] Y.U. Shen, Sep. Sci. Technol. 32 (1997) 2229–2235.
[12] M.A. Bezerra, A.R.A. Nogueira, L.A. Sergio, L.C. Ferreira, Int. J. Environ. Anal. Chem. 88 (2008) 131–142.
[13] V.A. Lemos, R.S. da Franca, Moreira, Sep. Purif. Technol. 54 (2007) 349–354.
[14] P.R. Aranda, R.A. Gil, S. Moyano, I.E. De Vito, L.D. Martinez, Talanta 75 (2008) 307–311.
[15] Y. Yamini, M. Faraji, S. Shariati, R. Hassani, M. Ghanbarian, Anal. Chim. Acta 612 (2008) 144–151.
[16] H. Sang, P. Liang, D. Du, J. Hazard. Mater. 154 (2008) 1127–1132.
[17] http://www.sigmaaldrich.com/catalog/search/ProductDetail/SIGMA/P4780/.
[18] http://www.iupac.org/goldbook/R05263.pdf.
[19] F. Shemirani, M. Baghdadi, R. Majid, M.R. Jamali, Anal. Chim. Acta 534 (2005) 163–169.
[20] J.L. Manzoori, H.A. Zadeh, M. Amjadi, Talanta 71 (2007) 582–587.
[21] A. Afkhami, T. Madrakian, H. Siampour, J. Hazard. Mater. 138 (2006) 269–272.
[22] J.L. Manzoori, K.M. Ghasem, Anal. Chim. Acta 521 (2004) 173–177.
[23] C. Jianrong, T.K. Chuan, Anal. Chim. Acta 450 (2001) 215–222.
[24] G.L. Donati, C.C. Nascentes, A.R.A. Nogueira, M.A.Z. Arruda, J.A. Nóbrega, Microchem. J. 82 (2006) 189–195.
[25] J. Chen, K.J. Teo, Anal. Chim. Acta 434 (2001) 325–330.
[26] A.E. Böyükbayram, M. Volkan, Spectrochim. Acta B 55 (2000) 1073–1080.
[27] J.L. Manzoori, A.B. Tabrizi, Anal. Chim. Acta 470 (2002) 215–221.
[28] A.N. Tang, D.Q. Jiang, X.P. Yan, Anal. Chim. Acta 507 (2004) 203–204.
[29] S.A. Kulichenko, V.O. Doroschuk, S.O. Lelyushok, Talanta 59 (2003) 767–773.
[30] A. Moghimi, H. Mossalayi, J. Korean Chem. Soc. 52 (2008) 144–148.
[31] U. Sahin, S. Kartal, A. Ulgen, Anal. Sci. 24 (2008) 751–757.
[32] Y. Surme, I. Narin, M. Soylak, H. Yuruk, M. Doğan, Microchim. Acta 157 (2007) 193–199.

Partition of horseradish peroxidase with maintained activity in aqueous biphasic system based on ionic liquid

Qing Cao[a], Li Quan[a], Chiyang He[b], Na Li[a], Kean Li[a], Feng Liu[a],*

[a] Beijing National Laboratory for Molecular Sciences, The Key Laboratory of Bioorganic Chemistry and Molecular Engineering,
Ministry of Education, College of Chemistry, Peking University, Chengfu Road, Beijing 100871, China
[b] Department of Chemistry, Anqing Normal College, Anqing 246011, China

ARTICLE INFO

ABSTRACT

Enzyme activity and partition behavior in aqueous biphasic systems (ABSs) consisting of ionic liquid (IL) and salt (IL-ABSs) were investigated to increase our understanding of IL-ABSs and shed light on their application potential as enzyme extraction system. With horseradish peroxidase (HRP) as the model enzyme, several effects of alkylimidazolium chloride–K_2HPO_4 ABSs on activity and partition behavior of enzyme were studied including alkyl chain length of ILs and concentrations of each component. High lyotropic ILs (1-butyl-3-methylimidazolium and 1-ethyl-3-methylimidazolium chloride) and adequate water content (>40%) were both essential for the activity maintenance of HRP in IL-ABS. 1-Butyl-3-methylimidazolium chloride ([C_4mim]Cl) was found to be an appropriate IL for phase forming and HRP activity retaining. After optimization of phase condition, about 80% HRP amount was distributed in the IL-rich upper phase, and greater than 90% enzyme activity was obtained. Moreover, compared with the commonly used polymer-based ABSs, this [C_4mim]Cl-ABS has a much lower viscosity, which is very beneficial to the experimental operation. Therefore, the tested IL-ABS could be considered as a potential enzyme extraction system.

© 2008 Elsevier B.V. All rights reserved.

1. Introduction

Ionic liquids (ILs) are sometimes called molten salts with melting point below 100 °C and composed entirely of ionic species. They have many fascinating features, such as negligible vapour pressure, high stability and widely tuneable properties by pairing different cations with any of a growing number of anions [1]. Therefore, ILs have received attention in recent years as "greener solvents" and "designer solvents" [2].

ILs have been proved to be a kind of very attractive extraction media as replacement of volatile organic compounds (VOCs). Effective extraction of metal ions, small organic compounds and DNA with hydrophobic IL–water systems have been reported [3–10]. However, IL is rarely applied to enzyme extraction. It might be due to several reasons: most enzymes are hardly soluble in hydrophobic ILs, causing the extraction process unavailable without extractant [11], while in hydrophilic ILs, inactivation of enzymes were frequently reported [12–14]. Moreover, hydrophilic ILs cannot be used directly for the extraction of analytes from aqueous solution due to their solubility. It is crucial to obtain both high enzyme activity and extraction efficiency for utilizing IL as enzyme extraction media.

Aqueous biphasic systems (ABSs) composed of ionic liquid and salt (IL-ABSs) might be a good choice for solving this problem. ABSs are comprised of two immiscible aqueous phases with variable concentrations of the solutes. Due to their relatively high content of water and no use of volatile organic compounds, ABSs are benign to proteins and friendly to environment, and therefore have been widely used for extraction and separation of organic compounds [15], inorganic ions [16], and biomolecules [17]. However, traditional ABSs composed of water-soluble polymer and salt or two incompatible polymers have high viscosity, form an opaque solution, and sometimes interfere with the analysis of analytes.

In 2003, IL-ABS was firstly reported for recycle, metathesis and study of the distribution ratios of short chain alcohols [18]. In our previous work, IL-ABS has been successfully applied to the extraction of steroids from human urine [19] and opium alkaloids from pericarpium papaveris [20]. Up to now, the preliminary application of IL-ABS on protein extraction was rarely reported, and the activity of protein after extraction was not determined [21,22]. Moreover, as far as we know, there is no report of enzyme partition or activity in IL-ABS. The investigation of the enzyme activity, stability and partition behavior would be helpful to largely expand its application.

The aim of this work is to increase our understanding of the influence of IL-ABSs on enzyme activity and investigate the enzyme partitioning in those systems. Horseradish peroxidase (HRP) was

---

* Corresponding author. Tel.: +86 10 62761187; fax: +86 10 62751708.
E-mail address: liufeng@pku.edu.cn (F. Liu).

chosen as the model enzyme, as it is one of the most widely used enzymes in bioanalysis and has been well-physicochemically characterized. Alkylimidazolium chloride ILs, as the most commonly used and inexpensive hydrophilic ILs, were used to form ABSs with K_2HPO_4, which has been reported as phase-forming salt of IL-ABS [19]. The phase-forming abilities of ILs with different alkyl chains were studied via phase diagrams. The HRP activities in corresponding IL-rich upper phase have been tested to understand how the property of IL may influence the enzyme activity. We also determined HRP stabilities in IL solutions with various water contents, in order to elucidate the water role in enzyme activity maintenance. Moreover, the partition behaviors and activities of HRP in [C_4mim]Cl-ABSs with different concentrations of IL, salt and enzyme were investigated in detail. Finally, the upper phase viscosity of the [C_4mim]Cl-ABS was determined and compared with that of poly(ethylene glycol) 4000 (PEG4000)-based ABS.

2. Experimental

2.1. Materials

Horseradish peroxidase (HRP) was acquired from Roche (Basel, Switzerland). Stock solution of HRP was prepared at 10.0 mg/mL in PBS (50 mM potassium phosphate buffer solution containing 100 mM NaCl, pH 7.0) and stored at −20 °C. 1-Hexyl-3-methylimidazolium chloride ([C_6mim]Cl, ≥97.0%) was purchased from Aldrich (St. Louis, MO, USA). 1-Ethyl-3-methylimidazolium chloride ([C_2mim]Cl, ≥98.0%), 1-butyl-3-methylimidazolium chloride ([C_4mim]Cl, ≥95.0%,) and 1-methyl-3-octylimidazolium chloride ([C_8mim]Cl, ≥97.0%) were obtained from Fluka (Steinheim, Germany). Hydrogen peroxide (30%, guaranteed reagent) was bought from Beijing Chemicals Plant (Beijing, China). 4-Aminoantipyrine was purchased from Shanghai Reagent First Factory (Shanghai, China). Poly(ethylene glycol) 4000 (PEG4000) was obtained from Tiantai Fine Chemicals (Tianjin, China). All chemicals were of analytical grade without special description. Deionised water was used for preparation of aqueous solutions. All the HRP solutions were prepared and diluted with PBS without special description.

2.2. Methods

A U-3010 UV–vis spectrophotometer (Hitachi Instruments Inc., Hitachi, Japan) was employed to accomplish all the absorption measurements. The viscosity tests were carried out with a RS-300 (Thermo Haake, Karlsruhe, Germany) rheometer.

2.2.1. Phase diagrams

To a 10-mL graduated test tube containing the solution of 0.5 g IL and 0.2 g water, K_2HPO_4 was added gradually and the content was vortexed until turbidity was observed. More water was added to get a clear one-phase system and then more salt was added again to form a two-phase system. The cycles for formation of two-phase system were repeated. After every two-phase system or one-phase system was obtained, the mixture was weighed. Then, the phase diagrams were constructed in terms of the concentrations of IL and salt (mol/kg) [17].

An empirical mathematical model developed by Merchuk et al. [23] was used to fit the binodal using the following equation:

$$y = M_1 \exp[(M_2 x^{0.5}) + M_3 x^3] \tag{1}$$

The tie lines, which describe the concentrations of IL and salt in the two phases, were measured with the procedure outlined in Ref. [21]. The water content in IL-rich phase was then calculated

by subtracting the IL and salt mass from the total amount of the upper phase. The water content of the same IL-rich phase was also measured with Karl Fisher titration, as a comparison with the calculation result. A Mettler Toledo DL39 Karl Fisher coulometer (Greifensee, Switzerland) was employed for the titration.

2.2.2. Preparation of IL-ABS

After a measured amount (see the following sections in "Section 2.2" for details) of IL and K_2HPO_4 was added into a 10-mL centrifugal tube, water was added until the total volume reached 5 mL. After vortexed for 30 s and allowed to stand for 5 min, the mixture turned into a clear IL-rich phase (the upper phase) and a salt-rich phase (the lower phase).

2.2.3. Activity assay of HRP

The HRP activity was determined by Worthington method [24] as described below. The substrate solution is mixture of 1.4 mL 4-aminoantipyrine solution (0.50 mg/mL 4-aminoantipyrine including 1.6 mg/mL phenol) and 1.5 mL H_2O_2 (0.006% v/v, in PBS). 0.1 mL HRP solution was added into this 2.9 mL substrate solution. Initial oxidation rate of 4-aminoantipyrine was monitored by the increase of absorbance at 510 nm. The activity was calculated with the following equation:

$$U = \frac{A_{510} \times 3}{6.58 \times m_{HRP}} \tag{2}$$

U is the activity contained in 1 mg HRP with unit of U/mg. A_{510} is the increment of absorbance at 510 nm per minute, and m_{HRP} is the mass of HRP added with unit of mg.

In the following experiments and discussions, the activity of the extracted HRP was expressed by the relative activity (U_r, %) which was defined as the following equation:

$$U_r (\%) = \frac{U_e}{U_n} \times 100 \tag{3}$$

U_e (U/mg) is the activity of HRP in the tested media (IL-rich phases or aqueous solutions of IL), and U_n (U/mg) as reference is the activity of HRP dissolved in PBS with the same concentration.

To investigate the effect of ILs on HRP activity, ABS composed of IL (0.2 g [C_4mim]Cl, [C_6mim]Cl, [C_8mim]Cl, or 0.4 g [C_2mim]Cl) and 3.5 g K_2HPO_4 with total volume of 5.0 mL was prepared. The upper phase of the ABS was withdrawn by a syringe, and subsequently 40 μL HRP solution (50 μg/mL) was added into it. The mixture was incubated at 25 °C for 30 min, and then diluted to 1.0 mL. The activity of HRP after incubation was determined. The relative activity was calculated.

The reaction kinetic profiles were prepared with the same process including incubation and activity test, except that the concentration of substrate solution was 1/10 of that for activity assay. The absorption at 510 nm was plotted as kinetic profile.

2.2.4. Evaluation of HRP stability

50 μL HRP (40 μg/mL) was added into [C_4mim]Cl/water mixtures to obtain solutions with water content of 20, 30, 40 and 50% (w/w), respectively. These solutions were incubated at 25 °C for 0.5, 1–8 h, and then diluted to 1.0 mL. The HRP activities in these solutions were determined. The stability was evaluated from U_r after different incubation time. The HRP stability in upper phase of IL-ABS (composed of 0.2 g [C_4mim]Cl and 3.5 g K_2HPO_4 with total volume of 5.0 mL) was tested following the similar procedure.

2.2.5. Determination of HRP partition

The partition behavior of HRP was studied in ABSs composed of [C_4mim]Cl and K_2HPO_4. IL, K_2HPO_4, and HRP were added to a 10-mL graduated tube, and then the mixture was diluted by water

to 5.0 mL. After the ABS formed clearly, the upper phase was completely removed by a syringe into a 2 mL centrifugal tube and then diluted by water to 1.0 mL for activity and concentration determination. The blanks were prepared with the identical ABSs without HRP.

To minimize the interference of IL, the first derivative spectra were used for the determination of HRP in ABS, and the measurement was carried out at 414 nm with the corresponding blank as reference. The HRP mass in upper phase was obtained from calibration curve. Then, the distribution ratio of HRP in the upper phase (W_u, %) was calculated with $W_u = m_u/m_s$, where m_s is the amount of HRP added, m_u is the amount of HRP distributed into the IL-rich upper phase.

2.2.6. The upper phase viscosity

The IL-ABS was composed of 4.8 g IL, 56 g K_2HPO_4 and water to a total volume of 80 mL. The polymer-based ABS was prepared with the same composition and concentration except that IL was replaced by PEG4000. All the upper phase viscosities were tested at 25 °C.

3. Results and discussion

3.1. Phase-forming abilities of alkylimidazolium chloride ILs

Phase diagrams of IL–K_2HPO_4 systems based on three alkylimidazolium chloride ILs with different alkyl groups were determined through cloud point titration at 25 °C. It was shown in Fig. 1 that with the same salt concentration, ABS formation required higher concentration of IL in [C_4mim]Cl/K_2HPO_4 system than that in 1-hexyl-3-methylimidazolium chloride ([C_6mim]Cl) or 1-methyl-3-octylimidazolium chloride ([C_8mim]Cl) system. With a higher concentration of K_2HPO_4 than that in [C_4mim]Cl system, 1-ethyl-3-methylimidazolium chloride ([C_2mim]Cl) can also form ABS. Unfortunately, in the [C_2mim]Cl system with the minimum K_2HPO_4 concentration for turbidity formation, the clear phase separation cannot be observed, so its phase diagram cannot be determined by the cloud point titration method. Therefore, the phase-forming abilities of alkylimidazolium ILs are in the order of [C_8mim]Cl ≈ [C_6mim]Cl > [C_4mim]Cl > [C_2mim]Cl.

The phase-forming abilities of ILs might be related to their chaotropicities. The weakly hydrated ions are usually called chaotropic ions [25]. According to Rogers and coworkers [26], those ILs which can form IL-ABSs more easily with phase-forming salt
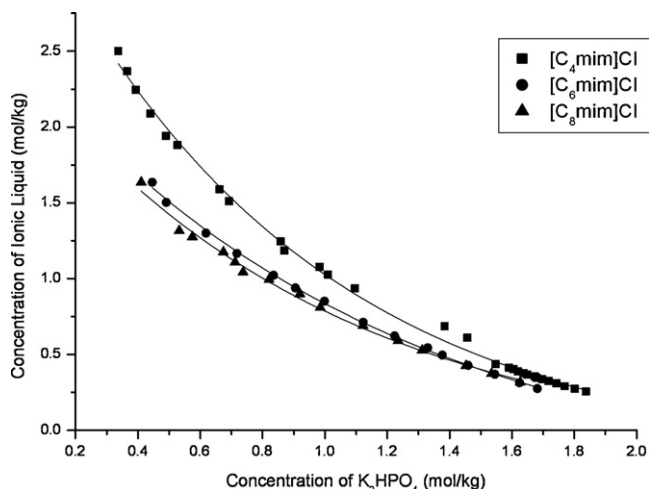
Fig. 1. Phase diagrams of alkylimidazolium chloride–K_2HPO_4 systems.
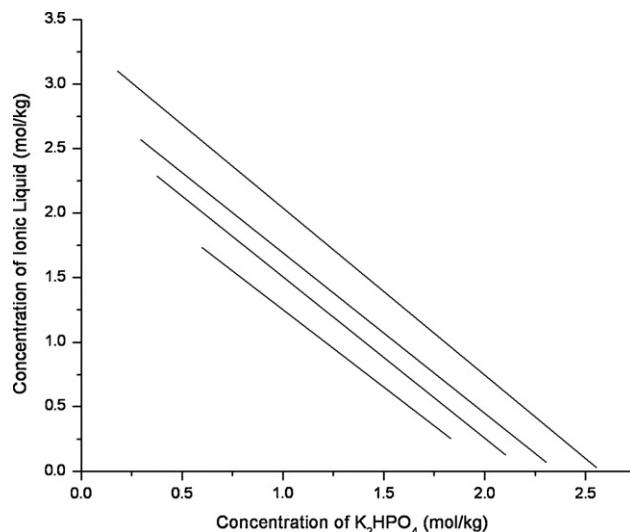
Fig. 2. Tie lines of [C_4mim]Cl–K_2HPO_4 ABS.

(e.g. K_2HPO_4) are more chaotropic. Therefore, it can be inferred that the chaotropicity of IL increases from [C_2mim]Cl to [C_8mim]Cl. The increase of chaotropicities with the alkyl chain length could be due to the increase of charge shielding on imidazolium cation.

Four tie lines of [C_4mim]Cl-K_2HPO_4 ABS were shown in Fig. 2. Points on one tie line represent ABSs having the same upper phase and lower phase composition, with different phase volumes.

3.2. Influence of disperse medium: HRP activity and stability in IL-ABSs

It has been reported that pure IL, as a disperse medium, usually strongly affected the enzyme structure and consequently caused enzyme inactivation [12,13,27]. In IL-ABS, the disperse medium of enzyme is the aqueous solution of IL, and water also played an important role in the enzyme activity maintenance. In the following discussion, both the IL property and water content in the disperse medium were considered as the key factors influencing enzyme activity.

3.2.1. HRP activities in ABSs based on ILs with different lyotropies

HRP activities in IL-ABSs based on four alkylimidazolium chloride ILs were studied. In PBS and the IL-rich upper phases of [C_2mim]Cl, [C_4mim]Cl, [C_6mim]Cl and [C_8mim]Cl-based ABSs, the HRP activity was 251, 265, 256, 114 and 40 U/mg, respectively. The reaction kinetic profiles were also determined by monitoring the increase of absorbance during the reaction process under the catalysis of HRP. As shown in Fig. 3, the inactivation of HRP occurred obviously in the upper phase of [C_6mim]Cl or [C_8mim]Cl system, while HRP activity was satisfactorily maintained in that of [C_2mim]Cl or [C_4mim]Cl system.

These differences amongst ILs in abilities in maintaining enzyme activity could be explained from their different lyotropies. "Lyotropy" is a special physicochemical property of ion, which means the ability to stabilize the quaternary structure of proteins. It is related to the chaotropicity of an ion. For cations, the ions with high chaotropicities are generally low in lyotropy [28]. As inferred from their phase-forming abilities, [C_6mim]$^+$ and [C_8mim]$^+$ are more chaotropic and therefore less lyotropic than [C_2mim]$^+$ and [C_4mim]$^+$. Hence, [C_6mim]$^+$ and [C_8mim]$^+$ disrupted the protein structure more seriously, and consequently caused in the obvious inactivation of HRP in the corresponding ABSs.
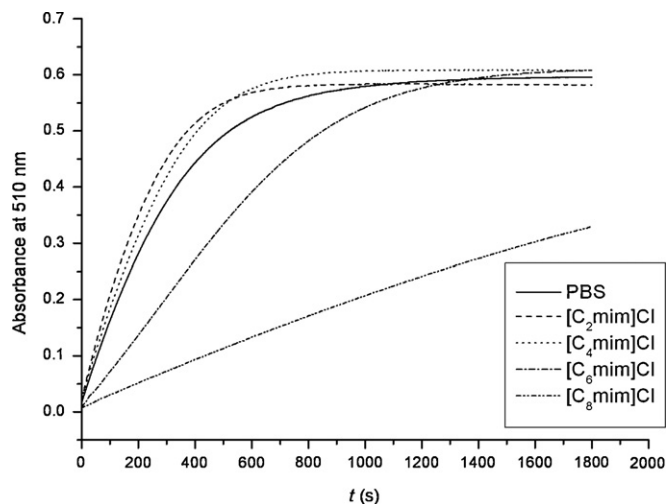
Fig. 3. Influence of alkylimidazolium chloride-ABS on HRP activity.

Fig. 5. Influence of IL mass on W_u (a) and U_r (b). IL-ABSs were composed of 3.6 g K_2HPO_4, 0.2 mg HRP and certain mass of IL shown in the figure and diluted by water to 5.0 mL.

In order to choose a proper IL for aqueous biphasic extraction of HRP, both the phase-forming ability and the enzyme activity preservation should be considered. As discussed above, more chaotropic ILs can form ABSs at a lower concentration, while less chaotropic ILs benefit the enzyme activity maintaining in the extraction procedure. Considering those two aspects, we chose [C$_4$mim]Cl as the ABS-forming IL for partition of HRP in the following study. In the [C$_4$mim]Cl-K$_2$HPO$_4$ ABS, the activity of HRP can be satisfactorily maintained in the period of test as demonstrated below.

3.2.2. The crucial role of water in the maintenance of HRP stabilities

Enzyme inactivation in the same IL ([C$_4$mim]Cl) with lower or no water content were reported [12,27]. Compared with those results, the avoidance of enzyme inactivation in some IL-ABSs may be attributed to the higher content of water. To support this point, we investigated the HRP stabilities in [C$_4$mim]Cl solution with different water contents and the upper phase of [C$_4$mim]Cl-K$_2$HPO$_4$ ABS (0.2 g IL, 3.5 g K$_2$HPO$_4$, with total volume of 5.0 mL). As shown in Fig. 4, in IL with 20% water, HRP became totally inactive within 0.5 h, and a fast inactivation of HRP also occurred in the IL with 30%

water. Whereas, in IL with 40% or 50% water, the results were optimistic: relative activity (U_r) varied little (90–110%) during the tested time of 8 h. The same stability of HRP was observed in the upper phase of [C$_4$mim]Cl–K$_2$HPO$_4$ ABS. With the procedure outlined in "Phase diagrams", the water content of the IL-ABS upper phase was calculated to be 42%. This calculated water content is accordant to that obtained with Karl Fisher titration (46%, R.S.D. = 3.0, n = 3). Obviously, the HRP stability in the upper phase of IL-ABS is close to that in IL solution with very similar content of water, which well supports the view about the water role in HRP stability maintenance.

Hydrogen binding between IL and enzyme was considered as the key factor that causes the unfolding of protein structures in IL [13]. Fortunately, water molecules can form hydrogen bound with IL, and consequently affect the bulk properties of IL [29]. From the result of our experiment, we can infer that water molecules could protect the enzyme structure by forming hydrogen bound with IL instead of enzyme. The protecting effect of water grows with its content in IL solution, until the hydrogen binding was totally weakened and HRP stability loss is completely avoided. The relatively high amount of water in IL-ABS is necessary for keeping enzymatic stability of HRP. That might be an essential merit of IL-ABS for bimolecular extraction.

3.3. Partition behavior and activity of HRP in [C$_4$mim]Cl–K$_2$HPO$_4$ ABS

The satisfactory activity maintaining and partition behavior of enzyme are required for the potential application of the IL-based ABS to enzyme extraction. In ABS composed of [C$_4$mim]Cl and K$_2$HPO$_4$, both higher relative activity (U_r) of HRP and higher distribution ratio of HRP in the upper phase (W_u) with less IL consumption were considered to obtain the optimal condition.

All W_u or U_r values were obtained from triplicate determinations and shown with error bars indicating the standard errors.

The effects of IL mass on W_u and U_r values were investigated in 5.0 mL IL-ABSs composed of 3.6 g K$_2$HPO$_4$, 0.2 mg HRP and IL (0.20, 0.25, 0.30, 0.35 and 0.40 g, respectively), as shown in Fig. 5. When 0.23-0.33 g IL was used, the W_u values reached 80–85%, indicating that an adequate IL mass is needed to get a high W_u. U_r values can be maintained satisfactorily (100–130%) within a wide IL mass range of 0.2–0.4 g.

The influence of K$_2$HPO$_4$ concentration on the W_u and U_r values of HRP in ABS was also investigated. Here, 0.3 g IL, 0.2 mg HRP

Fig. 4. HRP stability in [C$_4$mim]Cl-ABS and [C$_4$mim]Cl solutions with different water contents.
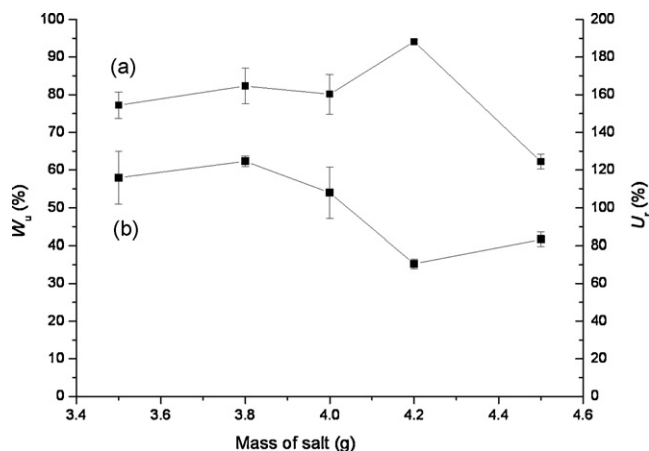
Fig. 6. Influence of K_2HPO_4 mass on W_u (a) and U_r (b). IL-ABSs were composed of 0.3 g IL, 0.2 mg HRP and certain mass of K_2HPO_4 shown in the figure and diluted by water to 5.0 mL.

and K_2HPO_4 (3.5, 3.8, 4.0, 4.2 and 4.5 g, respectively) were used for ABS formation. It can be seen in Fig. 6, with the increase of salt mass, W_u kept almost constant initially within 3.5–4.0 g salt, then increased to the maximum value when 4.2 g salt was used, and finally decreased obviously after that. While U_r values kept almost constant when the salt mass was 3.5–3.8 g, and then decreased considerably. It can be inferred that high-salt concentration causes strong salting-out effect, which benefits the partition of HRP into the upper phase. But meanwhile, the upper phase becomes more chaotropic, affecting the stability of enzyme structure, and consequently induces the decrease of activity and distribution ratio of enzyme.

With the optimal amount of IL (0.3 g) and K_2HPO_4 (3.6 g), the influence of HRP amount on its partition behavior was further studied. Within 0.1–0.5 mg, HRP mass did not affect W_u or U_r obviously (see Fig. 7), which provided a relatively wide range of enzyme concentration for its extraction.

Therefore, the optimal ABS were composed of 0.3 g [C_4mim]Cl, 3.6 g K_2HPO_4 and suitable amount of water with a total volume of 5.0 mL. The upper phase volume of this system was about 0.5 mL. Under this condition, the W_u was about 80% with well-retained activity ($U_r > 90\%$).
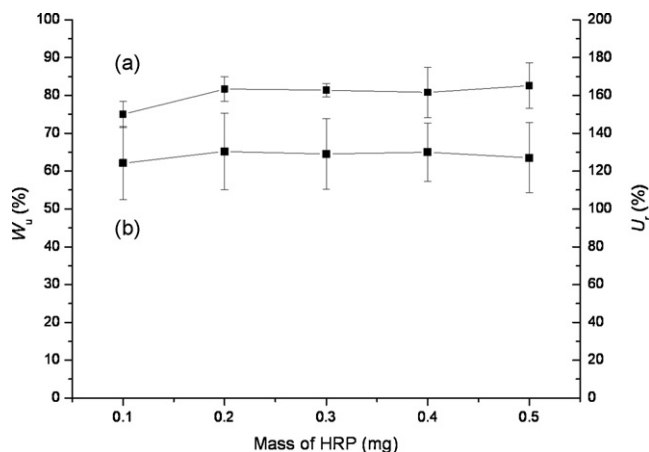
Fig. 7. Influence of HRP mass on W_u (a) and U_r (b). IL-ABSs were composed of 0.3 g IL, 3.6 g K_2HPO_4 and certain mass of HRP shown in the figure and diluted by water to 5.0 mL.

3.4. Comparison of the upper phase viscosities of [C_4mim]Cl–K_2HPO_4 and PEG4000–K_2HPO_4 ABS

The efforts required for phase equilibrium and upper phase removal highly depend on the viscosity of the upper phase. It was tested that the viscosity of the upper phase of [C_4mim]Cl-based IL-ABS was 4.12 mPa s, which was much lower than that of PEG4000-based ABS (79.6 mPa s). Obviously, the IL-ABS has a much lower viscosity than the traditional polymer-ABS. This unique character makes IL-ABS much easier to handle in several ways. For example, centrifugation is not needed for phase separation, and the upper phase can be drawn more easily. This is a significant improvement compared with the traditional polymer-ABSs.

4. Conclusion

In summary, we have systematically studied the activity and partition behavior of HRP in aqueous biphasic system consisting of alkylimidazolium chloride ionic liquid and salt for the first time. The chaotropicity of IL promotes phase forming, while its lyotropy is beneficial to enzyme activity maintaining. It is very important to consider both those properties when choosing proper IL-ABS as extraction system. Under the optimal conditions, HRP activity in [C_4mim]Cl–K_2HPO_4 ABS was proved to be stable in the test period, which could be attributed to the high content of water.

The [C_4mim]Cl-ABS was benign to the model enzyme and relatively friendly to environment because of its high content of water and avoidance of organic solvents. Moreover, it is less expensive compared with IL–water systems, due to the usage of relatively low-cost hydrophilic IL and less consumption of IL. In the optimized [C_4mim]Cl–K_2HPO_4 ABS, more than 80% HRP distributed into the upper phase with satisfactorily retained activity. Additionally, the upper phase viscosity of [C_4mim]Cl–K_2HPO_4 ABS was proved to be much lower than that of polymer based ABS, which facilitates the phase equilibrium and separation. If IL can be removed conveniently from the enzyme solution via a suitable method, IL-ABSs would be an effective alternative for enzyme extraction of traditional solvent extraction system or polymer-based ABSs. The tunable structures of ILs [30] and the controllable concentrations of phase-forming compounds will provide designable IL-ABSs as demand.

Acknowledgements

References

[1] R.D. Rogers, K.R. Seddon, Science 302 (2003) 792.
[2] G.A. Baker, S.N. Baker, S. Pandey, F.V. Bright, Analyst 130 (2005) 800.
[3] J.G. Huddleston, H.D. Willauer, R.P. Swatloski, A.E. Visser, R.D. Rogers, Chem. Commun. 16 (1998) 1765.
[4] E. Visser, R.P. Swatloski, W.M. Reichert, R. Mayton, S. Sheff, A. Wierzbicki, J.H. Davis Jr., R.D. Rogers, Chem. Commun. 1 (2001) 135.
[5] S. Chun, S.V. Dzyuba, R.A. Bartsch, Anal. Chem. 73 (2001) 3737.
[6] J.F. Liu, G.B. Jiang, Y.G. Chi, Y.Q. Cai, Q.X. Zhou, J.T. Hu, Anal. Chem. 75 (2003) 5870.
[7] H. Luo, S. Dai, P.V. Bonnesen, Anal. Chem. 76 (2004) 2773.
[8] H. Luo, S. Dai, P.V. Bonnesen, A.C. Buchanan, J.D. Holbrey, N.J. Bridges, R.D. Rogers, Anal. Chem. 76 (2004) 3078.
[9] K. Shimojo, M. Goto, Anal. Chem. 76 (2004) 5039.
[10] J.H. Wang, D.H. Cheng, X.W. Chen, Z. Du, Z.L. Fang, Anal. Chem. 79 (2007) 620.

[11] K. Shimojo, K. Nakashima, N. Kamiya, M. Goto, Biomacromolecules 7 (2006) 2.
[12] M.B. Turner, S.K. Spear, J.G. Huddleston, J.D. Holbrey, R.D. Rogers, Green Chem. 5 (2003) 443.
[13] F. van Rantwijk, F. Secundo, R.A. Sheldon, Green Chem. 8 (2006) 282.
[14] A.P. De Los Rios, F.J. Hernandez-Fernandez, F.A. Martinez, M. Rubio, G. Villora, Biocatal. Biotransform. 25 (2007) 151.
[15] S.H. Li, C.Y. He, F. Gao, D.B. Li, Z. Chen, H.W. Liu, K.A. Li, F. Liu, Talanta 71 (2007) 784.
[16] Y. Akama, A. Sali, Talanta 57 (2002) 681.
[17] P.Å. Albertsson, Partition of Cell Particles and Macromolecules, 3rd ed., Wiley, New York, 1986.
[18] K.E. Gutowski, G.A. Broker, H.D. Willauer, J.G. Huddleston, R.P. Swatloski, J.D. Holbrey, R.D. Rogers, J. Am. Chem. Soc. 125 (2003) 6632.
[19] C.Y. He, S.H. Li, H.W. Liu, K.A. Li, F. Liu, J. Chromatogr. A 1082 (2005) 143.
[20] S.H. Li, C.Y. He, H.W. Liu, K.A. Li, F. Liu, J. Chromatogr. B 826 (2005) 58.
[21] Z. Du, Y.L. Yu, J.H. Wang, Chem. Eur. J. 13 (2007) 2130.
[22] F.Z. Deng, D.F. Guo, Chin. J. Anal. Chem. 34 (2006) 1451.
[23] J.C. Merchuk, B.A. Andrews, J.A. Asenjo, J. Chromatogr. B: Biomed. Sci. Appl. 711 (1998) 285.
[24] B. Stellmach, Bestimmungsmethoden Enzyme für Pharmazie, Lebensmittelchemie, Technik, Biochemie, Biologie, Medizin, Steinkopff, Darmstadt, Germany, 1988.
[25] A. Berthod, M.J. Ruiz-Angel, S. Huguet, Anal. Chem. 77 (2005) 4071.
[26] N.J. Bridges, K.E. Gutowski, R.D. Rogers, Green Chem. 9 (2007) 177.
[27] S.F. Wang, T. Chen, Z.L. Zhang, D.W. Pang, Electrochem. Commun. 9 (2007) 1337.
[28] K.D. Collins, M.W. Washabaugh, Quart. Rev. Biophys. 18 (1985) 323.
[29] L. Cammarata, S.G. Kazarian, P.A. Salter, T. Welton, Phys. Chem. Chem. Phys. 3 (2001) 5192.
[30] D. Das, A. Dasgupta, P.K. Das, Tetrahedron Lett. 48 (2007) 5635.

Identification of individual DNA molecule of *Mycobacterium tuberculosis* by nested PCR-RFLP and capillary electrophoresis

Po-Ling Chang[a], Wen-Shyang Hsieh[b], Chia-Lien Chiang[b], Belinda Yen-Liberman[c], Gary W. Procop[c], Huan-Tsung Chang[a,*], Hsin-Tsung Ho[b,d,**]

[a] *Department of Chemistry, National Taiwan University, Taipei, Taiwan, ROC*
[b] *Department of Laboratory Medicine, Mackay Memorial Hospital, Taipei, Taiwan, ROC*
[c] *Section of Clinical Microbiology, Department of Clinical Pathology, The Cleveland Clinic, Cleveland, OH, USA*
[d] *Mackay Medicine, Nursing and Management College, Taipei, Taiwan, ROC*

ABSTRACT

The improvement of sensitivity and differentiation in rapidly identifying a small amount of mycobacteria in sputum has significant implications for reducing tuberculosis transmission. We previously applied the conventional PCR and capillary electrophoresis (CE) to establish the restriction fragment length polymorphism (RFLP) pattern of mycobacterial 65-kDa heat shock protein (*hsp65*) gene from colony specimens. However, the previous analysis did not provide enough sensitivity for sputum specimens in which the limitation of analysis might be hindered by PCR inhibitors and primer-dimers formation during amplification. In the current study, nested PCR (nPCR) had been redesigned for PCR-RFLP analysis (PRA) of mycobacterial *hsp65* gene using CE. The results show both *Mycobacterium tuberculosis* complex and mycobacteria other than tuberculosis could be identified in the presence of PCR inhibitors. The interference due to primer-dimers was also minimized. Based on the Poisson distribution, the repeatability of single DNA molecule detection was greatly affected by sampling probability and might be improved significantly by increasing the sample loading. The PRA using nPCR and CE is not only able to detect the individual mycobacterial DNA molecule but also potentially differentiate the species.

© 2008 Elsevier B.V. All rights reserved.

1. Introduction

Reduction of *Mycobacterium tuberculosis* (MTB) transmission is an important issue. One-third of the global population is believed to be infected with bacteria of the *M. tuberculosis* complex, the causative agent of tuberculosis. More than 8 million new cases of tuberculosis occur annually leading to 2 million deaths [1]. In addition, the mycobacteria other than tuberculosis (MOTT) also cause human diseases and are crucial to be correctly identified because of differences in antimicrobial susceptibility [2]. For rapid identification of MTB and MOTT, a wide-range of nucleic acid amplification tests has been developed. Several of them based upon species-specific probes are commercially available, including PCR-based Amplicor (Roche), transcription-mediated amplification (Gen-Probe), strand displacement amplification (Becton Dickin-

son), and ligase-chain reaction (Abbott) [3–6]. So far, limited numbers of identifiable species and high-cost of probe-based methods have restricted their routine use for clinical specimens. On the other hand, many endonuclease-based methods without costly probes have also been proposed for differentiating mycobacterial species [7–9]. These non-probe methods utilize enzymatic digestion of amplified genetic products and electrophoretic separation to obtain the restriction fragment length polymorphism (RFLP) pattern. Such a diagnostic algorithm, known as PCR-RFLP analysis (PRA), remains cumbersome and requires two or more restriction endonucleases to achieve a higher discriminatory power. Up to now, the sensitivity and specificity of both probe and non-probe methods are still insufficient to detect and differentiate a low copy number of DNA or a small amount of mycobacteria [10,11].

Capillary electrophoresis (CE) with laser-induced fluorescence has become a powerful analytical tool for bio-analysis mainly due to its high sensitivity, excellent efficiency, rapidity, less sample requirement, and thus, toward to system biology [12,13]. In the previous studies, our team demonstrated the performance of CE that could be applied to clinical microbiological diagnosis [14,15]. However, the PRA using conventional PCR and CE did not pro-

vide enough sensitivity for specimens directly from clinical isolates such as sputum. The limitation of analysis of sputum might be resulted from the presence of PCR inhibitors and primer-dimer formation during amplification. In the current study, nPCR had been re-designed for the PRA using CE in the presence of electroosmotic flow [16,17] to improve the sensitivity and specificity. The sampling impacts of identifying individual mycobacterial DNA were carefully estimated by rational explanation. The performance of this analysis, including the limit of detection, specificity of RFLP, and interferences by PCR inhibitors and primer-dimers, were evaluated for a limited number of specimens from colonies and sputum.

2. Materials and methods

2.1. Specimens and DNA preparation

We studied three mycobacterial strains, *M. tuberculosis* (ATCC 10709) from the American Type Culture Collection (Rockville, MD), *Mycobacterium heckashorne* (CCF 21) and *Mycobacterium celatum* (CCF 56); the latter two were from the culture collection of clinical microbiology section of Cleveland Clinic, Cleveland, OH, USA, and had been previously characterized using DNA sequencing. A loop from each cultured strain was suspended in 500 μL of TE buffer (10 mM Tris–HCl, 1 mM EDTA, pH 8.0) and inactivated by boiling for 10 min. The boiled specimen of *M. tuberculosis* was subjected to DNA extraction by Qiagen mini DNA purification kit (Gentra Systems, MN, USA) according to the manufacturer's instructions. The DNA concentration was determined using a Beckman DU-460 UV–vis spectrophotometer (Fullerton, CA, USA). For testing the interference of inhibitors, we did not treat the boiled specimens of *M. heckashorne* and *M. celatum* with DNA extraction. Nine specimens of sputum positive for acid-fast bacilli (AFB) collected at the department of laboratory medicine, Mackay Memorial Hospital, Taipei, Taiwan were also analyzed. All sputum specimens were digested with *N*-acetyl-L-cysteine and decontaminated with 4% NaOH. Each specimen was then concentrated by centrifugation ($3000 \times g$) before examination by Kinyoun stain and microscopy. The interpretation of AFB smear was scored as follows [18]. The scores 4+, 3+, 2+, and 1+, indicated >9 AFB per field ($1000\times$), 1–9 AFB per field, 1–9 AFB per 10 fields, and 1–9 AFB per 100 fields, respectively. Aliquots of sputum specimens were inoculated in both liquid (BACTEC MGIT 960, Becton Dickinson Bioscience, Sparks, MD) and solid (Löwenstein–Jensen) culture medium for the isolation and identification of mycobacteria. Identification at the species level was done by classical biochemical tests and further confirmed by DNA sequence analysis. Meanwhile, duplicate aliquots of sputum specimens were subjected to DNA extraction followed by PRA with CE (PRACE). The analytical laboratory performing CE was blinded with respect to the results of AFB smear and culture.

2.2. PCR amplification and enzymatic digestion

All specimens were investigated by using traditional PCR and nPCR for comparison. PCR mixtures contained 2.5 μL of 10× buffer concentrate, 0.4 μM (each) primer, 200 μM concentrations of each of four dNTPs, 1.0 unit of FastStart *Taq* DNA polymerase (Roche, Indianapolis, IN), and 1 or 10 μL of the DNA template (extracted from colonies or sputum) in a final volume of 25 μL. Amplification primers previously reported by Telenti et al. (Tb11 and Tb12) were chosen for traditional PCR [19]. The primers and other optimizations were redesigned for the nPCR protocol (Table 1). The external primers (Tb-ExF and Tb-ExR) were modified from the primers (M1 and M4) as reported by Bascunana and Belak [20]. Thermocycling of reaction mixtures was performed in a model 2700 Thermocycler (PerkinElmer—Applied Biosystems, USA) programmed for 40 cycles (30 s at 95 °C, 30 s at 60–68 °C, 60 s at 72 °C) and followed by a 7-min incubation at 72 °C (Table 1). Within the mycobacterial genome, a target of 461 bp fragment was amplified with external primers in first PCR of nPCR. Then, 1 μL out of 25 μL PCR products was transferred into a new reaction tube for second PCR of nPCR using internal primers. The internal primers (Tb-InF and Tb-InR) were elongated to 27 bp and annealed to the same locations from 5′ position of heat shock protein 65 (*hsp65*) gene as those by Telenti primers (Tb11 and Tb12). The size of nPCR products of *hsp65* gene that confirmed by sequencing were 441 bp (MTB and *M. celatum*) or 442 bp (*M. heckashorne* and *Mycobacterium abscessus*), respectively. Amplification products were then digested with restriction endonuclease HaeIII (Roche, Indianapolis, IN, USA). Thus 5 μL of the amplified reaction solution was added to a mixture containing 0.2 μL of enzyme (2 units), 2.5 μL of restriction buffer (10×), and 17.3 μL of sterile distilled water. The mixtures were incubated for 60 min at 37 °C for HaeIII digestion. We used a reference strain of MTB as positive control and healthy human genomic DNA as negative control. In no case were contaminations due to the transfer of PCR products into a new reaction tube observed. To examine the capability of single-molecule detection, we prepared mycobacterial DNA templates to the equivalent content of one bacillus by serial dilution with ribonuclease-free water (Invitrogen, Carlsbad, CA, USA).

2.3. Separation of PCR products by agarose gel electrophoresis and capillary electrophoresis

Undigested amplified reaction mixtures, 10 μL from conventional PCR or 2 μL from nPCR, were loaded in each well for 3% agarose gel electrophoresis. The gel was prepared in 0.5× TAE buffer containing 0.5 μg/mL ethidium bromide and the separation was run at 8 V/cm under ambient temperature. After electrophoretic separation, the band pattern was observed and demonstrated by ImageMastes recorder of Amersham Pharmacia Biotech (Piscat-

Table 1
Primers and thermocycles designed for conventional and nested PCR

Primers		Thermocycles				
Telenti primers of conventional PCR		40 cycles				
Tb11	5′-ACCAACGATGGTGTGTCCAT-3′	95 °C	95 °C	60 °C	72 °C	72 °C
Tb12	5′-CTTGTCGAACCGCATACCCT-3′	6 min	30 s	30 s	60 s	7 min
External primers of nested PCR		40 cycles				
Tb-ExF	5′-CCCCACGATCACCAACGATG-3′	95 °C	95 °C	61 °C	72 °C	72 °C
Tb-ExR	5′-CCGAGATGTAGCCCTTGTCGA-3′	6 min	30 s	30 s	60 s	7 min
Internal primers of nested PCR		40 cycles				
Tb-InF	5′-ACCAACGATGGTGTGTCCATCGCCAAG-3′	95 °C	95 °C	68 °C	72 °C	72 °C
Tb-InR	5′-CTTGTCGAACCGCATACCCTCGGTGAG-3′	6 min	30 s	30 s	60 s	7 min

away, NJ). We considered the band located within 400–500 bp range as *hsp65* gene product.

Amplicons and digested restriction fragments were analyzed by CE with laser-induced fluorescence using poly(ethylene oxide) (PEO) solution in the presence of electroosmotic flow. PEO with the molecular weight of 8,000,000 g/mol was purchased from Sigma–Aldrich (St Louis, MO, USA). Briefly, a high-voltage power supply (Gamma High Voltage Research Inc., Ormond Beach, FL) was used to drive electrophoresis. The entire detection system was enclosed in a black box with a high-voltage interlock. The high-voltage end of the separation system was put in a laboratory-made plexiglass box for safety. A 5.0-mW solid laser with 532 nm output from Uniphase (Mantence, CA, USA) was used for excitation. The light was collected with a $10\times$ objective (numerical aperture = 0.25). One RG 610 cut-off filter was used to block scattered light before the emitted light reached the phototube (Hamamatsu R928). The amplified currents were transferred directly through a 10-kΩ resistor to a 24-bit A/D interface at 10 Hz (Borwin, JMBS Developments, Le Fontanil, France) and stored in a personal computer. Bare fused-silica capillaries (Polymicro Technologies, Phoenix, AZ, USA) with an internal diameter of 75 μm were used for DNA separations without any further coating process. The capillary length was 40 cm and the length from the injection end to the detector was 30 cm. Anodic and cathodic vials were filled with 1.5% PEO solution that was prepared in 100 mM Tris–boric acid buffer (pH 9.0) containing 25 μg/mL ethidium bromide (Pharmacia Biotech, Sweden). A capillary was filled with 1.5 M Tris–boric acid buffer (pH 10.0) and then the DNA specimen was introduced from the inlet (anodic) end of the capillary by hydrodynamic injection at 30-cm height (the difference between the specimen vial and the cathodic vial) for 10 s. During the separation at 20 kV, neutral PEO molecules entered the capillary from the anodic end via electroosmotic flow. The DNA fragments migrating against electroosmotic flow entered PEO solution and were separated according to the sieving mechanism at ambient temperature and pressure.

3. Results and discussion

3.1. Comparison of the primer-dimer interference between conventional PCR and nested PCR

In order to assess the reduction of primer-dimers and the superior sensitivity of RFLP by the implementation of in PRACE, we simultaneously performed conventional PCR (Fig. 1) and nPCR (Fig. 2) amplifying mycobacterial *hsp65* genes for comparison. As the capillary electrophoregrams demonstrate, conventional PCR using Telenti primers require at least 5 pg of MTB DNA template to generate a 441-bp *hsp65* gene peak (Fig. 1C). Furthermore, it requires no less than 50 pg of MTB DNA template to obtain a full-range RFLP pattern (Fig. 1B). The formation of primer-dimers becomes obvious while MTB DNA templates less than 50 pg are applied (Fig. 1C and D). In contrast, nPCR is able to yield taller *hsp65* gene peaks and distinguishable species-specific RFLP patterns even with 5 fg of MTB DNA template (Fig. 2E). With enough PCR cycles [21], the heights of nPCR *hsp65* gene peaks remain almost identical regardless of declining MTB DNA template amounts (Fig. 2B–E). The primer-dimers seen in the first PCR using external primers (Fig. 2A) are no longer observed in the second PCR using internal primers (Fig. 2B–E). The disappearance of primer-dimers is partially due to a 25-fold dilution of the first PCR products which contribute a much higher product/primer ratio for the second PCR amplification. The
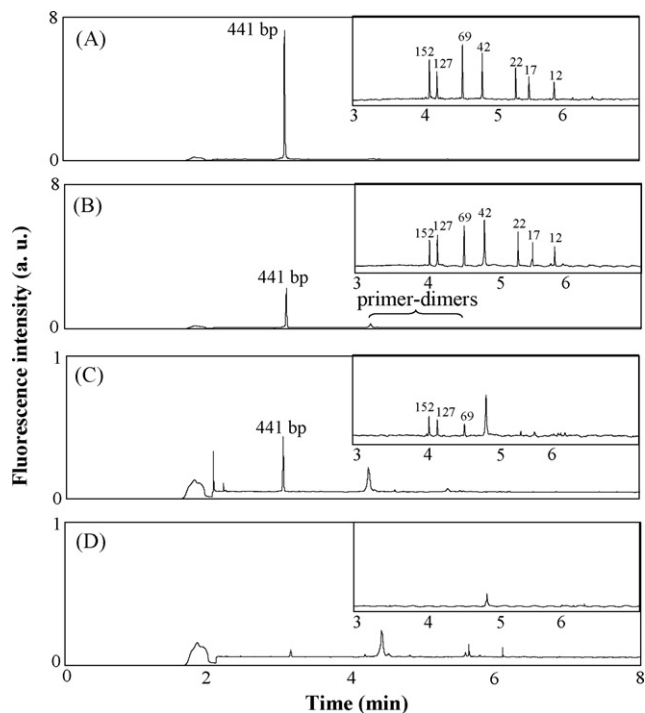
Fig. 1. CE of conventional PCR products using Telenti primers and MTB DNA templates in the amounts of 0.5 ng (A), 50 pg (B), 5 pg (C), and 0.5 pg (D). The inserts are corresponding RFLP patterns of 441-bp *hsp65* gene after enzymatic digestion.
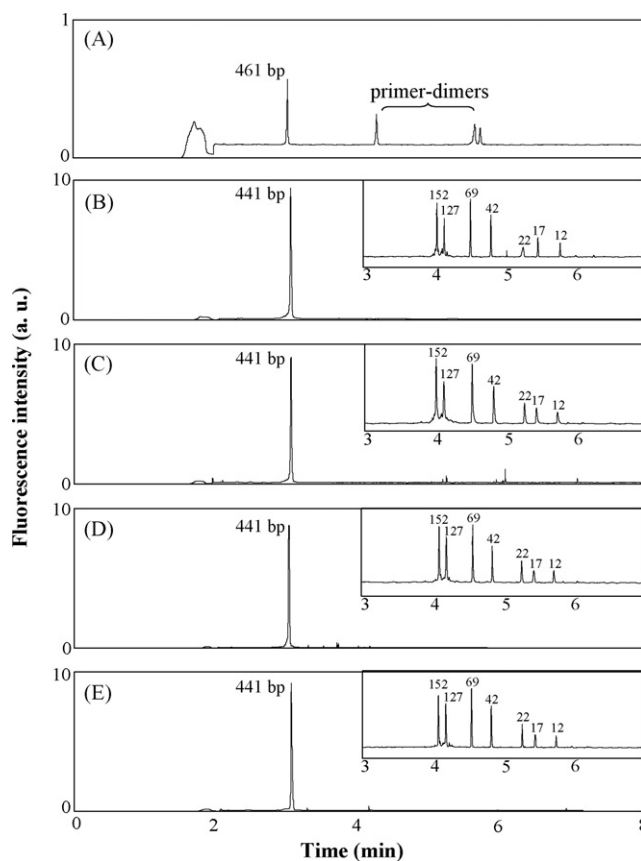
Fig. 2. CE of final nPCR products using MTB DNA templates in the amounts of 5 pg (B), 0.5 pg (C), 50 fg (D), and 5 fg (E). The first PCR with external primers yields 461-bp gene products (A). The second PCR with internal primers generate 441-bp *hsp65* gene products (B–E). The inserts are corresponding RFLP patterns of *hsp65* gene after enzymatic digestion.
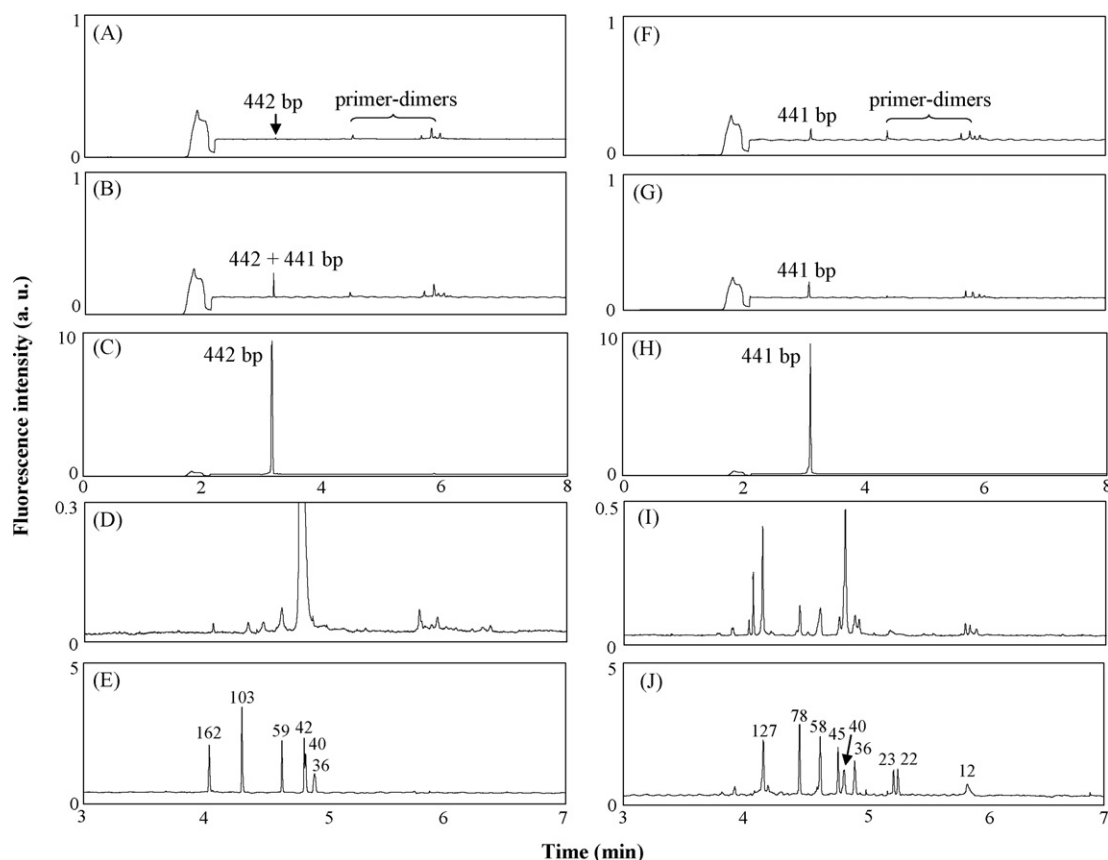
Fig. 3. CE of *M. heckashorne* (A–E) and *M. celatum* (F–J): conventional PCR products (A and F), poor enhancements of *hsp65* gene peaks following 50 pg spike of MTB DNA (B and G), the nPCR products (C and H), RFLP patterns of conventional PCR products (D and I), RFLP patterns of nPCR products (E and J).

7 °C increase of the second PCR annealing temperature also diminishes interactions between external and internal primers. Thus, as compared with conventional PCR, the implementation of nPCR not only avoids the interference of primer-dimers but also makes PRA 10,000 times more sensitive without losing specificity of RFLP pattern.

3.2. Comparison of the PCR inhibitor interference between conventional PCR and nested PCR

Unlike the existence of numerous bacilli in the cultured specimens, direct clinical isolates such as sputum frequently contain merely a few mycobacteria and sometimes inhibitors that interfere with the performance of PCR. Various attempts have been made to reduce PCR inhibition in diagnostic tests [22]. For respiratory and non-respiratory specimens studied by Böddinghaus et al. [23], the overall inhibition rate of PCR using Amplicor kit was 12.5% which could be reduced to 1.1% with the addition of silica membrane DNA purification. During previous RFLP study of multiple cultured mycobacteria, we found two specimens of *M. heckashorne* and *M. celatum* exhibiting potent inhibition of conventional PCR when the specimens were not treated with DNA extraction. Fascinatingly, the replacement of conventional PCR with nPCR can overcome the interference of inhibitors. As shown by capillary electrophoregrams, conventional PCR products of *M. heckashorne* and *M. celatum* contain tiny or small peak of *hsp65* gene (Fig. 3A and F). Coexistence of remarkable primer-dimers is also noted. The presence of inhibitors in both specimens is indicated by the poor enhancement of *hsp65* gene peak following 50 pg spike of MTB DNA (Fig. 3B and G). When analyzed by

nPCR in contrast to conventional PCR, the formation of primer-dimers and the inhibition of amplification disappear as evidenced by a solitary and sharp *hsp65* gene peak of 10-fold more height (Fig. 3C and H). After the enzymatic digestion, RFLP patterns of conventional PCR products are unrecognizable (Fig. 3D and I). On the contrary, RFLP patterns resulting from nPCR products are unambiguous and species-specific (Fig. 3E and J). The above examples of cultured MOTT demonstrate that mycobacteria could be identified without DNA extraction or even in the presence of inhibitors.

3.3. Sampling effect in identifying individual mycobacterial DNA molecule

Nested PCR is a more efficient approach towards identifying a low copy number of DNA and has been applied for the molecular diagnosis of tuberculosis [3–6]. Recently, Lu et al. modified this approach and proved its ability for the analysis of single DNA molecule, so called single-molecule PCR [24]. During single-molecule PCR, the single DNA molecule as a template is picked up by atomic force microscopy tips [24] or prepared by serial dilution [25,26]. To examine the capability of single-molecule detection, we conduct nPCR of *hsp65* gene using MTB DNA templates of following concentrations and volumes: 50 fg/μL × 1 μL, 5 fg/μL × 1 μL, and 0.5 fg/μL × 10 μL. For each preparation, 16 aliquots are subjected to nPCR for three times. The probability of nPCR gene production is evaluated by the presence of *hsp65* gene bands on 3% agarose electrophoretic gels. For 50 fg/μL × 1 μL aliquots (Fig. 4A), the probability reaches 100% (16/16, 16/16, 16/16). For 5 fg/μL × 1 μL aliquots (Fig. 4B), the probability ranges from 25 to
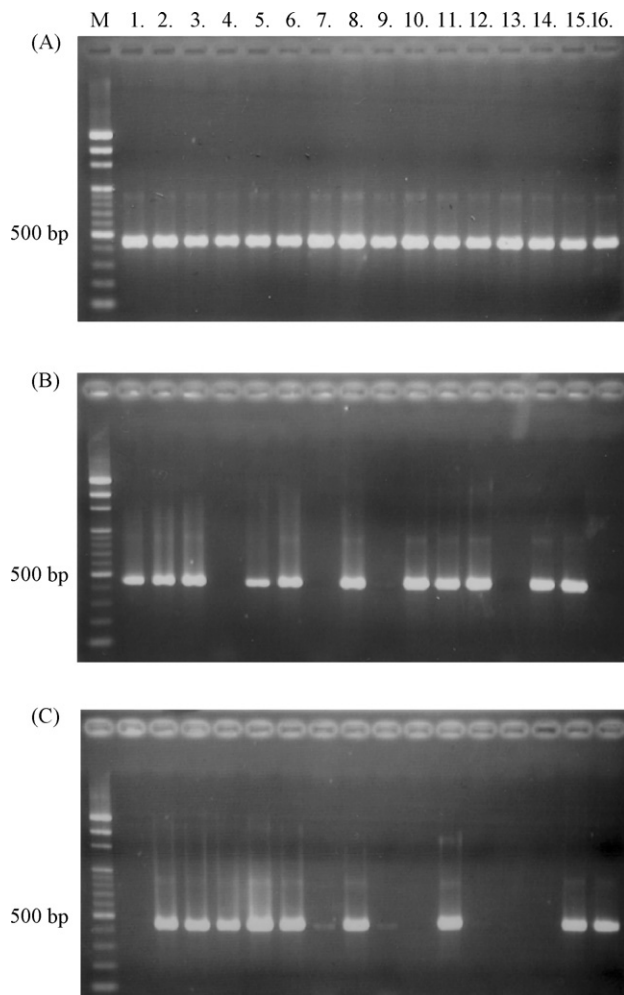
Fig. 4. Probabilities of nPCR gene production using MTB DNA templates prepared in 50 fg/μL × 1 μL (A), 5 fg/μL × 1 μL (B), and 0.5 fg/μL × 10 μL (C). Single-molecule DNA templates (B and C) are prepared by serial dilution. The final nPCR products are shown by the presence of *hsp65* gene bands on 3% agarose electrophoretic gels.

68.8% (4/16, 8/16, 11/16). For 0.5 fg/μL × 10 μL aliquots (Fig. 4C), the probability varies from 18.8 to 56.2% (3/16, 6/16, 9/16). Since the molecular weight of MTB DNA is 2.65×10^9 Da [27], the DNA molecule in one bacillus averages 4.4 fg [28]. Theoretically, MTB DNA prepared in 50 fg/μL × 1 μL (Fig. 4A), 5 fg/μL × 1 μL (Fig. 4B), and 0.5 fg/μL × 10 μL (Fig. 4C) aliquots approximate those from 10 bacilli/μL × 1 μL, 1 bacillus/μL × 1 μL, and 100 bacilli/mL × 10 μL, respectively. Although equivalent amounts of DNA aliquots are not exactly the same as those of intact bacilli, it is interesting enough to have an estimate of detectable mycobacterial concentration based upon above findings.

The probability of PCR amplification for detecting single DNA molecule could be calculated according to the equation of Poisson distribution.

$$p(x; \lambda) = \frac{\lambda^x e^{-\lambda}}{x!}, \quad x = 0, 1, 2, \dots$$

λ is the average number of template molecules before amplification, and x is an occurrence in a certain volume. If the average number of template molecules before amplification were 1, the probability of successfully taking DNA occurrences per microliter is 63.2%. Assuming that each single-molecule PCR reaction had a successful amplification, the sampling probability of single-molecule detection can be deduced by Poisson distribution [25]. Since the average number of template molecules before amplification is 1.14 (5 fg versus 4.4 fg), the probability of successfully taking DNA occurrences per microliter is 68.0%. Our probabilities for DNA molecule detection in one bacillus, 25–68.8% and 18.8–56.2%, are lower than Poisson distribution. The differences could be resulted from null sampling with single DNA molecule adsorbed on the surface of pipette tip. It may also due to inefficient amplification with only a few templates [25]. Thus, our nPCR results of probability indicate that all specimens with concentration of 10 bacilli/μL are detectable. For specimens with concentration of 1 bacillus/μL, the rate of detection is 25–68.8%. For specimens containing 100 bacilli/mL, the detection rate is 18.8–56.2% with 10 μL examined. Such a detection limit is much more sensitive than that of acid-fast bacilli smear (5000–10,000 bacilli/mL), and may reach the upper limit of sensitivity of culture method (10–100 bacilli/mL) [25].

3.4. Identification of the mycobacterium species from sputum

In the present study, we chose nine AFB-positive sputum specimens labeled from No.1 to No.9 and analyzed them with conventional PCR and nPCR for comparison. Before amplification, all sputum specimens had been treated with QIAamp DNA Mini Kit. The presence of amplification products were then demonstrated by 3% agarose electrophoretic gels. In PRA using conventional PCR (Fig. 5A), obvious formation of primer-dimers was noted. While PRA adopting nPCR (Fig. 5B), *hsp65* gene bands became brighter and primer-dimers formation disappeared. Among nine specimens, No.5 fails to generate *hsp65* gene band in PRA using conventional PCR, but it has remarkable *hsp65* gene products when analyzed with nPCR. As shown by capillary electrophoregrams, conventional PCR products of specimen No.5 separated by CE reveals a tiny 442-bp *hsp65* gene peak and some primer-dimers formation (Fig. 6A). The primer-dimers usually interfere with RFLP patterns by generating unrecognizable peaks after enzymatic digestion. The presence of inhibitors is indicated by the poor enhancement of *hsp65* gene peak following 50 pg spike of MTB DNA (Fig. 6B). When analyzed by nPCR, the formation of primer-dimers and the inhibition of amplification vanish as evidenced by a single 10-fold taller *hsp65* gene

Table 2
Comparison of results between AFB smear, culture, nPCR, and sequencing analysis for identification of mycobacteria in sputum

Specimen No.	AFB smear	Culture	nPCR	Sequencing
1	1+	*M. fortuitum*	*M. chelonae*	*M. chelonae*
2	1+	No growth	*M. tuberculosis*	*M. tuberculosis*
3	1+	*M. abscessus*	*M. chelonae*	*M. chelonae*
4	1+	*M. chelonae*	*M. chelonae*	*M. chelonae*
5	2+	*M. fortuitum*	*M. abscessus*	*M. abscessus*
6	2+	*M. tuberculosis*	*M. tuberculosis*	*M. tuberculosis*
7	2+	*M. tuberculosis*	*M. tuberculosis*	*M. tuberculosis*
8	3+	*M. abscessus*	*M. chelonae*	*M. chelonae*
9	3+	*M. tuberculosis*	*M. tuberculosis*	*M. tuberculosis*

Fig. 5. Agarose electrophoretic gels demonstrating *hsp65* gene bands generated from conventional PCR (A) and nPCR (B) of mycobacteria in sputum. Lanes 1–9: nine specimens with smear positive (1+ to 3+) for AFB, M: 100-bp DNA ladder, N: human genomic DNA as negative control, P: MTB DNA as positive control.

Fig. 6. CE of specimen No.5 (A–D): conventional PCR products (A), poor enhancement of *hsp65* gene peak following 50 pg spike of MTB DNA (B), the nPCR products (C), RFLP pattern of nPCR products (D). RFLP patterns of nPCR products from specimens No.1, 3, 4, 8 (E) and No. 2, 6, 7, 9 (F).

peak (Fig. 6C). A distinct full-range RFLP pattern is obtained from nPCR products after enzymatic digestion (Fig. 6D). According to the database of RFLP patterns established in previous study [25], specimen No.5 is consistent with *M. abscessus*. Specimens No.1, 3, 4, 8 are consistent with *Mycobacterium chelonae* (Fig. 6E) and specimens No.2, 6, 7, 9 are consistent with MTB (Fig. 6F).

The PRACE results of mycobacterial identification in sputum were compared with those of culture method and sequence analysis (Table 2). There are discrepancies of mycobacterium species identified between the culture method and PRACE. Of four specimens found to contain MOTT by culture, two differences were initially identified; specimen No.1 was identified as *M. chelonae* and specimen No.5 was identified as *M. abscessus* by PRACE, whereas they were later shown to be *Mycobacterium fortuitum* by culture. Similarly, specimen No.3 and No.8 were identified as *M. chelonae* by PRACE but were identified as *M. abscessus* by culture. These disagreements are not surprising because identification of rapidly growing mycobacteria to the species level relies on phenotypic tests in most laboratories [29]. The commonest error Ringuet et al. found in databases was the misidentification between *M. chelonae* and *M. abscessus* [30]. They are the most closely related species with *hsp65* sequences that differ by nearly 30 nucleotides, whereas their 16S rRNA genes differ by only four nucleotides. We selected the *hsp65* gene for our CE-based PRA, because its sequence has more variability than the 16S rRNA gene, and could be exploited to identify both slowly and rapidly growing mycobacteria. According to the sequence analysis of mycobacterial *hsp65* gene, PRACE was found to be more accurate than culture method in terms of species dif-

ferentiation for MOTT. One culture-negative specimen (specimen No.2) gives a positive result by PRACE. This specimen is AFB smear (1+), but reveals no growth despite prolonged incubation in both liquid and solid culture systems. It probably represents the presence of non-viable mycobacteria, which is identified as MTB by PRACE and sequence analysis.
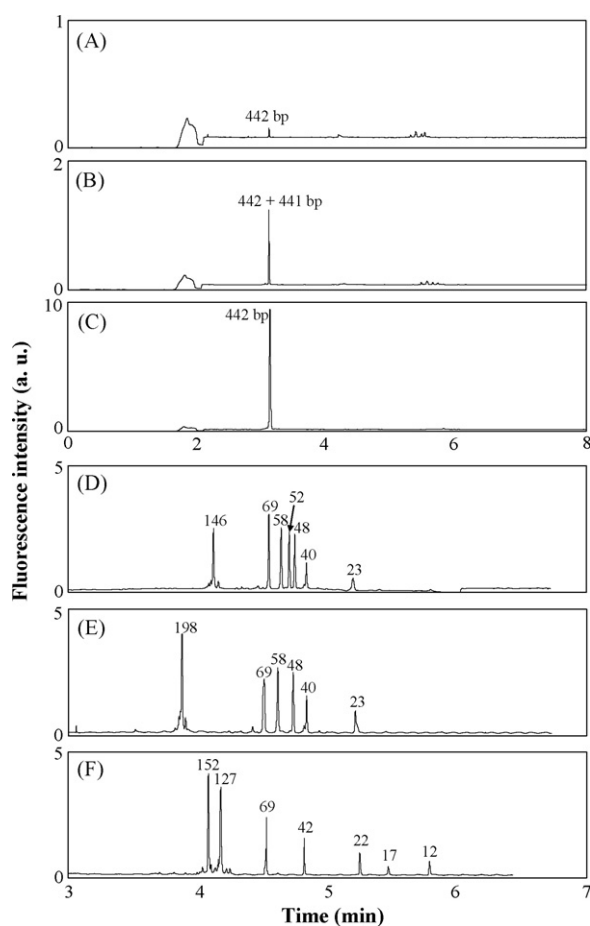
4. Conclusions

Practically speaking, there are at least two major problems in the rapid identification of mycobacterial species. One is the lack of an ultra-sensitive screening method for false smear-negative cases which are responsible for about 17% of tuberculosis transmission [10]. The other is the absence of a highly specific technique for diagnosing diseases caused by an increasing number of medically important MOTT species [2]. As our results shown, the advantages of nPCR and high-resolution CE enable PRACE to identify MTB and MOTT with minimal interferences of primer-dimers and inhibitors. For a limited number of specimens, the PRACE is not only able to differentiate the species, but detect the presence of individual DNA as well. Such an improvement is encouraging for our team to further evaluate a large quantity of specimens directly from clinical isolates, especially false AFB smear-negative cases and various species of MOTT. In conclusion, the PRACE using nPCR and high-resolution CE provides a potential alternative for rapidly identifying small amount of various mycobacterial species directly from sputum.

Acknowledgements

References

[1] F.A. Drobniewski, M. Caws, A. Gibson, D. Young, Lancet Infect. Dis. 3 (2003) 141.
[2] J.O. Falkinham, Clin. Microbiol. Rev. 9 (1996) 177.
[3] T.J. Brown, E.G. Power, G.L. French, J. Clin. Pathol. 52 (1999) 193.
[4] U. Reischl, N. Lehn, H. Wolf, L. Naumann, J. Clin. Microbiol. 36 (1998) 2853.
[5] C. Piersimoni, A. Callegaro, C. Scarparo, V. Penati, D. Nista, S. Bornigia, C. Lacchini, M. Scagnelli, G. Santini, G. De Sio, J. Clin. Microbiol. 36 (1998) 3601.
[6] T.J. Hellyer, T.W. Fletcher, J.H. Bates, W.W. Stead, G.L. Templeton, M.D. Cave, K.D. Eisenach, J. Infect. Dis. 173 (1996) 934.
[7] F. Brunello, M. Ligozzi, E. Cristelli, S. Bonora, E. Tortoli, R. Fontana, J. Clin. Microbiol. 39 (2001) 2799.
[8] A. Roth, U. Reischl, A. Streubel, L. Naumann, R.M. Kroppenstedt, M. Habicht, M. Fischer, H. Mauch, J. Clin. Microbiol. 38 (2000) 1094.
[9] E. Tortoli, Clin. Microbiol. Rev. 16 (2003) 319.
[10] M.A. Behr, S.A. Warren, H. Salamon, P.C. Hopewell, A.P. de Leon, C.L. Daley, P.M. Small, Lancet 353 (1999) 444.
[11] T.R. Frieden, T.R. Sterling, S.S. Munsiff, C.J. Watt, C. Dye, Lancet 362 (2003) 887.
[12] C.V.S. Babu, E.J. Song, S.M. Babar, M.H. Wi, Y.S. Yoo, Electrophoresis 27 (2006) 97.
[13] E.J. Song, S.M. Babar, E. Oh, M.N. Hasan, H.M. Hong, Y.S. Yoo, Electrophoresis 29 (2007) 129.
[14] P.-L. Chang, W.-S. Hsieh, C.-L. Chiang, M.J. Tuohy, G.S. Hall, G.W. Procop, H.-T. Chang, H.-T. Ho, Diagn. Microbiol. Infect. Dis. 58 (2007) 315.
[15] H.-T. Ho, P.-L. Chang, C.-C. Hung, H.-T. Chang, J. Clin. Microbiol. 42 (2004) 3525.
[16] H.-S. Chen, H.-T. Chang, Anal. Chem. 71 (1999) 2033.
[17] W.-L. Tseng, H.-T. Chang, Electrophoresis 22 (2001) 763.
[18] P.T. Kent, G.P. Kubica, Public Health Mycobacteriology: A Guide For The Level III Laboratory, US Department of Health and Human Services, Atlanta, 1985.
[19] A. Telenti, F. Marchesi, M. Balz, F. Bally, E.C. Bottger, T. Bodmer, J. Clin. Microbiol. 31 (1993) 175.
[20] C.R. Bascunana, K. Belak, J. Clin. Microbiol. 34 (1996) 2351.
[21] M.J. McPherson, S.G. Møller, PCR (The Basics), Springer-Verlag, New York, 2000.
[22] I.G. Wilson, Appl. Environ. Microbiol. 63 (1997) 3741.
[23] B. Böddinghaus, T.A. Wichelhaus, V. Brade, T. Bittner, J. Clin. Microbiol. 39 (2001) 3750.
[24] J.-H. Lu, H.-K. Li, H.-J. An, G.-H. Wang, Y. Wang, M.-Q. Li, Y. Zhang, J. Hu, J. Am. Chem. Soc. 126 (2004) 11136.
[25] G. Ruano, K.K. Kidd, J.C. Stephens, Proc. Natl. Acad. Sci. U.S.A. 87 (1990) 6296.
[26] E.T. Lagally, I. Medintz, R.A. Mathies, Anal. Chem. 73 (2001) 565.
[27] S.T. Cole, R. Brosch, J. Parkhill, T. Garnier, C. Churcher, D. Harris, S.V. Gordon, K. Eiglmeier, S. Gas, C.E. Barry III, F. Tekaia, K. Badcock, D. Basham, D. Brown, T. Chillingworth, R. Connor, R. Davies, K. Devlin, T. Feltwell, S. Gentles, N. Hamlin, S. Holroyd, T. Hornsby, K. Jagels, A. Krogh, J. McLean, S. Moule, L. Murphy, K. Oliver, J. Osborne, M.A. Quail, M.A. Rajandream, J. Rogers, S. Rutter, K. Seeger, J. Skelton, R. Squares, S. Squares, J.E. Sulston, K. Taylor, S. Whitehead, B.G. Barrell, Nature 393 (1998) 537.
[28] D. Hillemann, R. Warren, T. Kubica, S. Rusch-Gerdes, S. Niemann, J. Clin. Microbiol. 44 (2006) 302.
[29] S. Pai, N. Esen, X. Pan, J.M. Musser, Arch. Pathol. Lab. Med. 121 (1997) 859.
[30] H. Ringuet, C. Akoua-Koffi, S. Honore, A. Varnerot, V. Vincent, P. Berche, J.L. Gaillard, C. Pierre-Audigier, J. Clin. Microbiol. 37 (1999) 852.

Electrocatalytic activity of horseradish peroxidase/chitosan/carbon microsphere microbiocomposites to hydrogen peroxide

Xian Chen, Chengchao Li, Yanli Liu, Zhifeng Du, Shoujiang Xu, Limiao Li, Ming Zhang, Taihong Wang*

Key Laboratory for Micro-Nano Optoelectronic Devices of Ministry of Education, and State Key Laboratory for Chemo/Biosensing and Chemometrics, Hunan University, Changsha 410082, China

ARTICLE INFO

ABSTRACT

Colloidal carbon microspheres (CMS) are dispersed in chitosan (CHIT) solution to form an organic–inorganic hybrid with excellent micro-environment for the immobilization of biomolecules. A novel amperometric biosensor for the determination of hydrogen peroxide (H_2O_2) has been constructed by entrapping horseradish peroxidase (HRP) in as-synthesized CMS/CHIT hybrid. The modification of glassy carbon electrode is made by a simple solution-evaporation method. The electrochemical properties of the biosensor are characterized in electrochemical methods. The proposed biosensor shows high sensitive determination and fast response to H_2O_2 at −0.15 V. The constructed HRP/CHIT/CMS/GC electrode also exhibits a fine linear correlation with H_2O_2 concentration. The calculated value of the apparent Michaelis–Menten constant, 2.33 mM, suggests that the HRP in CMS/CHIT hybrid keeps its native bioactivity and has high affinity for H_2O_2.

© 2008 Published by Elsevier B.V.

1. Introduction

In recent years, amperometric biosensors based on horseradish peroxidase (HRP) have been considered as the most effective measure for the determination of hydrogen peroxide (H_2O_2), which is of practical importance in many fields, including chemistry, biology [1,2], industry, clinical control and environmental protection, etc. [3–5]. Conventional H_2O_2 detection methods, such as titrimetry [6], chemiluminescence [7–10], fluorimetry [11–13], and spectrometry [14], are generally time-consuming and cumbrous for operation. Now electrochemical sensors offer an attractive route because of their simplicity, high sensitivity, and selectivity.

Carbon-based materials, such as glassy carbon, graphite, and diamond, have been extensively used in electrochemistry due to their low background response, and good conductivity [15–17]. As one of the most interesting carbon nanostructures, carbon nanotubes (CNTs) have been extensively used in electrocatalysis and biosensing [18–22]. The insolubility of CNTs in most solvents, however, limits their application in designing CNTs-based biosensing devices. Oxidation with acids or ozone is used to be a conventional modification of carbon surface. The oxygenated functionalities such as carboxylic acid, esters are generated on the carbon surface. The subsequent reaction of thionyl chloride with the carboxylic groups makes it possible to graft and further elaborate the surface properties. However, the modification technique has a deadly disadvantage in the low degree of functionalization and the corrosion of the carbon surface during the oxidative treatment [23].

New kinds of biocompatible materials have attracted much interest to improve the behavior of biosensors. The carbon microspheres (CMS, colloidal carbon spheres [24]) are synthesized through a facile hydrothermal synthetic process. In contrast to other materials, two advantages become apparent: (1) The good biocompatibility and relatively active surface, which contains abundance of functional groups such as $-C=O$, $-OH$, is easily obtained by only one-step process without further modification. Partially dehydrated functional groups on the carbon frameworks improve the hydrophilicity and reactivity of the microspheres in aqueous systems. These functional groups, which provide a crucial chemical environment, make the microspheres that are easily solubilized in aqueous solution of a biopolymer, chitosan (CHIT), because of van der Waals force. At the same time, the effective attachment of the enzyme is occurred because of covalently binding through an amide bond between the CHIT and enzyme. (2) The preparation of the carbon microsphere is an absolutely environment friendly and low-cost approach. The hydrothermal reaction procedure involves none

---

* Corresponding author. Tel.: +86 731 8822332; fax: +86 731 8822332.
E-mail address: thwang@hnu.cn (T. Wang).

of the organic solvents or surfactants which are commonly used for preparation of polymer micro- or nanospheres. These advantages ensure that the microsphere is nontoxic, which enlarges their application in biosensor.

Herein we successfully utilize as-synthesized CMS as a new kind of biomaterial to construct a biosensor for the first time. CMS act as efficient conductor for electrons transfer, CHIT is an electrochemical promoting polymeric binder as backbone, and HRP is a biological catalyst that facilitates the transfer of substrate into product by lowering the activation energy. In contrast to previous sensors, the CMS-based H_2O_2 sensor has shown the advantages of low applied potential, high affinity, low background current and excellent sensitivity.

2. Experimental

2.1. Reagents

HRP (EC.1.11.1.7, 250 U/mg, from Horseradish) and CHIT were purchased from Sigma and used without further purification. H_2O_2 (30% v/v aqueous solution), glucose was obtained from Shanghai Chemical Reagent Co. (Shanghai, China). All other reagents were of analytical grade. All solutions were prepared with double distilled water, which was purified with a Milli-Q purification system. Phosphate buffer solution (PBS, 1/15 M, pH 6.98) was used as supporting electrolyte in all measurement.

2.2. Apparatus

Cyclic voltammetry was performed in 1/15 M PBS (pH 6.98) with CHI760B electrochemical workstation (Shanghai, China). The modified glassy carbon (GC) electrode was used as the working electrode, a Pt foil as the counter electrode and a saturated calomel electrode (SCE) as the reference electrode in a three-electrode cell (10 mL). Fourier transform infrared spectra (FT-IR) measured by KBr pellets was obtained on a WQF-410 Fourier transform infrared spectrophotometer (Beijing Secondary Optical Instruments, China). Transmission electron microscope (TEM) image was taken with a FEI Tecnai G^2 20 TEM (FEI, America).

2.3. Preparation of CMS

The carbon microspheres (CMS) were prepared through the polycondensation reaction of glucose under hydrothermal condition according to previously literature [25]. Briefly, 8 g of glucose was dissolved in 40 mL of deionized water. The mixture solution was then put into a Teflon-lined stainless steel autoclave with a capacity of 40 mL and maintained at 180 °C for over 8 h. The black product was precipitated with ethanol and distilled water followed by centrifugation. Finally the uniform CMS were obtained.

2.4. Preparation of HRP/CHIT/CMS/GC biosensor

Prior to modification, the GC electrodes (3 mm diameter) were polished with emery paper and 0.05 μm alumina powder, cleaned in nitric acid (dilute with distilled water to 1:1% v/v), ethanol and distilled water for 5 min, successively. Then thoroughly rinsed with distilled water and dried at room temperature. 125 mg of CHIT flakes were dissolved into 50 mL of 0.05 M acetic acid and the mixture was vigorously stirred for 2 h at room temperature. A viscous and translucent CHIT (0.25 wt %) solution was formed. 5 mg of CMS were ultrasonically dispersed into 20 mL of CHIT solution by ultrasonication for 2 h. Then equal volume of CMS/CHIT composite solution and the enzyme solution (5 μL of CMS/CHIT and 5 μL of 5 mg/mL HRP) were mixed adequately. The electrode
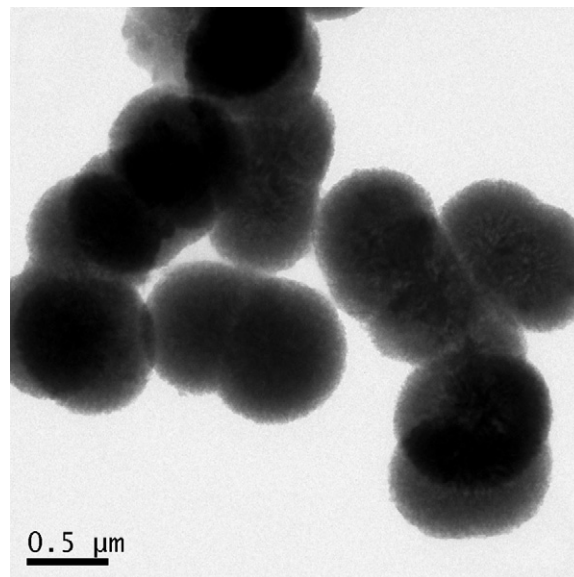
Fig. 1. TEM image of CMS of 500 nm prepared a 180 °C, 8 h.

modified by horseradish peroxidase/chitosan/carbon microspheres (HRP/CHIT/CMS) was prepared by casting 8 μL of the mixture solution onto the surface of a GC electrode. When the solution was dried at 4 °C overnight, a CHIT thin film contained CMS and HRP was prepared. As a comparison, the electrodes modified by HRP/CHIT and CMS/CHIT were also prepared by the similar manner.

3. Results and discussion

3.1. Characterization of the carbon microspheres (CMS)

Fig. 1 shows the typical TEM image of the sample prepared with reaction time of 8 h under the hydrothermal condition at 180 °C. The diameter of the particles is around 500 nm, with some large ones reaching about 800 nm. It can be seen that it is very coarse on the surface which contained some distributed uniformly nano-sized pores of the obtained CMS [25]. The coarse surface can not only increase the surface area, but also assist adsorption of reactive species. The diameters of the CMS were affected by temperature, concentration of the glucose and reaction time.

Fig. 2 shows the FT-IR spectra of the carbon spheres. The sample displays feature peaks for hydroxyl at 3383 cm^{-1} (O—H stretching),
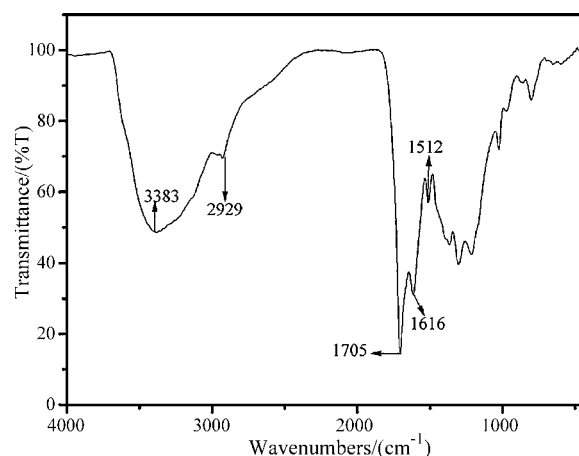
Fig. 2. FTIR spectra of carbon spheres.
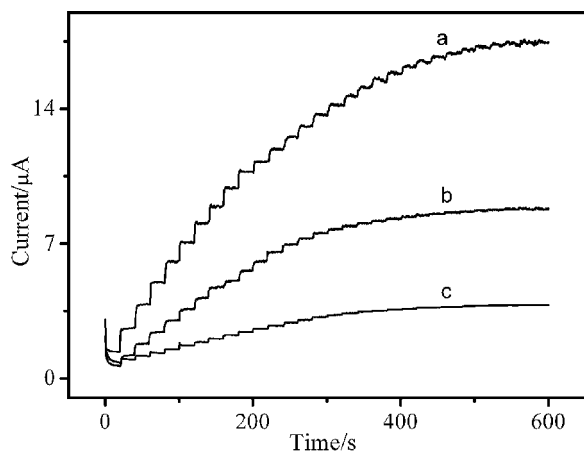
Fig. 3. Current–time responses for successive addition of 1 mM hydrogen peroxide at the (a) HRP/CHIT/CMS/GC, (b) CHIT/CMS/GC, (c) HRP/CHIT/GC electrodes in 1/15 M PBS (pH 6.98) containing 0.1 M hydroquinone. Operating potential, −0.15 V.

carbonyl at 1705 cm^{-1} (C=O stretching), and stretching peaks at 1616 and 1512 cm^{-1} (aromatic C=C). The bands in the range from 1000 to 1300 cm^{-1}, which include the C−OH stretching and −OH bending vibrations, imply the existence of large numbers of residual hydroxy groups. After dehydration, partial residues in which reductive −OH or −CHO groups are covalently bonded to the carbon frameworks improve the hydrophilicity and stability of the microspheres in aqueous systems. These residue groups improve the hydrophilicity and stability of the microspheres in aqueous systems.

3.2. Electrochemical behavior of the HRP/CHIT/CMS/GC/GC electrode

To distinguish the role of individual components and possible synergy between them, the electrochemical properties of HRP/CHIT/CMS/GC, CHIT/CMS/GC and HRP/CHIT/GC were monitored. The advantages of the HRP/CHIT/CMS/GC electrode are illustrated in connection with the detection of H$_2$O$_2$. Fig. 3 compares the response to increasing levels of H$_2$O$_2$ in 0.1 mM steps at the HRP/CHIT/CMS/GC electrode (Fig. 3a), CHIT/HRP/GC electrode (Fig. 3b) and CMS/CHIT/GC electrode (Fig. 3c) at potential of −0.15 mV. As expected from the curve, the CHIT/CMS/GC electrode gives a slight response signal to the addition of H$_2$O$_2$. Higher increase of the response signal is observed for the HRP/CHIT/GC electrode. In contrast, the HRP/CHIT/CMS/GC electrode responds rapidly to the changes of the concentration, reaching a steady-state signal within 5 s. The difference between these electrodes mainly attributes to the excellent properties of HRP immobilized on the CMS/CHIT hybrid. The micro-environment of the hybrid is advantageous to the incremental adsorption of HRP. The functional groups and the coarse surface of the carbon frameworks aid the large amount of distributing of CHIT in the hybrid through van der Waals between CMS and CHIT. HRP could be covalently bound to the functional surface mainly due to amide bonds between CHIT and HRP.

For the fabricated biosensor, the cyclic voltammograms (CVs) corresponding to various scan rates were also investigated. Both the anodic and cathodic peak currents clearly increase with increasing potential scan rate. As shown in Fig. 4, well-characterized redox peaks could be observed through the scan rate in a range from 20 to 200 mV s^{-1}. Moreover, it is found from Fig. 4 (inset) that the peak currents are proportional to the square roots of the scan rates, which suggest a typical the semi-infinite linear diffusion-controlled
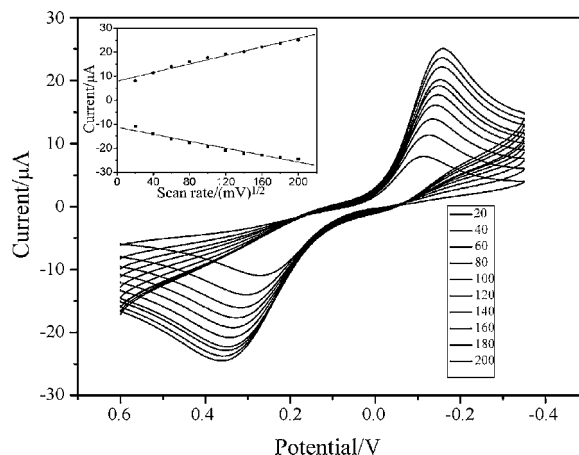
Fig. 4. Voltammetric responses of the GC electrode modified by HRP/CHIT/CMS films to 1 mM hydroquinone at different scan rates (inner to outer): 20, 40, 60, 80, 100, 120, 140, 160, 180, and 200 mV s^{-1}. The inset shows the anodic and cathodic peak currents plotted against the square root of the scan rate.

electrochemical behavior feature of the redox process. The catalytic process of HRP immobilized onto CHIT/CMS electrode surface can be expressed as follows [26]:

$$HRP(Fe^{3+}) + H_2O_2 \rightarrow compound\ I + H_2O \tag{1}$$

$$Compound\ I + H_2Q \rightarrow compound\ II + BQ \tag{2}$$

$$Compound\ II + H_2Q \rightarrow HRP(Fe^{3+}) + BQ + H_2O \tag{3}$$
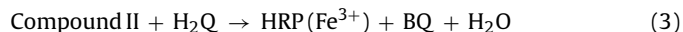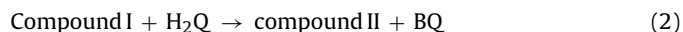
The net reaction is : $BQ + 2e^- + 2H^+ \rightarrow H_2Q$

where compound I (oxidation state + 5) and II (oxidation state + 4) represent the enzyme intermediates in the reaction H$_2$Q and BQ represent hydroquinone and benzoquinone, respectively. In the first two electrons transfer step, H$_2$O$_2$ is reduced to water and the HRP is oxidized to compound I. Compound I is then reduced in a one electron step to form compound II, and then compound II is reduced to the original form of HRP by the redox mediator (H$_2$Q). The BQ is subsequently reduced to H$_2$Q by a rapid reaction involving the consumption of two electrons from the electrode. The resulting cathodic currents are therefore correlated with the concentration of H$_2$O$_2$.

In order to observe the activity of HRP on the CMS/CHIT modified glassy carbon electrode, its response to the reduction of H$_2$O$_2$ was studied. Fig. 5 is the CVs of the HRP/CHIT/CMS/GC electrode in 1/15 M PBS (pH 6.98) in the absence (curve a) and in presence of 4 mM H$_2$O$_2$ (curve b) between −0.35 and 0.6 V at the scan rate of 100 mV s^{-1}. In blank PBS, the biosensor only exhibited the electrochemical behavior of hydroquinone, a pair of anodic and cathodic waves (curve a). With the addition of H$_2$O$_2$, an obvious increase of the cathodic and anodic current is observed. The reduction peak current increases greatly (from 18.67 to 73.66 μA) with slightly negative shift of peak potential. Meanwhile the oxidation peak current decreased markedly, indicating an obvious electrocatalytic process to the enzymatic reduction of H$_2$O$_2$ by the immobilized HRP. The inset shows the process of addition of successive aliquots of 1 mM H$_2$O$_2$ in PBS. The peak current enhances with the increase of H$_2$O$_2$ concentration. The excellent electrocatalytic activity of the electrode toward H$_2$O$_2$, which is a common product of a great many of oxidase-based enzyme reactions, means that the electrode can provide a signal transduction in the fabrication of biosensors.

The dependence of the biosensor response on the applied potential for determination of 0.1 mM H$_2$O$_2$ is shown in Fig. 6. The foot of the electrocatalytic reduction of H$_2$O$_2$ was observed around 0 V
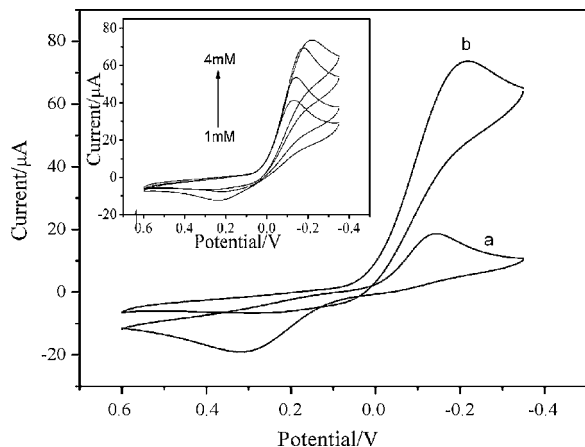
Fig. 5. CVs of the HRP/CHIT/CMS/GC electrode in 1/15 M PBS (pH 6.98) in the absence (a) and presence of 4 mM H_2O_2 (b). Inset: CVs of addition of successive aliquots of 1 mM H_2O_2 in PBS (pH 6.98).

and the maximum amperometric response value was at −0.15 V. As is well known, a lower potential can avoid or decrease the interference caused by some electroactive species and make the background current and noise levels reach their lowest value [27]. −0.15 V was chosen as the applied potential for the amperometric measurement. Fig. 7 displays a typical amperometric response of the CMS biosensor after addition of successive aliquots of 0.1 mM H_2O_2 in PBS (1/15 M, pH 6.98) under stirring. It can be seen that HRP/CHIT/CMS/GC electrode has a fast and sensitive response to H_2O_2 over a wide range of concentrations. The plot of current vs. H_2O_2 concentration is shown in inset A of Fig. 7. The equation of the fitting curve was:

$$I = 8.14 C_{H_2O_2} (mM) + 0.9146 (\mu A) \quad (R = 0.997, n = 13)$$

The calibration curve was linear with H_2O_2 concentration from 0.1 to 1.6 mM, the sensitivity was 120.17 $\mu A\,cm^{-2}\,mM^{-1}$ and the detection limit was calculated as 0.93 μM. It can be seen from the plot that the biosensor showed a rapid and sensitive response to the change of H_2O_2 concentration, indicating a good electrocatalytic property of the modified electrode. The sensor retained about 90% of its initial current response after intermittent use after 25 days. The response time for the electrode is less than 5 s. Fast responses may be due to the easy diffusion of H_2O_2 in the ultrathin CMS/CHIT hybrid film. The apparent Michaelis–Menten constant, K_M^{app}, which
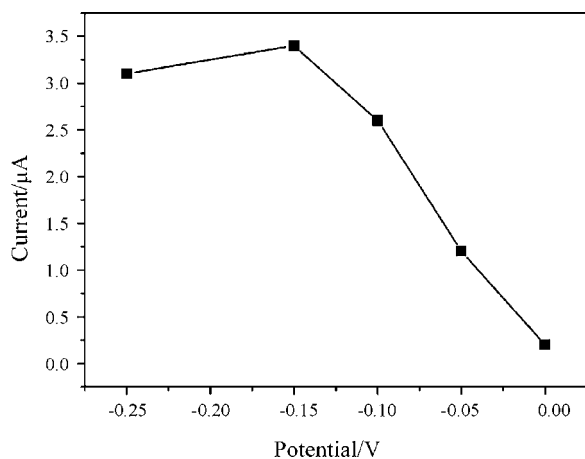
Fig. 6. Influence of applied potential on the amperometric response of the sensor to 0.1 mM H_2O_2.
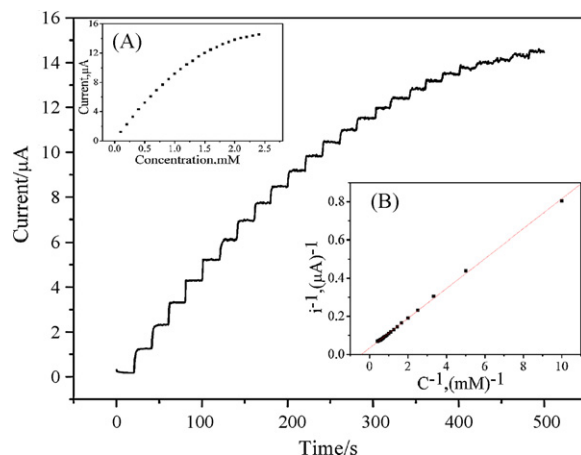
Fig. 7. Amperometric response of successive addition of 0.1 mM H_2O_2 at HRP/CHIT/CMS/GC electrode in PBS (pH 6.98, 1/15 M) containing 1 mM hydroquinone, −0.15 V constant potential, insets: (A) plot of chronoamperometric current vs. H_2O_2 concentration; (B) linear calibration curve for determination of K_M^{app}.

gives an indication of the enzyme-substrate kinetics and a reflection of the enzymatic affinity, could be calculated from the electrochemical version of the Lineweaver–Burk equation [28]:

$$\frac{1}{I_{ss}} = \frac{1}{I_{max}} + \frac{K_M^{app}}{I_{max} C}$$

where I_{ss} is the steady-state current after the addition of substrate, C is the bulk concentration of the substrate, and I_{max} is the maximum current measured under saturated substrate condition. The K_M^{app} is determined by analyzing the slope and intercept for the plot of the reciprocals of the current vs. H_2O_2 concentration. As is well known the smaller K_M^{app} shows the higher catalytic ability. The Michaelis–Menten constant of the system (K_M^{app}) in this work was found to be 2.33 mM, which was similar to that of 2.198 mM at polysaccharide–silica-modified electrode [29] and much smaller than the reported 23.85 mM based on the direct electrochemistry of HRP in sol–gel derived ceramic–CNT nanocomposite film [8]. The result implied that the HRP/CHIT/CMS/GC electrode exhibited a higher affinity for hydrogen peroxide.

4. Conclusions

In summary, a biosensor with excellent properties was successfully demonstrated based on the combination of CMS, CHIT, and HRP. Inorganic–organic hybrid, CMS/CHIT, allowed the necessary efficient electron tunneling and large amount of adsorption of HRP. With the help of CMS, nice electrochemical response of HRP was obtained. The H_2O_2 biosensors exhibited a variety of good electrochemical characteristics including high sensitivity, low applied potential, high affinity.

Acknowledgements

References

[1] X.L. Luo, J.J. Xu, W. Zhao, H.Y. Chen, Biosens. Bioelectron. 19 (2004) 1295.
[2] X. Cui, G. Liu, Y. Lin, J. Biomed. Nanotechol. 1 (2005) 1.
[3] S.Q. Liu, H.X. Ju, Biosens. Bioelectron. 19 (2003) 177.
[4] X.B. Lu, J.H. Zhou, W. Lu, Q. Liu, J.H. Li, Biosens. Bioelectron. 23 (2008) 1236.

[5] X.H. Shu, Y. Chen, H.Y. Yuan, S.F. Gao, D. Xiao, Anal. Chem. 79 (2007) 3695.
[6] N.V. Klassen, D. Marchington, H.C.E. McGovan, Anal. Chem. 66 (1994) 2921.
[7] D.W. King, W.J. Cooper, S.A. Rusak, B.M. Peake, J.J. Kiddle, D.W. O'Sullivan, M.L. Melamed, C.R. Morgan, S.M. Theberge, Anal. Chem. 79 (2007) 4169.
[8] S.H. Chen, R. Yuan, Y.Q. Chai, L.Y. Zhang, N. Wang, X.L. Li, Biosens. Bioelectron. 22 (2007) 1268.
[9] C.G. Shi, J.J. Xu, H.Y. Chen, J. Electroanal. Chem. 610 (2007) 186.
[10] J. Li, C. Lau, M. Morizono, K. Ohta, M. Kai, Anal. Chem. 73 (2001) 5979.
[11] M.C.Y. Chang, A. Pralle, E.Y. Isacoff, C.J. Chang, J. Am. Chem. Soc. 126 (2004) 15392.
[12] J. Li, P.K. Dasgupta, G.A. Tarver, Anal. Chem. 75 (2003) 1203.
[13] N. Jie, J. Yang, X. Huang, R. Zhang, Z. Song, Talanta 42 (1995) 1575.
[14] A. Lobnik, M. Cajlakovic, Sens. Actuators B 74 (2001) 194.
[15] K.P. Gong, M.N. Zhang, Y.M. Yan, L. Su, L.Q. Mao, S.X. Xiong, Y. Chen, Anal. Chem. 76 (2004) 6500.
[16] C. Terashima, T.N. Rao, B.V. Sarada, Y. Kubota, A. Fujishima, Anal. Chem. 75 (2003) 1564.
[17] P. Chen, R.L. McCreery, Anal. Chem. 68 (1996) 3958.
[18] R.H. Baughman, C. Cui, A.A. Zakhidov, Z. Iqbal, J.N. Barisci, G.M. Spinks, G.G. Wallace, A. Mazzoldi, D.D. Rossi, A.G. Rinzler, O. Jaschinski, S. Roth, M. Kertesz, Science 284 (1999) 1340.
[19] J. Wang, M. Musameh, Y.H. Lin, J. Am. Chem. Soc. 125 (2003) 2408.
[20] R.R. Moore, C.E. Banks, R.G. Compton, Anal. Chem. 76 (2004) 2677.
[21] H.J. Chen, S.J. Dong, Biosens. Bioelectron. 22 (2007) 1811.
[22] F.L. Qu, M.H. Yang, G.L. Shen, R.Q. Yu, Biosens. Bioelectron. 22 (2007) 1749.
[23] J.L. Bahr, J.M. Tour, J. Mater. Chem. 12 (2002) 1952.
[24] H.S. Qian, G.F. Lin, Y.X. Zhang, P. Gunawan, R. Xu, Nanotechnology 18 (2007) 355.
[25] X.M. Sun, Y.D. Li, Angew. Chem. Int. Ed. 43 (2004) 597.
[26] M. Delvaux, A. Walcarius, S. Demoustier-Champagne, Anal. Chim. Acta 525 (2004) 221.
[27] Y.X. Sun, J.T. Zhang, S.W. Huang, S.F. Wang, Sens. Actuators B 124 (2007) 494.
[28] R.A. Kamin, G.S. Wilson, Anal. Chem. 52 (1980) 1198.
[29] G.H. Wang, L.M. Zhang, J. Phys. Chem. B 110 (2006) 24864.

Identification of polyoxypregnane glycosides from the stems of *Marsdenia tenacissima* by high-performance liquid chromatography/tandem mass spectrometry

Juanjuan Chen[a], Xiaoyu Li[b], Cuirong Sun[a], Yuanjiang Pan[a,*], Urs Peter Schlunegger

[a] *Department of Chemistry, Zhejiang University, Zheda Road 38#, Hangzhou 310027, China*
[b] *Institute of Materia Medica, Zhejiang Academy of Medical Sciences, Hangzhou 310028, China*

ARTICLE INFO

ABSTRACT

A facile method based on high-performance liquid chromatography coupled with electrospray ionization tandem mass spectrometry (HPLC/(+)ESI-MS^n) has been established for the analysis of polyoxypregnane glycosides in the stems of *Marsdenia tenacissima*. The data reveals the ability of MS^n in the structural elucidation of polyoxypregnane glycosides including the nature of the polyoxypregnane core, the kinds of the substituents and the types of sugar residues. Offline Fourier transform ion cyclotron resonance mass spectrometry (FTICR-MS) is also performed to assign accurate elemental compositions. In this study, eighteen polyoxypregnane glycosides have been investigated. Among these components, five compounds are unambiguously identified as Marsdenoside K, Tencissoside A, B, C and D; two compounds are established as novel compounds based on mass spectral data; and the other eleven compound's structures are tentatively proposed. Furthermore, breakdown curves are constructed to distinguish five pairs of isomers among these eighteen compounds. As far as our knowledge, this is the first report on identification of polyoxypregnane glycosides in the stems of *M. tenacissima* by HPLC/ESI-MS^n directly, which could save time and material consuming efforts in traditional phytochemistry analyses.

Crown Copyright © 2008 Published by Elsevier B.V. All rights reserved.

1. Introduction

Marsdenia tenacissima (Roxb.)Wight et Arn. (Asclepiadaceae) is a perennial climber that grows from tropical to subtropical Asia. It is well known as "Tong-guang-teng" for the treatment of asthma, cancer, trachitis, tonsillitis, pharyngitis, cystitis, and pneumonia by its stems in Chinese folk medicine. Polyoxypregnane glycosides are the major bioactive constituents and rich in the stems of *M. tenacissima* [1–8]. To further investigate the pharmaceutical activities of these polyoxypregnane glycosides, identification of their chemical structures is necessary. However, traditional analytical protocols are tedious, laborious, time-consuming and insensitive, in which the minor constituents in plant extracts are easily ignored. Therefore, there is an increasing demand for methods for rapidly identifying and characterizing known or new structures.

The method of HPLC/ESI-MS^n has the advantage of high sensitivity, relatively short analysis time, considerable structural information, and low levels of sample consumption. It has the potential ability to rapidly screening of the minor constituents in plant extracts that are difficult to obtain by conventional phytochemical means [9–12]. Glycosides in crude plant extracts have been determined by HPLC/ESI-MS^n in the recent reports, demonstrating the advantages of mass spectrometry in phytochemistry [13–15]. However, to our knowledge, no previous studies of polyoxypregnane glycosides by HPLC/ESI-MS^n have been published in the stems of *M. tenacissima*.

This is the first report concerning the characterization of polyoxypregnane glycosides in *M. tenacissima* by HPLC/(+) ESI-MS^n. Based on the fragmentations behaviors of five known polyoxypregnane glycosides, eleven compounds were tentative proposed and two compounds were established as novel compounds. Breakdown curves were utilized to differentiate five pairs of isomers among these eighteen compounds. Results showed that two pairs of positional isomers and two pairs of stereochemical isomers in this study could be distinguished obviously.

2. Experimental

2.1. Reagents and chemicals

Polyoxypregnane glycosides used for identification purposes by HPLC and MS were isolated previously from the plant *M. tenacis-

* Corresponding author. Tel.: +86 571 87951285; fax: +86 571 87951629.
E-mail address: panyuanjiang@zju.edu.cn (Y. Pan).
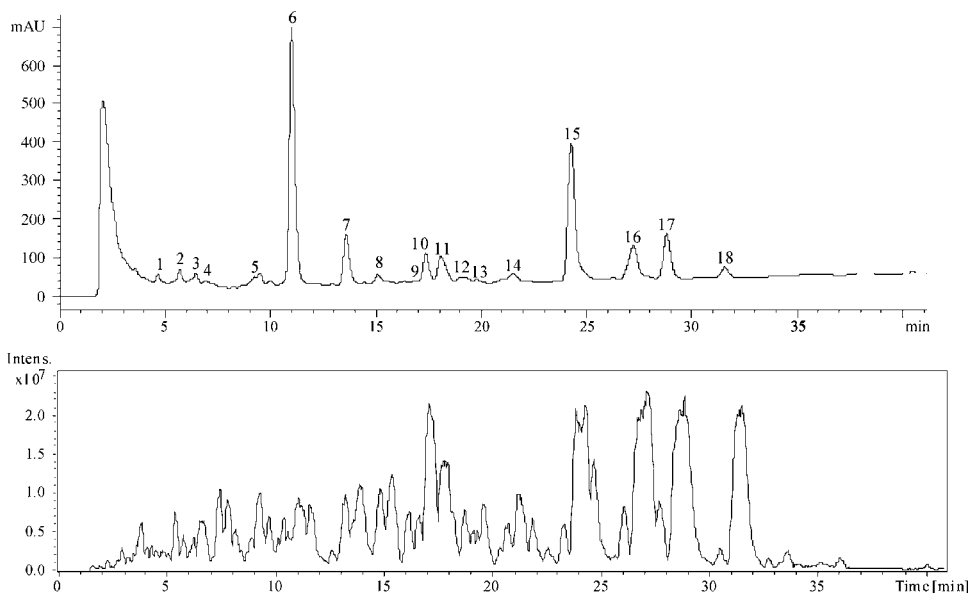
Fig. 1. HPLC/UV (220 nm) separation and total ion chromatography (TIC) of polyoxypregnane glycosides from the extracts of the stems of *Marsdenia tenacissima*.

sima in the laboratory of Institute of Materia Medica, Zhejiang Academy of Medical Sciences. Methanol (chromatographic grade) used for analytical HPLC and preparative HPLC was purchased from Merck (Darmstadt, Germany). Deionized water (18 MΩ) was obtained from a Milli-Q water purification system (Millipore, Bedford, MA, USA). The stems of *M. tenacissima* were obtained from Yunnan province, China.

2.2. Sample preparation

The dried and powdered stems of *M. tenacissima* (5 kg) were extracted three times with 95% ethanol under reflux for 2 h each time. The solvent in the extract was evaporated resulting in the ethanol extract residue which was extracted with chloroform under reflux, and a yellow residue was obtained on evaporation of the chloroform. The residue was subjected to column chromatography (silica gel, gradient $CHCl_3/MeOH$ (50:1, 20:1, 10:1, 5:1, v/v); thus eight main fractions were obtained. A sample of fraction 8 ($CHCl_3/MeOH$ 5:1, v/v) was dissolved in methanol, membrane-filtered (0.45 μm), and analyzed by HPLC/ESI-MS^n. The results obtained for this chloroform extract were reported and discussed in the following sections.

2.3. Analytical and preparative high-performance liquid chromatography

An Agilent 1100 analytical HPLC system with a G1312 Binpump, G1314A variable-wavelength detector (VWD), model 7725 injector fitted with a 20 μL sample loop, along with an Agilent ChemStation data system, was used. A reversed-phase Agilent Extend C18 column (4.6 mm × 150 mm, 3.5 μm) was used for separation; the column was maintained at room temperature. Chromatography was carried out in gradient mode with methanol and water; the percentage of methanol was changed linearly as follows: 0 min, 60%; 10 min, 65%; 30 min, 75%; 40 min, 80%; 42 min, 60%. The flow rate was 0.8 mL min^{-1}, and the detection wavelength was 220 nm.

Preparative HPLC system was performed using Waters 600 Separations Module equipped with Waters model 2996 diode array detector and Waters Empower System (Waters Co., Milford, MA, USA). A reversed-phase Shim-pack PRC ODS (20 mm × 250 mm,

10 μm) was used for preparation; the column was maintained at room temperature. The eluent for preparative HPLC was mixture of appropriate percentage of methanol and water: 72% methanol for **11**, **14** and **18**. The flow rate was 8.0 mL min^{-1}, and detection wavelength was 220 nm.

2.4. Mass spectrometry

HPLC/ESI-MS^n analyses were performed using the Agilent HPLC system described above combined with a Bruker Esquire 3000^{plus} ion trap mass spectrometer (Bruker–Franzen Analytik GmbH, Bremen, Germany) equipped with electrospray ionization (ESI). Instrument control and data acquisition were performed using Esquire 5.0 software. The ion source temperature was 250 °C, and needle voltage was always set at 4.0 kV. Nitrogen was used as the drying and nebulizer gases at a flow rate of 10 L min^{-1} and a back-pressure of 30 psi. Helium was introduced into the trap with an estimated pressure 6×10^{-6} mbar to improve trapping efficiency to act as the collision gas for the MS^n data; the mass spectrometer was optimized in the collision energy range of 0.6–1.0 V to maximize the ion current in the spectra. The MS^n spectral data of eighteen compounds are supported as the supplementary information.

The offline FTICR-MS experiments were performed using an Apex III Fourier transform ion cyclotron resonance mass spectrometer with 7.0T actively shielded superconducting magnet (Bruker Daltonics, Billerica, MA, USA) combined with an Apollo electrospray ionization source operated in the positive ion mode. The solutions were infused at a rate of 3.0 μL min^{-1} using a Cole-Parmer syringe pump. Accurate mass measurements were performed using NaI as an external calibration compound. Each spectrum was an average of eight transients, each composed of 512 K points, acquired using a workstation operating XMASS version 6.1.1.

2.5. NMR spectroscopy

1D and 2D NMR spectra were measured on a Bruker Advance DMX 500 spectrometer operating at 500MHz for ^{1}H and 125MHz for ^{13}C, using pyridine (C_5D_5N) as solvent and TMS as internal standard. The ^{13}C NMR spectral data of compounds **11**, **14** and **18** are supported as the supplementary information.

Fig. 2. Structures assigned to polyoxypregnane glycosides in the stems of *Marsdenia tenacissima*.

Compounds	R_1	R_2	R_3	Aglycone	MW
1	S	Ac, H*		1	872
2, 3, 5, 8		pairs of isomers		1	912
4	S	Ac	Ac	1	914
6	S	Tig	Ac	1	954
7	S	Ac	Bz	1	976
9	S	Tig	Tig	2	1012
10	isomer of S	Tig	Tig	1	994
11	S	Ac	Tig	1	954
12	S	Tig	Tig	3	996
13		isomer of 16		1	1016
14	S	Bz	Ac	1	976
15	S	Tig	Tig	1	994
16	S	Bz	Tig	1	1016
17	S	Bu	Tig	1	996
18	S	Bu	Bz	1	1018

*: R_2=Ac, R_3=H or R_2=H, R_3=Ac

3. Results and discussion

The HPLC/UV (220 nm) detection and total ion chromatography (TIC) of the polyoxypregnane glycosides in the extracts of stems of *M. tenacissima* are shown in Fig. 1. The target polyoxypregnane glycosides recorded at retention times were designed as **1** through **18**. All precursor ions were observed in the positive and negative ion mode spectra. Both of them had similar fragment pathways, but in the positive mode, the fragment information of sugar chain is more abundant than that in the negative mode. So singly charged sodium adducts of the molecules [M + Na]⁺ were studied in the following parts. Fig. 2 exhibits the structures of the investigated molecules and high-resolution FTICR-MS data are listed in Table 1.

3.1. Investigation of authentic compounds 6, 7, 15, 16 and 17

7, 6, 15, 16 and 17 could unambiguously be identified as Marsdenoside K, Tencissoside A, B, C and D, respectively, based on the comparison of the retention times with those of authentic reference substances and on the fragmentation behaviors observed in the MS^n experiments [4,6]. Generally, these five compounds gave similar fragmentations in MS^n experiments. Thus, the fragmentation patterns of **15** were discussed in detail below for elucidation of the molecular structure.

The mass spectra of **15** and proposed fragmentation pathways are shown in Fig. 3 and Scheme 1, respectively. ESI-MS analysis of **15** gave the [M + Na]⁺ ion at *m/z* 1017 which was further selected for MS/MS experiment. As demonstrated in Fig. 3, product ions at

Table 1
Accurate masses and assigned elemental compositions of eighteen polyoxypregane glycosides

Compounds	Composition	Measurement (m/z)	Theoretical (m/z)	Error (ppm)
1	$C_{43}H_{68}O_{18}Na^+$	895.4318	895.4298	2.2
2	$C_{46}H_{72}O_{18}Na^+$	935.4598	935.4611	−1.4
3	$C_{46}H_{72}O_{18}Na^+$	935.4613	935.4611	0.2
4	$C_{45}H_{70}O_{19}Na^+$	937.4388	937.4404	−1.7
5	$C_{46}H_{72}O_{18}Na^+$	935.4655	935.4611	4.7
6	$C_{48}H_{74}O_{19}Na^+$	977.4735	977.4717	1.8
7	$C_{50}H_{72}O_{19}Na^+$	999.4563	999.4560	0.3
8	$C_{46}H_{72}O_{18}Na^+$	935.4632	935.4611	2.4
9	$C_{51}H_{80}O_{20}Na^+$	1035.5105	1035.5135	−2.9
10	$C_{51}H_{78}O_{19}Na^+$	1017.5009	1017.5030	−2.1
11	$C_{48}H_{74}O_{19}Na^+$	977.4738	977.4717	2.1
12	$C_{51}H_{80}O_{19}Na^+$	1019.5174	1019.5186	−1.2
13	$C_{53}H_{76}O_{19}Na^+$	1039.4873	1039.4873	0
14	$C_{50}H_{72}O_{19}Na^+$	999.4574	999.4560	1.4
15	$C_{51}H_{78}O_{19}Na^+$	1017.5063	1017.5030	3.2
16	$C_{53}H_{76}O_{19}Na^+$	1039.4825	1039.4873	−4.6
17	$C_{51}H_{80}O_{19}Na^+$	1019.5222	1019.5186	3.5
18	$C_{53}H_{78}O_{19}Na^+$	1041.5011	1041.5030	−1.8

m/z 917 (A or B, shown in Scheme 1) and 817 (C) were generated by neutral loss of 100 Da and consecutive elimination of 100 Da from the precursor ion at m/z 1017, reasonably assigned as two (E)-2-methylbut-2-enoic acids from C-11 and C-12. In the MS[3] spectrum of ion at m/z 917 (A or B), elimination of 100 Da produced the ion at m/z 817 (C). Product ions at m/z 759 (D) and 655 (F) corresponded to the loss of C_3H_6O (58 Da) by cleavage within the oleandropyranose residue and terminal glucopyranose residue (162 Da) from the ion at m/z 817. Fragment ion at m/z 755 (E^b), by loss of 162 Da from ion at m/z 917, suggested the terminal glucopyranose residue. The whole sugar chain fragment ion at m/z 489 (G) resulted from the cleavage of the glycosidic bond between aglycone and the reducing end of the sugar chain, without containing the glycosidic oxygen atom. Fragment ion at m/z 345 (H) was achieved with the consecutive loss of reducing end oleandropyranose residue (144 Da) from ion at m/z 489 (G). Thus, with the analysis of the disaccharide fragment ion at m/z 345 (H) and terminal glucopyranose residue and the mass of second monosaccharide calculated as 160 Da, it could be inferred that it is consistent with allopyranose residue.

Based on the above analyses of the five authentic compounds, we could conclude that their fragmentation patterns were similar related to their structural characteristics. First, it was significant to stress that all the authentic substances only eliminated R_2OH and R_3OH on the C-11 and C-12 positions in the MS[2] experiments. Second, they had similar MS[3] fragmentation behaviors. The key fragment ions (m/z 489 (G) and 345 (H)) and neutral loss of 162 Da provided the mass information of sugar chain. Hence, according to the literatures and these fragmentation patterns, the structures of unknown polyoxypregnane glycosides could be proposed.

3.2. Identification of unknown compounds 1, 4, 9, 12, and 18

We also examined unknown polyoxypregnane glycosides in the extracts of stems of *M. tenacissima*. In the MS[3] spectra of compounds **1**, **4**, **9**, **12** and **18**, similar fragmentation pathways about sugar chain were observed to those of authentic compounds. Hence, the glycosyl ions of **1**, **4**, **9**, **12** and **18** were attributed to the Glc-Allo-Ole trisaccharide chain (**S**, as shown in Fig. 2).

The mass spectra of **1**, **4**, and **18** contained significant [M + Na]^+ ions at m/z 895, 937 and 1041, respectively. For compound **1**, neutral loss of 60 Da (acetic acid) and consecutive elimination of 18 Da (a molecular of water) were obtained from precursor ion at m/z 895 to produce fragment ions at m/z 835 and 817. These fragmentations indicated the presence of acetyl (**Ac**) and hydrogen atom on C-11 and C-12 positions. However, the acetyl located at C-11 or C-12

could not be confirmed by MS. As for **4**, loss of one and two 60 Da fragments produced the fragment ions at m/z 877 and 817, respectively, suggesting two acetyl substituents (**Ac**) on C-11 and C-12 positions. For **18**, the fragment ions at m/z 939, 919 and 817 were generated by neutral loss of 102 Da, 122 Da and sequential elimination of 102 Da from the precursor ion at m/z 1041, predicated the existing of benzoyl (**Bz**) and 2-methylbutyryl (**Bu**) groups.

Based on fragmentation behaviors and previous studies [1,2,6,7], **1** was proposed to be 3-O-β-D-glucopyranosyl-(1 → 4)-6-deoxy-3-O-methyl-β-D-allopyranosyl-(1 → 4)-β-D-oleandro-pyranosyl-11α-O-acetyltenacigenin B or 3-O-β-D-glucopyranosyl-(1 → 4)-6-deoxy-3-O-methyl-β-D-allopyranosyl-(1 → 4)-β-D-oleandropyranosyl-12β-O-acetyltenacigenin B. **4** was tentatively proposed as 3-O-β-D-glucopyranosyl-(1 → 4)-6-deoxy-3-O-methyl-β-D-allopyranosyl-(1 → 4)-β-D-oleandropyranosyl-11α, 12β-di-O-acetyltenacigenin B. Moreover, compound **18** has been purified by preparative HPLC and performed on 1D, 2D NMR. Based on the NMR data and previous studies[2,6], **18** was identified to be 3-O-β-D-glucopyranosyl-(1 → 4)-6-deoxy-3-O-methyl-β-D-allopyranosyl-(1 → 4)-β-D-oleandropyranosyl-11α-O-2-methyl-butyryl-12β-O-benzoyltenacigenin B, which has been reported as Tenacissoside E.

The [M + Na]^+ ion of **9** was concluded to be m/z 1035 (see Fig. 3). In the case of **9** neutral loss of 18 Da, 100 Da and consecutive loss of 100 Da and 18 Da from the [M + Na]^+ ion in the MS/MS spectrum, attributed to elimination of two molecules of water and two (E)-2-methylbut-2-enoic acid units. So it is hereby proven that there are two (E)-2-methylbut-2-enoyl (**Tig**) substituents on the C-11 and C-12 positions of **9**. Besides, a difference between **9** and the authentic compound **15** was observed in the MS[2] spectra. Compound **9** not only eliminated R_2OH and R_3OH, also loss two molecules of water. On the other hand, the 16 Da mass difference between [M + Na]^+ of **9** and **15**, indicated that the elemental composition of the aglycone of **9** contained one more oxygen atom than that of **15**. According to the literature [5,16], the polyoxypregnane aglycone core that the 8β-O-14β epoxy ring broke to form two hydroxyl groups on the C-8 and C-14 positions has been reported. So **9** was tentatively proposed as 3-O-β-D-glucopyranosyl-(1 → 4)-6-deoxy-3-O-methyl-β-D-allopyranosyl-(1 → 4)-β-D-oleandropyranosyl-11α-12β-O-di-tigloyl-5,6-dihydrosarcogenin.

In the MS/MS spectrum of [M + Na]^+ at m/z 1019 for **12**, fragment ions at m/z 919 and 819 were derived from neutral loss of 100 Da and sequential elimination of 100 Da, corresponding to the fact that **12** consisted of two (E)-2-methylbut-2-enoyl
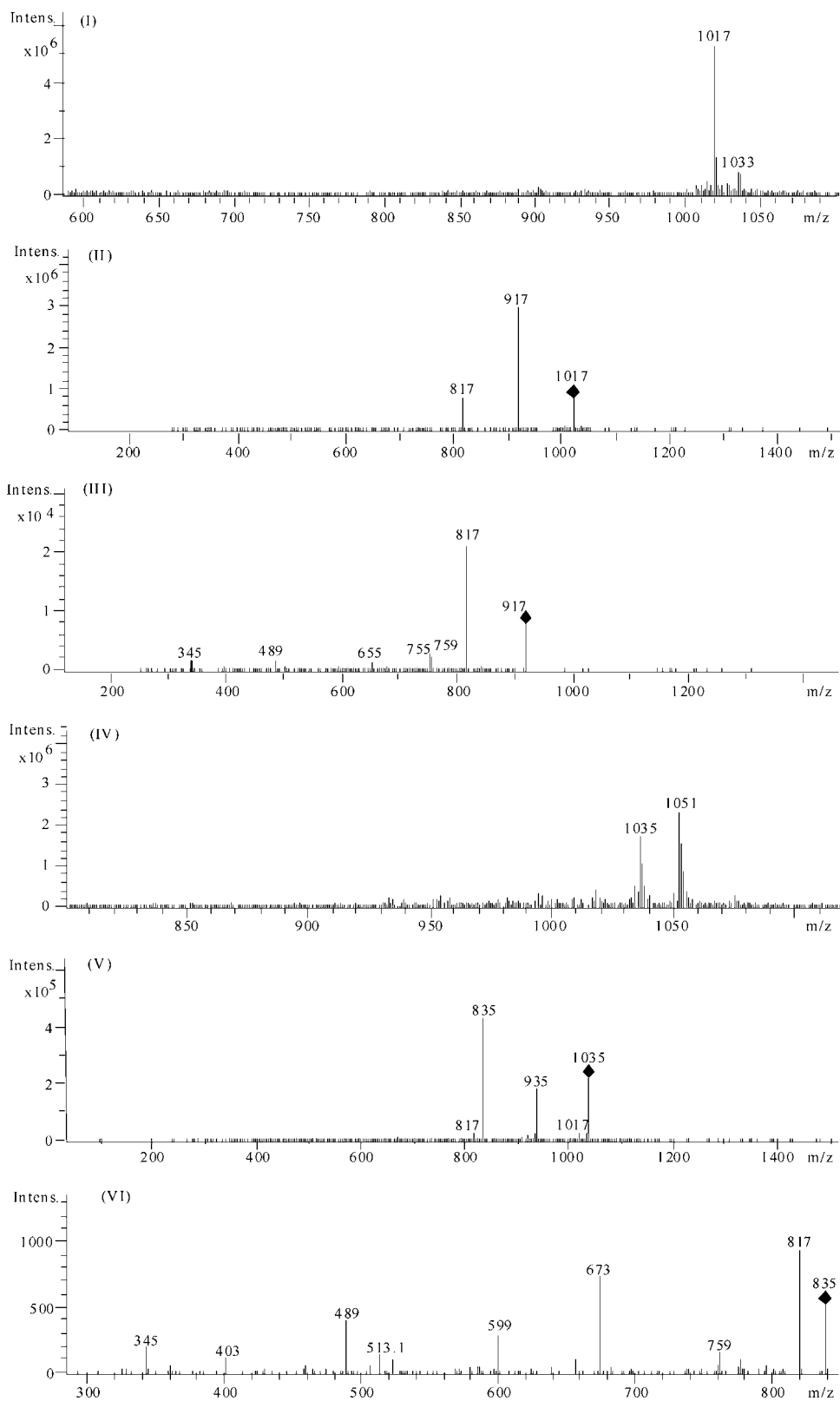
Fig. 3. Positive ions ESI-MS^n spectra: MS spectra of **15** (I) and **9** (IV); MS^2 spectra of **15** (II) and **9** (V); MS^3 of spectra **15** (III) and **9** (VI).

(**Tig**) substituents on the C-11 and C-12 positions of aglycone. The product ion at m/z 801 was generated by loss of 218 Da ([M + Na-100 Da-100 Da-18 Da]$^+$) from precursor ion at m/z 1019. The mass value of **12** was 2 Da higher than that of **15**. In a pre-

vious study [17], the polyoxypregnane glycoside that 8β-O-14β epoxy ring on C-8 and C-14 was broken to form hydroxyl group on C-14 from aglycone has been published. Consequently **12** was tentatively proposed as 3-O-β-D-glucopyranosyl-(1 → 4)-6-
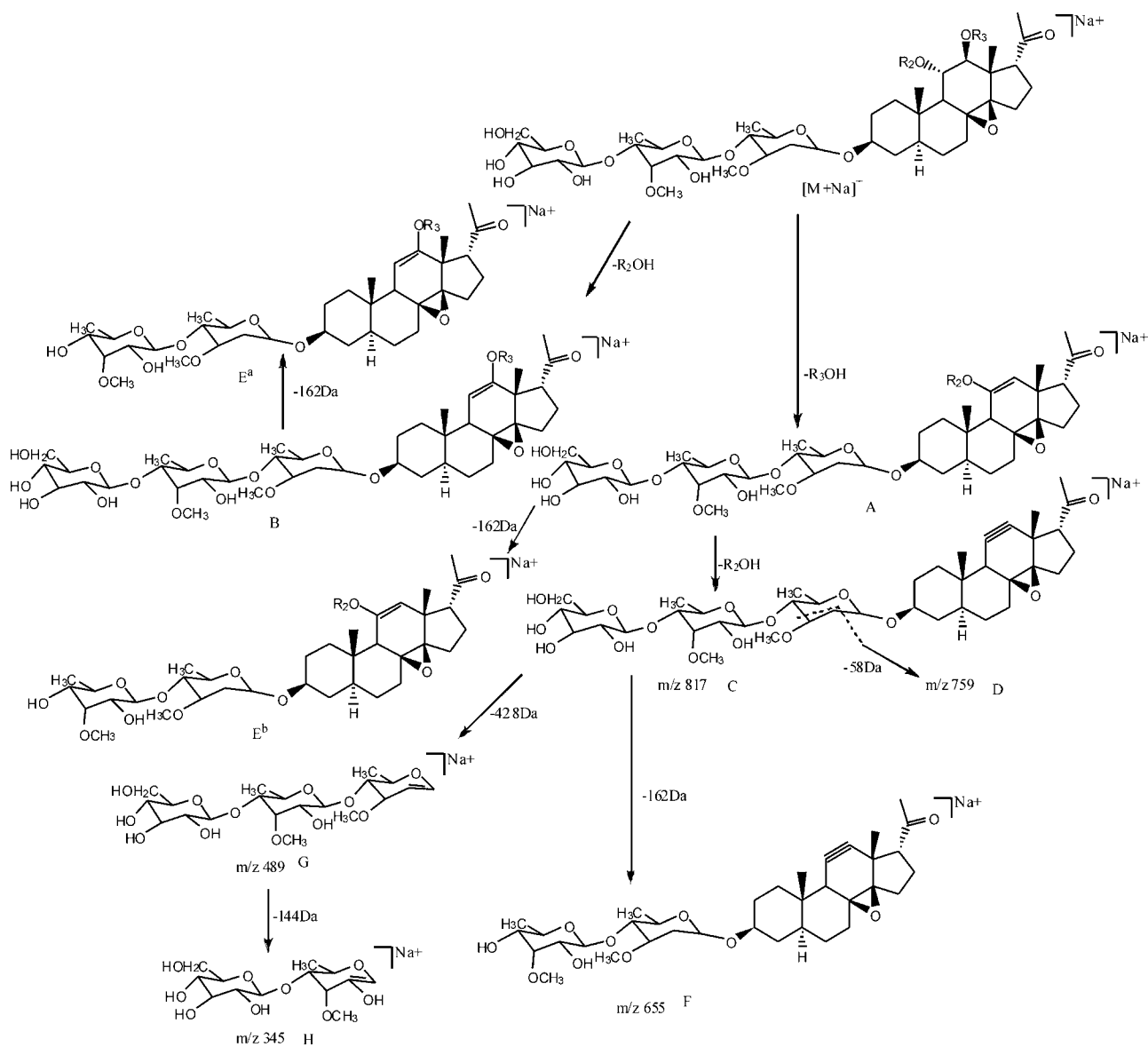
Scheme 1. Fragmentation pathways proposed for [M + Na]$^+$ of **6**, **7**, **15**, **16** and **17**. [a]: the ion E of 7; [b]: the ions E of 6, 15, 16 and 17.

deoxy-3-O-methyl-β-D-allopyranosyl-(1 → 4)-β-D-oleandropyra-nosyl-11α,12β-O-di-tigloyl-5, 6-dihydrodrevogenin P.

3.3. Differentiation of isomers 2, 3, 5, 8, 10, 11, 13 and 14 by breakdown curves

The [M + Na]$^+$ ions for unknown compounds **10**, **11**, **13** and **14** were observed at m/z 1017, 977, 1039 and 999, respectively. It is significant to note that they had similar molecular weights and MS^n spectra to authentic compounds **15**, **6**, **16** and **7**. Thus, **10**, **11**, **13** and **14** were proposed to be the isomers of **15**, **6**, **16** and **7**, respectively. Moreover, **10** had the two substituents (Tig) on C-11 and C-12 positions as **15**, which may be a consequence from the stereochemical difference of some monosaccharide residue of **15**. Compounds **11** and **14** have been purified by preparative HPLC and performed on 1D, 2D NMR. Based on the NMR data, it was confirmed that **11** was 3-O-β-D-glucopyranosyl-(1 → 4)-6-deoxy-3-O-methyl-β-D-allopyranosyl-(1 → 4)-β-D-oleandropyranosyl-11α-acetyl, 12β-O-tigloyltenacigenin B and **14** was identified as 3-O-β-D-

glucopyranosyl-(1 → 4)-6-deoxy-3-O-methyl-β-D-allopyranosyl-(1 → 4)-β-D-oleandropyranosyl-11α-O-benzoyl-12β-O-acetyl-tenacigenin B. To the best of our knowledge, compound **11** and **14** were reported here for the first time, as the positional isomers of authentic compounds **6** and **7**, respectively.

Evaluation of breakdown curves can provide information on fragmentation mechanisms such as distinguishing between competitive and consecutive fragmentation pathways, the stability of product ions and the identification of isomers and tautomers [18–20]. In order to distinguish these isomers, breakdown curves were generated by relative abundance of selected fragment ions versus collision energy.

11 and **14** were identified as the positional isomers of 6 and 7, respectively. Their breakdown curves were displayed in Fig. 4. The fragment ion at m/z 917 by loss of R$_3$OH from precursor [M + Na]$^+$ ion at 977 was the base peak in three MS^2 fragment ions of **6**. While product ion at m/z 877 generated by loss of R$_3$OH from **11** produced the highest relative abundance. The positional isomers **7** and **14** also represented similar phenomena. Therefore, it is proposed
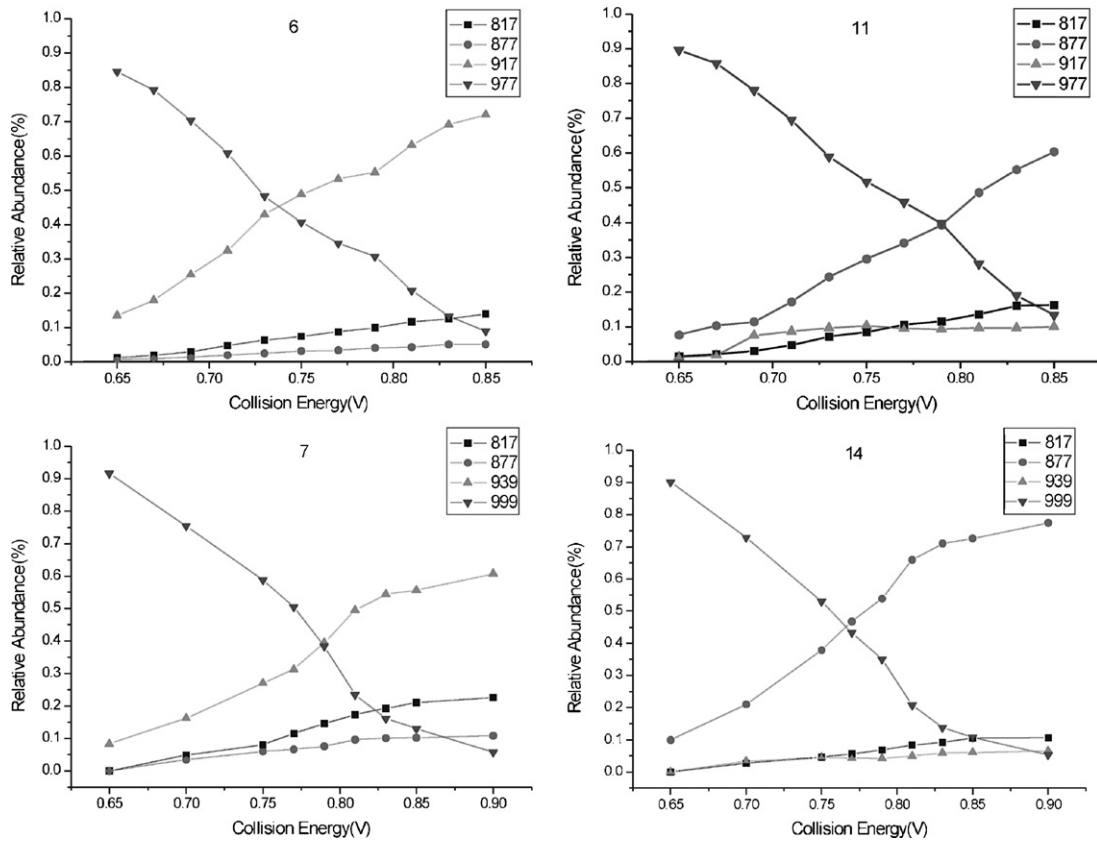
Fig. 4. Breakdown curves of MS^2 ions of positional isomers **6**, **11**, **7** and **14**.
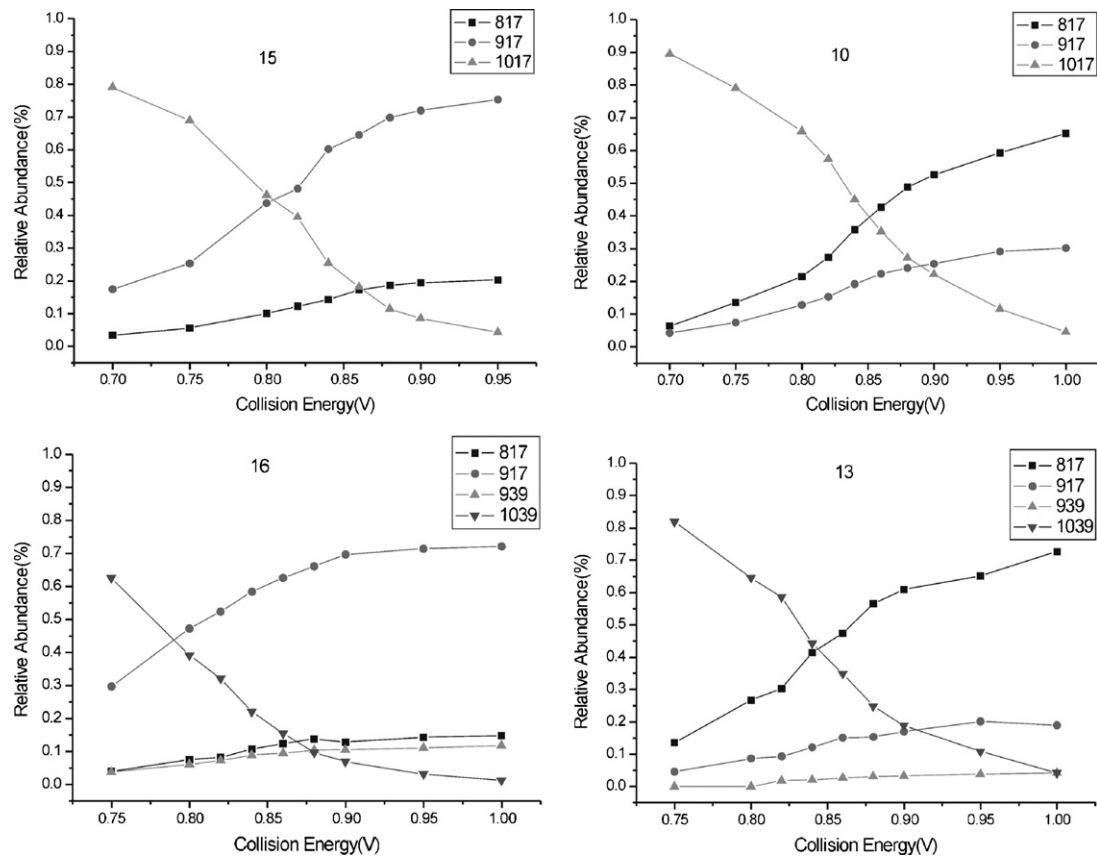
Fig. 5. Breakdown curves of MS^2 ions of **10**, **15**, **16** and **13**.

that product ions by loss of R_3OH had the highest relative abundance and these two pairs of positional isomers were differentiated conveniently by breakdown curves.

However, the breakdown curves (illustrated in Fig. 5) of **10** and **15** are different from the positional isomers discussed above. Both **10** and **15** had two fragment ions in MS^2 experiments. The ion at m/z 817 of **10** by loss of R_2OH and R_3OH had higher relative abundance than the ion at m/z 917; while for **15**, the circumstance was completely opposite. Thus, it was palpable that the breakdown curves were advantageous in distinguishing the stereochemical isomers **10** and **15**. The same phenomena were observed in isomers **13** and **16**. Accordingly, **13** might be proposed as the stereochemical isomers of **16**, with stereochemical difference in some monosaccharide residue.

Unknown compounds **2**, **3**, **5** and **8** not only had the same $[M+Na]^+$ ions at m/z 935, but also had similar MS^n spectra. Hence, these four compounds were proposed to be isomers. In the MS^2 spectra of ions at m/z 935, key fragment ions at m/z 835($[M+Na-100]^+$) and 817 ($[M+Na-100-18]^+$) demonstrated that there were (E)-2-methylbut-2-enoyl (Tig) and hydrogen groups on the aglycone. The MS^3 spectra were similar to authentic compounds. The breakdown curves of them were also investigated with little differentiation observed. It might be explained that these four compounds only have one substituent on C-11 or C-12 position, while the other four pairs mentioned above have two substituents on C-11 and C-12. However, the exact structures of these four compounds and differentiation of isomers need further studies.

4. Conclusions

The results illustrated the potential advantage of the method of HPLC/(+)ESI-MS^n for characterization of polyoxypregnane glycosides including the nature of the polyoxypregnane core, the kind of substituents and the types of sugar residues. Based on the fragmentation behaviors, eighteen polyoxypregnane glycosides are analyzed. Five compounds are identified by the fragmentations and authentic substances, eleven compounds are tentatively proposed and two compounds are established as novel compounds.

Moreover, breakdown curves assist in distinguishing the isomers, especially when the isomers yield the same product ions. Two pairs of positional isomers and two pairs of stereochemical isomers in some monosaccharide residue ascertained from this study could be promptly differentiated.

Appendix A. Supplementary data

Supplementary data associated with this article can be found, in the online version, at doi:10.1016/j.talanta.2008.05.054.

References

[1] J. Deng, Z. Liao, D. Chen, Phytochemistry 66 (2005) 1040.
[2] J. Deng, F. Shen, D. Chen, J. Chromatogr. A 1116 (2006) 83.
[3] Q. Li, X. Wang, L. Ding, C. Zhang, Chin. Chem. Lett. 18 (2007) 831.
[4] J. Deng, Z. Liao, D. Chen, Helvetica Chim. Acta 88 (2005) 2675.
[5] S. Qiu, S. Luo, L. Lin, G.A. Cordell, Phytochemisrry 41 (1996) 1385.
[6] S. Miyakawa, K. Yamaura, K. Hayashi, K. Kaneko, H. Mitsuhashi, Phytochemistry 12 (1986) 2861.
[7] S. Luo, L. Lin, G.A. Cordell, L. Xue, M.E. Johnson, Phytochemistry 34 (1993) 1615.
[8] J. Chen, Z. Zhang, J. Zhou, Acta Bot. Yunnan 21 (1999) 369.
[9] Q. Wu, M. Wang, J.E. Simon, J. Chromatogr. A 1016 (2003) 195.
[10] L. Ding, X. Biao Luo, F. Tang, J. Yuan, M. Guo, S. Yao, Talanta 71 (2007) 668.
[11] L. Tong, Y. Wang, J. Xiong, Y. Cui, Y. Zhou, L. Yi, Talanta 76 (2008) 80.
[12] X. Huang, F. Song, Z. Liu, S. Liu, J. Mass Spectrom. 42 (2007) 1148.
[13] Y. Tai, X. Cao, X. Li, Y. Pan, Anal. Chim. Acta 572 (2006) 230.
[14] X. Cao, Y. Tai, X. Li, Y. Ye, Y. Pan, Rapid Commun. Mass Spectrom. 20 (2006) 411.
[15] J. Liu, B. Chen, S. Yao, Talanta 71 (2007) 668.
[16] F.T. Halaweish, E. Huntimer, A.T. Khalil, Phytochem. Anal. 15 (2004) 189.
[17] N.P. Sahua, N. Panda, N.B. Mandal, S. Banerjee, K. Koike, T. Nikaido, Phytochemistry 61 (2002) 383.
[18] R.D. Hiserodt, B.M. Pope, M. Cossette, M.L. Dewis, J. Am. Soc. Mass Spectrom. 15 (2004) 1462.
[19] E.R. Filho, A.M.P. Almeida, M. Tabak, J. Mass Spectrom. 38 (2003) 540.
[20] J. Makowiecki, A. Tolonen, J. Uusitalo, J. Jalonen, Rapid Commun. Mass Spectrom. 15 (2001) 1506.

Visualized investigation of yeast transformation induced with Li+ and polyethylene glycol

Ping Chen[a], Hui-Hui Liu[b], Ran Cui[a], Zhi-Ling Zhang[a,*], Dai-Wen Pang[a],
Zhi-Xiong Xie[b,*,1], Hu-Zhi Zheng[a], Zhe-Xue Lu[a], Hua Tong[a]

[a] College of Chemistry and Molecular Sciences and State Key Laboratory of Virology, Wuhan University, Wuhan 430072, PR China
[b] College of Life Sciences, Wuhan University, Wuhan 430072, PR China

ARTICLE INFO

ABSTRACT

The effects of Li+ and polyethylene glycol (PEG) on the genetic transformation of *Saccharomyces cerevisiae* were investigated by using fluorescence microscopy (FM) to visualize the binding of plasmid DNA labeled with YOYO-1 to the surface of yeast cells, scanning electron microscopy (SEM) and atomic force microscopy (AFM) to image the change in surface topography of yeast cells, coupled with transformation frequency experiments. The results showed that under the same conditions, the transformation frequencies of yeast protoplasts were much higher than those of intact yeast cells. PEG was absolutely required for the binding of DNA to the surface of intact yeast cells or yeast protoplasts, and had no effect on the surface topography of intact yeast cells or yeast protoplasts. In the presence of PEG, Li+ could greatly enhance the binding of plasmid DNA to the surface of intact yeast cells, increase their transformation frequency, and affect their surface topography. On the other hand, no effect on the DNA binding to the surface of protoplasts and no increase in the number of transformants and no surface topography changes were found upon the treatment with Li+ to protoplasts. In the present work, the effects of Li+ and PEG on yeast genetic transformation were directly visualized, rather than those deduced from the results of transformation frequencies. These results indicate that cell wall might be a barrier for the uptake of plasmid DNA. Li+ could increase the permeability of yeast cell wall, then increase the exposed sites of DNA binding on intact yeast cells. The main role of PEG was to induce DNA binding to cell surface.

© 2008 Elsevier B.V. All rights reserved.

1. Introduction

Genetic transformation of *Saccharomyces cerevisiae* was first described by Oppenoorth [1] in 1960 and then demonstrated in a variety of papers [2–12]. It has been discovered that not only yeast protoplasts, the cell wall-removed yeast cells via enzymolysis [3], but also intact yeast cells can be transformed by plasmid DNA [4]. Various methods for pretreatment of yeast cells have been developed to increase the transformation efficiency, such as freezing and thawing, or treating cells with specific monovalent alkali cations or with thiol compounds, which can make yeast cells more competent for transformation.

For the transformation of intact yeast cells, a most-commonly-used efficient protocol makes use of polyethylene glycol (PEG) and Li+, which works well for most laboratory strains and is suitable for

high-efficiency transformation of plasmid DNA [8–10]. It has been shown that PEG is essential for yeast transformation with plasmid DNA [7,9], whose ability to induce membrane fusion seems important in transformation of yeast protoplasts [11–13]. The treatment of yeast cells with Li+ would modify cell wall porosity, then increasing their permeability [5,14]. However, almost all of the results are indirectly deduced from the results of the transformation frequencies, and never visualize clearly how plasmid DNA binds to yeast cells and what roles Li+ and PEG play in the transformation of the intact yeast cells. The elucidation of the manner in which plasmid DNA enters intact yeast cell is beneficial for optimization of the method of yeast transformation, and more importantly for general understanding of the processes of macromolecule uptake by cells, especially eukaryotic cells and the mechanism of horizontal gene transfer (HGT) in eukaryotic organisms.

It has been shown in our previous study that Li+ and PEG have an effect on DNA binding to the surface of intact yeast cells and can increase the permeability of yeast cells [15,16]. In order to specify the functions of Li+ and PEG in intact yeast transformation, in this paper the effects of Li+ and PEG on DNA uptake by both intact yeast cells and yeast protoplasts were investigated. The fluorescence

methods are convenient and powerful for the investigation of gene transformation or hormone receptors [17]. The binding of DNA labeled with a fluorescent intercalating reagent YOYO-1 to the surface of intact yeast cells or yeast protoplasts was observed using an inverted fluorescent microscope. Atomic force microscopy (AFM) and scanning electron microscopy (SEM) were used to study the effects of Li^+ and PEG on the surface topography of intact yeast cells or protoplasts. And the transformation frequency was calculated. A mechanism of genetic transformation of yeast was proposed.

2. Materials and methods

2.1. Strains and plasmids

S. cerevisiae AY (MATa/MATα *ura3–52 lys2–801* $_a$*ade2-101 trp1-*Δ63 *his3-*Δ200 *leu2–*Δ1) obtained from China Center for Type Culture Collection (CCTCC) were pre-cultured in YPD medium (1% yeast extract; 2% tryptone; 2% glucose; 2% agar) at 30 °C. Selective medium 1 for yeast transformation (Yeast N Base 0.67%, glucose 2%, agar 2.5%, L-lysine 30 μg/mL, L-leucine 60 μg/mL, L-histidine 20 μg/mL, L-tryptophan 40 μg/mL) and selective medium 2 (selective medium 1 + 17% sucrose) for protoplast transformation were used. Plasmid pUC18 DNA (Sino-American Biotechnology Co.) stained with YOYO-1 and pAJ161 prepared from the plasmid-bearing strain *Escherichia coli BL21* (from CCTCC) were used in transformation experiments.

2.2. Reagents

PEG 4000 was purchased from Sigma and Yeast Nitrogen Base (W/O Amino Acid & Ammonium Sulfate) from Sangon Shanghai. YOYO-1 was a product of Molecular Probes. Snailase was purchased from Boao Shanghai in China and cellulase from Baitai Beijing in China. Ultra-pure water (18.2 MΩ cm) was prepared by a Labconco system and used thoroughly.

2.3. Preparation and transformation of intact yeast cells

Yeast cells were grown in 5 mL of YPD (1% yeast extract, 2% tryptone, 2% glucose) with shaking at 30 °C overnight and a 2% dilution of the cells was grown in 50 mL of YPD with shaking at 30 °C for 5 h, harvested by centrifugation at 4000 rpm for 5 min and washed three times with sterile water, transferred to 1.5 mL microcentrifuge tubes and then washed once with TE (10 mM Tris/HCl, 1 mM EDTA, pH 7.5) buffer, harvested by centrifugation and the supernatant was discarded. Then the pellets were resuspended in 1.0 mL of transformation mixture (0.8 mL of 50% PEG 4000 (w/v) in TE buffer or 0.8 mL of TE buffer alone, 100 μL of 1.0 M CH_3COOLi in TE buffer or 100 μL of TE buffer, then adding TE buffer to a volume of 1.0 mL) and then incubated with unlabeled plasmid DNA pAJ161 with shaking at 30 °C for 30 min, kept at 42 °C in water bath for 15 min. The cell suspension was cooled to room temperature and washed twice with TE buffer. 0.2 mL of this cell suspension was spread on selective agar plate and then incubated at 30 °C. Transformants were counted after 72 h incubation.

2.4. Preparation and transformation of yeast protoplasts

Yeast cells were grown in 5 mL of YPD (1% yeast extract, 2% tryptone, 2% glucose) with shaking at 30 °C overnight and a 2% dilution of the cells was grown in 50 mL of YPD with shaking at 30 °C for 5 h, harvested by centrifugation at 4000 rpm for 5 min and washed three times with sterile water, transferred to 1.5 mL microcentrifuge tubes and then washed once with 1.0 M sorbitol in CPB (0.1 M citric acid, 0.2 M Na_2HPO_4, pH 7.5) buffer. The washed cells

were incubated in 1.0 mL of pretreatment solution (5 mM EDTA, 1% (v/v) 2-mercaptoethanol in 1.0 M sorbitol in CPB buffer) with shaking at 30 °C for 30 min. The cells were harvested by centrifugation at 1000 rpm for 6 min, and resuspended in 1.0 mL of 1.0 M sorbitol in CPB buffer containing 2 mg/mL of snailase and 2 mg/mL of cellulase. And then the cells were incubated with very gentle shaking at 30 °C for 30 min, harvested by centrifugation at 1000 rpm for 6 min and washed twice in 1.0 M sorbitol of CPB buffer and once in 1.0 M sorbitol in TE buffer. The transformation of yeast protoplasts was done just as intact yeast cells except all solutions were prepared in 1.0 M orbitol in TE buffer.

2.5. Inverted fluorescence microscopy

For fluorescence microscopy, pUC18 DNA as the model of plasmid DNA was stained with the fluorescent reagent YOYO-1. They were mixed at a ratio of about 15:1 of the base pairs of DNA to YOYO-1 molecules and stored at 4 °C in dark to react for ca. 2 h. The washed cells were resuspended in 1.0 mL of transformation mixture, and incubated with pUC18 DNA labeled with YOYO-1 with shaking at 30 °C for 30 min just as precedingly described for the transformation process. Several microlitres of the cell solution were placed on a microscope slide. Samples were examined and photographed under an inverted fluorescence microscope (Axiovert 200M, Zeiss, Germany) equipped with an oil immersion objective (Zeiss, 100 × objective, N.A. = 1.25).

2.6. Scanning electron microscopy

To illustrate the effects of Li^+ or PEG on the surface of intact yeast cells and yeast protoplasts, the cells incubated at 30 °C for 30 min in transformation mixture with Li^+ or PEG were fixed with 2.5% of glutaraldehyde in 0.1 M pH 7.0 phosphate buffer at room temperature for 2 h. After fixation, cells were washed with 0.1 M phosphate buffer for several times and dehydrated in a gradient ethanol series of 50%, 60%, 70%, 80%, 90%, and 100%. Samples were placed in the chamber of a critical point drier, using liquid CO_2 as the substituting fluid and then were coated with gold prior to the examination with a scanning electron microscope (Hitachi SEM-X650).

2.7. Atomic force microscopy

For AFM imaging, a drop of about 100 μL of the cell suspension treated with or without Li^+ as described above was deposited onto a piece of glass slide modified with poly-L-lysine. The sample was allowed to stand at room temperature for 20 min and rinsed several times with water and then air dried for atomic force imaging using a Picoscan atomic force microscope (Molecular Imaging, Tempe, AZ, USA) with commercial MAClever II tips (Molecular Imaging, USA) in contact mode.

3. Results and discussion

Previous study has supposed that the genetic transformation of bacteria can be divided into three steps: transformation DNA binding to cell surface, penetrating through cell wall/membrane into the interior of cells, and then replicating or transcripting into RNA in the cells [18]. To investigate the relationship between DNA binding to cell surface and DNA transformed into yeast cells, fluorescence microscopy was used to show pUC18 DNA labeled with the cell-impermeable YOYO-1 binding to cell surface, and the transformation frequencies of pAJ161 DNA in yeast cells were calculated based on the following points: (a) the role of yeast cell wall, and (b) the functions of Li^+ and PEG.

3.1. DNA binding to yeast surface

In order to show the effects of Li^+ and PEG on the DNA binding to the surface of intact yeast cells and yeast protoplasts, YOYO-1 was used to label pUC18 plasmid DNA. First, the dimeric cyanine dyes YOYO-1 is a kind of membrane-impermeable fluorescent probe and fluorescence enhancement by more than 3000 times will be found when it is bound to double-stranded DNA (dsDNA) [19], while the fluorescence from the conjugates of YOYO-1 with released nucleotides and small nucleic acid fragments is too weak to be detectable relative to that from the YOYO-1/dsDNA conjugates [20]. Second, under our experimental conditions, no fluorescence was found on the cell surface when the cells were incubated with YOYO-1 without plasmid DNA. That is to say that the observed fluorescence from the cells was caused by the YOYO-1-labeled DNA binding to the surface of yeast cells, i.e. fluorescent cells indicated that it was DNA that had bound to their surface. And the intensities of the fluorescence were directly proportional to the amount of DNA binding to cell surface [20].

Plasmid pUC18 DNA labeled with YOYO-1 was used to investigate the effects of Li^+ and PEG on the DNA binding to the surface of intact yeast cells and yeast protoplasts. PEG was indispensable for the binding of plasmid DNA to the surface of intact yeast cells and protoplasts. Without PEG, no labeled DNA was found on the surface of intact yeast cells (Fig. 1A and B) and yeast protoplasts (Fig. 2A and B). Our experiments showed that no matter for intact yeast cells or for protoplasts, DNA could bind to the cell surface when PEG was added only, suggesting that the treatment with PEG is a basic requirement for successful binding of DNA to the cell surface. Besides, PEG could also induce aggregation of both intact yeast cells (Fig. 1) and yeast protoplasts (Fig. 2).

The effect of Li^+ on yeast transformation was to increase the permeability of yeast cell wall. For intact yeast cells, the treatment of Li^+ could greatly affect the binding of DNA to cell surface (Fig. 1C and D), while no obvious effect of Li^+ was found on the binding of plasmid DNA to the surface of yeast protoplasts (Fig. 2C and D). The results indicate that Li^+ only has an effect on cell wall instead of cell membrane, for the only difference between intact yeast cells and yeast protoplasts lies in lack of cell wall for the protoplasts. The fluorescence sites of the intact yeast cells treated with Li^+ were much more than those of the cells pretreated without Li^+ (Fig. 1C and D), indicating that Li^+ evidently facilitated the transformation DNA penetrating through cell wall to bind to cell membrane under the induction of PEG.

Moreover, almost all the plasmid DNA attached to the surface of intact yeast cells or protoplasts could be removed by a washing step. When the cultured cells were harvested by centrifugation (1000 rpm, 6 min, 20 °C) and resuspended in TE buffer solution, almost all the fluorescence on the cells would disappear, suggesting that the binding of plasmid DNA to cell surface was reversible. Though it is not sure whether the interaction of plasmid DNA to cell surface is dependent on electrostatic force or hydrophobic interaction or receptor mediation, the interaction should not be
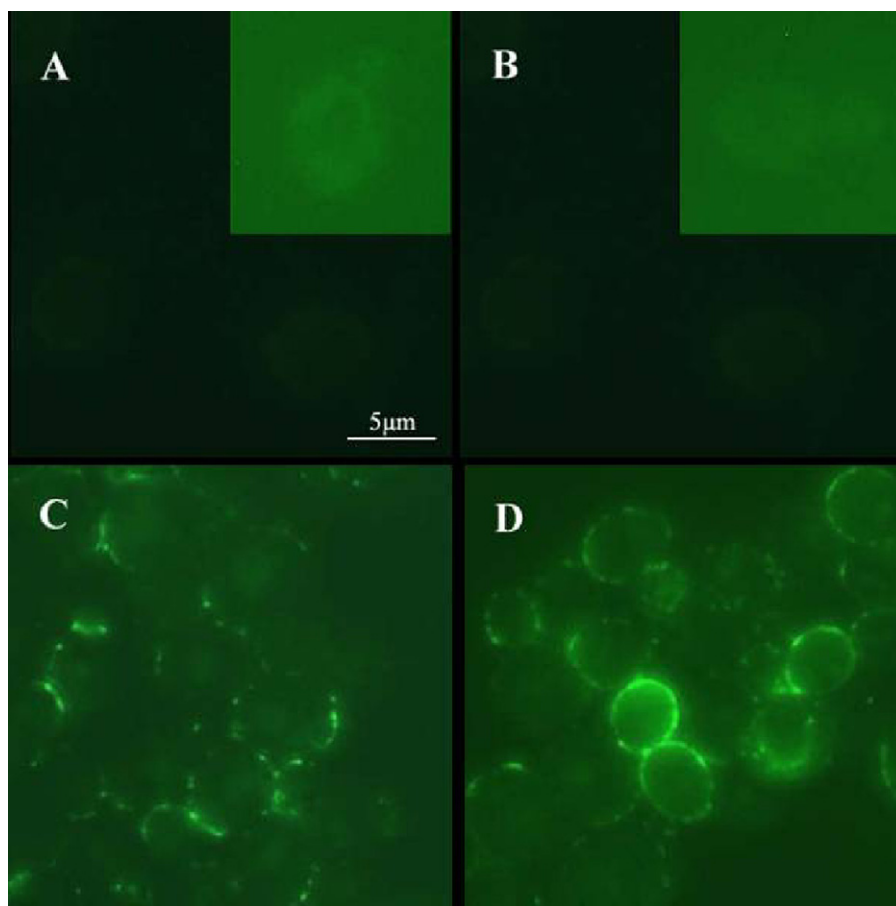
Fig. 1. Binding of pUC18 plasmid DNA labeled with YOYO-1 to the surface of living intact yeast cells. Yeast cells were suspended in the transformation mixture and incubated with labeled pUC18 DNA with shaking at 30 °C for 30 min, and then imaged with an inverted fluorescent microscope (ZEISS). (A) Yeast cells (no Li^+ and PEG were added), suspended in TE buffer solution, pH 7.5. (B) As in (A) but 0.1 M Li^+ was added. (C) As in A, but 40% PEG was added. (D) As in A, but 0.1 M Li^+ and 40% PEG were added. The exposure times of all images were adjusted to the same level, except the insets in (A and B), where the exposure times were increased to be able to show the details.
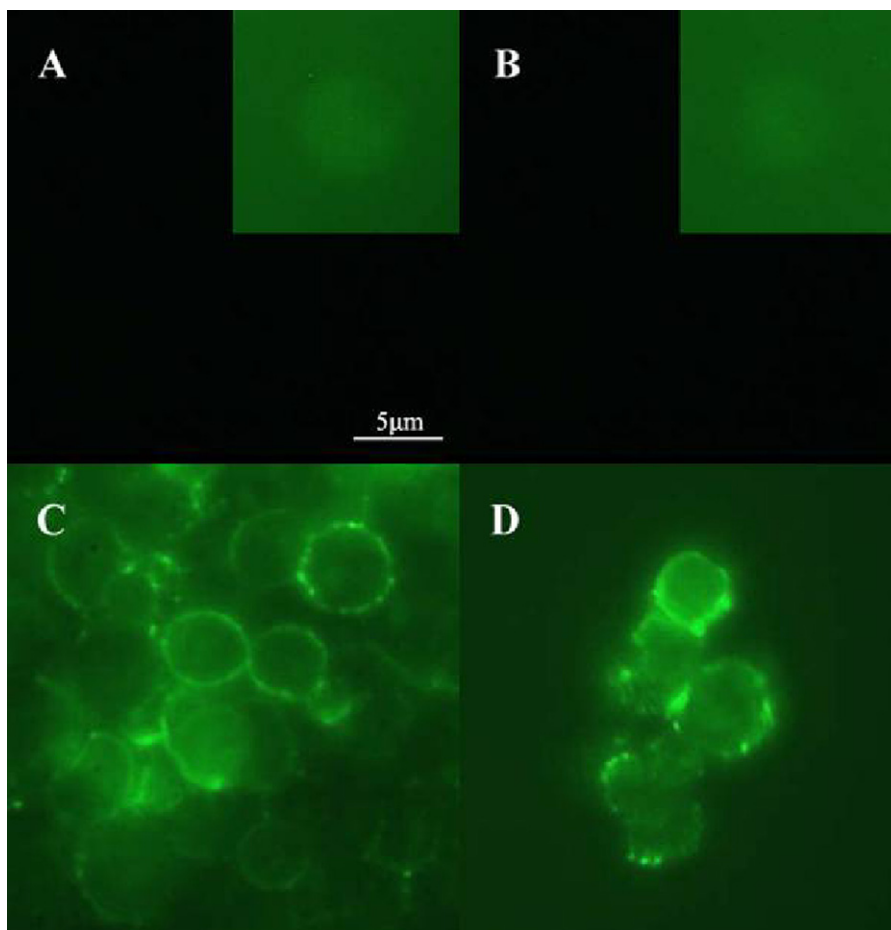
Fig. 2. Binding of pUC18 plasmid DNA labeled with YOYO-1 to the surface of living yeast protoplasts. Yeast cells were suspended in the transformation mixture and incubated with labeled pUC18 DNA with shaking at 30 °C for 30 min, and then imaged with an inverted fluorescent microscope (ZEISS). (A) Yeast cells (no Li^+ and PEG were added), suspended in 1.0 M sorbitol of TE buffer solution, pH 7.5. (B) As in A, but 0.1 M Li^+ was added. (C) As in A, but 40% PEG was added. (D) As in A, but 0.1 M Li^+ and 40% PEG were added. The exposure times of all images were adjusted to the same level, except the insets in (A and B), where the exposure times were increased to be able to show the details.

electrostatic since Li^+ cation did not affect the negatively-charged DNA binding to cell membrane as mentioned above (Fig. 2).

3.2. Transformation frequency

In order to confirm the effects of Li^+ and PEG on the binding of unlabeled pAJ161 DNA into intact yeast cells or protoplasts, the transformation frequencies were analyzed as listed in Table 1.

Table 1
Effects of Li^+ and PEG on the genetic transformation frequency

Cell	CH_3COOLi	PEG	Transformation frequency[a]
Intact yeast cells	+[b]	+	$(2.88 \pm 0.51) \times 10^{-4}$
	+	−	0
	−	+	$(4.45 \pm 0.43) \times 10^{-5}$
	−	−	0
Yeast protoplasts	+	+	$(5.18 \pm 0.24) \times 10^{-2}$
	+	−	$(5.31 \pm 0.64) \times 10^{-3}$
	−	+	$(4.69 \pm 0.68) \times 10^{-2}$
	−	−	$(5.37 \pm 0.24) \times 10^{-3}$

[a] Transformation frequency of intact yeast cells = number of transformants/number of living cells. Transformation frequency of yeast protoplasts = number of transformants/number of regenerated living cells.

[b] '+' shows the treatment of yeast cells with CH_3COOLi or PEG. On the other hand, cells treated with buffer solution instead of CH_3COOLi or PEG are indicated as '−'.

First, the frequencies of transformation of intact yeast cells treated with or without Li^+ or PEG were determined. Although treatment of intact yeast cells with PEG only could get some transformants, the number of transformants would considerably increase upon addition of Li^+. Without PEG, almost no transformants were found in our experiment, suggesting that treatment of intact cells with PEG is a minimal requirement for successful transformation and the treatment with Li^+ would increase the uptake of plasmid DNA for intact yeast cells.

For yeast protoplasts, despite no PEG relatively considerable transformants could be found, the frequency of transformation would be largely enhanced upon addition of PEG. Almost no increase in the number of transformants could be found when treated with Li^+. That is to say for yeast protoplasts, treatment with PEG was not a minimal requirement for successful transformation. Li^+ has no effect on the uptake of plasmid DNA as far as protoplasts.

Under the conditions described in Table 1, the transformation frequency of intact yeast cells was much less than that of yeast protoplasts, suggesting that cell wall was a barrier for transformation. In the presence of PEG, a higher frequency of transformation was obtained with the plasmid DNA upon treatment with Li^+ for intact yeast cells, while no effect could be found of the treatment with Li^+ for yeast protoplasts. The data are consistent with those obtained by fluorescence microscopy, confirming the results that Li^+ can only affect cell wall. As for the effect of PEG, no matter for intact yeast cells or yeast protoplasts, PEG can greatly enhance

the frequencies of transformation. Combining with the results of fluorescence experiments, PEG as a minimal requirement for DNA binding to cell surface does enhance the transformation frequency, and meanwhile the more DNA molecules bind to cell surface, the higher transformation frequency can be obtained. However, it is noteworthy that without PEG the fluorescence indicating the DNA binding to cell surface could not be observed though considerable transformants could be found for yeast protoplasts. The results indicated that PEG as a minimal requirement of DNA binding to cell surface was not a minimal requirement of protoplast transformation. The mechanism needs to be further explored.

3.3. Surface topography of yeast cells

To verify the effects of Li$^+$ and PEG on the transformation, the surface topography of intact yeast cells and protoplasts was examined by SEM and AFM. PEG did not have any effect on the surface topography of both intact yeast cells and yeast protoplasts. Li$^+$ affected the surface of cell wall. Protoplasts treated with or without Li$^+$ were examined by SEM (Fig. 3). By removing cell wall with enzyme, the lemon-like shape of yeast turns into a sphere covered with plasma membrane with smooth but a little and irregularly wrinkled surface. Globular forms in the images are substances secreted by yeast protoplasts [21]. As shown in Fig. 3, the surface topography of the protoplasts treated with Li$^+$ does not show any obvious difference

from the surface of those treated without Li$^+$, suggesting that Li$^+$ has no effect on the surface of protoplasts, i.e. cell membrane. On the other hand, though the surface of intact cells treated without Li$^+$ was homogenous and smooth, the surface became much rougher and more wrinkles appeared after incubated with Li$^+$ at 30 °C for 30 min (Fig. 4). Low-resolution SEM images of many intact yeast cells are shown in Fig. 4A and B, and higher resolution SEM images of yeast cells show more details as shown in Fig. 4C and D. The only difference between the cells in Fig. 4A and B was from the treatment of Li$^+$. So Li$^+$ did affect cell wall, which was consistent with the results mentioned above.

To get more detail information about the effect of Li$^+$, AFM as a complementary tool to SEM allowing the surface of cells to be explored at higher resolution [22], was used to observe the surface topography of intact yeast cells treated with Li$^+$ (Fig. 5). In the high-resolution AFM images of intact yeast cells, although the surface of cells treated without Li$^+$ was almost homogenous and much smoother, a large number of big protrusions would be found on the surface of the cells when treated with Li$^+$, indicating that Li$^+$ did change the surface of intact yeast cells and maybe damaged yeast cell wall making cell wall more porous to extracellular molecules.

3.4. Effect of PEG on genetic transformation

It has been indicated that the crucial role of PEG in transformation results from its ability to induce membrane fusion [11–13].
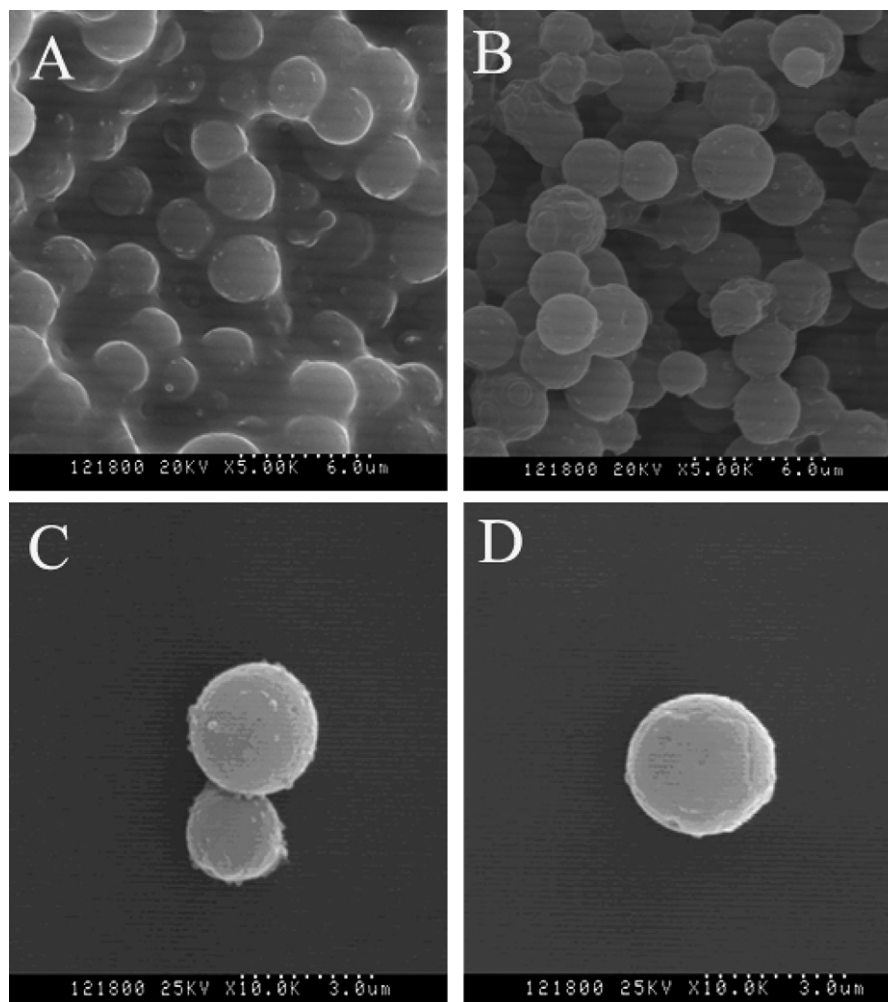
Fig. 3. Scanning electron microscopic images of the protoplasts of *S. cerevisiae*. (A and C) Protoplasts without treatment of Li$^+$. (B and D) Protoplasts after 30 min incubation with Li$^+$. (C and D) are higher-resolution SEM images of yeast cells to show more details.
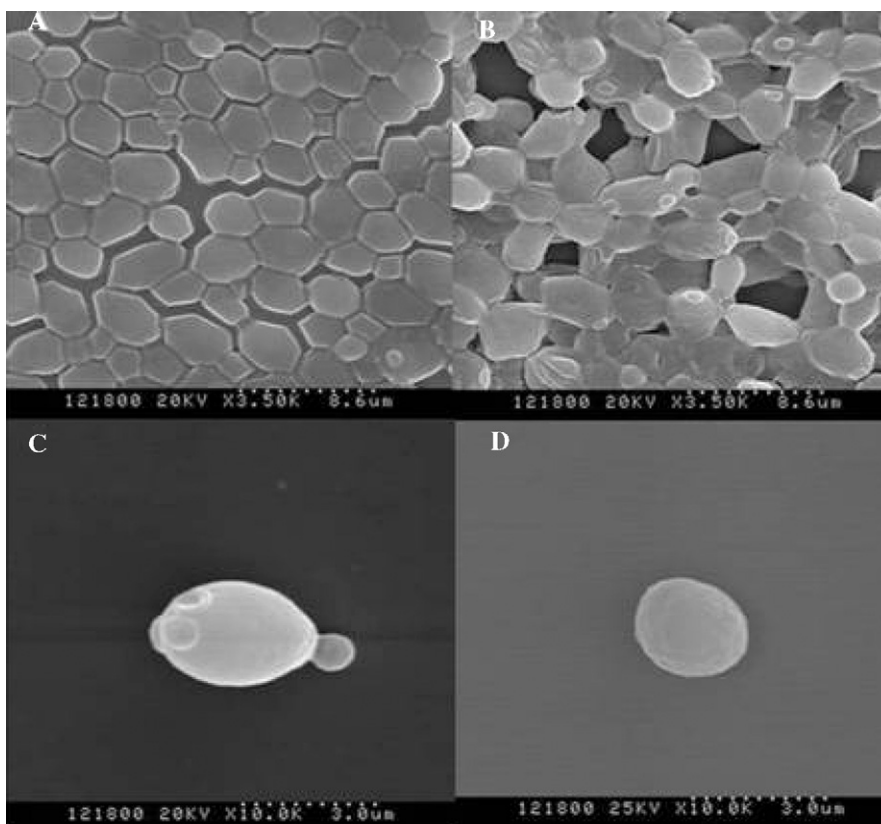
Fig. 4. Scanning electron microscopic images of intact yeast cells. (A and C) Intact yeast cells without treatment of Li$^+$. (B and D) Intact yeast cells after 30 min incubation with Li$^+$. Image size (for A and B) 25.8 μm × 25.8 μm. (C and D) are higher-resolution SEM images of yeast cells to show more details. Image size for C and D: 9 μm × 9 μm.

As for the transformation of yeast protoplasts, it seems true that PEG would induce membrane fusion of protoplasts because the fusion of protoplasts is dependent on the presence of PEG, and in the meanwhile, PEG can indeed induce the aggregation of protoplasts. But what about intact yeast cells? With the existence of cell wall, cell fusion can hardly be realized unless the yeast cells are haploid and of opposite mating type [14]. Our experiments showed that no matter for intact yeast cells or protoplasts, DNA could bind to the cell surface when PEG was added only. Evidently, the treatment with PEG is a basic requirement for successful binding of DNA to the cell surface. Furthermore, PEG could also induce aggregation of both intact yeast cells and yeast protoplasts. The main role of PEG in the transformation is to induce DNA binding to cell surface and make cells aggregate, making transformation DNA more accessible to cell surface, and most probably to facilitate DNA entering cells besides inducing membrane fusion.

3.5. Effect of Li$^+$ on genetic transformation

Though it was supposed that maybe Li$^+$ could modify the porosity of cell wall, the suppositions were all speculated from indirect
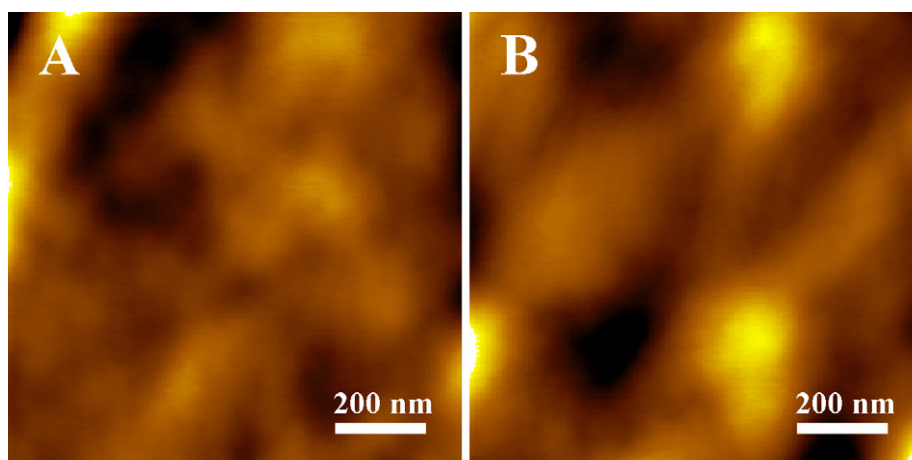
Fig. 5. AFM images of the surface of intact yeast cells. (A) Intact yeast cells without treatment of Li$^+$. (B) Intact yeast cells after 30 min incubation with Li$^+$. Image size: 1.0 μm × 1.0 μm.

studies, including examination of transformation frequencies or comparison of the effect of Li$^+$ with the effect of protease on cell wall, and finding the leakage of endogenous RNA from cells upon all the pretreatments [5,14]. And they never pointed out why it was cell wall but not cell membrane that Li$^+$ affected. In this study, the effect of Li$^+$ on genetic transformation was directly visualized using fluorescence microscopy, SEM and AFM. In fluorescence research, it was found that the fluorescence sites of intact yeast cells treated with Li$^+$ were much more than those of the cells treated without Li$^+$, but no effect of Li$^+$ on the fluorescence of yeast protoplasts were found. The results indicated that Li$^+$ only had an effect on yeast cell wall instead of cell membrane. AFM and SEM experiments also confirmed this. Although the surface topography of yeast protoplasts did not show any distinct difference after treated with Li$^+$, the surface became much rougher and a large number of wrinkles and big protrusions appeared after incubated with Li$^+$. The fact of the increase in transformation frequencies resulting from Li$^+$ for intact yeast cells and no effect of Li$^+$ on yeast protoplast transformation indicate that Li$^+$ can evidently facilitate transformation DNA penetrating through cell wall to bind to cell membrane and then enter into cells. The main role of Li$^+$ is to modify the porosity of cell wall and make more parts of cell membrane accessible to plasmid DNA.

4. Conclusion

In the present work, the effects of Li$^+$ and PEG on DNA transformation of yeast cells were studied for both intact yeast cells and yeast protoplasts. From the results obtained above, the treatment with PEG is a minimal requirement for the binding of DNA to yeast cell surface, which is an enhancer for the uptake of DNA into the interior of cells. Li$^+$ can break the integrality of yeast cell wall, a barrier for the uptake of plasmid DNA, and increase the DNA binding sites on cell surface to promote DNA uptake for intact yeast cells. Meanwhile, our experiments also show that the binding of plasmid DNA to cell surface is a prerequisite for intact yeast transformation. The more DNA molecules bind to cell surface, the more transformants will be obtained.

The results do suggest a mechanism of genetic transformation as follows: for yeast transformation, Li$^+$ modifies the porosity of yeast cell wall to facilitate transformation DNA breaking through cell wall, thus more DNA molecules can access cell membrane and bind to cell membrane under the promotion of PEG, and then enter cells.

References

[1] W.F.F. Oppenoorth, J. Microbiol. Serol. 26 (1960) 129–147.
[2] N.C. Khan, S.P. Sen, J. Gen. Microbiol. 83 (1974) 237–250.
[3] A. Hinnen, J.B. Hicks, G.R. Fink, Proc. Natl. Acad. Sci. USA 75 (1987) 1929–1933.
[4] H. Ito, Y. Fukuda, K. Murata, A. Kimura, J. Bacteriol. 153 (1983) 163–168.
[5] H. Ito, K. Murata, A. Kimura, Agric. Biol. Chem. 48 (1984) 341–347.
[6] H. Ito, K. Murata, A. Kimura, Agric. Biol. Chem. 47 (1983) 1691–1692.
[7] R.J. Klebe, J.V. Harris, Z.D. Sharp, M.G. Douglas, Gene 25 (1983) 333–341.
[8] R.D. Gietz, R.A. Woods, BioTechniques 30 (2001) 816–831.
[9] Y. Minoru, H. Fumio, G. Norio, Agric. Biol. Chem. 49 (1985) 869–871.
[10] R.D. Gietz, R.H. Schiestl, A.R. Willems, Yeast 11 (1995) 355–360.
[11] J.B. Hicks, A. Hinnen, G.R. Fink, Cold Spring Harbor Symp. Quant. Biol. 43 (1978) 1305–1313.
[12] S. Harashima, A. Takagi, Y. Oshima, Mol. Cell Biol. 4 (1984) 771–778.
[13] B. Brzobohaty, L. Kovac, FEBS 183 (1985) 211–214.
[14] B. Brzobohaty, L.J. Kovac, Gen. Microbiol. 132 (1986) 3089–3093.
[15] H.Z. Zheng, H.H. Liu, S.X. Chen, Z.X. Lu, Z.L. Zhang, D.W. Pang, Z.X. Xie, P. Shen, Bioconjugate Chem. 16 (2005) 250–254.
[16] P. Chen, H.H. Liu, Z.L. Zhang, D.W. Pang, Z.X. Xie, H.Z. Zheng, Z.X. Lu, H. Tong, Chin. Sci. Bull. 50 (2005) 1052–1053.
[17] T.-N. Noguerol, S. Boronat, S. Jarque, D. Barceló, B. Piña, Talanta 69 (2006) 351–358.
[18] R. Palmen, K.J. Hellingwerf, Gene 191 (1997) 179–190.
[19] A.N. Glazer, H.S. Rye, Nature 359 (1992) 859–861.
[20] R.P. Haugland, Handbook of Fluorescent Probes and Research Chemicals, 6th ed., Molecular Probes, Inc., 1996.
[21] M. Pardo, L. Monteoliva, J. Pla, C. Gil, Yeast 15 (1999) 459–472.
[22] F. Ahimou, A. Touhami, Y.F. Dufrene, Yeast 20 (2003) 25–30.

Application of thin-shielded mercury microelectrodes in anodic stripping voltammetry

Salvatore Daniele*, Carlo Bragato, M. Antonietta Baldo, Ilenia Ciani[1]

Department of Physical Chemistry, University of Venice, Calle Larga, S. Marta 2137, 30123 Venice, Italy

ABSTRACT

The performance in anodic stripping voltammetry (ASV) of hemispherical mercury microelectrodes, fabricated by electrodeposition of liquid mercury on the surface of Pt microdisks which were surrounded by a rather thick or thin insulating shield, was compared. The Pt microdisks were produced by sealing a wire of 25 μm diameter into a glass capillary, and by coating the cylindrical length of the Pt wire with a cathodic electrophoretic paint. The ratio of the overall tip radius b, to the basal radius of the electrode a, so-called RG = b/a, was equal to 110 ± 10 and 1.52 ± 0.01 for the thick- and thin-shielded microdisk, respectively. The mercury microelectrodes were characterized by cyclic voltammetry at 1 mV s^{-1}, in 1 mM Ru(NH$_3$)$_6^{3+}$ aqueous solution. The steady-state voltammogram recorded with the thin-shielded mercury microelectrode displayed less hysteresis, while the steady-state current was about 30% higher than that of the thicker one. This was a consequence of the additional flux due to diffusion from behind the plane of the electrode. The flux enhancement, which was operative at the thin-shielded mercury microelectrode during the deposition step in the ASV experiments, allowed recording stripping peaks for Cd and Pb, which resulted about 32% larger than those recorded at the thicker shielded mercury microelectrode, under same experimental conditions.

The usefulness of the thin-shielded mercury microelectrode for ASV measurements in real samples was verified by determining the content of heavy metal ions released in the pore water (pH 4.5) of a soil slurry.

© 2008 Elsevier B.V. All rights reserved.

1. Introduction

Anodic stripping voltammetry (ASV) [1] is an extremely sensitive technique for measuring a large variety of trace metals with low detection limits. Its remarkable sensitivity is achieved through a preconcentration step, in which the metal is accumulated into or onto working electrodes. This step is followed by the measurement step, in which the preconcentrated analyte is stripped back to the solution, a process resulting in a voltammetric response proportional to the concentration of the analyte in the sample. The sensitivity of an ASV procedure strongly depends on the metal ion flux, toward the electrode surface, generated during the preconcentration step. High fluxes can be achieved either by forced convection (i.e., electrode rotation or solution stirring) [1], or by diffusion only (i.e., quiescent solutions) when conventional electrodes or microelectrodes [2–4] are employed, respectively. At microelectrodes, the high flux is due to radial diffusion [2,3], which also allows a rapid

achievement of steady-state conditions in a relatively short time [2,3]. The accumulation of the target metal on the electrode surface through diffusion only is in general advantageous, because it makes the overall analytical procedure simpler and more reproducible, as less parameters have to be standardised [4,5]. For these reasons, since their introduction, microelectrodes have been widely used in ASV for the analysis of a variety of trace elements [4–7].

In recent years, microelectrodes with shields of thickness comparable to the electrode radius have been developed [8–16]. These microelectrodes have found applications in high spatial resolution measurements in combination with scanning electrochemical microscopy (SECM) [13–19], and for electroanalysis in small volume samples [8,9]. One of the characteristic features of a thin-shielded microelectrode is that, on the time scale of standard voltammetric measurements, the diffusion field undergoes a transition from linear to radial symmetry, and is established radially behind the plane of the electrode and shield [9–21] (Fig. 1A). Under these conditions, the flux, and consequently the current, is enhanced to an extent that depends on the relative size of the insulating shield ($b-a$) and the electrode radius (a). Such features have been verified, from both theoretical and experimental point of view, for disk [9–13,18–21], cone [13,14,18,19] and sphere cap [15,16,18,19] shaped microelectrodes under classical voltammetric or SECM operations. Because of

* Corresponding author. Tel.: +39 041 2348630; fax: +39 041 2348594.
  E-mail address: sig@unive.it (S. Daniele).
[1] Current address: School of Chemistry, University of Edinburgh, EH9 3JJ Edinburgh, UK.

(A)

$RG = b/a$

(B)

Inlaid disk

$2a$

h

Hg
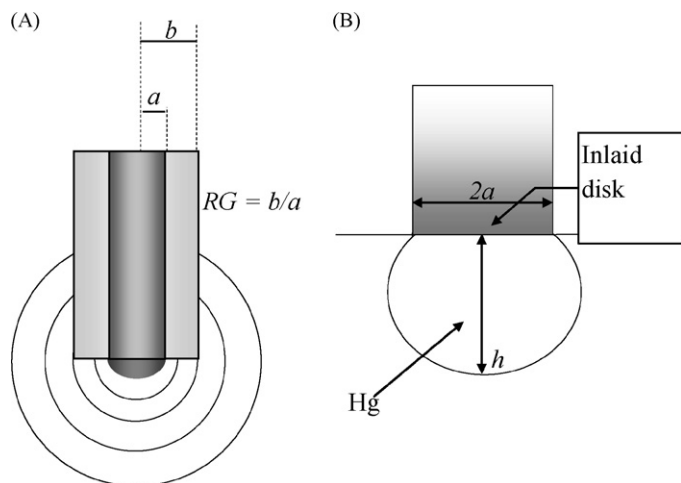
Fig. 1. Schematic representation of: (A) diffusion profiles at a thin-shielded micro-electrode and (B) shape and geometrical parameters of a hemispherical mercury microelectrode.

the above characteristics, the use of thin-shielded microelectrodes in ASV experiments should bring advantages in terms of sensitivity and analysis time with respect to thick-shielded microelectrodes.

In this paper, we report for the first time on the performance of thin-shielded mercury-coated platinum microelectrodes for ASV measurements of heavy metals. In particular, the effect of the flux enhancement during the preconcentration step in comparison with normal mercury microelectrodes, i.e., mercury microelectrodes surrounded by a thick insulating sheath, is investigated. Furthermore, the usefulness of thin-shielded mercury microelectrodes for in situ analysis of metal ions in real samples is verified by performing ASV measurements in a bauxitic soil sample.

2. Experimental

2.1. Chemicals

Perchloric, nitric and acetic acid, sodium acetate, mercurous nitrate, potassium nitrate and sodium chloride were of reagent grade and were purchased from Fluka. Titrisol cadmium and lead atomic absorption standards (Merck) were used to prepare stock standard solutions ($1000\,mg\,L^{-1}$) of these metal ions. Ruthenium(III) hexaammine trichloride was purchased from J. Matthey. All aqueous solutions were prepared with Milli-Q water (Millipore Corp.). All measurements requiring no oxygen were carried out in solutions that had been purged with pure nitrogen (99.99%) (from Siad).

2.2. Electrodes

The platinum microdisks, which served as the substrates for mercury deposition, were prepared either by sealing a Pt wire of $12.5\,\mu m$ radius into glass capillaries, or by coating the cylindrical length of the Pt wire with a cathodic electrophoretic paint as described previously [9,12]. The latter procedure was employed to prepare the Pt microdisk with a very thin insulating shield. In what follows, the microdisk characteristics are defined in terms of the parameter $RG = b/a$ (i.e., the ratio of the overall tip radius b, to the basal radius of the electrode a, Fig. 1A). For each microdisk, the radius of the insulating sheath, as is customary, was determined with an optical microscope or by SEM, while preparing the microtips. Moreover, for the thin-shielded microdisk, the cyclic voltammetric procedure described in Ref. [12] was also employed.

The microdisks used here had RG values of 1.52 ± 0.1 and 110 ± 10. Mercury microelectrodes were fabricated by cathodic deposition of liquid mercury onto the platinum microdisks [23–25]. The deposition was performed under potentiostatic conditions at $-0.1\,V$ against an Ag/AgCl reference electrode in a plating solution consisting of $5\,mM\,Hg_2(NO_3)_2$ in $1\,M\,KNO_3$ acidified with nitric acid to pH < 1. The height h of the mercury deposit (see Fig. 1B) was calculated from the sphere-cap volume (V) given by [22–24,26]: $V = \pi h\,(3a^2 + h^2)/6$ itself determined from the charge Q ($Q = V\rho F/M$, where ρ and M are the density and molar mass of mercury, respectively) [26] passed during the electrodeposition. The h values of the mercury microelectrodes employed here were equal to 12.7 and $13.1\,\mu m$. Prior to mercury deposition, the glass embedded microdisk was polished with graded alumina powder of different sizes (1, 0.3 and $0.05\,\mu m$) on a polishing microcloth.

The reference electrode was either a commercial available Ag/AgCl (Cl$^-$ saturated) electrode (AMEL), or a homemade Ag/AgCl electrode. The latter was constructed by using a silver wire coated electrochemically with a 100-μm thick silver chloride, on which a film of the anionic polymer exchanger Tosflex® resin was deposited. This membrane was then allowed to saturate with Cl$^-$ by prolonged immersion in a KCl saturated solution.

To measure the pH of the soil slurry, a standardised pH meter (Metrohm) with a glass electrode was employed.

2.3. Instrumentation

Voltammetric and potential step experiments were carried out by using an EG&G Mod. 283 potentiostat/galvanostat (PAR, Princeton), and the EG&G PAR 270 electrochemical analysis software. Unless otherwise stated, the measurements were carried out in a two-electrode cell, located inside a Faraday cage made of sheets of aluminium.

2.4. Samples and procedures

All ASV measurements were performed using linear sweep voltammetry in the stripping step. Unless otherwise stated, the scan rate employed was $50\,mV\,s^{-1}$. Lead and cadmium ions in acetate buffer were examined over the concentration range 0.01–$10\,\mu M$. A bauxitic soil sample collected at about $4\,m$ depth in Marghera industrial zone (Venice area) was also investigated. Linear sweep anodic stripping measurements (LSASV) were performed in the soil sample, which was equilibrated with an acidified aqueous solution as follows. A Teflon pot, 5-cm base diameter, was filled with $20\,g$ of soil and mixed with $7\,mL$ Milli-Q water containing $0.5\,M$ NaCl and HClO$_4$, under magnetic stirring. The slurry was left to equilibrate at least for $24\,h$ to achieve the uniform pH 4.5 throughout the sample. The LSASVs were then performed with the mercury microelectrodes visibly placed within the soil slurry.

3. Results and discussion

3.1. Characterization of the mercury microelectrodes

The mercury deposit on an inlaid microdisk of Pt, which is wettable by mercury, is usually in the shape of a sphere cap, with its basal plane coincident with the original inlaid disk [22–28] (Fig. 1B). This is a consequence of the large surface energy of the mercury/solution interface. The steady-state limiting current for a sphere cap (i_{Sc}) can be described by [22–29]:

$$i_{Sc} = k_{Sc}nFDc^b a \tag{1}$$

where k_{Sc} is a "geometric" coefficient that depends on both RG and h/a, and the other symbols have their usual meanings. Thus, for a

Table 1
Geometric parameters of the microelectrodes investigated and voltammetric data recorded in Ru(NH$_3$)$_6$Cl$_3$ aqueous solutions

Electrode type and geometric characteristics	k_{Sc}^{th}	i_{Sc}^{th} (nA)	$i_{Sc}^{exp} \pm 0.05$ (nA)	k_{Sc}^{exp}
Pt (RG = 110, b = 1375 μm, a = 12.5 μm)	4.00	3.82	3.85	4.03[a]
Hg/Pt (RG = 110, b = 1375 μm, h = 12.7 μm, a = 12.5 μm)	6.43	6.73	6.60	6.21[b]
Pt (RG = 1.52, b = 19.2 μm, a = 12.6 μm)	4.66	4.49	4.60	4.77[a]
Hg/Pt (RG = 1.52, b = 19.2 μm, h = 13.1 μm, a = 12.6 μm)	8.21	8.79	8.86	8.27[b]

th = theoretical, exp = experimental.
  [a] c^b = 1.08 mM.
  [b] c^b = 1.20 mM.

given experiment, on the basis of Eq. (1), the steady-state diffusion limiting current can be predicted once k_{Sc} is known. Recently, an analytical approximation that provides k_{Sc} as a function of RG and h/a parameters was reported [16]:

$$k_{Sc} = (4 + 0.5780(RG - 0.6734)^{-0.8348})$$
$$+ (2.2832 + 9.3279(RG + 1.0321)^{-2.2979})\left(\frac{h}{a}\right)^{1.3590} \quad (2)$$

This equation is valid for $1.04 \leq RG \leq 100$ and $0 \leq h/a \leq 2$, and therefore includes the coefficients for a microdisk and a hemisphere. For instance, setting in Eq. (2) $h/a = 0$ and RG $\rightarrow \infty$, or $h/a = 1$ and RG $\rightarrow \infty$, k_{Sc} values equal to 4 [30] or 6.28 [2,3] are found, which correspond to the coefficients expected for a disk or a shrouded hemisphere embedded on an infinite insulating plane, respectively. The theoretical k_{Sc} expected for the disk and spherical shaped microelectrodes employed here were determined by setting in Eq. (2) the b, a and h values determined experimentally, as described above. Table 1 summarizes the parameters thus evaluated.

The experimental geometric coefficients of the investigated electrodes were determined by cyclic voltammetry at a sufficiently low scan rate, in an aqueous solution containing Ru(NH$_3$)$_6$Cl$_3$ and 0.1 M KCl as supporting electrolyte. Fig. 2 shows typical voltammograms obtained at 1 mV s^{-1}, for the thin- and thick-shielded Pt microdisks and the corresponding Hg-coated Pt microelectrodes (Hg/Pt). As is evident, in all cases well-shaped sigmoidal curves with the forward and backward waves almost superimposed were obtained. The achievement of steady state conditions was assessed by using the criterion of the difference in half-wave potentials ($\Delta E_{1/2}$) observed on the forward and backward waves (see inset in Fig. 2) [10,12,31,32]. At steady state $\Delta E_{1/2}$ should be equal to zero [10,12,31,32]. The analysis of the voltammograms obtained with the investigated microelectrodes yielded $\Delta E_{1/2}$ values of

5.0($\pm$0.5) mV and 0.6($\pm$0.3) mV for the thick- and thin-shielded microelectrodes, respectively. This means that the thin-shielded microelectrodes approach the steady state faster. However, for both types of microelectrodes the diffusion limiting currents recorded under the adopted experimental conditions were very close (to within 2.5% deviation) to the true steady-state values.

From the steady-state limiting currents and Eq. (1), the experimental geometric coefficients of the various microelectrodes were found. These values, together with the experimental and theoretical diffusion steady state limiting currents, are included in Table 1. From this table it is evident that the thin-shielded microelectrodes display larger currents (and consequently higher geometric coefficients), which are clearly related to the flux enhancement due to the diffusion from behind the plane of the electrode. In particular, at the thin-shielded microelectrodes, the current is enhanced by about 17% and 30% for the disk and the spherical microelectrode, respectively.

The flux enhancement at the thin-shielded mercury microelectrode is expected to apply also during the preconcentration step of an ASV experiment, provided that a sufficiently long deposition time is employed to allow the achievement of a steady state. The performance of the thin- and thick-shielded mercury microelectrode for ASV measurements of lead and cadmium ions in aqueous solutions is compared in the next section.

3.2. ASV measurements with Hg/Pt microelectrodes in synthetic solutions

Fig. 3 shows typical LSASVs obtained at the thin- and thick-shielded mercury microelectrodes on a synthetic acetate buffer solution containing 0.5 μM each of lead and cadmium ions. The features of these voltammograms are similar in shape and position, regardless of the type of mercury microelectrode employed. In fact, peak potential (E_p) of −0.386($\pm$0.002) V for Pb and −0.560($\pm$0.002)
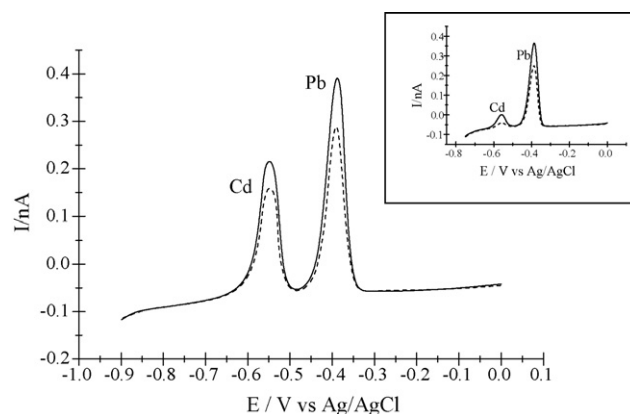
Fig. 2. Experimental cyclic voltammograms recorded in 1 mM Ru(NH$_3$)$_6$$^{3+}$ + 0.1 M KCl solution at: Hg/Pt (1) RG = 1.52 and h/a = 1.04, (2) RG = 110 and h/a = 1.02; Pt microdisk, (3) RG = 1.52, a = 12.6 μm and (4) RG = 110, a = 12.5 μm. Scan rate 1 mV s^{-1}. Inset: magnification of the indicated zone and indication of the meaning of $\Delta E_{1/2}$.

Fig. 3. ASV responses recorded in 0.5 μM each Pb^{2+} and Cb^{2+} at: Hg/Pt (—) RG = 1.52 and h/a = 1.04, and (⋯) RG = 110 and h/a = 1.02. E_d = −0.9 V, t_d = 100 s, scan rate 50 mV s^{-1}. Inset, as in the main figure and E_d = −0.75 V.

Fig. 4. Stripping peak charge against effective deposition time plots for 0.5 μM each (A) Pb and (B) Cd at (&z.cirf;) Hg/Pt RG = 1.52 and (○) Hg/Pt RG = 110. $E_d = -0.85$ V, scan rate 50 mV s^{-1}. Inset: magnification of the indicated zone.

V for Cd, and peak width at half height ($w_{1/2}$) of 44($\pm$2) mV and 50($\pm$2) mV for Pb and Cd, respectively, were obtained. However, both the stripping current (i_p) and charge (Q_a) of the stripping peaks were larger at the thin-shielded mercury microelectrode, congruently with a larger amount of metal accumulated during the deposition step at this type of electrode.

The effect of deposition time on the ASV responses was investigated in detail. Fig. 4 with symbols shows typical experimental stripping peak charge against effective deposition time (t_{eff}) data obtained in an acetate buffer solution containing 0.5 μM each of cadmium and lead ions, and using a deposition potential (E_d) equal to −0.85 V (similar trends, not shown, were also obtained for the stripping current against time plots). The effective deposition time was calculated by the following equation [24,33]:

$$t_{eff} = t_d + \frac{(E_p - E_d)}{v} \tag{3}$$

where t_d is the deposition time at E_d, and v is the scan rate. The term in parenthesis represents the deposition time while scanning. As is evident from Fig. 4, ASV peaks well emerging from the blank (about five times larger than the average signal of the blank) were recorded, after t_{eff} of about 9 and 14 s for lead and cadmium, respectively, by using the thin-shielded mercury microelectrode (see insets of Fig. 4). Instead, about 50 s for both ions were required to obtain valuable ASV peaks with the thick-shielded mercury microelectrode. Once again, this can be explained as due to

the higher flux involved at the thinner shielded mercury microelectrodes during the preconcentration step.

The experimental Q_a vs. t_{eff} plots showed good linearity (correlation coefficients >0.999) after 120 and 60 s for the thick- and thin-shielded mercury microelectrode, respectively. Moreover, the slope of the plot obtained with the thin-shielded mercury microelectrode was larger than that of the thicker shielded one. These results were rationalized on the basis of Eq. (4) [33]:

$$Q_a = nFc^b[1.13A(Dt_{eff})^{1/2} + k_{Sc}aDt_{eff}] \tag{4}$$

which was derived for sphere-cap microelectrodes embedded on an infinite insulating plane [33] and extended here to the thin-shielded one by the use of the proper geometric coefficient k_{Sc}. The latter, in fact, accounts for the different diffusion fields that apply at the two types of microelectrodes, when steady-state conditions are achieved. Eq. (4) was derived under the assumption that all metal accumulated in the mercury film during the deposition step is oxidized back during the stripping step [33].

Theoretical plots obtained from Eq. (4) for Cd and Pb are included in Fig. 4 with lines, using the diffusion coefficients 8.28×10^{-6} cm^2 s^{-1} (Pb^{2+}) and 6.90×10^{-6} cm^2 s^{-1} (Cd^{2+}) [34]. It is evident that theoretical and experimental data fit very well (within about 4%, experimental error). Interesting is also noting that above $t_{eff} = 120$ s, that is the time needed to achieve a steady state within about 6% deviation for both types of mercury microelectrodes, the stripping charge obtained at the thin-shielded electrode was on average 32 ± 3% larger than that recorded with the thicker shielded one. This charge enhancement is very close to the theoretical flux enhancement predicted above by steady-state measurements.

The effects of deposition potential, scan rate and concentration on the LSASVs were also investigated in an acetate buffer solution containing 0.5 μM each of cadmium and lead ions, using $t_d = 100$ s. The deposition potential was varied between −0.75 V (see inset in Fig. 3) and −0.9 V. It was found that, as the potential became more negative, while the stripping peak of lead increased slightly, in accordance with the increase of the effective deposition time (Eq. (4)), the stripping peak of cadmium increased significantly, especially at the thicker shielded microelectrode, in the range −0.75 to −0.85 V (compare LSASVs in Fig. 3 and inset); afterwards it changed slightly up to −0.9 V because of the increase of effective deposition time. These results indicated that optimum potential values for efficient deposition of both metal ions was in the range −0.85 to −0.9 V. The scan rate was varied over the range 20–200 mV s^{-1}; the current peak increased linearly with the scan rate, regardless of the electrode employed, as expected for restricted diffusion conditions, as typically observed at mercury microelectrodes [35]. The effect of concentration was evaluated over the range 0.05–10 μM, using $t_d = 120$ s, and $E_d = -0.85$ V; for both types of microelectrodes a linear trend was observed between Q_a and c^b. The linear regression analysis of experimental points provided the relationships summarized in Table 2.

3.3. Determination of metal ions in a soil sample by using the thin-shielded mercury microelectrode

Hg coated Pt microelectrodes surrounded by a thick insulating sheath were recently used for ASV measurements in soils [36,37]. In order to verify whether also the thin-shielded Hg coated Pt microelectrode was sturdy enough to withstand penetration within a soil slurry, a series of measurements were done in a bauxitic soil sample, which was acidified to pH 4.5, as described in Section 2. A typical LSASV obtained under these conditions is shown in Fig. 5, which displays three ASV peaks. On the basis of peak potentials, they were assigned to Cd (−0.65 V), Pb (−0.45 V) and Cu (−0.30 V).

Table 2
Linear regression equations (Q_a vs. c^b) evaluated at the two different mercury microelectrodes for the metal ions investigated $E_d = -0.85$ V and $t_d = 120$ s

Hg/Pt (RG)	Metal ion	Linear regression equation Q_a (nC) = $A + Bc^b$ (μM)		(R^2)
		A	B	
110	Pb^2	0.09	0.95	0.999
	Cd^{2+}	0.06	0.70	0.998
1.52	Pb^{2+}	0.10	1.42	0.999
	Cd^{2+}	0.11	0.98	0.999
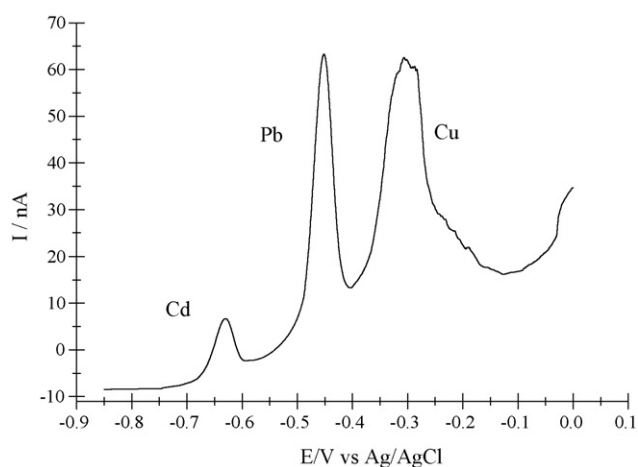
Fig. 5. ASV response recorded with an Hg/Pt RG = 1.52 and h/a = 1.04 located inside a soil slurry sample, pH 4.5. Scan rate 50 mV s^{-1}, $E_d = -0.85$ V and $t_d = 50$ s.

It must be noticed that while the stripping peaks of cadmium and lead are well shaped, the stripping peak of copper is rather broad. Broad ASV peaks for Cu reported in literature [1,37,38] attributed to several phenomena such as formation of adsorbed copper complexes due to organic matter and the presence of chloride ions and oxygen in the investigated media. Because of the complexity of the soil matrix investigated here and in view of the fact that oxygen from air was present within the soil slurry under the adopted experimental conditions, it is likely that all the above phenomena had a role in determining the shape of the copper stripping peak. The effects of deposition time, deposition potential and scan rate on these stripping peaks were similar to those discussed above in the aqueous synthetic solutions. Therefore, for the determination of the concentration of the metal ions, Eq. (4) was employed, all parameters involved in it being known. The diffusion coefficient values used were 2.2×10^{-6} cm^2 s^{-1} (Cd^{2+}), 2.8×10^{-6} cm^2 s^{-1} (Pb^{2+}) and 2.0×10^{-6} cm^2 s^{-1} (Cu^{2+}) [37,39]. These values, which are smaller than the above used in the homogeneous phase, account for porosity and tortuosity of pores in the soil [39,40]. To facilitate the calculations, the LSASVs obtained with t_d over the range 120–150 s were employed. Under these conditions, the steady-state contribution in Eq. (4) prevails, the time dependent term being in any case lower than 4%. Q_a vs. t_{eff} gave, as expected, linear trends, and from their slopes concentration values equal to 6.7 ($\pm$0.2) μM for Cd, 45 ($\pm$0.9) μM for Pb and 83 ($\pm$1.1) μM for Cu were obtained. The values thus calculated compare well with those found in the literature in similar media and under similar experimental conditions [37].

4. Conclusions

In this paper, it has been shown that a mercury microelectrode, fabricated by electrodeposition of liquid mercury on an inlaid Pt microdisk with a shield comparable to electrode radius, provided ASV responses which were sensibly greater than those obtained with classical mercury microelectrodes, i.e., electrodes surrounded by a relatively thick insulating sheath. In particular, for a hemispherical microelectrode RG = 1.52, because of diffusion from behind the plane of the electrode, the flux during the deposition step was enhanced by about 32%, and ASV peaks, well emerging from the background, could be recorded in 0.5 μM each Pb^{2+} and Cd^{2+} aqueous solution, only after a few seconds of effective deposition time. The thin-shielded mercury microelectrode revealed also high stability, such that ASV measurements could be performed in situ in soil slurry.

References

[1] J. Wang, Stripping Analysis: Principles, Instrumentation and Applications, VCH, Deerfield Beach, FL, 1985.
[2] R.M. Wightmann, D.O. Wipf, in: A.J. Bard (Ed.), Electroanalytical Chemistry, vol. 15, Marcel Dekker, New York, 1989, pp. 267–353.
[3] M.I. Queiros, in: M.A.J.L. Daschbach (Ed.), Microelectrodes: Theory and Applications, NATO ASI Series, Kluwer Academic Publishers, Dordrecht, 1991.
[4] S. Daniele, C. Bragato, M.A. Baldo, Curr. Anal. Chem. 4 (2008) 215.
[5] S. Daniele, M.A. Baldo, P. Ugo, G.A. Mazzocchin, Anal. Chim. Acta 219 (1989) 9.
[6] A. Economou, P.R. Fielden, Analyst 128 (2003) 205.
[7] J. Buffle, M.L. Tercier-Waeber, Trends Anal. Chem. 24 (2005) 172.
[8] R.A. Clark, S.E. Zerby, A.G. Ewing, in: A.J. Bard, I. Rubistein (Eds.), Electroanalytical Chemistry, vol. 20, Marcel Dekker, New York, 1998, pp. 227–294.
[9] X. Zhang, B. Ogorevc, M. Rupnik, M. Kreft, R. Zorec, Anal. Chim. Acta 378 (1999) 135.
[10] Y. Fang, J. Leddy, Anal. Chem. 67 (1995) 1259.
[11] G. Zhao, D.M. Giolando, J.R. Kirchoff, Anal. Chem. 67 (1995) 2592.
[12] I. Ciani, S. Daniele, Anal. Chem. 76 (2004) 6575.
[13] C.G. Zoski, M.V. Mirkin, Anal. Chem. 74 (2002) 1986.
[14] C.G. Zoski, B. Liu, A.J. Bard, Anal. Chem. 76 (2004) 3646.
[15] G. Lindsey, S. Abercrombie, G. Denuault, S. Daniele, E. De Faveri, Anal. Chem. 79 (2007) 2952.
[16] S. Daniele, I. Ciani, D. Battistel, Anal. Chem. 79 (2008) 2952.
[17] A.J. Bard, M.V. Mirkin (Eds.), Scanning Electrochemical Microscopy, Marcel Dekker, New York/Basel, 2001.
[18] Q. Fulian, A.C. Fisher, G. Denuault, J. Phys. Chem. B 103 (1999) 4387.
[19] Q. Fulian, A.C. Fisher, G. Denuault, J. Phys. Chem. B 103 (1999) 4393.
[20] D. Shoup, A. Szabo, J. Electroanal. Chem. 140 (1982) 237.
[21] D. Shoup, A. Szabo, J. Electroanal. Chem. 160 (1984) 27.
[22] S. Daniele, C. Bragato, M.A. Baldo, G.A. Mazzocchin, Ann. Chim. (Rome) 92 (2002) 203.
[23] Z. Stojek, J. Osteryoung, Anal. Chem. 66 (1989) 1305.
[24] M.A. Baldo, S. Daniele, M. Corbetta, G.A. Mazzocchin, Electroanalysis 7 (1995) 980.
[25] K.R. Wehmeyer, R.M. Wightman, Anal. Chem. 57 (1985) 1989.
[26] C.L. Colyer, D. Luscombe, K.B. Oldham, J. Electroanal. Chem. 283 (1990) 379.
[27] J.C. Myland, K.B. Oldham, J. Electroanal. Chem. 288 (1990) 1.
[28] L.C.R. Alfred, K.B. Oldham, J. Phys. Chem. B 100 (1996) 2170.
[29] R.L. Birke, Z. Huang, Anal. Chem. 64 (1992) 1513.
[30] Y. Saito, Rev. Polarogr. 15 (1968) 177.
[31] C.G. Zoski, A.M. Bond, C.L. Colyer, J.C. Myland, K.B. Oldham, J. Electroanal. Chem. 263 (1989) 1.
[32] C.G. Zoski, J. Electroanal. Chem. 296 (1990) 317.

[33] M.A. Baldo, S. Daniele, C. Bragato, G.A. Mazzocchin, Anal. Chim. Acta 464 (2002) 217.

[34] J. Heyrovsky, J. Kuta, Principles of Polarography, Czechoslovak Academy of Science, Prague, 1965, p. 106.

[35] M. Penczek, Z. Stojek, J. Electroanal. Chem. 191 (1985) 91.

[36] P.J. Brendel, G.W. Luther III, Environ. Sci. Technol. 29 (1995) 751.

[37] S. Daniele, I. Ciani, M.A. Baldo, C. Bragato, Electroanalysis 19 (2007) 2067.

[38] G.E. Batley, Anal. Chim. Acta 189 (1986) 371.

[39] R.N. Glud, K. Jensen, N.P. Revsbech, Geochim. Cosmochim. Acta 59 (1995) 231.

[40] N. Iversen, B.B. Jorgensen, Geochim. Cosmochim. Acta 75 (1993) 571.

Determination of chlorogenic acid in coffee using a biomimetic sensor based on a new tetranuclear copper(II) complex

Mirella Lucas de Carvalho, Murilo Santhiago, Rosely A. Peralta,
Ademir Neves, Gustavo Amadeu Micke, Iolanda Cruz Vieira *

Departamento de Química, Universidade Federal de Santa Catarina, CEP 88040-900 Florianópolis, SC, Brazil

ABSTRACT

A new tetranuclear copper(II) complex which mimics the active site of catechol oxidase was synthesized and characterized by IR, CHN, electronic spectroscopic and ^{1}H NMR methods. The title complex $[Cu_2(\mu\text{-}OH)(bpbpmp\text{-}NO_2)]_2[ClO_4]_2$ was employed in the construction of a novel biomimetic sensor and used in the determination of chlorogenic acid by square wave voltammetry. The performance and optimization of the resulting biomimetic sensor were studied in detail. The best response of this sensor was obtained for 75:15:10% (w/w/w) ratio of the graphite powder:nujol:Cu(II) complex, 0.1 mol L^{-1} phosphate buffer solution (pH 7.0), with frequency, pulse amplitude, and scan increment at 30 Hz, 100 mV, and 3.0 mV, respectively. The chlorogenic acid concentration was linear in the range of 5.0×10^{-6} to 1.45×10^{-4} mol L^{-1} ($r = 0.9985$) with a detection limit of 8.0×10^{-7} mol L^{-1}. This biomimetic sensor demonstrated long-term stability (250 days; 640 determinations) and reproducibility, with a relative standard deviation of 10.0%. The recovery study of chlorogenic acid in coffee samples gave values from 93.2% to 106.1% and the concentrations determined showed good agreement when compared with those obtained using capillary electrophoresis at the 95% confidence level.

© 2008 Elsevier B.V. All rights reserved.

1. Introduction

Coffee is among the most widely consumed pharmacologically active beverages in the world. It represents a giant global industry and ranks second only to petroleum in terms of dollars traded worldwide. Currently, 6.3 million tons of coffee is produced globally, with Brazil and Colombia contributing to nearly 44% of this figure. The major polyphenol in coffee is chlorogenic acid, an ester formed between *trans* cinnamic acids and quinic acid. The cinnamic acids most commonly encountered are caffeic, *p* coumaric and ferulic acid [1–6].

The acid content in coffee is an important indication of its quality, and is greatly dependent upon the degree of roasting, the type of roaster and method of infusion. The determination of chlorogenic acid in coffee is an important aspect of the quality control of the final product, since its aroma characteristics determine the commercial value [7]. The development of reliable, rapid, sensitive and simple methods for the quantification of this substance is of great importance. Methods for the determination of this acid include chromatography [8–11], capillary electrophoresis [12], flow injection chemiluminescence [13] and electrochemistry [14]. Križman

et al. [8] employed a reversed-phase HPLC method for analyzing phenolic compounds in fennel (*Foeniculum vulgare*). The limits of detection ranged from 0.05 to 1.0 μg mL^{-1}. The simultaneous determination of chlorogenic acid, caffeic and ferulic acid in coffee samples by micellar electrokinetic chromatography was used by Risso et al. [9]. The proposed method showed good linearity for chlorogenic acid and was able to resolve the two positional isomers of caffeoylquinic acid. A gas chromatographic–mass spectrometric method was used by Füzfai and Molnár-Perl [10] for the determination of flavonoids, sugars, carboxylic acids and amino acids in citrus fruits. The authors found 33 compounds in the fruit samples after hydrolysis with trifluoroacetic acid. Nishitani and Sagesaka [11] used high-performance liquid chromatographic (HPLC) for simultaneous determination of catechins, caffeine and other phenolic compounds in tea. The separation of polyphenolic compounds extracted from plant matrices using capillary electrophoresis has been proposed by Vaher and Koel [12]. Wang et al. [13] showed a new flow injection chemiluminescence method for the determination of chlorogenic acid in fruits based on the reaction of potassium permanganate with this acid in the presence of formaldehyde as an enhancer. The linearity of the method ranged from 5.0×10^{-8} to 5.0×10^{-5} g mL^{-1}. Mello et al. [14] developed a biosensor based on horseradish peroxidase for the determination of chlorogenic acid in tea and coffee samples. The analytical curve was linear from 1 to 50 μmol L^{-1} using chronoamperometry as the electrochemical

method. Electrochemical methods for the determination of this substance and other antioxidants are preferred over others because of their fast response time, low detection limits and relatively low costs [14–17].

Copper is an essential transition element that plays a fundamental role in the biochemistry of all aerobic organisms. Proteins exploit the unique redox nature of this metal to undertake a series of facile electron transfer reactions using copper as a cofactor in a select number of critical enzymatic pathways [18,19]. Copper complexes are synthesized and characterized widely as structural and functional models of active centers of oxidoreductase enzymes [20–22]. These complexes have been employed successfully in the development of biomimetic sensors. In addition, the models have an extraordinary advantage in relation to the natural enzyme, which is the high stability in relation to several factors (e.g. temperature, pH, and others) and, consequently, the biomimetic sensors offer a longer lifetime and greater number of determinations than other biosensors [22–24].

In this study, we synthesized and characterized by IR, CHN, electronic spectroscopy and ^{1}H NMR methods a new tetranuclear copper(II) complex $[Cu_2(\mu\text{-}OH)(bpbpmp\text{-}NO_2)]_2[ClO_4]_2$ which mimics the active site of catechol oxidase. This complex was employed in the construction of a novel biomimetic sensor. The experimental conditions (percentage of the Cu(II) complex, solution pH and square wave voltammetry parameters such as frequency, pulse amplitude, and scan increment) for the analytical performance of the sensor were optimized. The results obtained in the determination of chlorogenic acid in coffee samples using the biomimetic sensor were compared with those obtained using the capillary electrophoresis method.

2. Experimental

2.1. Chemicals

Chlorogenic acid was purchased from Sigma. Graphite powder (grade #38, FisherScientific) and mineral oil (Aldrich) of high purity were used in the preparation of the carbon paste. The tetranuclear copper(II) complex was used in the construction of the biomimetic sensor. Phosphate buffer ($0.1\,mol\,L^{-1}$, pH 7.0) solution was used as the supporting electrolyte. All reagents used in this study were of analytical grade and all solutions were freshly prepared with double distilled water. For the synthesis the ligand and complex were used: 2-(2-aminomethyl)pyridine, 5-nitrosalicylaldehyde, *p*-cresol, triethylamine, sodium hydroxide, formaldehyde, sodium bicarbonate, hydrochloric acid, anhydrous sodium sulfate, sodium borohydrate, thionyl chloride, copper(II) perchlorate hexahydrate purchased from Merck or Aldrich and used as received. 2-Pyridinecarboxaldehyde was distilled under reduced pressure before use. For the capillary electrophoresis analysis a stock solution of sodium tetraborate (STB), Na_2HPO_4 and sodium dodecyl sulfate (SDS) was prepared at $100\,mmol\,L^{-1}$, the standard stock solution of chlorogenic acid was prepared in methanol at $800\,mg\,L^{-1}$.

2.2. Complex characterization instrumentation

Elemental analysis for carbon, hydrogen, and nitrogen was performed using a Carlo Erba E-1110 analyzer. IR spectra (as KBr pellets or film, 4000–$500\,cm^{-1}$) were taken at $25\,^\circ C$ using a Perkin-Elmer FTIR-2000 spectrophotometer. ^{1}H NMR spectra were measured on a Bruker FT-200 MHz spectrometer. Chemical shifts were reported as δ values relative to an internal standard (Me_4Si) and the residual solvent proton peak. UV–vis spectra were recorded with a Perkin-

Elmer L-19 spectrophotometer, using quartz 10 mm path length cells.

2.3. Electrochemical and capillary electrophoresis instrumentation

Square wave voltammetry (SWV) measurements were performed with an Autolab PGSTAT12 potentiostat/galvanostat (Eco Chemie, The Netherlands). All electrochemical experiments were carried out in a conventional three-electrode cell at room temperature ($25.0 \pm 0.5\,^\circ C$). An Ag/AgCl electrode saturated with KCl solution was used as the reference electrode, against which all currents were measured and reported in this study. A platinum wire was used as the auxiliary electrode and the biomimetic sensor as the working electrode. The system was monitored with a personal computer for data acquisition and subsequent analysis.

Electropherograms were performed with an Agilent capillary electrophoresis system equipped with a diode array detector. The data processing was carried out with the HP Chemstation® software. The measurements were performed at $25\,^\circ C$ on an uncoated fused-silica capillary ($48.5\,cm \times 50\,\mu m$ I.D. $\times 375\,\mu m$ O.D., 8.5 cm of effective length) obtained from Microtube (Araraquara, SP, Brazil).

2.4. Synthesis and characterization of the ligand and biomimetic complex

The ligand *N*-(2-hydroxy-5-nitrobenzyl)(2-pyridylmethyl) amine (hbpa-NO_2) was obtained as follows: $20.0 \times 10^{-3}\,mol\,L^{-1}$ 2-(aminomethyl)pyridine was added to a methanolic solution of $20.0 \times 10^{-3}\,mol\,L^{-1}$ 2-hydroxy-5-nitrobenzaldehyde under stirring. After few minutes a yellow precipitate was observed. After 20 min, $10.0 \times 10^{-3}\,mol\,L^{-1}$ of sodium borohydrate was added slowly. The pH was then adjusted to 6.0 using $2.0\,mol\,L^{-1}$ HCl and the solvent was evaporated under reduced pressure. 3.9 g of a yellow solid (yield 75%) was obtained by recrystallization in methanol. mp: 158–$160\,^\circ C$. IR (KBr) in cm^{-1}: ν (N—H) 3440; ν (C—H$_{ar}$ and C—H$_{aliph}$) 3019–2909; ν (C=N and C=C) 1599–1440; δ (O—H) 1379; ν (C—O) 1279; δ (C—H$_{ar}$) 768. ^{1}H NMR, δ_H (CDCl$_3$), in ppm: 3.90 (s, 2H); 4.10 (s, 2H); 4.73 (s, 1H, NH); 6.83–6.92 (d, 1H); 7.19–7.30 (m, 2H); 7.62–7.77 (dt, 1H); 7.95 (s, 1H); 8.11–8.20 (m, 1H); 8.59–8. 71 (d, 1H).

The ligand 2-[*N*-bis-(2-pyridylmethyl)aminomethyl]-4-methyl-6-[*N*′-(2-pyridylmethyl)(2-hydroxy-5-nitrobenzyl)aminomethyl] phenol (H$_2$bpbpmp-NO$_2$) was synthesized adding $27.5 \times 10^{-3}\,mol\,L^{-1}$ of hbpa-NO_2 and 4.7 mL of triethylamine to $27.5 \times 10^{-3}\,mol\,L^{-1}$ of bpmamcf.HCl [25] previously dissolved in 50 mL of CH$_2$Cl$_2$. The mixtures were maintained under stirring and reflux for 30 h and then extracted with an aqueous solution of NaHCO$_3$ (8×40 mL). The organic layer was dried with anhydrous sodium sulfate and then rotaevaporated. The ligand was obtained by recrystallization in methanol. Yield 72%. mp: 80–$81\,^\circ C$. IR (KBr) in cm^{-1}: ν (C—H$_{ar}$ and C—H$_{aliph}$) 3059–2824; ν (C=C) 1589–1434; δ (O—H) 1373; ν (Ar—NO$_2$) 1335, ν (C—O$_{phenol}$) 1290; δ (C—H$_{ar}$) 754. ^{1}H NMR, δ_H (CDCl$_3$), in ppm: 2.19 (s, 3H); 3.80–3.97 (s, 12H); 6.82–6.91 (m, 3H); 7.15–7.29 (m, 2H); 7.37–7.41 (d, 3H); 7.59–7.67 (m, 3H); 7.97–8.06 (m, 3H), 8.57–8.59 (d, 3H).

The complex $[Cu_2(\mu\text{-}OH)(bpbpmp\text{-}NO_2)]_2[ClO_4]_2$ was synthesized by adding of a methanolic solution of $5.0 \times 10^{-4}\,mol\,L^{-1}$ of H$_2$bpbpmp-NO$_2$ and $1.0 \times 10^{-3}\,mol\,L^{-1}$ of Cu(ClO$_4$)$_2$·6H$_2$O, under stirring at $40\,^\circ C$, followed by the addition of 1.5 mL of a $1.0\,mol\,L^{-1}$ sodium hydroxide solution and $1.0 \times 10^{-3}\,mol\,L^{-1}$ of NaClO$_4$. After 5 min a green microcrystalline precipitate was obtained. Yield 40%. CHN calculated for C$_{74}$H$_{82}$Cl$_2$Cu$_4$N$_{12}$O$_{18}$ (MM = 1752.62 g mol^{-1}): C: 50.71%; H: 4.72%; N: 9.59%. Found C: 50.37%; H: 4.60%; N: 9.67%. IV (KBr), in cm^{-1}: ν (OH) 3380; ν (C—H$_{ar}$ and C—H$_{aliph}$) 3050–2900;

ν (C=N and C=C) 1608–1430; ν (Ar—NO$_2$) 1330; ν (C—O) 1287; ν (Cl—O) 1090. Although we have not to date encountered difficulties with the above compounds, perchlorate salts are potentially explosive and should be treated with care.

2.5. Biomimetic sensor construction

The biomimetic sensor was constructed according to the procedure reported elsewhere [22–24]. Briefly, the tetranuclear copper(II) complex (15 mg; 10%, w/w) and graphite powder (113 mg; 75%, w/w) were mixed in a mortar for 20 min. Subsequently, the mineral oil (22 mg; 15%, w/w) was added and mixed for at least 20 min. The resulting modified carbon paste was placed in a 1-mL syringe and a copper wire was inserted to obtain the external electrical contact. The biomimetic sensor was stored at room temperature when not in use.

2.6. Preparation and analysis of coffee samples

Four samples of coffee (vacuum packed roasted and ground coffee) were obtained from local supermarkets in Florianópolis (Santa Catarina, Brazil). For the determinations, 3.0 g samples were prepared in 50.0 mL of hot water in triplicate. For the electrochemical measurements, 200 μL of these coffee samples were used. These samples were used in the chlorogenic acid determination with the proposed biomimetic sensor and the capillary electrophoresis method.

2.7. Electrochemical and capillary electrophoresis measurements

Square wave voltammetry measurements were performed in an unstirred, non de-aerated, phosphate buffer solution (pH 7.0). In a typical run, 10.0 mL of the supporting electrolyte was transferred to a clean, dry cell and the required volume of the chlorogenic acid or coffee sample solution was added by micropipette. After a stirring period of 60 s to homogenize the solution, a square wave voltammogram was recorded. The measurements were performed applying a sweep potential between +0.4 and −0.2 V, at a pulse amplitude of 5.0–100 mV, frequency of 10–80 Hz and scan increment of 0.5–4.0 mV, after successive additions of chlorogenic acid.

Electropherograms were recorded as follows: standard solutions and samples were introduced from the outlet and injected hydrodynamically at 50 mbar (5.25 Pa) for 5 s with reverse pressure. UV detection was performed at 340 nm. The applied separation voltage was 30 kV positive polarity on the injection side. The electrolyte was composed of 20.0×10^{-3} mol L^{-1} NaH$_2$PO$_4$, 20.0×10^{-3} mol L^{-1} STB, and 20.0×10^{-3} mol L^{-1} SDS. At the start of each new working session, the capillary was conditioned at 25 °C and flushed with 1.0 mol L^{-1} sodium hydroxide for 10 min, followed by deionized water for 5 min and finally with the BGE for 10 min. Between runs with the same buffer, the capillary was rinsed for 0.5 min with BGE. At the end of the analysis, the capillary was rinsed for 5 min with 1.0 mol L^{-1} sodium hydroxide and for 10 min with deionized water.

3. Results and discussion

3.1. Characterization of the complex [Cu$_2$(μ-OH)(bpbpmp-NO$_2$)]$_2$[ClO$_4$]$_2$

The complex [Cu$_2$(μ-OH)(bpbpmp-NO$_2$)]$_2$[ClO$_4$]$_2$ is cationic in nature having ClO$_4^-$ as the counter anion, as shown in Fig. 1. The characteristic stretching vibration of ClO$_4^-$ was observed at 1090 cm^{-1}. Furthermore, the IR spectrum exhibited bands within the ranges 3050–2900 cm^{-1} (aromatic and aliphatic C—H),
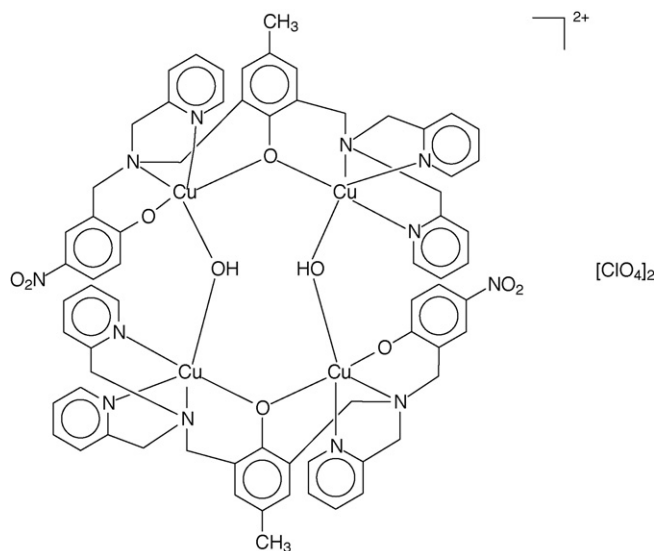
Fig. 1. Schematic representation of the [Cu$_2$(μ-OH)(bpbpmp-NO$_2$)]$_2$[ClO$_4$]$_2$ complex.

1608–1430 (C=C, C=N) and 1330 cm^{-1} (Ar—NO$_2$), which are consistent with those observed for the free ligand [25–27]. The band at 3380 cm^{-1} is consistent with the (μ-OH) proposed and observed in the X-ray structure of a similar complex containing the ligand H$_2$bpbpmp-CH$_3$ [28]. The chemical shifts and integration of the ^{1}H NMR spectrum allowed us to determine the number of H atoms present in the ligand H$_2$bpbpmp-NO$_2$. The electronic spectra of the complex show a broad band centered at 698 nm (ε = 246 L mol^{-1} cm^{-1}), typical of d–d copper(II) ion transitions and a band centered at 377 nm (ε = 10,525 L mol^{-1} cm^{-1}) which is attributed to the intraligand transition within the p-NO$_2$-phenolate group. The ligand-to-metal charge transfer band was not observed due to the superposition of the intense p-NO$_2$-aromatic band.

3.2. Reaction of the biomimetic complex with chlorogenic acid

The functional models of metalloenzymes for catalyst oxidation reactions are a very interesting idea and have attracting considerable attention. They have been employed successfully in the construction of sensors, showing high selectivity, stability and performance compared with those employing the enzyme [22–24].

Fig. 2 shows a schematic representation of the chlorogenic acid to quinone reaction at the sensor surface with the tetranuclear Cu(II) complex incorporated in the carbon paste. The reaction is based on the catalytic cycle proposed in other studies [29,30] and adjusted for the reaction involving this acid using the proposed biomimetic sensor.

The electrochemical behavior of chlorogenic acid using the plain carbon paste electrode and biomimetic sensor was investigated by cyclic voltammetry. In this study, cyclic voltammetry measurements were obtained by sweeping the potential between +0.5 and −0.5 V vs Ag/AgCl at a scan rate of 100 mV s^{-1}. Fig. 3 shows the cyclic voltammograms obtained using these sensors: (a) plain carbon paste electrode and (b) biomimetic sensor in 1.25×10^{-4} mol L^{-1} chlorogenic acid in 0.1 mol L^{-1} phosphate buffer solution (pH 7.0). As can be observed, the response to the oxidation of chlorogenic acid to its corresponding o-quinone and the electrochemical reduction back to chlorogenic acid using the biomimetic sensor, due to the addition of the [Cu$_2$(μ-OH)(bpbpmp-NO$_2$)]$_2$[ClO$_4$]$_2$ complex, was much better than that of the plain sensor and the carbon paste electrode.
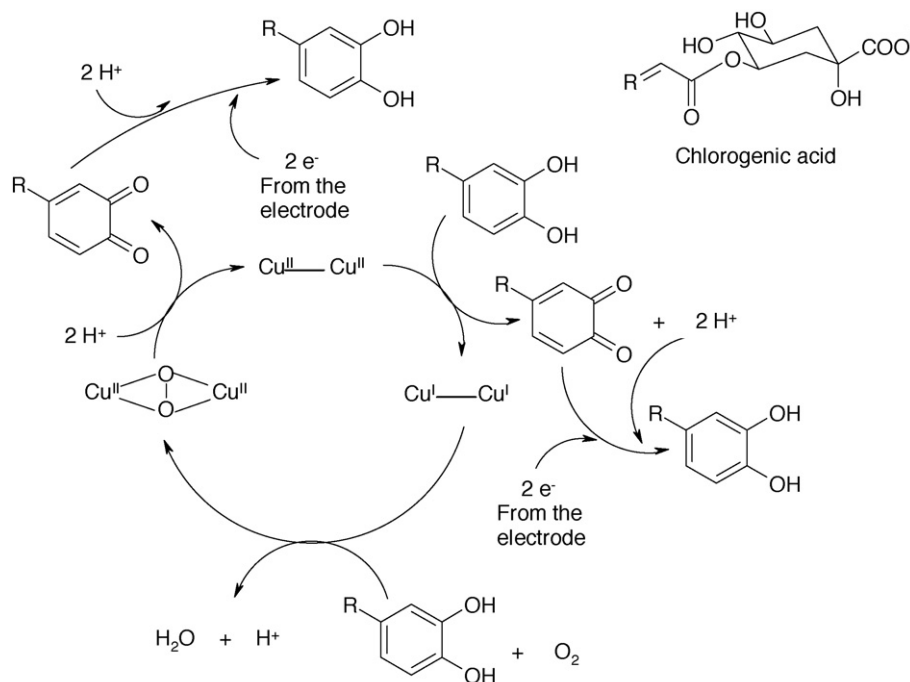
Fig. 2. Schematic representation of the reaction involving chlorogenic acid at the sensor surface with the tetranuclear Cu(II) complex incorporated in the carbon paste.

3.3. Influence of the pH and phosphate buffer concentration

To obtain the best biomimetic sensor performance, parameters such as pH (5.0–9.0) and concentration (0.01–0.25 mol L^{-1}) of the phosphate buffer solution were investigated using the square wave voltammetry technique.

The effect of the pH (5.0–9.0) was investigated in 9.80×10^{-4} mol L^{-1} chlorogenic acid solution. The maximum cathodic peak current was observed at pH 7.0, decreasing at other pH values, and this pH was therefore selected for further experiments.

The supporting electrolyte is an electrolyte that, when added in higher concentrations, can give some specific proprieties to the solution and the interface. The concentration of the supporting electrolyte (0.01–0.25 mol L^{-1}) phosphate buffer solution (pH 7.0) was studied at 9.80×10^{-4} mol L^{-1} chlorogenic acid solution. The current increased up to 0.1 mol L^{-1} and remained constant at higher concentrations, thus, the phosphate buffer solution concentration of 0.1 mol L^{-1} was selected for further experiments.

3.4. Optimization of the SWV parameters

The SWV method offers the best sensitivity and detection limit of the electrochemical signal. The cathodic peak current is dependent on various instrumental parameters such as frequency, pulse amplitude and scan increment. Thus, the effects of these parameters on the peak current response to 9.80×10^{-4} mol L^{-1} chlorogenic acid in 0.1 mol L^{-1} phosphate buffer solution pH 7.0 were investigated to obtain the best experimental conditions for the proposed biomimetic sensor.

The influence of the frequency from 10 to 80 Hz on the biomimetic sensor response was studied. The highest current response was obtained at 30 Hz decreasing for the other values studied. Thus, the frequency of 30 Hz was selected for further experiments. When the SWV pulse amplitude was varied between 5.0 and 100 mV, the peak current increased with increasing amplitude and reached a maximum at 100 mV, this value was therefore used for the subsequent measurements. The effect of the scan increment was investigated in the range of 0.5–4.0 mV. The current increased up to 3.0 mV and remained constant at higher values therefore this value was chosen as the optimum response. Overall, the optimized parameters can be summarized as follows: frequency 30 Hz; amplitude 100 mV and scan increment 3.0 mV.

3.5. Square wave voltammetry and analytical curve

After the optimization of the experimental parameters, the analytical curve obtained with the biomimetic sensor was linear from 5.0×10^{-6} to 1.45×10^{-4} mol L^{-1} of chlorogenic acid. The regression equation was found to be ($I_{pc} = -0.314 + 4.433 \times 10^{5}$ [chlorogenic acid]; $r = 0.9985$), where I_{pc} is the cathodic current
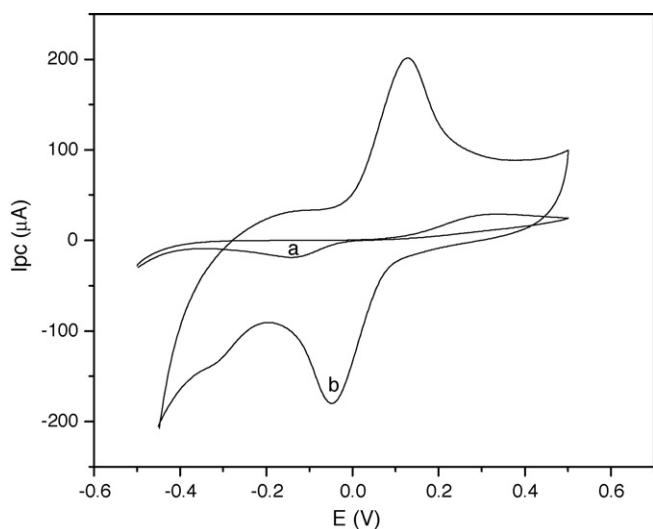
Fig. 3. Cyclic voltammograms obtained using (a) plain carbon paste electrode and (b) biomimetic sensor in 9.80×10^{-4} mol L^{-1} chlorogenic acid in 0.1 mol L^{-1} phosphate buffer solution (pH 7.0) at a scan rate of 100 mV s^{-1}.
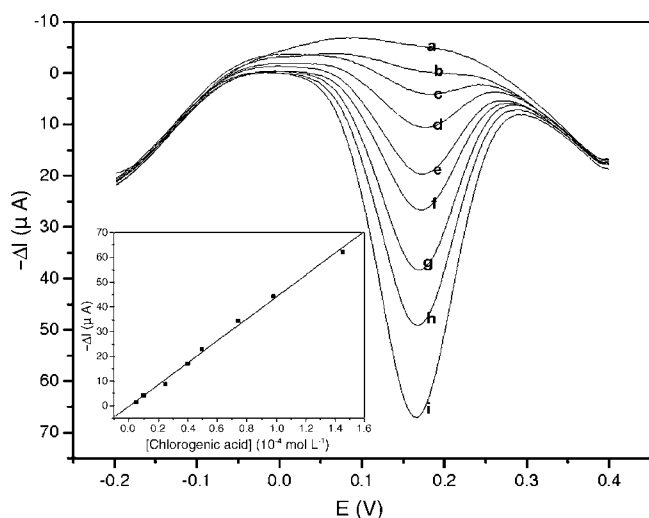
Fig. 4. Square wave voltammograms obtained using the proposed biomimetic sensor for (a) blank in phosphate buffer solution and chlorogenic acid solutions at the following concentrations: (b) 5.00×10^{-6}; (c) 9.98×10^{-6}; (d) 2.49×10^{-5}; (e) 3.97×10^{-5}; (f) 4.95×10^{-5}; (g) 7.39×10^{-5}; (h) 9.80×10^{-5}; and (i) 1.45×10^{-4} mol L^{-1} at frequency 30 Hz, pulse amplitude 100 mV and scan increment 3.0 mV. Inset: the analytical curve obtained for chlorogenic acid.

peak, [chlorogenic acid] is the chlorogenic acid concentration in mol L^{-1}, with a detection limit (three times the signal blank/slope) of 8.0×10^{-7} mol L^{-1} chlorogenic acid. Fig. 4 shows these voltammograms and the analytical curve can be seen in the inset.

3.6. Stability, reproducibility and repeatability

The long-term stability of the biomimetic sensor was investigated by measuring the electrochemical response (cathodic peak currents) to 9.80×10^{-4} mol L^{-1} chlorogenic acid solution (pH 7.0) over a 250-day period (over 640 samples were determined for each quantity of carbon paste used in the syringe). This involved consecutive measurements without surface renewal. When the sensor was stored at room temperature and measurements taken every 1–8 days, no noticeable change was observed. The high stability could be associated with the excellent ability of this tetranuclear Cu(II) complex to mimic the active site of the catechol oxidase enzyme and contributed to its successful use in the construction of the sensor.

The reproducibility was investigated using three biomimetic sensors prepared independently, and indicated an acceptable reproducibility with a relative standard deviation of 10.0% for the response to 9.80×10^{-4} mol L^{-1} chlorogenic acid solution (pH 7.0). In addition, the repeatability of the biomimetic sensor performance was studied and the relative standard deviation was 7.4% for 10 successive assays.

3.7. Study of selectivity, interference and recovery

Several phenolic compounds such as adrenaline, caffeic acid, carbidopa, catechol, chlorogenic acid, epigallocatechin gallate, ferulic acid, gallic acid, guaiacol, hydroquinone, L-dopa, luteolin, p-coumaric acid, rosmarinic acid, syringic acid, sinapic acid, tannic acid and vanillic acid were investigated, in order to determine the selectivity of the proposed biomimetic sensor. These compounds, only caffeic acid is present in the coffee samples. The sensors were sensitive to rosmarinic acid (100%), catechol (92.1%), chlorogenic acid (80.5%), hydroquinone (78.0%), adrenaline (71.0%),

Table 1
Recovery values for chlorogenic acid standard solutions in coffee using the proposed biomimetic sensor

Sample	Chlorogenic acid (mg L^{-1})		
	Added	Found	Recovery (%)
A	6.91	7.12 ± 0.1	103.0
	10.34	9.92 ± 0.1	95.9
	13.78	13.43 ± 0.2	97.5
B	6.91	7.24 ± 0.2	104.8
	10.34	9.74 ± 0.2	94.2
	13.78	13.25 ± 0.1	96.1
C	6.91	7.20 ± 0.1	104.2
	10.34	10.06 ± 0.1	97.3
	13.78	13.99 ± 0.1	101.5
D	6.91	7.33 ± 0.1	106.1
	10.34	10.95 ± 0.1	105.8
	13.78	12.85 ± 0.2	93.2

A and B = strong coffee; C and D = traditional coffee.

L-dopa (22.5%) and caffeic acid (12.0%). No response was observed for the other phenolic compounds studied.

To evaluate the interference of the biomimetic sensor, the influence of some possible interfering substance, i.e. caffeic acid, caffeine, citric acid, fructose, glucose, glutamic acid, sucrose and tartaric acid, on the determination the chlorogenic acid in coffee was investigated. The ratios of the concentration of chlorogenic acid to that of each substance were fixed at 1:1 and 1:5. Only caffeic acid caused a positive interference (12.0%) when present at the same concentration as the analyte. This positive interference observed was not critical, because caffeic acid is present at lower concentration levels than those investigated. None of these substances interfered in the proposed biomimetic sensor.

Vacuum packed roasted and ground coffee (A, B = strong and C, D = traditional) samples containing chlorogenic acid were selected for the recovery study. For this study, different standard chlorogenic acid concentrations (6.91, 10.34 and 13.78 mg L^{-1}) were added to the samples, followed by determination employing the propose sensor and the calculation of recovery percentage. The recoveries obtained for these samples were 93.2–106.1%, as shown in Table 1. It can be clearly observed that the recovery results obtained indicate an absence of matrix effects in these determinations.

3.8. Determination of chlorogenic acid in coffee using the biomimetic sensor and capillary electrophoresis

To evaluate the applicability of the biomimetic sensor, the chlorogenic acid concentrations of four coffee samples were determined applying the standard additions method to overcome the matrix effects. The results obtained using the proposed biomimetic sensor were close to those obtained using the capillary electrophoresis method (Table 2). Fig. 5A shows the electropherogram of the standard solution, and Fig. 5B and C show the electrophero-

Table 2
Determination of chlorogenic acid (mg L^{-1}) in coffee using the biomimetic sensor and capillary electrophoresis method

Sample	Capillary electrophoresis	Biomimetic sensor	Relative error (%)
A	444.8 ± 0.1	446.7 ± 0.1	+0.4
B	545.0 ± 0.1	544.3 ± 0.1	−0.1
C	522.7 ± 0.1	552.8 ± 0.1	+5.8
D	746.5 ± 0.1	755.0 ± 0.1	+1.1

A and B = strong coffee; C and D = traditional coffee.
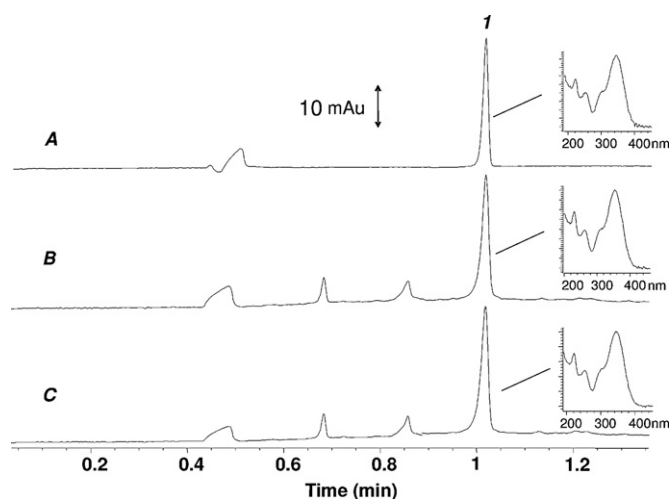
Fig. 5. Electropherogram and UV spectra obtained for chlorogenic acid: (A) $20\,mg\,L^{-1}$ standard solution of chlorogenic acid (peak 1); (B) strong coffee sample; (C) traditional coffee sample. Conditions: $20.0 \times 10^{-3}\,mol\,L^{-1}$ NaH_2PO_4, $20.0 \times 10^{-3}\,mol\,L^{-1}$ STB, and $20.0 \times 10^{-3}\,mol\,L^{-1}$ SDS. Capillary with 48.5 cm total length and 8.5 cm effective length, hydrodynamic injection reverse pressure 50 mbar for 6 s in short-end-injection mode, 30 kV positive polarity on the injection side; 25 °C; 340 nm.

gram of the strong and traditional coffee samples, respectively. As can be seen from the data, the results are in agreement at a 95% confidence level, within an acceptable range of error and it was therefore concluded that the biomimetic sensor is suitable for this application.

4. Conclusions

In this paper, a biomimetic sensor based on a tetranuclear copper(II) complex was constructed and optimized. This new complex was successfully synthesized and characterized as a mimetic of catechol oxidase. This sensor showed good long-term stability and good performance in terms of sensitivity, detection limit, response and linear calibration range. In addition, it was shown to be accurate, reliable, simple and quick to prepare, and of low cost, offering an alternative analytical procedure for the determination of chlorogenic acid in coffee.

References

[1] J.S. Bonita, M. Mandarano, D. Shuta, J. Vinson, Pharm. Res. 55 (2007) 187.
[2] K. Fujioka, T. Shibamoto, Food Chem. 106 (2008) 217.
[3] M.N. Clifford, W. Wu, N. Kuhnert, Food Chem. 95 (2006) 574.
[4] M.R. Olthof, P.C.H. Hollman, M.B. Katan, J. Nutr. 131 (2001) 66.
[5] C. Campa, S. Doulbeau, S. Dussert, S. Hamon, M. Noirot, Food Chem. 93 (2005) 135.
[6] D. Perrone, A. Farah, C.M. Donangelo, T. Paulis, P.R. Martin, Food Chem. 106 (2008) 859.
[7] N. Maeso, C. del Castillo, L. Cornejo, M. García-Acicollar, L.F. Alguacil, C. Barbas, J. Pharm. Biomed. Anal. 41 (2006) 1095.
[8] M. Križman, D. Baričevič, M. Prošek, J. Pharm. Biomed. Anal. 43 (2007) 481.
[9] E.M. Risso, R.G. Péres, J. Amaya-Farfan, Food Chem. 105 (2007) 1578.
[10] Z. Füzfai, I. Molnár-Perl, J. Chromatogr. A 1149 (2007) 88.
[11] E. Nishitani, Y.M. Sagesaka, J. Food Comp. Anal. 17 (2004) 675.
[12] M. Vaher, M. Koel, J. Chromatogr. A 990 (2003) 225.
[13] X. Wang, J. Wang, N. Yang, Food Chem. 102 (2007) 422.
[14] L.D. Mello, M.D.P.T. Sotomayor, L.T. Kubota, Sens. Actuators B 96 (2003) 636.
[15] S.C. Fernandes, I.R.W.Z. Oliveira, O. Fatibello-Filho, A. Spinelli, I.C. Vieira, Sens. Actuators B 133 (2008) 202.
[16] S.K. Moccelini, S.C. Fernades, I.C. Vieira, Sens. Actuators B 133 (2008) 364.
[17] S.C. Fernandes, I.R.W.Z. Oliveira, I.C. Vieira, Enzyme Microbial. Technol. 40 (2007) 661.
[18] S.B. Etcheverry, E.G. Ferrer, L. Naso, D.A. Barrio, L. Lezama, T. Rojo, A.M. Williams, Bioorgan. Med. Chem. 15 (2007) 6418.
[19] D. Kovala-Demertzi, A. Galani, M.A. Demertzis, S. Skoulika, C. Kotoglou, J. Inorg. Biochem. 98 (2004) 358.
[20] M.D.P.T. Sotomayor, A.A. Tanaka, L.T. Kubota, J. Electroanal. Chem. 536 (2002) 71.
[21] M.D.P.T. Sotomayor, A.A. Tanaka, L.T. Kubota, Electrochim. Acta 48 (2003) 855.
[22] I.R.W.Z. Oliveira, R.E.M.B. Osório, A. Neves, I.C. Vieira, Sens. Actuators B 122 (2007) 89.
[23] I.R.W.Z. Oliveira, A. Neves, I.C. Vieira, Sens. Actuators B 129 (2008) 424.
[24] M. Santhiago, R.A. Peralta, A. Neves, G.A. Micke, I.C. Vieira, Anal. Chim. Acta 613 (2008) 91.
[25] P. Karsten, A. Neves, A.J. Bortoluzzi, M. Lanznaster, V. Drago, Inorg. Chem. 41 (2002) 4624.
[26] R.M. Silverstein, G.C. Bassler, T.C. Morrill, Spectrometric Identification of Organic Compounds, 5th ed., John Wiley & Sons Inc., New York, 1991, 387 pp.
[27] K. Nakamoto, Infrared and Raman Spectra of Inorganic and Coordination Compounds., 3rd ed., John Wiley & Sons Inc., New York, 1978, 448 pp.
[28] R.A. Peralta, A. Neves, H. Terenzi, F. Nome, A.J. Bortoluzzi, E. Castellano, M.C.B. de Oliveira, Dalton Trans., unpublished results.
[29] C. Belle, K. Selmeczi, S. Torelli, J. Pierre, CR Chimie 10 (2007) 271.
[30] K. Selmeczi, M. Réglier, M. Giorgi, G. Speier, Coordin. Chem. Rev. 45 (2003) 191.

Review

Determination of Hg and organomercury species following SPME: A review

Sergi Díez [a,b,*], Josep M. Bayona [b]

[a] Institute of Earth Sciences "Jaume Almera", ICTJA-CSIC, Lluís Solé i Sabarís, s/n, E-08028 Barcelona, Spain
[b] Environmental Chemistry Department, IDÆA-CSIC, Jordi Girona, 18-26, E-08034 Barcelona, Spain

ARTICLE INFO

ABSTRACT

Mercury is ubiquitous in the environment and exists in a variety of chemical and physical forms as a result of both natural and man-made releases. Mercury, and specially, its organic species are toxic being the subject of much concern. Consequently, significant effort has been made to develop methods for its determination in environmental and biological samples. The state of the art of the analytical procedures based on solid-phase microextraction (SPME) and its applications to mercury and organomercury determination in abiotic and biotic matrixes are critically reviewed. Firstly, sample pretreatment prior to SPME is evaluated including a description of the most usual leaching procedures for sediment, soil and biological samples. Excluding the volatile organometallics that can be directly extracted from the sample by SPME, usually, those species lack of volatility and then a derivatization step is mandatory prior to gas chromatographic (GC) determination. The most common derivatization procedures used for mercury will be highlighted. The variables usually evaluated along the methodology to improve the sensitivity of the SPME, such as sampling size, stirring procedures and sampling temperature, polymer coating and thermal desorption have been reviewed.

© 2008 Elsevier B.V. All rights reserved.

Contents

* Corresponding author at: Institute of Earth Sciences "Jaume Almera", ICTJA-CSIC, Lluís Solé i Sabarís, s/n, E-08028 Barcelona, Spain. Tel.: +34 93 4095410; fax: +34 93 4110012.
E-mail address: sdiez@ija.csic.es (S. Díez).

1. Introduction

Since mercury (Hg) become a proved cause of concern due to its high neurotoxicity and widespread occurrence, its monitoring attracted special attention. Particularly, methylmercury (MeHg), the most toxic mercury species, can cause severe neurological damage to humans and wildlife [1,2]. Except for well-documented cases of severe mercury poisoning such as Minamata Bay [3] or Iraq [4], humans are generally exposed at non-toxic acute levels. Hence, potential health risks from low levels of mercury are a subject of intense debate and the accurate determination at low concentration levels is a current analytical challenge.

Mercury speciation in environmental samples requires an extraction step that usually involves a liquid–liquid or an acid or base digestion prior to detection [5]. Nevertheless, these leaching techniques are non-selective and can promote methylation of inorganic mercury during sample preparation or extraction steps [6].

To accomplish mercury speciation avoiding potential analytical errors, such as unintentional production of MeHg, solid-phase microextraction (SPME) in combination with gas chromatography (GC) determination [7] is a suitable method. Even though its moderate selectivity, SPME offers the possibility of a simple, fast, solvent-free, that can distinguish between organic and inorganic forms of trace elements.

During the last decade, the use of SPME for the extraction of analytes has been firmly established as a valuable alternative over traditional solid-phase extraction (SPE) techniques. Then, SPME advantages such as (a) non-exhaustive extraction technique, (b) low cost, (c) solventless, (d) reduction of the matrix effects and (e) the fully automation of the whole process can be highlighted. Moreover, its application to trace element speciation has been one of the areas of fast development since mid 1990s. Generally, for trace element speciation the analytical procedures based on SPME involve a derivatization step to transform the ionic species into neutral compounds that are equilibrated with a fiber by its exposure into the headspace (HS) followed by thermal desorption in the injector port of a gas chromatograph.

In this review, we will focus on the analytical procedures based on SPME of mercury species including abiotic and biotic matrixes. Critical steps and figures of merit of the different analytical procedures will be evaluated and compared with conventional methods. Recent trends involving new polymeric coating and sample size miniaturization will be also presented.

2. Sample pretreatment prior to SPME

2.1. Aqueous samples

Due to adsorption to the sample container and abiotic or biotic processes that could lead to a redistribution between chemical species, the sample pretreatment is a critical issue in trace Hg speciation. Several authors investigated the aqueous sample storage conditions to minimize the degradation–adsorption processes, which can lead to biased results. SPME can be a promising approach for sample storage of trace element species since they can be sorbed onto the SPME fiber. Then, determination of trace element by SPME in aqueous samples comprises several steps: (a) surrogate addition, (b) pH adjustment, (c) derivatization–extraction, and (d) determination. Filtration step is not necessary, avoiding analyte adsorption onto the filter. Then, aqueous phase derivatization and SPME are simultaneously performed under vigorous stirring to increase both the reaction and extraction kinetics. Then, the oganometallic species are extracted by the SPME while the non-

derivatizated species remain in solution because they exhibited a much lower distribution coefficient between the fiber and the aqueous phase.

2.2. Solid samples

2.2.1. Sediment and soil

A mild digestion or leaching technique to liberate the trace Hg compounds adsorbed onto the matrix into the liquid phase is required. Only highly volatile species (i.e. dimethylmercury, DMeHg) can be extracted directly from the headspace in equilibrium with the solid sample, otherwise a leaching step is mandatory prior to the SPME extraction. This leaching procedure usually involves an acid or basic conditions followed by a pH adjustment to perform the derivatization reaction. Once the leaching process is completed, an aliquot of the digested sample is transferred to another vessel where derivatization–extraction step is performed. For organomercury speciation, MeHg was extracted from marine sediments using microwave-assisted acid extraction or digestion [8]. Alternatively, MeHg was extracted from soil with subcritical water extraction [9], immersion in acetic acid/acetate buffer solution (pH 3, 24 h) with few drops of concentrated nitric acid for sediment [10] and soil [11].

2.2.2. Biota

For the determination of Hg species in biological matrixes, some methods use either HCl leaching from human hair [12], or basic digestion under sonication [13] or shaking for 4 h [14]. HCl 3 M (1 h) for fish tissue [14,15] or immersion in acetic acid/acetate buffer solution (pH 3, 96 h) with few drops of concentrated nitric for mink hair or skin [10] were described. Alternatively, microwave digestion has also been developed for the determination of MeHg in biological specimens [16].

3. Derivatization reactions used in trace Hg speciation

3.1. Alkylation–phenylation reactions

Traditional derivatization techniques have been based on the Grignard reaction, such as the identity of ethylmercury that was confirmed by converting $EtHg^+$ ion extracted from sediment samples to ethylbutylmercury (EtHgBu) using the Grignard derivatization and final chromatographic analysis [17]. However, the target species must first be extracted into a non-polar, aprotic solvent and then dried prior to derivatization, rendering sample preparation tedious and time consuming.

Although a variety of alkylation reactions have been used in trace element speciation, the most widely used method for mercury is by far ethylation and in less extent propylation by using sodium tetraalkylborates (i.e. $NaBEt_4$ or $NaBPr_4$). Tetraalkylborate compounds have gained great popularity as derivatization reagents for the speciation analysis of organomercury compounds as the reaction is accomplished in aqueous solution. This reduces analysis time and minimizes the use of organic solvents, which is one of their main advantages in comparison to Grignard reactions that require strictly anhydrous conditions.

Table 1 summarizes the derivatization procedures used in the SPME–GC methods. The most commonly used aqueous phase derivatization procedures are ethylation with sodium tetraethylborate ($NaBEt_4$), propylation with sodium tetrapropylborate ($NaBPr_4$) and phenylation with sodium tetraphenylborate ($NaBPh_4$). Ethylation does not let to distinguish between ethylmercury and inorganic mercury (Hg^{2+}). Moreover, stability of the ethylation solution is unsatisfactory and degradation can occur within hours [18]. Both $NaBPh_4$ and $NaBPr_4$ are commercially available and combine two

Table 1
SPME parameters for mercury speciation with GC separation

Analyte	Matrix	Technique	Derivatizing agent[a]	Fiber/extraction time	LOD (ng/L)	Reference
DMeHg	Gas condensate	MIP-AES	No derivatization	100 μm PDMS/30 s	240	[36]
Hg^{2+}					560	
DMeHg, DEtHg	Water	MIP-AES	No derivatization	100 μm PDMS/20 min	30–144	[42]
DMeHg, DEtHg					25–123	
MeHg	Water	AED	NaBPr$_4$	65 μm PDMS–DVB/5 min	0.016	[24]
Hg^{2+}	Seawater	ICP-MS	NaBEt$_4$	100 μm PDMS/5 min	1.6	[30]
MeHg					0.11	
Hg^{2+}	Seawater	ICP-MS	NaBPr$_4$	100 μm PDMS/5 min	0.35	[30]
MeHg					0.17	
Hg^{2+}	Seawater	MIP-AED	NaBPh$_4$	100 μm PDMS/5–45 min	100–300	[22]
MeHg, EtHg						
MeHg	Water	AFS	NaBEt$_4$	100 μm PDMS/5 min	3.0	[14]
	Fish tissue				6.6	
Hg^{2+}	Water	EI-MS	NaBEt$_4$	100 μm PDMS/15 min[*]	3.5–8.7	[13]
MeHg	Fish tissue				7.5–6.7	
MeHg	Soil	AAS	KBH$_4$	Fused silica/1.5–2 h	16[b]	[11]
EtHg					12[b]	
PhHg					7[b]	
MeHg	Soil	MS	NaBEt$_4$	100 μm PDMS/15 min	5	[9]
Hg^{2+}	Biological	MIP-AES	NaBPh$_4$	100 μm PDMS/15 min[*]	860	[23]
MeHg					120	
Hg^{2+}	Fish tissue	FAPES	NaBEt$_4$	100 μm PDMS/20 s[*]	60	[52]
MeHg					160	
Hg^{2+}	Fish tissue	FAPES	NaBPr$_4$	100 μm PDMS/40 s[*]	20	[18]
MeHg					60	
EtHg					30	
MeHg	Fish tissue	FAPES	NaBPh$_4$	100 μm PDMS/600 s[*]	650	[18]
EtHg					3500	
MeHg	Fish tissue	ICP-MS	No derivatization	65 μm PDMS-DVB/10 min	160	[15]
					190	
MeHg	Fish tissue	AAS	No derivatization	65 μm PDMS-DVB/90 min	60	[34]
MeHg	Fish tissue	AAS	NaBH$_4$	Fused silica/50 min	400	[34]
MeHg	Biological samples, sediments	AAS	KBH$_4$	Fused silica/1.5–2 h	26[b]	[10]
MeHg	Fish tissue	Py-AFS	NaBPr$_4$	100 μm PDMS/12 min	10[c]	[25]
MeHg	Biological samples	ICP-MS	NaBEt$_4$	100 μm PDMS/15 min	4.2[d]	[16]
Hg^{2+}	Biological samples	ICP–TOF-MS	NaBEt$_4$	75 μm CAR–PDMS/8 min	0.27[d]	[38]
MeHg					0.027[d]	
Hg^{2+}	Urine	EI-MS	NaBEt$_4$	100 μm PDMS/15 min	93	[55]
MeHg					303	
Hg^{2+}	Human	Py-AFS	NaBEt$_4$	100 μm PDMS/10 min	80[c]	[12]
MeHg	hair				50[c]	
MeHg	Fish tissue	ID–GC–MS	NaBPr$_4$	100 μm PDMS/10 min	37[c]	[28]
MeHg	Fish tissue	ID–GC–ICP-MS	NaBPr$_4$	100 μm PDMS/10 min	2.1[c]	[29]
MeHg	Fish samples	ID–GC–EI-MS	NaBPr$_4$	DVB-CAR-PDMS, 50 μm/30 μm	28[c]	[46]

MeHg, methylmercury; DMeHg, dimethylmercury; DEtHg, diethylmercury; NaBEt$_4$, sodium tetraethylborate; NaBPr$_4$, sodium tetrapropylborate; NaBPht$_4$, sodium tetraphenylborate; NaBH$_4$, sodium tetrahydroborate; KBH$_4$, potassium tetrahydroborate; DVB, divinylbenzene; AAS, atomic absorption spectroscopy; AED, atomic emission detector; AES, atomic emission spectrometry; Py-AFS, pyrolysis-atomic fluorescence spectrometry; EI-MS, electron impact ionization-mass spectrometry; FAPES, furnace atomization plasma emission spectrometry; ICP-MS, inductively coupled plasma-mass spectrometry; MIP, microwave induced plasma; PDMS, polydimethylsiloxane; TOF-MS, time-of-flight mass spectrometry.

[a] In all the cases acetate buffer solution was employed, for alkylation or phenylation at pH 4–5 and for hydride generation pH 3. All the extractions were performed in the HS mode except (*) that were carried out also in the DI.

[b] Absolute detection limit.

[c] ng/g.

[d] pg/g.

major advantages: ease of handling for in situ derivatization and extraction, and the possibility of distinguishing between ethyl- and inorganic mercury derivatives. The reagent solutions are also more stable than those of NaBEt$_4$, but after a long storage time (1 month) they also become inactive [19,20]. Phenylation using NaBPh$_4$ was firstly proposed by Luckow and Russel [21] as a means for achieving direct phenylation of mercury species such as MeHg and Hg^{2+} in aqueous solution. Then, phenylation is able to distinguish between EtHg and Hg^{2+}, but equilibration time, which is the time required for the amount of analyte extracted to reach a steady-state, is longer compared to ethylation and propylation, thus restricting sample throughput [18]. This method was further studied with some applications for the determination of methyl-, ethyl- and inorganic mercury compounds in seawater [22] or biological samples [23]. Finally, propylation with NaBPr$_4$,

that was firstly reported by De Smaele et al. [20]. It does not show the former drawbacks and has been, therefore, used for optimization of HS–SPME of MeHg throughout recent investigations [24,25].

The alkylation reaction yield depends on the pH of the medium. Usually the acetic/acetate buffer is used to bring the pH near to a value of 5 but also citrate buffer has been employed for trace level determination of organic mercury species. The amount of NaBEt$_4$ is strongly dependent on the matrix since it can react with some of its components. In addition, alkaline ions also might depress the derivatization yield, which can be particularly relevant in case of speciation studies in seawater. In case of aqueous matrixes, the amount needed is in the range of 0.8–1.0 mL of 1% (w/v) solution for a 150 mL sample. The reaction time is around 5 min under mechanical agitation.

Taking into consideration the variability in the derivatization yield according with the matrix, a structurally related compound or isotopically labelled surrogates are strongly recommended to correct concentration by their recovery. Nevertheless, if the surrogate does not possess a similar reactivity, this recovery correction could lead to invalid results.

In a validation study of aqueous ethylation with NaBEt$_4$, using isotopically labelled MeHg where the spike compound is Me^{201}Hg$^+$ followed by GC–ICP-MS determination, it was found that, in halide-containing solutions, a dealkylation of MeHg into elemental mercury occurred during ethylation [26]. That reaction does not occur with NaBPr$_4$ [20]. Moreover, NaBPr$_4$ has already been tested for the determination of MeHg in fish tissues by SPME using isotope dilution (ID) GC/MS [27–29]. Moreover, mercury speciation in seawater at sub-ppt levels with detection limits (LOD) down to a few picogram per liter for both Hg and MeHg have been achieved [30].

Despite ethylation with NaBEt$_4$ is nowadays the most widely used derivatization reagent, phenylation with NaBPh$_4$ [19,30–32] has been evaluated. The advantages of using phenylation with NaBPh$_4$ over ethylation with NaBEt$_4$ are few. The preference of the latter reagent allows MeHg, EtHg and inorganic mercury (Hg^{2+}) to be distinguished and concurrently determined. In fact, the phenylic forms of mercury do not occur in nature and the anthropogenic sources of phenyl mercury derivatives are negligible. In addition these forms are relatively stable and the reagent has a low cost. Anyway, their use for final SPME application has been tested for inorganic and organomercury compounds in seawater [22] and biological samples [23,33].

3.2. Hydride generation

Because of the high reactivity of metal hydrides, few researchers have reported results on the headspace sampling determination of metal hydrides using SPME techniques. Jiang and co-workers [10,11] developed a sampling method for organomercury species based on hydride generation using potassium tetrahydroborate (KBH$_4$) reagent. A home-made SPME device including a capillary fused-silica fiber was employed. The bottom (4 cm) of the fused-silica fiber, which was used to absorb the sample, was pretreated with concentrated hydrofluoric acid (HF) for 3.5 h and conditioned at 200 °C for 2 h. Further increases in this treatment time rapidly decreased the extraction capacity of the fiber. The optimum extraction time is relatively long and was reported to be 1.5–2 h. In this case, extraction is based on surface interactions between the organomercury hydrides and the treated fused-silica fiber; since it is mainly an adsorption phenomenon.

Later on, Bendicho and co-workers [34] compared chloride and hydride generation and headspace sampling of the volatile MeHg products. In this work, an easy-to-handle coupling of SPME and AAS without chromatographic interface, in combination with a rapid and selective ultrasound assisted procedure, was assessed for the determination of MeHg in seafood. Two different strategies for headspace sampling were tried (i.e., generation of the chloride or the hydride derivative) and different sorption materials (polydimethylsiloxane, PDMS; PDMS–divinylbenzene (DVB); fused silica and modified silica with L-cysteine, diethyldithiocarbamate and palladium nitrate) were compared. Best LODs were provided by the silica fiber for hydride (400 ng/L) and by the PDMS/DVB fiber for chloride (60 ng/L).

3.3. Direct determination

Neutral organometallic species are sufficiently volatile, then they can be sampled by SPME and determined by GC without a derivatization step [35]. For mercury species, a method for the determination of DMeHg in natural gas condensates with very short sampling times (30 s) was developed [36]. In this study, selective microwave induced plasma atomic emission detection (MIP-AED) system was used. However, serious problems were reported due to the extremely complex matrix analyzed including volatile organic material, which is also extracted with the DMeHg.

On the other hand, Mester et al. [15] reported the coupling of SPME with ICP-MS for the determination of mercury species. They utilized an SPME fiber coated with PDMS/DVD co-polymer and tried both direct liquid immersion and headspace extraction of a MeHg solution which was previously saturated with sodium chloride. This method was based on the relatively high vapor pressure of MeHg chloride. Sample introduction into an ICP-MS was achieved with an unique thermal desorption interface, consisting of a heated glass-lined splitless-type GC injector placed directly at the base of the torch to minimize the length of transfer line, which was provided for fast desorption and high sample introduction efficiency. The novelty of the method was that speciation could be achieved without employing any separation method (GC or HPLC), and was based entirely on the selectivity of the extraction procedure and the detection technique. Detection limits of 160 and 190 ng/L were obtained for direct and headspace sampling, respectively.

Hashemi and Rahimi [37] utilized a new simple and highly sensitive method for HS–SPME coupled with electrothermal atomic absorption spectrometric (ETAAS) for the determination of mercury. A gold wire, mounted in the headspace of a sample solution in a sealed bottle, is used for collection of Hg vapor generated by addition of sodium tetrahydroborate (NaBH$_4$). The gold wire is then simply inserted in the sample introduction hole of a graphite furnace of an ETAAS instrument. By applying an atomization temperature of 600 °C, Hg is rapidly desorbed from the wire and determined with high sensitivity. The method was applied for industrial wastewaters and tuna fish samples with a LOD of 6 ng/L and a precision better than 4.6% (RSD, relative standard deviation).

4. Speciation of Hg with SPME

Speciation studies for Hg by using SPME have been carried out mostly by using PDMS as preconcentration polymer since trace element species are mainly analyzed as methyl or ethyl derivatives. The species determined and the analytical conditions are reported in Table 1. The following variables have been evaluated to improve the extraction efficiency.

4.1. Extraction procedure

Headspace or direct sampling from the aqueous sample is the two procedures for trace element speciation with SPME. Given that ethylated trace element species have a relatively high volatility, headspace sampling is the preferred extraction procedure since carryover effect is minimized and fiber life-time increased. Derivatization reagents are used in the aqueous phase and they affect to the stability when it is exposed to high temperatures in the injector port during the desorption process [13]. The sensitivity in headspace analysis depends on their distribution coefficients, the longer the alkyl chain, the higher the sensitivity since they possess a higher distribution coefficient. The highest sensitivity was obtained for the propylated and phenylated derivatives (Table 1). The differences in the SPME response among the differ-

ent organomercury compounds according to the alkylation degree are even higher if they are underivatized or are analyzed as chlorides [34]. The use of adsorption fibers such Carboxen (CAR)–PDMS [24,38,39] or PDMS–DVB allows a higher extraction yield in comparison with PDMS for the shorter alkylchain organometallics and hydride derivatives [39].

Extraction time in SPME depends on the sample diffusion and the sampling procedure, either headspace or direct sampling by immersion of the SPME fiber in the aqueous sample. In some cases, headspace sampling is more time consuming than direct immersion and equilibrium conditions are not completely reached but it is preferred in terms of sensitivity and fiber lifetime.

Salting out effect has been evaluated in case of mercury species (MeHg and Hg^{2+}) [13] but it did not increase the extraction efficiency of the target analytes.

4.2. Extraction temperature

The equilibrium between the analyte sorbed into the SPME fiber coating and the concentration in the sample solution depends on both the solubility of analyte in the aqueous phase and its sorption affinity onto the SPME fiber coating. Increasing the temperature will increase the partial vapor pressure of analytes in the headspace but simultaneously decrease the distribution constant on to the fiber-headspace. In this regard, no significant improvement in the amount extracted of MeHg by the fiber was found when higher temperatures (35 or 50 °C) were investigated [12,13]. Moreover, it seems that MeHg extraction is significantly reduced by increasing the extraction temperature [25].

4.3. Polymer coating and fiber film thickness

The type and thickness of the coating material is probably the most important feature determining the analytical performance of SPME. The fiber film thickness plays an important role in the extraction and desorption kinetics. Hence, thicker coatings result in longer extraction times because diffusion is slow within the polymer phase, adsorption process is slower and higher desorption temperatures are needed [35].

Because of its high stability, the most popular fibers are those coated with 7–100 μm PDMS and PDMS combined with other polymers. PDMS fibers extract samples *via* absorption of analytes, which dissolve and diffuse into the coating material. The use of a thicker fiber needs a longer extraction time, however recoveries are generally higher. Accordingly, when thinner fibers are used (7 μm), the amount of analyte absorbed is lower and for most of the applications, the 100 μm film thickness is used because trace level determination of trace Hg species is required.

In addition to liquid polymeric coatings, other materials have been developed. Then, Carbowax (CW)–DVB, CAR–PDMS, DVB-CAR-PDMS and PDMS–DVB are mixed coatings where the extraction occurs *via* adsorption of analytes. The CAR–PDMS coating is a special case comprising a mixed carbon-phase containing micro and mesopores and has been particularly effective for the MeHg extraction [39].

The PDMS (100 μm) has been successfully employed for organomercury species. Furthermore, PDMS–DVB (65 μm) was used for the determination of MeHg and DEtHg in fish tissues [15] with direct immersion or headspace sampling getting similar LODs and RSDs; and MeHg in water samples with the lowest LODs (0.016 ng/L) ever reported [24]. Finally, DVB/CAR/PDMS was applied for multielement determination including lead and tin organometallics (TML, TEL, MBT, DBT and TBT) and mercury species (MeHg, Hg^{2+}) [40].

As it was described before, Jiang and co-workers [10,11] developed a new pretreatment of the silica as an alternative to commercial polymer coated by immersing the bottom 5 cm of fused-silica in concentrated HF. The adsorption efficiency increased initially with the pretreatment time, reaching a maximum between 3 and 4.5 h, but if the pretreatment process was longer than 4.5 h, the extraction efficiency dropped quickly because the surface can be destroyed by concentrated HF. In this case, extraction, which is based on surface interactions between the organomercury hydrides and the treated glass, was reported to be too long (2 h) and predominantly is an adsorption phenomenon. On the other hand, also described before, gold wires 2 cm in length and with diameters of 0.75 and 0.4 mm were used for the microextraction of Hg vapor [37]. As an alternative for liquid-phase and solid-phase coatings and fused silica, gold wires were successfully applied for industrial wastewaters and tuna fish samples.

4.4. Thermal desorption

Injection port temperature is critical for Hg speciation with GC since an inappropriate temperature could cause thermal decomposition or insufficient desorption of Hg species [12–14,41]. The desorption temperature has some effects on the peak areas of Hg species, especially for MeHgEt. It has been reported that the peak area of MeHgEt decreased with temperatures from 150 to 250 °C [14] or from 170 to 210 °C [12]. These results clearly indicate that MeHgEt is decomposed to Hg^0 at temperatures higher than 150–170 °C. Consequently, in case of MeHg lower injector port temperatures (i.e. 170 °C for PDMS) are strongly recommended in order to minimize its thermal degradation.

5. Linearity range, detection systems, selectivity, sensitivity

Speciation of organomercury compounds is most commonly performed by GC coupled to MS, AAS, AFS, CVAFS, ICP-MS, MIP-AES or furnace atomization plasma emission spectrometry (FAPES) with excellent sensitivity and selectivity.

GC coupled with MIP-AES detection is a highly sensitive technique for the determination of DMeHg and DEtHg with a working range in the μg/L and ng/g levels [42]. The main problem seems to be the conservation of environmental samples to avoid losses of these highly volatile species while sampling and storage. For Hg and MeHg quantification in seawater samples the lowest LODs were obtained by using ICP-MS. Ethylated and propylated mercury species analysis were tested to achieve LODs down to 2 ng/L for both [30] while precision was always better than 5% at a level of 100 ng/L of both species (Table 1). The lowest LODs were achieved by ICP-MS–TOF [39]. Finally, it should be pointed out the work performed by Geerdink et al. [24] where the LOD was 16 pg/L MeHg and the RSD was found to be 5%, whereas linearity of the GC–AED method was established over at least three orders of magnitude in the range 0–2000 pg/L.

Sturgeon and co-workers [18] compared aqueous phase ethylation, propylation and phenylation for MeHg determination by HS–SPME. Derivatizing agents were evaluated for use in speciating mercury in biological samples using SPME–GC–FAPES. Propylation proved to lead to lower LODs, robust and faster than the other ones. In this concern, Bravo-Sanchez et al. [30] also reported a 50–200% improvement in LODs for both inorganic- and MeHg when propylation was used instead of ethylation using HS–SPME.

For the determination of organomercury compounds in soils from orchards and wheat fields, He and Jiang [11] employed SPME–GC–AAS with absolute LODs for methyl-, ethyl- and

phenylmercury of 16, 12 and 7 ng, respectively and a range of 0.04–0.64 μg/g are detected in soils from different sites. On the other hand, extracted MeHg from spiked soil samples was performed by GC–MS after thermal desorption with a LODs of 5 ng/L [9]. An interesting application described by Gotzl and Riepe [43] employed a homemade SPME fiber for the aqueous phase enrichment of Hg. An ion-exchange material was glued to the tip of a small plastic rod and used it to preconcentrate mercury prior to photometric detection. The LOD is 300 ng/L of mercury in soil eluates.

In biological samples, Rodil et al. [23] employed headspace SPME and phenylation in conjunction with GC–MIP-AES with LODs and concentrations ranges of 120 and 200–3000 ng/L for MeHg; and 860 and 1000–8000 ng/L for inorganic Hg. Davis et al. [16] utilized headspace SPME GC–ICP-MS for the determination of MeHg in biological specimens and NIST Standard Reference Materials (SRMs) and reported an extremely low LOD of 4.2 pg/g based on 0.5 g sub-samples of material. Both Mester et al. [15] and Fragueiro et al. [34] employed SPME sampling with direct introduction of desorbed analyte into an atomic spectrometric detector for determination of MeHg. In both cases a custom designed thermal desorption interface was used and the analyte vaporized from the fiber was introduced into either an ICP-MS [15] or quartz tube-atomic absorption spectrometer [34]. Mester et al. [15] used saturated NaCl solution for the MeHg–Cl sampling directly from the aqueous phase with LODs of 160 ng/L for direct sampling and an upper range of linearity of 300 ng/mL using a 65 μm PDMS fiber. Fragueiro et al. [34] compared chloride and hydride generation and headspace sampling of the volatile MeHg products where the calibration curve was linear up to 20 ng/mL and LODs were 60 and 400 ng/L (as MeHg) for MeHgCl and MeHgH, respectively.

6. Matrix effect and calibration procedure

For low-level Hg speciation, SPME is a convenient alternative to other extraction methods because it integrates extraction, concentration and sample introduction into a single step without use of solvent reducing the possible interferences in the final detection. However, matrix effects can strongly affect to the quantitation, and hence the accuracy and precision can be compromised. In this regard, the HS–SPME approach seems to avoid the matrix effects because the fiber is not directly contacted with the matrix. In comparison with direct immersion, the HS reduces the possibility of interferences but not completely. In fact, HS was slightly less sensitive than immersion sampling for species-specific determination of MeHg [15] but offered a large linearity range. Immersion SPME was severely influenced by the matrix that leads to a 70-fold decrease in sensitivity. Thus, standard addition calibration procedures should be used with SPME. To avoid interferences, firstly a fiber blank should to ensure that neither the fiber nor the instrument cause interferences with the determination. Conditioning of the fiber should be usually accomplished by desorption in a GC. This operation ensures that the fiber does not introduce interfering species and it has to be repeated after analysis of any sample with high amounts of high molecular weight compounds.

Standard addition calibration, external calibration and isotope dilution are the usual methodologies to resolve matrix effects during quantification. In many cases, when the matrix is simple (e.g. groundwater) calibration might not be necessary, since the appropriate distribution constants, which define the external calibration curve, are available in the literature or can be calculated from chromatographic retention parameters. However, in complex-matrix samples (e.g. seawater or biological), the slope of the calibration graph differs from that obtained for standard solutions because the distribution constants depend on the composition and the polarity of the samples and the solutions.

Standard addition calibration is the most common methodology for the determination of trace levels of Hg in complex environmental samples in which matrix effects have been observed. In some cases, to evaluate matrix effects standard addition and external calibration have been compared [25]. In seawater, where matrix effects are obvious [30], standard addition calibration turned out to be mandatory for the reliable quantification of the mercury species because the simple use of an internal standard was insufficient to compensate for this strong effect.

On the other hand, the addition of water can reduce the matrix effect and enhance the release of analytes from the matrix. In fact, the matrix effects could be simply overcome by diluting the sample when the target analytes are in relatively high concentration and analysis could be performed with an adequately sensitive analytical system. Thus, dilution of the digest was successfully employed [33] in a cost-efficient analytical method based on alkaline sample digestion (KOH and NaOH), followed by aqueous phase phenylation (NaBPh$_4$) derivatization and SPME for the determination of MeHg in typical fish-containing food samples.

Application of species-specific isotope dilution (ID) determinations has been limited due to the need to synthesize species-specific spikes. In this regard, the recent certification of spike solutions such as ^{198}Hg [27] and ^{202}Hg-enriched spike solutions [44] and its commercial availability have opened new venues for the use of ID analysis as a routine technique. Thus, one of the main advantages is that the matrix effects are accounted for since quantization is done by ratio measurements. ID enables correction of differences between derivatization efficiencies in complex matrices. In most cases, the use of species-specific isotope dilution, it should avoid the calibration by standard addition, which is time consuming. In addition to providing the highest accuracy and precision, species-specific isotope-dilution analysis also enables tracking and correction of possible species transformations during the analytical procedure [28,29,45,46].

Finally, it should be pointed out that multiple solid-phase microextraction (MSPME) is a stepped procedure (in both immersion and headspace modes) suitable for avoiding matrix-effect errors in quantitative analyses of complex matrix samples by SPME. It is based on calculating the amount of analyte corresponding to complete extraction using the peak areas of a few consecutive extractions from the same sample [47]. Moreover, when is performed in the headspace mode, multiple headspace MHS–SPME is an interesting approach [48] that can be used to overcome matrix-effect errors in the quantitative determination of volatile compounds, particularly in solid samples, to which the standard addition method is unsuited. For liquid samples, the only advantage over the standard-addition method is the reduction in sample preparation. Applications to organomercury compounds have not been addressed yet; however potential applications including extraction of volatiles and semivolatiles (e.g. DMeHg) from environmental and physiological samples might be expected in future developments.

7. Validation

A point of primary importance before the application of the developed analytical procedures is their validation. Reference Materials (RMs) are available for MeHg in fish. To date, developed speciation studies using SPME have been validated in case of MeHg in biological samples by DORM-2, DOLT-2, TORT-1 or TORT-2 [8,14,18,25] SRM1566b (MeHg in oyster tissue) [8,16] and SRM 1946 Lake Superior Fish Tissue [16] and sediments SRM 1646a [8] or MeHg in human hair by NIES 13 [12,49].

Table 2
Validation of the organomercury content in biological certified reference material (CRM) DORM-2 by different SPME methods

CRM	MeHg	Reference
DORM-2 (ng/g as Hg)	4470 ± 320[a]	[56]
GC–AFS (n = 3)	4060 ± 140	[14]
GC–MIP-AES (n = 2)	4710	[8]
GC–FAPES (n = 3)	4460 ± 20[b]	[52]
GC–FAPES (n = 3)	4370 ± 70[c]	[18]
GC–ICP-MS (n = 5)	4720 ± 160	[15]
ID–GC–MS (n = 4)	4336 ± 91	[28]
ID–GC–ICP-MS (n = 4)	4484 ± 29	[29]
CG–Py-AFS (n = 3)	4850 ± 210	[25]
CG–ICP-TOF-MS (n = 3)	4280 ± 210	[39]
CG–MIP-AES (n = 6)	4496 ± 250	[23]

[a] Certified value.
[b] Derivatization with $NaBEt_4$.
[c] $NaBPr_4$.

For MeHg determination in biological matrixes by SPME, DORM-2 (dogfish muscle tissue) has been widely used for validation. The SPME–GC–MIP-AES method also provides a significant improvement compared with previous methods used for the certification of MeHg in mussel tissues SRMs [50,51]. Nevertheless, the GC–FAPES method [52] seems to be the most accurate offering an improvement over GC–AFS [14], GC–MIP-AES [8], GC–ICP-MS [15] or even over isotope dilution technique, ID–SPME–GC–MS [28] as it is shown in Table 2. It should be emphasized that the use of isotope dilution GC–ICP-MS [29] provides similar results, but generally is an expensive technique and isotopic enriched standards are not widely available. In addition, when the ID–SPME–GC–MS is applied with an isotopic element enriched spike, the mass balance equations should take into account the contributions of proton losses from the alkyl substituents, which add complexity into the calculations [30,40].

8. Concluding remarks

Applications of SPME to trace Hg speciation (metal and organometallic) are growing. Headspace–SPME sampling is definitively becoming popular, as this allows for easy and rapid extractions that avoid the use of solvents. Several methods can detect low nanogram or picogram per liter levels of organomercury species in water. One of the more sensitive methods developed includes the use of a CAR–PDMS fiber for speciation analysis of Hg at ultra-trace levels on the basis of SPME.

On the other hand, the method automation is another important aspect to increase the sample throughput and results reliability. Current developments in SPME automation allow the possibility to perform derivatization and extraction sequentially by using two robotic systems [53]. This topic has been recently reviewed [54]. This review discusses developments and future challenges in the automation of SPME, including discussion of recent developments that may have significant implications for automation such as superelastic fiber assemblies and internally cooled fiber-SPME.

Applications into more severe sampling environments, designing more robust fiber coatings, enhancing detection capabilities and securing calibration and validation strategies are new challenges and trends in speciation studies of Hg using SPME.

Acknowledgements

References

[1] T.W. Clarkson, L. Magos, G.J. Myers, J. Trace Elem. Experim. Med. 16 (2003) 321.
[2] P. Grandjean, R.F. White, A. Nielsen, D. Cleary, E.C.D. Santos, Environ. Health Perspect. 107 (1999) 587.
[3] M. Harada, Crit. Rev. Toxicol. 25 (1995) 1.
[4] M.R. Greenwood, J. Appl. Toxicol. 5 (1985) 148.
[5] J.E.S. Uria, A. Sanz-Medel, Talanta 47 (1998) 509.
[6] M. Leermakers, W. Baeyens, P. Quevauviller, M. Horvat, TrAC-Trends Anal. Chem. 24 (2005) 383.
[7] C.L. Arthur, J. Pawliszyn, Anal. Chem. 62 (1990) 2145.
[8] S. Tutschku, M.M. Schantz, S.A. Wise, Anal. Chem. 74 (2002) 4694.
[9] A. Beichert, S. Padberg, B.W. Wenclawiak, Appl. Organomet. Chem. 14 (2000) 493.
[10] B. He, G.B. Jiang, Z.M. Ni, J. Anal. At. Spectrom. 13 (1998) 1141.
[11] B. He, G.B. Jiang, Fresenius J. Anal. Chem. 365 (1999) 615.
[12] S. Diez, J.M. Bayona, J. Chromatogr. A 963 (2002) 345.
[13] Y. Cai, J.M. Bayona, J. Chromatogr. A 696 (1995) 113.
[14] Y. Cai, S. Monsalud, K.G. Furton, R. Jaffe, R.D. Jones, Appl. Organomet. Chem. 12 (1998) 565.
[15] Z. Mester, J. Lam, R. Sturgeon, J. Pawliszyn, J. Anal. At. Spectrom. 15 (2000) 837.
[16] W.C. Davis, S.S. Vander Pol, M.M. Schantz, S.E. Long, R.D. Day, S.J. Christopher, J. Anal. At. Spectrom. 19 (2004) 1546.
[17] Y. Cai, R. Jaffe, R. Jones, Environ. Sci. Technol. 31 (1997) 302.
[18] P. Grinberg, R.C. Campos, Z. Mester, R.E. Sturgeon, J. Anal. At. Spectrom. 18 (2003) 902.
[19] V. Minganti, R. Capelli, R. De Pellegrini, Fresenius J. Anal. Chem. 351 (1995) 471.
[20] T. De Smaele, L. Moens, R. Dams, P. Sandra, J. Van der Eycken, J. Vandyck, J. Chromatogr. A 793 (1998) 99.
[21] V. Luckow, H.A. Russel, J. Chromatogr. 150 (1978) 187.
[22] A.M. Carro, I. Neira, R. Rodil, R.A. Lorenzo, Chromatographia 56 (2002) 733.
[23] R. Rodil, A.M. Carro, R.A. Lorenzo, M. Abuin, R. Cela, J. Chromatogr. A 963 (2002) 313.
[24] R.B. Geerdink, R. Breidenbach, O.J. Epema, J. Chromatogr. A 1174 (2007) 7.
[25] L. Carrasco, S. Diez, J.M. Bayona, J. Chromatogr. A 1174 (2007) 2.
[26] N. Demuth, K.G. Heumann, Anal. Chem. 73 (2001) 4020.
[27] C. Bancon-Montigny, L. Yang, R.E. Sturgeon, V. Colombini, Z. Mester, Appl. Organomet. Chem. 18 (2004) 57.
[28] L. Yang, V. Colombini, P. Maxwell, Z. Mester, R.E. Sturgeon, J. Chromatogr. A 1011 (2003) 135.
[29] L. Yang, Z. Mester, R.E. Sturgeon, J. Anal. At. Spectrom. 18 (2003) 431.
[30] L.R. Bravo-Sanchez, J.R. Encinar, J.I.F. Martinez, A. Sanz-Medel, Spectrochim. Acta B: Atom. Spectros. 59 (2004) 59.
[31] Y. Cai, S. Monsalud, R. Jaffe, R.D. Jones, J. Chromatogr. A 876 (2000) 147.
[32] H.E.L. Palmieri, L.V. Leonel, Fresenius J. Anal. Chem. 366 (2000) 466.
[33] Z. Jokai, L. Abranko, P. Fodor, J. Agric. Food Chem. 53 (2005) 5499.
[34] S. Fragueiro, I. Lavilla, C. Bendicho, J. Anal. Atom. Spectrom. 19 (2004) 250.
[35] Z. Mester, R. Sturgeon, J. Pawliszyn, Spectrochim. Acta B 56B (2001) 233.
[36] J.P. Snell, W. Frech, Y. Thomassen, Analyst 121 (1996) 1055.
[37] P. Hashemi, A. Rahimi, Spectrochim. Acta B: Atom. Spectros. 62 (2007) 423.
[38] P. Jitaru, F.C. Adams, J. Chromatogr. A 1055 (2004) 197.
[39] P. Jitaru, H.G. Infante, F.C. Adams, J. Anal. At. Spectrom. 19 (2004) 867.
[40] G. Centineo, E. Blanco Gonzalez, A. Sanz-Medel, J. Chromatogr. A 1034 (2004) 191.
[41] L. Liang, M. Horvat, N.S. Bloom, Talanta 41 (1994) 371.
[42] S. Mothes, R. Wennrich, J. High Res. Chromatogr. 22 (1999) 181.
[43] A. Gotzl, W. Riepe, Talanta 54 (2001) 821.
[44] J.P. Snell, C.R. Quetel, L. Lambertsson, J. Qvarnstrom, J. Anal. At. Spectrom. 19 (2004) 1315.
[45] L. Yang, R.E. Sturgeon, J. Anal. At. Spectrom. 20 (2005) 724.
[46] G. Centineo, E.B. Gonzalez, J.I.G. Alonso, A. Sanz-Medel, J. Mass Spectrom. 41 (2006) 77.
[47] M.T. Tena, J.D. Carrillo, TrAC-Trends Anal. Chem. 26 (2007) 206.
[48] M. Hakkarainen, J. Biochem. Biophys. Methods 70 (2007) 229.
[49] P. Montuori, E. Jover, R. Alzaga, S. Diez, J.M. Bayona, J. Chromatogr. A 1025 (2004) 71.
[50] H. Emteborg, E. Bjorklund, F. Odman, L. Karlsson, L. Mathiasson, W. Frech, D.C. Baxter, Analyst 121 (1996) 19.
[51] M.K. Donais, R. Saraswati, E. Mackey, R. Demiralp, B. Porter, M. Vangel, M. Levenson, V. Mandic, S. Azemard, M. Horvat, K. May, H. Emons, S. Wise, Fresenius J. Anal. Chem. 358 (1997) 424.
[52] P. Grinberg, R.C. Campos, Z. Mester, R.E. Sturgeon, Spectrochim. Acta Part B 58B (2003) 427.
[53] D.R. Parkinson, I. Bruheim, I. Christ, J. Pawliszyn, J. Chromatogr. A 1025 (2004) 77.
[54] J. O'Reilly, O. Wang, L. Setkova, J.P. Hutchinson, Y. Chen, H.L. Lord, C.M. Linton, J. Pawliszyn, J. Sep. Sci. 28 (2005) 2010.
[55] M. Guidotti, M. Vitali, J. High Res. Chromatogr. 21 (1998) 665.
[56] DORM-2, Certified Reference Material DORM-2, Dogfish Muscle; National Research Council Canada: Otawa, Canada http://inms-ienm.nrc-cnrc.gc.ca/calserv/crm_files_e/DORM-2_e.pdf, Accessed July 2008.

Quantitative Structure-Retention Relationship study of the constituents of saffron aroma in SPME-GC–MS based on the Projection Pursuit Regression method

Hongying Du[a], Jie Wang[a,b], Zhide Hu[a,*], Xiaojun Yao[a]

[a] Department of Chemistry, Lanzhou University, Lanzhou 730000, China
[b] Department of Biomedical Engineering, Yale University, New Haven, CT, USA

ARTICLE INFO

ABSTRACT

Quantitative Structure-Retention Relationship (QSRR) studies were performed for predicting the retention times of 43 constituents of saffron aroma, which were analyzed by solid-phase micro-extraction gas chromatography–mass spectrometry (SPME-GC–MS). The chemical descriptors were calculated from the molecular structures of the constituents of saffron aroma alone, and the linear and non-linear QSRR models were constructed using the Best Multi-Linear Regression (BMLR) and Projection Pursuit Regression (PPR) methods. The predicted results of the two approaches were in agreement with the experimental data. The coefficients of determination (R^2) of the linear BMLR model were 0.9434 and 0.8725 for the training and test sets, respectively. The other non-linear PPR model gave a more accurate prediction with R^2 values of 0.9806 (training set) and 0.9456 (test set). The proposed models could also identify and provide some insights into structural features that may play a role on the retention behaviors of the constituents of saffron aroma in the SPME-GC–MS system. This study affords a simple but efficient approach for studying the retention behaviors of other similar plants and herbs.

1. Introduction

Saffron, the dried and dark-red stigma with a small portion of the yellowish style attached of *Crocus sativus* L., belongs to the Iridaceae family, and grows natively in Europe, Asia, and the Middle East [1,2]. It is a very expensive spice used mostly as a herbal medicine or a food coloring and flavoring agent in parts of the world [3–5]. Three main chemical compounds have been identified in saffron, the bright red coloring carotenoids, picrocron and safranal. In fact, freshly picked saffron is odorless, but the odoriferous substances develop a very pleasing flavor during the drying procedure. Most of the flavor compounds are formed by thermal and enzymatic degradation of picrocrocin [6]. Safranal and isophorone derivatives are the chief flavor components of the essential oil and are responsible for the characteristic of saffron aroma [7,8]. Nowadays, saffron is becoming more and more popular as a colorant for foodstuffs mainly due to its aromatic and flavoring properties.

Solid-phase micro-extraction (SPME) is a relatively new sample preparation technique that has been steadily increasing in popularity since its development by Arthur and Pawliszyn [9]. The SPME method is a particularly promising tool, which involves the use of a fiber coated with GC packing material for the extraction of sample molecules from their matrix [10]. It is also a useful sample preparation technique for the analysis of volatile and semi-volatile analytes. This method is most often coupled with gas chromatographic separation and mass spectrometric analysis (GC–MS), which is a method commonly used in food volatile analysis [11–15]. The SPME-GC–MS method was utilized by D'Auria to separate the aroma constituents of saffron [16] based on its solvent free sample processing, sensitivity and reliability.

Quantitative Structure-Retention Relationship (QSRR) is a statistical method linking the chromatographic retention behaviors of a series of analytes and their structures [17–19]. The advantage of this approach over the other methods lies in the fact that the descriptors used to build models are obtained only from the structures of the analytes, and it only depends on few experimental properties. The main objectives of the QSRR studies are to find mathematical models that are related to the retention behaviors of the given analytes and their physicochemical and structural parameters. In addition to their practical application in optimization strategies, the QSRR models can help us to gain insight into the separation mechanism that occurs at the molecular level [20–23]. At the same time, this kind of study can indicate the important structural factors that play a role in the determination of the retention behavior. The aims of this work were to establish a robust QSRR model that could be used for the prediction of the known aroma constituents of saffron; and to seek the most important structural features that were related to

* Corresponding author. Tel.: +86 931 891 2540; fax: +86 931 891 2582.
E-mail address: hu_zhide@yahoo.com.cn (Z. Hu).

the relative retention behaviors of saffron favor fractions strongly in SPME-GC–MS separation system.

In this investigation, Best Multi-Linear Regression (BMLR) method was utilized to reduce the number of descriptors and select the relevant ones. Two different QSRR models with the same five descriptors were built using the BMLR and PPR methods. The results from different methods were also compared in order to find the most suitable method for the prediction of SPME-GC–MS chromatography retention behavior. The ultimate aim is to establish a significant model with excellent prediction ability and obtain some useful information of the interaction retention behaviors between the aroma constituents of saffron and SPME-GC–MS separation. This work provides a simple but efficient approach in studying the retention mechanism of compounds in the application of chromatographic coupling technologies. It could also help us to optimize the separation conditions of some similar fields.

2. Experimental

2.1. Data set

The logarithm of the retention times ($\log t_R$) of 43 saffron flavor compounds is taken from the literature [16]. A complete list of the 43 aroma constituents of saffron's names and their corresponding experimental retention times ($\log t_R$) are shown in Table 1. The entire set of compounds was randomly divided into two subsets, a training set of 34 compounds and a test set of 9 compounds. The training set was used to select the most relevant molecular descriptors and develop QSRR models, and the test set was used to evaluate the performance of the different models.

Six dried samples of saffron derived from cultivation of *C. sativus* in the zone of Salerno (Southern Italy) were used. The retention times of the aroma constituents of saffron were obtained using the following apparatus: A 100-μm polydimethysiloxane-SPME module (57300-U, Supelco, Bellefonte, PA) was used; GC (HP 6890) equipped with a Phenomenex Zebron ZB-5 MS capillary column and linked with mass selective detector (HP 5973). All analyses were carried out in triplicates. The detailed description of the experimental condition can be found in Ref. [16].

2.2. Molecular descriptors generation and selection

All the molecular structures were drawn and pre-optimized using the molecular mechanics force fields (MM+) in HyperChem 7.0 program (HyperCube, Inc.) [24]. Afterward, a more precise optimization was done with the semi-empirical AM1 method in MOPAC 6.0 (Stewart Computational Chemistry), and then the structures with minimum energy were obtained. The resulting geometries formed the inputs of CODESSA software (University of Florida) [25] to calculate constitutional, topological, geometrical, electrostatic and quantum-chemical descriptors. Then a pre-selection was used to exclude the irrelevant descriptors, such as the ones with same values for the whole data set or missed values for some compounds. There were 381 molecular descriptors left for further analysis. The BMLR method was used to search for the best set of descriptors for multi-linear correlation.

The BMLR method is a very useful tool in searching for the best set of descriptors. It has several advantages, such as its ease of implementation and the interpretability of the resulting equations; it also offers a more systematic and thorough search of preferred descriptors. In BMLR, the number of orthogonal descriptors in the model was incrementally added up to the optimum as determined by the Fisher criterion at a given probability level and the cross-validated correlation coefficient. The model

Table 1
Experimental and predicted logarithm of retention times for the constituents of saffron aroma

No.	Compounds	$\log t_R$[a]	BMLR[b]	PPR[c]
1	2-Methylpropanal	0.350	0.357	0.376
2	Acetic acid	0.371	0.370	0.328
3	3-Methylbutanal	0.378	0.431	0.416
4[*]	2-Methylbutanal	0.474	0.476	0.469
5	1-Pentanol	0.573	0.604	0.542
6	Hexanal	0.635	0.701	0.643
7	1-*t*-Butylcyclopentadiene	0.782	0.963	0.880
8[*]	Heptanal	0.811	0.818	0.802
9	2(5H)-Furanone	0.828	0.838	0.821
10	4,4-Dimethylcyclopentenone	0.829	0.900	0.888
11[*]	Octanal	0.941	0.906	0.936
12[*]	b-Phellandrene	0.961	0.984	0.997
13	6-Methyl-5-hepten-2-one	0.965	0.945	0.933
14[*]	3,5,5-Trimethylcyclohex-3-en-1-one	0.980	0.951	1.003
15	2,5-Dimethyl-2,4-hexadiene	0.990	0.883	0.978
16	1-(1-Methylethyl)-4-methyl-2,4-cyclohexadiene	1.001	1.018	1.018
17	1,3,5-Trimethylbenzene	1.003	1.010	0.959
18	Benzaldehyde	1.026	0.993	1.003
19	1,1,3-Trimethylcyclopentadiene	1.033	0.999	1.014
20	Nonanal	1.035	1.004	1.049
21	6-Methyl-3,5-heptadien-2-one	1.036	0.952	1.028
22	5,5-Dimethyl-2-methylene-1-cyclohexylcarbaldehyde	1.038	0.928	1.016
23[*]	2-Phenylethanol	1.046	0.944	0.988
24	3,5,5-Trimethylcyclohexenone	1.049	0.989	1.031
25	4-(1-Methylethyl)-benzaldehyde	1.061	1.100	1.086
26	3,5,5-Trimethylcyclohex-2-en-1,4-dione	1.066	1.082	1.105
27	3,5,5-Trimethylcyclohexan-1,4-dione	1.083	1.019	1.056
28[*]	2-Hydroxy-3,5,5-trimethylcyclohexenone	1.103	1.066	1.100
29	Safranal	1.108	1.125	1.136
30	2-Isopropylidene-3-methylhexa-3,5-dien-1-al	1.118	1.163	1.178
31	2,7,7-Trimethyl-2,4-cycloheptadien-1-one	1.119	1.088	1.134
32[*]	2-Hydroxy-3,5,5-trimethylcyclohex-2-en-1,4-dione	1.155	1.226	1.197
33	4-Hydroxy-3,5,5-trimethylcyclohex-2-enone	1.166	1.080	1.101
34	2,4,5-Trimethylbenzaldehyde	1.172	1.149	1.123
35	2,6,6-Trimethyl-4-hydroxycyclohexa-1,4-dien-3-on-1-carbaldehyde	1.207	1.185	1.186
36	Dihydro-beta-ionone	1.227	1.260	1.204
37	Dihydro-beta-ionol	1.230	1.147	1.210
38	(E)-6,10-Dimethyl-5,9-undecadien-2-one	1.231	1.284	1.238
39	2,6-Di-(1,1-dimethylethyl)-4-hydroxy-4-methylcyclohexa-2,5-dien-1-one	1.239	1.282	1.277
40[*]	2,6,6-Trimethyl-4-hydroxycyclohexen-1-carbaldehyde	1.244	1.037	1.116
41	beta-Ionone	1.246	1.267	1.209
42	Pentadecane	1.248	1.233	1.254
43	2,6-Di-(1,1-dimethylethyl)-phenol	1.256	1.351	1.281

[a] Logarithm of experimental retention time for aroma compounds ($\log t_R$).
[b] Predicted $\log t_R$ by the BMLR method.
[c] Predicted $\log t_R$ by the PPR method.
[*] Test set.

obtained with this procedure was expected to yield maximum predictive ability. A stepwise addition of further descriptor scales was performed to find the best multi-parameter regression models with the optimum values of statistical criteria (highest values of R^2, the cross-validated R_{cv}^2, and the F value). The influence of the model's dimension on its prediction capability was tested by the

leave-one-out cross-validation procedure. The BMLR procedure correlations are usually much faster than other methods including the heuristic method with comparable quality. The strategy of multi-parameter regression with maximum prediction ability was described in detail in Ref. [26].

2.3. Projection Pursuit Regression (PPR)

PPR developed by Friedman and Stuetzle's [27] is a powerful tool for seeking interesting projections, which project the high-dimensional data into lower dimensional space by means of linear projections. Therefore, it can surmount the curse of dimensionality since it relies in estimation in at most tri-variate settings. At present, it has been successfully applied to tackle some chemical problems [28,29]. Friedman and Stuetzle's concept of PPR avoided many difficulties experienced with other existing nonparametric regression procedures. The sparsity limitation and poor performance in high dimensions (curse of dimensionality) encountered in kernel and nearest neighbor techniques are not encountered in PPR since all estimation (smoothing) is carried out in a univariate setting. PPR does not require specification of a metric in the predictor space. Unlike recursive partitioning, PPR does not split the sample, thereby allowing, when necessary, more complex models. In addition, interactions of predictors are directly considered [27]. The basic theory of PPR can be found in the references [27,30–32]. Here, we only give a brief description. The PPR method is based on an iterative two-stage process of projection (reduction of parameter space) and smoothing (establishing non-linear relation). The reduction of the parameter space is essential for the application of smoothing; smoothing in high-dimensional spaces quickly becomes impossible because of data sparsity [27]. In a regression work, several parameters should be given first: n, the number of objects under investigation (chemical structures); p, number of explanatory variables (molecular descriptors); y, vector of response or dependent variable ($n \times 1$) (property or activity); X, matrix of explanatory variables ($n \times p$). The projection process can be defined as $z_m = X\alpha_m$, where α_m is the mth projection vector (length p); and z_m is the vector of scores after projection of X on α_m (length n). After the projection, the smooth functions (ridge functions) are used, which are as follows:

$$y = \bar{y} + \sum_{m=1}^{M_0} \phi_m(z_m) + \varepsilon_{M_0} \tag{1}$$

where M_0 is the number of incorporated smooths; ε_{M_0} is the residual error after fitting M_0 smooths. Then it can produce a non-linear regression model by the summation of a number of ridge functions.

All calculation programs implementing PPR were written in R-file based on R script under R2.3.1 environment [33] running operating system on a Pentium IV with 512 M RAM.

2.4. Model performance evaluation

Model performance can be measured by different ways. In this investigation, the root mean square error (RMSE) was used to evaluate the predictive ability of the models. It was defined as the following:

$$\text{RMSE} = \sqrt{\frac{\sum_{i=1}^{n_s}(y_{ke} - y_{kp})^2}{n_s}} \tag{2}$$

where k represents kth molecule, y_{ke} is the experimental responses (desired output values), y_{kp} is the responses predicted by the regression model, and n_s is the number of compounds in the analyzed set. The smaller RMSE, the more accurate the proposed model.

3. Results and discussion

3.1. Principal component analysis (PCA) of the data set

The PCA method has been performed using all the molecular descriptors for the entire set of data. It aims to show the spatial location of samples, and verify the way of splitting the data into the training and the test set. The result of PCA gave us three major PCs that explained 65.97% of the variation in the data (30.29%, 24.04% and 11.64%, respectively). Fig. 1 illustrates the scores plot of PCA for the training set and the test set. From this figure, it can be seen that the samples in the training and the test sets are well balanced and scattered over the whole 3D-space. The compounds in both sets are representative and so this splitting method of the data set is reliable for the assessment of the predictive ability and performance of different models.

3.2. Result of the BMLR method

The BMLR method available in the CODESSA program was used to select the most important molecular descriptors based on the training set and develop the multi-linear QSRR model. A variety of subset sizes were investigated to determine the optimum number of the descriptors in a model. After adding another descriptor, the statistics of the model did not improve significantly; it was determined that the optimum subset size had been achieved. To avoid the "overparametrization" of the model, an increase of the "R^2" value of less than 0.02 was chosen as the breakpoint criterion. Fig. 2 shows the number of descriptors vs. the correlation coefficient (R^2) and leave-one-out (LOO) cross-validation (R_{cv}^2). It could be seen that five descriptors were sufficient for a successful regression model of $\log t_R$. The statistical parameters of the best model and the involved molecular descriptors are given in Table 2. The correlation matrix of these descriptors is shown in Table 3. From this table, it could be clearly seen that the linear correlation coefficient values of each of the two descriptors was less than 0.85, which demonstrated that the descriptors selected by the BMLR method were independent.

The predicted values for all the constituents of saffron aroma including the training set and the test set are given in Table 1. Fig. 3 showed the plot of the calculated vs. experimental values ($\log t_R$) for all saffron flavor constituents studied, for the training set and the test set. It could be concluded that the best linear correlations developed by the BMLR method had satisfactory predictive ability.
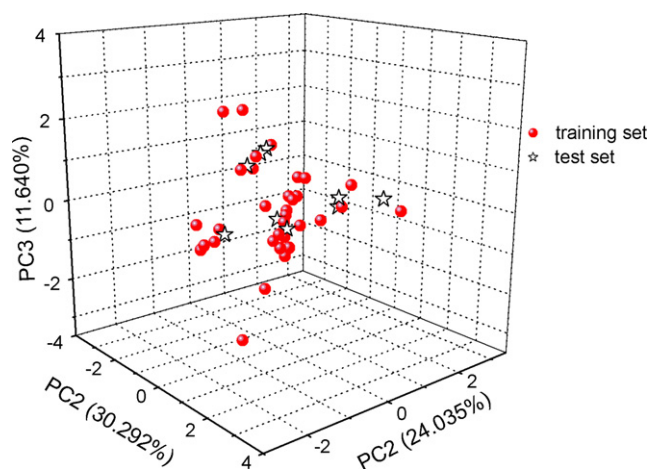
Fig. 1. Principal component analysis of the molecular descriptors for the data set.
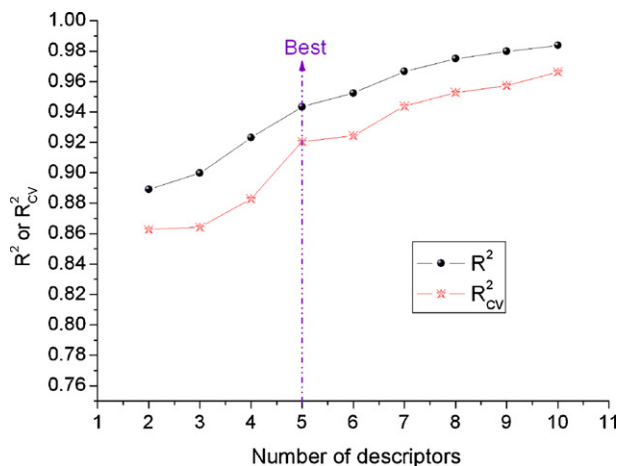
Fig. 2. R^2 and R^2_{cv} vs. the number of descriptors for the training set.

Table 2
Descriptors, coefficients, standard errors, and T-values for the BMLR model

Descriptors	Chemical meaning	Coefficient	Error	t-Test value
Constant	Intercept	2.17E+00	3.77E−01	5.7595
RNR	Relative number of rings	3.47E+00	5.76E−01	6.0132
ALFAP	ALFA polarizability (DIP)	4.24E−03	1.19E−03	3.5580
MAOEP	Min atomic orbital electronic population	−1.83E+00	3.47E−01	−5.2809
RRNCQ	RNCS Relative negative charged SA (SAMNEG*RNCG) [Quantum-Chemical PC]	−2.60E−02	5.21E−03	−4.9999
KSI2	Kier shape index (order2)	2.59E−02	7.02E−03	3.6967

$R^2 = 0.9434$; $F = 93.36$; $s^2 = 0.0044$; $R^2_{cv} = 0.9205$; $N = 34$. *Note*: Coefficient, standardized regression coefficients.

Table 3
The correlation matrix of the selected descriptors

	RNR	KSI2	RRNCQ	MAOEP	ALFAP
RNR	1.0000				
KSI2	−0.5357	1.0000			
RRNCQ	−0.0704	−0.2388	1.0000		
MAOEP	−0.0371	0.1897	−0.6264	1.0000	
ALFAP	−0.0374	0.4336	−0.7026	0.0568	1.0000
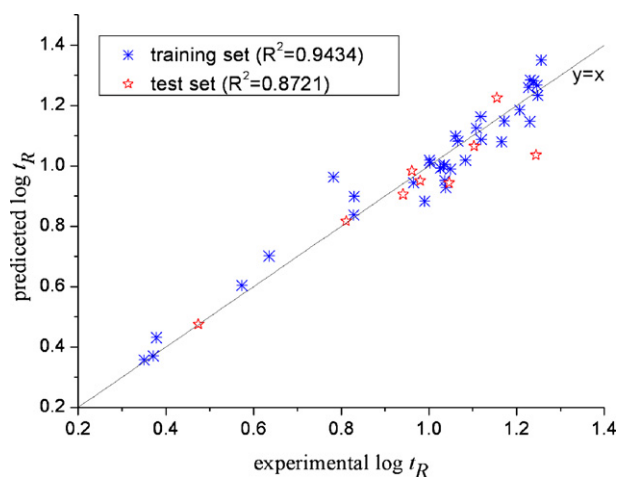
Fig. 3. Plot of predicted log t_R values vs. experimental values by BMLR.

3.3. Results of the PPR method

In order to get a more accurate prediction model, the PPR method was applied to build a non-linear model with the same selected descriptors. In the PPR approach, there are several parameters to be adjusted. The parameters 'nterms' and 'max.terms' represent the number of ridge terms to include in the final model and the number of maximum ridge terms to choose from when building the model, respectively. The algorithm first adds up to 'max.terms' ridge terms one at a time; it will use less if it is unable to find a term to add that makes sufficient difference. It then removes the least important term at each step until 'nterms' terms are left. The 'df' defines the smoothness of each ridge term by the requested equivalent degrees of freedom, if 'sm.method' is 'spline'. The levels of optimization (argument' optlevel') differ in how thoroughly the models are refitted during this process. At level 0 the existing ridge terms are not refitted. At level 1 the projection directions are not refitted, but the ridge functions and the regression coefficients are. Levels 2 and 3 refit all of the terms and are equivalent for one response; level 3 is more careful to re-balance the contributions from each regressor at each step and so is a little less likely to converge to a saddle point of the sum of squares criterion. In this investigation, the four parameters 'nterms', 'max.terms', 'optlevel' and 'df' were determined as 2, 10, 3, and 6, respectively. The ridge functions for 2-term projection pursuit regressions based on the optimized parameters can be depicted graphically in Fig. 4. It can be used to modify the major parameters of the procedure: the average smoother bandwidth and the terminal threshold. The predicted results and the statistical parameters of the optimal PPR model are shown in Tables 1 and 4, respectively. The scatter plot is given in Fig. 5. From Fig. 5 and Table 4, it could be seen that the predicted values are in good agreement with the experimental values log t_R for almost all the compounds.

3.4. Comparison of the results obtained by different approaches

In order to check the superiority of the two different methods (BMLR and PPR), the predicted accuracy for different data sets (training set and test set) by the two methods was collected together and shown in Table 4. As it can be seen from this table, the non-linear regression method PPR shows better predictive capability.

3.5. Discussion of the selected descriptors

By interpreting the descriptors in the regression model, it is possible to gain some insights into the factors that are likely to govern the retention times of the constituents of saffron aroma in SPME-GC–MS separation model. In the best linear model, there are five molecular descriptors: one constitutional descriptor (relative number of rings (RNR)), two quantum-chemical descriptors (ALFA polarizability (DIP) (ALFAP) and min atomic orbital electronic population (MAOEP)), one electrostatic descriptors (RNCS Relative negative charged SA (SAMNEG*RNCG) [Quantum-Chemical PC] (RNCSQ)) and one topological descriptor (Kier shape index (order 2) (KSI2)).

The first important descriptor is a constitutional descriptor—RNR, which accounts for the chain stiffness of small molecules. The number of rings [34] affects the aromatics density in a reduced forms the relative number of rings (the number of rings divided by the number of atoms). It is related to the size and shape of the molecule. This descriptor has a positive coefficient in the linear model, therefore it indicates that the molecules with larger number of rings are expected to bind more tightly to GC column. According to the coefficients of the best linear model, the second important parameter is a quantum-chemical descriptor MAOEP, it describes
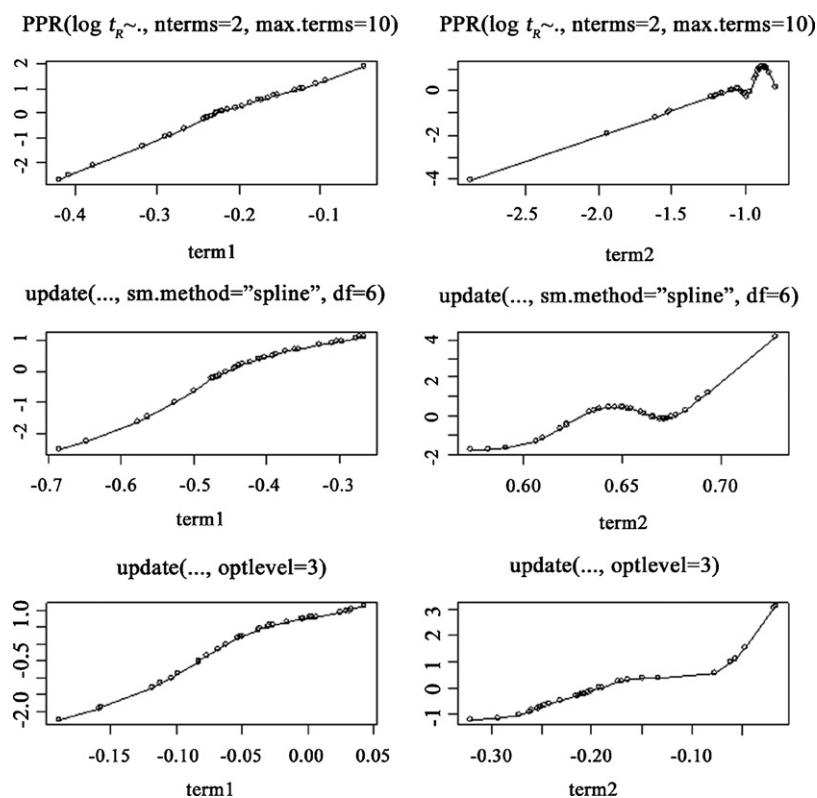
Fig. 4. Plots of the ridge functions for 2-term projection pursuit regressions based on the optimized parameters.

Table 4
Comparison of the square correlation coefficient (R^2) and the root mean square of error (RMSE) for different QSRR models

Methods	Data set	R^2	RMSE
MLR	Training set	0.9434	0.0604
	Test set	0.8725	0.0832
PPR	Training set	0.9806	0.0354
	Test set	0.9456	0.0509

the nucleophilicity of the molecule, which is directly related to the polarity of molecules [25]. So MAOEP for a given atomic species in the molecule is a simplified index to describe the electrophilic ability of a molecule. The negative coefficient of MAOEP in the model
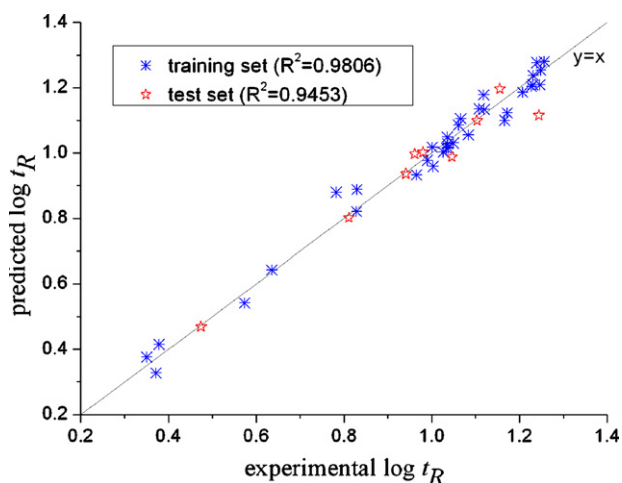
Fig. 5. Plot of predicted log t_R values *vs.* experimental values by PPR.

implies that increasing the value of this descriptor is in favor of elution procedure, so the retain will be shorter in the column. The descriptor RNCSQ belongs to an electrostatic descriptor. It reflects the characteristic of the charge distribution of the molecule and accounts for the electrostatic interaction between the constituents of saffron aroma and immobility phase. The negative coefficient of RNCSQ in the model implies that increasing the value of this descriptor can lead to a smaller log t_R value. The quantum-chemical descriptor ALFAP could reflect the size and volume of the molecule, the interaction between the medium and molecular, polarizability [35]. So it tightly relates to the hydrophobicity and electrophilicity of the molecular [36]. The positive coefficient of this descriptor indicates that the larger polarizability and hydrophobicity, the longer retention in SPME-GC–MS system. The last descripto-KSI2 [25] belongs to a topological descriptor. The Kier shape index (KSI) descriptors are intend to capture different aspects of the molecular shape. For N vertices, the maximal graph includes edges between all vertex pairs. For the minimal graph a linear path of N-1 edges connecting the vertices is taken. The Kier shape index is defined as:

$$K = \frac{2P_{min}P_{max}}{P^2} \tag{3}$$

where P is the number of edges in the graph. P_{max} is the number of edges in the maximal graph, and P_{min} is the number of edges in the minimal graph. The KSI2 encodes the branching information of the molecule. P, P_{min}, and P_{max} now denote the number of paths of length 2 in the corresponding graphs. The maximal graph is taken to be the star graph in which all atoms are adjacent to a common atom. Thus, $P_{max} = (N - 1)(N - 2)/2$. The linear graph is again taken as the minimal graph, so $P_{min} = N - 2$. Eq. (3) yields the following:

$$k_2 = \frac{(N - 1)(N - 2)^2}{P^2} \tag{4}$$

where k_2 is the value of KSI2.

From the above discussion, it can be seen that all the descriptors involved in the model have physical and chemical meanings. These descriptors can account for the structural features responsible for the retention behavior of the constituents of saffron aroma in SPME-GC–MS, such as hydrophobicity, electrophilicity, electrostatic interaction, polarizability, size, shape and the branching information of molecules. So the selected descriptors are related to the retention characteristics of the constituents of saffron aroma in this special chromatographic separation model.

4. Conclusions

This study focused on the development of QSRR models for predicting the retention times of constituents of saffron aroma in SPME-GC–MS. In order to obtain more reliable models with good predictive capabilities, it is advisable to consider selecting proper molecular descriptors and constructing different QSRR models with miscellaneous chemometric approaches. In this study, the BMLR was used to select the main structural descriptors and build a linear regression model at the same time, and it had good predictive capability. Considering the complex interaction mechanism of SPME-GC–MS separation system, the non-linear method—PPR was used to build the other QSRR model. According to the comparison of the results, it clearly shows that the PPR approach performed much better than the linear method BMLR. Therefore, it can be concluded that the PPR approach combined with BMLR method has superiority in solving the retention times of the compounds problems; meanwhile, this work also provides another simple and reasonable way to deal with other separation researches on other plants and herbs.

Acknowledgments

References

[1] J.A. Fernandez, Recent Res. Dev. Plant Sci. 2 (2004) 127.
[2] N. Xuabin, Zhongcaoyao 23 (1992) 100.
[3] S.C. Nair, B. Panikkar, K.R. Panikkar, Cancer Lett. 57 (1991) 109.
[4] S.C. Nair, S.K. Kurumboor, J.H. Hasegawa, Cancer Biother. 10 (1995) 257.
[5] D. Basker, M. Negbi, Econ. Bot. 37 (1983) 228.
[6] B.L. Raina, S.G. Agarwal, A.K. Bhatia, G.S. Gaur, J. Sci. Food Agric. 71 (1996) 27.
[7] J.L. Iborra, M.R. Castellar, M. Cánovas, A. Manjón, J. Food Sci. 57 (1992) 714.
[8] N.S. Zarghami, D.E. Heinz, Lebensm. Wiss. Technol. 4 (1971) 2.
[9] C.L. Arthur, J. Pawliszyn, Anal. Chem. 62 (1990) 2145.
[10] J. Pawliszyn, Solid-Phase Microextraction Theory and Practice, Wiley-VCH, New York, 1997.
[11] W.C. Chen, P.Z. Zhou, K.C. Wong-Moon, N.S. Cauchon, J. Pharm. Biomed. Anal. 44 (2007) 450.
[12] F. Augusto, A.L.P. Valente, E.d.S. Tada, S.R. Rivellino, J. Chromatogr. A 873 (2000) 117.
[13] W. Jahouach-Rabai, M. Trabelsi, V. Van Hoed, A. Adams, R. Verhé, N. De Kimpe, M.H. Frikha, Ultrason. Sonochem. 15 (2008) 590.
[14] A.J. Matich, D.D. Rowan, N.H. Banks, Anal. Chem. 68 (1996) 4114.
[15] M.E. Miller, J.D. Stuart, Anal. Chem. 71 (1999) 23.
[16] M. D'Auria, G. Mauriello, R. Racioppi, G.L. Rana, J. Chromatogr. Sci. 44 (2006) 18.
[17] L.C. Porto, É.S. Souza, B.d.S. Junkes, R.A. Yunes, V.E.F. Heinzen, Talanta 76 (2008) 407.
[18] F.P. Liu, Y.Z. Liang, C.Z. Cao, N. Zhou, Talanta 72 (2007) 1307.
[19] H.Y. Du, X.Y. Zhang, J. Wang, X.J. Yao, Z.D. Hu, Proteomics 11 (2008) 2185.
[20] S.K. Poole, C.F. Poole, J. Chromatogr. A 1182 (2008) 1.
[21] A.G. Fragkaki, M.A. Koupparis, C.G. Georgakopoulos, Anal. Chim. Acta 512 (2004) 165.
[22] A. Niazi, J. Ghasemi, M. Zendehdel, Talanta 74 (2007) 247.
[23] C. Sârbu, D. Casoni, M. Darabantu, C. Maiereanu, J. Pharmaceut. Biomed. Anal. 35 (2004) 213.
[24] HyperChem, Release 6.0 for Windows, Hypercube, Inc., 2000.
[25] A.R. Katritzky, V.S. Lobanov, M. Karelson, Comprehensive descriptors for structural and statistical analysis, in: Reference Manual, Version 2.0, University of Florida, 1994.
[26] A.R. Katritzky, V.S. Lobanov, M. Karelson, CODESSA: Training Manual, University of Florida, Gainesville, Florida, 1995.
[27] J.H. Friedman, W. Stuetzle, J. Am. Stat. Assoc. 76 (1981) 817.
[28] Y.P. Du, Y.Z. Liang, D. Yun, J. Chem. Inf. Comput. Sci. 42 (2002) 1283.
[29] H.Y. Du, J. Wang, X.Y. Zhang, X.J. Yao, Z.D. Hu, Chemometr. Intell. Lab. Syst. 92 (2008) 92.
[30] P.J. Huber, Ann. Stat. 13 (1985) 435.
[31] D. Donoho, I.M. Johnstone, Ann. Stat. 13 (1985) 496.
[32] P. Diaconis, M. Shahshahani, SIAM J. Sci. Stat. Comput. 5 (1984) 175.
[33] M. Birattari, G. Bontempi, R Manuals, The R Development Core Team, 2003.
[34] J. Wang, H.Y. Du, H.X. Liu, X.J. Yao, Z.D. Hu, B.T. Fan, Talanta 73 (2007) 147.
[35] H.A. Kurtz, J.J.P. Stewart, K.M. Dieter, J. Comput. Chem. 11 (1990) 82.
[36] M. Karelson, V.S. Lobanov, A.R. Katritzky, Chem. Rev. 96 (1996) 1027.

On-line and off-line quantification of trace elements associated to colloids by As-Fl-FFF and ICP-MS

S. Dubascoux *, I. Le Hécho, M. Potin Gautier, G. Lespes

LCABIE CNRS UMR 5254 IPREM, Helioparc, av du Président Pierre Angot, 64053 PAU, France

ARTICLE INFO

ABSTRACT

A quantification procedure of trace elements during colloid size fractionation was developed and validated. This procedure is based on the hyphenation between Asymmetrical Flow Field-Flow Fractionation (As-Fl-FFF) and Inductively Coupled Plasma Mass Spectrometer (ICP-MS). The optimisation of the procedure was performed on a soil leachate spiked with six trace elements selected for their environmental and health impact (As, Cd, Sb, Se, Sn and Pb). The elements in the spiked sample were on-line monitored during the fractionation. The validation was carried out by comparison with a second off-line quantification procedure based on fraction collection and total element analysis by ICP-MS. This off-line one was previously validated using reference materials. Finally, the analytical performances of the two procedures were compared.

1. Introduction

Colloids play a major role in the biogeochemical cycle of elements [1,2]. In aquatic media, the distribution of elements on colloids is not only directly linked to the considered elements themselves but also to the size and the nature of colloids [3,4]. Moreover, these parameters could also influence the reactivity and thus the mobility of colloids in the groundwater [5]. For all these reasons, the characterization of colloids and the determination of associated elements are of main interest especially in soil solutions where transfer could occur from dissolved to particulate part but also from soil to plants.

To fractionate environmental colloids as a function of their sizes, Flow Field-Flow Fractionation (Fl-FFF) has taken an important place among the different analytical tools because of its high resolution, its capability to fractionate over a wide range of size and the lower interactions with the analytical system in comparison to those observed in chromatography. Moreover, it can be easily coupled to various detectors (Ultra-Violet: UV, Multi-Angle Laser Light Scattering: MALLS, Fluorescence, Differential Refractive Index: RI, Atomic Mass Spectrometer...) and such coupling appears to give relevant data with regard to information needed [6].

Using Fl-FFF, the fractionation takes place in a channel under a field of mobile phase (crossflow) applied perpendicularly to a main parabolic flow. For a colloidal range from some nanometres to about 500 nm, the diffusive phenomenon leads to the discrimination in size of the colloids, according to the parabolic flow profile. The elution takes place from small colloids to larger ones (i.e. normal mode). The cut-off of the ultrafiltration membrane defines the part of the sample retained in the channel (all the macromolecules smaller than cut-off being removed in the crossflow) [7]. Asymmetrical Fl-FFF (As-Fl-FFF) is a sub-technique of Fl-FFF where the crossflow is generated by a pressure differential in a semipermeable channel. As-Fl-FFF permits to increase the fractionation speed and involves less dilution [7].

In order to obtain in the same time features about the colloidal size, distribution and concentration of elements bound to colloids, Fl-FFF can be associated with Inductively Coupled Plasma-Mass Spectrometer (ICP-MS) which insures a sensitive multi-elemental detection. In the last decade, some studies have focused on the coupling of Fl-FFF and ICP-MS for the qualitative analysis of environmental samples [3,8,9]. Others have focused on the on-line quantification and the possibility to link element concentration to colloidal fractionation [10–16]. However, very few works deal with analytical development of the coupling and quantification and no one with the analytical validation of quantification procedure [4,17]. This analytical lack is partly due to the high dilution of the sample during fractionation. The lack of available certified reference natural colloid with certified metal

* Corresponding author. Tel.: +33 559407762.
   E-mail address: stephane.dubascoux@univ-pau.fr (S. Dubascoux).

concentration also makes any validation critical to perform. In this work, an on-line trace element quantification procedure is proposed and validated, for the first time. The accuracy evaluation is performed by the way of an off-line quantification, this second procedure being previously validated by the use of reference materials (RM). Such approach has never been related before and appears useful especially with regard to insurance quality.

2. Materials and methods

2.1. Chemicals

Ammonium nitrate (NH_4NO_3: 99.5%) and sodium dodecyl sulfate (SDS: 98.5%) were purchased from Sigma–Aldrich (Seelze, Germany) and sodium hydroxide (NaOH: 99%) from Merck (Darmstadt, Germany). Nitric acid (HNO_3) was Instra Analyzed 69–70% from Baker (Atlantic-Labo, Bordeaux, France). 100 mg L^{-1} multi-elemental solutions (CCS-4, CCS-5 and CCS-6) was obtained from Analab (Strasbourg, France). The Milli-Q (MQ) water used was 18 MΩ (Millipore system, USA). Filters used for mobile phase were Durapore 0.1 μm from Millipore and 0.45 μm filters were hydrophilic mixed cellulose ester ones (Millipore, USA).

2.2. Samples

To evaluate the accuracy of the on-line quantification procedure results by comparison to the off-line ones, a soil leachate was spiked with metals and metalloids. The leaching test was performed according to a standardized protocol from the French Agency of Normalisation (AFNOR) [18]. This protocol is applied for polluted soils and waste in order to evaluate the pollutant concentrations in the soluble phase before treatment or disposal. The soil used was a referenced environmental sample: a ploughed layer of a densic podzol already described in previous studies [19]. The preparation was performed in three steps. The first one consists of the leaching of 100 g of soil with 1 L of Milli Q (MQ) water in a flask shaken during 16 h. Then the slurry was centrifuged at 3500 × g for 30 min. Finally, the supernatant was collected and filtered at 0.45 μm. Once the soil leachate obtained, it was spiked with a solution prepared from CCS multi-elemental solutions which contain trace elements with high environmental and health impact: arsenic (As), cadmium (Cd), antimony (Sb), selenium (Se), tin (Sn) and lead (Pb). This solution was previously adjusted at pH 7 with a 0.5 mol L^{-1} NaOH solution, in order to be close to the leachate pH. The spiking was carried out in order to have a soil leachate with a total elemental concentration of 100 μg L^{-1} for each element. The mixture was then shaken during 24 h.

To check the accuracy of the on-line quantification protocol, two reference samples known for their total metal concentration were analyzed: a certified reference waste water (CRM) named SPSWW1 (LGC Promochem, Oslo, Norway) with certified element concentrations (As, Cd and Pb, especially) and a laboratory reference material (LRM). The LRM was a landfill leachate containing colloids and already analyzed and described in previous studies [20]. It contains As, Cd, Sb, Se, Sn and Pb in known concentrations (named "known" or "expected values" later on in this paper).

For the on-line quantification procedure, multi-elemental solutions from CCS ones were prepared at different concentrations (0.5, 1, 2, 5, 10, 20 and 50 μg L^{-1}) in 1% of HNO_3. For the off-line quantification procedure, standard solutions with concentrations ranged from 50 ng L^{-1} to 20 μg L^{-1} were prepared in 7% of HNO_3 in order to insure the external calibration with matrix reconstitution.

2.3. Apparatus

A Flow Field-Flow Fractionation system, (Eclipse 2, Wyatt Technology, Dernbach, Germany) with an asymmetrical channel (As-Fl-FFF) was used in this work. The channel dimensions were 26.5 cm length and from 2.1 to 0.6 cm width. Its thickness was defined by a spacer of 250 μm height. Ultrafiltration membranes used were 10 kDa (cut-off) regenerated cellulose (Wyatt Technology, Dernbach, Germany). Flows were controlled with an Agilent 1100 series isocratic pump equipped with an Agilent series 1100 micro-vacuum degasser (Agilent Technologies, Tokyo, Japan).

The UV detector was an adjustable wavelength 1100 series (Agilent Technology, Tokyo, Japan) tuned at 270 nm. The ICP-MS was a 7500ce model (Agilent Technology, Tokyo, Japan) with a Meinhard nebulizer. The HPLC pump used for the standard injections was a HPLC Varian 9012 (Varian, Palo Alto, USA). The freeze drying was performed in an Alpha 1–4 LSC from Bioblock (Fischer Scientific Bioblock, Illkirch, France) and the mineralization carried out in an automated system (Digiprep, SCP science, Baie D'Urfé, Quebec, Canada).

The Multi-Angle Laser Light Scattering (MALLS), a DAWN DSP-F (Wyatt technology, Santa Barbara, USA) was used to measure the gyration radius (R_g) during the soil leachate fractionation in order to check the separation quality.

2.4. Quantification procedures

The two procedures described below are summarized in the Fig. 1. Each As-Fl-FFF analysis was realized in triplicate.

2.4.1. On-line quantification—Q1

In order to quantify the metals and metalloids linked to colloids as a function of the colloidal size separation, the quantification method developed (Q1) was based on the direct hyphenation of As-Fl-FFF and ICP-MS as presented in Fig. 2. The output of the MALLS detector was directly connected to the Meinhard nebulizer via a
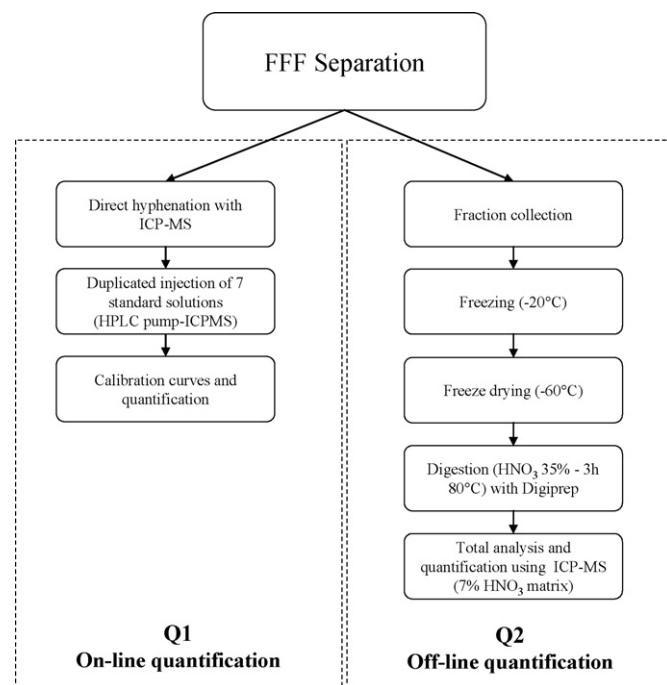
Fig. 1. Quantification procedures: on-line by As-Fl-FFF-ICP-MS (Q1) and off-line by ICP-MS analysis after fractionation and fraction collection (Q2).
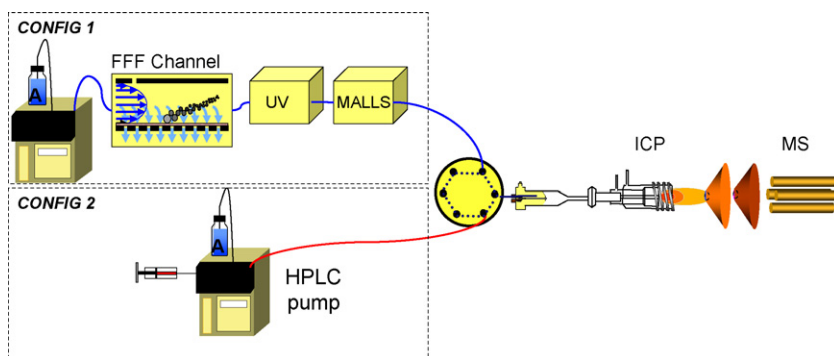
Fig. 2. Schematic presentation of CONFIG 1 (As-Fl-FFF-UV-ICP-MS coupling) and CONFIG 2 (direct injection in ICP-MS via HPLC pump).

capillary tube allowing the As-Fl-FFF effluent to be introduced in ICP-MS without any acidification. The coupling parameters are presented in Table 1. The H_2 collision cell mode was used to decrease spectral interferences especially for ^{80}Se (interfered by ^{40}Ar^{40}Ar). The different isotopes monitored in time resolved analysis mode were ^{75}As, ^{111}Cd, ^{113}Cd, ^{121}Sb, ^{123}Sb, ^{78}Se, ^{80}Se, ^{116}Sn, ^{118}Sn, ^{120}Sn, ^{206}Pb and ^{208}Pb. The As-Fl-FFF conditions were previously optimised to fractionate large colloids, with gyration radius ranging from 20 to 250 nm.

In CONFIG 1 (FFF-UV-MALLS-ICP-MS, see Fig. 2), the direct monitoring of elements associated to colloids was performed during the fractionation. When it was over, the position of the six-way valve was changed switching the HPLC pump to the ICP-MS system (CONFIG 2). The composition and flow rate of mobile phase were identical for the two configurations. This second configuration allowed the injection of multi-elemental solutions with a 100 µL sample loop according to an external calibration procedure.

2.4.2. Off-line quantification—Q2

This second quantification method was based on the concentration measurements in the fractions collected after As-Fl-FFF separation. It was developed in order to validate Q1 and reach extremely low detection limits required for the analysis of the As-Fl-FFF fractions collected because of the high dilution induced by the fractionation system (around 1:200). Colloidal fractions were collected in polypropylene vials (about 20 mL for each fraction) from the start to the end of the colloidal peak monitored by UV. Each fraction was first freezed at −20 °C and freeze dried at −60 °C in order to be pre-concentrated. Then, 2 mL of 35% HNO$_3$ was added

to each vial and heated in the Digiprep (ramp from room temperature to 80 °C and then 80 °C during 3 h). This step permits to digest the samples and thus homogenises the matrix. Acidic extracts were diluted with MQ water to obtain solutions at 7% of HNO$_3$. This procedure was applied to both reference materials and As-Fl-FFF fractions collected. Each sample was then analyzed by direct ICP-MS measurement in total analysis mode using an external calibration. The ICP stability was checked by measuring the ^{103}Rh (isotope not present in samples) during the ICP-MS runs and the deviation was found to be less than 8%.

3. Results and discussion

The general analytical approach was the following. First the analytical performances of Q1 and Q2 procedures were evaluated in order to determine the range of concentrations that can be reached. Then Q2 accuracy was checked with the help of reference materials in order to serve as reference method to Q1. Finally, trace metal concentrations determined by the two methods were compared and Q1 validated.

3.1. Analytical performances evaluation

The first step of the validation was to evaluate the analytical characteristics of the two external calibrations (on-line via the HPLC pump-Q1 and off-line-Q2). Fig. 3 gives as an example the ^{120}Sn signal obtained for the injection of 150 µL of spiked soil leachate using Q1. The left part of the Fig. 3 (CONFIG 1) corresponds to the

Table 1
As-Fl-FFF-UV-ICP-MS coupling and operating parameters

FFF-ICPMS operating parameters	
As-Fl-FFF and UV parameters (Wyatt eclipse 2)	
Channel flow rate (mL min^{-1})	1.0
Crossflow rate (mL min^{-1})	0.5
Injection flow rate (mL min^{-1})	0.15
Mobile phase	NH$_4$NO$_3$ 10^{-3} mol L^{-1} + SDS 3 10^{-4} mol L^{-1}/pH 8
Focus ratio	5.1%
Injection + focus time (min)	10
Focus time (min)	5
UV wavelength (nm)	270
ICP-MS parameters (Agilent 7500ce)	
Sample and skimmer cones	Ni
RF Power (W)	1500
Plasma gas flow rate (L min^{-1})	15
Carrier gas (L min^{-1})	0.95
Make up gas (L min^{-1})	0.15
Collision cell mode	H$_2$
Collision cell gas flow rate (mL min^{-1})	3.3
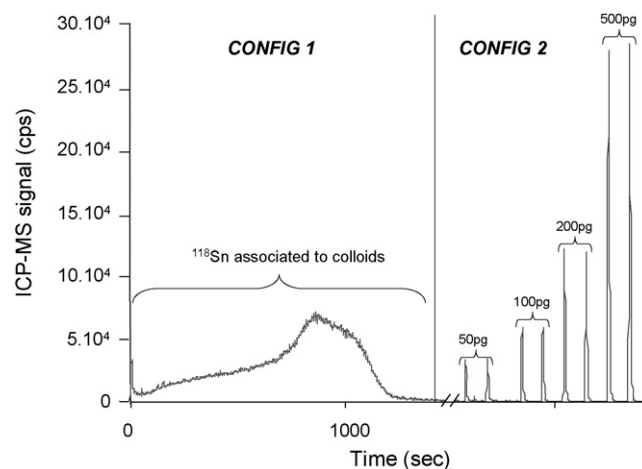
Fig. 3. Tin signals corresponding to Q1 quantification. CONFIG 1 presents the signal of tin associated to colloids during the As-Fl-FFF fractionation. CONFIG 2 shows four duplicated injections of standard solutions at different concentrations.

Sn signal associated to colloidal phase of the sample and the right part (CONFIG 2) corresponds to the eight first injections of standard solutions (from 50 to 500 pg). All the multi-elemental standard injections (from 50 to 2000 pg—total number of analyzed standard solutions: 12) allow the ICP-MS response to be evaluated and calibration curves to be plotted. Table 2 presents the Limits of Detection (LOD), the Limits of Quantification (LOQ) in pg and the determination coefficient (R^2) for the linear calibration curves of the two quantification methods.

The Q1 and Q2 methods give precise calibration according to the R^2 values. Absolute LOD and LOQ were calculated for the soil leachate prepared, over the whole analytical method, i.e. FFF fractionation and ICP-MS detection for Q1 and sample preconcentration and direct ICP-MS measurement for Q2. Concerning Q1, the LOD and LOQ were calculated with increasing sample volume injections (from 5 to 150 μL). Consequently, the LOD and LOQ calculated for Q1 depend on the peak shape and thus on the type (colloidal size range) of the injected sample [21]. Indeed, for the same peak area, the thinner the peak is, the lower the LOD and LOQ are. Sb and Se being not present in the colloidal part of the sample, LOD and LOQ could not be calculated because of the lack of signal. LOD and LOQ calculated for Q2 represent the lower absolute amount of element that can be detected in the collected fraction after As-Fl-FFF fractionation. They were calculated according to the linear regression curve method [22]. Q1 appears to be 1.5–2 times more sensitive than Q2.

3.2. Q2 accuracy checking

To evaluate the accuracy (i.e. trueness and precision according to the ISO 5725-1 norm) of Q2 quantification procedure and thus validate it, the CRM and LRM were first analyzed. In order to ensure measurable concentrations (close to those expected in As-Fl-FFF fractions) and prevent any leachate foaming during freeze drying, the reference samples were preliminary diluted in MQ water before freezing. The values obtained were compared to certified or known concentrations (see Table 3). Concentration values are presented as concentration (C) with its corresponding error (dC) calculated in a 95% confidence interval according to [23]:

$$dC = \frac{t_{\alpha/2,n-1} \cdot \text{S.D.}}{\sqrt{n}} \tag{3.1}$$

where t: student coefficient, $\alpha/2$: refers to the bilateral interval of confidence of $(1-\alpha)$, S.D.: standard deviation, n: number of replicates.

The lower Se concentration in the LRM and its higher LOQ cannot allow the concentration measurement in the LRM. Consequently Se results obtained later on in this article will only be informative. For As, Cd, Sb, Sn and Pb, the measured and certified/expected values are in agreement, according to the experimental uncertainty
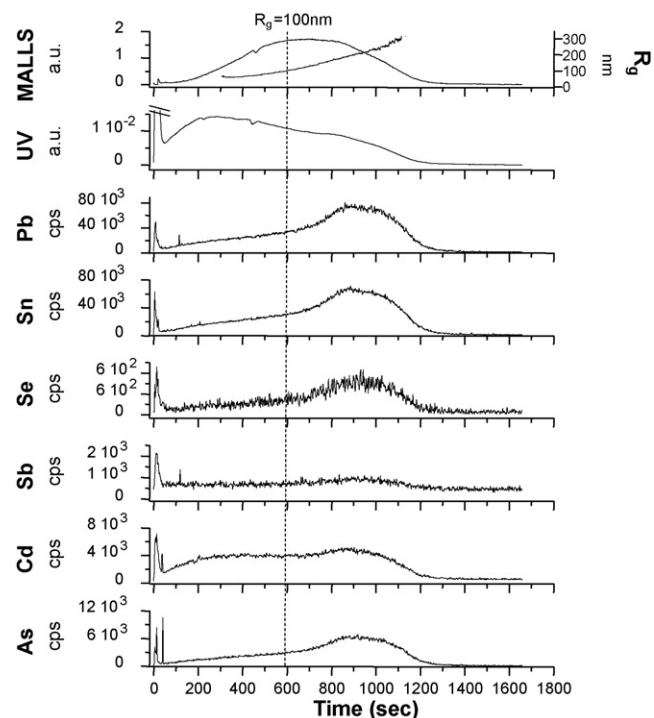
Fig. 4. UV, MALLS and ICP-MS signals from As-Fl-FFF fractionation of a soil solution spiked by Pb, Sn, Se, Sb, Cd and As—injected volume: 150 μL.

and the confidence interval. The relative standard deviation is not over 10% generally, which is satisfactory according to the studied concentration range. Neither loss nor contamination during the different steps of the procedure can be highlighted. With regard to trueness and precision criteria, Q2 method is, thus, validated for all the detected trace elements.

3.3. Element distribution and qualitative analysis

The colloids in the soil leachate sample present a gyration radius varying from about 30–250 nm during the fractionation (MALLS Zimm first order fit formalism calculation). The R_g variation being linear according to the retention time and with a positive slope, the elution during the fractionation occurred conveniently and as expected according to the normal mode.

The Fig. 4 presents UV, MALLS and trace element ICP-MS signals as a function of the elution time. From the replicate analyses, no significant difference of peak shapes was noticed between several runs. The variations of ICP-MS peak areas were ranging from 2% for Sn to 10% for Cd emphasizing the satisfactory repeatability between the different replicates.

Table 2
Limits of Detection (LOD), Limits of Quantification (LOQ) and determination coefficient (R^2) of the calibration curve for the two quantification procedures (Q1 and Q2)

Analytical performances						
	On-line quantification—Q1			Off-line quantification—Q2		
	Absolute LOD (pg)	Absolute LOQ (pg)	R^2 ($n=14$)	Absolute LOD (pg)	Absolute LOQ (pg)	R^2 ($n=14$)
As	334	649	0.9998	500	1160	1
Cd	323	628	0.9997	410	930	1
Sb	n.c.[a]	n.c.[a]	0.9989	470	1080	1
Se	n.c.[a]	n.c.[a]	0.9997	700	1620	0.9999
Sn	188	366	0.9993	370	830	0.9999
Pb	177	343	0.9995	240	530	0.9999

n: number of points. n.c.: not calculated.

[a] Element not present in the colloidal part.

Table 3
Comparison of certified (or known) and measured trace element concentrations in two reference materials (CRM and LRM) by Q2 procedure

Elements	Concentrations (μg L^{-1})			
	SPSWW1		Landfill leachate	
	Certified values	Measured values $C \pm dC$ (R.S.D.%)	Expected values	Measured values $C \pm dC$ (R.S.D.%)
As	100.0 ± 0.5	103 ± 8 (3%)	61 ± 1	60 ± 11 (10%)
Cd	20.0 ± 0.1	21 ± 2 (5%)	0.25 ± 0.07	0.21 ± 0.03 (5%)
Sb	not cer.	<LOD	14 ± 1	13 ± 3 (8%)
Se	not cer.	<LOD	0.36 ± 0.04	<LOQ[a]
Sn	not cer.	<LOD	316 ± 2	286 ± 76 (10%)
Pb	100.0 ± 0.5	100 ± 2 (1%)	5.6 ± 0.3	6 ± 2 (17%)

not. cer.: not certified; C: concentration; dC: error on the concentration and R.S.D.: relative standard deviation.

[a] Not quantified because of higher LOD and sample dilution to prevent foaming during sample preparation.

The first thin peak observed simultaneously for all signals corresponds to materials which are not retained during the fractionation. According to the separation conditions, the elution time and the important UV intensity, this peak could be associated to low-size organic colloidal materials (typically humic substances). The second broad peak corresponds to larger particles of the soil leachate eluted with increasing sizes, as confirmed by MALLS signal. In this part of the fractogram, the UV signal is widely less intense, which could indicate that UV responds either to the turbidity induced by particles or to organic coating on particles. With regard to the elemental distribution (Fig. 4) the colloidal part of the soil leachate shows different affinities according to the trace metal or metalloid considered and according to colloid type. Cd appears to have a bimodal distribution, comparable to UV one. As, Sn and Pb are mainly distributed on the largest particles corresponding to 100–250 nm gyration radius. Se has a similar distribution, despite its very low signal. Sb does not show any signal indicating that it is not significantly associated to colloidal particles. The elements present in dissolved phase and colloidal part with size lower than cut-off (i.e. mainly Sb and Se) were directly removed in the cross-flow.

The different distributions observed can be partly explained by the charge of the elements. In fact, Cd, Pb and Sn were in cationic forms which could induce a high sorption onto particles (mainly negatively charged) of the soil leachate. However, despite the same charge of these elements, significant differences in their respective distribution were previously noticed, suggesting that different types of colloids exist over 30–250 nm gyration radius range. This hypothesis could explain the observed bimodal shape of the UV. Arsenic was in neutral or anionic form but its affinity for inorganic particles (especially oxides) is well known and could explain the signal observed in Fig. 4 [24]. Sb and Se were also in neutral or negative forms inducing a lower sorption in the experimental conditions. Finally, this on-line monitoring directly gives information of the metal and metalloid distribution associated to the colloidal part of the sample and shows the importance of a multi-detection approach, preliminary to a quantitative approach.

3.4. Q1 validation and Q1/Q2 comparison

In order to evaluate the accuracy of the Q1 procedure, the elements associated to the soil leachate colloids were also quantified with Q2. According to the ICP-MS fractograms (see Fig. 4), fractions from the output of FFF channel were collected from the beginning ($t = 0$ s) to the end of the colloidal peak ($t = 1380$ s) and quantified according to the validated Q2 procedure. These values were compared to those obtained with Q1 procedure, integrating the same peaks than those collected. The concentrations obtained with both quantification procedures are presented in Table 4.

As expected and shown by the Sb profile in Fig. 4, the Sb concentration in the collected fractions is lower than the LOD of both quantification procedures. Some integration difficulties were noticed especially when peaks had important fronting as for As, leading to possible over evaluations. The concentration values obtained with the two methods are significantly the same in a 95% confidence interval, the relative standard deviation being satisfactory, in the range 3–11%. So, Q1 protocol is proved to be accurate and is thus validated.

As, Cd, Sn and Pb in the colloidal part can be also quantitatively compared, considering the fractograms presented in Fig. 4 and the qualitative analysis previously made. Thus, As, Pb and Sn concentrations were found to be in the range 30–60 μg L^{-1} significantly over Cd, Sb and Se. Moreover, As, Pb and Sn present also the same colloidal profiles, being mainly distributed on the largest particles (65 ± 5% for the three elements are present in the range 100–250 nm of gyration radius), as previously noticed. These observations suggest a significant affinity of the particles for these three elements. Cd concentration remains lower although this element was distributed over the whole colloidal range. More generally, Q1 procedure appears to be a suitable and a convenient quantitative approach to evaluate elemental concentration linked to colloids of soil solution for environmental applications. Q2 has the obvious convenience to permit fraction collection replicates and addition of these replicates to increase the amount of element in the freeze-dried product. The main advantages of Q1 method is that no sample preparation is needed and analysis is rapid compared to off-line process. The analysis could be carried out within 2 h whereas at least 4 days are needed for Q2 (2 days for the freezing and 2 days for the freeze drying). Moreover the hyphenation directly gives the distribution of the monitored element on the colloidal phase and thus, produces crucial and relevant additional information, also allowing the integration of elemental distribution on different colloidal populations and the determination of the corresponding metal concentrations.

Table 4
Concentrations of the studied trace elements in the colloidal part of the spiked soil leachate, evaluated by the two quantification protocols (Q1 and Q2)

Elements	Concentrations (μg L^{-1})	
	Q1 $C \pm dC$ (R.S.D.%)	Q2 $C \pm dC$ (R.S.D.%)
As	30 ± 3 (4%)	26 ± 5 (8%)
Cd	14 ± 4 (11%)	14 ± 5 (13%)
Sb	≤LOQ	≤LOD
Se	4.9 ± 0.8 (6%)	3 ± 2 (27%)
Sn	59 ± 5 (3%)	50 ± 8 (6%)
Pb	59 ± 5 (3%)	45 ± 10 (9%)

C: concentration; dC: error on the concentration and R.S.D.: relative standard deviation.

4. Conclusion

Two quantification strategies for metals and metalloids associated to colloidal fraction were applied on a natural soil leachate sample. The on-line quantification method gives accurate quantitative results. It is worth stressing that the direct coupling between As-Fl-FFF and ICP-MS presents the advantage to on-line monitor the distribution of the elements associated to colloids according to their size. The off-line quantification method permits to measure the element concentration when the hyphenation is not possible. However, it presents two major drawbacks. The procedure is time-consuming in comparison with Q1 and the high dilution induced by FFF fractionation can impede the quantification of the less abundant elements.

Finally, this work shows the applicability and the convenience of different quantification approaches of trace elements on colloidal phase and permits to enlarge the field of As-Fl-FFF applications.

Acknowledgments

References

[1] J.F. McCarthy, J.M. Zachara, Environ. Sci. Technol. 23 (1989) 496.
[2] J. Buffle, H.P. Van Leeuwen, Environmental Particles, vol. 1, Lewis Publishers, Chelsea, 1992, p. 554.
[3] H. Geckeis, T. Ngo Manh, M. Bouby, J.I. Kim, Colloids Surf. A 217 (2003) 101.
[4] M. Hassellöv, B. Lyven, C. Haraldson, W. Sirinawin, Anal. Chem. 71 (1999) 3497.
[5] J. Buffle, G.G. Leppard, Environ. Sci. Technol. 29 (1995) 2169.
[6] L.J. Gimbert, K.N. Andrew, P.M. Haygarth, P.J. Worsflod, Trends Anal. Chem. 22 (2003) 615.
[7] M.E. Schimpf, K.D. Caldwell, J.C. Giddings, Field-Flow Fractionation Handbook, Wiley Interscience, 2000, p. 616.
[8] D. Amarasiriwardena, A. Siripinyanond, R.M. Barnes, J. Anal. At. Spectrom. 16 (2001) 978.
[9] D.J. Chittleborough, S. Tadjiki, J.F. Ranville, F. Shanks, R. Beckett, Supersoil 2004, in: 3rd Australian New Zealand Soils Conference, 5–9 December, 2004, University of Sydney, Australia, 2004, Published on CDROM.
[10] E. Alasonati, B. Stolpe, M.A. Benincasa, M. Hassellöv, V.I. Slaveykova, Environ. Chem. 3 (2006) 192.
[11] E. Bolea, M.P. Gorriz, M. Bouby, F. Laborda, J.R. Castillo, H. Geckeis, J. Chromatogr. A 1129 (2006) 236.
[12] M. Baalousha, F.V.D. Kammer, M. Motelica-Heino, M. Baborowski, C. Hofmeister, P. Le Coustumer, Environ. Sci. Technol. 40 (2006) 2156.
[13] F.V.D. Kammer, M. Baborowski, S. Tadjiki, W.V. Tümpling, Acta Hydrochim. Hydrobiol. 31 (2003) 400.
[14] B. Lyven, M. Hassellöv, D.R. Turner, C. Haraldson, K. Andersson, Geochim. Cosmochim. Acta 67 (2003) 3791.
[15] A. Siripinyanond, R.M. Barnes, D. Amarasiriwardena, J. Anal. At. Spectrom. 17 (2002) 1055.
[16] B. Stolpe, M. Hassellöv, Geochim. Cosmochim. Acta 71 (2007) 3292.
[17] B. Stolpe, M. Hassellöv, K. Andersson, D.R. Turner, Anal. Chim. Acta 535 (2005) 109.
[18] Norme AFNOR X31-210 Déchets, essais de lixiviation, Association Française de Normalisation, 1992, pp. 13.
[19] D. Plenet, G. Lemaire, Plant Soil 216 (1999) 65.
[20] P. Pinel-Raffaitin, M. Ponthieu, I. Le Hecho, D. Amouroux, L. Mazeas, O.F.X. Donard, M. Potin-Gautier, J. Environ. Monit. 8 (2006) 1069.
[21] M. Hassellöv, F.V.D. Kammer, R. Beckett, in: K.J. Wilkinson, J.R. Lead (Eds.), Environmental Colloids and Particles—Behaviours, Separation and Characterization, John Wiley and Sons, Chichester, 2007, pp. 223–277.
[22] J. Mocak, A.M. Bond, S. Mitchell, G. Scollary, Pure Appl. Chem. 69 (1997) 297.
[23] R.L. Tranter, Design and Analysis in Chemical Research, Blackwell, 2000, p. 576.
[24] P.L. Smedley, D.G. Kinniburgh, Appl. Geochem. 17 (2002) 517.

Review

Stability-indicating determination of meropenem in presence of its degradation product

Nariman A. Elragehy [*], Ezzat M. Abdel-Moety, Nagiba Y. Hassan, Mamdouh R. Rezk [1]

Analytical Chemistry Department, Faculty of Pharmacy-Cairo University, Kasr El-Aini Street, ET-11562 Cairo, Egypt

A R T I C L E   I N F O

A B S T R A C T

Stability-indicative determination of meropenem (MERM) in the presence of its open-ring degradation product, the metabolite, is investigated. The degradation product has been isolated, *via* acid-degradation, characterized and confirmed. Selective quantification of MERM, singly in bulk form, pharmaceutical formulations and/or in the presence of its major degradate is demonstrated. The indication of stability has been undertaken under conditions likely to be expected at normal storage. Among the analytical techniques adopted for quantification are spectrophotometry [first-derivative (^{1}D), first-derivative of ratio spectra (^{1}DD) and bivariate analysis], as well as chromatography [coupled TLC-densitometry and HPLC].

Contents

 * Corresponding author. Fax: +20 2 23628426.
   E-mail address: n_a_ragehy@yahoo.com (N.A. Elragehy).
 [1] Part of Ph.D. study.

1. Introduction

Meropenem (MERM), is (4*R*,5*S*,6*S*)-3-[[(3*S*,5*S*)-5-(dimethyl carbamoyl)-3-pyrrolidinyl]thio]-6-[(1*R*)-1-hydroxyethyl]-4-methyl-7-oxo-1-azabicyclo [3.2.0]hept-2-ene-carboxylic acid, trihydrate (Fig. 1). It is a broad-spectrum carbapenem antibiotic with wide range of activity. It is used mainly for the treatment of serious bacterial infections, including lower respiratory tract, intraabdominal, obstetric/gynecological, urinary tract, skin structure, meningitis, cystic fibrosis and in febrile neutropenia [1–4].

MERM is metabolized inside the human body through hydrolysis to form the opened β-lactam ring product which is pharmacologically inactive [5,6]. In healthy volunteers, 70% of the administered dose is excreted unchanged in urine and 20% as the open-ring metabolite [7].

The literature survey reveals several analytical methods for quantitative estimation of MERM in body fluids and in pharmaceutical formulations. These methods include high-performance liquid chromatography (HPLC) [1,8–12], ultraviolet spectrophotometry [12] and microbiological assay [13]. A chromatographic method for the determination of polymerized impurities in MERM was proposed [14]. The stability of the drug was studied under various conditions [15–17]. Patel and Cook [15] studied the stability of MERM in 0.9% sodium chloride injection. The stability in PVC containers and other elastomeric infusion device was also investigated [16]. Quantification of MERM in plasma and cerebrospinal fluid by micellar electrokinetic capillary chromatography was done [18]. MERM was found to be stable at room temperature in solid state formulations for injection [19]. Carbon dioxide adduct of the drug in bicarbonate solution has been elucidated using ^{1}H NMR and flow-injection quadropole mass spectrometry [20].

In modern analytical laboratory, there is always a need for significant stability-indicating methods of analysis. The present work aimed to develop simple instrumental methods for the quantification of MERM in bulk form or in the presence of its acid-degradate; which is the open-ring metabolite [21]. These methods include first-derivative (^{1}D), first-derivative of the ratio spectra (^{1}DD) and bivariate analysis, as well as chromatographic methods; *namely*, TLC-densitometry method and HPLC.

2. Experimental

2.1. Instruments

Spectrophotometer: Shimadzu UV-1601 PC, dual-beam UV–vis spectrophotometer (Kyoto-Japan), with matched 1 cm quartz cells, connected to an IBM-compatible PC and an HP-600 inkjet printer. Bundled, UV-PC personal spectroscopy software version 3.7, was used to process the absorption and the derivative spectra. The spectral band width was 2 nm with wavelength-scanning speed of 2800 nm min^{-1}.

IR Spectrophotometer: Shimadzu 435 (Kyoto, Japan), sampling was undertaken as potassium bromide discs.

Gas chromatograph coupled to a mass spectrophotometer: GC–MS-QB 1000 EX, Finnigan Nat (USA).

pH-meter, Digital pH/MV/TEMP/ATC meter, Jenco Model-5005(USA). Graffin melting point apparatus model SMP1, Stuarts Scientific Co. Ltd. (UK). Precoated TLC-plates, silica gel 60 F$_{254}$ (20 cm × 20 cm, 0.25 mm), E. Merck (Darmstadt-Germany). Camag TLC scanner 3 S/N 130319 with winCATS software. Camag Linomat 5 autosampler (Switzerland). Camag microsyringe (100 μL).

A liquid chromatograph consisted of an isocratic pump (Agilent Model G1310A), an ultraviolet variable wavelength detector (Model G1314A, Agilent 1100 Series), a Rheodyne injector (Model 7725 I, Rohnert Park, CA, USA) equipped with 20 μL injector loop, Agilent (USA). Stationary phase; a 250 mm × 4.6 mm i.d. C$_{18}$ Lichrosorb^{TM} 10 μm analytical column, Alltech (USA). Mobile phase; 0.05 M ammonium acetate + acetonitrile + methanol + triethylamine, 75:15:10:0.1 (v/v/v/v). The final pH-value was adjusted to 3.0 ± 0.1 by using *o*-phosphoric acid; isocratically at 1 mL min^{-1}. The mobile phase was filtered through a 0.45 μm Millipore membrane filter and was degassed for ~15 min in an ultrasonic bath prior to use. UV-detection was done at 298 nm. The samples were filtered also through a 0.45 μm membrane filter, and were injected by the aid of a 25 μL Hamilton® analytical syringe.

2.2. Materials and reagents

Reference MERM standard (Meropenem trihydrate powder) was kindly supplied by Sumitomo Pharmaceuticals Co. Ltd. (Osaka, Japan). Its potency was found to be 1002 μg mg^{-1} (on anhydrous basis).

Pharmaceutical dosage form (Meronem^{TM}, 500 mg or 1 g) vials were kindly supplied by AstraZeneca Egypt Scientific Office and were claimed to contain 570 mg or 1140 mg (as meropenem trihydrate) equivalent to 500 mg or 1 g (as anhydrous form) of MERM and 104 mg or 208 mg, respectively, of the anhydrous sodium carbonate as excipient.

All calculations and samples preparation for reference material and pharmaceutical formulation were done regarding the anhydrous form.

$C_{17}H_{25}N_3O_5S \cdot 3H_2O$ M.W. (437.52)
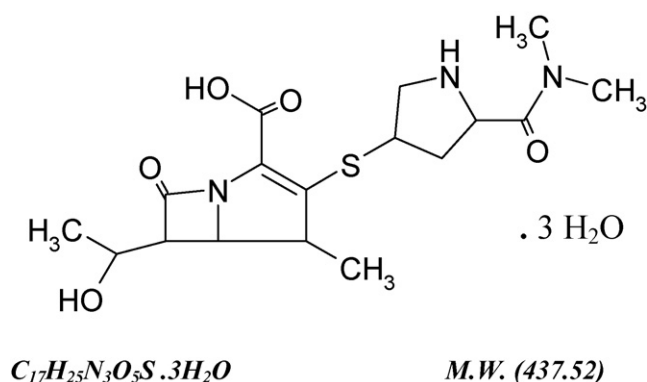
Fig. 1. Structural formula of meropenem trihydrate.

Reference cefotaxime sodium was kindly supplied by Egyptian International Pharmaceutical Industries Company [EIPICO] (10th of Ramadan, Egypt). Its purity was found to be 997 μg mg^{-1} according to the official HPLC method [1].

Hydrochloric acid, n-butanol, acetone, ammonium acetate and anhydrous sodium carbonate: Adwic, El-Nasr Pharm. Co. (Cairo, Egypt). Methanol and acetonitrile: HiPerSolv.®, HPLC-grade, E. Merck (Darmstadt, Germany). Triethylamine LR: Laboratory Rasayan s.d. Fine-Chem Ltd. o-Phosphoric acid (85%): AnalaR BDH-laboratory suppliers' (Poole, England). De-ionized water: Bi-distilled from "Aquatron" Automatic Water Still A4000, Bibby Sterillin Ltd. (Staffordshire, UK).

2.3. Standard solutions

MERM standard solution (1 mg mL^{-1}) in distilled water. Drug degradate standard solution (1 mg mL^{-1}) in distilled water. MERM standard solution (0.5 mg mL^{-1}) in the mobile phase for the HPLC method. Drug degradate standard solution (0.5 mg mL^{-1}) in the mobile phase for the HPLC method. Cefotaxime standard solution (1 mg mL^{-1}) in the mobile phase for the HPLC method. All solutions were prepared with respect to the anhydrous form. They were freshly prepared on the day of analysis and stored in a refrigerator to be used within 24 h.

2.4. Procedures

2.4.1. Degradation of meropenem
Accelerated acid-degradation was performed by dissolving 25 mg of pure MERM powder in ~25 mL of 0.1N hydrochloric acid (final pH was 1.0). The solution was set aside at room temperature for 2 h. Complete degradation was achieved; as investigated by thin layer chromatography. The acid degraded sample was neutralized by anhydrous sodium carbonate powder (to pH 7.0). The solution was evaporated under vacuum nearly to dryness then re-crystallized from methanol. The obtained degradate was characterized by UV-spectroscopy, TLChromatography, melting point, GC/MS- and IR-spectrometry.

2.4.2. Spectrophotometric methods
2.4.2.1. First-derivative (^{1}D) method.
2.4.2.1.1. Spectral characteristics of MERM and its degradate. Two aliquots (0.8 mL) of both MERM and its degradate standard aqueous solutions (each, 1 mg mL^{-1}) were, separately, transferred into two 25 mL volumetric flasks. The volume was completed with distilled water to obtain 32 μg mL^{-1} final concentration, for each. The zero-order and the first-derivative spectra of the prepared solutions were recorded.

2.4.2.1.2. Linearity. Portions equivalent to (0.1–1.5 mL) of MERM standard solution (1 mg mL^{-1}) were separately transferred to a series of 25 mL volumetric flasks. Each flask was completed to the volume with distilled water to reach the concentration range of 4–60 μg mL^{-1}. The amplitudes of the first-derivative peaks were measured at 281 and 315 nm with $\Delta\lambda = 4$ nm and a scaling factor = 100. Calibration graphs were constructed by plotting $\Delta A/\Delta\lambda$ versus concentration. The regression equations were then computed for the studied drug at the specified wavelengths and used for determination of unknown samples containing MERM.

2.4.2.2. First-derivative of ratio spectra (^{1}DD) method.
2.4.2.2.1. Linearity. Standard serial concentrations in the range of 4–60 μg mL^{-1} aqueous solutions of MERM were prepared as under Section 2.4.2.1.2. Accurately 0.8 mL of the degradate standard solution (1 mg mL^{-1}) was transferred into a 25 mL volumetric flask and the volume was completed with distilled water to get a final concentration of 32 μg mL^{-1} to be used as a divisor. The spectra of the prepared standard solutions were scanned (200–400 nm) and stored into the PC. The stored spectra of MERM were divided (amplitude at each wavelength) by the spectrum of 32 μg mL^{-1} of the degradation product. The first-derivative of the ratio spectra (^{1}DD) with $\Delta\lambda = 4$ nm and a scaling factor = 10 was obtained. The amplitudes of the first-derivative peaks of MERM were measured at 284 and 315 nm. Calibration graphs were constructed relating the peak amplitudes of (^{1}DD) to the corresponding concentrations. The regression equations were then computed for the studied drug at the two specified wavelengths and used for determination of unknown samples containing MERM.

2.4.2.3. Bivariate method.
Two series of standard aqueous solutions containing 4–60 μg mL^{-1} of MERM and its degradate were prepared from the stock solution (1 mg mL^{-1}, each) for the bivariate calibration. Spectra of the obtained solutions were recorded and stored into the PC. The regression equations were computed at $\lambda = 220$ and $\lambda = 298$ nm. The concentrations of MERM and its degradate were calculated using the parameters of the linear regression functions evaluated individually for each component at the same wavelength and substituting in the following equations

$$C_{\text{degradate}} = \frac{m_{A2}(A_{AB1} - e_{AB1}) + m_{A1}(e_{AB2} - A_{AB2})}{m_{A2}m_{B1} - m_{A1}m_{B2}}$$

$$C_{\text{MERM}} = \frac{A_{AB1} - e_{AB1} - m_{B1}C_{\text{degradate}}}{m_{A1}}$$

where e_{AB1} and e_{AB2} are the sum of the intercepts of the linear calibration at two wavelengths ($e_{AB1} = e_{A1} + e_{B1}$), m_A and m_B are the slopes of linear regression and C (μg mL^{-1}) is the concentration of MERM and its degradate.

The accuracy of the results was checked by applying the proposed bivariate calibration method for determination of different, blind samples of pure MERM and its degradate. The concentrations were obtained from the corresponding regression equations from which percentage recoveries were calculated.

2.4.3. Chromatographic methods
2.4.3.1. TLC-densitometric method.
2.4.3.1.1. Linearity. Aliquots 2–12 μL of MERM standard solution (1 mg mL^{-1}) were applied in the form of bands on a TLC plate. The band length was 4 mm and dosage speed was 150 nL s^{-1}. The bands were applied 14 mm apart from each other and 10 mm from the bottom edge of the plate. Linear ascending development was performed in a chromatographic tank previously saturated with n-butanol + acetone + water (4:3:3, v/v/v) for 1 h at room temperature. The developed plates were air-dried and scanned at 298 nm using deuterium lamp, absorbance mode at 3 mm × 0.45 mm slit dimension and scanning speed of 20 mm s^{-1}. A calibration curve relating the optical density of each spot to the corresponding concentration of MERM was constructed. The regression equation was then computed for the studied drug and used for determination of unknown samples containing it.

2.4.3.2. Liquid chromatographic method.
2.4.3.2.1. Linearity. Portions 0.1–2 mL from MERM standard solution (0.5 mg mL^{-1} in the mobile phase) were transferred separately into a series of 10 mL measuring flasks and mixed with 0.2 mL of cefotaxime-stock solutions (1 mg mL^{-1}) as an internal standard (IS). The contents of each flask were completed to volume with the mobile phase to get the concentrations of 5–100 μg mL^{-1} of MERM. The samples were then chromatographed using the following chromatographic conditions:

Stationary phase; a $250\,mm \times 4.6\,mm$, i.d. C_{18} Lichrosorb™ $10\,\mu m$ analytical column, Alltech (USA), mobile phase; 0.05 M ammonium acetate + acetonitrile + methanol + triethylamine, 75:15:10:0.1 (v/v/v/v). The final pH-value was adjusted to 3.0 ± 0.1 with *o*-phosphoric acid using a pH-meter. The mobile phase was filtered through a $0.45\,\mu m$ Millipore membrane filter and was degassed for about 15 min in an ultrasonic bath prior to use, flow rate; $1\,mL\,min^{-1}$ [isocratically at ambient temperature ($\sim 25\,^{\circ}C$)], with UV-detection at 298 nm. The samples were filtered also through a $0.45\,\mu m$ membrane filter, and were injected by the aid of a $25\,\mu L$ Hamilton® analytical syringe. To reach good equilibrium, the analysis was usually performed after passing ~ 50–60 mL of the mobile phase, just for conditioning and pre-washing of the stationary phase.

The relative peak area ratios were then plotted *versus* the corresponding concentrations of MERM to get the calibration graph and to compute the corresponding regression equation. Concentrations of unknown samples of MERM were determined using the obtained regression equation.

2.4.4. Analysis of laboratory prepared mixtures containing different ratios of MERM and its degradation product using the suggested methods

Mix aliquots of intact drug and the degraded drug to prepare different mixtures containing 10–90% (w/w) of the degradation product, and proceed as mentioned under each method. Calculate the concentrations from the corresponding regression equations.

2.4.5. Assay of pharmaceutical formulations (Meronem™ vials)

No sample preparation for vials was required other than dissolving the contents of the vial powder in the appropriate solvent for each method. Vials were dissolved in distilled water to get drug concentration of $1\,mg\,mL^{-1}$ for the spectrophotometric methods and the TLC-densitometric method. They were dissolved in the mobile phase to get drug concentration of $0.5\,mg\,mL^{-1}$ for the HPLC method and proceed as mentioned under each method.

2.4.6. Kinetic calculations

The stability of MERM in different solutions; namely, water, 0.1N HCl, 0.9% (w/v) saline and 5% (w/v) dextrose solution was studied. The degradation rate kinetics was determined by plotting log of concentration of drug remaining *versus* time. Each experiment was done in triplicate (analysis by HPLC method) and average values were taken for the analysis.

3. Results and discussion

3.1. Degradation of MERM

The main degradation product of MERM is the open β-lactam ring structure [5,6]. MERM is recommended to be used freshly by intravenous route, so if possibility of degradation to occur, the open β-lactam ring degradate will be formed. Degradation was examined under both acidic and alkaline media and even at elevated temperatures. It was noticed that the main degradate is the open β-lactam ring product which is also the major metabolite of the drug inside the human body. The double bond in the bicyclic structure of the carbapenem nucleus creates a considerable ring strain and increases the reactivity of the β-lactam ring to ring-opening reactions. Literature revealed that acid hydrolysis of imipenem, a carbapenem antibiotic, followed by neutralization is a convenient method to prepare its metabolite (Scheme 1) [21]. This method was used for MERM to prepare its metabolite. Accelerated drug degradation was carried out using 0.1N HCl as mentioned in the

procedures. The melting range of the degradate was 218–$220\,^{\circ}C$ while that of the intact was 208–$210\,^{\circ}C$. In the GC/MS chart, the parent peak was identified at *m/z* 402 (molecular weight of the open-ring metabolite). This proves that the prepared degradate is the main open β-lactam ring metabolite. No other degradation products were observed under the conditions used to prepare the open β-lactam ring degradate.

3.1.1. Spectral changes

A hypochromic effect was observed during degradation of MERM. Once completely degraded, the characteristic peak at 298 nm was vanished (Fig. 2).

3.1.2. TLC-fractionation

TLC-monitoring of the drug degradation was done on thin layer plates of silica gel F_{254} using *n*-butanol + acetone + water (4:3:3, v/v/v) as the developing solvent. The developed plates were visualized under short UV-lamp and/or by subjecting them to iodine vapors. The open-ring degradate (R_f value = 0.16); could be separated from the intact drug (R_f value = 0.34).

3.2. Spectrophotometric methods

3.2.1. First-derivative (^1D) method

Derivative spectrophotometry is a powerful tool in quantification of mixture of drugs. It can be also used as a stability-indicating method for the analysis of drugs in presence of their degradation products; as it can solve the problem of absorption bands overlapping.

A simple, rapid and selective spectrophotometric technique was proposed and applied for the determination of MERM in the presence of its degradation product, either as raw material or in pharmaceutical formulations. This was done by applying the first-derivative (^1D) ultraviolet spectrophotometry. The method can solve the problem of spectral bands overlapping between MERM and its degradate without sample pretreatment or separation steps of the analyzed drug and its degradate.

The absorption spectra of MERM and its degradation product (Fig. 2) show overlapping, little interference and error probability that make the use of direct spectrophotometry for determination of MERM in the presence its degradate inaccurate, especially at higher level of degradate (more than 5%, w/w). When the first-derivative spectra (Fig. 3) were examined, it was found that MERM can be determined at 281 and 315 nm, where its degradate has no contribution (zero crossing). The clear zero crossing of the degradate allows accurate determination of MERM in presence of any level of its degradate up to 60% (w/w). A linear relationship was obtained in the range of 4–60 $\mu g\,mL^{-1}$ for MERM (Fig. 4). The corresponding regression equations were computed and found to be:

$$^1D = 0.0543C + 0.0284 \qquad (r = 0.9995), \text{ at } 281\,nm$$

$$^1D = 0.0866C + 0.0262 \qquad (r = 0.9998), \text{ at } 315\,nm$$

where ^1D is the peak amplitude of the first-derivative curve ($\Delta A / \Delta \lambda$) at the corresponding wavelength, *C* is the concentration of MERM ($\mu g\,mL^{-1}$) and *r* is the correlation coefficient.

The precision of the proposed method was confirmed by the analysis of different concentrations of authentic samples in triplicates. The mean percentage recoveries were found to be 99.76 ± 0.52 at 281 nm and 100.11 ± 0.46 at 315 nm.

3.2.2. Derivative ratio spectrophotometric method

The derivative ratio spectroscopy is a useful tool in quantification of drugs. It could be applied as a stability-indicating method
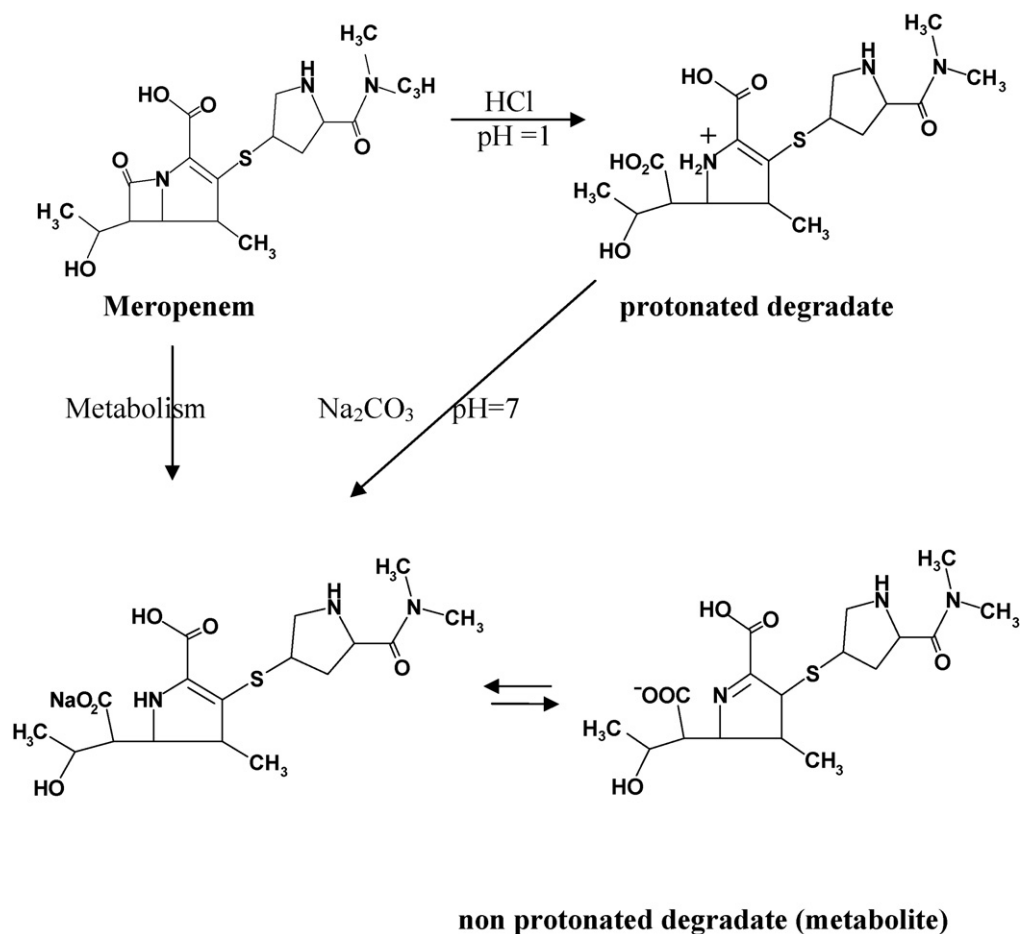
Scheme 1. Degradation of meropenem.

for the determination of MERM in presence of its degradate. It could determine MERM in the presence of higher degradation percentage than the first-derivative method does.

The zero order of the derivative ratio spectra of MERM and the first-order of the derivative ratio spectra are presented in Figs. 5 and 6, respectively. The concentration of the devisor was studied. It was found that upon dividing by $32 \mu g\,mL^{-1}$ of the degradation product led to the best results in terms of sensitivity, repeatability and signal to noise ratio.
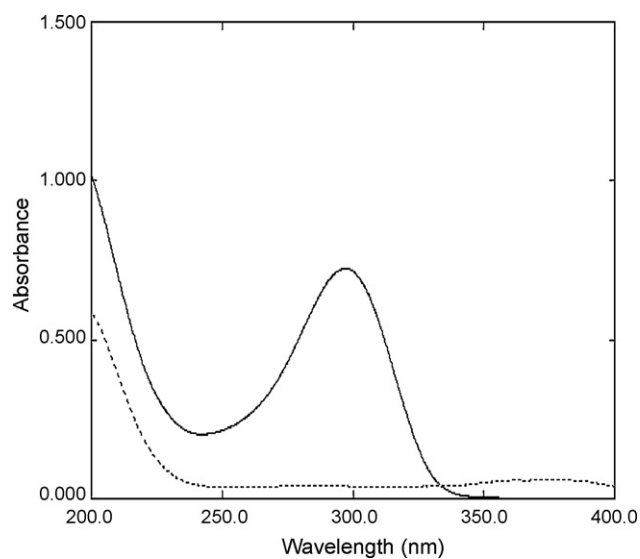
Fig. 2. Zero-order absorption spectra of $32 \mu g\,mL^{-1}$ pure (—) and $32 \mu g\,mL^{-1}$ degraded meropenem (. . .) in distilled water.
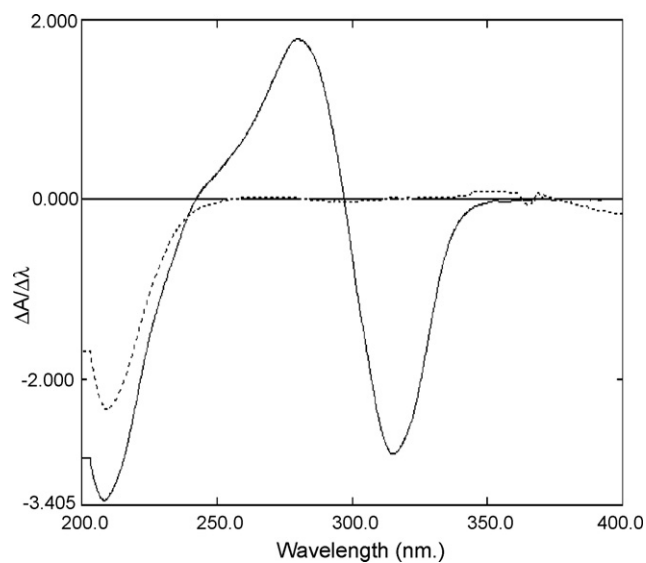
Fig. 3. First-derivative spectra of $32 \mu g\,mL^{-1}$ pure (—) and $32 \mu g\,mL^{-1}$ degraded meropenem (. . .) in distilled water.
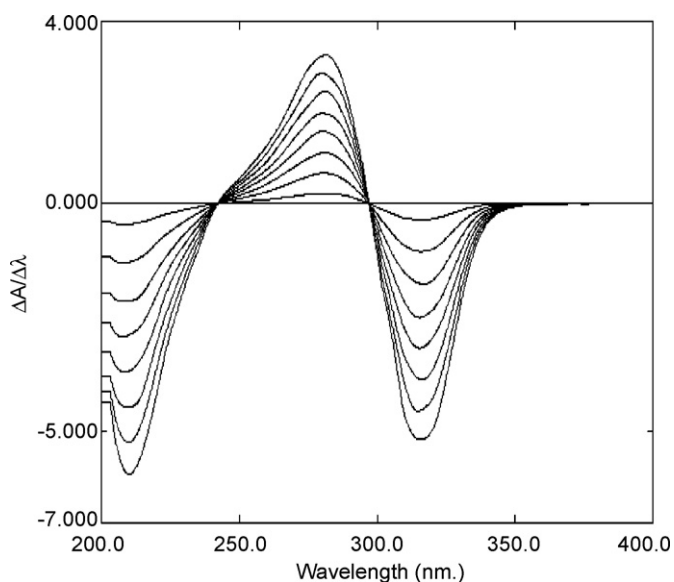
Fig. 4. First-derivative spectra for different concentrations (4, 12, 20, 28, 36, 44, 52 and 60 μg mL^{-1}) of meropenem in distilled water.

Linear calibration graphs were obtained for MERM in concentration range of 4–60 μg mL^{-1} by recording the peak amplitude at 284 and 315 nm using 32 μg mL^{-1} of the degradate as a devisor. The regression equations were computed and found to be:

$$^1DD = 0.1291C + 0.0582 \qquad (r = 0.9997), \text{ at } 284 \text{ nm}$$

$$^1DD = -0.2498C - 0.0805 \qquad (r = 0.9998), \text{ at } 315 \text{ nm}$$

where ^1DD is the peak amplitude of the first-derivative curve for (MERM/its degradate), C is the concentration of MERM (μg mL^{-1}) and r is the correlation coefficient.

The precision of the proposed method was checked by the analysis of different concentrations of authentic samples in triplicates. The mean percentage recoveries were found to be 100.51 ± 0.43 and 100.33 ± 0.31 at 284 and at 315 nm.
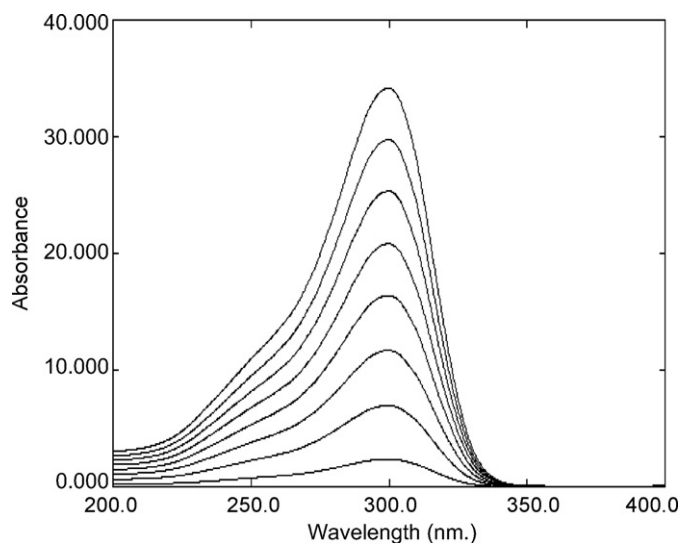
Fig. 5. Zero order of derivative ratio spectra of meropenem 4–60 μg mL^{-1} using 32 μg mL^{-1} of degradate as a divisor.
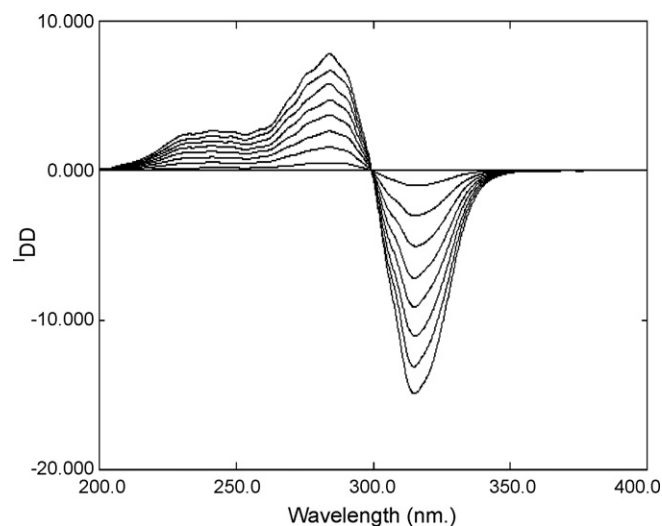
Fig. 6. First order of derivative ratio spectra of meropenem 4–60 μg mL^{-1} using 32 μg mL^{-1} of degradate as a divisor.

3.2.3. Bivariate method

Calibration function was calculated ($r > 0.9990$), m_i- and e_i-values were taken for the bivariate algorithm. The precision of the proposed method was checked by the analysis of different concentrations of both authentic and degradate samples in triplicates. The mean percentage recoveries were found to be 99.94 ± 0.64 for MERM and 100.10 ± 0.66 for the degradate.

The bivariate calibration method may be competitive and in some cases even superior to commonly used derivative spectrophotometric methods as applied for the resolution of binary mixtures. The advantage of bivariate calibration method is its simplicity and the fact that derivatization procedures are not necessary. Unlike other chemometric techniques, there is no need for full spectrum information and no data processing is required. In order to apply the bivariate method to the resolution of binary mixture of MERM and its metabolite, we first select the signals of the two components located at seven wavelengths: 220, 230, 250, 280, 298, 310 and 320 nm. The calibration curve equations and their respective linear regression coefficients are obtained directly with the aim of ensuring that there is a linear relationship between the signal and the concentration. All the calibration curves at the selected wavelengths showed a satisfactory linear regression coefficient ($r > 0.9990$). The slope values of the linear regression were estimated for both components at the selected wavelengths and used for determination of the sensitivity matrices K, proposed by Kaiser's method [22]. The determinants of these matrices were calculated as shown in Table 1. The wavelength set was selected for which

Table 1
Application of the method of Kaiser[a] for the selection of the wavelength set for the mixture meropenem and its degradate

$\lambda_{2(nm)}$	$\lambda_{1(nm)}$						
	220	230	250	280	**298**	310	320
220	0	1312	2265	7348	**10820**	8020	3316
230		0	713	2868	4356	3156	1140
250			0	958	1640	1090	166
280				0	744	144	864
298					0	600	1608
310						0	1008
320							0

The bold values refer to the highest matrix determinant value at which selection of the two wavelengths occur.

[a] The absolute values of determinants of sensitivity matrices K is multiplied by 10^{-8}.

Table 2
Linear regression calibration formulae used for the bivariate algorithm

Binary mixture	Component	Calibration equations[a]	
		$\lambda = 220$ nm	$\lambda = 298$ nm
Meropenem–degradate	Meropenem	$Y = 0.0125X + 0.0138$, $r = 0.9996$	$Y = 0.022X + 0.012$, $r = 0.9998$
	Degradate	$Y = 0.0056X + 0.0091$, $r = 0.9991$	$Y = 0.0012X + 0.0005$, $r = 0.9992$

[a] Where Y is the absorbance value at 220 nm and at 298 nm, X is the concentration in μg mL^{-1} and r is the correlation coefficient.

the highest matrix determinant value was obtained. For the bivariate determination of MERM and its degradate the wavelengths 220 and 298 nm were used. At these selected wavelengths, the one-component calibration curves were obtained in the range of 4–60 μg mL^{-1} for both components. The linear regression calibration formulae used for the bivariate algorithm are presented in Table 2. The mean percentage recoveries were 99.94 ± 0.64 and 100.10 ± 0.66, for MERM and its degradate, respectively. The advantage of this method over the other spectrophotometric methods is the ability for simultaneous determination of the intact drug and its degradate in mixtures.

3.3. Chromatographic methods

3.3.1. TLC-densitometry

A TLC-densitometric method is described for the determination of MERM in the presence of its degradate without prior separation. Different solvent systems were tried for the separation of MERM and its degradate. Satisfactory results were obtained by using a mobile phase composed of n-butanol + acetone + water (4:3:3, v/v/v), where $R_f = 0.34$ and 0.16 for MERM and its degradate, respectively. The separation allows the determination of MERM with no interference from its degradate. The linearity was confirmed by plotting the measured peak area *versus* the corresponding concentrations at 298 nm over a range of 2–12 μg spot^{-1}, where a linear response was obtained. Scanning profile of different concentrations of MERM at 298 nm was shown in Fig. 7. The regression equation was found to be: $A = 0.2421C + 0.1505$, $r = 0.9992$; where A is the

integrated area under the peak $\times 10^{-4}$ for MERM, C is the concentration of MERM in μg spot^{-1} and r is the correlation coefficient. The precision of the proposed method was checked by the analysis of different concentrations of authentic samples in triplicates. The mean percentage recovery was found to be 100.33 ± 0.58.

3.3.2. High-performance liquid chromatography

A simple isocratic high-performance liquid chromatographic method was developed for the determination of MERM in pure form and in pharmaceutical preparation using a 250 mm $\times$ 4.6 mm, i.d. C$_{18}$ Lichrosorb^{TM} 10 μm analytical column. The mobile phase was consisting of 0.05 mol L^{-1} ammonium acetate + acetonitrile + methanol + triethylamine (75:15:10:0.1, v/v/v/v) and the pH was adjusted to 3.0 ± 0.1 using o-phosphoric acid. The mobile phase was chosen after several trials to reach the optimum stationary/mobile-phase matching. Although MERM was degraded under drastic acidic conditions (pH 1) but it showed stability in the mobile phase (pH 3.0 ± 0.1) during the analysis. Most of the reported methods for MERM determination analyze the drug at pH 3 that practically showed the best separation of the drug from its degradate.

System suitability parameters were tested by calculating the capacity factor, tailing factor, the sensitivity factor and resolution. The average retention times under the conditions described are 2.74 min for the open-ring degradate, 3.94 min for intact MERM and 6.59 min for cefotaxime as internal standard. One sample can be chromatographed in 12 min (Fig. 8). The chromatographic sys-

Fig. 7. Scanning profile of different concentrations of meropenem by the TLC-densitometric method.
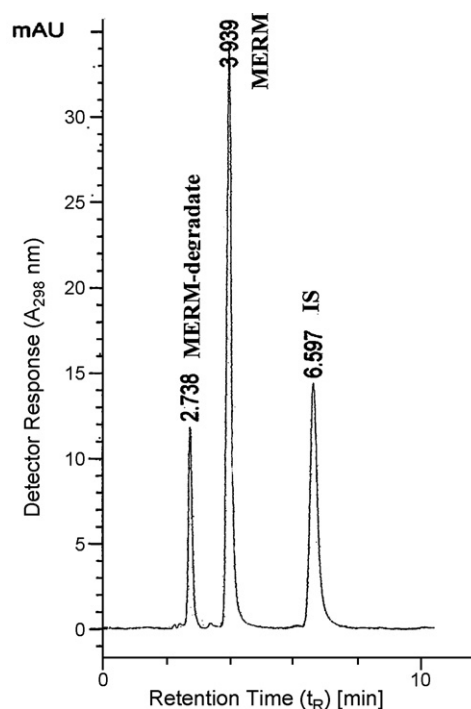
Fig. 8. Liquid chromatographic separation of MERM (3.939 min) from its degradate (2.738 min) and cefotaxime (IS) (6.597 min), experimental conditions (see Section 2).

Table 3
Determination of meropenem in laboratory prepared mixtures by the proposed methods

Determination of intact meropenem in lab. mix.	Methods						
	^{1}D-Method at 281 nm[a]	^{1}D-Method at 315 nm[a]	^{1}DD-Method at 284 nm[b]	^{1}DD-Method at 315 nm[b]	Bivariate method[b]	TLC-densitometric method[c]	HPLC method[c]
Mean ± S.D.	100.13 ± 0.528	100.07 ± 0.497	100.11 ± 0.491	100.09 ± 0.605	99.94 ± 0.641	100.76 ± 0.690	100.16 ± 0.577

[a] Up to 60% degradation product.
[b] Up to 80% degradation product.
[c] Up to 90% degradation product.

Table 4
Determination of meropenem in Meronem^{TM} vials by the proposed methods

Preparation	^{1}D-Method		^{1}DD-Method		Bivariate method	TLC-densitometric method	HPLC method
	At 281 nm	At 315 nm	At 284 nm	At 315 nm			
Meronem vial (0.5 g) Lot CV776							
Mean ± S.D.	99.99 ± 0.575	99.89 ± 0.571	100.37 ± 0.680	100.10 ± 0.543	100.40 ± 0.666	100.44 ± 0.657	100.42 ± 0.590
Meronem vial (1 g) Lot CH979							
Mean ± S.D.	100.15 ± 0.644	99.80 ± 0.712	100.21 ± 0.710	100.13 ± 0.616	100.06 ± 0.910	99.63 ± 0.595	100.07 ± 0.574

tem described in this work allows complete base line separation of meropenem from its degradation product and cefotaxime; (IS). Peak purity was confirmed for the HPLC peaks of both intact MERM and its degradate by a pilot run using a photodiode array detector. Spiking of both intact drug and its degradate assured the presence of only one degradate during preparation of the degradation product also by changing the mobile phase ratios, just one peak appeared corresponding to the drug at ~3.9 min and another one for the degradate at ~2.7 min. Calibration graph was obtained by plotting the peak area ratios (drug/IS) against concentration of MERM (μg mL^{-1}). Linearity range was found to be 5–100 μg mL^{-1} using the following regression equation:

$$A = 0.0819C - 0.0965 \qquad (r = 0.9999)$$

where A is the peak area ratio, C is the concentration of MERM (μg mL^{-1}) and r is the correlation coefficient.

The mean percentage recovery of pure sample was found to be 100.18 ± 0.39.

The robustness of the HPLC method was investigated by analysis of samples under a variety of experimental conditions such as small changes in the pH (3.0–3.5), small changes in acetonitrile/methanol ratio (from 15/10 to 13/12) in the mobile phase and changing the column using a 250 mm × 4.6 mm i.d. C$_{18}$ Zorbax^{TM} 5 μm analytical column, Agilent (USA). The effect on retention time and peak parameters was studied. It was found that the method was robust when the column and the mobile phase ratio were varied. During

these investigations, the retention times were modified, however the areas and peaks symmetry were conserved.

3.4. Stability indication

To assess the stability-indicating efficiency of the proposed methods, the degradation product of MERM was mixed with its intact sample in different ratios and analyzed by the proposed methods. Table 3 illustrates good selectivity in the determination of MERM in the presence of up to 60% (w/w) of its degradate in the first-derivative spectrophotometric method, up to 80% (w/w) by the derivative-ratio and bivariate methods and up to 90% (w/w) by the densitometric and HPLC methods.

The suggested methods were successfully applied for the determination of MERM in its pharmaceutical formulation, showing good percentage recoveries. The validity of the suggested methods was further assessed by applying the standard addition technique (Table 4).

The precision of the suggested methods was also expressed in terms of relative standard deviation of the interday and intraday analysis results (Table 5).

Results of the suggested methods for determination of MERM were statistically compared with those obtained by applying the official HPLC method [1]. The calculated t- and F-values [23] were found to be less than the corresponding theoretical ones, confirming good accuracy and excellent precision (Table 6).

Table 5
Assay parameters and validation sheet for determination of meropenem

Parameter	^{1}D-Method		^{1}DD-Method		Bivariate method	TLC-densitometric method	HPLC method
	At 281 nm	At 315 nm	At 284 nm	At 315 nm			
Range	4–60 μg mL^{-1}		4–60 μg mL^{-1}		4–60 μg mL^{-1}	2–12 μg spot^{-1}	5–100 μg mL^{-1}
Slope	0.0543	0.0866	0.1291	0.2498		0.2421	0.0819
Intercept	0.0284	0.0262	0.0582	0.0805		0.1505	−0.0959
Mean	99.76	100.11	100.51	100.33	99.94	100.33	100.18
S.D.	0.524	0.458	0.425	0.311	0.641	0.576	0.393
Variance	0.275	0.210	0.181	0.097	0.411	0.332	0.154
Coefficient of variation	0.525	0.457	0.423	0.310	0.642	0.574	0.392
Correlation coefficient (r)	0.9995	0.9998	0.9997	0.9998		0.9992	0.9999
R.S.D. (%)[a]	0.465–0.562	0.535–0.567	0.451–0.512	0.519–0.589	0.652–0.725	0.589–0.682	0.621–0.825
R.S.D. (%)[b]	0.439–0.575	0.657–0.518	0.449–0.562	0.551–0.628	0.591–0.684	0.521–0.591	0.598–0.782

[a] The interday (n = 6) relative standard deviations of (10 μg mL^{-1} and 50 μg mL^{-1}) of meropenem by the proposed methods and (5 μg spot^{-1} and 10 μg spot^{-1}) for the TLC-densitometric method.
[b] The intraday (n = 5) relative standard deviations of (10 μg mL^{-1} and 50 μg mL^{-1}) of meropenem by the proposed methods and (5 μg spot^{-1} and 10 μg spot^{-1}) for the TLC-densitometric method.

Table 6
Statistical comparison for the results obtained by the proposed methods and the official method for the analysis of meropenem

Parameter	[1]D-Method		[1]DD-Method		Bivariate method	TLC-densitometric method	HPLC method	Official HPLC method [1]
	At 281 nm	At 315 nm	At 284 nm	At 315 nm				
Mean	99.76	100.11	100.51	100.33	99.94	100.33	100.18	100.23
S.D.	0.524	0.458	0.425	0.311	0.641	0.576	0.393	0.415
Variance	0.275	0.210	0.181	0.097	0.411	0.332	0.154	0.172
n	8	8	8	8	8	6	10	6
F-test	1.60 (4.88)[*]	1.22 (4.88)[*]	1.05 (4.88)[*]	1.77 (4.88)[*]	2.39 (4.88)[*]	1.93 (5.05)[*]	1.117 (5.05)[*]	
Student's t-test	1.872 (2.179)[*]	0.512 (2.179)[*]	1.236 (2.179)[*]	0.495 (2.179)[*]	1.025 (2.179)[*]	0.345 (2.228)[*]	0.238 (2.145)[*]	

[*] The values in the parenthesis are the corresponding thoretical t- and F-values at $P = 0.05$ [23].

3.4.1. The kinetic order

Estimation of the kinetic order of the acid-degradation of MERM could be done by calculating the percentage of the remaining drug concentration and its logarithmic value at different time intervals during the hydrolysis process. Assay of MERM was carried out by adopting the developed HPLC method. The degradation process of meropenem follows pseudo-first-order kinetics during degradation as indicated by the straight line relationship between log the percentage of the remaining drug concentration *versus* time. Lower rate of degradation was observed for the dosage formulation (containing sodium carbonate additive) in water, 0.9% (w/v) saline solution and in 5% (w/v) dextrose solution. It was up to 5% degradation after 8 h in water or saline solutions and after 3 h in dextrose solution.

4. Conclusion

The suggested methods are found to be simple, accurate, selective and equally sensitive with no significant difference of the precision compared with the official HPLC method of analysis [1]. Application of the proposed methods to the analysis of MERM in its pharmaceutical formulation shows that neither the excipient nor the degradation product interferes with the determination.

References

[1] The United States Pharmacopeia, 28th ed., The United States Pharmacopeial Convention, Rockville, 2005, pp. 1218–1219.

[2] S.C. Sweetman (Ed.), Martindale The Complete Drug Reference, 34th ed., Pharmaceutical Press, London, UK, 2005, p. 229.
[3] M.A. Pfaller, R.N. Jones, Diag. Microbiol. Infect. Dis. 28 (1997) 157.
[4] J.R. Edwards, J. Antimicrob. Chemother. 36 (1995) 1.
[5] N.L. Matthew, M.L. Harriet, Drugs 60 (2000) 619.
[6] W.A. Craig, Clin. Infect. Dis. 24 (1997) 266.
[7] L.A. Burman, I. Nilsson-Ehle, M. Hutchison, S.J. Haworth, S.R. Norrby, J. Antimicrob. Chemother. 27 (1991) 219.
[8] S. Bomparde, L. Ferrante, M. De Martinis, L. Leone, J. Chromatogr. A 812 (1998) 249.
[9] M. Ehrlich, F.D. Daschner, K. Kummerer, J. Chromatogr. B 751 (2001) 357.
[10] Y. Ozkan, I. Kucukguzel, S.A. Ozkan, H.Y. Aboul-Enein, Biomed. Chromatogr. 15 (2001) 263.
[11] C. Robatel, T. Buclin, P. Eckert, M.D. Schaller, J. Biollaz, L.A. Decosterd, J. Pharm. Biomed. Anal. 29 (2002) 17.
[12] A.S.L. Mendez, M. Steppe, E.E.S. Schapoval, J. Pharm. Biomed. Anal. 33 (2003) 947.
[13] A.S.L. Mendez, V. Weisheimer, T. Oppe, M. Steppe, E.E.S. Schapoval, J. Pharm. Biomed. Anal. 37 (2005) 649.
[14] S.Y. Cai, C.Q. Hu, J. Pharm. Biomed. Anal. 37 (2005) 585.
[15] P.R. Patel, S.E. Cook, Am. J. Health-Syst. Pharm. 54 (1997) 412.
[16] D.L. Smith, S.M. Bauer, D.P. Nicolau, Am. J. Health-Syst. Pharm. 61 (2004) 1682.
[17] S. Jaruratanasirikul, S. Sriwiriyajan, Southeast Asian J. Trop. Med. Public Health 34 (2003) 627.
[18] Y.W. Chou, Y.H. Yang, J.H. Chen, C.C. Kuo, S.H. Chen, J. Chromatogr. B 856 (2007) 294.
[19] Y. Takeuchi, Y. Takebayashi, M. Sunagawa, Y. Isobe, Y. Hamazume, A. Uemura, T. Noguchi, Chem. Pharm. Bull. 41 (1993) 1998.
[20] O. Almarsson, M.J. Kaufman, J.D. Stong, Y. Wu, S.M. Mayr, M.A. Petrich, J.M. Williams, J. Pharm. Sci. 87 (1998) 663.
[21] R.W. Ratcliffe, K.J. Wildonger, L.D. Michele, A.W. Douglas, R. Hajdu, R.T. Goegelman, J.P. Springer, J. Hirshfield, J. Org. Chem. 54 (1989) 653.
[22] D.L. Massart, B.G.M. Vandeginste, S.N. Deming, Y. Michotte, L. Kaufman, Chemometrics: A Textbook, Elsevier, Amsterdam, 1988, p. 124.
[23] M.R. Spiegel, L.J. Stephns, Schaum Outline of Theory and Problems of Statistics, Schaum Outline Series, NY, 1999.

The effects of grinding methods on metals concentrations in soil

Deborah R. Felt [a],[*], Anthony J. Bednar [a], Thomas Georgian [b]

[a] U.S. Army Engineer Research and Development Center, 3909 Halls Ferry Road, Vicksburg, MS 39180, United States
[b] U.S. Army Environmental and Munitions Center of Expertise, 1616 Capitol Avenue, Suite 9200, Omaha, NE 68102-9200, United States

ARTICLE INFO

ABSTRACT

Multi-increment sampling (MIS) has been most extensively used for munitions constituents at environmental sites where a high degree of contaminant heterogeneity exits. A revised method (USEPA Method 8330B) for explosives that uses MIS was announced in the fall of 2006, but similar guidance has not been reported for testing metals in soils. Questions have been raised as how to prepare representative analytical samples for metals determination from field composites. Three different grinding procedures were used in this study for three soil types to determine if grinding (relative to homogenizing soil without grinding) increases metal concentrations and decreases variability. The performance of these procedures was demonstrated via the analysis of replicates ($n = 16$ for two soil types) using statistical evaluations that included calculations of various descriptive statistics (e.g., medians, means and standard deviations), Kruskal–Wallis (KW) tests for the medians and two tests for the variances (Bartlett's and Levene's test). There was a slight increase in concentrations for several of the metals in the clay loam soil after grinding, although the increases were a small percentage of the concentrations measured. The standard deviations (and variances) for replicate digestions and analyses generally decreased, although anomalies were observed. The grinding methods increased precision overall, however, the data indicated that the roller mill grinding was not as effective as the other grinding methods tested.

Published by Elsevier B.V.

1. Introduction

Studies done for training and firing ranges in both the United States and Canada have shown that munitions constituents, concentrations, fragment sizes and spatial distributions greatly vary within individual training ranges, as well as between different ranges [1,2]. In order to achieve representative field samples for ranges, multi-increment sampling (MIS) strategies have been developed for explosives analysis. MIS typically entails collecting 30 or more soil aliquots (e.g., using a coring device for surface soils) that are combined to produce a single composite sample of at least 1 kg [3–8]. The set of soil aliquots or "increments" is usually collected within some pre-defined boundary (referred to as the "decision unit") using either random or systematic random sampling. The single composite sample is then air-dried and ground to assure homogeneity for explosives analysis. Metals are also potential contaminants of concern for active and inactive training and firing ranges [9–11]. The Department of Defense has developed the Munitions Response Site Prioritization Protocol to assign priorities

for response action to defense sites containing these constituents [12,13].

However, questions have been raised as how to prepare representative analytical samples for metals analysis from these field composites. Traditional methods for the preparation of soil samples for metal analysis, such as USEPA Methods 3050B and 3051, recommend sample masses of 1 g or less for digestion and analysis. Although these methods recommend that about 200 g of sample be collected in the field, the sub-sampling of the 1-g masses for digestion and analysis typically entails little or no sample preparation. For example, guidance for sample preparation for sub-sampling in Method 3050B is limited to the following: "Mix the sample thoroughly to achieve homogeneity and sieve, if appropriate and necessary, using a USS #10 sieve." Multi-increment sampling typically entails collecting a larger sample mass in the field (e.g., at least 1000 g for explosives using Method 8330B) and doing extensive sample preparation (e.g., homogenization through grinding) prior to sub-sampling to reduce variability and sub-sampling errors. The non-routine sample preparation procedures and lack of experience with the MIS at some production laboratories have hindered its implementation.

Grinding is not an uncommon sample preparatory step, as it is recommended by the U.S. Geological Survey [14], the Canadian Society of Soil Science [15], and U.S. Environmental Protection

* Corresponding author. Tel.: +1 601 634 3576; fax: +1 601 634 3518.
E-mail address: Deborah.Felt@usace.army.mil (D.R. Felt).

Agency [16], however it is not specified in the traditional USEPA Method 3051. The Canadian Society of Soil Science recommends routine grinding of soil to pass through a 2 mm screen prior to most soil analyzes [15]. Another study modified USEPA Method 3050B by adding drying, grinding, and sieving procedures [17]. Specific grinding methods and equipment were not specified in these studies. Additionally, it has been suggested that stainless steel equipment was generally satisfactory, but should be used with caution because of the number of metals in that material [15]. In particular, soil samples prepared for USEPA Method 8330B are typically ground with ring puck mills with steel grinding surfaces that can introduce significant metal contamination for low-level analyses.

Homogenization using grinding with non-metallic grinding surfaces and containers for the preparation of soil samples for metals analysis at the laboratory was evaluated in the present study. The overall objective of this study was to obtain a better understanding of the technical requirements for processing large soil samples prior to metals analysis. Compared with samples that are homogenized without any grinding, it was expected that analyte concentrations in ground samples would not significantly increase (i.e., a large positive bias would not be observed) and that variability would decrease (i.e., better measurement precision would be achieved). This information will enable the development of practical strategies that support the MIS approach for environmental studies that require metal analyses.

2. Experimental

2.1. Materials and methods

Three different grinding procedures, all using non-metallic grinding surfaces and containers: (1) mortar and pestle (MP), (2) roller mill (RM) and (3) pulvisette (PS) were investigated; three different solid materials were used: (1) Ottawa Sand (2) Waterways Experiment Station (WES) soil and (3) Grenada Loring (GL) soil. The Ottawa Sand was purchased from Fisher Scientific and served as a contamination control for the grinding procedures. The WES soil has been classified as a loess (98% fines), with a cation exchange capacity of 5 meq/100 g, total organic carbon content of 3.14%, and a pH of 8.70. The Grenada Loring soil has been classified as a silty clay loam; its geochemical characteristics are described elsewhere [18]. Both WES and GL soils are representative of some soils found on training and firing ranges. The performance of the sample preparation procedure was demonstrated via the analysis of replicates using statistical evaluations as described below.

All acids, chemicals, and standards used for the digestions were of ultrapure reagent grade and were used as received. The deionized water had a resistivity of 18.3 MΩ cm. The mechanical grinding devices used in this study included a roller mill purchased from Sepor, Inc. (Wilmington, CA) and a Fritsch Pulverisette 7 (Idar-Oberstein, Germany). The Sepor roller mill was a continuous duty jar drive equipped with a variable-speed DC drive for an output range of 20–345 roller RPM, which can achieve a jar speed range of 5–86 revolutions per minute (RPM). One kilogram of solid material was processed for 6 h in grinding jars, which were constructed of ultra-high fired alumina (85% $A1_2O_3$). To each grinding vessel, 12 grinding balls were added. The body of each jar was externally coated with a thick layer of polyurethane to prevent breakage. The grinding jars were equipped with a positive lid locking bar and precision-fit covers with neoprene gaskets.

The Fritsch Pulverisette 7 is a laboratory planetary mill used for high-speed grinding of liquid or solid samples. Each sample was crushed in agate (SiO_2) grinding bowls by agate grinding balls. Approximately 35 g of soil was placed in each grinding bowl and processed in the pulverisette for 15 min. The 35-g aliquots were then combined before further processing was done. The soil in the bowl was ground by the centrifugal forces from the rotation of the grinding bowl around its own axis and the rotating supporting disc.

The mortars and pestles used in this study were made from hard chemical-porcelain ware. The mortars had a lip and were glazed on the outside. The pestles were glazed to the grinding surface. Soil aliquots of about 70 g were ground for about 15 min in the mortar with the pestle to pass the soil through a #40 sieve. The ground soil aliquots were then combined for additional sample preparation.

All solid samples (sample size $n = 16$ per treatment for the WES and GL soils and $n = 3$ for Ottawa Sand blanks) were acid digested following USEPA Method 3050B (4) using nitric acid and hydrogen peroxide in borosilicate glass digestion vessels. Samples were heated during digestion on a DigiPrep heating block purchased from SCP Science (Champlain, NY). Digested samples were analyzed for metals using a PerkinElmer Elan 6000 inductively coupled plasma mass spectrometer (ICP-MS) (Wellesley, MA). The plasma was operated at 1200 W, cross-flow nebulizer flow of 0.85 mL/min, sample flow rate of 1.5 mL/min and integration time per analyte of 50 ms with three instrumental replicates. Rhodium (internal standard) was added in-line prior to the nebulizer to correct for instrumental drift during analytical batches. Method detection limits of 0.2–0.5 μg/L and reporting limits of 2–5 μg/L were obtained, depending on the element. This produced reporting limits of 0.4–1 mg/kg (example 2 μg/L × 0.05 L digestate/0.5 g soil).

2.2. Quality control

The ICP-MS was calibrated using a series of blanks and calibration standards that contained all the metals of interest at concentrations of 0, 1, 10 and 100 μg/L. In addition to a number of target analyte list (TAL) metals, rare earth metals were included in the analyses to determine if grain size reduction through grinding increased metal concentrations (presumably, by increasing the efficiency of the acid extractions). The types of quality controls samples included in this study are listed in Table 1.

Two types of standard reference samples were analyzed for external quality control. One was a solid, standard reference material, #8704, procured from the U.S. National Institute of Standards and Technology (NIST) and the second (ERA) was a liquid quality control standard, #500, purchased from Environmental Resource Associates (Golden, CO).

2.3. Analytical sample preparation

Approximately 4 kg of each solid material was manually mixed and passed through a #10 stainless steel sieve, as recommended in USEPA Method 3050B. "Soil" was defined as the material that passed through the sieve. Each soil was then divided into four equal 1-kg aliquots by random sampling. One aliquot was left unground, whereas the three remaining 1-kg aliquots were ground using a mortar and pestle, roller mill or pulvisette, until the soil passed through a #40 sieve. A #40 sieve (425 μm openings) was used to reduce sub-sampling variability to a degree that a 0.5 g aliquot (sub-sample) would be expected to be representative of the 1 kg sample (according to Gy's sampling theory) [19]. Method 3050B recommends a 1-g (dry-weight) sample aliquot be diluted to 100 mL after acid digestion, whereas equivalent methods, such as Method 3051, recommend an aliquot of 0.2–0.5 g. Therefore, the 0.5 g aliquots were diluted to volumes of 50 mL after the acid digestions to maintain the same sample to reagent ratios as in Method 3050B. Soil sub-samples ($n = 16$ for soils, $n = 3$ for sand blanks) of 0.5 g for each of the four treatments were acid digested using nitric acid and hydrogen peroxide following USEPA Method 3050B. The digested samples

Table 1
Quality control samples used in this study

Abbreviation	Title	Comment
ICV	Initial calibration verification	Verifies calibration from a second source standard (relative to the initial calibration standard)
CCV	Continuing calibration verification	Verifies instrument calibration throughout sample analysis
CCB	Continuing calibration blank	Monitors carry over and reagent purity throughout sample analysis
PBS	Preparation blank sample	Monitors contamination for the digestion and analysis
LCS	Laboratory control sample	Verifies analyte recoveries for digestion and analysis
NIST	Buffalo River sediment, #8704	NIST-traceable solid standard (reference soil)
ERA	Quality control standard, Catalog #500, Lot# 07074	External source Quality Assurance (QA) standard
MS	Matrix spike – at least one per treatment	Verifies analytes can be recovered from each soil
R	Replicate – one per analysis	Monitors instrument precision
A	Analytical spike – one per analysis	Monitors instrument accuracy and bias

were then filtered, diluted to 50 mL and analyzed for metals using ICP-MS following USEPA Method 6020. The unground sub-samples (and analytical data) were labeled "UG." The remaining aliquots (and resulting analytical data) were labeled as follows: "RM" for roller mill, "PS" for the pulverisette and "MP" for the mortar and pestle.

2.4. Statistical evaluations

The statistical evaluation of the soil data included the calculation of various descriptive statistics such as the sample median, median, and standard deviation (e.g., to evaluate central tendency and dispersion, respectively). The following two-sample hypothesis tests were also done: The KW tests for the medians, two tests for the variances (Bartlett's and Levene's test) and the sign test (to evaluate overall differences between the medians). These tests were done using the commercial statistical software package, MINITAB Version 14.2. The 95% level of confidence was used for all of the statistical tests. For the KW tests and the tests for the variances, the null or baseline hypotheses were that all of the medians or variances are equal, where p-values <0.05 indicate one or more variances or medians are different. The Levene's test was typically used to evaluate the variances as many data sets were not normally distributed and Bartlett's test is sensitive to departures from normality. Similarly, the non-parametric KW tests were used for the statistical evaluations of the median metal concentrations.

Most of the statistical hypothesis tests were two-tailed, identifying non-directional differences for one or more of the data sets (e.g., changes in the medians rather than increases in the medians). Simple multi-sample two-tailed hypothesis tests such as the KW and Levene's test were primarily used for convenience. Large p-values indicated that there was no change in the medians or variances but small p-values needed to be carefully interpreted (for determining whether grinding increased the medians or reduced the variability). The thorium results for the WES soil illustrate how small p-values were interpreted. The small p-value for the KW test ($p < 0.05$) indicated that at least one of the treatment medians was statistically different. However, the treatment medians were different because the UG median was larger than the other treatment medians (3.71 compared with 3.53, 3.51 and 3.55), not because grinding increased the medians. Similarly, there was also at least one difference for the variances of the four treatments (p-values for the Levene's and Bartlette's tests <0.05). However, this occurred because the variance for the RM treatment was larger than the other variances, not because grinding reduced the variances.

A large number of statistical plots (e.g., normal probability and box plots) were done to support the statistical evaluations; a number of two-sample directional hypothesis tests were also done when the non-directional hypothesis test identified significant differences (e.g., to determine whether grinding increased the medians or reduced variability), but most of these results were not included (e.g., primarily for purposes of brevity).

3. Results and discussion

3.1. Quality control samples

The means of the experimental values obtained for the quality control samples are listed in Table 2. The certified NIST reference soil had low recoveries for some analytes (V, Cr, Sb, Ba, U, Ce and Th). However, overall the quality control samples had acceptable recoveries. Laboratory control sample (LCS) recoveries were all within acceptable limits and the preparation blank samples (PBS) had low metals concentrations, except for boron and phosphorus. It is likely that some of the boron observed in the digestion solutions was the result of the use of borosilicate glass digestion vessels and phosphorus can be a contaminant in nitric acid.

The low recoveries for some of the analytes can be attributed to the digestion method that was used. EPA Method 3050B utilizes nitric acid and hydrogen peroxide when the samples are analyzed using ICP-MS. The method also allows the use of hydrochloric acid for the digestion procedure (to increase its metal extraction

Table 2
Experimental results for quality control samples

Analyte	Average values of quality control samples		
	PBS (ug/g)	LCS (% REC)	NIST (% REC)
Be	<2	94.7	NA
Ti	<2	94.2	NA
V	<2	92.6	25.0
Cr	<2	91.8	59.7
Mn	<2	94.3	94.4
Co	<2	92.0	83.0
Ni	<2	91.3	88.1
Cu	<2	92.9	NA
Zn	<2	88.1	88.7
As	<2	86.1	NA
Se	<2	85.6	NA
Sr	<2	89.4	NA
Mo	<2	89.5	NA
Ag	<2	91.2	NA
Cd	<2	87.9	98.6
Sn	<2	98.7	NA
Sb	<2	91.8	15.9
Ba	<2	92.1	22.2
Tl	<2	92.0	NA
Pb	<2	95.5	98.0
U	<2	80.8	23.5
Ce	<2	NA	34.9
Gd	<2	NA	NA
La	<2	NA	NA
Nd	<2	NA	NA
Pr	<2	NA	NA
Sm	<2	NA	NA
Th	<2	76.9	37.6
B	16.5	NA	NA
P	17.0	NA	NA
Zr	<2	NA	NA
Rb	<2	NA	NA

Table 3
Recovery results for matrix spike samples

Analyte	Averages of matrix spike samples (% recoveries)									
	Sand		Grenada Loring soil				WES soil			
	UG	MP	UG	RM	PS	MP	UG	RM	PS	MP
Be	97.7	97.8	102.4	105.6	101.1	107.5	103.4	105.2	109.3	106.3
Ti	100.0	95.9	107.2	118.1	103.0	102.3	97.7	110.5	102.7	99.8
V	97.2	98.1	112.6	115.8	108.3	114.2	114.7	120.5	125.9	114.2
Cr	97.8	99.6	106.4	107.2	103.7	108.1	102.2	103.2	108.9	105.5
Mn	96.7	98.5	66.8	182.1	113.3	146.9	195.9	160.4	158.5	49.6
Co	95.8	96.6	96.0	99.5	95.8	99.0	99.6	98.9	105.2	99.9
Ni	95.7	95.3	96.1	97.8	95.9	99.5	97.6	99.6	102.8	97.7
Cu	98.4	96.3	97.5	91.9	95.7	99.0	95.3	95.5	99.5	93.8
Zn	88.5	90.0	93.2	96.4	94.0	95.1	95.1	95.6	97.4	95.0
As	91.2	90.9	93.7	96.1	93.2	98.1	92.9	94.7	96.6	93.8
Se	90.1	88.6	91.0	93.9	90.5	95.8	93.5	96.1	98.0	95.4
Sr	95.2	96.6	112.0	116.6	120.7	116.0	116.5	131.0	132.7	118.8
Mo	94.5	96.5	86.8	89.7	86.3	88.4	93.6	95.8	98.8	93.7
Ag	95.6	95.5	96.1	97.1	94.8	98.5	93.8	95.8	99.3	96.0
Cd	90.8	92.1	94.9	97.2	94.6	95.8	94.0	95.1	98.3	94.1
Sn	93.9	97.9	145.0	91.0	93.0	97.0	69.9	70.2	73.8	67.1
Sb	95.0	95.9	12.1	11.8	10.3	10.8	40.1	39.8	39.9	29.4
Ba	94.0	96.2	109.0	113.5	109.2	115.3	106.3	105.1	109.2	100.1
Tl	95.9	94.6	98.2	101.3	100.5	107.7	95.0	93.3	97.2	92.7
Pb	95.8	98.4	102.4	102.6	105.2	112.5	96.5	95.2	98.7	92.8
U	88.4	86.8	92.5	95.5	93.4	101.1	81.2	80.8	84.8	79.1
Th	86.2	81.9	88.4	94.3	89.3	99.2	77.8	79.4	90.9	76.7

efficiency) if the samples are analyzed by ICP-AES. Hydrochloric acid is not typically used for ICP-MS analyses because of isobaric interferences in the plasma from chloride ions (e.g., $^{40}Ar^{35}Cl$ on ^{75}As, $^{16}O^{35}Cl$ on 51 V and $^{16}O^{37}Cl$ on ^{53}Cr). ICP-MS analyses were used because trace element determinations were needed, as indicated by the low metal concentrations in the soil samples. The use of only nitric acid and hydrogen peroxide for the digestions could have resulted in the lower recoveries for some of the metals [20].

However, it should be noted that the recoveries were within acceptable limits for many of the elements determined. Furthermore, even if it is assumed that the use of only nitric acid resulted in lower recoveries (i.e., a low bias for the reported metal concentrations), this would not affect the comparability or reproducibility of the results. Bias from the digestion procedure would change the medians but not the differences between medians (e.g., for the KW tests). Method 3050B is not a total digestion technique for most samples; rather it is a very strong acid extraction that will dissolve most elements that could become "environmentally available." By design, elements bound in silicate structures are not normally dissolved by this digestion procedure as they are not usually mobile in the environment.

The matrix spike recoveries for most elements were within 15% of the nominal values, as shown in Table 3. Antimony recoveries are low because hydrochloric acid was not used in the digestion procedure as explained above [20]. The spike concentrations for elements such as Mn and Sr were small relative to the native concentrations in the samples (less than a 1:10 ratio); therefore, spike recoveries for these analytes were not considered to be representative. The matrix spike results for the Ottawa Sand samples that were ground using the RM and the PS were not included in Table 3 because the spike was inadvertently not added to those samples; however, the recoveries for the UG and MP Ottawa Sand samples are acceptable.

3.2. Ottawa Sand

Metals concentrations for the sand samples, ground and unground, were generally low with small standard deviations as shown in Table 4. This is attributable to the homogeneity of the parent material; Ottawa Sand is a primarily pure silica material with

uniform grain size. It was included in the study as a control to detect contamination from the sample processing. These results indicate that few, if any, metals were introduced into the samples during grinding, owing to the use of non-metallic grinding and digestion equipment.

3.3. GL soil

The analyte concentrations for the GL soil samples are listed in Table 5. The zinc results for the GL soil were typical of other metals that were evaluated during the study. There was a slight increase in analyte concentration in the ground samples versus the unground samples and the standard deviations for the ground samples tended to be smaller. The unground sample concentrations were typically within one standard deviation of the ground sample concentrations. For example, the zinc concentration in the unground GL soil was 27.7 μg/g with a standard deviation of 6.0 μg/g. The zinc concentrations in the ground samples were 35.0 ± 4.9, 28.5 ± 2.7, and 30.3 ± 3.2 μg/g for the RM, PS, and MP samples, respectively.

The medians and p-values derived for the GL soil data are listed in Table 6 and results of the sign test for the medians are illustrated in Table 7. The overall differences in the medians between the unground (UG) and ground samples (RM, PS, and MP) for most of the metals were initially evaluated using the sign test. (Metals in the GL soils at low concentrations at or below the reporting limits were not evaluated.) For each metal, the median of the UG results was subtracted from the corresponding median of PS, MP and RM results (producing 63 differences or data points – 3 grinding treatments × 21 metals per treatment). If grinding did not increase the medians on the average, then the number of positive and negative differences should have been roughly equal. A two-tailed sign test was done to determine if the differences were different from zero on the average. The sign showed a significant negative difference, suggesting that grinding increases the medians to some degree.

Statistically significant differences were observed for the KW tests for about half of the metals. Analytes in the GL soil that did not show statistically significant differences for the medians after grinding included Ti, V, Cr, Mn, Ni, Sr, Th, Rb, Cu and Co.

Table 4
Descriptive statistics for sand replicates

Analyte	Mean metals concentrations (µg/g) and one standard deviation (µg/g) in sand samples							
	UG		RM		PS		MP	
	Mean	S.D.	Mean	S.D.	Mean	S.D.	Mean	S.D.
Be	0.0	0.0	0.0	0.0	0.0	0.0	0.0	0.0
Ti	0.6	0.3	4.1	0.1	3.6	0.1	0.4	0.1
V	0.1	0.0	0.3	0.0	0.2	0.0	0.1	0.1
Cr	0.2	0.0	0.4	0.0	0.2	0.0	0.2	0.1
Mn	1.7	0.4	2.0	0.0	2.1	0.1	1.8	0.3
Co	0.0	0.0	0.0	0.0	0.0	0.0	0.0	0.0
Ni	0.2	0.0	0.3	0.0	0.7	0.5	0.2	0.1
Cu	0.2	0.0	18.9	28.0	0.8	0.8	0.4	0.3
Zn	0.8	0.3	4.8	0.1	2.7	1.0	0.8	0.3
As	0.1	0.0	0.1	0.0	0.1	0.0	0.1	0.0
Se	0.0	0.1	0.0	0.1	0.0	0.1	0.0	0.1
Sr	1.2	0.1	1.5	0.0	2.1	0.0	1.2	0.0
Mo	0.0	0.0	0.0	0.0	0.0	0.0	0.0	0.0
Ag	0.0	0.0	0.0	0.1	0.0	0.0	−0.1	0.0
Cd	0.0	0.0	0.0	0.0	0.0	0.0	0.0	0.0
Sn	1.3	0.0	1.3	0.0	1.3	0.0	1.3	0.1
Sb	0.0	0.0	0.0	0.0	0.0	0.0	0.3	0.6
Ba	0.3	0.0	1.1	0.0	2.5	0.1	0.4	0.1
Tl	0.0	0.0	0.0	0.0	0.0	0.0	0.0	0.0
Pb	0.3	0.2	0.5	0.2	0.9	0.7	0.7	1.0
U	0.0	0.0	0.1	0.0	0.1	0.0	0.0	0.0
Ce	2.9	0.2	3.3	0.2	3.8	0.1	3.1	0.4
Gd	0.2	0.0	0.3	0.0	0.3	0.0	0.2	0.0
La	1.0	0.1	1.2	0.1	1.5	0.1	1.1	0.2
Nd	1.2	0.1	1.4	0.1	1.6	0.1	1.3	0.2
Pr	0.3	0.0	0.3	0.0	0.4	0.0	0.3	0.1
Sm	0.2	0.0	0.2	0.0	0.3	0.0	0.2	0.0
Th	0.1	0.0	0.2	0.0	0.4	0.0	0.1	0.1
B	0.6	0.1	0.8	0.2	0.6	0.3	0.3	0.3
P	37.4	9.9	37.9	1.1	33.9	1.8	23.9	2.1
Zr	0.1	0.0	0.4	0.0	0.7	0.0	0.2	0.0
Rb	0.1	0.0	0.1	0.0	0.1	0.0	0.1	0.0

Although statistical differences occurred, all three grinding methods did not typically produce statistically different medians; a number of statistical differences seemed to be attributable to only one or two of the three grinding methods. If the increase in surface area from grinding had produced a large positive bias, statistical differences would have been expected for all three grinding methods. In addition, the most energetic grinding treatment, PS, would be expected to produce the largest increases in the medians. However, the PS treatment often produced medians that were numerically smaller than the corresponding medians for the least energetic grinding treatment, MP. The differences in the medians were also relatively small for the metals that exhibited statistically significant differences. These results suggested that grain size reduction did not greatly affect metal availability to the acid leach solutions.

The statistical evaluation indicated that the grinding methods reduced variability (increased precision) overall for the Grenada Loring soil. With the exception of Th, the p-values for all of the analytes were <0.05 by the Bartlett's test, Levene's test or both. The statistical differences were usually attributable to larger variances for the UG soil data, but larger variances (relative to the variances of the MP and PS data) were also observed for RM soil data. The larger overall variability of the UG data sets relative to the small increases in the medians after grinding supported the conclusion that the statistical differences in the medians observed for the KW tests were not of practical significance.

3.4. WES soil

The metal concentrations in the WES soil are summarized in Table 8. Most of the p-values for the WES soil using the KW test were >0.05, as shown in Table 9, which does not support the hypothe-sis that grinding increased the medians. One or more significantly larger medians were observed for some elements: Be, Ti, V, Cr, Mn, Zn, Mo, Ba, B and Rb (usually for either the RM or PS procedure). However, in general, when statistical differences between the medians occurred, they were relatively small and did not appear to be of practical significance. For example, the statistically larger median for the PS treatment for Ba in the WES soil was within 10% of the UG median (well within the typical tolerance for analytical error for ICP analyses).

Furthermore, when statistical differences occurred for the KW tests, the medians of all three grinding methods were not all statistically larger than the corresponded UG medians; that is statistical differences were not systematically observed for all of the grinding procedures. This did not support the hypothesis that grinding produces a large positive bias. For example, as shown in Table 9, the KW p-value for Ba is nearly zero, indicating that one or more medians are significantly different. However, the statistical difference for the KW test is attributable to the PS treatment only, as shown in Table 10, which summarizes the results of the two-sample Mann–Whitney (MW) test for Ba. (The MW test produces comparable results to KW test.) The baseline (null) hypothesis for the MW test was that the median of the grinding treatment (MP, PS or RM) is less than or equal to the median of UG treatment. With the exception of the PS grinding treatment, the p-values were all >0.05. Similarly, a statistically significant difference was noted for Zn for the RM treatment only, as shown in Table 11.

Overall, none of the grinding procedures appreciably reduced the variability of the WES soil data, unlike GL soil results, where grinding decreased the variances overall. The variances or standard deviations for the WES samples ground using a mortar and pestle were often the same or numerically larger than those for

Table 5
Descriptive statistics for Grenada Loring replicates

| Analyte | Mean metals concentrations and one standard deviation (µg/g) in GL soil samples | | | | | | | |
| | UG | | RM | | PS | | MP | |
	Mean	S.D.	Mean	S.D.	Mean	S.D.	Mean	S.D.
Be	0.6	0.2	0.5	0.1	0.5	0.1	0.6	0.1
Ti	57.0	12.2	61.2	7.4	59.8	7.6	65.1	4.3
V	25.4	7.4	25.1	3.0	25.8	1.6	25.0	1.0
Cr	13.3	2.8	13.4	2.2	13.5	1.1	13.0	0.9
Mn	578.0	273.1	580.4	207.6	571.1	60.7	564.0	59.4
Co	7.3	3.5	6.5	1.4	6.7	0.4	6.7	0.4
Ni	10.7	1.8	10.9	1.3	10.9	0.4	11.1	0.5
Cu	9.1	1.9	9.3	1.7	9.4	0.4	9.5	0.4
Zn	27.7	6.0	35.0	4.9	28.5	2.7	30.3	3.2
As	6.8	4.7	5.9	1.0	6.7	0.8	6.5	0.5
Se	0.8	0.3	0.7	0.2	0.8	0.3	0.8	0.4
Sr	7.7	1.1	8.0	0.9	8.1	0.4	8.1	0.4
Mo	0.2	0.2	0.2	0.1	0.2	0.0	0.2	0.0
Ag	0.1	0.0	0.1	0.0	0.1	0.0	0.1	0.0
Cd	0.1	0.0	0.1	0.1	0.1	0.0	0.1	0.0
Sn	0.3	0.1	0.2	0.1	0.3	0.1	0.3	0.1
Sb	0.0	0.0	0.0	0.0	0.0	0.0	0.0	0.0
Ba	68.4	12.6	79.1	28.4	76.6	3.6	74.1	2.9
Tl	0.2	0.0	0.2	0.0	0.2	0.0	0.2	0.0
Pb	14.4	3.8	15.0	2.2	15.8	0.6	16.2	1.0
U	1.2	0.2	1.2	0.2	1.3	0.1	1.3	0.1
Ce	44.6	6.7	46.5	5.1	48.7	1.9	49.2	1.6
Gd	3.1	0.6	3.3	0.4	3.5	0.1	3.5	0.2
La	19.5	3.0	20.5	2.2	21.4	0.9	21.6	0.9
Nd	18.1	2.7	19.0	2.0	20.1	0.7	20.3	0.7
Pr	4.7	0.7	5.0	0.5	5.2	0.2	5.3	0.2
Sm	3.2	0.5	3.4	0.3	3.6	0.1	3.6	0.2
Th	3.5	1.1	3.7	1.1	4.0	0.9	4.1	1.0
B	−3.7	3.8	−6.3	5.3	−10.6	7.4	−8.7	7.2
P	378.6	113.4	375.4	49.8	397.4	31.5	402.1	22.7
Zr	5.4	1.4	4.9	0.8	4.4	0.3	4.3	0.2
Rb	12.5	1.8	13.1	1.8	13.4	0.8	13.2	0.9

Table 6
Medians (µg/g) and p-values from statistical tests for the GL soil data

| Metal | Median | | | | p-value | | |
	MP	PS	RM	UG	KW	Levene	Bartlett's
Ti	66.4	57.15	59.45	58.6	0.08	0	0.002
V	24.9	25.4	24.15	22.85	0.121	0.029	0
Cr	12.75	13.25	12.95	12.55	0.385	0.066	0
Mn	548.7	538.2	532.5	496.6	0.478	0.041	0
Co	6.7	6.6	6.5	5.75	0.201	0.008	0
Ni	11.2	11.05	10.6	10.4	0.319	0	0
Cu	9.4	9.35	9	9	0.354	0	0
Zn	29.3	27.55	35.85	27.2	0	0.014	0.012
As	6.35	6.5	5.65	5.5	0.005	0.11	0
Sr	8	7.9	8.1	7.7	0.746	0	0
Ba	73.9	75.5	75.8	67.95	0.037	0.038	0
Pb	16	15.8	15.65	13.05	0.041	0.001	0
Ce	49.3	48.45	46.1	42.6	0.047	0	0
Gd	3.45	3.5	3.45	3	0.03	0	0
La	21.6	21.3	19.95	18.95	0.019	0	0
Nd	20.4	20.15	18.9	17.6	0.008	0	0
Pr	5.3	5.2	4.95	4.55	0.017	0	0
Sm	3.6	3.6	3.4	3.05	0.003	0.001	0
Th	3.6	3.5	3.5	3.2	0.123	0.66	0.927
Zr	4.15	4.4	5.05	5.2	0.002	0	0
Rb	13.55	13.55	12.4	11.6	0.072	0.081	0.001

Table 7
Sign test for GL soil

Variable	N	Below	Equal	Above	P	Median
Delta	63	56	1	6	0.0000	−0.7500

Variable	N	Mean	Standard deviation	Minimum	Median	Maximum
Delta	63	−2.85	10.49	−52.10	−0.75	33.30

Delta = {median (UG) − median(PS, MP or RM)} (µg/g). Delta = 0 versus ≠ 0.

Table 8
Descriptive statistics for WES soil replicates

Analyte	Mean metals concentrations and one standard deviation (μg/g) in WES soil samples							
	UG		RM		PS		MP	
	Mean	S.D.	Mean	S.D.	Mean	S.D.	Mean	S.D.
Be	0.3	0.0	0.3	0.0	0.3	0.0	0.3	0.0
Ti	173.6	4.4	180.3	14.7	212.1	14.1	182.0	7.5
V	20.6	0.7	20.8	1.4	23.1	1.1	21.1	0.6
Cr	11.9	0.5	12.2	0.7	13.0	0.7	12.1	0.4
Mn	404.3	66.6	398.4	33.2	428.4	26.8	464.0	90.3
Co	5.4	0.2	5.4	0.2	5.5	0.2	5.6	0.4
Ni	14.8	0.9	14.5	0.8	15.2	0.6	15.0	0.6
Cu	11.9	1.0	11.8	0.7	12.1	1.1	13.5	6.8
Zn	34.8	1.4	37.2	3.7	35.6	2.7	34.4	1.2
As	2.2	0.1	2.2	0.1	2.2	0.1	2.2	0.1
Se	0.4	0.1	0.4	0.1	0.4	0.1	0.4	0.1
Sr	34.4	1.0	34.3	1.9	35.0	0.9	34.4	1.0
Mo	0.3	0.0	0.3	0.0	0.3	0.0	0.3	0.0
Ag	0.1	0.0	0.2	0.0	0.2	0.0	0.2	0.0
Cd	0.2	0.0	0.2	0.0	0.2	0.0	0.2	0.0
Sn	0.5	0.1	0.6	0.2	0.6	0.1	0.5	0.1
Sb	0.0	0.0	0.0	0.0	0.0	0.0	0.0	0.0
Ba	72.0	7.0	70.5	4.3	75.6	2.5	75.1	10.2
Tl	0.1	0.0	0.1	0.0	0.1	0.0	0.1	0.0
Pb	6.0	0.3	6.3	1.0	5.8	0.3	5.9	0.3
U	0.6	0.0	0.6	0.0	0.6	0.0	0.6	0.0
Ce	34.7	1.3	34.2	2.0	34.5	1.4	34.8	1.3
Gd	3.4	0.1	3.4	0.2	3.4	0.1	3.4	0.1
La	16.0	0.5	15.8	0.8	16.0	0.5	16.1	0.5
Nd	16.7	0.7	16.5	1.0	16.6	0.7	16.6	0.6
Pr	4.2	0.2	4.1	0.3	4.2	0.2	4.2	0.2
Sm	3.2	0.1	3.2	0.2	3.2	0.1	3.2	0.1
Th	3.7	0.1	3.5	0.2	3.5	0.1	3.5	0.1
B	6.3	1.5	8.2	5.5	7.8	1.6	6.6	1.1
P	470.0	34.9	471.7	40.9	478.1	39.2	481.4	23.8
Zr	15.5	0.5	15.4	1.0	16.0	0.6	15.6	0.5
Rb	7.2	0.1	7.3	0.3	8.1	0.2	7.3	0.2

Table 9
Medians (μg/g × 10) and p-values from statistical tests for the WES soil data

Metal	Median				p-value		
	MP	PS	RM	UG	KW	Levene	Bartlett's
Be	3.3607	3.5152	3.4051	3.2366	0.008	0.128	0.078
Ti	1819.8	2125.3	1829.6	1738.8	0	0	0
V	212.2	233.45	208.35	208.09	0	0.001	0.007
Cr	120.32	129.29	121.95	117.37	0	0.04	0.05
Mn	4347	4318.6	4030.3	3960	0.01	0.34	0
Co	54.992	55.653	54.289	52.843	0.07	0.95	0.03
Ni	149.71	153.67	146.42	146.29	0.057	0.56	0.45
Cu	117.7	119.83	117.33	115.3	0.804	0.542	0
Zn	344.69	358.89	636.73	346.93	0.001	0.507	0
As	21.469	22.385	21.684	21.832	0.23	0.61	0.64
Se	3.86	3.802	3.909	4.368	0.159	0.882	0.853
Sr	342.78	350.86	345.78	343.62	0.32	0.04	0.01
Mo	2.631	2.816	2.622	2.593	0.01	0.732	0.144
Ag	1.571	1.565	1.5105	1.472	0.485	0.876	0.968
Cd	2.131	2.146	2.040	2.009	0.181	0.108	0.014
Sn	4.88	5.49	4.95	5.06	0.70	0.23	0
Sb	0.249	0.299	0.323	0.309	0.15	0.951	0.553
Ba	726.9	759.9	706.6	703.2	0.00	0.22	0
Tl	1.385	1.438	1.393	1.427	0.18	0.355	0.04
Pb	58.087	58.145	60.750	59.233	0.128	0.076	0
U	5.999	5.956	6.058	6.199	0.001	0.037	0.037
Ce	346.18	346.76	347.90	346.39	0.844	0.182	0.185
Gd	33.977	34.336	33.980	34.196	0.815	0.005	0.007
La	160.67	161.12	159.94	159.53	0.901	0.064	0.063
Nd	166.20	167.00	164.95	165.58	0.913	0.319	0.351
Pr	41.107	42.136	41.107	41.772	0.976	0.53	0.651
Sm	31.813	32.185	31.757	31.856	0.915	0.262	0.308
Th	35.308	35.160	35.561	37.125	0	0.001	0
B	64.13	71.46	63.00	56.90	0.026	0.235	0
P	4763.5	4835.3	4575.0	4748.6	0.661	0.022	0.206
Zr	157.31	160.99	155.35	153.88	0.175	0.059	0.018
Rb	73.561	81.420	73.942	71.923	0	0.003	0

The analyte concentrations in this table are in units of (μg/g)×10

Table 10
WES soil MW test results for Ba for UG and the MP, PS and RM treatments (μg/g)

Treatment	Ba, median (μg/g)	MW, p-value
UG	70.3	–
MP	72.7	0.141
PS	76.0	0.0039
RM	70.7	>0.95

Table 11
WES soil MW test results for Zn for UG and the MP, PS and RM treatments (μg/g)

Treatment	Zn, median (μg/g)	MW, p-value
UG	34.7	–
MP	34.5	>0.95
PS	35.9	0.1103
RM	36.4	0.0017

the unground samples, as illustrated by the Ba results. The Ba concentrations in the unground WES soil was $72 \pm 7 \mu$g/g and were 70.5 ± 4.3, 75.6 ± 2.5, and $75.1 \pm 10.2 \mu$g/g soil in the RM, PS, and MP ground samples, respectively. Similarly, numerically larger standard deviations were also noted for Mn, Cu, Ti, and Ce in the MP WES soil compared to the other grinding treatments. However, for the metals Ba, Mn, Cu, Ti and Ce, the Levene's test resulted in a statistically significant difference for the variances for Ti only.

The Levene's test identified some statistically significant differences owing to larger variances for one or more of the grinding treatments (Table 9). However, the statistically significant differences for the variances were sporadic; they were not attributable to any single grinding treatment. Therefore, it did not appear that the difference were of practical significance. It seems likely that the lack of substantial reductions in variability occurred because the WES soil was relatively homogeneous prior to sample processing and most of the metals concentrations were very low.

4. Conclusions

The first hypothesis, that analyte concentrations would not significantly increase in ground samples compared with unground samples, was validated for the sample matrices investigated. Overall, the KW p-values were greater than 0.05 and the medians of all three grinding treatments were not significantly larger than the corresponding UG treatment medians. Grinding resulted in statistically significant increases for about half the metals for the Grenada Loring soil, but these increases were relatively small, well within the typical tolerances for analytical uncertainty for environmental ICP-AES and ICP-MS metal analyses ($\pm20\%$ at the mid-quantitative range). Grinding also resulted in some statistically larger medians for the WES soil, but did not significantly change the median concentrations for most of the metals and the differences between the medians seemed to be well within analytical error. Therefore, there was no strong evidence that the larger medians derived from the grinding procedures were of practical significance.

The second hypothesis, that variability would be reduced (increased precision), was generally validated for the GL soil, although anomalies were observed. The grinding methods reduced variability overall; however, the data indicated that the roller mill was not as effective for this purpose as the mortar and pestle and the pulverisette grinding methods in the Grenada Loring soil. It is possible that the roller mill grinding time may have been inadequate for these samples. None of the grinding proce-

dures appreciably reduced the variability in the WES soil, which is attributed to its inherent homogeneity and very low metals concentrations. It is suggested that additional soils be tested to confirm this conclusion.

In summary, homogenization through mechanical grinding resulted in either no differences in the median metal concentrations or only small increases in medians for the acid-digested soil samples. If commercial and research laboratories use sample grinding techniques for sample preparation to increase precision, it is recommended that "metal free" grinding devices be used such as the equipment tested here to minimize positive bias owing to external contamination.

References

[1] J.C. Pennington, T.F. Jenkins, J.M. Brannon, J. Lynch, T.A. Ranney, T.E. Berry, C.A. Hayes, P.H. Miyares, M.E. Walsh, A.D. Hewitt, N. Perron, J.J. Delfino, ERDC/EL TR-01-13, 2001.
[2] J.C. Pennington, T.F. Jenkins, G. Ampleman, S. Thiboutot, J.M. Brannon, J. Lynch, T.A. Ranney, J.A. Stark, M.E. Walsh, J. Lewis, C.A. Hayes, J.E. Mirecki, A.D. Hewitt, N. Perron, D. Lambert, J. Clausen, J. J. Delfino, ERDC/EL TR-02-08, 2002.
[3] T.F. Jenkins, A.D. Hewitt, M.E. Walsh, T.A. Ranney, C.A. Ramsey, C.L. Grant, K.L. Bjella, J. Environ. Forensics 6 (2005) 45–55.
[4] United States Environmental Protection Agency (USEPA). Washington, DC, 2006, http://www.epa.gov/epaoswer/hazwaste/test/pdfs/8330b.pdf.
[5] M.E. Walsh, C.A. Ramsey, T.F. Jenkins, Chemosphere 49 (2002) 1265–1271.
[6] M.E. Walsh, D.J. Lambert, ERDC/CRREL TR-06-6, 2006.
[7] M.E. Walsh, C.A. Ramsey, C.M. Collins, A.D. Hewitt, M.R. Walsh, K. Bjella, D. Lambert, N. Perron, ERDC/CRREL TR-05-6, 2005.
[8] C.A. Ramsey, A.D. Hewitt, Environ. Forensics 6 (2005) 71–75.
[9] M.D. Chendorain, L.D. Stewart, B. Packer, Environ. Sci. Technol. 39 (2005) 2442–2447.
[10] J.L. Davis, S.L. Larson, D.R. Felt, C.C. Nestler, W.A. Martin, L. Riggs, E.J. Valente, G.R. Bishop, ERDC/EL TR-07-3, 2007.
[11] J.C. Pennington, F. Jenkins, S. Thiboutot, G. Ampleman, J. Clausen, A.D. Hewitt, J. Lewis, M.R. Walsh, M.E. Walsh, T.A. Ranney, B. Silverblatt, A. Marois, A. Gagnon, P. Brousseau, J.E. Zufelt, K. Poe, M. Bouchard, R. Martel, D.D. Walker, C.A. Ramsey, C.A. Hayes, S.L. Yost, K.L. Bjella, L. Trepanier, T.E. Berry, D.J. Lambert, P. Dubé, N.M. Perron, ERDC TR-05-2, 2005.
[12] Formerly Used Defense Sites Program, https://eko.uasce.army.mil/usacecop/pub/ecop/what_we_do/fuds.
[13] Munitions Response Site Prioritization Protocol, http://www.denix.osd.mil/denix/Public/News/OSD/MMRP/mmrp.html.
[14] U.S. Geological Survey, in: J.E. Taggart Jr. (Ed.), Open-File Report 02-223, 2002.
[15] M.R. Carter (Ed.), Soil Sampling and Methods of Analysis, Lewis Publishing, Boca Raton, FL, 1993.
[16] United States Environmental Protection Agency (USEPA), Washington, DC, EPA/600/R-92/128, 1992.
[17] G. Dewalt, P. Constant, B.E. Buxton, S.W. Rust, B.S. Lim, J.G. Schwemberger, Sampling and Analysis of Lead in Dust and Soil for the Comprehensive Abatement Performance Study (CAPS).
[18] A.J. Bednar, J.E. Mirecki, L.S. Inouye, L.E. Winfield, S.L. Larson, D.B. Ringelberg, Talanta 72 (2007) 1828–1832.
[19] G. Pierre, Sampling for Analytical Purposes, John Wiley and Sons, New York, NY, 1999.
[20] A.D. Hewitt, J.H. Cragin, ES&T 25 (5) (1991) 985–986.

Development of an electronic nose to identify and quantify volatile hazardous compounds

Daniel L.A. Fernandes, M. Teresa S.R. Gomes *

CESAM & Department of Chemistry, University of Aveiro, 3810-193 Aveiro, Portugal

ARTICLE INFO

ABSTRACT

A new electronic nose was developed to identify the chemical compound released when a 2.5-L flask was broken inside a 3 m × 3 m × 2.5 m store-room. Flasks of 10 different hazardous compounds were initially present in the room: ammonia, propanone, hexane, acetic acid, toluene, methanol, tetrachloromethane, chloroform, ethanol and dichloromethane. Besides identification, quantification of the compound present in the air was also performed by the electronic nose, in order to evaluate the risk level for room cleaning. An array of six sensors based on coated piezoelectric quartz crystals was used. Although none of the individual sensors was specific for a single compound, an artificial neural network made it possible to identify and quantify the released vapour, among a series of 10 compounds, with six sensors. The neural network could be simplified, and the number of neurons reduced, provided it was used just for the identification task. Quantification could be performed later using the individual calibration of the sensor most sensitive to the identified compound.

1. Introduction

Store-room in the University and in other laboratory facilities contain several glass containers of volatile compounds used as solvents. Among them, and in high quantities, are organic and inorganic solvents. The use of solvents is common to many industrial processes and different solvents are usually stored together.

All solvents should be considered potentially hazardous. The harmful effects may follow inhalation of the vapour, eye or skin contact with liquid or vapour, or ingestion. The severity and type of the effect due to vapour contact, depends on its concentration, time of exposure, and toxicity of the solvent. Long and repeated exposure to some solvents may impair perceptions and cause behavioural changes. Degeneration of nerve cells in the peripheral nervous system causes several organic malfunctions, some of them irreparable, and, in the most severe cases, death can follow. Permissible exposure limits have been settled for these compounds [1].

Accidents do happen, and a flask can be broken inside the store-room. Identification and quantification of the contaminant in the air must be performed before entering into the store-room, in order to determine if the concentration is below the time-weighted average limits (TWA) and if is safe to start the cleaning procedures.

Electronic noses can play a major role in the identification and quantification of the hazardous vapour. Electronic noses can employ different types of chemical gas sensors, based on different transducer technologies, including metal oxide and conducting polymers, bulk and surface acoustic wave devices, electrochemical sensors and others [2–4].

Bulk acoustic wave sensors are piezoelectric devices, highly sensitive to mass changes, besides being technologically simple are inexpensive. Each piezoelectric quartz crystal needs to be coated with a compound that interacts with the target solvent. This sensitive layer must be carefully chosen as it must be very stable and interact reversibly and selectively with the compound to be detected [5]. The interaction between the analyte and the coating produces a frequency decrease, which is proportional to the mass attached to the crystal electrodes. The interaction is ruled by the physicochemical affinity between the volatile compounds and the sensitive film. Adsorption can be of several types, from Van der Waals to hydrogen bonding, and depends upon polarity, steric hindrance and π-electron density [6]. However, no covalent bonding can be broken or formed, as the high energies involved would prevent sensor reversibility.

Selectivity to a single compound is hard to be accomplished, and arrays of several non-specific sensors are easier to be mounted.

Arrays of piezoelectric quartz crystal have been used to detect volatile organic compounds (VOCs). Recently Je et al. [7] measured the total VOCs level, while Sugimoto et al. [8] have classified the atmospheric VOCs in two groups: polar VOCs and non-polar VOCs.

* Corresponding author. Tel.: +351 234370722; fax: +351 234370084.
E-mail address: mtgomes@ua.pt (M.T.S.R. Gomes).

Si et al. [9] have also succeeded in separating low polar from non-polar VOCs and were able to determine toluene concentrations, but only in binary mixtures of toluene and ethanol. In this work, we will try not only to identify the compound in the air of the store-room but also to quantify it.

The arrays of sensors produce a big and complex amount of data, rendering data analysis difficult and delayed. Useful information can be extracted from the frequency shifts obtained for the samples, through pattern recognition techniques.

Artificial neural networks have been used as pattern recognition methods to identify volatile compounds with electronic noses. The main advantage of artificial neural networks is that the heavy process of computation occurs during the training.

Three sample sets are needed for neural network learning: a training set, a monitoring set and a test set. Calibration is done with the training set and with the monitoring set, which is used to decide when to stop the training of the network. The monitoring set is used to prevent overfitting by the neural network, and to make it more robust to noise.

The validation must be performed with the test set, composed of samples not used in the calibration. Once trained, the process of identification of a sample is fast, and it can be performed in the field [10].

Most authors try to avoid variations due to changes in concentration as they find difficulties in cluster separation. Case concentration change, several normalizations procedures are applied [11]. This is why most of the published work deals just with the identification of the compounds [2,10–17], although quantification is also very important for most of the problems.

In this work, neural network calculations will be initially performed with non-normalized data. A new electronic nose composed of an array of six acoustic wave home-made sensors was specially developed for the identification and quantification of a series of hazardous compounds ordinary found in a solvent store-room: ammonia, propanone, hexane, acetic acid, toluene, methanol, tetrachloromethane, chloroform, ethanol and dichloromethane.

The electronic nose was developed to solve the specific problem of identifying the compound released when a 2.5-L flask is broken inside a 3 m × 3 m × 2.5 m store-room. The identification and concentration of the hazardous compound in the air was determined with three different neural networks, two for data that has not been normalized, and a simpler one, used just for compound identification, which uses normalized data. If this last network is used, quantification can be achieved using the calibration of the most sensitive sensor to the identified compound.

2. Experimental

2.1. Reagents

The sensors were coated with: 1,10-decanodithiol (dithiol, TCI D0015), nafion 117 solution (nafion, Fluka 70160), manganese(II) phthalocyanine (Mn_pht, Aldrich 379557), polydimethylsiloxane (PDMS, ABCR 76189), tetramethylammonium fluoride tetrahydrate (TMAF, Aldrich 107212), and magnesium (II) phthalocyanine (Mg_pht, Aldrich 402737). Nitrogen was Alphagaz from ArLíquido.

Hazardous compounds were detected by the electronic nose in gas phase. Therefore, vapours were obtained from pure compounds: ammonia 25% (Riedel-de-Haën 30501), propanone (Riedel-de-Haën 32201), hexane (Lab-Scan C16C11X), acetic acid (Panreac 131008), toluene (Riedel-de-Haën 32249), methanol (Fluka 65543), tetrachloromethane (Riedel-de-Haën 32215),

chloroform (Lab-Scan A3505E), ethanol (Merck 100983) and dichloromethane (Lab-Scan C2510L).

2.2. Apparatus

Fig. 1 shows the experimental layout. Each sensor is housed in a separate cell and a constant stream of nitrogen is flowing through each one. Before distribution, total nitrogen flow was controlled by a flowmeter (Cole Parmer). Sample volumes ranging from 10 to 250 μL were injected through the injection port (OMNIFIT 3301), and a distribution valve (OMNIFIT 1103) divided the sample by the sensors. Each sensor was driven by an oscillator and the frequencies of oscillation of the sensors were simultaneously monitored and stored in a PC at intervals of 1 s. Frequencies were numerically and graphically displayed on the monitor.

Fig. 2 shows the cell design in detail. The PVC crystal cells were home-made and each one possesses two inputs, directed towards the crystal faces, and one output at the bottom. Inner volume of the cell was the smallest possible (350 μL). Before entering the crystal cell, the nitrogen stream was divided and directed to both entrances. Teflon tubes with Ø = 3.2 mm, as short as possible, were used in all the connections.

Assemblage of sensors in sequential array could not be performed, as dispersion of sample would prevent the response of the last three sensors.

Oscillators and software were home-made and specially designed to obtain the best precision in the frequency measurements [18]. Frequency was determined with a precision of 0.1 Hz.

The frequencies of oscillation of the sensors were simultaneously monitored with a Counter/Timer Device PXI 6608, from National Instruments, and stored in a PC.

9 MHz AT-cut quartz crystals with Au-electrode (Euroquartz) operating in the thickness-shear mode were used in this work.

2.3. Procedure

Six 9 MHz AT-cut quartz crystals were coated, on both sides, with: dithiol; nafion; Mn_pht; PDMS; TMAF; Mg_pht. The first two sensors were coated by dipping the quartz wafer into the coating solution, and all the other sensors were coated by spraying. The coated crystals were then allowed to dry for 24 h and, afterwards, each one of them was inserted into a cell. Frequency decreases due to coating of 8, 88, 20, 14, 17 and 11 kHz have been obtained for the sensors coated with dithiol, nafion, Mn_pht, PDMS, TMAF, and Mg_pht, respectively. Although homogeneous coating distribution is not assured by the techniques used for coating application, especially in case of dipping, coating amounts of these magnitudes are adequate to obtain the desired sensitivities. Each coated crystal is afterwards calibrated, which effectively deals with the fact of each similar coated crystal behaving slightly different in terms of sensitivity to the analytes.

Vapour samples of known concentration were obtained by placing each hazardous compound in a flask immersed into a thermostated bath at 20 °C. The samples of solvents were withdrawn from the gaseous phase of the flasks, through a septum, and injected into the system, which operates in the flow injection mode.

Nitrogen at a constant flowing rate of 10 mL/min is entering into the system, and is divided by the six sensors. The frequency of each sensor, under this constant flow, is from now on defined as baseline frequency. Then, the sample was injected and carried by the nitrogen flow, entered the distribution valve, where it was divided and directed to each sensor. Frequency of the six sensors were simultaneously monitored and stored at intervals of 1 s. The difference between baseline frequency and the minimum frequency observed after sample injection was computed, and used later in the artificial
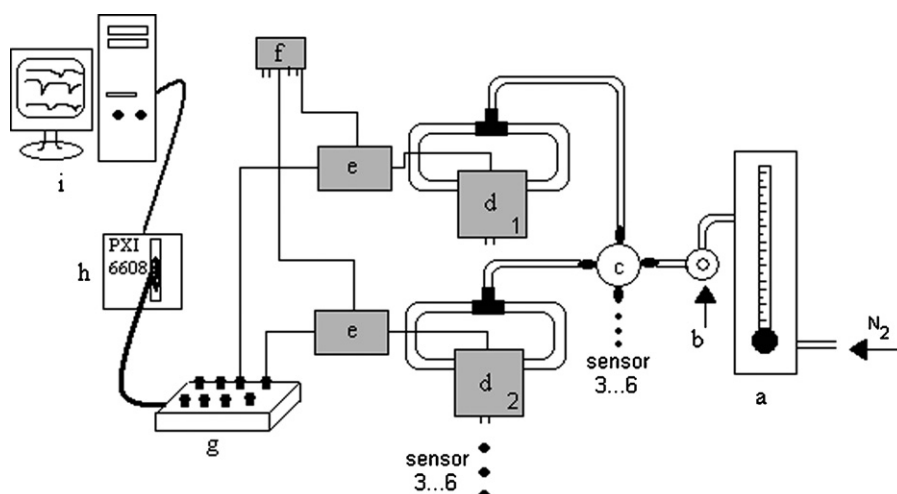
Fig. 1. Experimental layout: (a) flowmeter; (b) injection port; (c) distribution valve; (d) crystal cells; (e) oscillator; (f) power supply; (g) BNC 2121 box; (h) counter/timer PXI-6608; (i) computer.

neural network (ANN), for pattern recognition and quantification. After sample injection, a complete recover of the initial frequency of all the six crystals was achieved in less than 10 min, and no sample was injected before all baseline frequencies have been restored.

Artificial neural network was constructed as a multilayer network and was trained with backpropagation of error algorithm, with three sets of samples: training set, monitoring set and test set [19]. After training has started, the number of perceptrons and artificial neurons was removed or incremented until training was complete. The network was then applied to the monitoring set. After calibration, involving the training and monitoring sets, validation using the test set was performed.

3. Results and discussion

Several quantities of each of the 10 solvents were analyzed. Fig. 3 shows, as an example, the responses of the six sensors to an injection of 17 μg of methanol. Although detected with different sensitivities by the sensors, reversibility was completed in 5 min. The smallest quantity of each solvent was lower than the one that

would be present in 2.5 mL of the air in the store-room, in case a single 2.5-L flask of that solvent was broken. A total of 136 samples were injected. Samples were divided in three sets: a set of 80 samples for training the artificial neural network, a monitoring set with 10 samples, and the test set with 46 samples. The training set was composed of 4 samples of ammonia (quantities ranging from 1.07 to 10.70 μg), 5 samples of propanone (quantities ranging from 12.13 to 121.26 μg), 4 samples of hexane (quantities ranging from 31.11 to 124.45 μg), 12 samples of acetic acid (quantities ranging from 1.87 to 7.49 μg), 4 samples of toluene (quantities ranging from 5.48 to 27.40 μg), 11 samples of methanol (quantities ranging from 3.42 to 34.24 μg), 9 samples of tetrachloromethane (quantities ranging from 38.41 to 153.63 μg), 9 samples of chloroform (quantities ranging from 20.90 to 208.96 μg), 11 samples of ethanol (quantities ranging from 2.07 to 20.74 μg) and 11 samples of dichloromethane (quantities ranging from 32.42 to 324.22 μg).

The analysis extended for a period of 1 month, during which the frequency of the six coated sensors remained stable and the sensitivity of each one did not change significantly ($\alpha = 0.05$). Measurements have been performed at room temperature in a non-acclimatized laboratory and diurnal variations as well as day to day ordinary changes did not produce statistically significant changes
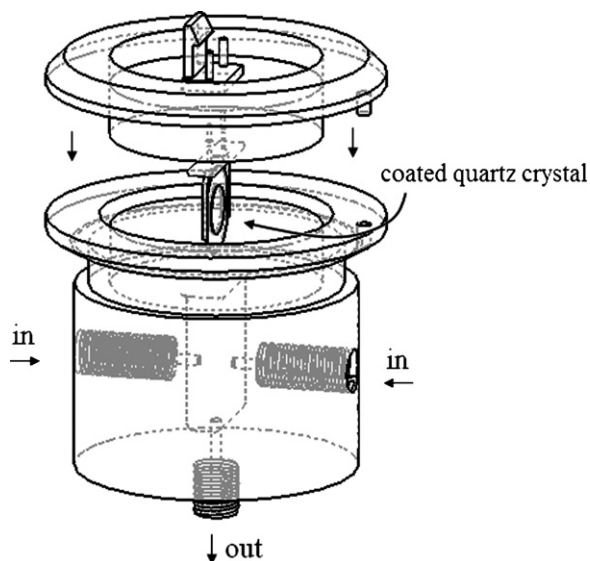
Fig. 2. Cell design used for sensors.
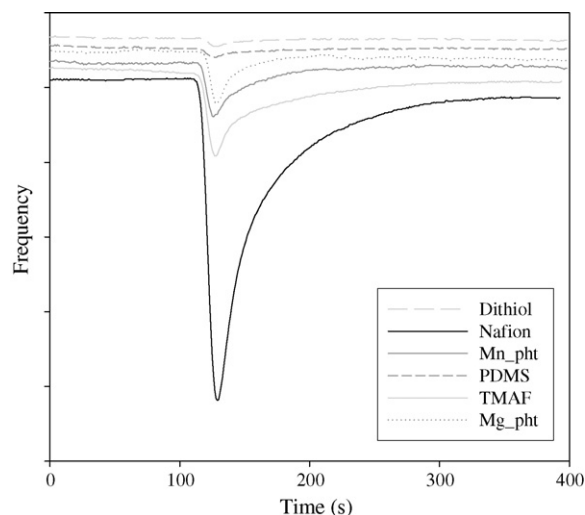
Fig. 3. Frequency decreases of all sensors when a standard of methanol was injected.

in the analytical signals of the sensors. Water vapour did not interfere, as the quantity of water present in 2.5 mL of air is not enough to produce a frequency change in any of the sensors.

The monitoring set was composed of a sample of each solvent, different from the ones used in the training set.

Fig. 4 shows the radar plots with the normalized fingerprints of the 10 compounds obtained with the sensor array. As can be seen, there are significant differences in the fingerprint of each compound. However, there were some similarities in the fingerprints. For instance, dichloromethane and chloroform are detected

with the highest sensitivity by the Mn_pht sensor, while hexane and tetrachloromethane were best detected by the PDMS sensor, and toluene was best detected both by the Mn_pht and the PDMS sensors. All the other solvents, ammonia, ethanol, methanol, propanone and acetic acid, which are more polar compounds, were detected with the highest sensitivity by the nafion sensor.

A neural network with 6 perceptrons and a total of 56 artificial neurons (17-10-1-17-10-1) was built, and applied to the data obtained with the array of 6 sensors. This network had two output layers, one to identify the solvent and the other to quantify it. An ID
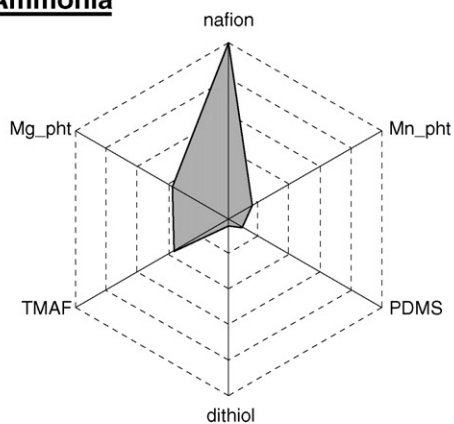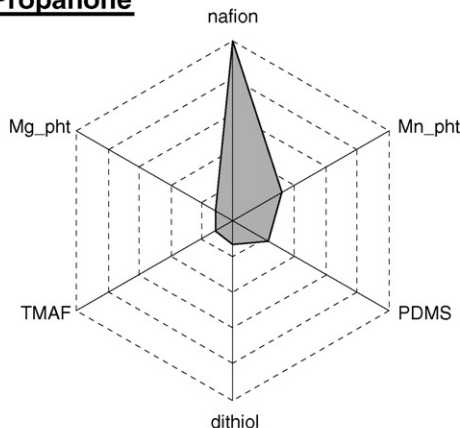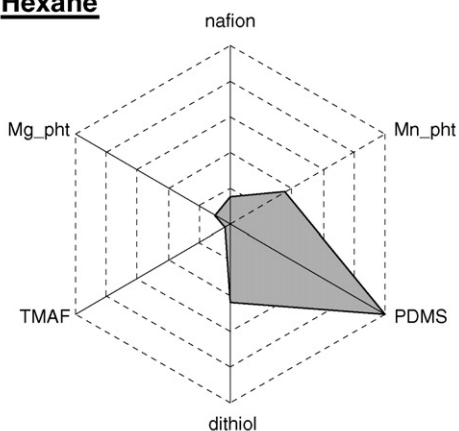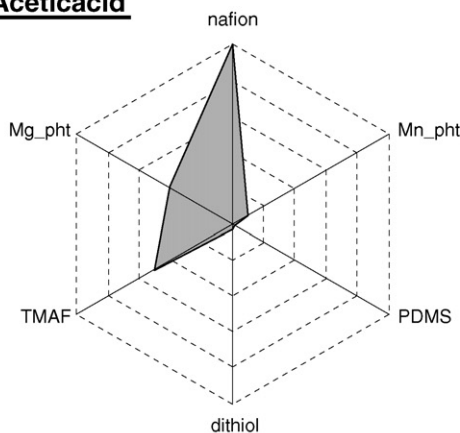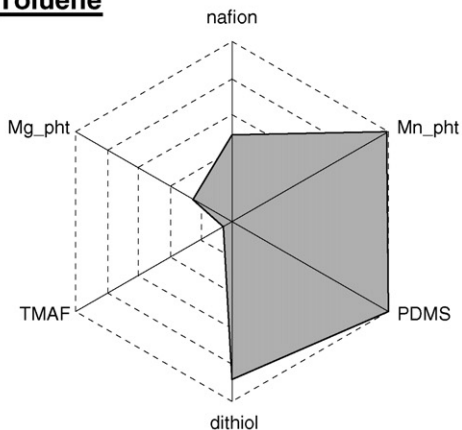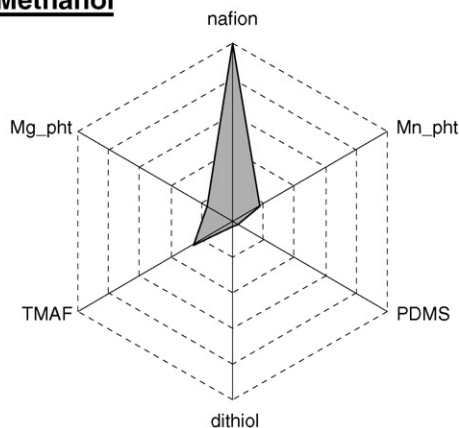
Fig. 4. Radar plots showing compound fingerprint obtained by the array of sensors, from normalized data.
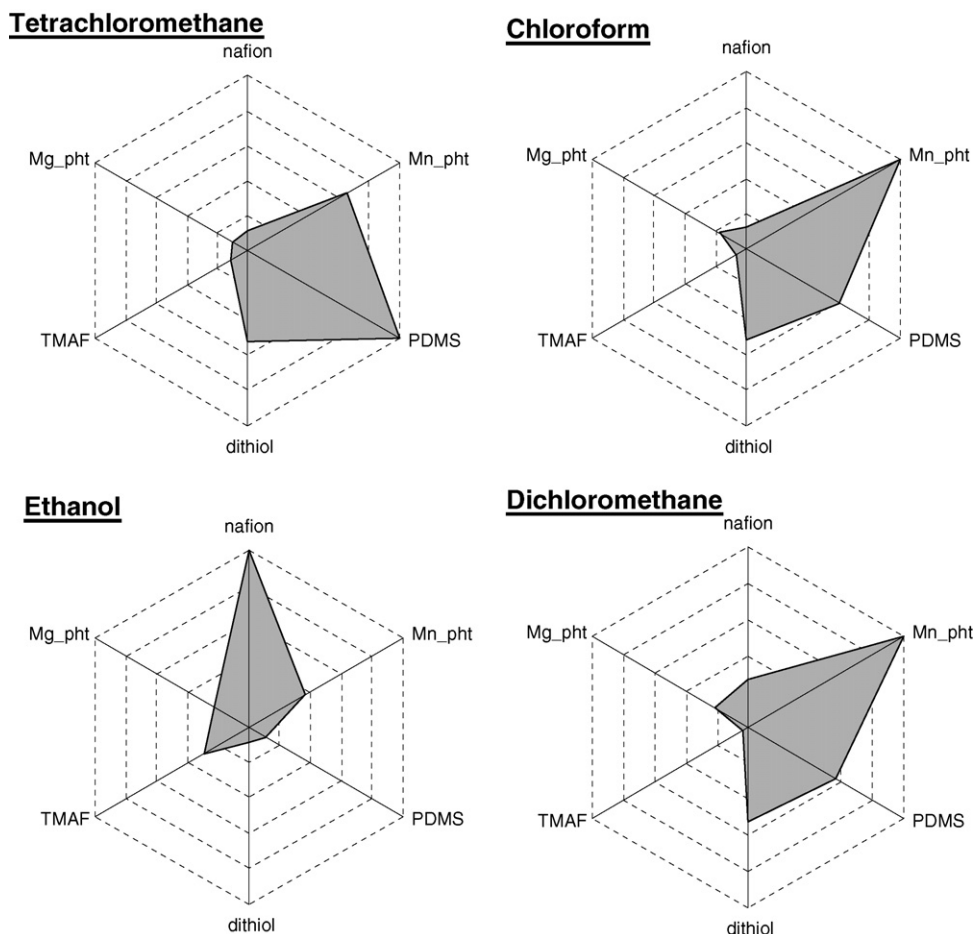
Fig. 4. (*Continued*).

number was attributed to each compound to introduce it in the network: ammonia, 1; propanone, 2; hexane, 3; acetic acid, 4; toluene, 5; methanol, 6; tetrachloromethane, 7; chloroform, 8; ethanol, 9; dichloromethane, 10.

Fig. 5 shows a plot of the predictions for compound identification (a) and quantification (b) *vs.* real values, for the 46 samples of the test set. The method of least square was applied, and the slopes of 1.00 and 1.01 show that both identification and quantification were achieved with success. Besides, regarding quantification, a paired *t*-test showed that there was no statistically significant difference ($\alpha = 0.05$) between the real and predicted values.

Principal component analysis was applied to the data to reduce its dimentionality, to identify the relevant sensors in the array, and to discard redundant information.

Table 1 shows the correlation coefficients for the six sensors in the array. As can be seen, some degree of correlation exists between the dithiol sensor, the Mn_pht sensor and the PDMS sensor, which leads to the conclusion that at least two of these sensors

Fig. 5. Predicted *vs.* real values for the test set, using the first neural network.

Table 1
Correlation coefficients for the six sensors in the array

	Dithiol	Nafion	Mn_pht	PDMS	TMAF	Mg_pht
Dithiol	1	−0.2139	0.9591	0.9415	−0.0778	0.5768
Nafion		1	−0.0747	−0.2157	0.8385	0.5441
Mn_pht			1	0.8246	0.0339	0.719
PDMS				1	−0.0648	0.427
TMAF					1	0.5851
Mg_pht						1
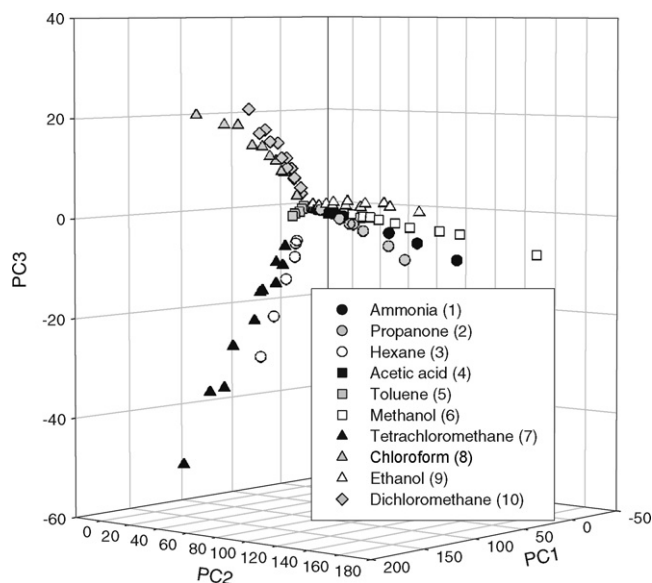
Fig. 6. Principal component representation of data.

Fig. 7. Predicted *vs.* real values for the test set, using the second neural network.

are redundant. Applying principal component analysis it was possible to reduce the dimensionality from six sensors to three variables. The first three principal components, explain 99% of the data variability. The graphic representation retaining just the three principal components can now be drawn and data are easier to interpret than before. Fig. 6 shows the data represented by the three first principal components (PC1, PC2 and PC3).

Data are preferentially oriented in three directions, according to their similarities. Dichloromethane and chloroform data are clearly oriented in the same direction, while hexane and tetrachloromethane are displayed in another direction, and ammonia, ethanol, methanol, propanone and acetic acid are in a distinct zone of Fig. 6. The way compounds joined in the same direction was the same as reported before, when the best sensors for each compound were selected. Toluene, which was described as a particular case, was detected with the highest sensitivity by two sensors, and is displayed between chloroform and hexane data.

A neural network with six perceptrons and a total of 49 artificial neurons (13-10-1-18-6-1) was built from the scores of the three principal components. Fig. 7 shows the regression between predicted and real values for the test set, obtained by this network. As can be seen, the identification and quantification of solvents with this network was also successful. A paired *t*-test showed no statistically significant differences ($\alpha = 0.05$) between the real and predicted values.

After principal component analysis, successful identification and quantification was obtained with a smaller number of artificial neurons than before. This simpler network allowed a faster learning process and a decrease in the calculation effort than before. These results suggest that the remaining PCs, which explained 1% of variability of data, should contain confused information and/or noise. The loads showed that the least important sensors for identification and quantification were the TMAF and Mg_pht sensors. These are also the two most significant sensors in the PC4, PC5 and PC6 not considered, and that explained the remaining 1% of data variability.

If normalized data were used in network building, quantification would be impossible. However, once the released compound was correctly identified, quantification could be performed through the
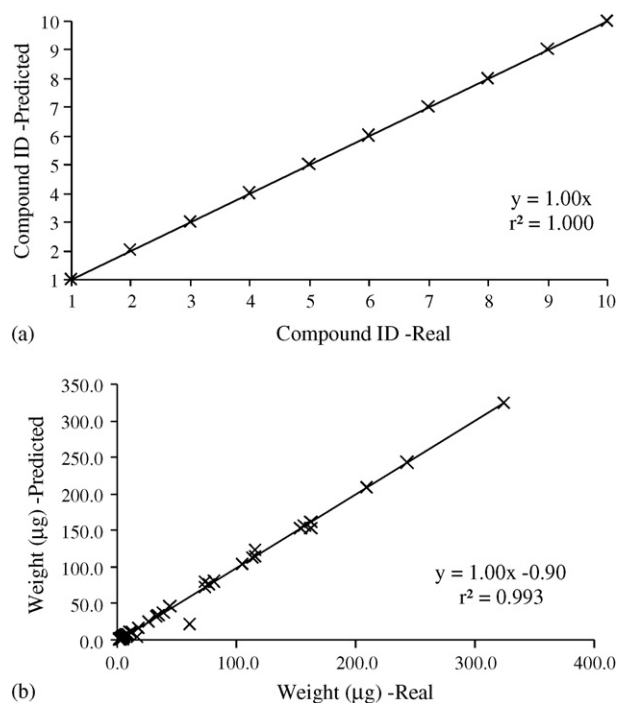
calibration line of the appropriate sensor. This would allow to use a simplified network, and to spare on network training and on calculation effort. Data for each sample was normalized by dividing by the highest signal observed within the array of the six sensors. Principal component analysis was then performed with the normalized data, and an artificial neural network was built, using the first three principal components. Table 2 shows the correlation coefficients. As can be seen, no significant correlation was observed between sensors. This result indicates that no sensor should now be discarded and that all the six sensors would be useful to identify the solvent.

Fig. 8 shows a representation of the data using the first three principal components (PC1, PC2 and PC3). These three PCs represent 97% of data variability and the loads showed that the least important sensor was the Mg_pht sensor.

Looking at the normalized data, the samples appear now clustered by compound. Clusters were clearly separated, with the exception of ammonia and methanol, which appeared slightly mixed. Clusters of polar compounds can be seen on the left side of the graph, while less polar compounds can be seen on the right side. Although quantification is now out of question, the artificial neural network was simpler, easy and fast to compute, and possess just 4 perceptrons and a total of 13 artificial neurons (2-5-5-1).

Fig. 9 shows the regression between predicted and real IDs for the test set, obtained by this network. The identification of sol-

Table 2
Correlation coefficients for sensors with normalized data

	Dithiol	Nafion	Mn_pht	PDMS	TMAF	Mg_pht
Dithiol	1	−0.8977	0.9074	0.9061	−0.7727	−0.3532
Nafion		1	−0.8187	−0.9228	0.7789	0.446
Mn_pht			1	0.712	−0.7592	−0.2833
PDMS				1	−0.781	−0.5359
TMAF					1	0.6059
Mg_pht						1
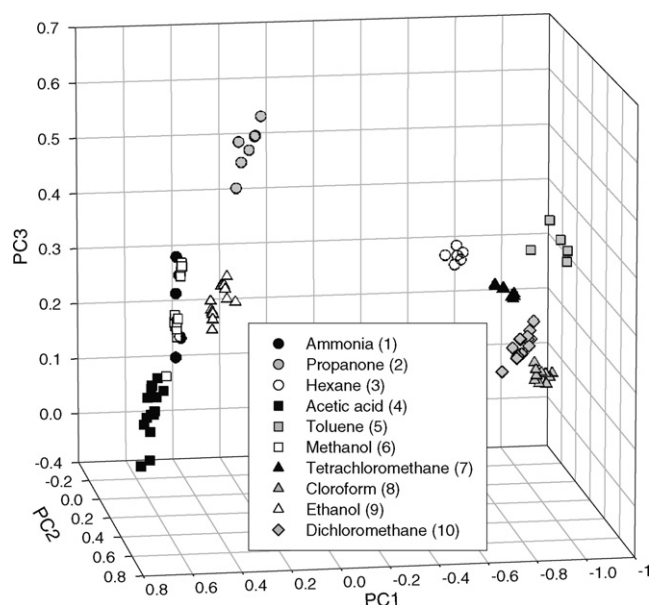
Fig. 8. Principal components representation of normalized data.
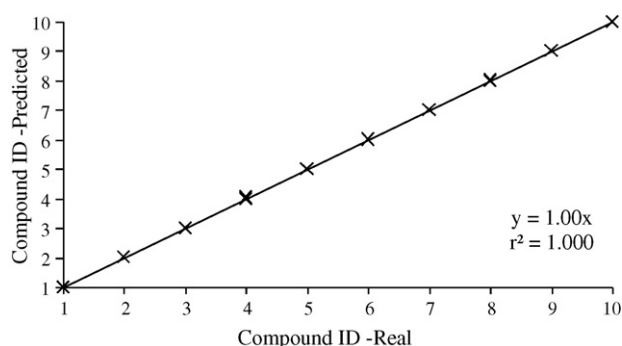
Fig. 9. Predicted *vs.* real values for the test set, using the third neural network.

Table 3
Calibration curves of the most sensitive sensors for each compound

Compound	Equation	Sensor
Ammonia	$\Delta F = 8.81M + 6.37$, $r = 0.9994$	Nafion
Propanone	$\Delta F = 0.67M + 7.98$, $r = 0.9954$	Nafion
Hexane	$\Delta F = 0.51M - 1.19$, $r = 0.9998$	PDMS
Acetic acid	$\Delta F = 1.93M + 1.35$, $r = 0.9689$	Nafion
Toluene	$\Delta F = 0.83M - 0.37$, $r = 0.9916$	Mn_pht
Methanol	$\Delta F = 33.35M - 0.91$, $r = 0.9897$	Nafion
Tetrachloromethane	$\Delta F = 0.86M - 4.39$, $r = 0.9787$	PDMS
Chloroform	$\Delta F = 0.64M + 1.90$, $r = 0.9911$	Mn_pht
Ethanol	$\Delta F = 3.21M + 0.55$, $r = 0.9607$	Nafion
dichloromethane	$\Delta F = 0.29M + 2.07$, $r = 0.9772$	Mn_pht

tion. This way, it is reasonable to postulate that the quantity of the compound would be determined even with best accuracy than with neural network prediction.

Calibration curves for each sensor for every compound are available. However, quantification should be performed using the calibration curve of the sensor with highest sensitivity. Table 3 shows the equations of the calibration curves of the sensors most appropriate for each compound. Frequency decrease (ΔF) was expressed in Hz, while the quantities of the solvent injected (M) were expressed in μg.

4. Conclusion

The objective of the work, the identification and quantification of a compound in a universe of 10 different hazardous compounds, when a flask with 2.5 L is broken in a store-room of $3\,m \times 3\,m \times 2.5\,m$, was completely fulfilled. The proposed array of sensors, with artificial neural network, is capable of giving a fast and correct answer, even when the individual sensors are not highly selective, and with a smaller number of sensors than compounds. This electronic nose allows the identification of any of the tested hazardous compounds, sampling less than 2.5 mL. The neural network can be simplified by applying principal component analysis. Identification can be achieved from normalized data with a neural network with less perceptrons and artificial neurons, and quantification was still possible using the calibration curves of the appropriate sensor.

References

[1] R.E. Lenga, The Sigma–Aldrich Library of Chemical Safety Data, vol. 1, II ed., 1988, USA.
[2] B.J. Doleman, M.C. Lonergan, E.J. Severin, T.P. Vaild, N.S. Lewis, Anal. Chem. 70 (1998) 4177.
[3] K.T. Lau, J. Micklefield, J.M. Slater, Sens. Actuators B 50 (1998) 69.
[4] E.J. Severin, B.J. Doleman, N.S. Lewis, Anal. Chem. 72 (2000) 658.
[5] M.T.S.R. Gomes, A.C. Duarte, J.A.B.P. Oliveira, Talanta 48 (1999) 81.
[6] N. Kasai, I. Sugimoto, M. Nakamura, Sens. Actuators B 65 (2000) 114.
[7] C. Je, R. Stone, S.G. Oberg, Sci. Total Environ. 382 (2007) 364.
[8] I. Sugimoto, T. Nagaoka, M. Seyama, M. Nakamura, K. Takahashi, Sens. Actuators B 124 (2007) 53.
[9] P. Si, J. Mortensen, A. Komolov, J. Denborg, P.J. Møller, Anal. Chim. Acta 597 (2007) 223.
[10] P.E. Keller, R.T. Kouzes, L.J. Kangas, IEEE Electro/94 International Conference in Boston USA, 1994, 378.
[11] G.J. Gouws, D.J. Gouws, Sens. Actuators B 91 (2003) 326.
[12] M. Sriyundthsak, A. Teeramongkolrasasmee, T. Moriizumi, Sens. Actuators B 65 (2000) 358.
[13] A. Ortega, S. Marco, T. Sundic, J. Samitier, Sens. Actuators B 69 (2000) 302.
[14] H. Zhang, M.Ö. Balaban, J.C. Principe, Sens. Actuators B 96 (2003) 385.
[15] A.K. Srivastava, Sens. Actuators B 96 (2003) 24.
[16] C.W. McCarrick, D.T. Ohmer, L.A. Gilliland, P.A. Edwards, Anal. Chem. 68 (1996) 4264.
[17] M. Penza, G. Cassano, Sens. Actuators B 89 (2003) 269.
[18] D.L.A. Fernandes, J.A.B.P. Oliveira, M.T.S.R. Gomes, Anal. Chim. Acta 617 (2008) 171.
[19] F. Despagne, D.L. Massart, Analyst 123 (1998) 157R.

vents was achieved with 100% success. Although quantification cannot be obtained by the network, as data have been normalized, non-normalized sample data can be used for solvent quantification using the appropriate calibration curve, after compound identifica-

Urea as new stabilizing agent for imipenem determination Electrochemical study and determination of imipenem and its primary metabolite in human urine

R. Fernández-Torres, M. Villar Navarro, M.A. Bello López, M. Callejón Mochón*, J.C. Jiménez Sánchez

Department of Analytical Chemistry, Faculty of Chemistry, University of Seville, 41012 Seville, Spain

ABSTRACT

Imipenem shows a fast chemical conversion to a more stable imin form (identical to that of biochemical dehydropeptidase degradation) in aqueous solutions and stabilizing agents used avoid its electrochemical study and determination.

The aim of this work is the proposal of urea as stabilizing agent which allows the electrochemical study of imipenem and the proposal of electrochemical methods for the determination of imipenem and its primary metabolite (M1) in human urine samples. Electrochemical studies were realized in phosphate buffer solutions over pH range 1.5–8.0 using differential-pulse polarography, DC-tast polarography, cyclic voltammetry and adsorptive stripping voltammetry. In acidic media, a non-reversible diffusion-controlled reduction involving a two steps mechanism which involves one electron and one proton in the first step and two electrons and two protons in the second step occurs and the mechanism for the reduction was suggested.

A differential-pulse polarographic method for the determination of imipenem in the concentration range 3.2×10^{-6} to 2×10^{-5} M (0.95–3.4 mg/L) and its primary metabolite in the concentration range 1.4×10^{-6} to 10^{-4} M (0.43–26.1 mg/L) with detection limits of 9.6×10^{-7} M (0.28 μg/L imipenem) and 4.3×10^{-7} M (0.14 μg/L M1) was proposed. Also, a method based on controlled adsorptive pre-concentration of imipenem on the hanging mercury drop electrode followed by voltammetric measure, allows imipenem determination in the concentration range 1.8×10^{-8} to 1.2×10^{-6} M (5.42–347 μg/L) with a detection limit of 5.4×10^{-9} M (1.63 μg/L). The proposed methods have been used for the direct determination of the analytes in a pharmaceutical formulation and human urine.

© 2008 Elsevier B.V. All rights reserved.

1. Introduction

Imipenem [5R-[5α,6α(R*)]]-6-(1-hydroxyethyl)-3-[[2-[(imino-methyl)amino]ethyl] thio]-7-oxo-1- azabicyclo[3.2.0]hept-2-ene-2-carboxylic acid (Fig. 1) is the *N*-formimidoyl derivative of thien-amycin, the first member of a new class of beta-lactam antibiotics, the carbapenems, having a broad-spectrum activity against aerobic and anaerobic bacteria. Because imipenem is hydrolysed by the renal brush border enzyme dehydropeptidase-I (DHP-I) [1], it is coadministered in clinical usage with cilastatin, a specific and highly active dehydropeptidase inhibitor, which improves the plasma concentration and markedly increases the urinary excretion of the unmetabolyzed drug [2].

The renal metabolism occurs by cleavage of beta-lactam ring, giving imipenemoic acid, the primary metabolite of imipenem (M1) (Fig. 1) [3]. A previous work has demonstrated that the enzymatically degraded antibiotic structure is the same as those obtained by deliberate chemical hydrolysis or by degradation on storage in aqueous solution [4]. A previous stability study of imipenem in aqueous solution has been realized [5] which revealed that rate determining beta-lactam ring opening preceded the formation of several products whose structures were not clearly established.

An excellent work about imipenem's degradation products using ^{1}H RMN and ^{13}C RMN has been published [4], and the conversion mechanisms (chemical and biochemical) were proposed (Fig. 2) with a tautomeric equilibrium of M1. Numerous other minor products were detected by HPLC in the decomposition mixtures derived from imipenem. However, Carlucci et al. [6] have reported that the only metabolite from real urine samples was the parent drug, thienamycin.

---

* Corresponding author.
E-mail address: mochon@us.es (M. Callejón Mochón).
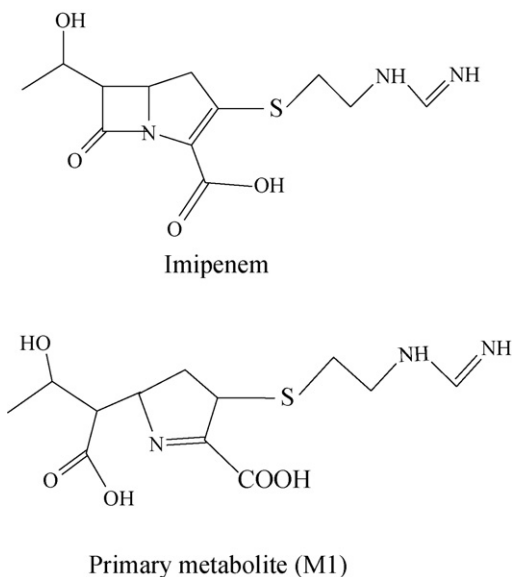
Fig. 1. Structures for imipenem and its primary metabolite (M1).

The degradation of imipenem's primary metabolite (M1) yields to a not well-defined product that absorbs strongly at 308 nm and it has been also studied under different conditions [7].

Bersier et al. [8] also described the fast chemical conversion of imipenem solutions to the imin form which is also electroactive and proposed the polarographic techniques as potential methods to determine carbapenem antibiotics.
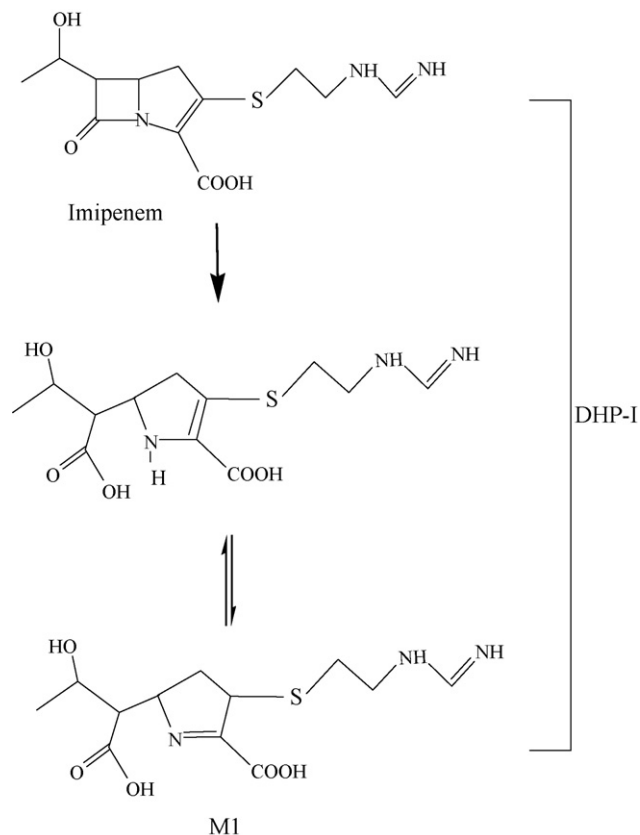
Fig. 2. Chemical and metabolic transformations of imipenem including M1 tautomeric rearrangement.

The stability of imipenem is well documented in literature. The stability in aqueous solution depends on the concentration of the drug and the pH [5], in general imipenem exhibits low stability in aqueous solutions and serum. Until now the most effective stabilizing substances for storing imipenem are non-nucleophilic inert buffers (pH 5–8) which are zwitterionic substituted morpholines such as 2-(N-morpholino)ethane sulfonate (MES) and 3-(N-morpholino)propane sulfonate (MOPS) and 4-(2-hydroxy-ethyl)piperazine-1-ethanesulphonic (HEPES) because they probably do not promote the cleavage of the beta-lactam ring [9]. Despite these facts, imipenem exhibits a great stability in urine samples [10].

Nowadays, no electrochemical procedures are available for the determination of imipenem, because the interference of the common stabilizing substances avoided its determination using electrochemical techniques. However, a study of the electrochemical behavior of its main metabolite has been developed [10].

In this work, a new stabilizing substance that permits to study the electrochemical behavior of imipenem have been assayed. The use of this stabilizing agent allows the electrochemical study of imipenem as well as the determination of imipenem and its main metabolite at low concentration levels using a simple, accurate and a non-time consuming procedure. The reduction mechanism has been suggested. A differential-pulse polarographic method for the determination of imipenem and its primary metabolite has been proposed. Also, a method based on controlled adsorptive pre-concentration of imipenem on the hanging mercury drop electrode have been proposed for the direct determination of the analytes in a pharmaceutical formulation, spiked human urine and real human-derived urine with good results and it should be appropriate for monitoring purposes.

2. Materials and methods

2.1. Chemicals and reagents

Imipenem was kindly provided by Merck Sharp & Dohme, Spain. All chemicals were of analytical-reagent grade and purchased from Merck (Darmstadt, Germany). High purity water was obtained from a Millipore (Milford, MA, USA) Milli-Q Plus system. Phosphate 0.05 M pH 3 buffer was used; suitable aliquots of 1 M H_3PO_4 and 1 M NaOH were added to adjust the pH at other values when it was necessary. Imipenem stock solutions of 10^{-3} M were daily prepared by dissolving it in urea aqueous solution (1 g/L). Aqueous solution of urea 1 g/L was used to prepare working solutions of imipenem. M1 standard solution was obtained from imipenem 10^{-3} M solution freshly prepared daily, and after its preparation, 2 h of storage at room temperature were necessary in order to warrant their complete conversion to the M1 [10].

2.2. Apparatus

An ECO-Chemie PGSTAT 10 (Eco Chemie B.V., Utrecht, The Netherlands) potentiostat–galvanostat was used in combination with a Metrohm VA-663 polarographic stand fitted with a PC provided with the appropriate GPES (General Purpose Electrochemical Software) version 4.2.

A three-electrode combination was used, consisting of a saturated KCl–Ag/AgCl reference electrode, a stationary dropping-mercury electrode (SDME) or hanging mercury drop electrode (HMDE) as working electrode and a platinum wire auxiliary electrode. A Crison (Barcelona, Spain) Model 2002 pH-meter with a combined glass-calomel electrode was also used.

A HPLC equipment (Merck-Hitachi) consisted of a L-7100 pump, a Rheodyne (Cotati, CA, USA) model 7725i injection valve with a 20 µL sample loop, a 25 cm × 4.6 mm Zorbax Eclipse® XDB-C$_8$, 5 µm column (Agilent technologies, Inc., Santa Clara, CA, USA) and a model L-7455 diode array detector controlled by a Merck-Hitachi D-7000 interface equipped with a HPLC System Manager® software was used to realize chromatographic determinations.

2.3. Stabilizing procedure

0.01 g of imipenem were placed into a 25 mL calibrated flask and diluted to volume with urea solutions of 15, 10, 1, 0.5, 0.2 g/L to get stock solutions of imipenem at different urea concentrations, in order to test the drug stability. Adequate aliquots of the stock solutions were used to record the corresponding polarograms according to the procedure describe in the following section. The study was also realized at different pH values (3, 6.5, 8.5, and 11) of the optimum stock solution (1 g/L).

2.4. Determination of imipenem and M1 by differential pulse polarography (DPP)

Aliquots containing 23.9–85 µg of imipenem (1 g/L) and 10.7–652 µg of M1 were placed into a 25 mL calibrated flask, 0.2 mL of urea 1 g/L and 5 mL of buffer solution (pH 3) were added. The solution was diluted to volume with water and mixed well. The solution was then transferred into a polarographic cell. The differential pulse polarogram was recorded from −0.1 to −1.5 V (pulse amplitude −70 mV, scan rate 10 mV s^{-1}) after deoxygenation with a stream of pure nitrogen during 10 min. A calibration plot obtained with known concentrations of imipenem was used to convert peak height into sample concentrations. Cyclic voltammetry experiments were carried out under identical conditions using a scan rate of 50 mV s^{-1}.

2.5. Determination of imipenem by adsorptive stripping voltammetry (AdSV)

An aliquot containing 0.13–9.0 µg of imipenem (1 g/L) was placed into a 25 mL calibrated flask, 0.2 mL of urea 1 g/L and 5 mL of buffer solution (pH 3) were added, and diluted to the mark with water. The solution was transferred into a polarographic cell and, after deoxygenation for 10 min with a stream of pure nitrogen, was measured from 0 to −1.5 V (pulse amplitude −70 mV, scan rate 10 mV s^{-1}) after a deposition step consisting in the application of a potential of 0.0 V for 15 s and an equilibration time of 5 s.

2.6. Determination of imipenem and M1 in human urine by DPP

Up to 2 mL of untreated urine were placed into a 25 mL volumetric flask and diluted with water to the mark. 0.5 mL of this solution with 0.2 mL of urea 1 g/L and 5 mL of buffer solution (pH 3) were diluted with water to 25 mL into a volumetric flask. The polarograms were recorded according to the above-recommended procedure. The voltammograms of samples without analytes do not show any signal that can interfere in the determination.

2.7. Determination of imipenem in human urine by AdSV

Up to 0.5 mL of untreated urine were diluted with water to 25 mL in a volumetric flask; a 20 µL aliquot of this solution was transferred into a 25 mL calibrated flask, 0.2 mL of urea 1 g/L and 5 mL of buffer solution (pH 3) were added and diluted with water to 25 mL into a volumetric flask. The samples were measured according to the procedure described in Section 2.5. The voltammograms of samples without imipenem do not show any signal that can interfere in the determination.

2.8. Determination of imipenem in pharmaceuticals

The proposed procedure for the determination of imipenem was applied to its direct determination in one pharmaceutical formulation (Tienam®).

Vials of Tienam® 500/500 mg were directly analysed, after solubilisation in urea 1 g/L solution. Adequate aliquots of the stock solution were prepared and measured according to the procedure described in Section 2.4.

2.9. Clinical study protocol

A dose of 500 mg imipenem-500 mg cilastatin was administered to two volunteers. Urine samples were collected after 2 h from the injection and immediately submitted to the above described procedures in order to determine imipenem and M1 contents.

3. Results and discussion

3.1. Stability of imipenem in urea solutions

As mentioned in Section 1, imipenem suffers a fast chemical degradation in aqueous solution so a stabilizing substance must be used to avoid such degradation.

Previously to the stability study, DC-tast and DP polarograms of urea solutions (15, 10, 1, 0.5, 0.2 g/L) were recorder in order to evaluate a possible interference. The absence of analytical signals confirms that urea does not interfere in the voltammetric analysis.

The stability study was realized at different urea concentration and different pH values of the optimum stock solution (3, 6.5, 8.5, 11) as mentioned previously. Results obtained are showed in Fig. 3a and b. As can be observed, imipenem solutions remain stable at least 48 h at concentrations equal or above 1 g/L of urea at pH values of 6.5 and 8.5. At a more acidic pH value imipenem suffers a chemical degradation, although it remains stable at least one hour, which allows its electrochemical determination at pH 3 where the height of the peak reaches a maximum value. At pH 11 the signal of imipenem is very weak and it disappear in 2 h.

3.2. Reduction waves for imipenem and M1

Imipenem is reduced on the SDME, in acidic media, producing two cathodic waves with peak potentials $E_{p1} = -1.0$ V and $E_{p2} = -1.25$ V (Fig. 4). The effect of pH on the DC-tast polarogram was investigated by recording the current–voltage curves, at a drop time of 1 s and 10 mV s^{-1} scan rate for a 10^{-5} M aqueous solution. Two cathodic waves were observed in the pH range 1.5–5.0. In Fig. 5a, the plot of $E_{1/2}$ versus pH is shown; as can be seen, when pH increases, the half-wave potential shifts towards more negative values for wave 2 and to less negative values for wave 1. Linear pH-dependence of the half-wave potential, for both waves shows that protons participate directly on the reduction process. The plot shows two segments which intersections leads to a pH value of 3.8 approximately, which is in agreement with theorical pK_a value 3.18 ± 0.09 [5].

The study of the influence of pH on limit currents was also carried out to determine whether the electroactive species participate in equilibria involving protons directly and to obtain the pH range for maximum signal. The limit current reaches a maximum around pH 2.0–3.0 (Fig. 5b), so pH 3.0 was chosen for the determination of imipenem because waves were better defined at this pH value.

Fig. 4. Differential pulse polarograms of imipenem ((a) 1.0×10^{-5} M, (b) 4×10^{-6} M, (c) 3.2×10^{-6} M, (d) blank) and M1 ((a)1.5×10^{-5} M, (b) 5×10^{-6} M, (c) 2×10^{-6} M) aqueous solution (pH 3, urea 1 g/L, pulse amplitude of 70 mV, drop time of 1 s and 10 mV s^{-1} scan rate).

yses of imipenem solutions were done for both of the two waves giving a number of exchange electrons of one for peak 1 and two for peak 2, indicating a reduction via one and two-electron steps on the electrode surface.

A cyclic voltammetry scan was recorded in order to determine the reversibility of the system. Imipenem yields two well-defined reduction waves but oxidation waves are not observed (Fig. 6). The reduction waves are displaced to more negative potentials when the scan rate, υ, increases, which is a characteristic behavior of irreversible processes. When plotting i_p versus $\upsilon^{1/2}$ a linear relationship was observed, which agrees with diffusion-controlled electrode processes, $I_{p1}(A) = 2.2 \times 10^{-10} - 9.9 \times 10^{-10} V_b^{1/2}$, $r_1 = 0.9992$ (peak 1); $I_{p2}(A) = 5.69 \times 10^{-10} - 2.06 \times 10^{-9} V_b^{1/2}$, $r_2 = 0.9991$ (peak 2). The αn_a (electron transfer coefficient) value and the number of protons (p) corre-

Fig. 3. (a) Effect of pH on stability of imipenem (10^{-5} M, urea concentration 1 g/L). (b) Effect of urea concentration on stability of imipenem (10^{-5} M, pH 6.5).

The electrochemical behavior of M1 have been previously detailed by Hilali et al. [10] and the presence of urea does not affect its electrochemical behavior.

3.3. Effect of operating parameters

The drop time was ranged from 0.5 to 2 s and an increase in the intensity of the peak with the drop time was observed. Plotting the intensity of the peak obtained by DPP versus $t^{2/3}$, a linear relationship was observed with a correlation coefficient of 0,9995. A time of 1 s was chosen.

The peak height increases linearly when pulse amplitude ranges from 10 to 100 mV; however, the peak potential was displaced towards more positive values. A pulse amplitude of 70 mV was selected as the optimum value as well defined peaks and high peak current were obtained.

3.4. Number of electrons transferred, reversibility of the system and mechanism of reduction of imipenem

Controlled-potential microcoulometry was used to determine n, the number of electrons transferred in the reduction process. This study was done at three pH values, 2.0, 3.0 and 4.0. Microelectrol-

Fig. 5. (a) Effect of pH on $E_{1/2}$ (10^{-5} M imipenem, urea 1 g/L, DC-tast voltammetry with a drop time of 1 s and 10 mV s^{-1} scan rate). (b) Effect of pH on peak current (10^{-5} M imipenem, urea 1 g/L, DC-tast voltammetry with a drop time of 1 s and 10 mV s^{-1} scan rate).
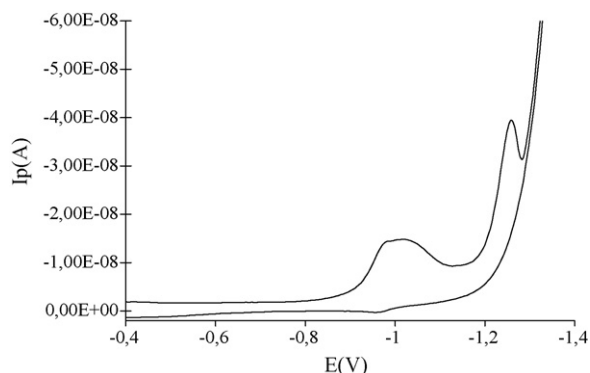
Fig. 6. Current–potential curve for cyclic voltammetry (10^{-5} M imipenem, urea 1 g/L).

sponding to the rate-determining step were calculated at different pH values. In the pH range 2–5, αn_a was found to be 0.85 ± 0.08 (wave 1) and 1.93 ± 0.04 (wave 2). Using the following expression: $\Delta E_{1/2}/\Delta pH = 0.059 p/\alpha n_a$, p was found to be 0.8 ± 0.1 (wave 1) y 2.2 ± 0.21 (wave 2).

From the results obtained and, on the basis of imipenem structure and the reduction potentials obtained, we suggest that the mechanism of reduction can be assigned to the break of the S—C bond (wave 1) giving a radical compound that would suffer a dimerization compound, which involves one electron and one proton as follows:
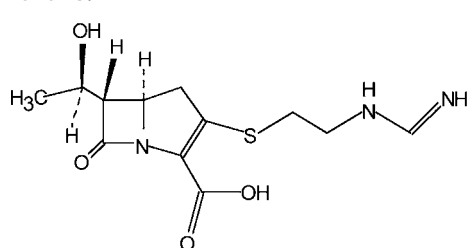
and to the direct reduction of the carboxylic acid group to aldehyde (wave 2), which involves two electrons and two protons as follows:
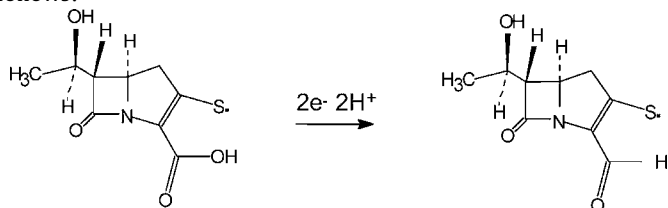
3.5. DPP: variation of peak intensity with the concentration of imipenem and M1

A calibration plot was obtained from known concentrations of imipenem and M1 using the peak current as analytical response. In the case of imipenem the peak 2 was used because it renders better sensibility. Series of standard solutions (three replicates) containing imipenem and M1 were prepared by following the procedures described in Section 2.6. The calibration graph was found to be linear over the range 3.2×10^{-6} to 2×10^{-5} M for imipenem (Eq. (1)) and 1.43×10^{-6}–10^{-4} M for M1 (Eq. (2))

$$-I_p \ (A) = (8.18 \pm 0.52) \times 10^{-9} + (1.26 \pm 0.06) \times 10^{-2} C \ (M)$$
$$(n = 10, \ r = 0.9996) \tag{1}$$

$$-I_p \ (A) = (5.91 \pm 0.60) \times 10^{-10} + (5.94 \pm 0.09) \times 10^{-4} C \ (M)$$
$$(n = 10, \ r = 0.9998) \tag{2}$$

Sensitivity parameters such as limit of detection (LOD) were calculated as the minimum concentration of an analyte that can be detected and reliably distinguished from zero and limit of quantitation (LOQ) as the minimum concentration of an analyte that can be determined quantitatively with an acceptable level of precision. To take into account the errors associated with the calibration line, the Long and Winefordner [11] approach was used where the LOD is calculated as:

$$X_{LOD} = \frac{2t(\nu, P)[s_{blank}^2 + s_a^2 + (a/b)^2 s_b^2]^{1/2}}{b}$$

and the LOQ was calculated from the X_{LOD} value according to the Analytical Methods Committee [12] changing LOD into LOQ.

Detection limits of 9.59×10^{-7} M (0.28 mg/L) and 4.30×10^{-7} M (0.14 mg/L) were obtained for imipenem and M1, respectively, and quantitation limits of 3.20×10^{-6} M (0.95 mg/L) and 1.43×10^{-6} M (0.43 mg/L) were obtained for imipenem and M1, respectively. In order to check the precision of the method [13,14], 3.2×10^{-6}, 5×10^{-6} and 1.5×10^{-5} M solutions of imipenem and 1.43×10^{-6}, 5×10^{-6} and 1.5×10^{-5} M solutions of M1 were prepared and measured in quintuplicated obtaining a relative standard deviation (R.S.D.) of 1.9%, 2.8% and 2.1% for imipenem, 2.3%, 2.1% and 3.1%
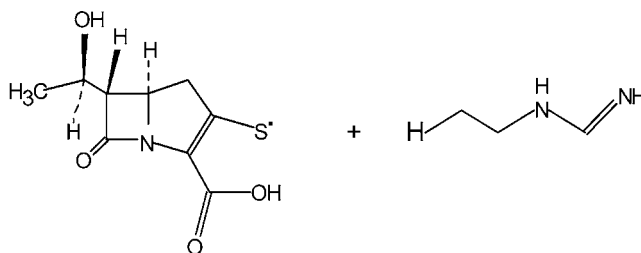
for M1, respectively; intermediate precision obtained measuring within a week 10^{-5} M solutions was 1.53% for imipenem and 2.85% for M1.

3.6. Adsorptive stripping voltammetry of imipenem (AdSV)

The electrochemical studies with hanging mercury drop electrode carried out indicate that an adsorption process occurs on the mercury electrode surface which can be used as an effective pre-concentration step prior to voltammetric measurement. An
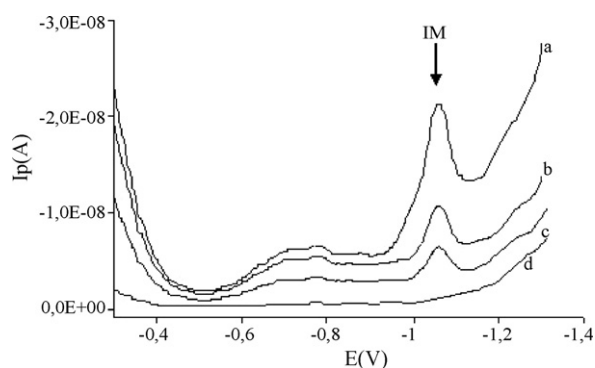
Fig. 7. Voltammograms corresponding to the AdSV of imipenem ((a) 7×10^{-7} M, (b) 3×10^{-7} M, (c) 8×10^{-8} M, (d) blank, urea 1 g/L).
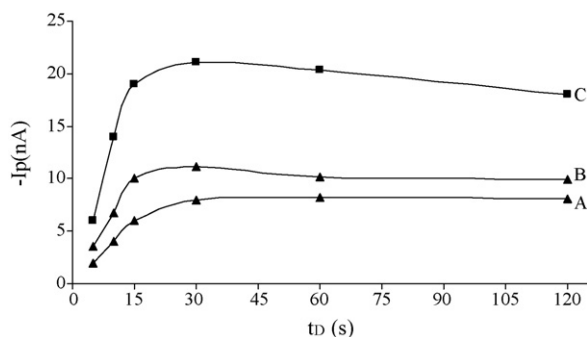
Fig. 8. Peak current versus deposition time for 2.8×10^{-8} (A), 3×10^{-7} (B) and 1.2×10^{-6} M (C) imipenem solutions.

exhaustive study of the dependence of adsorptive peak currents on accumulation potential and accumulation time, equilibration time and pH was performed using 3×10^{-7} M solutions. Voltammograms were recorded within a pH range 1.5–7.0 and a maximum intensity was obtained at pH 3; at this pH imipenem yields a well-defined peak at around -1.10 V (Fig. 7).

The influence of the deposition potential on the peak height shows that imipenem is not affected by the deposition potential applied, so 0 V was used as the accumulation potential for all the measurements. The influence of accumulation time on the peak current was studied in the range 5–120 s. The current versus deposition time plots at concentrations of 2.8×10^{-8}, 3×10^{-7} and 1.2×10^{-6} M appear in Fig. 8. An initial linear relationship was observed up to around 15 s. The influence of the equilibration time on the peak height was studied in the range 0–40 s, and no dependence between both magnitudes was found, a 5 s equilibration time was chosen for all the measurements.

A linear relationship of the adsorption holds between the peak current and the concentration of imipenem in the range from 1.8×10^{-8} to 1.2×10^{-6} M with a good precision and accuracy. The triplicate measurements of 10 solutions with concentration values within this range follow the expression:

$$-I_p\,(\mathrm{A}) = (7.22 \pm 0.42) \times 10^{-10} + (1.84 \pm 0.06) \times 10^{-2}\,C\,(\mathrm{M})$$

$$(r = 0.9992)$$

Using the expressions previously described in the above section, the LOD calculated was 5.43×10^{-9} M (1.63 µg/L) and the quantitation limit was 1.81×10^{-8} M (5.42 µg/L). In order to check the precision of the method [12,13], 5×10^{-8} and 4×10^{-7} M solutions of imipenem were prepared and measured in quintuplicate, obtaining a repeatability (intra-assay precision) of 4.3% and 5.1% for the relative standard deviation (R.S.D.), respectively; intermediate precision obtained measuring within a week 5×10^{-8} M solutions was 7.09%.

Fig. 9. Voltammogram corresponding to the reduction of real human urine containing M1 and imipenem. (A) Blank urine sample and (B) urine sample of patient 1.

3.7. Analysis of urine samples

Previously to the imipenem determination in urine samples, due to its 1:1 coadministration, the possible interference of cilastatin was checked. Both DPP and adsorptive stripping voltammetry of imipenem (AdSV) procedures were checked with cilastatin amounts up to 10-fold the corresponding imipenem amounts and no interference were observed.

Stability studies of imipenem into urine show that not significant hydrolysis occurs within 15 h at room temperature.

In order to avoid matrix effect the standard addition method was used. Urine blank samples were spiked with imipenem and M1 to obtain 250, 300 and 500 mg/L concentrations. These spiked samples were submitted, in triplicate, to the above-proposed procedures and the imipenem and M1 concentrations determined. The recoveries obtained are shown in Table 1. The accuracy of the proposed methods was statistically checked according to the *t*-test by comparison of the experimental mean with the known value [15]. As can be seen, the recoveries obtained shown an adequate accuracy for both methods.

3.8. Human study

Real human urine samples obtained from two volunteers as it has been previously described in Section 2.7, were submitted to the described procedures and measured by DPP and AdSV. The results obtained are shown in Table 2 and Fig. 9 shows the reduction peaks of imipenem (A) and M1 (B) corresponding to a real human urine sample measured by DPP.

Urine samples were also measured by a HPLC procedure [6] as another accuracy determination for the proposed methods [13,14]. The determination was realized with a reverse-phase C8 column using a mixture of sodium borate buffer (0.2 M, pH 7.2)-methanol (90:10, v/v) and detection at 300 nm. M1 and imipenem elute at 3.8 and 5.2 min, respectively. Urine samples (0.1 mL) were stabilized

Table 1
Imipenem and M1 recoveries from spiked urine samples

Spiked amount (mg/L)	DPP				AdSV	
	Imipenem[a] (mg/L)	M1[a] (mg/L)	*t*-test Imipenem	*t*-test M1	Imipenem[a] (mg/L)	*t*-test Imipenem
250	245 ± 4	235 ± 10	1.77	2.12	243 ± 8	1.23
300	290 ± 6	295 ± 7	2.35	1.01	305 ± 8	0.88
500	505 ± 11	480 ± 13	0.64	2.17	502 ± 9	0.31
		2.78[b]				2.78[b]

[a] Average of three determinations ± S.D.

[b] Critical values for *t* ($p = 0.05$).

Table 2
Imipenem and M1 contents in real urine samples with DDP and AdSV methods and compared with another HPLC method (for the statistical data treatment see text)

		Patient 1	Patient 2	Critical values for F and t ($p = 0.05$)
DDP	Imipenem[a] (mg/L)	570 ± 10	678 ± 7	
	F-test	2.77	1.36	39.00
	t-test	0.07	0.16	2.78
	M1[a] (mg/L)	255 ± 4	280 ± 6	
	F-test	1.0	1.36	39.00
	t-test	0.62	0.24	2.78
AdSV	Imipenem[a] (mg/L)	563 ± 9	690 ± 7	
	F-test	2.25	1.0	39.00
	t-test	0.21	0.12	2.78
HPLC	Imipenem[a] (mg/L)	575 ± 6	685 ± 6	
	M1[a] (mg/L)	245 ± 4	270 ± 7	

[a] Average of three determinations $\pm$ S.D.

Table 3
Validation parameters of HPLC method

		IM	M1
Linearity		$y = (9010 \pm 780.2)\,x + (60.80 \pm 458.6)$	$y = (1198 \pm 80.32)\,x + (37.80 \pm 596.0)$
Range (mg/L)		0.51–100	4.97–100
Precision[a]	5	2.6%	5.1%
	25	1.49%	7.73%
	100	2.89%	6.1%
Intermediate precision[b]		3.8%	5.9%
LOD (mg/L)		0.15	1.49
LOQ (mg/L)		0.51	4.97
Recoveries in spiked urine[c]	5	95.4 ± 1.7	89.0 ± 2.3
	40	97.6 ± 2.1	93.4 ± 3.8
	100	99.2 ± 0.9	91.9 ± 2.0

[a] R.S.D. of five determinations.
[b] R.S.D. of five determinations, 25 mg/L over 1 week.
[c] Average of three determinations $\pm$ S.D.

Table 4
Imipenem contents found in pharmaceuticals (Tienam® 500/500)

Sample	DPP			AdSV			HPLC
	Imipenem[a] (mg/L)	t-test	F-test	Imipenem[a] (mg/L)	t-test	F-test	Imipenem[a] (mg/L)
Vial 1	503 ± 7	0.25	1.31	510 ± 8	0.11	1.00	517 ± 8
Vial 2	515 ± 3	0.33	16.0	505 ± 5	0.18	5.76	490 ± 12
Vial 3	518 ± 7	0.11	2.04	512 ± 9	0.02	1.23	510 ± 10
		2.78[b]	39.00[b]		2.78[b]	39.00[b]	

[a] Average of three determinations $\pm$ S.D.
[b] Critical values for F and t ($p = 0.05$).

with a solution containing HEPES buffer (0.5 M, pH 6.8): ethylene glycol: water (2:1:1) and extracted with 1 mL of methanol, centrifuged at 4000 g for 10 min at 4 °C and the supernatant was injected onto the HPLC system. Validation parameters are shown in Table 3.

Table 2 shows the results obtained and as can be seen, good agreement was found between the HPLC and the two proposed methods, statistically proved according to the t-test for comparison of two experimental means, and two-tailed F-test, which indicates that the two proposed methods are accurate (null hypothesis accepted) [15].

Levels found of imipenem and M1 are in accordance to previous works [5–7], described in the Section 1.

3.9. Determination of imipenem in pharmaceuticals

Imipenem was determined in one pharmaceutical formulation (Tienam®) according to the procedure described in Section 2.8 by means of external calibration. Table 4 shows the results obtained. Samples were also measured by a HPLC procedure [6] and data

obtained were checked for statistical significance using t-test for comparisons of two experimental means, and two-tailed F-test [15]. Results obtained show no significant differences between data.

4. Conclusions

Urea is proposed as new stabilizing substance for the determination of imipenem and its primary metabolite that substitutes the biological buffers which cause a lot of interferences in some imipenem determinations and it also allows working at pH values different from 7.0. The use of urea permits the electrochemical study and determination. The reduction of imipenem under the conditions described in this work is an irreversible process controlled by diffusion. The proposed reduction mechanism involves two steps that imply one and two electrons, respectively. Also, an adsorption process occurs on the mercury electrode surface which can be used as an effective pre-concentration step prior the voltammetric measurement.

The results obtained show that the proposed methods may be useful to determine imipenem and M1 in human urine at the levels usually obtained after the administration of normal clinical doses and they would be methods of choice for monitoring this substance in patients.

The proposed procedures can be alternative methods to the chromatographic ones for the analysis of imipenem and M1, and they are easy, inexpensive, non-time consuming and also they do not require the use of organic solvents as well as they use simple sample treatment.

Acknowledgement

References

[1] H. Krop, J.G. Sundelof, J.S. Kahan, F.M. Kahan, J. Birnbaum, Antimicrob. Agents Chemother. 17 (1980) 993.
[2] S.R. Norrby, K. Alestig, B. Björnegard, L.A. Burman, F. Ferber, J.L. Huber, K.H. Jones, F.M. Kahan, J.S. Kahan, H. Kropp, M.A.P. Meisinger, J.G. Sundelof, Antimicrob. Agents Chemother. 23 (1983) 300.
[3] H. Kropp, J.G. Sundelop, R. Hajdu, F. Kahan, Antimicrob. Agents Chemother. 22 (1982) 62.
[4] R.W. Ratcliffe, K.J. Wildonger, L. Di Michele, A.W. Douglas, R. Hajdu, R.T. Goegelman, J.P. Springer, J. Hirshfield, J. Org. Chem. 54 (3) (1989) 653.
[5] G.B. Smith, E.F. Schoenewaldt, J. Pharm. Sci. 70 (3) (1981) 272.
[6] G. Carlucci, L. Biordi, C. Vicentini, M. Bologna, J. Pharm. Biomed. Anal. 8 (3) (1990) 283.
[7] D.G. Musson, R. Hajdu, W.F. Bayne, J.D. Rogers, Pharm. Res. 8 (1) (1991) 33.
[8] P.M. Bersier, J. Bersier, G. Sedelmeier, E. Hungerbühler, Electroanalysis 2 (5) (1990) 373.
[9] D.A. Gravallese, D.G. Musson, L.T. Pauliukonis, W.F. Bayne, J. Chromatogr. 310 (1984) 71.
[10] A. Hilali, J.C. Jiménez, M. Callejón, M.A. Bello, A. Guiraúm, J.Pharm. Biomed. Anal. 38 (2005) 768.
[11] L.G. Long, J.D. Winefordner, Anal. Chem. 55 (1983) 712A.
[12] Analytical Methods Committee. Analyst 112 (2) (1987) 99–204.
[13] International Conference on Harmonization (ICH), Q2b: Validation of Analytical Procedures: Methodology, US FDA Federal Register, vol. 60, May 1997, 27463.
[14] US Pharmacopeia 24. Validation of compendial methods, section 1225, United Sates Pharmacopeal Convention, Rockville, MD, 1999.
[15] J.C. Miller, J.N. Miller, Statistic for Analytical Chemistry, 4th ed., Prentice Hall, Chichester, 2000.

Pre-concentration procedure for determination of copper and zinc in food samples by sequential multi-element flame atomic absorption spectrometry

Hadla S. Ferreira[a], Ana C.N. Santos[a], Lindomar A. Portugal[a], Antonio C.S. Costa[a], Manuel Miró[b], Sérgio L.C. Ferreira[a],*

[a] Universidade Federal da Bahia, Instituto de Química, Campus Universitário de Ondina, Salvador, Bahia 40170-290, Brazil
[b] Department of Chemistry, Faculty of Sciences, University of Balearic Islands, Carretera de Valldemossa km 7.5, E-07122 Palma de Mallorca, Spain

A R T I C L E   I N F O

A B S T R A C T

In this paper is proposed a simultaneous pre-concentration procedure using cloud point extraction for the determination of copper and zinc in food samples employing sequential multi-element flame atomic absorption spectrometry (FS-FAAS). The reagent used is 1-(2-pyridylazo)-2-naphthol (PAN) and the micellar phase is obtained using the non-ionic surfactant octylphenoxypolyethoxyethanol (Triton X-114) and centrifugation. The optimization step was performed using Box–Behnken design for three factors: solution pH, reagent concentration and buffer concentration. A multiple response function was established in order to get an experimental condition for simultaneous extraction of copper and zinc.

Under the optimized experimental conditions, the method allows the determination of copper with a limit of detection ($3\sigma_b/S$, LOD) of 0.1 μg L^{-1}, precision expressed as relative standard deviation (R.S.D.) of 2.1 and 1.3% ($N = 10$), for copper concentrations of 10 and 50 μg L^{-1}, respectively. Zinc is determined with a LOD of 0.15 μg L^{-1} and precision as R.S.D. of 2.7 and 1.7% for concentrations of 10 and 50 μg L^{-1}, respectively. The enhancement factors obtained were 36 and 32 for copper and zinc, respectively. The accuracy was assessed by analysis of certified reference materials, namely, SRM 1567a – Wheat Flour and SRM 8433 – Corn Bran from National Institute of Standards & Technology and BCR 189-wholemeal flour from Institute of Reference Materials and Measurements.

The method was applied to the determination of copper and zinc in oats, powdered chocolate, corn flour and wheat flour samples. The copper content in the samples analyzed varied from 1.14 to 3.28 μg g^{-1} and zinc from 8.7 to 22.9 μg g^{-1}.

© 2008 Elsevier B.V. All rights reserved.

1. Introduction

Zinc, copper and iron are essential minerals that are required for a variety of biomolecules to maintain the normal structure, function, and proliferation of cells. These metals can be toxic in excessive amounts, especially in certain genetic disorders [1]. Foods are the principal sources of zinc and copper exposure for humans. Determination of these metals in foodstuffs is thus always opportune. Generally, trace level concentrations are found and pre-concentration procedures are required for these analyses when conventional techniques such as flame atomic absorption spectrometry (FAAS) and inductively coupled plasma optical emission spectrometry (ICP OES) are employed [2–7].

Cloud point extraction (CPE) is a separation technique which has been frequently used in procedures for determination of trace

level concentrations of organic and inorganic species in a plethora of sample types, employing a vast number of analytical techniques, such as FAAS [8–10], ICP OES [11], graphite furnace atomic absorption spectrometry [12], cold vapor atomic absorption spectrometry [13], hydride generation atomic absorption spectrometry [14], inductively coupled plasma mass spectrometry [15], molecular absorption spectrophotometry [16,17], laser induced-thermal lens spectrometry [18], fluorimetry [19], high performance liquid chromatography [20,21] and mass spectrometry [22]. However, most of the papers published so far reported univariate or first order models for investigation of the influence of experimental variables on the analytical responses [23,24].

Multivariate techniques have over the past few years played a relevant role in optimization of experimental factors involved in analytical methods [25–28]. Box–Behnken is a second-order multivariate design based on three-level incomplete factorial designs that received widespread application for assessment of critical experimental conditions, that is, maximum or minimum of response functions. The number of experiments (N) required for the

development of this design is defined as $N = 2K(K-1) + C_o$, where (K) is the factor number and (C_o) is the replicate number of the central point [29,30].

This paper proposes a pre-concentration procedure using CPE for determination of copper and zinc in food samples by fast sequential multi-element-FAAS. The ligand used is 1-(2-pyridylazo)-2-naphthol) (PAN) and the micellar phase is obtained using the non-ionic surfactant octylphenoxypolyethoxyethanol (Triton X-114). The optimization of the pre-concentration procedure is performed exploiting the Box–Behnken design.

2. Experimental

2.1. Instrumentation

A Varian Model SpectrAA 220 (Mulgrave, Victoria, Australia) flame atomic absorption spectrometer with fast sequential module (FS-FAAS), equipped with a conventional pneumatic nebulizer and nebulization chamber was used for the analysis. A multi-element hollow cathode lamp for determination of copper and zinc was used under the conditions suggested by the manufacturer and applying a current of 10.0 mA. The most sensitive wavelengths for copper at 324.8 nm and zinc at 213.9 nm were used with bandwidths of 0.5 and 1.0 nm for copper and zinc, respectively. The flame composition was acetylene (flow rate: 2.0 L min^{-1}) and air (flow rate: 13.5 L min^{-1}) and the burner height was set to 13.5 mm. The nebulizer flow rate aspiration was kept between 5.5 and 6.0 mL min^{-1}. A Fanem (São Paulo, Brazil) thermostatic bath was used to reach the cloud point temperature. A Janetzki T 32C (Berlin, German) centrifuge was employed to accelerate phase separation.

2.2. Chemicals and reagents

Ultrapure water was used for the preparation of the standard solutions. Copper and zinc solution (10.0 μg mL^{-1}) was prepared by diluting a 1000 μg mL^{-1} copper and zinc solution (Merck®) with 1% (v/v) nitric acid. A 0.025% (w/v) 1-(2-pyridylazo)-2-naphthol (PAN) solution was prepared by dissolving 0.025 g PAN and 3.2 g Triton X-114 in 10 mL of ethanol and making up to 100 mL with ethanol.

Tris buffer solution (pH 8.6) was prepared by dissolving 12.1 g Tris- (hydroxymethyl) aminomethane (Merck®) in 200 mL of deionised water and pH was adjusted with hydrochloric acid.

2.3. General procedure

A sample volume of 50 mL containing the analytes within the range of 0.34–220 μg L^{-1} for copper and 0.5–180 μg L^{-1} for zinc, plus 720 μL of 3.6 mg L^{-1} PAN in Triton X-114 solution and 750 μL of 1.5 mmol L^{-1} Tris buffer solution (pH 8.6) were transferred into a centrifuge tube. This system was heated thermostatically at 40 °C for 15 min. Separation of the two phases was achieved by centrifugation for 10 min at 2500 rpm. On cooling in an ice-bath for 10 min, the surfactant-rich phase became viscous. Then, the aqueous phase could be separated by inverting the tube. In the later, to reduce viscosity and facilitate sample handling, 300 μL ethanol solution containing 1% HNO$_3$ was added. This final solution was introduced into the flame by conventional aspiration.

2.4. Sample preparation and certified reference material

A mass of approximately 100 mg of homogenized samples in a blender was weighed and volumes of 2.0 mL of concentrated HNO$_3$ and 1.0 mL of 30% (v/v) H$_2$O$_2$ were added to the samples. After that, acid digestion bombs (4746 Model, ParrInstrument Company, USA) were closed and kept for 12 h at 150 ± 10 °C, which was the

optimized time to achieve the complete dissolution. After cooling down the solutions to room temperature, pH was adjusted to 8.6 with 1 mol L^{-1} NaOH before making up to 50.0 mL. All samples were analyzed in triplicate.

3. Results and discussion

3.1. Optimization of the pre-concentration procedure

The optimization step of the pre-concentration procedure was performed using a Box–Behnken design involving the following factors: sample pH, concentration of TRIS buffer solution and PAN reagent concentration. The time and temperature of heating were fixed to 15 min and 40° C respectively as reported in an earlier paper [31], wherein Triton X-114 was also used as surfactant. Sample volumes of 50 mL containing both copper and zinc at the 20.0 μg L^{-1} level were used in all experiments.

Table 1 shows the matrix with coded and real values and the responses as analytical signals (absorbances) for each individual metal. Replicates of the central point were performed for evaluation of the experimental error. All experiments were carried out in a random order. The final evaluation was done using a multiple response (MR) function in order to get a simultaneous condition for pre-concentration of both Cu(II) and Zn(II) ions, being (MR) calculated by the expression:

$$MR = Abs \frac{Cu}{0.0565} + Abs \frac{Zn}{0.1486},$$

where Abs is the analytical signal for each metal ion, 0.0565 and 0.1486 were the maximum values of absorbance obtained for copper and zinc, respectively, during the experimental protocol.

The equation below illustrates the relationship of the three variables, that is, solution pH, reagent concentration (RC) and buffer concentration (BC) and the multiple response.

$$MR = -5.9684 + 1.2827(pH) - 0.0751(pH)^2 + 0.3846(RC)$$
$$- 0.0874(RC)^2 2580.6551(BC) - 1102159.3873(BC)^2$$
$$+ 0.0006(pH)(RC) + 5.5937(pH)(BC) + 165.2179(RC)(BC)$$

The derivation of this general equation as (pH), (RC) and (BC) results in three new equations:

$$\frac{\delta(MR)}{\delta(pH)} = 1.2827 - 0.1502(pH) + 0.0006(RC) + 5.5937(BC)$$

$$\frac{\delta(MR)}{\delta(RC)} = 0.3846 - 0.1748(RC) + 0.0006(pH) + 165.2179(BC)$$

$$\frac{\delta(MR)}{\delta(BC)} = 2580.6551 - 2204.318,774(BC) + 5.5937(pH)$$
$$+ 165.2179(RC)$$

The critical point in the surface response are found by solving these equation systems for the conditions of $\delta(MR)/\delta(pH) = 0$, $\delta(MR)/\delta(RC) = 0$, $\delta(MR)/\delta(BC) = 0$. The way of calculating these critical points has been published in previous papers [32]. An evaluation using Analyses of Variance (ANOVA) demonstrated that there is no lack of fit in this model.

The calculated values for the critical point are as follows: solution pH of 8.6, RC of 3.61 mg L^{-1} and BC of 1.46 mmol L^{-1}. These results were calculated using the multiple response function, and a good agreement is found with the analytical results calculated for copper and zinc using individual absorbances, which were: pH 8.71,

Table 1
Box–Behnken design for optimization of the CPE extraction step

Experiment	pH	RC	BC	Cu	Zn	MR
1	4 (−1)	2.0 (−1)	0.0015 (0)	0.0112	0.0108	0.2709
2	9 (+1)	2.0 (−1)	0.0015 (0)	0.0526	0.1421	1.8872
3	4 (−1)	5.0 (+1)	0.0015 (0)	0.0154	0.0151	0.3742
4	9 (+1)	5.0 (+1)	0.0015 (0)	0.0565	0.1486	2.0000
5	4 (−1)	3.5 (0)	0.0010 (−1)	0.0100	0.0105	0.2477
6	9 (+1)	3.5 (0)	0.0010 (−1)	0.0509	0.1309	1.7818
7	4 (−1)	3.5 (0)	0.0020 (+1)	0.0121	0.0146	0.3124
8	9 (+1)	3.5 (0)	0.0020 (+1)	0.0542	0.1360	1.8745
9	6.5 (0)	2.0 (−1)	0.0010 (−1)	0.0445	0.1178	1.5803
10	6.5 (0)	5.0 (+1)	0.0010 (−1)	0.0371	0.1067	1.3747
11	6.5 (0)	2.0 (−1)	0.0020 (+1)	0.0293	0.0762	1.0314
12	6.5 (0)	5.0 (+1)	0.0020 (+1)	0.0350	0.1043	1.3214
13	6.5 (0)	3.5 (0)	0.0015 (0)	0.0518	0.1298	1.7903
14	6.5 (0)	3.5 (0)	0.0015 (0)	0.0525	0.1292	1.7987
15	6.5 (0)	3.5 (0)	0.0015 (0)	0.0533	0.1285	1.8081

RC: reagent concentration ($mg\,L^{-1}$), BC: buffer concentration ($mol\,L^{-1}$), and MR: multiple response function for simultaneous extraction of copper and zinc.

RC: 3.55 $mg\,L^{-1}$ and BC: 1.47 $mmol\,L^{-1}$ for copper, and pH 8.52, RC: 3.71 $mg\,L^{-1}$ and BC: 1.46 $mmol\,L^{-1}$ for zinc. Therefore, in this case, multiple response functions could be used because there is a tendency for all the answers to a common region of the experimental dominium studied. The overall experimental data were processed using a statistical program [33].

3.2. Validation studies

Limits of detection ($3\sigma/S$) and quantification ($10\sigma/S$), where (3σ) is the standard deviation of the blank and (S) slope of analytical curve, were calculated following IUPAC recommendations [34]. The precision was also determined and expressed as relative standard deviation. Table 2 compiles the analytical performance of the method.

The calibration equations obtained using the pre-concentration procedure were given as Abs = 0.0027 [Cu, $\mu g\,L^{-1}$] + 0.0006 for copper and Abs = 0.0067[Zn, $\mu g\,L^{-1}$] + 0.0018 for zinc with correlation coefficients >0.9991 for both metals. In order to determine the enhancement factor, analytical curves were prepared without CPE. The calibration equation obtained were Abs = 8.0×10^{-5} [Cu, $\mu g\,L^{-1}$] − 0.0010 and Abs = 0.0002 [Zn, $\mu g\,L^{-1}$] + 0.0031 for copper and zinc, respectively. The experimental enhancement factors calculated as the ratio of the slopes of the calibration graphs with and without pre-concentration were 36 and 32 for copper and zinc, respectively. The burner position of FS-FAAS was fixed during the sequential determination. The adjustment is made by the element of smaller sensitivity and/or lower concentration in the samples. In this work, this optimization was made for copper, because the sensitivity for this element is lower than that of zinc.

The accuracy of the procedure was confirmed by determination of copper and zinc in several certified reference materials, namely SRM 1567a – Wheat Flour and SRM 8433 – Corn Bran from NIST and BCR 189-Wholemeal flour from IRMM. The results are shown in Table 3. The t-test for comparison of means demonstrated that

Table 2
Analytical characteristics of the CPE method

Parameters	Copper	Zinc
Limit of detection ($\mu g\,L^{-1}$)	0.10	0.15
Limit of quantification ($\mu g\,L^{-1}$)	0.34	0.50
Precision as R.S.D. (10 $\mu g\,L^{-1}$)	2.1%	2.7%
Precision as R.S.D. (50 $\mu g\,L^{-1}$)	1.3%	1.7%
Enhancement factor	34	33
Concentration range ($\mu g\,L^{-1}$)	0.34–220	0.5–180

Table 3
Determination of copper and zinc in certified reference materials ($N = 3$)

Sample	Copper ($\mu g\,g^{-1}$)		Zinc ($\mu g\,g^{-1}$)	
	Certified	Found[*]	Certified	Found[*]
NIST 8433	2.47 ± 0.40	2.6 ± 0.3	18.6 ± 2.2	18.2 ± 1.3
BCR 189	6.4	6.5 ± 0.7	56.5	55.8 ± 1.7
NIST 1567a	2.1 ± 0.2	2.1 ± 0.3	11.6 ± 0.4	11.5 ± 0.6

[*] All results are expressed as interval confidence at 95% level.

Table 4
Determination of copper and zinc in food samples ($N = 3$)

Samples	Zinc ($\mu g\,g^{-1}$)[*]	Copper ($\mu g\,g^{-1}$)[*]
Oats	22.9 ± 1.4	3.3 ± 0.4
Powdered chocolate	9.0 ± 1.0	3.3 ± 0.1
Corn flour	16.8 ± 1.6	1.1 ± 0.3
Wheat flour	8.7 ± 1.1	1.2 ± 0.2

[*] All results are expressed as interval confidence at 95% level.

there is no significance difference between the certified values and the experimental results at the significance level of 0.05 [35].

3.3. Application

The optimized CPE pre-concentration method was applied to the determination of zinc and copper in powdered chocolate, oats, wheat flour and corn flour. The results obtained are showed in Table 4. The copper content in the samples analyzed varied from 1.14 to 3.28 $\mu g\,g^{-1}$ and zinc from 8.7 to 22.9 $\mu g\,g^{-1}$. These results do agree well with data reported in the literature as to the content of zinc and copper in the above foodstuffs [36].

The wheat flour sample was also analyzed employing ICP OES. The concentrations of Zn and Cu obtained via CPE were 8.7 ± 1.1 and $1.2 \pm 0.2\,\mu g\,g^{-1}$, respectively, while those calculated by ICP OES were 7.9 ± 0.2 and $1.39 \pm 0.08\,\mu g\,g^{-1}$ for zinc and copper, respectively. The statistical comparison by the t-test of comparison of means revealed the inexistence of significant difference between these values at the 95% confidence level.

4. Conclusions

The Box–Behnken design proved to be efficient for optimization of pre-concentration procedures using cloud point extraction for simultaneous determination of copper and zinc in food samples. The method proposed is inexpensive, precise and accurate and it has limit of quantification sufficient for determination of copper and zinc in food samples.

Acknowledgements

References

[1] Y. Zheng, X.K. Li, Y. Wang, L. Cai, Hemoglobin 32 (2008) 135.
[2] M.D.A. Korn, E.S.D.B. Morte, D.C.M.B. dos Santos, J.T. Castro, J.T.P. Barbosa, A.P. Teixeira, A.P. Fernandes, B. Welz, W.P.C. dos Santos, E.B.G.N. dos Santos, M. Korn, Appl. Spectrosc. Rev. 43 (2008) 67.
[3] V.A. Lemos, D.G. da Silva, A.L. de Carvalho, D.D. Santana, G.D. Novaes, A.S. dos Passos, Microchem. J. 84 (2006) 14.
[4] P. Pohl, B. Prusisz, Talanta 71 (2007) 1616.
[5] A. Pendergrass, D.J. Butcher, Microchem. J. 83 (2006) 14.
[6] V. Kienen, W.F. Costa, J.V. Visentainer, N.E. Souza, C.C. Oliveira, Talanta 75 (2008) 141.
[7] V.A. Lemos, E.M. Gama, A.D. Lima, Microchim. Acta 153 (2006) 179.
[8] V.A. Lemos, J.S. Santos, P.X. Baliza, J. Braz. Chem. Soc. 17 (2006) 30.
[9] M.A. Bezerra, A.L.B. Conceição, S.L.C. Ferreira, Microchim. Acta 154 (2006) 149.
[10] G.L. Donati, C.C. Nascentes, A.R.A. Nogueira, M.A.Z. Arruda, J.S. Nóbrega, Microchem. J. 82 (2006) 189.
[11] M.A. Bezerra, R.E. Bruns, S.L.C. Ferreira, Anal. Chim. Acta 580 (2006) 51.
[12] T.D. Maranhão, E. Martendal, D.L.G. Borges, E. Carasek, B. Welz, A.J. Curtius, Spectrochim. Acta Part B 62 (2007) 1019.
[13] I.M. Dittert, T.A. Maranhão, D.L.G. Borges, M.A. Vieira, B. Welz, A.J. Curtius, Talanta 72 (2007) 1786.
[14] A.E. Boyukbayram, M. Volkan, Spectrochim. Acta Part B 55 (2000) 1073.
[15] L. Liu, B. Hu, L. Xia, Z.C. Jiang, Talanta 70 (2006) 46.
[16] T. Madrakian, A. Afkhami, A. Mousavi, Talanta 71 (2007) 610.
[17] H.S. Ferreira, M.A. Bezerra, S.L.C. Ferreira, Microchim. Acta 154 (2006) 163.
[18] N. Shokoufi, F. Shemirani, Talanta 73 (2007) 662.
[19] C.C. Wang, M.O. Luconi, A.N. Masi, L. Fernandez, Talanta 72 (2007) 1779.
[20] L. Wang, Y.Q. Cai, B. He, C.G. Yuan, D.Z. Shen, J. Shao, G.B. Jiang, Talanta 70 (2004) 47.
[21] J. Zhou, S.W. Wang, X.L. Sun, Anal. Chim. Acta 608 (2008) 158.
[22] A.S. Lopes, J.S. Garcia, R.R. Catharino, L.S. Silva, M.N. Eberlin, M.A.Z. Arruda, Anal. Chim. Acta 590 (2007) 166.
[23] A. Shokrollahi, M. Ghaedi, S. Gharaghani, M.R. Fathi, M. Soylak, Quim. Nova 31 (2008) 70.
[24] N. Goudarzi, J. Braz. Chem. Soc. 18 (2007) 1348.
[25] F.S. de Oliveira, E.T. Sousa, J.B. de Andrade, Talanta 73 (2007) 561.
[26] A.F. Barbosa, M.G. Segatelli, A.C. Pereira, A.S. Santos, L.T. Kubota, P.O. Luccas, C.R.T. Tarley, Talanta 71 (2007) 1512.
[27] A. Alnajjar, A.M. Idris, H.H. AbuSeada, Microchem. J. 87 (2007) 35.
[28] E.T. Sousa, F.D. Rodrigues, C.C. Martins, F.S. de Oliveira, P.A.D. Pereira, J.B. de Andrade, Microchem. J. 82 (2006) 142.
[29] S.L.C. Ferreira, R.E. Bruns, H.S. Ferreira, G.D. Matos, J.M. David, G.C. Brandao, E.G.P. da Silva, L.A. Portugal, P.S. dos Reis, A.S. Souza, W.N.L. dos Santos, Anal. Chim. Acta 597 (2007) 179.
[30] S.L.C. Ferreira, M.G.A. Korn, H.S. Ferreira, E.G.P. da Silva, R.G.O. Araújo, A.S. Souza, S.M. Macedo, D.C. Lima, R.M. de Jesus, F.A.C. Amorim, J.M. Bosque-Sendra, Appl. Spectrosc. Rev. 42 (2007) 475.
[31] J. Cheng, K.C. Teo, Anal. Chim. Acta 450 (2001) 215.
[32] W.L. dos Santos, C.M.M. dos Santos, J.L.O. Costa, H.M.C. Andrade, S.L.C. Ferreira, Microchem. J. 77 (2004) 123.
[33] Statistics for Windows, StatSoft, Inc., 2300 East 14th Street, Tulsa, OK 741014, USA, 1999.
[34] IUPAC, Analytical Chemistry Division, Spectrochim. Acta Part B 33 (1978) 242.
[35] J.N. Miller, J.C. Miller, Statistics and Chemometrics for Analytical Chemistry, 5th edition, Pearson Education Ltd., Essex, 2005, pp. 41–45 (Chapter 3).
[36] Tabela Brasileira de Composição de Alimentos—TACO, http://dtr2004.saude.gov.br/nutricao/documentos/tab_bras_de_comp_de_alim_doc.pdf (accessed on April 01, 2008).

Development of an optical fibre reflectance sensor for *p*-aminophenol detection based on immobilised bis-8-hydroxyquinoline

Hayati Filik [a,*], Mustafa Hayvalı [b], Emine Kılıç [b], Reşat Apak [a], Duygu Aksu [a], Zeynep Yanaz [a], Tayfun Çengel [a]

[a] *Istanbul University, Faculty of Engineering, Department of Chemistry, Avcılar, 34320 Istanbul, Turkey*
[b] *Ankara University, Faculty of Science, Department of Chemistry, Tandogan, 06100 Ankara, Turkey*

ARTICLE INFO

ABSTRACT

2,2′-(1,4-Phenylenedivinylene)bis-8-hydroxyquinoline (PBHQ), a highly sensitive reagent used for the colorimetric determination of *p*-aminophenol (PAP), was successfully immobilised on XAD-7 and coupled with optical fibres to investigate a sensor-based approach for determining *p*-aminophenol. The solid-state sensor is based on the reaction of PAP with PBHQ in presence of an oxidant to produce an indophenol dye. The reflectance measurements were carried out at a wavelength of 647 nm since it yielded the largest divergence different in reflectance spectra before and after reaction with the analyte. The linear dynamic range of PAP was found within the concentration range of 0.1–$2.18\,\mathrm{mg\,l^{-1}}$ with its LOD of $0.02\,\mathrm{mg\,l^{-1}}$. The sensor response from different probes ($n = 7$) gave a R.S.D. of 4.4% at $1.09\,\mathrm{mg\,l^{-1}}$ PAP concentration. The response time of the optical one-shot sensor was 5 min for a stable solution. As this PAP sensor is irreversible, a fresh sensor has to be used for each measurement. All the experimental parameters were optimized for the determination of PAP. Using the optical sensing probe, PAP in pharmaceutical wastewater and paracetamol was determined. The effect of potential interferences such as inorganic and organic compounds was also evaluated. Potential on-site determination of PAP with such sensors can indirectly aid detection of organo-phosphorus nerve agents and pesticides in the field by inhibition of acetylcholine esterase-catalyzed hydrolysis of *p*-aminophenyl acetate to *p*-aminophenol.

© 2008 Elsevier B.V. All rights reserved.

1. Introduction

p-Aminophenol (PAP) has been widely used as raw chemical material and important intermediate in various fields, such as medicine, sulfur and azo dyes, rubber, feeding-stuff, petroleum, and photography, etc. [1–3]. As a result, large amounts of PAP may enter the environment as a pollutant. Moreover, *p*-aminophenol is a parent material for the production of paracetamol as one of the most produced pharmaceuticals worldwide. This compound is also an intermediate product of the decomposition of paracetamol and its analogs in the human body and during the storage of its medicinal preparations. It is known that paracetamol in aqueous solution is liable to undergo hydrolysis to form *p*-aminophenol, which is itself liable to degrade into quinoneimine [4]. *p*-Aminophenol tends to form oxidation products (e.g. quinonimine), which impart a characteristic pink color to the solutions. The rate of degradation of paracetamol increases with increasing temperature and light intensity [4]. This rate is minimal at a pH around 6 [5]. *p*-Aminophenol

is a harmful substance, because it increases the body temperature in humans, and its biological half-life (*i.e.*, the time required for half of PAP to be removed from the organism by biophysical and biochemical processes) is long. *p*-Aminophenol is a harmful substance for human organism because it increases body temperature and its biological half-life is long. It appears in environment mainly from the chemical and pharmaceutical industrial wastes (water and powdered pollutant emission). Thus, *p*-aminophenol shows both biochemical and environmental hazards, and the determination of its trace amounts is topical.

Historically, several analytical methods have been utilised for the determination of *p*-aminophenol, e.g., potentiometric titration, spectrophotometry, fluorophotometry, high-performance liquid chromatography (HPLC), capillary electrophoresis (CE), and chemiluminescence (CL) [6,7]. Classical analytical procedures are usually performed by means of sophisticated instrumentation which cannot be easily moved away from laboratory, thus requiring the transport of the sample to the lab. In contrast to such methods, chemical sensors provide a possibility of real-time analysis, which can be accomplished onsite. Ideally, such a sensor can be stuck directly into the sample and the result of the measurement is displayed within several minutes.

* Corresponding author. Tel.: +0212 4737070 17739; fax: +0212 4737180.
E-mail address: filik@istanbul.edu.tr (H. Filik).

Karousos and Reddy [8] first suggested the use of quartz crystal microbalance (QCM) sensor for the detection of PAP. To the best of our knowledge, reflectance spectroscopic detection of PAP has not been reported. The use of optical fibre chemical sensors (optodes) for such applications have increased in the past several years. Fibre-optic sensors are a class of sensors that use optical fibres to detect chemical contaminants [9]. In such sensor applications, the analyte is extracted onto a solid sorbent matrix loaded with a colorimetric reagent and then quantified directly on the adsorbent surface. Various types of solid supports such as cellulose, XAD polymers, nylon tape, and Nafion ion exchange membrane have been tested [10–15]. According to Oehme and Wolfbeis, the polymers not only act as solid supports onto (into) which indicator dyes are immobilized, but also can provide permeation selectivity for certain species while rejecting others [15]. Optical effects of the materials may be detected by conventional methods of absorbance, fluorescence and reflectance spectroscopy, and in various formats such as test strips and disposable tips [16,17]. In recent years, special attention has been devoted to the direct quantification of colored species retained on the surface of a solid support by diffuse reflectance spectroscopy [18,19]. Reflectance spectroscopy is the investigation of the spectral composition of surface-reflected optical radiation with respect to its angularly dependent intensity and the composition of the incident radiation. UV–vis diffuse reflectance spectroscopy proved to be a promising method for the quick and simple analysis of light-impermeable structures for which the classical transmittance spectrophotometric methods are difficult to implement [20].

Determination of organo-phosphorus (OP) insecticides may be achieved by irreversible inhibition of acetylcholine esterase. This enzyme, in uninhibited form, can hydrolyze p-aminophenyl acetate to p-aminophenol. Thus, estimation of PAP can indirectly detect OP insecticides and nerve agents. This means that rapid on-site determination of PAP can potentially aid develop measures against chemical (NBC) warfare [21,22].

Many reagents cannot be used in optical sensors because of unfavourable analytical wavelengths, poor photostability, low molar absorptivity or the need for additional reagents [23]. 2,2′-(1,4-Phenylenedivinylene)bis-8-hydroxyquinoline (PBHQ) is a known reagent and used as a coupling agent for the detection of PAP by a spectrophotometric method [24,23]. In the present study, we have evaluated the possibility of quantifying PAP as indophenol dye by combining solid-phase extraction (SPE) and UV–vis reflectance spectroscopy. The solid-state PAP sensor based on the Berthelot (or the indophenol dye) reaction responded to PAP sample fairly rapidly (∼5 min), and blue color was observed almost immediately upon addition of the test sample solution. The indophenol-blue reaction was actually used for ammonia sensor applications [16,17]. The performance of the immobilised PBHQ on XAD-7 as a reagent in the development of optical reflectance sensor for PAP determination has been demonstrated. The recovery of the proposed method was tested by replicate analysis of several samples with spiked PAP.

2. Experimental

2.1. Apparatus

The instrumentation set-up used for this experiment is as shown in Fig. 1. Experiments were carried out using a commercially available miniature fibre-optic-based spectrometer (Ocean Optics Inc., HG4000CG-UV-NIR) which utilises a small tungsten halogen lamp (Ocean Optics Inc.) as the light source and a CCD-based detector for reflectance measurements. Light reflected from the probe surface was transmitted by a bundle of optical fibres to a miniature
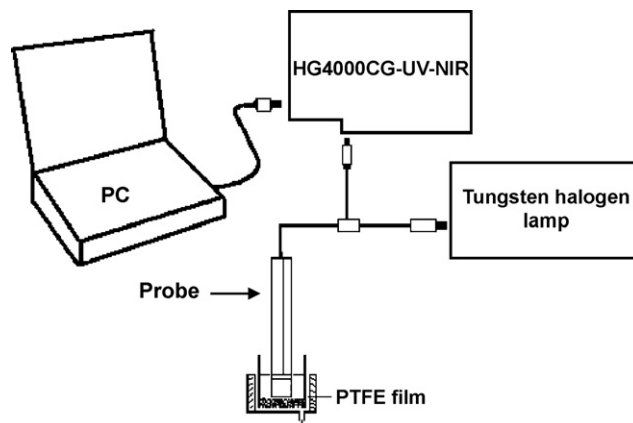
Fig. 1. Schematic diagram of the PAP fibre-optic sensor instrumentation.

fibre-optic spectrophotometer (Ocean Optic HG4000CG-UV-NIR) which on the other hand was connected to a PC (Dell-compatible) and also a printer. For optical isolation, the probe and the detector were kept in a black box to minimise any interference from ambient light. The spectral deconvolution was performed after smoothing the spectra by a 25-point Fourier transform filter using peak fitting module in OriginPro7.0 software (OriginLab Co., USA). A mechanical shaker (Nüve, Turkey) having speed control facility was used for batch equilibration.

2.2. Reagents

All chemicals used were of analytical grade. p-Aminophenol, m-aminophenol (m-AP), o-aminophenol (o-AP) and paracetamol (PCT) were obtained from Riedel de Haen (Fluka Chemie, Buchs, Switzerland). PCT stock standard solution (1.0×10^{-3} M) was prepared by dissolving pure PCT in 100 ml of distilled water using an ultrasonic water bath to ensure complete dissolution. PAP stock solution (1.0×10^{-3} M) was prepared by dissolving 54 mg of PAP in 100 ml of ethanol. The structural formula of PBHQ (synthesized) ligand is shown in Fig. 2. PBHQ stock standard solution (2.0×10^{-3} M) was prepared by dissolving PBHQ ligand in 100 ml of THF (Aldrich, Milwaukee, MI). More dilute solutions of the reagent were prepared as required. The borax buffer solution was prepared by dissolving 2.0 g NaOH and 2.0 g $Na_2B_4O_7 \cdot 10H_2O$ in 100 ml distilled water (pH 12.4 ± 0.2). Other metal salts were obtained either as chloride or nitrate salts from Fluka (Buchs, Switzerland) and Merck (Darmstadt, Germany). All metal salts and organic substances were used without further purification. Amberlite XAD-7 (surface area: 450 $m^2 g^{-1}$ and bead size: 20–50 mesh) were obtained from Fluka (Buchs, Switzerland).

2.3. Preparation of the analyzed samples

2.3.1. Pharmaceutical waste water analysis

The pharmaceutical wastewater samples were collected from a pharmaceutical factory in Turkey (Atabay Pharmaceutical Fine
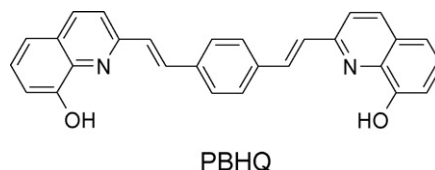
Fig. 2. Structural formula of the sensing layer constituent.
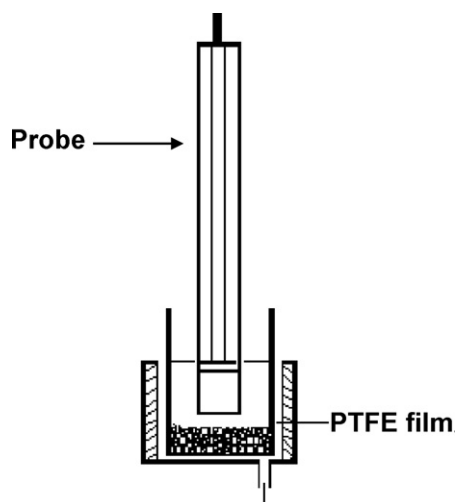
Fig. 3. The design of the PAP probe.

Fig. 4. Relative reflectance spectra of immobilized PBHQ before, curve (a), and after curve (b), coupling reaction with 0.545 mg l^{-1} PAP. Inset: Orginal reflectance signals of immobilized PBHQ before (a) and after (b) reaction with PAP without FT-smoothing of spectra.

Chemicals Inc., Kocaeli, Gebze). After filtration, the samples were stored at 4 °C in refrigerator to avoid exposure to light and air, and they were used for the determination of PAP without dilution. The pH values of the sample solutions were measured to be 3.5 and 5.0.

2.3.2. Paracetamol analysis

Different dosage forms of paracetamol were obtained commercially from different firms (Turkey). An average weight of five tablets was taken. The tablets were powdered, and 0.5 g of this homogenized material was dissolved in 50 ml ethanol and sonicated for 5 min. The sample solution was filtered through a 0.45-μm membrane filter into a 100-ml volumetric flask. The filtrate was made up to the volume. A volume of 5 ml of the diluted solution was assayed according to the general procedure.

2.4. Impregnation procedure

Amberlite XAD-7 resin obtained from the supplier contained organic and inorganic impurities. To remove the contaminants, it was washed successively with ethanol, water, 1 M NaOH and 1 M HCl. The XAD-7 beads were then washed with distilled water until neutral. The sensing material (PBHQ) was physically immobilised by adsorption onto Amberlite XAD-7 polymer. The resin beads were dried in an oven at 105 °C for 4 h. One gram dry resin (Amberlite XAD-7) beads were treated with 2 ml of 2.0×10^{-3} M PBHQ and 3 ml ethanol, and the mixture was shaken at room temperature for 5 min. The resulting yellow particles were filtered off from the supernatant solution, and were washed with water until reagent excess was eliminated from the resin. The resulting yellow resin beads were dried in air. The resin was left to expand in 1:1 alcohol–water before usage.

2.5. Sensor design

The model sensor design was similar to that described by Ahmad and Narayanaswamy [25,24]. The probe was built using disposable syringe tubes (i.d. = 4 mm) (SB Medical Center, Kartal, Istanbul). A syringe column (12 cm length and 1.0 cm diameter), with a nylon membrane and a stopcock, has been used for preconcentration of the PAP. Fig. 3 shows the design of the probe. The syringe tube was filled with 0.2 g (dry substance) Amberlite XAD-7-PBHQ resin. The filling height of the Amberlite XAD-7-PBHQ resin was approximately 5 mm. After swelling (in 1:1 alcohol–water), 1 ml of borax
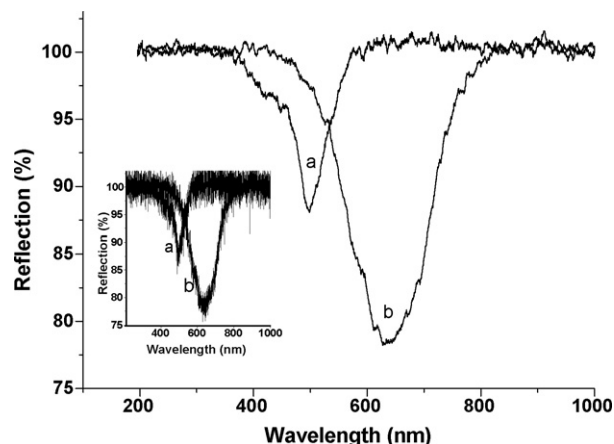
buffer solution and 0.1 ml of 1.0×10^{-3} M KIO$_4$ were added to the sensor; the probe was later attached to the distal end of a bifurcated fibre-optic.

2.6. Reflectance measurement

Ten milliliters of PAP standard solution (within the linear range of 0.1–2.18 mg l^{-1}) were added to the sensor. The reflectance measurement was carried out by recording the optical signal 5 min after placement of the bifurcated optical fibre in the analyte solution. Reflectance spectra were registered after 5 min (for full color development). Maximum reflectance signal was measured at 647 nm. The measurements were expressed in the units of relative reflectance, which is defined as the difference between the reflectance of the PAP-PBHQ dye (R_c) and that of the immobilised reagent alone (R_f), both recorded at the same wavelength (647 nm). The arbitrary unit and the detector were kept in a black box to minimise any interference from ambient light.

3. Results and discussion

3.1. Reflectance spectra of the sensor

The reflectance baseline was previously adjusted to 100 arbitrary units in the detector, which corresponds to the reflectance of the optode containing the immobilized PBHQ (R_f). Fig. 4 shows the reflectance spectrum of the immobilized PBHQ-XAD-7 reagent before and after the reaction with 1.09 mg l^{-1} PAP at pH 12.4 ± 0.2. It can be noted that the formation of the dye causes a decrease in reflectance signal due to a sharp change in color of the reagent phase from yellow to blue, with concomitant narrowing of the original spectrum. Diffuse reflectance spectra of immobilised PBHQ before (curve a) and after (curves b–e) coupling with PAP (0.545, 1.09, 1.635 and 2.18 mg l^{-1}, respectively) are shown in Fig. 5. Greatest reflectance difference was found at 647 nm, and this wavelength was used for all subsequent measurements of reflectance.

3.2. Influence of variables

The influence of different variables on the response of the sensor, immobilization of PBHQ, its concentration, pH of determination, and response time of the sensor was studied.
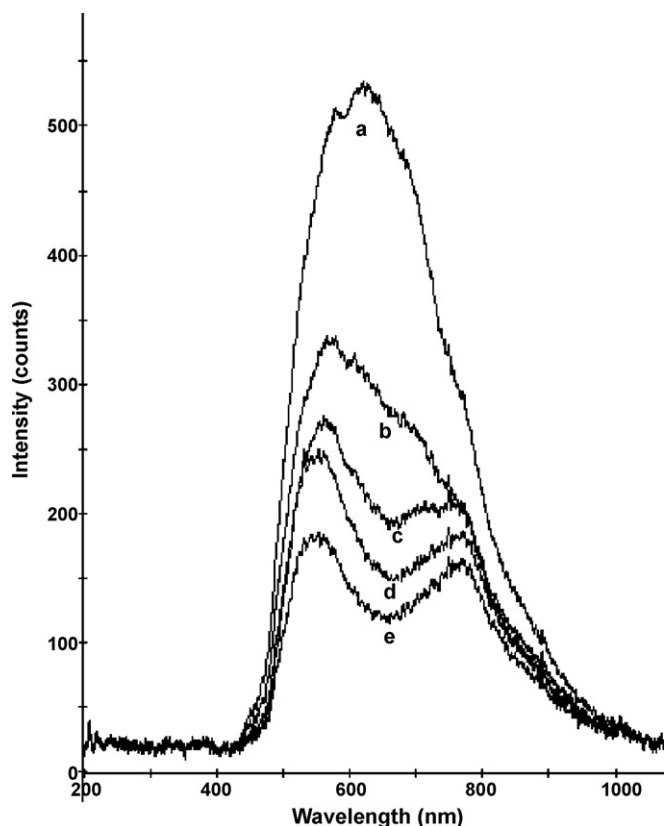
Fig. 5. Reflectance spectra of immobilised PBHQ in XAD-7 before (a) and after (b–e) coupling reaction with PAP solution, the analyte concentration being 0.548, 1.09, 1.635 and 2.18 mg l^{-1}, respectively.

Fig. 6. The effect of pH on the probe response. [PAP] = 1.09 mg l^{-1}. The inset shows the intensity profile of the original reflectance spectra.

The influence of time of immobilization on optical properties of the sensor is important because of its relationship with the response time and dynamic range of sensor. The results show that the amount of PBHQ adsorbed is increased by varying the soaking time of the XAD-7 resin in the PBHQ solution from 1 to 10 min. The best result was achieved for >5 min impregnation.

The concentration of the PBHQ solution used to prepare the sensing phase is probably the main parameter that must be investigated since it determines the signal intensity. The effect of the reagent concentration on the sensor response was studied by using different initial concentrations of the reagent during its impregnation. The results obtained indicated that the best option was the employment of 2 ml of 2.0×10^{-3} M PBHQ concentration. The reflectance of the sensing layer was measured at 497 nm (λ_{max} of PBHQ).

The influence of the sample pH on the response of sensor was also studied by measuring the reflectance at 647 nm when it is inserted for a fixed time into a solution containing 1.09 mg l^{-1} PAP at different pH values. The effect of pH was studied in the range 9–14 under the same experimental conditions by using NH$_3$/NH$_4$Cl buffer and NaOH solution for pH adjustment. As can be seen from Fig. 6, the sensor responded to PAP only above pH 9.0, and the response increased with pH up to a certain level. Optimum response was observed between pH 12 and 13. Reflectance intensity decreased above pH 13.0. In subsequent experiments, borax buffer solution of pH 12.4 ± 0.2 was used for adjustment to optimal pH.

Maximum reflectance of the optode was obtained with the oxidizing agent concentration of 1×10^{-4} M KIO$_4$; above this value, the reflectance intensity of sensing layer decreased gradually. Thus, a KIO$_4$ molar concentration of 1×10^{-4} was adopted.
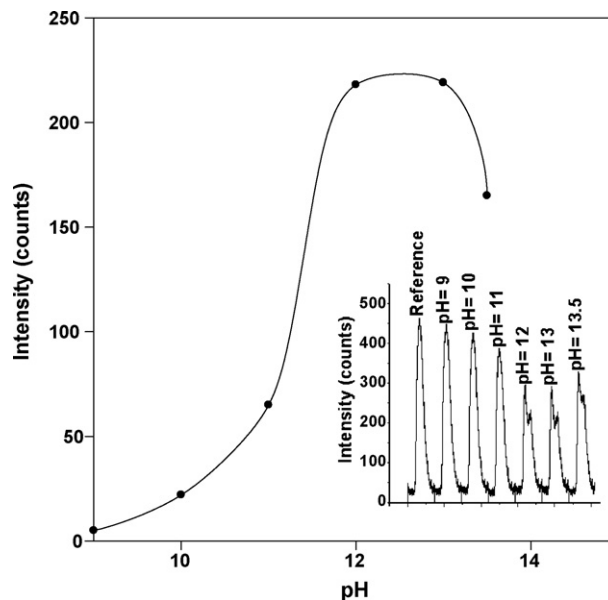
3.3. Stability and reproducibility

A study on stability of the sensing layer was carried out to detect the possibility of photo-leaching or photo-decomposition of the reagent phase when it was continuously exposed to a light source for a longer period of time. The stability of the immobilised reagent was evaluated by monitoring the sensor response continuously for 5 h when the sensor was immersed in an alkaline solution. The reflectance intensity recorded at 647 nm demonstrated that the reagent phase was very stable and no photo-decomposition occurred.

The sensing layer can be stored under air for 6 months without considerable loss in reflectance intensity or response function. When the sensing layer was continuously exposed to light, no drift in signal occurred, and the sensing layer was very stable throughout the experiment with no leaching of the PBHQ ligand.

The reproducibility of the sensing layer preparation was also checked for five separate sensing layers by measuring the reflectance of PBHQ (λ = 497 nm). The results showed that the chemical and physical characteristics of the sensor layer did not change during 6 months. In addition, the reproducibility for the determinations of PAP was tested by performing five replicate measurements of signal for the sensing layers using 0.545 and 1.09 mg l^{-1} PAP solutions. The relative standard deviation (R.S.D.) for these determinations was 4.06 and 3.73%, respectively.

3.4. Response time

The sensing time of the probe is a very important parameter for rapid measurement. Fig. 7 shows response spectra of the sensing probe at 647 nm as a function of time when the sensing layer was exposed to 1.09 mg l^{-1} PAP at pH: 12.4 ± 0.2. The results showed that after 5 min, the sensing probe reached the output signal equal to 96% of the steady-state response.

3.5. Interference study

Industrial and environmental waters are known to contain various inorganic and organic compounds. The effects of various metal

Fig. 7. Time-dependent responses of the optical sensor to a 1.09 mg l^{-1} PAP solution. The inset shows the intensity profile of the original reflectance spectra.

Fig. 8. Response to different PAP concentrations: (a) 0.0218; (b) 0.218; (c) 0.545; (d) 1.09; (e) 1.635; (f) 2.18 mg l^{-1}. The inset shows the linear response of PAP immobilized on PBHQ-XAD-7.

3.6. Calibration graph

As indicated in the "Procedure", the reflectance measurements were expressed as reflectance difference, which is defined as the difference between the reflectance of immobilized PBHQ alone (R_f) and the reflectance of the PAP-PBHQ dye (R_c). The regression curve obtained was reasonably linear and can be expressed by the following equation: $(R_f - R_c) = 0.1678C + 0.036$ where the concentration of PAP was expressed in mg l^{-1} with a correlation coefficient of 0.9934 ($n = 7$). The reflectance response of the optode under the selected experimental conditions for different PAP concentrations in the range 0.1–2.18 mg l^{-1} is shown in Fig. 8. The limited working range in this work is due to the saturated response that occurred at higher PAP concentrations. The limit of detection (LOD) achieved for PAP, estimated by $3s_B/m$ (where s_B is the standard deviation of 10 measurements of the blank and m is the slope of the calibration line) was 0.02 mg l^{-1} for the analyte. The reproducibility of the method, expressed as R.S.D., was checked on 7 individual samples containing 1.09 mg l^{-1} of PAP. The relative standard deviation was found to be 4.4% for PAP, which is a bit higher than those of spectrophotometric measurements carried out in homogenous solution, but is very acceptable in reflectance measurements of heterogenous phases.

3.7. Application to real samples

The method was used for the determination of PAP in pharmaceutical wastewater and pharmaceutical samples. All samples were spiked with standard stock solution of PAP at different concentration levels and then analyzed five times ($n = 5$). The recovery was between 98 and 102% (Tables 2 and 3). The results by using the present method were comparable with those by using sodium Berthelot hypochlorite–alkaline phenol spectrophotometric method [25]. We can see that the results were satisfactory. The performance of the proposed method was compared statistically in terms of the Student's t-test and the variance ratio F-test. At the 95% confidence level, the calculated t- and F-values did not exceed the theoretical values 2.78 (for $n = 5$) and 6.39 (for $n = 5$), respectively. Results are summarized in Table 2. From the results, it is apparent that the present sensor may be useful for the determination of PAP in real samples. The method allowed the determination of p-aminophenol in the presence of paracetamol without separation. Good recoveries were obtained, and the data are shown in Tables 2 and 3.

ions on the determination of PAP were studied under the optimal experimental conditions selected above. Synthetic sample solutions containing 1.09 mg l^{-1} PAP and different concentrations of the possible interferent compounds were tested, and the peak heights obtained were measured. The possible interferences of some inorganic cations, such as Mg^{2+}, Ca^{2+}, Ba^{2+}, Zn^{2+}, Ni^{2+}, Co^{2+}, Mn^{2+}, Cd^{2+}, Bi^{3+}, Pb^{2+}, Fe^{3+} and Al^{3+} were evaluated. Table 1 shows the maximum tolerable concentrations of various metal ions. As can be seen, several metal ions do not interfere even at high concentrations. During the interference studies, any precipitate formed was removed by centrifugation.

Organic contaminants, such as nitro- and chloro-substituted phenols, were tested for their effects on the PAP signals. The results are shown in Table 1. All the aminophenols (o-AP and m-AP) were found to influence the determination. The tolerable limit of a foreign species was taken as a relative error greater than $\pm 2\%$ in the recovery of 1.09 mg l^{-1} PAP.

Table 1
Effect of possible interferents on reflectance of the optode

Species	Added (mg l^{-1})	Found PAP (mg l^{-1})	Error (%)	Recovery (%)
Cu	127	1.11 ± 0.05	+2	97
Cr	103	1.10 ± 0.06	+1	101
Mn	109	1.12 ± 0.03	+3	96
Ni	117	1.06 ± 0.06	−3	97
Al	53	1.12 ± 0.05	+3	96
Pb	414	1.10 ± 0.05	+1	101
Ca	80	1.09 ± 0.09	0	100
Co	117	1.10 ± 0.06	+1	98
Mg	46	1.08 ± 0.07	−1	99
Fe	112	1.07 ± 0.04	−2	98
Zn	130	1.09 ± 0.08	0	100
Ba	274	1.06 ± 0.04	−3	97
Cd	224	1.08 ± 0.05	−1	99
Cl$^-$, PO$_4{}^{3-}$,NO$_3{}^-$	1000	1.07 ± 0.07	−2	98
p-Nitrophenol	100	1.05 ± 0.04	−4	96
o-Chlorophenol	100	1.05 ± 0.06	−4	101
o-Aminophenol	1	1.06 ± 0.04	−3	96
m-Aminophenol	1	1.05 ± 0.06	−4	96
Paracetamol	1000	1.10 ± 0.08	+1	101

Table 2
Determination of PAP in wastewaters ($n = 5$)

Sample	Reference method[a]	PAP added[b] (mg l^{-1})	Found[b] (mg l^{-1})	Recovery (%)
Wastewater A	1.05 ± 0.03	–	1.19 ± 0.06 $t = 2.46$; $F = 4.0$	
		0.55	1.75	102
		1.09	2.26	98
Wastewater B		–	0.45 ± 0.08 $t = 1.72$; $F = 2.56$	
		0.55	0.99	98
		1.09	1.55	101

[a] Literature method [25].
[b] This method.

3.8. Comparative evaluation of the proposed method in regard to sensor technologies

In this study, the synthesis of a reflectance-based sensor (manufactured by impregnating an alcoholic solution of the ligand PBHQ onto the XAD-7 copolymer resin) has been reported for the first time. The ligand PBHQ (being a raw material for the sensor manufacture) was previously used as a coupling reagent for spectrophotometric determination of PAP (hydrolyzed from paracetamol) in pharmaceutical formulations [23]. However, the linear range of the current sensing method (0.1–2.18 mg l^{-1}) is wider and covers smaller concentrations than that of the former spectrophotometric method (*i.e.*, 0.44–5.5 mg l^{-1}) [23]. The LOD of the current method (0.02 mg l^{-1}) is smaller than that of the former method (*i.e.*, 0.09 mg l^{-1}).

Actually, specific colorimetric sensors for PAP have not been previously synthesized. The solid state UV sensor is for paracetamol (which yields PAP only upon hydrolysis), and concentrates the parent drug on an anion-exchanger gel resin, Sephadex QAE A-25 [26]. The sensor measures the analyte at 300 nm, a UV wavelength which is open to interference by many other organic compounds. On the other hand, determination of PAP using a quartz crystal microbalance sensor based on indophenol dye formation from PAP, periodate, and phenols does not involve a linear calibration curve [8]. The current manuscript tries to fill in the gap of a flexible colorimetric sensor based on reflectance measurement.

In real life, there are cases where *p*-aminophenol has to be rapidly and sensitively assayed with a cheap, easily available optosensor with a considerable shelf-life so that the sensor used for this purpose is readily available. Example potential applications are:

(i) Indirect detection of organo-phosphorus nerve agents and pesticides in the field by inhibition of acetylcholine

esterase-catalyzed hydrolysis of *p*-aminophenylacetate to *p*-aminophenol [21].
(ii) Since the drug paracetamol is rapidly absorbed and excreted by humans largely in urine and its high doses have been associated with lethal hepatic necrosis and renal failure, development of a rapid, sensitive and selective assay of paracetamol is of vital importance for fast urinary screening and antidote administration [27] before applying more sophisticated, but costly and laborious hyphenated instrumental techniques of HPLC-SPE-NMR-MS.

Now, the proposed technology of optosensor preparation is based on the impregnation of the ligand PBHQ onto a XAD or a similar polystyrene–divinylbenzene resin which is readily available. Such an optosensor can be easily prepared at the location of requirement, or can be safely stored and transported without deterioration of the sensor material (the sensor was shown to be stable toward different conditions of storage such as air and light). On the other hand, when the sensor active material (PBHQ) is tried to be encapsulated in a PVC matrix in a tetrahydrofurane (THF) solution with plasticiser, then poured onto a petri dish, dried and strip sliced, the matrix does not respond to PAP. Even if such polymeric optosensors based on spectrophotometric measurement on transparent PVC or other polymeric membranes were to be prepared successfully, they would be subject to error over time, because the membrane material may first turn translucent and then opaque, and the sensor raw materials may accumulate at certain locations of the membrane upon prolonged storage probably as a result of phase separations of the originally compatible components of the polymeric composition, adversely affecting the homogenous appearance and light transmission of the membrane. Kimball and Munir [28] have shown that there may be a small decrease in the transmission of PVC, PET and polystyrene transparent films in the visible range upon weathering.

It should be added that the only competent technology for PAP assay (as a reasonable alternative to the proposed methodology) with repetitive use is an electrochemical-based (amperometric) biosensor capable of detecting PAP as the enzymatic hydrolysis product of *p*-aminophenylacetate [29,30]. Some electro-active substances (e.g., those showing electroactivity around the anodic oxidation potential of PAP at +0.25 V *vs.* Ag/AgCl) and organic substances strongly adsorbing on the electrode surface may interfere [29]. The glassy carbon electrode (GCE) used for PAP assay can also be modified with multi-wall carbon nanotubes (MWNTs)/Nafion [31], but these are high-cost materials not available to common laboratories.

4. Conclusion

This study has shown that the fibre-optic reflectance sensor based on immobilized PBHQ is rapid and simple for the on-site quantitative determination of PAP. The development of a new kind of sensor, namely a fibre-optic chemical sensor, brings about an alternative for environmental monitoring and pharmaceutical analysis especially for hazardous contaminants such as PAP. The sensor is small and of low-cost. Furthermore, it can be made into a portable instrument for *in situ* measurements. Using enzymatic inhibition techniques (e.g., using acetyl choline esterase as enzyme and *p*-aminophenyl acetate as substrate), such a sensor can potentially be used for on-site determination of organo-phosphorus nerve agents and insecticides. Thus, a simple method in detecting trace levels of PAP has been developed and validated.

Table 3
Determination of PAP in paracetamol ($n = 5$)

Sample	PAP added (mg U^{-1})	Found (mg U^{-1})	Recovery (%)
Tamol A	NF	NF	–
	0.55	0.56 ± 0.1	102
	1.10	1.11 ± 0.1	101
	2.18	2.20 ± 0.2	101
Tamol B	NF	NF	–
	0.55	0.56 ± 0.1	101
	1.09	1.10 ± 0.1	101
	2.18	2.19 ± 0.3	100

NF: not found.

Acknowledgement

References

[1] S. Mitchell, Kirk-Othmer Encyclopedia of Chemical Technology, vol. II, 4th ed., Wiley, New York, USA, 1992, p. 580.
[2] S. Afzal Khan, M. Hamayun, S. Ahmed, Enzyme. Microb. Technol. 38 (2006) 10.
[3] H. Xua, C.-F. Duana, Z.-F. Zhanga, J.-Y. Chena, C.-Z. Laia, M. Liana, L.-J. Liua, H. Cuia, Water Res. 39 (2005) 396.
[4] J.E. Fairbrother, Anal Profiles, Drug Subst. 3 (1974) 1.
[5] K.T. Koshy, L. Lach, J. Pharm. Sci. 50 (1961) 113.
[6] M.S. Bloomfield, Talanta 58 (2002) 1310.
[7] M.E. Bosch, A.J. Ruiz Sánchez, F.S. Rojas, C.B. Ojeda, J. Pharm. Biomed. Anal. 42 (2006) 291.
[8] N.G. Karousos, S.M. Reddy, Analyst 127 (2002) 368.
[9] J. Janata, Anal. Chem. 64 (1992) 196R.
[10] L.A. Saari, W.R. Seitz, Anal. Chem. 55 (1983) 667.
[11] B. Kuswandi, R. Narayanaswamy, J. Environ. Monit. 1 (1999) 109.
[12] B. Kuswandi, R. Narayanaswamy, Sens. Actuators 76 (1999) 183.
[13] N. Malcik, O. Oktar, M.E. Ozser, P. Caglar, A. Bushby, A. Vaughan, B. Kuswandi, R. Narayanaswamy, Sens. Actuators 53 B (1998) 211.
[14] S.A. Momin, R. Narayanaswamy, Anal. Chim. Acta 244 (1991) 71.
[15] I. Oehme, O.S. Wolfbeis, Microchim. Acta 126 (1997) 177.
[16] K.T. Lau, S. Edwards, D. Diamond, Sens. Actuators B 98 (2004) 12.
[17] Y.M. Martínez, R.H. Hernández, P.C. Falcó, Anal. Chim. Acta 534 (2005) 327.
[18] C.B. Ojeda, F.S. Rojas, Sensors 6 (2006) 1245.
[19] T. Surles, J.O. Erickson, D. Priesner, Int. Lab. (1975) 29.
[20] S. Andreescu, A. Avramescu, C. Bala, V. Magearu, J.-L. Marty, Anal. Bioanal. Chem. 374 (2002) 39.
[21] S. Andreescu, T. Noguer, V. Magearu, J.-L. Marty, Talanta 57 (2002) 169.
[22] B. Kuswandi, J. Ilmu Dasar 1 (2000) 18.
[23] H. Filik, M. Hayvali, E. Kilic, Anal. Chim. Acta 535 (2005) 177.
[24] M. Ahmad, R. Narayanaswamy, Anal. Chim. Acta 291 (1994) 255.
[25] T.T. Ngo, C.F. Yam, Anal. Lett. 17 (1984) 1771.
[26] A. Ruiz-Medina, M.L. Fernandez-de Cordova, M.J. Ayora-Canada, M.I. Pascual-Reguera, A. Molina-Diaz, Anal. Chim. Acta 404 (2000) 131.
[27] H. Filik, I. Sener, S. Demirci Cekic, E. Kilic, R. Apak, Chem. Pharm. Bull. 54 (2006) 891.
[28] W.H. Kimball, Z.A. Munir, Polym. Eng. Sci. 18 (2004) 230.
[29] C. La Rosa, F. Pariente, L. Hernandez, E. Lorenzo, Anal. Chim. Acta 308 (1995) 129.
[30] F. Pariente, C. La Rosa, F. Galan, L. Hernandez, E. Lorenzo, Biosens. Bioelectron. 11 (1996) 1115.
[31] Y. Cheng, Y. Liu, J. Huang, Y. Xian, W. Zhang, Z. Zhang, L. Jin, Talanta 75 (2008) 167.

Determination of asulam by fast stopped-flow chemiluminescence inhibition of luminol/peroxidase

F. García Sánchez*, A. Navas Díaz, C. Delgado Téllez, M. Algarra

Department of Analytical Chemistry, Faculty of Sciences, University of Málaga, Campus de Teatinos s/n, 29071 Málaga, Spain

ABSTRACT

An efficient, sensitive and fast stopped-flow method has been developed to determine asulam in water, based on its inhibition effect on the horseradish peroxidase–luminol–hydrogen peroxide chemiluminescence reaction, (HRP–luminol–H_2O_2). Ultra fast data acquisition (0.20 s) facilitates excellent selectivity because no interferences from concomitants in the matrix act in such short time scale. The precision as repeatability (expressed as relative standard deviation, $n = 10$) was 0.4% at a 40 pM level. The detection limit was 1.5 pM (0.35 ng/L) and 7.15 pM in pure and raw water, respectively. The calibration data over the range 5–60 pM present a correlation coefficient of $r = 0.9993$. The proposed method has been applied to determine asulam in water samples by using solid-phase extraction (SPE). Mean recovery value was $98.1 \pm 2\%$ at 50 pM level.

1. Introduction

Asulam (methyl 4-aminobenzenesulfanilyl carbamate) is a carbamate pesticide with a widely broad spectrum of biological activity, acts by stopping the cell division and growth of plant tissues, can accumulate and remain in environment. Due to its good solubility in water, creates a compromise to develop suitable analytical methods [1,2]. In literature, a great variety of analytical techniques are employed to quantified asulam at trace level. Currently, gas or liquid chromatography is the most used method for analyzing pesticides [3], and solid-phase extraction (SPE) is often performed for concentrating and purifying analytes in the samples, prior analysis [4–6]. Analytical determination by means of synchronous fluorescence with derivatization with fluorescamine [7], or based on its native fluorescence with a flow injection (FI) analysis system, has been used [8,9].

Chemiluminescence (CL) is a luminescence technique showing as main advantages its high sensitivity, easy of use and simple instrumentation, being actively applied for the detection of small amounts of chemical species at ultra-trace levels. Considering the kinetic characteristics of this technique, anyone of the reaction components, including CL substrate, oxidant, catalyst, cofactor, sensitizer, enhancer and inhibitor can be made rate limiting and hence be determined [10]. The oxidation is usually conducted in a basic solution in the presence of an oxidant: hydrogen peroxide [11], hypochlorite [12], iodine [13], or oxygen [14], and catalysts: peroxidases such as horseradish peroxidase (HRP) [15,16], or lactoperoxidase [17], and metals ions [18]. Among them, HRP–luminol–H_2O_2 system is most popular and has been employed in many assays [19,20]; moreover, this system has been employed to quantify analytes who act as enhancers [21,22] or inhibitors [23]. Particularly, in the determination of carbamates as analytes, only few contributions have been found based on the CL of Ru(bpy)$_3^{3+}$ reaction [24], and on the peroxyoxalate CL oxidation in the presence of a fluorophore [25]. This technique can be easily coupled to a flow injection manifold as detection mode or assembled to stopped-flow technique, where rapid chemical reactions are studied on the millisecond to second time scale [26].

In this study, we have found that the pesticide asulam produces an inhibition on the CL emission from the HRP–luminol–H_2O_2 system. Under the optimum experimental conditions, the very fast CL emission is proportional to the concentration of asulam, the whole transient signal can be recorded in about 200 ms. The main features of this technique are its ability to mix the sample and reagent solutions automatically, the possibility of making experiments shortly after mixing, a high overall precision, the minimization of potential interferences, and its suitability for fast and slow reactions. Based on these findings, a simple and fast new direct stopped-flow CL method has been developed for the determination of asulam in water by using solid-phase extraction.

* Corresponding author. Tel.: +34 952 131 972; fax: +34 952 131 884.
E-mail address: f_garcia@uma.es (F. García Sánchez).

2. Experimental

2.1. Reagents and solutions

Ultrapure water (Millipore 60 system, Bedford, MA, USA) was used for the preparation of all solutions, except asulam which was prepared in acetone. Luminol (5-amino-2,3-dihydrophthalazine-1,4-dione), horseradish peroxidase, type VI-A (16 U/mg) and Tris–HCl (99–99.5%) were purchased from Sigma (St. Louis, USA). Hydrogen peroxide (H_2O_2) 30% (p/v) by Merck (Darmstadt, Germany). Asulam (methyl[(4-aminophenyl)sulfonyl]carbamate) (98.1%), MCPA (4-chloro-o-tolyloxyacetic acid), 2,4,5-T (2,4,5-trichlorophenoxyacetic acid), amitrole (3-amino-1,2,4-triazole), and atrazine (2-chloro-4-(ethylamine)-6-(isopropylamine)-s-triazine) were purchased from Riedel de Häen, Seelze, Germany and employed without further purification. Diclorprop (2-(2,4-dichlorophenoxy) propanoic acid) and metamidofos (O,S-dimethyl phosphoramidothioate) was provided by Dr. Ehrenstoffer Laboratories (Augsburg, Germany).

The stock solution of luminol (2 mM) was prepared by dissolving 35.44 g of solid in a 0.1 M of Tris–HCl buffer solution (pH 8.4); this solution is stable when stored in the dark. 13.68 U/mg of lyophilized HRP was prepared in water by dissolving 1.3 mg of the parent HRP in 25 mL. H_2O_2 (1 M) was prepared in water by dissolving 752 μL in a volume of 25 mL. The concentration of H_2O_2 was determined daily by measuring the UV absorbance at 240 nm using $\varepsilon_{240} = 39.4 \, cm^{-1} \, M^{-1}$ [27]. Asulam (1 mM) stock solutions were prepared by dissolving in acetone 11.51 mg to a final volume of 50 mL.

2.2. Apparatus

A Perkin-Elmer LS-50 (Beaconsfield, UK) luminescence spectrometer with the light source switched-off was used. The apparatus was set in the phosphorescence mode with 0.00 ms delay time and 60 ms gate time. The slit-width of the emission monochromator was set at 20 nm with λ = 425 nm and photomultiplier voltage set manually to 700 V. The samples were placed in a quartz cuvette continuously stirred with a magnetic stirrer. The chemiluminescent reaction was triggered by injecting HRP solution with a syringe, through a septum.

The study of the CL emission at short times was carried out in an SLM-Aminco 48000s fluorometer equipped with a MilliFlow stopped-flow reactor (Urbana, IL), with the light source turned off and no optical filter before the photomultiplier. The stopped-flow reactor permits observation of the reaction velocity of the reactants which are forced through a mixing chamber and into an observation cell. The two 5 mL driving syringes were filled with the reactants and whose positions are simultaneously driven by a pressurized nitrogen-operated plunger. After leaving the observation cell, the mixed reactants advance the piston of a stopping syringe, which is brought to a "dead" stop against the tip of a micrometer. Just prior to stopping, a switch is closed, thereby supplying a triggering signal which opens the electronic data acquisition. The cell volume was 32 μL. Equal volumes of the two reagent solutions were introduced into the cell when a pressure of 4.5 bar was applied on the two supply syringes. The dead time was 1.0 ms, flow velocity 20 mL/s, and mixing efficiency was >98%. The intensity (in V) was collected throughout the reaction at a rate of 10 ms per point with a photomultiplier gain of 10 and a voltage of 900 V.

2.3. Methods

2.3.1. General procedure

For the study of the asulam signals at short times, a syringe of the stopped-flow apparatus was filled with HRP (0.6 U/mL) in 0.02 M buffer solution (pH 8.4) and the other with a mixture of luminol (3×10^{-5} M), H_2O_2 (2×10^{-3} M), 0.02 M buffer solution and variable volumes of asulam to obtain 5–60 pM concentrations. The initial rates (dI/dt) were measured by subtracting the signal values at 0.08 s from that at 0 s. All measurements were carried out at $25 \pm 0.1 \, °C$.

2.3.2. Procedure for the determination of asulam in water

Due to the good solubility of this pesticide in water [28], a preconcentration step is necessary to reach at trace level the limit of detection. Solid-phase extraction was performed with Lichrolut SPE RP-18 (500 mg, 6 mL) from Merck. Previously, the SPE cartridges were conditioned by passing, according to the manufacturer recommendations, 2 mL of methanol followed by 10 mL of LC-grade water through the cartridge at a flow rate of 3 mL/min. The extraction tubes were set with a Visiprep™ SPE Vacuum Manifold system purchased from Supelco. Fifty milliliters of asulam solution (10^{-8} M) were percolated through the C_{18} cartridges at a constant flow rate between 4 and 8 mL/min. After preconcentration, the extraction was eluted with 2 mL of methanol and evaporated to dryness with a gentle stream of nitrogen and reconstituted with 500 μL of water.

Equal volumes of the two reagent solutions were introduced into the cell when a pressure of 4.5 bar was applied on the two supply syringes. All measurements were carried out at $25 \pm 0.1 \, °C$.

3. Results and discussion

3.1. Optimization of the factors affecting the asulam determination at short times

The experimental conditions were optimized by means of the univariate approach. The efficiency of HRP–luminol–H_2O_2 system is highly dependent on reaction pH. Tris–HCl buffer pH has been reported previously to give a higher CL intensity with luminol as compared with other buffer solutions [19]. Therefore, in the proposed method, the effect of Tris–HCl concentration was studied in the range 0.01–0.1 M. The maximum CL inhibition with asulam was observed at a Tris–HCl concentration of 0.02 M. The effect of Tris–HCl buffer pH (0.02 M) was investigated in the range 8.2–9.5, and the maximum CL was observed at pH 8.4 (Fig. 1); therefore, Tris–HCl buffer (0.02 M and pH 8.4) was selected and used for subsequent studies. The effect of luminol concentration was studied in the range 5–150 μM, the best results were obtained
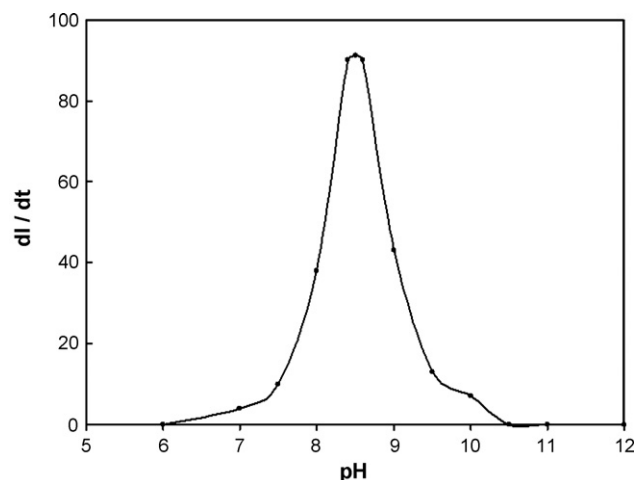
Fig. 1. Initial slope (0–80 ms) at several pH values. Experimental conditions: [Tris–HCl buffer] = 0.02 M; [HRP] = 0.6 U/mL; [luminol] = 3×10^{-5} M; H_2O_2 (2×10^{-3} M).

Table 1
Inhibition data for asulam ($n = 5$)

Asulam (pM)	Inhibition (%)	R.S.D. (%)
0	1.10	3.04
20	25.93	0.81
40	48.96	2.81
80	66.53	3.05
120	81.25	1.09
160	87.23	1.34
320	89.51	1.42
400	95.03	0.8

Table 2
Interference study at 50 pM asulam level

Interference	Asulam:interference (w/w)	Recovery (%)
2,4,5-T	1:1	88.2
	1:0.5	95.6
Diclorprop	1:1	98.6
MCPA	1:1	98.7
Atrazine	1:1	79.2
	1:0.5	86.9
	1:0.25	88.9
Metamidofos	1:1	98.1
Amitrole	1:1	98.9

at 30 μM, compromises between signal reproducibility and blank signal value. Further experiments were realized using 30 μM as optimum luminol concentration. The effect of hydrogen peroxide on the determination of asulam was investigated in the range of 0.2–3 mM, and the best result was obtained with 2 mM. Same procedure was carried out with the peroxidase (HRP) concentration, reaching the 0.6 U/mL as the optimum value of analysis.

3.2. Study of the CL with asulam at short time

The preliminary experiment, carried out in the SLM-Aminco apparatus, showed the CL reaction of luminol was inhibited by asulam, at very low level of concentrations (pM). Blank signals were obtained using the luminol–H_2O_2 system by itself and catalyzed by peroxidase. In Table 1 are presented the inhibition data of this system and illustrated in Fig. 2, measured between 0 and 120 ms and were obtained the slopes of the initial rates (dI/dt) versus asulam concentration over the range 20–400 pM. The data are obtained with the aid of the following expression:

$$\%I = \left(\frac{S_b - S}{S_b} \right) \times 100$$

where I is the inhibition (in %) and S_b and S are the mean of five separate measurements of the slope of the blank and signals, respectively.

3.3. Quantitative analysis and main analytical figures of merit

The calibration data of CL inhibition versus concentration of asulam were obtained over the range 0–400 pM. According to the experimental data, the linear analytical range was established between 5 and 60 pM. A calibration graph obtained by least-squares treatment was: $\%I_{CL} = 1.19$ [asulam] $+ 1.93627$ ($n = 5$), with a corre-

lation coefficient of 0.9993 and R.S.D. = 0.40%. The detection limit (1.5 pM, 0.35 ng/L) was calculated as three times the standard deviation of seven blanks divided by the slope of the calibration graph. Quantification limit (10σ) was 5 pM.

3.4. Interferences

In order to study the determination of asulam in real water samples, the effect of other pesticides that can be present in water at similar levels was studied. In Table 2 are ordered the results obtained over samples containing 50 pM asulam. The selectivity of the proposed methods against the pesticides checked is confirmed, except for atrazine that cause a severe interference (1:0.25, 88.9%).

3.5. Application

In order to assess the potential of the method described, the proposed method was applied to the recovery of asulam in tap water samples, collected from the university. After collection, samples were filtered through a cellulose membrane filter (cellulose acetate, pore size 0.45 μm, 47 mm diameter, Whatman, Maidstone, UK), to remove some possible suspended solids. Into a 50 mL calibrated flask were transferred an aliquot of 25 μL of 10^{-8} M asulam standard solution, the final concentration was of 5 pM (1.15 ng/L).

According to the procedure described above (see Section 2.3), the solid-phase extraction was applied and best recoveries were obtained when the pH of the solution was adjusted at pH 3. With this, a calibration graph was obtained from the kinetic curve (Fig. 3) at the 175 ms over the range 5–60 pM. Least-squares treatment gives $\%I_{CL} = 1.445$ [asulam] $- 6.603$ ($n = 5$), with a correlation coef-

Fig. 2. % Inhibition against asulam concentration (pM). Conditions as in Fig. 1.
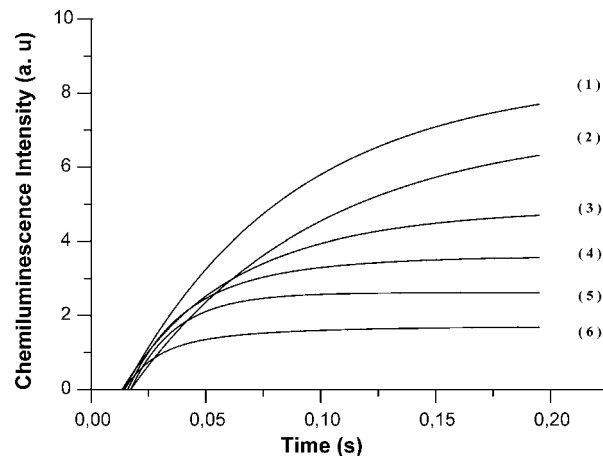
Fig. 3. Kinetic curves of the calibration graph for asulam in tap water. (1) 0 pM; (2) 20 pM; (3) 30 pM; (4) 40 pM; (5) 50 pM; (6) 60 pM. Analytical signal obtained at 175 ms.

Table 3
Comparison of the performances of the proposed method with the previously published one

Sample	DL	Recovery (%)	R.S.D. (%)	Technique
Tap water	0.35 ng/L	98	1.90	This method
Tap water	1 µg/L	86	6.50	MEKC-UV detection [29]
Tap water	0.8 µg/L	88	5.80	MEKC-electrochemical detection [29]
Tap water	0.04 ng	90–118	1.13	HPLC with derivatization [30]
Natural water	10.9 µg/L	53–98	<5.3	CE-UV detection [31]
Natural water	0.9 µg/L	82–102	<6.5	CE-electrochemical detection [31]
Water samples	40 µg/L	–	4.1	Photochemiluminometric [10]
Water samples	5 µg/L	–	1	FIA-fluorescence [8]
Soil	1 mg/L	–	–	TLC [32]
Peaches	43 µg/L	85–106	1.6	Synchronous fluorescence with derivatization [7]
Water samples	0.02 mg/L	93–96	1.16	Fluorometric [33]
Water samples	1.2×10^{-8} M	107	<5	FIA-amperometric [34]

ficient of $r = 0.994$ and R.S.D. = 0.78%. The detection limit (7.15 pM) was calculated as in Section 3.3. The mean recovery values of three separate determinations over 0.5 mL (50 mL reconstituted to 0.5 mL in the preconcentration step and transferred to a drive syringe of 5 mL) of water samples containing 50 pM spiked asulam was 98.14% with a R.S.D. = 1.90%.

The proposed method was compared with others described in literature; in Table 3 are depicted the analytical specifications of these methods [29]. As can be seen detection limit of the method described here is the best. Employing the compared techniques in natural waters, low recoveries are obtained [30]. It is known and well established that colloidal matter, suspended solids and dissolved organic material as humic substance may significantly affected the asulam partition and adsorption process from liquid to solid sorbent.

4. Conclusions

The kinetic information offered by the first instance (0.2 s) of the transient chemiluminescence signal from the system HRP–luminol–H_2O_2 when the pesticide asulam is present, allows us to perform a very sensitive analytical method for the determination of asulam at trace levels, based on the inhibition of the initial chemiluminescence of the base reaction. In addition to the high sensitivity, few interferences affect the method because data acquisition uses the initial steps of the chemiluminescent reaction and avoids side reaction from concomitant in the matrix having slower kinetic constants.

Acknowledgement

References

[1] P. Veerasekaran, R.C. Kirkwood, E.W. Parnell, Pestic. Sci. 12 (2006) 325.
[2] A. Kaufmann, A. Kaenzig, Food Addit. Contam. 21 (2004) 564.
[3] S.J. Lehotay, A. de Kok, M. Hiemstra, P. van Bodegraven, J. AOAC Int. 88 (2005) 595.
[4] F.A. Esteve-Turrillas, A. Pastor, M. de la Guardia, Anal. Chim. Acta 553 (2005) 50.
[5] H.G.J. Mol, A. Rooseboom, R. van Dam, M. Roding, K. Arondeus, S. Sunarto, Anal. Bioanal. Chem. 389 (2007) 1715.
[6] H. Kerkdijk, H.G.J. Mol, B. van der Nagel, Anal. Chem. 79 (2007) 7975.
[7] F. García Sánchez, A. Aguilar, C. Cruces, Talanta 39 (1992) 1195.
[8] I. Subova, A.K. Assandas, M.C. Icardo, J.M. Calatayud, Anal. Sci. 22 (2006) 21.
[9] M. Nakamura, T. Yasukawa, T. Igarashi, S. Yamada, S. Aizawa, Busenki Kagaku 49 (2000) 65.
[10] A. Chivulescu, M.C. Icardo, J. Mateo, J.M. Calatayud, Anal. Chim. Acta 519 (2004) 113.
[11] A. Navas Díaz, F. García Sánchez, J.A. González García, Chemiluminescence 327 (1996) 165.
[12] J.B. Claver, M.C.V. Mirón, L.F. Capitán-Vallvey, Anal. Chim. Acta 522 (2004) 267.
[13] T. Fujiwara, U. Mohammadzaii, H. Inoue, T. Kumamaru, Analyst 125 (2000) 759.
[14] H. Nakamura, Y. Abe, R. Koizumi, K. Suzuki, Y. Mogi, T. Hirayama, I. Karube, Anal. Chim. Acta 602 (2007) 94.
[15] A. Navas Díaz, F. García Sánchez, M.C. Ramos, M.C. Torijas, Sens. Actuators B: Chem. 82 (2002) 176.
[16] H.-C. Yeh, W.-Y. Lin, Talanta 59 (2003) 1029.
[17] Y. Yoshiki, K. Okubo, Y. Akiyama, K. Sato, M. Kawanari, Luminescence 15 (2000) 183.
[18] K. Sato, S. Tanaka, Microchem. J. 53 (1996) 93.
[19] F. García Sánchez, A. Navas Díaz, J.A. González García, Anal. Chim. Acta 310 (1995) 399.
[20] A. Navas Díaz, M.C. Ramos, M.C. Torijas, Anal. Chim. Acta 363 (1998) 221.
[21] N. Kuroda, R. Shimoda, M. Wada, K. Nakashima, Anal. Chim. Acta 403 (2000) 131.
[22] Y. Dotsikas, Y.L. Loukas, Talanta 71 (2007) 906.
[23] A. Navas Díaz, F. García Sánchez, J.A. González García, J. Photochem. Photobiol. A: Chem. 113 (1998) 27.
[24] T. Pérez-Ruiz, C.M. Lozano, V. Tomás, J. Martín, Analyst 127 (2002) 1526.
[25] E. Orejuela, M. Silva, J. Chromatogr. A 1007 (2003) 197.
[26] A. Navas Díaz, J.A. González García, Anal. Chem. 66 (1994) 988.
[27] J.S. Wang, H.K. Back, H.E. van Wart, Biochem. Biophys. Res. Commun. 179 (1991) 1320.
[28] B. Ingham, M.A. Gallo, Bull. Environ. Contam. Toxicol. 13 (1975) 194.
[29] M. Chicharro, A. Zapardiel, E. Bermejo, A. Sánchez, Anal. Chim. Acta 469 (2002) 243.
[30] F. Garcia Sánchez, A. Navas Díaz, A. García Pareja, V. Bracho, J. Liq. Chromatogr. Rel. Technol. 20 (1997) 603.
[31] M. Chicharro, A. Zapardiel, E. Bermejo, A. Sánchez, R. González, Electroanalysis 16 (2004) 311.
[32] A.E. Smith, L.J. Milward, J. Chromatogr. 265 (1983) 378.
[33] M. Nakamura, T. Yasukawa, T. Igarashi, S. Yamada, S. Aizawa, Bunseki Kagaku 41 (2000) 65.
[34] H.P.A. Nows, C. Delerue-Matos, J.L.F.C. Lima, E.M. Garrido, P. Vincke, N.A. Maes, Int. J. Environ. Anal. Chem. 82 (2002) 69.

Modeling the adsorption of dyes onto activated carbon by using experimental designs

Verónica Gómez, M. Pilar Callao *

Analytical and Organic Chemistry Department, Rovira i Virgili University, Marcel·lí Domingo s/n., Campus Sescelades, 43007 Tarragona, Spain

ARTICLE INFO

ABSTRACT

We used experimental design methodologies to obtain the response surface of the adsorption process for three acid dyes used in the dyeing step of a tanning process. The dyes were Acid Red 97, Acid Orange 61 and Acid Brown 425. The adsorption process was evaluated determining the concentrations of individual and total dyes remaining in solution at the end of the process. These concentrations were determined simultaneously in a single step using sequential injection analysis with multivariate curve resolution alternating least squares (SIA-MCR-ALS).

This method involves fractional factorial designs and the steepest ascent method to find a zone of efficient adsorption and a response surface-modeling step to fit the relevant adsorption factors for the response.

1. Introduction

The tanning industry uses a wide spectrum of dyes to impart a particular color to the leather matrix. About 60–80% of the dyes available are adsorbed onto the leather matrix and the unspent dyes are discharged in the wastewater, causing an environmental and economic problem.

There is considerable environmental interest in determining dyes because their biodegradability is poor and conventional wastewater treatment plants are not very efficient in removing them [1,2]. The discharge of dye-laden wastewater by the tanning industries has been severely criticized by the public for aesthetic reasons. Attempts have been made to remove unspent dyes by coagulation–flocculation [3], chemical oxidation [4–6], foam flotation [7], electrolysis [8,9], adsorption [10–12] and by the use of membranes [13]. Adsorption onto activated carbon has proven to be one of the most effective and reliable physicochemical treatment methodologies [14–18].

In a previous paper, we described a method for simultaneously determining three acid dyes in wastewater samples from the tanning industry [18] (Acid Red 97, Acid Orange 61 and Acid Brown 425). The ability of activated carbon to remove these acid dyes was also assessed [19]. From this last study, we could know the behavior of these dyes versus some variables maintaining the rest of variables constant. For example, we could predict the amount of dye adsorbed among the time, having the concentration of dyes and the amount of adsorbent fixed (kinetic study) or we could know the relation between the amount of dye adsorbed and the amount of dye in solution at equilibrium having the amount of adsorbent constant (thermodynamic study).

The objective of the present paper was to study the adsorption process, considering simultaneous variations of the factors that could affect to it, and to build a mathematical model for the percentage of dyes remaining in solution as a function of variables involved to find the experimental conditions in which the adsorption process was efficient. For finding efficient conditions in experimentation we used the design of experiments (DOE) [20,21] strategy. DOE is very important because it takes less time, effort and resources than univariate procedures, and it provides large quantities of information in a minimum number of experiments [22–26].

Our method uses fractional factorial designs and response surface methodologies to fit the relevant adsorption factors for the percentage of individual and total dyes remaining in solution. Dye concentrations were evaluated with a sequential injection analysis (SIA) system with a diode-array spectrophotometer and data treatment with a second-order calibration method, multivariate curve resolution with alternating least squares (MCR-ALS). The SIA-MCR-ALS based method permits quantification in the presence of interferents. In this case, no interferents were present but no simpler approach could be used because the three dyes had an

* Corresponding author. Tel.: +34 977558199; fax: +34 977558446.
E-mail address: mariapilar.callao@urv.cat (M.P. Callao).
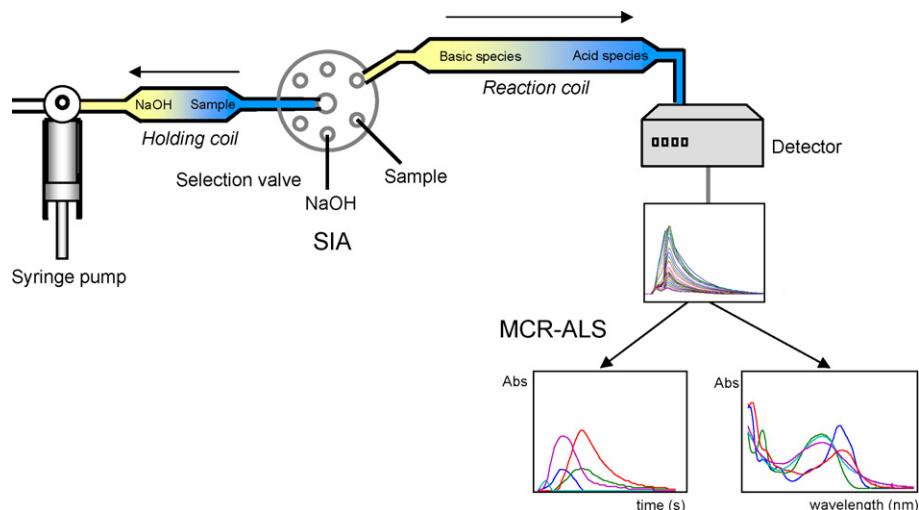
Fig. 1. Schematic illustration of the SIA-MCR-ALS method for determining three acid dyes used in tanning samples.

UV–visible overlapped signal and a univariate calibration would show the existence of bias.

2. Experimental

2.1. Materials

- Adsorbent: The commercial material activated carbon (CAC) was supplied by J.T. Baker (Holland).
- Adsorbates (analytes): Acid Red 97, Acid Orange 61 and Acid Brown 425 were selected as the adsorbates that would be used to investigate the adsorption selectivity of acid dyes. Dyes were of analytical grade from Trumpler, S.A. and were used without further purification.
- Reagents: The sodium hydroxide used was of analytical/ laboratory grade, provided by PROLABO. We used purified water from a Milli-Q water system from Millipore, USA.

2.2. Adsorption process

The adsorption of dyes onto activated carbon was studied by the immersion method. The desired amount of carbon was immersed in the solution of dyes for a certain amount of time, and the solution was agitated at ambient temperature (25 °C). All the dye solution was prepared with purified Milli-Q water.

The solution and solid phase were separated by filtration with nylon syringe filters from Sharlau. A 5 mL aliquot of the supernatant was removed and analyzed for dyes.

2.3. Analytical method

2.3.1. Instrument

The instrumentation used to determine the dyes consists of a sequential injection (SI) system. This system has the following components: a syringe pump (CAVRO XL 3000 stepper motor-driven) connected to a PC with an RS-232 interface; a 6-position automatic selection valve (Eurosas EPS 1306 BPB) connected to the computer through a PCL-711S PC-Lab-Card; a 70 cm × 0.8 mm Omnifit PTFE tubing reaction coil; a 200 cm × 0.8 mm holding coil; a diode-array spectrophotometer (HP8452A) with a Hellma 178.713QS flow-through cell controlled by an HP Vectra 5/75 computer equipped with an HP-IB IEEE 488 interface for communications.

2.3.2. Analytical procedure

The analytical process is outlined in Fig. 1. It consisted in obtaining a data matrix of absorbances recorded at different wavelengths and at different times when a reaction took place between sodium hydroxide and the sample. The synthetic dyes are polyprotic species so, with a pH gradient, the interdiffusion process of the sample and reactants led to a gradual fall in pH, and acid/basic species arrived sequentially at the detector [18]. The matrix obtained was treated with the second-order algorithm, MCR-ALS [27], available in Ref. [28] which enables quantitative and qualitative information of the analytes to be recovered.
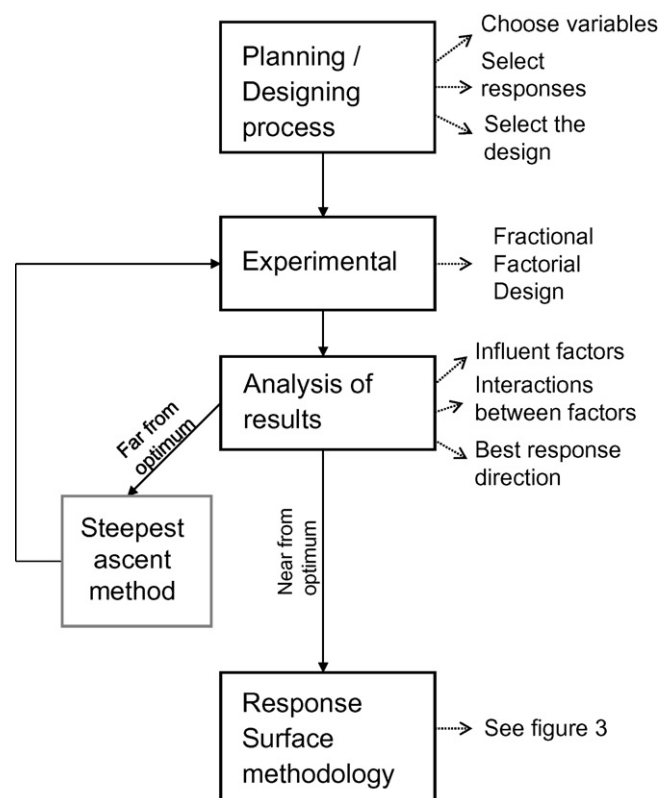
Fig. 2. Scheme of the procedure used in the modeling process.

Table 1
Experimental domain and responses of the first fractional factorial design

	Experimental domain					Dyes in solution (%)			
	A^a	B^b	C^c	D^d	E^e	Acid Red	Acid Brown	Acid Orange	Total
1	30	30	30	0.1	120	47.43	90.26	60.56	66.08
2	50	30	30	0.1	60	62.10	90.16	70.11	71.94
3	30	50	30	0.1	60	60.19	85.28	73.16	75.13
4	50	50	30	0.1	120	53.22	79.31	76.36	68.60
5	30	30	50	0.1	60	65.47	71.72	83.38	75.32
6	50	30	50	0.1	120	51.54	86.84	69.61	66.64
7	30	50	50	0.1	120	47.80	84.02	72.15	71.10
8	50	50	50	0.1	60	68.34	81.07	86.88	78.76
9	30	30	30	0.3	60	56.76	58.02	90.99	68.59
10	50	30	30	0.3	120	49.49	73.41	69.03	61.34
11	30	50	30	0.3	120	37.01	86.60	56.16	64.77
12	50	50	30	0.3	60	65.82	68.01	82.13	72.73
13	30	30	50	0.3	120	38.08	77.07	67.64	62.15
14	50	30	50	0.3	60	57.96	59.10	79.25	69.94
15	30	50	50	0.3	60	54.89	66.61	81.62	69.68
16	50	50	50	0.3	120	52.32	74.57	79.24	68.71

[a] Acid Red concentration (mg l^{-1}).
[b] Acid Brown concentration (mg l^{-1}).
[c] Acid Orange concentration (mg l^{-1}).
[d] Mass of carbon (g).
[e] Time of contact (min).

2.4. Modeling process

Fig. 2 shows a scheme of the procedure followed in this paper.

2.4.1. Definition of factors and responses

The following variables involved in the adsorption were studied: each initial dye concentration (i.e. of Acid Red 97, Acid Brown 425 and Acid Orange 61), mass of carbon, and contact time. Initial dyes concentrations were set as experimental design factors although these values cannot be modified by the experimenter but it was known that they influenced in the response (concentration of dyes remaining in solution), so they should be included in the model.

Because the main objective of this paper was to establish the conditions in which dyes can be efficiently adsorbed onto activated carbon, the studied responses were the percentage of the relative concentration of each dye at the end of the process (r_i), individual response, and the percentage of the relative concentration of the sum of dyes (r_t), total response, calculated as in Eqs. (1) and (2),

respectively:

$$r_i = \frac{c_{i,f}}{c_{i,0}} \times 100 \tag{1}$$

$$r_t = \frac{\sum c_{i,f}}{\sum c_{i,0}} \times 100 \tag{2}$$

where $c_{i,f}$ is the concentration of dye after the adsorption process and $c_{i,0}$ is the concentration of dye before the adsorption process.

2.4.2. Screening process with a fractional factorial design

Fractional factorial designs are good alternatives to full factorial designs for reducing the number of experiments, especially in the initial stage of a project [29].

In this paper, we worked with a fractional factorial design 2^{5-1}. With this design and with the four-factor interaction as the generator of the fifth-factor, the main effects are confounded with four-factor interactions, and two-factor interactions are confounded with three-factor interactions. Assuming that the interactions between three or more factors are negligible,
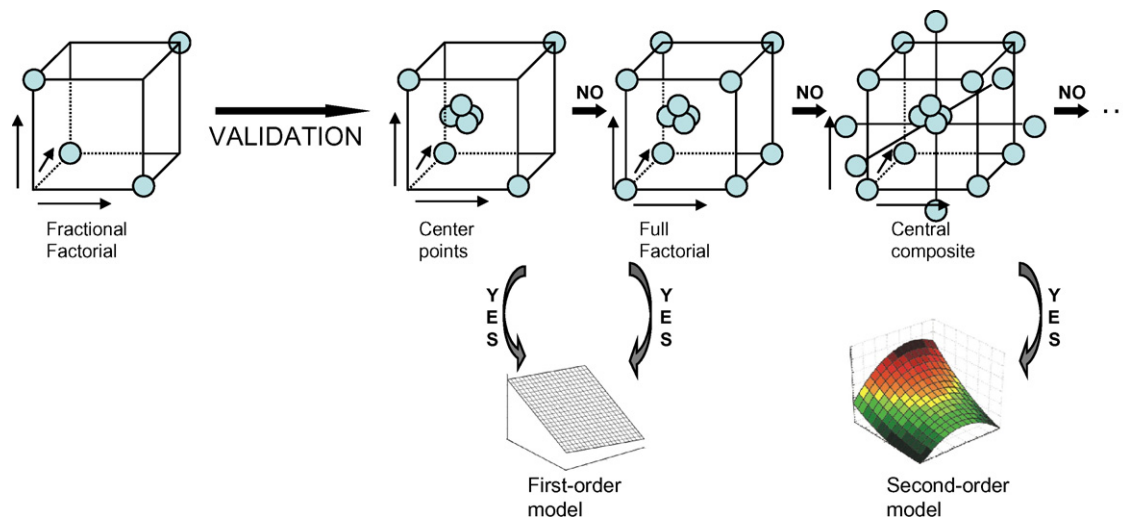
Fig. 3. Scheme used to establish and validate the response surfaces.

Table 2
Experimental points or experimental domain used in the optimization step

Step	Method	Factor			Response (%)[a]			
		A/B/C	D	E	Red	Brown	Orange	Global
1	STM	40	0.43	180	31	80	58	56
2	STM	40	0.56	240	10	67	50	42
3	FFD	30–50[b]	0.46–0.66[b]	210–270[b]	14	64	49	42
4	STM	40	1	180	9.5	48	28	28.5
5	STM	40	1.4	180	8	40	25	24
6	FFD	30–50[b]	1.3–1.5[b]	150–210[b]	11	38	23	24

STM: steepest ascent method, FFD: fractional factorial design.
[a] Average response in designs (percentage of dyes in solution).
[b] Experimental domain.

the main effects and the two-factor interactions can be determined.

In this paper, the significance of estimated effects is studied using the ANOVA test [30]. The importance of the effects can be visually studied with a Pareto chart, which shows important factors in the response in the form of a graph.

2.4.3. Application of the steepest ascent method [20]

When the initial estimate of the optimum operating conditions is a long way from the actual optimum, the steepest ascent method is a simple and economically efficient experimental procedure for getting into the general vicinity of the optimum.

This method moves sequentially along the path of steepest ascent; that is, in the direction of the maximum increase in the response. We assume that a first-order model is an adequate approximation to the true surface in the experimental domain.

The fitted first-order model is:

$$\hat{y} = \hat{\beta}_0 + \sum_{i=1}^{k} \hat{\beta}_i x_i \tag{3}$$

where $\hat{\beta}_i$ is the estimations of the effects of each factor, evaluated in the screening step.

For each factor (x_j), the step size (Δx_j) is affixed by the experimenter depending on the experiment and the step size for the rest of the factors (Δx_i) is evaluated as in the following equation:

$$\Delta x_i = \frac{\hat{\beta}_i}{\hat{\beta}_j / \Delta x_j} \quad i = 1, 2, \ldots, k; \ i \neq j \tag{4}$$

Finally, coded variables have to be converted into natural variables.

Experiments are conducted until no further increase in response is observed. Then a new first-order model can be fitted, a new steepest ascent path determined, and the procedure continued.

2.4.4. Establishing and validating the response surface

Once we know the experimental domain in which the response values are considered suitable, the experimental methodology for obtaining the response surface is established, following the scheme in Fig. 3. The eventual objective of response surface methods is to determine the optimum operating conditions for the system or to determine a region in the factor space in which operating requirements are satisfied.

When a fractional factorial design is used we can fit a first-order model but we should be alert to the possibility that a second-order model may be more appropriate. Replicating certain points (e.g. center points) is suitable to determine the presence of a curvature from second-order effects and also enables an independent estimate of error to be obtained. Validation consists of evaluating the pure quadratic curvature sum of squares (SS$_{\text{pure quadratic}}$) and applying an F-test to compare SS$_{\text{pure quadratic}}$ and SS$_{\text{residual}}$. If both values
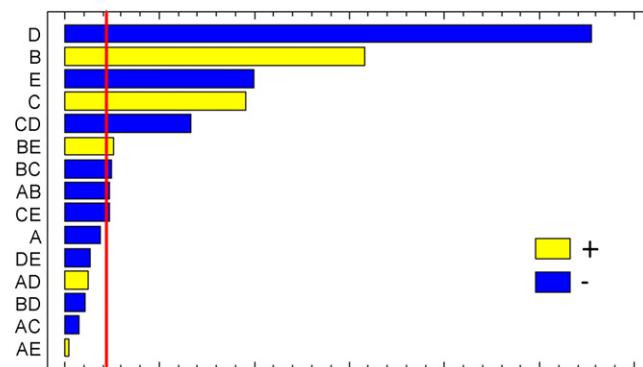
Fig. 4. Pareto chart from the fractional factorial design considering the % total dyes in solution as response.

are comparable, there is no quadratic curvature. On the other hand if they are not comparable, then quadratic curvature is present and we will have to assume a second-order model.

The pure quadratic curvature sum of squares in the analysis of variance is computed as follows:

$$SS_{\text{pure quadratic}} = \frac{n_F n_C (\bar{y}_F - \bar{y}_C)^2}{n_F + n_C} \tag{5}$$

where $\bar{y}_F$ is the average of the runs at the factorial points of the design and $\bar{y}_C$ is the average of the runs at the center point. n_F and n_C are the number of runs at the factorial design and at the center point, respectively.

To estimate the parameters of the quadratic terms, a central composite design is one option. Central composite designs contain imbedded full factorial designs with center points that are augmented with a group of axial (star) points that enable curvature to be estimated [31]. In a central composite design, the experimental domain can be carried out in a sequential way. In the first-step, the full factorial design is completed and validation for a first-order model is checked again, even though the initial hypothesis should be maintained and the obtained conclusions might be the same as with a fractional factorial design. If the first-order model is not validated, axial points are added.

Table 3
Analysis of the quadratic effects of the first-order model

	SS$_{\text{pure quadratic}}$	SS$_{\text{residual}}$	MS$_{\text{residual}}$	F-value
Total	2.12	17.78	1.11	1.91
Acid Red	33.61	30.87	1.93	17.42
Acid Brown	17.52	35.98	2.25	7.79
Acid Orange	14.18	131.37	8.21	1.73

Degrees of freedom (residual) = 3, degrees of freedom (pure quadratic) = 1, $F_{1,3,0.05} = 17.443$.

Table 4
External validation of the first-order model

Exp. no.	A	B	C	D	E	Experimental/predicted response			
						Total	Acid Red	Acid Brown	Acid Orange
1	35	50	50	1.45	165	25.7/24.7	13.4/13.3	36.2/36.3	21.9/21.0
2	45	35	35	1.35	195	21.7/22.7	9.1/8.3	38.1/39.8	21.5/25
3	35	45	45	1.35	165	25.6/27.1	13.6/12.7	34.9/39.0	22.6/27.5
4	35	45	35	1.5	195	20.6/20.6	11.8/12.1	28.2/30.4	15.2/16.4

3. Results and discussion

The experimental domain of the first design is based on previous knowledge [19]. The experimental domain and the results obtained are shown in Table 1. The notation of the variables will be maintained throughout the paper. The results revealed that approximately 70% of dyes remain in the solution. Acid Red 97 is the most adsorbed dye, with 54% of the dye being in solution, followed by Acid Orange 61 with 76% of the dye in solution and, finally, Acid Brown 425 with 80% of the dye in solution. These results agree with those obtained in previous papers [19].

From this first design, the individual and total responses show that all factors and interactions are significant. For the total response, the most significant factor was the contact time, followed by the mass of carbon.

Because the response of the initial design was a long way from the real optimum, we used the steepest ascent method. The new experimental conditions (see Table 2, step 1) are determined by taking into account that the effect of the mass of carbon on the total response is two-third of the effect of time. The initial dye concentrations are maintained constant because it is the most common range in wastewater tanning samples. We increased the highest level of time by 60 min and the highest level of mass of carbon by 0.13 g. The response improved and a second experimental point was reconsidered following the same criterion as in the first optimization (Table 2, step 2). The response was again better.

A new fractional factorial design (Table 2, step 3) was proposed to determine whether the influence of the factors changed given that adsorption is not linear over time [19], and in this case, approach a suitable experimentation. The experimental domain of this second design was established by considering that the experimental points of the second optimization step were the central points of the domain. We worked with a fractional factorial design that was analogous to the previous one.

When we studied the effect of the factors, we noticed that the time factor was not important in most of the responses, so the domain of this factor belonged to a flat zone in the kinetic adsorption. The most influential factor was the mass of carbon, followed by the initial concentration of the red dye. It seemed that the mass of carbon we were working with prevented the brown dye from competing with the orange dye and the red dye from being adsorbed onto the activated carbon.

Since our aim was to find a model that fitted the response to the factors considered, we used again the steepest ascent method and modified its direction. The new experimental point is shown in step 4 of Table 2. Contact time was fixed at the initial conditions of the optimization process (step 1) and the mass of carbon was increased so that response was better. In this way, response improved noticeably and the new experimental conditions were moved in this direction (see Table 2, step 5). At this last experimental point, response improved slightly, indicating that we were in a stable zone where the percentage of dyes in solution was 24% so we decided to conclude the optimization process.

These values were considered to be suitable because a high percentage of dyes could be eliminated at reasonable cost (time and mass of carbon). This is why the modeling strategy was initiated around experiment 5 of Table 2, following the scheme in Fig. 3 (Table 2, step 6).

Fig. 4 shows the Pareto chart obtained with the total concentration of dyes in solution as response. The vertical line corresponds to the p-value above which the effects are important.

It can be seen that, with the exception of factor A (initial concentration of red dye), all the factors were relevant. Some interactions were significant, but the only important one was the initial concentration of the orange dye with the mass of carbon. The initial concentration of the red dye was not important, which indicated that we worked in experimental conditions in which it was mainly adsorbed.

We established a first-order model with the fractional factorial design for the total response (a), Acid Red 97 (b), Acid Brown 425 (c) and Acid Orange 61(d):

(a) $y = 23.4 + 1.8X_B + 1.1X_C - 3.2X_D - 1.1X_E - 0.3X_AX_B - 0.3X_BX_C + 0.3X_BX_E - 0.8X_CX_D - 0.3X_CX_E$
(b) $y = 10.5 - 2.3X_A + 1.2X_B + 0.7X_C - 0.4X_AX_C + 0.4X_BX_E - 0.5X_CX_D$
(c) $y = 37.7 + 3.6X_A - 0.7X_B + 2.1X_C - 3.4X_D - 1.4X_E$
(d) $y = 23.1 + 1.4X_A + 1.4X_B - 6.3X_D - 1.9X_E - 1.2X_CX_D$

with responses expressed as a percentage of dyes remaining in solution and the variables X_A, X_B, X_C, X_D, X_E expressed as coded values (−1 the lowest level and +1 the highest level) of the last full factorial design (see Table 2, step 6).

We validated this surface with the central points of the design evaluating $SS_{pure\ quadratic}$ and $SS_{residual}$, and calculated the corresponding F-value. Table 3 shows the results of this validation process. All the surfaces obtained are validated for a significance level of 5%.

We also selected four other points in the domain to do an external validation of the model. The experimental factors and responses of each point are shown in Table 4. We applied a joint test of slope of unity and intercept of zero to the regression fitted between the experimental and predicted responses. We determined that they were statistically comparable with the predicted values from the model with 5% significance and concluded that the linear model fits the process studied.

Fig. 5 shows the fitted surface for the total response for 40 mg l^{-1} of each dye at different contact times and mass of carbon. The contour plot is also presented, which shows the different combinations of contact time and mass of carbon for achieving the same response.

In the experimental domain where the response surfaces were fitted, between 14.5 and 32.3% of total dyes were in solution, between 5 and 16% of Acid Red 97, between 26.5 and 48.9% of Acid Brown 425 and between 10.9 and 35.3% of Acid Orange 61, with the extremes of the domain being applied to all factors.

The obtained results could be attractive for the tanning industry although their wastewaters might be treated in treatment plants but this process would reduce their cost because these waters would be cleaner.
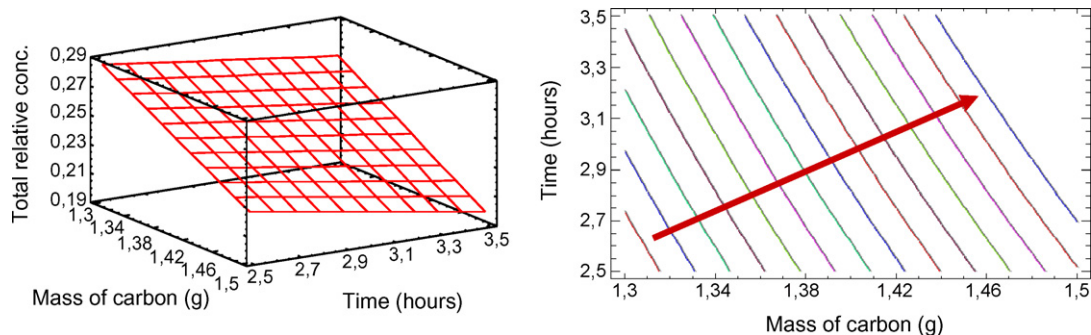
Fig. 5. Response surface and contour plot of the total percentage of dyes in solution after the dyes have been adsorbed onto activated carbon. Experimental conditions: 40 mg l^{-1} each dye.

Due to the simplicity of the adsorption process onto activated carbon, the strategy used could be suitable for industries which have limited technologies in many cases.

4. Conclusions

Our study of the adsorption of dyes onto activated carbon has demonstrated something we know from a previous paper [19]: adsorption process is competitive and the adsorption of the brown dye was clearly influenced by the presence of the other two dyes. The adsorption of the orange dye was less influenced by the red dye and the adsorption of the red dye was similar whether it was by itself in solution or in a mixture. In this paper where the three dyes are always present in the solution we could appreciate that the dye that is mostly adsorbed (lower independent term in the equations modeled) is the red dye, then the orange dye and finally the brown dye.

We established a first-order response surface for the adsorption of dyes onto activated carbon using the relative concentration of dyes at the end of the process. In the domain studied, 24% of the dyes were in solution, after the fractional factorial designs and the steepest ascent method had been applied. When the responses were individual concentrations, the first-order model was also fitted.

Although the dyes studied compete with each other in the adsorption process, conditions to obtain the best response were not opposite. Experimental conditions can depend on which dye we are interested in removing, for visual or toxic reasons, by obtaining response surfaces for the total and the individual responses.

The influence of the factors, whether they are principal effects or interactions between factors, is different in each model established. Overall, it is complicated to do physical interpretations about interactions between factors because we have to consider that the studied process is competitive and the equilibrium could or could not be reached when measurements are done. Although, many interactions show that the effect of the principal factors is reinforced.

Modeling the adsorption of dyes by using the classical approach of establishing kinetic equations or isotherms or by using empirical models using methodologies of DOE provides complementary information. In the first case, we obtain theoretical parameters in fixed conditions that allow you to predict the behavior of the dyes at the same conditions. Models obtained by using DOE allow you to predict the behavior of dyes when few parameters are modified simultaneously, whenever we are in the experimental domain where we have applied and validated the model. We think that before optimizing and modeling the process varying several factors it is worthy to know the behavior of the dyes at initial conditions of reference in order to reduce the number of experiments.

This methodology can be used as a strategy to reduce the percentage of dyes in wastewater samples. However, the presence of other species in the sample can affect the final function obtained, especially if the affinity of these species is greater than those of interest. In this case, the method can be applied in the same way.

References

[1] L.H. Ahlström, A. Sabine, L. Mathiasson, J. Sep. Sci. 28 (2005) 2407–2412.
[2] G.A. Umbuzeiro, H.S. Freeman, S.H. Warren, D. Palma de Oliveira, Y. Terao, T. Watanabe, L.D. Claxton, Chemosphere 60 (2005) 55–64.
[3] S. Papic, N. Koprivanac, A. Loncaric Bozic, J. Soc. Dyers Color. 116 (2000) 352–358.
[4] J. Oakes, P. Gratton, J. Chem. Soc., Perkin Trans. 2 (1998) 2201–2206.
[5] I. Poulios, I. Aetopoulou, Environ. Technol. 20 (1999) 479–487.
[6] J.X. Chen, L.H. Zhu, Chemosphere 65 (2006) 1249–1255.
[7] S.H. Lin, C.C. Lo, Environ. Technol. 17 (1996) 841–849.
[8] S.M. McClung, A.T. Lemley, Text. Chem. Color. 26 (1994) 17–22.
[9] V. Lopez-Grimau, M.C. Gutierrez, Chemosphere 62 (2006) 106–112.
[10] A. Bousher, X. Shen, R.G.J. Edyvean, Water Res. 31 (1997) 2084–2092.
[11] S.S. Tahir, N. Rauf, Chemosphere 63 (2006) 1842–1848.
[12] F.L. Fu, Y. Xiong, B.P. Xie, R.M. Chen, Chemosphere 66 (2007) 1–7.
[13] M. Arami, N.Y. Limaee, N.M. Mahmoodi, Chemosphere 65 (2006) 1999–2008.
[14] A. Pala, E. Tokat, Water Res. 36 (2002) 2920–2925.
[15] I.D. Mall, V.C. Srivastava, N.K. Agarwal, I.M. Mishra, Chemosphere 61 (2005) 492–501.
[16] K. Kadirvelu, C. Karthika, N. Vennilamani, S. Pattabhi, Chemosphere 60 (2005) 1009–1017.
[17] H. Metivier-Pignon, C. Faur, P. Le Cloirec, Chemosphere 66 (2007) 887–893.
[18] V. Gómez, J. Font, M.P. Callao, Talanta 71 (2007) 1393–1398.
[19] V. Gómez, M.S. Larrechi, M.P. Callao, Chemosphere 69 (2007) 1151–1158.
[20] D.C. Montgomery, Design and Analysis of Experiments, John Wiley & Sons, New York, 1997.
[21] T. Lundstedt, E. Seifert, L. Abramo, B. Thelin, A. Nystrom, J. Pettersen, R. Bergman, Chemometr. Intell. Lab. Syst. 42 (1998) 3–40.
[22] R.H. Myers, D.C. Montgomery, Response Surface Methodology, Process and Product Optimization using Designed Experiments, John Wiley & Sons, New York, 1995.
[23] J. Brandvik, Chemometr. Intell. Lab. Syst. 42 (1998) 51–61.
[24] N. Ortega, S.M. Albillos, M.D. Busto, Food Control 14 (2003) 307–315.
[25] C. Severini, A. Baiano, T. De Pilli, R. Romaniello, A. Derossi, Lebensm. -Wiss. Technol. 36 (2003) 657–665.
[26] J.V. Nardi, W. Acchar, D. Hotza, J. Eur. Ceram. Soc. 24 (2004) 375–379.
[27] R. Tauler, Chemometr. Intell. Lab. Syst. 30 (1995) 133–146.
[28] R. Tauler, A. de Juan, 2006, Multivariate Curve Resolution Homepage, http://www.ub.es/gesq/mcr/mcr.htm.
[29] G. Hanrahan, K. Lu, Crit. Rev. Anal. Chem. 36 (2006) 141–151.
[30] D.L. Massart, B.G.M. Vandeginste, L.M.C. Buydens, S. de Jong, P.J. Lewi, J. Smeyers-Verbeke, Handbook of Chemometrics and Qualimetrics Part A, Elsevier, Amsterdam, 1997.
[31] G. Hanrahan, J. Zhu, S. Gibani, D.G. Patil, Chemometrics: experimental design, in: Encyclopedia of Analytical Science, Elsevier, Oxford, 2005.

Sensitive and selective detection of aspartic acid and glutamic acid based on polythiophene–gold nanoparticles composite

Hongliang Guan, Peng Zhou, Xianglei Zhou, Zhike He*

College of Chemistry and Molecular Sciences, Wuhan University, Wuhan, Hubei 430072, PR China

ARTICLE INFO

ABSTRACT

In recent years, gold nanoparticles and water-soluble fluorescent conjugated polymers are promising materials in terms of their potential applications in a variety of fields, ranging from monitoring DNA hybridization to demonstrate the interaction between proteins, or detecting diseased cell, metal ions and small biomolecular. In order to exploit some new properties of the both, many attempts have been devoted to achieve nanoparticle–polymer composite via incorporating metal nanoparticle into polymer or vice versa, however, only few of them are put into practical application. In the present paper, we utilize the "superquenching" property of AuNPs to polythiophene derivatives for detecting aspartic acid (Asp) and glutamic acid (Glu) in pure water, and discuss the factors accounting for fluorescence quenching and recovery via modulating pH. Thus an exceptionally simple, rapid and sensitive method for detecting Asp and Glu is established with a limit of detection (LOD) is 32 nM for Asp and 57 nM for Glu, the linear range of determination for Asp is 7.5×10^{-8} M to 6×10^{-6} M and 9.0×10^{-8} M to 5×10^{-6} M for Glu. The system is applied to real sample detection and the results are satisfying. Otherwise the composite is very sensitive to pH change of solution, we expect it will be possible to use as pH sensor with wide range in the future.

© 2008 Elsevier B.V. All rights reserved.

1. Introduction

For decade years, the application of gold nanoparticles (AuNPs) and water-soluble fluorescent conjugated polymers (conjugated polyelectrolytes, CPEs) has gained great attention due to their unique performance for use as highly sensitive chemical and biosensors [1–10]. For AuNPs, several features make them exceptional appealing to many researchers. First, AuNPs possess high extinction coefficient in the visible region, the extraordinary optical features make AuNPs an ideal color reporting group for signaling molecular recognition events and render them to function as efficient quenchers for most fluorophores [11–15]; secondarily, by modification with thiol ligands, such as antibody, DNA/RNA, AuNPs could specifically recognize target biomolecular [16,17]; and thirdly, the good conductivity of AuNPs also makes them be widely used for electrochemical assay [18–20]. For example, Kim et al. used the AuNPs–RNA–dye conjugates to detect a complementary single-stranded DNA target through the fluorescence changes from the conjugates [21]; by taking advantage of different agglomeration states of AuNPs can result in distinctive color changes. Chen et al. [22] exploited AuNPs-based competitive colorimetric assay for

detection of protein–protein interactions. On the other hand, CPEs, characterized by a backbone with a π-delocalized electronic structure and pendant groups bearing ionic functionalities, also have been one of the best candidates as components in high performance and rapid response chemical and biological sensor applications [23–25]. The utility of these CPEs in biosensors comes from their high absorption coefficients (excellent "light harvesters") together with high fluorescent quantum yields, furthermore, when appropriately modified, they can detect, transduce, and possibly amplify chemical, biological and physical changes into measurable optical or electrical signals [26]. In order to exploit the best use of the both, several groups have focused their interests on incorporating metal nanoparticles into conducting polymers or vice verse to obtain integrated functional multicomponent devices [27–30]. However, these efforts are often restricted to study the structure of the composite, only few cases aim at practical application [31–33].

In this regard, we had for the first time utilized water-soluble fluorescent polythiophene derivative and AuNPs composite for detecting aspartic acid (Asp) and glutamic acid (Glu). Polythiophene derivatives have received widespread attention in chemical and biological sensing field, one hand, they are easy modification and preparation, thiophene polymer can be obtained through oxidation of the corresponding monomers by $FeCl_3$ or other coupling reagents [34]; on the other hand, the interactions between the side-chain (ligands) and different analytes (targets) can readily be

* Corresponding author. Tel.: +86 27 87162672; fax: +86 27 68754067.
E-mail address: zhkhe@whu.edu.cn (Z. He).
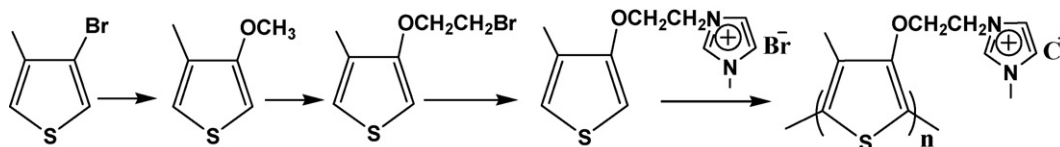
Scheme 1. The synthesis route of polythiophene derivate, (i) CH_3OH, CH_3ONa, CuBr, NMP; (ii) toluene, $NaHSO_4$, $BrCH_2CH_2OH$; (iii) CH_3CN, 1-methylimidazole; and (iv) $FeCl_3$, $CHCl_3$, Bu_4NCl/ion exchange.

detected from the changes in both side-chain and backbone conformations without any tagging process [35]. Glu and Asp both play critical roles in maintaining natural functions of body, high-level Glu content in plasma will lead to acute ischemic stroke [36], and Glu is precursor for γ-amino butyric acid, which is the main inhibitory neurotransmitter in the central nervous system [37]; while Asp can facilitate tricarboxylic acid cycle, potassium salt of Asp is used to cure heart, liver disease and diabetes [38,39]. The general approach for determination of free amino acids is by liquid, gas chromatography or electrochemical strategies [40–43], but these chromatography methods have some drawbacks, such as the lengthy cleanup and derivatization steps, electrochemical methods also need complex treatment of electrodes.

2. Experimental

2.1. Materials and methods

Poly(1*H*-imidazolium-1-methyl-3-{2-[(4-methyl-3-thienyl)-oxy]ethyl})chloride (PT) was synthesized according to the previously published literatures [44,25] (Scheme 1). $HAuCl_4 \cdot 3H_2O$ was purchased from Beijing Chemical Company. Trisodium citrate dehydrate was from Sinopharm Company, China. 20 free amino acids were obtained from Shanghai Sangon Biological Engineering Technology & Services Co., Ltd. Sample Asp and Glu were from Wuhan Hezhong Fine Chemical Factory ($90 \pm 2\%$ according to the label). Tris(hydroxymethyl)aminomethane (Tris) was purchased from Sigma. Unless other specified, the rest reagents were of analytical grade and used without further purification. The water used was purified through a Water Pro Plus system (Labconco Co., USA).

2.2. Preparation of gold nanoparticles (AuNPs)

All glassware used in the following preparations was thoroughly cleaned in a bath of fresh aqua regia (HNO_3:HCl = 3:1), rinsed in pure water prior to use. AuNPs were prepared by one-step citrate reduction of $HAuCl_4$ at ambient temperature following Grabar's method [45]. In short, 100 mL aqueous solution consisting of 1 mM $HAuCl_4$ was brought to a vigorous boil with stirring in a round-bottom flask fitted with a reflux condenser; 38.8 mM trisodium citrate (10 mL) was then added rapidly to the solution. The solution was heated under reflux for another 15 min, during which time its color changed from pale yellow to deep red. The solution was cooled to room temperature while being stirred continuously. After filtration and centrifugalization, the resulted solution was stored at 0–4 °C for further use. The sizes of the nanoparticles were verified by TEM (JEF2010, Japan) analysis with an average size of 13.8 ± 1.5 nm (about 60 particle samples) (Fig. 1). The particle concentration was 13.0 nM according to Beer's law using an extinction coefficient of 2.08×10^8 M^{-1} cm^{-1} at 517 nm.

2.3. Standard and sample solutions

The stock solutions of each amino acid (0.2 mM) were prepared in pure water and used by appropriate dilution of the stock solution.

Sample solutions, which were equivalent to about 20 mg of Asp and Glu according to the label content of the tablet supplier, were transferred to 100-mL volumetric flasks, sonicated for 15 min and stored for analysis.

2.4. Instrumentation

UV–vis absorption was taken on a TU-1900 Spectrophotometer (Beijing Purkinje General Instrument Co., Ltd). Fluorescence measurements were acquired in 3-mL quartz at room temperature using a LS-55 Luminescence Spectrometer (PerkinElmer, UK). The pH of solution was measured using Sartorius PB-10 pH Meter (Sartorius, Germany). TEM measurements were made on a transmission electron microscope operating at 200 kV. The sample for TEM was prepared by placing a drop of the colloidal solution on the carbon-coated micro-grid and drying at room temperature.

3. Results and discussion

In pure water, PT exhibited a strong emission with maximum wavelength at 514 nm (Fig. 3a), which had a perfect spectral overlap with the absorption of AuNPs, as a result, the fluorescence of PT could be quenched dramatically by AuNPs even at very low concentration via a highly efficient energy transfer between them (Fig. 3b). Linear Stern–Volmer plots thus provided a traditional and convenient means to determine K_{SV} value, the K_{SV} was related to PT efficiency via the relationship:

$$\frac{F^0}{F} = 1 + K_{SV} \quad [\text{quencher}] \tag{1}$$

where F^0 and F were PT fluorescent intensity in the absence and presence of quencher, respectively. A plot of F^0/F vs quencher concentration showed the highly efficient "superquenching" originated from the PT fluorophore–quencher pair, here the K_{SV} was 1.29×10^{10} M^{-1} with the concentration ranging from 0 pM to 26 pM.

Because of the adsorption of citrate during the preparation, AuNPs were typically negatively charged, did not quench the
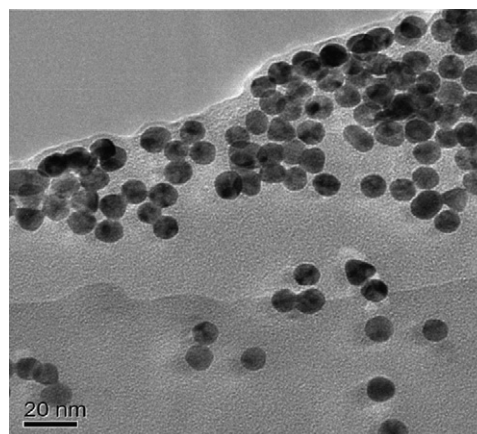
Fig. 1. TEM image and corresponding particle size of AuNPs.
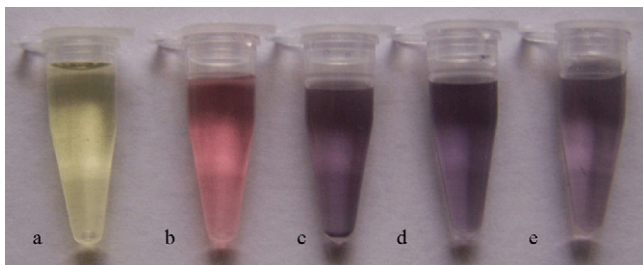
Fig. 2. Photographs of solutions ($c_{PT} = 5.0 \times 10^{-5}$ M, on repeat units; $c_{Au} = 1.3 \times 10^{-9}$ M, $c_{Asp} = c_{Glu} = 2 \times 10^{-4}$ M) of (a) PT, (b) AuNPs, (c) PT + AuNPs, (d) PT + AuNPs + Asp, and (e) PT + AuNPs + Glu. (For interpretation of the references to color in the artwork, the reader is referred to the web version of the article.)

anionic-conjugated polymer, such as poly[lithium 5-methoxy-2-(4-sulfobutoxy)-1,4-phenylenevinylene], but could easily quench the fluorescence of cationic charged PT. The quenching mechanism had been systematically investigated by Fan et al. [46], they ascribed the superquenching to the strong electrostatic nanoparticle–polymer complexation and the ability of gold nanoparticles to quench via efficient energy transfer. When wine-red AuNPs solution was added to yellow PT aqueous solution (Fig. 2a and b), the color of PT turned purple, meanwhile precipitation occurred due to the electrostatic adsorption of AuNPs to PT (Fig. 2c). When 20 free amino acids were added into the PT–AuNPs composite separately, the precipitation disappears (Fig. 2d and e), but only Asp and Glu could recover the quenched fluorescence of PT (Fig. 3c and d), the rest 18 amino acids still did not disturb the fluorescence of the system (Fig. 4). As we all know, Asp and Glu are acidic amino acids, the pI of which is 2.77 and 3.22. Compared with other amino acids, they can give out one more hydrion in aqueous solution, the electrolytic dissociation equilibrium was below (Eq. (2)), thus there was a competitive electrostatic interaction between the positively charged polymer and hydrion, hydrion was more prone to combine with AuNPs, whereas the PT was released to emit the fluorescence (Fig. 5):

$$HOOC(CH_2)nCHCOOH \rightleftharpoons HOOC(CH_2)nCHCOO^- \rightleftharpoons {}^-OOC(CH_2)nCHCOO^- + H^+$$
$$\overset{|}{NH_2} \qquad\qquad \overset{|}{NH_3} \qquad\qquad \overset{|}{NH_3}$$

$$n=1, Asp; n=2, Glu \qquad (2)$$

$$(2)$$
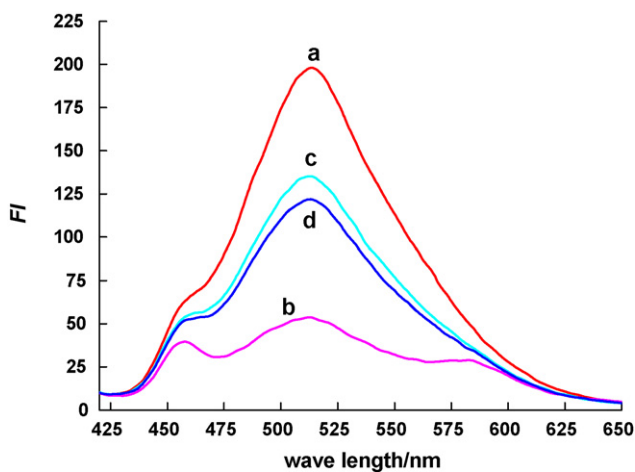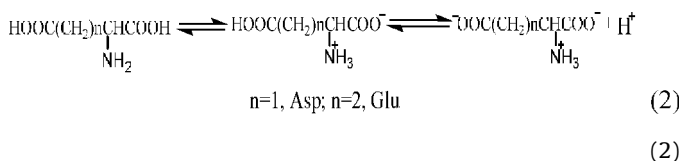
Fig. 3. Fluorescence spectra of (a) PT ($c_{PT} = 1.0 \times 10^{-6}$ M, repeat units), (b) PT + AuNPs ($c_{AuNPs} = 2.6 \times 10^{-11}$ M), (c) PT + AuNPs + Asp, (d) PT + AuNPs + Glu. $c_{Asp} = c_{Glu} = 5.0 \times 10^{-6}$ M. (For interpretation of the references to color in the artwork, the reader is referred to the web version of the article.).
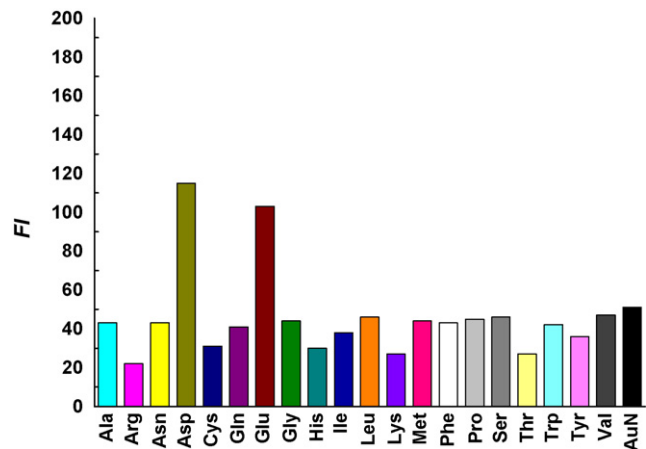
Fig. 4. The fluorescence recovery upon the addition of 20 α-amino acids into PT–AuNPs composite, the concentration of above amino acids is 5.0×10^{-6} M. (For interpretation of the references to color in the artwork, the reader is referred to the web version of the article.)

To confirm the hypothesis, controlled experiments were carried out in HCl and tris(hydroxymethyl) aminomethane solution (Tris). One key motive for this study was to evaluate how the pH value of different solutions affected the emission recovery. In pH 2.0 HCl solution, the fluorescence intensity of PT was nearly the same as in pure water. However, the addition of AuNPs could not quench the fluorescence of PT; also the addition of Asp, Glu and other 18 amino acids only lead to slightly intensity perturbation, although each of 20 free amino acids bears different pI (Fig. 6), such behavior might be the structure change of AuNPs in HCl solution, molar extinction coefficient of AuNPs was lower in HCl solution (pH 2.0) than that in pure water (Fig. 7). The same experiments were repeated in 0.01 M Tris aqueous solution (pH 10.2), the PT fluorescence intensity in Tris solution only equaled to about 30% that in pure water and in HCl solution. Furthermore, the addition of AuNPs could quench the intensity even lower, when 20 free amino acids were added, there was not pronounced change in intensity (Fig. 8). Tris, a biological base, can combine with H$^+$ after it dissolves in water, then the solution is alkaline, the extra OH$^-$ could quench the fluorescence of PT, but not so efficient as AuNPs. All these data indicated that pH of solution play a dominate role in the interaction between AuNPs and PT, when the solution was altered from neutral to acidic or to alkaline, the pH of the solution either weaken or strengthen the resonance energy transfer effect between the AuNPs and PT.
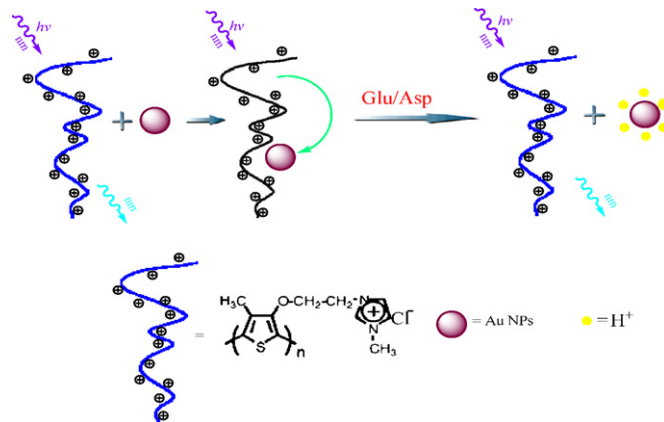
Fig. 5. Schematic description of the interaction between PT, AuNPs, and H$^+$. (For interpretation of the references to color in the artwork, the reader is referred to the web version of the article.)
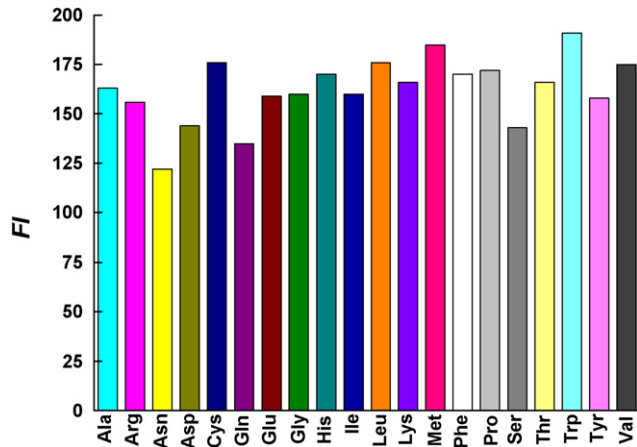
Fig. 6. The fluorescence intensity of AuNPs–PT composite upon the addition of 20 α-amino acids in 0.01 M HCl (pH 2) solution, the concentration of above amino acids is 5.0×10^{-6} M. (For interpretation of the references to color in the artwork, the reader is referred to the web version of the article.)
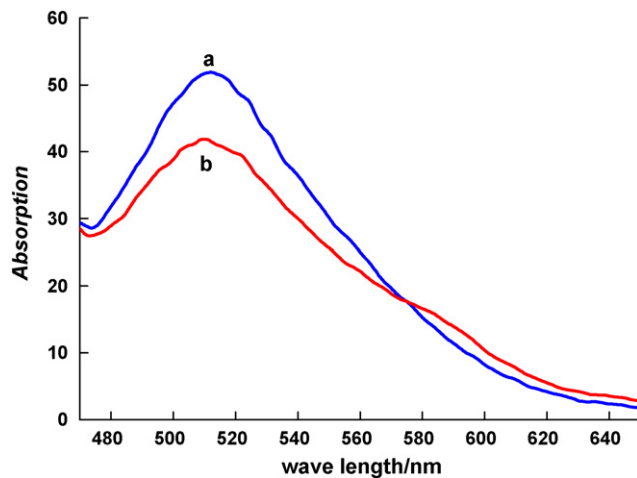
Fig. 7. The absorption spectra of AuNPs in (a) pure water and (b) HCl solution (pH 2). $c_{AuNPs} = 2.6 \times 10^{-11}$ M. (For interpretation of the references to color in the artwork, the reader is referred to the web version of the article.)
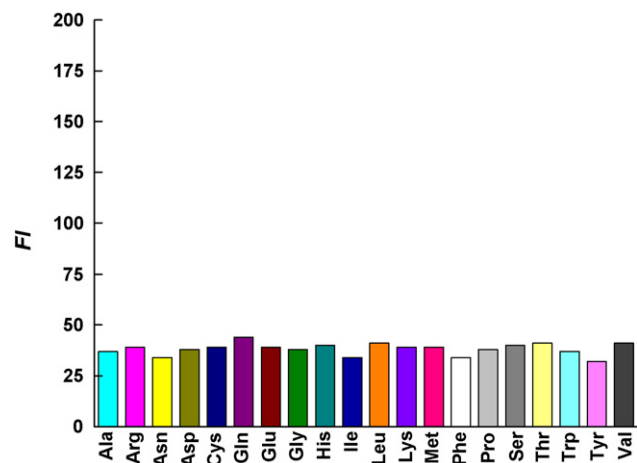
Fig. 8. The fluorescence intensity of AuNPs–PT composite upon the addition of 20 α-amino acids in 0.01M Tris solution (pH 10.2), the concentration of above amino acids is 5.0×10^{-6} M. (For interpretation of the references to color in the artwork, the reader is referred to the web version of the article.)
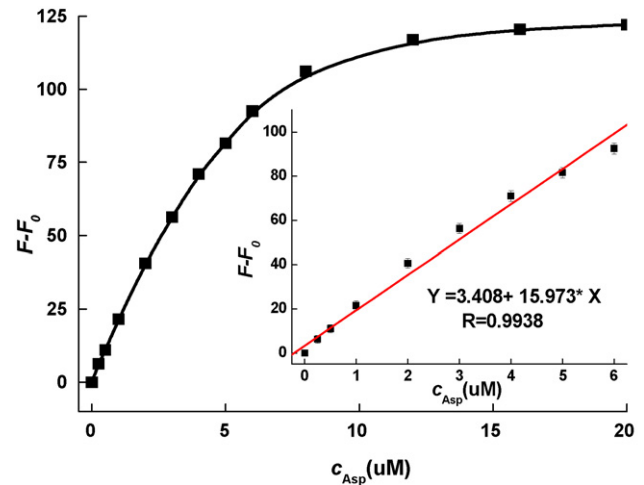
Fig. 9. Linear plots of increased fluorescence intensity ($F–F_0$, F_0 is the fluorescent intensity of AuNPs–PT composite) vs the addition of Asp. Error bars represent the standard deviation of three measurements.

From earlier studies we knew that at low pH or in pure water, the positively charged chains separated from each other to induce a more planar conformation of the polymer backbone, but high pH (pH > 10) would facilitate the aggregation of PT, which directed the quenching of PT [47]. Thus the addition of 20 amino acids to PT aqueous solution at pH > 10 could indeed perturb the fluorescence of PT, it was still difficult to categorize them according to emission intensity (Fig. 8). Interestingly, in pure water, the same concentration of Glu and Asp led to different recovered emission for the different pI (pI_{Asp} = 2.77, pI_{Glu} = 3.22), thus we could differentiate Asp from Glu in terms of the emission intensity, generally, and Asp intensity was stronger than that of Glu.

4. The determination of Asp and Glu

4.1. Optimization of the PT and AuNPs ratio

It should be noted that the proportion over the concentration of PT and AuNPs was critical in the detecting system. Either low or high amounts of PT present in the solution were found to deteriorate the system's sensitivity. For instance, when using much more AuNPs than needed to quench PT, the more Asp or Glu were used
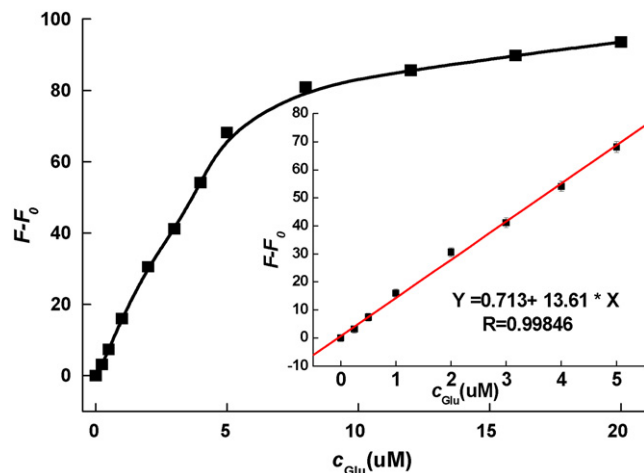
Fig. 10. Linear plots of increased fluorescence intensity ($F − F_0$, F_0 is the fluorescent intensity of AuNPs–PT composite) vs the addition of Glu. Error bars represent the standard deviation of three measurements.

Table 1
Repeatability of the proposed method ($n = 5$)

Sample	Asp			Glu		
	Added (μg mL^{-1})	FI	Found (μg mL^{-1})	Added (μg mL^{-1})	FI	Found (μg mL^{-1})
$\bar{X} \pm$ S.E.	0.50 ± 0	63.1 ± 2.03	0.493 ± 0.11	0.5 ± 0	46.4 ± 3.05	0.491 ± 0.12
S.D.	0	2.30	2.71	0	2.43	2.67
R.S.D. (%)	0	0.41	0.54	0	0.47	0.57

$\bar{X} \pm$ S.E.: mean $\pm$ standard error; S.D.: standard deviation; R.S.D.%: relative standard deviation.

Table 2
Recovery test for Asp ($n = 3$)

Sample	Original[a] (μg mL^{-1})	Added[b] (μg mL^{-1})	Found (μg mL^{-1})	Mean recovery (%)	R.S.D. (%)
Asp	0.30	0.10	0.39 ± 0.02	98.5	0.51
	0.30	0.20	0.49 ± 0.01	99.8	0.48
	0.30	0.30	0.60 ± 0.02	102.4	0.43

[a] Original: standard solution.
[b] Added: sample solution.

Table 3
Recovery test for Glu ($n = 3$)

Sample	Original[a] (μg mL^{-1})	Added[b] (μg mL^{-1})	Found (μg mL^{-1})	Mean recovery (%)	R.S.D. (%)
Glu	0.30	0.10	0.38 ± 0.02	97.6	0.52
	0.30	0.20	0.49 ± 0.01	98.5	0.50
	0.30	0.30	0.61 ± 0.01	102.1	0.45

[a] Original: standard solution.
[b] Added: sample solution.

to recover the emission and the perturbations from other amino acids would also be shielded; less AuNPs led to higher background signal due to the strong emission from free fluorophores, which affected the sensitivity of Asp and Glu detection, thus further LOD value was influenced. A serial of experiments with varied AuNPs/PT ratios had been carried out to ensure the right proportion. By measuring quenching efficiency, the optimized concentration of PT was 1×10^{-6} M, corresponding to 2.6×10^{-11} M AuNPs, all the presented data were acquired under optimized conditions. As expected, the increase of fluorescence from AuNPs–PT composite could quantitatively reflect the amounts of Asp or Glu added, as shown in Figs. 9 and 10, by monitoring the fluorescence intensity at 514 nm, a good linear relationship was obtained in the range of 7.5×10^{-8} M to 6×10^{-6} M for Asp and 9.0×10^{-8} M to 5×10^{-6} M for Glu. The limit of detection at an S/N ratio of 3 for Asp was 32 nM and Glu was 57 nM.

4.2. Reproducibility

In order to measure the reproducibility of the system, five same standard solutions containing 0.5 μg mL^{-1} Asp and Glu were added to polymer–AuNPs composite, the result was evaluated by considering fluorescent intensity, the added and found concentration, the precision values with their R.S.D. were shown in Table 1. The amount of Asp was found to be 0.493 ± 0.11 μg mL^{-1} with its R.S.D. of 0.54% and Glu 0.491 ± 0.12 μg mL^{-1} with its R.S.D. of 0.57%. These values implied that the proposed method possessed the high reproducibility for Asp and Glu analysis.

4.3. Recovery test for real samples

The system was applied to detect real samples from a fine chemical factory; samples were treated as described in the procedure for sample preparation. Recovery studies of the method were conducted by adding the different concentrations of three standard Asp and Glu solution and each solution was repeated for three times.

The acceptable recovery was set as between 95% and 105%, the mean recovery was between 98.5–102.4% for Asp and 97.6–102.1% for Glu, and R.S.D. was between 0.43–0.51% for Asp and 0.45–0.52% for Glu. The obtained results in Tables 2 and 3 were in good agreement with the label claim for Asp and Glu content.

5. Conclusion

In summary, here we have developed an exceptionally simple, rapid and sensitive method for detection of Asp and Glu without any complicated protocols or laborious modification. AuNPs can efficiently quench the fluorescence of PT, K_{SV} is high to 1.29×10^{10} M^{-1}, the quenching and recovery mechanism are ascribed to the electrostatic interactions and energy transfer between PT and AuNPs. Upon addition of Asp or Glu, two acidic amino acids, which could offer one more hydrion to combine with AuNPs via competition, thus the fluorescence of PT recovered, the recovered emission intensity is proportion to the concentration of two amino acids, whereas a new homogeneous assay measurement for Asp and Glu is established with a LOD as low as 32 nM and 57 nM respectively. Since AuNPs and PT composite are very sensitive to the environment pH change, it is expected for further use as high performance pH sensors or detection of other chemically/biologically important analytes.

References

[1] F. McKenzie, K. Faulds, D. Graham, Small 3 (2007) 1866.
[2] C.C. Huang, H.-Ts. Chang, Anal. Chem. 78 (2006) 8332.

[3] S.K. Pillalamarri, F.D. Blum, A.T. Tokuhiro, M.F. Bertino, Chem. Mater. 17 (2005) 5941.
[4] B.I. Ipe, K.G. Thomas, J. Phys. Chem. B 106 (2002) 18.
[5] P.V. Kamat, S. Barazzouk, S. Hotchandani, Angew. Chem. Int. Ed. 41 (2002) 2764.
[6] Ho-A. Ho, M. Leclerc, J. Am. Chem. Soc. 125 (2003) 4412.
[7] L. Chen, D.W. McBranch, H.L. Wang, R. Helgeson, F. Wudl, D.G. Whitten, Proc. Natl. Acad. Sci. 96 (1999) 12287.
[8] C. Li, M. Numata, M. Takeuchi, S. Shinkai, Angew. Chem. Int. Ed. 44 (2005) 6371.
[9] C.-H. Fan, T. Hirasa, K.W. Plaxco, A.J. Heeger, Langmuir 19 (2003) 3554.
[10] B. Liu, G.C. Bazan, Nat. Protocol. 1 (2006) 1698.
[11] J. Chen, A. Zheng, A. Chen, Y. Gao, C. He, X. Kai, G. Wu, Y. Chen, Anal. Chim. Acta 599 (2007) 134.
[12] H. Li, R. Liang, D.H. Turner, L.J. Rothberg, S. Duan, RNA-Publ. RNA Soc. 13 (2007) 2034.
[13] P. Hazarika, F. Kukolka, C.M. Niemeyer, Angew. Chem. Int. Ed. 599 (2007) 134.
[14] T.L. Jennings, M.P. Singh, G.F. Strouse, J. Am. Chem. Soc. 128 (2006) 5462.
[15] C. Burns, W.U. Spendel, S. Puckett, G.E. Pacey, Talanta 69 (2006) 873.
[16] A.K.R. Lytton-Jean, M.S. Han, C.A. Mirkin, Anal. Chem. 79 (2007) 6037.
[17] L. Wang, X. Liu, X. Hu, S. Song, C. Fan, Chem. Commun. 36 (2006) 3780.
[18] M.T. Castaneda, S. Alegret, A. Merkoci, Electroanalysis 19 (2007) 743.
[19] Y. Jin, W. Lu, J.Q. Hu, X. Yao, J. Li, Electrochem. Commun. 9 (2007) 1086.
[20] R. Chai, R. Yuan, Y. Chai, C. Ou, S. Cao, Xuelian Li, Talanta 74 (2008) 1330.
[21] J.H. Kim, R.A. Estabrook, G. Braun, B.R. Lee, N.O. Reich, Chem. Commun. (2007) 4342.
[22] C.S. Tsai, T.B. Yu, C.T. Chen, Chem. Commun. 34 (2005) 4273.
[23] D. Wang, X. Gong, P.S. Heeger, F. Rininsland, G.C. Bazan, A.J. Heeger, Proc. Natl. Acad. Sci. 99 (2002) 49.
[24] K.P.R. Nilsson, O. Inganäs, Nat. Mater. 2 (2003) 419.
[25] K. Faïd, M. Leclerc, Chem. Commun. 24 (1996) 2761.
[26] S.W. Thomas III, G.D. Joly, T.M. Swager, Chem. Rev. 107 (2007) 1339.
[27] M. Borrell, L.G. Leal, Langmuir 23 (2007) 12497.
[28] D. Li, Y. Cui, K. Wang, Q. He, X. Yan, J.B. Li, Adv. Funct. Mater. 17 (2007) 3134.
[29] Y. Leroux, E. Eang, C. Fave, G. Trippe, J.C. Lacroix, Electrochem. Commun. 9 (2007) 1258.
[30] D.I. Gittins, F. Caruso, Adv. Mater. 12 (2000) 1947.
[31] B.R. Panda, A.J. Chattopadhyay, Colloid Interf. Sci. 316 (2007) 962.
[32] L. Shang, C. Qin, T. Wang, M. Wang, L.X. Wang, S. Dong, J. Phys. Chem. C 111 (2007) 13414.
[33] H. Chen, S. Dong, Talanta 71 (2007) 1752.
[34] R.S. Loewe, S.M. Khersonsky, R.D. McCullough, Adv. Mater. 11 (1999) 250.
[35] M.J. Marsella, P.J. Carroll, T.M. Swager, J. Am. Chem. Soc. 117 (1995) 9832.
[36] Y.V. Tcherkas, A.D. Denisenko, J. Chromatogr. A 913 (2001) 309.
[37] S. Heger, M. Seney, E. Bless, G.A. Schwarting, M. Bilger, A. Mungenast, S.R. Ojeda, S.A. Tobet, Endocrinology 144 (2003) 2566.
[38] D.Q. Shi, T. Nakamura, J. Dai, L. Yi, J.H. Qin, D.Y. Chen, Z.H. Xu, Y. Wang, S. Ikegawa, Q. Jiang, J. Hum. Genet. 52 (2007) 664.
[39] S. Huang, K. Zhou, Z. Li, Trans. Nonferrous Met. Soc. China 17 (2007) 612.
[40] T. Farkas, J. Toulouee, LC GC Eur. (2003) 14.
[41] A. Mustafa, P. Aman, R. Andersson, A. Kamal-Eldin, Food Chem. 105 (2007) 317.
[42] T. Cserháti, Biomed. Chromatogr. 21 (2007) 780.
[43] G. Herzog, D.W.M. Arrigan, Analyst 132 (2007) 615.
[44] Ho-A. Ho, M. Boissinot, M.G. Bergeron, G. Corbeil, K. Doré, D. Boudreau, M. Leclerc, Angew. Chem. Int. Ed. 41 (2002) 1548.
[45] K.C. Grabar, R.G. Freeman, M.B. Hommer, M.J. Natan, Anal. Chem. 67 (1995) 735.
[46] C. Fan, S. Wang, J.W. Hong, G.C. Bazan, K.W. Plaxco, A.J. Heeger, Proc. Natl. Acad. Sci. 100 (2003) 6297.
[47] K.P.R. Nilsson, M.R. Andersson, O. Inganäs, J. Phys. Condens. Matter. 14 (2002) 10011.

A novel evanescent wave scattering imaging method for single gold particle tracking in solution and on cell membrane

Hua He, Jicun Ren*

College of Chemistry & Chemical Engineering, Shanghai Jiaotong University, 800 Dongchuan Road, Shanghai 200240, PR China

ARTICLE INFO

ABSTRACT

We propose a novel evanescent wave scattering imaging method using an objective-type total internal reflection system to image and track single gold nanoparticles (GNPs) in solution. In this imaging system, only a millimeter-scale hole is employed to efficiently separate GNPs scattering light from the background reflected beam. The detailed experimental realization of the imaging system was discussed, and the effect of the hole size on imaging was investigated. We observed that the hole diameters from 2.5 to 4 mm are suitable to perform the scattering imaging by adjusting the incidence angle. The technology was successfully applied to track single gold nanoparticles in solution and on live cell membrane via the anti-epidermal growth factor receptor antibody. Compared to total internal fluorescence microscopy, the resonance light scattering detection has no photobleaching or blinking inherent to fluorescent dyes and quantum dots. Compared to conventional dark-field microscopy, the evanescent wave illumination can be conveniently applied to study membrane dynamics in living cells. Additionally, the objective-based configuration provides a free space above the coverslip, and allows imaging and concomitant manipulation of live cells in culture by microinjection, patch-clamping, AFM and other techniques.

© 2008 Elsevier B.V. All rights reserved.

1. Introduction

Many cellular processes, such as signal transduction and membrane trafficking, are closely correlated with the motion of transmembrane and membrane-associated molecules at the plasma membrane of live cells. Tracking single molecules at the plasma membrane is becoming most useful for studying the spatial–temporal control of membrane molecular processes. These studies afford the advantage viewing individual characteristics of a membrane molecule that may be washed out in the ensemble averaging that is inherent in bulk studies. Total internal reflection fluorescence microscopy (TIRFM) uses an electromagnetic field called the "evanescent field" (or "evanescent wave") to excite the fluorophores within several hundred nanometers from the interface and is most suitable for surface/membrane studies [1]. Compared to differential interference contrast, confocal microscopy, theta microscopy, or multi-photon microscopy [2–6], this method provides a significant improvement to visualize the dynamic behavior and reaction kinetics of individual molecules near the plasma membrane without interference of signals from other parts of the cell. Due to the stochastic nature of single par-

ticle/molecule behavior, TIRFM provides another advantage over laser scanning technique that enables statistics over several hundred luminescent spots to be taken in a single measurement as well as faster tracking since TIRFM images are captured frame by frame with charge-coupled device (CCD) cameras.

Traditionally, fluorescence detection methods employ organic fluorescent dyes as optical probes [7–9]. However, fluorescent dyes suffer from rapid photobleaching, and cannot fluoresce continuously for extended periods of time when used in single-molecule detection. Recently, fluorescent semiconductor quantum dots (QDs) have also been introduced as optical probes [10,11]. QDs possess unique optical properties, such as good photostability, high brightness, narrow but tunable emission spectra, and a broad spectral excitation cross-section. These properties make them valuable tools for biological imaging [12–14]. Unfortunately, QDs are subject to strong blinking [15], which would result in missing segments in the particle trajectory. In addition, potential human toxicity and cytotoxicity of the semiconductor materials make QDs unsuitable for in vivo applications [16,17]. Another promising alternative optical label are gold nanoparticles (GNPs). Compared to fluorescent dyes and QDs, GNPs have unique optical properties such as absence of blinking and photobleaching. Additionally, GNPs show strong light scattering at the plasmon resonance wavelength owing to the collective oscillation of the conduction electrons. For example, the light scattering intensity of a 60-nm, gold particle is equivalent to about 5×10^5 fluorescein molecules [18,19]. Moreover, they are

readily synthesized with controlled diameters, relatively inert, and easily attached to other moieties [20–27]. So far, although the light scattering intensity of GNPs is so strong, the separation of scattering light signal from the background reflection signal represents a great challenge in the detection system. Conventionally, the tracking of single gold particles was achieved using video-enhanced differential interference contrast (DIC) microscopy [28–32], dark-field microscopy [33], and lately using laser scanning [34,35]. For the elegant evanescent field illumination, although it was reported that a prism-based TIR system was constructed to image single wide gold islands with diameters ranging from 68 to 260 nm that were prepared by electron-beam lithography [36], the long exposure time and use of white light source would make this system rather limited for single particle tracking. Additionally, due to its optical configuration restriction, the prism-based TIR system is inconveniently used in cell imaging. Here, we propose a novel evanescent wave scattering imaging method using a hole-based objective-type total internal reflection system to rapidly image and track single gold nanoparticles in solution and on cell membrane. In this imaging system, only a millimeter-scale hole is employed to efficiently separate GNPs scattering light from the background reflected beam. Furthermore, this technology was successfully used to rapidly track

single gold nanoparticles near or on live HeLa cell membrane based on interaction of epidermal growth factor receptor (EGFR) and EGFR antibody (anti-EGFR). Our results demonstrated that the novel imaging method is a promising tool to study membrane dynamics in living cells.

2. Experimental

2.1. Preparation of gold nanoparticles

GNPs were synthesized by using a reported method with a minor modification [20]. In brief, aqueous solution of $HAuCl_4$ (0.01%, w/w) and sodium citrate (1%, w/w) were prepared. A solution of $HAuCl_4$ (100 ml) was heated to boiling, and a given volume of sodium citrate solution (volume depended on the requirement size of GNPs) was added rapidly to the boiling solution. Heating was continued 30 min after the solution color remains unchanged. After cooling to room temperature, the GNP stock solution was placed in a refrigerator for further use. Representative TEM micrograph of GNPs is shown in Fig. S-1. All solutions were prepared with ultra-pure water (18.2 MΩ) purified on Millipore Simplicity (Millipore, USA). To prepare anti-EGFR (anti-epidermal growth
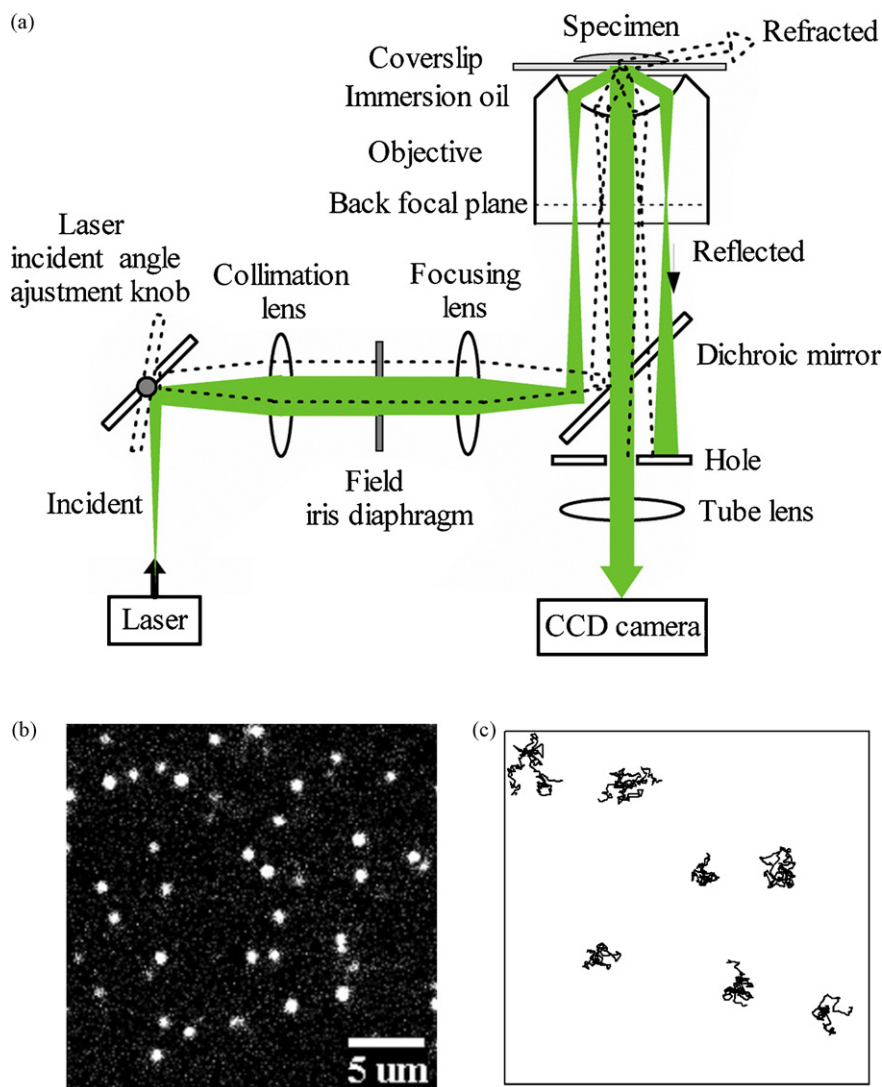
Fig. 1. (a) Schematic diagram of the hole-based objective-type total internal reflection system. (b) Evanescent wave scattering images of 40-nm GNPs in 50% (v/v) glycerin with a 3-mm hole under the system. Exposure time: 50 ms. (c) The experimental trajectories of GNPs near the interface shown in (b).

factor receptor)/GNPs conjugates, colloidal GNPs were diluted in 20 mM HEPES buffer (pH 7.4), and anti-EGFR antibodies (1 mg ml^{-1}, Beijing CellChip Biotechnology Co. Ltd., China) were reconstituted in the same buffer at 0.1 mg ml^{-1}. Then the solutions were mixed at a 1:1 volume ratio and allowed to interact for 20 min at room temperature. Polyethyleneglycol (MW 20,000) was added to the mixture up to a final concentration of 0.5 mg ml^{-1}, and the solution was centrifuged at 2000 rpm for 2 h to wash unbound antibodies. Then the anti-EGFR/GNPs pellet was redispersed in PBS buffer (pH 7.4) and stored at 4 °C.

2.2. Cell culture

Cervical cancer HeLa cells were cultured with high Dulbecco's Modified Eagle's medium supplemented with 10% fetal bovine serum (Hyclone) in a humidified incubator (MCO-15AC, Sanyo) at 37 °C in which the CO_2 level was kept constant at 5%. In our experiments, a 1-ml solution with approximately 8000 cells was seeded onto the coverslip, and then grown for 24 h at 37 °C under 5% CO_2. After washing three times with PBS, the cells on the coverslips were replaced in PBS buffer (pH 7.4). The anti-EGFR/GNPs (∼0.3 nM) were added to the medium for single particle tracking experiments. All measurements were performed at room temperature.

2.3. Imaging setup

Imaging of GNPs was accomplished on a custom modified Olympus IX 71 inverted microscopy (Olympus Optical Co., Tokyo, Japan). The excitation was performed by a Nd:YVO$_4$ laser operating at 532 nm and the laser power monitored in front of the microscopy objective (PlanApo N 60×/1.45 oil, Olympus) under epi-illumination was measured to be 5 mW. The mode could be switched between TIR and epi-illumination by adjusting the incidence angle through a laser incidence angle adjustment knob. Scattering light from the sample was collected by the same

objective, transmitted by suitable dichroic mirror (570 nm), and separated from the excitation light by a self-made hole with millimeter-scale diameter, and then focused into a cooled-CCD camera with a frame transfer device (Cascade 650, Photometrics, Tucson, AZ). The frame-transfer device has an imaging array of 653×492 with $7.4 \times 7.4\ \mu m^2$/pixel. Since the image can be quickly transferred from the sensor area to the frame transfer area, there is no need for a mechanical shutter. When operated in overlap mode, the camera is extremely useful in applications requiring continuous imaging (100% duty cycle) and can capture all the light emitted from the specimen. Image acquisition, particle tracking and analysis were carried out by using the MetaMorph software (Universal Imaging, Downingtown, PA, USA). Images were smoothed by averaging each pixel with its eight nearest neighbors, and the location of each particle was taken to be at the intensity centroid. For each trajectory, the mean squared displacement MSD (t) as computed from the formula

$$MSD(t) = \frac{1}{L-n} \sum_{s=0}^{L-n-1} (r(s+n) - r(s))^2$$

where $n = t/\Delta t$, L is the length of the trajectory (number of frames), and $r(s)$ is the two-dimensional position of the particle in frame s ($s = 0$ corresponds to the start of the trajectory) [37,38].

3. Results and discussion

3.1. The hole-based total internal reflection imaging system

Fig. 1a illustrates the schematic diagram of the hole-based total internal reflection system. TIR production and scattering light collection are performed by the same objective with a high numerical aperture. Under the objective-based configuration, similar to the widely used objective-type total internal reflection fluorescence microscopy, the fluorescence detection could be easily realized by
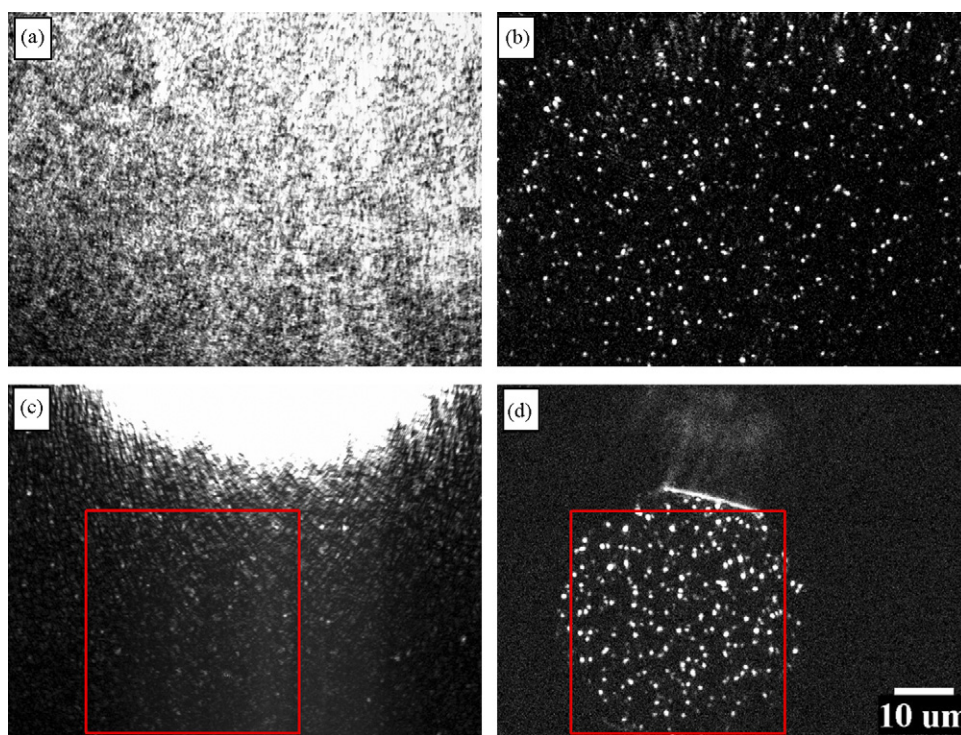
Fig. 2. Evanescent wave scattering images of GNPs over the entire CCD field of view in air. (a) Without a hole and (b) with a 3-mm hole under TIR illumination at the incidence angle of 63°; (c) before and (d) after reducing the field diaphragm opening diameter with a 3-mm hole at the incidence angle of 41.3°. Exposure time: 5 ms.

employing a set of filters to separate fluorescent light from the reflected incident light due to the wavelength change they involve (Stocke's shift). For scattering particles, however, the presence of the reflected incident light would make scattering signal impossible to be detected since the scattering light of a particle illuminated by monochromatic light (laser) has the same wavelength as the incident light. In our system, the laser beam is focused into the back focal plane (BFP) of the objective, and collimated to strike the glass-solution interface. When focused at the center position, the laser beam has an incidence angle of 0°. Except that most part of the laser beam is transmitting through the interface, another part will reflect back into the objective at the same angle. By adjusting the incidence angle, the path of the reflected beam is shifted from the center to the edge of the objective. In this case, a hole with millimeter-scale diameter is employed to efficiently separate particle scattering light from the reflected beam under total internal reflection or epi-illumination as shown in Fig. 1a. Fig. 1b shows the evanescent wave scattering images of 40 nm GNPs in 50% (v/v) glycerin with a 3-mm hole. Experimentally, Brownian motion of single gold particles was easily observed, and the corresponding video can be seen in the supplementary data (Video S-1). Here, the hole diameter and incidence angle play a decisive role on the experimental realization of scattering imaging system. Fig. 2a and b shows the scattering images of GNPs over the entire CCD field of view in air without holes and with a 3-mm hole, respectively. The

scattering images of GNPs with different diameter holes are shown in the supplementary data. Clearly, in the absence of holes or at the incidence angle of 0°, the reflected beam is projected directly onto the detector after passing through the dichroic mirror, and particles scattering signal would be totally flooded. The smaller the hole diameter and the higher the incidence angle, the less reflected incident light is projected onto the detector. Nevertheless, with the reduction of the hole diameter, the more scattering signal would also be rejected by the hole, and even the spatial resolution started to decrease when the hole diameter was reduced down to 2 mm (see Fig. S-2 in the supplementary data). In our experimental system, depending on the objective with a numerical aperture (NA) of 1.45, the incidence angle can be adjusted over a range of 0–73°, and a hole with diameter from 2.5 to 4 mm is suitable to perform the scattering imaging by adjusting the incidence angle. With a 3-mm hole, the reflected laser beam would be mostly rejected at the incidence angle of ∼59°. It is importantly noted that at the cost of the smaller field of view, the appropriate reduction of the field diaphragm opening diameter also helps to separate more effectively particle scattering light from the reflected beam, and moreover, the scattering signal can be detected at the lower incidence angle. For example, as shown in Fig. 2c, the particle scattering signal was almost flooded due to the strong disturbance of reflected beam at the incidence angle of 41.3° under the system with a 3-mm hole. When reducing the field diaphragm opening diameter, the particle signal was
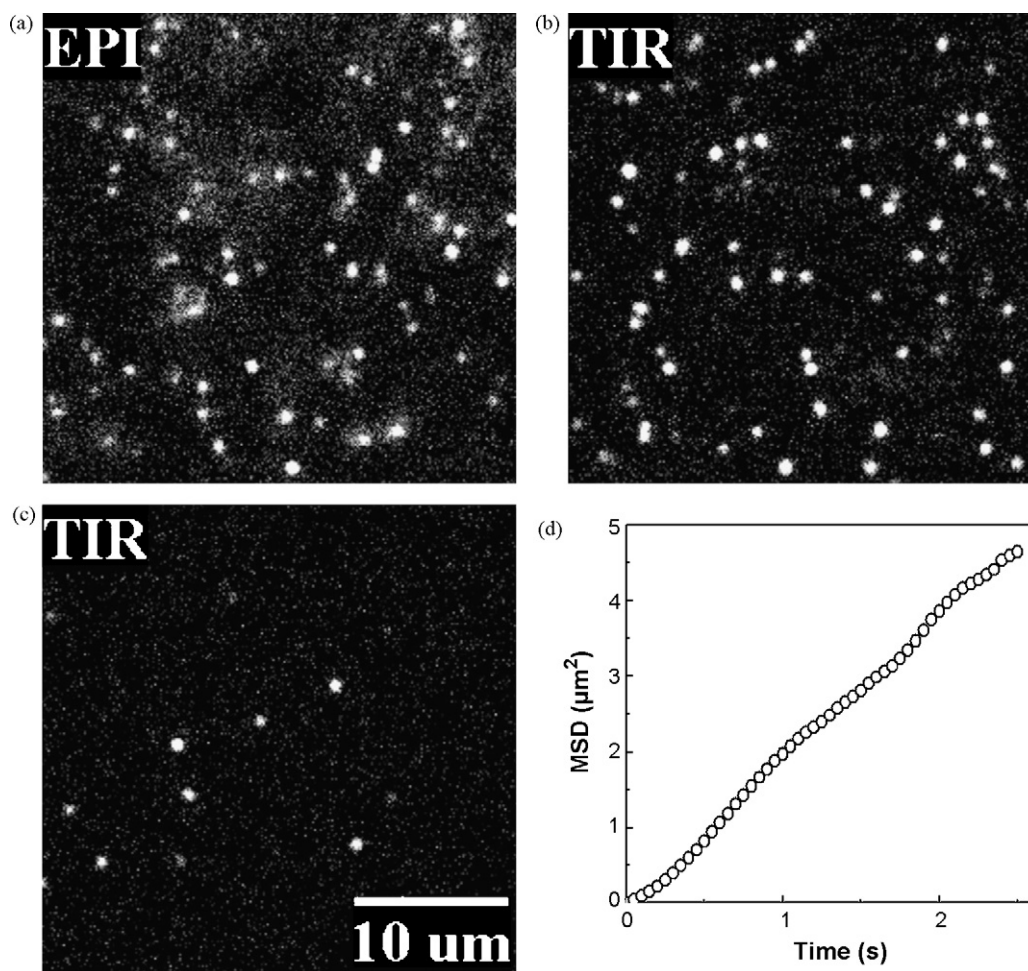
Fig. 3. Scattering images of GNPs in 50% (v/v) glycerin with a 3-mm hole. (a) Epi-illumination at the incidence angle of ∼61°, where the critical angle is 67°; (b) TIR illumination at the incidence angle of ∼68°; (c) TIR illumination at the incidence angle of ∼71°. Note that smaller amount of GNPs were observed in (c) due to the thinner excitation depth at large incidence angle and Brownian motion of particles (see Supplementary data Video S-1); (d) typical MSD–Δt plots from each trajectory for GNPs in 50% glycerin solution. Exposure time: 50 ms.

observed immediately (Fig. 2d). Therefore, experimentally, we can obtain high signal-to-noise ratio scattering images by optimizing hole diameter, incidence angle and field diaphragm opening diameter. In subsequent experiments, if not mentioned, the 3-mm hole and 40-nm gold nanoparticles will always be employed.

3.2. Evanescent wave scattering tracking of single gold nanoparticles in solution

To perform evanescent wave scattering imaging of GNPs, the incidence angle must be adjusted above the critical angles where total internal reflection only occur. For the glass–air and glass–water interface, the critical angles are 41.3° and 61.3°, respectively. As mentioned above, the lower limit of the incidence angle is ~59° for obtaining particle scattering images over the entire CCD field of view with a 3-mm hole. Thus, the hole-based total internal reflection system is quite suitable for evanescent wave scattering detection in solution due to the larger critical angle, and moreover, can be used to detect gold particles in solution under epi-illumination at the incidence angle over a range of 59–61.3°. Surprisingly, particle scattering images in solution under epi-illumination would have higher signal-to-noise ratios than ones in air over this incidence angle range where total internal reflection has occurred because total internal reflected beam causes greater disturbance than the reflected beam below the critical angle. Fig. 3 shows the scattering images of single GNPs in 50% (v/v) glycerin under epi- and TIR-illumination, respectively. The videos are shown in the supplementary data (Video S-1). As can be seen, the penetration depth of evanescent field is well controlled by changing the incidence angle. Furthermore, base on the strong res-

onance scattering, gold nanoparticles can be sensitively detected by our system. Generally, only 5 ms (or even less) exposure time is required for 40-nm gold particles. Thus, single gold particle tracking in solution is easily performed. For 15 μm $\times$ 15 μm images, the frame rate is up to 100 frames per second, which depends on the readout rate of CCD camera. As a key advantage over laser scanning, we can track simultaneously all GNPs in the field of view, and record their corresponding trajectories by computationally extracting particle positions in the stream images as presented in Fig. 1c. Here, we only tracked GNPs near the interface that was considered to undergo two-dimensional Brownian diffusion motion. Fig. 3d shows the mean square displacement (MSD)–time plot from each trajectory for GNPs in 50% glycerin solution shown in Fig. 1c. The corresponding diffusion coefficient value can be obtained by fitting the linear curve following the procedure described preciously [29]. For 40-nm gold particles in 50% and 25% glycerin solution, the diffusion coefficients are $(5.73 \pm 2.71) \times 10^{-9}$ cm^2 s^{-1} ($n = 20$) and $(5.18 \pm 3.31) \times 10^{-8}$ cm^2 s^{-1} ($n = 20$), respectively.

3.3. Single gold particle tracking on live cell membrane

A particularly promising application of our imaging method is in single gold particle tracking on live cell membrane, a unique advantage for evanescent wave microscopy. Fig. 4b shows the evanescent wave scattering image of live cell by our hole-based total internal reflection system. Because of the limited excitation depth of TIR, the cell scattered very weak light, and only the structures in the immediate proximity of the basal membrane were observed. Also, this thin optical section reduces greatly photodamage to living cells. When anti-EGFR/GNPs were added to live HeLa cells on the cover-
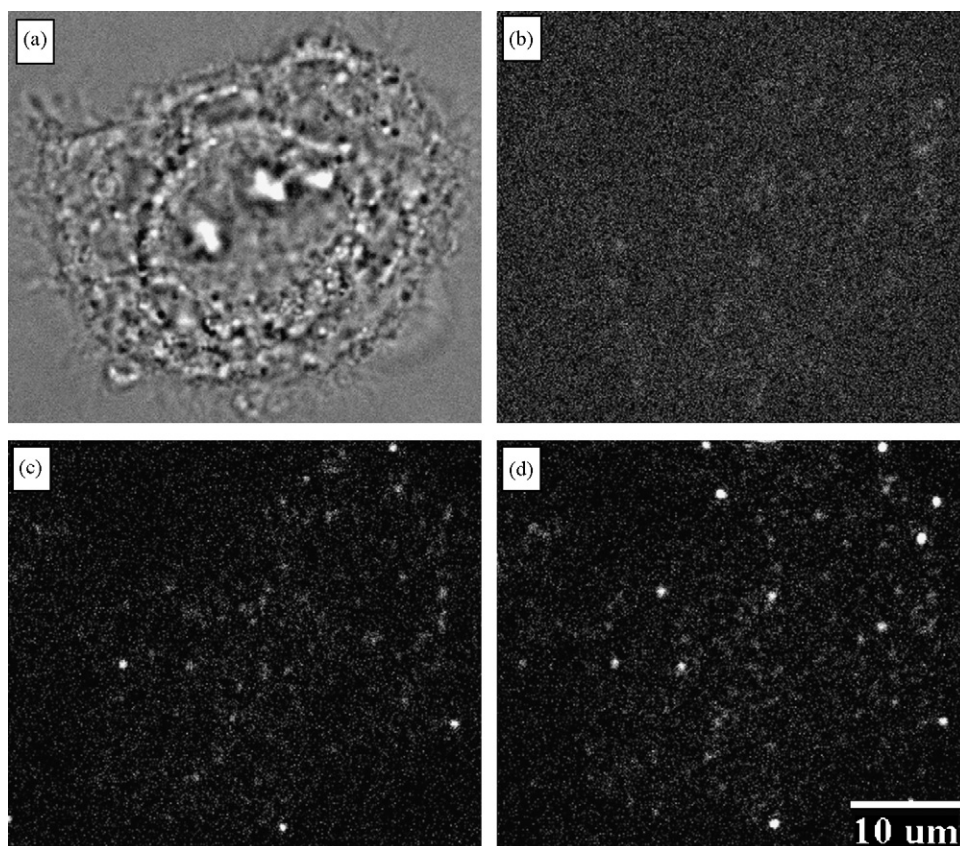
Fig. 4. (a) Typical bright field microscope image of HeLa cell; (b) evanescent wave scattering images on the basal plasma membrane of the cell shown in (a); (c) and (d): evanescent wave scattering images on the basal plasma membrane of the cell after 1 and 25 min for addition of anti-EGFR/GNPs, respectively. Laser incidence angle: ~72°. Exposure time: 50 ms.
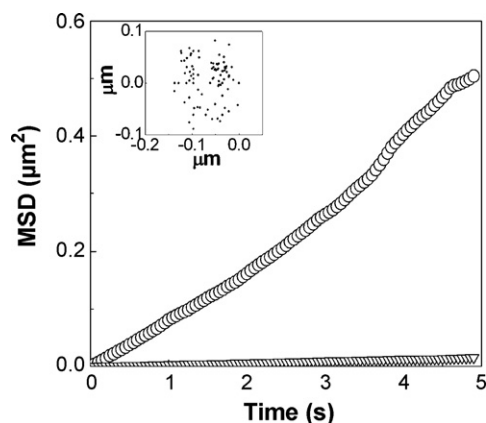
Fig. 5. Typical MSD–Δt plots from the trajectories for the diffusing GNPs ($\bigcirc$), and the stationary GNPs ($\triangledown$) on the basal plasma membrane. Inset: the corresponding trajectory of single diffusing GNPs on the basal plasma membrane.

slip on the microscope stage, they first underwent rapid Brownian motion in solution, and then some of them bound immediately to the cell periphery as shown in Fig. 4c. After 5 min, GNPs in solution started to drift into some narrow space between the bottom surface of the cell and the coverslip (Video S-2a). Fig. 4d shows the evanescent wave scattering image of cells after 25 min of addition of anti-EGFR/GNPs. In experiments, once bound to the basal membrane of cell, GNPs were either stationary or exhibited a random diffusion behavior, and then some of them struggled to leave the cell surface (Video S-2b). We performed a continuous tracking of these regions on the cell surface, and observed that some positions were visited and "kissed" more than once by gold nanoparticles (shown in Fig. S-3), suggesting that these were likely specific receptor sites, because HeLa cancer cells are derived from a human epithelial carcinoma, and it has been reported that they exhibit significantly elevated EGFR expression [39,40]. Fig. 5 shows MSD–Δt plots of single gold nanoparticles on the cell surface. The diffusion coefficient is $(13.7 \pm 14.6) \times 10^{-11}$ cm^2 s^{-1} ($n = 20$). For the stationary particles, they also show a diffusion-like motion but with a much smaller diffusion coefficient of $(7.64 \pm 3.12) \times 10^{-12}$ cm^2 s^{-1} ($n = 20$). These are in agreement with the previous results in the literatures [29].

4. Conclusions

In conclusion, we propose a novel evanescent wave scattering imaging method using a hole-based objective-type total internal reflection system to rapidly image and track single gold nanoparticles in solution and on cell membrane; we discussed the detailed experimental realization of the imaging system. The experimental results demonstrate that the hole-based total internal reflection system is quite suitable for evanescent wave scattering detection in solution, especially for single gold particle tracking on live cell membrane. Compared to fluorescent dyes or quantum dots, gold nanoparticles have no photobleaching and no blinking, and the evanescent wave scattering imaging methods based on gold nanoparticles will become a very useful tool to study membrane dynamics in living cells. Furthermore, our imaging method can be simply realized using the commercial objective-type total internal reflection fluorescence microscopy by only replacing the emission filters with a suitable small hole. The objective-based configuration

provides a free space above the coverslip, and allows imaging and concomitant manipulation of live cells in culture by microinjection, patch-clamping, AFM and other techniques.

Appendix A. Supplementary data

Supplementary data associated with this article can be found, in the online version, at doi:10.1016/j.talanta.2008.05.059.

References

[1] D. Axelrod, E.H. Hellen, R.M. Fulbright, in: J.R. Lakowicz (Ed.), Topics in Fluorescence Spectroscopy, Biochemical Applications, vol. 3, Plenum Press, 1992.
[2] S. Inoue, Video Microscopy, Plenum Press, New York, 1986.
[3] J.B. Pawley, Handbook of Biological Confocal Microscopy, 2nd ed., Plenum Press, New York, 1995.
[4] J.S. Park, C.K. Choi, K.D. Kihm, Exp. Fluids 37 (2004) 105.
[5] E.H.K. Stelzer, S. Lindek, Opt. Commun. 111 (1994) 536.
[6] W. Denk, J.H. Strickler, W.W. Webb, Science 248 (1990) 73.
[7] W.E. Moerner, M. Orrit, Science 283 (1999) 1670.
[8] X. Li, H. Ma, L. Nie, M. Sun, S. Xiong, Anal. Chim. Acta 515 (2004) 255.
[9] Z. Bao, S. Wang, W. Shi, S. Dong, H. Ma, J. Proteome Res. 6 (2007) 3835.
[10] M. Bruchez, M. Moronne, P. Gin, S. Weiss, A.P. Alivisatos, Science 281 (1998) 2013.
[11] R. Cui, H.C. Pan, J.J. Zhu, H.Y. Chen, Anal. Chem. 79 (2007) 8494.
[12] B. Dubertret, P. Skourides, D.J. Norris, V. Noireaux, A.H. Brivanlou, A. Libchaber, Science 298 (2002) 1759.
[13] M. Dahan, S. Levi, C. Luccardini, P. Rostaing, B. Riveau, A. Triller, Science 302 (2003) 442.
[14] X. Michalet, F.F. Pinaud, L.A. Bentolila, J.M. Tsay, S. Doose, J.J. Li, G. Sundaresan, A.M. Wu, S.S. Gambhir, S. Weiss, Science 307 (2005) 538.
[15] M. Nirmal, B.O. Dabbousi, M.G. Bawendi, J.J. Macklin, J.K. Trautman, T.D. Harris, L.E. Brus, Nature (London) 383 (1996) 802.
[16] A.M. Derfus, W.C.W. Chan, S.N. Bhatia, Nano Lett. 4 (2004) 11.
[17] C. Kirchner, T. Liedl, S. Kudera, T. Pellegrino, A.M. Javier, H.E. Gaub, S. Stolzle, N. Fertig, W.J. Parak, Nano Lett. 5 (2005) 331.
[18] J. Yguerabide, E.E. Yguerabide, Anal. Biochem. 262 (1998) 137.
[19] J. Yguerabide, E.E. Yguerabide, J. Cell. Biochem. (2001) 71.
[20] J.J. Storhoff, R. Elghanian, R.C. Mucic, C.A. Mirkin, R.L. Letsinger, J. Am. Chem. Soc. 120 (1998) 1959.
[21] T.A. Taton, C.A. Mirkin, R.L. Letsinger, Science 289 (2000) 1757.
[22] W. Yan, X. Feng, X. Chen, W. Hou, J.J. Zhu, Biosens. Bioelectron. 23 (2008) 925.
[23] H. Yao, C. Yi, C.H. Tzang, J. Zhu, M. Yang, Nanotechnology 18 (2007) 015102.
[24] Y.C. Cao, R.C. Jin, S. Thaxton, C.A. Mirkin, Talanta 67 (2005) 449.
[25] Z.L. Jiang, W.X. Huang, A.H. Liang, B. Chen, Talanta 73 (2007) 926.
[26] M. Hou, S.J. Sun, Z.L. Jiang, Talanta 72 (2007) 463.
[27] X. Xu, M.S. Han, C.A. Mirkin, Angew. Chem. Int. Ed. 46 (2007) 3468.
[28] M.P. Sheetz, S. Turney, H. Qian, E.L. Elson, Nature 340 (1989) 284.
[29] A. Kusumi, Y. Sako, M. Yamamoto, Biophys. J. 65 (1993) 2021.
[30] K. Ritchie, X.Y. Shan, J. Kondo, K. Iwasawa, T. Fujiwara, A. Kusumi, Biophys. J. 88 (2005) 2266.
[31] A. Kusumi, Y. Sako, Curr. Opin. Cell Biol. 8 (1996) 566.
[32] A.J. Borgdorff, D. Choquet, Nature 417 (2002) 649.
[33] C. Sonnichsen, A.P. Alivisatos, Nano Lett. 5 (2005) 301.
[34] V. Jacobsen, P. Stoller, C. Brunner, V. Vogel, V. Sandoghdar, Opt. Exp. 14 (2006) 405.
[35] D. Lasne, G.A. Blab, S. Berciaud, M. Heine, L. Groc, D. Choquet, L. Cognet, B. Lounis, Biophys. J. 91 (2006) 4598.
[36] C. Sonnichsen, S. Geier, N.E. Hecker, G. von Plessen, J. Feldmann, H. Ditlbacher, B. Lamprecht, J.R. Krenn, F.R. Aussenegg, V.Z.H. Chan, J.P. Spatz, M. Moller, Appl. Phys. Lett. 77 (2000) 2949.
[37] H. Ewers, A.E. Smith, I.F. Sbalzarini, H. Lilie, P. Koumoutsakos, A. Helenius, Proc. Natl. Acad. Sci. U.S.A. 102 (2005) 15110.
[38] M. Goulian, S.M. Simon, Biophys. J. 79 (2000) 2188.
[39] G.Y. Hu, W.B. Liu, J. Mendelsohn, L.M. Ellis, R. Radinsky, M. Andreeff, A.B. Deisseroth, J. Natl. Cancer Inst. 89 (1997) 1271.
[40] A. Hemminki, I. Dmitriev, B. Liu, R.A. Desmond, R. Alemany, D.T. Curiel, Cancer Res. 61 (2001) 6377.

Reversed-phase high performance liquid chromatography (RP-HPLC) characteristics of some 9,10-anthraquinone derivatives using binary acetonitrile–water mixtures as mobile phase

B. Hemmateenejad[a], M. Shamsipur[b], A. Safavi[a,*], H. Sharghi[a], A.A. Amiri[a]

[a] Department of Chemistry, Shiraz University, Shiraz, Iran
[b] Department of Chemistry, Razi University, Kermanshah, Iran

ABSTRACT

The retention behavior of 28 synthesized 9,10-anthraquinone derivatives in a reversed-phase (RP) high performance liquid chromatography (HPLC) system has been studied on a C18-RP column using acetonitrile–water mixtures as mobile phase. The influences of the composition of mobile phase and the solute structure on the retention times of 9,10-anthraquinone derivatives were investigated by linear solvation free energy relationship (LSFER) and quantitative structure-retention relationship (QSRR) analyses. Among different solvatochromic parameters of solvent systems, their polarity/polarizability parameter (π^*) was identified as the controlling factor affecting retention behavior of these compounds. A four-parametric QSRR model was obtained between solute structures and retention indices. Finally, a unified model containing both the molecular structure parameters and mobile phase properties was developed to describe the chromatographic behavior of the systems studied. The resulted QSRR models could explain and predict higher than 90% of variances in the retention indices. Among the solvent properties, polarity/polarizability parameter (π^*), and among the solute properties, HATS5v (leverage-weighted autocorrelation of lag 5/weighted by atomic van der Waals volumes, GETAWAY descriptors), Mor14p (3D-MoRSE-signal 14/weighted by atomic polarizabilities, 3D-MoRSE descriptors), GATS5p (Geary autocorrelation-lag 5/weighted by atomic polarizabilities, 2D autocorrelations) and R6u+(R maximal autocorrelation of lag 6/unweighted, GETAWAY descriptors) were identified as controlling factors in the RP-HPLC behavior of 9,10-anthraquinone derivatives in actonitrile–water binary solvents.

© 2008 Elsevier B.V. All rights reserved.

1. Introduction

9,10-Anthraquinone derivatives, as the largest group of naturally occurring quinines, have been widely used in chemistry, biochemistry, medicine and industry [1–3]. They are best known for their antioxidant activity [4], anti-tumor promotion, Epstein–Barr virus activation [5], and anti-human cytomegalovirus activity [6]. In addition, 9,10-anthraquinone (9,10-AQ) is the parent compound for a large palette of anthraquinone which are widely used in the textile dye industries [7,8]. Recently, high performance liquid chromatographic (HPLC) methods were used as analytical tools for determination of quinones using UV [9,10], fluorescence [11], electrochemical [12], and chemiluminescence (CL) detection systems [13,14].

However, the HPLC separations are still being developed in a nonsystematic manner, often by trial-and-error, which involves several disadvantages. The most distinct disadvantage is the long development time required to select experimental conditions which are not necessarily the optimum conditions. In order to overcome this problem, investigation and developments of mathematical models that are able to predict chromatographic retention data from chemical structures' data have received an increasing interest [15,16]. The quantitative structure-property relationships (QSPR) or quantitative structure-retention relationships (QSRR) help chemists to find the type of solute–solvent interactions in chromatography and also to predict the retention behavior of new or even unsynthesized molecules [17]. Nowadays QSPR/QSRR studies are in rapid progress and have been widely used by chemists for the prediction of different chemical and physical properties of different types of molecules [18,19]. Enormous numbers of publications are concerned with modeling QSRR in chromatography [20–23].

In recent years, we have been involved in the synthesis of some new derivatives of 9,10-anthraquinone and 9-anthrone [24], and have conducted widespread studies on their properties and applications, including pK_a determination [25,26], solubility deter-

mination in supercritical CO_2 [27,28], electrochemical behavior [29–32], spectrofluorometric studies [33,34] and their use as selective ion carriers in solid phase extraction [35,36], bulk liquid membrane transport [37] and in preparation of ion selective electrodes [38-40]. We have also employed QSPR and target factor analyses to find the effects of different structural properties of 1-hydroxy-9,10-anthraquinones on their acidity behavior [41,42] and electrochemical properties [43].

In this work, an experimental study was conducted in order to investigate those solvent properties and solute structure parameters affecting the retention behavior of 28 newly synthesized 9,10-anthraquinone derivatives. In order to predict solute retention from solvent composition, it will be very important to know the effects of mobile phase compositions of binary solvents on the chromatographic behavior. This has been extensively studied by the Kamlet–Taft solvatochromic comparison method [44,45]. Finally, the effect of the structural properties of the molecules on their retention times was investigated by the QSRR analysis. Multiple linear regression was used to find the quantitative relationships between the calculated descriptors and the retention behavior.

2. Experimental

2.1. Chemicals

HPLC grade acetonitrile (Merck) and deionized water were used as mobile phase. The anthraquinone derivatives used in this work (see Table 1) were synthesized in our research group [24] and used after recrystallization from reagent grade benzene (Merck) and vacuum drying. Potassium bromide (Merck) was used for establishing the dead time.

2.2. Apparatus

The chromatographic equipment consisted of two PU-2080 plus delivery pumps (Jasco, Japan), an injector valve Rheodyne 7725i (USA) with 20-μL sample loop and a variable-wavelength absorbance detector UV-2070 plus (Jasco, Japan) operating at 275 nm. The chromatographic system was controlled by HSS-2000 provided by Jasco using the LC-Net II/ADC interface. The data were processed using BORWIN software (version 1.50). Analysis was carried out at room temperature on a Finepak SIL C18, 100 Å pore size, 10 μm particle size, 250 mm × 4.6 mm I.D. column. The mobile phase was prepared using different percentages of acetonitrile in water. The flow-rate of the mobile phase was 1.0 mL min^{-1}.

2.3. Procedures

2.3.1. Determination of HPLC retention times

A 10 mg portion of each substance was dissolved in 10 mL of acetonitrile to obtain 1000 mg L^{-1} stock solutions. Working standards were prepared by appropriate dilution of the stock solutions with acetonitrile to yield a concentration of 100 mg L^{-1} for all anthraquinone derivatives. A 20 μL portion of these working standards was injected to HPLC system with a 20 μL loop at ambient temperature. A flow-rate of 1.0 mL min^{-1} and a detector wavelength of 275 nm were selected for all the experiments. The composition of acetonitrile–water mixed solvents as mobile phase was varied between 0.2 and 0.9 mole fraction of acetonitrile, with 0.1 mole fraction intervals. Therefore, for each 9,10-anthraquinone derivative, the chromatograms were reordered in 8 different mobile phase compositions and the resultant retention times of each compound were collected in a row vector.

The dead time, t_0, was established for each mobile phase by injection of 20 μL of a 0.01% potassium bromide solution in water

Table 1
Structural features of the AQ derivatives used in this study
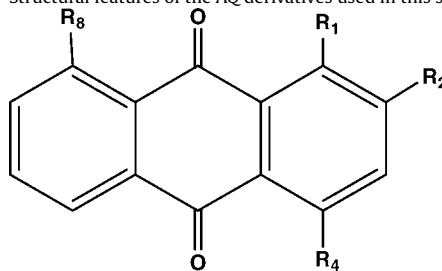
ID	R_1	R_2	R_4	R_8
AQ_1	H	H	H	H
AQ_2	H	CH_3	H	H
AQ_3	H	C_2H_5	H	H
AQ_4	OH	H	H	H
AQ_5	OH	CH_3	H	H
AQ_6	OH	CH_2I	H	H
AQ_7	OH	CH_2OCH_3	H	H
AQ_8	OH	$CH_2OC_2H_5$	H	H
AQ_9	OH	$CH_2OC_3H_7$	H	H
AQ_{10}	OH	$CH_2OC_4H_9$	H	H
AQ_{11}	OH	$CH_2OCH_2CH(CH_3)_2$	H	H
AQ_{12}	OH	CH_2OCOCH_3	H	H
AQ_{13}	OH	CH_2CHCH_2	H	OH
AQ_{14}	OH	H	H	OCH_2CHCH_2
AQ_{15}	OCH_2CHCH_2	H	H	OCH_2CHCH_2
AQ_{16}	OCH_2CHCH_2	H	H	H
AQ_{17}	OCH_2CHCH_2	H	OCH_2CHCH_2	H
AQ_{18}	OH	H	OH	H
AQ_{19}	OCH_3	CH_2Br	H	H
AQ_{20}	OCH_3	CH_2OCH_3	H	H
AQ_{21}	I	H	H	H
AQ_{22}	I	CH_3	H	H
AQ_{23}	I	C_2H_5	H	H
AQ_{24}	N_3	CH_3	H	H
AQ_{25}	N_3	C_2H_5	H	H
AQ_{26}	NO_2	CH_3	H	H
AQ_{27}	NO_2	C_2H_5	H	H
AQ_{28}	NH_2	C_2H_5	H	H

and monitoring at 200 nm [46]; for all mobile phases, the t_0 values were similar with an average of 2.5 min. The retention factors (k) for all selected compounds, at each mobile phase assayed, were determined using the expression $k = (t_R - t_0)/t_0$, where t_0 is the dead time and t_R is the retention time of each compound, obtained from the peak maximum. Then, the logarithm of retention factors ($\log k$) of all compounds were collected in a ($m \times n$) data matrix (**Y**), where m and n are the number of 9,10-anthraquinone derivatives (i.e., $m = 28$) and number of mobile phase acetonitrile–water binary mixtures (i.e., $n = 8$), respectively.

2.3.2. Modeling of solvent effect

The effect of solvent composition on the retention time was investigated for each 9,10-anthraquinone derivative, separately. In the case of each molecule, a multi linear model based on the general equation of Kamlet et al. [47] $\mathbf{yi} = \mathbf{y_0} + a\boldsymbol{\alpha} + b\,\boldsymbol{\beta} + s\boldsymbol{\pi}^*$ was constructed, where **yi** is vector of retention factor (i.e., $\log k$) for the ith solute measured in 8 solvent compositions and $\boldsymbol{\alpha}$, $\boldsymbol{\beta}$ and $\boldsymbol{\pi}^*$ are the vectors of solvatochromic parameters of the mixed solvents describing hydrogen-bonding acidity, hydrogen-bonding basicity and polarity/polarizability properties of solvent (Table 2), respectively. The parameters a, b and s are regression coefficients and $\mathbf{y_0}$ is the hypothetical value of retention time in a solvent with zero solvotochromic parameters. The solvatochromic parameters for acetonitrile–water binary mixed solvents were refined as reported elsewhere [48,49]. A linear interpolation was used to estimate solvatochromic parameters for all the solvent composi-

Table 2
Solvatochromic parameters for binary acetonitrile–water mixed solvents used in this study [48,49]

X_{AN}	α	β	π^*
0.20	0.89	0.39	0.98
0.30	0.87	0.41	0.93
0.40	0.87	0.40	0.87
0.50	0.86	0.41	0.85
0.60	0.84	0.42	0.84
0.70	0.81	0.43	0.81
0.80	0.70	0.42	0.79
0.90	0.49	0.33	0.77

tions used (Table 2). The LSFER models were developed for each molecule using a subset of solvatochromic parameters selected by a stepwise selection procedure, which uses a combination of both forward selection and backward elimination of variables. The degree of model fit was measured by conventional statistical parameters including square of multiple determination (R^2), standard error of regression (S.E.), Fisher's variance ratio (F) and its corresponding probability (P-value).

2.4. Modeling the effect of solute structure (QSRR analysis)

Prior to the calculation of the molecular descriptors, the chemical structures of molecules were drawn by the HyperChem release software (version 7.0). Then the Z-matrices of the structures were provided by the software and transferred to the Gaussian 98W program (version 5.2). The 3D geometry optimization was performed using HF/STO-3G quantum chemical calculation. The main step in every QSRR study is choosing and calculating the structural descriptors as numerical encoded parameters representing the chemical structures. In the present work, the molecular descriptors were generated using the Dragon software (version 2.1). This software has been frequently used for calculating chemical descriptors in many QSAR/QSRR studies [50,51]. A total of 1481 descriptors were calculated for each molecule using this software. A working subset of 579 descriptors was selected from the 1481 generated descriptors following the routine procedure: (1) constant descriptors were eliminated, (2) descriptors which were almost constant were eliminated and (3) for all pairs of remaining descriptors with a correlation coefficient greater than 0.95, only one of them was considered in developing the model. The 579 descriptors thus selected were considered for further investigations after discarding the descriptors with constant and inter-correlated ones.

In the case of each mixed solvent as mobile phase, a separate QSRR was developed to make a connection between solute's structure and retention time in a specified mobile phase composition. Multi linear equations in the form of $\mathbf{y} = b_0 + b_1\mathbf{x_1} + b_2\mathbf{x_2} + b_3\mathbf{x_3} + \ldots$ were built to find the quantitative relationships between molecular descriptors, as independent variables, and retention factors, as dependent variables. Here, $\mathbf{y}$ refers to the retention factor at a specified solvent composition, $\mathbf{x_1}$ through $\mathbf{x_n}$ denote the molecular descriptors and b_0 through b_n are the model coefficients. The multiple linear regressions with stepwise selection of variables of SPSS software were used to find the most convenient subset of descriptors for each solvent composition. The SPSS software produces some models and sorts them based on calibration statistics. It should be noted that, in some cases, SPSS proposes some over-fitted models. To overcome this problem, the accuracy and acceptability of the generated model were evaluated by leave-one-out cross-validation method, and the one represented a better cross-validation statistic (Q^2) with lower number of input variables was selected. The number of data points used for QSRR modeling

in each mobile phase composition was 20, which is equal to the number of 9,10-anthraqinone derivatives used for calibration in this study. Eight molecules i.e. AQ_2, AQ_3, AQ_4, AQ_7, AQ_8, AQ_9, AQ_{15} and AQ_{18} were selected as the test set.

3. Results and discussion

The molecular structures of the 9,10-anthraquinone derivatives used in this study are represented in Table 1. Obviously, the solutes have different substituents on the 1, 2, 4 and 8 positions of the anthraquinone backbone, where the high variations in the substitution patterns are observed at positions 1 and 2. We used these molecules to find the effect of the structural variations on the retention behavior of the 9,10-anthraquinones. Because of significant differences between the hydrogen-bonding, electronic and lipophilic properties of the substituents, it is not surprising to find a large dependency of the retention times of the molecules on the mobile phase properties. The concomitant effect of acetonitrile concentration and structure of substitution on the tested compounds were studied for all the solutes. Since a large number of these compounds have one or two –OH groups as substituent, the use of standard silica-based reversed-phase columns is not suggested because the analytes interact very strongly with the stationary phase support and result in peak broadening.

In this study a Finepak SIL C18 endcapped stationary phase with a very low metal content was used. The peak asymmetry for all of the compounds were evaluated using the expression $A_s = W_{5\%}/2 \times W_{1/2}$, where $W_{5\%}$ and $W_{1/2}$ are the peak widths at 5% and 50% of the peak height, respectively. Using this stationary phase, almost all peaks were symmetrical ($A_s = 1.1$–1.3). Some typical chromatograms recorded using a mobile phase $X_{AN} = 0.4$ are shown in Fig. 1. As can be seen from Table 1 and Fig. 1, with the exception of AQ_1 and AQ_4, in all cases, the retention times are increased with increasing the number of C atoms in the substituent groups. A comparison between the chemical structures of molecules shown in Table 1 revealed that AQ_1 does not have any substituent whereas AQ_4 has a hydroxy group on position 1. Thus, due to the possible hydrogen-bonding between the hydroxyl group of AQ_4 and mobile phase, AQ_4 is expected to elute faster than AQ_1. However, an inspection of Fig. 1 shows an opposite behavior, AQ_1 shows lower retention time with respect to AQ_4. This behavior can be attributed to the well-known intramolecular hydrogen-bonding between OH and adjacent C=O of the anthraquinone derivative, which in turn weakens the hydrogen-bonding between OH of AQ_4 and water molecules in the mobile phase.

The recorded chromatograms of molecules AQ_8 and AQ_{15} in different mole fractions of acetonitrile are shown in Fig. 2, and the variation of logarithm of retention factor as a function of acetonitrile mole fraction for all of 9,10-anthraquinone derivatives are plotted in Fig. 3. Both figures show that the retention of solutes in the stationary phase is significantly decreased by increasing the amount of acetonitrile in the binary mixed solvent. In addition, as can be seen from Fig. 2, by changing the mobile phase composition, retention times of compounds AQ_8 and AQ_{15} are varied in different manner, depending on their chemical structures.

The retention times data matrix for all the studied 9,10-anthraqinone derivatives in different mobile phase compositions are represented in Table 3. These data were used to derive the quantitative relationships between retention time and solvent composition, in one hand, and retention time and solute structure, in the other. Preliminary studies showed that logarithmic transformation of retention factor ($\log k$) resulted in more straightforward models, which is in agreement with LSFER concept. Thus, in all derived models, $\log k$ was used as a dependent variable.
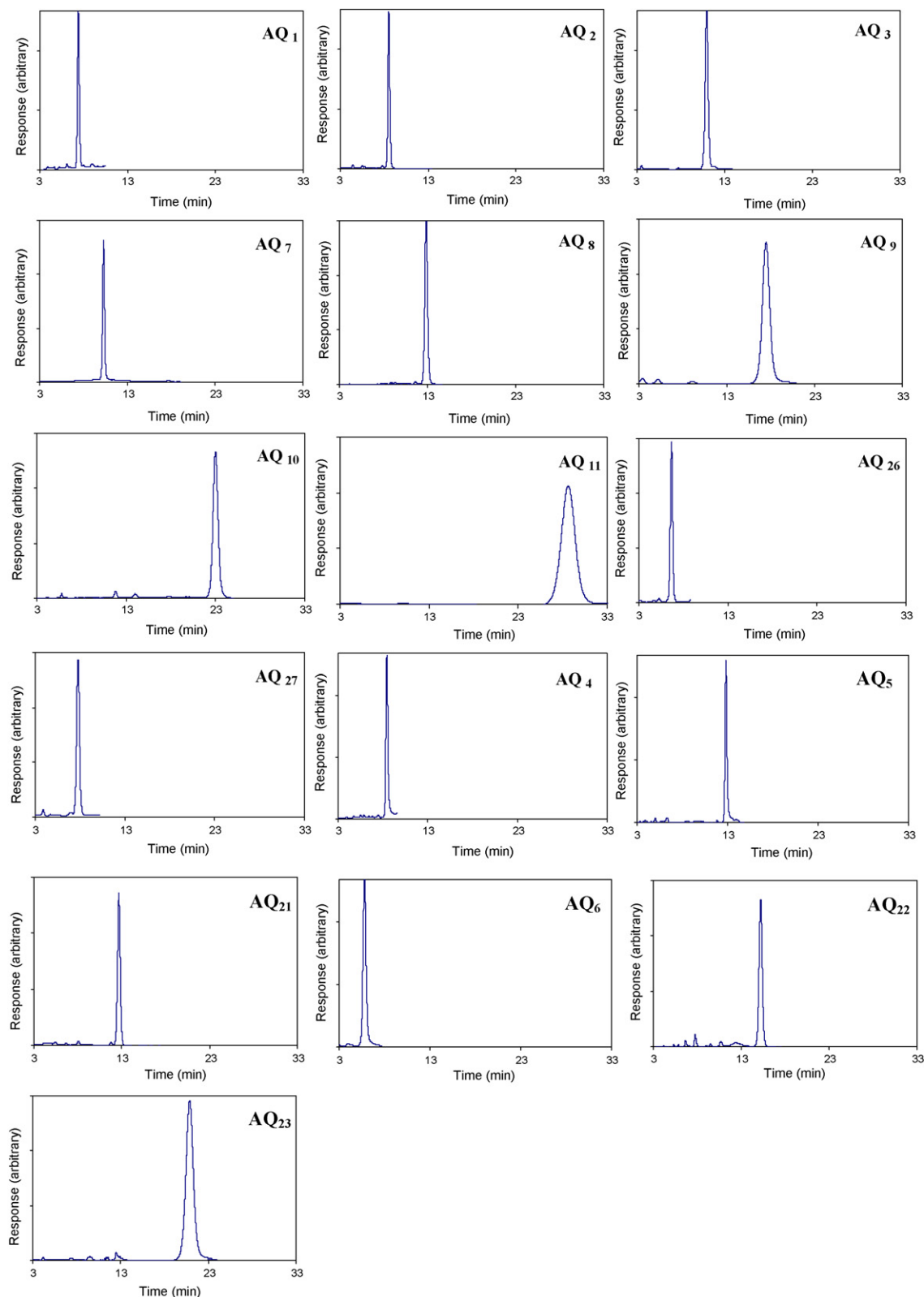
Fig. 1. Chromatograms of some 9,10-anthraquinone derivatives in mole fraction of 0.4 of acetonitrile.

3.1. LSFER models accounting the effect of mobile phase composition

Table 4 lists the LSFER equations obtained for each solute using solvatochromic parameters of solvents as independent (or pre-dictor) variables. For each substance, the significant independent variables were selected by applying a stepwise procedure to build up the model. As it is obvious from Table 4, for all solutes, the reduced Kamlet–Taft equations contain the polarity/polarizability parameter (π^*) as solvent parameter. Thus, the following equa-
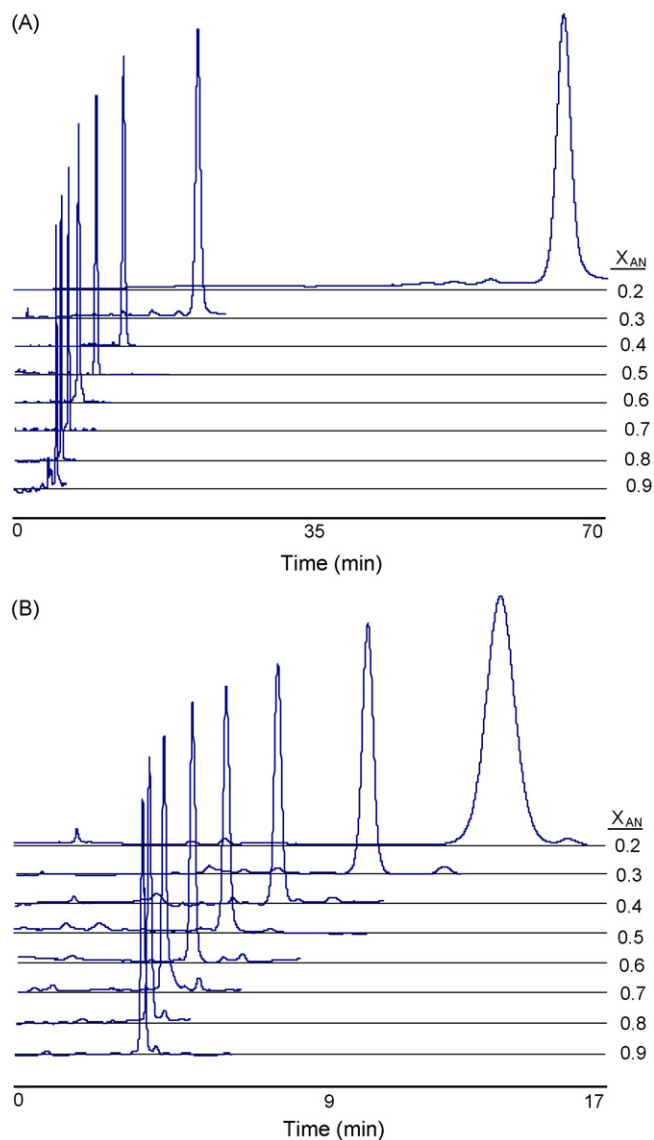
Fig. 2. The chromatograms of AQ_8 (A) and AQ_{15} (B) compounds in different mole fractions of acetonitrile.

tion was established between the logarithm of retention factors of anthraquinone derivatives and the solvatochromic parameters of acetonitrile–water binary solvents, as mobile phase.

$$\log k = \text{Const.} + s\pi^* \tag{1}$$

Eq. (1) suggests that the polarity/polarizability interactions are the main factors controlling the interaction of 9,10-anthraquinone derivatives with acetonitrile–water mixed solvents. The quality of each model was estimated by its coefficient of multiple determination (R^2), standard error of regression (S.E.) and variance ratio (F-value). As it is obvious from Table 4, all regression equations represented high statistical quality. The coefficient of multiple determinations for almost all models is higher than 0.95, indicating that 95% of variances in the retention data of each solute can be explained by polarity/polarizability interaction. In addition, the F-values are much higher than the critical value, which confirm the statistical significance of the resulting models. Moreover, the significance of selected parameters is confirmed by the high ratio of coefficients to their respective standard errors.
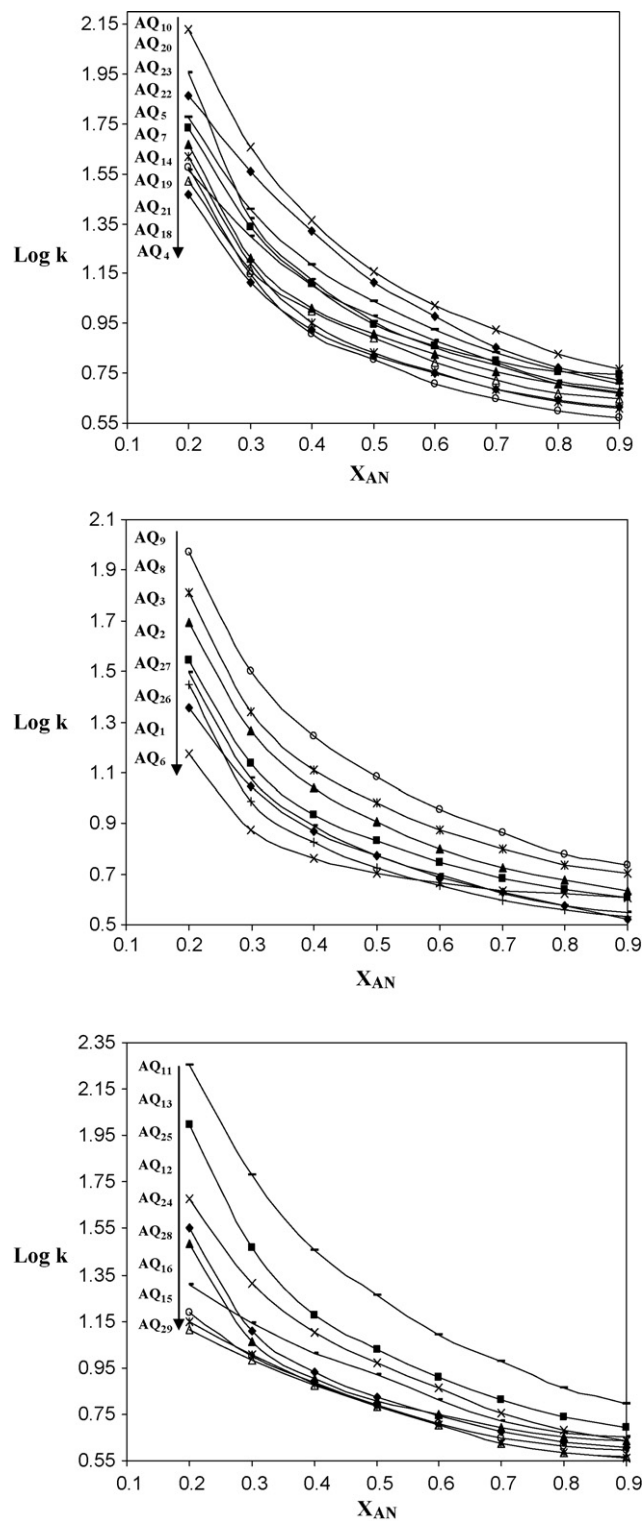
Fig. 3. Relationship between $\log k$ values and the acetonitrile concentration in the mobile phase for 28 of 9,10-anthraquinone derivatives.

The absence of β and α parameters of binary solvents in the resulted LSFER equations implies that the retardation of 9,10-anthraquinone derivatives does not obey the acid–base interactions. In fact, by changing the strength of hydrogen bond accepting ability or hydrogen bond donating ability of solvent as mobile phase, the retention times of these compounds should be almost constant.

Table 3
Retention time of the AQ derivatives obtained by HPLC equipment

ID	Mole fraction of acetonitrile in water							
	0.2	0.3	0.4	0.5	0.6	0.7	0.8	0.9
AQ_1	22.658	11.092	7.395	5.907	4.842	4.233	3.775	3.333
AQ_2	34.925	13.683	8.533	6.792	5.608	4.835	4.34	4.058
AQ_3	49.325	18.342	10.95	8.063	6.325	5.333	4.733	4.3
AQ_4	29.425	13.025	8.426	6.624	5.6	4.833	4.375	4.133
AQ_5	54.208	21.775	12.817	8.867	7.208	6.283	5.683	5.567
AQ_6	14.958	7.492	5.792	5.033	4.617	4.283	4.2	4.058
AQ_7	46.817	16.392	10.3	8.083	6.708	5.683	5.067	4.725
AQ_8	64.958	21.875	12.842	9.617	7.525	6.317	5.45	5.033
AQ_9	93.623	31.525	17.475	12.167	9.05	7.283	6.025	5.433
AQ_{10}	134.526	45.608	23	14.442	10.586	8.417	6.692	5.85
AQ_{11}	178.359	59.942	28.65	18.383	12.367	9.442	7.283	6.233
AQ_{12}	35.717	12.825	8.583	6.65	5.55	4.717	4.275	4.042
AQ_{13}	99.875	29.485	14.967	10.717	8.158	6.508	5.458	4.933
AQ_{14}	41.408	15.475	8.958	6.792	5.7	4.842	4.308	4.058
AQ_{15}	13.993	10.125	7.55	6.108	5.042	4.217	3.833	3.633
AQ_{16}	15.417	9.975	7.7	6.15	5.125	4.458	4.083	3.917
AQ_{17}	12.992	9.649	7.45	6.075	5.042	4.233	3.85	3.667
AQ_{18}	33.433	14.558	10.05	7.767	6.217	5.267	4.683	4.458
AQ_{19}	37.675	14.067	8.142	6.358	5.108	4.417	3.983	3.75
AQ_{20}	90.783	23.275	13.3	9.108	7.167	6.042	5.125	4.7
AQ_{21}	36.658	19.958	12.683	9.525	7.65	6.208	5.208	4.833
AQ_{22}	59.508	25.475	15.217	10.883	8.405	6.817	5.742	5.075
AQ_{23}	72.748	36.205	20.875	13.008	9.471	7.135	5.91	5.309
AQ_{24}	30.375	11.533	8.025	6.433	5.617	4.9	4.483	4.308
AQ_{25}	47.925	20.517	12.7	9.417	7.325	5.676	4.783	4.33
AQ_{26}	27.883	9.758	6.675	5.275	4.525	3.942	3.6	3.425
AQ_{27}	31.167	11.992	7.783	5.942	5.018	4.2	3.758	3.55
AQ_{28}	20.342	13.942	10.299	8.292	6.467	5.233	4.658	4.517

As it is seen from Table 4, the coefficients of π^* (i.e., s value) in the reduced Kamlet and Taft equations are positive for all the molecules, which indicate that the solutes should have higher retention times in a mobile phase with higher polarity/polarizability index. This means that, in the case of water rich

Table 4
Coefficient of LSFER models ($\log k = \text{Const.} + s\pi^*$) for different solutes and corresponding statistical parameters

ID	Const.	s	R^2	S.E.	F
AQ_1	−5.30 (±0.21)[a,b]	6.33 (±0.25)	0.991	0.047	641.2
AQ_2	−5.01 (±0.23)	6.17 (±0.27)	0.989	0.051	521.6
AQ_3	−5.31 (±0.23)	6.65 (±0.27)	0.99	0.051	614.6
AQ_4	−4.68 (±0.20)	5.77 (±0.23)	0.99	0.044	613.4
AQ_5	−4.63 (±0.33)	5.99 (±0.38)	0.976	0.073	243.1
AQ_6	−3.50 (±0.32)	4.17 (±0.37)	0.955	0.070	126.4
AQ_7	−4.75 (±0.29)	6.02 (±0.34)	0.981	0.064	313.0
AQ_8	−5.07 (±0.28)	6.51 (±0.32)	0.985	0.061	406.7
AQ_9	−5.40 (±0.24)	7.04 (±0.28)	0.991	0.053	639.8
AQ_{10}	−5.76 (±0.21)	7.59 (±0.25)	0.994	0.047	945.0
AQ_{11}	−5.99 (±0.22)	7.97 (±0.26)	0.994	0.049	945.0
AQ_{12}	−5.06 (±0.29)	6.21 (±0.33)	0.983	0.063	346.9
AQ_{13}	−5.86 (±0.27)	7.51 (±0.32)	0.989	0.060	558.4
AQ_{14}	−5.36 (±0.24)	6.61 (±0.28)	0.99	0.052	574.8
AQ_{15}	−4.16 (±0.34)	4.99 (±0.39)	0.964	0.074	161.3
AQ_{16}	−3.89 (±0.24)	4.72 (±0.28)	0.979	0.053	286.2
AQ_{17}	−3.95 (±0.34)	4.74 (±0.40)	0.959	0.076	140.0
AQ_{18}	−4.54 (±0.23)	5.70 (±0.27)	0.986	0.052	435.2
AQ_{19}	−5.65 (±0.23)	6.86 (±0.29)	0.99	0.054	568.4
AQ_{20}	−5.85 (±0.39)	7.42 (±0.43)	0.98	0.082	295.5
AQ_{21}	−4.38 (±0.30)	5.64 (±0.22)	0.991	0.042	654.6
AQ_{22}	−4.90 (±0.20)	6.36 (±0.20)	0.993	0.038	1000.1
AQ_{23}	−5.26 (±0.33)	6.88 (±0.35)	0.982	0.066	390.6
AQ_{24}	−4.46 (±0.30)	5.51 (±0.36)	0.975	0.069	229.4
AQ_{25}	−5.21 (±0.25)	6.60 (±0.26)	0.991	0.049	638.5
AQ_{26}	−5.61 (±0.29)	6.66 (±0.34)	0.985	0.063	390.7
AQ_{27}	−5.61 (±0.28)	6.75 (±0.26)	0.991	0.049	687.0
AQ_{28}	−3.76 (±0.24)	4.77 (±0.38)	0.963	0.072	157.8

[a] Values in parenthesis are the standard errors of coefficients.
[b] P-values for constant and s coefficients are lower than 0.001.

mobile phase with higher polarity, the solutes have higher retention times and eluted slower; the coefficient s is varied between 4.17 (for AQ_6) and 7.97 (for AQ_{11}). As expected, the higher the value of s for a solute, the larger the influence of solute polarity on the retention of that solute. It is worth mentioning that compounds AQ_9, AQ_{10}, AQ_{11}, AQ_{13} and AQ_{20} with the highest s values are those anthraquinone derivatives bearing bulky lipophilic alkyl groups on their R_2 position.

3.2. QSRR analyses

To derive quantitative relationship between solute structure and RP-HPLC retention, the logarithm of retention factors ($\log k$) for all analytes in different mobile phase compositions (reported in Table 3) were regressed against the selected descriptors obtained from Dragon software. Consequently, for each mobile phase, a separate QSRR model was obtained. When the most convenient subsets of descriptors were selected for each mobile phase composition, it was interestingly found that the structure-retention relationships in all compositions could be described by models containing the same descriptors.

As it is shown in Table 3, in each mobile phase composition, a significant variation in retention times is observed for 9,10-anthraquinone derivatives, which can be related to the variation of substituted groups on the backbone of 9,10-anthraquinone. Moreover, a deeper inspection of the results given in Table 3 clearly revealed that the observed variations in retention times are not similar from one mobile phase composition to another. For example, for a mobile phase composition of $X_{AN} = 0.9$, the retention times of compounds are varied between 3.333 and 6.233 min by changing the substitution groups on 9,10-anthraquinone (i.e., a difference in retention times of only 2.9 min), while for a mobile phase composition of $X_{AN} = 0.2$, this property is varied between 12.992 and 178.359 min (i.e., a large difference of 165.367 min in retention times).

Table 5
The quantities of selected descriptors by Dragon software

ID	GATS5p	Mor14p	HATS5v	R6u+
AQ$_1$	1.932	−0.354	0.098	0.057
AQ$_2$	1.94	−0.306	0.107	0.145
AQ$_3$	1.872	−0.135	0.125	0.146
AQ$_4$	1.961	−0.306	0.095	0.078
AQ$_5$	1.867	−0.302	0.116	0.129
AQ$_6$	1.966	−0.138	0.258	0.121
AQ$_7$	2.04	−0.279	0.129	0.122
AQ$_8$	1.849	−0.13	0.116	0.113
AQ$_9$	1.982	0.069	0.118	0.136
AQ$_{10}$	1.739	0.145	0.111	0.094
AQ$_{11}$	2.108	0.042	0.11	0.213
AQ$_{12}$	1.792	−0.196	0.139	0.092
AQ$_{13}$	2.018	−0.045	0.135	0.12
AQ$_{14}$	2.028	−0.337	0.108	0.158
AQ$_{15}$	2.054	−0.551	0.121	0.114
AQ$_{16}$	2.003	−0.35	0.108	0.164
AQ$_{17}$	2.052	−0.533	0.115	0.184
AQ$_{18}$	1.989	−0.31	0.091	0.07
AQ$_{19}$	2.041	−0.222	0.2	0.292
AQ$_{20}$	2.419	−0.203	0.137	0.208
AQ$_{21}$	2.309	−0.149	0.144	0.063
AQ$_{22}$	2.138	−0.114	0.141	0.131
AQ$_{23}$	3.203	0.082	0.245	0.15
AQ$_{24}$	1.909	−0.297	0.14	0.244
AQ$_{25}$	1.904	−0.059	0.184	0.244
AQ$_{26}$	1.8	−0.183	0.253	0.17
AQ$_{27}$	1.883	−0.03	0.204	0.186
AQ$_{28}$	1.921	−0.07	0.152	0.186

In this case, for mobile phase compositions of $X_{AN} = 0.2$ through $X_{AN} = 0.9$, the relationship obtained between the logarithm of retention factors of AQ derivatives and the selected descriptors was as follows:

$$\log k = b_o + b_1 \, GATS5p + b_2 \, Mor14p + b_3 \, HATS5v + b_4 \, R6u^+ \quad (2)$$

This four-parametric QSRR equation describes the significant effects of the GETAWAY descriptors (*i.e.*, leverage-weighted auto-correlation of lag 5/weighted by atomic van der Waals volumes, HATS5v and R maximal autocorrelation of lag 6/unweighted, R6u$^+$), 3D-MoRSE descriptor (*i.e.*, 3D-MoRSE-signal 08/weighted by atomic van der Waals volumes, Mor14p) and 2D autocorrelations (*i.e.*, Geary autocorrelation-lag 5/weighted by atomic polarizabilities, GATS5p) on the retention behavior of the 9,10-anthraquinone derivatives. The GETAWAY (GEometry, Topology, and Atom-Weights AssemblY) descriptors try to match 3D-molecular geometry provided by the molecular influence matrix and atom relatedness by molecular topology, with chemical information by using different atomic weights (atomic mass, polarizability, van der Waals volume, and electronegativity). The quantities of these descriptors for 28 molecules obtained by Dragon software are represented in Table 5. The presence of polarizability related descriptors in the resulting QSRR models is in direct agreement with the resulted solvotochromic LSFER models, which

Fig. 4. Plots of coefficients of QSRR model ($\log k = b_0 + b_1 \, GATS5p + b_2 \, Mor14p + b_3 \, HATS5v + b_4 \, R6u^+$) versus acetonitrile mole fraction.
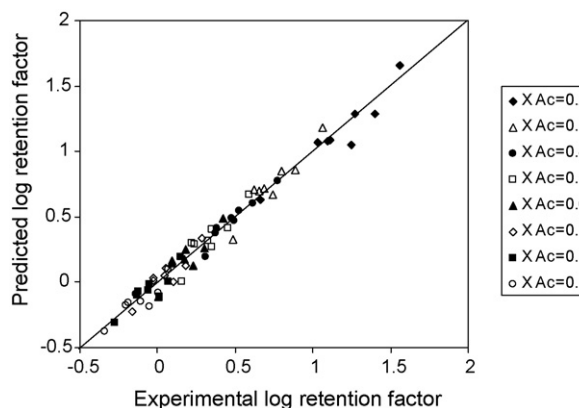
Fig. 5. Plots of experimental $\log k$ data versus predicted $\log k$ data for 8 compounds as prediction set in mole fraction of 0.2–0.9 of acetonitrile.

describe the significant influence of polarity/polarizability interaction on the RP-HPLC behavior of the studied AQ derivatives.

As it is shown in Fig. 4, there are systematic relationships between regression coefficients of the QSRR model and solvent composition.

Among the calculated regression coefficients, b_1, b_2 and b_4 are positive and b_3 is negative in all solvent compositions, where b_o is negative at $0.2 < X_{AN} > 0.7$ and is positive at $X_{AN} > 0.8$. Although the statistical quantities of the QSRR models (given in Table 6) are not very high, there is a balance between the statistical quantities of calibration cross-validation and the external prediction set. Fig. 5 shows the plot of predicted $\log k$ against the experimental

Table 6
Coefficients of QSRR models ($\log k = b_0 + b_1 \, GATS5p + b_2 \, Mor14p + b_3 \, HATS5v + b_4 \, R6u^+$) for different mixed solvent compositions and corresponding statistical parameters

X_{AN}	b_0	b_1	b_2	b_3	b_4	Q^2	R^2 calibration	R^2 prediction	F^a
0.20	1.40	0.22	1.56	−3.57	0.88	0.6118	0.6834	0.904	14.898
0.30	0.72	0.33	1.26	−3.44	0.63	0.7685	0.8427	0.8995	29.241
0.40	0.42	0.32	1.07	−3.01	0.47	0.788	0.871	0.8356	32.708
0.50	0.29	0.28	0.96	−2.80	0.41	0.7886	0.873	0.8045	32.095
0.60	0.16	0.25	0.89	−2.50	0.28	0.7716	0.8537	0.8015	28.668
0.70	0.08	0.23	0.87	−2.46	0.19	0.735	0.8146	0.8213	24.417
0.80	−0.02	0.20	0.78	−2.17	0.08	0.6425	0.7352	0.8059	16.661
0.90	−0.10	0.19	0.74	−2.05	0.13	0.508	0.6231	0.7632	10.301

[a] The P-values for obtained models are lower than 0.001 then not reported.

Fig. 6. Chromatogram of a mixture of prediction set compounds in mole fraction of 0.4 of acetonitrile (A) and calculated retention times by QSRR model (B).

Fig. 7. Plot of experimental $\log k$ data versus predicted $\log k$ data for 64 data set based on unified model.

results for eight AQ derivatives in all studied solvent compositions. These compounds did not contribute in any model development steps. The distribution of data around the ideal line (*i.e.*, slope 1 and intercept 0) with low scattering confirms the high prediction power of the QSRR models. Experimental chromatogram of a mixture of prediction compounds (AQ$_2$, AQ$_3$, AQ$_4$, AQ$_7$, AQ$_8$, AQ$_9$, AQ$_{15}$ and AQ$_{18}$) in mole fraction of 0.4 of acetonitrile together with the predicted retention times of these compounds are shown in Fig. 6. As can be seen there is a good agreement between experimental and calculated results.

3.3. Unified model for considering both solvent and solute effects

In the last step of the development of quantitative models for characterization of the RP-HPLC behavior of the studied 9,10-anthraquinone derivatives, attempts were made to obtain a model considering the effects of both solvent composition and solute chemical structure. As it was mentioned in the experimental section, the data set in this case are composed of 224 data points of retention factors (28 solutes in 8 mobile phases), among which 160 samples were used in the model development step (calibration phase) and the rest was used to evaluate the model prediction ability. Random design was used for data classification. Multi linear regression (MLR) with stepwise selection of variables resulted in the following equation:

$$\log k = -4.90\,(\pm 0.14) + 0.23\,(\pm 0.03)\,\text{GATS5p}$$
$$+ 0.97\,(\pm 0.06)\,\text{Mor14p} - 2.51\,(\pm 0.28)\,\text{HATS5v}$$
$$- 0.29\,(\pm 0.12)\,\text{R6u}^+ + 6.20\,(\pm 0.43)\pi^* \quad N = 160,$$
$$R^2 = 0.939, \quad \text{S.E.} = 0.117, \quad F = 475.2, \quad Q^2_{\text{LOO}} = 0.925,$$
$$Q^2_{L10O} = 0.917 \tag{3}$$

Obviously, this equation represents very high statistical quality with very good generalization and stability measured by leave-one-out and leave-10-out cross-validation correlation coefficient (*i.e.*, Q^2_{LOO} and Q^2_{L10O}, respectively) of about 0.92, which means that the resulting model can reproduce more than 92% of the variances in the retention factor data. A very small difference between the correlation coefficient of calibration and cross-validation confirms that the model is not over-fitted. The solute and solvent parameters used by Eq. (3) are those appeared in the LSFER and QSRR models dis-

cussed in previous sections. The effects of these parameters on the retention behavior of solutes can be explained in a similar manner as discussed previously. The only difference is the value of coefficients. In the LSFER models obtained for each solute (Table 4), the coefficients of π^* was different for various 9,10-anthraquinone derivatives, lying between 4.17 and 7.97. However, the corresponding value in Eq. (3) is fixed at 6.20, which is an approximate average of the values reported in Table 4. Similar trends are observed for the coefficients of GATS5p, Mor14p and HATS5v of solutes.
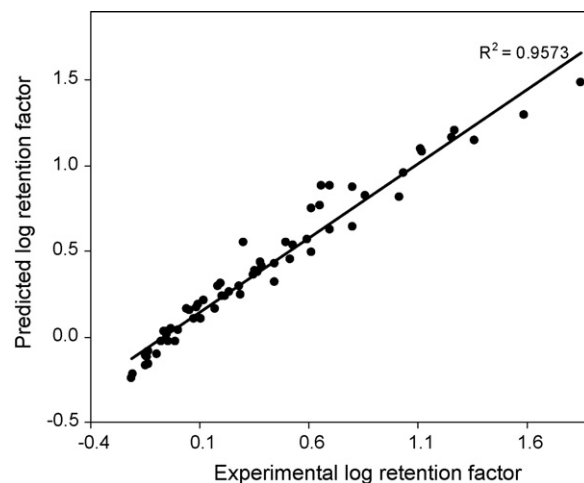
Eq. (3) not only represents qualitative information about solute–solvent interaction, but also shows a quantitative estimate of the new or non-tested compounds. When Eq. (3) was used to predict the retention factor of the data points which did not have any contribution to the model development step (prediction set), highly accurate results were obtained. To illustrate the retention predictions capabilities of the QSRR models specified above, the predicted retention factors against the corresponding experimental values were plotted for 64 data points which were selected randomly as external prediction set (Fig. 7). As can be seen from Fig. 6, the predicted retention factors can be represented by a linear equation of $\log k\,(\text{pred}) = -0.046 + 1.102\,\log k\,(\text{exp})$ with the respective correlation coefficient and root mean square error of 0.957 and 0.100, respectively.

4. Conclusions

Multi linear regression was used to find those properties of acetonitrile–water mixtures which affect the retention time of twenty-eight 9,10-anthraquinone derivatives in RP-HPLC. The polarity/polarizability parameter (π^*) of the binary mixed solvents was found to be significant and a reduced Kamlet–Taft equation $\log k = \text{Const.} + s\pi^*$ was obtained. Coefficient of π^* is positive which indicates that longer retention times are obtained in solvent systems of higher π^* values. In addition, the effect of molecular structure on the retention time in a specified mobile phase was studied by QSRR method and the model of $\log k = b_0 + b_1 \text{GATS5p} + b_2 \text{Mor14p} + b_7 \text{HATS5v}\ b_4 \text{R6u}^+$ was obtained. Finally, a unified model was built as $\log k = -4.90\ (\pm 0.14) + 0.23\ (\pm 0.03)\ \text{GATS5p} + 0.97\ (\pm 0.06)\ \text{Mor14p} - 2.51\ (\pm 0.28)\ \text{HATS5v} - 0.29\ (\pm 0.12)\ \text{R6u}^+ + 6.20\ (\pm 0.43)\ \pi^*$, which considers the effects of both solvent composition and solute chemical structure on the retention times of the 9,10-anthraquinone derivatives. By using this equation, one is able to obtain qualitative information about solute–solvent interaction

ID	AQ$_2$	AQ$_3$	AQ$_4$	AQ$_7$	AQ$_8$	AQ$_9$	AQ$_{15}$	AQ$_{18}$
Experimental t$_r$	8.59	10.95	8.46	10.29	12.84	17.47	7.56	9.98
Predicted t$_r$	8.91	11.22	8.38	9.87	12.44	17.41	6.41	10.13

and also to predict the quantitative estimate of retention times of new or non-tested compounds.

Acknowledgements

References

[1] R.H. Thomson, Naturally Occurring Quinones, Academic Press, New York, 1971.
[2] S. Routier, J.L. Bernier, J.P. Catteau, J.F. Riou, C. Bailly, Anticancer Drug Res. 13 (1998) 407.
[3] S. Das, A. Saha, P.C. Mandal, Talanta 43 (1996) 95.
[4] G.C. Yen, P.D. Duh, D.Y. Chuang, Food Chem. 70 (2000) 437.
[5] J. Koyama, I. Morita, K. Tagahara, M. Ogata, T. Mukainaka, H. Tokuda, H. Nishino, Cancer Lett. 170 (2001) 15.
[6] D.L. Barnard, D.W. Fairbairn, K.L. O'Neill, T.L. Gage, R.W. Sidwell, Antivir. Res. 28 (1995) 317.
[7] F. Nourmohammadian, I. Yavari, B. Mohtat, S.Z. Shafaei, Dyes Pigments 75 (2007) 479.
[8] M.G. Johonson, H. Kiyokava, S. Tani, J. Koyoma, S.L.M. Naschke, Org. Med. Chem. 8 (1997) 1469.
[9] O.T. Fahmy, M.A. Korany, H.M. Maher, J. Pharm. Biomed. Anal. 34 (2004) 1099.
[10] S.W. Sun, H.T. Su, J. Pharm. Biomed. Anal. 29 (2002) 881.
[11] Q. Zhou, B. Chowbay, J. Pharm. Biomed. Anal. 30 (2002) 1063.
[12] H. Wakabayashi, K. Onodera, S. Yamato, K. Shimada, Nutrition 19 (2003) 661.
[13] T. Perez-Ruiz, C. Martínez-Lozano, V. Tomas, J. Martín, Analyst 124 (1999) 197.
[14] S. Ahmed, S. Fujii, N. Kishikawa, Y. Ohba, K. Nakashima, N. Kuroda, J. Chromatogr. A 1133 (2006) 76–82.
[15] J. Jiskra, H.A. Claessens, C.A. Cramers, R. Kaliszan, J. Chromatogr. A 977 (2002) 193.
[16] T. Baczek, R. Kaliszan, J. Chromatogr. A 962 (2002) 41.
[17] A. Niewiadomy, J. Matysiak, A. Zabinska, J.K. Rozylo, B. Senczyna, K. Jozwiak, J. Chromatogr. A 828 (1998) 431.
[18] S. Wold, J. Trygg, A. Berglund, H. Antii, Chemom. Intell. Lab. Syst. 58 (2001) 131.
[19] B. Hemmateenejad, Chemom. Intell. Lab. Syst. 75 (2005) 231.
[20] T. Baczek, R. Kaliszan, K. Novotna, P. Jandera, J. Chromatogr. A 1075 (2005) 109.
[21] T. Baczek, R. Kaliszan, J. Chromatogr. A 987 (2003) 29.
[22] M. Markuszewski, R. Kaliszan, J. Chromatogr. B 768 (2002) 55.
[23] T. Baczek, R. Kaliszan, J. Biochem. Biophys. Methods 49 (2001) 83.
[24] H. Sharghi, A. Forghaniha, Iran J. Chem. Chem. Eng. 14 (1995) 16.
[25] S. Rouhani, R. Rezaei, H. Sharghi, M. Shamsipur, G. Rounaghi, Microchem. J. 52 (1995) 22.
[26] D. Almasifar, A. Forghaniha, Z. Khojasteh, J. Ghasemi, H. Sharghi, M. Shamsipur, J. Chem. Eng. Data 42 (1997) 1212.
[27] M. Shamsipur, A.R. Karami, Y. Yamini, H. Sharghi, J. Chem. Eng. Data 48 (2003) 171.
[28] M. Shamsipur, A.R. Karami, Y. Yamini, H. Sharghi, J. Supercrit. Fluid 32 (2004) 47.
[29] M. Shamsipur, T. Mohammadi, K. Alizadeh, H. Sharghi, R.J. Nichols, Polish J. Chem. 79 (2005) 1379.
[30] M. Shamsipur, A. Salimi, S.M. Golabi, H. Sharghi, M.F. Mousavi, J. Solid State Electrochem. 5 (2001) 68.
[31] M. Shamsipur, K. Alizadeh, S. Arshadi, J. Mol. Struct. Theochem. 758 (2006) 71.
[32] M. Shamsipur, B. Hemmateenejad, A. Babaei, L. Faraj-Sharabiani, J. Electroanal. Chem. 570 (2004) 227.
[33] M. Shamsipur, A. Yari, H. Sharghi, Spectrochim. Acta A 62 (2005) 372.
[34] M. Shamsipur, M.J. Chaichi, A.R. Karami, H. Sharghi, J. Photochem. Photobiol. A 174 (2005) 23.
[35] M. Shamsipur, A. Avanes, H. Sharghi, G. Aghapour, Talanta 54 (2001) 863.
[36] M. Shamsipur, A. Avanes, H. Sharghi, Sep. Sci. Technol. 39 (2004) 113.
[37] S. Dadfarnia, M. Shamsipur, F. Tamaddon, H. Sharghi, J. Membr. Sci. 78 (1993) 115.
[38] M. Shamsipur, T. Poursaberi, A. Avanes, H. Sharghi, Spectrochim. Acta A 63 (2006) 43.
[39] M. Barzegar, M.F. Mousavi, H. Khajehsharifi, M. Shamsipur, H. Sharghi, IEEE Sens. J. 5 (2005) 392.
[40] S. Riahi, M.F. Mousavi, M. Shamsipur, H. Sharghi, Electroanalysis 15 (2003) 1561.
[41] B. Hemmateenejad, M.A. Safarpour, R. Miri, N. Nesari, J. Chem. Inf. Model. 45 (2005) 190.
[42] B. Hemmateenejad, M.A. Safarpour, F. Taghavi, J. Mol. Struct. Theochem. 635 (2003) 183.
[43] M. Shamsipur, A. Siroueinejad, B. Hemmateenejad, A. Abbaspour, H. Sharghi, K. Alizadeh, S. Arshadi, J. Electroanal. Chem. 600 (2007) 345.
[44] N. Sanli, G. Fonrodona, J. Barbosa, G.A. Ozkan, J.L. Beltran, Anal. Chim. Acta 537 (2005) 53.
[45] N. Sanli, G. Fonrodona, D. Barron, G. Ozkan, J. Barbosa, J. Chromatogr. A 975 (2002) 299.
[46] R. Beges, V. Sanz-Nebot, J. Barbosa, J. Chromatogr. A 869 (2000) 27.
[47] M.J. Kamlet, J.L. Abboud, R.W. Taft, J. Am. Chem. Soc. 99 (1977) 6027.
[48] M. Roses, E. Bosch, Anal. Chim. Acta 274 (1993) 147.
[49] C. Reichardt, Solvents and Solvent Effects in Organic Chemistry, 3rd Ed., WILEY-VCH Verlag GmbH & Co. KGaA, Weinheim, 2003, pp. 389–452.
[50] F. Liu, Y. Liang, C. Cao, Chemom. Intell. Lab. Syst. 81 (2006) 120.
[51] A. Khalafi-Nezhad, M.N. Soltani Rad, H. Mohabatkar, Z. Asrari, B. Hemmateenejad, Bioorg. Med. Chem. 13 (2005) 1931.

Rate of phosphoantimonylmolybdenum blue complex formation in acidic persulfate digested sample matrix for total dissolved phosphorus determination: Importance of post-digestion pH adjustment

Xiao-Lan Huang [a,b,∗], Jia-Zhong Zhang [a]

[a] Ocean Chemistry Division, Atlantic Oceanographic and Meteorological Laboratory, National Oceanic and Atmospheric Administration, Miami, FL 33149, USA
[b] CIMAS, Rosenstiel School of Marine and Atmospheric Science, University of Miami, Miami, FL 33149, USA

A B S T R A C T

Acidic persulfate oxidation is one of the most common procedures used to digest dissolved organic phosphorus compounds in water samples for total dissolved phosphorus determination. It has been reported that the rates of phosphoantimonylmolybdenum blue complex formation were significantly reduced in the digested sample matrix. This study revealed that the intermediate products of persulfate oxidation, not the slight change in pH, cause the slowdown of color formation. This effect can be remedied by adjusting digested samples pH to a near neural to decompose the intermediate products. No disturbing effects of chlorine on the phosphoantimonylmolybdenum blue formation in seawater were observed. It is noted that the modification of mixed reagent recipe cannot provide near neutral pH for the decomposition of the intermediate products of persulfate oxidation. This study provides experimental evidence not only to support the recommendation made in APHA standard methods that the pH of the digested sample must be adjusted to within a narrow range of sample, but also to improve the understanding of role of residue from persulfate decomposition on the subsequent phosphoantimonylmolybdenum blue formation.

© 2008 Elsevier B.V. All rights reserved.

1. Introduction

Phosphorus is one of essential nutrients for life on earth, and occurs in soils, sediments, waters, and organisms. Among various forms of phosphorus, orthophosphate, the most frequently measured form of phosphorus, is considered to be the only form directly available and rapidly assimilated by bacteria, algae [1] and plants [2,3]. On the other hand, the role of organic phosphorus in different ecosystems is still a subject of intensive study [4–6]. This is in part due to the lack of reliable organic phosphorus data in many ecosystems because of complex procedures involved in determination of dissolved organic phosphorus [4,7]. To determine total dissolved organic phosphorus in the samples, breakdown of organic phosphorus, by digestion, to dissolved phosphate is often required. Several methods, including fusion, dry ashing, and boiling samples in perchloric, sulfuric or nitric acid on a hot plate, have been employed to digest samples for total dissolved phosphorus determination. More recently, autoclaving, UV photo-oxidation and microwave heating are widely used [8]. However, there are many uncertainties involved in the total dissolved phosphorus measurements [7–9]. The QUASIMEME laboratory performance studies (nutrient section) indicated that more than a half of laboratories participated the inter-comparison study on total dissolved phosphorus cannot produce consistent results and concluded that the total phosphorus was the most problematic parameter in routine water quality monitoring program [10]. Among various problems, incomplete recovery of organic phosphate compounds has been considered to cause the underestimate of the total dissolved phosphorus in the natural waters [4,11–13].

One of the most popular methods of total phosphorus digestion was based on the oxidation of organic phosphorus by persulfate in acidic solution. The oxidation processes were usually accelerated by autoclaving samples at a pressure of 137 kPa to 120 °C for a period of time (ranged from 30 min to 5 h) [12,14–17]. This procedure has been adapted for total dissolved phosphorus analysis in the standard method for the examination of water and wastewater [18] and USEPA Method 365.1 [19]. Because the digestion product of organic phosphorus is orthophosphate, same color reagents and procedures have been widely used for the determination of phosphate and total dissolved phosphorus in the same samples. Slow formation of the phosphoantimonylmolybdenum blue complex in persulfate digested samples has been reported [12,20,21]. This

* Corresponding author at: CIMAS, Rosenstiel School of Marine and Atmospheric Science, University of Miami, Miami, FL 33149, USA. Tel.: +1 305 361 4551; fax: +1 305 361 4447.
E-mail address: xiaolan.huang@noaa.gov (X.-L. Huang).

might cause an underestimate in determination of total phosphorus, particularly in automated analysis where the colored complex is usually detected less than 10 min after mixing the sample with reagents [22].

Previous studies have attributed the slow formation of the phosphoantimonylmolybdenum blue complex in the acidic persulfate digested samples to the decrease in sample pH resulting from decomposition of persulfate to sulfuric acid [12,20,21]. For the total dissolved phosphorus in the fresh water and wastewater, neutralization of digested solution with sodium hydroxide was recommended before the total phosphate determination [18,19,23]. For measuring total dissolved phosphorus in seawater samples, a modified mixed reagent with high molybdate and low acidity ($[H^+]/Mo = 46.5$) were recommended [12,15,17] to compensate newly formed sulfuric acid from decomposition of persulfate during the digestion process. The same strategy for seawater has recently been suggested for determination of total dissolved phosphorus in fresh water and wastewater samples [24]. Little attention has been paid to the difference in sample matrix, particularly the modification of sample matrix after addition of oxidizing reagents and subsequent digestion process. The influence of oxidation products on the subsequent phosphoantimonylmolybdenum blue formation has been largely ignored. So far, there is no study on the kinetics of formation of the phosphoantimonylmolybdenum blue complex in the persulfate digested sample matrix. To develop an optimal procedure for total dissolved phosphorus determination, it is necessary to understand the factors that control the rate of the color formation in these digested sample matrix. In this report, we explore the kinetics of formation of the phosphoantimonylmolybdenum blue complex in total dissolved phosphorus samples that have undergone the acidic persulfate digestion by a modified Murphy and Riley method [25,26]. The influences of persulfate and solution pH on the formation of the phosphoantimonylmolybdenum blue complex were separately examined and their combined effect was evaluated.

2. Experimental

2.1. Apparatus

Kinetics of phosphoantimonylmolybdenum blue complex formation as a function of time were measured on a Hewlett Packard 8453 UV–visible spectrophotometer in quartz cells of 50-mm path length at room temperature ($25 \pm 2\,^\circ C$) with the ChemStation software.

2.2. Reagents and standard solution

Deionized water (DIW) used for preparing standard and reagents was purified by a distilling unit followed by Millipore Super-Q Plus Water System that produce water with $18\,M\Omega\,cm$ resistance. All samples and reagents were stored in polypropylene bottles that were immersed in 10% HCl solution overnight, followed

by rinsing three times with deionized water and then drying at $60\,^\circ C$ in an oven for 5–10 h prior to their use.

All chemicals used were of analytical grade reagents or GR. Potassium dihydrogen phosphate (KH_2PO_4, Aldrich, AR) was used to prepare the stock orthophosphate (IP) standard solution (1.0 mM). The stock solutions were stored in a polyethylene bottle at $4\,^\circ C$ in a refrigerator. Working standard solutions were prepared daily from serial dilution of the stock solution with deionized water. Acidic 5% potassium persulfate solution (20 g potassium persulfate ($K_2S_2O_8$, Aldrich, AR) in 400 ml 0.5 M H_2SO_4) was made in a brown polyethylene bottle and stored at room temperature. Usually the stock persulfate solution can be used within month.

The model phosphorus compounds used in digestion are listed in Table 1, which included phosphate ester (C–O–P bonded compounds), phosphonates (C–P bonded compounds) and organic condensed phosphates (C–O–P–O–P bond) and inorganic polyphosphate. All the model phosphorus compounds were stored in a freezer as required by the manufacturers. Each of the model compounds were prepared as an 10 mM phosphorus stock solution in DIW and stored in a polyethylene bottle at $4\,^\circ C$ in a refrigerator were used within a week. The lower concentrations of these model phosphorus solutions in different sample matrix (DIW, LNSW and NaCl) were prepared daily.

Ammonium molybdate reagent was prepared by mixing 2.4 g of ammonium molybdate (($NH_4)_6MO_7O_{24}\cdot4H_2O$, Merck, GR), 25 ml of concentrated sulfuric acid (H_2SO_4, 96–98%, L.T. Baker) and 50 ml of 0.3% antimony potassium tartrate ($K(SbO)C_4H_4O_6)_2\cdot H_2O$, Fisher) solution and diluting mixture to 1 l with DIW. Ascorbic acids solution was prepared daily by dissolving 1 g of Ascorbic acid ($C_6H_8O_6$, Aldrich, AR) in 100 ml of DIW.

2.3. Procedures

A 20-ml of sample was pipetted into acid-washed 30-ml Teflon vial. An appropriate amount of acidic persulfate solution was added to each sample and mixed by swirling. To study the effect of persulfate, the amount of potassium persulfate used for digestion varied from 50 to 400 mg ($2.5–20\,mg\,ml^{-1}$ of sample). The autoclave pressure was set at 130 kPa for 5 h [12] to ensure that all the organic phosphorus was decomposed completely. The pH of the digested samples was monitored by a pH meter (Orion 420 A^+).

The orthophosphate determination was based on a modified method of Murphy and Riley, in which the pH of the test solution (sample and color reagent mixture) is 1.0 ($[H^+]/Mo = 70$) [26]. Prior to sample analysis, a single color reagent was prepared by mixing equal volumes of the molybdate reagent with the ascorbic acid solution. A 5-ml of color reagent was added to 20 ml of sample and mixed. The kinetics of absorbance of phosphoantimonylmolybdenum was recorded at 890 nm immediately after the mixing of sample with the color reagent.

Table 1
Characteristics of model phosphorus compounds used in digestion in this study

Name	Abbr	Formula	Origin	MW	Purity %
2-Aminoethylphosphonic acid	AEP	$C_2H_8NO_3P$	Aldrich	125.07	99
Glycerol-2-phosphate disodium salt hydrate	GLP	$C_3H_7Na_2O_6P\cdot xH_2O$	Sigma	216.04	99
Adenosine triphosphate	ATP	$C_{10}H_{14}N_5Na_2O_{13}P_3\cdot xH_2O$	Aldrich	551.2	99
Adenosine diphosphate	ADP	$C_{10}H_{14}KN_5O_{10}P_2\cdot2H_2O$	Sigma	501.3	95
Adenosine monophosphate	AMP	$C_{10}H_{14}N_5O_7P\cdot xH_2O$	Fluka	391.18	99
Phytic acid dipotassium	IP6	$C_6H_{16}K_2O_{24}P_6$	Sigma	736.2	95
Sodium tripolyphosphate	Poly-P	$Na_5P_3O_{10}\cdot6H_2O$	Sigma	475.86	98

3. Results and discussion

3.1. Effect of sample pH on the formation of phosphoantimonylmolybdenum blue complex

To separate the effects of pH and persulfate concentration on the color formation kinetics, the first set of experiments was designed to study the kinetic of formations of the phosphoantimonylmolybdenum blue complex as a function of pH in the absence of persulfate and without autoclaving. In this experiment, pH of samples containing 5-μM orthophosphate (IP) was adjusted from 0.64 to 10 using diluted HCl or NaOH solutions. The times taken to reach maximum absorbance levels of the blue phosphoantimonylmolybdenum complex (full color development) in samples of different pH are shown in Fig. 1. These results demonstrate considerable differences in the time needed for complete color development. It should be noted that the pH here was the pH of the original samples before addition of the color reagent and it is usually much higher than the pH of final mixture as usually referred in methodological papers [25–29]. When the sample pH is lower than 1.3 or higher than 10, the reaction become slow and would take hours to complete the color formation. For example, the times for the 95% color development at pH 0.9, 1.0, 1.05 and 1.22 are 25, 16.8, 11.5, and 3.9 min, respectively. However, in a pH range of 1.3 and 10, complete color development can be achieved within 3 min. It should be pointed out that the self-reduction of molybdate at high pH can result an overestimate of phosphate concentration in the sample [28,29].

3.2. Effect of concentration of persulfate used in digestion on the formation of phosphoantimonylmolybdenum blue complex

The effect of persulfate concentration (from 2.5 to 20 mg ml^{-1}) used in digestion on the formation of phosphoantimonylmolybdenum blue complex was studied by digesting model P compounds, AMP and ATP, in DIW matrix (Fig. 2). When the persulfate concentration was 2.5 mg ml^{-1}, the complete color development only took 3 min. When the persulfate concentration increased to 5.0 mg ml^{-1}, it took about 9–10 min to get 95% full color development. At a higher level persulfate concentration (20 mg ml^{-1}), only about 34–38% of full color can developed at 10 min and it took about 34–38 min to get 95% full color development. It noted that the amount of persulfate used in digestion in this study is in the range of the concentrations recommended by most researchers [11,14–19,23]. However, higher
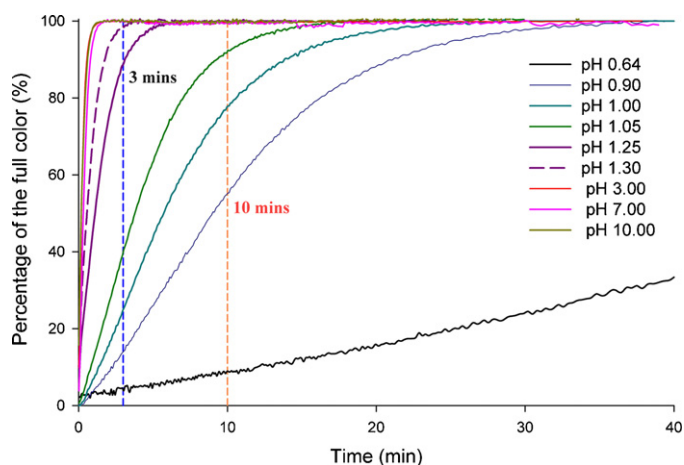
concentrations of persulfate have been used in previous studies. For example, Ridal and Moore [12] used have used 40 mg ml^{-1} adapted from Strickland and Parsons's recipe [30] used in DOC digestion, which is twice of our highest concentration used in this study (20 mg ml^{-1}).

In present study, the percentage of full color formation at a given time was negatively related to the persulfate concentration, especially at the short time (<10 min). For example, the relationship of percentage of full color of phosphoantimonylmolybdenum blue complex developed at 5 min (y) and the concentration of persulfate used in digestion (x) can be expressed by exponential equations as: $y_{(AMP, 5 min)} = 136.75\,e^{-0.12x}$, $r^2 = 0.982$ and $y_{(ATP, 5 min)} = 127.70\,e^{-0.11x}$, $r^2 = 0.996$, for 5-μM ATP and AMP, respectively. Since the persulfate oxidation can release proton, it is not surprising to notice that the greater amount of persulfate used, the lower pH in the final solution will be (Fig. 2). However, the change in pH is small and observed slowdown of color formation kinetics is dominated by the effect of persulfate concentration. These results strongly suggested the persulfate concentration used in digestion cause the slowdown of the color formation of phosphoantimonylmolybdenum blue complex.

3.3. Effect of sample matrix on the formation of phosphoantimonylmolybdenum blue complex

To investigate the effect of sample matrix on the formation of the phosphoantimonylmolybdenum blue complex in digested samples, samples contain 5-μM IP, AMP and ATP were prepared in matrix of
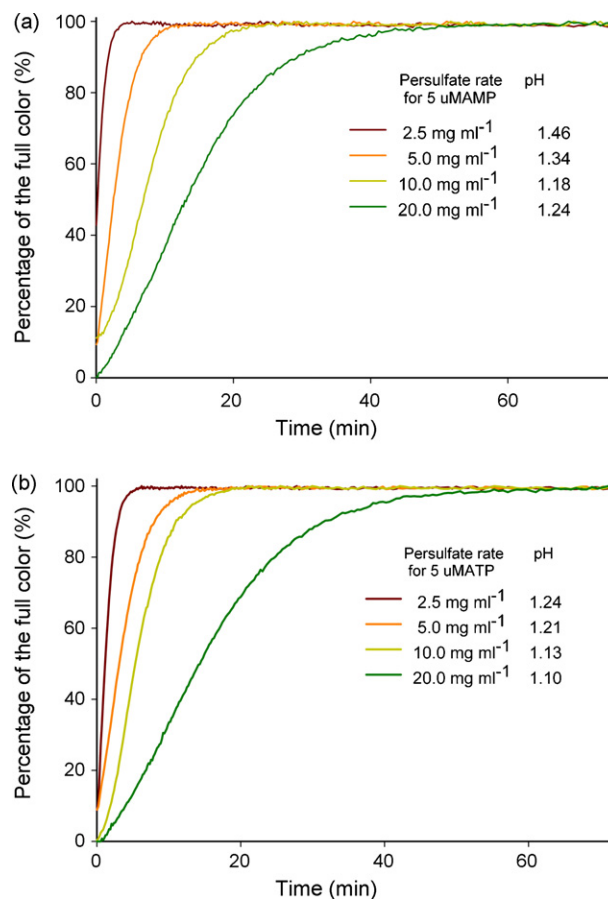
Fig. 2. Effect of different concentration of potassium persulfate on the time course of formation of phosphoantimonylmolybdenum blue complex. (a) Digested 5 μM AMP, and (b) 5-μM ATP in DIW matrix.

Fig. 1. Time course for the formation of phosphoantimonylmolybdenum blue complex at room temperatures ($25 \pm 2\,^\circ$C) in samples of different pH (0.64–10). All samples contain 5-μM IP in DIW matrix and the color was developed using a modified Murphy and Riley method [26].

Table 2
Effect of sample matrix on the percentage of full color of phosphoantimonylmolybdenum blue complex at 3–20 min in the acidic persulfate (5 mg ml^{-1}) digested samples solution containing 5 μM of IP, AMP and ATP, respectively

Matrix	Sample pH	Time (min)			
		3	5	10	20
IP (undigested, DIW)	1.00	25	64	88	99
IP (digested)					
DIW	0.98	4	6	18	48
LNSW	0.98	19	39	78	98
1% NaCl	0.98	14	21	40	72
2% NaCl	0.99	16	29	61	92
3% NaCl	0.98	47	70	95	99
AMP (digested)					
DIW	1.02	9	13	23	46
LNSW	1.18	22	36	73	99
50% DIW, 50% LNSW	1.04	19	26	51	85
25% DIW, 75% LNSW	1.05	24	39	75	97
1% NaCl	0.96	18	26	49	82
3% NaCl	0.99	20	36	72	98
ATP (digested)					
DIW	1.00	16	24	42	74
LNSW	1.13	20	38	76	97
50% DIW, 50% LNSW	1.05	15	25	57	90
25% DIW, 75% LNSW	1.09	13	23	56	90
1% NaCl	1.01	14	21	44	80
3% NaCl	0.96	21	40	78	98

Fig. 3. Time courses of formation of phosphoantimonylmolybdenum blue complex in persulfate digested samples containing IP, AMP and ATP and in an IP sample without persulfate digestion. All samples contained the same concentration phosphorus (5 μM) in DIW matrix and the same pH (1.00). The absorbances were measured at room temperatures (25 ± 2 °C).

DIW, different salinity of low-nutrient seawater and NaCl solution. The kinetic results presented as the percentage of full color development are listed in Table 2. In general, the color formation in seawater matrix is much rapid in comparison with that in DIW. The difference is greatest in the persulfate digested IP samples. After 5 min, the color development is 4 and 19% in DIW and seawater, respectively. After 20 min, it reached 98% in seawater but only 48% in DIW (Table 2). This might be due to lower concentration of organic compounds presented in DIW sample matrix than natural seawater for persulfate to react. It seems that the more remaining persulfate in the samples, the slower the color formation. Moreover, persulfate can react with chloride in seawater. It has been observed that free chlorine was formed from seawater during the persulfate digestion [15,20]. The chloride competing reaction for persulfate has been considered to cause incomplete persulfate digestion of dissolved organic carbon in seawater [31]. The effect of chlorine on the color formation was further investigated in solutions of different NaCl concentrations. The color formation of digested samples of ATP and AMP in high concentration of NaCl was much rapid than that in low concentration of NaCl or DIW matrix. After 10 min, the percentages of color formation of digested IP, AMP, and ATP samples in DIW matrix were only 18.3, 22.7 and 41.9, respectively. The corresponding values in 3% NaCl solution increased to 94.7, 72.4, and 77.9, respectively. No disturbing effects from chlorine were observed in our experiments, which do not support the previous view that the free chlorine cause serious error in total phosphorus measurement in seawater [15]. The chlorine effect was firstly reported by Koroleff in his technical report [20] but the report did not provide any experimental data to support his hypothesis.

We also made a series experiments to test the ascorbic acid concentration on the color formation. The rate of phosphoantimonylmolybdenum blue complex formation did not improved with higher ascorbic acid concentration used, even caused an adverse effect, which is completely different from the inorganic phosphate measurement [25,27,28]. For example, in a digested seawater matrix, the percentage of the color formation at 10 min when 0.5, 1, 2, 5 and 10% ascorbic acid were used were 69, 78, 79, 66 and 51%, respectively; and at 15 min, the corresponding value was 89, 92, 95,
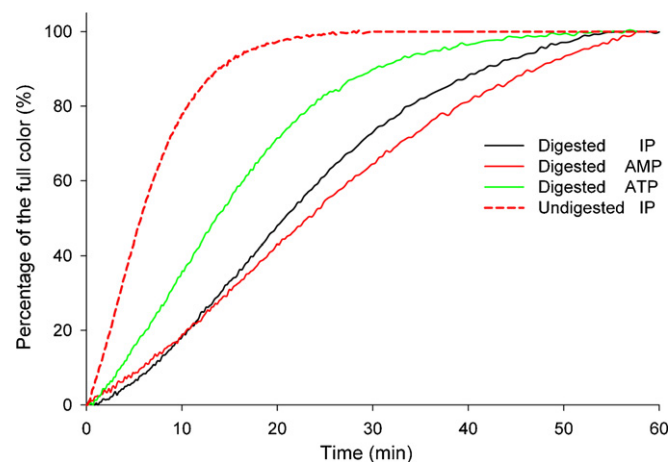
86 and 75%, respectively. Our laboratory routine total phosphorus analysis also demonstrates that it is not necessary to add additional ascorbic acid prior to addition of the mixed reagent.

3.4. Effect of types of organic phosphorus on the formation of phosphoantimonylmolybdenum blue complex in digested samples

In the acidic digestion method, the pH of the final digested solution of different organic phosphorus compounds is very close, around 0.98–1.00. The color formation in these digested samples becomes much slower in comparison with the samples without persulfate digestion at the same sample pH (Fig. 3). As mentioned before, it takes about 17 min to get 95% full color for the 5-μM IP at the pH 1.00 (DIW matrix) conditions, whereas the time for the 95% full color of 5-μM IP, AMP and ATP after digestion is 48, 51 and 36 min, respectively, though the final pH of the digestion solution was very close to 1.00.

It also found that there was significant difference in the rate of color formation after digestion among the different model phosphorus compounds in both DIW and seawater matrix. In seawater matrix, the percentage of full color development of the phosphoantimonylmolybdenum blue complex after 3–20 min was listed in Table 3. After 5 min, the percentage of full color of IP was around 39%, whereas the corresponding values of phytic acid dipotassium (IP6) and glycerol-2-phosphate disodium salt hydrate (GLP) was 49 and 37%, respectively. The order of percentage of the full color

Table 3
Effect of the acidic persulfate (5 mg ml^{-1}) digested samples of different phosphorus compounds in seawater matrix on the percentage of full color of phosphoantimonylmolybdenum blue complex at 3–20 min

Treatment (digested P compounds, LNSW)	Sample pH	Time (min)			
		3	5	10	20
Inorganic orthophosphate (IP)	0.98	19	39	78	98
2-Aminoethylphosphonic acid (AEP)	0.98	11	25	67	100
Glycerol-2-phosphate disodium salt (GLP)	0.98	19	37	77	99
Adenosine triphosphate (ATP)	0.98	11	25	64	95
Adenosine diphosphate (ADP)	0.98	16	32	71	97
Adenosine monophosphate (AMP)	0.98	13	23	57	92
Phytic acid dipotassium (IP6)	0.98	25	49	87	99
Sodium tripolyphosphate (Poly-P)	0.98	17	38	79	99

All samples contained 5 μM phosphorus.

at 10 min is IP6 (87%), tripolyphosphate pentasodium salt (Poly-P, 79%), IP (78%), GLP (77%), adenosine diphosphate (ADP, 71%), 2-aminoethylphosphonic acid (AEP, 67%), ATP (64%) and AMP (57%). Most of them achieved full color development ($\geq$95%) after 20 min except the AMP (92%). The pH of sample alone cannot explain the difference in rate of color development in these total phosphorus samples, since the final pH of these digestion solutions with the different phosphorus compounds was very close (around 0.98). All of these results further indicate that the low pH was not the only factor to impede the formation of phosphoantimonylmolybdenum blue complex.

3.5. Effect of persulfate concentration (no digestion) on the formation of phosphoantimonylmolybdenum blue complex

Our results clearly indicated the rate of color formation is decreased with increasing persulfate concentration. One possible explanation is the un-reacted persulfate after digestion causing the rate to decrease. To test this hypothesis, different concentration of potassium persulfate (0–50 mg ml^{-1}) was directly added to a 5-μM IP standard solution and color formation was measured in this modified sample matrix without undergoing digestion.

The effects of added persulfate on color formation were shown in Table 4. The color developments were closed to 100% in 3 min and maintained up to 30 min in variable persulfate concentrations. It should be noted that 50 mg ml^{-1} persulfate used in this study was higher than any concentrations reported in literature for organic phosphorus digestion [12,30]. These results clearly demonstrated that un-reacted persulfate, if any, does not influence the rate of formation of phosphoantimonylmolybdenum blue complex.

3.6. Intermediate products from persulfate digestion on the formation of phosphoantimonylmolybdenum blue complex

Because persulfate itself does not have any effect on the color formation, it is likely that intermediate products of persulfate oxidation caused the slow color formation. In order to verify the role of the intermediate products of persulfate oxidation in the color formation, kinetic measurements were made in the different mixtures of persulfate digested sample and undigested sample. Two samples containing 5-μM IP in DIW and 3% NaCl matrix, respectively, were prepared. After digestion with acidic persulfate (5 mg ml^{-1}), pH of digested sample was about 1.00. A series of sub-samples were prepared by mixing a portion of digested sample with different proportion of undigested sample. Kinetics of the color formation was measured in these samples after their pH was adjusted to the original digested samples.

Table 4
Effect of concentration of potassium persulfate and hydrogen peroxide (per-digestion) on the percentage of full color of phosphoantimonylmolybdenum blue complex at 3–30 min in samples containing 5 μM IP in DIW matrix

Treatments	Time (min)				
	3.0	5.0	10.0	20.0	30.0
Control (5 μM IP)	100	100	100	99	99
Potassium persulfate					
2.5 mg ml^{-1}	99	100	100	100	99
25 mg ml^{-1}	99	100	100	99	98
50 mg ml^{-1}	99	100	100	99	99
Hydrogen peroxide					
15 mg l^{-1}	100	100	99	99	98
75 mg l^{-1}	99	100	100	99	98
600 mg l^{-1}	96	100	100	100	99
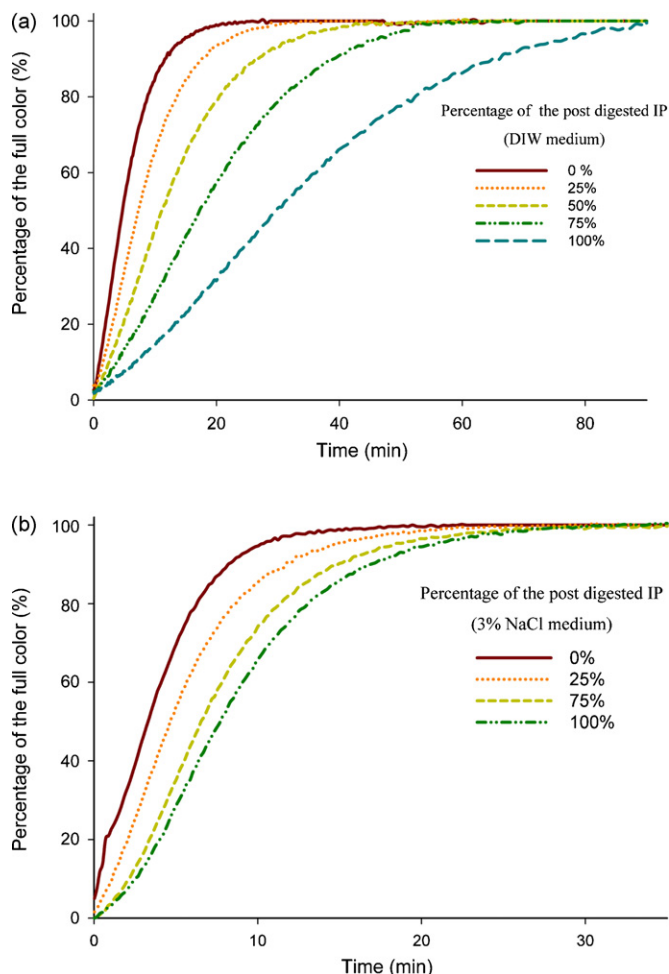
Fig. 4. Time courses of formation of phosphoantimonylmolybdenum blue complex in samples containing different percentage of post-persulfate digested IP sample matrix. (a) Post-persulfate digested IP in DIW matrix and (b) post-persulfate digested IP in 3% NaCl matrix. All samples contained 5 μM IP and adjusted to the same pH (1.00). The absorbances were measured at room temperatures (25 $\pm$ 2 °C).

The formations of the phosphoantimonylmolybdenum blue complex in the mixed samples with different fraction of digested samples are presented in Fig. 4. It is clear that the rates of color formation were the greatest in the undigested samples and decreased with increasing fraction of digested samples in both DIW and NaCl matrices (Fig. 4a and b). In agreement with the effect of persulfate concentration on color formation, the relationship between the percentage of full color formation (y) and the fraction of digested sample (x) can be described with exponential equations. In DIW matrices, the equations are $y_{(2\,min,\ DIW)} = 21.09\,e^{-0.018x}$, $r^2 = 0.996$; and $y_{(5\,min,\ DIW)} = 32.18\,e^{-0.017x}$, $r^2 = 0.988$, for time at 2 and 5 min, respectively. In 3% NaCl matrices, the corresponding equations are $y_{(2\,min,\ 3\%\ NaCl)} = 53.60\,e^{-0.019x}$, $r^2 = 0.999$; and $y_{(5\,min,\ 3\%\ NaCl)} = 68.50\,e^{-0.009x}$, $r^2 = 0.998$. It is clear that impediment effect of digested sample on the color formation was much less in 3% NaCl solution than that in DIW matrix.

Since hydrogen peroxide is usually assumed to be one of the main intermediate products of potassium persulfate oxidation after high temperature digestion [32–35], the effects of hydrogen peroxide (0–600 mg l^{-1}) on the color formation was studied by adding different amount of hydrogen peroxide to the digested samples. The results shown in Table 4 demonstrated that hydrogen peroxide does not influence the formation of phosphoantimonylmolybdenum blue complex. Therefore, the intermediate products other than

hydrogen peroxide should be accounted for the observed difference in rate of color formation.

Persulfate thermal decomposition is complex process involving many factors and complicate mechanisms, though it is generally recognized that the persulfate radical is one of the most probably intermediate products [31–36] and its decomposition follows an Arrhenius relationship between 50 and 130 °C [31,34]. It is suggested that the persulfate has a half-life of about 30 s at 130 °C and 4 h at 75 °C [37]. However, our data and many other studies have demonstrated that the persulfate decomposition requires much longer time [12,14,16,17]. Although the details of chemical composition of the intermediate products are still unknown, experimental data indicate that these intermediate products are quite stable at low pH (<1), but can decompose rapidly at neutral and alkaline pH (7–10). We also noted that the color formation became faster after digested solution was left on bench for 3–4 weeks (data not shown) possible due to decomposition of intermediate products over time.

All of these results further demonstrated that the intermediate products of persulfate decomposition were the main factors that control the rate of phosphoantimonylmolybdenum blue complex formation. The impediment effect will be relieved after pH adjusted to neutral since the intermediate products would be decomposed rapidly. In fact, both the standard method of total P in water and wastewater [18] and EPA method 365.1 [19] recommend neutralization of sample after digestion before determination the total phosphorus by the method of Murphy and Riley. It should further point out that the modified mixed reagent recipe does not provide neutral pH for the decomposition of the intermediate products of persulfate oxidation in the digested samples. Our work further indicated that different kinetics behaviors of phosphoantimonylmolybdenum blue complex in acidic persulfate digested matrix might lead the errors for the standard calibration, if the pH of the digested standard solution did not adjust before adding the mixed reagent, even the modified mixed reagent receipt.

4. Conclusion

The mechanism of slow formation of the phosphoantimonylmolybdenum blue complex in the acidic persulfate digested samples was investigated. The rate of color formation was related to the types of organic phosphorus compounds, the sample matrix, and the pH of the digested samples and, most important, the amount of persulfate used in the digestion.

- The intermediate products of persulfate oxidation caused the rate of the phosphoantimonylmolybdenum blue complex formation to decline in acidic persulfate digested samples.
- By adjusting digested solution's pH to be neutral, the intermediate products of persulfate oxidation can be readily decomposed, and the color of phosphoantimonylmolybdenum blue complex can be fully developed within 3 min.
- No disturbing effects from chlorine on the phosphoantimonylmolybdenum blue formation in seawater were observed and it is not necessary to add extra ascorbic acid prior to the mixed reagent for the seawater total dissolved phosphorus determination.
- It is critical to adjusting pH before mixed reagent addition to be near neutral for both the digested calibration standards and organic phosphorus samples solution due to the different kinetics behavior. Modification of mixed reagent recipe cannot provide near neutral pH for the decomposition of the intermediate products of persulfate oxidation.

In summary, this study provides experimental evidence to support the recommendation made in APHA standard methods that the pH of the digested sample must be adjusted to within a narrow range of sample, in order to avoid the effects of persulfate digestion on the kinetics of phosphoantimonylmolybdenum blue development.

References

[1] D.F. Currie, J. Kalff, Limnol. Oceanogr. 29 (2) (1984) 311–321.
[2] X.-L. Huang, Y. Chen, M. Shenker, Plant Soil 271 (1–2) (2005) 365–376.
[3] K.G. Raghothama, Ann. Rev. Plant Biol. 50 (1999) 665–693.
[4] D.M. Karl, K.M. Björkman, in: D.A. Hansell, C.A. Carlson (Eds.), Biogeochemistry of Marine Dissolved Organic Matter, Academic Press, San Diego, 2002, pp. 249–366.
[5] K.R. Reddy, G.A. O'Connor, C.L. Schelske, Phosphorus Biogeochemistry in Subtropical Ecosystems, Lewis, Boca Raton, Florida, 1999, pp. 707.
[6] B.L. Turner, E. Frossard, D.S. Baldwin (Eds.), Organic Phosphorus in the Environment, CAB International, Wallingford, UK, 2004, p. 380.
[7] I.D. McKelvie, in: B.L. Turner, E. Frossard, D.S. Baldwin (Eds.), Organic Phosphorus in the Environment, CABI International, Wallingford, UK, 2004, pp. 1–20.
[8] W. Maher, L. Woo, Anal. Chim. Acta 375 (1–2) (1998) 5–47.
[9] P.J. Worsfold, et al., Talanta 66 (2) (2005) 273–293.
[10] A. Aminot, D. Kirkwood, S. Carlberg, Mar. Poll. Bull. 35 (1–6) (1997) 28–41.
[11] F.I. Ormaza-González, P. Statham, Water Res. 30 (11) (1996) 2739–2747.
[12] J.J. Ridal, R.M. Moore, Mar. Chem. 29 (1) (1990) 19–31.
[13] L. Solórzano, J.H. Sharp, Limnol. Oceanogr. 25 (4) (1980) 754–758.
[14] M.E. Gales, J. EC, R.C. Kroner, J. Am. Water Works Assoc. 58 (1966) 1363–1368.
[15] F. Koroleff, in: K. Grasshoff, M. Ehrhardt, K. Kremling (Eds.), Methods of Seawater Analysis, Verlag-Chemie, Weinheim, 1983, pp. 167–173.
[16] D.W. Menzel, N. Corwin, Limnol. Oceanogr. 10 (1965) 280–282.
[17] E.J. Monagham, K.C. Ruttenberg, Limnol. Oceanogr. 44 (7) (1990) 1702–1714.
[18] L.S. Clescerl, A.E. Greenberg, A.D. Eaton (Eds.), 4500-P, Standard Methods for the Examination of Water and Wastewater, 20th ed., American Public Health Association, American Water Works Association, Water Environment Federation, Washington, DC, 1998.
[19] J.W. O'Dell (Ed.), Method 365. 1. Determination of Phosphorus by Semi-Automated Colorimetry, Environmental Monitoring Systems Laboratory, Office of Research and Development, USEPA, Cincinnati, OH, 1993.
[20] F. Koroleff, Determination of total phosphorus in natural waters by means of persulfate oxidation, in I.C.E.S. C.M./C. 1968. p. 5.
[21] J.P. Riley, in: J.P. Riley, G. Skirrow (Eds.), Chemical Oceanography, Academic Press, London, 1975, pp. 421–424.
[22] J.M. Estela, V. Cerda, Talanta 66 (2) (2005) 307–331.
[23] M. Chen, S.H. Daroub, V. Nadal, Commun. Soil Sci. Plant Anal. 37 (15–20) (2006) 2351–2363.
[24] M. Zhou, D.M. Struve, Water Res. 38 (18) (2004) 3893–3898.
[25] J. Murphy, J.P. Riley, Anal. Chim. Acta 27 (31–36) (1962) 31–36, 27.
[26] J.-Z. Zhang, C.J. Fischer, P.B. Ortner, Talanta 49 (2) (1999) 293–304.
[27] L. Drummond, W. Maher, Anal. Chim. Acta 302 (1) (1995) 69–74.
[28] X.-L. Huang, J.-Z. Zhang, Microchem. J. 89 (2008) 58–71.
[29] S.C. Pai, C.C. Yang, J.P. Riley, Anal. Chim. Acta 229 (1) (1990) 115–120.
[30] J.D.H. Strickland, T.R. Parsons, Bull. Fish. Res. Board Can., 1972, p. 311.
[31] G.R. Peyton, Mar. Chem. 41 (1–3) (1993) 91–103.
[32] P. Bartlett, J. Cotman, J. Am. Chem. Soc. 71 (1949) 1419–1422.
[33] D.A. House, Chem. Rev. 62 (1962) 185–203.
[34] I.M. Kolthoff, I.K. Miller, J. Am. Chem. Soc. 73 (7) (1951) 3055–3059.
[35] S. Swati, et al., J. Appl. Polym. Sci. 39 (5) (1990) 1061–1077.
[36] N.M. Beylerian, et al., Macromol. Chem. Phys. 203 (1) (2002) 212–218.
[37] A. Doyle, M.N. Weintraub, J.P. Schimel, Soil Sci. Soc. Am. J. 68 (2) (2004) 669–676.

Determination of cadmium, lead, copper and zinc in the acetic acid extract of glazed ceramic surfaces by anodic stripping voltammetric method

Jaroon Jakmunee [a,b,*], Jaroon Junsomboon [a]

[a] Department of Chemistry, Faculty of Science, Chiang Mai University, Chiang Mai 50200, Thailand
[b] Institute for Science and Technology Research and Development, Chiang Mai University, Chiang Mai 50200, Thailand

ARTICLE INFO

ABSTRACT

An anodic stripping voltammetric method has been developed for determination of cadmium, lead, copper and zinc in acetic acid extract of glazed ceramic surfaces. An aliquot of 4% (v/v) acetic acid solution was kept in a ceramic ware for 24 h in the dark, then 10 mL of the extracted solution was placed in a voltammetric cell. The solution was purged with oxygen free nitrogen gas for 3 min before deposition of the metals was carried out by applying a constant potential of -1.20 V versus Ag/AgCl to the hanging mercury drop electrode (HMDE) for 45 s. A square wave waveform was scanned from -1.20 to 0.15 V and a voltammogram was recorded. A standard addition procedure was used for quantification. Detection limits of 0.25, 0.07, 2.7 and 0.5 μg L^{-1} for cadmium, lead copper and zinc, respectively, were obtained. Relative standard deviations for 11 replicate determinations of 100 μg L^{-1} each of all the metals were in the range of 2.8–3.6%. Percentage recoveries obtained by spiking 50 μg L^{-1} of each metal to the sample solution were in the range of 105–113%. The method was successfully applied to ceramic wares producing in Lampang province of Thailand. It was found that the contents of cadmium, lead, copper and zinc released from the samples were in the range of <0.01–0.16, 0.02–0.45, <0.14 and 0.28–10.36 μg dm^{-2}, respectively, which are lower than the regulated values of the Thai industrial standard. The proposed method is simpler, more convenient and more sensitive than the standard method based on FAAS.

© 2008 Elsevier B.V. All rights reserved.

1. Introduction

Cadmium and lead are well-known toxic metals. These metals are found in glazed ceramic surfaces and are controlled by law for permissible amounts released from some ceramic products. Glaze is a thin layer of liquid, which is put on a piece of pottery and becomes hard and shiny when the pottery is heated in a hot oven. In Thailand, ceramic products are mainly produced in northern provinces, e.g., Lampang, Sukhothai and Chiang Mai. Release of cadmium and lead from ceramic ware, glass–ceramic ware and glass dinnerware intended to be used in contact with food is tested according to the Thai industrial standard (TIS 32-2546) or ISO-6486-1: 1999 [1]. The method involving extraction of the metals from the glaze by 4% (v/v) acetic acid, which is kept in the ceramic ware to be tested for 24 h in the dark, and determination of the metals in the extracted solution by flame atomic absorption spectrophotometry (FAAS). This method is tedious and time-consuming, and with relatively high

detection limits. To improve detection limit and precision, sample pretreatment of the extract, e.g., evaporating up of acetic acid and adding with hydrochloric acid before FAAS determination may be performed. On-line separation/preconcentration procedures, e.g., using column packing with Pb-Spec resin [2], Muramac A-1 chelating resin [3], thioureasulfonamide resin [4] and bead injection with renewable sorption material [5] are usually employed for the determination of trace amounts of cadmium/lead by FAAS or ETAAS. Flow injection analysis with on-line preconcentration column using Pb-Spec resin and spectrophotometric detection based on formation of Pb(II)–4-(2-pyridylazo)resorcinol complex was developed for determination of lead in acetic acid leachate of glazed ceramic surfaces [6]. Detection limit of 8 μg L^{-1} and relative standard deviation for five replicate determinations of 0.8 mg L^{-1} of 0.35% were reported. However, the method is quite complicated.

On the other hand, anodic stripping voltammetry (ASV) which has an in situ preconcentration (electrodeposition) step can be applied directly for simultaneous determination of cadmium and lead at trace levels [7–13]. Metal ions were electrochemically deposited on a working electrode, e.g., a hanging mercury drop electrode (HMDE), a mercury film electrode [7–9], or a more environment friendly bismuth film electrode [10–13]. Then, the determination was done in the stripping step by scanning potential

* Corresponding author at: Department of Chemistry, Faculty of Science, Chiang Mai University, Huay Keaw Road Suthep, Chiang Mai 50200, Thailand. Tel.: +66 5394 1909; fax: +66 5394 1910.
E-mail address: scijjkmn@chiangmai.ac.th (J. Jakmunee).

to positive (anodic) direction, where re-oxidation of the deposited metals was occurred at a specific potential for each metal. However, this method can detect free metal ions only and is suffered from interferences such as surface active organic substances [8]. Some modified electrodes have been developed for improving sensitivity and selectivity in the analysis of complicated samples [9–11]. Fortunately, the extract of ceramic glaze was free from organic substances, so the ASV method with a HMDE should be suitable for this sample. An electrolyte medium such as acetate buffer [7–11] is widely utilized in ASV determination of Cd and Pb. In this work, the acetic acid which has been used as an extractant for leaching of the metals from ceramic glaze surfaces, was investigated to be applied as an electrolyte in the ASV analysis.

In this paper, we developed a simple method based on anodic stripping voltammetry for simultaneous determination of cadmium, lead, copper and zinc in acetic acid leachate of glazed ceramic wares. The 4% (v/v) acetic acid extracted solution could be also used an electrolyte for voltammetric analysis, so the determination of the metals could be carried out without any sample pretreatment. A HMDE which is available in most analytical laboratories has been employed as a working electrode, making the developed method simple and convenient for quality control of ceramic wares.

2. Experimental

2.1. Chemicals

All chemicals used were of analytical reagent grade. Deionized water (obtained from a system of Milli-Q, Millipore, Sweden) was used throughout. Stock standard solution of lead(II) ($1000\,mg\,L^{-1}$) was prepared by dissolving 0.1615 g of lead nitrate (Merck, Germany) in 0.1 M nitric acid 100 mL. Stock standard solution of cadmium(II) ($1000\,mg\,L^{-1}$) was prepared by dissolving 0.1991 g of cadmium chloride (J.T. Baker, Canada) in 0.1 M hydrochloric acid 100 mL. Stock standard solution of copper(II) ($1000\,mg\,L^{-1}$) was prepared by dissolving 0.3968 g of copper sulphate (Merck, Germany) in 0.1 M sulfuric acid 100 mL. Stock standard solution of zinc(II) ($1000\,mg\,L^{-1}$) was prepared by dissolving 0.4443 g of zinc sulphate (Ajex Finechem, Australia) in 0.1 M sulfuric acid 100 mL. The working standard solutions were prepared daily by diluting the stock standard solution of each metal with 4% (v/v) acetic acid. The extracted solution (4% (v/v) acetic acid) was prepared by diluting 40 mL of glacial acetic acid in water and adjusting the final volume to 1000 mL. An oxygen free nitrogen (OFN) gas (99.9995%, TIG, Thailand) was used for purging the solution to remove dissolved oxygen.

2.2. Voltammetric system

A voltammetric analyzer (VA 757, Metrohm, Switzerland) including a voltammetric cell with a HMDE as a working electrode (WE), a platinum rod electrode as an auxiliary electrode (AE), and a Ag/AgCl electrode (3 M KCl) as a reference electrode (RE), was employed for anodic stripping voltammetric analysis. The voltammetric analyzer was controlled by a personal computer, using a VA Computrace version 2.0.000, SR1 software (8.757.8023, 757 VA Computrace, Metrohm).

2.3. Extraction procedure

Extraction of metals from glazed ceramic surfaces was carried out according to the standard method [1]. Briefly, the ceramic ware to be tested was cleaned to be free from grease or other matter likely to affect the test, then it was filled with 4% (v/v) acetic acid solution to produce an acid depth of >6 mm, covered the specimen and allowed to stand in the dark at $22\pm2\,^{\circ}C$ for 24 ± 0.5 h. Then, the extracted solution was collected in a polyethylene bottle for further voltammetric determination of the released metals. The surface area of the ceramic ware was accurately measured to $0.01\,dm^{-2}$.

2.4. Voltammetric analysis procedure

An aliquot of 10 mL of the extracted solution was put in a voltammetric cell and the solution was purged with OFN for 3 min. Then, a fixed potential of −1.20 V was applied to the WE for a period of 45 s, while the solution was stirred at 2000 rpm (deposition step). After that the stirring was stopped for 5 s, followed by anodically scanning of the potential from −1.20 to 0.15 V, employing a square wave waveform with amplitude of 40 mV, step potential of 10 mV, and frequency of 50 Hz (stripping step). A voltammogram was recorded. Peak potential and peak current corresponding to each metal was evaluated from the voltammogram. Standard addition procedure was carried out by adding standard solution of each metal to the sample solution, then the deposition and stripping steps were performed. Standard addition was repeated for four times. Concentration of each metal in sample was evaluated from the standard addition graph, with subtracting of concentration of metal in the blank solution. Amounts of the metal released from ceramic wares were reported as $\mu g\,dm^{-2}$, which were calculated from total amounts of the metal released into the extracted solution divided by contacted surface area.

3. Results and discussion

3.1. Effect of some parameters on voltammetric analysis

ASV method is based on electrochemical reduction of metal ions at WE to deposit the metals on the electrode surface with subsequent anodic striping by scanning the potential to anodic direction to allow electrooxidation of the deposited metals at a characteristic potential of each metal, as recorded as a voltammogram in this step. Conditions for deposition and stripping steps of ASV were investigated. A square wave waveform was employed in the stripping step, as it provided fast scanning and good sensitivity for the reversible redox reaction. A square wave waveform with amplitude of 40 mV, step potential of 10 mV, and frequency of 50 Hz was used. A solution of 4%(v/v) acetic acid that employing as the extracted solution was also used as an electrolyte. Standard solutions of Cd, Pb, Cu and Zn were added to the electrolyte solution and voltammetric measurement was carried out. Effect of deposition potential was investigated in the range of −0.90 to −1.30 V. It was found that the more negative potential used the higher sensitivity was obtained. Deposition potential of −1.20 V was chosen because too negative potential may lead to deposition of some interferences or evolving of hydrogen gas at the WE in the high acidic medium. Deposition time was studied for the determination of $50\,\mu g\,L^{-1}$ of each metal. A plot of peak current versus deposition time is depicted in Fig. 1. It was found that peak currents of all the metals, except Cu, are linearly proportional to deposition time up to 2 min. At too long deposition time, the deposited metals may saturate at the HMDE so no further increase in peak current was observed. While most ASV methods used acetate buffer as an electrolyte medium, in this work acetic acid (4%, v/v) should be employed because it has been used as an extractant for leaching of metals from ceramic surfaces. Effect of concentration of acetic acid on peak current of $50\,\mu g\,L^{-1}$ of each metal is investigated. Acetic acid in concentration range of 1–6% (v/v) did not affect either on peak potential or peak current of
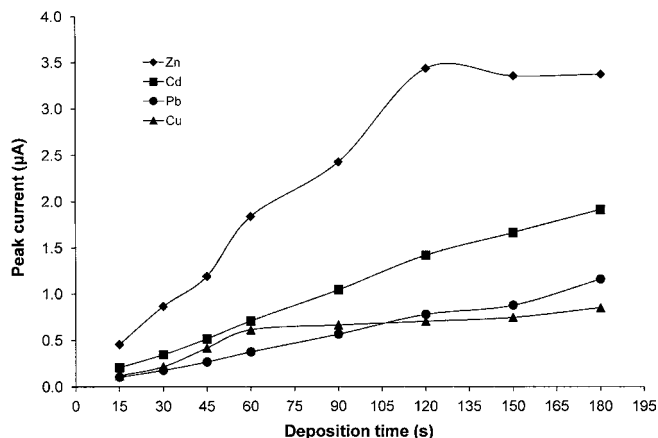
Fig. 1. Effect of deposition time on peak current. Condition: deposition potential −1.20 V, stirring rate 2000 rpm, scan rate 0.01 V s^{-1}, potential scan range −1.20 to 0.15 V.

all the metals studied. However, the higher concentration of acetic acid used, the higher zinc content in the electrolyte solution (blank) was observed. Acetic acid of 4% (v/v) was selected to be used as both the extractant and the electrolyte for ASV analysis.

3.2. Analytical characteristics

Under the selected condition: 4% (v/v) acetic acid as an electrolyte solution, deposition potential of −1.20 V, deposition time of 45 s, square wave waveform with amplitude of 40 mV, step potential of 10 mV, and frequency of 50 Hz, voltammograms were obtained as shown in Fig. 2. Linear calibration graphs in the concentration range of 0–200 µg L^{-1} of each metal were obtained as the followed calibration equations: Cd: $Y = 0.0094X + 0.0062$, $r^2 = 0.9996$, Pb: $Y = 0.0048X + 0.0065$, $r^2 = 1.0000$, Cu: $Y = 0.0033X + 0.0081$, $r^2 = 0.9990$, and Zn: $Y = 0.0159X + 1.5462$, $r^2 = 0.9999$, where Y is peak current (µA) and X is concentration (µg L^{-1}) of each metal. Detection limits calculated from three times standard deviation of blank/slope of the calibration graph [14] were 0.25, 0.07, 2.7 and 0.5 µg L^{-1} for Cd, Pb, Cu and Zn, respectively. Sensitivity and detection limit could be
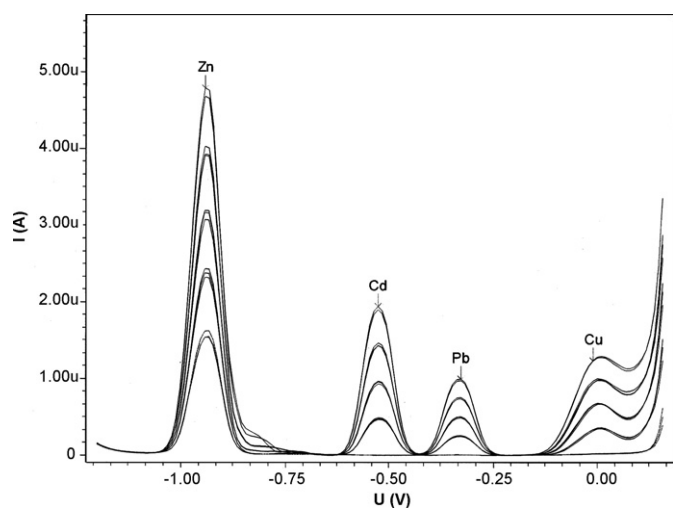
Fig. 2. Voltammograms of zinc, cadmium, lead and copper in 4% (v/v) acetic acid. Concentrations of each metal from bottom to top: 0, 50, 100, 150 and 200 µg L^{-1}. Condition: deposition potential −1.20 V, deposition time 45 s, stirring rate 2000 rpm, scan rate 0.01 V s^{-1}, potential scan range −1.20 to 0.15 V.

Table 1
Amounts of some metals released from ceramic wares

Sample	Released amounts (µg dm^{-2})*			
	Zn	Cd	Pb	Cu
1	10.36 ± 0.12	0.16 ± 0.01	0.394 ± 0.001	N.D.
2	6.31 ± 0.23	N.D.	N.D.	N.D.
3	6.00 ± 0.01	N.D.	0.447 ± 0.001	N.D.
4	0.88 ± 0.04	N.D.	0.006 ± 0.001	N.D.
5	2.84 ± 0.04	N.D.	0.272 ± 0.001	N.D.
6	0.46 ± 0.02	N.D.	0.290 ± 0.001	N.D.
7	5.65 ± 0.23	N.D.	0.109 ± 0.002	N.D.
8	6.56 ± 0.06	N.D.	0.261 ± 0.001	N.D.
9	1.18 ± 0.14	N.D.	0.299 ± 0.009	N.D.
10	1.30 ± 0.06	N.D.	0.065 ± 0.001	N.D.
11	2.89 ± 0.02	0.02 ± 0.00	0.096 ± 0.016	N.D.
12	5.25 ± 0.16	N.D.	0.064 ± 0.002	N.D.
13	4.17 ± 0.04	N.D.	0.097 ± 0.003	N.D.
14	0.64 ± 0.06	N.D.	0.056 ± 0.003	N.D.
15	2.41 ± 0.05	N.D.	0.126 ± 0.002	N.D.
16	0.28 ± 0.05	N.D.	0.076 ± 0.001	N.D.
17	2.50 ± 0.02	N.D.	0.200 ± 0.006	N.D.
18	7.24 ± 0.08	N.D.	0.431 ± 0.001	N.D.
19	3.63 ± 0.24	N.D.	0.096 ± 0.001	N.D.
20	3.53 ± 0.18	N.D.	0.127 ± 0.001	N.D.
21	1.33 ± 0.06	N.D.	0.041 ± 0.001	N.D.
22	2.29 ± 0.04	N.D.	0.316 ± 0.002	N.D.
23	0.84 ± 0.02	N.D.	0.020 ± 0.001	N.D.

*Mean of triplicated results, N.D. = not detected.

improved by using longer deposition time as described in Section 3.1. Relative standard deviations for 11 replicate determinations of 100 µg L^{-1} of each metal were 3.0, 2.8, 3.6 and 2.8% for Cd, Pb, Cu and Zn, respectively. Recoveries obtained from spiking of the metal standard solutions (50 µg L^{-1} each) into the extracted solution were found in the range of 105–113%. The analysis time is 5 min per sample by using standard addition procedure for determination of four metals, which is much faster than the standard method based on FAAS [1].

3.3. Application to real samples

The proposed method was applied to the determination of some metals extracted from the surface of ceramic wares. Standard addition method was employed for quantification in order to account for the effect of sample matrix. However, the results obtained by using calibration graph method were correlated well with those from the standard addition method (for Zn, $Y = 0.9322X − 0.8767$, $r^2 = 0.9631$). The results from standard addition method are summarized in Table 1. It was found that the contents of cadmium, lead, copper and zinc released from the samples were in the range of <0.013–0.16, 0.02–0.45, <0.14 and 0.28–10.36 µg dm^{-2}, respectively, which are lower than the permissible values of the Thai industrial standard. The developed method was convenient to be used and could be applied as an alternative method to the standard method for testing the releasing of cadmium and lead from ceramic products.

4. Conclusion

Anodic stripping voltammetric method was proposed for determination of Cd, Pb, Cu and Zn in an acetic acid extract of glazed ceramic wares. The extract can be analyzed directly by voltammetric method, where the extractant, 4% (v/v) acetic acid, also acts as an electrolyte solution. The method is simple, fast, sensitive and selective, and can simultaneously determine four metals with high accuracy using either standard addition or calibration methods. The developed method may be used in the routine determination of Cd

and Pb extracted by acetic acid from glazed ceramic wares, as an alternative to the standard method (TIS 32-2546).

Acknowledgements

References

[1] Thai industrial Standard, TIS-32-2546: Test method for ceramic ware, glass–ceramic ware and glass dinnerware in contact with food—Release of lead and cadmium.
[2] Y. Bakircioglu, S.R. Segade, E.R. Yourd, J.F. Tyson, Anal. Chim. Acta 485 (2003) 9.
[3] Y.H. Sung, S.D. Huang, Anal. Chim. Acta 495 (2003) 165.
[4] B.F. Senkal, M. Ince, E. Yavuz, M. Yaman, Talanta 72 (2007) 962.
[5] P. Ampan, J. Ruzicka, R. Atallah, G.D. Christian, J. Jakmunee, K. Grudpan, Anal. Chim. Acta 499 (2003) 167.
[6] M. Kuramochi, K. Tomioka, M. Fujinami, K. Oguma, Talanta 68 (2005) 287.
[7] J. Jakmunee, S. Suteerapataranon, Y. Vaneesorn, K. Grudpan, Anal. Sci. 17 (2001) i399.
[8] J. Jakmunee, L. Patimapornlert, S. Suteerapataranon, N. Lenghor, K. Grudpan, Talanta 65 (2005) 789.
[9] B.S. Sherigara, Y. Shivaraj, R.J. Mascarenhas, A.K. Satpati, Electrochim. Acta 52 (2007) 3137.
[10] S.B. Hočevar, I. Švancara, K. Vytřas, B. Ogorevc, Electrochim. Acta 51 (2005) 706.
[11] G.H. Hwang, W.K. Han, J.S. Park, S.G. Kang, Talanta 76 (2008) 301.
[12] L. Cao, J. Jia, Z. Wang, Electrochim. Acta 53 (2008) 2177.
[13] A. Economou, Trends Anal. Chem. 24 (2005) 334.
[14] G.D. Christian, Analytical Chemistry, 6th ed., Wiley, New York, USA, 2004.

Dedicated mother wavelet in the determination of antimony in the presence of copper

Małgorzata Jakubowska *, Robert Piech

Faculty of Materials Science and Ceramics, AGH University of Science and Technology, al. Mickiewicza 30, 30-059 Kraków, Poland

ABSTRACT

In this paper, a new signal-processing procedure is applied to the optimization of voltammetric determination of antimony in the presence of copper and the parallel determination of these two elements. The proposed numerical algorithm for the separation of the overlapping peaks utilizes the continuous wavelet transform and the inverse continuous wavelet transform. As the base function, the specially defined dedicated mother wavelet is used. In its construction the ideal, simulated voltammetric peak is intensively exploited. This approach, corresponding to the wavelet theory, gives satisfactory signals separation, even in the cases when they constitute one peak. The possibility of Sb(III) determination is presented in the case of different distances between copper and antimony peaks and also in 10-, 20- and 50-fold excesses of Cu. The parallel determination of Cu(II) and Sb(III) is possible even in the case of a 10-fold excess of copper. The quality of the obtained results fulfills the requirements of validation.

© 2008 Elsevier B.V. All rights reserved.

1. Introduction

Antimony, a naturally occurring element, is present in the aquatic environment as a result of rock weathering, soil runoff, atmospheric deposition and human activities. This element is found in two oxidation states (III and V) in environmental, biological and geochemical samples [1] but it is a non-essential element for plants, animals, and humans. Antimony and its compounds are considered strong pollutants. The mechanism of antimony toxicity is not well known, but it is related to the chemical state—the Sb(III) species is usually more toxic than Sb(V). Much analytical research has been devoted to the determination and speciation of antimony and its compounds, as a result of environmental and metabolic studies. Hydrid generation atomic absorption spectrometry (HG-AAS) is one of the most widely accepted techniques used for these purposes [2–4]. Other optical methods, such as the electrothermal atomic absorption spectrometry (ET-AAS) [5], inductively coupled plasma atomic emission spectroscopy (ICP-AES) [6] and inductively coupled plasma mass spectroscopy (ICP-MS) [7] have also been described. A variety of voltammetric methods have also been proposed, including anodic stripping voltammetry (ASV) on a hanging mercury drop [9–11] and mercury film electrodes [12], and adsorptive cathodic stripping voltammetry at a hanging mercury drop electrode [13–15]. The ASV method with hydrochloric acid as a supporting electrolyte is very easy to apply. Unfortunately, copper ions cause strong interferences with Sb(III) because of their similar reduction potential. To avoid this inconvenience, it is necessary to use a high concentration of hydrochloric acid (more than 1 M) [16].

Signal processing is a useful step which gives the possibility to obtain desirable results of determination in the optimized experiment. The main problems that are resolved in this type of work are the smoothing of signals and the separation of the overlapping peaks originating from antimony and copper. Depending on the experimental conditions, the distance between peaks may be greater or lower. The lowest distance or even complete overlapping is obtained in the case of the optimal experimental conditions (lowest concentration of HCl), which are more expected.

In electroanalysis, the close reduction energies of some electrochemical processes are the source of the overlapping signals, therefore the signal-processing numerical algorithms are applied to resolve these curves and enhance the resolution of the method of determination. In the effect, the quantitative analysis may be successfully realized. All the mathematical methods used in the case of the resolution of overlapping signals belong to soft modeling or hard modeling groups. From hard methods, curve fitting, Fourier self-deconvolution, or wavelet-based algorithms are often applied. The soft approach uses regression methods based on latent variables. Some combinations of the aforementioned approaches are also applied in quantitative determinations.

The curve-fitting methods used in the resolution of the overlapping peaks are based on the simulation of complex signals as the sum of single peak models, using iterative least-square

* Corresponding author. Fax: +48 12 6341201.
E-mail address: jakubows@agh.edu.pl (M. Jakubowska).

minimization [17–20]. In calculation, the arbitrary fitting function or simulated curves are applied. The other formalism applied in the separation of the overlapping signals is the Fourier self-deconvolution (FSD) technique. The principle of this method is to multiply the Fourier transform of the original signal by the weighting function in the frequency domain, which decays more slowly, and then to transform the multiplied signal back to the time domain. A detailed description of this algorithm in the case of voltammetric data was given by Pižeta [21] and is based on the theoretical backgrounds carried out by Engblom and Ivaška [22,23]. Some examples present the successful application of deconvolution in square-wave voltammetry [24], linear sweep voltammetry (LSV) [25] and differential pulse (DP) polarography [26,27].

There are some disadvantages of the FSD method, and therefore obtaining a successful effect is sometimes difficult. The results of deconvolution seriously depend on the selection of the apodization function, its width, the pre- and post-processing of the curves (analyzed and analyzing), and the filtration method (the cut-off frequency of the low-pass filter and its shape). Also, expert experience plays a great role and has influence on the final effect. The deconvolution function may be theoretical or even a measured curve of a single signal (not overlapped). An inaccurate correspondence of experimental data to prospective theoretical functions may generate problems. This often happens because voltammetric signals vary and depend on experimental condition. Additionally, it is necessary to know the number of signals present in the initial curve. This method is highly sensitive to noises in the original signal. An inappropriate effect in deconvolution is the high increase of noises. The procedure is ineffective in the resolution of overlapping peaks corresponding to electrode processes with various numbers of electrons when overlapping signals have a different half-width. In this case, it is very difficult to define an adequate analyzing function. Therefore, other algorithms also play an important role in the deconvolution of the overlapping voltammograms.

A new chemometric methodology based on the use of peak parameters as direct input data into different multivariate calibration methods is proposed in [28]. This strategy was studied as an alternative to procedures that apply pretreatment techniques to the full voltammograms. Good predictive and effective models were obtained.

The previously mentioned resolution methods still remain unsatisfactory, particularly when the analysis of interest is severely masked by components present in larger concentrations. Wavelet transformation (WT) has shown great advantages in this field and has also been intensively applied in the processing of electrochemical signals. The wavelets theory [29,30], which in the 1980s was only a mathematical formalism, found its place in many practical applications, from physics, medicine, image processing, acoustics, climatology, and seismology to the compression of data. The main feature of the wavelet transform is that it decomposes a signal into contributions which represent the information of different frequencies. They are labeled by a scale and a position parameter.

In literature there are many examples of the application of WT in the processing of electrochemical signals [31–40]. The application of WT to voltammetry was described in a work by Fang and Chen [31]. They investigated the wavelet packet transform for white noise and developed an adaptive wavelet filter which is useful for the study of fast electron transfer processes. Bao et al. [32] performed a comparison between spline wavelet smoothing and Fourier smoothing in processing the differential pulse stripping voltammograms and obtained high precision and good reproducibility. Also, a B-spline wavelet basis was applied in voltammetry [33,34]. An on-line wavelet transform algorithm and development of voltammetric analyzer with the on-line wavelet

transform (WT-voltammetric analyzer) is described [35] and successfully applied in analysis of mixtures of Pb(II) and Tl(I) and also in a mixture of Cd(II) and In(III).

WT is often applied in the resolution of overlapping signals, mainly in cases where FSD fails. In [36,37] the CWT with Marr wavelet is applied to find the peak positions in mixed solutions in voltammetry. The various multivariate calibration [38] methods (multilinear regression (MLR), partial least-square regression (PLS) and artificial neural networks (ANN)) may be applied when the wavelet transform is used for future selection prior to calibration. The DP anodic stripping and seriously overlapping voltammograms recorded with the mixture of lead and thallium were considered. In Ref. [39], a signal ratio method combined with a wavelet transform was proposed for a resolution of a voltammetric signal overlapped by other component, to remove or reduce the noise and background. To estimate the number of peaks and find the individual peak positions in an overlapped DPV curve, a new method called maximum spectrum of continuous wavelet transform was developed by extracting the maximum coefficients of continuous wavelet transformation [40].

The main scope of this work consists of the development of a new signal-processing procedure to be applied to the optimization of the voltammetric determination of antimony in the presence of copper and the parallel determination of the two ions. In the presented approach, the time–frequency signal analysis realized by the wavelet transform with specially defined mother wavelet is applied. The numerical calculations are realized through the application of the continuous wavelet transform (CWT) and the inverse continuous wavelet transform (iCWT). As the mother wavelet in these numerical operations, a specially defined mother wavelet, dedicated for voltammetry, is used. The main principle of this method is based on dissection of the signal into components of different frequency and taking for further interpretation only those components in which the peaks are separated and the noise levels are the lowest. The dedicated mother wavelet makes possible the precise resolution of the overlapping peaks originating from antimony and copper. Therefore, the presented signal-processing procedure based on wavelets may be useful in the determination of antimony in the presence of copper and parallel determination of antimony and copper. Also, the method of definition of the dedicated mother wavelet is described. The results of optimization of the signal-processing procedure which relies on selection of the proper parameters of CWT are presented. Evaluation of the proposed algorithm is realized in different experimental conditions. Because the antimony and copper peak position depends on the concentration of HCl, this parameter was intensively tested in the aim to discover how low concentration gives the possibility of signal separation by application of the proposed numerical procedure. Additionally, all measurements were realized by the short pre-concentration time. The short-lasting experimental procedure, done with a little consumption of the aggressive reagents followed by the proposed signal-processing algorithm, will have a practical application.

2. Theory

Signal processing is also one of the main fields in which wavelets are used, particularly in electroanalysis, when complex multicomponent systems are considered. Many papers present different applications of WT, but all of them exploit the base functions defined in the literature as a mother wavelet. The main novelty of the presented algorithm is the application of a specially constructed mother wavelet dedicated [41] to the problem under consideration, i.e. denoising and the separation of overlapping peaks.

In the work the CWT was applied, because this procedure does not limit the signal interpretation, leaving the possibility of a free choice of transformation parameters. The CWT of the input signal $x(t)$ is expressed as

$$\mathrm{CWT}_x(a, b) = \int\limits_{-\infty}^{\infty} x(t)\Psi_{ab}^*(t)\mathrm{d}t \tag{1}$$

where the asterisk stands for complex conjugation, while $\Psi_{ab}(t)$ can be derived from the mother wavelet $\Psi(t)$ by scaling and shifting according to the following formula:

$$\Psi_{ab}(t) = \frac{1}{|\sqrt{a}|}\Psi\left(\frac{t-b}{a}\right) \tag{2}$$

The result of the CWT are wavelet coefficients $\mathrm{CWT}_x(a, b)$, which are the functions of a and b. The a and b are called scale and translation parameters, respectively. There are no restrictions to the values of the indices a, b except that a must be higher than zero. The coefficient $1/a$ may be interpreted as a measure of frequency. The parameter b, on the other hand, indicates the location of the wavelet window along the time axis. Thus, by changing a and b, coefficients $\mathrm{CWT}_x(a, b)$ can be computed on the entire time–frequency plane. The observation of the transformed curve by the selected scales makes it possible to analyze the successive components of the signal.

Since the purpose of the inverse transform is to reconstruct the original function from its wavelet coefficients, it involves a two-dimensional integration over the scale, parameter a, and the translation, parameter b. The expression for the inverse wavelet transform iCWT is

$$x(t) = \frac{1}{c}\int\limits_{-\infty}^{\infty} \mathrm{d}b \int\limits_{-\infty}^{\infty} \frac{1}{a^2}\mathrm{CWT}_x(a, b)\Psi_{ab}(t)\mathrm{d}a \tag{3}$$

where c is a constant that depends on the choice of wavelet. Eq. (3) is essentially a superposition integral. Integration with respect to a sums all the contributions of the wavelet components at location b, while the integral with respect to b includes all locations along the y-axis. In the work, summing with respect to a is realized in a different way. Through the application of CWT and the various scales, the obtained components are analyzed. The components which include only noise are substituted by zero. Therefore, it may be said that only these components which are useful and are not distorted by noise take part in the reconstruction of the signal. The inverse CWT may be very useful because not only one frequency component is considered in calibration process. Whole useful information is included and therefore the quality of determination may be most satisfactory. In this case only distorting component are removed.

It is very important that WT is a linear transformation, which means that the linear relation between peak heights is preserved after CWT and iCWT operations. The calibration line may be calculated in the wavelet coefficient space, or after the reconstruction of the signal by iCWT.

In the approach described in the work, the model voltammetric curve was selected as the pattern shape. The generation of that curve was performed using the algorithm of simulation of electrode processes introduced by Feldberg [42] and [43]. This simulated signal was used as the input for the calculation of the mother wavelet, which was done through the application of the numerical method announced by Misiti et al. [44]. The algorithm yields as a result a function which is a mother wavelet, and is similar to the pattern signal in the sense of least squares. In Fig. 1, the model voltammetric peak is presented together with the obtained mother wavelet, which is also a peak-shaped discrete curve, taking the zero value
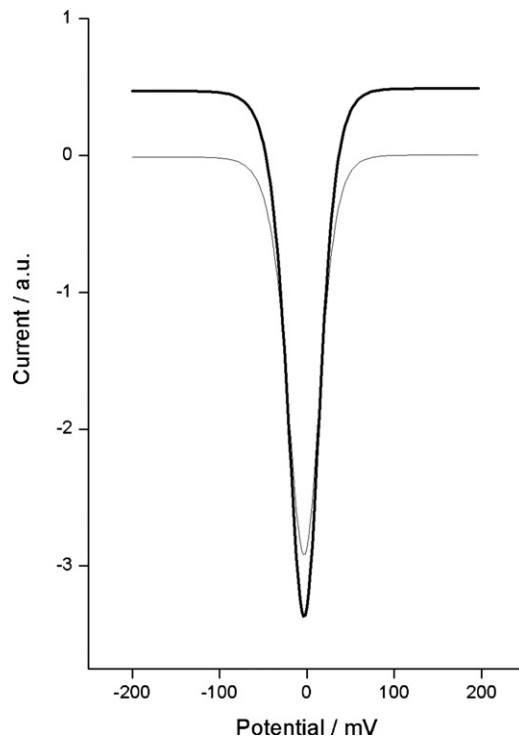
Fig. 1. Simulated voltammetric peak and the mother wavelet (thick line) defined on the base of it.

outside the area presented on the figure. The new wavelet dedicated for voltammetry is correctly defined—its square norm equals one and fulfils the condition of the zero mean.

In the work, the main proposed signal-processing procedure is the separation of overlapping peaks. Therefore, the degree of separation will be expressed using the coefficient R defined as [45]:

$$R = \frac{t_{\mathrm{p2}} - t_{\mathrm{p1}}}{0.5(w_{\mathrm{p1}} + w_{\mathrm{p2}})} \tag{4}$$

where t_{p1} and t_{p2} are the two peak positions on the time axis, and w_{p1} and w_{p2} are the widths of peak measured at the bottom. The results obtained by applying the proposed algorithm based on the dedicated wavelet may be compared with the effects presented in Ref. [37], where the Marr wavelet was utilized for determining the peak positions. In that work, successful separation was obtained for $R = 0.3$ (the same heights of the peaks) and for $R = 0.4$ (for different peak heights).

Selection of the optimal scale for CWT plays an important role to get maximum resolution and sensitivity. Since in the described experiment, peaks overlap with different overlap degrees, and the relation between peak heights also differs, the optimum value of the scale is dependent on the concentration of analytes and the concentration of the HCl. It is necessary to estimate the interval of optimal scales for the WT. In this work, signal-to-noise ratio (S/N) was an evaluation criterion used in the optimization process. As a signal amplitude, the difference between the peak extreme and the extreme value which separates peaks was calculated. The level of the noise was expressed by the standard deviation of it. The mentioned signal-to-noise ratio was calculated for each curve obtained by application of the CWT algorithm with the scales from 1 to 200 increasing by 1. The maximum of S/N points the optimal scale. The calculation was done separately for Cu(II) peak and Sb(III) peak. It was repeated for each curve in the set for calibration because the relation between the heights of the peaks differs. The described procedure is automatic but also a manual correction may be done

especially in the cases when the optimal scales in the set for calibration are different for each concentration and changes in the wide range. Often the low scales give the satisfactory separation effect but the level of the noise may be large. In greater scales curves are smoother and the absolute amplitude of them is greater, but the separation is unsuccessful. Therefore, the described criterion may be applied with great attention.

The generation of the dedicated wavelet and the wavelet transform were performed using Matlab for MS Windows, Version 7.3, with Wavelet Toolbox 3.1. The CWT and iCWT algorithm was written in Matlab software by the authors. Other computations were carried out by also homemade software written in C programming language, which expands the advanced version of the numerical environment EAGRAPH dedicated for the Electrochemical Analyzer EA9 (MTM-ANKO, Poland). For the remaining calculations, the OriginPro software (OriginLab Corporation, USA), Version 7.5, was used.

3. Experimental

3.1. Measuring apparatus and software

A multipurpose Electrochemical Analyzer M161 with the electrode stand M164 (both MTM-ANKO, Poland) was used for all voltammetric measurements. The classical three-electrode quartz cell with a volume of 20 mL, consisting of a controlled growth mercury drop electrode (CGMDE) as the working electrode, a double-junction reference electrode Ag/AgCl/KCl (3 M) with replaceable outer junction (3 M KCl), and a platinum wire as an auxiliary electrode. The ambient temperature was ~22 °C. The MTM-ANKO *EAGRAPH* software enabled electrochemical measurements, data acquisition and advanced processing of the results.

3.2. Chemicals and glassware

All reagents used were of analytical grade and were prepared using four times distilled water (two last stages from quartz). A 0.01 M standard stock solution of antimony(III) was prepared by dissolving SbCl$_3$ (Aldrich) in 0.4 M HCl. A 0.01 M standard stock solution of copper(II) was prepared by dissolving copper chloride (POCh, Poland). Solutions with lower antimony and copper concentration were made weekly by appropriate dilution of the stock solution. A new solution was analyzed in each measurement. Glassware was first immersed in 6 M nitric acid, and then rinsed repeatedly with distilled water.

3.3. Standard procedure of measurements

Measurements were performed using differential pulse anodic stripping voltammetry (DP ASV). The procedure of refreshing the mercury drop electrode was carried out before each measurement. A CGMDE electrode prepared in this way was used to determine antimony and copper. The determination was performed in the supporting electrolyte: 0.3–0.75 M (total volume 10 ml) contained in a quartz voltammetric cell. The potential of the electrode was changed in the following sequence: accumulation potential, $E_{acc} = -0.4$ V accumulation time, $t_{acc} = 45$ s. During the accumulation step, antimony and copper were deposited while the solution was being stirred (ca. 500 rpm) using a magnetic stirring bar. Then, after a rest period of 5 s, a differential pulse voltammogram was recorded in the anodic direction from −0.40 to 0.0 V. The other experimental parameters were as follows: step potential, $E_s = 2$ mV, pulse potential, $\Delta E = -25$ mV, time step potential, 40 ms (20 ms waiting + 20 ms sampling time). The measurements were carried out in deaerated solutions.

4. Results and discussion

Unfortunately, Cu(II) ions are a source of strong interference to Sb(III) determination, because of their similar reduction potential. Consequently, the recorded peaks overlap. This problem may be resolved in the experimental way, but in this case greater amounts of the high purity reagents are required, which increases the cost of the analysis. In this study, some experiments are described in which the separation of the peaks was realized by applying the proposed numerical algorithm.

The determination of Sb(III) was realized in the samples in which Cu(II) was present in a concentration of 20 ppb. The composition of the supporting electrolyte was: 10 ml of 0.3, 0.5 and 0.75 M HCl. Smaller concentrations of HCl yielded shorter distances between the peaks of Cu(II) and Sb(III), which made the determination of these elements more difficult, or practically impossible (for concentrations of HCl lower than 0.5 M). In addition, the problem of the numerical separation of the peaks becomes more complicated when they lie near each other or even have the same position. An algorithm which enables the resolution of this task is proposed. In all steps of calculation, the dedicated mother wavelet defined earlier was applied. The CWT was realized in the scales 1–250, in steps of 1.

Experimental curves obtained in the case of the addition of 10 ml 0.75 M HCl and for 0.5, 1, 1.5, 2, 2.5, 3 and 3.5 ppb Sb(III) are presented in Fig. 2a. The Cu and Sb peaks overlap ($R = 0.36$). The optimal scale for CWT calculated for curves obtained for increasing concentrations of Sb are equal to 30, 40, 46, 51, 55, 59 and 63, respectively. Because of the need for preservation of the relation between peak heights the same scale must be used for each signal. From the interval of optimal scales (30–63) the scale 35 was chosen (Fig. 2b) which is optimal for lower concentrations of Sb. In these cases, the separation is more difficult because the difference between peak heights is greater and the signal from Sb is lower. Additionally, in this scale the effect of increasing the Cu peak height was removed. The height of the peak is constant, which corresponds to the experiment. The next step of signal processing involved the application of the inverse CWT. Before this step, the signal components which delivered information only about noise (in this case, the scales from 1 to 19) and those in which peaks were not separated (over 80) were substituted by zero. The effect of the application of CWT and then the inverse CWT for the selected range of scales is presented in Fig. 2c. After this transformation, the peaks were also successfully separated. The obtained set of curves was ready for calibration. The transformation was then also performed for the curves recorded for unknown concentrations.

In the case of 10 ml of 0.5 M HCl, the distance between Cu and Sb peaks is shorter ($R = 0.25$). The optimal scales calculated for each concentration of Sb are changing from 15 to 57. The continuous wavelet transform realized in the scale 20, and next inverse continuous wavelet transform in the scales 15–25 gives the effect of successful peak separation. Consequently, in these cases the determination of Sb may be successfully performed. In the experiment in which 10 ml of 0.3 M HCl were added, effective application of the signal-processing procedures was the most difficult. This was due to the fact that the positions of the Cu and Sb peaks were so near that they constituted one peak. In this case the degree of separation, R, is equal to 0.15. Furthermore, in this instance the application of CWT in connection with inverse CWT using the dedicated mother wavelet gave successful peak separation. As the optimal transformation parameters, the scales 15–20 were used.

In each of the described experiments in which signal processing based on the CWT and dedicated mother wavelet was an important step, the calibration line was calculated. To satisfy the condition of linearity, for each curve in the set for calibration the same scale
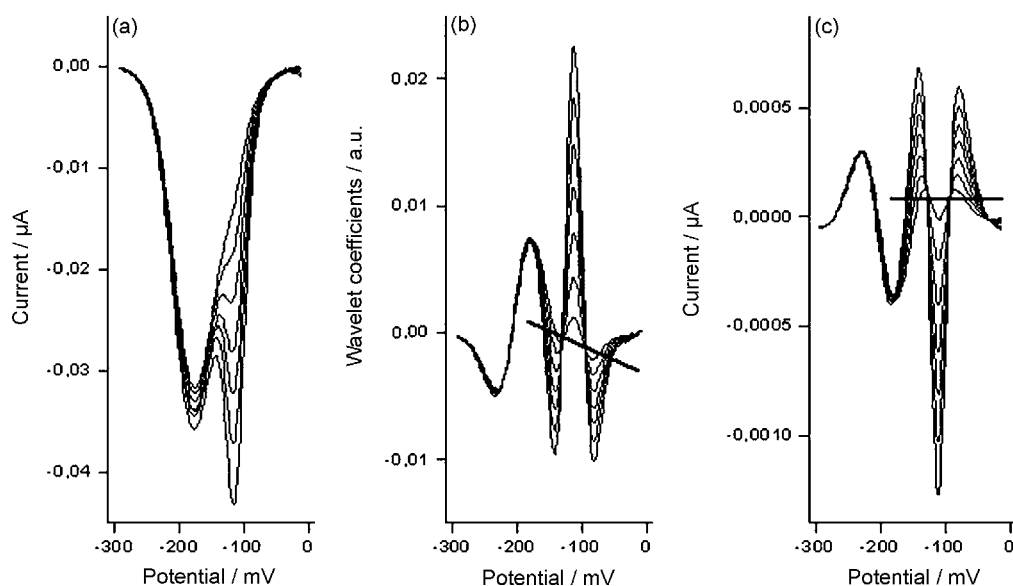
Fig. 2. The curves obtained for 0.5, 1, 1.5, 2, 2.5, 3 and 3.5 ppb Sb(III) in the presence of 20 ppb Cu(II) in 10 ml of 0.75 M HCl: (a) experimental, (b) the same curves after CWT transformation in the scales 35 and (c) the same curve after application of iCWT transformation in the scales 20–80.

in CWT must be chosen. Additionally, the curve recorded for an unknown concentration must be transformed in the same way as the other curves used in the calculation of the regression line. The evaluation of the obtained results was done by calculating the correlation coefficient *r*, which represents the quality of the calibration. In estimation of limit of detection, the propagation of errors approach was used [46]. The recovery for concentrations of Sb equal to 1.25 and 2.75 ppb were then calculated. The signal-to-noise ratio was also estimated for the middle concentration in each set of curves (2 ppb of Sb). The results are presented in Table 1. The obtained results were: *r* > 0.999, DL = 0.1 ppb, recovery between 96% and 101.4%. The detection limit for Sb(III) obtained in the comparative research was about 0.2 ppb (underground water, 10 ml of 1 M HCl, pre-concentration time 40 s) [47] and 0.01 ppb (coastal surface seawater samples, 10 ml of 0.5 M HCl + 0.5NaCl, very long pre-concentration time 600 s.) [16].

Next, the determination of Sb was realized in the presence of 10 ml of 0.5 M HCl and the considerable excess of Cu. The signals for calibration were recorded for 0.5, 1, 1.5, 2, 2.5, 3 and 3.5 ppb Sb(III). In the subsequent experiments the concentration of Cu(II) was 20, 40 and 100 ppb. The application of WT was preceded by optimization of the scale which results are presented in Fig. 3. The optimal scale for each concentration of Cu increases with increasing concentration of Sb. Similarly the optimal scales for greater excess of Cu are lower. Equivalently, it may be said that greater scales are dedicated for separation of the peaks which heights differ not so much. The optimal scale for CWT for each set of curves for calibration was selected from the interval determined by the values obtained for 0.5 and 3.5 ppb of antimony. Considerably lower scales were selected to reach satisfactory results for peaks which separation was more difficult (i.e. for lower concentrations of Cu). The

Fig. 3. Optimal values of scale for determination of Sb in 10 ml of 0.5 M HCl and considerable excess of Cu: squares, 20 ppb; circles, 40 ppb; triangles, 100 ppb.

inverse CWT was realized for scales in which peaks are clearly separated. The interval was larger than for optimization of scale for CWT. The results of calibration are presented in Table 2. In Fig. 4a, a set of curves is shown recorded in 0.5 M HCl for 0.5, 1, 1.5, 2, 2.5, 3 and 3.5 ppb of Sb and 100 ppb of Cu. A voltammograms have a shape of one peak. After iCWT realized by scales 12–35 peaks are successfully separated (Fig. 4b). The position of the peaks is identical like

Table 1
Evaluation of signal-processing procedures (CWT combined with iCWT) applied in the experiment of determination Sb in the presence of Cu in 10 ml of 0.3, 0.5 or 0.75 M

Electrolyte	*r*	DL (ppb)	Recovery (%)	S/N
10 ml 0.3 M HCl	0.9991	0.1	98–101	91
10 ml 0.5 M HCl	0.9996	0.1	96–101	186
10 ml 0.75 M HCl	0.9995	0.1	98.7–101.4	988

Table 2
Evaluation of signal-processing procedures (CWT and CWT followed by iCWT) applied in the experiment of determination of Sb in10 ml of 0.5 M HCl with excess of Cu

	r	DL (ppb)	Recovery (%)	S/N
Sb, 20-fold excess of Cu				
CWT	0.9997	0.08	95–101	63.3
CWT + iCWT	0.9989	0.14	90–106	99.5
Sb, 50-fold excess of Cu				
CWT	0.9994	0.11	95–102.5	58.6
CWT + iCWT	0.9983	0.17	95–104	49.9
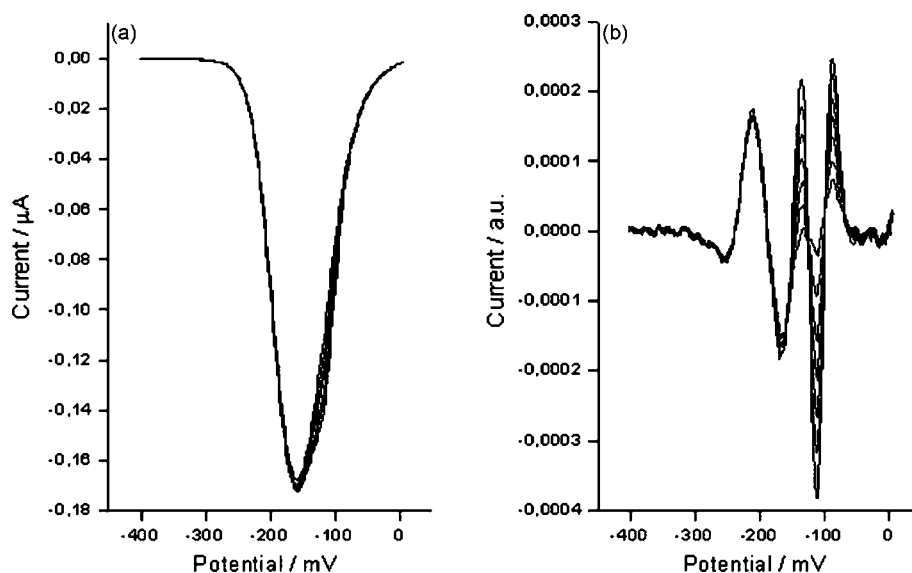
Fig. 4. Determination of Sb in 10 ml of 0.5 M HCl and 50-fold excess of Cu: (a) voltammograms Sb (0.5, 1, 1.5, 2, 2.5, 3 and 3.5 ppb) and constant concentration 100 ppb of Cu and (b) the same curves after CWT transformation followed by inverse CWT (scales 12–35).

in separate measuring voltammograms for Cu and Sb. The linearity of Sb(III) is greater than 0.998. Linearity and recovery fulfills the levels demanded in validation of the method.

The signal-processing procedures were then tested in the case of the parallel determination of the Cu and Sb. For calibration, Cu concentrations of 5, 10, 15, 20, 25, 30 and 35 ppb were selected (Fig. 5a). The corresponding concentrations of Sb were ten times lower in each case. The experiment was realized in a solution containing 10 ml of 0.5 M HCl. The optimization of the scale was realized separately for copper and antimony by calculation of the signal-to-noise ratio for each curve from the calibration set and for the scale from 1 to 200 increased by 1. The results of the optimization process are presented in Fig. 6. The optimal scale is the same for each concentration of Cu and for this element is equal to 43 or 44. There is a not great difference with the optimal scale for antimony which for all concentration takes the value 46 or 47. Lack of change in the scales is

connected with the fact that that relation between the peak heights in the curves is the same. The curves were transformed using CWT with the optimal scale 44 (Fig. 5b). The coefficients which are usually used to evaluate the quality of determination are presented in Table 3. The calculated values are separately given for calibration and determination of Cu and Sb, and additionally for two different signal-processing procedures: CWT only, and CWT combined with inverse CWT realized using the optimized parameters. The obtained coefficients fulfill the validation criteria which are most often required. The linearity expressed by the correlation coefficient is always greater than 0.995, the detection limit is equal to 1.6 ppb or even lower for copper, and 0.12 ppb for antimony. The DL achieved for Sb is one order of magnitude lower than that which is expected, as Cu and Sb concentrations can be found in such ratios in natural samples. Additionally, the obtained level of the determined concentrations is sufficient for the mentioned samples. The recov-
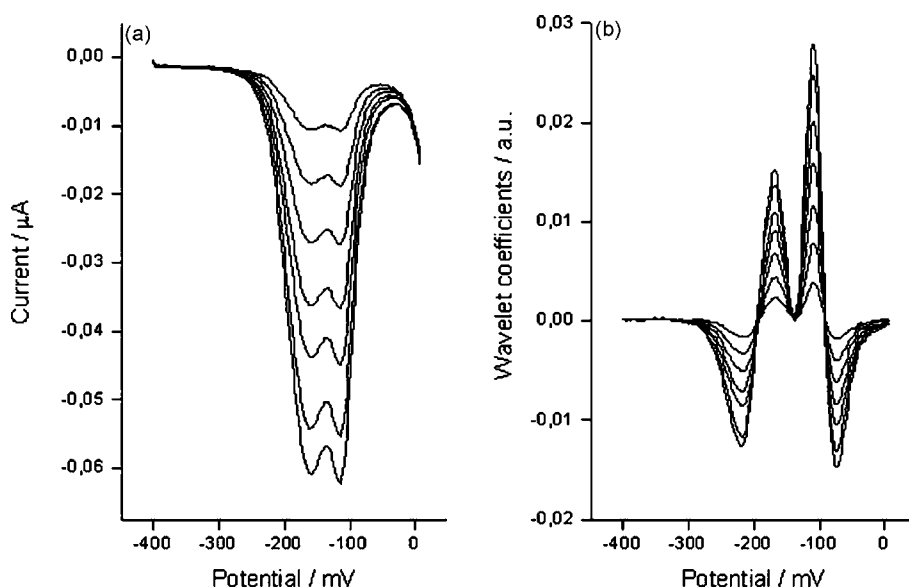
Fig. 5. Parallel determination of Cu and Sb in 10 ml of 0.5 M HCl: (a) voltammograms for Cu (5, 10, 15, 20, 25, 30 and 35 ppb) and Sb (0.5, 1, 1.5, 2, 2.5, 3 and 3.5 ppb) and (b) the same curves after CWT transformation by the scale 44.
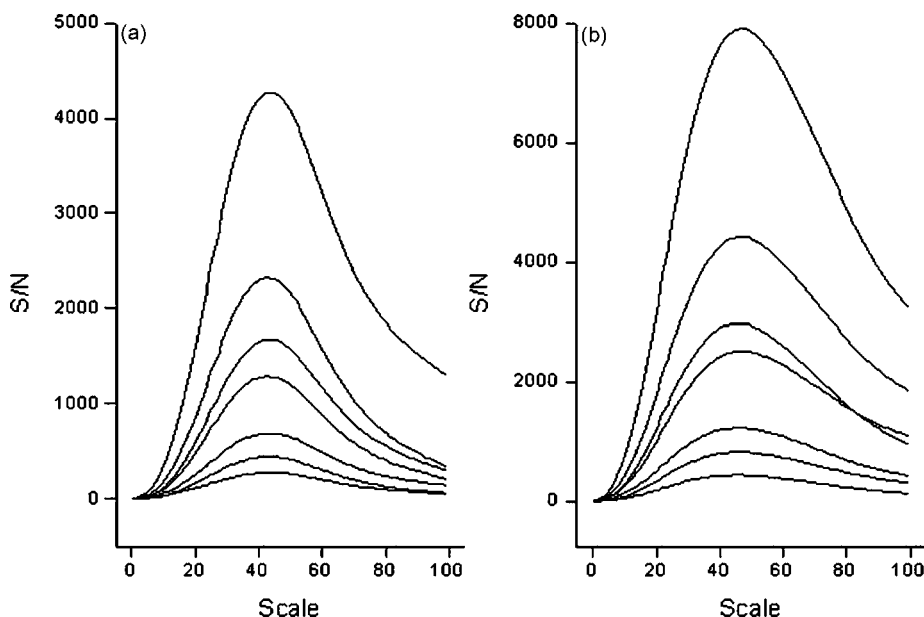
Fig. 6. Optimization of the scale in parallel determination of Cu and Sb in 10 ml of 0.5 M HCl: (a) S/N for Cu (5, 10, 15, 20, 25, 30 and 35 ppb) and (b) S/N for Sb (0.5, 1, 1.5, 2, 2.5, 3 and 3.5 ppb). S/N increases for increasing concentrations.

Table 3
Evaluation of signal-processing procedures (CWT and CWT connected with iCWT) applied in the experiment of parallel determination of Cu and Sb in 10 ml of 0.5 M HCl

	r	DL (ppb)	Recovery for 12.5 ppb (%)	Recovery for 27.5 ppb (%)	S/N
Cu					
CWT	0.9953	2.9	102.2	105.9	154.7
CWT + iCWT	0.9986	1.6	98.7	103.6	76.8
Sb					
CWT	0.9990	0.13	96.8	103.6	252.9
CWT + iCWT	0.9991	0.12	99.2	103.6	168.8

ery was measured and calculated for different concentrations, i.e. 12.5 and 27.5 ppb for Cu, and 1.25 and 2.75 ppb for Sb. The obtained recovery was between 96.8% and 105.9%. The signal-to-noise ratio changed in the range from 77 to 253. Finally, it was observed that the results did not differ much, regardless of which of the two different signal-processing procedures – CWT only, or CWT followed by the inverse CWT – was applied.

5. Conclusions

The new signal-processing procedure applied for the purpose of optimizing the determination of antimony in the presence of copper and the parallel determination of these two elements was described. The possibility of Sb(III) determination in the case of 10-, 20- and 50-fold excess of Cu(II) and the parallel determination of Cu(II) and Sb(III) even in the case of a 10-fold excess of copper was presented.

The algorithm operates using CWT only or CWT in connection with the inverse CWT. As the wavelet function, the specially dedicated for voltammetry mother wavelet was defined. The optimization of the experiment was realized in order to limit the usage of HCl. The mentioned limitation is connected with the decrease of the distance between Cu and Sb peaks positions. In this work, it was shown that even in the case of very little additions of HCl (10 ml of 0.3 M), when the two mentioned peaks constitute one peak, separation is still possible. The proposed method with dedicated wavelet allows for separate peaks when the degree of overlap R is equal to 0.15 and the heights of the peaks are different, what is far better than for any previously proposed method. The results

of the parallel determination of copper and antimony carried out with the application of the proposed signal-processing procedure, which intensively uses the specially constructed dedicated mother wavelet, are also satisfactory (r equal even to 0.9991, recovery between 96.9% and 105.9%, S/N = 155 for Cu and 253 for Sb). The optimized transformation parameters result in a DL of 1.6 ppb for copper, and 0.12 ppb for antimony. These detection limits are sufficient, e.g. for the determination of Cu and Sb in natural oceanic water samples. It is very important that the time of determination is very short because of the short pre-concentration step. The short-lasting experimental procedure done with a little consumption of the aggressive reagents followed by the proposed signal-processing algorithm has a practical application.

References

[1] M. Filella, N. Belzile, Y.-W. Chen, Earth Sci. Rev. 57 (2001) 125.
[2] R.E. Sturgeon, S.N. Willie, S.S. Berman, Anal. Chem. 57 (1985) 2311.
[3] S.C. Apte, A.G. Howard, J. Anal. At. Spectrom. 1 (1986) 221.
[4] M.B. De la Calle Guntiñas, Y. Madrid, C. Cámara, Anal. Chim. Acta 252 (1991) 161.
[5] I. Martinsen, B. Radziuk, Y.J. Thomassen, Anal. At. Spectrom. 3 (1988) 1013.
[6] L. Pretorius, P.L. Kemster, H.R. Van Vliet, J.F. Van Staden, Fresen. J. Anal. Chem. 342 (1992) 391.
[7] K. Chiba, I. Inamoto, M. Sasaki, J. Anal. At. Spectrom. 7 (1992) 115.

[9] G. Gillain, G. Duyckaerts, A. Disteche, Anal. Chim. Acta 106 (1979) 23.
[10] A.M. Bond, S. Kratsis, O.M.G. Newman, B.V. Pfund, Electroanalysis 9 (1997) 13.
[11] A.M. Bond, S. Kratsis, O.M.G. Newman, Electroanalysis 9 (1997) 681.
[12] R.C. Briner, S. Chouchoiy, R.W. Webster, R.E. Popham, Anal. Chim. Acta 172 (1985) 31.
[13] G. Capodaglio, C.M.G. Van den Berg, G. Scarponi, J. Electroanal. Chem. 235 (1987) 275.
[14] W. Wagner, S. Sander, G. Henze, Fresen. J. Anal. Chem. 354 (1996) 11.
[15] S. Sander, Anal. Chim. Acta 394 (1999) 81.
[16] F. Quentel, M. Filella, Anal. Chim. Acta 452 (2002) 237.
[17] S.P. Perone, W.F. Gutknecht, Anal. Chem. 42 (1970) 906.
[18] S.P. Perone, P.A. Boudreau, Anal. Chem. 51 (1979) 811.
[19] A.M. Bond, B.S. Grabarić, Anal. Chem. 48 (1976) 1624.
[20] S.V. Romanenko, A.G. Stromberg, E.V. Selivanova, E.S. Romanenko, CILS 73 (2004) 7.
[21] I. Pižeta, Anal. Chim. Acta 285 (1994) 95.
[22] S.O. Engblom, A.U. Ivaška, in: M.R. Smyth, J.G. Vos (Eds.), Electrochemistry, Sensors and Analysis (Analytical Chemistry Symposia Series, vol. 25), Elsevier, Amsterdam, 1986.
[23] S.O. Engblom, J. Electroanal. Chem. 296 (1990) 371.
[24] D.P. Binkley, R.E. Dessy, Anal. Chem. 52 (1980) 1335.
[25] S.O. Engblom, Anal. Chem. 64 (1992) 2530.
[26] I. Pižeta, M. Lovrić, M. Branica, J. Electroanal. Chem. 296 (1990) 395.
[27] X.-Q. Lu, X.-W. Wang, J.-W. Kang, J.-Z. Gao, Anal. Chim. Acta 404 (2000) 249.
[28] J.M. Palacios-Santander, L.M. Cubillana-Aguilera, I. Naranjo-Rodríguez, J.L. Hidalgo-Hidalgo-de-Cisneros, CILS 85 (2007) 131.
[29] I. Daubechies, Ten Lectures on Wavelets, SIAM Press, Philadelphia, 1992.
[30] D.F. Walnut, An Introduction to Wavelet Analysis, Birkhäuser, Boston, 2004.
[31] H. Fang, H.Y. Chen, Anal. Chim. Acta 346 (1997) 319.
[32] L.J. Bao, J.Y. Mo, Z.Y. Tang, Anal. Chem. 69 (1997) 3053.
[33] X. Zou, J. Mo, Anal. Chim. Acta 340 (1997) 115.
[34] X. Zheng, J. Mo, CILS 45 (1999) 157.
[35] X. Shao, C. Pang, S. Wu, X. Lin, Talanta 50 (2000) 1175.
[36] L. Nie, S. Wu, J. Wang, L. Zheng, X. Lin, L. Rui, Anal. Chim. Acta 450 (2001) 185.
[37] S. Wu, L. Nie, J. Wang, X. Lin, L. Zheng, L. Rui, J. Electroanal. Chem. 508 (2001) 11.
[38] M. Cocchi, J.L. Hidalgo-Hidalgo-de-Cisneros, I. Naranjo-Rodríguez, J.M. Palacios-Santander, R. Seeber, A. Ulrici, Talanta 59 (2003) 735.
[39] X. Zhang, Y. Fuchigami, J. Jin, Anal Bioanal. Chem. 380 (2004) 751.
[40] L. Xiaoquan, L. Hongde, X. Zhonghua, Z. Qiang, J. Chem. Inf. Comput. Sci. 44 (2004) 1228.
[41] M. Jakubowska, J. Electroanal. Chem. 603 (2007) 113.
[42] S.W. Feldberg, Electroanal. Chem. (Ed. Bard) 3 (1969) 199.
[43] D. Britz, Digital Simulation in Electrochemistry (Lecture Notes in Physics), Springer, 2005.
[44] M. Misiti, Y. Misiti, G. Oppenheim, J.M. Poggi, Les ondelettes et leurs applications, Hermes Science, Paris, 2003.
[45] M. Zhu (Ed.), Instrumental Analysis, Higher Education Press, Beijing, 1983.
[46] G.J. Long, J.D. Winefordner, Anal. Chem. 55 (1983) 712A.
[47] D. Rurikova, L. Dziackova, Chem. Listy 97 (2003) 1017.

Comparison of solvent mixtures for pressurized solvent extraction of soil fatty acid biomarkers

Richard Jeannotte [a,1], Chantal Hamel [a,2], Suha Jabaji [b], Joann K. Whalen [a,*]

[a] *Department of Natural Resource Sciences, Macdonald Campus, McGill University, 21 111 Lakeshore Road, Ste-Anne-de-Bellevue, Québec, H9X 3V9, Canada*
[b] *Department of Plant Science, Macdonald Campus, McGill University, 21 111 Lakeshore Road, Ste-Anne-de-Bellevue, Québec, H9X 3V9, Canada*

ARTICLE INFO

ABSTRACT

The extraction and transesterification of soil lipids into fatty acid methyl esters (FAMEs) is a useful technique for studying soil microbial communities. The objective of this study was to find the best solvent mixture to extract soil lipids with a pressurized solvent extractor system. Four solvent mixtures were selected for testing: chloroform:methanol:phosphate buffer (1:2:0.8, v/v/v), chloroform:methanol (1:2, v/v), hexane:2-propanol (3:2, v/v) and acetone. Soils were from agricultural fields and had a wide range of clay, organic matter and microbial biomass contents. Total lipid fatty acid methyl esters (TL-FAMEs) were the extractable soil lipids identified and quantified with gas chromatography and flame ionization detection. Concentrations of TL-FAMEs ranged from 57.3 to 542.2 n mole g^{-1} soil (dry weight basis). The highest concentrations of TL-FAMEs were extracted with chloroform:methanol:buffer or chloroform:methanol mixtures than with the hexane:2-propanol or acetone solvents. The concentrations of TL-FAMEs in chemical groups, including saturated, branched, mono- and poly-unsaturated and hydroxy fatty acids were assessed, and biological groups (soil bacteria, mycorrhizal fungi, saprophytic fungi and higher plants) was distinguished. The extraction efficiency for the chemical and biological groups followed the general trend of: chloroform:methanol:buffer ≥ chloroform:methanol > hexane:2-propanol = acetone. Discriminant analysis revealed differences in TL-FAME profiles based on the solvent mixture and the soil type. Although solvent mixtures containing chloroform and methanol were the most efficient for extracting lipids from the agricultural soils in this study, soil properties and the lipid groups to be studied should be considered when selecting a solvent mixture. According to our knowledge, this is the first report of soil lipid extraction with hexane:2-propanol or acetone in a pressurized solvent extraction system.

© 2008 Elsevier B.V. All rights reserved.

1. Introduction

Soil lipids are chemically and biologically diverse, since they come from plant, animal and microbial cells. The characterization of fatty acid biomarkers from the total lipids, phospholipids and neutral lipids, as well as their stable isotope composition [1], can reveal changes in the structure, nutritional status and living biomass of soil microbial communities [2–4]. Fatty acids that are unique or very abundant in the cell membranes of certain microbial groups (e.g., bacteria, fungi, algae, protozoa) serve as biomarkers for detecting the presence of these groups. Some biomarkers are specific for more narrowly defined groups, such as those that distinguish arbuscular mycorrhizal fungi from heterotrophic fungi or biomarkers that can discriminate microorganisms at the genus and species levels [5].

Fatty acid biomarkers are measured following the extraction and transesterification of soil lipids. The classical method of extracting soil lipids uses a solvent mixture containing a citrate or phosphate buffer, chloroform and methanol [6–8]. However, Tunlid and White [9] mentioned that the efficiency of chloroform:methanol:buffer mixture in extracting soil lipids was never fully investigated. Chloroform:methanol mixtures are efficient at extracting lipids from many biological media [10,11], but it is not known if these solvents are the best for extracting soil lipids, considering that clay particles and organic matter could interfere with lipid extraction [7,12,13]. Pressurized solvent extraction (PSE) is a technology that acclerates soil lipid extraction, reduces human contact with solvents, and reduces the volume of solvents used [14–17]. A comparative study of soil lipid extraction efficiency with different solvent mixtures in a PSE system remains to be performed.

Three solvent mixtures may be good alternatives to the chloroform:methanol:buffer mixture commonly used to extract soil lipids, namely chloroform:methanol, hexane:2-propanol and acetone. Lipids are extracted more rapidly with a chloroform:methanol mixture than with chloroform:methanol:buffer, which requires a lengthy post-extraction step of phase separation to remove non-lipid molecules such as amino acids and carbohydrates extracted by the buffer solution. Hexane:2-propanol is effective in extracting lipids from biological tissues and is considered to have the same extraction efficiency as chloroform:methanol, but with lower toxicity [6,18–20]. However, the performance of hexane:2-propanol varies among biological tissues. For example, Schäfer [21] showed that more fatty acids contained in cereal and yolk lipids were extracted using hexane:2-propanol than chloroform:methanol, but muscle lipids were extracted more efficiently with chloroform:methanol than other solvent mixtures. Acetone has lower toxicity than the other mixtures mentioned above, and is capable of extracting lipids from *Eucalyptus globulus* wood [22] and wheat grains [23]. Despite these findings, there are no reports describing the application of hexane:2-propanol or acetone to extract soil lipids, so this remains to be tested.

The objective of this research was to compare solvent mixtures for extracting lipids from soil with a PSE system and to characterize the extracts based on the chemical structure (e.g., saturated, mono unsaturated and poly unsaturated fatty acids) as well as the biological origin (e.g., fatty acid biomarkers of bacteria, mycorrhizal fungi, saprophytic fungi, higher plants/faunal biota) of their TL-FAMEs.

2. Experimental

2.1. Soil collection and handling

The soils used in this study (mixed, frigid Typic Endoaquents) were collected from the top 15 cm of agricultural fields in southwestern Québec, Canada in August 1999 (soil 4) and September 1999 (soils 1, 2 and 3), prior to crop harvest. Each soil sample was a composite of seven cores (15 cm long, 3 cm intenal diameter) collected randomly from the field. After collection, half of each soil sample was air-dried, passed through a 2 mm mesh sieve, stored at room temperature and used for soil physical and chemical analysis, while the other half was frozen immediately and stored at $-20\,^\circ$C until microbial biomass carbon and lipid analysis was conducted. Agricultural practices at the collection sites and selected soil characteristics are reported in Table 1.

2.2. Reagents and glassware

All organic solvents used in this study were high pressure liquid chromatography (HPLC) grade. Glassware was rinsed with methanol and chloroform or placed in a furnace at 360 $^\circ$C for at least 2 h before use. Laboratory equipment that did not tolerate heating

was rinsed with methanol and then chloroform, and allowed to dry at room temperature (20 $^\circ$C) before use.

2.3. Pressurized solvent extraction (PSE) system

Soil lipids were extracted with an ASE 200 accelerated solvent extractor (Dionex Corporation, Sunnyvale, CA, USA). Operating conditions consisted of one heating cycle at 80 $^\circ$C and 8280 kPa during 5 min, three static cycles of 15 min each at the same temperature and pressure, rinsing of the transfer lines and sample cell with the solvent and purging with N_2 for 180 s between each sample [14]. Triplicate samples of each composite soil (6–8 g of freeze-dried soil) were packed into separate 11 mL stainless steel ASE vessels, sealed at both ends with circular cellulose filters to prevent soil particles from entering the extractor. The following solvent mixtures were used: (a) chloroform:methanol:phosphate buffer (1:2:0.8, v/v/v), (b) chloroform:methanol (1:2, v/v), (c) hexane:2-propanol (3:2, v/v) and (d) acetone. Additional chloroform and buffer were added to the extracts from solvent mixture (a) to facilitate separation of the aqueous and organic phases, so the final composition of the chloroform:methanol:phosphate buffer was 2:2:1.8 (v/v/v). This procedure produced 48 extracts (four soils × three replicates × four solvent mixtures), each containing 20–25 mL of soil lipids and solvents. The organic phase was evaporated under N_2 gas.

2.4. Quantification and identification of TL-FAMEs from extractable soil lipids

TL-FAMEs were prepared by mild alkaline methanolysis of total soil lipid extracts [8]. After drying extracts completely under N_2, they were redissolved with 1 mL of iso-octane containing 25 ng μL^{-1} of methyl-nonadecanoate (C19:0) internal standard. The resulting mixture of TL-FAMEs (5 μL injected) were analyzed in split mode (50:1) with a gas chromatograph (Hewlett Packard 6890) equipped with a Simplicity Wax capillary column (cross-linked polyethylene glycol; length, 30 m; film thickness, 0.33 μm; Supelco 2-4326), He as carrier gas (constant at 9.5 psi) and a flame ionization detector. The oven temperature was initially set at 60 $^\circ$C, then raised to 150 $^\circ$C (10 $^\circ$C min^{-1}) and held for 5 min, after which it was raised by 3 $^\circ$C min^{-1} to a final temperature of 230 $^\circ$C and held for 20 min. Inlet and detector temperatures were 200 $^\circ$C and 250 $^\circ$C, respectively. The linear flow velocity was at 32 cm s^{-1}.

Identification of peaks was based on comparison of retention times to known standards (Supelco 37 Component FAME Mix cat.#47885-U; Supelco Bacterial Acid Methyl Esters cat.#47080-U; Matreya PUFA-2 cat.#1081; Matreya Bacterial Acid Methyl Esters CP Mix cat.#1114; Matreya cis-11-Hexadecenoic Acid cat.#1208 and Matreya 10-Methyloctadecanoate cat.#1763), used directly or derivatized if needed, containing FAMEs with chain length ranging from 8 to 24 carbon atoms. These standards permitted the identification and quantification of 53 different FAMEs from the total

Table 1
Selected properties of the soils (Typic Endoquents, 0–15 cm depth) used in the experiment

Soil	Tillage system[a]	Crop	pH[b]	OM[c] (g kg^{-1})	Sand[d] (g kg^{-1})	Silt[d] (g kg^{-1})	Clay[d] (g kg^{-1})	Textural class	SMB-C[e] (mg C kg^{-1})
1	CT	Soybean	8.0	23.5	211	339	450	Clay	153.7 ± 10.3
2	NT	Soybean	6.8	45.1	543	283	174	Sandy loam	215.3 ± 18.4
3	NT	Soybean	7.0	69.1	0	205	795	Clay	384.8 ± 11.1
4	CT	Bean	6.1	263.3	149	418	433	Silty clay	452.3 ± 23.2

[a] CT: conventional tillage, NT: no-tillage.
[b] Soil:water extracts (1:2 soil:solution ratio) [43].
[c] Organic matter (OM) determined by loss on ignition (360 $^\circ$C for 4 h).
[d] Particle-size analysis [44].
[e] SMB-C is soil microbial biomass C, mean (±standard error of mean) of three replicate measures. SMB-C = chloroform labile C/K_{EC}, using a K_{EC} of 0.45 [45].

soil lipid extract, hereafter defined as a TL-FAME (single FAME) or TL-FAMEs (groups of FAMEs with similar chemical or biological characteristics).

The concentration of each identified TL-FAME (nmoles per gram dry soil (DS)) was calculated relative to the C19:0 internal standard, which was present in each sample at 25 ng μL^{-1} (0.080 nmol C19:0 μL^{-1}). The contribution of each identified TL-FAME to the total concentration of TL-FAMEs (summed concentration of all extracted soil lipids that were identified with the standards listed above) in a sample was expressed as mole fraction (relative richness, % mole) and used in the multivariate analysis.

2.5. FAME nomenclature, chemical and biological groups

We used the standard ω-nomenclature (A:BωC) for designating the fatty acids [24] where "A" represents the number of carbon in the fatty acid, "B" the number of unsaturation and "C" the position of the double bond closest to the omega (distal) carbon. Identified FAMEs were grouped according to their chemical group (straight and branched saturated, mono- and poly-unsaturated, and hydroxy substituted fatty acids) and biological origin (biomarkers of bacteria, mycorrhizal fungi, saprophytic fungi, higher plant/faunal biota, general biota). Biological groups were distinguished with the following TL-FAMEs: bacteria (i-15:0, a-15:0, 15:0, i-16:0, 16:1ω7, i-17:0, 3-OH-12:0, 17:0, 17:1ω7, 17:0cy, 18:1ω7, 10Me18:0), mycorrhizal fungi (16:1ω5c), saprophytic fungi (18:1ω9c/t, 18:2ω6c/t, 18:3ω6, 18:3ω3) and a general biotic marker (16:0) [2,4,25–32]. All TL-FAMEs with 20 and more carbons (20:0, 21:0, 22:0, 23:0, 24:0, 20:1ω9, 20:2ω6, 20:3ω3, 20:3ω6, 20:4ω6, 20:5ω3, 22:1ω9, 22:2ω6, 22:4ω6, 22:5ω3, 22:6ω3, 24:1ω9) were categorized as TL-FAMEs ≥20 C because of the diverse origins (bacterial and fungal cells, plants, protozoa and other animals) of soil lipids in this group [2,4,33–36].

2.6. Statistical analysis

The effect of solvent mixtures on the quantity of TL-FAMEs (nmol g^{-1} DS, %mole) in the chemical and biological groups was determined with one-way analysis of variance using CoStat, version 6.003 (CoHort Software, Monterey, CA, USA). A post-hoc least sig-

nificant difference test at $\alpha = 0.05$ was used to compare treatment means. Discriminant analysis (DA) were performed with the TL-FAMEs dataset (in %mol, transformed with $\log_{10}(x+1)$ to achieve normality in the dataset) to test the discrimination of TL-FAMEs due to solvent mixture and soil type using SYSTAT software, version 10 (Systat Software Inc., Richmond, CA, USA). Values presented in graphs and tables are untransformed means followed by the standard errors of the mean ($n = 3$) for each soil.

3. Results and discussion

Soils had diverse characteristics (Table 1), but are representative of agricultural soils in southwestern Québec. The TL-FAME concentrations ranged from 57.3 to 542.2 nmol g^{-1} DS (Table 2). This range is similar to the 160.8–341.2 nmol g^{-1} DS of TL-FAMEs reported for agricultural soils from the Central and San Joaquin Valleys of California using the Microbial Identification System (MIS, Microbial ID Inc., Newark, DE, USA), another method for characterizing soil lipids [37]. In soils 1 and 2, the TL-FAME concentration of the soil lipids was more efficiently extracted with chloroform:methanol:buffer than other used solvents (Table 2). Chloroform:methanol:buffer and chloroform:methanol mixtures gave higher TL-FAME concentrations than hexane:2-propanol or acetone in soil 3, whereas in soil 4, chloroform:methanol:buffer, chloroform:methanol and acetone extracted soil lipids more efficiently, when compared to hexane:2-propanol (Table 2). These results are consistent with other studies showing chloroform:methanol mixtures to be the most efficient for extracting lipids from biological materials [10,38,39]. Regardless of the solvent used, the TL-FAME concentration followed the order soil 4 > soil 3 > soil 2 > soil 1, which may be related to the organic matter and soil microbial biomass carbon content of these soils.

3.1. Chemical and biological groups of TL-FAMEs

Lipids can be selectively solubilized by organic solvents, depending on structural features such as the proportion of nonpolar hydrocarbons in the fatty acids or other aliphatic moieties and the presence of polar functional groups, such as phosphate and sugar moieties [10]. Soil TL-FAMEs contained between 26.8 and 342.0 nmol g^{-1} DS of total saturated fatty acids (SAFAs), the sum

Table 2
Summed concentration (total TL-FAMEs) and chemical groups (SAFAs, saturated fatty acids; UFAs, unsaturated fatty acids; HYFA, hydroxyl fatty acid) of soil lipids extracted with various solvents using a PSE system (All values are in nmol g^{-1} DS)

Solvent mixture	Total TL-FAMEs	StraightSAFAs	BranchedSAFAs	MonoUFAs	PolyUFAs	HYFAs
Soil 1						
Acetone	59.7 c	25.0 c	1.8 c	11.0 c	21.6 c	0.3 c
Chloroform:methanol	101.0 b	38.2 b	5.6 b	21.5 b	34.7 b	0.9 b
Chloroform:methanol:buffer	167.1 a	49.4 a	16.7 a	51.1 a	47.0 a	2.8 a
Hexane:2-propanol	57.3 c	26.4 c	1.8 c	9.7 c	19.1 c	0.4 c
Soil 2						
Acetone	136.1 c	66.4 b	4.4 c	21.5 c	42.9 c	0.9 c
Chloroform:methanol	216.2 b	91.7 a	13.2 b	41.9 b	66.7 b	2.6 b
Chloroform:methanol:buffer	282.1 a	93.4 a	31.5 a	73.0 a	79.4 a	4.8 a
Hexane:2-propanol	137.2 c	63.4 b	4.1 c	20.2 c	48.9 c	0.7 c
Soil 3						
Acetone	242.9 b	85.7 b	4.0 c	28.9 b	124.3b c	0.0 c
Chloroform:methanol	360.6 a	122. 2a	13.5 b	69.8 a	153.3 a	1.9 b
Chloroform:methanol:buffer	361.7 a	121.8 a	30.6 a	70.1 a	135.6 b	3.6 a
Hexane:2-propanol	216.8 b	77.6 b	4.8 c	20.2 b	114.3 c	0.0 c
Soil 4						
Acetone	493.5 ab	297.8 a	6.4 c	24.1 b	164.8 a	0.7 b
Chloroform:methanol	542.2 a	321.7 a	20.3 b	43.7 a	153.2 a	3.2 a
Chloroform:methanol:buffer	438.8 b	233.9 b	27.7 a	54.7 a	119.8 b	2.6 a
Hexane:2-propanol	346.2 c	215.3 b	6.0 c	18.0 b	107.0 b	0.0 c

For each soil (Typic Endoquents), mean values in a column with the same letters are not significantly different (LSD Test, $p < 0.05$, $n = 3$).

Table 3
Summed concentration (total TL-FAMEs) and biological groups (described in the Experimental section) of soil lipids extracted with various solvents using a PSE system (All values are in nmol g^{-1} DS)

Solvent mixture	Total TL-FAMEs	Bacteria	Mycorrhizae	Fungi	FAMEs ≥ 20C	General biomass marker 16:0
Soil 1						
Acetone	59.7 c	5.8 c	1.4 c	12.4 c	30.6 c	4.5 c
Chloroform:methanol	101.0 b	15.3 b	3.7 b	16.5 b	49.8 b	8.1 b
Chloroform:methanol:buffer	167.1 a	44.7 a	10.6 a	25.2 a	61.0 a	13.7 a
Hexane:2-propanol	57.3 c	6.2 c	1.3 c	9.9 d	31.0 c	4.2 c
Soil 2						
Acetone	136.1 c	13.0 c	3.7 c	19.1 c	82.1 b	8.4 c
Chloroform:methanol	216.2 b	31.7 b	7.8 b	28.5 b	117.1 a	16.1 b
Chloroform:methanol:buffer	282.1 a	72.9 a	15.4 a	37.1 a	118.2 a	22.5 a
Hexane:2-propanol	137.2 c	11.6 c	3.5 c	14.4 d	91.8 b	7.3 d
Soil 3						
Acetone	242.9 b	9.6 c	3.6 c	42.7	160.1 c	13.8 c
Chloroform:methanol	360.6 a	26.1 b	8.5 b	46.9	236.1 a	22.2 b
Chloroform:methanol:buffer	361.7 a	68.3 a	17.1 a	47.7	178.8 b	28.1 a
Hexane:2-propanol	216.8 b	9.6 c	3.7 c	36.2	143.8 d	12.8 c
Soil 4						
Acetone	493.5 ab	15.8 c	2.4 c	39.5 a	321.3 a	37.1 bc
Chloroform:methanol	542.2 a	45.5 b	5.7 b	49.4 a	283.9 b	59.1 a
Chloroform:methanol:buffer	438.8 b	61.0 a	9.6 a	39.8 a	216.3 c	46.5 b
Hexane:2-propanol	346.2 c	14.1 c	2.0 c	27.1 b	204.8 c	30.8 c

For each soil (Typic Endoquents), mean values in a column with the same letters are not significantly different (LSD Test, $p < 0.05$, $n = 3$).

of straight SAFAs and branched SAFAs (Table 2). Straight SAFAs were the most common, accounting for 29.6–62.2% of the total soil TL-FAMEs. The concentration of total unsaturated fatty acids (UFAs), which are composed of monoUFAs (monounsaturated fatty acids) and polyUFAs (polyunsaturated fatty acids), ranged from 28.8 to 223.1 nmol g^{-1} DS (Table 2). MonoUFAs accounted for 4.9–30.6% of the soil TL-FAMEs, but the polyUFAs were more common (27.3−52.7% of the soil TL-FAMEs). The 3-OH-12:0 hydroxy fatty acid (HYFA) was less than 2% of the soil TL-FAMEs and concentrations ranged from 0.0 to 4.8 nmol g^{-1} DS (Table 2). Soils extracted with chloroform:methanol:buffer or chloroform:methanol mixtures had higher straight SAFA, branched SAFA, monoUFA, polyUFA and HYFA concentrations than soils extracted with hexane:2-propanol or acetone, except in soil 4, where chloroform:methanol and acetone yielded the highest concentrations (Table 2).

The TL-FAMEs were used to distinguish the biological origin of soil lipids. We found that bacteria contributed 3.2−26.8% of TL-FAMEs, mycorrhizal fungi 0.5−6.3% of TL-FAMEs and saprophytic fungi 7.8−20.8% of TL-FAMEs (Table 3). The general microbial biomass marker, 16:0, represented 5.3−10.9% of the TL-FAMEs (Table 3). We also found that 36.5−66.9% of the TL-FAMEs were ≥20C, which suggests these lipids were derived from higher plants and animals (Table 3). Data on TL-FAMEs ≥20C are not often presented in papers oriented towards soil microbial community dynamics because these fatty acids are not typically biomarkers of bacteria and fungi. However, when they are monitored, TL-FAMEs ≥20C normally represent a larger pool of fatty acids than those of microbial origin [35,40]. Jandl et al. [35] reported that these long chain TL-FAMEs came from above- and below-ground crop residues, animal manure and a variety of soil organisms (protozoa, nematodes, etc.). Soils extracted with chloroform:methanol:buffer or chloroform:methanol mixtures had higher concentrations of all investigated biomarkers than soils extracted with hexane:2-propanol or acetone (Table 3). An exception was found for soil 4, where acetone extracted more efficiently fungal biomarkers and TL-FAMEs ≥20C (Table 3).

The chloroform:methanol:buffer mixture contains an aqueous buffer as well as polar solvents (chloroform and methanol)

and it has been suggested that this type of monophasic solution should have a greater ability to break polar bonds and extract lipids from biological materials than the chloroform:methanol mixture alone [6]. Certainly, the chloroform:methanol:buffer and chloroform:methanol mixtures were generally more efficient at extracting TL-FAMEs from soil than hexane:2-propanol and acetone. Hexane (a hydrocarbon solvent) was expected to extract nonpolar lipids efficiently, while polar lipids should be soluble in 2-propanol (a polar sol-
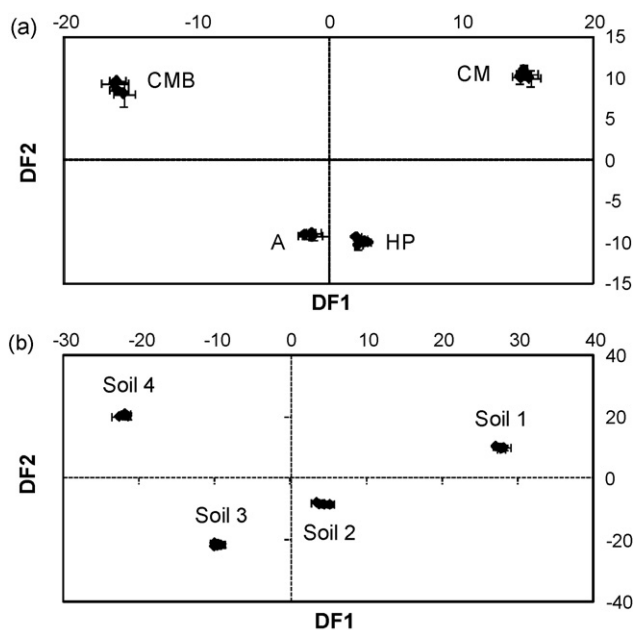
Fig. 1. Discriminant analysis of the TL-FAMEs from soil lipids extracted with four solvent mixtures using a PSE system. Scores plots of discriminant analysis were grouped according to (a) the solvent mixture, and (b) the soil type. Solvent mixtures are identified as A (acetone), CM (chloroform:methanol), CMB (chloroform:methanol:buffer) and HP (hexane:2-propanol). Soil types are described in Table 1. Data are mean scores and the standard errors of the mean ($n = 3$).

vent). However, 2-propanol has lower polarity than methanol, which explains the lower recovery of polar lipid classes and total TL-FAMEs with the hexane:2-propanol mixture than with the chloroform:methanol:buffer and chloroform:methanol mixtures. Acetone is a solvent of medium polarity often used to extract simple lipids and glycolipids or precipitate phospholipids [11], but it was not generally efficient at extracting soil TL-FAME from different chemical groups and diverse biological origins.

Discriminant analysis, based on the individual TL-FAMEs identified from soil lipid extracts, provided significant discrimination between solvent mixtures and soil types (Wilks' lambda = 0.000 at *p* < 0.00005 for all discriminant analysis tests) (Fig. 1a and b). The best discriminating variables selected by the automatic backward stepwise procedure allowed us to correctly classify 98% of the solvent mixtures and 100% of soils (Fig. 1a and b). There is a clear difference in the chemical and biological groups of TL-FAMEs extracted by the four solvents tested in this study. Discriminate analysis also confirms that lipid profiles, revealed by TL-FAME analysis, can distinguish soils that are known to have diverse chemical, physical and biological properties. Whether more subtle changes in the chemical and biological groups of TL-FAMEs within a particular soil (i.e., as a result of experimental treatments or environmental changes) can be detected with this technique is beyond the scope of this study, but has been demonstrated by other researchers [9,16,32,41].

4. Conclusions

Fatty acids are major building blocks for many classes of lipids, including acylglycerols and phospholipids, and are widely used as biomarkers in microbial ecology and to characterize soil microbial communities. We found that chloroform:methanol:buffer or chloroform:methanol extracted TL-FAMEs from soil more efficiently than the hexane:2-propanol and acetone solvent mixtures. The TL-FAME concentration attributed to relevant soil chemical and biological groups was affected by the type of solvent used, with improved extraction efficiency for chloroform:methanol:buffer ≥ chloroform:methanol > hexane:2-propanol = acetone. It is challenging to determine whether solvent mixtures permit quantitative extraction of soil lipids. Spiking a soil with a known concentration of a particular lipid may seem like a plausible option to evaluate the extraction efficiency of solvent mixtures, except that soils are biologically active and there is a high probability that newly-added lipids would be rapidly metabolized by soil microorganisms. Real soil lipids are probably stabilized physically or chemically and thus resist microbial breakdown. Some reports [7,12,13] indicate that solvent mixtures can become saturated in soils with high soil organic matter content, due to the presence of readily available organic molecules (not necessarily lipids). In such cases, longer extraction times, a higher solvent mixture:sample ratio, or a solvent mixture containing more chloroform would be required to generate a representative lipid sample. For example, Iverson et al. [42] showed that marine tissues containing > 2% lipids were extracted more efficiently with a chloroform:methanol (2:1, v/v) mixture than a chloroform:methanol (1:2, v/v) mixture. These considerations deserve further investigation in soils.

References

[1] H.T.S. Boschker, J.J. Middelburg, FEMS Microbiol. Ecol. 40 (2002) 85.
[2] J.R. Vestal, D.C. White, BioScience 39 (1989) 535.
[3] D.C. White, S.J. Macnaughton, in: C.E. Pankhurst, M.M. Doube, V.V.S.R. Gupta (Eds.), Biological Indicators of Soil Health, CAB International, Oxon, 1997, pp. 371–396.
[4] L. Zelles, Biol. Fert. Soils 29 (1999) 111.
[5] H. Lechevalier, M.P. Lechevalier, in: C. Ratledge, S.G. Wilkinson (Eds.), Microbial Lipids, vol. 1, Academic Press, London, 1989, pp. 869–902.
[6] E.G. Bligh, W.J. Dyer, Can. J. Biochem. Physiol. 37 (1959) 911.
[7] Å. Frostegård, A. Tunlid, E. Bååth, J. Microbiol. Methods 14 (1991) 151.
[8] D.C. White, D.B. Ringelberg, in: R.S. Burlage, R. Atlas, D. Stahl, G. Geesey, G. Sayler (Eds.), Techniques in Microbial Ecology, Oxford University Press, New York, 1998, pp. 255–272.
[9] A. Tunlid, D.C. White, in: G. Stotzky, J.M. Bollag (Eds.), Soil Biochemistry, vol. 7, Marcel Dekker, New York, 1992, pp. 229–262.
[10] F. Shahidi, P.K.J.P.D. Wanasundara, in: C.C. Akoh, D.B. Min (Eds.), Food Lipids: Chemistry, Nutrition, and Biotechnology, Marcel Dekker, New York, 2002, pp. 133–167.
[11] W.W. Christie, in: W.W. Christie (Ed.), Advances in Lipid Methodology, 2, Oily Press, Dundee, 1993, pp. 195–213.
[12] R.J. Hance, G. Anderson, Soil Sci. 96 (1963) 94.
[13] P. Nielsen, S.O. Petersen, Soil Biol. Biochem. 32 (2000) 1241.
[14] S.J. Macnaughton, T.L. Jenkins, M.H. Wimpee, M.R. Cormiér, D.C. White, J. Microbiol. Methods 31 (1997) 19.
[15] H. Dinel, M.C. Nolin, Soil Sci. Soc. Am. J. 64 (2000) 177.
[16] T.A. Spedding, C. Hamel, G.R. Mehuys, C.A. Madramootoo, Soil Biol. Biochem. 36 (2004) 499.
[17] B. Jansen, K.G.J. Nierop, M.C. Kotte, P. de Voogt, J.M. Verstraten, Appl. Geochem. 21 (2006) 1006.
[18] A. Hara, N.S. Radin, Anal. Biochem. 90 (1978) 420.
[19] E.D. Dodds, M.R. McCoy, A. Geldenhuys, L.D. Rea, J.M. Kennish, J. Am. Oil Chem. Soc. 81 (2004) 835.
[20] A. Tanamati, C.C. Oliveira, J.V. Visentainer, M. Matsushita, N.E. de Souza, J. Am. Oil Chem. Soc. 82 (2005) 393.
[21] K. Schäfer, Anal. Chim. Acta 358 (1998) 69.
[22] F.J. González-Vila, J.M. Bautista, A. Gutiérrez, J.C. Del Rio, A.G. González, J. Biochem. Biophys. Methods 43 (2000) 345.
[23] R. Zarnowski, Y. Suzuki, J. Food Compos. Anal. 17 (2004) 649.
[24] IUPAC-IUB, Lipids 12 (1977) 455.
[25] T.W. Federle, in: F. Megusar, M. Ganthar (Eds.), Perspectives in Microbial Ecology, Slovene Society for Microbiology, Ljubljana, 1986, pp. 493–498.
[26] A. Frostegård, E. Bååth, A. Tunlid, Soil Biol. Biochem. 25 (1993) 723.
[27] J.H. Graham, N.C. Hodge, J.B. Morton, Appl. Environ. Microbiol. 61 (1995) 58.
[28] P.A. Olsson, E. Bååth, I. Jakobsen, B. Söderström, Mycol. Res. 99 (1995) 623.
[29] A. Frostegård, E. Bååth, Biol. Fertil. Soils 22 (1996) 59.
[30] L. Zelles, Chemosphere 35 (1997) 275.
[31] P.A. Olsson, FEMS Microbiol. Ecol. 29 (1999) 303.
[32] G.T. Hill, N.A. Mitkowski, L. Aldrich-Wolfe, L.R. Emele, D.D. Jurkonie, A. Ficke, S. Maldonado-Ramirez, S.T. Lynch, E.B. Nelson, Appl. Soil Ecol. 15 (2001) 25.
[33] H.-R. Schulten, M. Schnitzer, Soil Sci. Soc. Am. J. 55 (1991) 1603.
[34] T. Rezanka, J. Votruba, Anal. Chim. Acta 465 (2002) 273.
[35] G. Jandl, P. Leinweber, H.-R. Schulten, K. Ekschmitt, Soil Biol. Biochem. 37 (2005) 1033.
[36] A. Otto, C. Shunthirasingham, M.J. Simpson, Org. Geochem. 36 (2005) 425.
[37] R.E. Drenovsky, G.N. Elliott, K.J. Graham, K.M. Scow, Soil Biol. Biochem. 36 (2004) 1793.
[38] M.J. Fishwick, A.J. Wright, Phytochemistry 16 (1977) 1507.
[39] R.G. Ackman, in: C.K. Chow (Ed.), Fatty Acids in Foods and Their Health Implications, Marcel Dekker, New York, 2000, pp. 47–65.
[40] G. Jandl, H.-R. Schulten, P. Leinweber, J. Plant Nutr. Soil Sci. 165 (2002) 133.
[41] C. Hamel, V. Vujanovic, R. Jeannotte, A. Nakano-Hylander, M. St-Arnaud, Plant Soil 268 (2005) 75.
[42] S.J. Iverson, S.L. Lang, M.H. Cooper, Lipids 36 (2001) 1283.
[43] W.H. Hendershot, H. Lalande, M. Duquette, in: M.R. Carter (Ed.), Soil Sampling and Methods of Analysis, Lewis, Boca Raton, 1993, pp. 141–145.
[44] B.H. Sheldrick, C. Wang, in: M.R. Carter (Ed.), Soil Sampling and Methods of Analysis, Lewis, Boca Raton, 1993, pp. 499–511.
[45] R.G. Joergensen, Soil Biol. Biochem. 28 (1996) 25.

Quick analysis of baicalin in Scutellariae Radix by enzyme-linked immunosorbent assay using a monoclonal antibody

Katsumi Kido [a], Osamu Morinaga [b], Yukihiro Shoyama [b], Hiroyuki Tanaka [a],*

[a] *Department of Phamacognosy, Graduate School of Pharmaceutical Sciences, Kyushu University, Fukuoka 812-8582, Japan*
[b] *Faculty of Pharmaceutical Sciences, Nagasaki International University, Huis Ten Bosch 2825-7, Sasebo, Nagasaki 859-3298, Japan*

ABSTRACT

To establish an immunoassay for baicalin (BA), a hybridoma cell line (9D6) secreting a monoclonal antibody (MAb) against BA was prepared by cell fusion with splenocytes derived from a mouse immunized with BA–bovine serum albumin (BSA) conjugate and a myeloma cell line, SP2/0-Ag14. MAb 9D6 shows specific reactivity against BA and its aglycone, baicalein, but not against other natural products. We developed an enzyme-linked immunosorbent assay (ELISA) using MAb 9D6 in a competitive manner, ranging from 200 ng/mL to 2 μg/mL. After validating the developed ELISA on the basis of intra- and inter-assays and a recovery experiment, it was found that the ELISA was not only simple, but also sufficiently reliable and accurate for quality control of Scutellariae Radix. It allowed determination of BA in complex and mixed materials, such as Kampo medicines.

© 2008 Elsevier B.V. All rights reserved.

1. Introduction

Baicalin (BA) is the most abundant compound among more than 30 kinds of flavonoids, such as baicalein, wogonin, and wogonin 7-*O*-β-ᴅ-glucuronide, in *Scutellaria baicalensis* Georgi (Fig. 1 Labiatae). BA has been reported to have anti-allergic [1], anti-inflammatory [2], anti-HIV [3,4], anti-cancer [5,6], anti-oxidant, and free-radical scavenging effects [7,8]. Recently, we found that BA must be the most important component in the defense mechanism including oxidative burst against plant disease and insect attack [9,10]. Scutellariae Radix (S. Radix), which is the dried root of *S. baicalensis*, is one of the most important crude drugs used widely in Kampo medicines in Japan. Because BA shows these characteristics, the concentration of BA in S. Radix used clinically should be ≥10% (w/w), as defined by the 15th edition of Japanese Pharmacopoeia. Kampo medicines containing S. Radix, which are clinically important, occasionally cause side effects [11]. For example, interstitial pneumonia has been aggravated if Shosaikoto containing S. Radix and interferon (IFN)-α are used for treatment of chronic liver diseases. In this case, baicalein is believed to be a candidate in this side effect [12]. Therefore, concentrations of baicalein and BA which is hydrolyzed to give baicalein in body fluids should be monitored precisely in Kampo medicines.

Various analytical approaches have been investigated for the determination of BA in S. Radix, Kampo medicines, and biogenic materials. Thin-layer chromatography and gas chromatography–mass spectrometry were applied to qualitative analysis of BA [13]. High-performance liquid chromatography (HPLC) with ultraviolet detection has been adopted as a quality control for S. Radix in Japanese Pharmacopoeia. HPLC with electrochemical detection showed a high sensitivity in the pharmacokinetic study of BA [14–16]. To establish the fingerprints of S. Radix, micellar electrokinetic capillary electrophoretic methods were also reported to separate and determine BA and flavonoids [17–19].

We have been focusing on an immunochemical approach for determination of phytochemicals [20–24] because it is reproducible, rapid, and highly sensitive for simultaneous analysis. However, since immunoassays for BA have not yet been reported, a monoclonal antibody (MAb) against BA was prepared successfully, and then applied to an enzyme-linked immunosorbent assay (ELISA) for the quantitative analysis of BA in this study.

2. Experimental

2.1. Regents and materials

BA and baicalein were purchased from Wako Pure Chemicals (Osaka, Japan). Bovine serum albumin (BSA) and human serum albumin (HSA) were purchased from Sigma (Steinheim, Germany). Freund's complete and incomplete adjuvants were obtained from Difco (Detroit, MI, USA). Peroxidase-labeled anti-mouse IgG was

* Corresponding author. Tel.: +81 92 642 6668; fax: +81 92 642 6668.
E-mail address: htanaka@phar.kyushu-u.ac.jp (H. Tanaka).
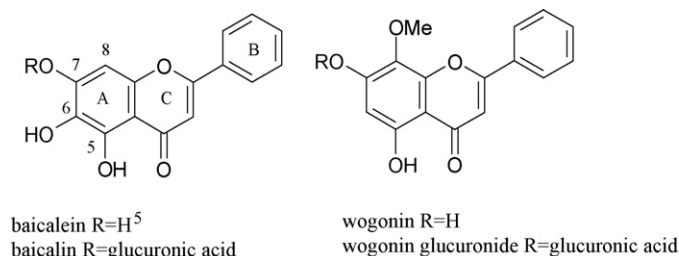
Fig. 1. Structure of baicalin (BA) and its related compounds.

purchased from MP Biomedicals (Solon, OH, USA). All other chemicals were standard commercial products of analytical-reagent grade.

Samples of various S. Radixes were purchased from Tochimototenkaido Corporation (Osaka, Japan), Takasago Yakugyo Corporation (Osaka, Japan), Daido Corporation (Osaka, Japan), and Yamada Corporation (Osaka, Japan). Kampo medicines were procured from Tsumura & Co. (Tokyo, Japan), Sanwa Shoyaku Co., Ltd. (Tochigi, Japan), and Kotaro Kampo Seiyaku Co., Ltd. (Osaka, Japan).

2.2. Synthesis of immunogen

1-Ethyl-3-(3-dimethylaminopropyl) carbodiimide hydrochloride (EDC; 5 mg) was added to a mixture of BA (5 mg) and BSA (5 mg) in 50 mM carbonate buffer (pH 9.6). The mixture was stirred at room temperature for 6 h. After the solution was dialyzed five times against H_2O, the dialysate was lyophilized to yield the BA–BSA conjugate (8.6 mg). BA–HSA conjugate was also synthesized in the same manner.

2.3. Determination of hapten number in BA–carrier protein conjugates by matrix-assisted laser desorption/ionization (MALDI)-TOF mass spectrometry

The hapten number of the BA–BSA and BA–HSA conjugates was determined by MALDI-TOF-MS as previously described [25,26]. A small amount (1–10 pmol) of the antigen conjugate was mixed with a 1000-fold molar excess of sinapinic acid in an aqueous solution containing 0.15% trifluoroacetic acid. The mixture was analyzed with a JEOL Mass Spectrometer (JMS) time-of-flight (TOF) mass monitor and irradiated with an N_2 laser (337 nm, 150 ns pulse). The ions formed by each pulse were accelerated by a 20-kV potential into a 2.0-m long evacuated tube. The data were analyzed using the GRAMS/386 software (Galactic Industries, Salem, NH, USA).

2.4. Preparation of anti-BA MAb

Male BALB/c mice (5 weeks old) were purchased from KBT Oriental Co. (Saga, Japan). Food (MF; Oriental Yeast Co., Tokyo, Japan) and water were provided *ad libitum*. Procedures and animal care were approved by the Committee on Ethics of Animal Experiments, Graduate School of Pharmaceutical Sciences, Kyushu University, Japan, and were conducted according to the Guidelines for Animal Experiments of the Graduate School of Pharmaceutical Sciences, Kyushu University.

The mice were injected with BA–BSA four times. Immunization was initiated by intraperitoneal injection of the conjugate (50 μg) in phosphate-buffered saline (PBS) emulsified with an equal volume of Freund's complete adjuvant. As a second immunization, 50 μg of the conjugate in Freund's incomplete adjuvant was injected intraperitoneally 2 weeks after the initial injection. Mice were bled 4 days after the boosts, and the sera were monitored

for antibodies recognizing BA by indirect and indirect competitive ELISAs using BA–HSA as a solid-phase antigen. On the fourth day after the final immunization (100 μg protein), splenocytes were isolated and fused with an aminopterin-sensitive mouse myeloma cell line, SP2/0-Ag14, by the polyethylene glycol (PEG) method [27]. SP2/0-Ag14 used for the cell fusion was obtained from RIKEN BioResource Center (Ibaragi, Japan). Hybridomas were obtained selectively by cultivation in a medium containing hypoxanthine–aminopterin–thymidine (HAT); those producing MAb reactive to BA were cloned by the limiting dilution method [28]. An established hybridoma was cultured in eRDF medium (Toyko, Japan) supplemented with 10 μg/mL insulin, 35 μg/mL transferrin, 20 μM ethanolamine, and 25 nM selenium [29].

2.5. Indirect ELISA

The reactivity of MAb to BA–HSA was determined by an indirect ELISA. BA–HSA (5 molecules of BA per molecule of HSA) (100 μL, 1 μg/mL) dissolved in 50 mM carbonate buffer at pH 9.6 was adsorbed to the wells of a 96-well immunoplate. It was then treated with 300 μL of PBS containing 5% skim milk (SPBS) for 1 h to reduce non-specific adsorption. The plate was washed three times with PBS containing 0.05% of Tween 20 (TPBS) and reacted with 100 μL of MAb solution to be tested for 1 h. The plate was washed three times with PBS containing 0.05% Tween 20 (TPBS) and incubated with 100 μL of a 1000-fold diluted peroxidase-labeled anti-mouse IgG solution for 1 h. After washing the plate three times with TPBS, 100 μL of substrate solution [0.1 M citrate buffer (pH 4) containing 0.003% H_2O_2 and 0.3 mg/mL of 2,2′-azino-bis (3-ethylbenzothiazoline-6-sulfonic acid) diammonium salt (ABTS)] was added to each well and incubated for 20 min. Absorbance at 405 nm was measured using a microplate reader. All reactions were carried out at 37 °C.

2.6. Indirect competitive ELISA

BA–HSA (100 μL, 1 μg/mL) dissolved in 50 mM carbonate buffer (pH 9.6) was adsorbed to the wells of a 96-well immunoplate. It was then treated with 300 μL SPBS for 1 h to reduce non-specific adsorption. Fifty microliters of various concentrations of BA or samples dissolved in 10% methanol were incubated with 50 μL of MAb solution (1.7 ng/mL) for 1 h. The plate was washed three times with TPBS, and then incubated with 100 μL of a 1000-fold diluted peroxidase-labeled anti-mouse IgG solution for 1 h. After washing the plate three times with TPBS, 100 μL of ABTS solution was added to each well and incubated for 20 min. The absorbance at 405 nm was measured using a microplate reader. All reactions were carried out at 37 °C.

2.7. Specificity and sensitivity of the assay

The cross-reactivities (CRs, %) of BA and related compounds were determined according to Weiler's equation [30]:

$$CR(\%) = \frac{\text{Concentration of BA at } A/A_0 = 50\%}{\text{Concentration of cross-reacting substance at } A/A_0 = 50\%} \times 100$$

A and A_0 are the absorbance in the presence and absence of the test compound, respectively.

2.8. HPLC instruments and conditions

The chromatography system used in this study consisted of a LC-10AD (Shimadzu, Kyoto, Japan), a UV-8 model II detector (Tosoh,

Tokyo, Japan), and a Chromatopac C-R5A data analyzer system (Shimadzu). The analytical column was Cosmosil 5C$_{18}$-AR column (4.6 mm i.d. × 150 mm, Nacalai Tesque, Kyoto, Japan) maintained at room temperature. The mobile phase comprised CH$_3$CN–H$_2$O (3:7) containing 60 mM H$_3$PO$_4$ and a flow rate of 1.0 mL/min. A 10-μL aliquot of each sample was injected and monitored at 254 nm.

2.9. Sample preparation

Dried samples (10 mg) of various S. Radixes and Kampo medicines were powdered, and extracted five times with MeOH (1 mL) under sonication. The extracted solution was filtered, and the combined extracted solution was adjusted to a volume of 10 mL with MeOH. The adjusted solution was diluted with H$_2$O to prepare a sample solution suitable for the indirect competitive ELISA.

2.10. Recovery experiment

Various amounts of BA were added to a dried powder of S. Radix (10 mg). The amount of BA in the unspiked sample was determined to be 1.09 mg. The spiked sample was extracted with MeOH by sonication and filtered. The combined extract was adjusted to 10 mL with MeOH, diluted to prepare a 10% MeOH solution, and assayed by the indirect competitive ELISA. The recovery rate of BA was calculated from the spiked and recovered amounts in the same concentration ranges.

$$\text{Recovery}(\%) = \frac{\text{Measured amount} - 1.09}{\text{Spiked amount}} \times 100$$

3. Results and discussion

3.1. Synthesis of the BA–BSA conjugate and direct determination of the hapten–carrier protein conjugates by MALDI-TOF mass spectrometry

Since a low molecular weight compound (hapten) like BA is poorly immunogenic, a hapten–protein conjugate should be synthesized and used as an immunogen for developing antibodies against such compounds. BA possessing a carboxylic acid group in a molecule, can be conjugated with a protein by carbodiimide system. Therefore, BSA was selected as a carrier protein and readily coupled with BA using 1-ethyl-3-(3-dimethylaminopropyl) carbodiimide hydrochloride (EDC) as a coupling reagent in this study. Fig. 2 shows the MALDI-TOF mass spectrum of the BA–BSA conjugate to validate its hapten number. A broad peak coinciding with the conjugate of BA and BSA appeared from m/z 66,900 to 74,900, centering at ∼m/z 70,200. Using the experimental result and a molecular weight of 66,433 for BSA, the calculated value of the BA component in the conjugate was 3767, suggesting 9 molecules of BA (on average) conjugated with a BSA molecule. This result revealed that adequate numbers of BA molecules were coupled with BSA, which meant that the BA–BSA conjugate could be used as an immunogen to evoke anti-BA antibodies in mice. BA–HSA was prepared as a solid-phase antigen for ELISA, and the hapten number of BA–HSA conjugate was also determined reliably from its spectrum to be at ∼5 molecules.

3.2. Production and characteristics of MAb against BA

BALB/c mice were immunized with BA–BSA until the absorbance of more than 0.5 in the indirect ELISA was observed using 1600-fold diluted sera after 10 min of color development. After confirming the
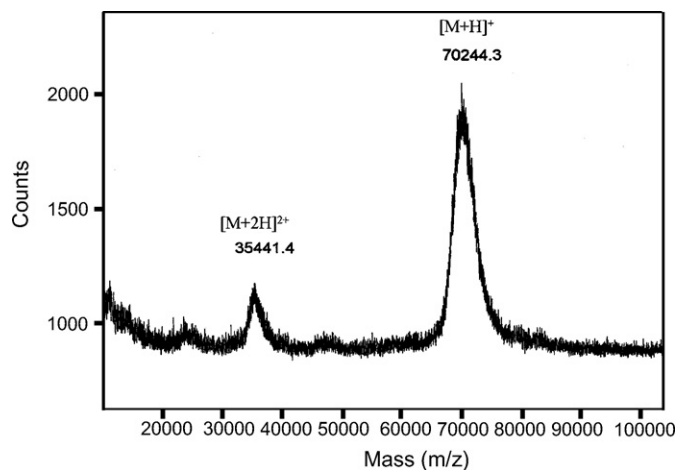
Fig. 2. Direct determination of BA–BSA conjugates by matrix-assisted laser desorption/ionization time-of-flight mass spectrometry (MALDI-TOF-MS). [M+H]$^+$ and [M+2H]$^{2+}$ are single- and double-protonated molecules of BA–BSA, respectively.

production of antibodies by the immunized mice, their spleen was extirpated to prepare splenocytes including antibody-secreting cells for cell fusion. Cell fusion was performed with the splenocytes and SP2/0 myeloma cells following the procedure established in this laboratory [31]. A hybridoma producing MAb reactive to BA was obtained through a series of screenings with the indirect and indirect competitive ELISAs and cloning by the limiting dilution method. The MAb, designated 9D6, was classified as IgG$_{2a}$ having κ light chains.

3.3. Assay sensitivity and assay specificity

An optimal concentration of anti-BA MAb applied to the indirect competitive ELISA was measured by the indirect ELISA with various concentrations of MAb 9D6. This optimal concentration was 1.7 ng/mL, which was selected for the indirect competitive ELISA to define sensitivity and specificity of the MAb because it was the minimum concentration of the MAb providing a sufficient signal to detect the interaction between the MAb and BA–HSA as a solid-phase antigen. The indirect competitive ELISA was developed using this concentration of MAb and polystyrene microtiter plates precoated with 1 μg/mL of BA–HSA. In addition, a 10% MeOH was used as a diluted solution for standard BA and samples, because addition of MeOH improved solubility of BA in the solutions at circumneutral condition. Fig. 3 shows inhibition of the interaction between the MAb and BSA–HSA using various concentrations of BA, providing a standard curve of BA in the indirect competitive ELISA. Under these conditions, a calibration curve for BA was generated in the linear range from 200 ng/mL to 2.0 μg/mL (R^2 = 0.994), which revealed that the sensitivity of the assay with a detection limit of 100 ng/mL was improved at least 5-fold compared with the HPLC method [32].

Specificity of MAb 9D6 was analyzed by comparing its cross-reactivities to compounds structurally related to BA and other natural products. Table 1 lists the CRs of the MAb examined by the indirect competitive ELISA, and calculated using the concentration of BA yielding midrange values on the basis of the method reported by Weiler et al. [30]. MAb 9D6 recognized not only BA, but also baicalein (CR: 51.4%) indicating a slight reactivity to wogonin (0.73%), although no detection against other flavonoids such as rutin, hesperidin, and daidzein (Table 1). It is easily suggested that all of function in ring A of BA might be immunized because MAb 9D6 strongly reacts BA structurally related compounds. Com-
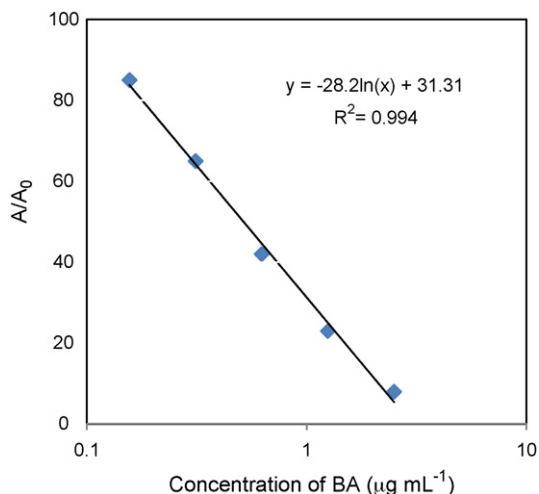
Fig. 3. Standard curve of inhibition by BA using MAb 9D6 in indirect competitive ELISA. Various concentrations of BA were incubated with MAb 9D6 (1.7 ng/mL) in a 96-well immunoplate precoated with BA–HSA (1 μg/mL).

pared to baicalein and wogonin, two hydroxyl groups at C5 and C7 positions are same, but two functions at C6 and C8 are completely different. Since the MAb recognizes BA and baicalein more than wogonin, it is supposed that a hydroxyl group at C6 position of BA, which is uncommon among flavonoids, evoked specificity of MAb 9D6 to BA and baicalein.

3.4. Variation and accuracy of the indirect competitive ELISA using anti-BA MAb 9D6

Intra- and inter-assays were performed to evaluate the indirect competitive ELISA using anti-BA MAb 9D6. In the standard curve for the ELISA obtained using various concentrations of BA from 0 to 2.5 μg/mL, variations were calculated using relative standard deviations (R.S.D.s) of measurements obtained from triplicate wells

Table 1
Cross-reactivities of anti-BA MAb (9D6) against flavonoids contained in Scullellariae Radix and other natural products

Compound	Cross-reactivity (%)
Flavonoids	
Flavone	
Baicalin	100
Baicalein	51.41
Wogonin	0.73
Flavonol	
Rutin	<0.21
Flavanone	
Hesperidin	<0.21
Isoflavone	
Daidzein	<0.21
Flavan-3-ol	
(+)-Catechin	<0.21
Glycyrrhizic acid	<0.21
Geniposide	<0.21
Saikosaponin a	<0.21
Magnolol	<0.21
Sennoside B	<0.21
Ginsenoside Rb1	<0.21
Berberine	<0.21

Table 2
Variations among the indirect competitive ELISA runs using anti-BA MAb 9D6

BA concentration (ng/mL)	R.S.D.[a] (%)	
	Intra-assay	Inter-assay
0	3.01	1.82
156	1.29	2.38
313	1.14	5.92
625	2.01	5.29
1250	7.50	5.06
2500	4.05	4.90

The measured values were mean ± S.D. for 3 plates and triplicate wells for each concentration within one plate from 3 consecutive days. The variation on replicates from well to well and plate to plate are defined as intra- and inter-assay variation, respectively.

[a] Relative standard deviation.

(intra-assay) and from plate-to-plate (inter-assay) on 3 consecutive days. Among the ELISA runs, the R.S.D.s were <8% in intra-assay, and <6% in inter-assay, which is one of the verifications that this assay is sufficiently reliable (Table 2).

Recovery rates of each spiked BA in S. Radix were calculated by the spiked and recovered amounts of BA in the same concentration ranges (Table 3). Table 3 indicates good recovery rates (av = 98%) with <7% of R.S.D.s ($n = 3$) from 0.25 to 1.0 mg of spiked BA. Taken together, these results suggest that the ELISA is sufficiently accurate to be applicable for quantitative determination of BA in products including S. Radixes.

3.5. BA determination in S. Radixes and Kampo medicines by the indirect competitive ELISA

After the validation and optimization of the assay, concentrations of BA in various S. Radixes and Kampo medicines were determined by the indirect competitive ELISA using the anti-BA MAb, and were compared with those determined by HPLC method. As shown in Table 4, the ELISA showed good linearity ($R^2 = 0.943$) with HPLC method in case of the determination of BA in all the dried S. Radixes. However, the data by the ELISA are overall higher than those by HPLC method. From this result, it is speculated that other BA structurally related compounds in S. Radix like baicalein and wogonin may react with MAb 9D6 and influence on those quantitative data by the ELISA. In addition, these concentrations of BA by HPLC method were relatively lower than those in the S. Radixes defined by Japanese Pharmacopoeia ($\geq$10%, w/w). This might depend on the not complete extraction by MeOH from S. Radixes. We realize that sample preparation should be improved to extract BA from samples as complete as possible. In the analytical trial of several Kampo medicines, the concentrations of BA in each sample except Kakkonto which does not contain S. Radix were

Table 3
Recovery of BA in spiked samples determined by the ELISA

Spiked amount (mg)	Measured amount (mg)[a]	R.S.D.[b]	Recovery (%)[c]
0	1.09 ± 0.11	[10.0]	
0.25	1.30 ± 0.07	[5.38]	84
0.5	1.62 ± 0.03	[1.85]	106
1	2.13 ± 0.15	[7.04]	104
			av = 98.0

[a] Baicalin in spiked samples was extracted by methanol with sample preparation. Data were mean ± S.D. from triplicate samples for each level.

[b] Relative standard deviation.

[c] The zero spiked level was used as control when the percentage of recovery was calculated as follows: recovery (%) = (measured amount − 1.09)/spiked amount × 100.

Table 4
BA concentrations in various Scutellariae Radixes and Kampo medicines determined by the ELISA and HPLC method

Sample	ELISA Concentration (mean ± S.D., w/w%) [R.S.D.][a]	HPLC Concentration (mean ± S.D., w/w%) [R.S.D.]
S. Radix 1	10.0 ± 0.5 [5.0]	7.5 ± 0.2 [2.7]
S. Radix 2	13.8 ± 0.7 [5.1]	10.9 ± 0.4 [3.7]
S. Radix 3	10.1 ± 0.3 [3.0]	6.7 ± 0.5 [7.5]
S. Radix 4	11.9 ± 1.0 [8.4]	8.5 ± 0.6 [7.1]
Daisaikoto	2.63 ± 0.06 [2.3]	
Shosaikoto	2.87 ± 0.11 [3.8]	
Ogonto	2.62 ± 0.20 [7.6]	
Saikokeishito	2.74 ± 0.29 [11]	
Saikokaryukotsuboreito	2.75 ± 0.04 [1.5]	
Saikokaryukotsuboreito 2	2.41 ± 0.15 [6.2]	
Kakkonto	N.D.[b]	

Data were mean ± S.D. from triplicate analyses for each sample.
  [a] Relative standard deviation.
  [b] N.D.: not detected.

determined correctly without complicated sample pretreatments (Table 4).

4. Conclusion

This is the first time to prepare MAb against BA and apply an indirect competitive ELISA for determination of BA in S. Radixes and Kampo medicines. It was evaluated that the ELISA was simple, rapid, and as reliable as compared with other instrumental analyses. The ELISA can be used as the next-generation quality control method of crude drugs and products containing BA, particularly Kampo medicines. Our data confirmed that the newly developed ELISA had sufficient sensitivity and accuracy to detect the total amount of BA and baicalein in Kampo medicine samples, resulting circumvention of side effects.

Acknowledgments

References

[1] K. Nishikawa, H. Furukawa, T. Fujioka, H. Fujii, K. Mihashi, K. Shimomura, K. Ishimaru, Phytochemistry 52 (1999) 885.
[2] A. Koda, S. Watanabe, Y. Yanagihara, H. Nagai, K. Sakamoto, Jpn. J. Pharmacol. 27 (1977) 31.
[3] B.Q. Li, T. Fu, W.H. Gong, N. Dunlop, H.F. Kung, Y.D. Yan, J. Kang, J.M. Wang, Immunopharmacology 49 (2000) 295.
[4] B.Q. Li, T. Fu, Y.D. Yan, N.W. Baylor, F.W. Ruscetti, H.F. Kung, Cell Mol. Biol. Res. 39 (1993) 119.
[5] J.A. Wu, A.S. Attele, L. Zhang, C.S. Yuan, Am. J. Chin. Med. 29 (2001) 69.
[6] T. Konoshima, M. Kokumai, M. Kozuka, M. Iinuma, M. Mizuno, T. Tanaka, H. Tokuda, H. Nishino, A. Iwashima, Chem. Pharm. Bull. 40 (1992) 531.
[7] S. Ikemoto, K. Sugimura, N. Yoshida, R. Yasumoto, S. Wada, K. Yamamoto, T. Kishimoto, Urology 55 (2000) 951.
[8] Z.H. Gao, K.X. Huang, H.B. Xu, Pharmacol. Res. 43 (2001) 173.
[9] S. Morimoto, N. Tateishi, T. Matsuda, H. Tanaka, F. Taura, N. Furuya, N. Matsuyama, Y. Shoyama, J. Biol. Chem. 273 (1998) 12606.
[10] S. Morimoto, N. Tateishi, M. Inuyama, F. Taura, H. Tanaka, Y. Shoyama, J. Biol. Chem. 274 (1999) 26192.
[11] F. Ikegami, M. Sumino, Y. Fujii, T. Akiba, T. Satoh, Hum. Exp. Toxicol. 25 (2006) 481.
[12] Z.L. Liu, S. Tanaka, H. Horigome, T. Hirano, K. Oka, Biol. Pharm. Bull. 25 (2002) 37.
[13] M.C. Lin, M. Tsai, K.C. Wen, J. Chromatogr. A 830 (1999) 387.
[14] L.C. Wang, Y.H. Cao, X.P. Xing, J.N. Ye, Chromatographia 62 (2005) 283.
[15] L. Zhang, D. Xing, Y. Ding, R. Wang, X. Wang, L. Du, Biomed. Chromatogr. 19 (2005) 494.
[16] A. Kotani, S. Kojima, H. Hakamata, F. Kusu, Anal. Biochem. 350 (2006) 99.
[17] Y.M. Liu, S. Sheu, Anal. Chim. Acta 288 (1994) 221.
[18] K.L. Li, S. Sheu, Anal. Chim. Acta 313 (1995) 113.
[19] H. Zhang, K. Tian, J. Tang, S. Qi, H. Chen, X. Chen, Z. Hu, J. Chromatogr. A 1129 (2006) 304.
[20] H. Yanagihara, R. Sakata, H. Minami, H. Tanaka, Y. Shoyama, H. Murakami, Anal. Chim. Acta 335 (1996) 63.
[21] H. Tanaka, W. Putalun, C. Tsuzaki, Y. Shoyama, FEBS Lett. 404 (1997) 279.
[22] S.J. Shan, H. Tanaka, Y. Shoyama, Anal. Chem. 73 (2001) 5784.
[23] W. Phrompittayarat, W. Putalun, H. Tanaka, K. Jetiyanon, S. Wittaya-Areekul, K. Ingkaninan, Anal. Chim. Acta 18 (2007) 411.
[24] S. Sakamoto, W. Putalun, R. Tsuchihashi, S. Morimoto, J. Kinjo, H. Tanaka, Anal. Chim. Acta 607 (2008) 100.
[25] Y. Shoyama, R. Sakata, R. Isobe, H. Murakami, Org. Mass Spectrosc. 28 (1993) 987.
[26] Y. Shoyama, T. Fukuda, T. Tanaka, A. Kusai, K. Nojima, Biol. Pharm. Bull. 16 (1993) 1051.
[27] G. Galfre, C. Milstein, Methods Enzymol. 73 (1981) 3.
[28] J.W. Goding, J. Immunol. Methods 39 (1980) 285.
[29] H. Murakami, H. Masui, G.H. Sato, N. Sueoka, T.P. Chow, T. Kano-Sueoka, Proc. Natl. Acad. Sci. U.S.A. 79 (1982) 1158.
[30] E.W. Weiler, H. Kruger, M.H. Zenk, Planta Med. 39 (1980) 112.
[31] R. Sakata, Y. Shoyama, H. Murakami, Cytotechnology 16 (1994) 101.
[32] M.C. Chih, M.J. Tsai, K.C. Wen, J. Chromatogr. A 830 (1999) 387.

Determination of lecithin and soybean oil in dietary supplements using partial least squares–Fourier transform infrared spectroscopy

J. Kuligowski, G. Quintás, S. Garrigues, M. de la Guardia*

Department of Analytical Chemistry, Universitat de València, Edificio Jeroni Muñoz, 50th Dr. Moliner, 46100 Burjassot, Spain

ABSTRACT

Lecithin and soybean oil in dietary supplements were determined by Fourier transform infrared spectrometry transmission measurements in dichloromethane in combination with a partial least squares (PLS) regression. Two different PLS models were developed, using 16 synthetic mixtures of analytes in dichloromethane, making measurements in the spectral range from 931.8 to 1252.3 cm^{-1} for lecithin and from 911.4 to 1246.9 cm^{-1} and 1695.3 to 1774.5 cm^{-1} for soybean oil. Seven products from the Spanish market with lecithin concentrations between 21.1% and 99.1% and soybean oil concentrations between 0% and 37.2% were analyzed by the proposed method and the data was compared to a chromatographic reference procedure obtaining accurate results. For samples spiked with amounts between 50 and 250 mg of lecithin and soybean oil recovery percentages between 98.0% and 102.1% and between 93.6% and 102.0% with an average precision of 0.35% and 0.41% were achieved for lecithin and soybean oil, respectively. This method can be applied for the quality control of dietary supplements.

© 2008 Elsevier B.V. All rights reserved.

1. Introduction

Lecithin is a phospholipids mixture, mainly composed by three compounds: phosphatidylcholine (PC), phosphatidylethanolamine (PE), and phosphatidylinositol (PI). Lecithin is formulated together with soybean oil in a number of dietary products at percentage concentration levels. Manufacturers and food control agencies should use analytical methods for the characterization of dietary products to guarantee their composition and to detect the replacement of expensive ingredients with cheaper substitutes.

Lecithin determination in dietary supplements can be carried out applying the AOAC official method 999.14 [1]. This enzymatic method is based on the colorimetric determination of choline after an alkaline digestion of the sample [2]. An alternative to this method is the use of the Bartlett arseno-molibdate procedure [3], based on the measurement of the total amount of phospholipids by acid digestion and subsequent phosphorous analysis. Phospholipid analysis can also be carried out by liquid chromatography [4,5] or gel permeation chromatography [6,7]. On the other hand, the conventional methods for oil analysis involve the hydrolysis and methylation of fatty acids for a further determination by gas chromatography (GC). Therefore, a simple strategy for the simultaneous determination of total phospholipids and the soybean oil content in dietary supplements is desirable.

The concentration range in which lecithin and soybean oil are present in dietary supplements, as well as their characteristic absorption bands in the mid-IR region, make Fourier transform infrared (FTIR) spectrometry an appropriate approach for the quantification of these analytes in this type of samples. However, we have found only three references focusing on the analysis of the total phospholipid content in vegetable oil samples by FTIR using univariate [8,9] and multivariate [10] regression models.

Soy lecithin phospholipids in vegetable oils were determined by peak area measurements between 1200 and 970 cm^{-1} using a series of standards prepared from dilution a standard mixture of 39% phosphatidylcholine, 22% phosphatidylinositol and 27% phophatidylethanolamine, which corresponds to the best representation of phospholipids present in soybean oil in the authors opinion [8,9]. Samples were treated with distilled water at 90 °C for 30 min and centrifuged for 20 min. The phospholipids-rich layer was decanted and washed three times with 100 mL acetone before measurement.

On the other hand, a direct partial lease squares (PLS)–FTIR procedure was developed for phospholipid determination in rapeseed oil at various steps of a technological process. The method is based on the use of first order derivative transmission spectra in the wavenumber range between 1760 and 860 cm^{-1} using seven standards in hexane of a mixture of 34% phosphatidylcholine, 18% phosphatidylethanolamine, 19% phosphatidylinositol,

* Corresponding author. Tel.: +34 96 3544838; fax: +34 96 3544838.
E-mail address: miguel.delaguardia@uv.es (M. de la Guardia).

5% phosphatidylserine and 20% phosphatidic acid to build the calibration model with three factors [10].

So, it can be concluded that the determination of lecithin by FTIR is still controversial and there is a lack of a simple method to determine lecithin in dietary supplements. Moreover, the available methods are not suitable for the simultaneous determination of oil and lecithin in samples containing both compounds.

In this study, FTIR spectrometry was used for a fast characterization of lecithin containing dietary products with and without soybean oil. The proposed method entails the analytes extraction in dichloromethane and a further determination by PLS–FTIR spectrometry based on the use of transmission measurements. The spectral range, as the main parameter affecting the performance of the PLS procedure, was selected by interval-PLS. The predictive error sum of squares (PRESS) value was employed as an indicator to select the appropriate number of factors for each PLS model. Recovery and precision of the method were evaluated via synthetic standards. Moreover, a survey of dietary supplements from the Spanish market was carried out to test the performance of the developed procedure and found results were compared with those obtained by a chromatographic method.

2. Experimental

2.1. Apparatus and reagents

FTIR spectra acquisition for the FTIR–PLS procedure was carried out using the Bruker Tensor 27 FTIR spectrometer, equipped with a DLaTGS detector. The scanner for the interferometer was operated at a HeNe laser modulation frequency of 10 kHz. A flow cell with BaF_2 and ZnSe windows and a pathlength of 100 μm was used for the transmission measurements. FTIR spectra were acquired between 4000 and 400 cm^{-1} in the stopped-flow mode using a spectral resolution of 4 cm^{-1} and averaging 25 scans for each spectrum which yielded a spectra acquisition frequency of 3 spectra min^{-1}. A spectrum of the flow cell filled with dichloromethane was used as background.

A Hewlett-Packard (Palo Alto, CA, USA) HP1050 high performance liquid chromatograph system, equipped with two Waters (Barcelona, Spain) Envirogel GPC columns (19 mm $\times$ 150 mm, 19 mm $\times$ 300 mm) and a sample injection loop of 2 mL was employed for chromatographic separations [11]. Dichloromethane was used as mobile phase at a flow rate of 5 mL min^{-1}.

A Bruker (Bremen, Germany) IFS 66/v FTIR spectrometer equipped with a liquid nitrogen refrigerated mercury–cadmium–telluride (MCT) detector and a vacuum system was used for the detection of the chromatographically separated compounds. The scanner for the interferometer was operated at a HeNe laser modulation frequency of 100 kHz. Transmission measurements of the samples were carried out in a flow cell with BaF_2 and ZnSe windows and a pathlength of 100 μm. Accumulating 20 scans per spectrum from 4000 to 750 cm^{-1} with a spectral resolution of 8 cm^{-1} and a zerofilling factor of 2 provided a spectra acquisition frequency of 20 spectra min^{-1}.

For instrumental and measurement control and data acquisition, the OPUS software (version 4.1) from Bruker was employed. Spectra treatment and data manipulation were carried out using Matlab 7.0.1 from Mathworks Inc. (Natick, MA, USA). For the calculation of the iPLS models the MatLab iToolbox developed by Norgaard [12] was used. PLS regressions were obtained with the TurboQuant-Analyst software (version 6.0) from Thermo Nicolet Corp. (Madison, WI, USA).

Granulated soybean lecithin standard (97%, w/w) was supplied by Guinama (Valencia, Spain). Seven formulated lecithin samples,

four powdered ones and three pills as well as refined soybean oil, were obtained from local markets. Dichloromethane was provided by Scharlau (Barcelona, Spain).

2.2. FTIR procedure

One gram of sample was weighed in a volumetric flask, diluted with 10 mL dichloromethane and sonicated for 5 min. The solutions were centrifuged at 3000 rpm for 5 min and then filtered through a 0.22 μm PTFE membrane. To determine the recovery, samples of 500 mg were spiked with different amounts of lecithin and soybean oil in the range between 49.9 and 255.7 mg and 51.7 and 229.2 mg, respectively.

16 synthetic mixtures of lecithin and soybean oil, prepared from different amounts of lecithin standard and soybean oil dissolved in 10 mL of dichloromethane, were used as calibration standards. The concentrations covered a range from 24.8 to 106.5 mg mL^{-1} and from 2.4 to 27.4 mg mL^{-1} for lecithin and soybean oil, respectively. Calibration and sample solutions were directly introduced into the flow cell using a peristaltic pump.

2.3. Gel permeation chromatography reference procedure

An appropriate amount of sample between 100 and 600 mg, according to the analyte concentration, was accurately weighed in a volumetric flask, filled up to 10 mL with dichloromethane and treated in the ultrasonic water bath for 5 min. The sample solutions were centrifuged at 3000 rpm and then filtered trough a 0.22 μm PTFE membrane. Two millilitres of sample extracts or CH_2Cl_2 solutions of standards were injected in the chromatographic system. The concentrations of lecithin and soybean oil were calculated from peak area values of the extracted chromatograms using the first order derivative intensities at 1034 and 1138 cm^{-1}, respectively. These values were interpolated in external calibration lines established with six solutions of both analytes in concentration ranges of 0–40 mg mL^{-1} and 0–30 mg mL^{-1} for lecithin and soybean oil, respectively. The calibration lines provided a very good linearity up to 100 and 50 mg mL^{-1} concentration for lecithin and soybean oil, respectively.

2.4. Selection of spectral ranges for the PLS models

The iPLS algorithm [13] was developed to simultaneously give an overview of the data to facilitate their interpretation, and to optimize the prediction capabilities of PLS regression models. The procedure develops local PLS models on equidistant subintervals of the spectrum applying a user defined range of latent variables. Results are presented in a plot where the prediction capabilities of the global model (which uses the whole spectrum) and the different local models are compared. In this work, the selection of the spectral regions used for the determination of lecithin and soybean oil was based on the validation parameter RMSECV (root mean square error of cross validation).

3. Results and discussion

For model development and method validation the measured FTIR spectra were divided in three sets called calibration, validation 1 and validation 2. The calibration set included FTIR spectra of 16 standard solutions. The standard solutions covered a range of lecithin/soybean oil concentration ratios between 1.0 and 40.4. During the cross validation process, for each iteration one calibration solution was left out calculating a calibration model and using the left out solution as validation sample. Validation set 1 was composed by seven samples directly obtained from the Spanish market
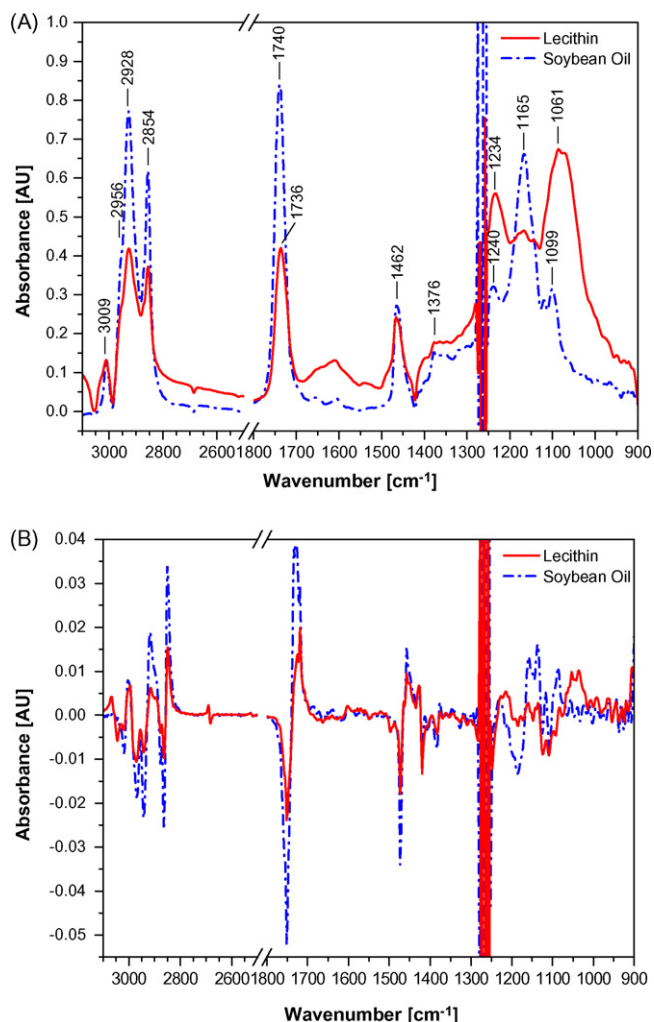
Fig. 1. (a) FTIR zero order absorption spectra of lecithin and soybean oil standard solutions in dichloromethane. (b) FTIR first order derivative spectra of lecithin and soybean oil standard solutions in dichloromethane. *Note*: Concentrations of lecithin and soybean oil: 50 mg/mL; pathlength of the flow cell: 100 μm; number of scans: 25; background spectrum: empty sample compartment.

with different contents of lecithin and soybean oil. Additionally, these samples were analyzed by a chromatographic reference procedure. Furthermore, the seven real samples were spiked with known amounts of lecithin and soybean oil to evaluate the recovery percentage of the method. The spectra of these spiked samples were used to build up validation set 2. Further information on the concentrations of standards and samples used in the different sets is given in Table 1.

3.1. FTIR spectra of lecithin and soybean oil

Fig. 1 shows typical FTIR spectra of standard solutions of soybean oil and lecithin in dichloromethane. In the lecithin spectra the most characteristic bands in the mid-IR region are: (i) the alkane bands corresponding to symmetric CH_2, antisymmetric CH_2, antisymmetric CH_3 stretching and CH_2 scissoring vibrational modes at 2854, 2928, 2956 and 1462 cm^{-1}, respectively; (ii) the carbonyl stretching vibration at 1736 cm^{-1}; and (iii) the highly overlapped PO_2^- and P–O–C infrared active vibrations in the region between 1200 and 970 cm^{-1}, with a maximal absorbance at 1061 cm^{-1}.

On the other hand, various bands can be identified in the soybean oil spectrum including the carbonyl C=O stretching band

Table 1
Characteristics of the different sets used in this study

Set	Type of sample	Number of samples	Number of spectra	Mean value (mg mL⁻¹)		Maximum value (mg mL⁻¹)		Minimum value (mg mL⁻¹)		Standard deviation (mg mL⁻¹)	
				Lecithin	Soybean oil	Lecithin	Soybean oil	Lecithin	Soybean oil	Lecithin	Soybean oil
Calibration	Standard mixtures	16	48	56.6	13.9	106.5	27.4	24.8	2.4	34.5	10.3
Validation 1	Real samples	7	21	68.2	13.3	95.3	36.5	20.6	26.9	28.1	16.8
Validation 2	Spiked samples	7	21	34.8	18.6	48.5	24.0	11.3	6.7	13.3	5.7
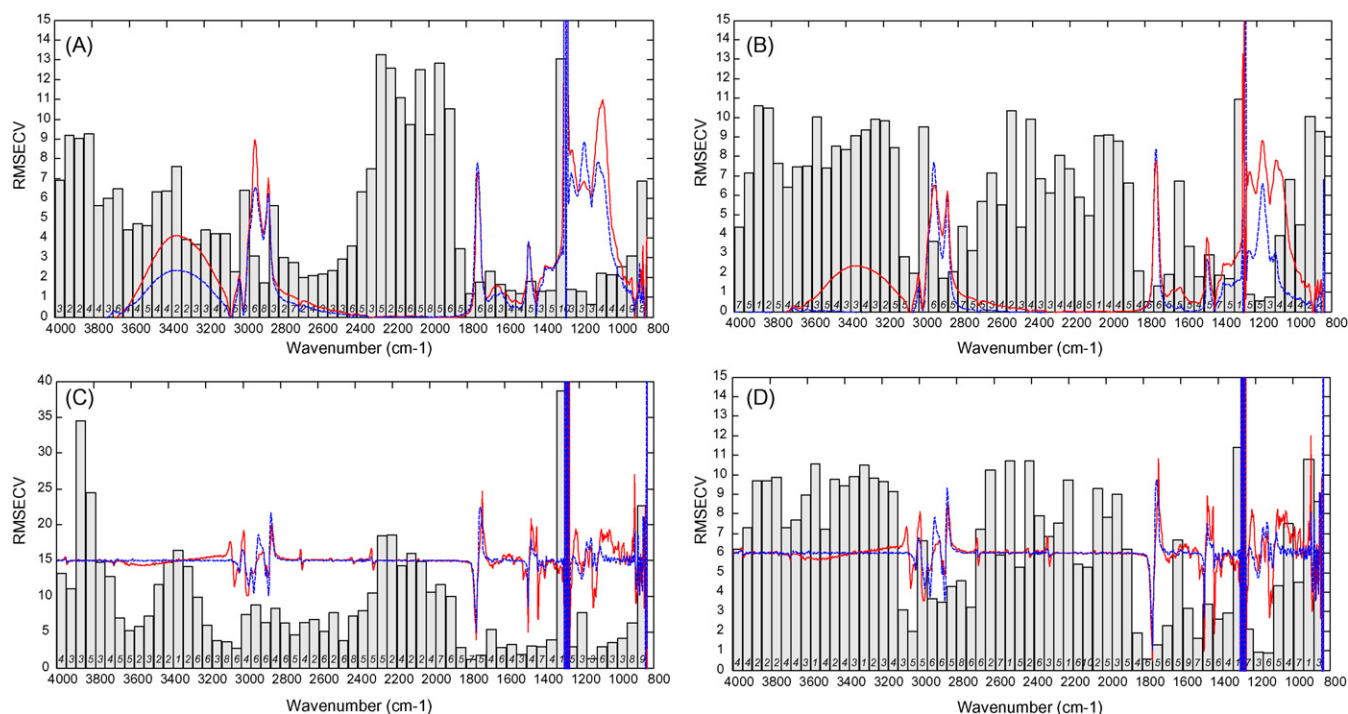
Fig. 2. Plots of the root mean square error of cross validation obtained using four iPLS analysis of zero order spectra of: (a) lecithin and (b) soybean oil, and of first order derivative spectra of: (c) lecithin and (d) soybean oil. *Note*: The spectra of both, lecithin (red) and soybean oil (blue) are shown to facilitate the interpretation of the iPLS analysis. The spectra have been shifted in the *y*-axis for a better visualization. (For interpretation of the references to color in this figure, the reader is referred to the web version of the article.)

at $1740\,cm^{-1}$, the CH_2 and CH_3 scissoring vibrations at 1462 and $1376\,cm^{-1}$, as well as intense $C=O$ stretching bands at 1165 and $1099\,cm^{-1}$. Absorption bands located at 2854, 2956 and $3009\,cm^{-1}$ arise due to the symmetric CH_2 stretching and the asymmetric CH_3 and CH_2 stretching, respectively [8,9].

The spectra in Fig. 1 show that it is not possible to select characteristic absorption bands of each one of the two considered compounds neither in the absorption nor in the first order derivative spectra because of the high spectral overlapping. Therefore the use of a multivariate calibration method such as PLS becomes essential for a direct determination of the two analytes in samples containing both products.

3.2. iPLS variable selection

As mentioned in Section 2.4, the variable selection was carried out by interval-PLS. The whole spectra using both, absorbance and first order derivative spectra of the 16 lecithin and soybean oil solutions included in the calibration set were split in 60 intervals of equal spectral width, and a PLS calibration model was calculated using up to 10 factors for each interval. To evaluate the performance of the calculated calibration models, the use of RMSECV using five segments for the cross validation, was selected. Obtained results for each compound are shown in Fig. 2. To facilitate the interpretation of the results the absorption spectra of the analytes are also shown in the figure. Comparing the results of the iPLS analysis of zero order absorption and first order derivative spectra, the RMSECV values provided the same trend for lecithin and for soybean oil. The absolute RMSECV values of the iPLS analysis of lecithin first order derivative spectra were higher throughout the whole spectral range than those obtained from lecithin zero order absorption spectra. On the other hand, the RMSECV values calculated in the iPLS analysis of the soybean oil absorption and first order derivative spectra provided similar results. Results from plots shown in

Fig. 2 are very useful to undertake an initial discrimination between the different spectral regions. It is clear that the spectral regions which provide lower RMSECV values were comprised between 900 and $1800\,cm^{-1}$ for lecithin and between 1050 and $1800\,cm^{-1}$ for soybean oil.

In order to obtain an optimal PLS model for unknown sample analysis a combination of the aforementioned intervals was carried out. Moreover, for the calculation of the PLS model zero order and first order derivative spectra were used simultaneously to obtain the best prediction performance. As indicated in Table 2, the spectral interval from 931.8 to $1252.3\,cm^{-1}$ using the zero order absorbance spectra was selected for the determination of lecithin, whereas for the soybean oil determination the interval from 911.36

Table 2
Summary of the most important parameters of the PLS calibration models developed for lecithin and soybean oil determination by FTIR

Component	Lecithin	Soybean oil
Spectral region 1 (cm^{-1})	931.82–1252.32	911.36–1246.91
Spectral region 2 (cm^{-1})	–	1695.31–1774.46
Baseline criteria	None	Single point BLC at 2000 cm^{-1}
Spectral order	Zero order spectra	Region 1: zero order spectra, region 2: first derivative Spectra
Factors	5	5
r_{CAL}	0.99992	0.99990
RMSEC (mg mL^{-1})	0.44	0.14
r_{CV}	0.99964	0.99985
RMSECV (mg mL^{-1})	0.98	0.5

Notes: BLC stands for "baseline correction" and was done to eliminate the influence of fluctuations of the baseline, FD means first derivative, r_{CAL} is the correlation coefficient of the calibration, RMSEC is the root mean square error of calibration, r_{CV} is the correlation coefficient of the cross validation, RMSECV is the root mean square error of cross validation.
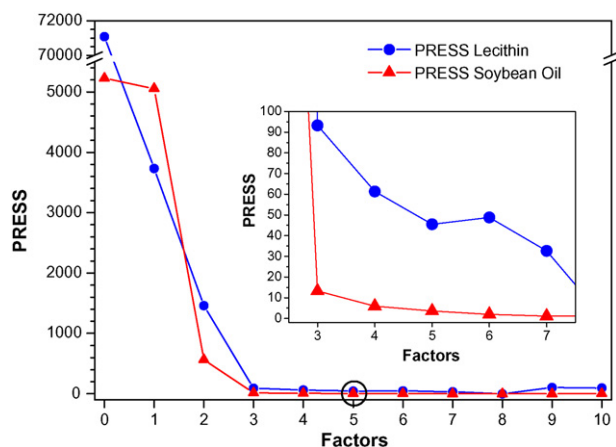
Fig. 3. PRESS values of lecithin (blue) and soybean oil (red) as a function of the number of factors used calculating the PLS model. Inset: close up of the region between 3 and 7 factors. (For interpretation of the references to color in this figure, the reader is referred to the web version of the article.)

to 1246.91 cm^{-1} using zero absorbance spectra and the interval from 1695.3 to 1774.5 cm^{-1} using the first order derivative spectra were chosen. The number of PLS factors is one of the most critical parameters in the application of a PLS model. In this work, the optimum number of factors in each model was chosen according to the PRESS. Fig. 3 shows calculated PRESS values as a function of the number of PLS factors for determining both, lecithin and soybean oil, using the absorbance and first order derivative spectra in the previously selected wavenumber regions. As it can be seen in Fig. 3 for lecithin the first minimum of the PRESS value was found using five factors for model building. For soybean oil five factors were selected because the use of a higher number of factors did not provide a significant improvement in the predictive capacity of the model and could easily lead to overfitting. To evaluate the calibration models, the correlation coefficient of the calibration (r_{CAL}), the root mean square error of calibration

(RMSEC), the correlation coefficient of the cross validation plot (r_{CV}) and the RMSECV were used. To determine the RMSECV, a leave-one-sample-out cross validation was performed. So, the spectrum of one sample of the training set was deleted from this set and a PLS model was built with the remaining spectra. The sample which was left out was used to assess the performance of the calculated regression model. The calculated parameters are listed in Table 2.

3.3. Accuracy and precision of the method

To assess the performance of the PLS models and to validate the accuracy of the method, a series of recovery experiments was carried out. Seven commercially available samples were spiked with both, lecithin and soybean oil, at different concentration levels. The FTIR spectra of the spiked samples were processed by PLS and results found for lecithin and soybean oil were used to calculate the recovery level of the procedure. Table 3 shows recoveries, precision levels (measured as relative standard deviation of three independent replicates) and the amounts of each compound added to the samples. The average recovery levels of both target compounds were satisfactory ranging in the interval between 98.0% and 102.1% for lecithin and between 93.6% and 102.0% for soybean oil. The precision of the obtained results was also appropriate for the analysis of lecithin and soybean oil in dietary products, with values of 0.35% and 0.41% for lecithin and soybean oil, respectively.

3.4. Sample analysis

Seven different dietary supplements, four powdered ones and three pills, which are all commercially available and contain markedly different concentrations of lecithin and soybean oil, were analyzed using the proposed method. The obtained results indicated in Table 4 confirmed the precision of the method. The found contents vary between 21.0% and 99.1% for lecithin and between 0% and 37.2% for soybean oil. To verify the accuracy of the method, the same samples were subsequently analyzed by a GPC–FTIR pro-

Table 3
Results of the analysis of seven spiked samples

Sample	Lecithin			Soybean oil		
	mg added	%Recovery ± s	%RSD	mg added	%Recovery ± s	%RSD
Powder 1	117.6	101.3 ± 0.2	0.2	67.1	97.9 ± 0.7	0.8
Powder 2	100.7	98.7 ± 0.4	0.4	150.8	93.60 ± 0.08	0.08
Powder 3	255.7	101.4 ± 0.3	0.3	199.9	95.8 ± 0.5	0.5
Powder 4	205.8	98.0 ± 0.3	0.3	210.0	98.3 ± 0.2	0.17
Pill 1	66.8	102.0 ± 0.8	0.8	79.5	97.4 ± 0.4	0.4
Pill 2	120.8	100.8 ± 0.3	0.3	51.7	96.4 ± 0.4	0.5
Pill 3	49.9	98.7 ± 0.1	0.14	53.1	101.9 ± 0.5	0.5

Note: s is the standard deviation; RSD is the relative standard deviation in %.

Table 4
Results of the analysis of seven market samples by using both the developed PLS–FTIR procedure and a reference GPC–FTIR method [8]

Sample	Lecithin		Soybean oil	
	Concentration found (%,w/w) ± s		Concentration found (%,w/w) ± s	
	GPC–FTIR (%RSD)	PLS–FTIR (%RSD)	GPC–FTIR (%RSD	PLS–FTIR (%RSD
Powder 1	20.6 ± 0.3 (1.5)	21.02 ± 0.05 (0.2)	0	0
Powder 2	97.7 ± 0.9 (0.9)	99.1 ± 0.5 (0.5)	0	0
Powder 3	96.88 ± 0.4 (0.4)	96.4 ± 0.8 (0.8)	0	0
Powder 4	98.21 ± 0.5 (0.5)	98.2 ± 0.4 (0.4)	0	0
Pill 1	56.7 ± 0.2 (0.3)	56.9 ± 0.2 (0.3)	30.0 ± 0.2 (0.7)	30.16 ± 0.2 (0.7)
Pill 2	54.86 ± 0.3 (0.6)	61.3 ± 0.2 (0.3)	27.2 ± 0.3 (1.1)	27.5 ± 0.1 (0.4)
Pill 3	55.03 ± 0.4 (0.7)	55.60 ± 0.07 (0.1)	37.7 ± 0.3 (0.8)	37.20 ± 0.03 (0.5)

Note: s is the standard deviation; RSD is the relative standard deviation in %.

cedure. The obtained results for both, lecithin and soybean oil, were statistically comparable for a 95% significance level in six of the seven samples. The lack of agreement between the content of lecithin in pill 2 found by PLS–FTIR (61.3%) and that found by GPC–FTIR (54.86%) could be explained by the presence of an unidentified compound in this sample which presents absorbance bands between 931.8 and 1252.3 cm^{-1}. In spite of the inherent limitations of the PLS-based model, the presented data shows the effectiveness of the method for the analysis of different formulations, such as powders without oil in their declared composition, or pills with high oil contents.

4. Conclusions

PLS–FTIR provides a fast and accurate way for the simultaneous determination of lecithin and soybean oil in dietary supplements. Compared to previously available procedures this methodology neither requires a time-consuming sample preparation [8,9] nor the use of mixtures of phospholipids to build the corresponding calibration models, using granulated soybean lecithin and refined soybean oil as standards.

The analytical figures of merit of the developed procedure compare well with those achieved using a PLS–FTIR model based on the use of phospholipids mixtures [9] in terms of recovery percentage and repeatability. Applying the new PLS method on real samples the found data agrees with those found by the chromatography method [7]. Furthermore, the PLS method require less time and reagents consume, thus providing an environmentally friendly methodology [14,15].

References

[1] Official Methods of Analysis of AOAC, Method 999.14, AOAC International, Gaithersburg, MD, USA.
[2] J.I. Rader, C.M. Weaver, M.W. Trucksess, J. AOAC Int. 87 (2004) 1297.
[3] G. Bartlett, J. Biol. Chem. 234 (1959) 446.
[4] B. Montañés, J.J. Permanyer, Food Chem. 60 (4) (1997) 675.
[5] R. Szücs, K. Verleysen, S.M.J.E. Guus, P. Duchateau, B.G.M. Sandra, Vandeginste, J. Chromatogr. A 738 (1) (1996) 25.
[6] R.E. Shansky, R.E. Kane, J. Chromatogr. 589 (1–2) (1992) 165.
[7] J. Kuligowski, G. Quintas, F.A. Esteve-Turrillas, S. Garrigues, M. de la Guardia, J. Chromatogr. A 1185 (2008) 71–77.
[8] J.M. Nzai, A. Proctor, J. Am. Oil Chem. Soc. 76 (1999) 61.
[9] J.M. Nzai, A. Proctor, J. Am. Oil Chem. Soc. 75 (1998) 1281.
[10] A. Szydlowska-Czerniak, Food Chem. 105 (2007) 1179.
[11] Gel Permeation Chromatography Cleanup System. Operator's Guide, Waters, MA, USA, WAT022516TP.
[12] L. Norgaard, iToolbox Manual, www.models.kvl.dk.
[13] L. Noorgaard, A. Saudland, J. Wagner, J.P. Nielsen, L. Munck, S.B. Engelsen, Appl. Spectrosc. 54 (2000) 413.
[14] M. de la Guardia, J. Ruzicka, Analyst 2 (1995) 17N.
[15] M. de la Guardia, J. Braz, Chem. Soc. 10 (6) (1999) 429.

Direct determination of uranium in seawater by laser fluorimetry

Sanjukta A. Kumar[*], Niyoti S. Shenoy, Shailaja Pandey, Suvarna Sounderajan, G. Venkateswaran

Analytical Chemistry Division, Bhabha Atomic Research Centre, Mumbai 400085, India

ARTICLE INFO

ABSTRACT

A method for estimation of uranium in seawater by using steady state laser flourimetry is described. Uranium present in seawater, in concentration of approximately $3\,ng\,ml^{-1}$ was estimated without prior separation of matrix. Quenching effect of major ions (Cl^-, Na^+, SO_4^-, Mg^+, Ca^+, K^+, HCO_3^-, Br^-) present in seawater on fluorescence intensity of uranium was studied. The concentration of phosphoric acid required for maximum enhancement of fluorescence intensity was optimized and was found to be 5%. Similarly the volume of concentrated nitric acid required to eliminate the quenching effect of chloride and bromide completely from 5 ml of seawater were optimized and was found to be 3 ml. A simple equation was derived using steady state fluorescence correction method and was used for calculation of uranium concentration in seawater samples. The method has a precesion of 1% (1 s, $n = 3$). The values obtained from laser fluorimetry were validated by analyzing the same samples by linear sweep adsorptive stripping voltametry (LSASV) of the uranium–chloranilic acid (2,5-dichloro-3,6-dihydroxy-1,4-benzoquinone) complex. Both the values are well in agreement.

© 2008 Elsevier B.V. All rights reserved.

1. Introduction

Uranium is a naturally occurring radioactive element which is important for nuclear technology. However, mineral resources for uranium are limited [1]. Seawater is a major source of uranium. The total estimated quantity of uranium in seawater is around four and a half billion tones [2]. Thus, the oceans have the potential to become the most eco-friendly and long sustainable resource for uranium. A number of countries in the world are in search of techniques to recover uranium from seawater economically. For this purpose and also for the environmental monitoring, the determination of uranium in seawater is very much important.

Estimation of uranium in seawater is a difficult task because of the very low concentration of uranium and high salt content of seawater. Instruments capable of uranium analysis in ppb range needs matrix separation prior to analysis. Literature involving analysis of uranium in seawater, are very few. Recently N. L. Misra et al. [3] used TXRF for uranium estimation in seawater after selective extraction of uranium in diethyl ether. P.G. Barbano et al. [4] and Dj. Dojozan et al. [5] determined uranium in seawater by spectrophotometric and differential pulse polarographic method respectively

after separating and preconcentrating it. M. Nagj [6] et al. used X-ray fluorescence spectroscopy for the estimation of uranium in seawater after its separation and preconcentration by co-precipitation and adsorption methods.

The approaches made for analysis of uranium in seawater as found in literature involve prior separation of matrix. In the present work we made an attempt to analyse uranium in seawater using laser fluorimetry without prior separation of matrix. Chemical processes have been used to minimize the quenching effect of concomitants. The slight quenching remaining is then corrected using steady state fluorescence method for the calculation of uranium concentration. The values obtained from laser fluorimetry were validated by analyzing the same samples by linear sweep adsorptive stripping voltametry (LSASV) of the uranium–chloranilic acid (2,5-dichloro-3,6-dihydroxy-1,4-benzoquinone) complex.

Laser-induced fluorescence is a very sensitive, selective and versatile technique mainly for uranium ultratrace analysis in various fields [7–10]. Uranium is a strong fluorophore which absorbs well in the region of 260–350 nm and emits strongly in the region 450–600 nm with a quantum yield of almost unity. However, in a real life sample, complications in fluorimetric estimations arise as the fluorescence may be quenched by a number of other species that may be present in the analyte solution [11,12]. It must be pointed out that this problem of quenching is not unique to uranium but applies to almost all fluorophores [11]. Quenching therefore

* Corresponding author. Fax: +91 22 25505151.
E-mail address: sanjukta_k@rediffmail.com (S.A. Kumar).

is a problem that must be considered and corrected for, in any fluorescence measurement.

2. Experimental

2.1. Instrumentation: laser fluorimeter

All fluorescence measurements have been made with the commercially available laser fluorimeter LF 003 uranium analyzer fabricated by Laser Applications and Electronics Division, R.R. Centre for Advanced Technology (CAT), Department of Atomic Energy, Indore, India. In LF 003 uranium analyzer, a compact sealed-off nitrogen laser emitting very intense but short lived (7 ns) UV (337.1 nm) pulses of maximum energy of 10 μJ per pulse, with a repetition rate of 10 pulses per second is used.

Voltammetric experiments were performed with Autolab PG Stat 20 (eco-chemie, Netherlands) coupled with the Metrohm make electrode system (Model 663 VA Stand) comprising of HMDE/Ag-AgCl (3 M KCl)/Pt rod electrode system. The cell solution was maintained at 298 ± 0.1 K.

2.2. Reagents

AR grade UO_2 powder was dissolved in hot concentrated nitric acid and the excess nitric acid was removed by evaporating to dryness. The residue was then dissolved in 1% nitric acid and suitably diluted to yield a stock solution of 1 mg/ml uranium. The concentration of uranium in this stock solution was verified using the method of Davies and Gray [13]. From this stock solution 100 ng/ml uranium solution was prepared for further use. 5% phosphoric acid was used as fluorescence enhancer during the fluorescence measurements. The phosphoric acid used was of AR grade. To verify the quenching effects of various cations and anions, stock solutions of appropriate concentrations were prepared from their AR grade salts. Nano pure water of 18.2 MΩ cm specific resistance collected from a Bransted Easy pure RF compact ultra pure water system was used through out the experiments. Nitric acid (65%) used was of suprapur grade procured from E. Merck.

2.3. Sample preparation

Samples/solutions in which uranium has to be estimated were subjected to a common procedure before measuring the fluorescence intensity as described here: appropriate amount of the samples/solutions were taken in 50 ml beakers and 5 ml of concentrated nitric acid was added to them. The content of the beakers was evaporated to dryness by heating on a sand bath. On completion of the evaporation, 2 ml of 25% phosphoric acid each was added to the beakers. The solutions were then made up to 10 ml by nano pure water and taken for fluorescence measurement. A blank was prepared for all experiments by taking only nitric acid in the beakers and treating it in the same way as samples/solutions.

3. Results and discussion

3.1. Flourescence enhancing reagent

Uranium phosphate species show very high fluorescence quantum efficiencies [14], and hence can be studied at very low concentrations. Reagents containing phosphate like sodium pyrophosphate, penta-sodium tri-poly phosphate, sodium hexam-eta phosphate, ammonium dihydrogen phosphate, phosphoric acid etc. are well known uranium fluorescence enhancing agents. In literature various concentrations of these reagents either alone or
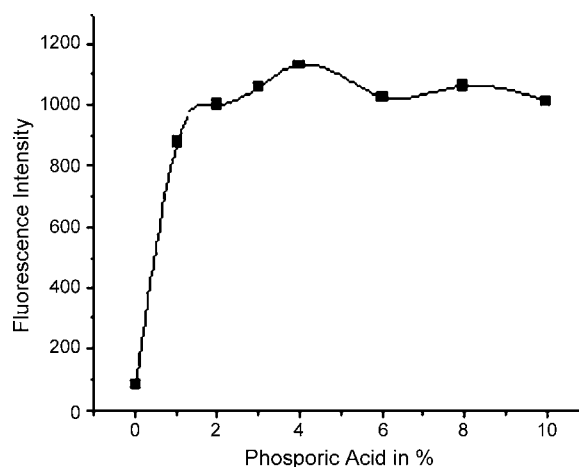
Fig. 1. Effect of phosphoric acid percentage on uranium fluorescence. 5 ng ml^{-1} of uranium is present in all solutions of varying phosphoric acid percentage.

in combination were found to be used for enhancement of uranium fluorescence [8–10,15]. In all our experiments phosphoric acid (H_3PO_4) was used as a fluorescence enhancing reagent owing to its easy availability. Since no literature is available regarding the concentration of phosphoric acid required for maximum enhancement of uranium fluorescence in seawater, an attempt has been made to establish that. It avoids the use of excess reagents which may contribute to the blank value of uranium determination. It was evaluated by measuring fluorescence intensity of a set of solutions containing 5 ng/ml uranium with increasing percentages of phosphoric acid. These solutions were prepared following the procedure mentioned in Section 2.3. From the Fig. 1 it is clear that without phosphoric acid, the fluorescence intensity (FI) of 5 ng/ml uranium is almost equal to blank. FI is found to increase with phosphoric acid concentration. Up to 4% phosphoric acid there is an enhancement in fluorescence intensity and then it remains constant up to 10%. This experiment has shown that phosphoric acid is very much essential for the enhancement of uranium fluorescence.

3.2. Influence of ions present in seawater on fluorescence intensity of uranium

Seawater is a complex matrix having about 3.5 wt% of dissolved salt content. The bulk of the dissolved salts (>99.99%) is made up of only 11 elements as listed in Table 1 and their concentrations vary only marginally [16,17]. Experiments were carried out to see the quenching effect of these cations and anions on fluorescence intensity of uranium. For this, solutions containing 5 ng/ml uranium and increasing concentrations of required cations and anions were prepared following the procedure described in Section 2.3. Fluorescence intensities of uranium for all these solutions were measured. Concentrations of cations and anions were varied from zero to a value higher than the amount present in actual seawater as per Table 1. From Fig. 2 it is clear that while sodium has no

Table 1
Concentrations of the Major Nonvolatile Constituent of 35‰ salinity seawater

Constituent	Concentration (mg/kg)	Constituent	Concentration (mg/kg)
Chloride	19,350	Bicarbonate	142
Sodium	10,760	Bromide	67
Sulphate	2,710	Strontium	8
Magnesium	1,290	Boron	5
Calcium	413	Fluoride	1
Potassium	387		
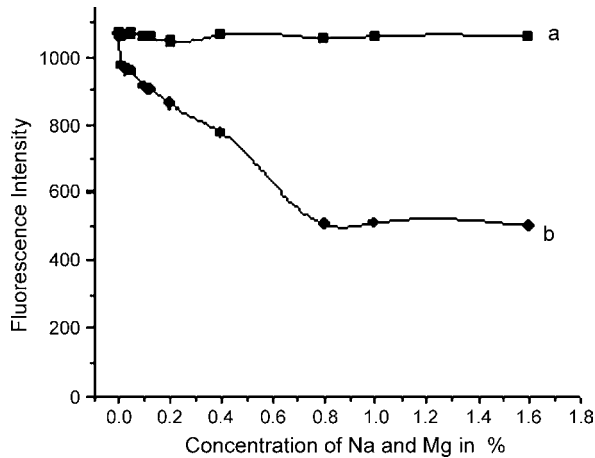
Fig. 2. a: Effect of Na percentage on Fluorescence intensity of uranium, b: Effect of Mg percentage on fluorescence intensity of uranium. Concentration of uranium: $5 \, ng \, ml^{-1}$.

effect through out the range, Mg shows a quenching effect. Fig. 3 shows the effect of potassium and calcium on uranium fluorescence intensity. In the concentration range mentioned in Table 1, a very marginal quenching effect due to these ions was observed. Chloride and bromide are found to have drastic quenching effect even in small concentrations of 0.06% as shown in Fig. 4. Sulphate and bicarbonate do not have any effect on fluorescence intensity of uranium as shown in Fig. 5.

3.3. Removal of major quenching effect due to chloride and bromide

Nitric acid is known to expel halides from solutions on heating. Rathore et al. [7] have used this property to remove fluoride from experimental solutions. Here this has been applied to seawater which contains approximately 2% of chloride which is the major fluorescence quencher. This necessitates the complete removal of chloride and bromide and thereby the quenching effect due to these ions is eliminated. For this, required quantity of nitric acid was added to the experimental solutions and then it was evaporated to dryness. It was found that chloride and bromide are evaporated off completely from the experimental solutions by this nitric acid treatment. Complete removal of chloride and bromide was confirmed by

Fig. 4. Effect of chloride percentage on fluorescence intensity of uranium. a: Before nitric acid treatment, b: after nitric acid treatment. Uranium in all solutions is $5 \, ng \, ml^{-1}$.

measuring these ions in the experimental solution before and after nitric acid treatment using ion selective electrode. Removal of chloride and bromide ensures total elimination of quenching effect due to these two anions as shown in the Fig. 4.

3.4. Effect of amount of nitric acid used for sample treatment

As seen from various experiments, except chloride and bromide, all other ions have relatively less quenching effect and can be corrected using steady state fluorescence correction method [15]. However, in presence of chloride, this correction cannot be applied as fluorescence of uranium is found to be quenched completely. As mentioned in Section 3.3 chloride and bromide was removed completely by treating the experimental solution with nitric acid and evaporating it to dryness.

Seawater contains uranium in ppb level and chloride in percentage level. Excess addition of nitric acid to seawater, for complete removal of chloride may increase the blank level for uranium determination. Hence, it is necessary to optimize the volume of concentrated nitric acid required for complete removal of chloride and bromide from 5 ml of seawater. It was evaluated by taking increasing volume of concentrated nitric acid and processing 5 ml

Fig. 3. a: Effect of Ca percentage on fluorescence intensity of uranium, b: effect of K percentage on fluorescence intensity of uranium. Uranium in all solutions is $5 \, ng \, ml^{-1}$.
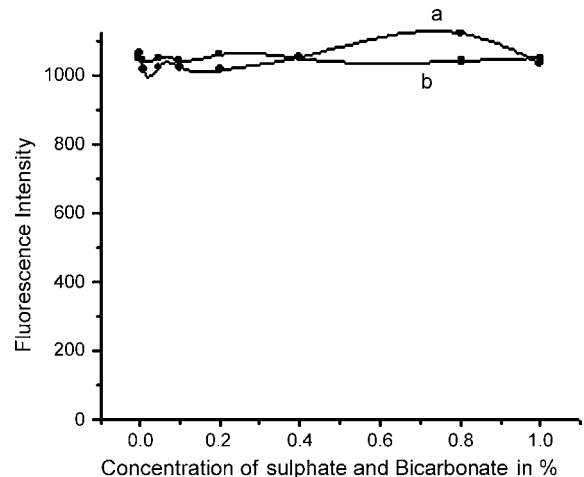
Fig. 5. a: Effect of sulphate percentage on fluorescence intensity of uranium, b: effect of bicarbonate percentage on fluorescence intensity of uranium.
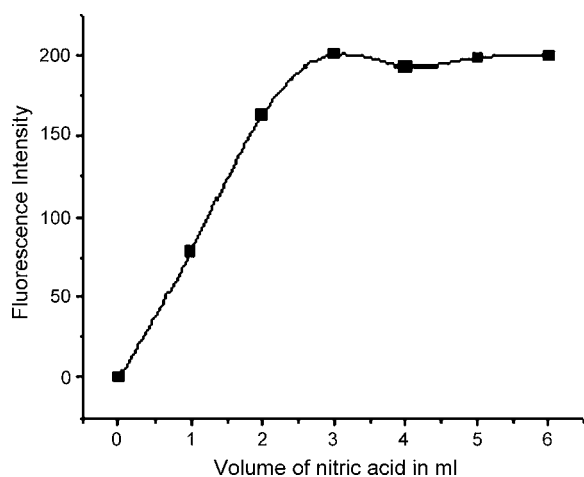
Fig. 6. Evaluation of nitric acid volume for removal of chloride completely from 5 ml of seawater.

of seawater as described in Section 2.3. It can be seen from Fig. 6 that fluorescence intensity is increasing with nitric acid volume with a maximum for 3 ml of concentrated nitric acid and then FI remains constant up to 6 ml nitric acid. This means 3 ml nitric acid is sufficient for removing all the chloride and bromide ions completely from 5 ml seawater. However, in all other experiments 5 ml nitric acid was used to avoid the doubt of complete removal of all the chloride and bromide ions.

3.5. Estimation of uranium in seawater by laser fluorimeter

After establishing various factors like phosphoric acid percentage required for maximum enhancement of fluorescence intensity, quenching effects of various ions present in seawater, removal of major quenching effects of chloride and bromide ions by nitric acid treatment, uranium concentration in actual seawater samples is determined using a steady state laser fluorimeter. The minor quenching effect caused due to ions other than chloride and bromide is corrected by steady state fluorescence correction method. The method is based on the fact that slope of the plot of fluorescence intensity versus concentration of the analyte is a function of the quencher concentration. The slope is the highest for the free analyte and decreases as the quencher concentration increases. Therefore, comparison of the slope of the plot of fluorescence intensity versus
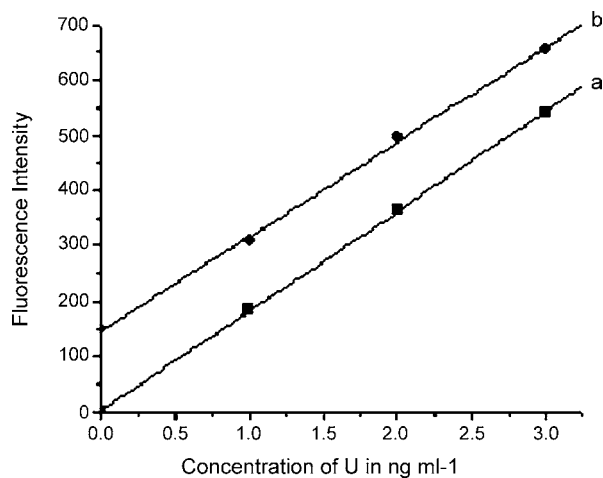
Fig. 7. Steady state fluorescence method for calculating uranium concentration. a: Standard addition curve without seawater, b: standard addition curve with seawater.

Table 2
% R.S.D. of slopes obtained for fluorescence intensity verses uranium concentration plot for five seawater samples analysed in triplicate. Uranium concentration varies from 0 to 3 ng/ml

Sample	Slope	% R.S.D.
SW-1	170.9	
	170.0	
	171.0	
SW-2	168.0	
	169.2	
	168.5	
SW-3	169.5	1.02
	170.2	
	171.3	
SW-4	172.3	
	173.0	
	170.5	
SW-5	173.2	
	173.8	
	172.9	

concentration of the free analyte to that for the sample (in presence of quenchers) indicates the extent of quenching due to the concomitant ions of the sample. To determine uranium in seawater sample, two sets of experiments were carried out simultaneously. In the first experiment 5 ml concentrated nitric acid and 0, 1, 2, and $3 \, \text{ng ml}^{-1}$ uranium were taken. In second experiment along with nitric acid and increasing concentration of uranium, 5 ml seawater also was taken. The solutions were processed as described in Section 2.3. Uranium fluorescence intensity was measured in the processed solutions. A plot of fluorescence intensity versus uranium concentration was made as shown in Fig. 7. Fig. 7(a), shows the plot of the fluorescence intensity versus concentration for free uranium over the concentration range of 0–$3 \, \text{ng ml}^{-1}$ where as Fig. 7(b) shows the same plot in presence of 5 ml seawater. The straight line shown in these plots are the least square fits of the corresponding data. As expected, the slope of the plot involving seawater sample ($S_s = 170.9$) is smaller than the slope of the plot without the seawater ($S_0 = 180$). Now as per S. Maji et al. [15] we can write:

$$\frac{I_0}{I_s} = \frac{S_0}{S_s} \tag{1}$$

where I_0 and I_s are the fluorescence intensity corresponding to a particular concentration of uranium without sample and with sample, respectively. Maji et al. have used the ratio of the slopes to convert the quenched fluorescence intensity I_s to a corrected value, I_0 using Eq. (1) as follows.

$$I_{0,\text{corrected}} = \left(\frac{S_0}{S_s} \right) I_s \tag{2}$$

Now this corrected fluorescence intensity ($I_{0,\text{corrected}}$) is used in the fluorescence intensity versus uranium concentration plot for free uranium (i.e. without sample) to read the concentration of uranium in the sample. However, this two-step calculation of uranium concentration in a given sample (first $I_{0,\text{corrected}}$ for a measured I_s and then uranium concentration from the fluorescence plot for free analyte) is a little tedious. Instead we have derived an equation which is then used to find out the uranium concentration in a single step calculation.

The fluorescence intensity (FI) versus uranium concentration ([U]) plot is a straight line and hence it can be fitted into the equation:

$$\text{FI} = S[\text{U}] + C \tag{3}$$

where S is the slope and C is the intercept of the plot. The plot for free analyte (i.e. without sample) will not have an intercept and

Table 3
Uranium in seawater sample

Samples	Uranium conc. in ng/ml ($n=3$) Laser Fluorimetry	Uranium conc. in ng/ml ($n=3$) LSASV
SW 1	2.50 ± 0.12	2.56 ± 0.14
SW 2[a]	4.45 ± 0.20	5.00 ± 0.18
SW 3	3.03 ± 0.15	2.98 ± 0.13
SW 4	3.12 ± 0.18	3.07 ± 0.15
SW 5	3.22 ± 0.13	3.10 ± 0.16

[a] SW 2: collected from the out let of a reverse osmosis plant where seawater is 1.5 times concentrated.

hence;

$$FI = S_0[U] \qquad (4)$$

When FI becomes $I_{0,corrected}$ (fluorescence intensity of analyte in sample after quenching correction), [U] becomes U_s (concentration of uranium in sample). Then we can write;

$$I_{0,corrected} = S_0 U_s \qquad (5)$$

or,

$$U_s = \frac{I_{0,corrected}}{S_0} \qquad (6)$$

Expansion of equation (6) gives;

$$U_s = \left(\frac{S_0}{S_s}\right)\frac{I_s}{S_0} = \frac{I_s}{S_s} \qquad (7)$$

where U_s is the uranium concentration in the sample and I_s is its fluorescence intensity as measured by the instrument. Therefore, by using Eq. (7) uranium concentration in the sample can be directly calculated in a single step and there is no need to plot the fluorescence intensity versus uranium concentration plot for free uranium (i.e. without sample). The quenching effect contributes to both I_s and S_s and hence when the ratio is taken for U_s calculation it gets nullify.

3.6. Final methodology followed for uranium estimation in seawater

Taking the various factors studied and Eq. (7) in to account the following procedure is outlined for analysis of uranium in seawater.

5 ml seawater was taken each in four 50 ml beaker and to them 5 ml concentrated nitric acid was added. In these beakers 0, 100, 200 and 300 μl of 100 ng ml^{-1} uranium standard solution was added respectively. The content of the beakers were evaporated to dryness on a sand bath and then to them 2 ml of 25% phosphoric acid solution was added. The solutions were then made up to 10 ml and fluorescence intensity was measured. Blank (fluorescence intensity of only 5 ml nitric acid processed as sample) fluorescence intensity was subtracted from all the four fluorescence intensity measured for samples and sample with standards. Fluorescence intensity of sample without any standard gives I_s. Let others are I_{s1}, I_{s2} and I_{s3}. Now these I_s, I_{s1}, I_{s2} and I_{s3} are plotted against the added uranium concentration in the final solution that is 0, 1, 2 and 3 ng ml^{-1}. The slope of this plot is S_s. Once I_s and S_s is known, uranium concentration in the sample U_s can be calculated by using Eq. (7). Using this method five seawater samples were analysed. The precision of the method was found to be within 1%.

S_s was found to vary within 1% R.S.D. for same type of samples as shown in Table 2. For calculating the % R.S.D. five seawater samples from different locations were taken. Therefore, it is not required to do standard additions in every sample for finding the S_s for each sample. Instead standard addition in one sample is sufficient to calculate S_s. This S_s can be used for other samples having same matrix for calculation of uranium concentration.

3.7. Validation of values obtained from laser fluorimeter

The values were validated by analyzing the same samples by linear sweep adsorptive stripping voltametry (LSASV) of the uranium–chloranilic acid (2,5-dichloro-3,6-dihydroxy-1,4-benzoquinone) complex. The values were found to agree well with the values obtained from laser fluorimetry measurements and are presented in Table 3.

4. Conclusion

By a simple nitric acid treatment method, uranium can be estimated precisely using a laser fluorimeter in a complex matrix like seawater. This method does not require any tedious matrix separation and analyte pre-concentration steps and have good precession.

References

[1] M. Tamada, N. Seko, F. Yoshii, Radiat. Phys. Chem. 71 (2004) 221.
[2] Uranium from seawater report, issued by United Kingdom Atomic Energy Authority, October 1976.
[3] N.L. Misra, S. Dhara, K.D. Singh Mudher, Spectrochimica Acta Part B 61 (2006) 1166.
[4] P.G. Barbano, L. Rigali, Anal. Chim. Acta 96 (1978) 119.
[5] Dj. Dozozan, M.H. Pournaghi-Azar, J. Toutounchi-Asr, Talanta 46 (1998) 123.
[6] M. Nagj, J. Makjanic, I. Orlic, S. Tomic, V. Valkovic, J. Radioanal. Nuclear Chem. 97 (1986) 373.
[7] D.P.S. Rathore, M. Kumar, Talanta 62 (2004) 343.
[8] J.C. Veselsky, B. Kwlecinsk, E. Wehrstein, O. Suschny, Analyst 113 (1988) 451.
[9] A. Rani, S. Singh, Health Phys. 91 (2006) 101.
[10] A. Premadas, P.K. Srivastava, J Radioanal. Nuclear Chem. 242 (1999) 23.
[11] J.R. Lakowicz, Topics in Fluorescence Spectroscopy-Principles, Vol. 2, Plenum Press, New York, 1991.
[12] T. Matsui, H. Fujimori, K. Suzuki, J. Nucl. Sci. Tech. 25 (1988) 868.
[13] W. Davies, W. Grey, Talanta 11 (1964) 1203.
[14] G. Geipel, Coordination Chemistry Reviews 250 (2006) 844.
[15] S. Maji, K. Sundararajan, K.S. Viswanathan, Spectrochimica Acta part A 56 (2000) 1251.
[16] R.P. Thomas Gibb, Jr., Editor, Analytical Methods in Ocenography, Advances in chemistry series 147, American Chemical Society, Washington D.C., p-2, 1975. ISBN 0-8412-0245-1.
[17] F. Culkin, in: J.P. Riley, G. Skirrow (Eds.), Chemical Ocenography, Vol 1, Academic, 1965, p- 121.

Development of a new sequential injection in-line cloud point extraction system for flame atomic absorption spectrometric determination of manganese in food samples

Valfredo Azevedo Lemos [a,*], Patrícia Xavier Baliza [b], Anaildes Lago de Carvalho [a], Rafael Vasconcelos Oliveira [a], Leonardo Sena Gomes Teixeira [c], Marcos Almeida Bezerra [a]

[a] *Universidade Estadual do Sudoeste da Bahia, Núcleo de Química Analítica da Bahia (NQA), Laboratório de Química Analítica (LQA), Campus de Jequié, 45.506-191 Jequié, Bahia, Brazil*
[b] *Universidade Federal da Bahia, Instituto de Química, Campus Universitário de Ondina, 40.170-280 Salvador, Bahia, Brazil*
[c] *Universidade Salvador, Departamento de Engenharia e Arquitetura, Av. Cardeal da Silva 132, 40220-141 Salvador, Bahia, Brazil*

ARTICLE INFO

ABSTRACT

A preconcentration method for manganese determination by sequential injection cloud point extraction with subsequent detection by flame atomic absorption spectrometry (FAAS) has been developed. The enrichment of Mn was performed after a preliminary on-line cloud point extraction and entrapment of manganese-containing surfactant aggregated within a minicolumn packed with cotton. The laboratory-made reagent 4-(5′-bromo-2′-thiazolylazo)orcinol (Br-TAO) and the surfactant Triton X-114 were used for cloud point extraction. The manganese ions were eluted with sulphuric acid solution and directly introduced into the FAAS. Chemical and flow variables affecting the preconcentration were studied. Using a sample volume of 2.80 mL the limit of detection and enrichment factor were calculated to be 0.5 μg L^{-1} and 14, respectively. The sample frequency is 48 h^{-1}, considering a total run cycle of 75 s. The accuracy of the proposed method has been demonstrated by the analysis of the certified reference biological materials rice flour and tomato leaves. The method has been applied to determination of manganese in food samples.

© 2008 Elsevier B.V. All rights reserved.

1. Introduction

Manganese is an essential trace element that can be found in several food items, such as tea, grains, rice, soya beans, eggs, nuts and cereals. This metal is essential for humans and other species of the animal kingdom. Some organisms, such as diatoms, mollusks and sponges, can accumulate manganese. However, excessive levels of manganese are detrimental to the organism. People exposed to very high levels of manganese for long periods of time can develop mental and emotional disturbances and slow and clumsy body movements. Therefore, the determination of trace amounts of manganese in several matrices samples is very important for some areas, such as environmental chemistry and food control [1,2].

Manganese determination at trace levels in real samples is frequently difficult because of low concentration of the metal and matrix interferences. In this manner, the determination generally is associated to preliminary step for enrichment and elimination of interfering species. Several enrichment procedures have been developed for the determination of Mn, involving different analytical techniques such as coprecipitation [3,4], liquid–liquid [5], solid-phase extraction (SPE) [6,7] or cloud-point extraction (CPE) [8–10]. Among the various analytical techniques, CPE has been largely applied in preconcentration procedures due to advantages obtained such as reducing of disposal costs and extraction time, simplicity and achievement of high recoveries. This separation technique has received great attention because of its great potential in separation of toxic solutes from several matrices.

Cloud point extraction has been successfully coupled to on-line systems in order to determine several species in different matrices [11,12]. This combination is advantageous because it eliminates manual operations typical of batch systems, such as heating, centrifugation, cooling, removal of supernatant and dilution. The on-line incorporation of CPE to FIA was reported for the first time for the determination of coproporphyrin in pretreated urine samples [13]. Low levels of mercury(II) have been determined in water samples using a flow injection system involving CPE and spectrophotometric detection [14]. A flow injection on-line micelle-mediated preconcentration and separation procedure was used for ETAAS determination of trace lead in biological samples [15]. A comparison of traditional cloud-point extraction and on-line flow-injection

cloud-point extraction has been presented in a detailed discussion of several preconcentration conditions for both CPE procedures [16]. The authors highlighted the principal advantages of on-line FI CPE, especially preconcentration factor, extraction efficiency and analysis time. The dye 2-(5-bromo-2-pyridylazo)-5-diethylaminophenol (Br-PADAP) has been used as complexing agent in on-line CPE methodologies for the preconcentration and determination of gadolinium [17], dysprosium [18,19] and iron [19] content in urine samples.

Pyridylazo and thiazolylazo dyes have been used as extractants for various metal ions in different preconcentration methods. The use of these substances in extraction procedures is advantageous duo their great capacity to form insoluble complexes with many metallic substances [20–22]. Several pyridylazo and thiazolylazo reagents have been used for cloud-point extraction of metals. This paper reports the development of a new on-line CPE system with sequential injection for FAAS determination of trace manganese in food samples. A thiazolylazo dye (Br-TAO) has been prepared for the first time for this application. The study of variables affecting the on-line system was followed by application of the procedure in the determination of Mn in food. No reports were found in the literature on CPE on-line systems with sequential injection.

2. Experimental

2.1. Chemicals and reagents

All the reagents were of analytical grade. Deionized water was used to prepare all solutions. The laboratory glassware was kept in dilute nitric acid at least overnight and subsequently washed with deionized water. Manganese stock solution containing $1000 \mu g \, mL^{-1}$ was purchased from Merck, Darmstadt, Germany. Working manganese standards of between 5.0 and $100.0 \mu g \, L^{-1}$ were prepared on a daily basis by serial dilution from this stock standard. Solutions of the non-ionic surfactant Triton X-114 (Sigma–Aldrich, Milwaukee, USA) were prepared in high purity deionized water. Br-TAO solutions were prepared by dissolving appropriate amounts of 4-(5′-bromo-2′-thiazolylazo)orcinol (Br-TAO) laboratory-prepared in absolute ethanol (Merck). Hydrochloric, nitric and sulphuric acid solutions were prepared by direct dilution with deionized water from the concentrated solutions (Merck). KCl–HCl (3.0), acetate (4.7–6.0), borate (7.0–8.0) and ammonia (8.5–9.2) buffers were used to adjust the sample pH [23]. Sodium carbonate (Vetec, Rio de Janeiro, Brazil), 2-amino-5-bromothiazole (Sigma–Aldrich), sodium nitrite (Vetec), orcinol (Merck) and ethanol (Merck) were used for synthesis of Br-TAO. The accuracy of the method was assessed by analyzing the following certified reference materials (CRM): SRM 1568a rice flour and SRM 1573a tomato leaves from the National Institute of Standards and Technology (Gaithersburg, MD, USA).

2.2. Instrumentation

A PerkinElmer Instruments (Shelton, USA) model AAnalyst 200 flame atomic absorption spectrometer equipped with an air–acetylene burner was used for absorbance measurements. A manganese hollow cathode lamp (PerkinElmer instruments) was used as the light source at a wavelength of 279.5 nm and operated at 15.0 mA, with a 0.2 nm spectral bandpass. Deuterium lamp background correction was also used. The flame composition was acetylene (flow rate: $2.0 \, L \, min^{-1}$) and air (flow rate: $13.5 \, L \, min^{-1}$). Nebulizer flow rate was $5.0 \, ml \, min^{-1}$. Digestion of food samples and certified reference materials was carried out in a Parr Instrument 4749 (Moline, IL, USA) acid digestion bomb enclosing a chemically inert Teflon sample cup of 23 mL. Infrared spectrum was recorded
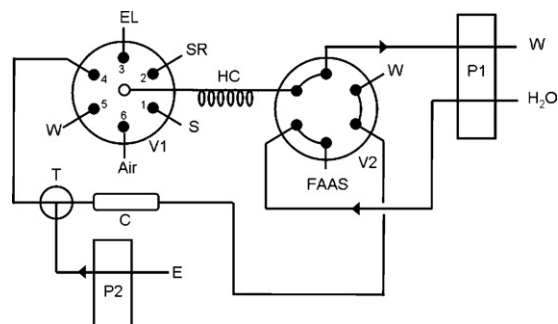
Fig. 1. Schematic diagram of on-line CPE system with sequential injection for FAAS determination of trace manganese. P1 and P2, peristaltic pumps; V1, six-position rotary valve; V2, four-way rotary valve; C, minicolumn packed with cotton; T, T-piece connected to two-way valve; HC, holding coil; S, sample solution; SR, surfactant-reagent solution; EL, electrolyte solution; E, eluent; W, waste.

in an ABB Bomen MB series model MB100 Fourier transform IR spectrometer.

The sequential injection preconcentration system is illustrated in Fig. 1. The SI manifold consists of a Rheodyne (Cotati, USA) model 5011 six-position rotary valve, a Rheodyne model 5041 four-way rotary valve (Cotati, USA) and two multichannel peristaltic pumps model 204 from Millan (Colombo, Brazil) furnished with silicone tubes to delivery the solutions. A T-piece connected to a laboratory-made Teflon two-way valve (T) was inserted into the system. This manually operated valve is open only when P2 is on. A minicolumn manufactured from a PVC tube (3.50 cm length and 0.4 cm i.d.) packed with 100 mg of cotton was also used. All connections of flow system were made using fittings, unions and tees made of plastic and PEEK materials. The manifold was built up with PTFE tube of 0.5 mm bore. All pH measurements were made with a Digimed DM 20 model (Santo Amaro, Brazil) digital pH meter.

2.3. Synthesis of Br-TAO

For Br-TAO preparation, a modified procedure based in the synthesis of similar reagents [20,24] has been performed. 2-Amino-5-bromothiazole (2.0 g) was dissolved in 50 mL of a $6.0 \, mol \, L^{-1}$ hydrochloric acid solution at 0–5 °C. A solution of 0.53 g of sodium nitrite in 20 mL of water was added dropwise. The mixture was stirred and kept at 0–5 °C for 45 min. For coupling, 0.96 g of orcinol was added to 20 mL of $1.0 \, mol \, L^{-1}$ sodium carbonate solution and the mixture was cooled to 0–5 °C. This solution was added dropwise to the above diazotized compound at vigorous stirring. The system was allowed stand overnight in refrigerator at 0–5 °C. The product was filtered and rinsed with cold water. The dark-red precipitate resulting was purified by recrystallization with ethanol and active carbon.

Solubility tests, melting point and IR instrumental techniques have been used for Br-TAO characterization. The solubility of dye was tested and it was found that Br-TAO is soluble in a 5% (w/v) NaOH solution, methanol and ethanol, and insoluble in water. Melting point was determined seven times and varied in the range of 205–207 °C°C. The IR spectrum of the dried product showed bands in the region ranging from 3400 to 3200, 1300 to 1100 and $1050 \, cm^{-1}$ corresponding to –OH, C–O, and –C–N frequencies, respectively. Fig. 2 shows a proposed structure for Br-TAO.

2.4. Operating procedure

The steps of the complete cycle for on-line CPE system with sequential injection for FAAS determination of trace manganese are summarized in Table 1. The analysis procedure started when

Table 1
Sequence steps of a complete measurement cycle for the determination of manganese

Step	Time (s)	Valve 1 position	Valve 2 position	Pump 1	Pump 2	Action
1	20	1	1	On	Off	Aspirate sample
2	5	2	1	On	Off	Aspirate reagent and surfactant
3	5	3	1	On	Off	Aspirate electrolyte solution
4	30	4	2	On	Off	Propulsion through minicolumn
5	10	5	2	Off	On	Elution and reading washing of holding coil
6	5	6	1	On	Off	Deliver water from holding coil
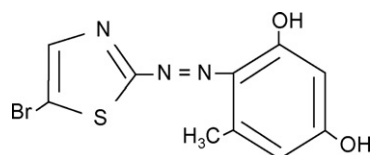
Fig. 2. Proposed structure for Br-TAO.

the pump 1 (P1) is on, and valve 2 is in position 1. In these conditions, the pump 2 (P2) is turned off and water is carried to FAAS. Firstly, 2800 μL of the sample solution (S), 700 μL of surfactant-reagent solution (SR) and 700 μL of electrolyte solution (EL) were aspirated from ports 1, 2 and 3, respectively, into the holding coil (HC, 200 cm) at a flow rate of 140 μL s^{-1}. When the reaction mixture entered for whole the holding coil, the valves 1 and 2 were simultaneously switched to its 4 and 2 positions, respectively. The reaction mixture was then propelled to the minicolumn (C) through port 4 at a flow rate of 140 μL s^{-1}. After loading, the valve 1 was then switched to position 5. Simultaneously, the pump 2 was turned on and the two-way valve was opened. In this situation, a stream of eluent (E) passes through the minicolumn to release manganese ions directly into the nebulizer of the spectrometer. At the same time, water is dispensed to flow through the holding coil in order to eliminate any loosely adhering concomitants from the tube walls to waste (W). Thereafter, air was aspirated into the holding coil from port 6 in order to deliver the water. The cycle time was 75 s (48 determinations per hour). The transient signal from the detector was recorded as a peak. Peak height values were adopted for quantification, considering that a good precision was achieved within the concentration range studied.

2.5. Samples and sample pre-treatment

Two NIST certified reference biological materials were used for method validation: SRM 1568a (rice flour) and SRM 1573a (tomato leaves). Food samples (rice flour, infant formula and corn flour) were purchased at supermarkets from Jequié, Bahia, Brazil. Approximately 0.10 g for dry sample (food or certified reference biological material) were weighed into PTFE vessels and digested in a mixture of 4.0 mL of 1:1 (v/v) nitric acid solution on a stove. After digestion, the resultant solution was allowed to cool at room temperature. These solutions were adjusted to pH 9.0 with a 10% (w/v) sodium hydroxide and 10 mL of an ammonia buffer solution. The mixtures were finally diluted to final volume by double deionized water. Spiked samples were also prepared in order to calculate the recovery of the digestion procedure. Blanks were prepared in the same way as the samples. The final concentration of Mn in all these samples was in the linear range of the method.

3. Results and discussion

In the optimization of the method, a known amount of manganese (100 μg L^{-1}) has been injected in the system. The

parameters potentially influencing the manganese extraction were investigated through the analytical signals.

3.1. Optimisation of chemical variables

The firstly studied parameter was the influence of pH in the cloud point extraction of Mn. The pH of the manganese solution was adjusted by the addition of 10 mL of buffer solution. The pH of buffer solution had been varied in the range of 3.0–10.0. The results are shown in Fig. 3. It can be observed that the analytical signal is maximum at pH 9.0. Therefore, a pH 9.0 (ammonia buffer) manganese solution was used in the following studies.

The addition of electrolytes has been employed as a good alternative in CPE on-line procedures for an efficient preconcentration of hydrophobic substances from an aqueous phase into a non-ionic surfactant phase. The salting-out effect caused by the presence of electrolytes induces the phase separation resulting in a more efficient extraction. The electrolytes Na_2SO_4, NaCl, KCl, K_2SO_4, and KNO_3 were tested as salting-out agents in the proposed CPE system. Best results were provided by NaCl. In this manner, a saturated NaCl solution was used in all subsequent experiments.

The influence of Br-TAO concentration on the cloud point extraction of manganese has also been investigated. Surfactant-reagent solutions (SR) were prepared and the Triton X-114 concentration was fixed at 2.5×10^{-2}% (v/v). Several Br-TAO amounts varying in the range between 3.0×10^{-7} and 1.6×10^{-5} mmol L^{-1} were tested. The analytical signal increases up to a Br-TAO concentration of 3.0×10^{-6} mmol L^{-1} and reaches a maximum value. So a Br-TAO concentration of 1.0×10^{-5} mmol L^{-1} was chosen for further experiments.

The surfactant chosen for cloud point extraction was Triton X-114, which possesses a low cloud-point temperature and high density. In CPE procedures, it is necessary to determine the surfactant concentration for sufficient extraction of target analytes. In this manner, the effect of Triton X-114 concentration on the cloud point extraction of manganese has also been studied. This
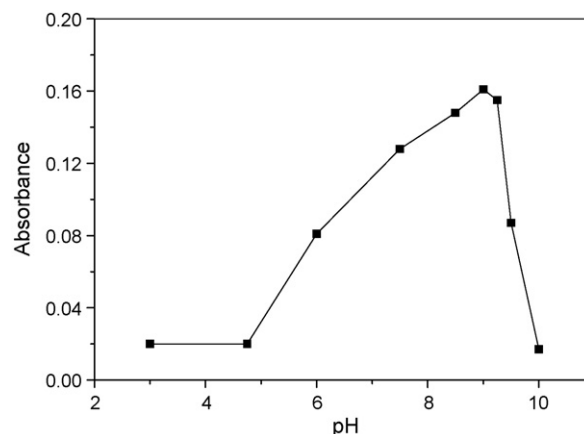
Fig. 3. Effect of pH on CPE on-line preconcentration of manganese.
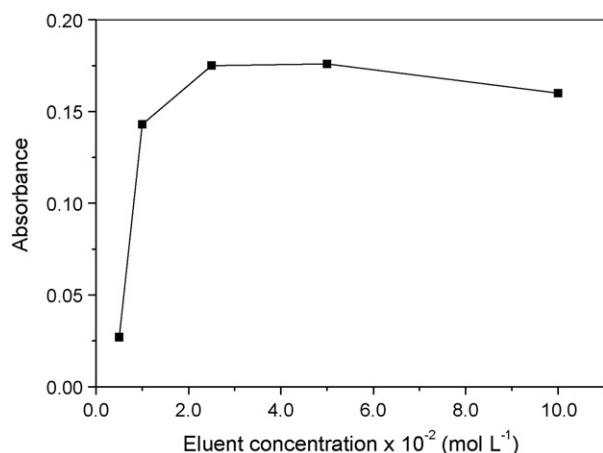
Fig. 4. Effect of eluent concentration on CPE on-line preconcentration of manganese.

effect was examined in the range of 1.0×10^{-3} to $2.5 \times 10^{-2}\%$ (v/v). The highest analytical signals for manganese were found in the range between 5.0×10^{-3} and $2.5 \times 10^{-2}\%$ (v/v) surfactant concentrations. A $1.0 \times 10^{-2}\%$ (v/v) Triton X-114 solution was chosen for subsequent work.

After the preconcentration step, an appropriate solvent should be used to remove the manganese-containing surfactant aggregated within the minicolumn. This eluent is also employed to transport the metal ions to FAAS hence the selection of proper eluent is an essential factor determining the analytical signal of manganese. Desorption of the retained manganese from the cotton minicolumn has been investigated. Several synthetic mixtures of varying composition with respect to ethanol and their acid mixtures were employed as eluents to achieve reasonable desorption efficiency and at the same time a favorable analytical signal for manganese. Mixtures containing ethanol were found to be efficient for the elution but these eluents were not able to provide a good analytical signal for manganese. The use of ethanol or water alone resulted in poor elution. Therefore, mixtures containing ethanol were not used as eluent in subsequent experiments. Solutions of hydrochloric, nitric and sulphuric acid presented the best results in terms of elution and response. Sulphuric acid has been chosen for subsequent experiments because this eluent provided more precise results. Different H_2SO_4 concentrations in the range of 5.0×10^{-3} to 1.0×10^{-1} mol L^{-1} were tested for the quantitative elution of manganese ions from the minicolumn. The signals obtained for manganese as a function of sulphuric acid concentration are shown in Fig. 4. The results indicated that the signal for manganese is maximum when the concentration of sulphuric acid is up to 2.5×10^{-2} mol L^{-1}. A 5.0×10^{-2} mol L^{-1} sulphuric acid aqueous solution was used as eluent in all subsequent experiments.

Table 2
Features of the sequential injection on-line CPE preconcentration system for manganese determination (A, absorbance; C, Mn concentration, μg L^{-1})

Enrichment factor	14
Sample consumption (μL)	2800
Consumptive index (mL)	0.20
Sample frequency (h^{-1})	48
Limit of detection (μg L^{-1})	0.5
Limit of quantification (μg L^{-1})	1.7
Linear range (μg L^{-1})	1.7–150.0
Precision (R.S.D.%)	6.3% (50 μg L^{-1}) and 5.4% (100 μg L^{-1})
Calibration function	$A = 5.00 \times 10^{-3} + 2.49 \times 10^{-3} C$

Table 3
Tolerance limits for coexisting ions for determination of manganese (100 μg L^{-1})

Substance	Maximum tolerable amount
Al^{3+}	1.0 mg L^{-1}
Cl$^-$	10.0 g L^{-1}
Co^{2+}	1.0 mg L^{-1}
Cu^{2+}	0.1 mg L^{-1}
Fe^{3+}	1.0 mg L^{-1}
K$^+$	5.0 g L^{-1}
Mg^{2+}	1.0 g L^{-1}
Na$^+$	10.0 g L^{-1}
Ni^{2+}	1.0 mg L^{-1}
Pb^{2+}	0.1 mg L^{-1}
Zn^{2+}	1.0 mg L^{-1}
NO$_3^-$	5.0 g L^{-1}

3.2. Optimization of FI flow conditions

The influence of flow rate of surfactant-rich phase passing through minicolumn has also been investigated. Flow rate values ranging from 75 to 180 μL s^{-1} were tested. The most favorable collecting conditions were achieved when using flow rates in the range from 130 to 155 μL s^{-1}. The flow rate of surfactant-rich phase was fixed at 140 μL s^{-1}. This value was also chosen for aspiration flow rate described in Section 2.4 in order to facilitate the operation.

In the proposed procedure, the eluent flow rate controls the velocity of desorption of manganese from the cotton minicolumn. Experiments were carried out by pumping a 5.0×10^{-2} mol L^{-1} sulphuric acid solution in order to achieve an analytical signal as high as possible. Best results were found within the range of 3.5–7.0 mL min^{-1}. An eluent flow rate of 5.0 mL min^{-1} was selected, which provides good sensitivity and combines aspiration (FAAS) and desorption flow rates.

In order to verify the effect of temperature and incubation time in CPE of manganese, a temperature controlled water-bath has been integrated into the SIA manifold. The holding coil was inserted in the water-bath and the temperature was varied in the range of 30–70 °C. In this experiment, the electrolyte has not been added and the step 3 in Table 1 was modified. At this step, when the reaction mixture entered the holding coil, the flow was stopped for periods from 0 to 60 s. Temperatures exceeding 70 °C were not tested due to the formation of air bubbles. No significant change on analytical signal of manganese was observed if the temperature of holding coil varied from 25 (room temperature) to 70 °C for any incubation time. Therefore, all experiments were carried out at a room temperature of 25 °C and the period for incubation time was suppressed.

After the phase separation, a filtering material should be used in order to retain the micelle phase. Based in previous methodologies [13,17], glass wool, cigarette filter and cotton were tested as filtering material. Best results, in terms of analytical signal and reproducibility, were obtained when cotton was used. The amount of cotton in

Table 4
Results obtained for manganese determination in food samples ($n = 4$)

Sample	Manganese content (μg g^{-1})		R (%)
	Added	Found	
Rice flour	0.0	2.2 ± 0.1	98
	5.0	7.1 ± 0.3	
Infant formula	0.0	6.9 ± 0.3	106
	5.0	12.2 ± 0.5	
Corn flour	0.0	4.3 ± 0.1	104
	5.0	9.5 ± 0.5	

Confidence interval, 95%; R, recovery.

Table 5
A comparison of the analytical features of the present method against some of the on-line preconcentration procedures for Mn with detection by FAAS

Separation technique	EF	f (h^{-1})	V (mL)	LOD (μg L^{-1})	Sample	Reference
SPE	30	10	15	12.0	Natural water	[7]
SPE	26	60	–	1.5	Biological samples	[29]
SPE	47	60	4.2	0.9	Mussel and non-fat milk	[30]
SPE	80	30	7.0	0.5	Seawater	[31]
SPE	21.3	12	2.5	0.8	Urine	[32]
Precipitation	55	–	8 24	2.0 1.0	Biological samples	[33]
Precipitation	30	–	150.0	2.6	Water, soil and sediment	[4]
CPE	49.1	–	50.0	0.39	Milk and water	[34]
CPE	20	–	10.0	1.45	Water	[35]
CPE	84	–	70.0	0.60	Saline effluents	[36]
CPE	20	–	100.0	5.0	Water	[37]
CPE	57.6	–	50.0	0.28	Water	[38]
CPE	14	48	2.8	0.5	Food	[This work]

EF, enrichment factor; f, sampling frequency; V, sample volume; LOD, limit of detection; CI, consumption index; SPE, solid-phase extraction; CPE, cloud point extraction.

the minicolumn was varied from 50 to 150 mg. It was found that 100 mg of cotton is sufficient for the maximum analytical signal. The amount of cotton was limited by the backpressure produced by the minicolumn. A cylindrically shaped polyvinyl chloride minicolumn (3.50 cm × 4.0 mm id) packed with 100 mg of cotton was then used in further experiments.

3.3. Features of the proposed analytical method

Under the optimal working conditions, the analytical properties of merit obtained for the on-line cloud point extraction system for Mn were summarized in Table 2. Regression curve without preconcentration resulted in the following equation: $A = -2.00 \times 10^{-3} + 1.75 \times 10^{-4} C$ (Mn 50–3000 μg L^{-1}), where A is the absorbance and C is the manganese concentration in solution, in μg L^{-1}. This equation was obtained under optimum conditions of the spectrometer. The relative standard deviation (R.S.D.%, $n = 7$, $C = 1000$ μg L^{-1}) for direct measurement of absorbance is 0.8%.

An enrichment factor of 14 was obtained by aspirating a sample loading volume of 2.8 mL into on-line preconcentration system. Enrichment factor was calculated as the ratio of the slopes of the linear section in calibration graphs for preconcentration and direct aspiration, respectively [25]. Consumptive index (CI) was also calculated. This parameter is defined as the volume of the sample consumed to achieve a unit of EF [25]. It was calculated by the ratio of the sample volume, in milliliters, and EF. The calibration graph for manganese is linear up to 150 μg L^{-1}.

From the calibration curve, the detection limit (LOD) was calculated as LOD = 3 (s/m), where s is the standard deviation of 12 measurements of a reagent blank, and m is the slope of the calibration curve. The quantification limit (LOQ) was calculated as LOQ = 10 (s/m). From these equations, LOD and LOQ were found to be 0.5 and 1.7 μg L^{-1}, respectively. The precision, assessed as the relative standard deviation of Mn determination was obtained by measuring the analytical signal for seven cycle times at levels of 50 and 100 μg L^{-1} Mn. The R.S.D. obtained were 6.3% (50 μg L^{-1}) and 5.4% (100 μg L^{-1}).

3.4. Effect of foreign ions

To evaluate the interference of co-existing ions on the determination of manganese, solutions of the Mn(II) and a single coexisting ion were prepared. Various kinds of ions were added to the aqueous solution containing 100 μg L^{-1} Mn(II). Manganese was determined by the on-line CPE proposed system. A relative error of less than 5% was considered to be within the range of experimental error. The

NaCl interference was studied without considering the salt amount added as electrolyte. As shown in Table 3, the presence of tested species caused no appreciable interferences in the determination of manganese.

3.5. Analysis of standard reference materials

In order to study the accuracy of the proposed procedure, two standard reference materials were analyzed. The samples were digested by using the dissolution procedure described in section 2.5. The standard rice flour (SRM 1568a) and tomato leaves (SRM 1573a) reference materials have a certified manganese value of 20.0 ± 1.6 and 246 ± 8 μg g^{-1}, respectively. The metal content established by the present procedure (NIST 1568a, 19.3 ± 1.2 μg g^{-1} and NIST 1573a, 239 ± 5 μg g^{-1}) agrees well with the certified values. The results indicate the effectiveness and accuracy of the proposed method.

3.6. Determination of manganese in commercial food samples

The proposed method was applied to the determination of manganese in food samples (rice flour, infant formula and corn flour), collected from supermarkets and street markets in Jequié city, Bahia, Brazil. These samples were subjected to digestion, preconcentration and manganese determination using the proposed procedure. The results are listed in Table 4. The percentage recovery (R) was determined by using the equation: $R = \{100(C_m - C_o)/m\}$. Where C_m is a value of metal in a spiked sample, C_o is a value of metal in a sample and m is the amount of metal spiked. The obtained recoveries were satisfactory for all samples and varied between 98 and 104%. These results demonstrate the applicability of the proposed CPE on-line system in the determination of manganese in food matrices.

4. Conclusion

The proposed on-line sequential injection cloud point extraction system was successfully applied for on-line preconcentration and determination of manganese in food samples by FAAS. This study allowed the development of a new, rapid, easy to use, safe and inexpensive methodology for the determination of trace manganese in food samples. The proposed methodology was compared to a variety of methods for determination of manganese reported recently in the literature. The distinct characteristics are summarized in Table 5. As can be seen from the table, except enrichment factor, the obtained analytical features by the proposed procedure

are comparable to or even better than most of the other methods. The significant features of the proposed method are the sample frequency and the consumptive index obtained by using the on-line system. Other interesting feature is the low sample volume required in this method. Due to good analytical characteristics s the proposed procedure has been demonstrated to be promising for trace element analysis. The wide spectrum of potential methods for inorganic and organic substances make thiazolylazo dyes very promising reagents for analytical purposes, especially in precipitation, cloud point and solid-phase extraction [21]. The use of these reagents in separation systems can result in very interesting and versatile procedures [26–28]. Some studies on this direction are a focus of future work in this laboratory.

Acknowledgements

References

[1] H.A. Mckenzie, L.E. Smythe, Quantitative Trace Analysis of Biological Materials, Elsevier, Amsterdam, 1988.
[2] S.L.C. Ferreira, A.S. Souza, G.C. Brandão, H.S. Ferreira, W.N.L. Dos Santos, M.F. Pimentel, M.G.R. Vale, Talanta 74 (2008) 699.
[3] M. Soylak, B. Kaya, M. Tuzen, J. Hazard. Mater. 147 (2007) 832.
[4] F.A. Aydin, M. Soylak, Talanta 73 (2007) 134.
[5] M. Alkan, D. Kara, J. Trace Microprobe Tech. 21 (2003) 479.
[6] A.P. Dos Anjos, L. Cornejo-Ponce, S. Cadore, N. Baccan, Talanta 71 (2007) 1252.
[7] M. Knap, K. Kilian, K. Pyrzynska, Talanta 71 (2007) 406.
[8] P. Liang, Z.M. Sun, J. Cao, At. Spectrosc. 28 (2007) 62.
[9] P. Liang, H. Sang, Z.M. Sun, J. Colloid Interface Sci. 304 (2006) 486.
[10] M.A. Bezerra, M.A.Z. Arruda, S.L.C. Ferreira, Appl. Spectrosc. Rev. 40 (2005) 269.
[11] J.L. Burguera, M. Burguera, Talanta 64 (2004) 1099.
[12] C. Lu, G. Song, J.M. Lin, C.W. Huie, Anal. Chim. Acta 590 (2007) 159.
[13] Q. Fang, M. Du, C.W. Huie, Anal. Chem. 73 (2001) 3502.
[14] M. Garrido, M.S. Di Nezio, A.G. Lista, M. Palomeque, B.S. Fernández Band, Anal. Chim. Acta 502 (2004) 173.
[15] J. Nan, Y. Jiang, X.P. Yan, J. Anal. At. Spectrom. 18 (2003) 946.
[16] G.Q. Song, C. Lu, K. Hayakawa, J.M. Lin, Anal. Bioanal. Chem. 384 (2006) 1007.
[17] C. Ortega, M.R. Gomez, R.A. Olsina, M.F. Silva, L.D. Martinez, J. Anal. At. Spectrom. 17 (2002) 530.
[18] C. Ortega, S. Cerutti, R.A. Olsina, M.F. Silva, L.D. Martinez, Anal. Bioanal. Chem. 375 (2003) 270.
[19] C. Ortega, S. Cerutti, R.A. Olsina, L.D. Martinez, M.F. Silva, J. Pharm. Biomed. Anal. 36 (2004) 721.
[20] S.L.C. Ferreira, M.G.M. Andrade, I.P. Lobo, A.C.S. Costa, Anal. Lett. 24 (1991) 1675.
[21] V.A. Lemos, E.S. Santos, M.S. Santos, R.T. Yamaki, Microchim. Acta 158 (2007) 189.
[22] S.L.C. Ferreira, M.L.S.F. Bandeira, V.A. Lemos, H.C. dos Santos, A.C.S. Costa, D.S. de Jesus, Fresen. J. Anal. Chem. 357 (1997) 1174.
[23] D.D. Perrin, B. Dempsey, Buffers for pH, Metal Ion Control, Chapman Hall, London, UK, 1974.
[24] E.M. Gama, A.D. Lima, V.A. Lemos, J. Hazard. Mater. 136 (2006) 757.
[25] Z. Fang, Flow Injection Separation, Preconcentration, Wiley, New York, 1993.
[26] R.J. Cassella, V.A. Salim, L.S. Jesuíno, R.E. Santelli, S.L.C. Ferreira, M.S. De Carvalho, Talanta 54 (2001) 61.
[27] V.A. Lemos, J.S. Santos, P.X. Baliza, J. Braz. Chem. Soc. 17 (2006) 30.
[28] W.N.L. dos Santos, C.M. dos Santos, S.L.C. Ferreira, J. Braz. Chem. Soc. 16 (2005) 727.
[29] M. Zougagh, A.G. De Torres, J.M.C. Pavón, Anal. Lett. 36 (2003) 1115.
[30] C.G. Bruhn, F.E. Pino, V.H. Campos, J.A. Nóbrega, Anal. Bioanal. Chem. 374 (2002) 131.
[31] K.A. Tony, S. Kartikeyan, B. Vijayalakshmy, T.P. Rao, C.S.P. Iyer, Analyst 124 (1999) 191.
[32] R.M. Cespón-Romero, M.C. Yebra-Biurrun, Anal. Chim. Acta 609 (2008) 184.
[33] C. Dittfurth, E. Ballesteros, M. Gallego, M. Valcarcel, Spectrochim. Acta B 51 (1996) 1935.
[34] A.R. Rod, S. Borhani, F. Shemirani, Eur. Food Res. Technol. 223 (2006) 649.
[35] Z.M. Sun, P. Liang, Q. Ding, J. Cao, Anal. Sci. 22 (2006) 911.
[36] M.D. Bezerra, A.L.B. Conceição, S.L.C. Ferreira, Microchim. Acta 154 (2006) 149.
[37] V.O. Doroschuk, S.O. Lelyushok, V.B. Ishchenko, S.A. Kulichenko, Talanta 64 (2004) 853.
[38] K.C. Teo, J.R. Chen, Analyst 126 (2001) 534.

Short communication

A novel amperometric biosensor based on NiO hollow nanospheres for biosensing glucose

Chengchao Li, Yanli Liu, Limiao Li, Zhifeng Du, Shoujiang Xu, Ming Zhang, Xiaoming Yin, Taihong Wang*

Key Laboratory for Micro-Nano Optoelectronic Devices of Ministry of Education, and State Key Laboratory of Chemo/Biosensing and Chemometrics, Hunan University, Changsha 410082, China

ARTICLE INFO

ABSTRACT

NiO hollow nanospheres were synthesized by controlled precipitation of metal ions with urea using carbon microspheres as templates, which were for the first time adopted to construct a novel amperometric glucose biosensor. Glucose oxidase was immobilized on the surface of hollow nanospheres through chitosan-assisted cross-linking technique. Due to the high specific active sites and high electrocatalytic activity of NiO hollow nanospheres, the constructed glucose biosensors exhibited a high sensitivity of 3.43 μA/mM. The low detection limit was estimated to be 47 μM (S/N = 3), and the Michaelis–Menten constant was found to be 7.76 mM, indicating the high affinity of enzyme on NiO hollow nanospheres to glucose. These results show that the NiO hollow nanospheres are a promising material to construct enzyme biosensors.

© 2008 Published by Elsevier B.V.

1. Introduction

Numerous efforts have been focused on the development of biosensors in recent years because of their applications in biological and chemical analysis, clinical detection, environmental monitoring, and food processing industries [1,2]. There is always a demand for highly sensitivity, stable and disposable biosensors in determining glucose in blood and urine for the diagnosis of diabetes. Enzyme immobilization is considered as an important factor in biosensor technologies. The search for novel materials to design electrochemical biosensors is of significant at present. Recently, nanostructures such as ZnO nanowires, ZrO_2 nanoparticles, carbon nanotubes, polyaniline nanofibers, and polypyrrole nanotubes have been widely investigated as alternative matrices for immobilization of enzyme due to their exceptional electrical, optical, biocompatible properties [3–6]. Besides, their large surface area can immobilize more enzyme molecules and provide direct electron transfer between the active sites of enzyme and electrode. Among the nanomaterials, NiO nanostructures have received considerable attention in recent years due to their broad applications such as catalyst, battery cathode, gas sensors, electrochromic films, and magnetic material [7–9]. However, the application of

NiO nanostructures in biosensors is rare. As NiO is a biocompatible material with a high isoelectric point (IEP) of about 10.7, which make it suitable for adsorption of proteins with low IEPs by electrostatic interaction. Moreover, NiO nanostructures with high chemical stability, high electrocatalysis, and high electron transfer capability are promising for biosensor application. In this letter, a biosensor with high sensitivity based on NiO hollow nanospheres was fabricated. NiO hollow nanospheres were synthesized by a controlled precipitation of Ni^{2+} in the presence of carbon microspheres as templates. Due to the hollow structure of NiO nanomaterials, the immobilized glucose oxidase (GO_x) showed high loading and fast electron transfer rate. The resulting biosensor exhibited high sensitivity, low detection limit to glucose. All the results provided that NiO hollow nanospheres were good matrices for protein immobilization and biosensors preparation.

2. Experimental details

2.1. Reagents

The glucose oxidase (GO_x, E.C 1.1.3.4, *from Aspergillus niger*, 200 units mg^{-1}), β-D-(+)-glucose, and chitosan (CHIT) were obtained from Sigma–Aldrich. All the other chemicals were of analytical grade supplied by Shanghai Chemical Reagent (Shanghai, China) and were used without further purification. The phosphate

---

* Corresponding author. Tel.: +86 731 8822332; fax: +86 731 8822332.
E-mail address: thwang@hnu.cn (T. Wang).
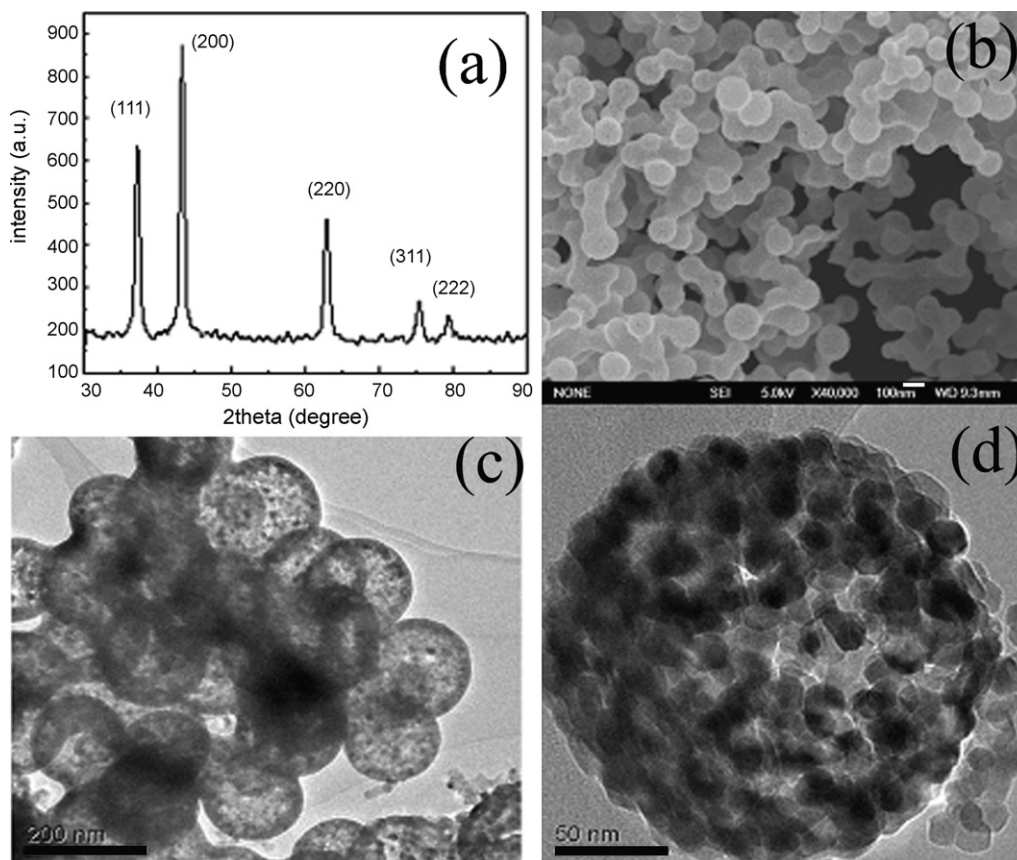
Fig. 1. (a) XRD pattern of as-grown NiO hollow nanospheres. (b) SEM image of NiO hollow nanospheres. (c) and (d) TEM images of a single hollow nanosphere.

buffer solutions (PBS, pH 6.98) were prepared from 0.04 M Na_2HPO_4 and 0.027 M KH_2PO_4. All the solutions were prepared with doubly distilled water, which was purified with a Milli-Q purification system.

2.2. Apparatus

The electrochemical experiments were carried out with a CHI 660A electrochemical workstation (Shanghai, China) with a conventional three-electrode cell. The modified or unmodified glassy carbon (GC) electrodes were used as the working electrode. The Pt wire and a saturated calomel electrode (SCE) were used as the counter and reference electrodes, respectively. All the solutions were purged with high purity nitrogen for at least 20 min prior to experiments and a nitrogen environment was then kept over the solution in the cell. The morphology and size of the synthesized NiO hollow nanospheres were characterized by scanning electron microscopy (SEM) [JSM-6700F] and transmission electron microscope [JEOL-3010F]. The operating voltage of SEM and TEM were 5 kV and 200 kV, respectively. The crystal structure of the sample was determined by X-ray diffraction (XRD) [D/max 2550V, Cu Kα radiation].

2.3. Synthesis of NiO hollow nanospheres

The NiO hollow nanospheres were synthesized by controlled precipitation method and the as-prepared carbon microspheres were used as templates [10,11]. Briefly, the carbon microspheres were synthesized through the polycondensation reaction of glucose under hydrothermal condition. In a typical procedure, 8 g of glucose was dissolved in 40 ml of deionized water. The solution was

then transferred to a 40 ml Teflon-lined autoclave and maintained at 180 °C for 6 h. Black products were obtained after centrifugation. 5 mmol of $Ni(NO_3)_2$ was dissolved in a mixture of 10 ml of deionized water and 80 ml of ethanol to form a clear solution. 0.5 g of as-prepared carbon microspheres was dispersed in the solution above with the aid of ultrasonication to give a suspension. 3 g of urea was then added to the suspension with vigorous stirring. Finally, the mixture was transferred into a round bottom flask, and kept at 60 °C for 2 days. The obtained products were subjected to four centrifugation/water and ethanol wash/redispersion cycles and then dried at 80 °C for 12 h in an oven, followed by calcinations at 500 °C in air atmosphere. Then an ashen product was collected.

2.4. Preparation of CHIT/GO$_x$/NiO/GC electrode

The GC electrode was polished by 0.3 and 0.05 μm aluminum slurries, and then was cleaned by dipping into 1:1 (v/v) aqueous solution of HNO_3, deionized water and ethanol with the assistance of ultrasonication prior to the experiment. The as-prepared NiO hollow nanospheres were dispersed in ethanol by ultrasonication for 1 h to give a 3 mg/ml suspension. Firstly, 8 μl of the mixture of NiO hollow nanospheres and ethanol was firstly cast on the surface of GC electrode and dried at room temperature. Secondly, 5 μl of GO$_x$ solution (10 mg/ml, dissolved in 0.067 M PBS, pH 6.98) was dropped onto the surface of GC electrode modified by NiO nanospheres. Finally, 5 μl of 0.5 wt.% CHIT solution dissolved in acetic acid solution was dropped onto the surface of GO$_x$/NiO/GC electrode to avoid the leakage of the enzyme. The device was dried at 4 °C overnight in a refrigerator, followed by washing step to remove the unimmobilized GO$_x$. The CHIT/GO$_x$/NiO/GC electrode was stored in PBS and kept at 4 °C in a refrigerator when not in use.

3. Results and discussions

3.1. Characterization of NiO hollow nanoshperes

The XRD pattern of the as-prepared product is shown in Fig. 1(a), where all the diffraction peaks could be well assigned to cubic-phase of NiO (JCPDS file No. 01-1239) with a lattice parameter of 0.4195 nm. The absence of impurity peaks suggests the high purity of NiO hollow nanospheres. The crystal size of the NiO particles is estimated by Scherrer formula ($D = 0.9\lambda/(\beta \cos \theta)$) from the (200) crystal surface to be about 12 nm [12], which is in agreement with the TEM image (Fig. 1(c)). Fig. 1(b) is a typical SEM image of the NiO hollow nanospheres with diameters of about 150 nm. And it clearly shows that the product consists of interconnecting hollow nanospheres. TEM image (Fig. 1(c) and (d)) shows that the hollow nanospheres are composed of many NiO nanocrystals, which are interconnected with each other to form the NiO hollow nanospheres. The brighter region around the nanocrystals indicates a large amount of pores exist in the NiO hollow nanospheres, which is useful for the adsorption of proteins.

3.2. Electrochemical performance of the modified electrodes

The enzyme electrode was characterized by cyclic voltammetry between the potentials of −0.3 V and 0.5 V, as shown in Fig. 2(a). Curves a and b are the cyclic voltammetric responses of CHIT/GO$_x$/NiO/GC electrode in stirred 0.067 M (pH 6.98) PBS in the absence and presence of 1 mM hydroquinone. No electrochemical response is observed in the absence of hydroquinone (curve a). The results indicate that hydroquinone could be used as a diffusional electron-transferring mediator. In the present of hydroquinone, a pair of redox peaks with formal potential at −0.14 V and +0.35 V versus reference electrode was clearly observed, which can be assigned to two-electron reversible redox reaction of benzoquinone/hydroquinone. With the addition of 2 mM, 3 mM, 4 mM, 5 mM glucose into the buffer solution containing hydroquinone, a sharp current increase at potential above 0.35 V was observed. The electrocatalytic peak current increases with the increasing concentration of glucose in PBS. These results indicate that the immobilized GO$_x$ on NiO nanoparticles retains its electrocatalytic activity for the oxidation of glucose. The typical enzyme-dependent catalytic process can be described as follows:

$$QH_2 - 2e \rightarrow Q \tag{1}$$

$$GO_x(FAD) + G \underset{k_{-1}}{\overset{k_1}{\rightleftharpoons}} GO_x(FAD - G) \overset{k_2}{\rightarrow} GO_x(FADH_2) + GI \tag{2}$$

$$GO_x(FADH_2) + Q \overset{k_3}{\rightarrow} GO_x(FAD) + QH_2 \tag{3}$$
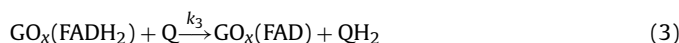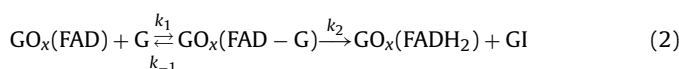
where GO$_x$ (FAD) and GO$_x$ (FADH2) represent oxidized and reduced forms of glucose oxidase, Q and QH$_2$ are the benzoquinone and hydroquinone, and G and GI are β-D-(+)-glucose and glucono-D-lactone, respectively. As the addition of glucose, the cathodic current decreased because the reduced form of the enzyme restrained the reduction of the benzoquinone at the electrode. Simultaneously, hydroquinoe was regenerated and then reoxidized at the electrode, resulting in the increase of oxidation current. In the absence of mass transport limitations, the increase of the oxidation current (i_{cat}) can be expressed as

$$\frac{1}{i_{cat}} = \frac{1}{2Fk_3S\Gamma_E^0}\frac{1}{[Q]_0} + \frac{1}{2FS\Gamma_E^0}\left(\frac{1}{k_2} + \frac{1}{k_{red}[G]}\right),$$

where F is the Faraday's constant, S the electrode area, Γ_E^0 the surface concentration of enzyme, $[Q]_0$ the mediator concentration, G the glucose concentration in PBS, $k_{red} = k_1k_2/(k_{-1} + k_2)$
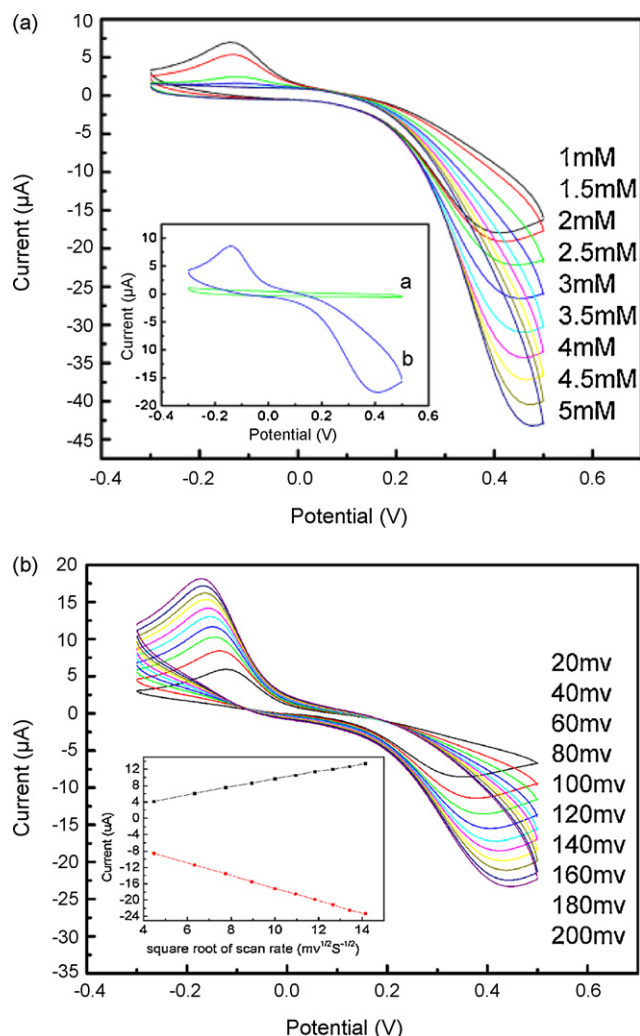
Fig. 2. (a) CVs of the electrode in the presence of glucose with different concentrations. Inset: CVs of the electrode in the presence (curve a) and absence (curve b) of hydroquinone. (b) CVs of the electrode in 0.067 M PBS (pH 6.98) containing 1 mM hydroquinone at different scan rate.

[13,14]. According to the equation, the surface concentration of GO$_x$ immobilized on the electrode surface was estimated to 1.7×10^{-13} mol/cm^2, which is due to the large surface-to-volume ratio and high IEP of NiO hollow nanospheres.

Fig. 2(b) shows the cyclic voltammograms (CVs) of CHIT/GO$_x$/NiO/GC electrode in PBS (pH 6.98) at different scan rates. Peak-to-peak separation increases with increasing scan rate, suggesting a quasireversible behavior. Both the cathodic and anodic peaks currents are linearly proportional to the square root of scan rate in the range from 20 to 200 mV/s (Linear regression equations: Pa: $y = 0.09717 + 0.94924x$, $r = 0.999$; Pc: $y = -1.68145 - 1.53808x$, $r = -0.999$), which shows a typical diffusion-controlled electrochemical behavior.

Fig. 3(a) is a typical amperometric response of the glucose biosensor after addition of successive aliquots of 0.3 mM glucose in PBS (pH 6.98) at an applied potential of 0.35 V. It is found that the biosensor shows a rapid and sensitive response to the change of glucose concentration, which is ascribed to the good electrocatalytic property of CHIT/GO$_x$/NiO/GC electrode. Besides, the response time is around 8 s for the electrode to reach 95% steady-state current, indicating a fast electron exchange between GO$_x$ and NiO. The corresponding calibration curve is shown in Fig. 3(b). The

Table 1
Glucose content determination in serum sample

Samples	Content determined by local hospital (mmol^{-1})	Content determined by current method[a] (mmol^{-1})	R.S.D. (%)	Relative error (%)
1	5.51	5.35 ± 0.06	2.3	−2.90
2	4.72	4.90 ± 0.05	2.8	+3.81
3	4.85	5.05 ± 0.1	3.5	+4.12
4	4.90	4.74 ± 0.06	2.5	−3.26
5	5.24	5.38 ± 0.08	3.2	+2.67

[a] Average of the three measurements.

linear detection range of NiO hollow nanospheres-based glucose biosensor is 1.5–7 mM. This kind of biosensor has a low detection limit of 47 μM (be estimated based on the signal-to-noise characteristics of these data (S/N = 3)) and a high sensitivity of 4.3 μA/mM. The high sensitivity of the enzyme electrode can be attributed to the excellent adsorption ability, high electrocatalytic activity and good biocompatibility of the NiO hollow nanospheres. The Michaelis–Menten constant of the system (K_M^{app}) in this work can be calculated from the well-known Lineweaver–Burk equation and is found to be 7.76 mM, which gives an indication of the enzyme–substrate kinetics for the glucose biosensor. The value of K_M^{app} for GO$_x$ in this work is much smaller than GO$_x$ immobilized by sol–gel organic–inorganic hybrid material, 22 mM, GO$_x$ immobilized by chitosan and gold nanoparticles, 10.5 mM, GO$_x$ entrapped in polypyrrole films, 19 mM, and glucose oxidase in Nafion film, 14.91 mM [15–18]. The results implied that the GC electrode modified by NiO hollow nanospheres exhibits a higher affinity to glucose.

3.3. Repeatability and reproducibility

The reproducibility of response current of the GO$_x$ enzyme electrode was investigated by comparing the response currents of 8 enzyme electrodes. The relative standard deviation (R.S.D.) was 5.3% at a glucose concentration of 0.2 mM. In order to evaluate the repeatability, an enzyme electrode was used to determine 1 mM glucose for 10 times continuously, and the R.S.D. of the response current was 3.5%.

3.4. Stability of the enzyme electrode

The CHIT/GO$_x$/NiO/GC electrode was stored in PBS (pH 6.98) at 4 °C when not in use. The stability of the biosensor was investigated using the same PBS containing 1 mM glucose. Every few days the cyclic voltammogram was recorded and using the same electrode. The peak current decreased with the increase of storage time. However, the electrode can still retain about 85% of the initial response after 20 days storage. The above results indicate that the CHIT/GO$_x$/NiO/GC electrode has a good stability.

3.5. Interference and real sample analysis

We also examined the interference of some electroactive compounds to the glucose response. The deviation of response was calculated according to $(I_i - I_g)/I_g$, where I_i and I_g were the steady-state current recorded for solutions containing glucose and interferent or glucose alone. The interference was investigated in the presence of physiological normal level with a glucose concentration of 5.6 mM. At CHIT/GO$_x$/NiO/GC electrode, the deviations caused by ascorbic acid (0.1 mM) and uric acid (0.5 mM) were 1.9% and 3.2%, respectively. This indicates that the biosensor suffers some influence from the coexistents in serum samples. However, the influence of ascorbic acid and uric acid on the glucose response was weak under the testing conditions. In order to validate the reliability of the biosensor, the determination of glucose in human serum samples was performed with the CHIT/GO$_x$/NiO/GC electrode. Fresh serum samples were first analyzed in the local hospital with ASCA AG-II Chemistry System (Landmark, USA). The samples were then reassayed with the CHIT/GO$_x$/NiO/GC electrode. For current method, a serum sample was added into the stirred 5 ml PBS (pH 6.98), and amperometric response was recorded at 0.35 V. The results were shown in Table 1. The glucose levels determined in this work were close to the values declared by local hospital, indicating that the fabricated glucose biosensor has practical potential.

4. Conclusions

We have fabricated an amperometric glucose biosensor by immobilizing glucose oxidase on the surface of NiO hollow nanospheres, which were synthesized by controlled precipitation
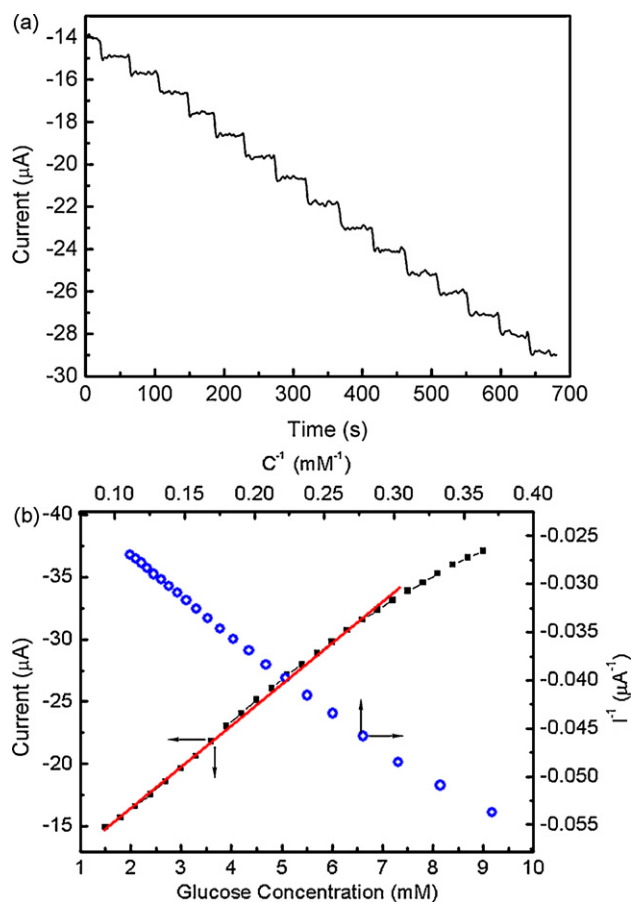
Fig. 3. (a) Amperometric responses of CHIT/GO$_x$/NiO/GC electrode with the successive addition of 0.3 mM glucose to the 0.067 M PBS (PH 6.98) under stirring. (b) The calibration curve of NiO/GO$_x$ biosensor and the Lineweaver–Burk plot. The straight line is the linear fit to the calibration curve. A potential of +0.35 V (vs SCE) was applied on the working electrode in the measurement.

of metal ions with urea. The fabricated CHIT/GO$_x$/NiO/GC electrode exhibits high sensitivity and linear response in the range of 1.5–7 mM glucose concentration due to the large specific surface area and high electrocatalytic activity of NiO hollow nanospheres. The low value of Michaelis–Menten constant of 7.76 mM indicated high enzyme affinity of glucose oxidase. The results clearly suggest that NiO hollow nanospheres provide an attractive matrix for effective immobilization of biomolecules.

Acknowledgements

References

[1] N.A. Rakow, K.S. Suslick, Nature (London) 406 (2000) 710.
[2] R.W. Keay, C.J. McNeil, Biosens. Bioelectron. 13 (1998) 963.
[3] A. Wei, X.W. Sun, J.X. Wang, Y. Lei, X.P. Cai, C.M. Li, Z.L. Dong, W. Huang, Appl. Phys. Lett. 89 (2006) 123902.
[4] Y. Liu, M. Wang, F. Zhao, Z. Xu, S. Dong, Biosens. Bioelectron. 21 (2005) 984.
[5] Y. Xian, Y. Hu, F. Liu, Y. Xian, H. Wang, L. Jin, Biosens. Bioelectron. 21 (2006) 1996.
[6] E.M.I. Mala Ekanayake, D.M.G. Preethichandra, Keiichi Kaneto, Biosens. Bioelectron. 23 (2007) 107.
[7] C.L. Carnes, K.J. Klabunde, J. Mol. Catal. A, Chem. 194 (2003) 227.
[8] V. Biju, M. Abdul Khadar, Mater. Sci. Eng.: A 304–306 (2001) 814.
[9] Y. Ichiyanagi, N. Wakabayashi, J. Yamazaki, S. Yamada, Y. Kimishima, E. Komatsu, H. Tajima, Physica B 329–333 (2003) 862.
[10] X.M. Sun, Y.D. Li, Angew. Chem. Int. Ed. 43 (2004) 597.
[11] H.S. Qian, G.F. Lin, Y.X. Zhang, Poernomo Gunawan, R. Xu, Nanotechnology 18 (2007) 355602.
[12] Hyo-Jin Ahn, Hyun-Chul Choi, Kyung-Won Park, Seung-Bin Kim, Yung-Eun Sung, J. Phys. Chem. B 108 (2004) 9815.
[13] C. Bourdillon, C. Demaille, J. Gueris, J. Moiroux, J.M. Saveant, J. Am. Chem. Soc. 115 (1993) 12264.
[14] S. Zhang, Y. Niu, C. Sun, Electrochim. Acta 49 (2004) 4777.
[15] B. Wang, B. Li, Q. Deng, S. Dong, Anal. Chem. 70 (1998) 3170.
[16] D.W.M. Arrigant, P.N. Bartlett, Biosens. Bioelectron. 13 (1998) 293.
[17] B.Y. Wu, S.H. Hou, F. Yin, J. Li, Z.X. Zhao, J.D. Huang, Q. Chen, Biosens. Bioelectron. 22 (2007) 838.
[18] K.I. Ozoemena, T. Nyokong, Electrochim. Acta 51 (2006) 5131.

Review

Recent development of interaction of transition metal complexes with DNA based on biosensor and its applications

Feng Li, Wei Chen, Chenfei Tang, Shusheng Zhang*

Key Laboratory of Eco-Chemical Engineering, Ministry of Education, College of Chemistry and Molecular Engineering, Qingdao University of Science and Technology, Qingdao 266042, PR China

ARTICLE INFO

ABSTRACT

In this article interaction of transition metal complexes with DNA and its applications in electrochemical DNA biosensors as hybridization indicator or electroactive marker of DNA are reviewed. Special emphasis has been given to the efforts for the development of new transition metal complexes and their interaction to DNA. DNA and polymers covalently conjugated with transition metal complexes were also reviewed.

© 2008 Elsevier B.V. All rights reserved.

Contents

Fig. 1. Recognition interface consisting of the immobilized DNA probe and steps in the detection of a specific DNA target strand (reproduced from Ref. [7], Copyright (2007) with permission from Royal Society Chemistry).

1. Introduction

Deoxyribonucleic acid (DNA) offers chemists a very powerful tool. The detection of specific DNA sequences provides the fundamental basis for monitoring a wide variety of genetic diseases, viral infections and infectious diseases. Moreover, an understanding of how small molecules interact with DNA is potentially useful in the design of new drugs and diagnostic reagents. DNA biosensors based on nucleic acid recognition processes have received considerable attention in rapid and inexpensive DNA assays [1,2]. Different detection methods including fluorescence, surface plasmon resonance, quartz crystal microbalance and electrochemistry have been employed to study DNA hybridization or its interactions with various molecules. Amongst them, electrochemical transducers offer powerful tools for interfacing DNA recognition at the molecular level and converting the hybridization event into an analytical signal [3–6]. Due to attractive advantages such as high sensitivity, low cost and minimal power requirements, electrochemical DNA biosensors represent a dynamically developing field in the fields of clinical diagnosis, environmental monitoring and drug analysis.

Electrochemical DNA biosensors rely on the conversion of DNA base pair recognition events into a useful electrical signal. In such devices, the sensitive recognition layer was coupled to a signal transducer. Detection based on the use of electroactive hybridization indicators is still of attractive significance. In brief, single-stranded DNA (ssDNA) probe is immobilized onto different electrodes to recognize its complimentary target sequence via base pairing. The conversion of hybridization/recognition event into measurable electrochemical signals was achieved by using an electroactive compound [2,4]. Nowadays, transition metal complexes have been widely used as electrochemical hybridization indicators or electroactive markers of DNA. Moreover, it has been reported that many transition metal complexes have activity of chemistry nuclease, such as splitting DNA with specificity. Development of new transition metal complexes and utilization of their interaction with DNA will be potentially useful in clinical diagnosis for the design of new drug or reactive probes.

2. Electrochemical hybridization indicators and electroactive markers of DNA

Fig. 1 illustrates the recognition interface consisting of the immobilized DNA probe and steps in the detection of a specific DNA target strand [7]. Electrochemical DNA biosensors rely on the conversion of the DNA base pair recognition events into a useful electrical signal. Electrochemical hybridization indicators are usually electroactive compounds with small molecular weight and different affinities for ssDNA relative to double-stranded DNA (dsDNA). Binding of small molecules to DNA are normally defined as three modes including electrostatic interaction, groove binding, and intercalation. It is well known that grooves are formed only within the double helix. As a result, groove-binders have greater affinity for dsDNA than ssDNA, whereas, electrostatic binders have the poorest duplex-specific affinity. For intercalators, they usually have much higher duplex affinity and binding stability.

The desired properties [7] of an ideal electrochemical hybridization indicator can be summarized as follows:

(1) Stable reduced and oxidized forms.
(2) Duplex-specific affinity was highlighted and ssDNA affinity should be negligible or, at least, as low as possible.
(3) Fast and reversible electron transfer between the electrochemical hybridization indicator and electrode.
(4) Redox potential should be outside those for the oxidation and reduction processes of the nucleobases. Low redox potentials are preferred.
(5) Ease of preparation, low toxicity and cost.

In summary, hybridization was detected by redox-active complexes that associated selectively and reversibly with hybrid duplex. As a result, the electrochemical signal (peak current) corresponding to the indicator increases in proportion to the amount of hybrid duplex formed, which relates to the amount of complementary target sequence.

Redox label of DNA using transition metal complexes is outstanding over the past few years, despite interaction with dsDNA formed after hybridization. The covalent attachment of metal complexes probes to DNA or polymers have been reported recently [8,9]. The combination of redox characteristics and photophysical properties of transition metal complexes might meet the multifunctional analysis of DNA and possess potential application in biochip device.

3. Interaction of transition metal complexes with DNA and their application as hybridization indicator

Nowadays, transition metal complexes show potential and have been successfully applied as the mostly used electroactive hybridization indicators for DNA analysis. In general, transition metal complexes usually consist of one or several transition metal ion(s) as center ion(s) and several organic heterocycles as ligands.

Cationic metal complexes that interact in a different way with ssDNA and dsDNA are usually applied. Transition metal complexes used as electrochemical hybridization indicators could be classed based the center transition metal ions.

3.1. Ruthenium(II) complexes

Ruthenium(II) complexes was useful for studying DNA binding with transition metal complexes owing to their attractive characteristics including ease of preparation, intense optical absorption and emission, and inertness towards substitution and racemization. Ruthenium(II) complexes containing mixed ligands are usually investigated [10,11]. The structure blocks commonly used for the synthesis of ruthenium(II) complexes included 2,20-bipyridine (bpy), 1,10-phenanthroline (phen), 2,20-bipyridine (bipy) and their derivatives.

Ji group synthesized asymmetric bidentate ruthenium(II) complex and systematically investigated their interaction with DNA [10]. Ruthenium(II) complex $[Ru(bpy)_2(PYNI)]^{2+}$ (PYNI = 2-(20-pyridyl)naphthoimidazole) could bind to calf thymus DNA (CT-DNA) in an intercalative mode. Using asymmetric ligands, 3-(pyrazin-2-yl)-*as*-triazino[5,6-*f*]acenaphthylene (dta) and 3-(pyrazin-2-yl)-*as*-triazino[5,6-*f*]phenanthrene (dpt), three ruthenium(II) complexes $[Ru(bpy)_2(L)][ClO_4]_2$ (L = ddt (complex 1), dta (complex 2) and dpt (complex 3), ddt = 3-(pyrazin-2-yl)-5,6-diphenyl-*as*-triazine) were also synthesized and investigated [11]. Results showed that the planar extension of intercalative ligand increased the interaction with DNA. They also found that the size and shape of the intercalated ligand had remarkable effect on the strength of interaction. $[Ru(bpy)_2(dta)][ClO_4]_2$, and $[Ru(bpy)_2(dpt)][ClO_4]_2$ could enantioselectively interact with CT-DNA but not $[Ru(bpy)_2(ddt)][ClO_4]_2$, as showed by circular dichroism (CD) signals of the dialysates of the racemic complexes against CT-DNA. It was interesting that $[Ru(bpy)_2(PYNI)]^{2+}$, $[Ru(bpy)_2(dta)][ClO_4]_2$, and $[Ru(bpy)_2(dpt)][ClO_4]_2$ could promote cleavage of plasmid pBR 322 DNA from the supercoiled form I to the open circular form II upon irradiation.

A series of enantiomeric polypyridyl ruthenium(II) complexes including $[Ru(bpy)_2CNOIP](PF_6)_2$ (CNOIP = 2-(2-chloro-5-nitrophenyl)imidazo[4,5-*f*][1,10]phenanthroline), $[Ru(bpy)_2HPIP]$ $(PF_6)_2$ (HPIP = 2-(2-hydroxyphenyl)imidazo[4,5-*f*][1,10]phenanthroline), $Ru(bpy)_2DPPZ](PF_6)_2$ (DPPZ = dipyrido[3,2:α-2'-3':*c*]-phenazine), $[Ru(bpy)_2TAPTP](PF_6)_2$ (TAPTP = 4,5,9,18-tetraazaphenanthreno-[9,10-*b*]triphenylene) were also prepared by Ji group [12]. Though all the enantiomers bound to DNA through intercalative mode, the binding affinity of each chiral complex to DNA was different due to the different shape and planarity of the intercalative ligand. Upon irradiation at 302 nm, $[Ru(bpy)_2HPIP](PF_6)_2$, $Ru(bpy)_2DPPZ](PF_6)_2$, and $[Ru(bpy)_2TAPTP](PF_6)_2$ could promote the cleavage of plasmid pBR 322 DNA from supercoiled form I to nicked form II. Additionally, obvious enantioselectivity was observed on DNA cleavage for the enantiomers of $[Ru(bpy)_2HPIP](PF_6)_2$ and $[Ru(bpy)_2TAPTP](PF_6)_2$. PMIP (PMIP = 2-(4-methylphenyl)imidazo[4,5-*f*]1,10-phenanthroline) was also used to synthesize three Ru(II) complexes, including $[Ru(bpy)_2PMIP]^{2+}$, $[Ru(phen)_2PMIP]^{2+}$ and $[Ru(dmp)_2PMIP]^{2+}$ (dmp = 2,9-dimethyl-1,10-phenanthroline) [13]. The theoretical calculations using density functional theory (DFT) on the level of B3LYP/LanL2DZ basis were used to investigate the binding strength or binding constants (K_b). Results showed that $[Ru(bpy)_2PMIP]^{2+}$ and $[Ru(phen)_2PMIP]^{2+}$ could bind to CT-DNA through intercalation, while $Ru(dmp)_2PMIP]^{2+}$ via partial intercalative mode. Ancillary ligands of polypyridyl Ru(II) complexes had significant effects on the spectral properties and the DNA binding behaviors. They [14] also synthesized two polypyridyl ligands with substituent
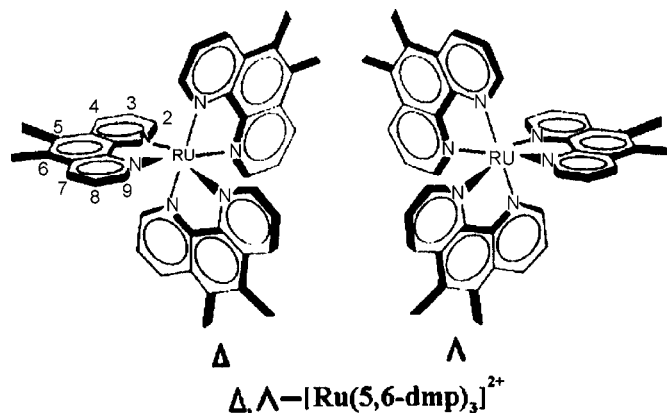
Fig. 2. Schematic view of *rac*-[Ru(5,6-dmp)$_3$]$^{2+}$ (reprinted with permission from Ref. [18]. Copyright (2006) American Chemical Society).

Br at different positions in the phenyl ring, including OBIP (OBIP = 2-(2-bromophenyl)imidazo[4,5-*f*]-1,10-phenanthroline) and PBIP (PBIP = 2-(4-bromophenyl)imidazo[4,5-*f*]-1,10-phenanthroline). $[Ru(dmp)_2(OBIP)]_2$ bound to CT-DNA via a semi-intercalative mode while $[Ru(dmp)_2(PBIP)]_2$ strongly bound to CT-DNA through intercalation. Some experimental regularities or trends were reasonably explained by the theoretical results.

Palaniandavar group synthesized a serial of Ru(II) mixed ligand complexes including $[Ru(NH_3)_4(L)]^{2+}$, L = bipy, phen, 5,6-dmp, 4,7-dmp, 22,9-dmp, 3,4,7,8-tetra-methyl-1,10-phenanthroline (Me$_4$phen), imidazo[4,5-*f*][1,10]phenanthroline (ip), 2-phenylimidazo[4,5-*f*][1,10]phenanthroline (pip), 2-(2-hydroxyphenyl)imidazo[4,5-*f*][1,10]phenanthroline (hpip), 4,7-diphenyl-1,10-phenanthroline (dip), naphtha[2,3-*a*]dipyrido[3,2-*h*:2′,3′-*f*]phenazine-5,18-dione (qdppz), and 5,18-dihydroxynaphtho[2,3-*a*]dipyrido[3,2-*h*:2′,3′-*f*]phenazine (hqdppz) [15,16]. Those complexes interacted with DNA through their diimine face, which was supported by the hydrogen bonding of the ammonia co-ligands. When the diimines in these complexes are different as methyl-substituted 1,10-phenanthrolines [15] and modified 1,10-phenanthrolines [16], the DNA binding affinities were higher than those with phen and bpy co-ligands. The interaction between CT-DNA and Ru(II) complexes with 5,6-dmp as primary ligand and phen, bpy, pyridine (py) and NH$_3$ as co-ligands was also investigated [17]. The DNA binding constants decreased in the order of tris(5,6-dmp)Ru(II) > bis(5,6-dmp)Ru(II) > mono(5,6-dmp)Ru(II). The phenomenon that they depend upon the number of 5,6-dmp ligands revealed hydrophobic interaction between 5,6-dimethyl groups and DNA surface. For the bis(5,6-dmp)Ru(II) complexes, those with monodentate py or NH$_3$ as co-ligands showed slightly higher DNA binding affinities than the bpy and phen analogues. The phenomena suggest that the complexes interact with DNA through the co-ligands while 5,6-dmp ligand interacted with the exterior of the DNA surface. Two DNA binding modes including surface/electrostatic and strong hydrophobic/partial intercalative DNA interaction were given for such mixed-ligand complexes. Interaction of *rac*-[Ru(5,6-dmp)$_3$]$^{2+}$ with CT-DNA was also investigated [18]. The X-ray crystal structure of the complex *rac*-[Ru(5,6-dmp)$_3$]Cl$_2$ revealed a distorted octahedral coordination geometry with the Ru–N bond distances shorter than its phen analogue. Schematic view of *rac*-[Ru(5,6-dmp)$_3$]$^{2+}$ was given in Fig. 2. The K_b for the interaction between CT-DNA and the complex was $(8.0 \pm 0.2) \times 10^4 \, M^{-1}$, which was much more strong compared with its phen analogue. Moreover, the emission intensity of the 5,6-dmp complex was dramatically enhanced when bound to DNA, which was also higher than that of the phen analogue. The ^{1}H NMR
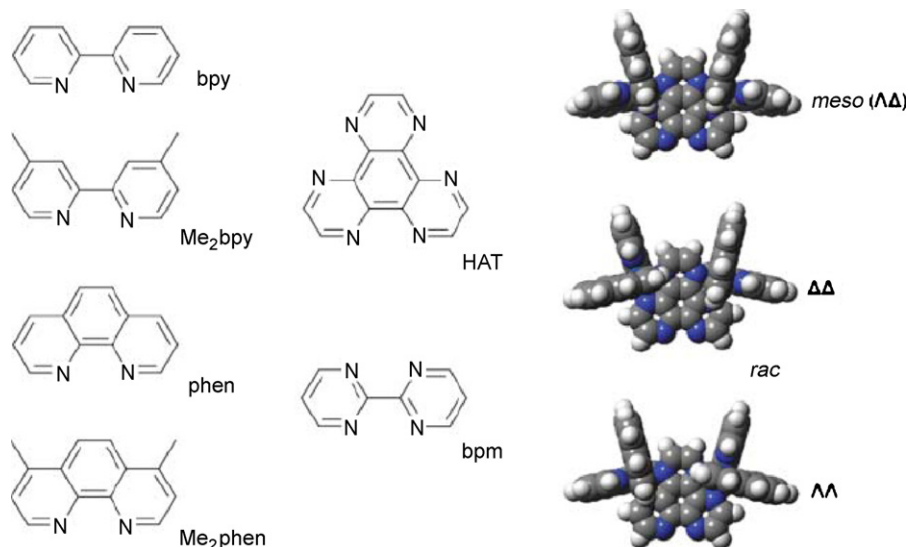
Fig. 3. Structures of the ligands used and models of the three stereoisomeric forms of the compound [{Ru(phen)$_2$}$_2$(μ-HAT)]$^{4+}$ (reproduced from Ref. [20], Copyright (2006) with permission from Royal Society Chemistry).

spectra of *rac*-[Ru(5,6-dmp)$_3$]$^{2+}$ bound to poly d(GC)$_{12}$ revealed that the complex closely interacted in the major grooves of DNA. Electrochemical studies showed that 5,6-dmp complex stabilized CT-DNA from electrocatalytic oxidation of its guanine base.

The preferential binding of the Δ-enantiomer of mixed-ligand complex, *rac*-[Ru(5,6-dmp)$_2$(dppz)]Cl$_2$ [dppz = dipyrido[3,2-*a*:2′,3′-*c*]phenazine], to the right-handed CT-DNA was found [19]. The 5,6-dmp complex exhibited preferential binding to [d(AT)$_6$]$_2$ over [d(GC)$_6$]$_2$ and the complex aggregated formed with six [Ru(5,6-dmp)$_2$(dppz)]$^{2+}$ cations per base pair of [d(AT)$_6$]$_2$. For [Ru(phen)$_2$(dppz)]$^{2+}$, however, only one cation per base pair was involved in DNA binding.

Smith et al. [20] used ^{1}H NMR spectroscopy and fluorescent intercalator displacement (FID) assays to investigate the DNA binding abilities of two series of dinuclear polypyridyl ruthenium(II) complexes including [{Ru(L)$_2$}$_2$(μ-BL)]$^{4+}${L = bpy, 4,4′-dimethyl-2,2′-bipyridine (Me$_2$bpy), phen, or 4,7-dimethyl-1,10-phenanthroline (Me$_2$phen); BL = 2,2′-bipyrimidine (bpm) or 1,4,5,8,9,12-hexaazatriphenylene (HAT)}. Structures of the ligands used in the investigation and models of the three stereoisomeric forms of [{Ru(phen)$_2$}$_2$(μ-HAT)]$^{4+}$ were given in Fig. 3. *Meso*-[{Ru(phen)$_2$}$_2$(μ-HAT)]$^{4+}$ was proven to be a high-affinity DNA hairpin probe.

Vrabel et al. [21] prepared purines bearing phenanthroline or bipyridine ligands and their Ru(II) complexes in position 8. The complexes were investigated as model compounds for electrochemical DNA labeling. Using carbon paste and mercury electrodes, the electrochemistry of the modified purines and the Ru(II) complexes was studied by cyclic or square-wave voltammetry. The experimental redox potentials of such compounds were compared with quantum chemical calculations. A very good agreement between experiment and theory was obtained. Several compounds of this series exhibited considerable cytostatic effect and activity against the hepatitis C virus (HCV).

Gaudry et al. [22] used surface enhanced resonance raman scattering (SERRS) to study the interaction between DNA and Ru(bpy)$_2$(Hcmbpy)(PF$_6$)$_2$ (Hcmbpy = 4-carboxy-4′-methyl-2,2′-bipyridine). In the presence of DNA, the intensity of SERRS spectra for such complexes reduced in particular for the specific bands assigned to the Hcmbpy ligand. As a result, such Ru complex bound to DNA through the Hcmbpy moiety via an intercalation mode.

DNA binding with enantiopure Ru complex was more efficient than with the corresponding racemic complexes.

Steichen et al. [23] proposed an electrochemical detection of DNA hybridization method based on electrostatic interactions of [Ru(NH$_3$)$_6$]$^{3+}$ cations with DNA. Peptide nucleic acid (PNA) molecules, which contained no anionic phosphate groups, were firstly immobilized as capture probes on the gold substrate. [Ru(NH$_3$)$_6$]$^{3+}$ adsorbed onto the anionic phosphate backbone of target DNA after hybridization. Consequently, a clear hybridization detection signal was observed. Very good discrimination against the single-base mismatch A2143G, internal to the 23S rRNA gene of *Helicobacter pylori*, was obtained.

3.2. Copper(II) complexes

Palaniandavar group [24] investigated DNA binding properties of mixed-ligand copper(II) complexes of iminodiacetic acid. The complexes were Cu(imda)(phen)(H$_2$O) (H$_2$imda = iminodiacetic acid, and phen = 1,10-phenanthroline), Cu(imda)(5,6-dmp) (5,6-dmp = 5,6-dimethyl-1,10-phenanthroline) and Cu(imda)(dpq) (dpq = dipyrido-[3,2-*d*:20,30-*f*]-quinoxaline). K_b for binding of such three complexes with CT-DNA was $0.60 \pm 0.04 \times 10^3$ M^{-1}, $3.9 \pm 0.3 \times 10^3$ M^{-1}, and $1.7 \pm 0.5 \times 10^4$ M^{-1}, respectively. Cu(imda)(phen)(H$_2$O) and Cu(imda)(dpq) bound to DNA through partial intercalation while Cu(imda)(5,6-dmp) was involved in groove binding. All the three complexes showed cleavage of pBR322 supercoiled DNA in the presence of ascorbic acid and showed hydrolytic DNA cleavage activity in the absence of light or a reducing agent. Three linear unsymmetrical tridentate ligands N-methyl-N′-(pyrid-2-ylmethyl)ethylenediamine (L1), N,N-dimethyl-N′-(pyrid-2-ylmethyl)ethylenediamine (L2) and N,N-dimethyl-N′-((6-methyl)pyrid-2-ylmethyl)ethylenediamine (L3) were used to prepare complexes of Cu(L1)Cl$_2$, Cu(L2)Cl$_2$ and Cu(L3)Cl$_2$ [25]. A covalent binding mode was revealed with coordination of most possibly guanine N7 nitrogen of CT-DNA to form a CuN$_4$ chromophore. The complexes could also induce the cleavage of pBR322 plasmid DNA and Cu(L1)Cl$_2$ was more efficient. DNA-fiber EPR study of the orientation of Cu(II) complexes of 1,10-phenanthroline ([Cu(phen)]$^{2+}$) and its derivatives ([Cu(phen)$_X$aa]$^{n+}$ (X standed for an aa-amino acid) bound to DNA was performed by the same group [26]. The phenanthroline moiety
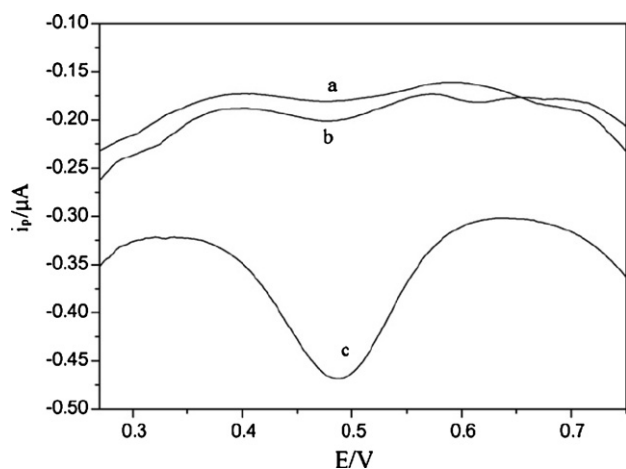
Fig. 4. Differential pulse voltammograms of [Cu(dmp)(H$_2$O)Cl$_2$] on the electrode (a) of target ssDNA immobilized, (b) after hybridization with complementary sequence, and (c) after hybridization with mismatched sequence (reproduced from Ref. [29], Copyright (2007) with permission from Elsevier).

Table 1
Examples of transition metal complexes used for the biosensing of DNA hybridization.

Metal atom	Indicator	Detection mode transducer	Electrode	Refs.
Os	[Os(bpy)$_3$]$^{3+}$	DPV	Gold	[42]
Os	[Os(phen)$_3$]$^{3+}$	DPV	Gold	[42]
Os	[Os(bpy)$_2$Cl$_2$]$^+$	CV	Gold	[43]
Os	[Os(bpy)$_2$Cl$_2$]$^+$	CV	GCE	[44]
Os	[Os(bpy)$_2$(phe-dione)]$^{3+}$	DPV	Gold	[45]
Os	[Os(DA-bpy)$_2$DPPZ]$^{2+}$	DPV	Gold	[46]
Mn	([Mn(Im)$_6$](teph)·4H$_2$O)	DPV	GCE	[47]
Fe	{[Fe(phen)(H$_2$O)$_3$]$_2$O}(SO$_4$)$_2$	DPV	Gold	[48]
Ni	Ni(NCS)$_2$(Mim)$_4$	CV	GCE	[49]

intercalated to DNA. The amino acids in the ternary complexes of glycine, leucine, serine, threonine, cysteine, methionine, and asparagine were partly substituted with some coordinating groups in DNA, whereas the ternary complexes of lysine, arginine, and glutamine remained intact on DNA.

Jiao group [27] synthesized a new copper complex of [Cu(bpy)(pba)$_2$H$_2$O]0.5H$_2$O (pba = *p*-methylbenzoate). The complex bound to DNA through intercalation mode via 2,20-bipyridine ring into DNA base pairs. Such copper complex could cleave pBR322 DNA effectively in the presence of ascorbic acid. Zhang group [28] prepared copper complex of 4,5-diazafluorene-9-one (dafone) and bromine ligands ([Cu(dafone)$_2$]Br$_2$). Its interaction with salmon sperm DNA was studied. The intercalation mode was revealed. Using Cu(dafone)$_2$Br$_2$ as a new electrochemical DNA indicator, detection of human hepatitis B virus (HBV) DNA fragment by differential pulse voltammetry (DPV) was achieved with a detection limit of 3.18×10^{-9} M. They also developed an electrochemical DNA biosensor using [Cu(dmp)(H$_2$O)Cl$_2$] as a new hybridization indicator [29]. Numerous factors affecting the probe immobilization, target hybridization, and indicator binding reactions were optimized to maximize the sensitivity and speed the assay time. Signal of [Cu(dmp)(H$_2$O)Cl$_2$] was observed after hybridization with complementary sequence in DPV, as shown in Fig. 4. A sequence of HBV could be detected with a detection limit of 7.0×10^{-8} M. [CuL(H$_2$O)$_2$](ClO$_4$)$_2$(H$_2$O)$_2$, (L = *N*-(5-sulfosalicylidene) 4′-bromoaniline) [30], [CuL(C$_6$H$_5$N$_2$O$_2$)(ClO$_4$)$_2$H$_2$O, CuL) (L = *N*-(5-sulfosalicylidene)-4′-nitraniline) [31], tetraploid (imidazole) Copper(II) Terephthalate [32], and mononuclear copper(II), nickel(II) and cobalt(III) tetracoordinate macrocyclic complexes [33] were also prepared by the same group. Interactions of the complexes with DNA were also systematically investigated.

3.3. Cadmium(II) and cobalt(II)complexes

Zhang et al. [34] developed DNA biosensor using diaquabis[*N*-(2-pyridinylmethyl)benzamide-κ^2*N,O*]-cadmium(II) dinitrate, {[CdL$_2$(H$_2$O)$_2$](NO$_3$)$_2$, L = *N*-(2-pyridinylmethyl) benzamide}, as a new electroactive indicator for detecting of HBV DNA. The binding ratio between [CdL$_2$]$^{2+}$ and salmon sperm DNA was calculated to be 2:1 and the binding constant was 25.56 M$^{-1/2}$. Target HBV DNA could be quantified ranged from 1.01×10^{-8} to 1.62×10^{-6} M with a detection limit was 7.19×10^{-9} M. Nucleic acid biosensor for the detection of short sequence related to HBV

using bis(benzimidazole)cadmium(II) dinitrate as electrochemical indicator was also developed [35]. They [36] also obtained the crystal of three hexakis(imidazole)metallo complexes of Cd, Co and Ni. Such complexes all interact with DNA mainly by intercalation.

Zhang group [37] studied the interaction mechanism between 1,10-phenanthroline cobalt(II) complex [Co(phen)$_2$ClH$_2$O]Cl and salmon sperm DNA. An intercalative mode was identified. Electrochemical DNA biosensor was developed by covalent immobilization of probe ssDNA related to HIV on the activated glassy carbon electrode (GCE). With [Co(phen)$_2$ClH$_2$O]$^+$ being the novel electrochemical hybridization indicator, selective detection of complementary ssDNA was achieved using DPV. The complex [Co(phen)$_2$IP]·2ClO$_4$·3H$_2$O (IP = imidazo[*f*] phenanthroline) was also synthesized by the group [38]. The binding ratio between [Co(phen)$_2$IP]$^{2+}$ and salmon sperm DNA was calculated to be 1:1 and the binding constant was 3.74×10^5 M^{-1}. A HIV DNA biosensor was developed by covalent immobilizing of single-stranded HIV DNA fragments to a modified GCE. Using [Co(phen)$_2$IP]$^{2+}$ as electrochemical indicator, a detection limit of 27 pM was achieved using DPV. Karadeniz et al. [39] also investigated the using of the intercalator, [Co(phen)$_3$]$^{3+}$, for the detection of DNA hybridization.

Erdem et al [40] accomplished the detection of hybridization using Co(III) complex, [Co(phen)$_3$$^{3+}$] as indicator species. The reversible electroactivity of such complex and strong association with the immobilized dsDNA segment lead to significantly enhanced voltammetric signals.

Electrochemical and spectroscopic studies on the interaction between tetracoordinate macrocyclic cobalt(III), copper(II) and nickel(II) complexes and DNA were also performed by Zhang et al. to find highly efficient ligands for hepatic asialoglycoprotein receptor(ASGPR) [33]. Four cluster galactosides with different scaffolds were synthesized. Results showed that trivalent cluster galactosides behaved better than divalent analogues. The cluster galactosides with aryl groups on their scaffolds presented better binding affinity than those with aliphatic chain scaffolds. Jiao et al. [41] synthesized a new bis(*N*-benzyl-benzotriazole)dichloro (bbt) Co(II) complex (Co(bbt)$_2$Cl$_2$). The interaction of such complex with fish sperm DNA was studied. The binding of DNA with the complex contained electrostatic binding and intercalation.

3.4. Other metal complexes

Transition metal complexes used for the biosensing of DNA were given in Table 1. As shown, the central metal atom included Os, Mn, Fe and Ni. The ligands contained bpy, phen, 1,10-phenantroline-5,6-dione, 4,4-diamino-2,2-bipyridine, imidazole, 1-methylimidazole, terephthalate and thiocyanate [42–49].
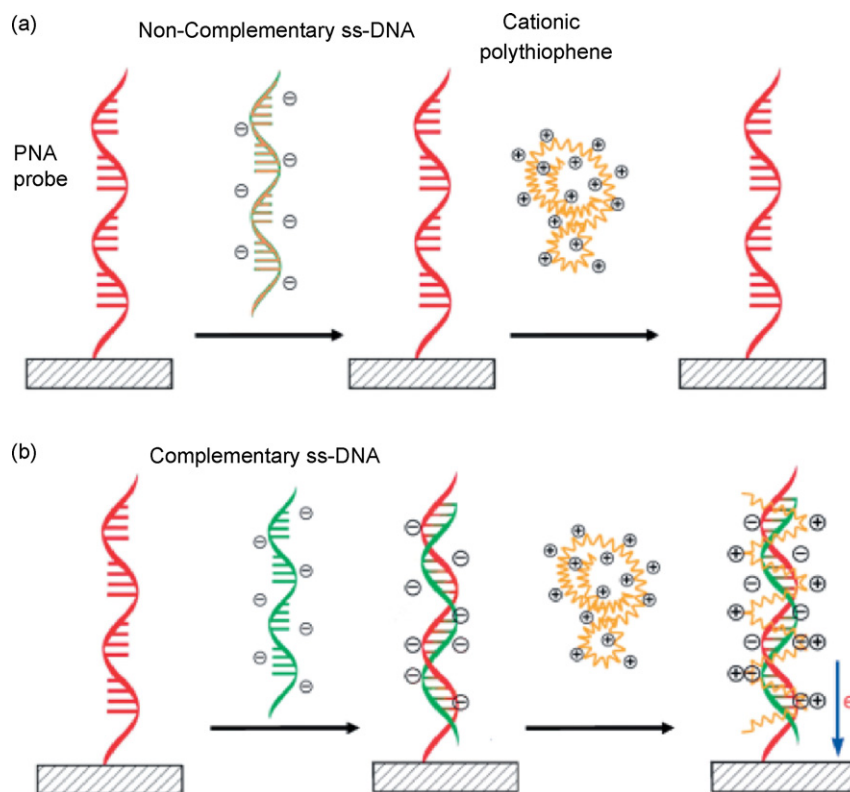
Fig. 5. Schematic description of the electrochemical detection of unlabelled DNA targets, (a) without and (b) with complementary ssDNA (reproduced from Ref. [8], Copyright (2005) with permission from Wiley-VCH Verlag GmbH & Co. KGaA).

4. Transition metal complexes as electroactive marker of DNA

Attachment of electroactive probes based on transition metal complexes to a nucleobase via conjugate linkers should increase the efficiency of charge transfer and thus enhance sensitivity. There are many examples of such probes connected to pyrimidine nucleobases. The attached probe could be used to probe DNA hybridization and charge transfer through DNA. The strategy also possesses potential application in multifunction analysis of DNA by combining the redox characteristic and photophysical properties of transition metal complexes. The ferrocenyl group was well suited for the development of redox-active oligonucleotides owing to its stability, diverse substitution chemistry and amenable stereochemistry. There have some reports on terminal attachment of ferrocenyl groups to oligonucleotides. The attachment of other redox-active metal complexes, e.g. polypyridine Ru(II) and Os(II) complexes, was also attempted.

Hurley and Tor [50] reported a general and versatile method for site-specific incorporation of polypyridine Ru(II) and Os(II) complexes into DNA oligonucleotides using solid-phase phosphoramidite chemistry. Novel nucleosides were synthesized by covalent attachment of $[(bpy)_2M(3\text{-ethynyl-1,10-phenanthroline})]^{2+}$ (M = Ru, Os) to 5-position in 2′-deoxyuridine. A well-defined $M^{2+/3+}$ wave could be obtained in electrochemical experiments. Photophysical experiments showed that the Ru(II) nucleoside exhibits a rather long-lived excited state in phosphate buffer at pH 7.0 ($\tau = 1.08\,\mu s$) associated with a relatively high emission quantum efficiency ($\phi = 0.051$). CD spectra confirmed that the global conformation of the double helix was not altered by the presence of these polypyridyl complexes in the major groove.

Vrabel et al. [51] synthesized 2′-deoxyadenosine nucleosides bearing bipyridine-type ligands and their Ru-complexes in posi-

tion 8 through cross-coupling reactions. The ligand for modification 2′-deoxyadenosine was bipyridine, phenanthroline or terpyridine ligands.

5. Transition metal complexes as electroactive marker of polymer

Polymers covalently conjugated with transition metal complexes have also enabled the transduction of hybridization events into an electrical signal without labeling of the DNA target. In addition, the combination with other techniques, e.g. layer-by-layer self-assembly could be easily achieved and their potential application in biochip device is promising.

Le Floch et al. [8] reported specific and sensitive label-free electrochemical detection of unlabeled target DNA at room temperature through ferrocene-functionalized cationic polythiophene. The schematic description of such label-free electrochemical detection using gold-bound peptide nucleic acid (PNA) probes and such ferrocene-functionalized cationic polythiophene was shown in Fig. 5. The PNA probe was neutral. The electrochemical detection occurred when the PNA probe hybridized with a complementary DNA target. Afterwards, the electrostatic interaction with the cationic polythiophene transducer was achieved.

Liu et al. [9] prepared a poly(4-vinylpyridine) (PVP) derivative bearing redox-active osmium complexes, $PVP\text{-}[Os(5,6\text{-dmphen})_2Cl]^{2+}$ (5,6-dmphen = 5,6-dimethyl-1,10-phenanthroline), as shown in Fig. 6. It was employed as a hybridization indicator for electrochemical DNA sensors. Due to polymeric effects, such polymeric indicator exhibited similar to 1000 times higher sensitivity than the corresponding monomeric analogue ($[Os(5,6\text{-dmphen})_2Cl]^{2+}$) for DNA determination. The detection limit of the present sensor was 0.5 aM. Moreover, the redox potential using
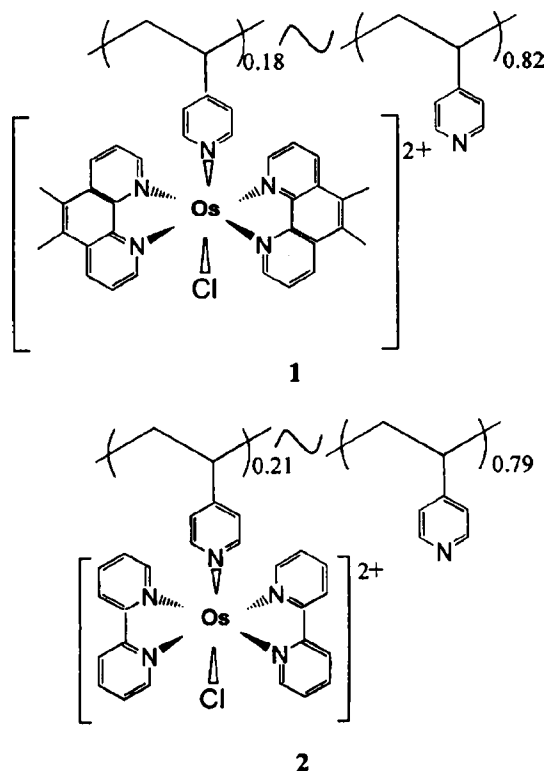
Fig. 6. Chemical structures of polymic indicators PVP-[Os(5,6-dmphen)$_2$Cl]$^{2+}$ (reprinted with permission from Ref. [9]. Copyright (2004) American Chemical Society).

such polymeric indicator was +360 mV (vs. Ag/AgCl), which was significantly lower than that reported for the monomeric analogue (+672 mV). The polymeric indicator can be repeatedly used by removing from the electrode surface via rinsing the electrode in a high-temperature buffer for 6 min. Polyelectrolyte multilayer (PEM) films were also constructed on the surface of gold (Au) electrodes using a layer-by-layer self-assembly method by the same group. The PEM films contained polycationic Os bipyridyl (bpy) complex-attached PVP derivative, [Os(bpy)$_2$Cl]$^{2+}$-PVP (Os-PVP) and polyanionic calf thymus CT-DNA [52]. For such PEM layer, a diffusion-free electron transfer from the Os complex moieties in the films to the electrode surface was observed. Electrocatalytic oxidation of ascorbic acid (AA) by this DNA-containing PEM film-covered electrode was also obtained.

Le Floch et al. [53] proposed label-free electrochemical detection of protein based on a ferrocene-bearing cationic polythiophene and aptamer. Human alpha-thrombin could be detected by using a water-soluble, ferrocene-functionalized polythiophene transducer and a single-stranded oligonucleotide aptamer probe. The approach using ferrocene-functionalized polythiophene was a direct method in which the recorded current decreased upon the addition of targeted protein.

Farre et al. [54] investigated electropolymerization of pyrrole-ferrocene derivatives. The monomer was functioned with ferrocene group and the obtained poly(pyrrole) derivatives had potential application in biochip device.

6. Conclusions

The interaction of small molecules with DNA and electrochemical DNA analysis remains a dynamically developing field in clinical diagnosis, environmental monitoring and drug analysis. Application of transition metal complexes achieved significant success in electrochemical DNA biosensors as hybridization indicator or electroactive marker of DNA. Development of new transition metal complexes with high sensitivity are still of attractive significance. Polymers covalently conjugated with redox metal complexes are outstanding. Such functional polymers enable the combination with other techniques such as layer-by-layer self-assembly. Their potential application in biochip device is promising. For labeling of DNA using transition metal complexes, the attachment of metal complexes probes to nucleobase possesses potential application in multifunction analysis of DNA by combination the redox characteristic and photophysical properties of transition metal complexes.

References

[1] P. Palaska, E. Aritzoglou, S. Girousi, Talanta 72 (2007) 1119.
[2] A. Erdem, Talanta 74 (2007) 318.
[3] J. Wang, Trends Anal. Chem. 21 (2002) 226.
[4] A. Shabani, A.W.H. Mak, I. Gerges, L.A. Cuccia, M.F. Lawrence, Talanta 70 (2006) 615.
[5] X.H. Lin, P. Wu, W. Chen, Y.F. Zhang, X.H. Xia, Talanta 72 (2007) 468.
[6] L. Wu, M. McIntosh, X. Zhang, H. Ju, Talanta 74 (2007) 387.
[7] K.J. Odenthal, J.J. Gooding, Analyst 132 (2007) 603.
[8] F. Le Floch, H.A. Ho, P. Harding-Lepage, M. Bedard, R. Neagu-Plesu, M. Leclerc, Adv. Mater. 17 (2005) 1251.
[9] A.H. Liu, J. Anzai, Anal. Chem. 76 (2004) 2975.
[10] Y.J. Liu, H. Choa, L.F. Tan, Y.X. Yuan, W. Wei, L.N. Ji, J. Inorg. Biochem. 99 (2005) 530.
[11] H. Deng, J. Cai, H. Xu, H. Zhang, L.N. Ji, Dalton. Trans. 3 (2003) 325.
[12] Q.L. Zhang, J.H. Liu, J.Z. Liu, X.Z. Ren, P.X. Zhang, Y. Liu, Y. Huang, L.N. Ji, J. Inorg. Biochem. 98 (2004) 1405.
[13] H. Xu, K.C. Zheng, H. Deng, L.J. Lin, Q.L. Zhang, L.N. Ji, New J. Chem. 27 (2003) 1255.
[14] H. Xu, K.C. Zheng, Y. Chen, Y.Z. Li, L.J. Lin, H. Li, P.X. Zhang, L.N. Ji, Dalton Trans. 11 (2003) 2260.
[15] P. Uma Maheswari, M. Palaniandavar, Inorg. Chim. Acta 357 (2004) 901.
[16] P.U. Maheswari, M. Palaniandavar, J. Inorg. Biochem. 98 (2004) 219.
[17] P.U. Maheswari, V. Rajendiran, M. Palaniandavar, R. Thomas, G.U. Kulkarni, Inorg. Chim. Acta 359 (2006) 4601.
[18] P.U. Maheswari, V. Rajendiran, H. Stoeckli-Evans, M. Palaniandavar, Inorg. Chem. 45 (2006) 37.
[19] P.U. Maheswari, V. Rajendiran, M. Palaniandavar, R. Parthasarathi, V. Subramanian, J. Inorg. Biochem. 100 (2006) 3.
[20] J.A. Smith, J.L. Morgan, A.G. Turley, J.G. Collins, F.R. Keene, Dalton Trans. 26 (2006) 3179.
[21] M. Vrabel, M. Hocek, L. Havran, M. Fojta, I. Votruba, B. Klepetarova, R. Pohl, L. Rulisek, L. Zendlova, P. Hobza, I.H. Shih, E. Mabery, R. Mackman, Eur. J. Inorg. Chem. 12 (2007) 1752.
[22] E. Gaudry, J. Aubard, H. Amouri, G. Levi, C. Cordier, Biopolymers 82 (2006) 399.
[23] M. Steichen, Y. Decrem, E. Godfroid, C. Buess-Herman, Biosens. Bioelectron. 22 (2007) 2237.
[24] B. Selvakumar, V. Rajendiran, P.U. Maheswari, H. Stoeckli-Evans, M. Palaniandavar, J. Inorg. Biochem. 100 (2006) 316.
[25] A. Raja, V. Rajendiran, P.U. Maheswari, R. Balamurugan, C.A. Kilner, M.A. Halcrow, M. Palaniandavar, J. Inorg. Biochem. 99 (2005) 1717.
[26] M. Chikira, Y. Tomizawa, D. Fukitia, T. Sugizaki, N. Sugawara, T. Yamazaki, A. Sasano, H. Shindo, M. Palaniandavar, W.E. Antholine, J. Inorg. Biochem. 89 (2002) 163.
[27] F.Q. Liu, Q.X. Wang, K. Jiao, F.F. Jian, G.Y. Liu, R.X. Li, Inorg. Chim. Acta 359 (2006) 1524.
[28] G.J. Li, N. Liu, S.F. Liu, S.S. Zhang, Electrochim. Acta 53 (2008) 2870.
[29] X.M. Li, H.Q. Ju, C.F. Ding, S.S. Zhang, Anal. Chim. Acta 582 (2007) 158.
[30] S.Y. Niu, G.F. Jie, S.S. Zhang, Y. Li, F. Yang, Chem. Res. Chin. Univ. 21 (2005) 149.
[31] S.S. Zhang, S.Y. Niu, G.F. Jie, Y. Li, K. Jiao, F. Yang, J. Indian Chem. Soc. 82 (2005) 393.
[32] S.Y. Niu, S.S. Zhang, X. Shi, K. Jiao, J. Chem. Soc. Pakistan 27 (2005) 480.
[33] S.S. Zhang, S.Y. Niu, G.F. Jie, X.M. Li, B. Qu, Chin. J. Chem. 24 (2006) 257.
[34] S.S. Zhang, Q.Q. Tan, F. Li, X.R. Zhang, Sens. Actuator B:Chem. 124 (2007) 290.
[35] X.M. Li, H.Q. Ju, L.P. Du, S.S. Zhang, J. Inorg. Biochem. 101 (2007) 1165.
[36] S.S. Zhang, S.Y. Niu, G.F. Jie, X.M. Li, H. Xu, X. Shi, K. Jiao, Chin. J. Chem. 24 (2006) 51.

[37] S.Y. Niu, F. Li, S.S. Zhang, L. Wang, X.M. Li, S.Y. Wang, Sensor 6 (2006) 1234.
[38] S.Y. Niu, S.S. Zhang, L. Wang, X.M. Li, J. Electroanal. Chem. 597 (2006) 111.
[39] H. Karadeniz, B. Gulmez, A. Erdem, F. Jelen, M. Ozsoz, E. Palecek, Front. Biosci. 11 (2006) 1870.
[40] A. Erdem, B. Meric, K. Kerman, T. Dalbasti, M. Ozsoz, Electroanalysis 11 (1999) 1372.
[41] K. Jiao, Q.X. Wang, W. Sun, F.F. Jian, J. Inorg. Biochem. 99 (2005) 1369.
[42] M.V. Del Pozo, C. Alonso, F. Pariente, E. Lorenzo, Biosens. Bioelectron. 20 (2005) 1549.
[43] H.X. Ju, Y.K. Ye, J.H. Zhao, Y.L. Zhu, Anal. Biochem. 313 (2003) 255.
[44] H.T. Zhao, H.X. Ju, Electroanalysis 16 (2004) 1642.
[45] M.V. Del Pozo, C. Alonso, F. Pariente, E. Lorenzo, Anal. Chem. 77 (2005) 2550.
[46] K. Maruyama, Y. Mishima, K. Minagawa, J. Motonaka, Anal. Chem. 74 (2002) 3698.
[47] S.S. Zhang, S.Y. Niu, B. Qu, G.F. Jie, H. Xu, C.F. Ding, J. Inorg. Biochem. 99 (2005) 2340.
[48] Q.X. Wang, K. Jiao, W. Sun, F.F. Jian, X. Hu, Eur. J. Inorg. Chem. 1838 (2006) 1838.
[49] Q.X. Wang, K. Jiao, F.Q. Liu, X.L. Yuan, W. Sun, J. Biochem. Biophys. Methods 70 (2007) 427.
[50] D.J. Hurley, Y. Tor, J. Am. Chem. Soc. 124 (2002) 3749.
[51] M. Vrabel, R. Pohl, B. Klepetarova, I. Votruba, M. Hocek, Org. Biomol. Chem. 5 (2007) 2849.
[52] A.H. Liu, J. Anzaib, J. Wang, Bioelectrochemistry 67 (2005) 1.
[53] F. Le Floch, H.A. Ho, M. Leclerc, Anal. Chem. 78 (2006) 4727.
[54] C. Farre, N. Spinelli, A. Bouchet, C. Marquette, B. Mandrand, F. Garnier, C. Chaix, Synth. Met. 157 (2007) 125.

Stacking and separation of urinary porphyrins in capillary electrophoresis: Optimization of concentration efficiency and resolution

Jinhua Li, Zongwei Cai *

Department of Chemistry, Hong Kong Baptist University, Kowloon Tong, Kowloon, Hong Kong SAR, China

ARTICLE INFO

ABSTRACT

We demonstrated that anionic porphyrins could be stacked and separated in micellar electrokinetic chromatography (MEKC) and microemulsion electrokinetic chromatography (MEEKC) by applying acetonitrile and high salt content in human urine sample matrix. The introduction of sample containing acetonitrile and sodium chloride into the CE capillary at more than 10% of the total capillary volume resulted in the improvement of peak resolution and the enhancement of detection sensitivity. The achieved acetonitrile stacking enrichment factors of six porphyrins ranged from 12 to 32 in MEKC and from 28 to 33 in MEEKC, respectively. The stacking technique was successfully applied for analyzing porphyrins present in urine samples that were deproteinized with acetonitrile. For the analysis of coproporphyrin isomers, addition of the sodium cholate (SC) into micelle and microemulsion solutions provided adequate resolution. Calibration curves obtained for the determination of coproporphyrin isomers were found linear between 30 and 400 nmol L^{-1}, and the limit of detection (LOD) was 20 nmol L^{-1} in MEEKC. Intra- and interday precisions ($n = 11$) in the microemulsion separation system for the isomers at spiked concentrations of 40–400 nmol L^{-1} in urine were in the range of 0.1–0.4% and 0.7–7.6% for migration time and peak area, respectively. Coproporphyrin III, coproporphyrin I and uroporphyrin were detected at levels of 80.7 nmol L^{-1}, 32.3 nmol L^{-1} and 19.8 nmol L^{-1}, respectively, in the urine samples collected from healthy individuals. Different porphyrin profiles, however, were observed in urine samples from porphyria cutanea tarda (PCT) patients.

© 2008 Elsevier B.V. All rights reserved.

1. Introduction

Capillary electrophoresis (CE) has become a well-established separation technique for pharmaceutical research and clinical application with the high resolving power, rapidity, and small amount of samples and reagents required [1–4]. However, CE with absorbance detection yields relatively poor sensitivity, which is attributed to the limited optical pathway of on-capillary photometry and the small sample injection volume [5]. Two basic approaches can be distinguished to overcome the sensitivity problem, either with special detectors that are more sensitive than UV such as laser-induced fluorescence (LIF) [6], and electrochemical mode [7], or with increased analyte amounts by using on column and/or off column preconcentration methods [8]. The preconcentration based on stacking effect has been demonstrated to allow the significant improvement of the detection sensitivity in CE. One of the simple and practical methods to perform stacking is to dissolve a sample in an organic solvent and to inject directly a large volume of the sample into the capillary. Acetonitrile has been conveniently employed for the stacking [9]. Samples from physiological materials normally contain many salts, which can be loaded on the capillary and can cause peaks broadening, especially when the sample volume exceeds 1% of the capillary volume. However, the presence of salts together with acetonitrile was found to provide more efficient sample enrichment than that obtained with pure acetonitrile [9]. The de-proteinization by acetonitrile minimizes the effect of protein adsorption onto the capillary wall. Acetonitrile also counteracts the deleterious effects of the high concentrations of inorganic ions. The distinct difference of conductivity between acetonitrile (low) and the salts (high) leads to stacking. Thus, the use of acetonitrile allows the introduction of a large volume of sample. The sensitivity may be enhanced when high concentrations of inorganic ions are present in the samples [10–12]. The stacking technique is especially useful for the sample extracts from urine, serum and food with higher detection sensitivity.

It is important to determine the all and individual porphyrins in medicinal research and clinical application [13]. However, porphyrins are always present in biological specimens at very low concentrations. The increased deposition of porphyrins in a tissue or the porphyrin excretion by an organism is often the result

---

* Corresponding author. Fax: +852 3411 7348.
E-mail address: zwcai@hkbu.edu.hk (Z. Cai).

of certain metabolic aberration. The identification and measurement of various porphyrins are essential for the diagnosis of the disease known as porphyria. Porphyria is a class of liver disorders caused by disruptions in heme biosynthesis due to specific enzyme deficiency [14]. For instance, the deficiency of the enzyme uroporphyrinogen descarboxylase may result in porphyria cutanea tarda (PCT). A simple and effective diagnosis of PCT is to monitor the by-products of heme biosynthesis, such as urinary porphyrins. Patients suffered from PCT have been found to excrete elevated levels of heptacarboxylic acid porphyrins and uroporphyrins, while the healthy individuals excrete predominantly coproporphyrins. Therefore, the diagnosis of certain porphyrias may be accomplished by determining the relative abundance of the urinary porphyrins excreted. More recently, a number of conventional methods have been developed and applied for the separation of porphyrins in biological samples, including gas chromatography (GC) [15], flow-injection analysis (FIA) [16], thin-layer chromatography (TLC) [17], and high-performance liquid chromatography (HPLC) [18,19]. Detection techniques such as fluorometry [20] and mass spectrometry (MS) [21–23] have also been implemented successfully. Traditionally, HPLC has been widely employed for the separation of porphyrins. However, CE has recently been shown to be an alternative for the determination of porphyrins and their analogues [24,25].

In this work, a preconcentration method based on the stacking effect of acetonitrile and salt for the determination of the six urinary porphyrins was presented. The feasibility of employing acetonitrile–salt mixture to induce band narrowing in micellar electrokinetic chromatography (MEKC) and microemulsion electrokinetic chromatography (MEEKC) was investigated. The method was validated and applied for the analysis of real urine samples from normal and porphyric persons.

2. Experimental

2.1. Chemicals

A chromatographic marker kit containing 10 nmole of each of mesoporphyrin (MP), coproporphyrin (CP), pentacarboxylic acid porphyrin (PENTAP), hexacarboxylic acid porphyrin (HEXAP), heptacarboxylic acid porphyrin (HEPTAP) and uroporphyrin (UP) was purchased from Porphyrin Products (part No. CMK–1A; Logan, UT, USA). CP, PENTAP, HEPTAP and UP were the type I porphyrins, while MP was type IX, and HEXAP included two possible isomers (HEXAP-a and HEXAP-b). MP-IX is not a biological porphyrin but is also included as a representative dicarboxylic acid porphyrin. The individual porphyrins as well as the type III of CP (CP-III) were obtained from the same source. The structures of these compounds are shown in Fig. 1.

Sodium dodecyl sulphate (SDS) was purchased from Sigma–Aldrich (St. Louis, MO, USA). Sodium cholate (SC), 3-Cycolohexyl-amino-1-propanesulfonic acid (CAPS), *N*-tris(hydroxymethyl) methyl-2-aminoethanesulfonic acid (TES), acetonitrile, 1-butanol and 1-octanol were obtained from Acros (Pittsburg, PA, USA). Dimethylformamide (DMF) was from LAB-SCAN (Patumwan, Bangkok, Thailand). Methanol (MeOH) was purchased from Fisher Chemicals (Loughborough, Leics, UK).

2.2. Apparatus

The analysis was carried out on a computer controlled CE-L1 capillary system supplied from CE Resources Pte. Ltd. (Singapore) equipped with an auto-sampler, a UV detector model and a CSW 1.7 software programme. An uncoated used silica capillary (Polymicro

Technologies, Phoenix, AZ, USA) of 55 cm length (40 cm effective length $\times$ 75 μm ID $\times$ 365 μm OD) was used for the separation. The detection wavelength was set at 400 nm. All CE experiments were carried out at 25 °C. Hydrodynamic injection was made by pressure at 0.5 psi for the injection time as indicated. Injection was done at the anode and detection at the cathode. The separation potential was positively high voltage (over 10 kV). New capillaries were conditioned firstly with MeOH for 10 min, followed by doubly distilled deionized (DDI) water for 10 min, 1 mol L^{-1} NaOH for 30 min, 0.1 mol L^{-1} NaOH for 20 min, DDI water for 10 min, and finally running buffer for 10 min. Prior to the daily use, the capillary was flushed for 5 min with DDI water, 5 min with 1 mol L^{-1} NaOH, 5 min with 0.1 mol L^{-1} NaOH, 3 min with water, and 10 min with the running buffer. Between each run, the capillary was rinsed for 5 min with running buffer.

2.3. Preparation of standards, micellar and microemulsion solutions

Stock solution of the porphyrin standard mixture (50 μmol L^{-1}) was prepared in 200 μL DMF. Injection standard solutions were prepared by diluting the stock solution with appropriate amount of specific solutions as indicated. Stock and sample solutions were stored at 4 °C in darkness prior to the analysis.

Micellar solutions were prepared by mixing specific buffer with appropriate amount of surfactant (SDS or SC), and/or organic modifier or other additives. Microemulsion solutions were obtained by mixing a buffer with an appropriate amount of the surfactant, oil (1-octanol), cosurfactant (1-butanol), and/or organic modifiers (acetonitrile or MeOH). Except for the organic modifiers that were prepared on volume basis, all organic solvents added into the microemulsion running buffers were prepared on weight basis. The solution mixtures for the MEEKC systems were sonicated for 30 min, which led to the formation of stable and optically transparent microemulsion solutions. The running buffers were prepared in DDI water that was obtained from a Milli-Q Water System (Millipore, Bedford, MA, USA). The buffers were filtered through a 0.45 μm membrane filter prior to use.

2.4. Preparation of urine samples

The 24 h pooled urine samples collected from two healthy adults (one female and one male) and two male patients (#1 and #2) suffering from PCT were analyzed. Three aliquots were collected from each of the healthy persons within 2 months. One aliquot was obtained from each of the two PCT patients. The urine was filtered through a 0.45 μm membrane filter. 1 mL filtered sample and 2 mL acetonitrile were vortex-mixed for 15 s, and centrifuged at 12,000 rpm for 5 min. The supernatant was introduced directly into the capillary by pressure injection at 0.5 psi.

3. Results and discussion

3.1. On-line stacking and MEKC separation of porphyrins

The mixture of porphyrin standards at the concentration of 1.0 μmol L^{-1} was injected for 1 s and 15 s and their results are shown in Fig. 2a and b, respectively. The separation buffer was used as the sample matrix for the analysis of the standards. The increase of sample volume resulted in more intensive peaks, but with lower separation efficiency and resolution (Fig. 2b). The 60 nmol L^{-1} sample present in the matrix of *ca.* 2:1 (v/v) mixture of acetonitrile and 1.1% NaCl was injected for 5 s, which showed the peaks with very low signal intensity (Fig. 2c). The percentage of sample volume related to the total volume of capillary was determined with
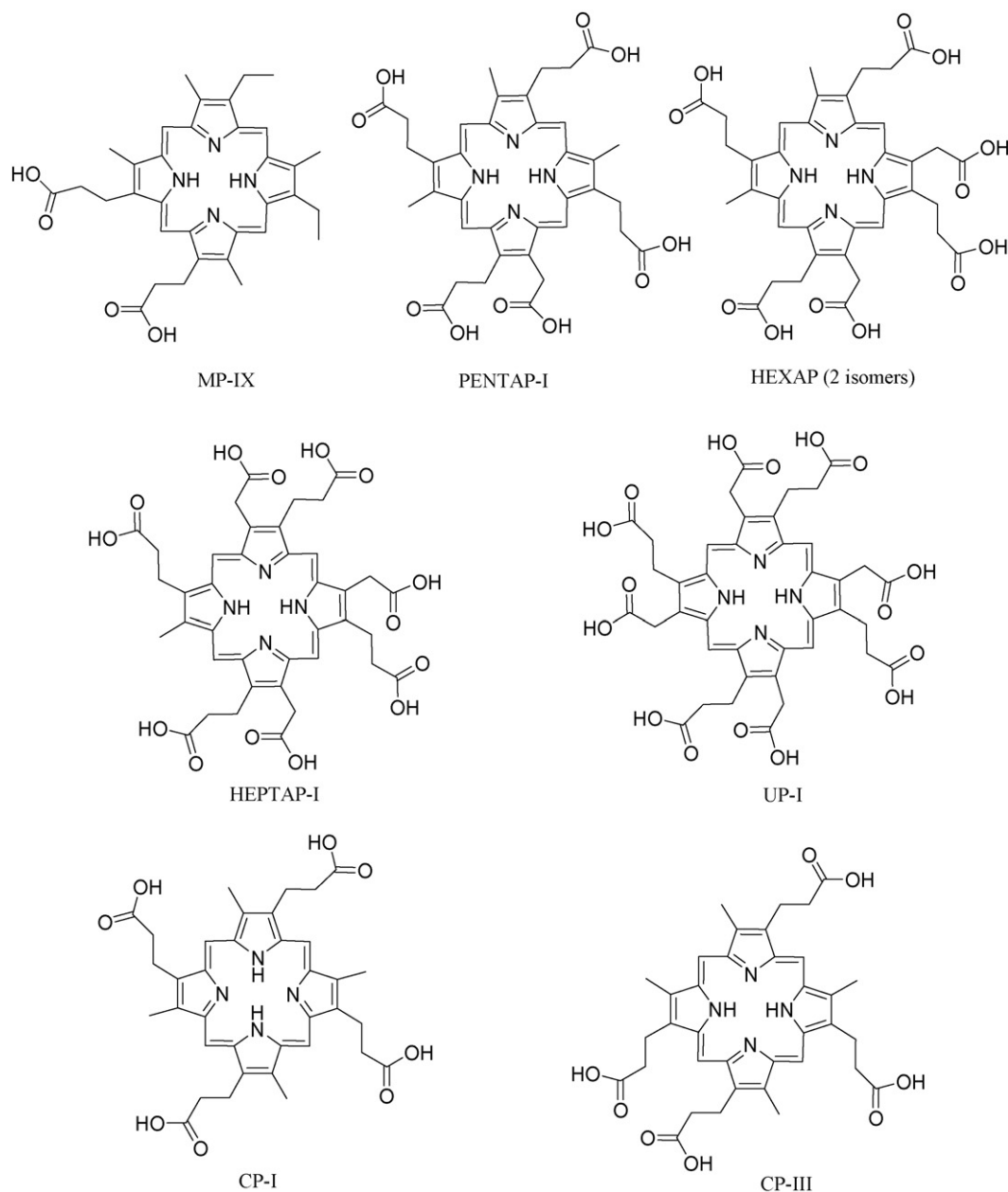
Fig. 1. Chemical structures of the urinary porphyrins.

the reported method [26]. In the current system, the injection of 5 s occupied about 1% of the capillary volume. When the injection amount was increased from 1% to 12% of the capillary volume or 60 s injection with the same sample matrix, the signal intensities (in terms of UV absorbance units) of the 60 nmol L^{-1} sample shown in Fig. 2d were larger than those obtained from the injection of the 1.0 μmol L^{-1} sample in Fig. 2a demonstrating a more than 17-fold increase in sensitivity. The resolution was increased significantly, too, as shown in Fig. 2d. For the 80 s injection of the same sample of 60 nmol L^{-1}, however, the migration window was shortened, which was accompanied with a marked decrease in separation resolution and efficiency. Three porphyrins, namely HEXAP, HEPTAP and UP were detected with poor resolution, while the other three porphyrins were seen in an unresolved broad peak (Fig. 2e).

The obtained result shown in Fig. 2d clearly demonstrated the stacking effect on the on-line concentration of the low content sample. Trace enrichment will occur in chromatographic or elec-

trophoretic separations when the solute's velocity is greater in the injection medium than in the separation medium [27]. The stacking effect was due to the high field strength of acetonitrile (low conductivity). Injected for 60 s, a large volume of sample in acetonitrile and 1.1% NaCl matrix was introduced into the capillary. The sample matrix was high electric resistant; as soon as the voltage (e.g., 12 kV) was applied, the salts ions moved rapidly in the high electric field. Because the region was vacated by the salt ions, the porphyrin ions began to move quickly. When salt ions migrated into the separation buffer, they became exposed to the low electric field and as a result, their migration velocity decreased. Those porphyrin ions in front or close to the salt ions slowed down and remained behind. However, the porphyrin ions remaining in the injection zone were still exposed to the high electric field strength and thus migrated with high speed. As a result, they were compressed at the rear of the injection zone. Therefore, porphyrins were concentrated and gave intensive signals (Fig. 2d). Palmer studied the
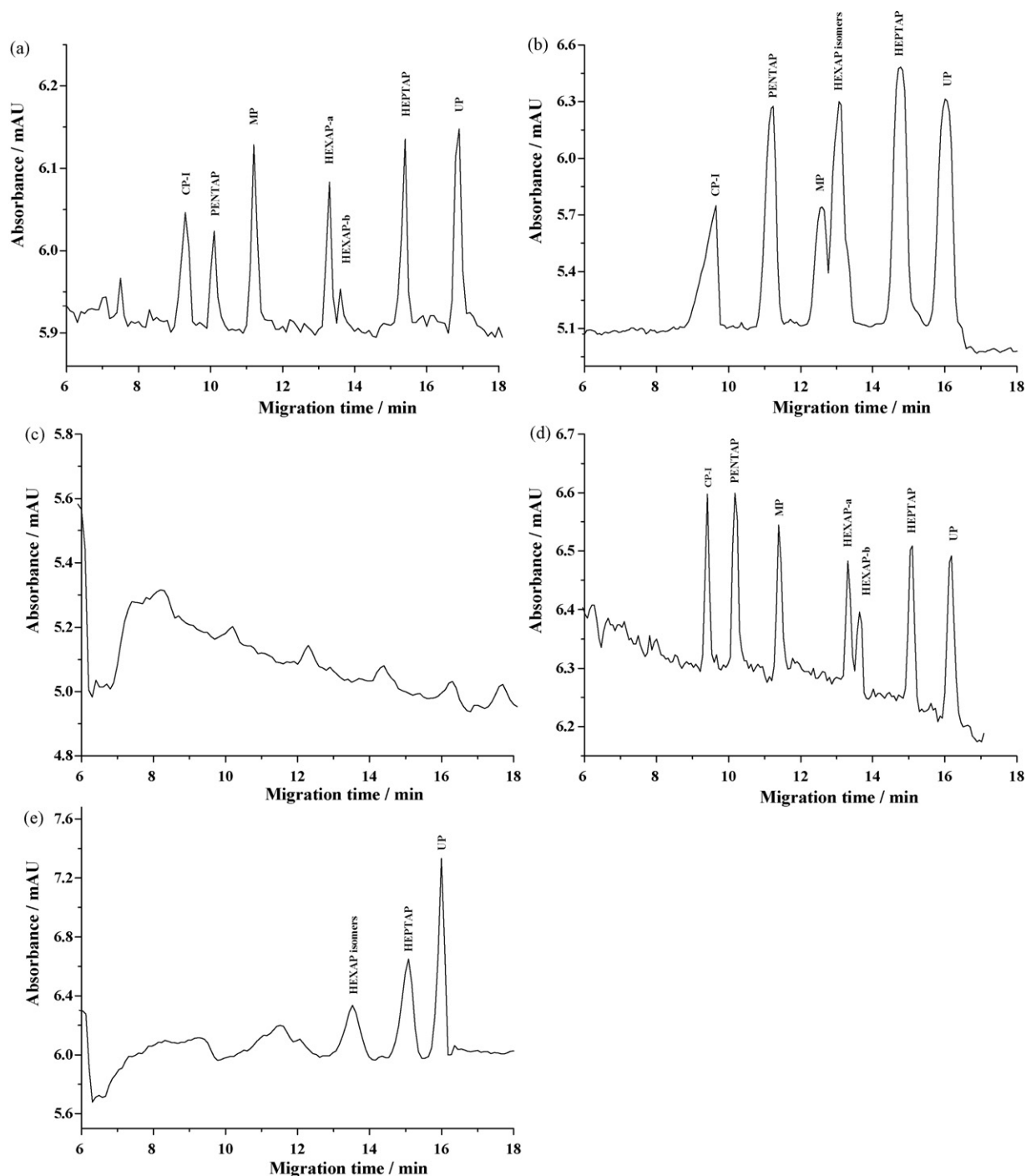
Fig. 2. MEKC separation of the porphyrin standards at a concentration of (a) and (b) with 1 μmol L^{-1}; (c–e) with 60 nmol L^{-1}. For (a) and (b): the pressure injection was at 0.5 psi for 1 s and 15 s, respectively. For (c), (d) and (e): the injection time was 5 s, 60 s and 80 s, respectively. The sample matrices were the separation buffer for (a) and (b) as well as the mixture of acetonitrile and 1.1% NaCl (2:1, v/v) for (c), (d) and (e). The separation buffer consisted of 20 mmol L^{-1} CAPS (pH 11.00), 60 mmol L^{-1} SDS and 15% (v/v) MeOH. The applied voltage was +12 kV.

high salt stacking in MEKC [28]. When the conductivity of sample matrix exceeds that of the separation buffer, the electric field will decrease significantly inside the sample zone. The sample matrix needs to contain a co-ion with a higher intrinsic electrophoretic mobility than cholate. In the present work, the presence of chloride as the co-ion, in 188 mmol L^{-1} or 1.1% NaCl, ensured the formation of a pseudo-steady-state boundary between the micelle and co-ion component in the sample matrix. The chloride acted as the leading ion, while the acetonitrile was the trailing ion. The salt moved

rapidly in acetonitrile and slowly at the separation buffer interface. Therefore, the porphyrins in a large injection plug (over 10% capillary volume) were compressed into a narrow band (Fig. 2d). As a result, high efficiency and resolution were attained for the separation of porphyrins. However, the resolution was decreased and the peak shape was degraded when the salt concentrations were higher than 1.1% (data not shown). This is probably due to the disappearance of the pseudo-steady-state boundary between the micelle and co-ion component. As the conductivity of the sample

matrix was further increased, the electrophoretic movement of co-ion against electroosmotic flow (EOF) was slowed down, resulting in poor stacking.

The effect of acetonitrile present in the sample matrix on MEKC separation has been reported [10,29,30]. Compared to the results obtained by using acetonitrile alone, the presence of NaCl in the acetonitrile matrix produced higher concentration efficiency. The optimal volume ratio of 2 to 1 for acetonitrile and 1.1% NaCl was used to concentrate the urinary porphyrins. The stacking efficiency was closely related to the conductivity of the salts and the content of the organic solvent in the sample matrix of acetonitrile and NaCl. The feasibility of exploiting high salt sample matrices for the stacking of neutral or charged analytes in MEKC was recently reported [31]. Kong investigated the influence of various salts on stacking and concluded that anions were the important factors for stacking negatively charged glutathione and found that the effect of the salts was similar to that of the isotachophoresis process (ITP) [32]. However, the acetonitrile–salt stacking is easier to perform when compared to the conventional ITP because there are no strict requirements for matching the mobility of the leading/terminating ions, samples mobility and pH value. At the same time, the stacking process can eliminate the effect of proteins from the sample. Furthermore, both anions and cations can be concentrated simultaneously by using acetonitrile stacking. The stacking method has been combined with MEKC for the on-line concentration and separation [9,25,33,34]. In the present work, the stacking efficiencies were obtained for the 12% injection sizes (Fig. 2d). The achieved stacking enhancement factor ranged from 12 to 32 for the six porphyrins. However, as the sample plug was further increased, the peaks became wide. The larger salt contents and ionic strength between the sample zone and the separation zone may result in the dispersive effect on the focused bands [35]. The sample volume injected was therefore limited.

In the alkaline buffer, all these six porphyrins were completely ionized with negative charges, and the use of elevated pH was also likely to maximize the negative charges on the capillary wall to enhance electrostatic repulsion between the porphyrins and the capillary wall. The large difference in charges of the six porphyrins leads to a highly different water solubility. Therefore, buffer additives such as surfactants and/or organic modifiers were employed to enhance the solubility of the porphyrins, especially for CP and MP. In Fig. 2, the elution order was consistent with the charge on each porphyrin for a counter migration mechanism. The exception to this rule was MP, which migrated to the detector after PENTAP. MP has both of its carboxyl groups located on adjacent indoles. Therefore, the anionic charges were highly localized and the opposite side of the molecule was free to interact with SDS without experiencing electrostatic repulsion. All of the other porphyrins have a more uniform distribution of carboxyl groups throughout their structures, as a result of more uniform charge distribution and interact minimally with the micelles. SDS was used to bind some electrostatic or hydrophobic sites on the capillary wall that might interact with the anionic analyte, rather than contribute to the separation mechanism.

3.2. MEEKC separation of porphyrins and the comparison to MEKC

While the on-line stacking and MEKC provided the separation for porphyrins at low concentrations within a short period of time and with good resolution, the separation of the more hydrophobic components in the mixture might be unsatisfactory. The separation basis of MEEKC is similar to MEKC. For MEKC, the surfactant monomers group together to form micelles, while in MEEKC the microemulsion is pseudophase. Hydrophobic solutes may reside
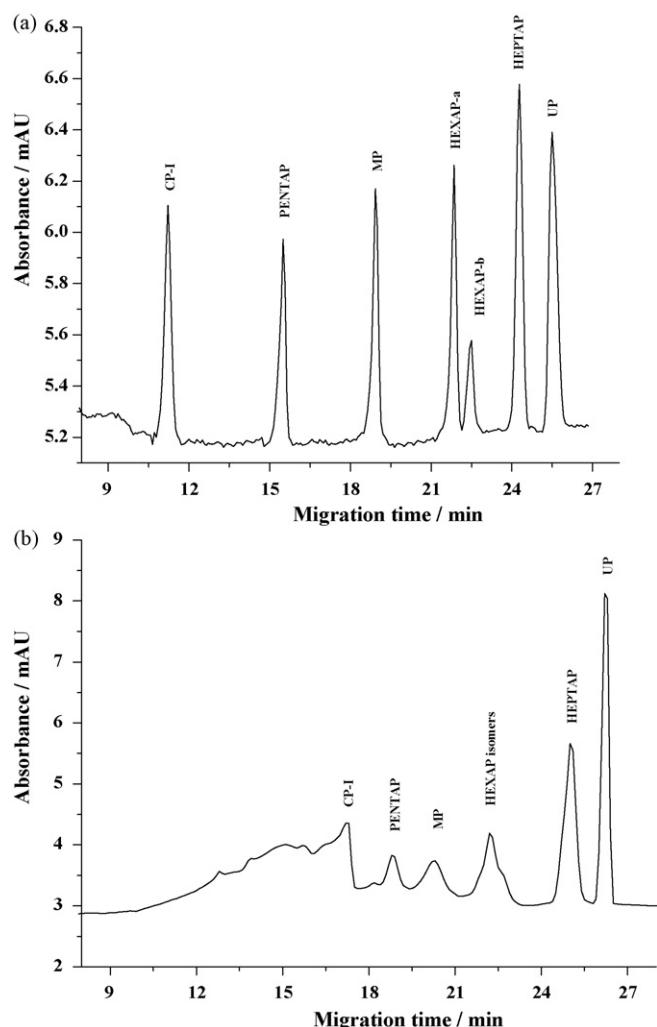
Fig. 3. MEEKC separation of the porphyrin standards at 60 nmol L^{-1}. The injection was at 0.5 psi for (a) 60 s and (b) 80 s. The sample matrix was a mixture of acetonitrile and 1.1% NaCl (2:1, v/v). The separation buffer was the mixture of 20 mmol L^{-1} TES (pH 7.50), 60 mmol L^{-1} SDS, 6.61% (w/w) 1-butanol, 0.82% (w/w) 1-octanol and 20% (v/v) acetonitrile. The applied voltage was +15 kV.

more frequently in the oil droplet than water-soluble solutes, allowing MEEKC to be applicable for a wider range of solutes than MEKC. Compared to the results, as shown in Fig. 2d, the better resolution and efficiency were obtained in the enlarged separation windows when the 60 nmol L^{-1} sample was introduced for 60 s injection by MEEKC (ref. Fig. 3a). The microemulsion manifested better separation performance for the more hydrophobic porphyrins, especially for CP and MP (Table 1). The peaks of the more hydrophilic HEPTAP and UP had better shape than those in MEKC, while the other four more hydrophobic porphyrins gave the significant improvement in efficiency and resolution. Although the higher injection volume of 16% gave similar results (Fig. 3b) as those in MEKC, better peak shape and resolution of the HEPTAP and UP were obtained. The peaks of MP, PENTAP, CP and HEXAP could be resolved, although the separation efficiency was low.

CP gave a peak with front-tailing in the MEKC. The fronting-peak was not observed in the MEEKC. The separation efficiency of 17702 was obtained in MEEKC, which was nearly 6-fold of that in MEKC (Table 1). The isomers of HEXAP were successfully separated with the resolution increased from 0.9 to 1.8. The improvement in peak sharpness and resolution may be due to the solubility increase of the solutes in the microemulsion. Importantly, the enhancement

Table 1
Separation parameters of six porphyrins by MEKC and MEEKC with acetonitrile–salt sample stacking

Porphyrins	MEKC[a]				MEEKC[b]			
	R_s[c]	N[d]	R.S.D.[e] (%, $n = 6$)		R_s	N	R.S.D.[e] (%, $n = 6$)	
			Area	Time			Area	Time
CP	2.4	2958	3.6	0.4	7.9	17702	2.9	0.2
PENTAP	2.4	11192	2.9	0.3	7.9	18013	1.8	0.2
MP	3.6	10883	3.5	0.3	8.2	38991	2.5	0.1
HEXAP-a	4.2	10759	3.4	0.2	6.2	26076	2.1	0.2
HEXAP-b	0.9	4219	3.7	0.5	1.8	27735	3.5	0.3
HEPTAP	4.0	28533	2.5	0.2	3.3	32270	2.4	0.1
UP	3.4	41717	2.1	0.1	2.2	26977	2.1	0.1

[a] Experimental conditions as in Fig. 2d.
[b] Experimental conditions as in Fig. 3a.
[c] Resolution.
[d] Theoretical plate number.
[e] Relative standard deviation.

capacity of the stacking was also improved from 20 to 28 folds for CP and from 15 to 32 folds for MP. The precision data of migration time and peak area demonstrated better stability of microemulsion than micelle in separation. Nevertheless, both MEKC and MEEKC separations of the six-porphyrin standards were achieved by the on-line concentration with the acetonitrile–NaCl stacking.

3.3. Analysis of the porphyrins in human urine

Fig. 4a shows a MEEKC electropherogram obtained from the analysis of the urine sample collected from a healthy human. The sample solution consisted of a mixture of acetonitrile and urine (2:1, v/v). The introduction amount was 1% capillary volume.
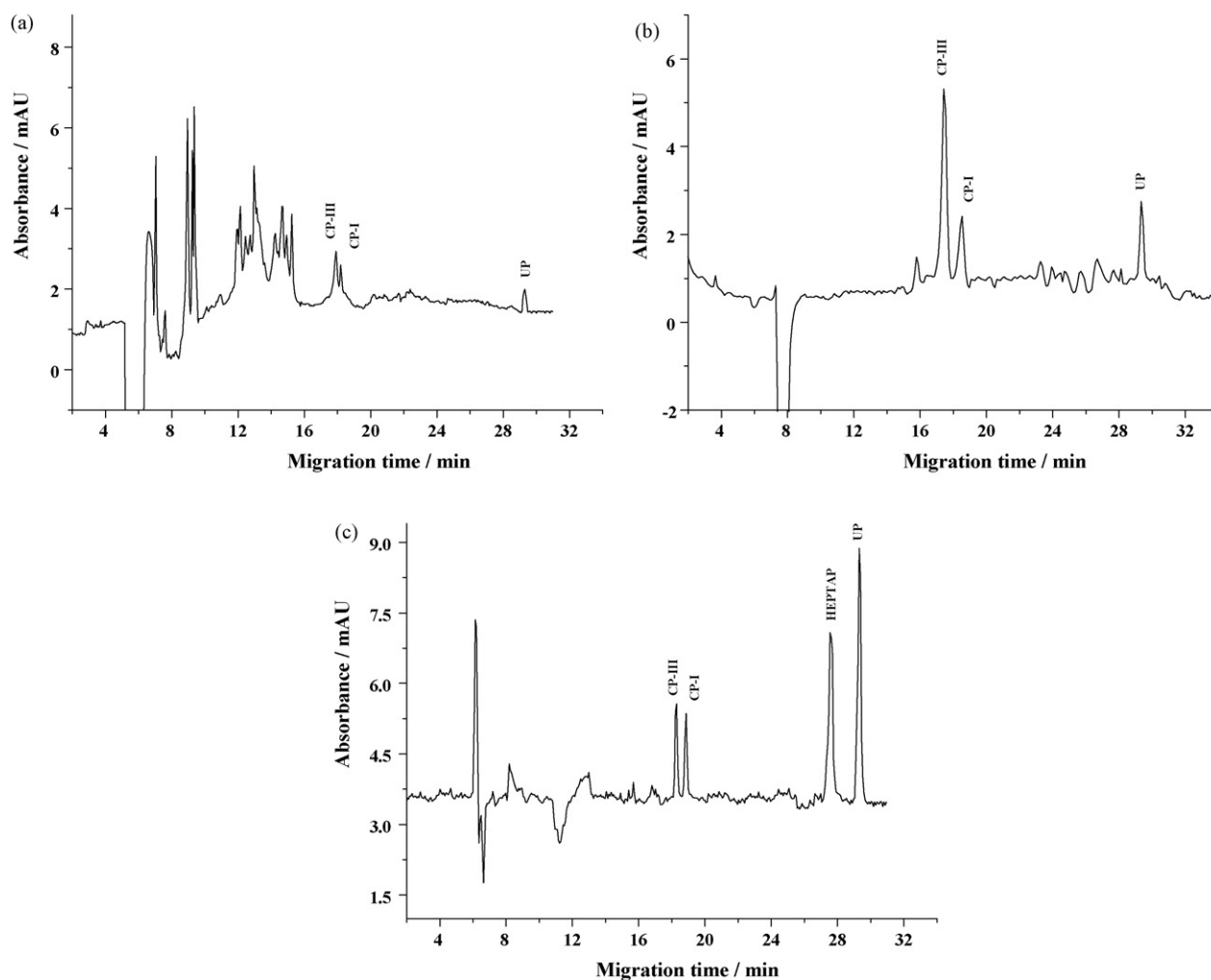
Fig. 4. MEEKC separation of porphyrins in human urine samples (a) and (b) from healthy individuals and (c) from PCT patients. The urine sample matrix: one volume of urine with two volumes of acetonitrile. For (a) and (b): the pressure injection was at 0.5 psi for 5 s and 60 s, respectively. For (c): the injection time was 60 s. The running buffer consisted of 20 mmol L^{-1} CAPS (pH 9.00), 60 mmol L^{-1} SC, 6.50% (w/w) 1-butanol, 0.81% (w/w) 1-octanol and 15% (v/v) acetonitrile. The applied voltage was +15 kV.

CP and UP were observed with low intensity in the 5 s injection. The healthy human urine normally contains predominant CP, some UP and small amounts of porphyrins with five, six and seven carboxyl groups. When the injection time was increased to 60 s without changing the composition of the sample solution, the peak intensities and the resolution were increased remarkably (Fig. 4b). The addition of acetonitrile into the urine increased deproteinization and stacking. When using SDS, the difference in migration time between the ionized CP isomers was too small to allow for separation (data not shown). Interestingly, the two isomers were resolved by using a running buffer containing SC instead of SDS because the CP-I interacted more strongly with the bile salt, resulting in a longer migration time during the separation process. It appeared that the peak area of CP-III was about three times of that of CP-I (Fig. 4b). The endogenous 1% NaCl content in the urine benefited the stacking. However, higher salt content in urine may render the sample zone much more conductive than the buffer zone, resulting in sample de-stacking [36]. Therefore, a higher injection size of 20% capillary volume brought partial resolution of the isomers and a marked decrease in efficiency (data not shown). The obtained porphyrin profiles for healthy individuals were consistent with those reported in the literatures [22,36–38].

To further evaluate the method applicability, the healthy human urine sample was spiked with the standards of CP-III, CP-I, UP and an internal standard of MP-IX. Under the same experimental conditions as those described in Fig. 4b, the spiked urine sample was analyzed by using the internal standard method. The obtained porphyrin peak areas were plotted versus the corresponding concentrations to establish the MEEKC calibration curves. The curves obtained from the analysis of the spiked urine sample at the concentrations ranged from 30 to 400 nmol L^{-1} yielded the following two linear equations: $y = 0.0124x + 0.826$, with $R^2 = 0.9994$ for CP-III and $y = 0.0112x + 1.04$, with $R^2 = 0.9991$ for CP-I. The analysis of the spiked UP over the range of 30–415 nmol L^{-1} also yielded linear correlation, namely, $y = 0.0230x + 0.0160$, with $R^2 = 0.9988$. Three linear curves were also achieved for the CP isomers and UP in MEKC systems.

Proteins in urine can be adsorbed irreversibly onto the capillary wall, resulting in the changes of EOF magnitude and thus poor reproducibility. In order to eliminate the hysteresis effects of protein adsorption in the sample, acetonitrile was added prior to the separation procedure [36,39]. By using acetonitrile, the matrix effects were drastically reduced and the method reproducibility was optimized. Better precision in migration time and peak area for the determination of CP and UP was obtained (Table 2). Even with the injection of the relatively large sample volume, good precision in migration time was achieved within days, indicating that the use of acetonitrile to induce deproteination was able to minimize irreproducibility associated with the precipitation and/or adsorption of various proteins within the CE capillary.

Averaged recoveries from 95.7 to 99.4% were obtained for the spiked porphyrins by using MEKC and MEEKC, respectively. The LOD based on S/N of 3 was determined. For MEKC method, LOD of 27 nmol L^{-1} was obtained for the CP isomers and 16 nmol L^{-1} for UP. Lower LOD was achieved in MEEKC, namely 20 nmol L^{-1} for the CP isomers and 15 nmol L^{-1} for UP. The LOD represents an improvement in sensitivity of almost 20 folds and 50 folds of magnitude over the previous reports of CE-fluorescence and CE-absorbance analyses of the same porphyrin mixture, respectively [27]. The averaged concentrations of endogenous CP and UP in urine samples collected from the healthy individuals were determined as 78.9 nmol L^{-1} for CP-III, 29.4 nmol L^{-1} for CP-I and 20.2 nmol L^{-1} for UP by MEKC. The MEEKC method gave results of 80.7 nmol L^{-1} for CP-III, 32.3 nmol L^{-1} for CP-I and 19.8 nmol L^{-1}

Table 2
Intraday and interday precisions (R.S.D., $n = 11$) of peak area and migration time for the determination of CP isomers and UP spiked in the healthy human urine[a]

Concentration (nmol L^{-1})	MEKC[b]												MEEKC[c]											
	Intraday						Interday						Intraday						Interday					
	Area			Time			Area			Time			Area			Time			Area			Time		
	CP-III	CP-I	UP	CP-III	CP-I	UP	CP-III	CP-I	UP	CP-III	CP-I	UP	CP-III	CP-I	UP	CP-III	CP-I	UP	CP-III	CP-I	UP	CP-III	CP-I	UP
40	0.8	1.4	1.6	0.4	0.5	0.3	6.9	3.1	2.8	0.3	0.4	0.3	0.7	1.3	1.2	0.4	0.4	0.3	7.6	3.4	3.0	0.3	0.2	0.3
100	1.2	2.4	1.0	0.4	0.3	0.2	4.6	3.6	3.2	0.3	0.3	0.3	1.0	1.0	0.6	0.3	0.2	0.1	4.4	3.2	2.8	0.1	0.2	0.2
400	0.8	2.4	1.0	0.4	0.4	0.3	8.7	2.6	2.2	0.2	0.2	0.1	0.7	2.1	0.6	0.3	0.3	0.1	3.5	2.6	1.8	0.1	0.1	0.1

[a] Intraday and interday precisions were calculated from samples based on a total of 11 consecutive injections for each of the three spiked concentrations. MP-IX was as internal standard. The samples employed for interdays were the same (stored in capped sample vials over 24 h).

[b] Run buffer consisted of 20 mM CAPS (pH 11.00), 60 mM SC and 15% (v/v) acetonitrile. Injection time 60 s. Normal voltage 12 kV.

[c] Experimental conditions were the same as those described in Fig. 4b.

Table 3
Porphyrins excreted values (μg) in 24 h human urine determined by MEEKC[a]

Urine source	MP	CP-III	CP-I	PENTAP	HEXAP	HEPTAP	UP
Healthy female	ND[b]	54.1 ± 18.9[c]	21.7 ± 10.2	ND	ND	ND	16.9 ± 5.5
Healthy male	ND	51.5 ± 14.7	20.1 ± 11.5	ND	ND	ND	16.1 ± 10.2
PCT male #1	ND	15.7	16.0	ND	ND	460.8	520.8
PCT male #2	ND	21.8	22.1	ND	ND	375.5	476.9

[a] Acetonitrile stacking and electrophoresis conditions were the same as those described in Fig. 4b.

[b] Not detected.

[c] Averaged from three samples.

for UP. The differences between the MEKC and MEEKC determinations were 2.2% for CP-III, 8.8% for CP-I and 1.8% for UP. Thus, both MEKC and MEEKC methods were applicable for the quantitative analysis of the porphyrins in human urine. Also, these results are consistent with values reported for healthy human urine. By using reversed phase HPLC–UV, Li et al. determined that CP-III ranged from 43.6 to 121.2 nmol L^{-1} and CP-I ranged from 17.4 to 42.6 nmol L^{-1} [40]. CP was detected at 34 nmol L^{-1} by using CE-LIF [38]. CP-III and CP-I were detected at 17.9 μg L^{-1} and 13.9 μg L^{-1}, respectively, in MEKC with high salt and acetonitrile stacking [9]. Furthermore, a method coupling the offline salting-out extraction and the on-line stacking provided the determination of CP-III and CP-I at 29.3 ng mL^{-1} and 9.5 ng mL^{-1}, respectively [25].

The urine specimens from two male patients suffered from PCT were also analyzed. Fig. 4c exemplified the porphyrin pattern and the elevated levels of HEPTAP and UP, which virtually demonstrated the diagnostic symptom of PCT. CP isomers, were also detected with lower total contents and decreased ratio of CP-III to CP-I compared to the corresponding distributions in the healthy human. The healthy individual showed a pattern with dominated CP-III over the CP-I (Fig. 4b).

The determinations of porphyrins in human urine allowed the calculation of excretion rates (μg/24 h) of urine porphyrins from both healthy persons and PCT patients (Table 3). The total levels of CP isomers and the UP levels were detected in the ranges of 47–105 μg/24 h and 17–49 μg/24 h, respectively, while other porphyrins were not detected in the urines from the healthy persons. The obtained data indicated that CP and UP might be excreted predominantly in the urine from a healthy person. HEPTAP were determined in PCT patients at 376–461 μg/24 h, while it was not detected in the urine from healthy persons. High excretion rates of UP were also observed over the range of 477–521 μg/24 h, which was 30 folds higher than those in the healthy persons. It is noted that the contents of HEPTAP and UP in PCT patients were roughly 6-fold and 7-fold of total excretion rates of the CP isomers from the healthy individuals, respectively. The obtained data from the MEEKC analysis were comparable with those reported in the literatures [41–43]. UP and CP in the normal male population was determined in the ranges of 8–44 μg/24 h and 10–109 μg/24, respectively, while in the patients with PCT, the levels of UP, HEPTAP and CP were much higher, ranging from 104 to 5177 μg/24 h, 43 to 1508 μg/24 h and 7 to 263 μg/24 h, respectively [41]. Urinary porphyrins excretions in the healthy adults were 12 μg/24 h for UP, 62 μg/24 h for CP. However, 469 μg/24 h of UP, 177 μg/24 h of HEPTAP and 105 μg/24 h of CP were found in the PCT urines [42]. The excretion amounts of 13 μg/24 h of UP and 50 μg/24 h of CP in the urine from a healthy male were detected by using fluorometric detection with HPTLC separation [43]. The reasonable results in this work indicated that the on-line stacking CE with UV technique might be employed for the determination of urinary porphyrin contents and the diagnosis of porphyria in clinical studies.

4. Conclusions

On-line concentration by using acetonitrile with high salt content significantly improved the detection sensitivity of the urinary porphyrins by MEKC and MEEKC. The stacking method provided effective concentration for the ionized porphyrins with 188 mmol L^{-1} salt ions (1.1% NaCl). The enhancement of detection sensitivity via the addition of an appropriate salt to induce concentration after acetonitrile deproteinization provided sensitive detection of the porphyrins by using CE. The stacking technique is particularly helpful when large injection must be employed to increase the sensitivity while maintaining the characteristic efficiency and resolution of CE.

Low levels of CP and UP in human urine were determined with good reproducibility. The healthy persons were found to excrete predominantly the CP isomers and some uroporphyrins in urine. The results suggested that the CE methods might be useful for the clinical application as an alternative analytical tool for the determination of porphyrins present in biological samples. Although only two urine samples from the PCT patients were analyzed, the obtained results demonstrated that the detection of the trace amounts of certain porphyrins in human urine could allow the diagnosis of the porphyrin-associated diseases.

References

[1] Q.L. Wang, L.Y. Fan, W. Zhang, C.X. Cao, Anal. Chim. Acta 580 (2006) 200.
[2] M. Hernandez, C. Aquilar, F. Borrull, M. Calull, J. Chromatogr. B 772 (2002) 163.
[3] U.B. Soetebeer, M.O. Schierenberg, H. Schultz, G. Hempel, P. Andresen, G. Blaschke, Anal. Chem. 73 (2001) 2178.
[4] S.Y. Chang, W.L. Tseng, S. Mallipattu, H.T. Chang, Talanta 66 (2005) 411.
[5] M. Molina, M. Silva, Electrophoresis 21 (2000) 3625.
[6] J. Jiang, C.A. Lucy, Talanta 72 (2007) 113.
[7] T. Li, Y. Du, B.L. Li, S.J. Dong, Electrophoresis 28 (2007) 3122.
[8] M. Urbanek, L. Krivankova, P. Bocek, Electrophoresis 24 (2003) 466.
[9] S.K.S. Terence, J. Li, C.W. Huie, Electrophoresis 22 (2001) 2159.
[10] M.A. Friedberg, M. Hinsdale, Z.K. Shihabi, J. Chromatogr. A 781 (1997) 35.
[11] Z.K. Shihabi, Electrophoresis 21 (2000) 2872.
[12] Z.K. Shihabi, J. Chromatogr. A 744 (1996) 231.
[13] M. Biesaga, K. Pyrzynska, M. Trojanowicz, Talanta 51 (2000) 209.
[14] M. Doss, E. Schermuly, in: M. Doss (Ed.), Porphyrins in Human Diseases, 1976, p. 189.
[15] Z.Q. Yu, G.Y. Sheng, J.M. Piu, P.A. Peng, J. Chromatogr. A 903 (2000) 183.
[16] Q. Fang, M. Du, C.W. Huie, Anal. Chem. 73 (2001) 3502.
[17] R.J. Hift, B.P. Davidson, C.V. Hooft, D.M. Meissner, P.N. Meissner, Clin. Chem. 50 (2004) 915.
[18] R. Mateo, G. Castells, A.J. Green, C. Godoy, C. Cristofol, J. Chromatogr. B 810 (2004) 305.
[19] P. Macours, F. Cotton, Clin. Chem. Lab Med. 44 (2006) 1433.
[20] A. Tronin, J. Strzalka, X. Chen, P.L. Dutton, J.K. Blasie, Langmuir 16 (2000) 9878.
[21] W. Bu, N. Myers, J.D. McCarty, T. O'Neill, S. Hollar, P.L. Stetson, D.W. Sved, J. Chromatogr. B 783 (2003) 411.

[22] X. Ausio, J.O. Grimalt, D. Ozalla, C. Herrero, Anal. Chem. 72 (2000) 4874.
[23] R. Giovannetti, V. Bartocci, F. Pucciarelli, M. Ricciutelli, Talanta 63 (2004) 857.
[24] Q. Li, C.K. Chang, C.W. Huie, Electrophoresis 26 (2005) 3349.
[25] Q. Li, C.W. Huie, Electrophoresis 27 (2006) 4219.
[26] M. Friedberg, Z.K. Shihabi, J. Chromatogr. B 695 (1997) 1193.
[27] R. Weinberger, E. Sapp, J. Chromatogr. 516 (1990) 271.
[28] J. Palmer, J.P. Landers, Anal. Chem. 72 (2000) 1941.
[29] Z.K. Shihabi, J. Capillary Electrophoresis 2 (1995) 267.
[30] Z.K. Shihabi, M.E. Hinsdale, J. Chromatogr. B 669 (1995) 75.
[31] J. Palmer, N.J. Munro, J.P. Landers, Anal. Chem. 71 (1999) 1679.
[32] Y. Kong, J. Liquid Chromatogr. R. Tech. 29 (2006) 1561.
[33] T.M.H. Choy, W.H. Chan, A.W.M. Lee, C.W. Huie, Electrophoresis 24 (2003) 3116.

[34] C.C. Florentina, K. Athena, P. Patrice, M. Philippe, S.G. David, D. Stephanie, T. Myriam, J. Chromatogr. A 1068 (2005) 123.
[35] J. Quirino, S. Terabe, J. Capillary Electrophoresis 4–5 (1997) 233.
[36] Z.K. Shihabi, in: J.P. Landers (Ed.), Handbook of Capillary Electrophoresis, CRC Press, Boca Raton, FL, 1997, p. 457.
[37] C.K. Lim, M.F. Li, T.J. Peters, J. Chromatogr. 429 (1988) 123.
[38] J.E. Melanson, C.A. Lucy, Electrophoresis 23 (2002) 1689.
[39] J.F. Wu, L.X. Chen, G.A. Luo, Y.S. Liu, Y.M. Wang, Z.H. Jiang, J. Chromatogr. B 833 (2006) 158.
[40] C.B. Li, M.L. Wang, W.L. Wang, Acta Acad. Med. Inner Mongolia 20 (2) (1998) 75.
[41] R.E. Ford, C.N. Ou, R.D. Ellefson, Clin. Chem. 27 (1981) 397.
[42] W.E. Schreiber, V.A. Ralsys, R.F. Labbe, Clin. Chem. 29 (1983) 527.
[43] C.W. Huie, W.R. Williams, Anal. Chem. 61 (1989) 2292.

Study of the electrochemical behavior of isorhamnetin on a glassy carbon electrode and its application

Ai-Lin Liu [a,b], Shao-Bo Zhang [a], Wei Chen [a,b], Li-Ying Huang [a], Xin-Hua Lin [a,*], Xing-Hua Xia [b,**]

[a] Department of Pharmaceutical Analysis, Faculty of Pharmacy, Fujian Medical University, Fuzhou 350004, PR China
[b] Key Laboratory of Analytical Chemistry for Life Science, School of Chemistry and Chemical Engineering, Nanjing University, Nanjing 210093, PR China

ARTICLE INFO

ABSTRACT

The electrochemical behavior of isorhamnetin (ISO) at a glassy carbon electrode was studied in a phosphate buffer solution (PBS) of pH 4.0 by cyclic voltammetry (CV) and differential pulse voltammetric method (DPV). A well-defined redox wave of ISO involving one electrons and one proton appeared. The electrode reaction is a reactant weak adsorption-controlled process with a charge transfer coefficient (α) of 0.586. Based on the understanding of the electrochemical process of ISO at the glassy carbon electrode, analysis of ISO can be realized. Under optimal conditions, the oxidation peak current showed linear dependence on the concentration of ISO in the range of 1.0×10^{-8} to 4.0×10^{-7} M and 1.0×10^{-6} to 1.0×10^{-5} M. The detection limit is 5.0×10^{-9} M. This method has been successfully applied to the detection of ISO in tablets.

© 2008 Elsevier B.V. All rights reserved.

1. Introduction

Currently, herbal medicines, especially, anticancer herbal drugs are gaining more attention from modern pharmaceutical institutes, as scientists are aware that herbal medicine is an almost infinite resource for drug development. Furthermore, the toxicity of the herbal drug is very low and most of them have no side effects. Flavonoids are polyphenolic compounds, widely found in the plant kingdom. As intrinsic components of fruits, vegetables and beverages such as wine and tea, most of the 4000 different flavonoids known to-date belongs to part of a regular diet. In recent years, scientists have accomplished extensive research on the flavonoids' biological activities, and found that the flavonoids could be the potential therapeutic agents against a large variety of diseases, such as anti-viral, anti-allergic, anti-platelet and anti-inflammatory, and possibly protective effects against chronic diseases [1–3]. It has also reported that flavonoids showed anti-tumors promoting activity, providing useful chemopreventive agents in human carcinogenesis [4–8]. Evidences have shown that flavonoids are an important class of antioxidants [3,9,10]. Isorhamnetin (4′,5,7-trihydroxy-3′-methoxyflavone, ISO) is one of the most bioactive flavonoids. Its chemical structure is shown in

Fig. 1. ISO appears to cause many beneficial effects on human health, including cardiovascular protection, anticancer activity, anti-ulcer effects, anti-allergy activity, and anti-inflammatory effects.

Up to now, various analytical methods have been suggested for the determination of ISO in flavonoids, including thin-layer chromatography [11], gas chromatography (GC) [12,13], high-performance liquid chromatography (HPLC) [14–17], capillary electrophoresis (CE) [18–20] and a quartz microchip [21] coupled with various detection techniques, such as UV–vis spectrometry. The coupling of these techniques may provide high selectivity of the assay, but brings also some disadvantages of operating complexity, time and reagent consuming, and high cost. The application of HPLC in the analyses of traditional Chinese medicines is often subjected to short lifetime of columns due to contamination.

Flavonoids and related polyphenols generally consist of two benzene rings linked by an oxygen containing heterocycle. Therefore, all flavonoids including ISO are electroactive. The oxidation reaction of flavonoids is strongly related to their structure, which contains several free phenolic hydroxyl groups, particularly ortho-phenolic hydroxyl groups [8,22,23]. It has been shown that the antioxidant activity of flavonoids resides in their aromatic OH groups [24–27]. To our knowledge, there are few reports on the electrochemical behavior of flavonoids, especially on that of ISO (chemical structure of the monomer is illustrated in Fig. 1). The objective of this study aimed to investigate the mechanism of ISO oxidation by cyclic voltammetry (CV) and differential pulse
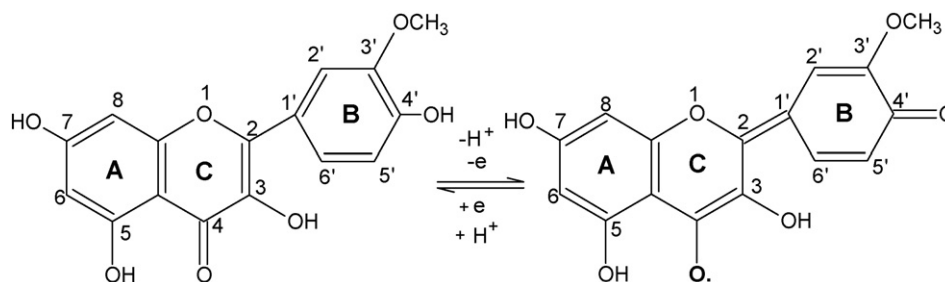
Fig. 1. The electrochemical reaction of ISO on a glassy carbon electrode.

voltammetric method (DPV), and finally a DPV method was developed for the measurement of ISO.

2. Experimental

2.1. Reagents and solutions

ISO was purchased from the National Institute for the Control of Pharmaceutical and Biological Products (Beijing, China). The standard solution of 1.0×10^{-3} M ISO was prepared by dissolving ISO in ethanol, and then it was stored in the dark. All reagents were of analytical grade and used without any further purification. Phosphate buffer solutions (PBS) were prepared by mixing the stock solutions of 0.05 M NaCl and 0.05 M NaH_2PO_4–Na_2HPO_4, and then adjusting the pH with 0.05 M H_3PO_4 or 0.05 M NaOH. All solutions were prepared with double-distilled water. ISO tablets (5 mg per tablet, Shan Xi ShunTian Pharmaceutical Co., Ltd, no. Z20050520) were purchased from local drug store.

2.2. Apparatus

CHI 660C electrochemical workstation (Shanghai CH Instruments, China) was used for electrochemical measurements. A conventional three-electrode system was used throughout the experiments, including a bare GCE working electrode, a platinum wire counter electrode, and an Ag/AgCl reference electrode. All potentials mentioned in this paper refer to this reference. The experiments were conducted in PBS (0.05 M, pH 4.0) at room temperature. All cyclic voltammetric experiments were carried out with scan rate of 100 mV s^{-1} unless otherwise stated. The pH measurements were carried out with a pHS-3B pH-meter (Shanghai Precision & Scientific Instruments, China) at room temperature.

2.3. GCE pretreatment

The bare GCE was polished successively with 0.3 and 0.05 μm Al_2O_3 slurry on silk. Then it was rinsed with doubly distilled water, and sonicated in 1:1 aqueous HNO_3 solution (volume ratio of water to HNO_3 = 1:1), acetone and doubly distilled water for 10 min, respectively. After being cleaned, the electrode was immersed in 0.05 M H_2SO_4 and was conditioned by cyclic sweeping from −0.4 to 1.6 V at 100 mV s^{-1} for 20 scan times before use.

2.4. Tablet sample preparation

Ten tablets (5 mg per tablet) were finely pulverized, then weighted the average mass and dissolved with 50 mL ethanol. After sonication and filtration, a suitable aliquot of the clear filtrate was diluted with pH 4.0 PBS to form appropriated sample solutions. The sample was then added with ISO for recovery experiments.

2.5. Analytical procedure

The required volume of standard solution or sample solution of ISO was added to 10 mL PBS (pH 4.0), and underwent a preset adsorption potential for the analyte accumulation. Then, the CV or DPV was recorded. The CV was recorded from −0.2 to 0.8 V at scan rates from 20 to 500 mV s^{-1}. The DPV was recorded from 0.0 to 0.6 V with amplitude of 0.05 V, pulse width of 0.05 s, and pulse period of 0.2 s.

3. Results and discussion

3.1. Electrochemical behavior of ISO

The cyclic voltammograms of ISO on a bare GCE in PBS (pH 4.0) are shown in Fig. 2. It is clear that the electrochemistry of ISO on the bare GCE shows a reversible redox couple (peak 1 and peak 3) at lower potential ($E_{pa1} = 0.357$ V, $E_{pc1} = 0.282$ V), and an irreversible oxidation peak (peak 2) at higher positive potentials ($E_{pa2} = 1.15$ V). The reversible oxidation peak 1 located at $E_{pa1} = 0.357$ V corresponds to the oxidation of the 4′-hydroxy substituent on the ring-B of ISO. The corresponding reduction (peak 3) of the 4′-quinone occurs at $E_{pc1} = 0.286$ V. The second oxidation (peak 2) occurred at $E_{pa2} = 1.15$ V is due to an irreversible reaction which involves the 5,7-dihydroxy group on the ring-A [28,29]. The separation of the redox peak potentials ($\Delta E_p = E_{pa1} - E_{pc1}$) is 71 mV, which is close to $2.3RT/nF$ (or $59/n$ mV at 25 °C). The number of electrons involved in the reaction was $n = 1.20 \approx 1$, and the ratio of the anodic peak current to the cathodic peak current is almost equal to unity ($I_{pa}:I_{pc} = 1.31:1.65 \approx 1:1$), demonstrating that one electron is involved in the reversible redox reaction [30]. The transfer coefficient (α) can be deduced from the peak width at half-height in terms of the method developed by Laviron [31]. According to this
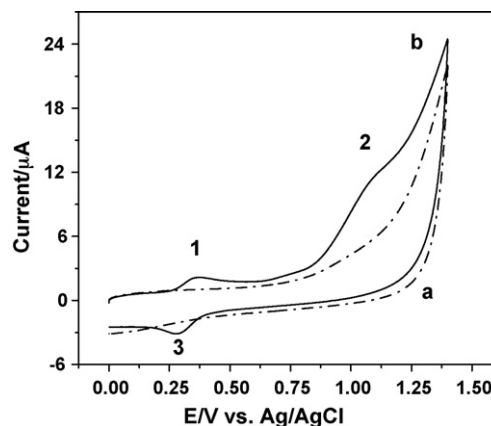
Fig. 2. Cyclic voltammograms (a) in the absence and (b) in the presence of 2 μM ISO in pH 4.0 PBS at a scan rate of 100 mV s^{-1}.
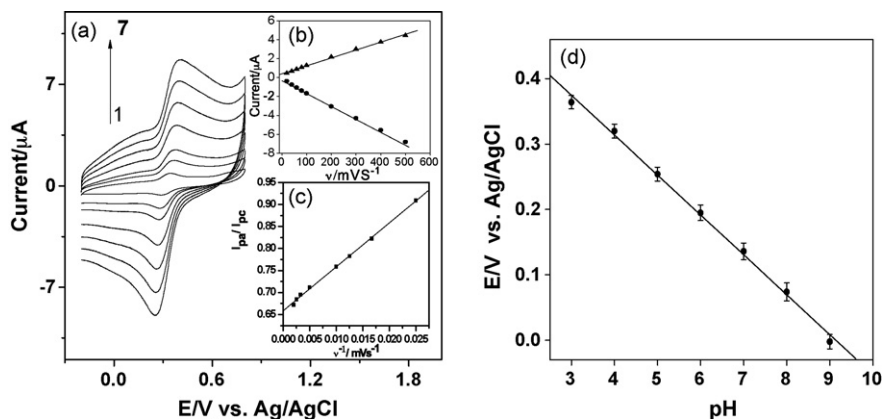
Fig. 3. (a) CVs of 2 μM ISO on glassy carbon electrode at different scan rate. Insets show the dependence of peak currents on the scan rate of 20, 40, 80, 100, 120, 140, 200, 300, 400, and 500 mV s^{-1} (b) and peak current ratio vs. scan rate from the cyclic voltammograms when the ISO is weakly adsorbed (c). (d) The effect of pH on the peak potential (E_{pa1}) of the reversible couple for ISO in phosphate buffer solutions.
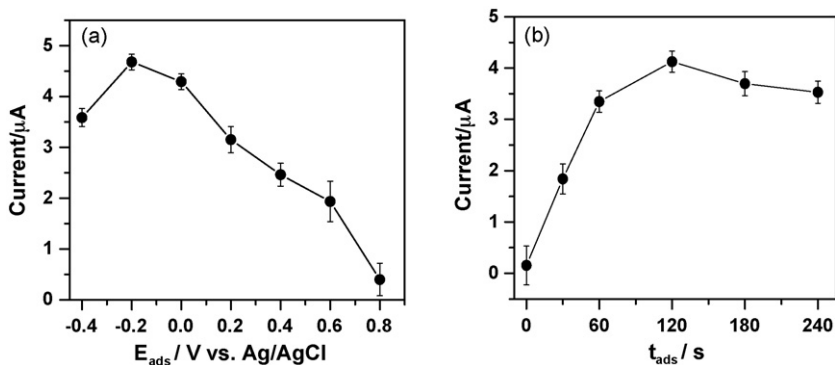
Fig. 4. (a) Effect of the preconcentration potential on peak current of 2 μM ISO by DPV in pH 4.0 PBS, t_{ads} = 120 s. (b) Effect of the preconcentration time on peak current of 2 μM ISO by DPV in pH 4.0 PBS at adsorption potential of E_{ads} = −0.2 V. Scan rate: 100 mV s^{-1}.

method, the width at half anodic peak was 62.5/(1 − α) mV. The width at half anodic peak of ISO was 151 mV at a scan rate of 100 mV s^{-1}, so α = 0.586 was obtained.

The scan rate is probably the most important experimental parameter for evaluating the effects due to adsorbed reactant and/or due to reactant reaching the electrode via diffusion. Fig. 3a shows that the peak currents for the reversible redox couple of ISO increases with increasing the scan rate. An increase in cathodic peak current is obvious, while change of the anodic peak current is not significant. A separate post-wave does not appear, because there is a larger amount of product of ISO near the electrode during the reversal scan. As indicated in the inset of Fig. 3a, plots of the reversible redox couple currents (I_p) versus scan rate (v) (Fig. 3b) yield straight lines in the range from 20 to 500 mV s^{-1} ($I_{pa,ISO}$ (μA) = 0.3926 + 0.00835v, r = 0.9989; $I_{pc,ISO}$ (μA) = −0.27439 − 0.01325v, r = −0.9992). In addition, the ratio, I_{pa}/I_{pc}, is a function of v (I_{pa}/I_{pc} (μA) = 0.6585 + 9.9841v^{-1}, r = −0.9991), and is smaller than the value of unity (Fig. 3c). These results imply that the reaction of this reversible couple is a surface weak adsorption-controlled process of the ISO, which is in agreement with the previous reports [32–35].

In addition the solution pH on the CVs of ISO was also studied. Fig. 3d shows that the peak potentials (E_{pa1}) of this reversible couple shift to more negative values with the increase of solution pH. A linear dependence of the anodic peak potential (E_{pa1}) on the solution pH is obtained (E_{pa1} = 0.557 − 0.061 pH, r = 0.9984). The slope of this linear line was −61 mV/pH in the pH range of

2–8, following the Nernst equation slope. This demonstrates that one electron and one proton are involved in the electrochemical reaction.

Based on the electrochemical results of ISO at the GCE, a mechanism for the oxidation of ISO can be illustrated. As shown in Fig. 1, the electrooxidation of ISO involves in losing a proton to give the monoanionic species followed by a one electron, one proton oxidation of the monoanionic species to form a radical anion, and then yield the final product of 4′-quinone [28,29,36].
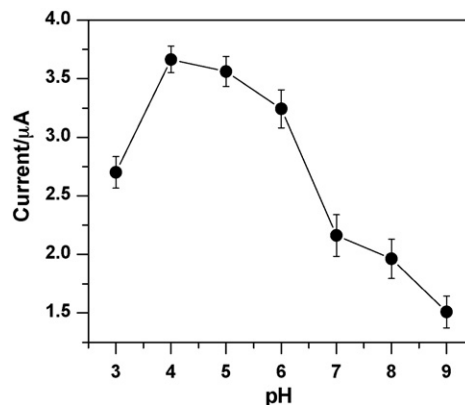
Fig. 5. Effect of solution pH on the peak current of 2 μM ISO by DPV, E_{ads} = −0.2 V, t_{ads} = 120 s. Scan rate: 100 mV s^{-1}.
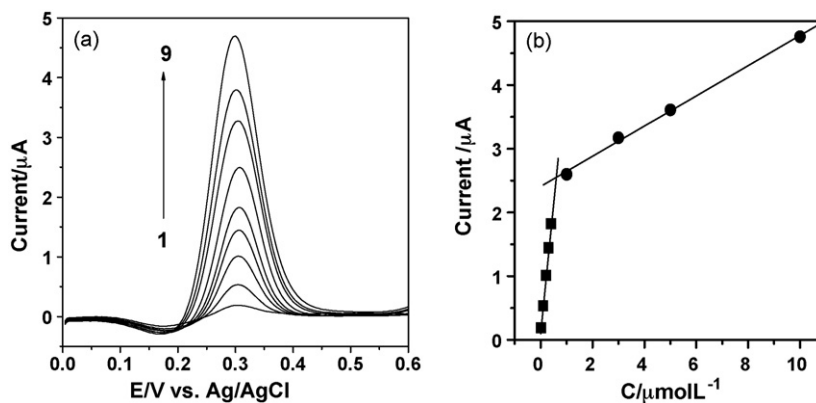
Fig. 6. (a) DPVs of different ISO concentrations at a glassy carbon electrode. ISO concentrations (from 1 to 9, μM): 0.0, 0.1, 0.2, 0.3, 0.4, 1.0, 3.0, 5.0 and 10.0. (b) The relationship between ISO concentrations and peak current. Scan rate: 100 mV s^{-1}.

3.2. DPV determination of ISO at GCE

3.2.1. Influence of preconcentration potential and time

Since the reaction of ISO on GCE is an adsorption-controlled electrode process, the peak current increases with the amount of adsorbed ISO. Therefore, sensitive determination of ISO can be achieved by using preconcentration technique. In this case, DPV technique coupled with a preconcentration procedure was used to determine ISO using the GCE surface. The effect of preconcentration potential (E_{ads}) and time (t_{ads}) was studied in stirring solution. Effect of preconcentration potential on DPV peak current of ISO is shown in Fig. 4a. It is clear that the dependence of the peak current on preconcentration potential shows a bell shape. At the preconcentration potential of −0.2 V, the maximum peak current was reached. The decrease of the ISO adsorption at −0.4 V compared to that at −0.2 V could be due to the strong evolution of hydrogen via the reduction of hydrogen ion at more negative potentials. Thus, the optimal adsorption potential was performed at −0.2 V.

Fig. 4b shows the dependence of peak current on preconcentration time. It is clear that the peak current increases rapidly within the preconcentration time of 120 s. Then, it decreases gradually with increased preconcentration time. This decrease in peak current could be due to the low conductivity of the large amount of the adsorbed ISO. For preconcentration time of 120 s, the response sensitivity of ISO on GCE is significantly improved about 30 times (Fig. 4b).

3.2.2. Influence of solution pH

The effect of solution pH on the electrochemical response of ISO was also studied. Variation of the peak current as a function of solution pH in the range of 3.0–9.0 is shown in Fig. 5. Due to the acidic hydroxyl groups of ISO (Shown in Fig. 1) at the 7, 4′ carbon position, the pK_a value of ISO is about 4 and slight less than 7, which is in agreement with previous reports [36–38]. Therefore, a maximum DPV peak current of ISO at around pH 4 is expected. In fact, it is clear that the DPV peak current of ISO increases rapidly with the increase of solution pH (Fig. 5). At pH 4.0, it reaches maximum and then it decreases rapidly with the further increase of pH. Therefore, solution pH of 4.0 was chosen in the subsequent measurements.

3.2.3. Linearity, detection limit and reproducibility

Under the optimum conditions (preconcentrated at −0.2 V for 120 s in pH 4.0 solution), the peak current of ISO was measured by DPV. From the electrochemical responses in Fig. 6, it can be seen that the peak current increases linearly with the concentration of ISO in the range of 1.0×10^{-8} to 4.0×10^{-7} M (I_{Pa} (μA) = 0.1383 + 4.2661C (μM), r = 0.9992) and 1.0×10^{-6} to 1.0×10^{-5} M (I_{pa} (μA) = 2.4088 + 0.2369C (μM), r = 0.9989). The detection limit is down to 5.0×10^{-9} M. The relative standard deviation of nine repetitive measurements of standard solution containing 2.0 μM ISO is 2.54%, showing good reproducibility.

3.2.4. Interferences

To evaluate the interferences of foreign species on the determination of ISO, possible interferents (μM) such as lysine (100), cysteine (100), citric acid (200), tartaric acid (200), glucose (200), cyclodextrin (200), lactose (200) and saturated starch (200) were individually added into the standard solution containing 2.0 μM ISO. The results indicated that no interference (signal change >5%) on the determination of ISO was observed.

3.2.5. Samples analysis

ISO in tablets was determined by the DPV method described here. The results are listed in Table 1. It shows that the proposed method could be used to determine ISO in tablet.

4. Conclusion

The electrochemical behavior of ISO at glassy carbon electrode was studied by using the electrochemical methods. It showed a reversible process corresponding to oxidation of the catechol 4′-hydroxyl group and another irreversible at high potentials corresponding to the oxidation of the 5,7-dihydroxyl groups. Since the reaction corresponding to the reversible couple is a surface reactant weak adsorption controlled electrode process, its peak current can be enhanced by the amount of adsorbed ISO. After optimizing the preconcentration potential and time and solution pH, determination of ISO with good stability, high sensitivity and selectivity is developed. This approach can be successfully used to determine ISO in tablets.

Table 1
Determination of ISO in tablet (n = 6)[a]

Analyst	Labeled (mg)	Added (mg)	Found (mg)	R.S.D. (%)	Recovery (%)
ISO	3.64	0	3.625	1.9	
	3.64	0.50	4.173	2.1	106.6
	3.64	1.00	4.625	2.3	98.5
	3.64	1.50	5.158	2.8	101.2

[a] n is six repetitive measurements number.

Acknowledgements

References

[1] H.K. Kim, B.S. Cheon, Y.H. Kim, S.Y. Kim, H.P. Kim, Biochem. Pharmacol. 58 (1999) 759.
[2] K.V.N.S. Srinivas, Y.K. Rao, I. Mahender, B. Das, K.V.S.R. Krishna, K.H. Kishore, U.S.N. Murty, Phytochemistry 63 (2003) 789.
[3] D. Ozyurt, B. Demirata, R. Apak, Talanta 71 (2007) 1155.
[4] H. Fujiki, Plant Flavonoids in Biology and Medicine: Biochemical, Pharmacological and Structure Activity Relationships, AlanR. Liss, Inc., New York, 1986, p. 429.
[5] E.E. Deschner, J. Ruperto, G. Wong, H.L. Newmark, Carcinogenesis 12 (1991) 1193.
[6] V. Elangovan, N. Sekar, S. Govindasamy, Cancer Lett. 87 (1994) 107.
[7] W.S. Chang, Y.L. Lee, F.J. Lu, H.C. Chiang, Anticancer Res. 13 (1993) 2165.
[8] S. Buratti, S. Benedetti, M.S. Cosio, Talanta 71 (2007) 1387.
[9] C.L. Bourvellec, D. Hauchard, A. Darchen, J.L. Burgot, M.L. Abasq, Talanta 75 (2008) 1098.
[10] M.N. Peyrat-Maillard, S. Bonnely, C. Berset, Talanta 51 (2000) 709.
[11] P.P.S. Schmid, J. Chromatogr. A 157 (1978) 217.
[12] R. Christov, V.J. Bankova, J. Chromatogr. A 623 (1992) 182.
[13] M.R. Koupai-Abyazani, C.S. Creaser, G.R. Stephenson, Phytochem. Anal. 3 (1992) 80.
[14] R.X. Liu, Q. Wang, H.Z. Guo, L. Li, K.S. Bi, J. Pharm. Biomed. Anal. 39 (2005) 469.
[15] S.P. Wang, K.J. Huang, J. Chromatogr. A 1032 (2004) 273.
[16] Q.L. Zhang, H. Cui, J. Sep. Sci. 28 (2005) 1171.
[17] Y.G. Zu, C.Y. Li, Y.J. Fu, C.J. Zhao, J. Pharmac. Biomed. Anal. 41 (2006) 714.
[18] P.I. Mólnar, F.F. Zhou, J. Chromatogr. A 1073 (2005) 201.
[19] M.J. Dubber, I. Kanfer, J. Chromatogr. A 1122 (2006) 266.
[20] M.E. Yue, T.F. Jiang, Y.P. Shi, Talanta 62 (2004) 695.
[21] B. Ma, X.M. Zhou, G. Wang, H.Q. Huang, Z.P. Dai, J.H. Qin, B.C. Lin, Electrophoresis 27 (2006) 4904.
[22] X.Q. Xu, H.Z. Ye, W. Wang, L.S. Yu, G.N. Chen, Talanta 68 (2006) 759.
[23] X.K. Wang, Y.Z. He, L.L. Qian, Talanta 74 (2007) 1.
[24] C.G.M. Heijnen, G.R.M.M. Haenen, J.A.J.M. Vekemans, A. Bast, Environ. Toxicol. Pharmacol. 10 (2001) 199.
[25] Z. Spáčil, L. Nováková, P. Solich, Talanta 76 (2008) 189.
[26] M. Jesus, O. López, M. Innocenti, C. Giaccherini, F. Ieri, A. Romani, N. Mulinacci, Talanta 73 (2007) 726.
[27] J.J. Xu, H.Y. Zhang, G. Chen, Talanta 73 (2007) 932.
[28] A.M.O. Brett, M.E. Ghica, Electroanalysis 15 (2003) 1745.
[29] P. Janeiro, A.M.O. Brett, Electroanalysis 17 (2005) 733.
[30] A.J. Bard, L.R. Faulkner, Electrochemical Methods, Fundamentals and Applications, Wiley, New York, 2000, pp. 239–243.
[31] E.J. Laviron, J. Electroanal. Chem. 101 (1979) 19.
[32] R.H. Wopschall, I. Shain, Anal. Chem. 39 (1967) 1514.
[33] R.H. Wopschall, I. Shain, Anal. Chem. 39 (1967) 1527.
[34] R.H. Wopschall, I. Shain, Anal. Chem. 39 (1967) 1535.
[35] A.J. Bard, L.R. Faulkner, Electrochemical Methods: Fundamentals and Applications, 2nd ed., Wiley, New York, 2000, pp. 595–600.
[36] X.S. Yao, L.J. Wu, J.Z. Wu, Natural Pharmaceutical Chemistry, 4th ed., People's Medical Publishing House, Beijing, 2006, pp. 173–193.
[37] S.V. Jovanovic, S. Steenken, M. Tosic, B. Marjanovic, M.G. Simic, J. Am. Chem. Soc. 116 (1994) 4846.
[38] H. Wagner, V.M. Chari, J. Sonnenbichler, Tetra. Lett. 17 (1976) 1799.

Validated hydrophilic interaction LC–MS/MS method for simultaneous quantification of dacarbazine and 5-amino-4-imidazole-carboxamide in human plasma

Yanhong Liu[a], Weihua Zhang[b], Yuhui Yang[c],*

[a] Key Laboratory of Animal Virology of Ministry of Agriculture, State Key Laboratory of Veterinary Etiological Biology, Lanzhou Veterinary Research Institute, Chinese Academy of Agricultural Sciences, Lanzhou 730046, PR China
[b] Gansu Provincial Cancer Hospital, No. 2 Xiaoxihu Eastern Street, Lanzhou 730001, PR China
[c] Chrom-Matrix Inc., 2455 George Washington Way, Suite M271, Richland, WA 99354, USA

ARTICLE INFO

ABSTRACT

A hydrophilic interaction high performance liquid chromatography–tandem mass spectrometric method has been developed and validated for simultaneous quantification of dacarbazine (DTIC) and its terminal metabolite, 5-amino-4-imidazole-carboxamide (AIC) in human plasma. The plasma samples are first extracted by a C8 + SCX mixed-mode 96-well plate to extend the extraction stability of DTIC and AIC. The extracted residues are further cleaned by a primary and secondary amine (PSA) adsorbent for minimization of matrix effect. Analyses are done on an Amide-80 HPLC column coupled to a tandem mass spectrometer fitted with an atmospheric pressure turbo ion spray ionization interface in the positive-ion mode. Both DTIC and AIC have reproducible retention times on the Amide-80 HPLC column. This type of column not only has an excellent column life (over 4000 injections), but also has zero carryover effect. The injection volume should be limited at 10 μL or less to avoid the peak splitting. The validated concentration ranges are from 0.5 to 500 ng/mL for DTIC and from 2.0 to 500 ng/mL for AIC. The validated method has been successfully applied to determine the pharmacokinetic profiles for human patients receiving DTIC infusions.

© 2008 Elsevier B.V. All rights reserved.

1. Introduction

Dacarbazine, 5-(3,3-dimethyl-1-triazenyl)-imidazole-4-carbox amide (Fig. 1), is one of the most important chemotherapeutic agents [1–8]. Single-administration dacarbazine (DTIC) (850–1000 mg/m^2), once every 3 weeks, remains the reference standard therapy in patients with metastatic melanoma [1–4]. There is no difference in overall survival time and only a small, statistically non-significant increase in tumor response for stage IV melanoma patients treated with combination chemotherapy compared with the single-agent dacarbazine monotherapy while at the same time causing a significant increase in toxicity [1,2]. DTIC offers a short-lived response rate of around 10–25% with less than 5% of patients achieving a complete response, with a median survival of 8 months [1–6]. Dacarbazine has also been used in combination with other drugs for treating renal adenocarcinoma, soft tissue sar-

coma, malignant lymphomas, brain cancer and Hodgkin's disease [7,8].

The pharmacokinetics profiles of DTIC and its metabolites are determined mainly by conventional liquid–liquid extraction and reversed-phase HPLC methods [9–13]. After intravenous administration of DTIC, its disappearance from the plasma is biphasic with initial half-life from 5 to 20 min and a terminal half-life of a few hours [9,10]. In human, DTIC undergoes *N*-demethylation by the liver microsomal enzymes to form 5-aminoimidazole-4-carboxamide (AIC) (Fig. 1). Substantial concentration of AIC in plasma implicates metabolism as a major route of DTIC elimination [8–10]. Safgren et al. [11] developed and validated a reversed-phase HPLC method for simultaneous determination of DTIC and its two reactive metabolites, 5-(3-hydroxymethyl-3-methyl-1-triazeno)imidazole-4-carboxamide and 5-(3-methyl-1-triazeno)imidazole-carboxamide. Joukhadar et al. [12] investigated the penetration of DTIC and AIC into cutaneous metastases of human malignant melanoma and concluded that the relative lack of response to antineoplastic therapy with DTIC might be explained by resistance of melanoma cells at a molecular level rather than by an inability of DTIC and

---

* Corresponding author. Tel.: +1 2146369175; fax: +1 9726925198.
E-mail address: yyang@chrom-matrix.com (Y. Yang).
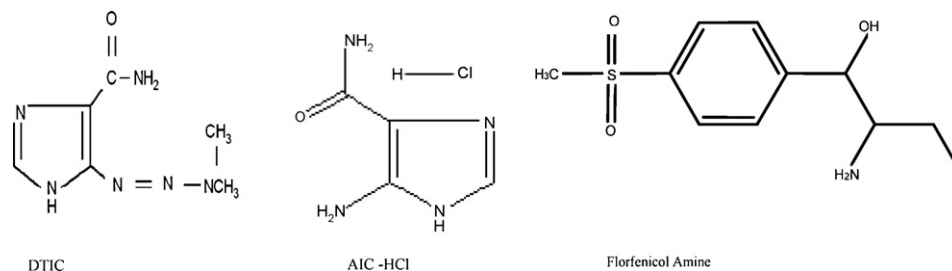
Fig. 1. Chemical structures of DTIC (CAS No. 4342-03-4), AIC-HCl (CAS No. 360-97-4) and florfenicol amine (76639-93-5).

AIC to penetrate into the interstitium of meastatic malignant melanoma. Fazeny-Dörner et al. [13] investigated the combined therapy of DTIC and fortemutine in glioblastoma multiforme patients and the data showed no significant gender-dependent difference. In addition, Chowdhury et al. [14] used DTIC as an internal standard and validated a LC–MS/MS method for the pharmacokinetics study of 5-(3-N-methyltriazen-1-yl)-imidazole-4-carboxamide, a pharmacologically active hydrolysis product of temozolomide.

Reliable clinic pharmacokinetics data are very important for optimization of the clinical dosage of DTIC and the development of better combination therapies [9–13]. However, the current methods for determination of DTIC and AIC pharmacokinetics are not perfect. First, our experiments in the present study reveals that various liquid–liquid extraction protocols cannot provide sufficiently long extraction stability for both DTIC and AIC from human plasma. A typical analytical run includes not only the real clinical samples but also the calibration and quality control standards. The rapid degradation and DTIC and AIC extracted from plasma implies a high risk for under-estimation of their concentrations. Second, most previous publications [9–14] are based on reversed-phase HPLC methodology. DTIC and particularly AIC are very polar compounds, thus having no sufficient retention and isolation on various commercial reversed-phase HPLC columns. Some investigators [9,10,12,13] even used conventional C18 columns under nearly 100% aqueous mobile phase. Under such a circumstance, the hydrophobic C18 HPLC columns themselves have very short life. In addition, it is difficult to separate AIC from the background of the extracted plasma. Safgren et al. [11] used a cyano column for the determination of DTIC. In comparison with conventional C18 columns, cyano columns are much more hydrophilic and has questionable reversed-phase retention for polar compounds like DTIC and AIC.

The present study successfully develops and validates an innovative and robust LC–MS/MS bioanalytical method for simultaneous quantification of DTIC and its final metabolite, AIC in K$_3$EDTA plasma in support of clinical studies. The key steps to the success include the use of a silica-based C8 + SCX mixed-mode SPE as the first extraction step to greatly extend the extraction stability, the use of a weak-anionic adsorbent for elimination of matrix effect, and finally the use of an Amide-80 column for retention and isolation of DTIC and AIC. Since the extraction method is very reproducible, a generic internal standard used in our labs, florfenicol amine (Fig. 1), is able to readily track the extraction and injection.

It is believed that both the extraction method and the hydrophilic LC–MS/MS method in the validation may have extensive applications in the bioanalytical industry. Thus, the present study also discusses how to use cationic mixed-mode SPE, the value of weak-anionic adsorbent (WAX) for reduction and elimination of matrix effect, the merits of hydrophilic interaction chromatography and an observed peak-distorted phenomenon.

2. Experimental

2.1. Standards and reagents

Dacarbazine (98% purity) and AIC (5-amino-4-imidazole-carboxamide hydrochloride, 98% purity) were from Sigma (St. Louis, MO, USA). Florfenicol amine was from Huajia Chemical Sciences Co. (Changsha, Hunan Province, PR China). Seven different lots of K$_3$EDTA human plasma were from Gansu Province Cancer Hospital (Lanzhou, Gansu Province, China). HPLC-grade acetonitrile, methanol, formic acid and ammonium hydroxide were from Beijing Chemical Factory (Beijing, PR China). Innovation™ C8 + SCX mixed-mode SPE 96-well plate and primary and secondary amine (PSA) bulk material were from Chrom-Matrix Inc. (Richland, WA, USA). DTIC-Dome® formulation (200 mg brown-red powder per bottle) was from Bayer Corporation, Shanghai, PR China and it was manufactured by Ben Venue Laboratories, Bedford, Ohio, USA. A 5 μm 10 cm × 4.6 mm HPLC column was from Tosoh Bioscience (Montgomeryville, PA, USA).

2.2. Making stock and spiking solutions

Stock solutions, corresponding to 100 μg/mL DTIC and AIC (all corrected as the free base with 100% purity) were prepared with ice-cold methanol. The stock solutions of both DTIC and AIC were made in duplicates. The stocks were stored in plastic bottles protected against light at −40 °C. Only plastic bottles should be used in order to avoid undesired adsorption of DTIC and AIC on glassware. Stock solution stability was determined by freshly preparing two new stock solutions and comparing it to the old stock solutions. It was found that the DTIC stock solution was stable for 2 months and the AIC stock solution was stable for 1.5 months when they were stored at −40 °C.

One of the two set stocks was used to make nine calibration standard spiking solutions by a serial dilution into methanol:water (v/v). The other set of stock solutions were used to make five quality control standard spiking solutions in methanol:water (50:50). The spiking solutions were stored at plastic bottles protected against light at −40 °C. Spiking solution stability was determined by freshly preparing new spiking solutions and comparing it to the old spiking solutions. One-and-half-month storage stability was established for both DTIC and AIC spiking solution standards.

2.3. Preparation of the calibration standards and quality control standards

Nine calibration standards were freshly made daily. 10 μL of a DTIC spiking solution and 10 μL of an AIC spiking solution were spiked into 980 μL K$_3$EDTA human plasma for homogenization in an Eppendorf 1.5 mL microcentrifuge polypropylene tube with a snap top to make a calibration standard. The dilution factor from the spiking solution to the corresponding calibration standard was

Table 1
Analytical performance of DTIC and AIC quality control samples from three core runs

Analyte (QC)	Inter-assay CV (%) ($n = 18$)	Measured concentration (ng/mL)	Accuracy derivation (%)	Intra-assay CV (%) ($n = 6$)	Inter-assay CV (%) ($n = 18$)
DTIC (LLOQ)	NA	0.491	98.2	7.6	NA
DTIC (low)	3.5	1.42	94.7	4.9	3.5
DTIC (mid)	1.1	21.7	98.6	4.1	1.1
DTIC (high)	4.1	762	95.2	5.5	4.1
DTIC (dilution)	NA	20,320	101.6	8.7	NA
AIC (LLOQ)	NA	2.12	106	11.6	NA
AIC (low)	3.1	5.80	96.7	10.6	3.1
AIC (mid)	2.7	44.1	98.0	5.1	2.7
AIC (high)	1.8	820	102.5	3.6	1.8
AIC (dilution)	NA	19,817	99.1	9.1	NA

100. For the calibration standard curve, the final concentrations of DTIC and AIC in human plasma were as follows: 0.500, 1.30, 3.50, 9.00, 22.0, 60.0, 150, 400 and 1000 ng/mL for DTIC, and 2.00, 4.50, 10.0, 20.0, 45.0, 100, 200, 450 and 1000 ng/mL for AIC.

The quality control standards were made at the beginning of the project initialization. A 1.000 mL DTIC spiking solution and a 1.000 mL AIC spiking solution were added into 98.00 mL K_3EDTA human plasma for homogenization. The theoretical concentrations of DTIC and AIC in human plasma were listed in Table 1.

The QC samples were divided into 1.0 mL and stored at −70 °C in Eppendorf 1.5 mL microcentrifuge polypropylene tubes with snap tops prior to use. Only one tube of QC standard at each concentration level was taken out to be melted at ice for use at each run.

2.4. Preparation of internal standard spiking solution

Florfenicol amine was used as the internal standard. The initial concentration was 100 μg/mL in methanol and the final IS-SS concentration was 50 ng/mL, prepared by serial dilution in 80:20 of water:methanol in plastic bottles.

2.5. Extraction process

All the sample preparation steps were process in the yellow light.

2.5.1. Sample pretreatment

A 10 μL of DTIC diluted QC standard and a 10 μL of AIC diluted QC standard were added into 980 μL K_3EDTA human plasma for homogenization to dilute 100 times.

A 10 μL of the patient plasma sample was added into 990 μL K_3EDTA human plasma for homogenization to dilute 100 times.

100 μL of the matrix blanks, calibration standards, quality control standards, and diluted clinical samples were added into Eppendorf 1.5 mL microcentrifuge polypropylene tubes with snap tops by Microman positive displacement pipettes. Then 10 μL of the internal standard and 90 μL of 0.1 M HCl solution were added into each tube using an Eppendorf repeater. A 30-s vortex-mixing was used for homogenization. The pretreatment was done in an ice bath.

2.5.2. C8 + SCX mixed-mode SPE cleanup

Chrom-Matrix C8 + SCX mixed-mode SPE 96-well (100 mg per well) plate was used for the cleanup.

Each well in the 96-well plate was conditioned with 1 mL of methanol (at least for 1 min) prior to a positive-pressure CEREX Multi-channel SPE system, and equilibrated with 1 mL 0.1 M HCl solution. Then 200 μL of each acidic sample above was loaded. During the loading process, attention was paid to keep the wet state of the unloaded wells by adding more 0.1 M HCl solution. After loading, each well in the plate was washed by 1 mL 0.1 M HCl, 1 mL

water and 1 mL methanol. After drying for 3 min under a high vacuum setting (∼15-in. Hg), a clean deep-well collection plate was placed under the SPE plate in the vacuum manifold. The analytes were eluted with 1.0 mL methanol/ammonium hydroxide (95:5). The eluants were evaporated to dryness under nitrogen at 45 °C.

2.5.3. PSA cleanup

The dry eluant in each well was reconstituted with 1 mL acetonitrile:water (95:5). Approximately 50 mg of PSA (silica-based primary and secondary amine adsorbent, average particle size: 60 μm) particle was added into each well. The components with negative charges were adsorbed on the PSA particles via a 10-min vortex-mixing. After another 5-min centrifugation at 3000 rpm, 700 μL of the supernatants were transferred onto a blank 96-well plate via a Tom-tec. The supernatants were evaporated to dryness under nitrogen at 45 °C. The final extracts were reconstituted with 700 μL of water:acetonitrile:formic acid (30:70:0.1) for LC–MS/MS analysis.

2.6. LC–MS/MS analysis

The instruments used were a Perkin-Elmer Series LC-200 HPLC system, a CTC high-throughput autosampler and a Sciex API 4000 triple quadrupole mass spectrometer with a turbo ion spray interface and the positive mode. The Analyst software (version 1.4.2) was used to operate the integrated system.

The current HPLC method employed a hydrophilic interaction chromatography with a Tosoh BioSep TSKgel Amide-80 column (5 μm 10 cm × 4.6 mm i.d.). The flow rate was 1.0 mL/min; mobile phase A: acetonitrile; mobile phase B: 0.1% formic acid in water. Injection volume: 10 μL. The 6.0-min HPLC gradient program was described below: in the first 2 min, an isocratic run by 70% (v/v) mobile phase A and 30% mobile phase B (v/v); from 2.0 to 5.0 min, a linear gradient from 70% (v/v) mobile phase A to 35% (v/v) mobile phase A; from 5.0 to 5.2 min, an isocratic run at 35% (v/v) mobile phase A; from 5.2 to 5.5 min, a linear gradient from 35% (v/v) mobile phase A to 70% (v/v) mobile phase A; from 5.5 to 6.0 min, an isocratic run by 70% (v/v) mobile phase A and 30% mobile phase B (v/v).

Florfenicol amine, DTIC and AIC were determined by MRM scan mode. Dwell times were 200 ms for all the compounds. MRM transitions were 248 → 130 (florfenicol amine), 183 → 138 (DTIC) and 127 → 110 (AIC). In the original infusion experiment, another MRM transition (183 → 166) was selected for the detection of DTIC. Chowdhury et al. [14] also used the transition. However, such a transition suffered a saturation of the mass detector when the concentration was over 500 ng/mL. In addition, there was a strong background peak in the corresponding MRM chromatogram (not shown). The second strong transition (183 → 123) had the similar problems. Thus, the transition above was selected. With the transition (183 → 138), only the peak assigned to DTIC was observed.

2.7. Method validation

The validation was done according to US FDA guidance for industry on bioanalytical method validation [15].

Three days of calibration curves, with six replicates of quality controls at each concentration level were performed to determine intra-assay and inter-assay variation and accuracy. After the LC–MS/MS bioanalysis, the third batch was stored at 4 °C for a re-injection to establish the extraction stability.

In the third batch, the true recovery and absolute matrix effect were evaluated in both Low QC and High QC levels. Six extracted matrix blank were dried and then spiked with 1.0 mL of acetonitrile:water:formic acid (70:30:0.1) containing Low QC or High QC concentration levels of DTIC and AIC. In addition, six replicate of 1.0 mL of acetonitrile:water:formic acid (70:30:0.1) containing Low QC or High QC concentration levels of DTIC and AIC were added at the end of the running sequence. The absolute matrix effects were calculated using the peak area ratios of Low QC (or High QC) vs. post-spiked Low QC (or High QC). The true recoveries were calculated using the peak area ratios of post-spiked Low QC (or High QC) vs. the same concentrations of quality standards in the reconstituted solvents.

The fourth batch was used to evaluate the relative matrix effect from six unique matrix lots, at the Low QC level.

Finally, the 4 °C matrix stability, the matrix freeze/thaw (F/T) stability and a 2-month −70 °C storage stability for quality control standards were evaluated.

MRM chromatograms were automatically integrated using Analyst software and then the data were transferred into Watson LIMS (Innaphase, version 6.4.0.02) to perform the regression, calculate the regression constants, and calculate the concentration of the analyte in unknown samples and QCs using the peak area ratios of analyte vs. internal standard. Individual precision and accuracy for the calibration standards and QC samples were determined by Watson.

2.8. Patients and chemotherapy

The study was performed after approval by the local ethics committee. Two patients with advanced melanoma and four patients with proven glioblastoma multiforme were administrated into Gansu Province Cancer Hospital. All patients volunteered to participate in the study and gave their written informed consent before start of chemotherapy. The two patients with histological confirmation of advanced melanoma were treated with a single-agent DTIC standard monotherapy. The four patients with histologically proven glioblastoma multiforme were treated with a DTIC and fotemustine combined chemotherapy. The patients exhibited normal bone marrow (leukocyte, >3500 mm^{-3}; platelets, >100,000 mm^{-3}), hepatic (bilirubin, <1.2 mg/dL) and renal (serum creatinine, ≤1.2 mg/dL; creatinine clearance, ≥60 mL/min) functions.

The patients with advanced melanoma received DTIC at a dose of 950 mg/m^2 (mean body surface area 1.71 m^2, n = 2) every 3 weeks. The patients with glioblastoma multiforme received DTIC at a dose of 200 mg/m^2 followed 24 h later by fotemustine at a dose of 100 mg/m^2 (mean body surface area 1.78 m^2, n = 4) every 4 weeks. Every DTIC dose (200 mg/bottle) was quickly reconstituted with 19.7 mL of sterile water. The total dose was diluted to a final volume of 200 mL 0.9% saline. Fotemustine dose (100 mg/vial) was diluted into 250 mL 5% glucose. All the bottles and flasks were protected from light. Both DTIC and fotemustine were given intravenously in an outpatient setting. Both DTIC and fotemustine were intravenously infused over a mean period of 60 ± 4 min.

2.9. Pharmacokinetics

Pharmacokinetics was investigated during the administration of the first cycle of DTIC.

Blood samples were collected before infusion, during the infusion and periodically for 24 h after the completion of the infusion. The blood samples were placed into light-protected tubes containing EDTA as anticoagulant. Immediately after blood sampling, the tubes were centrifuged at 3000 rpm for 5 min. The plasma supernatant was transferred to another light-protected tube and stored at −70 °C prior to a dry-ice shipment.

The collected plasma was extracted according to the established method described above. The majority of the clinical samples had to be diluted 100 times with blank plasma prior to the extraction. When the clinical samples were analyzed, only three replicates of quality control standards at each concentration level were used in each LC–MS/MS run, and the clinical samples were incubated between quality standards. The validated LC–MS/MS bioanalytical method was used to investigate the time courses of DTIC and AIC.

The plasma concentration data were fitted using Kinetica^{TM} version 4.0 pharmacokinetic software (Innaphase Corporation, PA, USA), to calculate the area under the concentration–time curve (AUC), half-life of the terminal phase of the plasma concentration decay curve ($T_{1/2}$), maximum concentration (C_{max}).

3. Results and discussion

3.1. HPLC method development

The first technical challenge is how to develop a robust HPLC method.

In the previous studies, reversed-phase HPLC methods had been used [9–14]. Unfortunately, DTIC and particularly AIC are extremely hydrophilic, thus having no sufficient retention on all kinds of reversed-phase HPLC columns as well as polar-embedded RP-HPLC columns.

An alternative strategy is to use hydrophilic interaction chromatographic modes (HILIC) [16–18]. Hydrophilic interaction chromatography (HILIC) is used primarily for the separation of polar and hydrophilic compounds that are either weakly retained or eluted in the void volume of reversed-phase chromatography columns. Nevertheless, on typical HILIC phases such as cyano, diol and amino phases [16], no retention happens for both DTIC and AIC. Another versatile HILIC phase [17,18], silica column, offers distorted peaks for both the hydrophilic compounds.

Finally, a novel HILIC method is successfully developed with Tosoh Bioscience TSKgel Amide-80 column. TSKgel Amide-80 column consists of non-ionic carbamonyl groups that are chemically bonded to the silica gel [16]. This type of column is widely used for the separation of carbohydrates, peptides and amino acids [16]. On the other hand, to the best of our knowledge, only one publication has reported regarding the application of this kind of column for LC–MS bioanalysis of small basic molecules [19].

The representative chromatogram is shown in Fig. 2.

In the hydrophilic interaction chromatography, organic solvent such as acetonitrile represents weak mobile phase and water represents strong mobile phase [16]. In Fig. 2, florfenicol amine eluted first at 2.2 min since it is the most hydrophobic compound, followed by DTIC at 2.6 min and finally AIC at 3.3 min.

HILIC mode offers three significant advantages. First, the Amide-80 column is proven to be very robust and it performs well over 4000 injections of the extracted samples. Second, HILIC also offers unique advantages for mass spectrometric detection of water soluble polar compounds when compared to reversed-
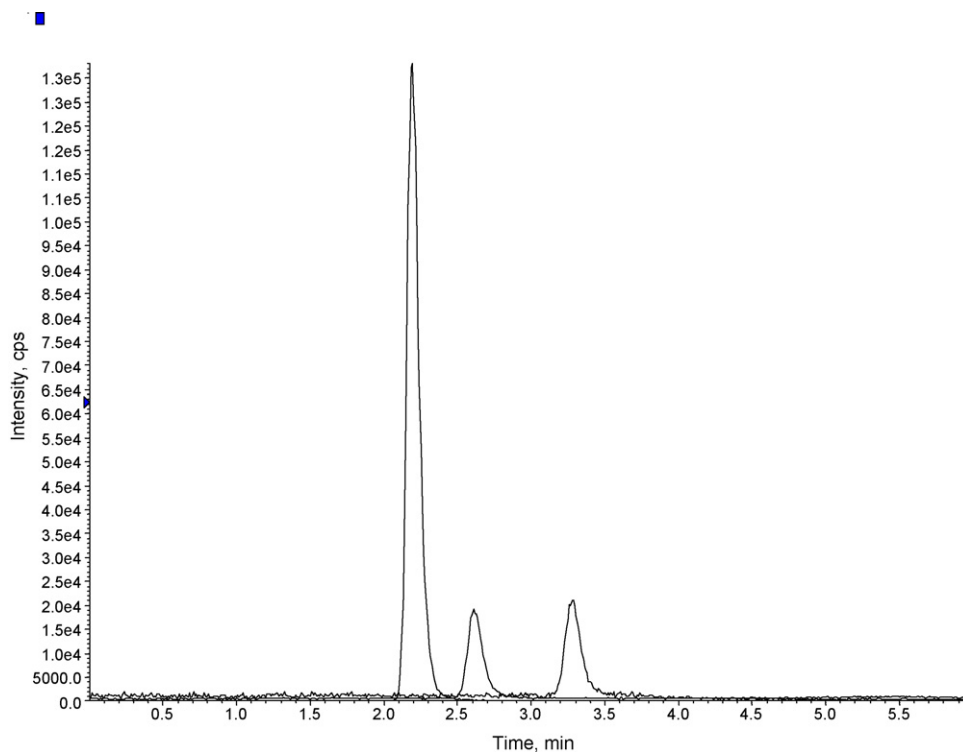
Fig. 2. A representative LC–MS/MS MRM chromatogram of florfenicol amine, DTIC and AIC extracted from a human plasma sample.

phase chromatography. The higher organic content of the eluent in HILIC supports efficient evaporation of the solvent, thus enhancing sensitivity. Third, in comparison with reversed-phase LC–MS/MS methodologies, hydrophilic interaction chromatography using Amide-80 has zero carryover, possibly because of weak

dipole–dipole interaction between the polar stationary phase and the compounds.

As a typical example, the MRM chromatograms of the highest calibration standard and the corresponding matrix blank injection are shown in Figs. 3 and 4. According to US FDA Bioanalytical Vali-
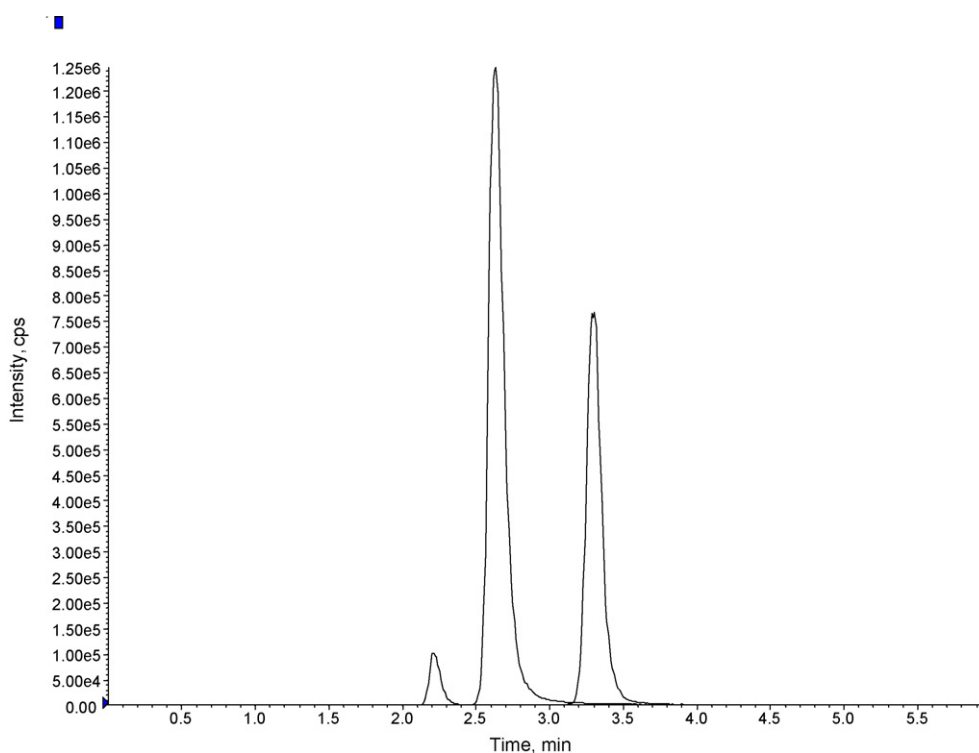
Fig. 3. LC–MS/MS MRM chromatogram of the highest calibration standard.
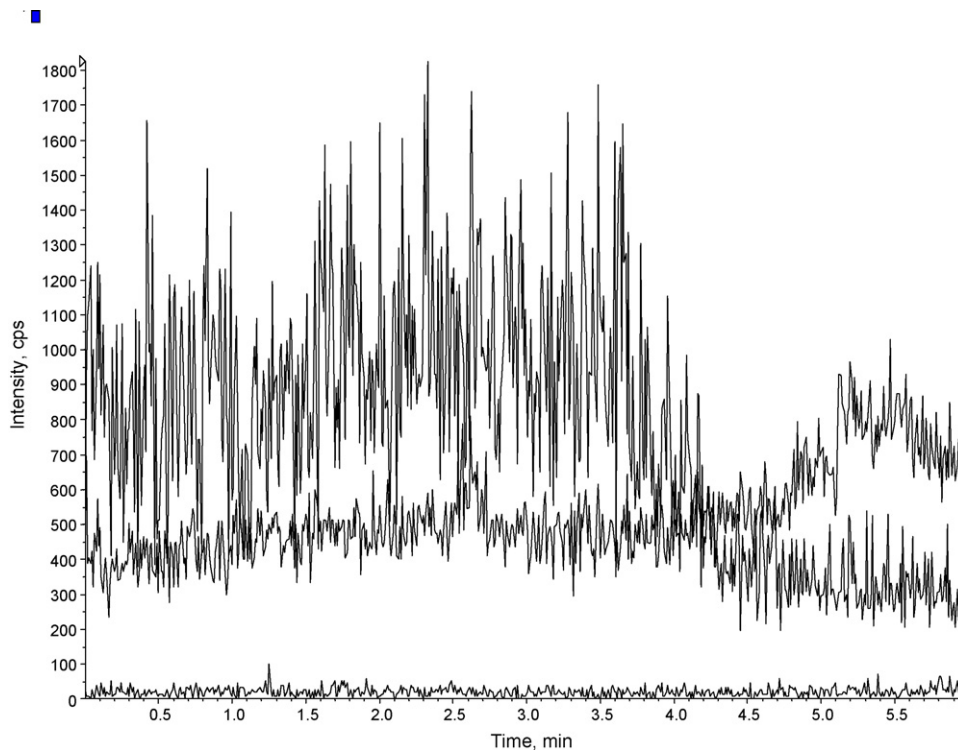
Fig. 4. Carryover from the highest calibration standard.

dation Guidance, the carryover of the highest calibration standard should be less than 20% of the integration area of lower limit of quantitation (LLOQ) [15]. No carryover is observed in the present study for all the compounds. Therefore, the LLOQ of DTIC is set at 0.5 ng/mL. Since AIC exists in some blank human plasma lots at endogenous levels of 0.2–0.5 ng/mL, the LLOQ value has to be set at 2.0 ng/mL for AIC.

Based on our experimental observation, one of the major limitations using hydrophilic interaction LC–MS/MS methodology is the peak distortion and even splitting phenomenon when the injection volume is over a limit. A typical chromatogram is shown in Fig. 5.

In Fig. 5, the MRM signal starts from 1.93 min with a tailing peak. The signal lasts flatly until 2.35 min, and then appeared as a major frontal peak. The phenomenon happens in all DTIC MRM transitions such as $183 \rightarrow 123$ and $183 \rightarrow 138$ (Fig. 5). When the injection volume is set at 20 μL, about 15% of the injected samples have such a distorted peak or a two-peak splitting for DTIC (Fig. 5) and about 10%
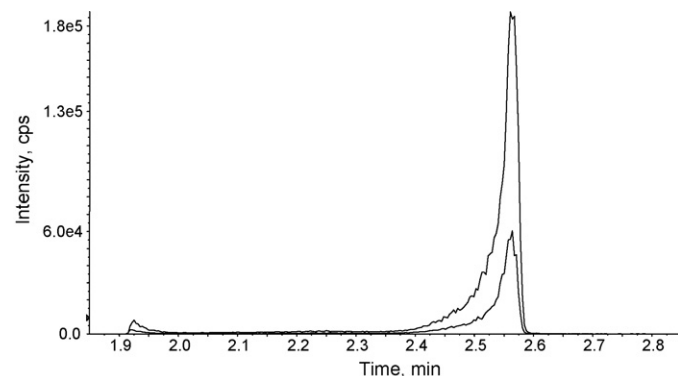
Fig. 5. LC–MS/MS MRM chromatogram of DTIC extracted from human plasma. Injection volume: 20 μL. Upper line: MRM transition $183 \rightarrow 123$ and lower line: MRM transition $183 \rightarrow 138$.

for AIC (not shown). The intrinsic mechanisms remain unknown, but the problem can be well solved via the limitation of the injection volume as 10 μL.

Similar phenomenon is quite frequently observed when other hydrophilic interaction phases, such as silica, diol and cyano phases are used. For silica-based hydrophilic interaction LC–MS/MS bioanalysis, the current literatures [17,18] only use 2 μL injection volume and our in-house studies for many compounds also show that distorted peaks are observed at 5 μL injection or higher injection volume when a silica column is used for hydrophilic interaction LC–MS/MS bioanalysis. It is hard to control the variety from injection to injection when such a small injection volume (<5 μL) has to be used.

The popular phenomenon might mean that hydrophilic interaction chromatography has a limited volume capacity.

Another major limitation, specific to the separation of basic drugs and metabolites by the TSKgel Amide-80 phase, is that all the peaks are broad. It means that the column efficiency is quite low (about 20,000 theoretical plates per meter in the current application). On the other hand, it is reported that the same type of column offers 80,000 theoretical plates per meter for mannitol [16]. The inherent mechanism remains unclear.

3.2. Method development for extraction of DTIC and AIC from human plasma

The previous researches [9–14] reported the successful extraction of DTIC from plasma samples by methanol. However, in the present study, it is found that methanol extraction does not have sufficient extraction stability. Similar problem happens when other organic solvents such as ethyl acetate, acetonitrile and acetone are used. Among all the liquid–liquid extraction trials, the methanol:acetonitrile extraction in the presence of weak anion-exchange adsorbent offers reproducible data with a 6-h extraction ability. The role of weak-anionic exchange (WAX) is to remove

all negative and zwitterionic interferences such as fatty acids and phospholipids [20].

Nevertheless, the 6-h extraction ability is still not long enough for completion of one batch of assay.

Another challenge is how to choose a right internal standard. Since both DTIC and AIC are very unstable, the corresponding isotope-labeled internal standards are very difficult to be made. Thus, we have to focus on the development of a robust extraction process with use of a generic internal standard. The role of a generic internal standard, even with very different chemical structure, is just to compensate the injection variations. A cheap generic standard, florfenicol amine (Fig. 1), is chosen. It has some common characters with DTIC and AIC. For example, all of them are hydrophilic and basic compounds, thus probably having similar performance in both the sample cleanup processes by generic cationic exchange or C8 + SCX mixed-mode SPE methodologies.

Since DTIC and AIC are too hydrophilic to be retained on conventional reversed-phase stationary phases, the selection of solid-phase extractions should focus on ion-exchange and mixed-mode methodologies. Weak cationic exchange usually requires that the internal standards must be very similar to the compounds for compensation of extraction variation. Strong cationic exchange (SCX) SPE is found to work perfectly with AIC. Nevertheless, the experiments show that DTIC extraction by SCX SPE cannot be readily tracked by the generic internal standard, florfenicol amine.

Among cation mixed-mode SPE products, evidences show that polymer-based mixed-mode SPE resulted in higher background. Müller et al. [21] investigated ion-suppression effects during electrospray-ionization mass spectrometry caused by different sample preparation. Severe ion-suppression effects for codeine and glafenine were observed when the sample preparation was done by the convention protein precipitation combined with Oasis MCX cleanup [21]. On the other hand, no ion suppression was detected with the second fraction of the silica-based C8 + SCX mixed-mode SPE [21]. It should be noted that the serum sample was loaded onto the SPE cartridge at pH 6 in the study [21]. In another study, Shen et al. [22] found that a silica-based SCX SPE was better than Waters MCX, a polymer-based mixed-mode SPE, for minimization of matrix effect. It should be noted that in the study [22] the sample was loaded onto the SPE cartridge under acidic pH and the matrix effect significantly existed.

The C8 + SCX mixed-mode SPE 96-well plate from Chrom-Matrix Inc. is applied to the present study. The product has a significantly high cationic ion-exchange capacity, and thus offers significantly higher recovery for hydrophilic basic drugs [23].

The performance of the mixed-mode SPE product is very dependent on the loading pH. Generally, when the plasma samples are loaded at pH 6, the eluates are most cleaned, and matrix effect is minimal [21]. The background becomes dirty when the pH is adjusted lower [23]. Since both DTIC and AIC has no hydrophobic interaction with C8, pH 3.5 is initially selected as the loading condition in order to strengthen ionic exchange interaction. The data for DTIC are listed as Table 2.

Table 2
Effect of loading pH on the extraction of DTIC by C8 + SCX mixed-mode SPE

DTIC	True recovery (%)	Suppression/ enhancement (%)	Process efficiency (%)
Loading at pH 3.5			
Low QC	48.4	91.1	44.1
CV (%) (*n* = 6)	17.5	21.5	18.3
Loading at pH 1.0			
Low QC	89.6	62.8	56.3
CV (%) (*n* = 6)	13.2	14.5	13.5

True recovery is evaluated by comparing the mean peak areas in the extracted QCs to those mean peak areas obtained from post-spiked QCs. The post-spiked QCs are matrix blanks that have been reconstituted after extraction with solvent QCs prepared to mimic final extraction concentrations assuming 100% recovery. The extraction recovery for DTIC is 48.4%, implying that the ion-exchange interaction is still insufficient for full retention of DTIC on the SPE. In addition, the integration ratio of DTIC and the response factor (DTIC vs. the internal standard) are highly variable, because of quite poor reproducibility regarding DTIC. Thus, the imprecision (CV %) for DTIC is high (Table 2). Furthermore, AIC is even more hydrophilic (shown in Fig. 2) and thus has even worse reproducibility at pH 3.5 loading condition.

The absolute matrix effect is calculated by comparing the mean integration areas of post-spiked QCs to the mean peak areas of the solution QCs. A value of less than 100% indicates suppression and a value greater than 100% indicates enhancement. The value is 91.1% and thus the ion-suppression effect for DTIC is only 8.9% (Table 2).

Process efficiency, also called as apparent recovery, is evaluated by comparing peak areas in the extracted QCs to the mean peak areas obtained from solvent QCs. The data was also shown in Table 2.

Although the ion-suppression effect in LC–MS/MS bioanalysis is minimal at pH 3.5 loading condition, the loading pH has to be set at pH 1 for DTIC and AIC in order to ensure the strong retention of both compounds on C8 + SCX mixed-mode SPE and obtain reproducible data. The plasma samples are diluted by 0.1 M HCl and the C8 + SCX mixed-mode SPE 96-well plate is also conditioned by 0.1 M HCl. A test batch is done and the data for DTIC is also shown in Table 2. The extraction recovery is greatly enhanced to 89.6% due to stronger ion-exchange interaction at pH 1, and the precision (CV %) is better.

However, a significant matrix effect happens and the ion-suppression effect is 37.2% (Table 2). Furthermore, the biospecificity data from six unique lots for DTIC and AIC do not meet the acceptance criteria.

Cationic mixed-mode SPE products and SCX SPE products play a limited role for minimization of the matrix effect at acidic loading pH. When plasma (or serum or urine) samples are loaded on silica-based cationic mixed-mode SPE phases at neutral pH, the background of the final elutant is very clean and the matrix effect is nearly zero. Unfortunately, the reproducibility of the data for hydrophilic compounds is frequently too poor to be acceptable [20]. In order to improve the precision of the data, the hydrophilic samples have to be loaded at acidic pH, usually pH 1–2. Let us use phospholipids as the example to explain why at acidic pH the matrix effect becomes significant. Phospholipids have been confirmed as one of the major causes of ionization suppressions in bioanalysis [24]. As a class of zwitterionic compounds [24], phospholipids are removed by the methanol washing step via hydrophobic interaction mechanism when the samples are loaded on the mixed-mode SPE products under neutral pH. However, as the pH value moved towards acidic environment, phospholipids possessed positive charge and thus they would retained on the mixed-mode SPE cartridges during the methanol washing and elute into the final fraction to interference with the analysis. In case when cationic mixed-mode SPE adsorbents are used for enrichment of the target compounds from biological fluids, such a step also concentrates phospholipids and thus enlarges ion-suppression effect.

Therefore, an additional clean-up step is required to minimize and eliminate the matrix effect. It is done by PSA cleanup [20]. PSA is very effective to remove all the negative and zwitterionic components such as fatty acids, heparin, EDTA, triglycerides, glucuronides, oligosaccharides, phospholipids, lipids, lipid–proteins and glyco-proteins, while ensuring full recoveries of basic and neutral compounds [20]. Under acidic loading pH conditions,

mixed-mode SPE itself is sufficient for removal of neutral and negative components, but insufficient for removal of phospholipids and zwitterion interferences. The additional PSA cleanup further removes the remained interferences that induced the matrix effect.

Finally, a mixed-mode SPE process at the loading pH 1, followed by a WAX cleanup is developed in the present study to give the optimum results for extraction efficiency, minimized matrix effect and precision. The two-step extraction process offers very reproducible results. Although florfenicol amine has a very different chemical structure (Fig. 1), the generic internal standard tracks the bioanalysis of DTIC and AIC very well. It is assumed that the role of the generic internal standard is to just compensate the injection variation at the autosampler. The data would be further shown and discussed in Section 3.3.

3.3. Validation

3.3.1. Precision and accuracy

Over the concentration range of 0.5–1000 ng/mL for DTIC, the calibration curve is better fitted with quadratic regression model using $1/x^2$ weight factor. Over the concentration range of 2–1000 ng/mL for AIC, the calibration curve fits will linear regression model using $1/x^2$. The least-squares linear regression constants (r^2) are always equal to or higher than 0.994 for both DTIC and AIC. Concentrations of quality control standards are calculated from each curve. The accuracy is obtained by comparing the averaged calculated concentrations to their nominal values (% of nominal) and the precision by the percent coefficient of variation (%CV). The results from a 3-day precision and accuracy batches are listed in Table 1. The current US FDA regulatory requirements expect that the LLOQ standard back-calculated concentrations must be within ±20% of theoretical nominal concentrations and all other standards' back-calculated concentrations must be within ±15% of their nominal theoretical concentrations. The results in Table 1 completely meet with the acceptance criteria.

3.3.2. Absolute matrix effect, true recovery and process efficiency

Matrix effect, recovery and process efficiency are evaluated according to Matuszewski et al.'s method [25].

The data for DTIC and AIC are shown in Table 3.

Comparing the absolute matrix effect data between Tables 2 and 3, PSA cleanup minimizes the matrix effect very much. The imprecision (CV%) is also improved very much. On the other hand, the recovery becomes somewhat lower after the additional cleanup. It is realistic that a small portion of loss frequently happens in each sample preparation step.

3.3.3. Specificity

The data are shown in Table 4.

Since the absolute matrix effect is very small, it is not surprised that the relative matrix effect among the seven lots of QC samples is absent.

Table 3
True recoveries, absolute matrix effect and process efficiencies of DTIC and AIC

Compound	True recovery (%)	Suppression/ enhancement (%)	Process efficiency (%)
DTIC			
Low QC	82.5	94.4	77.9
Mid QC	84.4	92.5	78.1
High QC	84.7	96.6	81.8
Mean	83.9	94.5	79.3
CV (%)	1.4	2.1	1.8
AIC			
Low QC	65.4	91.8	60.0
Mid QC	68.5	90.4	61.9
High QC	69.2	90.2	62.4
Mean	67.7	90.8	61.4
CV (%)	4.5	3.8	4.4

Table 5
Stability of DTIC and AIC in human plasma

Analyte (QC)	Concentration (ng/mL)	Accuracy derivation (%)	CV (%) ($n = 6$)
Three free–thaw cycles			
DTIC (low)	1.50	96.5	5.1
DTIC (high)	800	94.9	3.2
AIC (low)	6.00	108	6.4
AIC (high)	800	101	3.6
36-h refrigerated extraction stability			
DTIC (low)	1.50	91.2	7.2
DTIC (high)	800	94.2	8.4
AIC (low)	6.00	93.5	4.0
AIC (high)	800	97.8	7.1
24-h refrigerated stability in matrix			
DTIC (low)	1.50	89.7	4.5
DTIC (high)	800	87.5	4.8
AIC (low)	6.00	96.1	4.8
AIC (high)	800	104.0	11.2
Two-month storage stability			
DTIC (low)	1.50	91.7	9.5
DTIC (high)	800	87.8	7.8
AIC (low)	6.00	95.6	5.6
AIC (high)	800	102	4.7

3.3.4. Freeze–thaw stability, refrigerated stability and extraction stability

The three-cycle freeze–thaw stability, the 36-h refrigerated extraction stability (4 °C), and the 24-h refrigerated stability (4 °C) in the plasma have been validated. The data were shown in Table 5.

3.3.5. Transportation and long-term storage stability

A 1-week dry-ice transportation and then 2-month QC standard storage stability at −70 °C are established. The data are listed in Table 5.

Table 4
Relative matrix effect from six unique low QC standards on quantitative assessments

	Lot 1	Lot 2	Lot 3	Lot 4	Lot 5	Lot 6
DTIC						
Mean concentration found (ng/mL)	1.60	1.49	1.50	1.52	1.56	1.47
%CV	5.7	4.0	2.8	4.2	5.1	2.0
Accuracy derivation (%)	6.7	−0.7	0	1.3	4.0	−2.0
n	6	6	6	6	6	6
AIC						
Mean concentration found (ng/mL)	6.15	6.36	6.07	5.64	5.72	6.21
%CV	3.1	4.8	1.8	7.2	4.8	5.1
Accuracy derivation (%)	2.5	6.0	1.1	−6.0	−4.7	3.5
n	6	6	6	6	6	6
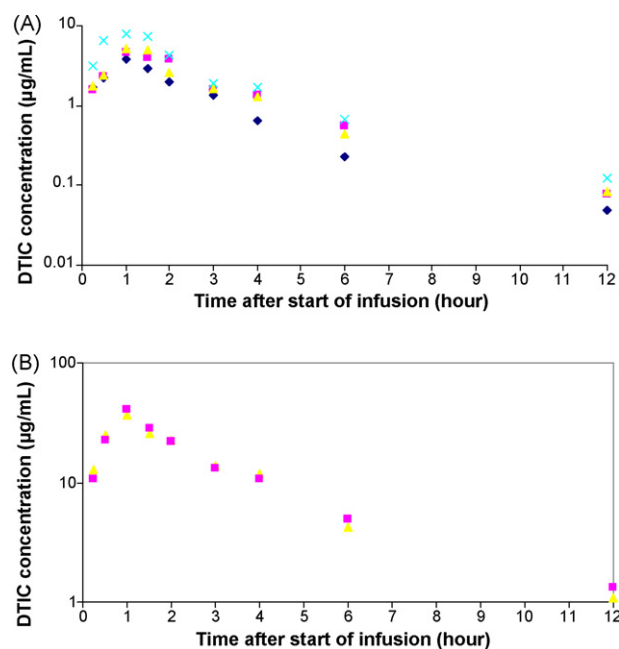
Fig. 6. (A) Time vs. concentration profiles of dacarbazine from human plasma. DTIC dosage: 200 mg/m². Four patients with histologically proven glioblastoma multiforme were treated with a DTIC and fotemustine combined chemotherapy. (B) Time vs. concentration profiles of dacarbazine from the human plasma. DTIC dosage: 950 mg/m². Two patients with histological confirmation of advanced melanoma.

Fig. 7. (A) Time vs. concentration profiles of 5-aminoimidazole-4-carboxamide. DTIC dosage: 200 mg/m². Four patients with histologically proven glioblastoma multiforme were treated with a DTIC and fotemustine combined chemotherapy. (B) Time vs. concentration profiles of 5-aminoimidazole-4-carboxamide from human plasma. DTIC dosage: 950 mg/m². Two patients with histological confirmation of advanced melanoma.

3.4. Pharmacokinetics

The validated LC–MS/MS method is used for the simultaneous determination of DTIC and AIC in human plasma after the intravenous administration of DTIC to cancer patients.

Four patients with histologically proven glioblastoma multiforme were treated with a DTIC and fotemustine combined chemotherapy. According to Fazeny-Dörner et al. [13], the combined chemotherapy has recently been established as an interesting first- and second-line therapy for glioblastoma multiforme. The standard protocol is to administrate a single intravenous dose of DTIC at 200 mg/m² and then fotemustine at 100 mg/m². Fig. 6A illustrates the DTIC concentration–time profile in the plasma. Analysis of plasma collected before the start of the infusion does not reveal the presence of DTIC. The pharmacokinetic parameters are shown in Table 6.

Two patients with histological confirmation of advanced melanoma were treated with a single-agent DTIC standard monotherapy at a dose of 950 mg/m². Fig. 6B illustrates the DTIC concentration–time profile in the plasma. Analysis of plasma collected before the start of the infusion does not reveal the

presence of DTIC. The pharmacokinetic parameters are shown in Table 6.

Fig. 7A and B demonstrates the corresponding AIC concentration–time profile in the plasma. Analysis of plasma collected before the start of the infusion shows endogenous level of AIC at 0.2–0.5 μg/mL. The pharmacokinetic parameters for AIC are also listed in Table 6.

We cannot follow the methods in the previous publications [9–14] to make a side-by-side comparison regarding the pharmacokinetic parameters because liquid–liquid extraction offers too short-lived extraction stability for both DTIC and AIC. Nevertheless, it is not unreasonable to expect that the current methods for the pharmacokinetic investigations may under-estimate the concentrations of DTIC and AIC.

DTIC has been the mainstay of chemotherapy for metastatic melanoma [1–6]. However, the majority of metastatic melanomas respond poorly to dacarbazine therapy. New effective therapies are urgently needed for this treatment-refractory disease [1–6]. The method and protocols validated in the present study would be valuable to support DTIC pharmacokinetic analysis and development of more effective combined chemotherapies.

Table 6
Pharmacokinetic parameters of DTIC and AIC

	Patient 1	Patient 2	Patient 3	Patient 4	Patient 5	Patient 6
DTIC						
C_{max} (μg/mL)	3.88	4.55	5.12	8.08	36.3	40.9
AUC_{0-720} (μg min/mL)	457	521	594	943	4378	4641
T_{max} (min)	67	78	64	70	72	75
$t_{1/2}$ (min)	55	67	52	65	65	71
AIC						
C_{max} (μg/mL)	3.22	3.81	4.01	5.78	13.5	14.4
AUC_{0-720} (μg min/mL)	800	1120	1187	1427	4780	5160
T_{max} (min)	74	69	78	84	75	72
$t_{1/2}$ (min)	140	150	125	210	340	370

4. Conclusions

By the present study, a robust and sensitive method for simultaneous determination of DTIC and its final metabolite, AIC has been successfully developed and validated. The data for the validation indicated that the method is specific, reproducible and accurate to support the assay of DTIC and AIC in K_3EDTA human plasma samples. The method would be valuable to support both DTIC pharmacokinetic analysis and development of more effective combined chemotherapies.

In addition, DTIC and AIC, due to their extreme hydrophilic and unstable character, are very difficult to be extracted and assayed by current methods in the literatures. The two-step extraction process, C8 + SCX mixed-mode 96-well plate extraction for extending the extraction stability and PSA cleanup for minimizing the matrix effect, and the hydrophilic interaction LC–MS/MS developed in the present study may contribute as important options in support of versatile LC–MS/MS bioanalysis.

Acknowledgements

References

[1] P.B. Chapman,.H. Einhorn, M.L. Meyers, S. Saxman, A.N. Destro, K.S. Panageas, C.B. Begg, S.S. Agarwala, L.M. Schuchter, M.S. Ernstoff, A.N. Houghton, J.M. Kirkwood, J. Clin. Oncol. 17 (1999) 2745.

[2] L. Serrone, M. Zeuli, F.M. Sega, F. Cognetti, J. Exp. Clin. Cancer Res. 19 (2000) 21.

[3] M. Huncharek, J.F. Caubet, R. McGarry, Melanoma Res. 11 (2001) 75.

[4] A.M.M. Eggermont, J.M. Kirkwood, Eur. J. Cancer 40 (2004) 1825.

[5] P. Queirolo, M. Acquati, Cancer Treat. Rev. 32 (2006) 524.

[6] C.J.A. Punt, S. Suciu, M.A. Gore, J. Koller, W.H.J. Kruit, J. Thomas, P. Patel, D. Lienard, A.M.M. Eggermont, U. Keilholz, Eur. J. Cancer 42 (2006) 2991.

[7] V.T. DeVita Jr., in: V.T. DeVita Jr., S. Hellman, S.A. Rosenburg (Eds.), Cancer: Principles and Practice of Oncology, 7th ed., Lippincott Williams & Wilkins, 2005.

[8] Ben Venue Laboratories, DTIC-Dome® product manual, 2006.

[9] H. Breithaupt, A. Dammann, K. Aigner, Cancer Chemother. Pharmacol. 9 (1982) 103.

[10] J.M. Buesa, E. Urréchaga, Cancer Chemother. Pharmacol. 28 (1991) 475.

[11] S.L. Safgren, J.M. Reid, R. Rios, M.M. Ames, J. Chromatogr. B 754 (2001) 91.

[12] C. Joukhadar, N. Klein, R.M. Mader, C. Schrolnberger, B. Rizovski, E. Heere-Ress, H. Pehamberger, N. Strauchmann, B. Jansen, M. Müller, Cancer 92 (2001) 2190.

[13] B. Fazeny-Dörner, R.M. Mader, M. Piribauer, B. Rizovski, B. Stögermaier, C. Marosi, Anti-Cancer Drugs 15 (2004) 495.

[14] S.K. Chowdhury, D. Laudicina, N. Blumenkrantz, M. Wirth, K.B. Alton, J. Pharm. Biomed. Anal. 19 (1999) 659.

[15] Department of Health and Human Services, Food and Drug Administration, Guidance for Industry on Bioanalytical Method Validation, Fed. Regist. 2001, 66 (100), 28526 (Docket No. 98D-1195).

[16] T. Ikegami, K. Tomomatsu, H. Takubo, K. Horie, N. Tanaka, J. Chromatogr. A 1184 (2008) 474.

[17] W.Z. Shou, W. Naidong, J. Chromatogr. B 825 (2005) 186.

[18] W. Naidong, J. Chromatogr. B 796 (2003) 209.

[19] T. Nakagawa, J. Jang, M. Yotsu-Yamashita, Anal. Biochem. 352 (2006) 142.

[20] Y. Yang, Methods for matrix cleanup and analysis of drugs and metabolites in biological matrices, US Patent, Publication No. US-2008-0050838-A1.

[21] C. Müller, P. Schäfer, M. Störtzel, S. Vogt, W. Weinmann, J. Chromatogr. B 773 (2002) 47.

[22] J.X. Shen, R.J. Motyka, J.P. Roach, R.N. Hayes, J. Pharm. Biomed. Anal. 37 (2005) 359.

[23] Y.H. Liu, J. Liq. Chromatogr. Relat. Technol. 29 (2006) 1405.

[24] P. Bennett, K.C. Van Horne, 2003 AAPS Annual Meeting and Exposition, Salt Lake City, UT, October, 2003.

[25] B.K. Matuszewski, M.L. Constanzer, C.M. Chavez-Eng, Anal. Chem. 75 (2003) 3019.

Speciated isotope dilution analysis of Cr(III) and Cr(VI) in water by ICP-DRC-MS

H.-L. Ma, P.A. Tanner *

Department of Biology and Chemistry, City University of Hong Kong, Tat Chee Avenue, Kowloon, Hong Kong S.A.R., PR China

ARTICLE INFO

ABSTRACT

An isotope dilution method has been developed for the speciation analysis of chromium in natural waters which accounts for species interconversions without the requirement of a separation instrument connected to the mass spectrometer. The method involves (i) *in-situ* spiking of the sample with isotopically enriched chromium species; (ii) separation of chromium species by precipitation with iron hydroxide; (iii) careful measurement of isotope ratios using an inductively coupled plasma mass spectrometer (ICP-MS) with a dynamic reaction cell (DRC) to remove isobaric polyatomic interferences. The method detection limits are $0.4\,\mu g\,L^{-1}$ for Cr(III) and $0.04\,\mu g\,L^{-1}$ for Cr(VI). The method is demonstrated for the speciation of Cr(III) and Cr(VI) in local nullah and synthetically spiked water samples. The percentage of conversion from Cr(III) to Cr(VI) increased from 5.9% to 9.3% with increase of the concentration of Cr(VI) and Cr(III) from 1 to $100\,\mu g\,L^{-1}$, while the reverse conversion from Cr(VI) to Cr(III) was observed within a range between 0.9% and 1.9%. The equilibrium constant for the conversion was found to be independent of the initial concentrations of Cr(III) and Cr(VI) and in the range of 1.0 (at pH 3) to 1.8 (at pH 10). The precision of the method is better than that of the DPC method for Cr(VI) analysis, with the added bonuses of freedom from interferences and simultaneous Cr(III) determination.

1. Introduction

Chromium mainly occurs as the hexavalent and trivalent oxidation states in the environment and a brief survey of their chemistries is now given. Cr(III) is a hard acid which forms octahedral coordination complexes with ligands such as water, sulfate, urea, ammonia, and organic acids [1]. When Cr(III) exists as $Cr(H_2O)_6^{3+}$, its deprotonated forms (which are formulated shortly as $CrOH^{2+}$, $Cr(OH)_2^+$ and $Cr(OH)_3$) are dominant within pH 4–10. $Cr(OH)_3$ is sparingly soluble, however, it forms the readily soluble $Cr(OH)_4^-$ complex at higher pH [2]. Manganese oxides were found to be the most effective oxidation pathway for Cr(III) rather than molecular oxygen and H_2O_2 in environmental systems [3].

Cr(VI) is present in the aqueous phase as chromate (CrO_4^{2-}, $HCrO_4^-$ and H_2CrO_4) or dichromate ($Cr_2O_7^{2-}$) ions, the proportions of which depend on both pH and the total concentration of Cr(VI). $HCrO_4^-$ is the predominant form within the pH range 2–6, since H_2CrO_4 is deprotonated at pH > 1 and CrO_4^{2-} only exists in the solution above pH 6 [4].

Above a certain concentration of Cr(VI), orange-red $Cr_2O_7^{2-}$ ions are formed but with increase in the basicity, the color changes from orange-red to yellow due to the formation of CrO_4^{2-} ions. Cr(VI)

ions are easily reduced to Cr(III) by electron donors such as organic matter, e.g. humic acid at low pH [5], and inorganic species such as Fe^{2+}, which is thermodynamically possible over the entire pH field [6]. Phosphate and sulfide also influence the rate of reduction of Cr(VI) [7,8].

Because of differences in chemical behavior, toxicity and bioavailability of (essential) Cr(III) and (carcinogenic) Cr(VI), speciation is important in their environmental analyses. The 1,5-diphenylcarbazide (DPC) method is a well-known Cr(VI) determination method [9,10]. It is based on the reaction of DPC with Cr(VI) at the pH of 1.0 ± 0.3 forming a colored complex which can be detected by UV–vis spectrophotometry at 540 nm. However, isolation of Cr(VI) from sample extracts containing Fe(II) is needed before spectrophotometric measurement is made because the acidic environment would facilitate reduction of Cr(VI) by Fe(II) [11] which would result in low recovery of Cr(VI). This method also suffers from the presence of interfering species such as humic acid, which is able to compete with DPC for Cr(VI) and which also absorbs at 540 nm [8]. Other separation techniques for Cr(VI) and/or Cr(III) have utilized ion chromatography [2,11,12], capillary electrophoresis [13–16], and in particular, high performance liquid chromatography coupled with an inductively coupled plasma mass spectrometer (ICP-MS) is a convenient technique for simultaneously distinguishing both chromium species with low detection limit [17–19]. The conventional speciation methods including the colorimetric method, capillary electrophoresis and chromatogra-

* Corresponding author. Tel.: +852 2788 7840; fax: +852 27887406.
E-mail address: bhtan@cityu.edu.hk (P.A. Tanner).

phy, are prone to error due to Cr(III)–Cr(VI) interconversion during sample processing. Speciated isotope dilution mass spectrometry (SIDMS) has been developed to address species transformations that can occur in the steps of sampling, storage, sample preparation and measurement. Accordingly it provides accurate analysis of the original sample concentrations of the different chemical species. No other measurement method can provide this information. The procedures of SIDMS include the preparation of enriched isotopic spikes that have each been chemically converted into a single species, sample collection and spiking, species separation, isotope ratio measurement, and deconvolution of species concentrations. The isotopically enriched species will undergo the same reactions as the corresponding naturally occurring species so that the interconversions that occur after spiking are traceable and can be corrected by use of the isotope ratios [20,21]. To illustrate SIDMS, the speciation of Cr(III) and Cr(VI) in water samples has been carried in this study. We have combined the SIDMS technique with the species separation method using iron hydroxide precipitation. The co-precipitation speciation method is based on the specific scavenging effect of Fe(III) hydroxide on Cr(III) to form a precipitate which can be subsequently dissolved in order to obtain the Cr(III) concentration [22–24]. On the other hand, the total Cr concentration is determined by adding Fe(II) hydroxide into the sample. The Fe(II) hydroxide reduces the *in situ* Cr(VI) to Cr(III), which is subsequently scavenged by Fe(III) hydroxide formed in the redox reaction, thus resulting in the removal of all dissolved Cr species. The concentration of Cr(VI) can be found by the difference of total and Cr(III) concentrations. Therefore this method is capable of determining both dissolved Cr(VI) and Cr(III) simultaneously. Besides, it requires minimal sample preparation and the equipment can easily be employed in the field. The speciation of Cr(III) and Cr(VI) was further simplified in our method by only carrying out a single scavenging step where Fe(III) hydroxide scavenges Cr(III) so that Cr(VI) remains in the sample. Therefore, by analyzing the dissolved precipitate and the filtrate, both Cr(III) and Cr(VI) can be determined separately. Finally, the problems of accurately measuring chromium isotopic ratios due to polyatomic isobaric interferences such as $^{34}S^{16}O^+$, $^{40}Ar^{12}C^+$, $^{1}H^{35}Cl^{16}O^+$, $^{40}Ar^{13}C^+$, $^{37}Cl^{16}O^+$, etc. have been surmounted by employing dynamic reaction cell (DRC) technology [25,26]. The reaction gas ammonia was found to be more efficient than oxygen in breaking up such molecular ions.

2. Materials and methods

2.1. Instrumentation

An Elan 6100 DRC-ICP-MS system (PerkinElmer SCIEX Instruments, USA) equipped with a peristaltic pump, Meinhard quartz nebulizer, cyclonic spray chamber, nickel skimmer and sample cones was employed. The instrument was optimized daily with consideration of background count, sensitivity, as well as doubly charged and oxides formation in the standard mode. The pH of water samples was measured by a Metrohm 744 pH Meter.

2.2. Reagents and materials

Argon gas (99.995%) and ammonia reaction gas (99.999%) were purchased from the Hong Kong Oxygen Co. and the Hong Kong Special Gas Co., respectively. Isotopically enriched materials ^{50}Cr metal with 96.9% enrichment (Lot# I1-8991B) and ^{53}Cr oxide with 97.9% enrichment (Lot# I1-8991A) were obtained from Cambridge Isotope Laboratories Inc., USA. Standard reference material (SRM) 979 (isotopic standard for chromium) was purchased from the

National Institute of Standards and Technology, USA. Purified water (18.2 MΩ), from a Milli-Q water purification system (Millipore, Billerica, MA, USA) was used to prepare all the solutions. Other reagents employed are itemized in the Supplementary information.

2.3. ICP-DRC-MS optimization for isotope ratio measurements

The instrument parameters are listed in Table S1. The DRC conditions were optimized independently from the remainder of the ICP-MS system. The cell gas flow rate of ammonia and the high-pass rejection parameter (Rpq) value (the low-pass parameter (Rpa) was set at 0) were optimized to achieve the highest signal to noise ratio. Two solutions were used for the DRC optimization. The *blank solution* was the solution containing the possible interfering species of Cr and was composed of 1 mg L^{-1} S, 400 mg L^{-1} Cl, 0.5% CH$_3$OH, 2% HNO$_3$. The *standard solution* contained the interfering matrix (blank solution) together with a 2 μg L^{-1} Cr spike. Studies of the NH$_3$ flow rate in the range from 0.1 to 1 ml min^{-1} using different Rpq values changing from 0.4 to 0.7 on these solutions were investigated (Fig. S1).

2.4. Dead-time correction

For accurate isotope ratio determination, both the detector dead time and mass discrimination effects have to be corrected [27–30]. The dead time concerns the amount of time required for the detector and its associated electronics to process the signal from an incident ion and since this effect becomes increasingly stronger as the ion count rate increases it leads to significant biases in the measured ion intensity and therefore induces inaccuracy. For dead-time correction, an optimum dead-time value for which the isotope ratio is independent of concentration should be determined. The influence of dead time on the isotope ratios of $^{50}Cr/^{52}Cr$ and $^{53}Cr/^{52}Cr$ was determined by measuring different concentrations of natural isotopic abundance Cr standard SRM 979 with respective certified ratios of 0.052 and 0.113. A sweep is counted each time the instrument scans from the lowest to the highest mass specified. Results were unsatisfactory using 20 sweeps so that 400 sweeps were employed and then the instrument dead time of 50 ns was found to maintain constancy in both interested isotope ratios (Fig. S2).

2.5. Mass discrimination correction

Mass discrimination occurs when ions of different mass to charge ratios are transmitted or detected through the mass spectrometer with different efficiencies within the ICP-MS instrument, and this results in non-uniform response across the mass range [29]. The natural isotopic abundance standard SRM 979 was employed to determine the external correction mass bias factors from measurements of $^{50}Cr/^{52}Cr$ and $^{53}Cr/^{52}Cr$ isotope ratios at the determined optimum dead time.

The exact concentrations of the $^{50}Cr(III)$ and $^{53}Cr(VI)$ enriched spikes were determined by inverse IDMS. 0.0125 ml of $^{50}Cr(III)$ and $^{53}Cr(VI)$ enriched spike solutions were separately spiked into two 100 ml of 10 μg L^{-1} SRM 979 solutions, i.e. each containing 19.2 nmol of Cr. The dead-time corrected isotope ratios $^{50}Cr/^{52}Cr$ and $^{53}Cr/^{52}Cr$ were measured in both enriched $^{50}Cr(III)$ and $^{53}Cr(VI)$ spiked standard solutions by ICP-DRC-MS, and corrected by the mass bias factors (Table S2).

2.6. Sample collection and spiking

Local nullah water samples were collected in Shek Kip Mei Nullah on 8 and 15 March 2006, using a plastic bracket attached to a

nylon wire, and stored in acid-cleaned 2 L polythene bottles. Samples were filtered by a cellulose mixed-ester filter in a syringe before spiking. Each sample was then spiked with a known quantity of $^{50}Cr^{III}$ and $^{53}Cr^{VI}$. The optimal ratio would be $^{50}Cr^{III}$ and $^{53}Cr^{VI}$ in a concentration that approaches approximately a 1:1 ratio with the natural $^{50}Cr^{III}$ and $^{53}Cr^{VI}$ respectively, and therefore the concentrations of spikes depend upon the amounts of Cr(III) and Cr(VI) in the original sample.

2.7. Species separation by iron hydroxide co-precipitation

1 ml of 0.01 M of iron(III) hydroxide solution prepared from adding 1 ml of 10% (w/w) ammonium hydroxide to 50 ml of 0.01 M iron(II) ammonium sulfate solution and shaking for 24 h, was added to the 140 ml sample. The sample was shaken for 1 h by a mechanical shaker (Julabo SW-21C, Germany) and then suction filtered through a 0.4 μm Nucleopore membrane filter pre-cleaned with 10% (v/v) HNO_3 and milli-Q water. The sample filtrate was collected for Cr(VI) analysis. The filter paper containing the green precipitate was sonicated with 5 ml of 50% (v/v) HNO_3 for 30 min to extract Cr(III). The extract was filtered through a cellulose filter and then diluted to 50 ml with milli-Q water prior to ICP-DRC-MS measurement for Cr(III). Additional scavenging experiments were carried out with Fe(II) hydroxide to check the total chromium concentrations and the results were in agreement and not reported herein.

2.8. Isotope ratio measurement and calculation

The four isotope ratios of $^{50}Cr^{III}/^{52}Cr^{III}$, $^{53}Cr^{III}/^{52}Cr^{III}$, $^{50}Cr^{VI}/^{52}Cr^{VI}$ and $^{53}Cr^{VI}/^{52}Cr^{VI}$ were measured and corrected. The number of moles of Cr(III) and Cr(VI) in the sample and the degree of conversion between Cr(III) and Cr(VI) that occurred after spiking in sample were calculated by Eq. (1)–(4):

$$R^{III}\left(\frac{50}{52}\right) = \frac{(N_x^{III50}A_x + N_s^{III50}A_s^{III})(1-\alpha) + (N_x^{VI50}A_x + N_s^{VI50}A_s^{VI})\beta}{(N_x^{III52}A_x + N_s^{III52}A_s^{III})(1-\alpha) + (N_x^{VI52}A_x + N_s^{VI52}A_s^{VI})\beta} \tag{1}$$

$$R^{III}\left(\frac{53}{52}\right) = \frac{(N_x^{III53}A_x + N_s^{III53}A_s^{III})(1-\alpha) + (N_x^{VI53}A_x + N_s^{VI53}A_s^{VI})\beta}{(N_x^{III52}A_x + N_s^{III52}A_s^{III})(1-\alpha) + (N_x^{VI52}A_x + N_s^{VI52}A_s^{VI})\beta} \tag{2}$$

$$R^{VI}\left(\frac{50}{52}\right) = \frac{(N_x^{VI50}A_x + N_s^{VI50}A_s^{VI})(1-\beta) + (N_x^{III50}A_x + N_s^{III50}A_s^{III})\alpha}{(N_x^{VI52}A_x + N_s^{VI52}A_s^{VI})(1-\beta) + (N_x^{III52}A_x + N_s^{III52}A_s^{III})\alpha} \tag{3}$$

$$R^{VI}\left(\frac{53}{52}\right) = \frac{(N_x^{VI53}A_x + N_s^{VI53}A_s^{VI})(1-\beta) + (N_x^{III53}A_x + N_s^{III53}A_s^{III})\alpha}{(N_x^{VI52}A_x + N_s^{VI52}A_s^{VI})(1-\beta) + (N_x^{III52}A_x + N_s^{III52}A_s^{III})\alpha} \tag{4}$$

and since the subscripts x and s refer to the sample and spike, respectively: $R^z(y/52)$ is the isotope ratio of ^yCr to ^{52}Cr of Cr(z) ($z = III$ for $y = 50$ and $z = VI$ for $y = 53$) in the *spiked* sample; A_x is the relative abundance of the respective isotope of Cr in the original sample; A_s^{III} and A_s^{VI} are the relative abundances of the respective isotopes of Cr in the enriched $^{50}Cr^{III}$ and $^{53}Cr^{VI}$ isotopic standard spikes, respectively; N_s^z is the number of moles of Cr(z) in the enriched $^{50}Cr^z$ ($z = III$) and $^{53}Cr^z$ ($z = VI$) isotopic standard spikes, respectively; N_x^{III} and N_x^{VI} are the numbers of moles of Cr(III) and Cr(VI) initially in the sample, respectively; α is the percentage of Cr(III) oxidized to Cr(VI) after spiking; and β is the percentage of Cr(VI) reduced to Cr(III) after spiking.

The calculated α and β are related to the equilibrium constant (K_c) between Cr(III) and Cr(VI) by Eq. (5):

$$K_c = \frac{N_x^{VI}(1-\beta) + \alpha N_x^{III}}{N_x^{III}(1-\alpha) + \beta N_x^{VI}} \tag{5}$$

The method detection limits (MDL) were determined as three times the standard deviation of the concentrations of seven replicates of blank reagent that were processed through the entire analytical method with a sample and were 0.4 and 0.04 μg L^{-1} for the analysis of Cr(III) and Cr(VI), respectively, following the described procedures.

3. Results and discussion

3.1. ICP-DRC-MS optimization for isotope ratio measurements

The DRC optimization now discussed was used for isotope ratio measurements on solutions. The first consideration of an accurate determination of the isotopic ratios of chromium concerns the interferences upon the interested isotopes $^{50,52,53}Cr$. The concentrations given above of the predominant interfering species arising from Cl, C, S and N were estimated from the average concentrations of Cl$^-$, total organic carbon, S^{2-}, inorganic nitrogen (NO$_3^-$ and NO$_2^-$) and organic nitrogen from measurements in Hong Kong inland waters by the Hong Kong Environmental Protection Department [31]. In this study, DRC technology was found to successfully overcome the problem of polyatomic interferences on Cr by using ammonia gas under optimized operating conditions. Investigations on varying the NH$_3$ flow rates as well as the Rpq values were carried again to obtain reliable DRC operation parameters. Among the ranges of Rpq and cell gas flow rate studied, the operation at the high- and low-pass rejection parameters Rpq = 0.45, Rpa = 0, and flow rate of 0.45 ml min^{-1} provided a good estimated detection limit, as well as strong signal intensity for all Cr isotopes, and were thus selected to be the subsequent operating conditions (Fig. S1).

By consideration of the ionization energies of Cr (6.77 eV) and NH$_3$ (10.16 eV), the electron transfer from NH$_3$ to Cr$^+$ is therefore endothermic, so that the interference removal mechanism is expected to be preferentially by conversion into new species, rather than by forming new cluster ions with Cr at different masses. Our results (not shown) demonstrated that Cr does not readily react to form Cr(NH$_3$)$_n^+$ ($n = 2, 3, 4, \ldots, 6$) species and that only the signal intensities of $^zCr(NH_3)^+$ ($n = 1$; $z = 50, 52, 53, 54$) increased linearly with different concentrations of Cr standard solutions. However, the signal intensity of $^{52}Cr(NH_3)^+$ was too weak to provide an accurate determination.

Using 400 sweeps of the mass spectrometer and the optimized dead time of 50 ns, the isotope ratios obtained were 0.048 and 0.119 for $^{50}Cr/^{52}Cr$ and $^{53}Cr/^{52}Cr$ respectively, which are only correspondingly 8% and 4% in error with the certified values. The mass discrimination factors per unit mass of $^{50}Cr/^{52}Cr$ and $^{53}Cr/^{52}Cr$ were both calculated as 4.0%, which were then used for the mass discrimination corrections of $^{50}Cr/^{52}Cr$ and $^{53}Cr/^{52}Cr$ in the sample by applying Eqs. (S1, S2) (Table S2).

3.2. Preparation of $^{50}Cr(III)$ and $^{53}Cr(VI)$ enriched spike solutions

The isotopic abundances of the $^{50}Cr^{III}$ and $^{53}Cr^{VI}$ enriched spike solutions prepared were determined and are shown in Table 1. The measured abundances were determined by calculating the ratio of the net intensity of a specific isotope to the total intensity of the element (sum of intensity for all isotopes). The results showed good agreement between the certified and the measured abundances in both enriched spike solutions, with good precision. The concentrations of the $^{50}Cr^{III}$ and $^{53}Cr^{VI}$ enriched spikes were determined by

Table 1
Determination of isotopic abundance of the ^{50}Cr(III) and ^{53}Cr(VI) spike solutions prepared (identical values were obtained for two replicates)

Isotope	^{50}Cr^{III} spike solution		^{53}Cr^{VI} spike solution	
	Certified abundance (%)	Measured abundance (%)	Certified abundance (%)	Measured abundance (%)
^{50}Cr	96.9	96.6	–	0.1
^{52}Cr	–	3.2	–	1.9
^{53}Cr	–	0.2	97.9	97.9
^{54}Cr	–	0	–	0.1

inverse IDMS using SRM 979 and were found to be 90 and 67 mg L^{-1}, respectively.

3.3. Assessment of interconversion between Cr(III) and Cr(VI)

To investigate the influence of initial concentrations upon the distribution between Cr(III) and Cr(VI) in water, six sets of iron hydroxide co-precipitation experiment were performed using 140 ml nullah water samples (pH 7.52). The water sample was filtered by a syringe cellulose mixed-ester filter before spiking. Since the total chromium concentration in the neat nullah water samples (labeled A, B) was found to be only 0.9 μg L^{-1}, additional solutions in duplicate (labeled C. . .L) were made up with natural abundance Cr(III) and natural abundance Cr(VI) spikes of up to 100 μg L^{-1}. Appropriate concentrations (in a roughly 1:1 species ratio) of isotopically enriched ^{50}Cr^{III} and enriched ^{53}Cr^{VI} were also spiked into the samples. An aliquot of 140 ml milli-Q water without any spikes acted as a blank sample. Following iron(III) hydroxide treatment and subsequent manipulations described above, the isotope ratio measurements of ^{50}Cr^{III}/^{52}Cr^{III}, ^{53}Cr^{III}/^{52}Cr^{III}, ^{50}Cr^{VI}/^{52}Cr^{VI} and ^{53}Cr^{VI}/^{52}Cr^{VI} were made separately for the speciated Cr(III) and Cr(VI) samples. These isotope ratios were employed in the set of Eqs. (1)–(4) to calculate the initial amounts of Cr(III) (N_x^{III}) and Cr(VI) (N_x^{VI}) in the sample, as well as the respective concentrations which are listed in Table 2.

A and B are the samples without any natural Cr spikes (i.e. only nullah water with subsequent enriched isotopic spikes). The initial Cr(VI) concentrations were found to be 0.7 μg L^{-1}, which is similar to the total Cr concentration of 0.9 μg L^{-1} in the nullah water

sample analyzed by ICP-DRC-MS. Thus about 90% of Cr in the nullah water existed as Cr(VI). This may be due to the immobility or absence of Cr(III) in this water system since it: (i) has a strong tendency to complex with many inorganic or organic ligands; (ii) is adsorbed by naturally occurring solids; and (iii) precipitates out under neutral to basic condition. Thus Cr(VI) is generally the most mobile Cr form in natural waters. The calculated concentrations of both Cr(III), Cr(VI) and total Cr (i.e. labeled as C_x: corresponding to the amount of natural abundance spikes plus the original small amount present in the nullah water) are in good agreement with their true concentrations. Subtraction of the natural isotopic abundance spike concentrations ($^{nat}C_s^{total}$) from the total determined Cr concentration (C_x^{total}) gives the concentration of Cr present in the original nullah water in the last column of Table 2. Good agreement is obtained for this small concentration (samples A–F inclusive) except when two large numbers are being subtracted (samples G–L).

Satisfactory recoveries (of between 94% and 107%) were obtained by using the proposed speciation method as shown in Table 3. The percentage of conversion from Cr(III) to Cr(VI) (α) increases from ~6% to ~10% with increase of the initial concentrations of Cr(III) and Cr(VI) each from <1 to >50 μg L^{-1}, while the percentage of conversion from Cr(VI) to Cr(III) (β) was between 1.6% and 0.9% in these ranges (Table 3, columns 7 and 8). This relatively small degree of interconversion from Cr(VI) to Cr(III) is expected under the basic medium since Cr(VI) then has a negative redox potential ($E^0 = -0.13$ V) and exhibits thermodynamic stability under aerobic conditions [32] whereas dissolved oxygen rapidly reacts with reducing agents such as S^{2-}, Fe^{2+} and organic matter usually

Table 2
Concentrations of Cr(III), Cr(VI) and total Cr in the samples and the determined mean ± standard deviation values from replicate samples

Sample labels	Concentration (μg L^{-1})						
	$^{nat}C_s^{III}$	$^{nat}C_s^{VI}$	$^{nat}C_s^{total}$	C_x^{III}	C_x^{VI}	C_x^{total}	$C_x^{total} - {}^{nat}C_s^{total}$
A, B	0	0	0	<DL[a]	0.7 ± 0	0.8 ± 0.1	0.8 ± 0.1
C, D	5.2	5.4	10.6	5.2 ± 0.1	6.2 ± 0	11.4 ± 0.1	0.9 ± 0.1
E, F	10.7	10.5	21.2	10.5 ± 0.1	11.6 ± 0.1	22.1 ± 0.1	0.9 ± 0.1
G, H	20.7	20.9	41.6	18.9 ± 0.4	23.2 ± 0.5	42.1 ± 0.1	0.5 ± 0.1
I, J	49.1	52.3	103.9	46.9 ± 1.7	53.7 ± 0.7	100.7 ± 2.5	-3.4 ± 2.5
K, L	103.3	103.2	206.5	97.8 ± 0.5	106.6 ± 1.4	204.4 ± 1.9	-2.2 ± 1.9

$^{nat}C_s^z$: initial concentration of natural abundance Cr(z) spiked into the sample; $^{nat}C_s^{total}$: total natural abundance Cr concentration in the sample; C_x^{III}, C_x^{VI} and C_x^{total} are the determined concentrations of Cr(III), Cr(VI) and total Cr in the sample.

[a] The detection limit for Cr(III) is 0.4 μg L^{-1} (3σ value; N = 7).

Table 3
Chromium recoveries, interconversions and equilibrium constants for samples A–L (mean ± S.D.; N = 2)

Sample	Recovery of Cr (%)			Cr existing in the sample (%)		Percentage of conversion (%)		Equilibrium constant, K_c
	Cr(III)	Cr(VI)	Cr(total)	Cr(III)	Cr(VI)	α	β	
A, B	–	–	94.2 ± 4	(9.8 ± 0.4)	90.3 ± 0.4	5.9 ± 1.8	1.6 ± 0.1	nd[a]
C, D	97.9 ± 1	102.4 ± 0	99.7 ± 0.5	45.1 ± 0.3	54.9 ± 0.3	8.5 ± 0.2	1.1 ± 0.1	1.4 ± 0
E, F	97.5 ± 1.2	103 ± 1.4	99.9 ± 0.1	47.7 ± 0.7	52.4 ± 0.7	8.0 ± 0.5	1.9 ± 0.6	1.2 ± 0
G, H	91 ± 2.2	107.3 ± 2.2	99.1 ± 0.1	44.9 ± 1.1	55.1 ± 1.1	8.4 ± 1.2	1.0 ± 0.1	1.4 ± 0.1
I, J	90.7 ± 3.3	101.4 ± 1.4	96.1 ± 2.3	46.6 ± 0.6	53.4 ± 0.6	12.1 ± 0.4	0.9 ± 0.1	1.4 ± 0
K, L	94.6 ± 0.5	102.6 ± 1.3	98.6 ± 0.9	47.9 ± 0.2	52.2 ± 0.2	9.3 ± 2	0.9 ± 0.1	1.3 ± 0

[a] This value was not determined since the initial concentrations of Cr(III) (C_x^{III}) in samples A and B were below detection limit.

Table 4
Summary of the determined Cr(III) and Cr(VI) in samples M–R, the percentage of interconversion, and the equilibrium constant between Cr(VI) and Cr(III) at different days of analysis under different pH conditions

Sample label	Day of storage	pH	Concentration of Cr in the sample ($\mu g\,L^{-1}$)		Percentage of Conversion (%)		K_c
			C_x^{III}	C_x^{VI}	α	β	
M, N	1	3.00	201.6 ± 1.3	204.5 ± 0.3	1.4 ± 0.1	2.7 ± 0.1	1.0 ± 0.0
	2	2.89	201.1 ± 0.4	205.0 ± 0.3	1.6 ± 0.1	2.8 ± 0.1	1.0 ± 0.0
	5	2.88	201.7 ± 0.1	203.5 ± 0.1	1.7 ± 0.1	3.3 ± 0.1	1.0 ± 0.0
O, P	1	7.00	201.0 ± 0.6	205.2 ± 0.1	1.1 ± 0.0	1.7 ± 0.1	1.0 ± 0.0
	2	6.36	200.4 ± 0.0	206.7 ± 0.0	6.6 ± 0.0	2.4 ± 0.1	1.1 ± 0.0
	5	6.26	200.5 ± 0.2	204.8 ± 0.5	3.7 ± 0.5	3.4 ± 0.0	1.0 ± 0.0
Q, R	1	10.02	202.6 ± 3.2	204.7 ± 1.7	30.8 ± 0.1	1.2 ± 0.0	1.8 ± 0.0
	2	9.45	201.3 ± 0.2	207.2 ± 1.1	25.4 ± 2.5	1.1 ± 0.2	1.7 ± 0.1
	5	9.35	201.8 ± 0.3	205.1 ± 0.1	30.0 ± 2.5	1.3 ± 0.0	1.8 ± 0.1

Values represent the mean ± S.D. ($N = 2$). The initial concentrations of Cr(III) and Cr(VI) were 201.3 $\mu g\,L^{-1}$ and 204.0 $\mu g\,L^{-1}$, respectively.

present. On the other hand, the basic medium destabilizes Cr(III) and converts it to Cr(VI) in the presence of oxidizing agents. However, the manganese oxidation state existing in natural waters is generally Mn(II) and not the potential oxidant Mn(IV). Besides, the oxidation of Cr(III) by dissolved oxygen was reported to be slow [32] and the reaction was found to be insignificant when compared with MnO_2 [33].

As expected, the equilibrium constant (K_c: Table 3, last column) calculated from α and β was independent of the initial concentrations of Cr(III) and Cr(VI) and maintained at the constant value of 1.3 at room temperature and pH 7.52. Thus, the percentage of conversion from Cr(III) to Cr(VI) increases more significantly than the conversion from Cr(VI) to Cr(III) with the increase of initial concentrations of Cr(III) and Cr(VI).

3.4. Effect of pH and storage time

The proposed speciation method only allows co-precipitation of Cr(III) with $Fe(OH)_3$ to form $Cr_xFe_{1-x}(OH)_3$ when the pH is above 4 [32,34]. Thus, to investigate the influence of pH and storage time on the distribution between Cr(III) and Cr(VI) in water, the pH values of three bottles each of 1.2 L of synthesized water samples were adjusted to pH 3, 7 and 10, respectively, by using NaOH or HNO_3. Then, natural isotopic abundance Cr(III) and Cr(VI), and isotopically enriched Cr(III) and Cr(VI) spikes were added, with the final concentrations of each being 200 $\mu g\,L^{-1}$ in each sample. Two replicates of 140 ml sample at each adjusted pH (together with an aliquot of 140 ml milli-Q water without any spikes acting as a blank sample), were analyzed after days 1, 2 and 5 by the SIDMS method. Immediately before the Fe(III) co-precipitation, the pH of each sample was adjusted to 7. Then the isotope ratio measurements of $^{50}Cr^{III}/^{52}Cr^{III}$, $^{53}Cr^{III}/^{52}Cr^{III}$, $^{50}Cr^{VI}/^{52}Cr^{VI}$ and $^{53}Cr^{VI}/^{52}Cr^{VI}$ were made as described before. The calculated concentrations of Cr(III) and Cr(VI) in the different samples labeled M–R and their corresponding α and β are shown in Table 4. The calculated concentrations of both Cr(III), Cr(VI) and total Cr in the sample over the whole pH range studied agreed with their true concentrations (i.e. corresponding to the amount of natural abundance spikes added). According to the results, a greater extent of the conversion from Cr(VI) to Cr(III) was found under an acidic medium, whereas the oxidation from Cr(III) to Cr(VI) dominated at higher pH. These results are expected since Cr(VI) exhibits a high positive redox potential under acidic media. By contrast, a negative potential occurs under basic media which destabilizes Cr(III) and converts it to the Cr(VI) oxidation state in the presence of oxidizing agents. The equilibrium constant, K_c (final column, Table 4) changed with pH from 1 (pH 3) to 1.8 (pH 10) but was temporally constant for a given pH value.

Table 5
Concentrations of Cr(VI) ($\mu g\,L^{-1}$) determined in samples analyzed by SIDMS and DPC methods. The initial concentrations were 405 $\mu g\,L^{-1}$

Sample label	Day of storage	pH	SIDMS method	DPC method
			$^{nat+iso}C_x^{VI}$	$^{nat+iso}C_x^{VI}$
S, T	1	3.00	404.5 ± 0.3	386.2 ± 0.1
	2	2.89	405.0 ± 0.3	411.2 ± 0.6
	5	2.88	403.5 ± 0.1	407.3 ± 0.2
U, V	1	7.00	405.2 ± 0.1	378.7 ± 0.5
	2	6.36	406.7 ± 0.0	403.6 ± 0.4
	5	6.26	404.8 ± 0.5	396.8 ± 0.4
W, X	1	10.02	404.7 ± 1.7	381.3 ± 0.2
	2	9.45	407.2 ± 1.1	403.3 ± 0.5
	5	9.35	405.1 ± 0.1	398.7 ± 0.1

3.5. Comparison of SIDMS with DPC method for Cr(VI) analysis

The DPC method for Cr(VI) analysis, with experimental details as described in the Supplementary information, was also employed for temporal and accuracy comparisons with the proposed SIDMS analysis method. Table 5 shows the concentration of the natural abundance Cr spikes in the samples analyzed by the SIDMS and DPC methods at different pH and after storage for different times. The Cr(VI) concentrations obtained from the DPC method fluctuated more over the period of study (maximum error 6.5%) under different pH conditions than those from SIDMS (maximum error 0.5%). Besides the problems of chemical and spectral interferences mentioned in Section 1, the much simpler spectrophotometric DPC method has the usual problems of colorimetric methods in ensuring uniform color development and reproducibility.

4. Conclusions

Species-specific isotope dilution methods for Cr(III)/Cr(VI) analysis using mass spectrometry have been previously employed together with the separation techniques HPLC [19] and ion chromatography [12]. The present method withdraws the requirement for a separation technique. Furthermore, the mass spectrometry component becomes more accurate with the incorporation of a dynamic reaction cell into the instrument. The advantages of the present method over the conventional spectrophotometric Cr(VI) speciation methods are that it is more accurate and precise, and that species interconversions prior to, and during the analysis, are eliminated. The present method has the added bonus that there is a built-in check upon the total chromium concentration in solution by scavenging with Fe(II) hydroxide.

Appendix A. Supplementary data

Supplementary data associated with this article can be found, in the online version, at doi:10.1016/j.talanta.2008.06.005.

References

[1] California Air Resources Board, Chromium and compounds, hexavalent chromium Report ARB/SSD/SES, 1997, Available at www.arb.ca.gov/toxics/tac/factshts/chromium.
[2] J. Kotas, Z. Stasicka, Environ. Pollut. 107 (2000) 263.
[3] C. Seigneur, E. Constantinou, Environ. Sci. Technol. 29 (1995) 222.
[4] F.A. Cotton, G. Wilkinson, Advanced Inorganic Chemistry, Wiley-Intersci., New York, 1988 (Chapter 18).
[5] P.R. Wittbrodt, C.D. Palmer, Environ. Sci. Technol. 29 (1995) 255.
[6] D.L. Sedlak, P.G. Chan, Geochim. Cosmochim. Acta 61 (1997) 2167.
[7] M. Pettine, F.J. Millero, R. Passino, Marine Chem. 46 (1994) 335.
[8] M. Pettine, S. Capri, Anal. Chim. Acta 540 (2005) 231.
[9] APHA, AWWA, WEF, Standard Methods for the Examination of Water and Wastewater, 20th ed., APHA, Washington, DC, 1998, pp. 3–65.
[10] United States Environmental Protection Agency, Method 7196A, 1992.
[11] K. Ashley, A.M. Howe, M. Demange, O. Nygren, J. Environ. Monit. 5 (2003) 707.
[12] K. Tirez, W. Brusten, A. Cluyts, J. Patyn, N. De Brucker, J. Anal. At. Spectrom. 18 (2003) 922.
[13] Y.M. Lui, J.K. Cheng, Electrophoresis 24 (2003) 1993.
[14] B. Baraji, M. Martinez, A. Sastre, M. Aguilar, J. Chromatogr. A 695 (1995) 103.
[15] G.Y. Jung, Y.S. Kim, H.B. Lim, Anal. Sci. 13 (1997) 463.
[16] S. Himeno, T. Nakashima, K.I. Sano, Anal. Sci. 14 (1998) 369.
[17] Y.L. Chang, S.J. Jiang, J. Anal. At. Spectrom. 16 (2001) 858.
[18] Z. Grosser, W. Reuter, P. Perrone, K. Neubauer, Water Environ. Lab. Solut. 11 (2004) 1.
[19] J. Meija, L. Yang, J.A. Caruso, Z. Mester, J. Anal. At. Spectrom. 21 (2006) 1294.
[20] H.M. Kingston, D. Huo, Y. Lu, S. Chalk, Spectrochim. Acta Part B: Atom. Spectrosc. 53 (1998) 299.
[21] United States Environmental Protection Agency, Elemental and speciated isotope dilution mass spectrometry, U.S. Environmental Protection Agency, USEPA 6800, 1998.
[22] H.E. Cranston, J.W. Murray, Anal. Chim. Acta 99 (1978) 275.
[23] R.J. Kieber, G.R. Heiz, Environ. Sci. Technol. 26 (1992) 307.
[24] S.E. Kaczynskl, R.J. Kieber, Environ. Sci. Technol. 27 (1993) 1572.
[25] S.F. Kan, P.A. Tanner, Environ. Chem. 3 (2006) 149.
[26] S.F. Kan, P.A. Tanner, J. Anal. At. Spectrom. 19 (2004) 639.
[27] S.M. Nelms, C.R. Quetel, T. Prohaska, J. Vogl, P.D.P. Taylor, J. Anal. At. Spectrom. 16 (2001) 333.
[28] F. Vanhaecke, L. Balcaen, I. Deconinck, I.D. Schrijver, C.M. Almeida, L. Moens, J. Anal. At. Spectrom. 18 (2003) 1060.
[29] L. Yang, R.E. Sturgeon, J. Anal. At. Spectrom. 18 (2003) 1452.
[30] K.G. Heumann, S.M. Gallus, G. Rädlinger, J. Vogl, J. Anal. At. Spectrom. 13 (1998) 1001.
[31] Hong Kong Environmental Protection Department, River water quality in Hong Kong 2003, Report EPD/TR1/04, 2004, Available at http://www.epd.gov.hk/epd/english/environmentinhk/water/river_quality/rwq_report03.html.
[32] F.Y. Seleh, T.F. Parkerton, R.V. Lewis, J.H. Huang, K.L. Dickson, Sci. Total Environ. 86 (1989) 25.
[33] D. Rai, L.E. Eary, J.M. Zachara, Sci. Total Environ. 86 (1989) 15.
[34] H. Zhang, R. Bartlett, Environ. Sci. Technol. 33 (1999) 588.

Application of the Bahe's pseudolattice theory to water–1-butyl-3-methylimidazolium tetrafluoroborate (bmimBF$_4$) mixtures at 298.15 K
Part II. Acidity scales

I. Bou Malham [a,b], P. Letellier [a,b], M. Turmine [a,b,*]

[a] Laboratoire d'Electrochimie et Chimie Analytique, UMR 7575, Université Pierre et Marie Curie-PARIS6, Ecole Nationale Supérieure de Chimie Paris-ENSCP, CNRS, UMR7575, Paris F-75005, France
[b] Energétique et Réactivité aux Interfaces, UPMC, case 39, 4 place Jussieu, 75252 Paris cedex 05, France

ARTICLE INFO

ABSTRACT

Molten salts at room temperature and their mixtures with water or molecular solvents are excellent candidates for future replacement of most of organic solvents used in many industrial processes. To make this possible and to allow efficient application, it is necessary to determine physico-chemical parameters (such as the acidity scales) for these reaction media. This work follows a study of the autoprotolysis constants (K_s) of water–1-butyl-3-methylimidazolium tetrafluoroborate (bmimBF$_4$) mixtures at 298.15 K over the composition range of 0–77.43 vol.% bmimBF$_4$ [I. Bou Malham, P. Letellier, M. Turmine, Talanta 72 (2007) 155–164]. In this second analysis, we determined the values of the dissociation constant (pK_a) of various conjugate acid–base pairs for the same water–bmimBF$_4$ mixtures, to establish acidity scales for each medium. These data can be used to produce proton buffer solutions and thus to control the acidity level of water–ionic liquid (IL) mixtures. We compare the values of pK_a for acid–base pairs in water–bmimBF$_4$ mixtures with published values for water–methanol mixtures.

© 2008 Elsevier B.V. All rights reserved.

1. Introduction

The need of chemical industries that respect the environment while remaining efficient has stimulated active research in recent years on new non-polluting solvents. Particular attention has been paid to molten salts at room temperature (known as green solvents) [1–5]. These ionic liquids (IL), flexible in their nature (anions and cations) and properties, have very low vapour pressures, can dissolve molecular species and salts, and display substantial thermal stability in addition to various other interesting features. They are thus possible alternative reaction media to the standard organic solvents used in industrial processes. Numerous studies of these pure compounds and their mixtures with various molecular solvents have extensively described their physico-chemical properties using diverse approaches [6–8]. The main feature of these media is that they are strongly structured [9–13]. An important issue concerning ionic liquids involves the reactions [14,15] and processes [16,17], that can be achieved using them.

Many published studies directly compare the evolution (kinetic and mechanism) of a given reaction in a medium (where it is usually carried out) and in molten salts. In these exploratory experiments, the acidity levels of the solutions are not controlled. In such conditions, it can be difficult to assess the true impact of the ionic liquid on reactivity for a given process. In some cases, the acidity of the molten salt is fixed for catalyzing certain reactions: this is the case for acidic or very basic ionic liquids. There is interest in acidic ionic liquids [18] because they are candidates to replace traditional homogenous and heterogeneous acids in chemical processes. Such acidic ionic liquids have potential as dual solvent-catalysts for organic reactions. Thus, properties of [bmim]HSO$_4$ have been exploited for catalytic activity: for example, its tendency to form biphasic systems has been used in the synthesis of coumarin and the monotetrahydropyranylation of diols. The acidity of such media is generally determined by means of Hammett functions [19]. Basic ionic liquids, mainly 1-butyl-3-methylimidazolium hydroxide [20], are also used to catalyze some reactions, such as Markovnikov addition of imidazole to vinylacetate [21], Michael addition and alkylation of active methylene compounds [22].

* Corresponding author at: Laboratoire d'Electrochimie et Chimie Analytique, UMR 7575, Université Pierre et Marie Curie-PARIS6, Ecole Nationale Supérieure de Chimie Paris-ENSCP, CNRS, UMR7575, Paris F-75005, France.
E-mail address: mireille.turmine@upmc.fr (M. Turmine).

Apart from these particular cases, there has been little work concerning the proton acidity level [23] and dissociation constant values of conjugate acid–base pairs [24] in ionic liquids, or even in simple concentrated salt solutions [25].

We therefore studied the acidity scales in water–bmimBF$_4$ mixtures [26]. Molten salt behaves like an aprotic solvent. In the first part of this study, we published the pK_s values of these mixtures over the composition range of 0–77.43 vol.% bmimBF$_4$ [26]. We showed that the values of autoprotolysis products could be suitably described by the quasi-lattice theory proposed by Bahe as supplemented by Varela et al. [27,28]. In this approach, concentrated saline solutions are considered as media in which the ions are distributed according to a face-centred cubic structure with strong short-range ion–ion interactions. We continued this analysis by determining values of dissociation constants (pK_a) for various acid–base pairs in these same media. The goal was primarily operational: to provide experimental data allowing proton buffer solutions in water–bmimBF$_4$ mixtures to be prepared and to control the acidity levels for efficient use of these water–ionic liquid mixtures as reaction media.

2. Experimental

2.1. Reagents and products

Sodium tetrafluoroborate (98%), 1-methylimidazole (99%), 1-bromobutane (99%) and acetonitrile (99%) were from Acros Organics. Acetone (Normapur) was from Prolabo, ethyl acetate (purex for analysis) and dichloromethane were from SDS. Sodium hydroxide (1 M), hydrochloric acid (1 M) and buffer solutions (pH 4, pH 7, pH 10) were obtained from SDS. 4-Cyanophenol (99%), ammonium tetrafluoroborate (99.999%) and phenol (99%) were obtained from Aldrich, and acetic acid (purex for analysis) was from SDS. Pyridine was purchased from prolabo and was distilled twice before use.

All mixtures were prepared in ultrapure water (all water used was distilled and then filtered with an ELGA UHQ II system, $\kappa = 18$ MΩ). Imidazolium salts were synthesised according to the procedure described in the first part of this study [26].

2.2. Electrochemical measurements

For all measurements, the temperature was maintained at a constant 298.15 ± 0.10 K.

The electrochemical cell used can be described as follows:

KCl-saturated calomel electrode	agar–agar gel salt bridge aqueous 2M NaBr solution	water–bmimBF$_4$ mixture H$^+$ and/or AH/A$^-$ or BH$^+$/B	High alkalinity glass electrode
E$_{ref}$	E$_j$	E$_{mes}$	
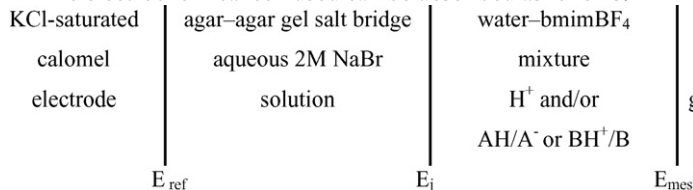
The electromotive force (emf), E, of the corresponding cells is

$$E = E_{mes} + E_j - E_{ref} \tag{1}$$

The pH sensitive electrode is a "high alkalinity" glass electrode made by Inforlab Chimie. The behaviour of this electrode in water–ionic mixtures is similar to those observed in pure water, particularly, its response time is about less than 1 min (typically about 30 s for the studied solutions). This membrane electrode has a potential, E_{mes} that follows the Eisenman–Nikolsky's equation [29],

$$E_{mes} = cste + m \log(a_{H^+} + k_M \sum a_M) \tag{2}$$

where a_{H^+} is the proton activity in solution, a_M is the interfering cation activities and k_M is the selectivity coefficient. m is the experimental slope of the electrode. If the glass membrane is perfectly selective with the protons then, $m = RT \ln(10)/F$. In the concentrated saline solutions, the activities, with reference to the infinitely diluted state in the medium, are given in terms of concentration. As will be shown in the experimental study, the imidazolium cation interferes very little with the electrode response ($k_M \approx 0$). E_j is the junction potential between the measurement compartment and the agar–agar salt bridge. The concentrations of acids and bases introduced into the medium are low ($C < 10^{-1}$ mol L^{-1}). The value of E_j depends only on the concentration of the two electrolytes involved: molten salt and NaBr. We used this salt in the bridge because potassium tetrafluoroborate is slightly soluble in water and then KCl-saturated calomel electrode cannot be directly soaked in the compartment containing the solution being studied. Moreover, we tested in the first part of this study [26], three types of junctions between the two compartments. We chose a junction with a salt bridge made of a capillary Teflon tube filled with a saline gel of 2 M NaBr in agar–agar which avoids the diffusion between the two compartments (reference electrode and solution). After each series of measurement, the junction was regenerated by cutting the end of the bridge salt.

E_{ref} is the potential of the KCl-saturated calomel reference electrode. Under these conditions, the liquid-junction potential ($E_j - E_{ref}$) was found to be stable over time (to within ± 0.1 mV). The cell's emf is thus reduced to

$$E = A + m \log a_{H^+} \tag{3}$$

where A is the constant term of the electrochemical cell.

2.3. Experimental determination of dissociation constants

First, the measuring cell, E_a, is calibrated with various solutions of known hydrochloric acid concentrations in ionic liquid–water mixtures. Thus, values of the slope, m, of the electrode and the constant, A, can be determined.

Then, a mixture of an acid (for example, AH) and its conjugated base (A$^-$) is introduced into the measurement compartment. The emf of this cell will be E_C. The dissociation constant of AH/A$^-$, K_a, is related to the proton activity in the solution according to

$$\log K_a = \log \frac{|A^-|}{|AH|} + \log a_{H^+} \tag{4}$$

Thus, a simple relation between E_C and the ratio of acid and base concentrations can be established

$$Y = \frac{A - E_C}{m} = pK_a + \log \frac{|A^-|}{|AH|} \tag{5}$$

Y is plotted against $\log(|A^-|/|AH|)$. The slope of this straight-line must be equal to one; the value of pK_a corresponds to the y-axis intercept value.

3. Results

To simplify the procedures for pK_a determination and to obtain numerous experimental points, we generally carried out potentio-
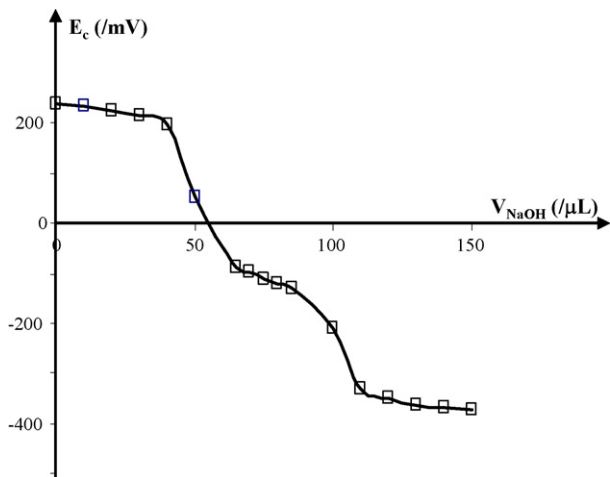
Fig. 1. Curve of neutralization of an equimolar mixture of 10^{-2} mol L^{-1} HCl and 4-cyanophenol by 1 mol L^{-1} NaOH in 38.67 vol.% ionic liquid mixture ($x_{IL} = 0.0569$).
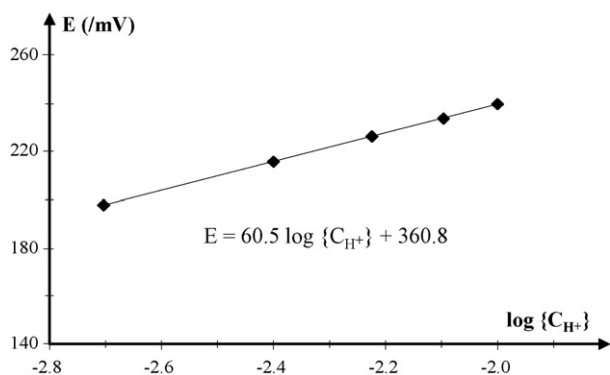
Fig. 2. Electrochemical cell calibration from the first part of the curve (Fig. 1), $A = 360.8$ mV, $m = 60.5$ mV/decade.

metric measurements on equimolar solutions of HCl and weak acid (generally at 10^{-2} mol L^{-1}) which were neutralized with concentrated (1 mol L^{-1}) NaOH. The first part of the titration curve allows the parameters of the electrochemical cell (i.e., A and m) to be determined, the second part leads to the pK_a value. Our method is illustrated by Figs. 1–3. For example, we determined values of E_C for ionic liquid–water binary with $x_{IL} = 0.0569$ (38.67% in volume of ionic liquid) for a mixture HCl (10^{-2} M)–acid acetic (10^{-2} M) neu-
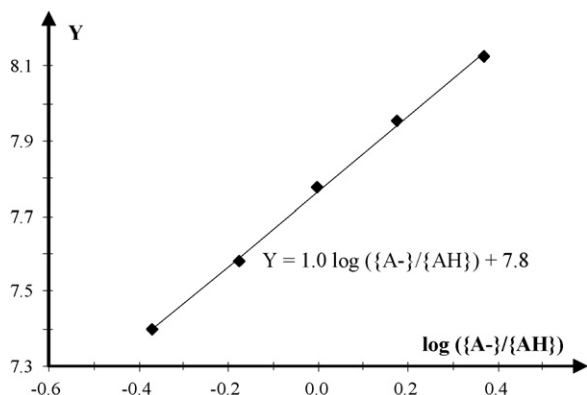
Fig. 3. Determination of pK_a for 4-cyanophenol/4-cyanophenolate in 38.67 vol.% ionic liquid solution. Y values of Eq. (5) are plotted against log ({A−}/{AH}). The slope of this straight-line is equal to one, pK_a = 7.8.

tralized with 1 M NaOH (Fig. 1). Calibration of the system is shown in Fig. 2 and the determination of pK_a in Fig. 3.

The results for various water–bmimBF$_4$ mixtures are reported in Table 1.

4. Discussion

The behaviour of conjugate acid–base pairs in these water–ionic liquid mixtures is somewhat different from that observed in hydro-organic media such as water–methanol, and water–DMSO. Fig. 4 shows the comparison between pK_a values of some acid–base pairs in water–bmimBF$_4$ (Fig. 4a) and in water–methanol mixtures [30] (Fig. 4b).

The main feature of hydro-organic media is that these mixtures combine solvents with antagonistic properties. Water stabilizes ionic species strongly and solubilises molecular species weakly. By contrast, the organic solvent often solubilises molecules strongly and, in the case of DMSO for example, destabilizes ions weakly [31]. As the literal form of pK_a variation is established with the nature of the solvent, the effect of an organic solvent added to water is generally easy to interpret, as shown by considering the case of the protonic exchange between an acid AH and its conjugated base A$^-$. The properties of BH$^+$/B pairs can be established by analogy.

Consider the acid – base equilibrium AH = A$^-$ + H$^+$. In solvent S, the equilibrium condition is

$$^S\mu_H + {}^S\mu_A - {}^S\mu_{AH} = 0 \tag{6}$$

The chemical potentials can be expressed with respect to the concentration referenced to the ideal dilute behaviour in S, as:

$$^S\mu_H^\infty + {}^S\mu_A^\infty - {}^S\mu_{AH}^\infty + RT \ln \frac{{}^S a_H {}^S a_A}{{}^S a_{AH}} = 0 \tag{7}$$

$^S\mu_H^\infty$, $^S\mu_{A^-}^\infty$ and $^S\mu_{AH}^\infty$ are the standard chemical potentials of H$^+$, A$^-$ and AH, respectively, referenced to the ideal dilute behaviour in S. These parameters being constant,

$$^S\mu_H^\infty + {}^S\mu_A^\infty - {}^S\mu_{AH}^\infty + RT \ln {}^S K_a = 0 \tag{8}$$

$^S K_a$ is the equilibrium constant of acid dissociation in the solvent S. Its value can be compared with that in water by writing

$$\frac{{}^S\mu_H^\infty - {}^W\mu_H^\infty}{2.3RT} + \frac{{}^S\mu_A^\infty - {}^W\mu_A^\infty}{2.3RT} - \frac{{}^S\mu_{AH}^\infty - {}^W\mu_{AH}^\infty}{2.3RT}$$
$$- \log {}^W K_a + \log {}^S K_a = 0 \tag{9}$$

For each species, i, an activity coefficient of transfer between water and the medium S can be defined such as

$$\frac{{}^S\mu_H^\infty - {}^W\mu_H^\infty}{2.3RT} = \log \gamma_{t(H^+)}$$
$$\frac{{}^S\mu_A^\infty - {}^W\mu_A^\infty}{2.3RT} = \log \gamma_{t(A^-)} \tag{10}$$
$$\frac{{}^S\mu_{AH}^\infty - {}^W\mu_{AH}^\infty}{2.3RT} = \log \gamma_{t(AH)} = -\log \frac{{}^S C_{sat,}}{{}^W C_{sat,}}$$

The value of the activity coefficient of transfer of AH is related to the molecule solubility in water and in the solvent S, for low free concentration saturated solutions. The following general relation can be then written as

$$^S pK_a = {}^W pK_a - \log \gamma_{t(AH)} + \log \gamma_{t(H^+)}\gamma_{t(A^-)} \tag{11}$$

By introducing the solubility of the molecular species, this leads to

$$^S pK_a = {}^W pK_a + \log \frac{{}^S C_{sat,AH}}{{}^W C_{sat,AH}} + \log \gamma_{t(H^+)}\gamma_{t(A^-)} \tag{12}$$

Table 1
Values of pK_s (from Ref. [26]) and pK_a of several conjugate acid–base pairs at 298 K for various water–bmimBF$_4$ mixtures

% Vol. bmimBF$_4$	0	19.80	38.67	49.48	58.97	77.43
X_{sel}	0	0.0231	0.0569	0.0856	0.1208	0.2470
C_{IL}/mol L^{-1}	0	1.038	2.032	2.573	3.081	4.069
pK_s/±0.1	13.96	13.76	14.21	14.51	14.89	15.87
Ethanoic acid/ethanoate	4.62	4.7	4.75	4.8	5.1	6.45
Pyridinium/pyridine	5.17	5.1	5.15	5.25	5.4	6.1
1-Methylimidazolium/1-methylimidazole	7.00	6.7	6.8	7.05	7.3	7.8
4-Cyanophenol/4-cyanophenolate	8.00	7.7	7.8	8.1	8.5	9.3
NH$_4^+$/NH$_3$	9.17	8.7	8.8	8.9	9.0	9.1
Phenol/phenolate	9.87	9.9	10.05	10.3	10.4	10.9
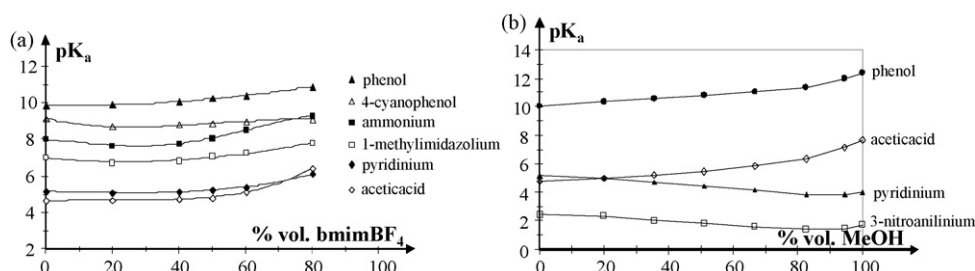
Fig. 4. Comparison of the acidity scales in water–bmimBF$_4$ (a) and water–methanol (b) (from Ref. [30]) mixtures.

By analogy, the following equation would be found for BH$^+$/B

$$^SpK_a = {}^WpK_a + \log \gamma_{t(B)} + \log \frac{\gamma_{t(H^+)}}{\gamma_{t(BH^+)}} \tag{13}$$

and

$$^SpK_a = {}^WpK_a - \log \frac{{}^SC_{sat,B}}{{}^WC_{sat,B}} + \log \frac{\gamma_{t(H^+)}}{\gamma_{t(BH^+)}} \tag{14}$$

For AH/A$^-$ or BH$^+$/B pairs, variations in ^SpK_a with the composition of the mixture are the result of two contributions: one due to the molecular species and the other to the ions. Consider the variation in ^SpK_a for BH$^+$/B as expressed in Eq. (14). The activity coefficient of transfer of ionic species appears in a ratio. Thus, for the smallest additions of organic solvent this ratio can be supposed to be close to the one. This implies that ^SpK_a will vary like the logarithm of the solubility of the molecular species. In the case of organic solvents, the solubility of the organic species increases implying that ^SpK_a will decrease, and the acid then becomes stronger [32]. Gaboriaud and Schaal [33] showed that for water–methanol mixtures variations in ^SpK_a of 3-nitro and 4-nitroaniline follow the variations in their solubility. This property is lost for the most concentrated organic solvent media, the destabilization of the proton being greater than that of BH$^+$. This explains why the ^SpK_a values of conjugate BH$^+$/B pairs in most hydro-organic mixtures (see Fig. 4b) decrease for the first additions of organic solvent to water, then substantially increase as the mixture composition approaches pure organic solvent. In the case of conjugate AH/A$^-$ pairs the variations in ^SpK_a expressed in Eq. (13) include only positive terms, because the term of solubility of AH is positive and the activity coefficients of transfer intervene as a product. As a result, the pK_a of conjugate AH/A$^-$ pairs increases with the organic solvent content even at low organic solvent concentrations.

Concerning water–bmimBF$_4$ mixtures, the situation is different because the properties of water and ionic liquid are not necessarily antagonistic. The saline co-solvent, like water, also stabilizes the ionic species. For molecules, although bmimBF$_4$ has a solubilising capacity much higher than water for gases such as CO$_2$ or hydrocarbons [34], it is not certain that this property applies to all molecular species. This can be assessed by examining the behaviour of pyridine/pyridinium pairs. The ^SpK_a value is almost unaffected

by the addition of ionic liquid. Relation 14 indicates that pyridine is not strongly stabilized by bmimBF$_4$. For 1-methylimidazolium and ammonium, a small decrease in ^SpK_a is observed at low concentrations of ionic liquid, which means that the molecular species are stabilized by the ionic liquid, but the effect is very limited.

When considering the behaviour of conjugate AH/A$^-$ pairs, it is not possible to separate the contributions of ionic species from those of molecular species. It is thus not possible to conclude about the evolution of the activity coefficient of transfer for molecules with the mixture composition of ionic liquid. The trend of the pK_a variation of conjugate acid–base pairs for hydro-organic media can be envisaged by considering the antagonistic properties of water and of the co-solvent but this is not true for water–ionic liquid binaries. No standard behaviour can be established because ionic liquid, like water, stabilizes ionic species and for molecules, the effects seem specific to each molecule.

5. Conclusion

This study shows that the acidity levels of water–bmimBF$_4$ mixtures can be fixed and controlled with precision using proton buffer solutions. These mixtures can thus be used, like reaction media, in a rational way. The behaviour of the conjugate acid–base pairs in these mixtures differs from that observed in hydro-organic mixtures and leads to interesting behaviours in particular with regard to the inversions of acidity. This behaviour was observed and described in detail, in particular for the amino-benzoic and, amino-naphthoic acids [35] in water–methanol mixtures. In water–bmimBF$_4$ mixtures, an inversion of acidity between pyridinium salt and acetic acid is observed and the ^SpK_a of ammonium and acetic acid move substantially towards each other (see Fig. 4a). This raises interesting issues about the behaviour of these compounds in mixtures whose compositions are close to pure ionic liquid and about that of amino acids. This study was limited to a composition of 80% ionic liquid by volume, which corresponds to the operation range of glass electrodes. We believe that the acid–base behaviour of bmimBF$_4$-rich media, near to pure salt will be interesting to explore. 1,3-Dialkylimidazolium salts are very weak acids [36] with an aprotic character. For the richest media in ionic liquid, we can hope to open the acidity scale of water–ionic

    I.B. Malham et al. / Talanta 77 (2008) 48–52

liquid media and to reach pK_a of the weakest acids. This study will require techniques other than potentiometric methods, including, for example, the use of Hammett acidity functions.

References

[1] T. Welton, Chem. Rev. 99 (1999) 2071.
[2] S.A. Forsyth, J.M. Pringle, D.R. MacFarlane, Aust. J. Chem. 57 (2004) 113.
[3] M.C. Buzzeo, R.G. Evans, R.G. Compton, Chem. Phys. Chem. 5 (2004) 1106.
[4] M. Yoshizawa, A. Narita, H. Ohno, Aust. J. Chem. 57 (2004) 139.
[5] R.D. Rogers, Nature 447 (2007) 917.
[6] I. Bou Malham, P. Letellier, A. Mayaffre, M. Turmine, J. Chem. Thermodyn. 39 (2007) 1132.
[7] H. Markusson, J.P. Belieres, P. Johansson, C.A. Angell, P. Jacobsson, J. Phys. Chem. A 111 (2007) 8717.
[8] J.M. Slattery, C. Daguenet, P.J. Dyson, T.J.S. Schubert, I. Krossing, Angew. Chem. Int. Ed. 46 (2007) 5384.
[9] J. Sung, Y. Jeon, D. Kim, T. Iwahashi, T. Iimori, K. Seki, Y. Ouchi, Chem. Phys. Lett. 406 (2005) 495.
[10] L.P.N. Rebelo, V. Najdanovic-Visak, Z.P. Visak, M. Nunes da Ponte, J. Szydlowski, C.A. Cerdeirina, J. Troncoso, L. Romani, J.M.S.S. Esperanca, H.J.R. Guedes, H.C. de Sousa, Green Chem. 6 (2004) 369.
[11] J. Hao, T. Zemb, Curr. Opin. Colloid Interface Sci. 12 (2007) 129.
[12] I. Bou Malham, P. Letellier, M. Turmine, J. Phys. Chem. B 110 (2006) 14212.
[13] J. Bowers, C.P. Butts, P.J. Martin, M.C. Vergara-Guttierrez, R.K. Heenan, Langmuir 20 (2004) 2191.
[14] P. Wasserscheid, T. Welton (Eds.), Ionic Liquids in Synthesis, Wiley-VCH, Weinheim, Germany, 2003.
[15] W.L. Hough, M. Smiglak, H. Rodrıguez, R.P. Swatloski, S.K. Spear, D.T. Daly, J. Pernak, J.E. Grisel, R.D. Carliss, M.D. Soutullo, J.H. Davis Jr., R.D. Rogers, New J. Chem. 31 (2007) 1429.
[16] M.L. Pusey, M.S. Paley, M.B. Turner, R.D. Rogers, Cryst. Growth Des. 7 (2007) 787.
[17] N. Winterton, J. Mater. Chem. 16 (2006) 4281.
[18] N. Gupta, Sonu, G.L. Kad, J. Singh, Catal. Commun. 8 (2007) 1323.
[19] H. Xing, T. Wang, Z. Zhou, Y. Dai, J. Mol. Catal. A 264 (2007) 53.
[20] B.C. Ranu, S. Banerjee, Org. Lett. 7 (2005) 3049.
[21] H. Sun, D. Zhang, F. Wang, C. Liu, J. Phys. Chem. A 111 (2007) 4535.
[22] B.C. Ranu, S. Banerjee, R. Jana, Tetrahedron 63 (2007) 776.
[23] C. Thomazeau, H. Olivier-Bourbigou, L. Magna, S. Luts, B. Gilbert, J. Am. Chem. Soc. 125 (2003) 5265.
[24] N. Benlhima, D. Lemordant, P. Letellier, J. Chim. Phys. 86 (1989) 1919.
[25] G. Senanayake, Miner. Eng. 20 (2007) 634.
[26] I. Bou Malham, P. Letellier, M. Turmine, Talanta 72 (2007) 155.
[27] (a) L.W. Bahe, J. Phys. Chem. 76 (1972) 1062;
(b) L.W. Bahe, J. Phys. Chem. 76 (1972) 1608;
(c) L.W. Bahe, D. Parker, J. Am. Chem. Soc. 97 (1975) 5664;
(d) L.W. Bahe, K.A. Jung, Can. J. Chem. 54 (1976) 824.
[28] L.M. Varela, M. Garcia, F. Sarmiento, D. Attwood, V. Mosquera, J. Chem. Phys. 107 (1997) 6415.
[29] J. Koryta, Principles of Electrochemistry, J. Wiley, New York, 1987.
[30] R. Gaboriaud, Ann. Chim. 2 (1967) 201.
[31] A.J. Parker, Chem. Rev. 69 (1969) 1.
[32] J.C. Halle, F. Terrier, R. Schaal, Bull. Soc. Chim. 4 (1973) 1225.
[33] R. Gaboriaud, R. Schaal, C.R. Acad. Sci. Paris 263 (1966) 353.
[34] G. Honga, J. Jacquemin, M. Deetlefs, C. Hardacre, P. Husson, M.F. Costa Gomes, Fluid Phase Equilib. 257 (2007) 27.
[35] I. Mentre, Ann. Chim. 7 (1972) 333.
[36] Y. Chu, H. Deng, J.P. Cheng, J. Org. Chem. 72 (2007) 7790.

NMR metabolic profiling of organic and aqueous sea bass extracts: Implications in the discrimination of wild and cultured sea bass

L. Mannina[a,b], A.P. Sobolev[b,*], D. Capitani[b], N. Iaffaldano[c], M.P. Rosato[c],
P. Ragni[b], A. Reale[a], E. Sorrentino[a], I. D'Amico[a], R. Coppola[a]

[a] Dipartimento STAAM, Università degli Studi del Molise, Via De Sanctis, 86100 Campobasso, Italy
[b] Istituto di Metodologie Chimiche, CNR, 00016 Monterotondo Staz., Roma, Italy
[c] Dipartimento SAVA, Università degli Studi del Molise, Via De Sanctis, 86100 Campobasso, Italy

ARTICLE INFO

ABSTRACT

The nuclear magnetic resonance (NMR) technique was used as analytical tool to determine the complete metabolic profiling of sea bass extracts: water-soluble metabolites belonging to different classes such as sugars, amino acids, dipeptides and organic acids as well as metabolites soluble in organic solvent such as lipids, sterols and fatty acids were identified. The metabolite profiling together with a suitable statistical analysis were used to discriminate between wild and cultured sea bass samples. Preliminary results show that discrimination between wild and cultured sea bass was obtained not only using fatty acid composition but also cholesterol and phosphatidylethanolamine and some water-soluble metabolites such as choline, trimethylamine oxide, glutamine, fumaric and malic acids.

© 2008 Elsevier B.V. All rights reserved.

1. Introduction

Given the importance of fish as a source of polyunsaturated fatty acids, the major part of metabolic studies on fish has been limited up to now to the analysis of fatty acids composition, almost completely disregarding water-soluble metabolites that are, indeed,

important from the nutritional point of view. Currently there is an increasing requirement for proper analytical methods capable to give a complete picture of fish metabolism and to assess the nutritional quality of the product. These methods should be based on the analysis of a variety of metabolites and not only of a few specific classes of compounds.

As a non-specific high-throughput analytical method, nuclear magnetic resonance (NMR) spectroscopy is well suited to the requirements of metabolic profiling [1,2]. It has been extensively used as analytical tool to analyze metabolites of food either of animal [3] or vegetable origin such as olive oils [4], tomatoes [5], lettuce [6], truffles [7] and coffee [8].

In this paper, we report a detailed study of the NMR spectra of the organic and aqueous extracts of the Sea bass (*Dicentrarchus labrax*), a very popular ocean-going fish with peculiar sensory and nutritional qualities. Due to the increased demand for this fish, in the last decade the aquaculture production has significantly increased and sea bass has become one of the most important commercial fish cultured in Mediterranean area (Greece, Turkey, Italy, Spain, Croatia and Egypt). Therefore, the intensive sea bass production has raised concerns over the quality of cultured fish in comparison with that of wild fish and has given rise to the development of robust analytical tools to distinguish cultured and wild samples [9–12].

The choice of NMR analytical approach for the food analysis depends on the specific problem. Four different approaches can be used: *target analysis*, *metabolic profiling*, *metabolomics* and

metabolic fingerprinting [13]. The *target analysis* is used when one is interested in a specific metabolite: in this case a selective extraction can be performed before the NMR analysis to concentrate the selected metabolite and to avoid interference from other compounds. The *metabolic profiling* is used when you are interested in the specific role of a selected metabolic pathway: it requires the NMR identification and quantification of a selected number of pre-defined metabolites in a given sample. *Metabolomics* requires a complete analysis in which all the metabolites are quantified and identified. Finally, the *metabolic fingerprinting* is used when the sample classification without quantification of individual specific metabolites is required: in this case, the NMR spectrum can be considered as a fingerprint of the product and all the NMR resonances are measured without any identification.

In this study a mixed *metabolic profiling–metabolomics* approach was followed: the ^{1}H spectra of sea bass extracts in aqueous and organic solvents were analyzed, all the NMR signals were assigned using 2D NMR spectra, and finally the intensity of the identified metabolites were measured and submitted to a suitable statistical analysis. Although a complete assignment of the ^{1}H spectra in aqueous and organic solvents was performed, we prefer not to define our analytical approach as *metabolomics* since some metabolites present in extremely low concentrations could be not revealed due to the intrinsic low sensitivity of the NMR technique. The detection limit of a given metabolite, analyzed in a 5 mm tube using one-dimensional ^{1}H NMR spectroscopy at high field (11–16 T), is ~100 μM [1].

Finally, the analytical metabolic profile was used to investigate the potentiality of the NMR methodology to discriminate between wild and cultured sea bass.

2. Materials and methods

2.1. Materials

Four cultured sea bass (average length and weight: 35 ± 3 cm and 600 ± 10 g, respectively) were purchased from a sea bass breeding located in Molise, Italy, whereas three wild sea bass (average length and weight: 46 ± 3 cm and 800 ± 10 g, respectively) were purchased from fishermen in Naples, Tyrrhenian Sea.

The commercial feed (Biomar, Ecolife 66F n. 6.5) used for cultured sea bass contained proteins (42%), fats (26%), carbohydrates (20%), ash (6.1%), fiber (3.0%), methionine and cysteine (1.34%) and total phosphorus (0.90%).

2.2. Sample preparation

Sea bass were killed by immersing in ice-cold water (*hypothermia*), packed into polystyrene containers with ice, and delivered to the laboratory within 90 min after the harvesting. Sea bass were washed with potable water and stored at 2 °C.

Bligh and Dyer [14] method was used to extract and separate water-soluble and liposoluble metabolites. Four portions (each portion ~8 g) of skin and four portions (each portion ~8 g) of muscle were accurately sampled from each fish and put into a ceramic mortar adding 24 mL of a chloroform/methanol (1:1, v/v) mixture. The sample was grinded and homogenized with a ceramic pestle; 8 mL of distilled water was then added. The homogenate was centrifuged at a speed of 4000 rpm for 20 min at 4 °C. The liquid chloroform and water/methanol phases were separated and dried. The lipidic fraction was dissolved in 2 mL of CDCl$_3$; 0.7 mL of solution was placed into a standard 5 mm tube for the NMR measurements. The water-soluble residue was dissolved in 3 mL of D$_2$O; 0.35 mL of the solution was placed into a 5 mm NMR tube adding 0.35 mL of D$_2$O

phosphate buffer (400 mM, p*D* = 6.5). Finally, the NMR tubes were flame-sealed.

2.3. NMR measurements

NMR spectra of sea bass extracts were recorded at 300 K on a Bruker AVANCE AQS600 spectrometer operating at the proton frequency of 600.13 MHz and equipped with a Bruker multinuclear *z*-gradient inverse probehead capable of producing gradients in the *z*-direction with a strength of 55.4 G cm^{-1}. ^{1}H spectra were referenced to DSS (sodium 3-(trimethylsilyl)-1-propanesulfonate) signal (δ = 0.00 ppm) in D$_2$O phosphate buffer and to the CH$_3$ signal (δ = 0.88 ppm) of the oleic fatty chain in CDCl$_3$. ^{13}C spectra were referenced to the CH$_3$ resonance of alanine (δ = 16.8 ppm) in D$_2$O and to the CH$_3$ resonance of the oleic fatty chain (δ = 14.1 ppm) in CDCl$_3$.

The ^{1}H spectrum of the aqueous extract was acquired by co-adding 512 transients with a recycle delay of 3 s and using a 90° flip angle pulse of 15.5 μs, and 32 K data points. The water signal was suppressed using a solvent presaturation (NOESY-presaturation scheme) during the relaxation delay and the mixing time of 160 ms [15].

The ^{1}H spectra of the CDCl$_3$ extracts were acquired by co-adding 16 transients with a recycle delay of 2 s and using a 90° flip angle pulse of 10 μs and 64 K data points.

The ^{13}C spectrum of the CDCl$_3$ extract was acquired by co-adding 7000 transients with a recycle delay of 6 s and using a 60° flip angle pulse of 10 μs and 64 K data points. A standard Bruker pulse sequence with power-gated proton decoupling and composite pulse GARP decoupling sequence was used. The *sn*1,3 and *sn*2 percentages of fatty acids on the glycerol moiety were calculated by means of the integration of the corresponding ^{13}C carbonyl resonances; the sum of all integrals was normalized to 100.

2D NMR experiments, namely ^{1}H–^{1}H COSY, ^{1}H–^{1}H TOCSY, ^{1}H–^{13}C HSQC and ^{1}H–^{13}C HMBC [15], were performed using the same experimental conditions previously reported [7]; the delay for the evolution of long-range couplings in ^{1}H–^{13}C HMBC experiments was 80 ms, the mixing time for the ^{1}H–^{1}H TOCSY was 80 ms. Pulsed field gradient spin echo (PGSE) experiments were performed with a pulsed field gradient unit producing a magnetic field gradient in the *z*-direction with a strength of 55.4 G cm^{-1}. The stimulated echo pulse sequence using bipolar gradients with a longitudinal eddy current delay was used. The strength of the sine-shaped gradient pulse with a duration of 1.4 ms, was logarithmically incremented in 32 steps, from 2% up to 95% of the maximum gradient strength, with a diffusion time of 200 ms and a longitudinal eddy current delay of 25 ms. After Fourier transformation and a baseline correction, the diffusion dimension was processed using the DOSY subroutine of the Bruker Xwinnmr^{TM} software package.

2.4. Measurement of the metabolic content in aqueous extract

The intensity of 19 ^{1}H resonances due to water-soluble assigned metabolites were measured with respect to the intensity of DSS signal (0.2 mM) used as internal standard and normalized to 10. The 19 measured resonances, see Fig. 1, Fig. 2 and the list of abbreviations, are due to ILE (**1**, 1.02 ppm), VAL (**3**, 1.05 ppm), LA (**4**, 1.33 ppm), ALA (**5**, 1.49 ppm), LYS (**6**, 1.74 ppm), GLU (**7**, 2.07 ppm), SA (**9**, 2.41 ppm), GLN (**8**, 2.46 ppm), ASN (**11**, 2.86 ppm), CR/PCR (**12**, 3.04 ppm), CHN (**25**, 3.22 ppm), TMAO (**14**, 3.28 ppm), TAU (**15**, 3.43 ppm), GLY (**16**, 3.57 ppm), GB (**13**, 3.91 ppm), MA (**10**, 4.31 ppm), α-GLC (**20**, 5.24 ppm), FA (**21**, 6.53 ppm), ANS (**23**, 7.22 ppm).
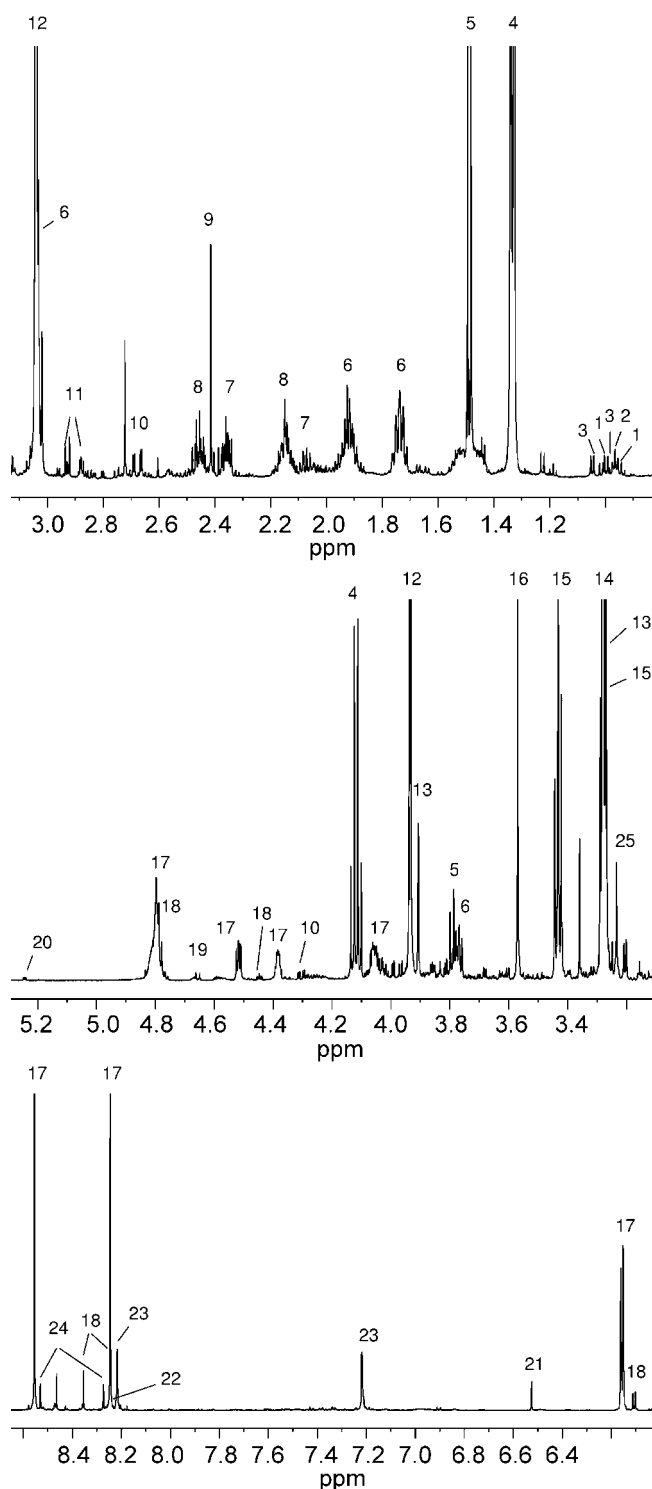
Fig. 1. 600.13 MHz ^{1}H NMR spectrum of a sea bass aqueous extract. The assignment of some peaks is also reported: **1**, ILE; **2**, LEU; **3**, VAL; **4**, LA; **5**, ALA; **6**, LYS; **7**, GLU; **8**, GLN; **9**, SA; **10**, MA; **11**, ASN; **12**, CR/PCR; **13**, GB; **14**, TMAO; **15**, TAU; **16**, GLY; **17**, IMP; **18**, INO; **19**, β-GLC; **20**, α- GLC; **21**, FA; **22**, HYP; **23**, ANS/carnosine; **24**, ATP/ADP; **25**, CHN.

2.5. Measurement of the metabolic content in organic extract

The integrals of 10 ^{1}H resonances due to assigned liposoluble metabolites were measured and used to obtain the normalized integrals, see Fig. 3. The resonances are due to CH$_3$-18 of CHO (**1**,
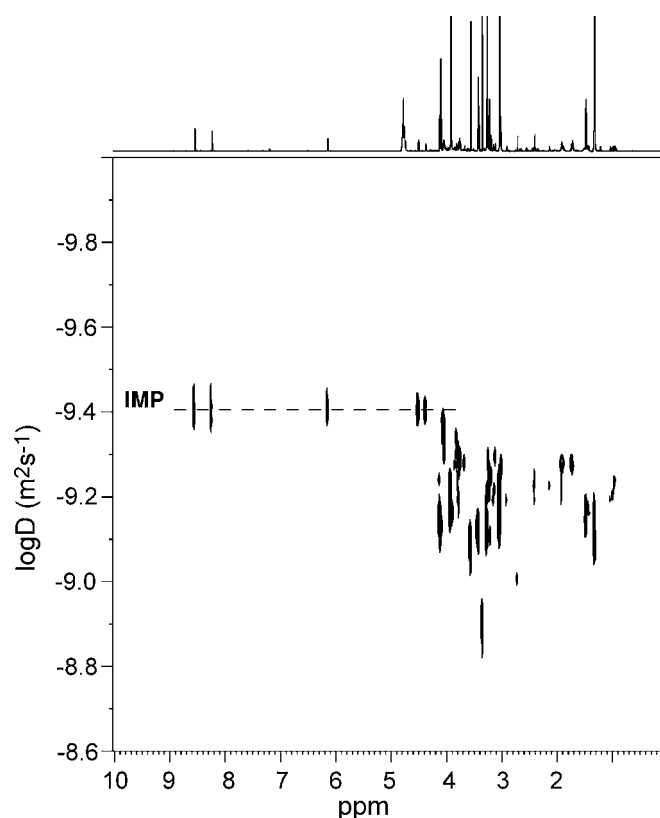
Fig. 2. 2D DOSY map of a sea bass extract in D$_2$O phosphate buffer at 300 K. All signals from a given molecule show the same diffusion coefficient as indicated for the case of IMP. The ^{1}H spectrum of the aqueous extract is also reported as horizontal projection.

0.68 ppm), CH$_3$ of all fatty acids except PUFA (**2**, 0.88 ppm), CH$_3$ of PUFA (**3**, 0.97 ppm), CH$_2$-3 of EPA (**6**, 1.70 ppm), all allylic protons except C3 allylic protons of DHA (**7**, 2.08 ppm), CH$_2$-2 of all fatty acids except DHA (**8**, 2.31 ppm), CH$_2$-2 and CH$_2$-3 of DHA (**9**, 2.38 ppm), CH$_2$ diallylic protons of DUFA, (**10**, 2.77 ppm), CH$_2$N of PC (**14**, 3.76 ppm), *sn*3 CH$_2$ diglycerides of PC + PE (**15**, 3.94 ppm), *sn*1,3 CH$_2$ of glycerol moiety of TG (**16**, 4.15 ppm). The normalized integrals were calculated according to the following equations:

$$nI_X = (I_X/(I_2 + I_3)) \times 10 \text{ if } X = CH_3$$

$$nI_X = (I_X/(I_2 + I_3)) \times 15 \text{ if } X = CH_2$$

$$nI_X = (I_X/(I_2 + I_3)) \times 30 \text{ if } X = CH$$

where nI_X is the normalized integral of the X signal, I_x is the integral of the X signal, $I_2 + I_3$ is the sum of integrals of all fatty acid CH$_3$ signals.

The normalized integrals were used to calculate the normalized integral of other metabolites or class of metabolites:$I_{DHA} =$ nI_9 /(2nI_8 + nI_9); $I_{EPA} =$ nI_6 /(nI_8 + nI_9/2); $I_{PUFA} =$ nI_3/(nI_2 + nI_3); $I_{UFA} =$ (nI_7 + nI_9)/(2nI_8 + nI_9); $I_{STA} = 1 - I_{UFA}$; $I_{DUFA} =$ nI_{10}/(nI_8 + nI_9/2); $I_{MUFA} = I_{UFA} - I_{PUFA} - I_{DUFA}$; $I_{PE} = I_{(PC + PE)} - I_{PC}$.

Four portions of each fish were analyzed separately, the data were averaged and the mean values were used in statistical analysis.

2.6. Statistical analysis

The statistical processing of the NMR data was performed using the STATISTICA package for Windows (version 5.1, 1997). Before per-

Table 1
Summary of the metabolites identified in the 600 MHz ^{1}H spectrum of the aqueous extract of wild and cultured sea bass

Compound	Assignment	^{1}H (ppm)	Multiplicity: J (Hz)	^{13}C (ppm)
Carbohydrates				
β-Glucose (β-GLC) **19**	CH-1	4.66	d: 8.0	96.5
	CH-2	3.26		74.7
	CH-3	3.51		76.3
	CH-4	3.42		70.5
	CH-5	3.48		76.4
	CH$_2$-6,6′	3.73, 3.89		61.3
α-Glucose (α-GLC) **20**	CH-1	5.24*	d: 3.8	92.7
	CH-2	3.54		71.9
	CH-3	3.72		
	CH-4	3.41		70.2
	CH-5	3.84		72.2
	CH$_2$-6,6′	3.77, 3.84		61.1
Organic acids				
Malic acid (MA) **10**	α-CH	4.31*	dd: 10.0; 3.1	70.9
	β,β,-CH$_2$	2.38	dd: 15.4; 10.0	43.2
		2.68	dd: 15.4; 3.1	
Fumaric acid (FA) **21**	α,β-CH=CH	6.53*	s	
Succinic acid (SA) **9**	α,β-CH$_2$	2.41*	s	34.6
	1,4-COOH			181.8
Lactic acid (LA) **4**	α-CH	4.12	q: 6.9	20.7
	β-CH$_3$	1.33*	d: 6.9	69.1
	COOH			183.1
Amino acids and dipetides				
Valine (VAL) **3**	α-CH	3.61		61.0
	β-CH	2.28	m	20.7
	γ-CH$_3$	1.00	d: 7.0	17.3
	γ′-CH$_3$	1.05*	d: 7.0	18.5
	COOH			175.0
Leucine (LEU) **2**	α-CH	3.73		54.1
	β-CH$_2$	1.72	m	40.2
	γ-CH	1.73	m	24.5
	δ-CH$_3$	0.97	d: 6.2	22.6
	δ′-CH$_3$	0.96	d: 6.1	21.6
Lysine (LYS) **6**	α-CH	3.77	m	55.0
	β-CH$_2$	1.92	m	30.4
	γ-CH$_2$	1.49	m	21.9
	δ-CH$_2$	1.74*	m	26.9
	ε-CH$_2$	3.03	t: 7.6	39.6
	COOH			175.4
Alanine (ALA) **5**	α-CH	3.79		51.2
	β-CH$_3$	1.49*	d: 7.3	16.8
	COOH			176.4
Asparagine (ASN) **11**	α-CH	4.01		
	β,β′-CH$_2$	2.86*	dd: 17.0; 7.6	
		2.95	dd: 17.0; 4.3	
Isoleucine (ILE) **1**	α-CH	3.68		60.2
	β-CH	1.98		36.4
	γ-CH$_3$	1.02*	d: 7.1	15.3
	γ-CH$_2$	1.26, 1.47		25.2
	δ-CH$_3$	0.94	t: 7.5	10.2
	COOH			
Glutamate (GLU) **7**	α-CH	3.77	m	55.1
	β,β′-CH$_2$	2.07*, 2.14	m	27.6
	γ-CH$_2$	2.36	m	34.1
	δ-CO			181.8
	COOH			175.1
Glutamine (GLN) **8**	α-CH	3.77		55.1
	β,β′-CH$_2$	2.15	m	26.8
	γ-CH$_2$	2.46*	m	31.5
	δ-CO(NH$_2$)			178.3
	COOH			174.6

Table 1(*Continued* **)**

Compound	Assignment	^{1}H (ppm)	Multiplicity: J (Hz)	^{13}C (ppm)
Glycine (GLY) **16**	α-CH$_2$	3.57*	s	42.1
	COOH			173.0
Creatine/phosphocreatine (CR)/(PCR) **12**	N–CH$_2$	3.95	s	54.4
	N–CH$_3$	3.04*	s	37.6
	N=C			
N(α)-(β-Alanyl)-L-1-methylhistidine (ANS) or N(α)-(β-alanyl)-L-1-histidine **23**	α-CH$_2$ (β-Ala)			
	β-CH$_2$ (β-Ala)			
	α-CH (His)	4.51		53.6
	β-CH$_2$ (His)	3.07; 3.26		
	4-CH (His)	7.22*		120.2
	2-CH (His)	8.22	d: 1.1	136.1
Osmolytes and nucleoside derivatives				
TMAO **14**	N–CH$_3$	3.28*	s	60.1
Glycine-betaine (GB) **13**	N–CH$_3$	3.27	s	54.0
	α-CH$_2$	3.91*	s	66.7
	COOH			170.0
Taurine (TAU) **15**	S–CH$_2$	3.28	t: 6.7	48.0
	N–CH$_2$	3.43*	t: 6.7	35.9
Inosine 5'-phosphate (IMP) **17**	CH-1', ribose	6.16	d: 5.7	88.0
	CH-2' ribose	4.80	m	75.2
	CH-3' ribose	4.52	dd: 3.8;5.0	71.2
	CH-4'ribose	4.38	m	85.3
	CH-5' ribose	4.05	m	64.3
	CH-2, ring	8.55	s	140.6
	C4, ring			149.6
	C5, ring			124.3
	CH-8, ring	8.25	s	
Inosine (INO) **18**	CH-1', ribose	6.11	d: 5.7	88.9
	CH-2', ribose	4.77	m	74.8
	CH-3', ribose	4.45	dd: 4.0; 5.1	70.9
	CH-4', ribose	4.28	m	86.2
	CH-5', ribose	3.87	m	71.8
	CH$_2$, ring	8.36	s	140.9
	C4, ring			149.0
	C5, ring			125.1
	C6, ring			159.1
	CH-8, ring	8.25	s	146.8
Hypoxanthine (HYP) **22**	CH-8	8.21	s	146.2
	CH-2	8.23	s	
Adenosine triphosphate (ATP)/adenosine diphosphate (ADP) **24**	CH-8	8.27	s	
	CH-2	8.53	s	
Choline (CHN) **25**	N–CH$_3$	3.22*	s	54.7

Abbreviations and identification numbering are reported. Signals selected for the statistical analysis are denoted by asterisk, see Section 2.4.

forming the statistical analysis all 29 selected variables, namely, 19 variables of the aqueous extracts and the 10 variables of the organic extracts, were mean-centred and each variable was divided by its standard deviation (autoscaling). Principal component analysis (PCA) was performed on the 29 variables: the percentage of variance for each specific principal component is reported. PCA results are shown reporting the scores of the principal components and also as a plot of the variable loadings. In the analysis of the variance (ANOVA) the variables with the highest index of variability were selected according to their p-level and F values. The p-level represents decreasing index of the reliability of a result and gives the probability of error involved in accepting a result as valid. A p-level of 0.05 (5% probability of error) is usually treated as a borderline acceptable error level. The F value is the ratio between groups' variability to within-group variability: the larger is this ratio, the larger is the discrimination power of the corresponding variable.

3. Results and discussion

3.1. NMR metabolic profiling

The NMR characterization of the sea bass extracts in aqueous solution and in organic solvent will be discussed separately. The assignments of ^{1}H and ^{13}C NMR spectra were obtained using standard two-dimensional experiments such as ^{1}H–^{1}H COSY, ^{1}H–^{1}H TOCSY, ^{1}H–^{13}C HSQC, ^{1}H–^{13}C HMBC and the literature data [1].

3.1.1. NMR analysis of aqueous extracts

Metabolites soluble in water are important nutrients responsible also for specific taste of the fish. The ^{1}H NMR spectrum of the aqueous extract and the corresponding assignment are reported in Fig. 1 and Table 1, respectively. Many signals due to different compounds are present. In order to assign this mixture a diffusion ordered NMR spectroscopy (DOSY) experiment together with
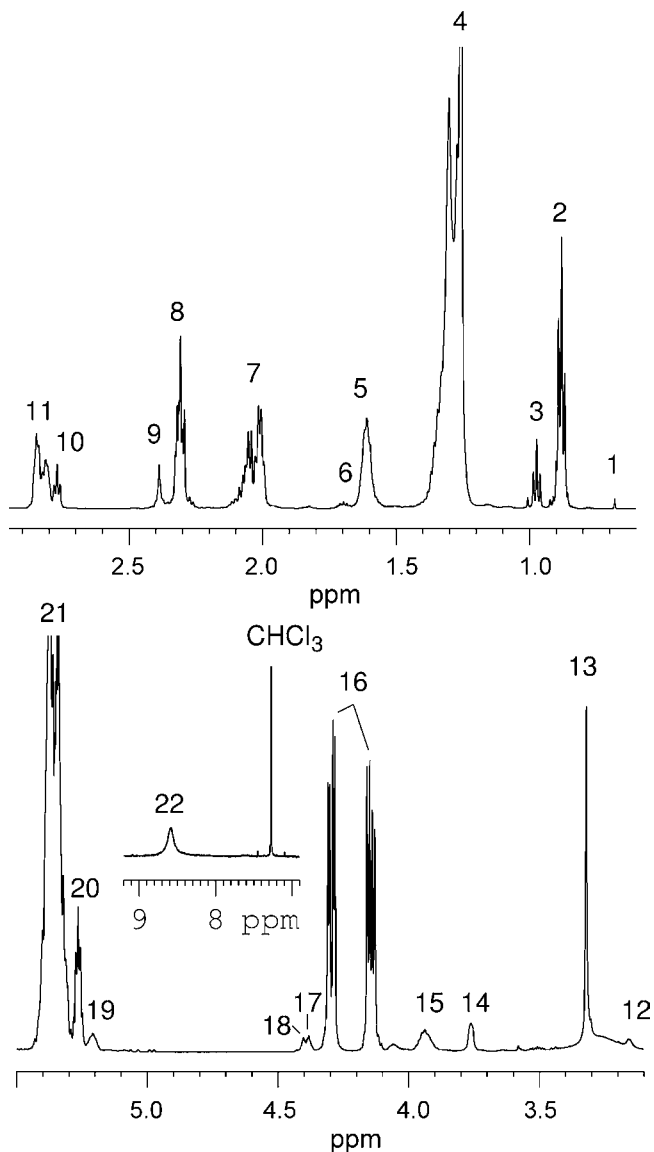
Fig. 3. 600.13 MHz ^{1}H NMR spectrum of a sea bass organic extract. The assignment of some peaks is also reported: **1**,CH$_3$-18 of CHO; 2, CH$_3$ of STA, MUFA and DUFA; **3**, CH$_3$ of PUFA; **4**, CH$_2$ of all fatty chains; **5**, CH$_2$-3 of all fatty chains except DHA and EPA; **6**, CH$_2$-3 of EPA; **7**, CH$_2$ allylic protons of all fatty chains except DHA; **8**, CH$_2$-2 of all fatty chains except DHA; **9**, CH$_2$-2 and 3 of DHA; **10**, CH$_2$, diallylic of DUFA; **11**, CH$_2$ of PUFA; **12**, CH$_2$N of PE; **13**, (CH$_3$)$_3$N of PC; **14**, CH$_2$N of PC; **15**, *sn*3 CH$_2$ diglycerides of PE and PC; **16**, *sn*1,3 CH$_2$ of TG; **17**, *sn*1 CH$_2$ diacylglycerols of PE and PC; **18**, CH$_2$OP of PC; **19**, *sn*2 CH diacylglycerols of PE and PC; **20**, *sn*2 CH$_2$ of TG; **21**, CH=CH of fatty chains; **22**, NH$_2$ of PE.

the standard two-dimensional experiments were preformed [16]. DOSY is a particular convenient way of displaying the molecular self-diffusion information in a bi-dimensional array, with the NMR spectrum in one dimension and the self-diffusion coefficient in the other one. DOSY has been successfully used for the analysis of mixtures [17], for the study of intermolecular interactions [18,19], for the characterization of aggregates [20], for the molecular weight determination of uncharged polysaccharides [21]. Here, we report the DOSY map of the aqueous extract (Fig. 2). As expected for a mixture, also in the case of aqueous extract, many signals with different diffusion coefficients and therefore with different molecular weights are present due to different metabolites; on the other hand, signals from the same molecule show the same diffusion coefficient, as it is shown in Fig. 2 for the case of IMP.

Using DOSY information and 2D experiments a full assignment of the spectra was obtained, see Fig. 1 and Table 1.

3.1.1.1. Sugars. A small amount of glucose was present in the sea bass aqueous extract. It was identified by means of the diagnostic anomeric doublets at 4.66 ppm (β-form) and 5.24 ppm (α-form) and by 2D experiments.

3.1.1.2. Free amino acids and dipeptides. The elevated content of proteins in fish [22] contributes to the total high nutritional value of fish based products. The ^{1}H spectrum of the aqueous extract allowed the free amino acid composition to be obtained: at least eight amino acids, namely, VAL, LEU, LYS, ALA, ILE, GLU, GLN and GLY were detected and assigned using 2D experiments and literature data.

Creatine (CR) or/and phosphocreatine (PCR), important energy sources, were also identified by means of characteristic singlets at 3.04 and 3.94 ppm, whereas the presence of taurine (TAU), a conditionally essential amino acid with many metabolic actions [23,24] was indicated by the resonances at 3.28 and 3.43 ppm.

Characteristic ^{1}H signals at 7.22 and 8.22 ppm can be ascribed to N(α)-(β-alanyl)-L-1-methylhistidine (anserine, ANS) or N(α)-(β-alanyl)-L-1-histidine (carnosine), dipeptides, which differ for the presence of a N–Me group in the imidazole ring of histidine. The ^{1}H chemical shift reported in literature for N–Me of ANS [25] is 3.75 ppm. In the specific case of the sea bass ^{1}H spectrum, due to the strong signal overlapping between 3 and 4 ppm, it was impossible to establish whether the signal at 3.75 ppm was present or not, and therefore to assign the signals at 7.22 and 8.22 ppm unambiguously.

3.1.1.3. Organic acids. Some organic acids such as MA, FA, SA and LA were also identified in the ^{1}H spectrum.

3.1.1.4. Nucleoside derivatives and osmolytes. Trimethylamine-N-oxide (TMAO) plays an important role in the osmotic regulation of body fluids [26]. TMAO was identified in the ^{1}H spectrum by the singlet at 3.28 ppm due to methyl group. The presence of TMAO in the extract suggested a good preservation state: in fact, during the
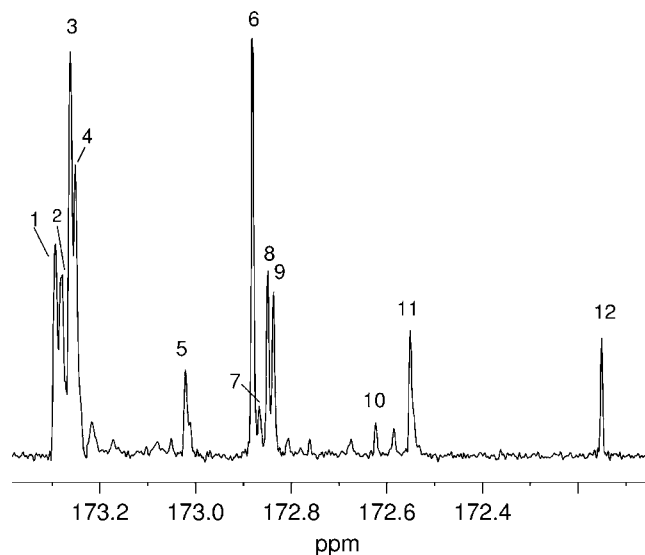
Fig. 4. 150 MHz, ^{13}C NMR spectrum of the sea bass muscle organic extract (carboxyl spectral region). Labeled peaks assignments: **1**, *sn*1,3-saturated chains; **2**, *sn*1,3 −18:1 Δ^{11} and *sn*1,3 −20:1 Δ^{11}; **3**, *sn*1,3 −18:1Δ^9 and *sn*1,3 −16:1Δ^9; **4**, *sn*1,3 −18:2Δ^{9,12} (linoleic fatty chain); **5**, *sn*1,3 −20:5 Δ^{5,8,11,14,17} (EPA); **6**, *sn*2-saturated chains; **7**, *sn*2 −18:1Δ^{11} and *sn*2 −20:1Δ^{11}; **8**, *sn*2 −18:1Δ^9 and *sn*2 −16:1 Δ^9; **9**, *sn*2 −18:2 Δ^{9,12}; **10**, *sn*2 −20:5 Δ^{5,8,11,14,17} (EPA); **11**, *sn*1,3 −22:6Δ^{4,7,10,13,16,19} (DHA);**12**, *sn*2 −22:6 Δ^{4,7,10,13,16,19} (DHA).

Table 2
Summary of the metabolites identified in the 600 MHz ^{1}H spectrum of the CDCl$_3$ extract of wild and cultured sea bass

Compound	Assignment	^{1}H (ppm)	Multiplicity: J (Hz)	^{13}C (ppm)[a]
Sterols				
Cholesterol (CHO)	CH$_2$-1	1.86; 1.10		37.30
	CH$_2$-2	1.85; 1.52		31.69
	CH-3	3.52		71.79
	CH$_2$-4	2.31; 2.26		42.35
	C-5			140.82
	C-6	5.36		121.70
	CH$_2$-7	2.00		31.94
	CH-8			
	CH-9	0.95		50.19
	C-10			36.54
	CH$_2$-11	1.51		21.12
	CH$_2$-12	2.02; 1.97		39.83
	C-13			
	CH-14	1.01		56.81
	CH$_2$-15			24.32
	CH$_2$-16			28.25
	CH-17	1.11		56.20
	CH$_3$-18 **1**	0.68	s	11.88
	CH$_3$-19	1.01		19.41
	CH-20			35.81
	CH$_3$-21	0.92		18.74
	CH$_2$-22			36.22
	CH$_2$-23			23.86
	CH$_2$-24			39.55
	CH-25	1.53		28.03
	CH$_3$-26	0.88		22.83; 22.60
Lipids: triglycerides				
Triacylglycerols (TG)	CH *sn*2 **20**	5.26	m	69.0
	CH$_2$ *sn*1,3 **16**	4.30	dd: 11.9; 4.2	62.1
		4.15	dd: 11.9; 6.0	
Lipids: diacylglycerophospholipids				
Phosphatidylcholine (PC)	CH *sn*2 **19**	5.21		70.4
	CH$_2$ *sn*1 **17**	4.38; 4.13		62.9
	CH$_2$ *sn*3 **15**	3.94		63.7
	CH$_2$OP **18**	4.40		59.5
	CH$_2$N **14**	3.76		66.3
	N(CH$_3$)$_3$	3.32	s	54.5
Phosphatidylethanolamine (PE)	CH *sn*2 **19**	5.21		70.4
	CH$_2$ *sn*1 **17**	4.38; 4.13		62.9
	CH$_2$ *sn*3 **15**	3.94		63.9
	CH$_2$OP	4.11		62.9
	CH$_2$N	3.16		40.6
	NH$_2$ **22**	8.55		
Lipids: fatty acid chains				
Saturated fatty chains (STA)	COO (*sn*1,3)			173.29
	COO (*sn*2)			172.88
	CH$_2$-2 (*sn*1,3) **8**	2.31	t: 7.8	34.06
	CH$_2$-2 (*sn*2) **8**	2.31	t: 7.8	34.23
	CH$_2$-3	1.61	m	24.8
	C H$_2$	1.28–1.30	m	28.9–29.7
	CH$_2$-n3	1.26	m	31.9
	CH$_2$-n2	1.30	m	22.7
	CH$_3$-n1 **2**	0.88	t: 7.2	14.12
cis-Monounsaturated fatty chains C18:1 Δ^{11}, C20:1 Δ^{11} (MUFA)	COO (*sn*1,3)			173.28
	COO (*sn*2)			172.87
	CH$_2$-2 (*sn*1,3) **8**	2.31		34.06
	CH$_2$-2 (*sn*2) **8**	2.31		34.23
	CH$_2$-3	1.61		24.8
	CH$_2$-4–9	1.33	m	29.7–30.2
	CH$_2$-10	2.01	m	27.2
	CH$_2$-11,12 **21**	5.35		129.7
	CH$_2$-13	2.01	m	27.2
	CH$_2$-14–15 (14–17)[b]	1.30	m	29.7–30.2
	CH$_2$-16 (18)[b]	1.26	m	31.9
	CH$_2$-17 (19)[b]	1.30	m	22.7
	CH$_3$-18 (20)[b] **2**	0.88	t: 7.2	14.12
cis-Monounsaturated fatty chains C16:1 Δ^9, C18:1 Δ^9 (MUFA)	COO (*sn*1,3)			173.26
	COO (*sn*2)			172.85

Table 2 (*Continued***)**

Compound	Assignment	^{1}H (ppm)	Multiplicity: J (Hz)	^{13}C (ppm)[a]
	CH$_2$-2 (*sn*1,3) **8**	2.31		34.06
	CH$_2$-2 (*sn*2) **8**	2.31		34.23
	CH$_2$-3	1.61		24.8
	CH$_2$-4–7	1.33	m	29.7–30.2
	CH$_2$-8	2.01	m	27.2
	CH$_2$-9,10 **21**	5.35		129.7
	CH$_2$-11	2.01	m	27.2
	CH$_2$-12–15 (12–13)[c]	1.30	m	29.7–30.2
	CH$_2$-16 (14)[c]	1.26	m	31.9
	CH$_2$-17 (15)[c]	1.30	m	22.7
	CH$_3$-18 (16)[c] **2**	0.88	t: 7.2	14.12
Linoleic fatty chain C18:2 $\Delta^{9,12}$ (DUFA)	COO (*sn*1,3)			173.25
	COO (*sn*2)			172.84
	CH$_2$-2 **8**	2.31		34.1–34.2
	CH$_2$-3	1.61		24.8
	CH$_2$-4–7	1.29–1.31		29.0–29.8
	CH$_2$-8,14	2.01–2.05	q: 7.0	27.2
	CH-9,13 **21**	5.35	m	130.2
	CH-10,12 **21**	5.35	m	127.8
	CH$_2$-11 **10**	2.77	t: 6.7	25.6
	CH$_2$-15	1.30	m	29.6
	CH$_2$-16	1.30	m	31.9
	CH$_2$-17	1.31	m	22.7
	CH$_3$-18 **2**	0.88	t: 7.2	14.08
Linolenic fatty chain C18:3 $\Delta^{9,12,15}$	COO (*sn*1,3)			173.24
	CH$_2$-2 **8**	2.31		34.1–34.2
	CH$_2$-3	1.61		24.8
	CH$_2$-4–7	1.29–1.31		29.0–29.8
	CH$_2$-8	2.05		27.2
	CH-9 **21**	5.35		130.27
	CH-10 **21**	5.35		127.8
	CH-13,12 **21**	5.35		128.2
	CH$_2$-11,14	2.81	t: 6.0	25.6
	CH-15	5.32		127.14
	CH-16	5.39		131.97
	CH$_2$-17	2.08		20.57
	CH$_3$-18 **3**	0.97	t: 7.5	14.29
Docosahexaenoic fatty acid chain C22:6 $\Delta^{4,7,10,13,16,19}$ (DHA)	COO (*sn*2)			172.15
	COO (*sn*1,3)			172.55
	CH$_2$-2 (*sn*2)	2.38		34.05
	CH$_2$-2 (*sn*1,3) **9**	2.38		33.90
	CH$_2$-3 **9**	2.38		22.6
	CH-4 (*sn*2) **21**	5.35		129.48
	CH-4 (*sn*1,3) **21**	5.35		129.50
	CH-5 (*sn*2) **21**	5.35		127.66
	CH-5 (*sn*1,3) **21**	5.35		127.68
	CH$_2$-6,9,12,15,18	2.85–2.81		25.6–25.4
	CH-19	5.31		127.04
	CH-20	5.31		132.04
	CH$_2$-21 **7**	2.08		20.58
	CH$_3$-22	0.97	t: 7.5	14.28
Eicosapentaenoic fatty acid chain C20:5 $\Delta^{5,8,11,14,17}$ (EPA)	COO (*sn*2)			172.62
	COO (*sn*1,3)			173.02
	CH$_2$-2 (*sn*2) **8**	2.31		33.61
	CH$_2$-2 (*sn*1,3)			33.42
	CH$_2$-3 **6**	1.70		24.80
	CH$_2$-4 (*sn*2)	2.11		26.51
	CH$_2$-4 (*sn*1,3)			26.53
	CH-5 **21**	5.35		128.99
	CH-6 **21**	5.35		128.81
	CH$_2$-7,10,13,16	2.85–2.81		25.6–25.4
	CH-17	5.31		127.04
	CH-18	5.31		132.04
	CH$_2$-19	2.08		20.58
	CH$_3$-20	0.97	t: 7.5	14.28
Docosapentaenoic fatty acid chain C22:6 $\Delta^{7,10,13,16,19}$ (DPA)	CH$_2$-6	2.01		27.06
Stearidonic fatty acid chain C18:4 $\Delta^{6,9,12,15}$	CH$_2$-5	2.01		26.93

Signals used to measure the integrals are labeled using the corresponding numbering as reported in Section 2.5.

[a] The chemical shifts reported with two decimal digits were measured from 1D spectra, while those reported with one decimal digit were taken from less resolved 2D experiments.

[b] In the case of C20:1 Δ^{11}.

[c] In the case of C16:1 Δ^9.

storage TMAO is degraded to the volatile trimethyl ammine (TMA) responsible for the unpleasant fish odor.

Glycine-betaine (GB), an important osmoprotectant, was also identified in the ^{1}H spectrum.

The ^{1}H spectrum shows the diagnostic singlets of hypoxanthine (HYP) at 8.21 and 8.23 ppm, inosine (INO) at 8.36 and 8.25 ppm, inosine 5′-phosphate (IMP) at 8.55 and 8.25 ppm. These purine derivatives are formed during the adenosine triphosphate (ATP) degradation according to the sequence: ATP → adenosine diphosphate (ADP) → adenosine 5′-phosphate (AMP) → IMP → inosine (INO) → hypoxanthine (HYP) → xanthine → uric acid. These metabolites have been used for an estimation of the fish freshness [27] and have been measured by NMR technique in sea bass samples submitted to modified atmosphere and γ-irradiations [28].

3.1.2. NMR analysis of chloroform extracts

The ^{1}H and ^{13}C NMR spectra of a sea bass chloroform extract are shown in Fig. 4Figs. 3 and 4. The assignment of ^{1}H and ^{13}C NMR spectra was obtained using two-dimensional experiments and the literature data [29–31].

3.1.2.1. Triacylglycerols and diacylglycerophospholipids.
The presence of triacylglycerols (TG) as the major components of the organic fraction is indicated by the strong ^{1}H signals at 4.30 and 4.15 ppm and at 5.28 ppm of the glycerol moiety.

Different diacylglycerophospholipids were present in the organic extract: in particular, phosphatidylcholine (PC) and phosphatidylethanolamine (PE) can be distinguished by means of the ^{1}H resonances of their head group or tail. PC can be easily identified by the characteristic singlet at 3.32 ppm due to the $N^+(CH_3)_3$ group, whereas PE can be identified by the characteristic resonance at 3.16 ppm due to NCH_2 group [7].

3.1.2.2. Fatty acids.
The ^{1}H spectrum of the organic extract shows the presence of fatty acids easily assigned by means of 2D spectra and literature data [4]. Fatty acid composition of fish lipids depends on various factors: species, diet, season, part and tissue of the body etc. The sea bass organic extract contains a high amount of polyunsaturated fatty acids (PUFA) very important for human diet and disease prevention [32–34]. In particular, eicosapentaenoic acid (EPA, $20:5n-3$) is shown to be beneficial in coronary heart disease and inflammatory pathologies, whereas docosahexaenoic acid (DHA, $22:6n-3$) has fundamental role for the development of neural tissue in infants and for the maintenance of the brain functions in adults.

It has been also reported [35,36] that ^{13}C NMR spectroscopy can be useful to characterize fatty acid chains; in fact, the ^{13}C NMR spectrum gives information not only about the fatty acids composition but also about the positional distribution of fatty acid chains in the glycerol moiety of triacylglycerols usually assessed using an enzymatic cumbersome and inaccurate method.

In particular, the ^{13}C resonances of fatty acid carboxylic groups are usually well resolved, see Fig. 4, and can be used for a qualitative and quantitative analysis of fatty acid chains and for the determination of the fatty acid acyl positional distribution in the glycerol moiety: in fact, the ^{13}C carboxyl resonances of fatty acids esterified in $sn1,3$ positions are downfield shifted (ca 0.4 ppm) with respect to the corresponding resonances of fatty acids esterified in the $sn2$ position. The assignment, reported in Table 2, was confirmed by 2D experiments and literature data: saturated, *cis*-11-monounsaturated, *cis*-9-monounsaturated, diunsaturated, and polyunsaturated fatty acids (EPA, DHA and linolenic fatty acid) were identified and their content in the $sn1,3$ and $sn2$ positions together

Table 3
Fatty acid content and positional distribution in the glycerol moiety of triacylglycerols obtained from ^{13}C spectrum of cultured sea bass muscle extract

Fatty acid chain	Content (%)		$sn1,3$:$sn2$ ratio
	$sn1,3$	$sn2$	
Saturated fatty acids (STA)	9.3	13.3	0.7
cis-11-Monounsaturated fatty acids.	12.9	2.8	4.5
cis-9-Monounsaturated fatty acids	18.3	5.8	3.1
Diunsaturated fatty acids (DUFA)	12.8	5.7	2.2
EPA	4.8	1.4	3.4
DHA	6.3	3.6	1.7
Linolenic acid	3.0	n.d.	n.d.

n.d. = not detectable.

with the $sn1,3$/$sn2$ ratio are reported in Table 3. Fatty acid distribution in vegetal and animal triacylglycerols is of crucial importance from a nutritional point of view; in fact, when fish is assumed by animals and humans, during digestive processes, triacylglycerols are transformed into 2-monoacyl-*sn*-glycerols successively absorbed by the intestines and utilized as such [37]. Different fish species can have different fatty acid distribution. Our results show that the acyl positional distribution of sea bass muscle samples is notably different from those reported for Atlantic tune and Atlantic salmon [38,39].

In the case of sea bass extract, saturated fatty chains (STA) are preferentially distributed in $sn2$ position, whereas for Atlantic tune and Atlantic salmon a random distribution is reported. DUFA, EPA and DHA fatty acids of sea bass lipids are distributed preferentially in $sn1,3$ positions, whereas for Atlantic salmon and Atlantic tune a preferential distribution in position $sn2$ is reported [38,39]. Finally, monounsaturated fatty acids (MUFA) are distributed preferentially in $sn1,3$ positions, in agreement with the distribution obtained in Atlantic tune and Atlantic salmon [38,39].

3.1.2.3. Sterols.
It is possible to obtain information about the sterolic composition by observing the ^{1}H resonance of the CH_3-18 in the 0.6–0.7 ppm spectral region [40]. In the case of the sea bass organic extract, the ^{1}H spectrum shows a characteristic resonance at 0.68 ppm, see Fig. 3, due to the CH_3-18 of cholesterol (CHO); the assignment was verified by 2D experiment and reported in Table 2.

3.2. Wild and cultured sea bass discrimination: preliminary results

The NMR analytical profile reported above was used to test the potentiality of the NMR methodology to compare the chemical composition of wild and cultured sea bass. Therefore, a preliminary study was carried out on four cultures sea bass and three wild sea bass. Although usually muscle samples have been used to perform analyses, we chose to analyze also skin samples to detect possible differences in the chemical composition of sea bass skin and muscle.

Water-soluble and liposoluble metabolites of cultured (C) and wild (W) sea bass extracted from skin (s) and muscle (m) were analyzed by ^{1}H NMR: in particular, the intensity of the signals corresponding to 29 metabolites or class of metabolites (column 1 in Table 4) were measured and submitted both to principal components analysis to analyze the multivariate structure of the data set and to ANOVA analyses (Table 4) to select the most discriminant variables between cultured and wild sea bass samples.

Fig. 5A shows a PCA plot of sample scores (PC1 versus PC2). These first two PCs account for the 70.3% of the variability within the data. PC1 provides mostly the discrimination between cultured and

Table 4
ANOVA applied to 29 metabolites to discriminate between cultured and wild sea bass samples

	F (fisher)	p-level
ANS	0.0006	0.9805
FA	**13.3090**	**0.0033**
α-GLC	0.6148	0.4482
MA	**12.5691**	**0.0040**
GB	0.8664	0.3703
GLY	4.4542	0.0565
TAU	2.2111	0.1628
TMAO	**59.3023**	**5.54E−06**
CHN	**12.7507**	**0.0038**
CR/PCR	0.7020	0.4185
ASN	1.3786	0.2631
GLN	**7.7089**	**0.0168**
SA	4.1880	0.0633
GLU	0.5888	0.4577
LYS	2.2329	0.1609
ALA	1.4561	0.2508
LA	1.9404	0.1889
VAL	3.9345	0.0707
ILE	1.4830	0.2467
CHO	**6.0802**	**0.0297**
PC	4.1521	0.0643
TG	**9.5390**	**0.0094**
DHA	**55.9547**	**7.43E−06**
EPA	**65.6672**	**3.3E−06**
PUFA	**21.1836**	**0.0006**
STA	1.1580	0.3030
DUFA	**157.4345**	**2.94E−08**
MUFA	**5.9335**	**0.0314**
PE	**4.8627**	**0.0477**

Variables with p-level lower than 0.05 are reported in bold type.

Fig. 5. (A) PCA performed on 29 metabolites measured in three wild (W_1, W_2, W_3) and four cultured (C_4, C_5, C_6, C_7) sea bass. Four portions of each fish were analyzed separately and averaged. Muscle samples were labeled as "m" whereas skin samples as "s". (●) Wild, (▲) cultured fish. (B) PCA plot of loadings.

wild sea bass samples, whereas PC2 is mostly responsible for the discrimination between muscle and skin samples, especially in the case of cultured samples.

Variables with the highest contribution to PC1 are responsible for wild and cultured samples separation and can be selected using the plot of loadings reported on Fig. 5B. The following variables were selected: DUFA, TG, CHN, MA, FA and GLN with loadings lying on the left side of PC1 axis and DHA, EPA, TMAO, PUFA, MUFA, CHO, PE and PC with loadings lying on the right side of PC1 axis. The mean values and standard errors of these variables are reported in Fig. 6. It is worth noting that DUFA, TG, CHN, MA, FA and GLN are more abundant in cultured samples (grey bars), whereas the levels of DHA, EPA, TMAO, PUFA, MUFA, CHO, PE and PC are higher in wild samples (white bars).

To verify the significance of the observed differences in the content of water-soluble and liposoluble metabolites between wild and cultured sea bass samples, an ANOVA analysis was performed (Table 4). Assuming that the borderline acceptable error for a significant difference between two group means (p-level) should be less than 5%, the level of the following 13 metabolites was significantly different in wild and cultured sea bass: DUFA, TG, CHN, MA, FA, GLN, DHA, EPA, TMAO, PUFA, MUFA, CHO and PE. This result confirms the observations obtained using PCA.

The content of DUFA in cultured samples is about six times as high as that in wild fish and can be attributed to the dietary of cultured fish. This result, in agreement with literature data [9,10,11], confirms that commercial aquafeed, containing terrestrial-derived raw materials with a lipid content of 20% and only a small amount of marine products, causes an accumulation of DUFA. Moreover, due to their terrestrial dietary, cultured fish are poor in PUFA, DHA and EPA fatty acids which, in turn, are more abundant in wild fish due to the marine dietary.
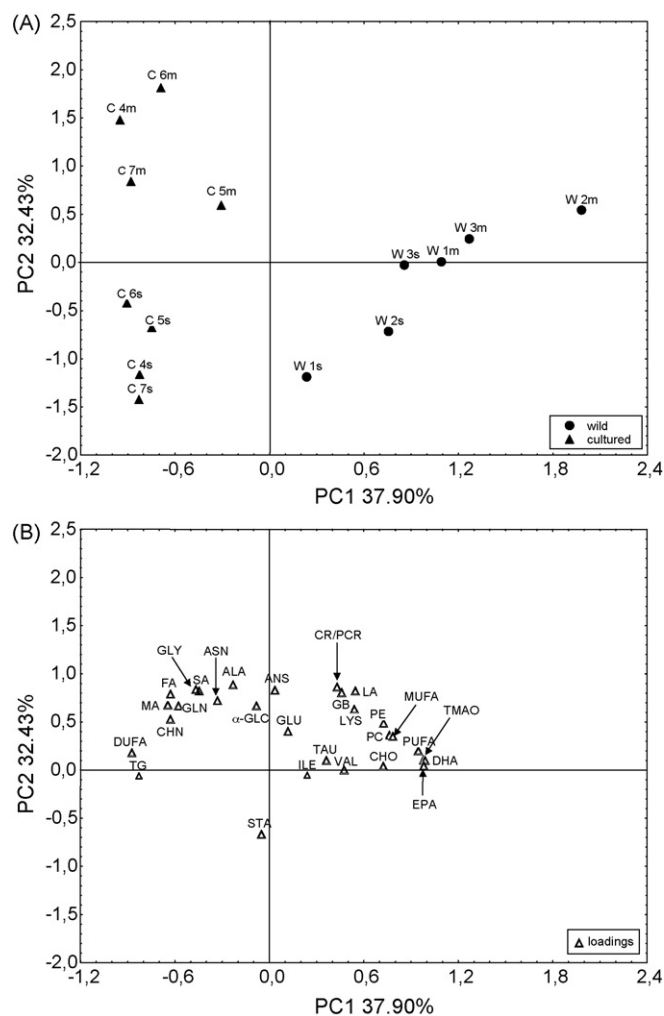
Among the water-soluble metabolites CHN, FA, MA, GLN are more abundant in cultured fish respect to wild ones, especially in muscle tissues. The higher level of FA and MA, components of Krebs cycle, could be due to a different level of energy metabolism in cultured fish with respect to wild ones. The accumulation of GLN in cultured fish is probably correlated to the higher level of FA and MA since GLN and GLU anabolism is closely related to Krebs cycle activity. Moreover, high level of GLN, marketed as supplement for muscle growth, gives an additional dietary value to cultured fish [41].

The level of CHN (choline) in cultured samples is about two times as high as that in wild ones. Again this result gives an additional value to the cultured samples since CHN as a precursor of acetylcholine and methyl donor in various metabolic processes is considered an essential nutrient for human diet.

The comparison between muscle and skin sea bass samples of cultured fish shows that their fatty acid composition as well as the TG and CHO content are not significantly different. On the other hand, muscles of cultured fish have a higher value of phospholipids (PC and PE), CHN, MA, FA and GLN with respect to skin samples suggesting an additional nutritive value of fish muscles.
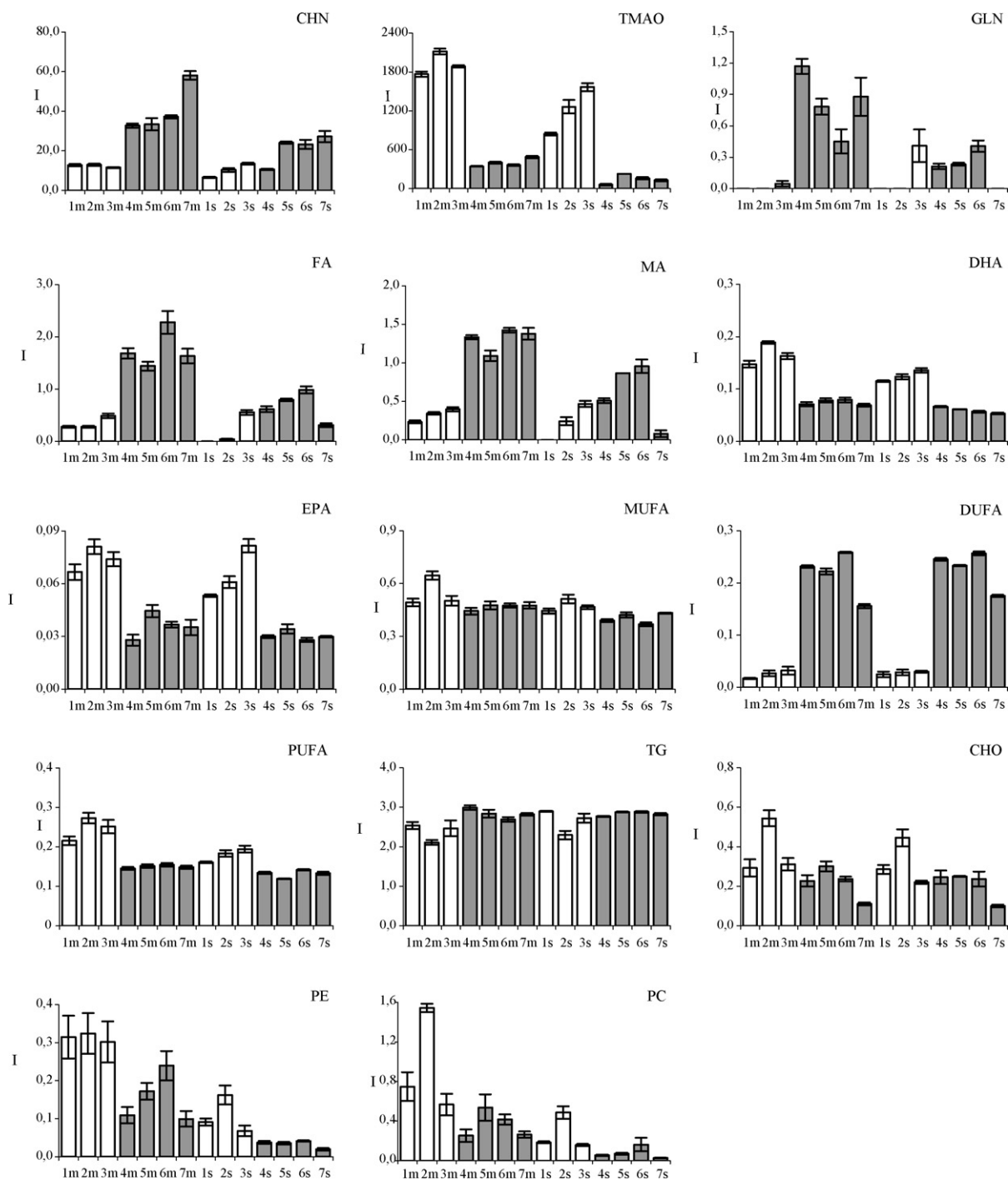
Fig. 6. Histograms relative to the intensity of selected metabolites (arbitrary units), see list of abbreviations. Mean values and standard errors for each fish are reported. Grey and white bars are due to cultured and wild fish respectively; *m* = muscle samples, *s* = skin samples.

Acknowledgement

References

[1] T.W.M. Fan, Prog. Nucl. Magn. Reson. 28 (1996) 161.
[2] L. Mannina, A.P. Sobolev, A.L. Segre, Spectroscopy 15 (2003) 6 (and references therein).
[3] O. Al-Jowder, F. Casuscelli, M. Defernes, E.K. Kemsley, R.H. Wilson, I.J. Colquhoun, in: G.A. Webb, P.S. Belton, A.M. Gil, I. Delgadillo (Eds.), Magnetic Resonance in Food Science: A View to the Future, The Royal Society of Chemistry, Cambridge, 2001, pp. 232–238.
[4] L. Mannina, A.L. Segre, Grasas y Aceites 53 (2002) 22.
[5] A.P. Sobolev, A.L. Segre, R. Lamanna, Magn. Res. Chem. 41 (2003) 237.
[6] A.P. Sobolev, E. Brosio, R.R. Gianferri, A.L. Segre, Magn. Res. Chem. 43 (2005) 625.
[7] L. Mannina, M. Cristinzio, A.P. Sobolev, P. Ragni, A. Segre, J. Agric. Food Chem. 52 (2004) 7988.
[8] M. Bosco, R. Toffanin, D. Palo, L. Zatti, A.L. Segre, J. Sci. Food Agric. 79 (1999) 869.
[9] J.G. Bell, T. Preston, R.J. Henderson, F. Strachan, J.E. Bron, K. Cooper, D.J. Morrison, J. Agric. Food Chem. 55 (2007) 5934.

[10] C. Alasalvar, K.D.A. Taylor, E. Zubcov, F. Shahidi, M. Alexis, Food Chem. 79 (2002) 145.
[11] K. Grikorakis, M.N. Alexis, K.D.A. Taylor, M. Hole, Int. J. Food Sci. Technol. 37 (2002) 477.
[12] I.U. Grün, H. Shi, L.N. Fernando, A.D. Clarke, M.R. Ellersieck, D.A. Beffa, Lebensm. Wiss. u. Technol. 32 (1999) 305.
[13] O. Fiehn, Plant Mol. Biol. 48 (2002) 155.
[14] E.G. Bligh, W.J. Dyer, Can. J. Biochem. Physiol. 37 (1959) 911.
[15] S. Braun, H.O. Kalinowski, S. Berger, 150 and More Basic NMR Experiments, second ed., Wiley-VCH, Weinheim, Germany, 1998.
[16] K.F. Morris, C.S. Johnson, J. Am. Chem. Soc. 114 (1992) 3139.
[17] K.F. Morris, P. Stilbs, C.S. Johnson, Anal. Chem. 66 (1994) 211.
[18] G.S. Kapur, E.J. Cabrita, S. Berger, Tetrahedron Lett. 41 (2000) 7181.
[19] S. Viel, L. Mannina, A.L. Segre, Tetrahedron Lett. 43 (2002) 2515.
[20] K.F. Morris, C.S. Johnson, J. Am. Chem. Soc. 115 (1993) 4291.
[21] S. Viel, D. Capitani, L. Mannina, A.L. Segre, Biomacromolecules 4 (2003) 1843.
[22] G. Özyurt, A. Polat, Eur. Food Res. Technol. 222 (2006) 316.
[23] H.P. Redmond, P.P. Stapleton, P. Neary, D. Bouchier-Hayes, Nutrition 14 (1998) 599.
[24] S. Shaffer, K. Takahashi, J. Auma, Amino acids 19 (2000) 527.
[25] P. Lundberg, T. Vogel, A. Malusek, P.O. Lundquist, L. Cohen, O. MDL Dahlqvist, The Magnetic Resonance Metabolomics Database (mdl.imv.liu.se), ESMRMB, Basel, Switzerland, 2005.
[26] N. Howell, Y. Shavila, M. Grootveld, S. Williams, J. Sci. Food Agric. 72 (1996) 49.
[27] I. Karube, H. Matsuoka, S. Suzuki, E. Watanabe, K. Toyama, J. Agric. Food Chem. 32 (1984) 314.
[28] A. Reale, E. Sorrentino, N. Iaffaldano, M. P. Rosato, P. Ragni, R. Coppola, D. Capitani, A. P. Sobolev, P. Tremonte, M. Succi, L. Mannina, World J. Microbiol. Biotechnol. (2008) http://dx.doi.org/10.1007/s11274-008-9802-7.
[29] F.D. Gunstone, Chem. Phys. Lipids 59 (1991) 83.
[30] F.D. Gunstone, S. Seth, Chem. Phys. Lipids 72 (1994) 119.
[31] M. Aursand, H. Grasdalen, Chem. Phys. Lipids 62 (1992) 239.
[32] P.C. Calder, Lipids 36 (2001) 1007.
[33] P. Calder, Clin. Sci. 107 (2004) 1.
[34] A.W.G. Moses, C. Slater, T. Preston, M.D. Barber, K.C.H. Fearon, Br. J. Cancer 90 (2004) 996.
[35] L. Mannina, C. Luchinat, M. Patumi, M.C. Emanuele, E. Rossi, A.L. Segre, Magn. Reson. Chem. 38 (2000) 886.
[36] L. Mannina, C. Luchinat, M.C. Emanuele, A.L. Segre, Chem. Phys. Lipids 103 (1999) 47.
[37] M.C. Carey, D. Small, C.M. Bliss, Ann. Rev. Physiol. 45 (1983) 651.
[38] R. Sacchi, I. Medina, S.P. Aubourg, I. Giudicianni, L. Paolillo, F. Addeo, J. Agric. Food Chem. 41 (1993) 1247.
[39] M. Aursand, J.R. Rainuzzo, H. Grasladen, J. Am. Oil Chem. Soc. 70 (1993) 971.
[40] W.R. Crasmun, R.M.K. Carlson, in: W.R. Crasmun, R.M.K. Carlson (Eds.), Two Dimensional NMR Spectroscopy: Applications for Chemists and Biochemists, VHC Publishers, New York, 1994, pp. 785–832.
[41] Y. Lin, X. Qiu-Zhou, Aquaculture 256 (2006) 389.

Relevance of NH_4F in acid digestion before ICP-MS analysis

Clarisse Mariet*, Oulfa Belhadj, Stéphanie Leroy, Francine Carrot, Nicole Métrich

Laboratoire Pierre Süe CEA – CNRS, UMR 9956 Centre de Saclay, Bât. 637, 91191 Gif sur Yvette Cedex, France

ABSTRACT

In order to implement a simpler, less expensive and more safe sample dissolution procedure, we have substituted the HF–$HClO_4$ mixture by NH_4F. By testing three certified reference materials, lichen 336, basalt BE-N, soil 7, it was found that the three-reagents digestion without HF and $HClO_4$ ($HNO_3 + H_2O_2 + NH_4F$ was used) was very effective for the pretreatment of ICP-MS measurement. The comparison was based on the measurement results and their uncertainties. All are reference material for amount contents of different trace elements. The accuracy and precision of the developed method were tested by replicate analyses of reference samples of established element contents. The accuracy of the data as well as detection limits (LODs) vary among elements but are usually very good (accuracy better than 8%, LODs usually below 1 μg/g in solids). ICP-MS capabilities enable us to determine routinely 13 and 16 minor and trace elements in basalt and soil.

© 2008 Elsevier B.V. All rights reserved.

Atomic spectrometry is useful for analysis of solid samples of environmental and geological interest. To overcome the heterogeneous nature of the specimens, most of these samples are investigated for bulk analysis by atomic absorption spectrometry (AAS), inductively coupled plasma-atomic emission spectrometry (ICP-AES), or inductively coupled plasma-mass spectrometry (ICP-MS). ICP-MS is the method with the highest potential with respect to its detection limits, sensitivity, precision and multi-elemental determinations and speed.

Solution nebulisation is commonly used for the sample introduction system of these methods. Although improvements have been made in the existing solid sampling techniques (laser ablation and electrothermal vaporizer), the liquid introduction remains most widespread. Solid sample introduction offers some main advantages over liquid sample [1]. Sample preparation time and handling are reduced, thus diminishing the likelihood of cross-contamination from other samples or reagents. Because no solvent is present, molecular ion spectral interferences derived from solution are absent. However, the lack of primary standards limits the quantitative viability of solid sample analysis [2,3].

Finding the correct procedure for the complete dissolution of the samples by chemical digestion is the most critical aspect of ICP-MS analysis. The common dissolution techniques are the acid decomposition in open vessel, the microwave digestion and the alkali fusion. Alkali fusion requires a high flux to sample ratio (4:1) necessary to completely decompose the sample. This entails a strong matrix effect and the introduction of a great amount of polluting elements also leading to a possible contamination of the torch and other parts of the analytical apparatus (e.g. boron rich flux) [4–6]. By a consequence the solution must be strongly diluted (f_d, dilution factor, $f_d = 5000$) dramatically lowering the detection limits. Moreover Si-rich samples generally result in solutions enriched in total dissolved solids (TDSs) which can cause analytical drift by reducing the diameter of the cone orifice [5]. Furthermore high Si content may involve important isobaric interferences which prevent the determination of such element as ^{45}Sc (interference: $^{17}OH + ^{28}Si$). Except alkaline fusion, multi-elements analyses of geological samples, as basalts, are mainly carried out following acid digestion [7–11] and less with microwave digestion [12,13]. The microwave digestion with open or closed oven frequently leaves undissolved residues [5,14–16], making necessary the addition of flux, thus causing similar inconvenience of the alkali fusion. On the other hand, protocols requiring evaporations related to the change of medium are time consuming with even with microwave digestion.

Open vessel acid decomposition was chosen because it warrants low detection limits and the complete sample digestion while keeping a low pollution and limited matrix effect. It has the disadvantage of being the most time consuming and requiring a great quantity of acid [14]. A possible limitation of this procedure is represented by the incomplete sample decomposition due to the presence of refractory accessory minerals. A combination of HNO_3 and HF is conventionally employed in the acid digestion of silicate matrix. However, some recent studies have reported that good recoveries of many elements can be achieved without HF addition [6,15,17–19]. This information is essential because it has been recommended that the use of HF, very corrosive and toxic, should be avoided for safety

* Corresponding author. Tel.: +33 1 69 08 49 60; fax: +33 1 69 08 69 23.
E-mail address: clarisse.mariet@cea.fr (C. Mariet).

Table 1
Summary of the working conditions used in the digestion procedures applied in the present investigation

Procedure	Reagents	Volume (ml)	Initial contact time
A	HNO_3:HF:$HClO_4$	2:1:1	10 h
	H_2O_2	1	Overnight
	HNO_3	1	Three successive evaporations with intermediate addition of HNO_3
	H_2O	1	15 min
B	HNO_3:NH_4F	2:1	10 h
	H_2O_2	1.5	Overnight
	HNO_3	1	Three successive evaporations with intermediate addition of HNO_3
	H_2O	5	15 min

reasons. Par consequent, new approaches to improve the digestion samples in elemental analysis are needed.

Our work aims at providing a simpler, less expensive and more safe dissolution procedure for lichen, soil and basalt leading to accurate ICP-MS determination of a few transition elements: Cr, Co, Ni, Zn, Pb, rare earth elements (La, Ce, Nd, Sm, Eu, Gd, Tb, Yb) and other trace elements like Sc, As, Rb, Sr, Mo, Ba, Cs, Hf, Ta, Th, U more seldom determined in such matrix. It is why we decided to remove the reagents more penalizing ($HClO_4$ and HF) and to replace them by NH_4F. This last reagent has the same aptitudes that HF from the point of view of acid digestion without the disadvantages related to safety. To the knowledge of the authors, this is the first time NH_4F is used in a digestion procedure. Only tertiary ammonium or tetramethylammonium hydroxide (TMAH) are used in for biological samples [20,21]. NH_4OH appears in soils analysis in extraction procedures before ICP-MS but not in acid digestion [20].

1. Experimental

1.1. Materials and equipment

The quality control of the analytical technique was ascertained by applying digestion and analytical procedures for ICP-MS to the following reference materials: the basalt geostandard BE-N from the SARM (Service of the Rocks and Minerals Analyses), the lichen 336 and soil 7 both provided by IAEA (International Atomic Energy Agency). We chosed these samples because they illustrate most of the environmental and geological samples.

Trace analysis in solid materials with amount in the lower microgram per gram level requires clean working conditions and specialized sample handling equipment in order to keep the blank contribution and contamination risks small. Teflon flasks were rinsed with ultrapure water and then heated for at least 2 h with HNO_3 (2%) followed by another rinsing and a drying step.

Table 2
Instrumental parameters

ICP Parameters	
Plasma gas	Argon
rf power	1350 W
Nebulizer gas flow	0.74 L min^{-1}
Auxiliary gas flow	0.90 L min^{-1}
Coolant gas flow	13.8 L min^{-1}
Spray chamber water-cooled at 3 °C	
Mass spectrometer	
Interface vacuum	1.9×10 hPa
Analyser vacuum	3.6×10^{-7} hPa
Ni made Xi sampler (Ø1 mm) and skimmer (Ø0.7 mm)	
Acquisition parameters	
Full quantitative scan mode	
Dwell time	10 ms/element
Replicates	4
Ion collection mode	Pulse counting
Measuring time	90 s

1.2. Chemicals and spike materials

For all dilutions and sample treatments, high purity deionized water (resistivity 18.2 MΩ cm) obtained using a Milli-Q water purification system (Millipore, Bedford, MA, USA) was used throughout. All reagents used for digestion procedures are® VWR Normatom purity grade. For the ICP-MS method, calibration solutions were prepared from certified stock multi-elemental 1000 mg g^{-1} solutions SPEX, Jobin Yvon. Analytical calibration standards were prepared daily over the range of 0–20 ng g^{-1} for all elements by suitable serial dilutions of multi-element stock solution in 2% (v/v) HNO_3. Rhodium and rhenium were used as internal standards at the concentration of 2 ng g^{-1}. The internal standards were diluted from 1000 mg g^{-1} stock standard.

All solutions were stored in high-density polyethylene bottles. Plastic bottles and glassware materials were cleaned by soaking in 10% (v/v) HNO_3 for 24 h, rinsing five times with Milli-Q water and dried in a class 100 laminar flow hood before use. All operations were performed in a clean bench.

1.3. Digestion procedures

The general conditions of the two digestion procedures are summarised in Table 1. About 50 mg (100 mg for lichen 336) of the sample were weighed into Teflon flasks.

Table 3
Limits of detection

Element	Analytical mass	Solution (ng g^{-1}) with 2% HNO_3	Sample blank (μg g^{-1})
Sc	45	<0.01	0.52
Cr	52	<0.01	0.35
Co	59	0.10	0.20
Ni	60	0.19	0.52
Zn	66	0.69	3.6
As	75	0.73	0.70
Rb	85	0.16	0.20
Sr	88	0.18	0.43
Mo	95	0.78	0.89
Sb	121	0.38	0.50
Cs	133	0.05	0.10
Ba	137	0.06	0.09
La	139	0.10	0.39
Ce	140	0.11	0.35
Nd	146	0.88	0.90
Sm	147	0.89	0.89
Eu	153	0.43	0.43
Gd	157	1.04	1.05
Tb	159	0.20	0.20
Yb	172	1.01	1.01
Hf	178	0.61	0.67
Ta	181	2.21	2.26
Pb	208	0.4	1.75
Th	232	0.19	0.23
U	238	0.29	0.29

Table 4
Analytical results obtained by HF–ClO$_4$ and NH$_4$F for lichen 336 (ppm)

Element	X_A HF–ClO$_4$ (4)	R.S.D. (%)	X_B NH$_4$F (10)	R.S.D. (%)	Certified values	Standard deviation
^{45}Sc	<LD		<LD		0.17	0.01
^{52}Cr	<LD		1.07	14.6	1.06	0.085
^{59}Co	0.31	12.5	0.27	7.1	0.29	0.025
^{60}Ni[a]	<LD		<LD			
^{66}Zn	32.8	3.1	29.7	3.4	30.4	1.7
^{75}As	<LD		0.62	8.5	0.63	0.04
^{85}Rb	1.8	3.1	1.9	7.1	1.76	0.11
^{88}Sr	9.1	2.5	10.0	6.9	9.3	0.55
^{95}Mo[a]	<LD		<LD		0.15	
^{121}Sb	<LD		<LD		0.073	0.005
^{133}Cs	<LD		0.110	5.8	0.11	0.0065
^{137}Ba	6.8	2	6.38	3.2	6.4	0.55
^{139}La	0.64	7.9	0.61	10.2	0.66	0.05
^{140}Ce	1.3	6	1.24	7.0	1.28	0.085
^{146}Nd	<LD		0.63	8.2	0.6	0.09
^{147}Sm	<LD		0.11	8.6	0.106	0.007
^{153}Eu	<LD		<LD		0.023	0.002
^{157}Gd[a]	<LD		<LD		0.5	
^{159}Tb	0.017	39.1	0.017	17.3	0.014	0.001
^{172}Yb	<LD		<LD		0.037	0.006
^{178}Hf[a]	<LD		<LD		0.06	
^{181}Ta[a]	<LD		<LD		0.01	
^{208}Pb	4.4	4.6	4.8	8.9	4.9	0.3
^{232}Th	<LD		0.12	13.0	0.14	0.01
^{238}U[a]	<LD		0.05	11.6	0.037	

[a] Recommended values; (n) number of independent determinations (% R.S.D. = 100 σ/m).

In the case of A procedure, an HF–HNO$_3$–ClO$_4$ mixture composed of 2 ml of HNO$_3$ (65%), 1 ml HClO$_4$ (68%) and 1 ml HF (47%) was added to the sample. The flasks were closed and put on a sand bath at 240 °C during 10 h. The Teflon flasks were cool down during 1/2 h, then 1 ml of H$_2$O$_2$ (30%) was added. After 1/2 h, the flasks were closed again and put on the sand bath at 190 °C overnight. The flasks were cool down. Then, after adding 1 ml HNO$_3$, the flasks were opened and left on the sand bath at 240 °C for evaporation up to dryness. The operation has been repeated three times. One millilitre of H$_2$O purified with a Milli-Q system was added, the flasks were closed and put on a sand bath at 240 °C during 15 min. The resulting solution was transferred to a 50 ml flask and brought to volume with purified water.

As concerned B procedure, it is the same thing with a HNO$_3$–NH$_4$F mixture using 1 ml NH$_4$F (47%) in the first step, then 1.5 ml H$_2$O$_2$ in the second and 5 ml H$_2$O were added in the last. This is an attractive procedure because it does not require the more expensive acid HClO$_4$ or the more hazardous acid HF.

A dilution factor f_d was applied to transform the concentration in solution (μg l^{-1}) into the concentration in solid (μg g^{-1}). f_d was

Table 5
Results obtained by HF–ClO$_4$ and NH$_4$F for Basalt BEN (ppm)

Element	X_A HF–ClO$_4$ (4)	R.S.D. (%)	X_B NH$_4$F (7)	R.S.D. (%)	Certified values	Standard deviation
^{45}Sc	22	0.7	21	4.2	22	4.08
^{52}Cr	378.	1.8	378	6.7	360	48.84
^{59}Co	60.	24.7	63	1.0	60	7.78
^{60}Ni[a]	279	1.4	274	1.6	267	26.48
^{66}Zn	201	1.8	159	6.7	120	49.67
^{75}As	1.5	2.1	2.2	6.7	1.8	0.56
^{85}Rb	52	4.6	46	6.9	47	8.79
^{88}Sr	1494	7.3	1318	7.1	1370	100
^{95}Mo[a]	3.0	0.2	2.8	6.0	2.8	–
^{121}Sb	0.3 < LD	15.9	0.5	2.4	0.26	0.08
^{133}Cs	0.8	13.2	1.0	3.6	0.8	0.33
^{137}Ba	1058	3.2	1181	1.3	1025	125
^{139}La	86	4.0	90	6.2	82	3
^{140}Ce	160	3.7	168	2.6	152	24.08
^{146}Nd	72	3.5	75	5.3	67	2.6
^{147}Sm	13	20.6	13.	4.7	12.2	0.6
^{153}Eu	4.0	4.8	3.13	3.9	3.6	0.52
^{157}Gd[a]	12.3	2.0	10.9	1.4	9.7	1.4
^{159}Tb	1.3	8.6	1.4	3.1	1.3	0.28
^{172}Yb	2.0	8.0	2.0	3.4	1.8	0.68
^{178}Hf[a]	5.8	8.2	5.2	2.7	5.6	0.37
^{181}Ta[a]	6.1	5.1	6.8	4.8	5.7	0.88
^{208}Pb	3.8	2.6	3.5	5.8	4	5.38
^{232}Th	10.0	1.7	10.0	7.1	10.4	2.01
^{238}U[a]	2.6	2.1	2.8	5.9	2.4	0.49

[a] Recommended values; (n) number of independent determinations.

Table 6
Analytical results obtained by HF–HClO$_4$ and NH$_4$F for soil 7 (ppm)

Element	X_A HF–HClO$_4$ (4)	R.S.D. (%)	X_B NH$_4$F (6)	R.S.D. (%)	Certified values	Standard deviation
^{45}Sc	8.1	0.8	8.3	13.1	8.3	5.5
^{52}Cr	60	1.2	63	3.1	60	4.5
^{59}Co	9.0	0.7	8.2	6.7	8.9	0.4
^{60}Ni[a]	28	1.0	24	16.6	26	2.5
^{66}Zn	107	2.8	106	1.8	104	3
^{75}As	14	18.7	14	9.2	13.4	1.3
^{85}Rb	49	4.1	49	0.8	51	0.05
^{88}Sr	113	3.1	109	0.5	108	0.5
^{95}Mo[a]	1.4	0.5	2.8	16.1	2.5	18.5
^{121}Sb	1.8	0.3	2	9.3	1.7	0.5
^{133}Cs	5.3	0.2	5.8	8.4	5.4	1
^{137}Ba	152	1.0	165	1.2	159	2
^{139}La	27	0.4	30	0.8	28	0.2
^{140}Ce	63	5.5	61	0.5	61	0.15
^{146}Nd	28	2.5	33	8	30	
^{147}Sm	5	0.3	5	8.4	5.1	0.15
^{153}Eu	1.0	0.1	1.0	8.8	1	0.1
^{157}Gd[a]	5.0	0.5	4.2	11.8	3.9	0.2
^{159}Tb	0.6	0.1	0.7	10.1	0.6	0.1
^{172}Yb	1.9	0.2	2.0	5.6	2.4	5.5
^{178}Hf[a]	2.5	0.2	2.7	4.4	5.1	0.25
^{181}Ta[a]	0.7 < LD	0.0	0.9	6.2	0.8	0.35
^{208}Pb	62	5.3	57	0.1	60	5.5
^{232}Th	8.2	0.7	8.2	2.1	8.2	4.5
^{238}U [a]	2.5	0.2	2.5	0.6	2.6	0.4

[a] Recommended values; (n) number of independent determinations (% R.S.D. = 100 σ/m).

calculated using the equation:

$$f_d = \frac{\text{final solution volume (ml)}}{\text{sample weight (mg)}}$$

The resulting dilution factor is 1000; the reagent blank was prepared in the same manner.

1.4. Instrumentation

ICP-MS measurements have been performed using a quadrupole ICP-MS spectrometer X7 series ICP-MS (*Thermo Fisher Corporation*) equipped with a concentric nebulizer. Instrumental parameters were fixed as indicated Table 2. Although this instrument can be used in the CCT (collision cell technology) mode to remove polyatomic interferences, we operated it solely in standard mode, i.e., with the CCT valve vented, for the determination of metals.

Signal optimization is obtained by using a 10 ng g^{-1} solution of Be, Mg, Co, Ni, In, Ce, Ba, Pb, Bi and U. The spectrometer is optimised to provide minimal values of the ratios CeO$^+$/Ce$^+$ and Ba^{2+}/Ba$^+$ and optimum intensity of the analytes. The optimum measurement conditions are summarised in Table 2; the isotopes used for analysis are listed in Table 3. Standards calibrations curves are built by measuring successively a mixed at different concentration levels 0, 0.1, 0.5, 2, 5, 10, 20 and 100 ng g^{-1} (calibration solutions were prepared from certified stock multi-elemental solutions). This method requires the use of internal standards to check for instrumental gain and to monitor short-term analytical drifting. That is suitable by a 2 ng g^{-1} standard solution of Rh and Re added simultaneously to all samples just before the nebulize admission.

2. Results and discussion

In order to avoid ICP-MS pollution, H$_3$BO$_3$ is not used to eliminate fluorides. Moreover it has a negative matrix effect [22]. This is why, although it is longer, we chosed evaporation to remove fluorides from geological and plant samples as volatile SiF$_4$ [18,23].

After the digestion, all samples formed yellowish solutions in the two procedures with no apparently visible residue.

2.1. Detection limits

The ICP-MS lower limits of detection (LODs) were determined for each element (Table 3), with each procedure, in the following way: 15 individual chemical blanks prepared along with the other samples were measured as an unknown in three replicates. The detection limit in the solid sample was then assumed to three times the standard deviation of the blank solution counts, taking into account the dilution factor (1 mg of sample in 1 ml of solution). No difference was observed between the two procedures. Detection limits of ICP-MS mainly depend upon the cleanliness of digestion vessels, the purity of reagents adding during the mineralisation and on ICP-MS working conditions. In order to discriminate these different factors, about 20 solutions: H$_2$O with 2% HNO$_3$ were analysed in the same manner than the samples blanks. We remark that there is a slight pollution for Zn, Mo and Pb most likely due to the cleanliness of digestion vessels or to the purity of reagents adding during the mineralisation. The interferences ^{57}Fe^{16}O^{1}H$^+$ plus ^{58}Ni^{16}O^{1}H$^+$ on ^{75}As$^+$ severely damage the detection limit. Meanwhile the LOD was generally below the lowest concentration observed in the samples.
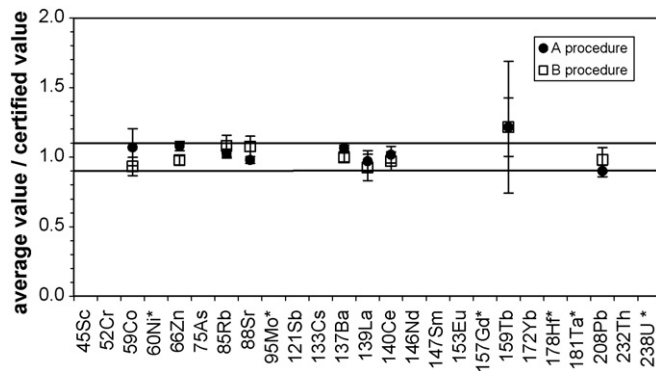
Fig. 1. Ratio of the average values obtained with the certified values for each dissolution procedure for lichen 336. The solid lines indicate a variation of 10% compared to the certified value. *When there is only recommended value.
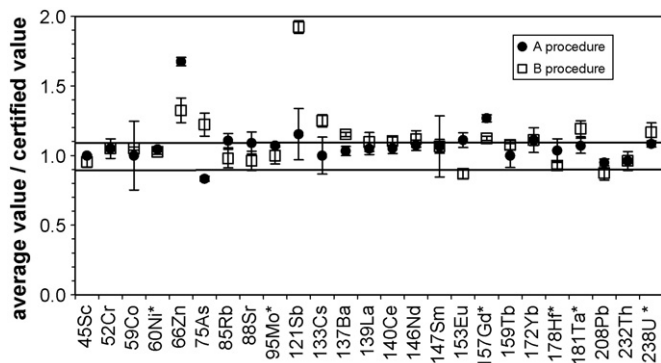
Fig. 2. Ratio of the average values obtained with the certified values for each dissolution procedure for basalt BEN. The solid lines indicate a variation of 10% compared to the certified value. *When there is only recommended value.

2.2. Reproducibility and accuracy

As a test of procedure reproducibility, different aliquots (four aliquots for A procedure and the remainder for B one) of the same sample were dissolved and analysed. The average value X_i and the relative standard deviation (% R.S.D.) were calculated (Tables 4–6). For the three references, the precision of analytical results characterized by the relative standard deviation was generally better than 8%.

In the lichen 336 samples, the low reproducibility for Co (% R.S.D. = 12%) and Tb (% R.S.D. = 9.1%) is dependant on the low analyte concentration and sensibility in the sample. In the basalt BEN sample, the worse elements are Co (% R.S.D. = 24.7%), Sb (% R.S.D. = 15.9%), Cs (% R.S.D. = 13.2%) and Sm (% R.S.D. = 20.6%) with A procedure.

As concerned soil 7, the elements for which the reproducibility is worse are Ni (% R.S.D. = 16.6%), Mo (% R.S.D. = 16.1%), Gd (% R.S.D. = 11.8%) and Tb (% R.S.D. = 10.1%) and with B procedure this time.

In order to compare the accuracy of the two procedures A and B, the measured concentrations were averaged and normalized against the certified values. There is a good agreement between the results and the reference values within 10% relative error, as illustrated in Figs. 1–3, respectively, for lichen 336, basalt BEN and soil 7.

First, one notes the procedure B is as good as procedure A for the majority of the elements.

The values obtained for Sb, Cs, Ba, Ta, and Pb quite match the theoretical values by using A procedure. Whereas we though the use
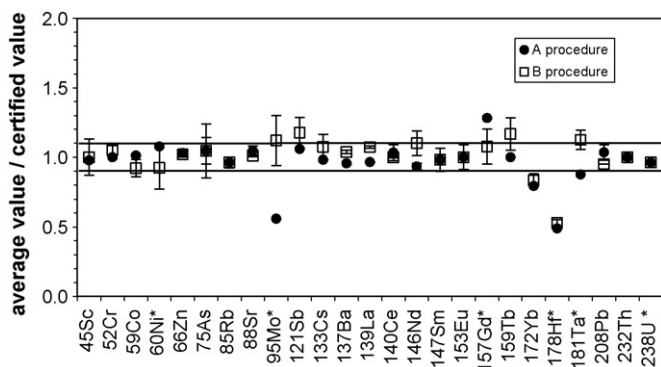
Fig. 3. Ratio of the average values obtained with the certified values for each dissolution procedure for soil 7. The solid lines indicate a variation of 10% compared to the certified value. *When there is only recommended value.

of NH_4F brings to the digestion solution a new possible complexant because NH_3 forms stable complexes with 3d elements [24], for others elements there is not only complexes but also precipitates. As an illustration, Ta, As, Sb easily form colloidal hydroxides in partially ammoniacal solution [25]. Besides, we can observe that these three elements are over-estimated in basalt BEN.

The measurement of [121]Sb and [137]Ba is always worst after the B procedure, most likely because of isobaric interferences respectively with the adducts $^{103}Rh(^{15}NH_3)^+$ and $^{103}Rh(^{14}NH_3)_2^+$ dependent on the addition of the internal standard. In the basalt BEN, the concentration of Sb is only of 0.26 ppm. Consequently, the contribution of the interference is all the more important as the concentration in the sample is weak. Selected interfering polyatomic ions can then be eliminated through ion molecule reaction cell with a small amount of gas [26]. A way of reducing these interferences consists in performing CCT mode with a mix collision gas O_2 8% in He, oxygen being used to oxidize NH_3 [2].

In contrast, the B procedure strongly improves the results for Gd even if its measured concentration remains over-estimated. One can imagine that the formation of $^{140}Ce^{16}OH^+$ is put at a disadvantage.

In lichen 336, 6 traces elements ([66]Zn, [85]Rb, [88]Sr, [139]La, [140]Ce, and [208]Pb) were founded in good agreement with the certified or recommended values, with R.S.D. (%) near to 10% or lower (Table 4, Fig. 1). Since the concentrations of the other were lower than LODs, no data were given for them. [59]Co is slightly over-estimated in lichen 336, but it should be noted that the required content is close to the LOD.

In basalt BEN (Table 5), 13 elements ([45]Sc, [52]Cr, [59]Co, [60]Ni, [85]Rb, [88]Sr, [95]Mo, [139]La, [140]Ce, [159]Tb, [178]Hf, and [232]Th) are accurately analysed and their normalized concentrations lie between 1.1 and 1.15 for 5 others ([121]Sb, [137]Ba, [146]Nd, [157]Gd, and [172]Yb). Nd is overestimated in basalt BEN. This overestimation is possibly caused by the isobaric interference $^{130}Ba^{16}O^+$, when Ba is highly concentrated in the sample (as As it is the case of basalt BEN). This statement is confirmed by the good agreement between the Nd measured concentrations and the certified value in the Ba poor, Soil 7 reference, whatever the procedure used.

In the case of Soil 7 (Table 6, Fig. 3), the normalized values fall within the interval 1 ± 0.1, for 16 elements ([45]Sc, [52]Cr, [59]Co, [60]Ni, [66]Zn, [75]As, [85]Rb, [88]Sr, [137]Ba, [139]La, [140]Ce, [147]Sm, [153]Eu, [208]Pb, [232]Th, and [238]U) with R.S.D. (%) lower than 8%.

As previously demonstrated (Xu et al. [6]), the optimization of the digestion conditions without HF nor $HClO_4$ led to the increase in the contribution of H_2O_2. This observation appears logical since the role of hydrogen peroxide is to increase the oxidizing capacity of the acids [27]. Thus, a part of the oxidizing effect of $HClO_4$ is replaced by that of H_2O_2.

3. Conclusion

As expected, for a multi-elemental analysis covering wide ranges of atomic masses and levels of occurrence, a single extraction method is not adequate. However, we developed a routine method for simultaneous determination of 13 and 16 elements (minor or trace) by ICP-MS, respectively, in basalt and soil. The final solutions are suitable for the ICP-MS instrument because total dissolved solid is kept low and possible interferences mainly due to the use of HCl or $HClO_4$ are avoided.

A clear advantage of the digestion procedure with NH_4F is the reduction of the number of acids used and the replacement of a prohibited acid of handling in laboratory for safety question by such an effective salt. The additional economic interest is obvious since ICP-MS is the most popular method for trace element analysis.

Moreover, accurate determination of large spectra of trace elements has a broad interest for the knowledge of the geochemical cycles and element transfer through the different terrestrial reservoirs and in fine for Environmental and Earth Sciences. The NH_4F-based digestion procedure applies to micro-samples (mass lower than 20 mg), too. The analytical precision is then strongly improved by the introduction of spiking aliquots.

Acknowledgement

References

[1] J.-F. Gravel, et al., Anal. Chem. 75 (6) (2003) 1442–1449.
[2] A. Montaser, Inductively Coupled Plasma Mass Spectrometry, Wiley–VCH, Washington, 1998, p. 964.
[3] P. Roper, Applications of Reference Materials in Analytical Chemistry, Royal Society of Chemistry, 2001.
[4] I. Jarvis, I.M.M. Totland, K.E. Jarvis, Chem. Geol. (1997) 27–42.
[5] A. Tsolakidou, J.B. Garrigós, V. Kilikoglou, Anal. Chim. Acta 474 (2002) 177–188.
[6] Y. Xu, et al., Talanta 66 (2005) 58–64.
[7] D. Beauchemin, et al., in: D. Barcelo (Ed.), Discrete Sample Introduction Techniques for Inductively Coupled Plasma Mass Spectrometry, vol. 24, Elsevier, Amsterdam, 2000.
[8] X.-J. Yang, C. Pin, The Analyst 125 (2000) 453–457.
[9] T. Meisel, et al., The Analyst 126 (2001) 322–328.
[10] A. Makishima, E. Nakamura, Spectrochim. Acta Part B 15 (2000) 263–267.
[11] G. Quitte, F. Oberli, J. Anal. At. Spectrom. 21 (2006) 1249–1255.
[12] V. Valaram, S.L. Ramesh, K.V. Anjaiah, Fresenius J. Anal. Chem. 353 (1995) 153.
[13] M.M. Totland, I. Jarvis, K.E. Jarvis, Chem. Geol. 124 (1995) 21–28.
[14] J. Ivanova, et al., Talanta 54 (2001) 567–574.
[15] A. Iwashita, et al., Fuel 85 (2006) 257–263.
[16] H. Lachas, et al., The Analyst 124 (1999) 177–184.
[17] J. Wang, et al., Anal. Chim. Acta 514 (2004) 115–124.
[18] G. Knapp, et al., in: H.M. Kingston, S.J. Haswell (Eds.), Microwave-Enhanced Chemistry, American Chemical Society, Washington, 1997.
[19] J.G.S. Gupta, N.B. Bertrand, Talanta 42 (1995) 1947–1957.
[20] J.A. Nobrega, et al., Spectrochim. Acta Part B 61 (2006) 465–495.
[21] B.L. Batista, et al., Talanta (in press).
[22] I. Rodushkin, M.D. Axelsson, E. Burman, Talanta 51 (2000) 743–759.
[23] V.F. Taylor, A. Toms, H.P. Longerich, Anal. Bioanal. Chem. 372 (2002) 360–365.
[24] A. Ringbom, Complexation in Analytical Chemistry, J. Wiley and Sons, New York, 1963.
[25] G. Charlot, L'analyse qualitative et les réactions en solution, Masson, Paris, 1963, p. 433.
[26] B.E. Erickson, Anal. Chem. 71 (1999) 811A.
[27] J.M. Mermet, in: H.M. Kingston, S.J. Haswell (Eds.), Fundamentals, sample preparation and applications, American Chemical Society, Washington, 1997, p. 772.

Comparison of microwave-assisted digestion procedures for total trace element content determination in calcareous soils

B. Marin [a,*], E.I.B. Chopin [a], B. Jupinet [a], D. Gauthier [b]

[a] GEGENA² EA 3795, University of Reims Champagne-Ardenne, 2 esplanade Roland Garros, 51100 Reims, France
[b] Municipal and Regional Laboratory, 2 esplanade Roland Garros, 51100 Reims, France

ARTICLE INFO

ABSTRACT

The aim of the study was to determine total trace (Cd, Co, Cr, Cu, Mn, Pb and Zn) and major (Al and Fe) element concentrations in calcareous soils using microwave-assisted digestion procedures. The literature showing lack of consensus regarding digestion procedures and unsatisfying recoveries for calcareous materials, four procedures using various acid combinations (HCl, HNO_3, H_2O_2, HF) and volumes were tested using a certified reference material (CRM 141R) and natural calcareous soil samples. Digests were analysed by inductively coupled plasma-atomic emission spectrometry (ICP-AES). Repeatability (R.S.D. <5%) and recoveries (82–116%) showed that the procedures were precise and accurate for most elements. Five calcareous soil samples from a Champagne vineyard plot were, then, subjected to these procedures. In calcareous materials, the presence of HF resulted in Al being severely underestimated (recovery <5%) and Co overestimated (recovery >124%) due to complex formation or spectrochemical interferences, respectively. As digestion was not significantly influenced by the addition of H_2O_2, the procedure corresponding to *Aqua regia* (HCl–HNO_3) appeared as the best compromise and was selected for further multielemental environmental studies on calcareous materials, even if the absence of HF could lead to incomplete digestion of accessory silicate minerals. Results for a vineyard plot showed that the soils were contaminated (3.65 mg kg⁻¹ Cd, 67 mg kg⁻¹ Cr, 278 mg kg⁻¹ Cu, 143 mg kg⁻¹ Pb and 400 mg kg⁻¹ Zn) as a consequence of urban waste and copper-treatment applications.

© 2008 Elsevier B.V. All rights reserved.

1. Introduction

Elevated concentrations of trace elements, when mobile, can cause great environmental concern by accumulating in and contaminating soils, fauna, vegetation or waters [1–3]. Therefore, guidelines and legislations have been issued concerning maximum allowable total trace element concentrations in soils [4–6]. Total concentrations should, thus, be accurately determined.

Concentrations are analysed using a range of analytical methods including inductively coupled plasma-atomic emission spectrometry (ICP-AES). However, these techniques have a major drawback since they require the solid sample to be put into solution. To this effect, a range of digestion systems (open and closed systems) and reagents have been used [4,5,7,8].

Pressurised closed-vessel microwave systems have the advantages of reducing digestion time, contamination and loss of volatile species, requiring less reagents and sample, and enhancing

operator safety [4,5,8,9]. Moreover, microwave digestion usually produces more controlled and reproducible results than conventional hot plate methods [4,9].

Depending on the reagents used, residues can remain after digestion suggesting that the digestion was incomplete and the concentrations are merely pseudo-total [5]. Moreover, actual total concentrations are required, particularly for further comparison with results from sequential extractions which determine trace element partitioning and mobility. Among reagents, HNO_3, HCl and HF are the most commonly used for calcareous soil digestion [8–10], H_2O_2 being also sometimes used [5,11,12]. In the literature, a very large range of digestion procedures exists from HNO_3 [13–15], HNO_3–HCl [4,5,8,15–21], HNO_3–HF [9,12,22], HNO_3–H_2O_2 [23], HNO_3–HCl–HF [8,9,24,25], HNO_3–HCl–H_2O_2 [26], HNO_3–HF–$HClO_4$ [15,27,28] to HNO_3–HF–$HClO_4$–H_2O_2 [5,29]. No concensus seems to exist as to the most appropriate procedure for a given type of soil, leaving choice to select any procedure and risking obtaining unsuitable results.

Most studies emphasize the need for HF in order to achieve a total digestion as it breaks down silicates [4,7]. However, in calcareous soils, HF could react with Ca to form Ca–F complexes which could trap trace elements [9,12]. In the literature, recoveries

---

* Corresponding author. Tel.: +33 3 29 77 36 85; fax: +33 3 29 77 36 36.
E-mail address: beatrice.marin@univ-reims.fr (B. Marin).

for calcareous reference materials when using HF range from extremely poor (down to 45%) to very elevated (up to 173%) depending on the element [9,12,22,24,30]. Therefore, the use of HF might be appropriate to determine certain elements and prove to be inacceptable when considering others. In the case of an environmental multielemental study, the digestion procedure used should represent the best compromise for a range of elements in terms of result reliability and measured concentrations. To verify whether the use of HF for calcareous soil digestion in environmental multielemental studies is appropriate or could cause under- or over-estimation of certain element concentrations, reference materials with high $CaCO_3$ content (>10%) are digested and recoveries calculated.

The purpose of this study was to compare total microwave-assisted digestion procedures using various mixtures of these four reagents for the determination of total trace (Cd, Co, Cr, Cu, Mn, Pb and Zn) and major (Al and Fe) element concentrations. The main aim consisted in testing the procedures using a certified reference material (CRM) and natural soil samples and suggesting the most appropriate procedure(s) for calcareous soils depending on the element considered, in terms of data quality, digestion efficiency, instrumentation protection and operator safety. A secondary aim involved digestions of calcareous vineyard soils in an environmental monitoring perspective.

2. Experimental

2.1. Samples

Five mollisol (sub-order rendoll, commonly known as Rendzina or Rendosol) soil samples were collected in a Champagne vineyard plot at Mailly-Champagne, 15 km SE of Reims, eastern France (Fig. 1). Soils were developed on Mesozoic chalk. The samples were wet-sieved to less than 2 mm in a plastic sieve to avoid contamination and ground to a fine powder using agate pestle and mortar. The soils showed alkaline pH (mean 7.9; 7.7–8.0), high organic carbon (mean 5.6%; 4.0–7.7%; NF ISO 14235) and $CaCO_3$ content (mean 14.9%; 10.0–20.8%; NF ISO 10693).

To validate the digestion procedures, a CRM 141R supplied by the Community Bureau of Reference of the European Community was chosen. This calcareous loam soil displays a $CaCO_3$ content (20.8%) similar to that of the five sampled soils. CRM 141R is certified for total element concentrations [31]. Contents and uncertainty values are reported within the results.

2.2. Reagents

The reagents used (36% HCl, 69% HNO_3, 30% H_2O_2 and 48% HF) were all of analytical grade (Prolabo, VWR International, France).

Table 1
Reagents and volumes used in microwave-assisted digestion procedures

	HCl (mL)	HNO_3 (mL)	HF (mL)	H_2O_2 (mL)
Procedure 1	6	2	1	1
Procedure 2	6	2	–	2
Procedure 3	6	2	2	–
Procedure 4	7.5	2.5	–	–

These reagents are commonly used in environmental studies. HCl and HNO_3 dissolve carbonates [5], H_2O_2 or HNO_3 oxidise organic matter [5], and HF breaks down the aluminosilicate phases [4,7]. They were chosen in accordance with previously used methods [5,8,9,32] and the microwave manufacturer (Milestone, USA) recommendations [33]. Distilled water was purified using a Milli-Q water purification system (Millipore, USA) to achieve a conductivity of 0.054 µS.

2.3. Microwave-assisted digestion procedures

Microwave PTFE vessels were cleaned before each digestion using 10 mL 69% HNO_3 heated for 15 min at 180 °C (800 W) and then rinsed with ultrapure water. PTFE evaporation vials were cleaned overnight with 4 mL 69% HNO_3 at 100 °C on a hot plate and then rinsed with ultrapure water.

Samples were accurately weighted to approximately 0.3 g directly in microwave vessels. They were subjected to four different digestion procedures using various acid combinations and volumes but keeping the same solid sample—reagent volume ratio (0.3 mg to 10 mL; Table 1). Relative volumes of each reagent were derived from the *Aqua regia* digestion procedure. For the first three procedures, a 3:1 HCl–HNO_3 ratio was kept, with the remaining volume being made up with either HF, H_2O_2 or both reagents. Procedures 1 and 2 required a pre-oxidation step using H_2O_2 to take place overnight before the actual microwave-assisted digestion. Procedure 4 corresponded to an *Aqua regia* digestion. The digestion program itself consisted in a 10-min gradual increase in temperature to 200 °C, a 15-min step at 200 °C (1000 W; 10^6 Pa) and then a ventilated cooling stage. This program was chosen in agreement with manufacturer recommendations and earlier studies on microwave-assisted digestion optimisation [9,33,34].

After cooling to room temperature, all the digests from the four procedures were filtered through a 0.45-µm PTFE minisart SRP filter (Sartorius, Vivascience, Germany) and then evaporated on a hot plate set at 60 °C. Evaporation was a necessary step since acid concentrations would have been too high for the ICP-AES and would have required dilutions to take place to such an extent that trace element could not have been detected. Care was taken to avoid burning
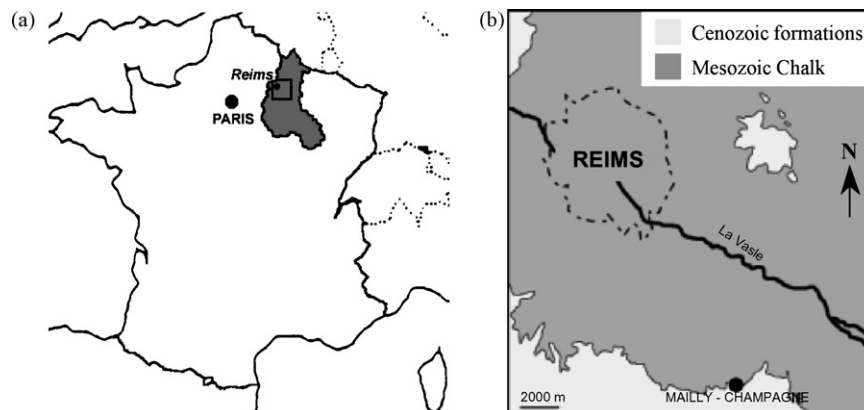
Fig. 1. Location of (a) the Champagne wine-producing region in France and (b) Mailly-Champagne, SE of Reims.

Parameter (unit)	Value
RF power (W)	1150
Plasma flow (L min^{-1})	14
Auxiliary flow (L min^{-1})	0.5
Nebulizer model	Cross-flow
Nebulizer flow (PSI)	28.0
Sample flow (mL min^{-1})	1.85
Rinse delay (s)	40
Read delay per replicate (s)	60
Number of replicates	3
Measurement processing mode	Area
Wavelengths (nm)	
Al	**237.312**–308.215
Cd	**214.438**–226.502
Co	**228.616**–237.862
Cr	**267.716**–**283.563**
Cu	224.700–**324.754**
Fe	**238.204**–**259.940**
Mn	**257.610**–**260.569**
Pb	220.353
Zn	**206.200**–**213.856**

Values in bold indicate wavelengths chosen.

of the evaporation residues. Residues were dissolved into a 0.9 mL 36% HCl and 0.3 mL 69% HNO$_3$ solution. Solutions were diluted to 50 mL with ultrapure water, resulting in HCl and HNO$_3$ concentrations of 0.58 mol L^{-1} and 0.14 mol L^{-1}, respectively. Solutions were stored in polyethylene vials at 4 °C until analysis.

2.4. Instrumentation

A pressurised closed-vessel microwave system (Ethos Touch Control, Milestone, USA) was used to digest the samples. It is equipped with a 10-position rotor (SK 10 T) and self-regulates its power to reach and maintain specified pressure and temperature. This last parameter was controlled by a sensor placed into one of the vessels.

Sample solutions were then analysed by ICP-AES (Iris Advantage, Thermo Jarrell Ash Corp., USA). A 100 mg L^{-1} multielement standard solution (Plasma Cal, SCP Science, Canada) was diluted to produce five calibration solutions containing 0 mg L^{-1}, 0.5 mg L^{-1}, 1 mg L^{-1}, 2 mg L^{-1} and 3 mg L^{-1} of elements, respectively. ICP-AES operating conditions and measured wavelengths are presented in Table 2. Three measurements were made at two wavelengths, apart for Pb. If one wavelength was affected by interferences, only the other one was considered and element concentration was given as the mean concentrations of three measurements (Cd, Co, Cu). In the case of both wavelengths being chosen, concentration was calcu-

lated as the mean of the two results (i.e. six measurements; Al, Cr, Fe, Mn, Zn).

3. Results and discussion

3.1. Detection and quantitation limits

Limits of detection (LOD) and limits of quantitation (LOQ) were calculated, over 10 measurements of the chemical blank from each procedure, as 3σ and 10σ, respectively [35]. Values are presented in Table 3. LODs ranged from 0.5 µg L^{-1} to 30 µg L^{-1} and LOQs from 2 µg L^{-1} to 99 µg L^{-1}, apart for Al with LOD and LOQ values of 59 µg L^{-1} and 195 µg L^{-1}, respectively. Both LOD and LOQ values were low and comparable with those calculated by Sandroni and Smith [9], who also used ICP-AES. However, Sandroni and Smith [9] limits were lower since they based their calculations on analytical blanks instead of chemical blanks in our study. Chemical blanks, unlike analytical blanks, are subjected to digestion procedures and are, thus, expected to provide higher LOD and LOD values.

3.2. Procedure repeatability

The term repeatability is generally used to quantify the closeness of the results obtained under the same conditions [36]. A natural soil sample was digested and analysed in triplicates for each procedure in order to calculate the relative standard deviation (R.S.D.) and therefore, the chemical and analytical repeatabilities. The deliberate choice of a natural sample corresponded to the worst possible conditions since it is less homogeneous than reference materials and could provide higher R.S.D. values.

In most cases, R.S.D. values were lower than 5% (Table 4). Some ranged from 7% to 13% (Cu and Pb following Procedures 1 and 3; Fe following Procedure 3). All these values were extremely satisfactory to very acceptable since they concerned triplicates of a natural complex matrix sample [36]. Moreover, they compared well with similar studies [4,5,9].

On the other hand, Procedure 3 gave very high R.S.D. value for Al (29.7%; Table 4) which was probably due to the very low Al concentration as a result of Al–F complex formation and/or inclusion of unknown amounts of Al in Ca–F complexes [9,12]. These complexes and the elements they contained could have been filtered out at the end of the procedure. High R.S.D. for Pb following Procedure 4 (48.3%) could be explained by an external contamination of one of the triplicates. Lead concentration for this sample was calculated as the mean of the other two triplicates. This value for Pb following Procedure 4 was used in the rest of the study. Other element concentrations for this natural sample were calculated as the mean of the triplicates ± S.D.

Table 3
Limits of detection and quantitation (LOD/LOQ; µg L^{-1}) for the 4 procedures after ICP-AES analysis

	Cd	Co	Cr	Cu	Pb	Zn	Mn	Al	Fe
Procedure 1: HCl–HNO$_3$–H$_2$O$_2$–HF	0.5/2	2/6	30/99	4/14	10/33	2/8	1/2	25/83	7/24
Procedure 2: HCl–HNO$_3$–H$_2$O$_2$	1/3	2/7	25/84	5/15	9/29	3/10	1/2	48/160	2/5
Procedure 3: HCl–HNO$_3$–HF	1/3	1/4	24/81	3/9	8/26	3/9	1/2	42/141	1/5
Procedure 4: HCl–HNO$_3$	1/3	2/8	26/85	3/10	7/24	4/12	1/2	59/195	2/5

Table 4
Chemical and analytical repeatability (σ/mean; R.S.D., %) obtained from a natural soil sample triplicate

	Al	Cd	Co	Cr	Cu	Fe	Mn	Pb	Zn
Procedure 1: HCl–HNO$_3$–H$_2$O$_2$–HF	4.6	1.2	0.3	1.6	12.6	1.3	0.7	7.3	1.0
Procedure 2: HCl–HNO$_3$–H$_2$O$_2$	3.0	1.2	0.9	0.7	4.6	4.2	1.5	3.8	0.7
Procedure 3: HCl–HNO$_3$–HF	29.7	2.0	5.4	1.8	8.3	9.1	1.5	9.2	2.1
Procedure 4: HCl–HNO$_3$	4.3	5.8	4.0	1.4	3.5	6.1	3.1	48.3	3.4

3.3. Procedure recovery

CRM 141R concentrations obtained after the four digestion procedures were compared to the BCR certified total contents (Table 5.). These certified concentrations were obtained following different digestion procedures on open hot plate systems, generally involving the use of HNO_3–HF–$HClO_4$ and sometimes H_2O_2, H_2SO_4 or H_3BO_3 [31]. Solutions were analysed using various analytical techniques.

Recoveries were calculated as [(measured value/certified total value) × 100]. Most results showed good agreement between measured and certified total concentrations with values ranging from 89% to 111% (Table 5). These recoveries agreed with similar studies where CRM 141R [5,8,22] and other certified calcareous materials [7,11,34,37] were digested using various digestion procedures.

A review of the available literature showed that calcareous soil digestion using HF often resulted in inacceptably elevated or low recoveries depending on the element. In our study, Cd and Co were relatively overestimated following procedures using HF (116% for Cd following Procedure 3, 124% and 140% for Co following Procedures 1 and 3, respectively). Adamo et al. [22] also found elevated recoveries of Cd and Co (147% and 115%, respectively) in CRM 141R digested with HF. Elevated recoveries of Co were probably due to interferences on Co wavelength 228.616 nm when HF was used. In other studies, digestion of CRM 141R using HF led to elevated recoveries of Cu, Ni and Pb of 139%, 144% and 173%, respectively [22,24,30]. Moreover, digestion of other calcareous reference materials using HF also resulted in inacceptably elevated recoveries of Cd, Cr, Cu, Mg and Ni of 118%, 118%, 126%, 133% and 129%, respectively [9,12].

On the other hand, Al recoveries were very poor in presence of HF (<5% following Procedures 1 and 3; Table 5) due to the formation of Al–F complexes and/or inclusion of Al in Ca–F complexes [9,12]. Other studies showed that digestion of CRM 141R using HF led to recoveries of Cd, Cr and Mn of 78%, 77% and 74%, respectively [22,24]. Digestion of other calcareous reference materials using HF also resulted in inappropriately low recoveries of Cr, Mg and Fe of 61, 45% and 56%, respectively [9,12]. Perchloric acid ($HClO_4$) or H_3BO_3 could be added to prevent complex formation [4,7,8,37]. In our study, recoveries of all the other elements following procedures using HF proved that use of $HClO_4$ or H_3BO_3 was not indispensable, as stated by other authors [9,34].

In absence of HF, Fe was slightly overestimated (114% following Procedure 2). On the other hand, Al, Cr and Pb showed low recoveries indicating that digestions for these elements were incomplete when no HF was added. Chromium and Pb showed recoveries ranging from 82% to 87%. Other calcareous reference materials showed similar recoveries (e.g., Pb recovery of 84% for CRM 320) when digested without HF [13,21]. Aluminium was a more problematic element with largely insufficient recoveries (72% and 63%, respectively).

Moreover, in the literature, calcareous soil digestion without HF produced better results than procedures using HF, with recoveries generally ranging from 80% to 114% and from 45% to 173%, respectively, depending on the reference material and the element [5,8,13,21]. In comparison, recoveries from our study were satisfying for Cd, Cr, Cu, Fe, Mn, Pb and Zn, with ranges from 82% to 116% independently of the procedure used (Table 5).

To summarize, recoveries from Procedures 1 and 3 and literature review showed that HF should not be added when digesting calcareous soil to avoid complex formation and interferences [4,7–9,12,22,24,30,37]. Therefore, Procedures 2 and 4, showing similar recoveries, provided the best results for multielemental determination.

On the other hand, studies on non-calcareous materials showed recoveries ranging from 85% to 118% when HF was used and from

Table 5
Results and recoveries obtained for CRM 141R (calcareous loam soil; BCR) after four digestion procedures and ICP-AES analysis

		Al (wt.%)	Cd (mg kg⁻¹)	Co (mg kg⁻¹)	Cr (mg kg⁻¹)	Cu (mg kg⁻¹)	Fe (wt.%)	Mn (mg kg⁻¹)	Pb (mg kg⁻¹)	Zn (mg kg⁻¹)
Certified values	Total content	5.09 ± 0.22	14.6 ± 0.5	10.5 ± 0.4	195 ± 7	46.4 ± 1.8	2.73 ± 0.10	683 ± 16	57.2 ± 1.2	283 ± 5
Procedure 1: HCl–HNO₃–HF–H₂O₂	Obtained value	0.22 ± 0.01	15.4 ± 0.1	13.1 ± 0.1	173 ± 3	44.0 ± 0.5	2.95 ± 0.06	696 ± 21	57.9 ± 0.1	286 ± 7
	Recovery	*4%*	**105%**	*124%*	*89%*	**95%**	**108%**	**102%**	**101%**	**101%**
Procedure 2: HCl–HNO₃–H₂O₂	Obtained value	3.67 ± 0.22	15.3 ± 0.1	11.0 ± 0.1	167 ± 5	44.4 ± 0.4	3.11 ± 0.06	622 ± 35	49.9 ± 1.5	290 ± 6
	Recovery	*72%*	**105%**	**104%**	*86%*	**96%**	*114%*	**91%**	*87%*	**102%**
Procedure 3: HCl–HNO₃–HF	Obtained value	0.02 ± 0.01	16.9 ± 0.4	14.7 ± 0.1	192 ± 1	44.4 ± 0.7	3.02 ± 0.08	692 ± 28	62.5 ± 2.3	309 ± 3
	Recovery	*0.5%*	*116%*	*140%*	**99%**	**96%**	*111%*	**101%**	*109%*	*109%*
Procedure 4: HCl–HNO₃	Obtained value	3.22 ± 0.06	14.4 ± 0.1	10.3 ± 0.1	164 ± 6	43.5 ± 0.1	2.58 ± 0.04	608 ± 33	46.9 ± 0.4	284 ± 12
	Recovery	*63%*	**98%**	**98%**	*84%*	**94%**	**94%**	**89%**	*82%*	**101%**

Values in bold indicate recoveries; values in italics indicate unsatisfactory recoveries.

80% to 119% without HF [4,5,8,13,29]. These values indicated that non-calcareous materials could be digested with or without the use of HF providing suitable results for a wide range of elements. Recoveries derived from calcareous and non-calcareous materials emphasized the issues associated specifically to digestion of the formers.

3.4. Procedure comparison for natural soil samples

The four procedures were tested using five natural soil samples from the studied vineyard plot as their matrix differed from that of reference materials. This could result in different matrix effects or analytical interferences.

The main difference could again be made between procedures using HF or not (Fig. 2). Those using HF (Procedures 1 and 3) showed, in general, higher concentrations which could be correlated to more complete digestion of environmental samples by adding HF or to interferences during spectrochemical analysis. This was particu-

larly the case for Cd, Co, Cr, Pb, and to a lesser extent Zn and Mn (Fig. 2). Hydrofluoric acid had a strong influence on microwave-assisted digestion since it breaks down silicates and enhanced results [4,5,7,34]. Its use could, however, also result in interferences with a range of elements [9,12,22,24,30].

In the case of Al, the use of HF and subsequent formation of F complexes caused Al to be nearly undetectable in natural samples (Procedures 1 and 3; Fig. 2a). However, results from Procedures 2 and 4 should be considered with caution since digestions were possibly incomplete (i.e. Al present in aluminosilicates not destructed in HF absence).

Results for Cu were not as marked, all procedures giving similar results (Fig. 2e). This leaves a wide choice of procedures when aiming at measuring Cu.

Procedure 2 gave the highest Fe concentrations (Fig. 2f). However, recoveries have shown an overestimation of Fe following Procedure 2 (Table 5). Procedures 1 and 3, which showed acceptable recoveries, gave the best results due to silicate destruction by HF.
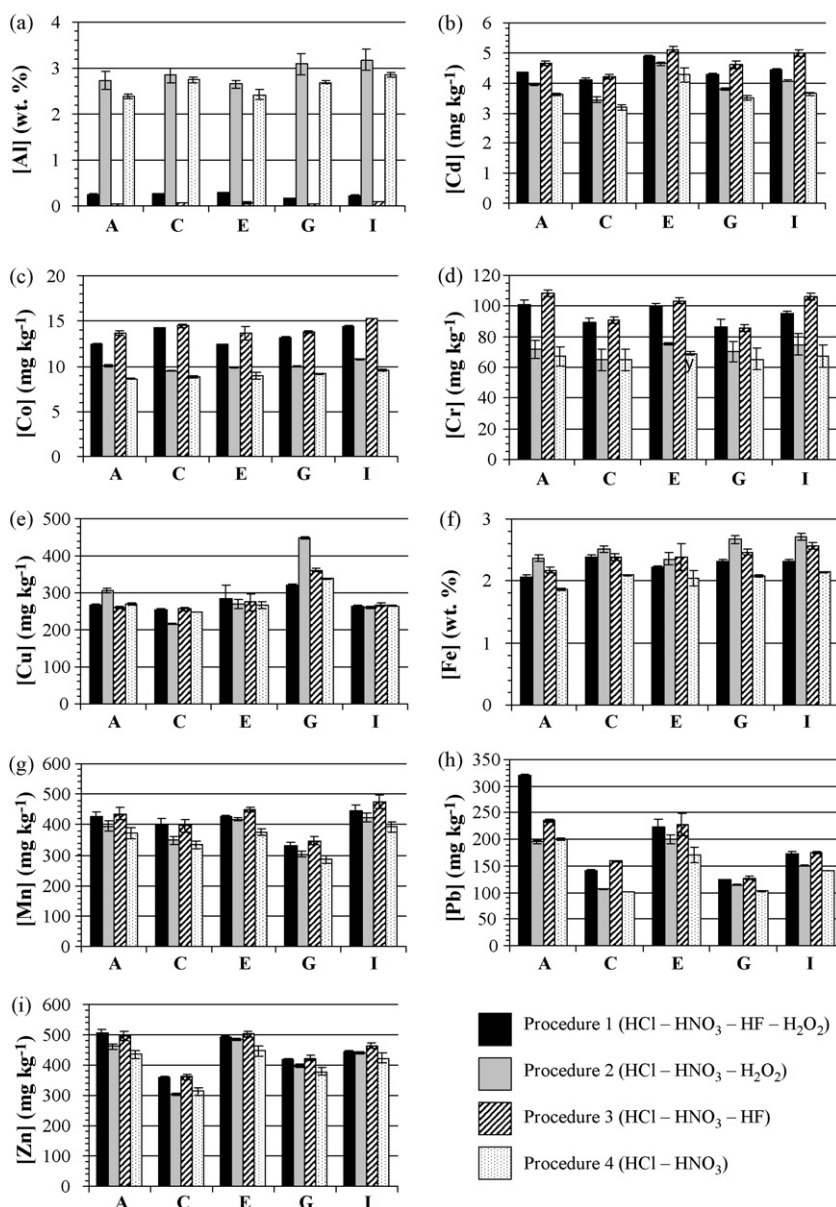
Fig. 2. Comparison of trace and major element concentrations in calcareous soils (A–I) given by four microwave-assisted digestion procedures (Procedures 1–4).

Table 6
Total soil trace element concentrations in a vineyard calcareous plot and French threshold values

Element values	Mean concentration ± standard deviation[a] (mg kg^{-1})	French threshold[b] (mg kg^{-1})
Cd	3.65 ± 0.39	2
Cr	67 ± 2	100
Cu	278 ± 35	100
Pb	143 ± 43	100
Zn	400 ± 55	300

[a] Calculated as mean (±standard deviation) of data obtained in vineyard soil samples with Procedure 4 (HCl–HNO$_3$; n = 5).

[b] AFNOR [39].

Overall, Procedures 1 and 3 gave similar results though higher for Procedure 3 (e.g., Cd, Cr, Co; Fig. 2). This was probably due to different volumes of HF being used, 1 mL and 2 mL for Procedures 1 and 3, respectively. Two millilitres were still an acceptable volume when considering instrumentation protection [9].

Depending on the elements to be studied, procedures should be chosen considering both the recoveries for the reference material and the results from natural samples. In the case of multielemental environmental study, the procedures using HF should be avoided due to overestimation of certain elements and severe underestimation of Al following complex formation. Only slight differences could be found between results from Procedures 2 and 4 (Fig. 2). Thus, adding H$_2$O$_2$ seems useless as previously mentioned by Sandroni et al. [12]. Nitric acid was totally capable of breaking down all organic matter present in the samples (<10% in our samples; [5]). In this case, Procedure 4 (*Aqua regia*, HCl–HNO$_3$) appeared the most suitable procedure for calcareous soil digestion.

3.5. Trace element concentrations for a vineyard plot

Overall trace element concentrations were calculated for the vineyard plot as the mean ± S.D. (n = 5) of concentrations from Procedure 4 (Table 6). Concentrations were elevated when compared to the world average trace element concentrations in non-contaminated surface soils (20 mg kg^{-1} Cu, 29 mg kg^{-1} Pb and 64 mg kg^{-1} Zn; [38]). Moreover, they overall displayed concentrations exceeding French quality guideline values (Table 6; [39]), which are used as thresholds for metal concentrations above which soils are unsuitable for sewage sludge application and, therefore, considered to be contaminated.

Trace multielemental contamination derived from combined urban waste application and yearly copper-based fungicide treatments (i.e. Bordeaux mixture Ca(OH)$_2$ + CuSO$_4$) to prevent mildew. Urban wastes were applied in our studied plot before planting in 1986 to improve soil stability since Champagne vineyard soils are susceptible to erosion. As it was a major source of trace element contamination, urban waste applications have been prohibited since 1993 [3,6]. Total soil concentrations were comparable to those found in other wine-growing regions [16,19], except for Brazilian vineyard soils with very high contents (up to 3216 mg kg^{-1} Cu; [28]).

Elevated concentrations of certain trace elements, when mobile, can cause great environmental concern by accumulating in and contaminating soils, vegetation, fauna or surface and groundwater [3,6,38]. Therefore, trace element partitioning will be investigated in order to determine their mobility and their environmental impact.

4. Conclusion

Total trace (Cd, Co, Cr, Cu, Mn, Pb and Zn) and major (Al and Fe) element concentrations in calcareous soils were determined using microwave-assisted digestion procedures and ICP-AES analysis. Four different digestion procedures using various HCl, HNO$_3$, H$_2$O$_2$ and HF combinations and volumes were tested.

Repeatabilities were extremely satisfactory (<5%) or very acceptable (7–13%). Most recoveries for CRM 141R ranged from 82% to 116%, except for Al (<5% with HF due to complex formation; <75% without HF due to incomplete digestion) and Co with HF (124–140% due to analytical interferences). However, digestion procedures for a calcareous reference material gave overall better recoveries without the use of HF. This was further confirmed by a literature review [5,8,13,21] and results derived from natural calcareous soil samples. Calcareous soil specificity with regards to HF resulted in questioning the appropriateness of HF use for calcareous material digestion, despite the many procedures found in the literature which are still often using it. Consequently, HF should be avoided in multielemental studies when digesting calcareous materials as it resulted in overestimation or underestimation of certain elements.

Procedure 4 (*Aqua regia*, HCl–HNO$_3$) gave the best compromise for the range of analysed elements in terms of result reliability, measured concentrations and safety considerations. It was selected for studies in a multielemental environmental context and, thus, will be used for further calcareous Champagne vineyard soil investigations.

References

[1] J.L. Fernandez-Turiel, P. Aceñolaza, M.E. Medina, J.F. Llorens, F. Sardi, Environ. Geochem. Health 23 (2001) 65.
[2] C.G. Lee, H.-T. Chon, M.C. Jung, Appl. Geochem. 16 (2001) 1377.
[3] H.M. Selim, D.L. Sparks (Eds.), Heavy Metals Release in Soils, Lewis Publishers, Boca Raton, FL, 2001, p. 249.
[4] S. Melaku, R. Dams, L. Moens, Anal. Chim. Acta 543 (2005) 117.
[5] J. Sastre, A. Sahuquillo, M. Vidal, G. Rauret, Anal. Chim. Acta 462 (2002) 59.
[6] B.J. Alloway, Heavy Metals in Soils, Blackie Academic & Professional, London, 1995, p. 368.
[7] D. McGrath, Talanta 46 (1998) 439.
[8] M. Bettinelli, G.M. Beone, S. Spezia, C. Baffi, Anal. Chim. Acta 424 (2000) 289.
[9] V. Sandroni, C.M.M. Smith, Anal. Chim. Acta 468 (2002) 335.
[10] M. Toribio, J.F. García, G. Rauret, R. Pilviö, M. Bickel, Anal. Chim. Acta 447 (2001) 179.
[11] A. Chatterjee, R.N. Banerjee, Sci. Total Environ. 227 (1999) 175.
[12] V. Sandroni, C.M.M. Smith, A. Donovan, Talanta 60 (2003) 715.
[13] U.S. Environmental Protection Agency, Microwave-Assisted Acid Dissolution of Sediments, Sludges, Soils and Oils, 2nd ed., USEPA Office of Solid Waste and Emergency Response, Washington, DC, 1996, p. 22.
[14] T. Chirenje, L.Q. Ma, M. Reeves, M. Szulczewski, Geoderma 119 (2004) 113.
[15] U. Pietrzak, D.C. McPhail, Geoderma 122 (2004) 151.
[16] L.A. Brun, J. Le Corff, J. Maillet, Environ. Pollut. 122 (2003) 361.
[17] D.H. McNear, R.L. Chaney, D.L. Sparks, Geochem. Cosmochem. Acta 71 (2007) 2190.
[18] M.C. Ramos, J. Environ. Manage. 78 (2006) 209.
[19] O. Schrammel, B. Michalke, A. Kettrup, Sci. Total Environ. 263 (2000) 11.
[20] P. Tume, J. Bech, L. Longan, L. Tume, F. Reverter, B. Sepulveda, Ecol. Eng. 27 (2006) 145.
[21] B. Vandecasteele, B. De Vos, F.M.G. Tack, Environ. Pollut. 122 (2003) 7.
[22] P. Adamo, M. Arienzo, M.R. Bianco, F. Terribile, P. Violante, Sci. Total Environ. 295 (2002) 17.
[23] D. Rusjan, M. Strlič, D. Pucko, Z. Korošec-Koruza, Geoderma 141 (2007) 111.
[24] I. Maiz, M.V. Esnaola, E. Millán, Sci. Total Environ. 206 (1997) 107.
[25] S. Van Herreweghe, R. Swennen, V. Cappuyns, C. Vandecasteele, J. Geochem. Explor. 76 (2002) 113.
[26] M. Kaplan, S. Orman, I. Kadar, J. Koncz, Agric. Ecosyst. Environ. 111 (2005) 41.
[27] M.-H. Feng, X.-Q. Shan, S. Zhang, B. Wen, Environ. Pollut. 137 (2005) 231.
[28] N. Mirlean, A. Roisenberg, J.O. Chies, Environ. Pollut. 149 (2007) 10.
[29] L. Hernandez, A. Probst, J.L. Probst, E. Ulrich, Sci. Total Environ. 312 (2003) 195.

[30] E. Campos, E. Barahona, M. Lachica, M.D. Mingorance, Anal. Chim. Acta 369 (1998) 235.

[31] P. Quevauviller, H. Muntau, U. Fortunati, K. Vercoutere, The certification of the total contents (mass fractions) of Cd, Co, Cr, Cu, Hg, Mn, Ni, Pb and Zn and the *Aqua regia* soluble contents (mass fractions) of Cd, Co, Cr, Cu, Hg, Mn, Ni, Pb and Zn in a calcareous loam soil CRM 141R, BCR Information, European Commission, 1996, p. 80.

[32] EPA 3052, Microwave-assisted acid digestion of siliceous and organically based matrices, EPA, 1996, p. 20.

[33] Milestone, Digestion Application Note, Soil Total Digestion, Milestone Editions 1.2i, 2004.

[34] C.Y. Zhou, M.K. Wong, L.L. Koh, Y.C. Wee, Anal. Chim. Acta 314 (1995) 121.

[35] C. Vandercasteele, C.B. Block (Eds.), Modern Methods in Trace Elements Determination, Wiley, New York, 1993.

[36] B. Marin, M. Valladon, M. Polve, A. Monaco, Anal. Chim. Acta 342 (1997) 91.

[37] P. Navarro, J.C. Raposo, G. Arana, N. Etxebarria, Anal. Chim. Acta 566 (2006) 37.

[38] A. Kabata-Pendias, H. Pendias, Trace Elements in Soils and Plants, CRC Press, Boca Raton, 2001, p. 432.

[39] AFNOR, Qualité des sols, Recueil de normes françaises, Paris, 1996, p. 534.

A novel biamperometric biosensor for urinary oxalate determination using flow-injection analysis

Stjepan Milardović*, Irena Kereković, Marijana Nodilo

Department of General and Inorganic Chemistry, Faculty of Chemical Engineering and Technology, University of Zagreb, Marulićev trg 19, HR-10000 Zagreb, Croatia

ABSTRACT

A biosensor for determination of oxalate concentration in urine has been developed by immobilisation of oxalate oxidase and peroxidase on the surface of an interdigitated gold electrode. Enzyme immobilisation was performed using BSA and glutaraldehyde. Biamperometric measurements were made in flow conditions both in aqueous oxalate solutions (tested concentration range between 50 μM and 10 mM) and in real urine samples (tested measuring range between 5 and 100 μM). Optimal working conditions were examined for flow-injection analysis, and good correlation was achieved between added oxalate quantity and the one measured by biosensor in urine matrix ($R^2 = 0.9983$). The influence of some interferences (ascorbic acid, uric acid, paracetamol, acetylsalicylic acid) was also studied using biamperometric measurement mode.

© 2008 Elsevier B.V. All rights reserved.

1. Introduction

Calcium oxalate is the main component of urinary tract stones. Basically, oxalate is a product of protein metabolism and becomes toxic at high concentration due to production of insoluble complex salts with divalent cations (mainly calcium). Determination of oxalates in urine is important for diagnosis of many diseases and mostly indicates the presence of kidney stones. Many methods have been recommended for oxalate determination in clinical laboratory analyses but some of them are time-consuming [1] (as chromatographic and spectrophotometric) while some others need a chemically pre-treated sample [2].

Enzyme-based biosensors are user-friendly devices offering good analytical precision, specificity, sufficiently short response time and durability. Amperometric biosensors have been used routinely for metabolite determination in biochemical laboratories since 1975.

Two enzymes catalyse oxalate degradation: oxalate decarboxylase and oxalate oxidase. Bioreactions of oxalate in the presence of oxalate oxidase can be described by Eq. (1):
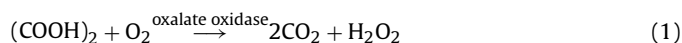
$$(COOH)_2 + O_2 \xrightarrow{\text{oxalate oxidase}} 2CO_2 + H_2O_2 \qquad (1)$$

According to Eq. (1) oxalate concentration is proportional to carbon dioxide and hydrogen peroxide concentration. Therefore, some of previously developed oxalate biosensors were based on pCO$_2$ or pH measurements [3] (pH changes proportionally with released CO$_2$). Amperometric-based oxalate biosensors mainly determine hydrogen peroxide concentration [4]. Some other biosensors are based on measurements of oxygen consumption during oxalate presence [5].

Hansen et al. suggested urinary oxalate determination by oxalate oxidase immobilised on silanised glass beads and chemiluminescence detection of hydrogen peroxide with luminol [6].

An amperometric biosensor for oxalate determination based on immobilisation of oxalate oxidase in gelatine using glutaraldehyde on top of the oxygen probe was reported by Dinçkaya and Telefoncu [7].

Reddy et al. described a biosensor for determination of human urinary oxalates [8]. They co-immobilised oxalate oxidase in bovine serum albumin by glutaraldehyde, between haemodialysis and cellulose acetate membrane, to prevent some chemical and electrochemical interferences.

Recently Capra et al. described an enzymatic electrode for oxalate determination with extended analytical range and better stability [9]. Quantification of oxalic acid in urine by employing an amperometric Clarck-type electrode imprinted by spinach tissue layer was suggested by Sezgintürk and Dinçkaya [10]. Bienzymatic amperometric biosensor for oxalate determination was described by Perez et al. [11]. Sotomayor et al. proposed bienzymatic optode as a detection system for oxalate determination [12],

---

while Pundir offered oxalate bienzymatic biosensor obtained by co-immobilisation of oxalate oxidase and peroxidase into glass beads [13].

Electrochemical determination of oxalate at pyrolytic graphite electrode was described by Sjukić et al. [14]. Stefan et al. described an oxalate ion selective electrode for determination of urinary oxalate [15].

Biamperometric detection has been applied in flow-injection analysis because of high selectivity of measurements (low potential imposed between electrodes) and increased sensitivity as a result of low sample dispersion.

Biamperometry is based on detection with two identical working electrodes polarised with a small voltage difference in a solution containing indicating reversible redox couple. Direct biamperometric measurements exploit one part of the redox pair while the second part of the redox pair is produced by chemical or biochemical interaction with the analyte. The most used indicating systems [16], for biamperometric determination include $Fe^{3+}|Fe^{2+}$, $I_2|I^-$, $Br_2|Br^-$, $VO_3^-|VO^{2+}$, Ce (IV)|Ce (III) and $Fe(CN)_6^{3-}|Fe(CN)_6^{4-}$ and lately $DPPH^+|DPPH$ and $ABTS^+|ABTS$ redox couple [17,18]. The application of biamperometric detection for flow-injection analysis was proposed by Tougas et al. [19]. Due to high selectivity of the method, biamperometric measurements were used for determination of various analytes as components of complex biological samples (urine, blood) [20,21].

Application of a microelectrode with interdigitated array is an efficient method for miniaturisation of electrochemical sensors and biosensors because of the features such as rapid rise to steady state, high sensitivity and high current response.

Sanderson and Anderson explained the application of interdigitated electrode (IDE) as an electrochemical detector almost 20 years ago [22].

Carbon-based interdigitated array electrodes utilised for electrochemical measurements in batch mode and in flow system were studied by Morita et al. [23], while application of multi microelectrode array of eight different sizes for biological electrochemistry, was presented by Kudera et al. [24]. Application of interdigitated array electrodes for determination of enzyme activity was also described [25].

A detection system consisting of four pairs of thin gold interdigitated electrodes and two auxiliary electrodes fixed on micro-fluidic platform was described as a chip-based detector for rapid detection and quantification of nucleic acids [26]. Interdigitated ultra microelectrode arrays (IDUAs) as transducers in a portable micro-fluidic based biosensor were designed with the aim to maximise signal-to-noise ratio [27]. A chip with four separated parallel arrays of iridium-made ultra microelectrodes and miniaturized flow device for trace heavy metal measurements in water was proposed by Xie et al. [28].

In the present paper, a two-enzyme (bienzymatic) biosensor based on biamperometric determination of oxalate in urine is described. Oxalate oxidase enzyme immobilised on the surface of an interdigitated electrode converted oxalate to carbon dioxide and hydrogen peroxide according to Eq. (1).

Co-immobilised peroxidase catalysed the reaction between hexacyanoferrate(II) and hydrogen peroxide as indicated by Eq. (2). Hexacyanoferrate(II) was a component of the buffer carrier solution.

$$H_2O_2 + 2[Fe(CN)_6]^{4-} + 2H^+ \xrightarrow{peroxidase} 2H_2O + 2[Fe(CN)_6]^{3-} \qquad (2)$$
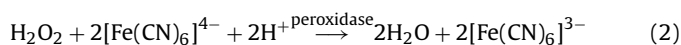
The produced hexacyanoferrate(III) was then reduced at the interdigitated electrode as denoted by Eq. (3).

$$[Fe(CN)_6]^{3-} + e^- \rightarrow [Fe(CN)_6]^{4-} \qquad (3)$$

Biamperometric current was proportional to hexacyanoferrate(III) concentration and thus also to oxalate concentration. Biamperometric measurement mode was used to avoid some electrochemical interferences. Optimisation of pH, flow rate, hexacyanoferrate(II) concentration and working potential was made to obtain good current sensitivity and to perform oxalate determination in flow-injection analysis. The influence of urine dilution on the proper working of biosensor was also studied.

2. Materials and methods

2.1. Chemicals and reagents

Commercially available chemicals of the highest purity were used. Oxalate oxidase (from barley seedlings, lyophilised powder, 0.70 units mg^{-1} solid), peroxidase (147 U mg^{-1}), bovine serum albumin (BSA), glutaraldehyde (GLA, mass fraction 25%) were obtained from Sigma–Aldrich (USA). Potassium hexacyanoferrate(III) trihydrate, potassium hexacyanoferrate(II), succinic acid, oxalic acid dihydrate, hydrochloric acid, potassium chloride, disodiummethylenediamintetraacetic acid dihydrate, L (+) ascorbic acid, uric acid and ethanol (96%) were from Kemika, Croatia. Paracetamol (from a Panadol pill) and acetylsalicylic acid (from an aspirin pill) were from Glaxo SmithKline, Croatia.

Deionised water was purified using a Milipore-MilliQ system.

2.2. Electrode preparation

Interdigitated electrode (IDE) IME 1525.3 FD Au P (ABTCH, Richmond, USA) was employed as a supporting electrode.

Prior to measurement, the interdigitated electrodes were cleaned and preconditioned according to manufacturer's recommendations. The conditioning was made in 0.8 M sulphuric acid by 3-fold cycling in the potential range between 600 and 1000 mV using 50 mV s^{-1} scan rate. The preconditioning was repeated for each part of the IDE pair using $Hg_2Cl_2|3$ M KCl as a reference electrode, and a disc glassy carbon electrode as an auxiliary electrode.

Oxalate oxidase and peroxidase were co-immobilised by glutaraldehyde-bovine serum albumin cross-linking procedure on top of the gold interdigitated electrode array. Two-enzyme layer was prepared by mixing 0.3 mg oxalate oxidase and 0.3 mg peroxidase into 20 μL 10% bovine serum albumin solution (BSA (M(BSA)) = 45,000 g mol^{-1}; solution prepared by dissolving 100 mg BSA in 1 mL of succinic buffer, pH 3.6). The solution was homogenised for 30 min. After 30 min, the albumin–enzyme solution was well mixed with 10 μL 5% glutaraldehyde and finally 2 μL of this mixture were deposited by micropipette on top of IDE and left to dry. Thus, prepared enzyme electrode was conditioned overnight in succinic buffer solution (pH 3.8) at 7 °C.

2.3. Urine samples

The urine samples were taken daily.

Biosensor testing was performed by recovery test (amount added *vs.* amount found) based on addition of the known concentration of oxalic acid to urine samples with very low natural oxalate content (after dilution, c(oxalate) < 1 μM).

2.4. Apparatus

Electrochemical measurements were carried out on the Potentiostat 273 A (Princeton Applied Research, USA) connected to the computer for data collection and analysis. Interdigitated electrode (IDE) IME 1525.3 FD Au P (ABTCH, Richmond, USA) was coated
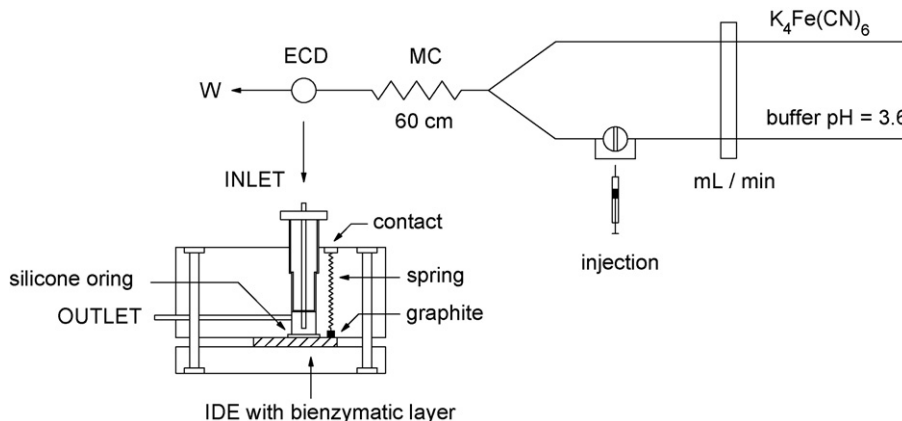
Fig. 1. Schematic presentation of optimized FIA device used for oxalate determination and the scheme of applied flow measuring cell. MC—mixing coil, ECD—electrochemical detector, W—waste.

by co-immobilised enzyme layer. The electrode is a microlitographically fabricated sensor chip consisting of two separated working gold electrode arrays on the chip ($6.4\,mm \times 5.5\,mm$, digit length (W_a) = 2.985 mm, digit width (W_g) = 15 μm, interdigit space (W) = 15 μm and the number of digit pairs = 25). For current–time measurements, a pair of interdigitated electrodes fixed in a flow-through measurement cell was used. Transportation of the carrier solution in FIA mode (Fig. 1) was made by double tubing peristaltic pump. Sample injection into carrier stream was done by a syringe using injector valve Rheodyne Model 7125 and sample loops of 10 μL and 100 μL. Knitted coil reactor was made using a Teflon tube (1 mm in diameter, 60 cm long).

Homogenisation of enzyme–BSA layer was done using ultrasonic mixer Transsonic 460/H, Elma, Germany, pH electrode (Blueline 17 pH, pH 0–14/−5 100 °C/3 M KCl, SCHOTT, Germany) and pH-meter MA 574O, Iskra, Slovenia.

3. Results and discussion

Fig. 2a shows *I–E* curves characteristic for $[Fe(CN)_6]^{4-}|[Fe(CN)_6]^{3-}$ redox pair determined in a classic electrochemical cell (batch mode) using the interdigitated electrode in biamperometric measurement mode. 1 mL 20 mM $K_4[Fe(CN)_6]$ was added to succinic buffer solution (8 mL 200 mM, pH 3.6) containing 50 mM EDTA and the curve designated as 0 was recorded. Curves 1–4 were recorded after successive addition of 100 μL 10 mM $K_3[Fe(CN)_6]$. According to Fig. 2a, there was insignificant current response due to existence of only $K_4[Fe(CN)_6]$ in the solution. The addition of $K_3[Fe(CN)_6]$ resulted in linear current response confirming that biamperometric response depends linearly on the concentration of $K_3[Fe(CN)_6]$, i.e. the response is proportional to that part of redox pair that is present in the solution at lower concentration. Fig. 2b represents calibration curve derived from Fig. 2a for potential of 100 mV. Five-point curve can be described with the following equation:

$$I = (0.0934 \pm 0.043)\,\mu A + (7.183 \pm 0.165)\,\mu A\,mM^{-1}$$

$$\cdot c(K_3[Fe(CN)_6])mM; \quad R^2 = 0.9992.$$

It is also notable that potential changes to higher values are followed by higher current response; however, at potentials higher than 100 mV, the difference in current response is negligible. According to Eq. (1), $[Fe(CN)_6]^{3-}$ concentration is proportional to oxalate concentration, confirming that IDE is suitable as a supporting electrode for oxalate biosensor construction.

3.1. Optimisation of the measuring system

It is well known that physiological concentration of oxalate is in the range between 50 and 2000 μM. Furthermore, many different species, contained in urine, strongly affect oxalate oxidase and therefore samples must be diluted to almost 20-fold, or even higher to avoid denaturation of the enzyme by constituents of urine matrix [6]. After dilution, oxalate concentrations in samples are in the range between 2.5 and 100 μM. In the case of flow-injection analysis, retention time of sample in the biosensor measuring cell is short, which also decreases the current response. Very low enzyme (oxalate oxidase) activity (production of hydrogen peroxide in small quantity per enzyme mass) causes further decrease of the current response. Thus, optimisation of the measurement system is required to obtain sufficient sensitivity of the developed biosensor.

3.1.1. Optimisation of potassium hexacyanoferrate(II) concentration

Optimal hexacyanoferrate(II) concentration was determined by injection 10 μL of 2 mM oxalate into the carrier stream containing succinic buffer pH 3.6. The applied potential difference to biosensor was 100 mV and the flow rate of 1.28 mL min^{-1} was used. Optimisa-
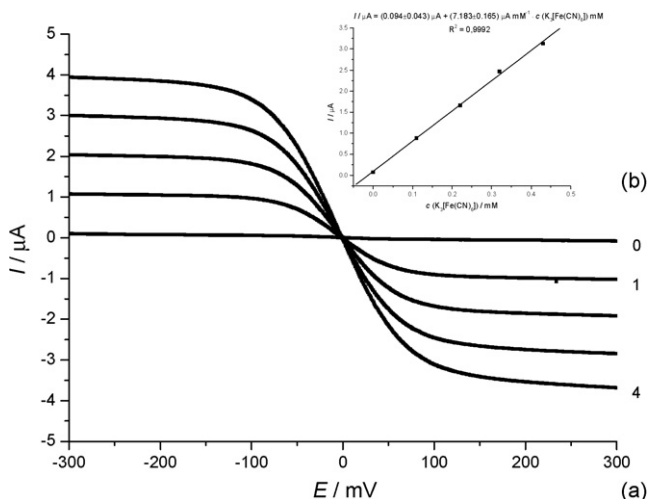
Fig. 2. (a) Biamperometric response of interdigitated electrode in the succinic buffer solution containing only $[Fe(CN)_6]^{4-}$ (curve 0) and after successive addition of $[Fe(CN)_6]^{3-}$ (curves 1–4) to the measurement cell. The scan rate used was 10 m V s^{-1}. (b) Calibration graph of hexacyanoferrate(III). Experimental conditions were the same as in (a).
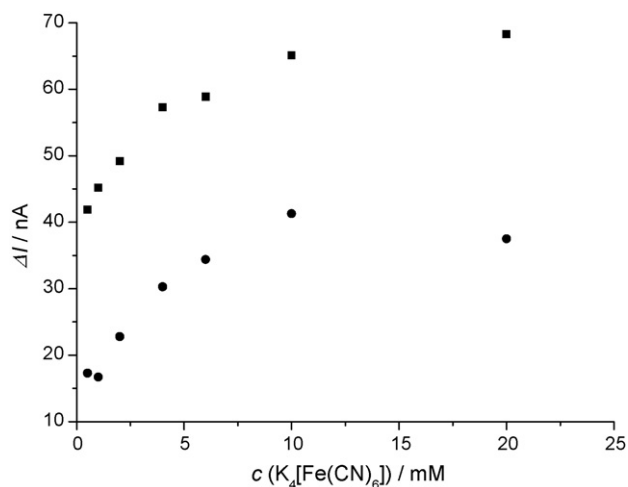
Fig. 3. Biosensor current response is shown as a function of potassium hexacyanoferrate(II) concentration. The applied potential was 100 mV, flow rate 1.28 mL min^{-1}, oxalate concentration 2 mM, injection volume 10 µL, carrier solution containing succinic buffer pH 3.6. The squares represent background current; the circles represent biosensor current peaks. The tested potassium hexacyanoferrate(II) concentration was in the range from 0.5 to 20 mM.

tion was done using biamperometric flow-injection analysis set-up (Fig. 1). The tested potassium hexacyanoferrate(II) concentrations were in the range from 0.5 to 20 mM.

The gradual increase in biosensor response was evident in the concentration range between 0.5 and 10 mM. Increasing concentration, of potassium hexacyanoferrate(II) above 10 mM (circle) cannot enhance current response (Fig. 3). Therefore, all subsequent experiments were done using 10 mM potassium hexacyanoferrate(II) concentration. The same gradual increase in background current (squares) was expected because concentrated potassium hexacyanoferrate(II) solutions contain an increased level of potassium hexacyanoferrate(III) produced by oxidation from air oxygen.

3.1.2. Optimisation of pH

Biosensor response obtained in succinic buffer solution with different pH values is shown in Fig. 4. Measurement conditions: working potential 100 mV, flow rate 1.28 mL min^{-1}, 10 mM K$_4$[Fe(CN)$_6$], oxalate concentration 2 mM, injected volume 10 µL. The tested pH values were in the range from 3.07 to 5.61.
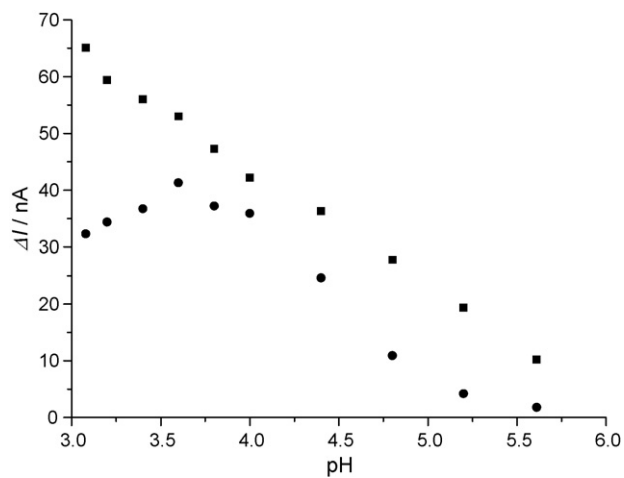
Fig. 4. pH influence on oxalate biosensor response. The squares represent background current, the circles represent biosensor current peaks.
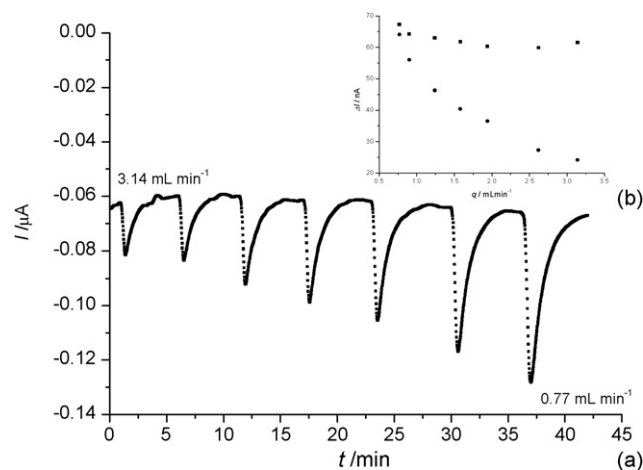
Fig. 5. (a) Influence of flow rates to oxalate biosensor response. Experimental conditions: working potential 100 mV, carrier solution (0.1 M succinic buffer pH 3.6 and 10 mM K$_4$[Fe(CN)$_6$], injection volume 10 µL, oxalate concentration 2 mM. (b) Peak currents (circles) and background currents (squares) determined in Fig. 5a were used.

The current peak height–pH graph shows the highest value at pH 3.6 and linear decrease at increased pH values (circles). Background current (squares) decreases linearly with increasing pH because redox air oxygen potential lowers by 59 mV pH^{-1} reducing the production of [Fe(CN)$_6$]$^{3-}$. Background current becomes negligible at pH 7. Despite the fact that the background current has no influence on the proper working of a developed biosensor, it can be strongly reduced by simple buffer deoxygenation.

According to literature, optimum pH for peroxidase is in the range between pH 6 and 6.5 and for oxalate oxidase between 3.8 and 4. The highest biosensor response is close to the pH optimum of oxalate oxidase indicating that the produced hydrogen peroxide concentration is low due to low oxalate oxidase activity, and becomes a limiting reagent for further enzymatic reactions with peroxidase. To obtain the highest biosensor response, the pH values of tested urine samples were adjusted to a value compatible with the pH maximum of the immobilised enzymes (pH 3.6). Peroxidase was co-immobilised onto the electrode due to signal amplification because of great sensitivity to H$_2$O$_2$ [29], even at very small concentration. Activity of peroxidase is reduced in acidic medium and thus the applied activity of the used peroxidase enzymes was increased (2.94 U/electrode) than the activity of the utilised oxalate oxidase (0.014 U/electrode). Amounts of immobilised enzymes were selected according to enzymatic assay solution for oxalate determination (Sigma, USA) [31].

Succinic buffer and EDTA were used as the oxalate oxidase activators, based on the literature overview of biosensor applications [9]. Concentration of the used cross-linker was previously optimised [30].

3.1.3. Flow rate optimisation

The optimum flow rate was determined by injection of 10 µL 2 mM oxalate into the carrier stream containing succinic buffer (0.1 M) pH 3.6 and 10 mM K$_4$[Fe(CN)$_6$]. The working potential imposed to electrode was 100 mV and the tested flow rates ranged between 3.14 and 0.77 mL min^{-1} (Fig. 5a).

It is evident (Fig. 5b) that there was no influence of the flow rate on the background current (squares). However, the biosensor response rose as the flow rate decreased (circles). Increase of peak current at lower flow rate was the result of extended reaction time between biosensor enzymes and oxalate. A flow rate of 1.24 mL min^{-1} was chosen for further experiments because it
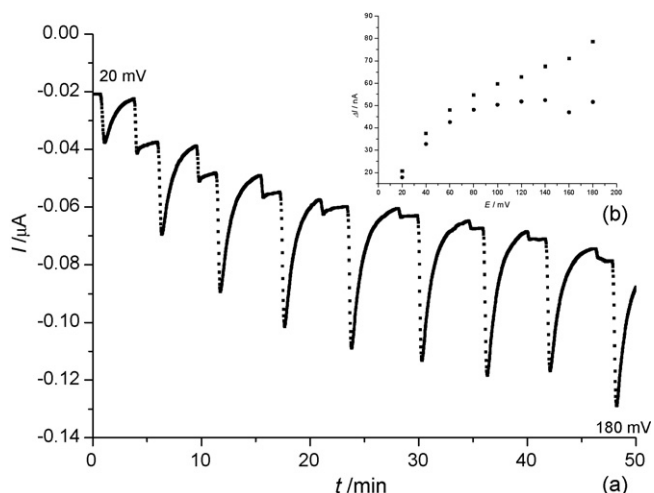
Fig. 6. (a) Current sensitivity of oxalate biosensor as a function of working potentials. Experimental conditions: carrier solution (0.1 M succinic buffer pH 3.6 and 10 mM $K_4[Fe(CN)_6]$, injection volume 10 μL, oxalate concentration 2 mM, flow rate 1.24 mL min^{-1}. Squares—background current, circles—peak current. Tested potential range: 20–180 mV.

offers sufficient current sensitivity and yields analytically acceptable response time (20 analyses per hour).

3.1.4. Optimisation of the working potential

The optimal working potential was determined by injection of 10 μL 2 mM oxalate into the carrier stream containing succinic buffer (0.1 M, pH 3.6) and 10 mM $K_4[Fe(CN)_6]$. The tested working potentials were in the range between 20 and 180 mV and the used flow rate was 1.24 mL min^{-1}.

As evident in Fig. 6a and b, the increase in potential was followed by a gradual increase in current response (circles). At the potentials higher than 100 mV, further current increase was insignificant and the potential of 100 mV was chosen for further experiments. The background current (squares) should show linear rise with potential according to the Ohm's law, but changes in the carrier solution resistance ($[Fe(CN)_6]^{3-}$ concentration rises with time) cause some deviation from linearity.

3.1.5. Biosensor calibration

After optimisation of various parameters, as described above, the biosensor was used for FIA calibration. Oxalate standards were prepared by serial dilution of a 0.1 M stock solution using succinic buffer pH 3.6. The testing range of oxalate concentration was between 25 μM and 10 mM.

A series of standard oxalate solutions were injected in triplicates, as shown in Fig. 7a.

The biosensor showed linearity in the range between 50 μM and 10 mM with injection volume of 10 μL. Such small volume of injected substrate caused enzyme saturation at high oxalate concentration, while very small current response was obvious in the urine oxalate range (10–200 μM). Fig. 7b shows the nine-point calibration curve derived from Fig. 7a, and it is represented with the following equation:

$$\Delta I = (-2.521 \pm 1.156)\,\text{nA} + (0.019 \pm 3.027 \cdot 10^{-4})\,\text{nA}\,\mu\text{M}^{-1}$$

$$\cdot c(\text{oxalate})\,\mu\text{M}; \quad R^2 = 0.9992$$

To obtain the higher current response in the range between 10 and 200 μM, the injection volume of 100 μL was used. Eight-point cali-
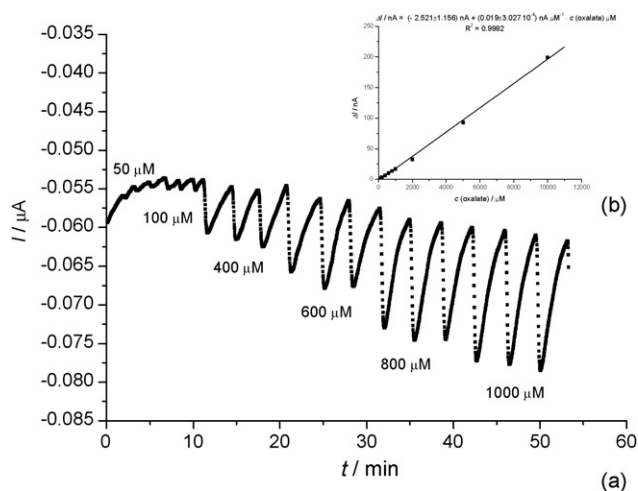
Fig. 7. (a) Diagram of oxalate biosensor obtained under optimised conditions. (b) represents calibration graph based on data from (a).

bration, made with sample loop of 100 μL, is denoted by equation:

$$\Delta I = (0.653 \pm 0.425)\,\text{nA} + (0.129 \pm 0.005)\,\text{nA}\,\mu\text{M}^{-1}$$

$$\cdot c(\text{oxalate})\,\mu\text{M}^{-1}; \quad R^2 = 0.9960$$

3.1.6. Influence of urine dilution

Achieving good linearity for aqueous standards did not improve the practical application of the developed biosensor for real sample measurements. Oxalate oxidase is inhibited by the sodium salts of chloride, phosphate, citrate and acetate which are the standard constituents of urine. To overcome that inhibitory influence, urine samples should be diluted before the measurement, as previously suggested [2,6].

The results of urine dilution on biosensor response for four dilution ratios (V(urine)/V(buffer); 1:3, 1:7, 1:11 and 1:19) are given in Table 1.

50 μM oxalate solutions were prepared with 4-, 8-, 12- and 20-fold diluted urine and succinic buffer–EDTA solution. Another 50 μM oxalate solutions were prepared using buffer–EDTA solution without urine. Both of the solutions were injected into the sample loop. The current response obtained in the solutions of diluted urine was compared with the current response obtained from buffer solutions. Only at 1:20 urine buffer ratio was the biosensor response equal for both prepared solutions.

3.1.7. Correlation of results using added-found method

Urine samples were taken daily fresh and were not preserved by concentrated HCl. Before preparation of urine–oxalate solutions, urine was 5-fold diluted by succinic buffer pH 3.8. A serial of oxalate urine solutions in the range 20–400 μM were prepared by sequential dilution of 0.1 M oxalate stock solution using 5-fold diluted urine. All prepared solutions were injected into the FIA system

Table 1
Influence of urine dilution on biosensor response

Dilution factor	I_s(urine)/I_s(buffer) (%)
4	63.2
8	86.0
10	89.0
20	99.8

Experimental conditions: working potential 100 mV, flow rate 1.24 mL min^{-1}, $c(K_4[Fe(CN)_6]) = 10$ mM, sample loop 100 μL, $c(\text{oxalate}) = 50$ μM, succinic buffer solution pH 3.6 containing 50 mM EDTA.

Table 2
Comparison of the oxalate concentration analytically prepared in urine and determined by the biosensor using buffer oxalate standards

c(sample, added, μM)	c(sample, found, μM)	c(oxalate in cell, added, μM)	c(oxalate in cell, found, μM)
20	14.20 ± 2.40	5	3.55 ± 0.60
40	36.10 ± 0.75	10	9.02 ± 0.19
60	64.16 ± 1.51	15	16.04 ± 0.38
80	79.60 ± 5.24	20	19.90 ± 1.31
100	94.92 ± 4.49	25	23.73 ± 1.12
150	150.10 ± 2.99	37.5	37.52 ± 0.75
200	185.64 ± 3.74	50	46.40 ± 0.94
400	384.51 ± 2.99	100	96.12 ± 0.75

Column 1—analytically prepared oxalate samples using 5-fold diluted urine, column 2—oxalate concentration determined by the biosensor, column 3—oxalate concentration in the measurement cell after 4-fold sample dilution, column 4—oxalate concentration in the measurement cell determined by the biosensor.

which additionally offered 4-fold sample dilution automatically (in total, a 20-fold dilution).

Oxalate determination in the solution prepared by 20-fold diluted urine is shown in diagram (Fig. 8a). Experimental conditions were the same as used before. Each sample was double injected.

The first two peaks indicate the biosensor response for pure, 20-fold diluted urine samples, while other peaks designate diluted urine samples with some added oxalate. The two peaks for the same concentration (Fig. 8a) are actually equal in height, however the second peak appears to be higher because of the background current variations.

Double curves (Fig. 8b) show the biosensor response to a series of oxalate solutions prepared in diluted urine. The curves have identical slope, however some differences in intercept are evident. Curve 1 (squares) was obtained by using ΔI as difference between peak current and background current for each tested concentration (y-axis) $vs.$ oxalate urine concentration (x-axis). Curve 2 (circles) was obtained by using ΔI as difference between Δ peak current and Δ peak current obtained in diluted urine (the sample without added oxalate) for all tested solutions.

The current obtained in diluted urine (first two peaks in Fig. 8a) represent the biosensor response for physiological urine oxalate concentration, therefore ΔI (curve 2) represents current response for added oxalate only (circles).

Physiological oxalate concentration for the used urine sample was very low, and it was the same for each of prepared urine solutions. Equations that denote the curves are as follows:

$$\Delta I = (2.4358 \pm 0.8406)\,\text{nA} + (0.1296 \pm 0.0048)\,\text{nA}\,\mu\text{M}^{-1}$$
$$\cdot c(\text{oxalate})\,\mu\text{M}; \quad R^2 = 0.9959 \; (\text{squares})$$

$$\Delta I = (-0.0642 \pm 0.8406)\,\text{nA} + (0.1296 \pm 0.0048)\,\text{nA}\,\mu\text{M}^{-1}$$
$$\cdot c(\text{oxalate})\,\mu\text{M}; \quad R^2 = 0.9959 \; (\text{circles})$$

Results of measurements obtained in the experiment (Fig. 8a and b) described above showed linear dependence between oxalate biosensor response and oxalate concentration for prepared urine samples.

For determination of oxalate concentration (added) for each prepared oxalate–urine solution, the equation obtained by three-point calibrating curve was used (three oxalate water standards were injected at the end of urine oxalate sample testing). Table 2 presents the results of concentration established by biosensor measurement (right column) and of analytically prepared concentration (added, left column).

Comparison of the oxalate concentration analytically prepared in urine and the one determined by the biosensor using buffer oxalate standards gave the slope equal to 1, low intercept (0.9596 μM) and the correlation coefficient of 0.9983. Correlation graph is represented by the following equation:

$$c(\text{det. by bios.}) = (0.959 \pm 0.765)\,\mu\text{M} + (1.007 \pm 0.017)$$
$$\cdot c(\text{added})\,\mu\text{M}; \quad R^2 = 0.9983.$$

Good correlation of results over a wide range of urinary oxalate concentration supports the practical application of the developed biosensor for oxalate determination in urine.

The stability of the biosensor was tested for 8 weeks on daily basis for almost 8 h. When not in use, the measurement cell with biosensor was filled with succinic buffer and stored at 7 °C. In the testing period, the sensitivity change from 0.135 nA μM^{-1} to 0.094 nA μM^{-1} signified that the half-life time of the electrode was >2 months. The detection limit calculated as LOD = 3 × standard deviation/slope was found to be 4.76 μM in the measurement cell corresponding to 19.04 μM in undiluted samples. To improve the good performance of the developed biosensor, a comparison with two amperometric oxalate biosensors of similar construction was made. The results of comparison between the developed biosensor and amperometric biosensors are given in Table 3. Biosensors [4], without Prussian blue layer and the proposed biosensor showed almost the same sensitivity while biosensor [9], showed significantly lower sensitivity.

Fig. 8. (a) Biosensor response for real, 20-fold diluted urine samples. Tested c(oxalate) = 20–400 μM (5–100 μM in the measurement cell). Double peaks indicate each tested concentration. Experimental conditions: working potential 100 mV, flow rate 1.24 mL min^{-1}, c(K$_4$[Fe(CN)$_6$]) = 10 mM, sample loop 100 μL, c(oxalate) = 50 μM, succinic buffer solution pH 3.6 contained 50 mM EDTA. Graphs (b) for a series of oxalate solutions prepared in the 20-fold diluted urine (squares) and the one obtained according to equation I(sample) = I(urine solution with added oxalate) − I(pure urine) (circles).

Table 3
Comparison of the performance of the developed biosensor and other previously reported biosensors

Slope (nA mM^{-1})	A(electrode) (cm^2)	Amount of immobilised enzyme (U)	Sensitivity (mA M^{-1} cm^{-2})	Reference
129	0.0113	0.014	11.42	Developed biosensor
883	0.0707	0.010	12.5	[4]
88	0.0314	0.016	2.8	[9]

3.1.8. Interferences

Possible interferences in urine are ascorbate, homovanilic acid, ascorbic acid, acetylsalicylic acid, uric acid and many others. Serious interferences were observed only for ascorbic acid while acetylsalicylic acid, paracetamol, and uric acid had no influence on the proper working of the biosensor. Interference study was done in a classic electrochemical cell (batch mode) using interdigitated electrode without enzyme layer connected to a potentiostat in biamperometric measuring mode. The supporting electrolyte contained 8 mL succinic buffer pH 3.8, 1 mL 20 mM $K_4[Fe(CN)_6]$ and 400 μL 10 mM $K_3[Fe(CN)_6]$). Addition of ascorbic acid to the measurement cell reduced biamperometric current response because ascorbic acid can reduce $K_3[Fe(CN)_6]$ to $K_4[Fe(CN)_6]$), causing significant chemical interference. However, many procedures have been suggested in order to avoid the interference of ascorbic acid with oxalate biosensor response [6]. Determination of urine oxalates by the described biosensor measurement cell together with a reference measurement cell (containing only interdigitated electrode without enzyme layer) for elimination of interference is in progress.

4. Conclusion

Results of the recovery test demonstrated the reliability of the proposed bienzymatic electrode in biamperometric measurement mode for urinary oxalate determination. According to literature there is no published method related to oxalate determination based on biamperometric measurements by interdigitated electrode.

Application of an interdigitated electrode as a two-electrode detector makes a reference electrode unnecessary. It is well known that the reference electrode for continuous flow measurement must be constructed very carefully, otherwise the reference electrode becomes the weak point of any flow-through system.

Interdigitated electrode as a planar electrode offers some additional advantages such as small size of the produced biosensor, high precision and accuracy, small sample volume and reduced cost of manufacturing.

The applied interdigitated electrode could be part of a microfluidic platform (biochip) offering a new possibility in urinary oxalate determination. Response time of 172 s (peak forming) for the highest expected oxalate concentration (200 μM) offered almost 20 analyses per hour. No need for sample preparation except sample dilution additionally confirmed the high value of this method for practical application.

Interference of ascorbic acid was noticed while acetylsalicylic and uric acid did not interfere with the function of the biosensor.

References

[1] C.J. Farrington, A.H. Chalmers, Clin. Chem. 25 (1979) 1993.
[2] N. Potezny, R. Bais, P.D. O'Loughlin, J.B. Edwards, A.M. Rofe, R.A.J. Conyers, Clin. Chem. (29/1) (1983) 16.
[3] J.R. Fernandes, C.D. Neto, L.T. Kubota, M. Tubino, Anal. Commun. 33 (11) (1996) 397.
[4] P.A. Fiorito, S.I. Córdoba de Torresi, Talanta 62 (2004) 649.
[5] E. Dinçkaya, E. Akylmaz, S. Akgol, Indian J. Biochem. Biophys. 37 (1) (2000) 67.
[6] H. Hansen, K.S. Winther, M. Gundstrup, Anal. Lett. 27 (7) (1994) 1239.
[7] E. Dinçkaya, A. Telefoncu, Indian J. Biochem. Biophys. 30 (1993) 282.
[8] S.M. Reddy, S.P. Higson, P.M. Wadgama, Anal. Chim. Acta 343 (1997) 59–68.
[9] R.H. Capra, M. Strumia, P.M. Vadgama, A.M. Baruzzi, Anal. Chim. Acta 530 (2005) 49.
[10] M.K. Sezgintürk, E. Dinçkaya, Talanta 59 (2003) 545.
[11] E.F. Perez, G.O. Neto, L.T. Kubota, Sens. Actuators B 72 (1) (2001) 80.
[12] M.D.P.T. Sotomayor, I.M. Raimundo Jr., G.O. Neto, L.T. Kubota, Anal. Chim. Acta 447 (2001) 33.
[13] C.S. Pundir, N.K. Kuchhal, A.K. Bhargava, Biotech. Appl. Biochem. 27 (1998) 103.
[14] B. Sjukić, R. Baron, R.G. Compton, Electroanalysis 19 (9) (2007) 918.
[15] R.I. Stefan, I. Draghici, G.E. Baiulescu, Sens. Actuators B 65 (2000) 250.
[16] A. Moreno Gálvaz, J.V. García Mateo, J. Martinez Calatayud, Anal. Chim. Acta 396 (1999) 161.
[17] S. Milardovic, D. Iveković, V. Rumenjak, B.S. Grabarić, Electroanalysis 17 (2005) 1847.
[18] S. Milardovic, I. Kereković, R. Derrico, V. Rumenjak, Talanta 71 (2007) 213.
[19] T.P. Tougas, J.M. Jannetti, W.G. Collie, Anal. Chem. 57 (1985) 1377.
[20] C. Zhao, J. Zhang, J. Song, Anal. Biochem. 297 (2001) 170.
[21] J. Michałowski, M. Trojanowicz, Anal. Chim. Acta 281 (1993) 299.
[22] D.G. Sanderson, L.B. Anderson, Anal. Chem. 57 (1985) 2388.
[23] M. Morita, O. Niva, T. Horiuchi, Electrochim. Acta 42 (1997) 3177.
[24] M. Kudera, H. Allen, O. Hill, P.J. Dobson, P.A. Leigh, W.S. McIntire, Sensors 1 (2001) 18.
[25] U. Wollenberg, M. Paeschke, R. Hintsche, Analyst 119 (1994) 1245.
[26] M. Gabig-Ciminska, A. Holmgren, H. Andersen, K. Bundvig Barken, M. Wümpelmann, J. Albers, R. Hintsche, A. Breitenstein, P. Neubauer, M. Los, A. Czyz, G. Wegrzyn, G. Silfversparre, B. Jürgen, T. Scweder, S.-O. Enfors, Biosens. Bioelectron. 19 (2004) 537.
[27] J.H. Min, A.J. Baeumner, Electroanalysis 16 (9) (2004) 724.
[28] X. Xie, D. Stüben, Z. Berner, J. Albers, R. Hintsche, E. Jantzen, Sens. Actuators 97 (2004) 168.
[29] H.B. Dunford, J.S. Stillman, Coord. Chem. Rev. 19 (1976) 187.
[30] R.H. Capra, A.M.B. Aruzzi, L.M. Quinzani, M.C. Strumia, Sens. Actuators B - Chem. 124 (2) (2007) 466.
[31] M.F. Laker, A.F. Hoffman, J.D. Meeuse, Clin. Chem. 26 (1980) 827.

Use of biotin–streptavidin system for developing a viable, sensitive and specific antigen heterologous assay for hapten

Seema Nara [a,b], Vinay Tripathi [a,b], Shail K. Chaube [a], Kiran Rangari [a], Harpal Singh [b], Kiran P. Kariya [c], Tulsidas G. Shrivastav [a,*]

[a] *Department of Reproductive Biomedicine, National Institute of Health and Family Welfare, Munirka, New Delhi 110067, India*
[b] *Center for BioMedical Engineering, Indian Institute of Technology, New Delhi 110016, India*
[c] *Department of Chemistry, VMV Com. JMT Arts & JJP Science College, Nagpur 444008, India*

ARTICLE INFO

ABSTRACT

The present study demonstrates improvement in sensitivity and specificity of hapten assay by using antigen heterology in conjunction with low molecular weight biotin label as compared to high molecular weight horseradish peroxidase (HRP) label. For generation of antiserum, cortisol-3-*O*-carboxylmethyl-oxime-bovine serum albumin (F-3-CMO-BSA) was used as immunogen whereas, for the preparation of primary label, corticosterone-3-carboxymethyl oxime (B-3-CMO) was coupled with biotinylcaproylhydrazide and HRP by employing *N*-hydroxysuccinimide mediated carbodiimide reaction. The data of the present study revealed that the antigen heterologous assay which employed high molecular weight HRP label showed 100% cross-reaction with corticosterone. On the contrary, when HRP was replaced with low molecular weight biotin label, less than 0.1% cross-reaction was observed with all analogous C_{18}, C_{19}, C_{21} and C_{27} steroids including corticosterone (0.2%). Moreover, the sensitivity of the later assay was 0.09 μg/dL, which is appreciable as compared to previously reported enzyme based assays. The recovery of the exogenously spiked serum pools lies in the range of 90.3–104.2%. The intra-assay and inter-assay coefficient of variation (CVs) ranged from 3.3% to 7.8% and 2.3% to 7.7%, respectively. The serum cortisol values obtained by this method correlated well with those obtained by radioimmunoassay; $r = 0.9$ ($n = 50$). The use of much stable biotin label in place of HRP has made the antigen heterologous enzyme linked immunosorbent assay (ELISA) of cortisol assay highly specific and sensitive.

© 2008 Elsevier B.V. All rights reserved.

1. Introduction

The high affinity antigen–antibody (Ag–Ab) interaction is the most specific one encountered in the biological systems and thus forms the basis for the development of sensitive and specific immunoassay techniques [1]. The overall objective of immunoassay is to determine low concentration of analyte with high throughput and precision. It is possible to develop immunoassay for low molecular weight (M.W.) compounds (haptens, M.W. <1000 Da) such as steroids that have very subtle differences among their chemical structures. The specificity and sensitivity of an immunoassay for steroids are primarily dictated by the structure of the immunogen and label used [2–4] along with the coupling chemistry involved in their preparation [5]. The antibody specificity is directed primarily at that portion of the hapten furthest removed from the

functional group linking the hapten to the carrier protein [6]. While preparing an immunogen, direct linkage to the functional groups or heteroatoms of hapten might lead to changes in polarity of the group and reduction in the number of potential sites contributing to antibody binding [7]. The use of heterologous combinations (hapten, site, bridge, etc.) results into greater sensitivity and selectivity in steroidal enzyme immunoassay due to improved fitting of steroid into antibody binding pocket and reduced bridge recognition. The influence of various heterologies (hapten, site or bridge) on the sensitivity and specificity of steroid hormone enzyme linked immunosorbent assays (ELISAs) was first recognized by Weeman and Schuurs [8]. Hosoda et al. [9], has demonstrated increase in the sensitivity of cortisol ELISA that uses a shorter bridge in the label than in immunogen. Since then, this concept has been utilized in developing immunoassays for many steroids [10–12]. But antigen heterology has not been widely used as compared to bridge or site heterology.

In an antigen heterologous chemiluminescent assay for measurement of estradiol in serum, estriol/estrone (E3/E1) was used as immobilized antigen with acridinium ester labeled estradiol

---

* Corresponding author. Tel.: +91 11 26165959.
E-mail addresses: drtg.srivastav@gmail.com,
tgsrivastava.nihfw@nic.in (T.G. Shrivastav).

(E2) antibody and 3-fold increase in the sensitivity was observed [13]. Similarly, antigen heterologous ELISA for testosterone and progesterone has also been developed. In the former assay, the cross-reaction with 5α-DHT was reduced to 6.7% [14], whereas, latter has achieved a sensitivity of 0.11 ng/mL with very low cross-reaction with 17α-OH-progesterone [15]. However, the influence of antigen heterology on functional parameters of cortisol assay has not been studied so far adopting antibody-immobilized format.

The direct enzymatic, fluorescent and chemiluminescent labeling of steroids although has achieved excellent detection limit but they still have several limitations [16]. These limitations could be avoided by using biotin–avidin/streptavidin system. This system has been extensively used for the detection of antibodies, ribonucleic acid (RNA) and deoxy-ribonucleic acid (DNA). Very few steroid immunoassays have been reported in literature involving biotin–avidin/streptavidin system.

The biotin–streptavidin technology has been utilized in two ways in competitive immunoassays for steroid measurement. Firstly, as a part of detection system wherein antibody bound biotinylated antigen is detected through streptavidin coupled reporter molecule [17–21] and secondly, as a separation system wherein streptavidin coated plate is used for immobilization of biotinylated Ag/Ab [22,23].

In the present study, biotin–streptavidin technology has been utilized as a part of detection system where biotin was coupled to corticosterone. The use of biotin as a primary probe features the advantage of a versatile end point determination, i.e. this tracer molecule can be used in laboratories equipped with ELISA readers, TR-fluorometers, potentially with luminometers using streptavidin labeled organic dye, lanthanide chelates [24], quantum dots [25], upconverting phosphors [26] or in conventional γ-counting, wherein [125I] streptavidin is employed as the secondary probe [27]. By virtue of using biotin-labeled steroid in present competitive binding reaction of the immunoassay, the molecular weight of analyte and the tracer molecule are of comparable size and similar to that of 125I-labeled steroid. In contrast to 125I-labeled tracers, it offers the advantage of virtually unlimited stability and their specific activity is not affected by storage time. The difference in the nature of bonds present in immunogen (amide bond), and in label (hydrazide bond) reduces the bridge recognition by the antibody. Further, label once prepared can be used to develop assays in both the antigen- and antibody-immobilized formats [28]. Besides its several advantages, biotin–streptavidin system has one limitation that it has an additional incubation step with labeled streptavidin after the immunoreactions and before signal detection. Nevertheless, the above-mentioned features, which label acquires, outweigh this limitation.

Thus, in the present work, the influence of antigen heterology and label type on the sensitivity and specificity of cortisol assay in serum has been investigated.

2. Experimental

2.1. Reagents and chemicals

All solvents, chemicals and salts used in the present study are of analytical grade and were used without prior purification. All the steroids used for the synthesis and cross-reactivity was obtained from Sterloids Inc. PO Box 689, Newport, RI 02840-0600, USA. Bovine serum albumin (BSA), *N*-hydroxysuccinimide (NHS), 1-ethyl-3-(3-dimethylaminopropyl) carbodiimide hydrochloride (EDAC), Freund's complete adjuvant (FCA), gelatin, and thimerosal were purchased from Sigma Chemical Company, St. Louis, MO, USA.

Streptavidin-horseradish peroxidase was procured from Bangalore Genei, Bangalore, India. Tetra-methyl-benzidine/H_2O_2 solution was purchased from Arista Biochemical, USA. Microtitre plates were procured from Greiner, Germany.

2.2. Buffers

(1) The most frequently used buffer was 10 mM phosphate (10 mM PB), pH 7.0, containing 0.9% NaCl (10 mM PBS) and 0.1% NaN_3.
(2) HRP conjugate dilution buffer was 18 mM acetate buffer (18 mM AB), pH 4.0, containing 0.1% thimerosal and dextran T-70, 0.3% BSA.
(3) Antibody dilution buffer used was 10 mM PB containing BSA (2 g/L) and 0.01% thimerosal as preservative.
(4) Microtitre well blocking and stabilizing buffer was 10 mM PB containing 0.9% NaCl, 0.2% BSA, 0.1% gelatin, thimerosal, dextran T-70, ethylene diamine tetra acetic acid:di-potassium salt (EDTA:K salt), and 0.01% gentamicin sulphate.

2.3. Norma rabbit serum (NRS)

The normal rabbit serum (NRS) was collected from non-immunized New Zealand white rabbits and stored in aliquots at −30 °C after ammonium sulphate precipitation.

2.4. Preparation of corticosterone-3-CMO-biotin conjugate

Fig. 1 shows the reaction scheme for preparation of corticosterone-3-CMO-biotin conjugate. Corticosterone-3-CMO (B-3CMO) was coupled with biotinylcaproylhydrazide by NHS-ester method with some modification described elsewhere [29]. In brief, to 5 mg of B-3CMO, 200 μL of each, dioxan and dimethyl formamide was added. To this solution 100 μL of water containing 10 mg NHS and 20 mg EDAC was added; the reaction mixture was activated for 24 h at 4 °C. Activated B-3-CMO solution was added to the solution of biotinylcaproylhydrazide (25 mg/mL of dimethyl sulphoxide), vortex-mixed and kept for 24 h at 4 °C. The B-3CMO-biotinylcaproylhydrazide conjugate was dried under the stream of nitrogen. The dried residue was extracted with 9:1 mixture of alcohol and dimethyl sulphoxide and passed through LH-20 column. The B-3CMO-biotinylcaproylhydrazide conjugate was kept at 4 °C for future use.

2.5. Preparation of corticosterone-3-CMO-HRP conjugate

The conjugation reaction was carried out as previously described by an active ester method [29]. In brief, to 5 mg of B-3-CMO, 200 μL of each, dimethyl formamide and dioxan was added. To this solution 100 μL of water containing 10 mg NHS and 20 mg EDAC was added; the reaction mixture was activated for 24 h at 4 °C. Activated B-3-CMO solution was added to the aqueous solution of HRP (1 mg/mL) and kept at 4 °C for 24 h. After incubation the reaction mixture was passed through a G-25 column, previously equilibrated with 10 mM PBS containing 0.1% thimerosal. The brown colored fractions containing enzyme activity were pooled and, to it, 1% (w/v) of sucrose, ammonium sulphate, BSA and an equal volume of ethylene glycol were added. The solution was kept at −30 °C in aliquots for future use.

2.6. Immunogen (F-3-CMO-BSA) preparation

Cortisol-3-CMO (F-3CMO) was coupled with BSA by NHS-ester method with modification described elsewhere [29]. To 5 mg of F-3CMO, 200 μL of each, dioxan and dimethyl formamide was added.

Step 1. Preparation of corticosterone-3-CMO avtive ester derivative

Step 2. Coupling of corticosterone-3-CMO active ester to biotinylcaproyl hydrazide
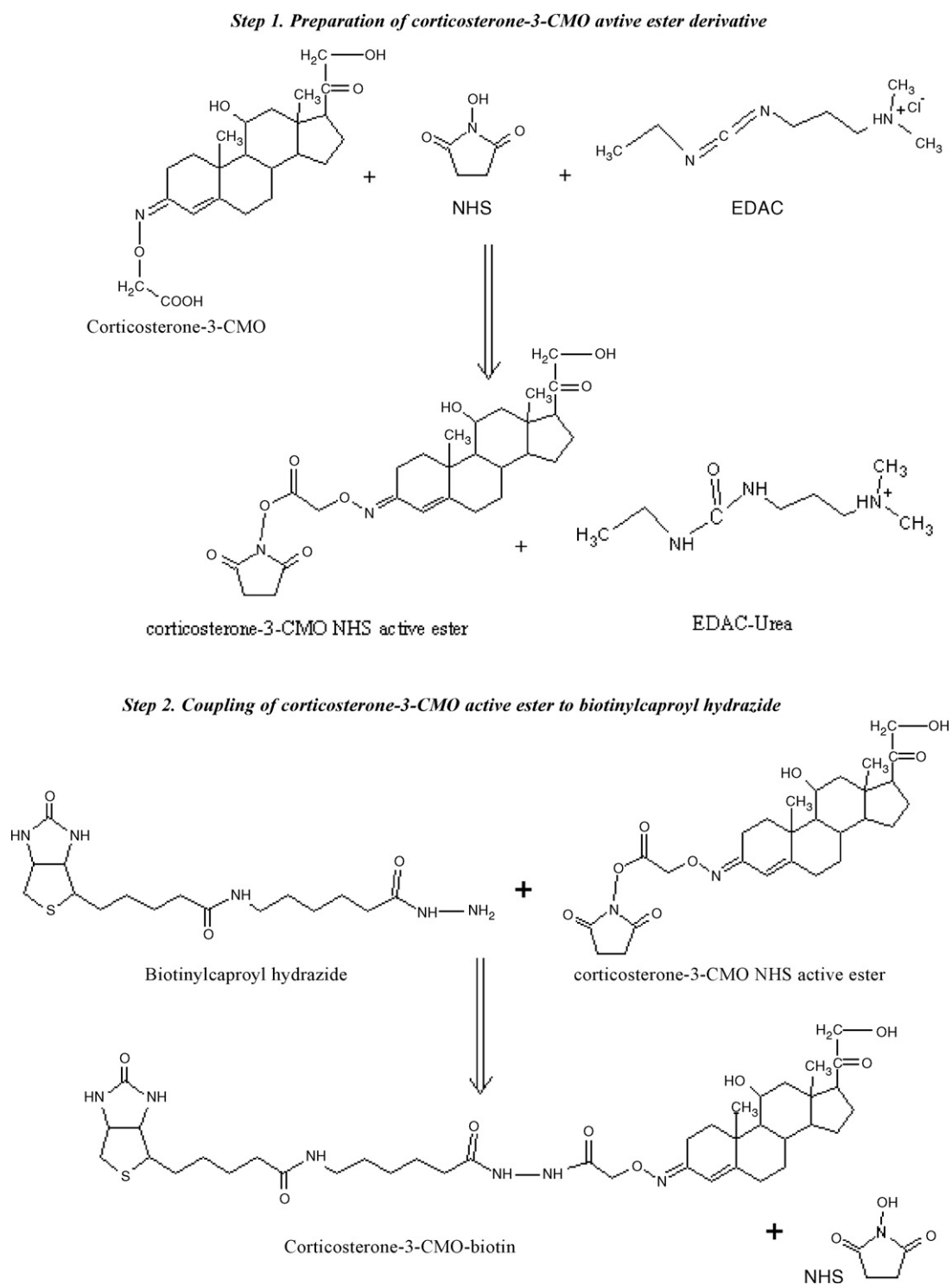
Fig. 1. Reaction scheme for the preparation of corticosterone-3-carboxymethyloxime-biotinylcaproyl hydrazide conjugate.

To this solution 100 μL of water containing 10 mg NHS and 20 mg EDAC was added; the reaction mixture was activated for 24 h at 4 °C. Activated F-3CMO solution was added to the aqueous solution of BSA (3.3 mg/mL), vortex-mixed and kept for 24 h at 4 °C. The F-3CMO-BSA conjugate was dialyzed against 3–4 changes of water. The dialysate was frozen, lyophilized and kept at 4 °C in aliquots of 1 mg for immunization.

2.7. Immunization

The intramuscular injections were given to New Zealand white rabbits as per method reported elsewhere [30]. F-3CMO-BSA (1 mg) was dissolved in saline (0.5 mL) and emulsified with Freund's complete adjuvant (0.5 mL). The emulsion (250 μL) was injected intramuscularly in the limbs of rabbits. The 5 weekly primary

injections were given followed by the monthly booster doses. The booster doses were given in Freund's incomplete adjuvant and rabbits were bled 10 days after the booster injection of each month. Antiserum was collected after centrifugation at 2500 rpm for 10 min and stored at −30 °C.

2.8. Checkerboard assay

2.8.1. Coating of microtitre plates

The 96-well microtitre plates were coated using the immuno-bridge technique for primary antibody immobilization described elsewhere [31]. In brief, 250 μL of the NRS diluted (1:250) in buffer "1" was dispensed into each well and incubated at 37 °C overnight. Following incubation, the plate was washed under running tap water. To the NRS coated wells, 250 μL of 1:1000 diluted goat anti rabbit gamma globulin (ARGG) was added and incubated for 2 h at 37 °C. After incubation, the contents of the plate were decanted and washed under running tap water. To the ARGG coated microtitre plates, 200 μL of appropriately diluted (1:4000) F-3-CMO-BSA antiserum in buffer "3" was dispensed. The plate was incubated at 37 °C for 2 h. Unadsorbed antibody was then washed off and 250 μL of buffer "4" was then added to block the unoccupied sites of the plate. The plate was kept at 37 °C for 1 h. The contents were decanted and the plate was dried at room temperature (RT) and kept at 4 °C for future use.

2.8.2. Determination of optimum dilution of antibody and biotin-steroid conjugates

To determine the amount of immobilized primary antibody and biotinylated steroid required to develop the assay, 100 μL of various dilutions (200, 100, 50, 5 ng/mL) of B-3-CMO-biotin was added in above coated plates (one dilution per two wells in vertical fashion). The plate was kept at RT for 1 h. Unbound contents were washed off and 100 μL of SA-HRP was added to all the wells and kept at RT for 20 min. The plate was washed under tap water to remove the unbound SA-HRP. For measuring bound enzyme activity 100 μL of TMB/H_2O_2 substrate was added to all the wells and kept at RT for 15 min. The reaction was stopped by adding 100 μL of 0.5 M H_2SO_4 and the color intensity was measured at 450 nm in a Tecan-spectra ELISA plate reader. The dilutions of antiserum and B-3-CMO-biotin showing maximum zero binding and least non-specific binding were selected for assay development.

2.9. Standard preparation

A parent stock solution of cortisol was prepared in ethanol and kept at −30 °C. A working stock of 600 μg/dL was made after air drying the desired amount of parent stock and reconstituting it in buffer "2". The nine standards of 0, 0.125, 0.5, 1, 3 10, 30, 60 and 90 μg/dL were made from the working stock in same buffer and kept at 4 °C for further use.

2.10. Assay design

2.10.1. For HRP conjugates

To the antibody-coated wells, 25 μL of cortisol standards (0–90 μg/dL) were added along with 100 μL of suitably diluted B-3-CMO-HRP in duplicate. The plate was kept at RT for 1 h. Unbound contents were washed off, 100 μL of TMB/H_2O_2 substrate was added to the wells and kept at RT for 15 min. The bound enzyme activity was measured with Tecan-spectra ELISA plate reader at 450 nm after terminating the reaction with 0.5 M H_2SO_4 (100 μL).

2.10.2. For Biotin conjugates

To the antibody-coated wells, 25 μL of cortisol standards (0–90 μg/dL) were added along with 100 μL of B-3-CMO-biotin (5 ng/mL) conjugates in duplicate. The plate was kept at RT for 1 h. Unbound contents were washed off. 100 μL of SA-HRP was added as secondary reporter molecule and kept at RT for 20 min. The plate was washed under tap water to remove the unbound SA-HRP. TMB/H_2O_2 substrate (100 μL) was added to the wells and kept at RT for 15 min. The bound enzyme activity was measured with Tecan-spectra ELISA plate reader at 450 nm after terminating the reaction with 0.5 M H_2SO_4 (100 μL).

2.11. Recovery

To 10-mL aliquots of six serum pools, we added 0, 0.5, 1, 2, 4, and 6 μg of cortisol (corresponds to 0, 5, 10, 20, 40 and 60 μg/dL). The %recovery is calculated as $O/E \times 100$, where O is the observed concentration and E is the sum of the amount of analyte added and inherent concentration in the matrix.

2.12. Precision

Serum pools of low, medium and high cortisol concentrations were utilized for determining the level of imprecision in assay by estimating cortisol in each pool for six time in assay and in six different assays. The %coefficient of variation (CVs) is calculated as (S.D./mean) × 100.

2.13. Validation of the assay

2.13.1. By using Bio-Rad External Quality Assurance Services (EQAS), USA

Bio-Rad External Quality Assurance Services (EQAS) programmes are designed to provide laboratories with accurate comparison of performance with laboratories using the same methodology and/or instrument/reagents. It is used in conjunction with the daily quality controls to give valuable information for monitoring performance. Various laboratories all over the world participate in the EQAS programme. In this programme, different methods including radioimmunoassay, chemiluminescent, enzymatic and automated systems were used for serum cortisol measurement in the "Bio-Rad EQAS control samples". Our laboratory participated in 22nd, 23rd and 24th cycles of EQAS programme. The mean ± 3 S.D. of the cortisol concentrations as estimated by all methods was set as the acceptable performance limits. The immunoassays, which determine the cortisol concentration outside this acceptable limit, are considered invalid. We have validated our assay by measuring cortisol in the control samples of 23rd and 24th cycles.

2.13.2. Comparing the assay with established radioimmunoassay kit (RIA)

The correlation coefficient was calculated by comparing serum cortisol concentrations as determined by developed ELISA with an established radioimmunoassay (RIA) kit (Immunotech, France).

3. Results

3.1. Standard curve

Fig. 2 depicts the semi-log standard curve of cortisol using B-3-CMO-biotin tracer. The increasing concentrations of cortisol (μg/dL) are plotted as their log values on X-axis against the % of bound fraction on the Y-axis. The graph was plotted using MS-Excel.
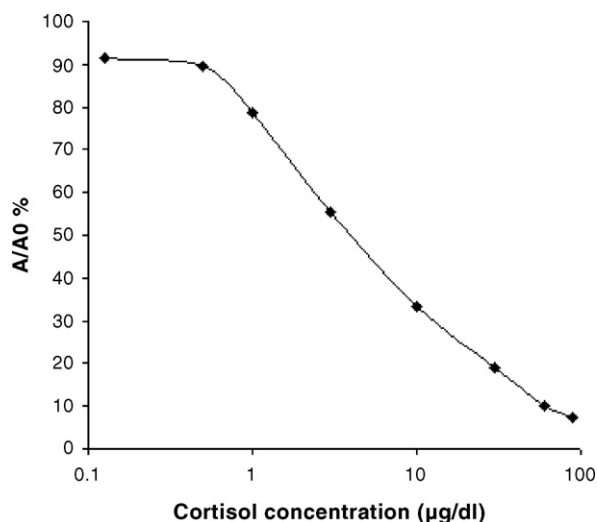
Fig. 2. Standard curve of cortisol using F-3-CMO-BSA antibody and B-3-CMO-Biotin tracer.

3.2. Specificity

The specificity of the F-3-CMO-BSA antibody was estimated as the percentage of cross-reaction with commercially available C_{27}, C_{21}, C_{19}, and C_{18} steroids. The %cross-reaction of cortisol antiserum was less than 0.1% with naturally occurring C_{18}, C_{19}, C_{21} and C_{27} steroids using biotinylated B-3-CMO tracer except cortisone with 4.5% cross-reaction. Another distinguishing feature is that the antibody is strongly recognizing corticosterone when it is labeled with biotin but is giving 0.2% cross-reaction with unlabeled corticosterone. This makes the assay much more specific to cortisol. On the other hand, HRP labeled corticosterone is 100% inhibited by unlabeled corticosterone. It shows that biotin label plays some crucial role in increasing the specificity of an antigen heterologous ELISA for low molecular weight haptenic molecules like steroids.

Since, the biotin based assay was very specific, it was further validated for other analytical parameters.

3.3. Sensitivity

The lower detection dose is the lowest concentration of analyte (A) giving a response statistically different from that observed in the absence of analyte (A_0). It is calculated as $A_0 - 2 \times$ S.D., after 20-fold determination of A_0. The assay has achieved a sensitivity of 0.09 μg/dL.

3.4. Recovery

Table 1 represents the recovery profile of the assay that lies in the range of 90.3–104.2%.

Table 2
Inter- and intra-assay coefficient of variation for the measurement of cortisol in three serum pools

Variation	Sample value (mean ± S.D.)	Coefficient of variation (%)
Intra-assay	17.5 ± 1.37	7.8
$n = 6$	22.83 ± 0.75	3.3
	25.33 ± 1.5	5.9
	28.8 ± 1.83	6.3
Inter-assay	16.86 ± 0.51	3.1
$N = 6$	21.79 ± 1.68	7.7
	25.79 ± 0.59	2.3
	28.18 ± 1.76	6.2

n = Number of times same sample analyzed for intra-assay variation. N = number of times assays carried out for inter-assay variation.

3.5. Precision

Table 2 depicts the inter- and intra-assay variation. The coefficient of variation of three serum pools for intra- and inter-assay variation ($n = 6$, replicate of each pool) was <8%.

3.6. Performance of developed assay as validated by EQAS samples

Table 3 shows a comparison of cortisol serum concentration estimated by our assay in Bio-Rad control samples and the values provided by Bio-Rad. All the values lie in the acceptable performance limits set by EQAS.

3.7. Correlation with RIA

The correlation coefficient for values of cortisol in human serum samples ($n = 50$) measured both by RIA kit (Immunotech, France) and ELISA was calculated and found to be significant, i.e. $r = 0.9$, $P < 0.0001$. The linear regression curve of the correlated data (plotted by GraphPad Prism version 3.00 for Windows, GraphPad Software, San Diego California USA) is given in Fig. 3.

4. Discussion

In the present study, we have developed an antigen heterologous ELISA for cortisol and explored the potential of biotin as a label in enhancing the specificity of this antigen heterologous assay. The application of streptavidin–biotin system in the development of immunoassays is mainly attributed to Guesdon et al. [32]. Since then, this system has been used in two different formats. Firstly, as a part of detection system wherein antibody bound biotinylated antigen is detected through streptavidin coupled reporter molecule [17–21] and secondly, as a separation system wherein streptavidin coated plate is used for immobilization of biotinylated Ag/Ab [22,23].

On the other hand, heterology has been often incorporated as a means for improving assay sensitivity or reagent stability. Antigen (hapten) heterology has been reported to be superior to bridge

Table 1
Recovery of cortisol from exogenously spiked serum pools

Serum pool	Cortisol added (μg/dL)	Cortisol observed (μg/dL)	Cortisol expected (μg/dL)	%Recovery
Pool A	–	11.0	–	–
Pool B	5.0	16.5	16.0	103.1
Pool C	10.0	22.0	21.0	104.0
Pool D	20.0	30.0	31.0	96.7
Pool E	40.0	46.0	51.0	90.3
Pool F	60.0	74.0	71.0	104.2

Table 3
Serum cortisol concentrations determined by the present ELISA in 12 samples of each 23rd and 24th cycle of External Quality Assurance Services (EQAS)

Sample no.	23rd cycle			24th cycle		
	No. of laboratories participated	EQAS cortisol concentrations (mean ± 3 S.D.) (μg/dL)	Cortisol concentrations by present ELISA (μg/dL)	No. of laboratories participated	EQAS cortisol concentrations (mean ± 3 S.D.) (μg/dL)	Cortisol concentrations by present ELISA (μg/dL)
1	160	7.05 ± 0.87	9.9	152	35.8 ± 4.84	40
2	178	29.5 ± 4.24	28	167	14.9 ± 1.5	18
3	180	18.5 ± 2.88	18	183	26.0 ± 3.0	31
4	182	42.4 ± 5.56	31	187	26.9 ± 4.76	26.2
5	192	18.6 ± 2.21	21	204	15.0 ± 1.61	15.5
6	178	42.2 ± 5.30	46	194	35.5 ± 5.43	43
7	193	7.19 ± 0.85	9.7	190	26.0 ± 2.73	30
8	194	30.0 ± 3.39	31	195	14.9 ± 1.47	18
9	196	18.7 ± 2.23	23	187	27.1 ± 4.98	22.5
10	174	42.3 ± 5.33	37	160	26 ± 3.09	22.5
11	194	30.3 ± 3.88	30	204	36.2 ± 5.38	35
12	183	7.28 ± 0.9	6.6	191	27.2 ± 4.58	30

and site heterologies as it involves highly defined epitope changes, thus allowing better control over the reagents in immunoassays and more basic interpretation of results in basic immunochemical studies [33]. The improvement in the assay sensitivity has been reported in the hapten heterologous assays for triiodothyronine (T3) and thyroxine (T4) [34]. This heterology has not been widely employed for developing steroid immunoassays. Therefore in this work, we have utilized a combination of F-3-CMO-BSA immunogen and B-3-CMO-HRP/biotin labels.

The cross-reaction comparison between the B-3-CMO-HRP and B-3-CMO-biotin label based assays showed that biotin as a label has strikingly reduced the cross-reaction with unlabeled corticosterone to 0.2% as compared to HRP as label (100%). Moreover the sensitivity of the biotin assay was also better than a site heterologous ELISA for cortisol where HRP was used to label cortisol-21-hemisuccinate and has a sensitivity of 0.28 μg/dL [23]. A lower detection limit of 0.05 μg/dL was achieved by introducing bridge heterology in the enzyme label [35]. The use of antigen heterology in the present work in conjunction with biotin label has brought the lower detection limit to 0.09 μg/dL. The % cross-reaction of the developed assay has been further reduced for analyte like corticosterone (0.2%), 17α-OH-P (0.9%) and cortisone (4.5%), as compared to previously developed bridge and site heterologous ELISA of cortisol [36].

The thrust of developing an immunoassay is always towards improved sensitivity and specificity. To achieve this aim, research is currently oriented towards introduction of new labels and more specific molecular recognition elements that mimic antibodies. Aptamers (artificial nucleic acid molecules) generated

Fig. 3. Regression graph of correlation between the serum cortisol concentrations as estimated by the developed ELISA and an established RIA kit (plotted by Prism 3 software).

against drugs, amino acids or proteins, molecularly imprinted molecules made against toxins, hormones, pesticides and other small molecules, and engineered antibody fragments are presently the area of research anticipating to enhance the immunoassay specificity [37]. Another area of interest is the use of particulate reporters such as quantum dots, upconverting phosphors, cantilevers, and gold nanoparticles, which possess very high specific activity that excludes the label as a sensitivity-limiting factor. However, the sensitivity limitation caused by non-specific binding still remains [38]. These new labels are singly charged species and may alleviate the problem associated with protein labels like HRP where the analyte is attached at multiple sites with varying electronic environments that could affect the fitting of labeled molecule in the Ab binding pocket. But the large size and the uneven shape of the particulate labels cause additional issues to the performance of immunoassay like steric hindrance and increased non-specific binding, which reduce reproducibility. These problems could be solved by using low molecular weight label like biotin to directly label the steroid, where the amplification of the signal can still be achieved using streptavidin-HRP or streptavidin labeled with these particulate reporter molecules.

It seems that the increased sensitivity and specificity of present assay is due to the combined effects of low molecular weight biotin label and heterology at antigen and bridge level. Sensitivity enhancement by heterology has been explained previously by assuming that the affinities of labeled and the unlabeled steroid approaches to approximately same levels as against the homologous label for which antibody displays high affinity but no direct experimental evidence in this support has yet been presented [39]. Low molecular weight of primary probe might have facilitated the easy and selective access of competing analyte present in the serum to compete with the antigen-binding pocket of antibody that might have reduced steric hinderance, resulting in the detection of as low as 0.09 μg/dL of analyte specifically. It is also possible that the difference in the nature of bonds, i.e. the presence of amide bond between cortisol and immunizing protein, and the hydrazide bond between corticosterone-biotin is remarkable enough to decrease the recognition of the bridge and thus resulted in obtaining adequate sensitivity and specificity [40]. The developed assay has been validated for accuracy, precision, and correlation.

To conclude, we say that biotinylcaproylhydrazide is a more effective label for hapten molecules like steroids due to its low molecular weight and the inherent 24.7 Å long spacer arm that provides efficient interaction with streptavidin probes. Together with the heterologous antigen, it improves the assay sensitivity and specificity. The effect of biotin as a label on the assay parameters could be studied for other haptens too.
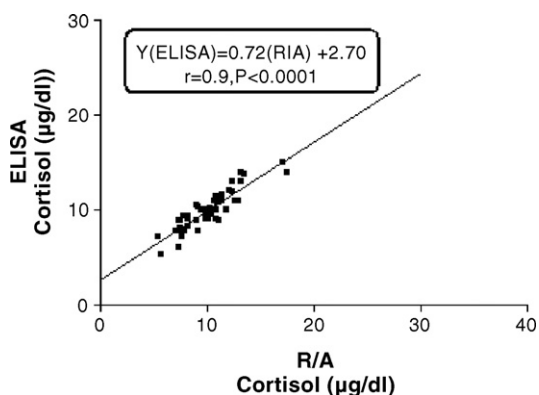
Acknowledgements

References

[1] H. Dent, M. Aslam, Bioconjugation: Protein Coupling Techniques for the Biomedical Sciences, Bath Press, London, 1998, p. 13.
[2] G. Hatzidakis, A. Stefanakis, E. Kramboiti, J. Reprod. Fertil. 97 (1993) 557.
[3] G.L. Kumari, R.N. Dhir, J. Immunoassay Immunochem. 24 (2003) 173.
[4] M. Mirasoli, S.K. Deo, J.C. Lewis, A. Roda, S. Daunert, Anal. Biochem. 306 (2002) 204.
[5] K.M. Rajkowski, N. Cittanova, J. Steroid Biochem. 14 (1981) 861.
[6] P. Luppa, S. Hauck, I. Schwab, C. Birkmayer, H. Hauptmann, Clin. Chem. 41 (1995) 564.
[7] P. Englebienne, Immune and Receptor Assays in Theory and Practice, CRC press, Florida, 2000, p. 86.
[8] K.V. Weeman, A.H.W.M. Schuurs, Immunochemistry 12 (1975) 667.
[9] H. Hosoda, N. Kobayashi, N. Ishii, T. Nambara, Chem. Pharm. Bull. 34 (1986) 2105.
[10] M. Mitsuma, A. Kambegawa, S. Okinaga, K. Arai, J. Steroid Biochem. 28 (1987) 83.
[11] K. Hoffmann, P. Samarajeewa, E.R. Smith, A.E. Keie, J. Steroid Biochem. 6 (1975) 91.
[12] T. Tanaka, M. Yanagi, A. Kubodera, Steroids 63 (1998) 516.
[13] H. Sato, H. Mochizuki, Y. Tomita, T. Kanamori, Clin. Biochem. 29 (1996) 509.
[14] P.N. Rao, I.B. Taraporewala, Steroids 57 (1992) 154.
[15] A. Basu, T.G. Shrivastav, S.K. Maitra, Steroids 71 (2006) 222.
[16] S.S. Deshpande, Enzyme Immunoassay: From Concept to Product Development, Chapman and Hall, New York, 1996.
[17] M.A. Mares, J. Deboever, G. Stans, E. Bosmans, F. Kohen, J. Immunol. Methods 183 (1995) 211.
[18] P. Luppa, C. Bruckner, I. Schwab, S. Hauck, S. Schmidmayr, C. Birkmayer, B. Paulus, H. Hauptmann, Clin. Chem. 43 (1997) 2345.
[19] S.E. Kakabakos, M.J. Khosravi, Clin. Chem. 38 (1992) 725.
[20] E.P. Diamandis, V. Bhayana, K. Conway, E. Reichstein, A. Papanastasiou-Diamandi, Clin. Biochem. 21 (1988) 291.
[21] J.H.F. Erkens, S.J. Dieleman, R.A. Dressendorfer, C.J. Strasburger, J. Steroid Biochem. Mol. Biol. 67 (1998) 153.
[22] M.A. Pesce, S.A. Bodourian, M. Sheehan, C.F. Henkel, Clin. Biochem. 25 (1992) 451.
[23] M. Wilchek, E.A. Bayer, Anal. Biochem. 171 (1988) 1.
[24] H. Harama, T. Soukka, A. Shavel, N. Gaponik, H. Weller, Anal. Chim. Acta 604 (2007) 177.
[25] L.J. Charbonniere, N. Hildebrandt, R.F. Ziessel, H.G. Lohmannsorben, J. Am. Chem. Soc. 128 (2006) 12800.
[26] K. Kuningas, T. Rantanen, T. Ukonaho, T. Lovgren, T. Soukka, Anal. Chem. 77 (2005) 7348.
[27] R.A. Dressendorfer, C. Kirschbaum, W. Rohde, F. Stahl, C.J. Strasburger, J. Steroid Biochem. 43 (1992) 683.
[28] M. Bodmer, L.X. Tiefenauer, L.Y. Andres, J. Steroid Biochem. 6 (1989) 1161.
[29] P.K. Pandey, T.G. Shrivastav, G.L. Kumari, P.N. Rao, P.K. Grover, H.G.K. Murthy, Clin. Chim. Acta 190 (1990) 175.
[30] A. Basu, T.G. Shrivastav, J. Immunoassay 21 (2000) 39.
[31] T.G. Shrivatsav, A. Basu, K.P. Kariya, J. Immunoassay Immunochem. 24 (2003) 205.
[32] J.L. Guesdon, T. Ternynck, S. Avrameas, J. Histochem. Cytochem. 27 (1979) 1131.
[33] U. Piran, D.S. Shostek, E.H. Barlow, Clin. Chem. 39 (1993) 879.
[34] U. Piran, W.J. Riordan, D.R. Silbert, J. Immunol. Methods 133 (1990) 207.
[35] T.G. Shrivastav, A. Basu, K.P. Kariya, J. Immunoassay Immunochem. 24 (2003) 191.
[36] A. Basu, S. Nara, S.K. Chaube, K. Rangari, K.P. Kariya, T.G. Shrivastav, Clin. Chim. Acta 366 (2006) 287.
[37] J.M.V. Emon, Immunoassay and Other Bioanalytical Techniques, CRC Press, New York, 2007, pp. 113–166.
[38] T. Ukonaho, T. Rantanen, L. Jamsen, K. Kuningas, H. Pakkila, T. Lovgren, T. Soukka, Anal. Chim. Acta 596 (2007) 106–115.
[39] P.A. Elder, K.H.J. Yeo, J.G. Lewis, J.K. Clifford, Clin. Chim. Acta 162 (1987) 199.
[40] M.J. Khosravi, R.C. Morton, Clin. Chem. 37 (1991) 58.

The extraction and speciation of arsenic in rice flour by HPLC–ICP-MS

Tomohiro Narukawa*, Kazumi Inagaki, Takayoshi Kuroiwa, Koichi Chiba

Inorganic Analytical Chemistry Division, National Metrology Institute of Japan (NMIJ), National Institute of Advanced Industrial Science and Technology (AIST), Tsukuba Central 3, 1-1-1 Umezono, Tsukuba, Ibaraki, 305-8563, Japan

ABSTRACT

Several solvent mixtures and techniques for the extraction of arsenic (As) species from rice flour samples prior to their analysis by HPLC–ICP-MS were investigated. Microwave-assisted extraction using water at 80 °C for 30 min provided the highest extraction efficiency. Total recoveries of extracted As species were in good agreement with the total As concentrations determined by ICP-MS after microwave-assisted acid digestion of the samples. Arsenite [As(III)], arsenate [As(V)] and dimethylarsinic acid (DMAA) were the main species detected in rice flour samples.

© 2008 Elsevier B.V. All rights reserved.

1. Introduction

Exposure to toxic inorganic arsenic (As) is linked to an increased risk of cancer [1,2]. Thus, methods capable of separating and measuring specific chemical forms of As in dietary components are necessary for accurate risk assessment. Food is the most obvious vehicle for toxic chemicals to enter the human body and therefore methods to evaluate the safety of foods from the aspect of contaminants are of great importance. In addition, food analysis can provide a measure of the degree to which the agricultural production system might be polluted. As the toxicity of elements such as As depend upon their molecular environment, it is important to determine which chemical species are present in a foodstuff as well as the total concentration of the element.

High concentrations of As are sometimes found in environmental waters. Severe health problems in some areas of south Asia are caused by high concentrations of inorganic As in ground water used as drinking water. In Japan, 80% of dietary As comes from seafood. It is well known that the As concentrations in seafoods such as fish, shellfish and seaweeds are much higher (generally $\mu g\,g^{-1}$ level) than those of other foods such as grains, vegetables and meat (generally $ng\,g^{-1}$ level) [3–18], and that most As in seafood is in the form of non-toxic arsenobetaine. Of agricultural products, rice is

the biggest contributor of As to the Japanese diet, but there has been little published information on the chemical forms of As in rice.

At the present time, the food sanitation law in Japan does not regulate for the As concentration in rice. The Codex Alimentarius Commission (CAC) also does not regulate for As concentrations in rice; indeed, discussions on the regulation of As in foodstuffs have been suspended since 1999 but the CAC concluded at that time that it was necessary to set standards for inorganic As in foodstuffs in the near future [19].

Arsenic speciation analyses of biological and environmental samples, including food, have been published [20,21], including reports on the As species in rice [22–31]. Speciation analysis usually requires the extraction of the species of interest into solvent before they can be identified and measured. Acids such as trifluoroacetic acid and solvent mixtures including water have been used to extract arsenic species from samples prior to speciation analysis [32–36]. However, there is a possibility that As(V) in samples could be sometimes reduced to As(III) during the extraction procedure [25].

This paper reports a study to determine the optimal extraction procedure for As species in rice samples prior to their analysis by high performance liquid chromatography coupled to inductivity coupled plasma mass spectrometry (HPLC–ICP-MS). Several extraction procedures were tested and the total amount of As extracted in each case was compared with the total As concentration obtained after microwave-assisted digestion of the samples. Results of speciation analyses of the samples are presented.

* Corresponding author.
E-mail address: tomohiro-narukawa@aist.go.jp (T. Narukawa).

2. Experimental

2.1. Instrumentation

An ICP-MS (Agilent 7500c, Agilent, Tokyo, Japan) equipped with a micromist nebulizer (100 μL, natural aspiration) and a Scott spray chamber (2 °C) was used. The ICP-MS normal operating parameters were as follows; incident rf power was 1500 W, outer Ar gas flow rate 15 L min^{-1}, intermediate Ar gas flow rate 0.9 L min^{-1}, carrier Ar gas flow rate 0.8 L min^{-1} and make-up Ar gas flow rate 0.4 mL min^{-1}. The ICP-MS was operated with He as the collision cell gas (3 mL min^{-1}) to reduce $^{40}Ar^{35}Cl^+$ interfering with ^{75}As. The ion count was monitored at $m/z = 75$. Arsenic species were separated by HPLC (L-6000 pump, Hitachi High Technologies Co. Ltd., Tokyo, Japan) with an automatic sample injector (Nanospece SI-2, Shiseido Co. Ltd., Tokyo, Japan) and direct introduction into the ICP-MS. An ODS L-column (150 mm × ID 4.6 mm, Chemicals Evaluation and Research Institute, Tokyo, Japan) was used with the mobile phase containing 10 mM sodium 1-butanesulfonate/4 mM malonic acid/4 mM tetramethylammonium hydroxide/0.05% methanol (pH 3.0). The HPLC system was connected to the nebulizer of the ICP-MS with PEEK tubing.

A MarsX system (CEM, Matthews, NC, USA) was used for the microwave-assisted extraction, and a MLS 1200-mega (Milestone MLS, Leutkirch, Germany) was used for the microwave digestion. An accelerated solvent extractor, ASE 200 (Dionex, Sunnyvale, CA, USA), was used for pressurized liquid extraction.

2.2. Reagents

The Japan Calibration Service System (JCSS) As standard solution (1000 mg L^{-1} As, made from high purity As_2O_3) used as the As(III) source standard solution, was purchased from Kanto Chemical Industries, Ltd. (Tokyo, Japan). The stock standard As(V) solution was prepared by oxidizing the JCSS As solution with HNO_3. Arsenobetaine (AB) solution certified reference material, NMIJ CRM 7901-a (National Institute of Advanced Industrial Science and Technology, NMIJ/AIST, Japan) was used as the AB source standard solution. Stock standard solutions of As(III), As(V) and AB were traceable to SI.

Monomethylarsonic acid (MMAA), dimethylarsinic acid (DMAA), trimethylarsine oxide (TMAO), tetramethylarsonium chloride (TeMA), and arsenocholine bromide (AsC), all of which were provided by Tri-Chemical Co. Ltd., were dissolved in water to prepare stock standard solutions containing 1000 mg As kg^{-1}. Working mixed standard solutions (0.5–10 ng As g^{-1}) were prepared daily by mixing the stock solutions and diluting with water.

2.3. Certified reference materials (CRMs)

The rice flour CRMs analyzed here were NIST SRM 1568a Rice Flour (National Institute of Standards and Technology, NIST, USA) and NIES CRM no. 10 Rice Flour series – Unpolished (National Institute for Environmental Studies, Japan) which consists of three CRMs with different cadmium concentrations (Cd level: low, medium and high). The certified value of total As in NIST SRM 1568a is 0.29 ± 0.03 mg kg^{-1}, and the reference values of total As in NIES CRM no. 10 are 0.17 (low Cd), 0.11 (medium Cd) and 0.15 (high Cd) mg kg^{-1}. These reference materials were made from unpolished brown rice.

2.4. Preparation of a sample of polished white rice flour

A sample of polished white rice flour was also prepared. The brown rice (unpolished type) used as the starting material was col-

lected in the northeast of Japan. After drying at 60 °C for 8 h, the brown rice was polished with a rice mill and freeze-pulverized. The white rice flour obtained was homogenized using a splitter, and then placed into clean amber glass bottles. After sterilization with ^{60}Co gamma radiation (20 kGy), the white rice flour was used as an analytical sample.

2.5. Procedures

2.5.1. Determination of total arsenic

A gravimetric method was employed in all preparations in this study. Total As concentrations in the CRMs and the white rice flour sample were determined by ICP-MS following microwave digestion with a mixture of HNO_3, $HClO_4$ and HF. Blank tests were performed to investigate possible As contamination; none was detected. Dry weight factors were obtained by measuring the weight loss after drying portions of the samples at 85 °C in an oven for 4 h.

2.5.2. Extraction procedure for speciation

Four extraction procedures (shaking, ultrasonication, accelerated solvent extraction and microwave-assisted extraction) were tested and their extraction efficiencies compared based on (i) total As extracted as measured by ICP-MS, and (ii) species dependency as determined by HPLC–ICP-MS.

The standard condition for extraction was a liquid/solid ratio of 10 to 1 (extraction solvent 10 g/sample 1 g). Five different extraction solvents (water, 25%, 50%, and 75% aqueous methanol, and 100% methanol) were tested for each extraction technique, and 6 samples were prepared in each case. When water was used as the extraction solvent, the rice flour-water suspension was centrifuged at 4000 rpm for 10 min and the supernatant was passed through a 0.45 μm syringe-type PVDF membrane filter and the filtrate analyzed. When an extraction solvent containing methanol was used, the solid was removed with a 0.45 μm membrane filter. The filtrate was evaporated to remove methanol and then diluted to 10 g with water. The solution was passed through a 0.45 μm syringe-type PVDF membrane filter again prior to analysis. Blank tests were performed in all cases.

2.5.2.1. Extraction by shaking.
An aliquot of the white rice flour was placed in a 50 mL polypropylene tube and extraction solvent was added. The capped tube was placed on a horizontal rotating shaker and shaken for 2 h at room temperature.

2.5.2.2. Ultrasonic extraction.
A capped 15 mL polypropylene tube containing white rice flour and extraction solvent was placed in an ultrasonic bath and ultrasonicated for 1 h.

2.5.2.3. Accelerated solvent extraction.
An aliquot of white rice flour was extracted using the accelerated solvent extraction system. Operating parameters were as follows; cell size was 11 mL, pressure 10 MPa, static time 10 min, flush 100%, purge 1 cycle and 90 s at 100 °C.

2.5.2.4. Microwave-assisted extraction.
A sample of white rice flour and the extraction solvent were placed in a PTFE vessel, which was then screwed into position on the microwave instrument. The operating program of the system was as follows: the temperature was raised from room temperature to 80 °C over 5 min, held at 80 °C for 30 min, and then cooled to room temperature over 10 min. Seven vessels were used for each run; six contained samples for extraction and the seventh was used for monitoring of temperature.
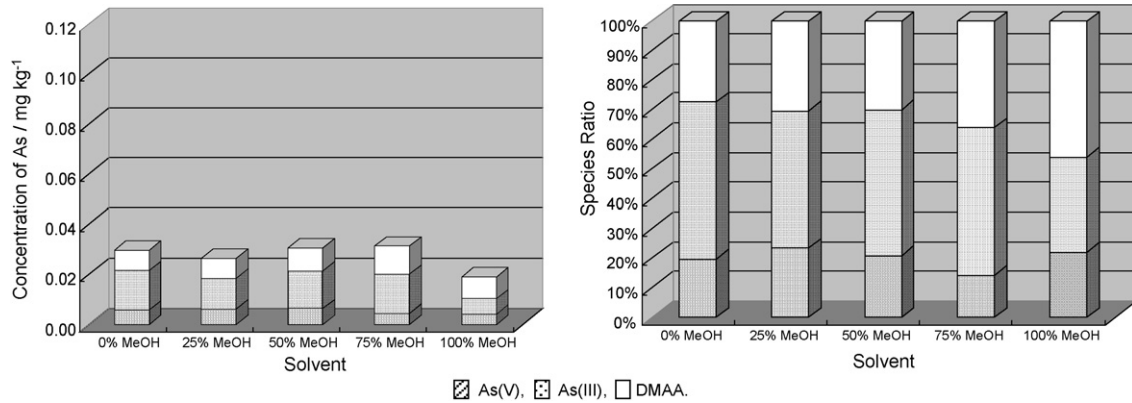
Fig. 1. Extraction of As species in white rice flour by shaking.
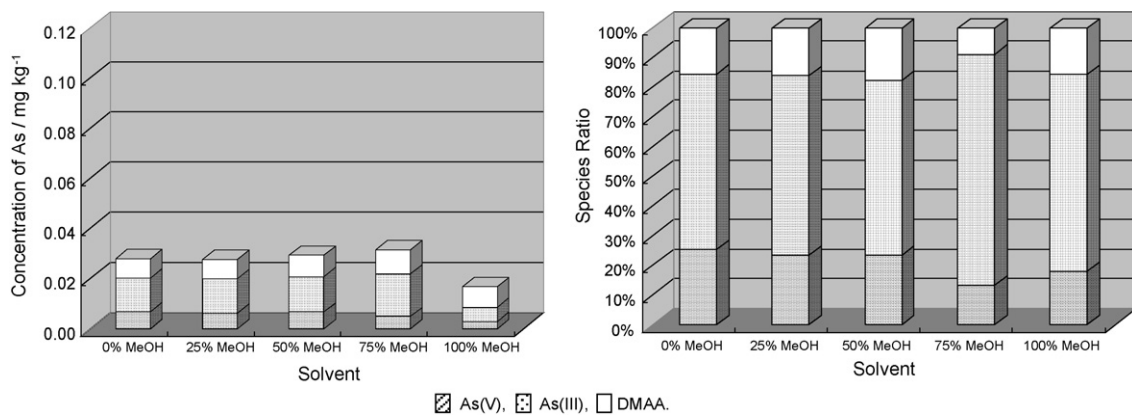
Fig. 2. Extraction of As species in white rice flour by ultasonication.

3. Results and discussion

3.1. Determination of total arsenic following microwave digestion

The analytical result ($n = 3$) for NIST SRM 1568a by ICP-MS was 0.285 ± 0.002 mg kg^{-1} As, which was in good agreement with the certified value. The results ($n = 3$) for NIES CRMs no. 10 were 0.172 ± 0.002 mg kg^{-1} (low Cd), 0.114 ± 0.003 mg kg^{-1} (medium Cd) and 0.157 ± 0.002 mg kg^{-1} (high Cd), which agreed well with their reference values. The total As concentration of the white rice sample ($n = 6$) was 0.096 ± 0.003 mg kg^{-1}.

3.2. Extraction efficiency for arsenic species

The white rice flour was used to compare the extraction efficiencies of the five solvents and four extraction techniques.

3.2.1. Extraction by shaking

Results are shown in Fig. 1. With water, the total As extracted from the rice flour was 0.029 mg kg^{-1}, and the extraction efficiency was 31%. The amount of As extracted remained constant when the proportion of methanol in the extraction solvent was increased, and the total As extracted was 0.031 mg kg^{-1} (efficiency 33%) with 75%
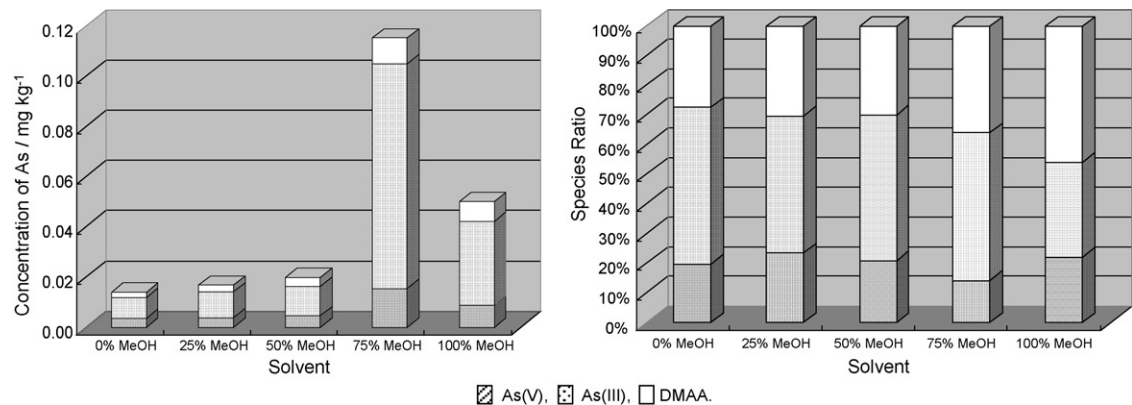
Fig. 3. Accelerated solvent extraction of As species in white rice flour.
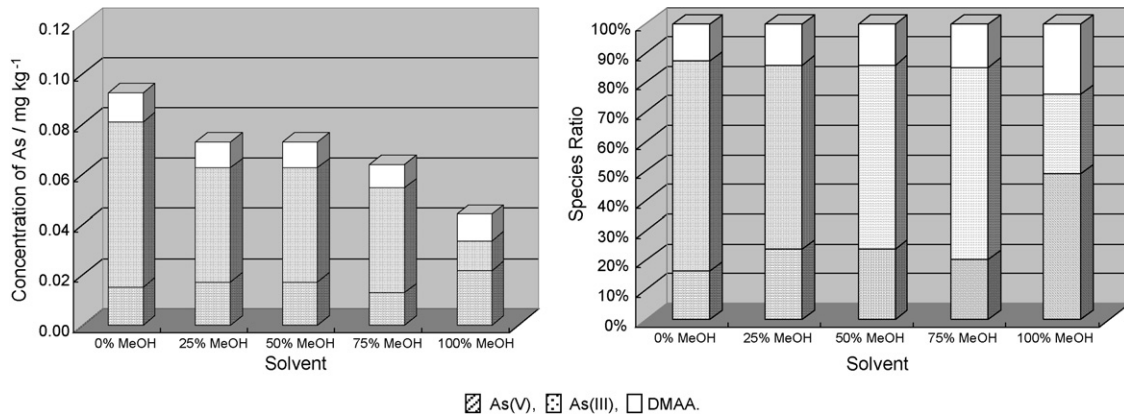
Fig. 4. Microwave-assisted extraction of As species in white rice flour.
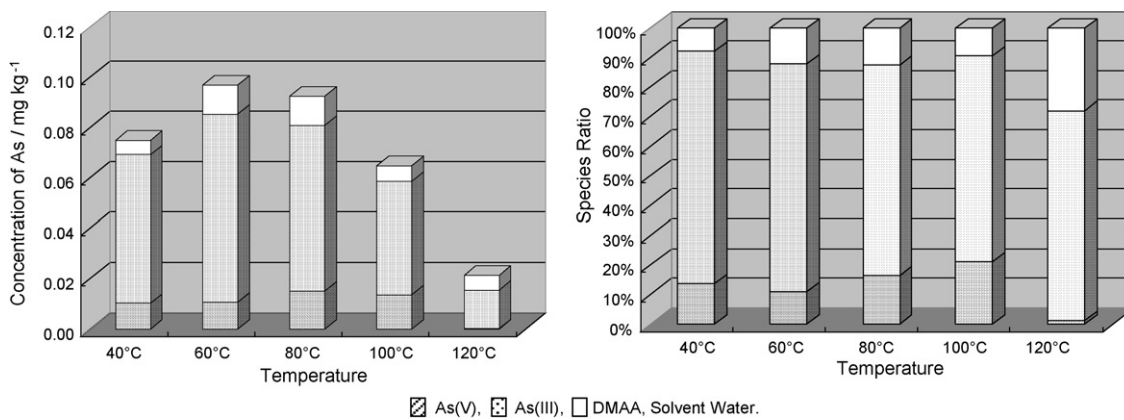
Fig. 5. Effect of operating temperature on microwave-assisted extraction.

methanol. However, when 100% methanol was used, the extraction efficiency dropped to 20%. As(III), As(V) and DMAA were found in all extracts. The extraction efficiencies for the As species in each extract were constant although the total amounts of As extracted were low compared with the total present in the rice flour (20–30%).

3.2.2. Ultrasonic extraction

The results shown in Fig. 2 were very similar to those obtained by shaking. As(III), As(V) and DMAA were detected in all extracts and their extraction efficiencies were the same as those obtained by shaking.

D'Amato et al. reported that shaking and ultrasonic extraction for 1 h or 2 h at room temperature did not yield satisfactory results. They demonstrated that four 2 h cycles at 50 °C were required to achieve quantitative extraction of As species from SRM 1568a using 1:1 water–methanol and ultrasonication [37]. However, the procedure needed much time and the extraction efficiency was not 100% when tested using 50% methanol solvent in the current study.

3.2.3. Accelerated solvent extraction

Results are shown in Fig. 3. The extraction efficiency depended very much on the solvent used. When water was used at high tem-
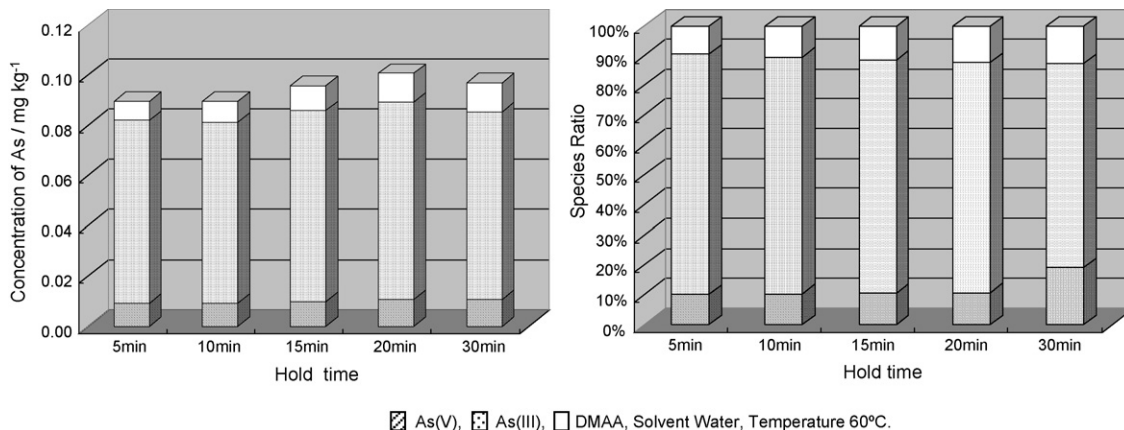
Fig. 6. Effect of extraction time on microwave-assisted extraction.

Table 1
Speciation results of As in rice sample by HPLC-ICP-MS

Sample	As(V)	As(III)	MMAA	DMAA	Total	Certified value (mg kg^{-1})	Recovery (%)
NIST 1568a	0.044 ± 0.002 (15%)	0.052 ± 0.001 (18%)	0.012 ± 0.0008 (4%)	0.173 ± 0.002 (60%)	0.281 ± 0.002	0.29 ± 0.03	97.0
NIES no. 10 low	0.059 ± 0.001 (35%)	0.096 ± 0.002 (56%)	0.003 ± 0.0004 (2%)	0.015 ± 0.0008 (9%)	0.173 ± 0.002	0.17[a]	101.9
NIES no. 10 medium	0.039 ± 0.001 (35%)	0.069 ± 0.002 (63%)	0.003 ± 0.0008 (3%)	0.005 ± 0.0004 (5%)	0.117 ± 0.003	0.11[a]	106.0
NIES no. 10 high	0.039 ± 0.001 (26%)	0.098 ± 0.002 (65%)	0.005 ± 0.0007 (3%)	0.017 ± 0.001 (11%)	0.159 ± 0.002	0.15[a]	105.8
White rice flour	0.013 ± 0.0007 (14%)	0.071 ± 0.001 (74%)	0.000 (0%)	0.011 ± 0.0006 (12%)	0.095 ± 0.003	0.096[b]	99.0

[a] Reference value.
[b] Result of total As in white rice flour with microwave digestion.

perature, the extraction efficiency was low, about 20%, even at high pressure, as the rice flour became gelatinous. The amounts of As extracted increased with increasing methanol concentration and 75% methanol solvent provided the highest extraction efficiency. The apparent efficiency was 130%; an anomaly resulting from difficulty in controlling the volume of extraction solvent and poor replication precision (10%). It was concluded that the accelerated solvent extraction technique was difficult to apply to rice samples.

3.2.4. Microwave-assisted extraction

Results are shown in Fig. 4. As(III), As(V) and DMAA were detected in the water extract, and the sum of the amounts of the extracted species was approximately 100% of the total As in the sample. The extraction efficiency decreased when the methanol concentration in the solvent was increased. It was finally about 50% when the extraction solvent was 100% methanol.

Interestingly, only the amount of As(III) extracted decreased with an increase in the methanol concentration of the extracting solvent; the extraction efficiencies of As(V) and DMAA remained constant. In addition, heating was necessary to completely extract the As species in rice samples, although inorganic As and the water-soluble organic As compounds can usually be extracted effectively from biological samples without heating. As(III) tends to bind tightly to thiol groups in proteins [38–40], which is a likely reason for the strong extraction conditions necessary to extract all the As(III) from the rice samples.

As(III), As(V) and DMAA were extracted from the white rice flour to some extent with all the extraction conditions and techniques investigated here, but no other As species were detected by HPLC–ICP-MS, even with elution times as long as 30 min.

3.3. Conditions for microwave-assisted extraction

Microwave-assisted extraction was the most efficient of the techniques tested here. The effect of extraction temperature was investigated using water and varying temperature from 40 °C to 120 °C. Results are shown in Fig. 5. The best extraction efficiency was obtained at temperatures of about 80 °C. When the operating temperature was 120 °C the rice flour charred and the extraction solvent volatilized during microwave irradiation. When charring occurred the amount of As extracted was reduced. When the extraction solvent volatilized recoveries of As were increased by factors of 1.2–1.5, so precision could not be determined. It was concluded that the optimum operating temperature was 80 °C.

The extraction time was investigated for each operating temperature using water as the extraction solvent; results for an operating temperature of 80 °C are shown in Fig. 6. The As extraction efficiency became constant (100% in this case) at 15 min and above. Also, the liquid/solid ratio was investigated by varying the liquid weight from 5 to 20 g and the solid weight from 0.5 to 2 g. When the ratio was 10 (liquid/solid = 10 g:1 g), the recoveries of As species were constant and could not be improved.

Thus, the optimum conditions for microwave extraction were as follows: an extraction temperature of 80 °C, an extraction time of 30 min, water as the extraction solvent, and a ratio of water to rice flour of 10 to 1 by weight.

3.4. Additional test of arsenic standards

An essential requirement for As speciation analysis is that the chemical forms of As remain unchanged during the extraction process. This is particularly important when the extraction is assisted by heating. Recoveries of As(III), As(V), MMAA, DMAA, TMAO, TeMA AB and AsC were investigated using the above extraction process. Rice flour samples were spiked with each of the As species standards (5–10 ng g^{-1} as As) and their recoveries were determined following the proposed extraction procedure (n = 3). Recoveries of all species were nearly 100%, which demonstrated that they are not chemically altered to any significant extent during the extraction.
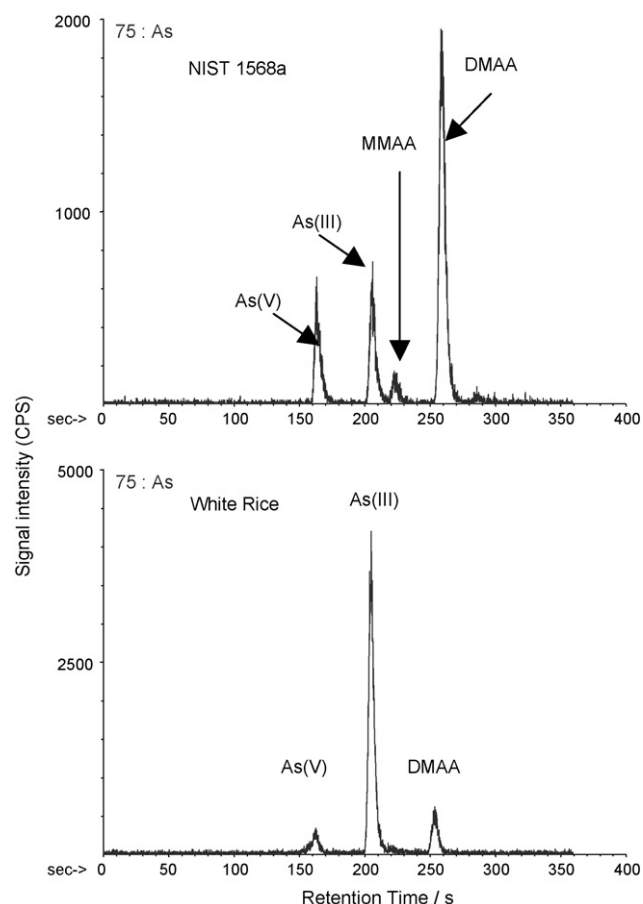
Fig. 7. Chromatograms of As species in rice sample.

In addition, no chemical changes were observed when the standard solutions alone were subjected to the extraction procedure.

3.5. Application to CRMs

The optimal extraction conditions established in this study were applied to CRM rice flour samples. Analytical results and typical chromatograms are shown in Table 1 and Fig. 7 (NIST SRM and white rice flour sample).

Standard solutions were used to construct the calibration curves, with concentration ranges from 0.5 ng g^{-1} to 10 ng g^{-1}. The detection limits for all As species were 0.1 ng g^{-1}.

When the white rice flour was analyzed (6 sub-samples, 1 from each of 6 bottles; $n = 6$), As(III), As(V) and DMAA were detected, with the quantities As(III) (74%) > As(V) (14%) > DMAA (12%). Three sub-samples were analyzed for each of the CRMs. In NIES no. 10 (all three Cd levels), As(III), As(V), DMAA and a small amount of MMAA were detected. The relative amounts were As(III) (26–35%) > As(V) (56–65%) > DMAA (5–11%) > MMAA (2–3%) for all types. As(III), As(V), MMAA and DMAA were detected in NIST SRM 1568a, and the relative quantities were DMAA (60%) > As(III) (18%) > As(V) (15%) > MMAA (4%). The proportion of DMAA in NIST CRM was very high compared with the other samples. When the sums of the concentrations of each arsenic species in each CRM were compared with the total for each CRM, the recoveries were 97–106%, and the results were in good agreement with the certified value and reference values.

4. Conclusions

Methods were investigated to extract the As species from rice flour prior to their analysis by HPLC–ICP-MS. Microwave-assisted extraction using water as the solvent provided good extraction efficiency without chemical alteration of the As species.

The concentrations of total As in the rice samples examined in this study were very low and are therefore unlikely to pose any health risks for human consumers. However, it is very important to know the total As concentration and its chemical species in foods to facilitate accurate risk evaluation related to food safety.

Five rice flour samples were used for the speciation study. A white rice flour sample and NIES CRM no. 10 unpolished rice flour, both collected in Japan, were found to contain high proportions of inorganic As species. In contrast, DMAA was the most abundant As species in NIST SRM 1568a, which was made from unpolished rice grown in the USA. The As species in the rice plants are likely to reflect the environment (soil, water, etc.) in which they were grown. DMAA has been used as a herbicide in the USA and it may persist in the NIST SRM. MMAA was not found in the white rice flour sample, but it was detected in NIES no. 10 and NIST 1568a, which were made from unpolished rice. There is thus a possibility that the different As species are in different parts of the rice plants; MMAA may tend to accumulate in bran for example. It is necessary to analyze a wider range of samples to acquire a comprehensive knowledge of As species in rice.

References

[1] Arsenic and Arsenic Compounds, IARC Monographs, Suppl. 7, International Agency for Research on Cancer, WHO, Lyon, France, 1987, pp. 100–106.
[2] The Arsenic in Food Regulation, SI number 831, Food Standard Agency, UK Government, 1959.
[3] K.J. Lamble, S.J. Hill, Anal. Chim. Acta 334 (1996) 261.
[4] S. Branch, L. Ebdon, P. O'Neill, J. Anal. At. Spectrom. 9 (1994) 33.
[5] D. Vélez, N. Ybáñez, R. Montoro, J. Anal. At. Spectrom. 12 (1997) 91.
[6] W. Goessler, D. Kuehnelt, C. Schlagenhaufen, Z. Slejkovec, K.J. Irgolic, J. Anal. At. Spectrom. 13 (1998) 183.
[7] J. Kirby, W. Maher, J. Anal. At. Spectrom. 17 (2002) 838.
[8] M.C. Villa-Lojo, E. Alonso-Rodríguez, P. López-Mahía, S. Muniategui-Lorenzo, D. Prada-Rodríguez, Talanta 57 (2002) 741.
[9] K. Wrobel, K. Wrobel, B. Parker, S.S. Kannamkumarath, J.A. Caruso, Talanta 58 (2002) 899.
[10] A. El Moll, R. Heimburger, F. Lagarde, M.J.F. Leroy, E. Maier, Fresenius' J. Anal. Chem. 354 (1996) 550.
[11] J.W. McKiernan, J.T. Creed, C.A. Brockhoff, J.A. Caruso, R.M. Leorenzana, J. Anal. At. Spectrom. 14 (1999) 607.
[12] P.A. Gallagher, J.A. Shoemaker, X. Wei, C.A. Brockhoff-Schwegel, J.T. Creed, Fresenius' J. Anal. Chem. 369 (2001) 71.
[13] M. Van Hulle, C. Zhang, X. Zhang, R. Cornelis, Analyst 127 (2002) 634.
[14] S. McSheehy, P. Pohl, D. Vĕlez, J. Szpunar, Anal. Bioanal. Chem. 372 (2002) 457.
[15] S. McSheehy, J. Szpunar, J. Anal. At. Spectrom. 15 (2000) 79.
[16] R. Schaeffer, C. Soeroes, I. Ipolyi, P. Fodor, N.S. Thomaidis, Anal. Chim. Acta 547 (2005) 109.
[17] A.D. Madsen, W. Goessler, S.N. Pedersen, K.A. Francesconi, J. Anal. At. Spectrom. 15 (2000) 657.
[18] J. Yoshinaga, Y. Shibata, T. Horiguchi, M. Morita, Accred. Qual. Assur. 2 (1997) 154.
[19] "Profile report", The Ministry of Agriculture, Forestry and Fisheries of Japan, http://www.maff.go.jp/syohi_anzen/profiles/arsenic.pdf.
[20] Y. Nakamura, T. Narukawa, J. Yoshinaga, J. Agric. Food Chem. 56 (2008) 2536.
[21] K. Sutton, R.M.C. Sutton, J.A. Caruso, J. Chromatogr. A 789 (1997) 85.
[22] R.A. Schoof, L.J. Yost, E. Crecelius, K. Irgolic, W. Goessler, H.-R. Guo, H. Greene, Hum. Ecol. Risk Assess. 4 (1998) 117.
[23] L.J. Yost, R.A. Schoof, R. Aucoin, Hum. Ecol. Risk Assess. 4 (1998) 137.
[24] R.A. Schoof, L.J. Eickhoff, E.A. Crecelius, D.W. Cragin, D.M. Meacher, D.B. Memzel, Food Chem. Toxicol. 37 (1999) 839.
[25] D.T. Heitkeper, N.P. Vela, K.R. Stewart, C.S. Westphal, J. Anal. At. Spectrom. 16 (2001) 299.
[26] C.-G. Yuan, G.-B Jiang, B. He, J. Anal. At. Spectrom. 20 (2005) 103.
[27] V.G. Mihucz, E. Tatár, I. Virág, C. Zang, Y. Jao, G. Záray, Food Chem. 105 (2007) 1718.
[28] E. Sanz, R. Muñoz-Olivas, C. Cámara, M.K. Sengupta, S. Ahamed, J. Environ. Sci. Health 42 (2007) 1695.
[29] E. Sanz, R. Muñoz-Olivas, C. Cámara, J. Chromatogr. A 1097 (2005) 1.
[30] S. Fostera, W. Mahera, F. Krikowaa, S. Apte, Talanta 71 (2007) 537.
[31] I. Pizarro, M. Gómez, C. Cámara, M.A. Palacios, Anal. Chim. Acta 495 (2003) 85.
[32] D. Kuehnelt, J. Lintschinger, W. Goessler, Appl. Organomet. Chem. 14 (2000) 411.
[33] A. Schmidt, W. Reisser, J. Mattusch, P. Popp, R. Wennrich, J. Chromatogr. A 889 (2000) 83.
[34] I. Koch, L. Wang, C.A. Ollson, W. Cullen, K.J. Reimer, Environ. Sci. Technol. 34 (2000) 22.
[35] I.J. Pickering, R.C. Prince, M.J. George, R.D. Smith, G.N. George, D.E. Salt, Plant Physiol. 122 (2000) 1171.
[36] L.Q. Ma, K.M. Komar, C. Tu, W. Zhang, Y. Cai, E.D. Kennelley, Nature 409 (2001) 579.
[37] M. D'Amato, G. Forte, S. Caroli, J. AOAC Int. 87 (2004) 238.
[38] O. Muñoz, D. Vélez, R. Montoro, Analyst 124 (1999) 601.
[39] O. Muñoz, D. Vélez, M.L. Cerver, R. Montoro, J. Anal. At. Spectrom. 14 (1999) 1607.
[40] M. Styblo, M. Hughes, D. Thomas, J. Chromatogr. B 677 (1996) 161.

Short communication

Improvement of acetylcholinesterase-based assay for organophosphates in way of identification by reactivators

Miroslav Pohanka [a,b,c,*], Daniel Jun [a,c], Kamil Kuca [a,c,d]

[a] Center of Advanced Studies, Faculty of Military Health Sciences, University of Defence, Hradec Kralove, Czech Republic
[b] Center of Biological Defense, Central Military Institute of Health, Techonin, Czech Republic
[c] Department of Toxicology, Faculty of Military Health Sciences, University of Defence, Hradec Kralove, Czech Republic
[d] Department of Chemistry, Faculty of Sciences, J.E. Purkinje University, Usti nad Labem, Czech Republic

ARTICLE INFO

ABSTRACT

Organophosphates present serious fulmination in several aspects of human life. Detection of organophosphates is frequently based on following acetylcholinesterase (AChE) inhibition. Although limit of detection and sensitivity for AChE-based assays seem to be intriguing, the identification of organophosphates is not currently efficient in this way. We introduce an improvement of AChE-based assay by reactivators using a selective come-back of AChE activity after previous inhibition. We have chosen four organophosphates: paraoxon-ethyl, paraoxon-methyl, trichlorfon, methamidophos as representative pesticides and the three most available reactivators: HI-6, obidoxime, pralidoxime. Reactivation was realized in the 96-wells photometric microplates and activity of human recombinant AChE was followed by reaction of Ellman's reagent with one of enzyme digestion product: thiocholine. Distinguishing of reactivation efficacy was judged by the independent two population *t*-test. The most significant identification was based on methamidophos inhibited AChE reactivation by HI-6 or pralidoxime and paraoxon-ethyl inhibited AChE by obidoxime; moreover, identification of trichlorfon and paraoxon-methyl was possible, too. Practical impact of described method is discussed.

© 2008 Elsevier B.V. All rights reserved.

1. Introduction

Organophosphates represent a wide group of toxic compound exerting inhibitory effect toward important enzymes in a body: acetylcholinesterase (AChE, EC 3.1.1.7), most commonly known from neurosynapses and butyrylcholinesterase (BChE, EC 3.1.1.8) with not unambiguous function. The group of organophosphates is well known due to practical importance of related compounds. Especially, nerve agents such as tabun (known also in shortened name GA), sarin (GB), soman (GD), cyclosarin (GF) and pesticides such as chlorpyrifos, diazinon, dimethoate, malathion, methamidophos, paraoxon (ethyl and methyl) are good examples of military or industrially widespread representatives.

Investigation of alignments in the primary and secondary structure proved close relation between AChE from evolutionary far species *Drosophila melanogaster, Mus musculus, Homo sapiens*, and *Torpedo californica* [1]. Although organophosphates can strongly inhibit different origin AChEs, some strategies for reactivation by some oximes were recommended [2]. Monoquaternary prali-

doxime (2-hydroxyiminomethyl-1-methylpyridinium chloride), and bisquaternary HI-6 [1-(2-hydroxyiminomethylpyridinium)-3-(4-carbamoylpyridinium)-2-oxa-propane dichloride], obidoxime [1,3-bis(4-hydroxyiminomethylpyridinium)-2-oxa-propane dichloride] and K048 [1-(4-hydroxyiminomethylpyridinium)-4-(4-carbamoylpyridinium) butane dibromide] were investigated for reactivation of VX, tabun, sarin, and cyclosarin [3]. The further study compared efficacy of pralidoxime, HI-6, obidoxime, trimedoxime, methoxime for seven organophosphates including nerve agents [4]. Reactivation potency of HI-6, obidoxime and pralidoxime was examined on *in vitro* paraoxon inhibited AChE [5]. Inhibition between alternative substrate acetylthiocholine and HI-6 for different origin AChE and BChE was studied and this fact was presented as partial disadvantage of HI-6 [6]. Reactivators were also found suitable for regeneration of biosensors based just on AChE; trimedoxime [TMB-4′; 1,3-bis(4-hydroyiminomethylpyridinium) propane dibromide] and pralidoxime (2-PAM; 1-methyl-2-hydroxyiminomethylpyridinium iodide) were referred for these purposes [7,8].

Several methods can be employed for organophosphates assay. The most common ones are either gas chromatography or nowadays more approachable liquid chromatography with tandem mass spectrometry detection [9]. Liquid chromatography–mass

spectrometry was also found applicable for diagnosis of organophosphates inhibited BChE [10]. Contemporary effort has led to development of new methods. Liu and Lin [11] proved feasibility zirconia nanoparticles as selective sorbents for organophosphate pesticides assay; potentiometric biosensor based on *Escherichia coli* cells expressing organophosphorus hydrolase was found suitable for paraoxon, methyl parathion, and diazinon assay [12]. Microchips employing capillary electrophoresis [13] and micellar electrokinetic chromatography [14] were described as useful tool for fast screening of organophosphate nerve agents. In another way performed assay was described by Mulchandani et al., organophosphorus hydrolase was proven suitable for an amperometric biosensor construction [15].

Inhibition of AChE and BChE by organophosphates is widely used for construction of detection devices. Detection kits were successfully designed [16,17]. Cholinesterases were found as a convenient recognition component for biosensors construction, e.g. BChE immobilized on platinum working electrode and AChE immobilized on a nanoporous carbon matrix was referred [18,19]. AChE is applicable for photometric assay, too [20]. A sensor with cholinesterase as recognition element was found promising for routinely assays of pesticides in beverages samples [21]. History of cholinesterase biosensors and expectancies for the future was extensively reviewed by Andreescu and Marty [22].

AChE reactivators are widely referred as important medicaments for treatment of individuals intoxicated with organophosphates. Some works appointed at possibility to employ reactivators for repeated assay with AChE-based biosensors. In the presented works, we are appointing at alluring performance of reactivators for analytical purposes especially due to diverse efficacy of inhibited AChE reactivation.

2. Materials and methods

2.1. Chemicals

Human recombinant AChE in lyophilized form (2000 U/mg of protein), acetylthiocholine chloride (ATChCl), DTBN [5,5′-dithiobis (2-nitrobenzoic acid)]—Ellman's reagent was purchased from Sigma–Aldrich (St. Louis, MO, USA). Organophosphates paraoxon-ethyl [O,O-diethyl O-(4-nitrophenyl) phosphate], paraoxon-methyl [O,O-dimethyl O-(4-nitrophenyl) phosphate], methamidophos [O,S-dimethyl phosphoramidothioate] and trichlorfon [(2,2,2-trichloro-1-hydroxyethyl) phosphonic acid dimethyl ester] were obtained as an analytical standards from the Labor Dr. Ehrenstorfer-Schafers (Augsburg, Germany). The monopyridinium and bispyridinium oximes (reactivators) were synthesized at the Department of Toxicology of the Faculty of Military Health Sciences, University of Defence (Czech Republic) according referred procedures [21–25]. The purities of prepared reactivators were analysed using a HPLC technique. The stock of reactivators was investigated by a NMR technique (Varian Gemini 300, Palo Alto, CA, USA) subsequently. Deionized water was prepared by the Millipore system. All other chemicals were supplied by the certified distributors in a *p.a.* quality.

2.2. Measuring setup

96-wells (8 × 12) photometric microplates were obtained from Gama (Ceske Budejovice, Czech Republic). The absorbance reader MRX (Dynatech Laboratories, Chantilly, VA, USA) was used as measuring device. Lyophilized AChE was suspended into phosphate buffered saline (PBS) up final activity 0.01 U/μl and injected into each well in final volume 1 μl and mixed with another 1 μl of 50 μM organophosphate (in PBS). The mixture was gently shaked in wet chamber for half an hour. After that, 100 μl of the fresh mixture of 1 mM ATChCl and DTBN 0.4 μg/ml in PBS was injected per well commonly with reactivator in final concentration from 10^{-4} to 10^{-8} M. Absorbance at 412 nm was measured against PBS (blank; four wells per one plate) after the given time interval (5, 10, and 20 min). Ever concentration of reactivator for used organophosphate was measured four times.

2.3. Data processing

The percent of reactivation R was taken as an outputting parameter. The value of the R was calculated according following equation:

$$R = \frac{\Delta A_r - \Delta A_i}{\Delta A_0 - \Delta A_i} \times 100(\%)$$

The symbol ΔA_0 is absorbance provided by mixture with intact AChE (in the final mixture was no organophosphate as well as no reactivator); ΔA_i is absorbance of mixture with inhibited AChE (inhibition by organophosphate, no reactivator). Absorbance provided by mixture where AChE activity was influenced by organophosphate and consequently by reactivator was presented by the last symbol ΔA_r.

The percentage of reactivation was drawn vs. reactivator concentration and fitted with an exponential decay using software Origin 6.1 (Northampton, MA, USA). Proper form of exponential decay equation will be discussed in Section 3. The correlation coefficient r was calculated for each curve. The collation of experimental values was realized by the independent two population t-test on significance level 0.05 (using Origin 6.1).

3. Results and discussion

Human recombinant AChE was inhibited with methamidophos, paraoxon-ethyl, paraoxon-methyl, and trichlorfon. After that, wells with inhibited AChE were reactivated with HI-6, pralidoxime, or obidoxime in different concentrations. Percent of reactivation R was calculated from experimental data and reactivation efficacy could be estimated from the dependence of R on final molar concentration of reactivator (from 10^{-8} to 10^{-4}) for ever preincubation time interval (5, 10, and 20 min). Calculated points were fitted with exponential decay function (Origin 6.1) and the coefficients of determination (r^2) were obtained. The correlation coefficients r (root of determination coefficients) was compared with the critical value on the probability level 0.05. Although the most of curves were described properly by the exponential decay; analysis of correlation coefficients and estimation of curves tendency proved that, *in vitro*, HI-6 was not significantly suitable for reactivation for trichlorfon and pralidoxime for paraoxon-ethyl inhibited AChE because of random fluctuation of R. Curves presenting efficacy of reactivation are presented in Fig. 1 for the most important 10 min preincubation. Due to lack of space and better lucidity, the coefficients of exponential decays and correlation coefficients are summarized in Table 1 for ever or the three times of preincubation. The common form of performed exponential decay equation found suitable for data processing is following:

$$R = R_0 + Ae^{-c/t}$$

Expression of the proportion rule between percent of reactivation (R) and molar concentration of reactivator (c) is given by this equation. The symbol R_0 indicates bottom limit of reactivation (when blank applied – spontaneous dissociation of
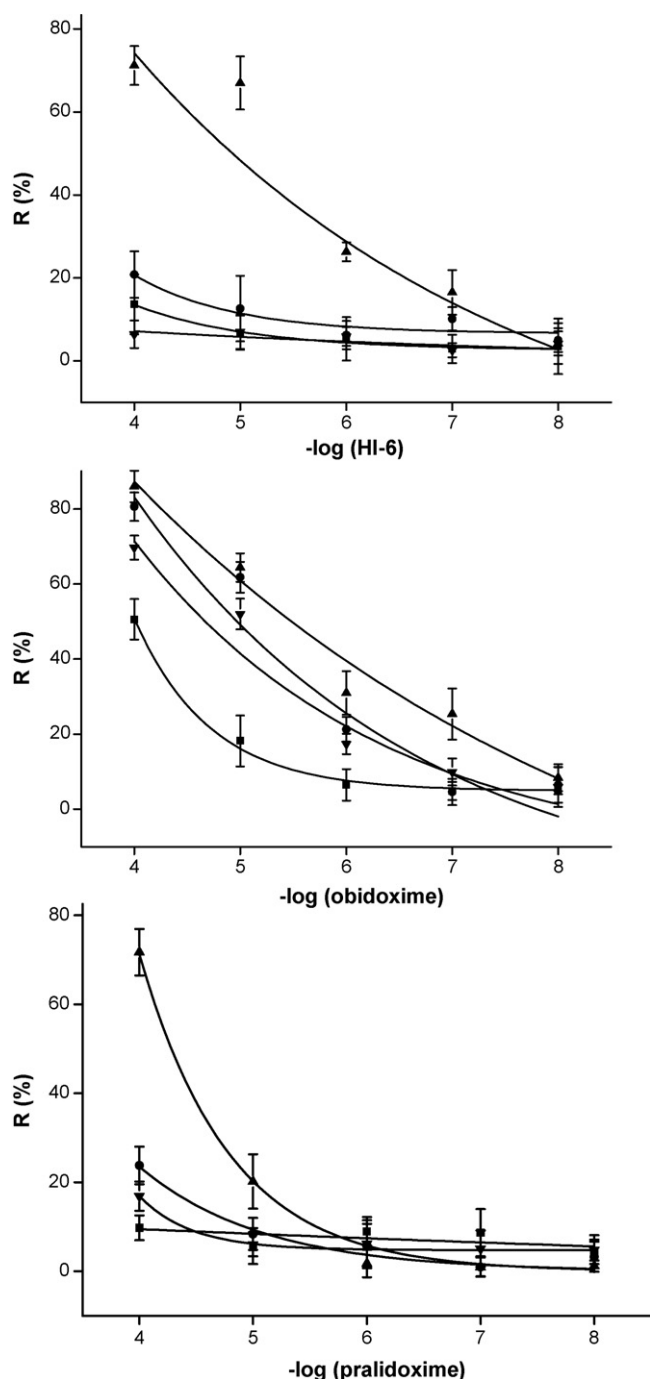
Fig. 1. AChE reactivation by HI-6, obidoxime and pralidoxime. The percent of reactivation R vs. molar concentration of reactivator is presented. Plots are for a 10 min preincubation with the reactivator. Preincubation 5 and 20 min are mentioned in the text. Inhibitors were following: methamidophos (▲), paraoxon-methyl (●), paraoxon-ethyl (■), and trichlorfon (▼). The error bars are expressed by standard deviation ($n = 4$). The experimental points were fitted by an exponential decay.

Table 1
Summarizing of exponential decay coefficients

	Paraoxon-ethyl	Paraxon-methyl	Methamidophos	Trichlorfon
HI-6, 5 min				
R_0	7.14	8.72	88.4	2.43
A	580	76.5	330	15.5
t	1.03	2.21	6.33	4.71
r	0.95	0.88	0.97	0.90
HI-6, 10 min				
R_0	2.58	6.60	−32.0	−0.89
A	400	988	324	17.0
t	1.11	0.94	3.59	5.30
r	0.98	0.87	0.96	0.73
HI-6, 20 min				
R_0	2.10	0.67	1.74	1.90
A	2.76×10^3	378	703	11.5
t	0.71	1.39	1.63	3.60
r	0.99	0.93	0.92	0.73
Obidoxime, 5 min				
R_0	8.04	−1.11	−77.4	1.13
A	3.15×10^4	2.70×10^3	335	2.26×10^3
t	0.61	1.20	6.00	1.05
r	0.99	0.95	0.98	0.99
Obidoxime, 10 min				
R_0	4.89	−27.1	−51.7	−13.7
A	1.27×10^4	482	323	481
t	0.71	2.71	4.75	2.31
r	0.99	0.97	0.99	0.98
Obidoxime, 20 min				
R_0	1.28	0.11	5.50	4.41
A	2.49×10^3	984	1.19×10^3	574
t	1.02	1.63	1.44	1.77
r	0.99	0.94	0.98	0.94
Pralidoxime, 5 min				
R_0	2.41	2.57	5.05	1.41
A	52.2	225	7.00×10^4	150
t	2.05	1.62	0.59	1.89
r	0.84	0.98	0.99	0.99
Pralidoxime, 10 min				
R_0	9.08	0.11	0.19	4.80
A	23.5	931	1.09×10^4	7.02×10^4
t	17.1	1.09	0.80	0.46
r	0.65	0.98	0.99	0.99
Pralidoxime, 20 min				
R_0	3.50	0.15	0.12	3.80
A	2.86×10^3	5.54×10^3	1.60×10^3	7.42×10^4
t	0.66	0.76	0.73	0.46
r	0.89	0.99	0.98	0.99

The correlation coefficients r was obtained as root of coefficient of determination (r^2) obtained throughout Origin software.

organophosphate), t, decay constant, and A, amplitude of exponential decay curve.

The values R in Fig. 1 were investigated using the independent two population t-test. The aim of presented work is not estimate reactivators efficacy for pharmaceutical study but follow differences in reactivation for qualitative analysis purposes. The most significant was difference in reactivation of methamidophos inhibited AChE by 10^{-4} and 10^{-5} M HI-6 and 10^{-4} M

pralidoxime in all time intervals. Reactivation of methamidophos inhibited AChE was significant on probability level 0.01. Obidoxime seems to be quite effective for reactivation of AChE inhibited by all tested organophosphates; however, paraoxon-ethyl inhibited AChE was significantly less reactivated (even on probability level 0.01) by 10^{-4}–10^{-5} M obidoxime and by pralidoxime in time interval 5 and 10 min. In further investigation, we observed that trichlorfon inhibited AChE can be significantly distinguished by 10^{-4}–10^{-5} M obidoxime from paraoxon-ethyl (bottom efficacy) and paraoxon-methyl and methamidophos (upper efficacy of reactivation) in 10 min preincubation interval. Some other differences were observed during statistical evaluation; nevertheless, above mentioned information is the most demonstrable for qualitative analysis purposes. It seems that preincubation of inhibited AChE with reactivator for 10 min is the most promising for analytical purposes. On the other side, preincubation for the longer time (20 min) has only a reduced analytical importance.

The obtained data are suitable for new approach in AChE-based organophosphate assay. The differences in reactivation efficacy confirmed that reactivators can be used for organophosphates identification. We should mention that total number of currently available organophosphates exceed tens and reach hundreds. On the other side, reactivators are currently investigated resulting in continuous increasing of its known amount [23–28]. Our experiments have proved possibility to distinguish each tested organophosphate from the other using AChE reactivators. The most relevantly can be identified paraoxon-ethyl by obidoxime and methamidophos by pralidoxime and HI-6; however, others organophosphates can be identified, too. The achievement is a possibility to distinguish two similar organophosphates: paraoxon methyl and ethyl. In all experimental curves, there was obvious reactivation efficacy for reactivator in concentration approximately above 10^{-6} M. We expect practical impact of reactivators in assays of organophosphates performed by biosensor or any photometric device based on AChE. Reactivators could be employed in electrochemical analysis without important interferences. In this way, tested HI-6 was not oxidized by applied voltage in our previous study [6]. We consider reactivators performance as a great challenge for contemporary AChE-based assays [29]. This study is only preliminary study and it is not possible to identify all known pesticides by the three tested reactivators. On the other side, the data are quite promising and the future research could introduce more extensive feasibility of cholinesterase-based assays. Presented way of reactivator's application was based on the reactivation of totally inhibited AChE. The future application should be also correlated on real samples and different concentration of organophosphate—there should be followed shift of activity after sample and then reactivator application.

4. Conclusions

The possibility to improve AChE-based assays by reactivators was tested. On the beginning, there was an idea used reactivator as an analytical reagent allowing distinguishing organophosphates according different reactivation rate (efficacy). We confirmed this idea. All four organophosphates can be distinguished one from each other when at least two reactivators are applied (obidoxime and either HI-6 or pralidoxime). The practical impact of proposed approaching is expected and we hope that further studies confirm promising suggestions promoted in this work.

References

[1] J. Wiesner, Z. Kriz, K. Kuca, D. Jun, J. Koca, J. Enzyme Inhib. Med. Chem. 22 (2007) 417.
[2] K. Kuca, D. Jun, K. Musilek, Mini Rev. Med. Chem. 6 (2006) 269.
[3] K. Kuca, J. Kassa, J. Enzyme Inhib. Med. Chem. 18 (2003) 529.
[4] K. Kuca, D. Jun, J. Bajgar, Drug Chem. Toxicol. 30 (2007) 31.
[5] M. Pohanka, D. Jun, K. Kuca, J. Enzyme Inhib. Med. Chem. (in press).
[6] M. Pohanka, D. Jun, K. Kuca, Anal. Lett. 40 (2007) 2351.
[7] S. Okazaki, H. Nakagawa, K. Fukuda, S. Asakura, H. Kiuchi, T. Shigemori, S. Takahashi, Sens. Actuators B 66 (2000) 131.
[8] K.C. Gulla, M.D. Gouda, M.S. Thakur, N.G. Karanth, Biochim. Biophys. Acta 1597 (2002) 133.
[9] M.G. Margariti, A.K. Tsakalof, A.M. Tsatsakis, Ther. Drug Monit. 29 (2007) 150.
[10] D. Noort, A. Fidder, M.J. van der Schans, A.G. Hulst, Anal. Chem. 78 (2006) 6640.
[11] G. Liu, Y. Lin, Anal. Chem. 77 (2005) 5894.
[12] A. Mulchandani, P. Mulchandani, I. Kaneva, W. Chen, Anal. Chem. 70 (1998) 4140.
[13] J. Wang, M.P. Chatrathi, A. Mulchandani, W. Chen, Anal. Chem. 73 (2001) 1804.
[14] J. Wang, M. Pumera, M.P. Chatrathi, A. Escarpa, M. Musameh, G. Collins, A. Mulchandani, Y. Lin, K. Olsen, Anal. Chem. 74 (2002) 1187.
[15] A. Mulchandani, P. Mulchandani, W. Chen, Anal. Chem. 71 (1999) 2246.
[16] H.Y. No, Y.A. Kim, Y.T. Lee, H.S. Lee, Anal. Chim. Acta 594 (2007) 37.
[17] B.M. Kim, A.M. Abd El-Aty, T.E. Hwang, L.T. Jin, Y.S. Kim, J.H. Shim, Bull. Korean Chem. Soc. 28 (2007) 929.
[18] P. Skladal, J. Krejci, Collect. Czech. Chem. Commun. 61 (1996) 985.
[19] S. Sotiropoulou, N.A. Chaniotakis, Anal. Chim. Acta 530 (2005) 199.
[20] F. Eyer, P. Eyer, Hum. Exp. Toxicol. 17 (1998) 645.
[21] M. Pohanka, K. Kuca, D. Jun, Anal. Lett. (in press).
[22] S. Andreescu, J.L. Marty, Biomol. Eng. 23 (2006) 1.
[23] J. Bajgar, J. Fusek, K. Kuca, L. Bartosova, D. Jun, Mini Rev. Med. Chem. 7 (2007) 461.
[24] K. Musilek, L. Lipka, V. Racakova, K. Kuca, D. Jun, V. Dohnal, M. Dolezal, Chem. Pap. 60 (2006) 48.
[25] K. Musilek, K. Kuca, D. Jun, V. Dohnal, M. Dolezal, Biorg. Med. Chem. Lett. 16 (2006) 622.
[26] K. Kuca, P. Stodulka, M. Hrabinova, P. Hanusova, D. Jun, B. Dolezal, Def. Sci. J. (in press).
[27] K. Kuca, K. Musilek, P. Stodulka, J. Marek, P. Hanusova, D. Jun, M. Hrabinova, J. Kassa, B. Dolezal, Lett. Drug Des. Discuss. 4 (2007) 510.
[28] K. Musilek, K. Kuca, D. Jun, M. Dolezal, Curr. Org. Chem. 11 (2007) 229.
[29] M. Pohanka, D. Jun, H. Kalasz, K. Kuca, Protein Pept. Lett. (in press).

Enzyme-Linked Immunosorbent Assay (ELISA) based on superparamagnetic nanoparticles for aflatoxin M_1 detection

A. Radoi[*], M. Targa, B. Prieto-Simon, J.-L. Marty

IMAGES, Université de Perpignan, 52 Avenue Paul Alduy, 66860 Perpignan Cedex, France

ABSTRACT

Five different clones of antibodies developed against the aflatoxin M_1 were investigated by using the classical indirect and direct competitive Enzyme-Linked Immunosorbent Assay (ELISA) formats, and also the direct competitive ELISA based on the use of the superparamagnetic nanoparticles. The purpose of this study was to assess if not so friendly time classical ELISA procedures can be further improved, by reducing the coating, blocking and competition time. Here we showed that a complete dc-ELISA (coating, blocking and competition step) based on the use of superparamagnetic nanoparticles can be performed in basically 40 min, if coating step (20 min) should be taken into account. Moreover, the standard analytical characteristics of the proposed method fulfil the requirements for detecting AFM_1 in milk, in a wide linear working range (4–250 ng/L). The IC_{50} value is 15 ng/L. The matrix effect and the recovery rate were assessed, using the European Reference Material (BD282, zero level of AFM_1), showing an excellent percentage of recovery, close to 100%.

© 2008 Elsevier B.V. All rights reserved.

1. Introduction

Aflatoxins are highly toxic and carcinogenic secondary metabolites produced by *Aspergillus flavus* and *Aspergillus parasiticus* on a variety of agricultural commodities [1] and [2]. These fungi grow under particular conditions of temperature and humidity on a great variety of food commodities and animal feed materials. Contamination, either before or after harvest, of corn, peanuts, cereal crops, figs, etc., is a common occurrence [3–5].

Aflatoxin M_1 (AFM_1) is the hydroxylated metabolite of aflatoxin B_1 (AFB_1). Mammals that ingest aflatoxin B_1 contaminated diets excrete amounts of the principal 4-hydroxylated metabolite known as aflatoxin M_1 into milk, and subsequently it can be found in a large variety of dairy products. The toxic and carcinogenic effects of AFM_1 have been convincingly demonstrated in laboratory investigations [6]. The demonstrated toxic and carcinogenic effects of AFM_1 recently lead WHO-IARC to change its classification from group 2 to group 1 [7]. AFM_1 is relatively stable during pasteurisations, storage, and preparation of various dairy products [6] and [8] and therefore AFM_1 contamination poses a significant threat to human health, especially to children, who are the major consumers of milk. European Community legislation limits the concentration of aflatoxin M_1, in milk and dried or processed milk products intended for adults, at 0.050 ppb (μg/kg) [9] and at 0.025 ppb (μg/kg) for milk

intended for infants or for baby-food production [10]. The official methods of sampling and analysis are regulated by the European Commission Directives [11]. A high performance liquid chromatography analysis with fluorimetric detection (HPLC-FD) coupled with a clean-up treatment by immunoaffinity columns (IC) is the reference method used for the determination of aflatoxins in milk [12]. This procedure is long and laborious and requires expensive equipment and well-trained personnel. Other methods for AFM_1 determination have also been proposed. Of significant importance are thin-layer chromatography [13], fluorescence detection after immunoaffinity clean-up [14], liquid chromatography coupled to mass spectrometry [15], and immunoenzymatic assays. Immunochemical assays are rapid, simple, specific, sensitive and even in portable format, have become the most common quick methods for the routine analysis of mycotoxins in food and feed materials [16–20].

ELISA (Enzyme-Linked Immunosorbent Assay) is well-established as a high throughput assay with low sample volume requirements, and often has less sample clean-up procedures compared to conventional HPLC methods, and its standardisation for the application to milk sample analysis has been reported in International Standards Organisation guidelines [21].

2. Experimental

2.1. Safety note

Aflatoxins are highly carcinogenic and should be handled with extreme care. Aflatoxin contaminated labware should be

---

* Corresponding author.
E-mail address: radoiantonio@yahoo.com (A. Radoi).

decontaminated with an aqueous solution of sodium hypochlorite (5%).

2.2. Materials and apparatus

Polystyrene microtitre plates, MaxiSorp^{TM} and PolySorp^{TM}, were purchased from NUNC^{TM} (Roskilde, Denmark). The ERM (European Reference Material) BD282 (zero level of AFM$_1$) was purchased from the Institute for Reference Materials and Measurements (IRMM, Belgium). I'screen AFLA M$_1$ MILK test kit was from Tecna S.r.l. (Trieste, Italy). Milk samples were obtained from local supermarkets.

Aflatoxin M$_1$ (AFM$_1$, A6428), aflatoxin M$_1$ linked to bovine seric albumin (BSA-AFM$_1$, A6412), anti-rat goat IgG linked to alkaline phosphatase (rat Ab$_{II}$-AP, A8438), anti-mouse IgG linked to alkaline phosphatase (Ab$_{II}$-AP, A3562) or to horseradish peroxidase (Ab$_{II}$-HRP, A4416), 3,3′,5,5′-tetramethylbenzidine (TMB, T0440) liquid substrate for ELISA, bovine seric albumin (A9647) were purchased from Sigma (St. Louis, MO, USA). Alkaline phosphatase substrate (*p*-nitrophenol) was from Fluka Chemie (Buchs, Switzerland).

Superparamagnetic nanoparticles ($d = 300$ nm) coated with affinity purified goat anti-mouse IgG (Bio-Adembeads Antibodies Goat anti-Mouse IgG) and Bio-Adembeads Protein G (uniform sized superparamagnetic nanoparticles conjugated with protein G) were from Ademtech S.A. (Pessac, France).

Five different types of monoclonal antibodies against aflatoxin M$_1$ were tested: clone 1C6 (Acris Antibodies GmbH, Hiddenhausen, Germany, 0.5 mg/mL), clones 3G11 and 6G4 (Soft Flow Biotechnology Ltd., Gödöllő, Hungary, 1 mg/mL) and clones (confidential source) ATX9 (1.78 mg/mL) and ATX2 (0.93 mg/mL).

All other reagents were from Sigma (St. Louis, MO, USA).

A Multiskan EX (Thermo Life Sciences, Cergy-Pontoise, France) microplate photometer was utilised for colorimetric measurements.

Adem-Mag 96 (adapted for 96-well microtitre plates) and Adem-Mag SV (single magnet position adapted for both 1.5 mL or 2 mL microtubes) were from Ademtech S.A. (Pessac, France).

A horizontal shaker (IKA, Vibrax-VXR) was also utilised.

2.3. Samples preparation

Milk samples (available on local markets) were centrifuged (10 min, $3000 \times g$, 10 °C, Beckman centrifuge-model J2-21), and the skimmed milk was assayed. All the samples were also assayed using the I'screen AFLA M$_1$ MILK test kit, following the recommendations indicated by the supplier.

The ERM-BD282 milk powder was handled as recommended in the instructions for use, data provided with the certified material. For recovery studies, it was spiked before centrifugation (10 min, $3000 \times g$, 10 °C) and recovery percentage was calculated.

2.4. Spectrophotometric ELISA

2.4.1. Indirect competitive ELISA (ic-ELISA) protocol

In the indirect competitive ELISA (ic-ELISA) format, the BSA-AFM$_1$ was adsorbed onto the wells of the microtitre plate (MaxiSorp^{TM}) during the coating step, performed in 50 mM carbonate buffer (CB), pH 9.80. The coating volume was 100 μL/well and the plate was incubated at 4 °C, over night (ON). Then the incubated ELISA plate was covered with 150 μL/well of 1% (w/v) BSA solution (blocking step) prepared in 15 mM phosphate buffer saline (PBS), pH 7.40, for 45 min, at room temperature (RT, 22 °C). The competition was allowed to proceed, by adding inside the wells non-labelled aflatoxin M$_1$ (90 μL) and primary (Ab$_I$) anti-AFM$_1$ antibody (10 μL); solutions were prepared in PBS and the

competition time was 1 h, at room temperature. Then a solution (100 μL) prepared in PBS of secondary (Ab$_{II}$) anti-IgG antibody was added and allowed to react (1 h), at RT. Finally, 100 μL of substrate solution was added and the absorbance was read. Washing (3×200 μL) was performed after each step, by using a solution of 0.05% (v/v) of Tween prepared in PBS (2×200 μL) followed by only PBS (1×200 μL).

All the five antibodies (clones 1C6, 3G11, 6G4, ATX9 and ATX2) developed against AFM$_1$ were assayed in the ic-ELISA format. The optimised conditions (coating concentrations and dilutions of primary antibody), for the three different clones, when using an alkaline phosphatase labelled secondary antibody (Ab$_{II}$-AP, 1/1000, v/v), were:

3G11 (1/1280, v/v) and BSA-AFM$_1$ (25 ng/mL);
6G4 (1/1280, v/v) and BSA-AFM$_1$ (25 ng/mL);
ATX2 (1/1600, v/v) and BSA-AFM$_1$ (12.5 ng/mL).

A solution of para-nitrophenyl phosphate (*p*-NPP, 2 mg/mL) solubilised in 10% diethanolamine buffer (DEA, pH 9.80) was used as substrate. The absorbance was read after 30 min, using the 405 nm filter.

When using as secondary antibody an anti-mouse IgG labelled with horseradish peroxidase (Ab$_{II}$-HRP, 1/2500, v/v) the dilutions of primary antibodies were kept constant as before (i.e. for clones 3G11 and 6G4 the dilution was 1/1280, v/v and for ATX2 clone it was 1/1600, v/v), only the coating concentration varied (25 ng/mL of BSA-AFM$_1$). The Ab$_{II}$-HRP was allowed to bind the anti-AFM$_1$ primary antibody during an incubation time of 30 min, and the absorbance was read also after 30 min. TMB liquid substrate for ELISA was used as chromogen, the absorbance being measured at both 650 and 450 nm (after quenching with 100 μL/well of 1N H$_2$SO$_4$).

2.4.2. Direct competitive ELISA (dc-ELISA) protocol

In the direct competitive ELISA (dc-ELISA) assay, the 96-well ELISA plate (MaxiSorp^{TM}) was coated with anti-AFM$_1$ antibodies (clones G11, 6G4, and ATX2). The coating step (100 μL/well, 4 °C, ON) was performed in 50 mM carbonate buffer, pH 9.80. The blocking step (45 min) was performed at 22 °C, using 150 μL/well of 1% (w/v) BSA solution (prepared in 15 mM PBS, pH 7.40). The competition was allowed to proceed for 45 min and at RT, by adding inside the wells non-labelled aflatoxin M$_1$ (90 μL) and horseradish peroxidase labelled aflatoxin M$_1$ (AFM$_1$-HRP, 10 μL).

Finally, 100 μL of substrate solution was added and the absorbance was read 15 min after the TMB solution was added inside the wells, at both 650 and 450 nm (after quenching with 100 μL/well of 1N H$_2$SO$_4$).

Washing (3×200 μL) was performed after each step, by using a solution of 0.05% (v/v) of Tween prepared in PBS (2×200 μL) followed by only PBS (1×200 μL).

The optimised conditions (coating and dilution of labelled AFM$_1$) for the three different clones were:

3G11 (0.4 μg/mL) and AFM$_1$-HRP (1/180, v/v);
6G4 (0.2 μg/mL) and AFM$_1$-HRP (1/180, v/v);
ATX2 (0.5 μg/mL) and AFM$_1$-HRP (1/120, v/v).

2.5. Direct competitive ELISA based on Bio-Adembeads Protein G

This simplified version of dc-ELISA format relies on the use of uniform sized superparamagnetic nanoparticles conjugated with protein G as support for immobilizing the anti-AFM$_1$ antibodies. No blocking step was necessary and as working buffer a solution at 0.05% (v/v) of Tween prepared in PBS was employed for all the steps:

coating, competition and washing. Prior to use the nanoparticles were washed twice with working buffer (1400 μL) for removing the Proclin 300.

Briefly the optimised procedure was the following:

coating: 14 μL of superparamagnetic nanoparticles conjugated with protein G were dispersed into 1400 μL of antibody solution prepared in working buffer and allowed to react for 20 min; then the particles were collected using the Adem-Mag SV and washed twice with working buffer (1400 μL) and finally resuspended in 1400 μL; 30 μL of this dispersion were added inside the wells and the buffer was removed, meanwhile the nanoparticles were collected onto the inner wall of the well by using the Adem-Mag 96;
competition: 90 μL of AFM$_1$ and 10 μL of AFM$_1$-HRP were allowed to compete (PolySorp^{TM} microtitre plates were utilised) for the antibody binding sites, during 20 min; during coating and competition, an horizontal shaker (200 rpm) was employed.

Washing steps were performed (300 μL/well, 1 min) and when the different solutions were discarded from the wells, the superparamagnetic nanoparticles were collected by using the magnets available on the Adem-Mag 96. The TMB liquid substrate for ELISA was utilised (150 μL/well) and the absorbance was read 15 min after the substrate solution was added inside the wells, at both 650 and 450 nm (after quenching with 100 μL/well of 1N H$_2$SO$_4$).

The optimised amount of antibody against AFM$_1$ and the dilution of AFM$_1$-HRP used, for each of the three tested clones, is:

3G11 (0.2 μg/mL) and AFM$_1$-HRP (1/150, v/v);
6G4 (0.2 μg/mL) and AFM$_1$-HRP (1/150, v/v);
ATX2 (0.5 μg/mL) and AFM$_1$-HRP (1/120, v/v).

2.6. Direct competitive ELISA based on Bio-Adembeads anti-Mouse IgG

This simplified version of dc-ELISA format relies on the use of superparamagnetic nanoparticles coated with affinity purified goat anti-mouse IgG as support for antibody binding. The procedure is similar with the one previously described, when the Bio-Adembeads Protein G superparamagnetic particles were utilised. Prior to use the nanoparticles were washed twice with working buffer (1400 μL) for removing the Proclin 300.

The optimised procedure was the following:

coating: 13 μL of superparamagnetic nanoparticles coated with affinity purified goat anti-mouse IgG were dispersed into 1400 μL of antibody solution prepared in working buffer and allowed to react for 20 min; then the particles were collected using the Adem-Mag SV and washed twice with working buffer (1400 μL) and finally resuspended in 1400 μL; 100 μL of this dispersion were added inside the wells and the buffer was removed;
competition: 90 μL of AFM$_1$ and 10 μL of AFM$_1$-HRP were allowed to compete (PolySorp^{TM} microtitre plates were utilised) for the antibody binding sites, during 20 min; during coating and competition, an horizontal shaker (200 rpm) was employed.

Washing steps were performed as described above. The TMB liquid substrate for ELISA was utilised (150 μL/well) and the absorbance was read 15 min after the substrate solution was added inside the wells, at both 650 and 450 nm (after quenching with 100 μL/well of 1N H$_2$SO$_4$).

The optimised amount of antibody against AFM$_1$ and the dilution of AFM$_1$-HRP used, for each of the three tested clones, is:

3G11 (0.2 μg/mL) and AFM$_1$-HRP (1/150, v/v);
6G4 (0.2 μg/mL) and AFM$_1$-HRP (1/150, v/v);
ATX2 (1.5 μg/mL) and AFM$_1$-HRP (1/80, v/v).

2.7. Calibration curves for spectrophotometric ELISA

Spectrophotometric ELISA standard curves were obtained using AFM$_1$ standard solutions prepared in PBS or in BD282 reference material.

Each experiment was performed in triplicate and the mean of each value was used for curve fitting. The calibration curves (absorbance at 650 or 405 nm *vs.* antigen concentration) were fitted using "non-linear four parameter logistic calibration plots" [22].

To allow the direct comparison of different calibration curves, absorbance values were converted into their corresponding test inhibition values (A/A_0, %) as follows:

$$\% \frac{A}{A_0} = \frac{A - A_{\text{sat}}}{A_0 - A_{\text{sat}}} \times 100 \tag{1}$$

where A is the absorbance value of competitors, A_{sat} and A_0 are the absorbance values corresponding to the saturating and the non-competition antigen, respectively (as evaluated by the four parameters logistic function).

The matrix effect, the recovery percentage and the limit of detection were assayed using blank samples prepared using the ERM-BD282 (zero level of AFM$_1$) powder milk. Recovery was assessed by spiking blank milk samples with a known amount of AFM$_1$ standard solution. The detection limit (LOD) was calculated as the concentration corresponding to 90% of A/A_0 [23]. The midpoint value (IC$_{50}$) was evaluated as the concentration of AFM$_1$ at 50% A/A_0. The working range was evaluated as the toxin concentration that gives test inhibition values of 80 and 20% of A/A_0. The data obtained for each curve were plotted and fitted using a SigmaPlot software (SPSS), and a regression analysis on the linear portion of the sigmoidal curves was also performed. The slopes obtained from the regression analysis were used to evaluate the matrix effect and the recovery of the assay.

3. Results and discussion

3.1. Spectrophotometric ELISA

Indirect and direct competitive ELISA formats were assayed to characterise analytically 5 clones of antibodies developed against AFM$_1$. This study was aimed also towards the possibility to reduce the time of analysis with respect to the classical ELISA competitive techniques.

The indirect competitive format of ELISA was utilised to ascertain how many of the five antibodies (clones 1C6, 3G11, 6G4, ATX9 and ATX2) available in our laboratory were able to bind the aflatoxin M$_1$. Three of them (clones 3G11, 6G4 and ATX2) were able to recognise and compete for the free AFM$_1$ during the competition step, meanwhile the other two clones were not able to recognise AFM$_1$ (data not shown). Two types of secondary antibodies, labelled with alkaline phosphatase (Fig. 1) or horseradish peroxidase (Fig. 2), were used to trace the AFM$_1$, but no significant difference, with respect to linear working range or midpoint value, was achieved (Table 1), since the determining factor for this format is the coating step. In fact, maintaining constant the amount of one primary antibody (for example ATX2, 1/1600, v/v) and varying the coating concentrations (50, 25 and 12.5 ng/mL of BSA-AFM$_1$), the midpoint value shifted from 430 to 120 and from 120 to 47 ng/L, respectively, when an Ab$_{II}$-AP was used. When using an Ab$_{II}$-HRP only the time analysis was shortened by 30 min, since it was possible to reduce the binding time with the primary antibody,
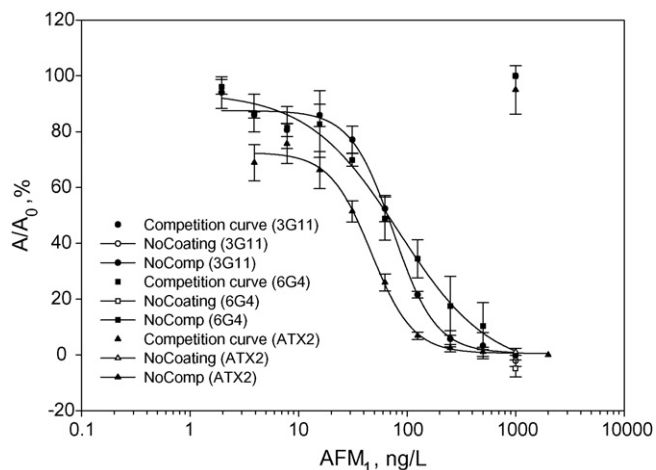
Fig. 1. Indirect competitive ELISA; secondary antibody labelled with alkaline phosphatase; over night coating, at 4 °C; blocking step (45 min) performed at room temperature; 60 min competition time.
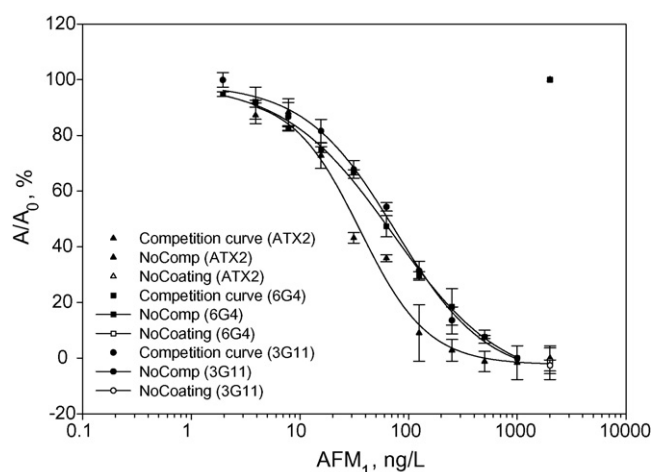
Fig. 2. Indirect competitive ELISA; secondary antibody labelled with horseradish peroxidase; over night coating, at 4 °C; blocking step (45 min) performed at room temperature; 60 min competition time.

Table 1
Analytical parameters for spectrophotometric ELISA

Clone	LWR (ng/L)	IC$_{50}$ (ng/L)	LOD (ng/L)
ic-ELISA (Ab$_{II}$-AP)-165 min			
3G11	15–250	75	15
6G4	15–500	84	15
ATX2	15–125	47	15
ic-ELISA (Ab$_{II}$-HRP)-135 min			
3G11	15–250	76	15
6G4	8–500	72	8
ATX2	8–125	35	8
dc-ELISA-90 min			
3G11	12.5–80	36	12.5
6G4	12.5–80	40	12.5
ATX2	12.5–100	36	12.5
dc-ELISA Bio-Adembeads Protein G-20 min			
3G11	4–250	15	4
6G4	12–500	50	12
ATX2	30–500	150	30
dc-ELISA Bio-Adembeads anti-Mouse IgG-20 min			
3G11	8–125	30	8
6G4	10–500	50	10
ATX2	10–250	50	10

LWR: linear working range; IC$_{50}$: midpoint value; LOD: limit of detection.
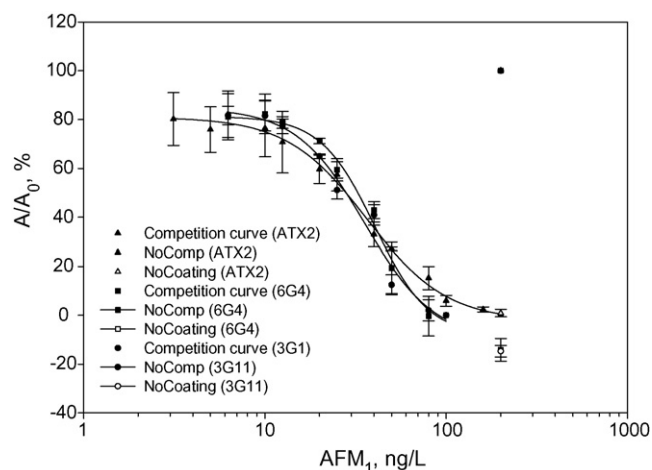
Fig. 3. Direct competitive ELISA; over night coating, at 4 °C; blocking step (45 min) performed at room temperature; 45 min competition time.

presumably due to a better affinity of Ab$_{II}$-HRP towards the primary antibody.

When the three clones (3G11, 6G4 and ATX2) were assayed in the direct competitive format (Fig. 3), all of them showed, more or less, an identical midpoint value (around 40 ng/L). The linear working range (LWR) was narrower then the one obtained in the ic-ELISA procedure but the limits of detection were comparable with the ones obtained for the ic-ELISA. However, the dc-ELISA format is more rapid then the ic-ELISA format (90 min against 165 or 135 min) therefore it was further optimised, by transferring the entire procedure (coating, competition, etc.) onto the superparamagnetic nanoparticles coated with protein G or anti-IgG.

One of the main advantage of using nanoparticles resides in the short interaction time between the biological components and the protein G or anti-IgG coated nanoparticles. The whole process could be defined as "homogeneous", since the interaction between the Ag and the Ab takes place at "nano" level. Moreover, being superparamagnetic, these nanoparticles can be easily separated from bulk solution, allowing also a versatile manipulation. Confronted with the ic- and dc-ELISA, the coating time was reduced to 20 min, instead of an over night incubation time (12–14 h). Moreover, the already incubated nanoparticles could be stored separately as ready to use nanobeads for performing just the competition step in a dc-ELISA. One time consuming factor was *a priori* overcame, since no blocking step was necessary. This was achieved by adding a non-ionic surfactant into the working buffer, as described before. Then, the competition time was even further reduced, when compared with an ic- or dc-ELISA, till 20 min (Figs. 4 and 5). When the competition curves performed by the aid of superparamagnetic nanoparticles were compared with the ones obtained from ordinary ic- and dc-ELISA, a different shape of these curves was evident, since the affinity of the tested clones towards the reactive coating biomaterial of the nanoparticles, protein G and anti-IgG, respectively, hardly depends on this factor. When a dc-ELISA based on Bio-Adembeads anti-Mouse IgG was performed, the behaviour of the clones 3G11, 6G4 and ATX2 was more or less identical, and similar with the one observed in the classical ic- and dc-ELISA. A better discrimination was further achieved when a dc-ELISA based on Bio-Adembeads Protein G was assayed. The clone 3G11 showed to be the best antibody, with the lowest IC$_{50}$ (15 ng/L) and it was further used to assess the matrix effect, the recovery percentage, when ERM-BD282 powder milk was fortified with known amounts of AFM$_1$, and to test locally available milk samples.
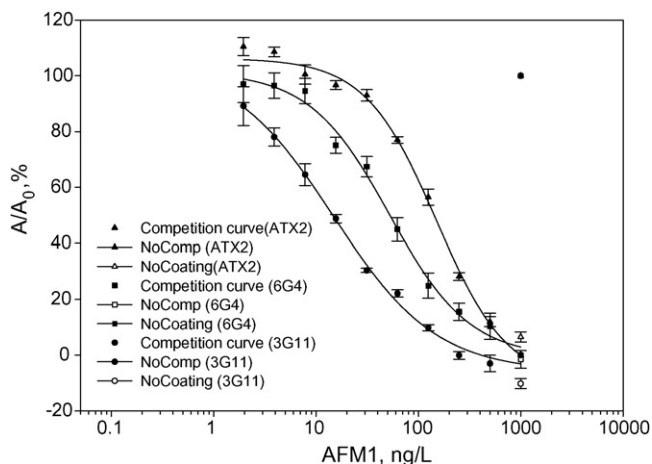
Fig. 4. Direct competitive ELISA based on Bio-Adembeads Protein G; coating (20 min) performed at room temperature; no blocking step; 20 min competition time.

3.2. Matrix effect, recovery and real sample analysis

Certified reference material (BD282, zero level of AFM_1) was reconstituted as indicated in the certification report supplied by the IRMM, Belgium. After reconstitution and centrifugation, a calibration curve in matrix was performed and it was observed that the calibration curve in milk was influenced by the new environment (Fig. 6). The IC_{50} shifted almost 3 times (41 ng/L) then the midpoint value obtained in buffer (15 ng/L). The linear working range (4–250 ng/L) was slightly modified, being essentially the same as for the standard competition curve performed in PBS. This is very important since the maximum accepted level of AFM_1 (50 ng/L) is well fitted into this linear working range.

Recovery was assessed (Table 2) by spiking with aflatoxin M_1 the BD282 reconstituted material.

The fortified (30, 60 120 ng/L of AFM_1) blank milk samples were interpolated from the calibration curve performed using reconstituted certified reference material.

The precision was determined by calculating the relative standard deviation (%R.S.D.) for the replicate measurements and the accuracy (%R.E.) was calculated by assessing the agreement between measured and nominal concentration of the fortified samples.
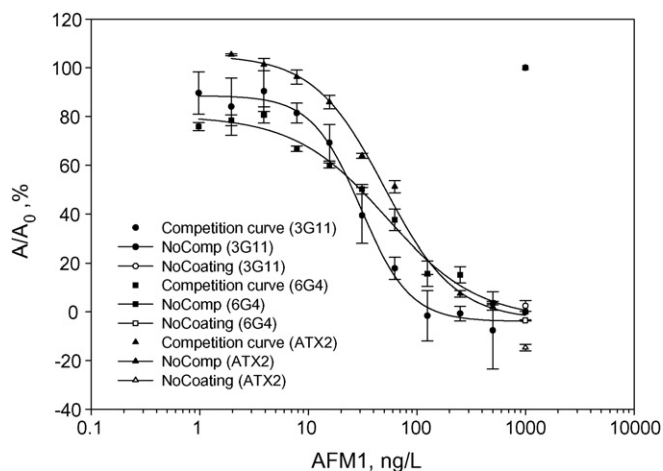
Fig. 5. Direct competitive ELISA based on Bio-Adembeads anti-Mouse IgG; coating (20 min) performed at room temperature; no blocking step; 20 min competition time.
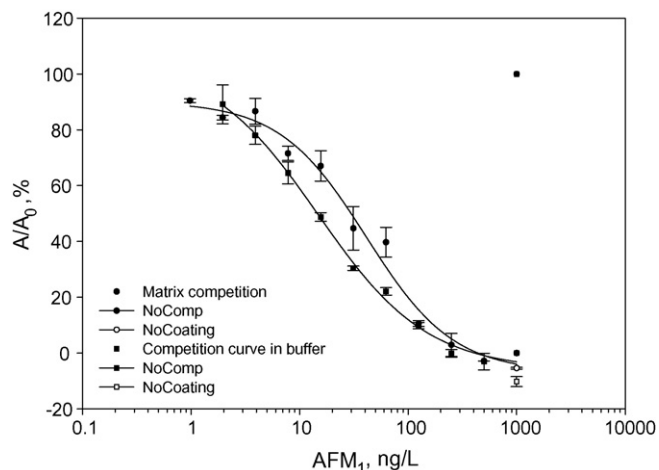
Fig. 6. Competition curves performed in buffer and in certified reference material (BD282, zero level of AFM_1); clone 3G11 immobilised on Bio-Adembeads Protein G was utilised to assess the matrix effect.

Table 2
BD282, zero level of AFM_1 certified reference material was employed; clone 3G11 immobilised on Bio-Adembeads Protein G was utilised to asses the recovery efficiency

AFM_1 added (ng/L)	AFM_1 found (ng/L)	R.S.D. (%)	R.E. (%)	Recovery (%)
30	28	7	−7	93
60	58	5	−3	97
120	118	3	−2	98

%R.E. (relative error) = [(measured value − true value)/true value] × 100; %R.S.D. (relative standard deviation) = standard deviation/mean × 100; $n = 6$.

Six different brands of commercially available milk samples, three declared to be produced following the rules of biological agriculture and three as fresh milk, were assayed and for all of them the response was negative, since the absorbance values were at the same level as for the "no competition" point of the standard calibration curve. The obtained results were confronted with the response obtained by using a commercial available kit for aflatoxin M_1 detection (AFLA M_1 MILK), and again a negative response was obtained.

4. Conclusions

In this work, five different antibodies developed against the aflatoxin M_1 were investigated by using different ELISA schemes based on classical indirect and direct competitive formats, and on the use of superparamagnetic nanoparticles. From all the five investigated antibodies, the most powerful, i.e. showing the best IC_{50} value and limit of detection, was the clone 3G11. Superparamagnetic nanoparticles conjugated with protein G and anti-mouse IgG were utilised to further reduce the coating (till 20 min, instead of 12–14 h necessary for the over night coating procedure) and the competition time. Also, one time consuming factor was *a priori* minimised, since no blocking step was necessary. Being superparamagnetic, these nanoparticles are easily separated from the bulk solution, allowing also a versatile manipulation. The use of superparamagnetic nanoparticles allowed us to demonstrate that the classical ELISA procedures, which sometimes are time consuming, could be further improved by decreasing the coating and competition time and by eliminating steps that cannot be neglected, like the blocking step. The feasibility of this dc-ELISA based on the use of pre-coated (protein G or anti-IgG) nanoparticles was confirmed by performing

competition curves in milk reference material, showing that the matrix effect is not greatly affecting neither the linear working range, neither the recovery rate nor the midpoint value.

In conclusion, we have demonstrated that a competitive immunoassay for AFM_1 based on the use of superparamagnetic nanoparticles is reliable, easy to perform and time efficient.

Acknowledgement

References

[1] W.F. Busby Jr., G.N. Wogan, Food-Borne Infections and Intoxications, second ed., Academic Press, New York, 1979, pp. 519–610.
[2] W.H. Butler, Mycotoxins, Elsevier Scientific Publishing, New York, 1974, pp 1–28.
[3] J.W.O. Ellis, P. Smith, B.K. Simpson, Food Sci. Nutr. 30 (1991) 403.
[4] J.P. Jouany, Anim. Res. 51 (2002) 81.
[5] D. Miller, J. Stor. Prod. Res. 30 (1994) 1.
[6] L. Stoloff, J. Food Prot. 43 (1989) 226.
[7] IARC, International Agency for Research on Cancer, Monograph on the Evaluation of Carcinogenic Risk to Humans, vol. 82, World Health Organisation, Lyon, France, 2002, p. 171.
[8] R.D. Stubblefield, G.M. Shannon, J. Assoc. Off. Anal. Chem. 57 (1974) 847.
[9] European Commission Regulation, No. 466/2001/EC of 8 March 2001, Setting Maximum Levels for Certain Contaminants in Foodstuffs, Official Journal of European Communities L077, 2001, pp. 1–13.
[10] European Commission Regulation, No. 683/2004/EC of 13 April 2004, Amending Regulation (EC) No. 466/2001 as Regards Aflatoxins and Ochratoxin A in Foods for Infants and Young Children, Official Journal of European Communities L106, 2004, pp. 3–5.
[11] European Commission Directive, 2002/26/EC of 13 March 2002 Laying Down the Sampling Methods and the Methods of Analysis For The Official Levels of Ochratoxin A in Foodstuffs, Official Journal of European Communities L075, 2002, pp. 38–43.
[12] ISO, Milk and milk powder. Determination of aflatoxin M1 content, in: Clean-up by Immunoaffinity Chromatography and Determination by High-Performance Liquid Chromatography. Standard 14501, International Standards Organisation, Geneva, Switzerland, 1998.
[13] F. Grosso, J.M. Fremy, S. Bevis, S. Dragacci, Food Addit. Contam. 21 (2004) 348.
[14] E. Chiavaro, C. Cavicchioli, E. Berni, E. Spotti, Food Addit. Contam. 22 (2005) 1154.
[15] C. Cavaliere, P. Foglia, E. Pastorini, R. Samperi, A. Lagana, J. Chromatogr. A 1101 (2006) 69.
[16] M. Magliulo, M. Mirasoli, P. Simoni, R. Lelli, O. Portanti, A. Roda, J. Agric. Food Chem. 53 (2005) 3300.
[17] L. Micheli, R. Greco, M. Badea, D. Moscone, G. Palleschi, Biosens. Bioelectron. 21 (2005) 588.
[18] M.L. Rodriguez Velasco, M.M. Calonge Delso, D. Ordonez Escudero, Food Addit. Contam. 20 (2003) 276.
[19] J. Stroka, E. Anklam, Trends Anal. Chem. 21 (2002) 90.
[20] K. Thirumala-Devi, M.A. Mayo, A.J. Hall, J. Agric. Food Chem. 50 (2002) 933.
[21] ISO, Milk and milk products, in: Guidelines for a Standardized Description of Competitive Enzyme Immunoassays-Determination of AFM1 Content. Standard 14675, International Standards Organisation, Geneva, Switzerland, 2002.
[22] M.J. Warwick, Immunoassay, in: A Practical Guide, Taylor & Francis Ltd., London, UK, 1996, p. 160.
[23] A. Dankwardt, Encyclopedia of Analytical Chemistry, Wiley, Chichester, 2001, pp. 1–25.

Review

Advances in technologies for the measurement of uranium in diverse matrices

D.P.S. Rathore *

Chemical Laboratory, Atomic Minerals Directorate for Exploration & Research, Department of Atomic Energy, Pratap Nagar, Sector-V Extension, Sanganer, Jaipur 302030, India

A R T I C L E   I N F O

A B S T R A C T

An overview of the advances in technologies, which can be used in the field as well as in a laboratory for the measurement of uranium in diverse matrices like, waters, minerals, mineralized rocks, and other beneficiation products for its exploration and processing industries is presented. Laser based technologies, ion chromatography, microsample X-ray analysis method followed by energy dispersive X-ray fluorescence technique (MXA–EDXRF), sensors for electrochemical detection followed by cyclic voltammogram and alpha liquid scintillation counting techniques are the most promising techniques. Among these techniques, laser fluorimetry/spectrofluorimetry, in particular, is the technique of choice because of its high performance qualification (PQ), inherent sensitivity, simplicity, cost effectiveness, minimum generation of analytical waste, rapidity, easy calibration and operation. It also fulfills the basic essential requirements of reliability, applicability and practicability (RAPs) for the analysis of uranium in solution of diverse matrices in entire nuclear fuel cycle. A very extensive range of uranium concentrations may be covered. Laser fluorimetry is suitable for direct determination of uranium in natural water systems within the $\mu g\,L^{-1}$ and $mg\,L^{-1}$ range while differential technique in laser fluorimetry (DT-LIF) is suitable for mineralized rocks and concentrates independent of matrix effects (uranium in samples containing >0.01% uranium). The most interesting feature of TRLIF is its capability of performing speciation of complexes directly in solution as well as remote determination via fiber optics and optrode. Future trend and advances in lasers, miniaturization and automation via flow injection analysis (FIA) has been discussed.

© 2008 Elsevier B.V. All rights reserved.

Contents

1. Introduction

Uranium, thorium and plutonium are the basic elements for utilization of "nuclear fission" energy [1]. On average, the earth's crust contains nearly about $4\,mg\,kg^{-1}$ uranium, $12\,mg\,kg^{-1}$ thorium and practically no plutonium. Natural uranium has two main isotopes, ^{238}U (99.3%) and ^{235}U (0.7%). ^{235}U is the only naturally occurring 'fissile' material. The extra available neutrons after maintaining the chain reaction are utilized in transmuting the naturally occurring ^{238}U and ^{232}Th isotopes to produce man-made fissile isotopes ^{239}Pu and ^{233}U, respectively. ^{238}U and ^{232}Th are called 'fertile' isotopes. The fission energy is utilized in a nuclear power reactor

* Fax: +91 141 2791126.
E-mail addresses: dpsr2002@yahoo.com, dpsrathore.amd@gov.in.

for generation of electricity or in a nuclear explosive device for blast and thermal radiation damage. The fission process emits about 200 MeV per fission while a chemical reaction occurring in fossil fuels releases about 2–4 eV only per atom of carbon. The fissile and fertile materials are used only for generating fission energy and additional fissile materials, respectively, while fossil fuels like coal or oil have several applications other than generating energy. These fissile materials led to the development of 'nuclear explosive devices' based on weapon grade ^{239}Pu (<10% ^{240}Pu) and high enriched uranium (HEU: >90% ^{235}U). Since there is no formal exchange of uranium as is for other commodities like gold or oil, uranium is, therefore, an element of strategic importance.

Uranium is nearly ubiquitous, [2–4] due to its polyvalence (+4, +6), large atomic radius (0.97 Å), high chemical reactivity, relative solubility of U(VI) compounds in aqueous solution, and relative insolubility of U(IV) compounds. Uranium forms many compounds, enters in to the structure of many minerals and disperses readily. Due to charge discrepancy, some limited U(IV) substitution occurs for Ca(II) in apatite, sphene, and fluorite but it undergoes extensive isomorphism with Th(IV) due to similar charge and radius. In primary minerals, such as pitchblende/uraninite or coffinite, uranium occurs in the quadrivalent state. Under oxidizing conditions, hexavalent uranium appears as the uranyl ion, UO_2^{2+} (VI), which is linear and polar in nature. Uranyl ion is very stable, maintains identity through many chemical transformations, as found in many secondary uranium minerals. Cations in these secondary minerals are loosely held, added or removed by base exchange reactions without touching the UO_2 keyed layer structures in solids represented by the general compositions, such as, $A[(UO_2)(RO_4)]XH_2O$; $B[(UO_2)(RO_4)_2]XH_2O$; $B[(UO_2)(CO_3)_2]XH_2O$; where A = K(I), Na(I), H(I); B = Ca(II), Ba(II), Mg(II), Cu(II), Fe(II), Pb(II); R = P(V), As(V), V(V). These secondary minerals are variably soluble in aqueous solution. Uranium in significant concentrations may be transported throughout a wide range of Eh and pH conditions as various uranyl complexes. In this way, uranium is a relatively mobile element in many surface or near-surface environments. Geochemical exploration methods and its prospecting can be based on the measurement of trace quantities of the metal itself in waters, soils, sediments or rocks. Since, uranium is its own best indicator, therefore, a better precision at all concentration levels is essential.

It is only hexavalent uranium [4,5], U(VI), present in the uranyl ion, UO_2^{2+} (VI) phosphoresces with a relatively long lifetimes of μs, while uranium of other valencies being essentially non-luminescent at the wavelengths of excitation used for its determination by fluorimetry [6]. Laser-induced spectroscopic studies of uranium(IV) have shown fluorescence properties observed in the UV–vis region with the lifetime <20 ns at room temperature by excitation light at 245 nm, which is corresponding to the 5f–5f electronic transition (=40820 cm^{-1}) of this element in this oxidation state [6]. Thus, uranyl compounds have a distinct well-known characteristic long-lived green luminescence which can be isolated by optical filters and measured as intensity with a photodetector to give an indication of the uranium concentration in a sample. In an ion as heavy as UO_2^{2+} (VI), it is in fact arguable whether or not electronic states of pure character exists [8,9]. The origin of the visible luminescence of the uranyl ion has been attributed to both fluorescence and phosphorescence [7,8]. The luminescence intensity, radiative lifetimes and spectral resolution in the emission from the optically excited uranyl ion were all remarkably enhanced in the presence of high concentrations of acid (protons), base (hydroxide ions) and pyrophosphate. This enhancement effects are partly due to increases in absorptivity at the excitation wavelengths used, but mostly arise from the formation of chemical complex having vibronic structure, in which the UO_2^{2+} (VI) ion acquires a higher probability for radiative transitions. The green emission charac-

teristic of the uranyl ion originates in a triplet states and decays exponentially. The emission spectrum is quite characteristic, with three regularly spaced peaks at approximately, 494, 516 and 540 nm of strong O—U—O bonds [4]. Thus, this enhancement of fluorescence effects in laser-dyes is brought about by imposing rigidity on the flexible molecular framework by internal chemical bonding or by freezing-out rotational motion by use of a highly viscous solvent. Moreover, whether excitation occurs in the ultraviolet, the so-called singlet absorption, or in the visible region, triplet absorption, the emission spectrum, lifetime, and intensity of optically excited solutions of uranyl nitrate are comparable [8].

There are many methods for the determination of uranium in geological materials [9]: gravimetric, volumetric, spectrophotometric, fluorimetric, radiometric and XRF analyses. Choice of a particular method depends primarily on the nature of the sample being analysed and on the amount of uranium in it. Analytical techniques with sufficient sensitivity in aqueous solutions include neutron activation [10], fission track [11] and optical fluorimetry [12]. In conventional fluorimetric method [12,13], after solvent-extractive separation of uranium from accompanying matrix, the liquid sample containing uranium compound is first evaporated carefully to dryness and the residue is fused at a high temperature with a carbonate–fluoride flux to produce a solid disc. The disc is then placed in an optical fluorimeter where it is illuminated by ultraviolet light to cause the fluorescence of uranium. This conventional fluorimetric method of analysis for uranium in aqueous samples suffers from a lack of sensitivity, limited precision, and complicated time-consuming preparative chemistry. More recently, Hou and Roos [14] reviewed the critical comparison of radiometric and mass spectrometric methods for the determination of uranium and other radionuclides in biological, environmental and waste samples. In this article, different radiometric methods, such as gamma (γ)-spectrometry, alpha (α)-spectrometry, and beta (β)-counting, and mass spectrometric methods, such as ICP-MS, accelerator mass spectrometry (AMS), thermal ionization mass spectrometry (TIMS), resonance ionization mass spectrometry (RIMS), secondary ion mass spectrometry (SIMS) and glow discharge mass spectrometry (GDMS) and their application for the determination of radionuclides are compared. The application of on-line methods (flow injection/sequential injection) for separation of radionuclides and automated determination of radionuclides is also discussed. This review paper will be helpful to the analysts and researchers to select the most suitable techniques as well as to improve upon the analytical capabilities for such applications.

With advancements in electronics, instrumentation and automation at microlitre liquid delivery lines controlled by microcomputers, there is a great pressure to change/or replace the age old conventional time-consuming extractive methods [9,12,13] for uranium determination in diverse matrices, owing to the skilled manpower necessity, minimization of generated analytical wastes and rising costs, even in the developed countries [15,16].

In this review article, an overview of the advances in technologies for the determination of uranium in diverse matrices is presented. Special emphasis is placed on the wide utility of laser fluorimetry/spectrofluorimetry.

2. Available technologies

2.1. Laser based instrumental techniques

The laser based instrumental techniques, such as, fluorimeter/spectrofluorimeters/phosphorimeters were evolved during the past three decades, utilizing the half-life of phosphorescent uranyl compounds and its decay as a diagnostic method for the low cost,
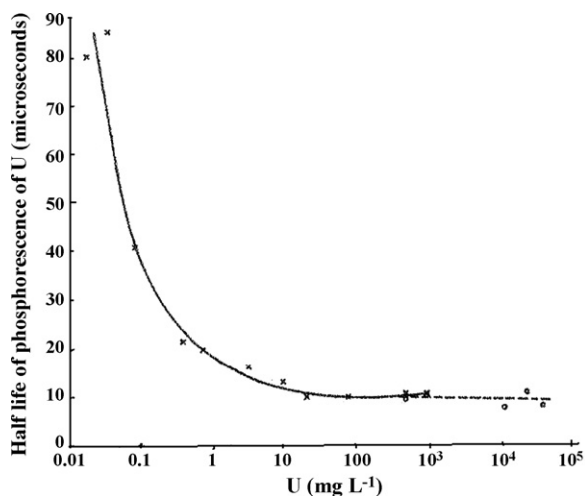
Fig. 1. Variation of the time constant of decay of intensity of the phosphorescence of uranium (VI) with the concentration of uranium, in an aqueous solution [5].

simple and direct determination of uranium at μg L^{-1} levels in natural water samples for hydro-geochemical reconnaissance surveys for uranium.

2.1.1. Laser fluorimetry

In this technique [4], the heart of the system is the light source – a compact sealed nitrogen laser, which emits ultraviolet (337 nm) short-lived pulses ($3–4 \times 10^{-9}$ s) at a repetition rate of 15 pulses per second. A laser is used in preference to other sources of ultraviolet light because the resultant pulse is intense yet self-terminating, monochromatic, and highly directional; the full output power is thus easily directed and focused on the sample cell. The phosphorescence in the cell is detected by a photomultiplier tube (PMT) isolated by a green-transmitting filter (480–540 nm). This technique comprises the steps of exciting the uranyl ion in the sample by projecting electromagnetic energy of suitable wavelengths and measuring the decay with time of the uranium phosphorescence after the termination of the incident electromagnetic radiation.

This technique is based mainly on the following observations [5]: (1) At a very low concentrations (U less than 1 mg L^{-1}), the half-life of phosphorescence of uranium in an aqueous solution increases very rapidly as the concentration decreases, (Fig. 1). (2) At low uranium concentrations, the effect of adding certain anions, notably polyphosphates, to the sample to be tested is to increase markedly the initial quantum yield. At the same time there is no enhancement of organic luminescence by the addition of these anions, and, thus such addition can be used to enhance the uranium luminescence selectively. A phosphate taken from the group pyrophosphate, tripolyphosphate, tetraphosphate, trimetaphosphate, tetrametaphosphate and hexametaphosphate is effective. This family of reagent is sensitive to acid and will decompose eventually to simple monophosphates in highly acidic solutions. The monophosphate solutions so generated are considerably less effective in stimulating the luminescent efficiency of the uranyl ion. A buffer is, therefore, added to reduce the acidity of the solution. Since the phosphorescence enhancement is pH-dependent. The polyphosphate was added to buffer in the ratio of about 1 to 10. The primary function of the fluorescence-enhancing agent (complexing agent + buffer) is the formation of the single phosphorescent uranyl species, but it also acts as a strong complexing agent for other metals in solution to reduce their effects on uranyl luminescence. The pH of the polyphosphate (pyrophosphate) solution was maintained at the optimum value for phosphorescent inten-

sity at pH $\sim$ 8 by adding a phosphate buffer as well as for optimum masking efficiency for other interfering metals.

During these years, this technique has grown and utilized the potentialities for its wide and diverse applications for the determination of uranium in rocks, minerals, mineralized rocks, mineral beneficiation products, concentrates, etc. for exploration programmes and U-processing industries. Different laser fluorimeters are shown in Fig. 2(a–c).

In view of the rapidity and simplicity of measurement by laser fluorimetry, the main emphasis was either on developing new fluorescence-enhancing reagents or on methods of measurements for different types of sample matrices. Several workers have developed methods for the determination of uranium in matrices, like rocks, soils and sediments, mineralized rocks, concentrates and other U-rich materials, in which sample matrix effects are either eliminated by dilution of sample solution to such an extent that quenching by impurities no longer influences the analysis, or the separation of the uranium from the quenchers by extraction, compensation of matrix effects by use of an internal standards (standard addition), or other methods. Romanovskaya et al. [17] suggested the possible use of polysilicates instead of Fluran reagent. A method involving the separation of uranium from water samples by co-precipitation with calcium fluoride and measurement of its laser-excited fluorescence has been developed by Perry et al. [18]. The reported detection limit of uranium is 10^{-5} μg L^{-1}. Harms et al. [19] proposed a method for the determination of uranium in plant ashes and McHugh [20] analysed various minerals by laser fluorimetry by fusing the samples with solid KOH. Tikoo and Murty [21] determined uranium in water and geological samples by decomposing the materials with HNO$_3$–HF and fusing the residue with Na$_2$O$_2$ using a mixture of ammonium dihydrogen phosphate and phosphoric acid as a fluorescence-enhancing reagent. However, it was found that this fluorescence-enhancing buffer is unsuitable for water samples due to severe quenching by halides, in particular, chlorides [15]. The quenching effect in laser fluorimetry has also been studied repeatedly [22,23]. Campen and Bachmann [22] presented a comparative analytical performance of laser fluorimetry with other techniques. Zook et al. [23] developed a versatile, direct method for the determination of trace amounts of uranium in solution utilizing pulsed laser fluorimetry and a pyrophosphate fluorescence-enhancing reagent. Authors claimed the measurement with a 2–3% relative standard deviation and accurate to better than 1% in the 0.01–4 mg U kg^{-1} range. The detection limit is 0.005 μg L^{-1} uranium. Time required per determination was 6 min. A special feature of the method was the use of a standard addition technique to eliminate sample matrix effects. The most interesting and simplified application of standard addition method is in the determination of uranium by laser-induced fluorescence technique in hydro-geochemical samples (water samples) each differing widely in its matrix composition [9,23,24].

Whitkop [25] reported a method for trace analysis of uranium in plutonium process stream samples containing large quantities of fluorescence quenchers. The effect of quenchers was eliminated by selective extraction of uranium from an aqueous sample into tri-n-butyl phosphate, with subsequent stripping into dilute phosphoric acid phase, and followed by its determination using the standard addition method by laser fluorimetry. The reported detection limit of uranium is 1 μg L^{-1}. The precision of the analysis was in the range of $\pm$7% relative standard deviation. Veselsky et al. [26] have developed a procedure for determination of uranium in minerals by decomposing the samples with HNO$_3$–HF–HClO$_4$ in Teflon beakers, the sample residue was then dissolved in 2 ml of HNO$_3$ (1 + 25) + 10 ml of Ca(NO$_3$)$_2$–EDTA solution (400 g of calcium nitrate and 6 g of disodium EDTA + 100 ml of water; warm until dissolved), followed by extraction with isobutyl methyl ketone (IBMK)

Fig. 2. (a) UA-3 Uranium analyser (Scintrex, Canada). (b) Digital laser fluorimeter (fabricated by India). (c) Laser uranium analyser (miniaturized – fabricated by RRCAT, INDORE, India).

by laser-induced luminescence registration of its polysilicate complexes. Premadas and Saravanakumar [28] used laser fluorimetry for the direct determination of uranium at trace level using sodium pyrophosphate as fluorescence-enhancing reagent and used the calibration method as well as standard addition/spiking in rutile, zircon, and monazite minerals and after separation in ilmenite, soil, sediment, coal fly ash and red mud samples. The major problems in the uranium determination of these minerals are: (i) preparation of a clear sample solution, (ii) presence of interfering elements at very high concentrations and (iii) accurate determination of uranium at trace level ($10 \, \text{mg kg}^{-1}$ or less). Ilmenite sample is decomposed by heating with ammonium fluoride. Rutile, zircon and monazite minerals are decomposed by fusion using a mixture of potassium bifluoride and sodium fluoride. Environmental and industrial waste materials were brought into solution by treating with a mixture of hydrofluoric and nitric acid. Rathore et al. [15] studied acidic buffer mixtures containing different dihydrogen phosphates plus phosphoric acid as a uranyl fluorescence-enhancing reagents in laser fluorimetry. An accurate and precise method for uranium determination in mineralized rocks and concentrates was developed, in which interferences were eliminated by dilution of sample aliquot using push-button microlitre pipettes (taking advantage of high sensitivity and selectivity of laser fluorimetry) thereby bringing the concentration of uranium within the operational range of the instruments and computing the results using differential technique. These single push-button pipettes [29] combine superior accuracy ($\pm 0.6\%$) and precision (<0.2%) over the volume range from 100 to 1000 μL, with ease of use for applications where one cannot afford to make mistakes, and were found to be most suitable for single step large dilutions. The authors utilized the technique used in differential spectrophotometry for selecting the appropriate reference standard concentration to obtain the maximum precision possible in any given analysis and introduced differential technique in laser fluorimetry (DT-LIF). Differential technique (DT) [15,16] is based on the comparison of the fluorescence of the reference solutions or certified reference materials with a sample of similar but unknown concentration on the same sample weight or dilution basis, wherein all samples are subjected to exactly the same procedures and measurement steps such that the whole methodology is checked [9]. A simple one- or two-step dilution of sample solution with distilled water removes matrix effects (linear decrease in uranium content but an exponential decrease in quenching effects). This method is free from high concentration of nitric acid and matrix effects because of microlitre sample volumes as per the prescribed procedure [15,16]. It was interesting to note that in practice, the accuracy and precision of DT was found to be comparable with differential spectrophotometric technique as well as to classical titrimetry and gravimetric methods. Since DT fulfills the essential requirements of both equipment and method calibration [30], it is, therefore, a self-standardized and an absolute methodology by using standards of accurately known concentrations, such as, certified reference materials [16,30].

In laser fluorimetry, the choice of the fluorescence-enhancing reagent is of great importance and depends mainly on the matrix composition (presence of quenching and/or absorbing species) and uranium concentration level. The desired acceptable precision at different concentration levels in an instrumental technique is achieved by the choice of mainly two aspects [31]: (1) choice of ideally suited (fluorescence-enhancing) reagent systems, and (2) different methods of measurement.

A comparison of different techniques for the determination of uranium in diverse matrices [9,16,31] is presented in Table 1.

Later, a digital read-out laser fluorimeter [32] was fabricated by Laser Applications and Electronics Division, RRCAT, Department of Atomic Energy, Indore, India (weighing 15 kg), Fig. 2(b) [15,32]. The

and back extraction with 10 ml of 0.001 M HNO_3 and subsequent measurement using laser fluorimeter. Kochan and Shuktomova [27] reported a method for microamounts of uranium determination in soils after separation of uranium from luminescence quenchers from liquid preparations by precipitation in strongly basic carbonate medium in the presence of activated charcoal (as a collector of precipitate) and subsequent uranium determination

Table 1
Comparison of the performance of the differential technique with other techniques for the determination of uranium

Conventional fluorimetry[9,16]	Solvent-extractive spectrophotometry[9,16]	Classical titrimetric and gravimetric methods[9,16]	Differential technique in laser fluorimetry[9,16]
1. Time consuming, multiple steps	1.Time consuming, multiple steps	1. Time consuming, multiple steps	1. Simple, rapid, easy calibration operation, and high PQ
2. Separation step is mandatory	2. Separation step is mandatory	2. Separation step is required except in Davies and Gray titrimetric method	2. No separation step is needed, thus saving of manpower per hour.
3. Less precision	3. Less precision	3. High precision	3. High precision
4. Moderate accuracy	4. Moderate accuracy	4. Most accurate	4. Most accurate
5. Applicable up to 500 mg kg^{-1} U$_3$O$_8$	5. Applicable to >500 mg kg^{-1} to 1% U$_3$O$_8$	5. Applicable to more than 5% U$_3$O$_8$	5. Applicable to dynamic range of concentration (<0.01% U$_3$O$_8$)
6.Analytical waste generated is maximum	6. Analytical waste generated is maximum	6. Analytical waste generated are maximum	6. Analytical waste generated are minimum (microlitre sample volumes, no effect of high acidity of nitric acid)
7. It is a laboratory technique	7. It is a laboratory technique	7. It is a laboratory technique	7. It is a laboratory as well as field technique

laser intensity response was found to be unaffected with prolonged use of the instrument up to more than 3 years [15,16,32]. This is beyond doubt a significant breakthrough in laser design. But, this instrument lacks the sensitivity control and range knobs vis-a-vis UA-3 uranium analyser. These two features in Scintrex UA-3 laser fluorimeter have significant advantages. Range knob facility (low and high range) is useful to increase the concentration range of the instrument (without the need for dilution of samples) as well as to exactly know and facilitate the appropriate dilution of samples containing high concentration of uranium. Likewise, sensitivity control facility again is more advantageous to calibrate the instruments in the desired range of concentration and necessary scale-expansion.

2.1.2. Time-resolved laser-induced fluorimetry (TRLIF)

This technique [33] specifically has additional features over the laser fluorimetry such as: (1) it has a dispersive system making it possible to obtain the spectrum giving the fluorescence intensity as a function of the emission wavelength. This spectrum is perfectly characteristic of uranium; its recording is the only way of ensuring that the actual measured signal corresponds to uranium, and (2) this technique makes it possible to measure the lifetime of the excited states of the uranyl species or, this amount to the same thing, to follow the decay of its fluorescence over a period of time. Thus, it provides vital information concerning the composition of the solution.

The process for the determination of traces of uranium in solution by the known spectrofluorimetry method comprises of exciting the fluorescence of the uranium molecules in solution in the acid phosphate medium (H$_3$PO$_4$) by a pulsed nitrogen laser shot operating on a wavelength of 337 nm and which emits at a frequency of 30 Hz pulses lasting 5 ns, wherein the exponential decay curve of said fluorescence is studied for a given wavelength, the value of F_0 of said same fluorescence is deduced at the end of each laser pulse and it is compared with the value F_0' obtained for a standard uranium solution containing a known uranium quantity. Behind the measuring cell is positioned a monochromator, which selects the wavelength chosen for examining the fluorescence. The photomultiplier, which on its output line, supplies electrical signals corresponding at all times to the intensity of the fluorescence emitted in the measuring compartment. These signals are distributed between an oscilloscope, thus making it possible to display the signals received and an averaging means which making it possible to both position the time reading window beyond time t_1 and measuring the intensity corresponding to said window position. The computer makes it possible to acquire the data from averaging

means, as well as to control monochromator and the position of the measuring window.

This technique [33] is based on the fact that it is possible, by measuring the decay curve of the fluorescence intensity of uranium, to obtain the value of F_0 of said fluorescence immediately at the end of each pulse of the laser shot. Thus, the fluorescence, which is a function of the time $F(t)$ can be written at all instants in accordance with the Eq. (1),

$$F(t) = F_0 e^{-t/\tau} \tag{1}$$

in which, F_0 is the value of said fluorescence at the end of each pulse of the laser shot. Moreover, the value F_0 of this initial fluorescence can be written according to Eq. (2);

$$F_0 = k\varepsilon I t_{\text{irr.}} [\text{UO}_2^{2+}] \tag{2}$$

in which k is an equipment factor, F_0 is the initial fluorescence, ε is the molar extinction coefficient of the uranyl at the wavelength of the laser, I is the intensity of the laser line, $t_{\text{irr.}}$ is the irradiation time of each pulse, usually approximately 5 ns and $[\text{UO}_2^{2+}]$ is the concentration of the uranyl molecules in the solution to be examined.

It can be seen that for given laser operating conditions, value F_0 is proportional to the uranium concentration which is wished to measure. However, this quantity F_0 is not generally accessible due to the spurious emission phenomena (due to organic substances), which mask the fluorescence of the uranium by being superimposed thereon for a varyingly long time t_1 after each excitation pulse.

Conversely, on measuring $F(t)$ for different values of the time t chosen beyond t_1, in such a way that the spurious fluorescence has disappeared, it is possible to plot the straight line, whose equation corresponds to the logarithm of Eq. (1), i.e.:

$$LF(t) = L F_0 e^{-t/\tau} \tag{3}$$

By experimentally plotting several points, it is possible to plot a straight line, whose slope gives the value of $1/\tau$, and the ordinate at the origin, the value of the logarithm of F_0, which finally makes it possible to calculate the value of F_0. It was found in a remarkable manner that, under certain fixed experimental conditions (characteristics of the emitting laser and the geometrical shape of the measuring container), said value F_0 is a constant which is independent of the measuring medium. Thus, it is possible by measuring the value of F_0 obtained on a sample to be determined with the corresponding value F_0' obtained on a standard solution sample produced in the laboratory and containing a known uranium quan-

tity, to obtain the direct determination of a solution by external calibration, which consists of comparing the result obtained on the sample with that of a reference solution.

The studies carried out by Mauchien et al. [33–40] and Moulin et al. [41–53] on time-resolved laser-induced fluorimetry (TRLIF) are commendable. Highly methodical and extensive studies related to the quenching and inner-filter effects were carried out and presented a general formula accounting for both these effects.

The great advantage of TRLIF is its triple resolution: (1) excitation resolution by the proper choice of the laser wavelength (N_2, tripled, or quadrupled Nd:YAG, dye, etc.); (2) emission fluorescence, which gives characteristic spectra of the fluorescent cation (free or complexed); and (3) fluorescence lifetime, which is characteristic of its environment (complexation, quenching).

These two later types of data provide useful information on the chemical species present in solution. A detailed studies were reported related with the uranyl absorption spectra in various nitric acid solutions, ($[HNO_3]$ from 0.5 to 4.1 M), [43,46]; uranium fluorescence spectrum close to the limit of detection in nitric acid; influence of nitric acid on uranyl time-resolved fluorescence spectrum; uranyl fluorescence decay curves for various nitric acid concentrations; uranyl fluorescence decay curves at various nitric acid concentrations for different temperatures [43] and uranyl fluorescence spectra and main spectroscopic parameters in various media used in TRLIF [50]. From these studies, it is concluded that the use of an appropriate gate position eliminates both quenching and prefilter effects associated with nitric acid concentration in TRLIF.

Complexation studies of radionuclides (such as uranium) are important in order to predict their migration behaviour in natural systems as well as in nuclear reprocessing medium. Moulin et al. [46] reported various studies related with uranium speciation in solution by TRLIF. The most interesting feature of TRLIF is its capability of characterizing species present in solution by modification of the fluorescence spectrum (and lifetime) and thus performing speciation (determination of complexes directly in solution). Studies were reported on the variations in the uranyl fluorescence spectrum at low concentration ($100\,\mu g\,L^{-1}$) as a function of pH in a non-complexing medium ($NaClO_4$); speciation diagram of uranium(VI) and compared uranyl fluorescence spectrum at pH 1 and first hydroxide complex fluorescence spectrum [46]. A total of nine uranyl species appear in the pH range 2–10 but primarily hydroxide and carbonate complexes. Hence, at pH 1, only UO_2^{2+} is present in solution; at pH 4, UO_2OH^+ appears; at pH 7, several uranyl-hydroxide complexes are present (UO_2OH^+, $UO_2(OH)_2$, $UO_2(OH)_3^-$, $UO_2(OH)_4^{2-}$, $(UO_2)(OH)^{3+}$) as well as uranyl-carbonate complexes (UO_2CO_3, $UO_2(CO_3)_2^{2-}$); at pH 10, uranyl tricarbonate, $UO_2(CO_3)_3^{4-}$ is the predominant species. Second, the lifetimes observed for pH 7 are of the same magnitude and direct speciation at this pH is not straightforward as too many species are present. Since lifetime obtained for pH 1 (where UO_2^{2+} is only present) and pH 4 (where UO_2OH^+ appears) are distinctly different, namely, 2 and 80 μs, respectively, speciation by time resolution is performed. Thus, placing a gate 40 μs after the laser pulse allows only the fluorescence due to UO_2OH^+, which was compared with the fluorescence of the free uranyl obtained at pH 1. The same spectrum (for free uranyl) is obtained at pH 4 by placing a gate only 1 μs after the laser pulse and with a short duration (to avoid the important contribution of the long-time component). Through these measurements, fluorescence wavelengths are shifted 10 nm between the free uranyl and the first hydroxide complex and lifetimes move from 2 (for UO_2^{2+}) to 80 μs (for UO_2OH^+). By varying pH and uranium concentration in the absence of carbonate ions and at fixed ionic strength, it was possible, together with free uranyl UO_2^{2+}, to identify spectrally and temporally all the uranium-hydroxo complexes, namely, UO_2OH^-, $UO_2(OH)_2$, $UO_2(OH)_3^-$, $(UO_2)_2(OH)_2^{2+}$,

$(UO_2)_3(OH)_5^+$ and $(UO_2)_3(OH)_7^-$ [46]. Moulin et al. [48] also used convolution procedure for speciation of uranyl species, UO_2^{2+} and UO_2OH^+). Couston et al. [49] reported speciation of uranyl species in nitric acid medium by TRLIF based on the assumptions made on spectral distortion, leading to a spectral deconvolution model. With the use of very well characterized chemical conditions (uranium concentration, pH, ionic strength, atmospheric partial pressure) and whenever possible, time resolution and then spectral deconvolution, acquisition of precise fluorescence spectra and lifetimes for different uranium-hydroxo complexes proved to be feasible. Some more reported results are interesting, such as, speciation diagram of uranium in nitric acid [52] and also uranium fluorescence spectrum in nitric acid, together with the theoretical spectrum obtained for the contribution from free uranyl and the first and second nitrate complexes. Thus, the applications of TRLIF coupled with spectral convolution will be particularly promising to validate the existence and proportion of uranium species.

The state of the arts in time-resolved laser-induced fluorescence for actinides analysis and trends towards the use of TRLIF for remote determination via fiber optics and optrode as well a speciation, are well documented in the literature [54]. The instrumentation has progressed [47,54]; gas laser have been replaced by solid state laser (tripled to quadrupled Nd-YAG) and monocanal detection (photomultiplier) has been replaced by multi-channel detection (pulsed intensified photodiodes array). Imaging detectors based on an image intensifier have been used for the measurement of luminescence [55]. Time-resolved optical array detectors and charge-coupled device (CCD) cameras have been used for more than a decade by several companies in equipment designed for studying the transient, unstable luminescence phenomena. To measure fast spectral changes, for example in the nanosecond range, the above devices may be generally coupled with a fast, gatable, proximity-focused image intensifier [56,57]. By the use of these imaging detectors, speciation studies of this tetravalent uranium ion can be expected. The evolution of the TRLIF instrument was finalized by the commercial apparatus FLUO 2001 (DILOR) under CEA license, which is now in operation in several laboratories of COGEMA, ANDRA, CEA for various applications in nuclear fuel cycle. The main laser source used in TRLIF, nitrogen laser, has several drawbacks for remote uranium determination in nitric acid; non-negligible nitric acid absorption at 337 nm, poor beam quality and fiber optics transmission loss. The use of tripled Nd-YAG laser (355 nm) for such purpose has several advantages: lower nitric acid absorption, better beam quality, better fiber transmission and solid state technology. Despite lower uranium absorption coefficient at 355 nm compared to 337 nm, tripled Nd-YAG laser seems promising as laser source for on-line uranium determination by TRLIF [47]. Another interesting feature of TRLIF is the possibility to perform remote measurements via fiber optics and optrode [46,54]. Such instrumentation has been developed to carry out determinations in glove-box and shield cell. Jia et al. [58] have reported the application of laser-induced optical fluorimetry to the analysis of ultralow level of uranium. The fluorescence spectrometer includes five major components: a pulsed nitrogen laser, optical fibers, an optrode, a detector and a boxcar. The fluorescence intensity of uranyl ions is linear with respect to uranium. The detection limit of uranium in 1 M phosphoric acid is 24 $\mu g\,L^{-1}$. This technique can be used for the remote, on-line measurement of low-level uranium. Wangen and co-workers [59] have reported the determination of uranyl in aqueous solutions using a fiber-optic-based, time-resolved luminescence sensor. They have coupled TRLIF with the use of a remote optical sensing device, a flow optrode, by using fiber-optic cables in order to probe for uranyl in aqueous solutions. The flow optrode incorporates a Nafion membrane through which UO_2^{2+} can diffuse into a reaction/analysis chamber which contains phosphoric acid,

a reagent which enhances the uranyl luminescence intensity and excited-state lifetime. The excited-state lifetime measurement provides information on the chemical environment within the sensor. More compact and portable systems using new laser technology (microchip laser pumped by diode) [44,54,60] are now being developed for tracer experiment or uranium monitoring.

The fast and sensitive methods were developed for use in the nuclear fuel cycle for ultratrace determinations of actinides and lanthanides [39]. Among the actinides and lanthanides, the ones that are fluorescent in solution are uranium, curium, americium, and europium, terbium, dysprosium, samarium, gadolinium, cerium, thulium [39]. These elements have been studied in different complexing media (nitric, phosphoric, sulphuric, carbonate, micellar) and have been analysed from the μg L^{-1} to the ng L^{-1}). It is worth mentioning that the results of an inter-laboratory round-robin study of the application of time-resolved emission spectroscopy [61] to the speciation of uranium(VI) in aqueous media were presented. As concluded based on these studies, (i) electronic excitation is localized within the $UO_2{}^{2+}$ group. (ii) Vibronic fine structure is observed in both absorption and luminescence spectra, and it depends on both the nature and symmetry of the species. The spectroscopic signature of a given U(VI) species can be made through its emission spectrum, not through its lifetime value. (iii) A complete description of the medium (chemical composition and total ionic strength value) is necessary to allow comparison of lifetime for free U(VI), and probable uranyl complexes. Indeed different spectral signatures are observed for each emitting uranyl species.

2.1.3. Laser-induced kinetic phosphorimetry

In this technique, a pulsed visible-region dye laser [8,62,63], can selectively excite the normally spin-forbidden transition to the excited triplet state in a given vibronic fine structure band of $UO_2{}^{2+}$ and phosphores with a lifetime characteristic of its matrix environment.

A method is described for measuring uranium in aqueous solution comprising [8,62,63]: (a) adding 1.5 ml of 1 M phosphoric acid to a 10 ml aliquot of a suitable sample to convert any uranium present to a uranyl phosphate complex; (b) irradiating the sample with a laser light pulse having a wavelength of 425 nm, (laser light produced by a nitrogen laser pumped broad band dye laser using stilbene 420 dye) a band width of 10 nm, peak power of 50 kW, and pulse duration of 5 ns; (c) observing any resultant emissions at a wavelength of 520 nm at timed intervals of 10 μs duration during the time from 50 to 400 μs after the laser light pulse; wherein the natural logarithm of the emission intensity observed in step (c) is plotted as a function of time yielding an intercept value which is directly proportional to uranium concentration.

In this method, the induced phosphorescence may be masked by laser and Raman scattering, prompt fluorescing organic species, and matrix quenching [33,62]. The scattering and prompt fluorescence may be screened out by ignoring those photons generated in the first 50 μs after the laser pulse. The basis for correction of matrix quenching is derived directly from the photo kinetics of the emitting state. If a given population of the uranyl phosphate is placed in the emitting excited state then its evolution may be described by the simple first order differential equation,

$$\frac{dU}{dt} = (K_p + K_q)U \tag{4}$$

where U, is the concentration of uranium in the emitting excited state, K_p is the intrinsic rate constant for phosphorescence decay and K_q is a summation for all the various channels of radiation less deactivation. The integrated form of this equation is:

$$U(t) = U(o) \exp{^{(-(K_p + K_q)t)}} \tag{5}$$

which can be linearized to,

$$\ln(U(t)) = \ln(U(o)) - (K_p + K_q)t \tag{6}$$

Extrapolation to $t = 0$ leads to

$$\ln(U(t)) = \ln(U(o))_{t=0} \tag{7}$$

i.e., the quenching disappears.

This principle was verified, for the quenching effect of chloride ions and proved up to an effect of 80%.

Thus, plotting the natural logarithm of the emission intensity as a function of time yields an intercept of $\ln(U(o))$, a direct measurement of the initially created population, independent of matrix quenching effects. The decay lifetime, τ, is the reciprocal of $(K_p + K_q)$, which is the negative reciprocal of the slope in Eq. (6). In this technique, the time resolution parameters are computer controlled and can be varied in order to obtain the set most suitable for the species to be determined. The number of laser pulses was set at 200, unless otherwise specified and can be increased to 2000 to enhance the sensitivity. In this method, using phosphoric acid as phosphorescence enhancing reagent, the severe quenching is due to the presence of chloride ions, which necessitates either large dilution or boiling the sample to dryness with ca. 10% HNO$_3$; the residue was redissolved with ca. 2 M HNO$_3$ and then diluted to a final volume. Detection limits [7,8,33,62,63] of 1 ng L^{-1} have been demonstrated, and in samples with concentrations greater than 100 ng L^{-1}, relative standard deviations of less than 3% are achieved routinely. In addition to KPA-11, other different models of kinetic phosphorescence analysis (KPA) (KPA-11A, 11R and 11T) are available in the market [63].

2.2. Ion chromatography

A review [64] is available detailing the development of ion chromatography (IC) as a selective analytical tool for the determination of toxic metals and their organic species in many environmental sample matrices. A brief outline of ion chromatographic principles, together with an overview of the stationary phases used to separate metals, namely ion exchangers, modified ion pair sorbents and chelating ion exchangers, and the methods for detecting metal ions including hyphenation with spectroscopy and sample preparation schemes are also given. Developed methods are critically examined for various metals including arsenic, chromium, cadmium, lead, mercury, beryllium, aluminium and uranium since 1990. Chelation ion chromatography [65], involving a high efficiency neutral polystyrene-divinylbenzene resin dynamically coated with 2,6-pyridinedicarboxylic acid, has been reported as a novel technique for the quantitative determination of uranium in complex matrices. An isocratic separation method, using an eluent consisting of 1 M KNO$_3$, 0.5 M HNO$_3$ and 0.1 mM 2,6-pyridinedicarboxylic acid, allowed the uranyl ion to elute away from matrix interferences in under 10 min. Detection was achieved using an Arsenazo III post-column reaction system. Good recoveries were obtained from spiked mineral water and sea water and the standard addition curves produced good linearity ($r^2 > 0.997$) with a detection limit, calculated as twice baseline noise, of 20 μg L^{-1}. The procedure was applied to the determination of trace uranium in standard reference water and sediment samples. The results obtained compared well with the certified values for uranium. Two methods are described for the determination of uranium [66] in process liquors using ion chromatography based on cation separation and cation–anion separation with ammonium sulphate–sulphuric acid as the eluent. The uranium species is detected spectrophotometrically at 520 nm after post-column reaction with 4-(2-pyridylazo) resorcinol. Chromatographic and detector variables, such as eluent

composition and concentration, metallochromic indicator concentration and eluent and indicator flow-rates, are discussed. The method is linear for peak heights up to 15 mg L^{-1} and has a quantitation limit of 0.04 mg L^{-1} using direct injection. A method has been reported based on chelation ion chromatography [67], which combines selective chelation concentration with analytical separation and specific detection The selective post-column derivitization of uranium is accomplished by using Arsenazo III. The detection limit by direct injection (50-μL loop) is 20 μg L^{-1} of uranium. The Eppendorf-Biotronik Portable Ion Chromatograph Model IC 2001-2 is a field-portable ion chromatography instrument made in Germany [68]. This instrumental technique measures anions and cations in aqueous samples. The instrument is light weight (approximately 16.5 kg) and is powered by either a rechargeable battery pack or 110 AC. EB-IC used the following configuration for this test: two pumps, one for transfer of the mobile phase sample (eluent), and one for pumping the uranium complexing agent; a uranium separation column; a UV–vis detector; and a notebook computer running the Winpeak light. A single time dependent peak which is directly proportional to the uranium concentration in the sample is detected by the UV–vis detector.

This instrumental technique rapidly detected the uranium concentration in water, and has a detection limit in the low μg L^{-1} range without using the sample concentrating feature. Additional comparisons with on-site laboratory instrumental techniques, such as, kinetic phosphorimetry and laser-induced fluorimetry are reported. As claimed by authors, overall, the ion chromatography technique performed exceptionally well providing a detection limit of <10 μg L^{-1} and giving rapid (<5 min) accurate and reproducible results for the water samples with uranium concentrations in the region of interest (10–40 μg L^{-1}). The per sample operating cost for this instrument technique is equivalent to the per sample cost for the currently used kinetic phosphorimetry. The time required to analyse a sample and provide a result is approximately the same for the ion chromatography, kinetic phosphorimetry, and laser-induced fluorimetry.

2.3. Microsample X-ray analysis method followed by Energy dispersive X-ray fluorescence technique (MXA–EDXRF)

XRF is a convenient, accurate, and versatile instrument for qualitative and quantitative analysis. XRF is used in a variety of areas, and there continue to be many innovations and new developments [69–71]. Dewberry [72] outlined a method for determination of total uranium amount in solutions. The concentrations of uranium examined in that study were 1–15 g L^{-1} (uranium solutions in 2 M nitric acid). 5 ml aliquots of liquid samples were pipetted in to plastic vials, then each was spiked with 50 μl of 40 μCi/ml ^{109}Cd source. The U L-line measurements were used to determine the amount of uranium. Turner et al. [73] reported a sample preparation method called microsample X-ray analysis (MXA). A 50 μL droplet of sample was deposited on an ultra thin (0.15 μm) X-ray window film support to dry completely. The resulting residue was then analysed by XRF for various elements other than uranium over a wide range of concentration. MXA results from river water samples were all within 12–14% of the known concentrations. Overall MXA results were in good agreement with ICP, and GFAA. It was concluded that this method is suited for determination of metal ions at low concentrations in environmental waters. MXA procedure was later adopted for determination of U(VI) in water. Quantitative determination of trace uranium in water by microsample X-ray analysis sample preparation method [74], followed by the EDXRF analysis, has been reported. The dried sample residues were analysed on Philips Analytical (Natick, MA) PW4025 Mini Pal EDXRF Spectrometer. The instrument is controlled by a personal computer (Software

supplied by EDXRF). The MXA sample preparation method offers a much higher sample turnout compared to other characterization methods available. The XRF analysis is one of the most rapid means of spectrometry, and the MXA sample preparation procedure takes only about 5 min. The method is very inexpensive. Only supplies (besides reagents) needed for sample preparation are XRF sample cups, X-ray window films, and some micropipettes of appropriate volume settings. The simplicity of the MXA sample preparation method may allow application and adaptation for other target elements. The amount of radioactive waste water generated from the MXA sample preparation procedure is minimal, which is extremely favourable in terms of environmental protection. The minimum detection limit of MXA samples is around 180 μg L^{-1}. The application of this method includes the tracking of uranium leaching behaviour in a simulated ground water storage condition and the analysis of surface water sample. To verify the effectiveness of the MXA sample preparation method, UA-3 uranium analyser was used to measure the same set of uranium sample solutions.

Some adaptations (to suits the needs for different target elements) include acidification of samples for spot size control for dilute samples, switching the X-ray film to a thinner kind, sample volume reduction, and XRF parameter adjustments. As long as the samples used for calibration and the real samples have the same matrices similar to each other, matrix effects are minimized. Minimizing the matrix effects improves data accuracy. Thus, the MXA sample preparation method, followed by the XRF analysis, can provide an affordable, quick, and simple alternative to materials characterization.

2.4. Calixarenes and calixarence-based sensors (calixarenes coated gold electrode as a sensors for electrochemical detection of uranium)

Extensive literature survey review is available on "calixarenes" since their discovery as by-products of the phenol formaldehyde bakelites, their different modifications and potential applications [75–77]. Calixarenes are of particular interest to synthetic organic chemists as well as to analytical chemists because they have two regions where the molecule can be modified. Each calix [4] arene molecule has four positions at the top and bottom that can react. Therefore, there is enormous potential for making a large number of molecules. The calixarene molecule is very symmetrical, which means that certain positions may often be of equivalent reactivity (it can either be a help or hinderance). Additionally, some positions may be more or less reactive than others; some will react with electron-rich atoms, some will react with electron-deficient atoms. These principles can be used to design a calixarene molecule. Metals in solution have certain sizes and shapes; so do the different calixarene cavities. The different members of calixarene groups can be made with differently sized and charged cavities which will accommodate other entities, such as metal cations and anions. The invention has been reported [76,77] describing methods of synthesizing the novel uranium-attractive calixarene dimers and their incorporation in to sensors having good sensitivity suitable for use in electrochemical analysis for the detection of uranium in solution. Depending upon the conditions, chemicals will react either at top or the bottom of the cup, i.e., the upper or lower rim. By adding different chemical groups to the calixarene, the chemical and physical properties of the molecule can be radically changed. For example, it is possible, by adding certain groups, to make calixarenes adhere to surfaces. Sulphur-containing groups are particularly good at adhering to gold surfaces and by attaching sulphur-containing groups to calixarenes it has been shown that they can be anchored to gold surfaces. Once the calixarenes are anchored, they can be used as sensors by examining changes in the properties of the surface, for

example when the calixarene surface comes into contact with metals or vapours. Thus, by anchoring the uranium-loving calixarenes to a gold surface a sensing method for uranium could be developed.

As reported, when the gold surface of an electrode was exposed to a solution of the sticky calixarene, a monolayer film of the calixarene disulphide formed. Thus, a film just one molecule thick was easily prepared and no specialised or expensive film preparation equipment was required. Once coated, the modified gold surface was used as an electrode. Gold allows good adsorption of the calixarene dimers on to the surface of the electrode.

The calixarene coated gold electrode was then dipped in a test solution containing uranium and used in an electrochemical technique known as cyclic voltammetry. The potential applied to the electrode was varied and the resulting current measured. In the presence of uranium ions, the monolayer film generated a distinct signal, which was proportional to the uranium concentration in the solution. A typical response was obtained using the cyclic voltammogram technique; by measuring the peak height, the concentration of uranium solution could be determined. Thus, by allowing the calixarene molecule to form a film on gold which is only one molecule thick, it becomes highly sensitive to the presence of uranium cations and can be used as an electrochemical sensor. As reported, the proximity of both the uranyl ion and the calixarene group undergoing redox reactions to the electrode surface probably contribute to the superior performance of the sensors in accordance with the invention [78]. The composition of the real waste sample was (μg L^{-1}): uranium, 15; beryllium, <1; chromium, 2; iron, 850; nickel, 13; copper, 11; zinc, 75; cadmium, <1; lead, 4; mercury, <1; chloride, 380; nitrate, <200. The wastes were analysed using the calixarene modified electrode connected to standard cyclic voltametry apparatus, either using the bench top instrument or a portable mini-potentiostat connected to a lap-top. The methodology has shown excellent response to laboratory generated uranium solutions and with real uranium containing wastes [76–78]. Therefore, in effect, Atomic Weapons Establishment (AWE), UK has developed a portable, novel, inexpensive and reliable field device having a uranium-sensitive electrode. As claimed by authors, the film in the current device has demonstrated a limit of detection of 5 μg L^{-1} of uranium in dilute sulphuric acid. In addition, studies with uranium have shown that calixarenes have fluorescent properties themselves, but the addition of a fluorescent group may be necessary to increase sensitivity for environmental levels. Fluorescence spectroscopy is an inherently sensitive technique because it measures absolute emission and is likely to provide the most viable detection method. Likewise, developing sensors for other actinides in particular, plutonium is underway at AWE.

2.5. Alpha liquid scintillation counting

The advantages of alpha liquid scintillation counting (LSC) over other types of detector are the easy sample preparation and the high counting efficiency (nearly 100%) due to the large ($\approx 4\pi$) solid angle and the absence of self-absorption [14]. The various extractive methods that have been reported for uranium determination using LSC can be divided in to two types: non-extractive methods [79,80] in which the sample is dissolved in a miscible scintillator cocktail, and methods in which the sample is measured by extracting the nuclide of interest in to the organic phase of a non-miscible cocktail. The principal reagents used in the extractive method are bis(2-ethylhexyl) phosphoric acid (HDEHP) [79–83] and tertiary amines [84,85]. Based on the latter type of extractant, Oak Ridge Laboratory Inc. (ORDELA) has developed uranium extractive cocktail URAEX® for measuring aqueous samples. A review of this and other trade extraction cocktails together with their principal components, has been published by McDowell and McDowell [86].

McDowell [87] used the Photon-Electron Rejecting Alpha Liquid Scintillation (PERALS®) alpha spectrometer to perform uranium measurements using only 1 ml of URAEX®. The specific measurement of uranium without extraction of other alpha emitters is based on a methodology first developed by Abuzeida et al. [81] and applied by Duffey et al. [88] for the measurement of uranium in water samples by selective and quantitative extraction from diethylenetriaminepentaacetic acid (DTPA) solution in to an extractive scintillator containing di-2-ethylhexylphosphoric acid (HDEHP) acidic extractant and alpha-counting by PERALS® spectrometry. This method offers several advantages over the current EPA and ASTM standard test methods for uranium in drinking water, including speed, simplicity, and isotopic information and has been proposed as a new ASTM standard test method.

Aupiais [89] further studied the above system and proposed a rapid, robust and simple method to measure uranium in all kinds of water samples, even those with very high salinity (e.g. 130 g kg^{-1}). The method is based on simple chemical treatment, only involving addition of DTPA, 0.1 M instead of 0.01 M. Sample preparation is carried out within 2 h for 100 ml samples. One optional step has been inserted for a few samples to specifically remove Po because of interference with the ^{232}U spike in the alpha energy spectrum. Chemical yield is about 100% for most of water samples. A particular deconvolution process of alpha energy spectra is applied to perform accurate determination. The reported detection limit is equal to 0.2 μg kg^{-1} i.e., 0.003 Bq kg^{-1} for 240,000 s counting time. Reproducibility of the method is within 5%. This method showed very good agreement with international and national intercomparison exercises for various water samples using other techniques such as, KPA, time-resolved laser-induced fluorimetry and fluorimetry.

3. Conclusions and trends

With the advancement in improved laser design and detector systems, there is a challenging trend in designing miniaturized as well as automated microanalytical systems via FIA and its sequels. Ruzicka [90] described the unique features of flow injection analysis (FIA), which will change the concept of solution handling in the chemical laboratory and make chemical analyses truly compatible with tools of the computer age by enabling us to design microchemielectronic devices. Christian [91] discussed the role and importance of flow analysis in analytical sciences. A review by Luque de Castro and co-workers [92] on valves and flow injection manifolds is commendable. In this review, the functions of valves—both injection and selection valves—in flow injection (FI) for manipulating the manifold as a function of both necessities and imagination of the user is reported. Hansen and Wang [93] reviewed the characteristic of the three generations of FIA, that is, FIA, sequential injection analysis (SIA), and bead injection-lab-on-valve. Recently, Hansen and Miro [94] discussed and summarized on the impact of FIA over the last 25 years on our way of performing chemical analyses and touched upon many of the novel and unique analytical chemical possibilities that FIA and its sequels, SIA and lab-on-valve (LOV), have offered. The challenges of microanalytical systems for routine diverse applications are now well understood and documented [95,96]. A review article by Schwarz and Hauser [97] on development of detection methods for microfabricated analytical devices is worth mentioning. A lot of current work is also focused on electrochemical methods as these represent the most direct approach to the signal conversion. Calixarene based electrochemical sensors seem more promising [76–78]. More compact and portable systems using new laser technology (microchip laser pumped by diode) [54,60,98] are now being developed for tracer experiment or uranium monitoring.

Table 2
Figures of merit of different microchemielectronic technologies for the determination of uranium concentration

Type of instrument	Technique used	Instruments make/manufacturers	Detection limits[a]	References
Laser based instrument	Laser fluorimetry	UA-3, Uranium analyser (Scintrex, Canada)	$0.05 \, \mu g \, L^{-1}$	[4,5,23]
	Laser fluorimetry	Digital read-out laser fluorimeter, RRCAT, Indore, India.	$0.05 \, \mu g \, L^{-1}$	[32]
		Miniaturized digital read-out laser fluorimeter, RRCAT, Indore, India	$0.1 \, \mu g \, L^{-1}$	
	Time resolution spectrofluorimetry	Time-resolved laser-induced spectrofluorimetry (TRLIS)	$1 \, ng \, L^{-1}$	[33,37]
	Kinetic phosphorescence analyser	The Chemcheck kinetic phosphorescence analyser (KPA), KPA-11 and others (KPA-11A, 11R and 11T), Inc., USA	$\sim 1 \, ng \, L^{-1}$	[7,8,62,63]
Ion chromatography	Field-portable ion chromatography instrument	The Eppendorf-Biotronik Portable Ion Chromatograph Model (IC 2001-2 EB-IC), Germany and distributed in US by Analytical Magnetics Inc. (AMI).	$10 \, \mu g \, L^{-1}$	[68]
XRF	Microsample X-ray analysis (MXA)–EDXRF analysis	Philips Analytical PW4025 Mini Pal EDXRF Spectrometer, Natick, MA	$\sim 1 \, mg \, L^{-1}$	[74]
Sensors for electrochemical detection	Calixarenes coated gold electrode based sensors followed by cyclic voltammogram technique	Portable-field device having a uranium-sensitive electrode, AWE, UK	$5 \, \mu g \, L^{-1}$	[76,77]

[a] Detection limit: as reported by authors as per the IUPAC definition, $3\sigma_{blank}/$slope.

The success of laser-induced fluorescence detection is due to its high sensitivity. Recently [99], laser instrumentation section, developed world's smallest sealed-off nitrogen laser module measuring only 145 mm × 75 mm × 50 mm with integrated H.V. power supply. Now, they are successful in miniaturizing the digital read-out laser fluorimeter (Fig. 2(c)) version 8.5, specifications: detection limit: $0.1 \, \mu g \, L^{-1}$, range: $20 \, \mu g \, L^{-1}$, excitation source: sealed-off nitrogen laser, size: 180 mm × 100 mm × 80 mm, power: 12 V DC, weighing only 2.5 kg and incorporated the software for scale-expansion, spiking and counting mode. Although, this miniaturized device was found to be more suited for field conditions for the measurement of uranium in hydro-geochemical samples for survey work. But, this miniaturized version of the instrument unlike the previously fabricated laser fluorimeter (weighing 15 kg; Fig. 2(b)), lacks in consistencies in the signal response (low performance qualification, PQ) for its varied utility for the determination of uranium in the aqueous solutions of diverse matrices on routine basis as well as for control laboratory. Rathore and Kumar [16] discussed and outlined the designing of automated compact micro devices based on DT-LIF coupled with flow injection for uranium determination. The advantages will include accurate spatial control of reagents and samples, minimum steps, increased throughput, automation, minimum generation of radioactive waste, cost effective, etc., without the need for skilled operators or special equipments.

Among the various technologies, laser-induced fluorimetry is the method of choice for such applications, which can be used in the field as well as in a control laboratory. It also fulfills the basic essential requirements of RAPs: reliability (accuracy and high precision), applicability (applicable to diverse sample matrices for wide applications in entire nuclear fuel cycle) and practicability (inherent high sensitivity, high PQ, simple, rapid and direct, easy calibration and operation, cost effective). A very extensive range of concentrations may be covered, macro quantities in mineralized rocks and concentrates to traces in rocks (by using either by standard addition method or after solvent-extractive separation); directly in natural waters. Time-resolved laser-induced spectrofluorimetry (TRLIS) is a variant, and complementary to laser fluorimetry for both fundamental and applied reasons. It is used to evaluate the speciation, oxidation state, equilibrium distribution, structure, and bonding of fluorescent elements. Fluorescence lifetimes often provide accurate information about the physical state of a fluorophore, its hydration status, molecules in its vicinity as well as possible association with a like fluorophore. Unlike laser fluorimetry, the TRLIS can be used for the analysis of other fluorescent actinides and lanthanides in solution, such as, curium, americium, and europium, terbium, dysprosium, samarium, gadolinium, cerium, and thulium.

In principle, such other reagent systems/analytical procedures based on differential technique having minimum steps and direct determination of analytes (which need microlitre sample volume and measurement at nano or micro level) may prove valuable absolute methods in other fields of applications of fluorimetry and also in other modern instrumental techniques, in the areas of clinical pathology, biochemistry, medical research, pharmaceutical industry, inorganic analysis and other related diverse applications.

In summary, a judicious use of various available techniques to provide quick feed back of analytical results at each phase of uranium exploration programme is essential, with the overall objective of greatly increasing the chances of discovering an economic deposit at the least possible cost.

The figures of merit of different techniques and their commercial instruments available in markets for the determination of uranium concentration are summarized in Table 2. The unique relationship between uranium and fluorimetry can be described as: An excellent marriage with unlimited versatility.

In future, new generations of automated microfabricated devices (microanalytical systems/compact portable devices) having high PQ either based on laser fluorescence or calixarene based electrochemical sensors will become a reality in analytical laboratories.

encouragement. Author is thankful to Dr. Vijay Kumar for critical discussions for improving the manuscript. Author is extremely grateful to the reviewers of the manuscript for their invaluable comments and suggestions in improving the manuscript in the present form.

References

[1] R. Chidambaram, C. Ganguly, Curr. Sci. 70 (1996) 21.
[2] Editorial Staff, Significance of Mineralogy in the Development of Flowsheets for Processing Uranium Ores, Technical Report Series no. 196, IAEA, 1980.
[3] B. Mason, C.B. Moore, Principles of Geochemistry, fourth ed., Wiley Eastern Limited, New Delhi, India, 1985, pp. 46–47.
[4] J.C. Robbins, CIM Bull. 71 (1978) 61.
[5] J.C. Robbins, J.D. Kinrade, United States Patent, patent no. 4,239,964 (December 16, 1980).
[6] A. Kirishima, T. Kimura, O. Tochiyama, Z. Yoshida, Chem. Commun. (7) (2003) 910.
[7] R. Kaminski, F.C. Purcell, E. Russavage, Anal. Chem. 53 (1981) 1093.
[8] G.A. Kenney-Wallace, J.P. Wilson, J.F. Farrell, B.K. Gupta, Talanta 28 (1981) 107 (and other references cited therein).
[9] Editorial Staff, Analytical Techniques in Uranium Exploration and Ore Processing, Technical Report Series no. 341, IAEA, 1982.
[10] W.W. Bowman, Neutron activation Analysis for Uranium and Associated Elements: HSSR Symposium, 1977, Grand Junction, Colorado.
[11] R. Fleischer, A.C. Delaney, Anal. Chem. 48 (1976) 642.
[12] G.R. Waterbury, Fluorimetric Analysis for Uranium in Natural Waters: HSSR Symposium, 1977, Grand Junction, Colorado.
[13] P.K. Tarafder, P. Murugan, L. Kunkal, D.P.S. Rathore, J. Radioanal. Nucl. Chem. 253 (2002) 135.
[14] X. Hou, P. Roos, Anal. Chim. Acta 608 (2008) 105.
[15] D.P.S. Rathore, P.K. Tarafder, M. Kayal, M. Kumar, Anal. Chim. Acta 434 (2001) 201.
[16] D.P.S. Rathore, M. Kumar, Talanta 62 (2004) 343.
[17] G.I. Romanovskaya, V.I. Pogonin, A.K. Chibisov, Talanta 34 (1987) 207.
[18] D.L. Perry, S.M. Klainer, H.R. Bowman, F.P. Milanovich, T. Hirschfield, S. Miller, Anal. Chem. 53 (1981) 1048.
[19] T.F. Harms, F.N. Ward, J.A. Erdman, J. Geochem. Expl. 15 (1981) 617.
[20] J.B. McHugh, Anal. Lett. 15 A (1982) 1009.
[21] B.N. Tikoo, D.S.R. Murty, Curr. Sci. 49 (1980) 861.
[22] W. Campen, K. Bachmann, Mikrochim. Acta II (1979) 159.
[23] A.C. Zook, L.H. Collins, C.E. Pietri, Mikrochim. Acta II (1981) 457.
[24] J.C. Robbins, C. Castledine, W. Kostiak, Analytical Procedures for UA-3 Uranium Analysis—Applications Manual, Scintrex Limited, Ontario, Canada, 1985 Oct.
[25] P.G. Whitkop, Anal. Chem. 54 (1982) 2575.
[26] J.C. Veselsky, B.K. Wiecinska, E. Wehrstein, O. Suschny, Analyst 113 (1988) 451 (and references cited therein).
[27] I.G. Kochan, I.I. Shuktomova, J. Radioanal. Nucl. Chem. 188 (1994) 27.
[28] A. Premadas, G. Saravanakumar, J. Radioanal. Nucl. Chem. 266 (2005) 95 (and other references cited therein).
[29] BDH, Laboratory Supplies Catalogue (Merck), 1995, p. 4–571.
[30] M. Valcarcel, Principles of Analytical Chemistry—A Text book, Springer, Berlin, Heidelberg, 2000, p. 263.
[31] D.P.S. Rathore, EARFAM 17 (2007) 145.
[32] http://www.cat.gov.in/lil/main.html.
[33] P. Mauchien, P. Cauchetier, United States Patent, patent no. 4,641,032 (February 3, 1987).
[34] P. Mauchien, Dosage de l'Uranium par spectrofluorimetrie a' Source d'Excitation Laser, CEA Rep., R.5300 (1985).
[35] T. Berthoud, P. Decambox, B. Kirsch, P. Mauchien, C. Moulin, Anal. Chem. 60 (1988) 1296.
[36] T. Berthoud, P. Decambox, B. Kirsch, P. Mauchien, C. Moulin, Anal. Chim. Acta 220 (1989) 235.
[37] C. Moulin, C. Beaucaire, P. Decambox, P. Mauchien, Anal. Chim. Acta 238 (1990) 291.
[38] P. Decambox, P. Mauchien, C. Moulin, Appl. Spectrosc. 45 (1991) 116.
[39] C. Moulin, P. Decambox, P. Mauchien, J. Phys. IV (1991) C7-677-680 (and reference cited therein).
[40] C. Moulin, P. Decambox, P. Mauchien, V. Moulin, M. Theyssier, Radiochim. Acta 52–53 (1991) 119.
[41] C. Moulin, P. Reiller, C. Beaucaire, D. Lemordant, J. Colloid Interface Sci. 157 (1993) 411.
[42] C. Moulin, P. Reiller, C. Beaucaire, D. Lemordant, Appl. Spectrosc. 47 (1993) 2172.
[43] H. Deniau, P. Decambox, P. Mauchien, C. Moulin, Radiochim. Acta 61 (1993) 23.
[44] C. Moulin, S. Rougeault, D. Hamon, P. Mauchien, Appl. Spectrosc. 47 (1993) 2007.
[45] P. Reiller, D. Lemordant, C. Moulin, C. Beaucaire, J. Colloid Interface Sci. 163 (1994) 81.
[46] C. Moulin, P. Decambox, V. Moulin, J.G. Decaillon, Anal. Chem. 67 (1995) 348.
[47] C. Moulin, P. Decambox, L. Couston, D. Pouyat, J. Nucl. Sci. Technol. 31 (1994) 691.
[48] C. Moulin, I. Laszak, V. Moulin, C. Tondre, Appl. Spectrosc. 52 (1998) 528.
[49] L. Couston, D. Pouyat, C. Moulin, P. Decambox, Appl. Spectrosc. 49 (1995) 349.
[50] V. Moulin, C. Moulin, Appl. Geochem. 10 (1995) 573.
[51] C. Moulin, P. Decambox, L. Trecani, Anal. Chim. Acta 321 (1996) 121.
[52] C. Moulin, P. Decambox, P. Mauchien, D. Pouyat, L. Couston, Anal. Chem. 68 (1996) 3204.
[53] S. Scapolan, E. Ansoborlo, C. Moulin, C. Madic, J. Radioanal. Nucl. Chem. 226 (1997) 145.
[54] C. Moulin, P. Decambox, P. Mauchien, J. Radioanal. Nucl. Chem. 226 (1997) 135 (and other references cited therein).
[55] C. Morgan, European Patent, patent no. EP 0 519 930 B1 (July 22, 1998).
[56] E. Gratton, M.V. Ven, B. Barbieri, European Patent, patent no. EP 0 600 633 B1 (May 31, 2000) (and other references cited therein).
[57] E. Gratton, M.V. Ven, B. Barbieri, United States Patent, Patent no. 5,323,010 (June 21, 1994) (and other references cited therein).
[58] W.J. Jia, A.D. He, Z.L. Wang, C.T. Chin, J. Radioanal. Nucl. Chem. 108 (1987) 33.
[59] P.T. Varineau, R. Duesing, L.E. Wangen, Appl. Spectrosc. 45 (1991) 1652.
[60] J.J. Zayhowski, Opt. Mater. 11 (1999) 255.
[61] I. Billard, E. Ansoborlo, K. Apperson, S. Arpigny, M.E. Azenha, D. Birch, P. Bros, H.D. Burrows, G. Choppin, L. Couston, V. Dubois, T. Fanghanel, G. Geipel, S. Hubert, J.I. Kim, T. Kimura, R. Klenze, A. Kronenberg, M. Kumke, G. Lagarde, G. Lamarque, S. Lis, C. Madic, G. Meinrath, C. Moulin, R. Nagaishi, D. Parker, G. Plancque, F. Scherbaum, E. Simoni, S. Sinkov, C. Viallesoubranne, Appl. Spectrosc. 57 (2003) 1027.
[62] B.A. Bushaw, United States Patent, patent no. 4,599,512(July 8, 1986). (http://www.freepatentsonline.com/4,599,512.html; http://osti.gov/energycitations/product.biblio.jsp?osti_id=5334198).
[63] R. Brina, A.G. Miller, Anal. Chem. 64 (1992) 1413.
[64] M.J. Shaw, P.R. Haddad, Environ. Int. 30 (2004) 403.
[65] M.J. Shaw, S.J. Hill, P. Jones, P.N. Nesterenko, Chromatographia 51 (2000) 695.
[66] J.J. Byerley, J.M. Scharer, G.F. Atkinson, Analyst 112 (1987) 41.
[67] DIONEX- Application Note 79: Determination of Uranium and Thorium in Complex Matrices Using Chelation Ion Chromatography (http://www.1.dionex.com/en-us/literature/lp53336.html).
[68] M.S. Anderson, S.J. Weeks, March 28, 1997, OSTI ID: 537304 (http://www.osti.gov/energycitations/servlets/purl/537304-uDEBKK/webviewable/).
[69] P.J. Potts, A.T. Ellis, P. Kregsamer, C. Streli, M. West, P. Wobrauschek, J. Anal. At. Spectrom. 14 (1999) 1773.
[70] P.J. Potts, A.T. Ellis, P. Kregsamer, J. Marshall, C. Streli, M. West, P. Wobrauschek, J. Anal. At. Spectrom. 16 (2001) 1217.
[71] M.R. Cave, O. Butler, S.R.N. Chenery, J.M. Cook, M.S. Cresser, D.L. Miles, J. Anal. At. Spectrom. 16 (2001) 194.
[72] R.A. Dewberry, Nucl. Instrum. Meth. A 403 (1998) 383.
[73] D.C. Turner, M. Benson, A. Wilson, J. Moore, W. Watson, Am. Lab. 32 (2000) 92.
[74] N. Shibuya, Determination of Uranium concentration in Water by Microsample X-Ray Analysis (MXA), A Thesis Presented to the Graduate School of the University of Florida in Partial Fulfillment of the Requirements for the Degree of Master of Science, University of Florida, 2003 (http://etd.fda.edu/UF/UFE0000972/shibuya_n.pdf).
[75] P. Jose, S. Menon, Bioinorg. Chem. Appl. 2007, Article ID 65815 (2007) 16 p. (doi:10.1155/2007/65815) (and reference cited therein).
[76] G.P. Nicholson, M.J. Kan, C.J.E. Thompson, C.W. Hall, A.H. Jones, United States Patent, patent no. 6,924,380 B2 (August 2, 2005) (and reference cited therein).
[77] C.W. Hall, Discovery, The Science & Technology Journal of AWE, CALIXARENES—Sensors for Actinides (http://www.awe.co.uk/images/calixarene_sensors_tcm6-1983.pdf) (and other references cited therein).
[78] C.E. Thompson, S.E. Field, A.H. Jones, M.J. Kan, C.W. Hall, G.P. Nicholson, W.M.'02 Conference, February 24–28, 2002, Tucson, AZ, USA (and reference cited therein).
[79] L. Salonen, Sci. Total Environ. 130–131 (1993) 23.
[80] A.V. Zelensky, M.G. Buzinny, I.P. Los, in: J.E. Noakes, F. Schonhofer, H.A. Polach (Eds.), Liquid Scintillation Spectrometry, The University of Arizona, Tucson, 1992, p. 405.
[81] M. Abuzeida, B.H. Arebi, Y.A. Zolatarev, N.A. Komarov, J. Radioanal. Nucl. Chem. 116 (1987) 285.
[82] H.M. Prichard, A. Cox, in: H. Ross, J.E. Noakes, J.D. Spaulding (Eds.), Liquid Scintillation Counting and Organic Scintillators, Lewis Publishers Inc., Michigan, 1991, p. 385.
[83] E.A. Venso, H.M. Prichard, C.L. Dodson, in: J.E. Noakes, F. Schonhofer, H.A. Polach (Eds.), Measurement of Isotopic Uranium in Texas drinking Water Supplies by Liquid Scintillation Spectrometry, The University of Arizona, Tucson, 1993, p. 425.
[84] J.E. Bouwer, J.W. McKlveen, W.J. McDowell, Nucl. Technol. 40 (1979) 102.
[85] R. Metzger, J.W. McKlveen, R. Jenkins, W.J. McDowell, Health Phys. 39 (1980) 69.
[86] W.J. McDowell, B.L. McDowell, Liquid Scintillation Alpha Spectrometry, CRC Press, Boca Raton, Fla., 1994.
[87] W.J. McDowell, Radioact. Radiochem. 3 (1992) 26.
[88] J.M. Duffey, F.I. Case, R.L. Metzger, B.J. Jessop, G.K. Schweitzer, J. Radioanal. Nucl. Chem. 221 (1997) 115.
[89] J. Aupiais, Anal. Chim. Acta 517 (2004) 221 (and other references cited therein).
[90] J. Ruzicka, Anal. Chem. 55 (1983) 1040A (and references cited therein).
[91] G.D. Christian, Anal. Chim. Acta 499 (2003) 5.
[92] R.C. Prados-Rosales, J.L. Luque-Garcia, M.D. Luque de Castro, Anal. Chim. Acta 480 (2003) 181.

[93] E.H. Hansen, J. Wang, Anal. Lett. 37 (2004) 345.
[94] E.H. Hansen, M. Miro, Trends Anal. Chem. 26 (2007) 18 (and references cited therein).
[95] A. Rios, A. Escarpa, M.C. Gonzalez, A.G. Crevillen, Trends Anal. Chem. 25 (2006) 467 (and references cited therein).
[96] M.D. Luque de Castro, F.P. Capote, Anal. Bioanal. Chem. 390 (2008) 67.
[97] M.A. Schwarz, P.C. Hauser, Lab Chip 1 (2001) 1.
[98] J.M. Lupton, Nature 453 (2008) 459.
[99] http://www.cat.gov.in/lil/latest.htm.

The use of headspace solid phase microextraction for the characterization of volatile compounds in olive oil matrices

Laila H. Ribeiro [a], Ana M. Costa Freitas [b], Marco D.R. Gomes da Silva [a,*]

[a] REQUIMTE, Departamento de Química, Faculdade de Ciências e Tecnologia, Universidade Nova de Lisboa, 2829-516 Caparica, Portugal
[b] Departamento de Fitotecnia, Instituto de Ciências Agrárias e Mediterrânicas-ICAM, Universidade de Évora, Apt 94 7002-554 Évora, Portugal

ABSTRACT

Two different fibre coatings, for solid phase microextraction (SPME) sampling, poly(dimethylsiloxane) (PDMS) and poly(acrylate) (PA), were studied in order to test, for olive oil matrixes, two mathematical models that relate the directly proportional relationship between the amount of analyte absorbed by a SPME fibre and its initial concentration in the sample matrices. Although the PA fibre was able to absorb higher amounts of compounds from the olive oil sample, the equilibrium was reached later then with the PDMS fibre. In both cases, the amount of analyte present affected the time profile or the equilibrium time in two of the concentrations studied, 0.256 µL/kg, 2.56 µL/kg and for 2-ethylfuran, pentan-3-one, pent-1-en-3-one, hexanal, *trans,trans*-non-2,4-dienal and in the four concentrations studied, 0.256 µL/kg, 2.56 µL/kg, 6.25 µL/kg and 400 µL/kg, for 4-methyl-pent-3-en-2-one, 2-methylbutan-1-ol, methoxybenzene, hexan-1-ol, *cis*-hex-3-en-1-ol, *trans*-hex-2-en-1-ol, 2-ethyl-hexan-1-ol and *trans,trans*-dec-2,4-dienal. Comparing the mathematical models of both fibres, the PA-coated fibre showed direct proportionality between the initial concentration and amount extracted, that allows the possibility of relative quantification in a non-equilibrium state in non-aqueous media. The same was not observed for the PDMS fibre.

© 2008 Elsevier B.V. All rights reserved.

1. Introduction

In the overall quality of olive oil, the aroma plays an important role in directing consumer preference. Some components present in low concentration, contribute to the pleasant aroma note in olive oils, but when they are present in higher concentrations their contribution seems to be negative [1]. So it is important to determine, at least, the relative amounts of the aroma components of olive oil.

Compared to several techniques of sample preparation for gas chromatographic (GC) analysis of aroma compounds, headspace solid phase microextraction (HS-SPME) shows some advantages such as solvent-free extraction, low sample volumes and low cost. SPME is an equilibrium method, which does not require exhaustive extraction of a volume of sample [2].

It is known that olive oil is a complex matrix, with a high content of natural volatile compounds that have differences, among other physicochemical properties, in volatility and polarity. These different compounds are expected to present different equilibrium times. As HS-SPME is a multiphase equilibrium process [3], the

maximum sensibility is obtained by allowing the analyte(s) to reach equilibrium. It is not practical to do so when equilibration times are excessively long. Ai [4] presented a mathematical model (Eq. (1)) to demonstrate that SPME quantification, in aqueous solution, using fibres coated with a polymeric liquid, is feasible before absorption equilibrium is reached, if the amount of analyte absorbed (n) is proportional to the initial concentration in the sample matrix (C_0):

$$\frac{n}{n^\infty} = [1 - \exp(-a_h t)] \qquad (1)$$

$n\infty$ represents the amount extracted at equilibrium and the parameter a_h is a measure of how fast partition equilibrium can be reached in the HS-SPME process. The parameter a_h is controlled by mass transfer coefficients, equilibrium constants and the physical dimensions of the sample matrix, headspace and the polymeric film. It has different magnitudes depending on the rate-determining step of the mass transfer process: matrix/headspace and headspace/polymer, diffusion in the polymeric film and evaporation from the matrix phase as described by Ai [4,5].

However, in Eq. (1) the initial period of extraction is neglected. In fact, during the sampling process, when the equilibrium between sample and headspace is reached, it is disturbed by the introduction of the fibre needle into the headspace. This disturbance is not considered in the model described by Eq. (1). Moreover, in complex

---

* Corresponding author. Tel.: +351 21 2948351.
E-mail addresses: lailarib@yahoo.com (L.H. Ribeiro), afreitas@uevora.pt (A.M. Costa Freitas), mdr@dq.fct.unl.pt (M.D.R. Gomes da Silva).

Table 1
Typical concentrations and odour characteristics of compounds identified as odorants in olive oil

No.	Compound	Concentration in olive oil (μg/kg)	Odour quality [6]
1	2-Ethylfuran	–	Powerful, sweet, ethereal, burnt odour, coffee taste on dilution
2	Pentan-3-one	153–1053 [7]	–
3	Pent-1-en-3-one	634 [7]	Pungent, mustard
		40–300 [8]	
		26 [9]	
4	Hexanal	169–6367 [7]	Fatty, green, grassy, powerful, penetrating
5	4-Methyl-pent-3-en-2-one	–	Unpleasant, pungent, vegetable, acrylic
6	2-Methylbutan-1-ol	2809 [7]	–
		230–10,260 [8]	
7	Methoxybenzene	–	Phenolic, gasoline, ethereal, anise
8	Hexan-1-ol	685–50,200 [7]	Herbaceous, woody, fragrant, mild, sweet, green
		680–10,260 [8]	
9	*cis*-Hex-3-en-1-ol	252–8587 [7]	Fresh, green grass
		460–870 [8]	
		684 [9]	
10	*trans*-Hex-2-en-1-ol	1118–89,100 [7]	Powerful, leafy, green, wine-like, fruity
11	2-Ethyl-hexan-1-ol	–	Mild, oily, sweet, slight rose
12	*trans,trans*-Non-2,4-dienal	49 [9]	Strong, fatty, floral
13	*trans,trans*-Dec-2,4-dienal	127–918 [9]	Powerful, fatty, citrus

matrices, such as olive oil, this disturbance is even more important, since more equilibria are now being influenced by fibre needle introduction. Ai [5] proposed a biexponential equation (Eq. (2)) that accounts for this fact:

$$\frac{n}{n^{\infty}} = \alpha[1 - \exp(-ct)] + \beta[1 - \exp(-c_1 t)] \tag{2}$$

Hybrid parameters α, c, β and c_1 are defined as

$$\alpha = \frac{b_1}{c - c_1}; \quad \beta = \frac{a_1}{c_1} - \frac{b_1}{c - c_1}; \quad c = k + \frac{A_f m_f K_{fh}}{V_h}; \quad c_1 \frac{2A_f m_f}{V_f};$$

$$a_1 = A_f m_f K_{fh} a; \quad b_1 = 2A_f m_f K_{fh} b; \quad a = \frac{kK_{hs}V_h}{kV_h + A_f m_f K_{fh}} C_0;$$

$$b = \frac{A_f m_f K_{fh} K_{hs}}{kV_h + A_f m_f k_{fh}} C_0$$

where A_f is the surface area of the SPME polymer film; m_f is the mass transfer coefficient of the analyte in polymer film phase; k is the evaporation rate constant; V_h and V_f are the volumes of the headspace and the coating, respectively; K_{fh} is the polymer/headspace distribution constant; K_{hs} is the headspace/matrix distribution constant. Since α and β (in mol, accounting for the variation of the quantity of a particular compound present in the headspace when the equilibrium is disturbed) are directly proportional to C_0 then n is directly proportional to C_0. This fact implies that quantitative determination can be performed in a non-equilibrium state.

Since both mathematical models (Eqs. (1) and (2)) describe an absorption process, poly(dimethylsiloxane) (PDMS) and poly(acrylate) (PA) fibres were chosen for the present study. The methyl groups of PDMS make this film relatively apolar, whereas PA is a more polar fibre due to the presence of carbonyl groups.

This work aims the application of the mathematical models to a non-aqueous matrix, in this case an oily matrix, such as olive oil. This type of matrices are a better solvent for the majority of the volatile components of olive oil. It is intended to demonstrate that an important and complex matrix such as olive oil can also be studied considering the estimation parameters calculated according to one or to both mathematical models studied. A SPME sampling method was developed procedure for reproducible qualitative and relative quantitative determination of aroma compounds

using non-equilibrium extraction conditions. We intended to determine not only which model describes better the experimental data obtained with each of the fibres studied, but also which fibre is more efficient for non-equilibrium state extraction in a non-aqueous medium.

2. Experimental

2.1. Standards

The standard compounds, 2-ethylfuran, pentan-3-one, 4-methyl-pent-3-en-2-one, pent-1-en-3-one, 2-methylbutan-1-ol, hexanal, methoxybenzene, hexan-1-ol, *cis*-hex-3-en-1-ol, *trans*-hex-2-en-1-ol, 2-ethyl-hexan-1-ol, *trans,trans*-non-2,4-dienal and *trans,trans*-dec-2,4-dienal were purchased from Aldrich (Deisenhofen, Germany). The internal standard (IS) used was nonan-2-ol also from Aldrich (Deisenhofen, Germany).

2.2. Sample preparation and analysis

Standard compounds were dissolved directly in refined olive oil. Four concentrations, 0.256 μL/kg, 2.56 μL/kg, 6.25 μL/kg and 400 μL/kg were used. Fifteen grams of olive oil with the dissolved standards were placed in a 22 mL vial and kept in a water-thermostatized bath at 37 °C for 30 min before the HS-SPME extraction. The septum covering the vial was pierced with a SPME needle and the fibre was exposed to the olive oil headspace for 1 min, 5 min, 15 min, 30 min, 60 min, 90 min and 120 min. During sampling, the oil phase was stirred with a magnetic stirrer at a constant and defined stirring rate. After sampling, the fibre was inserted manually into the GC injection port for 5 min and desorbed at 260 °C.

2.3. SPME fibres and conditioning

SPME device and fused silica fibres were purchased from Supelco Inc. (Bellefonte, Pennsylvania, USA). Poly(acrylate) (PA) and poly(dimethylsiloxane) (PDMS) SPME fibres with coating thicknesses of 85 μm and 100 μm, respectively were used. Prior to use, the fibres were conditioned according to manufacturer instructions.
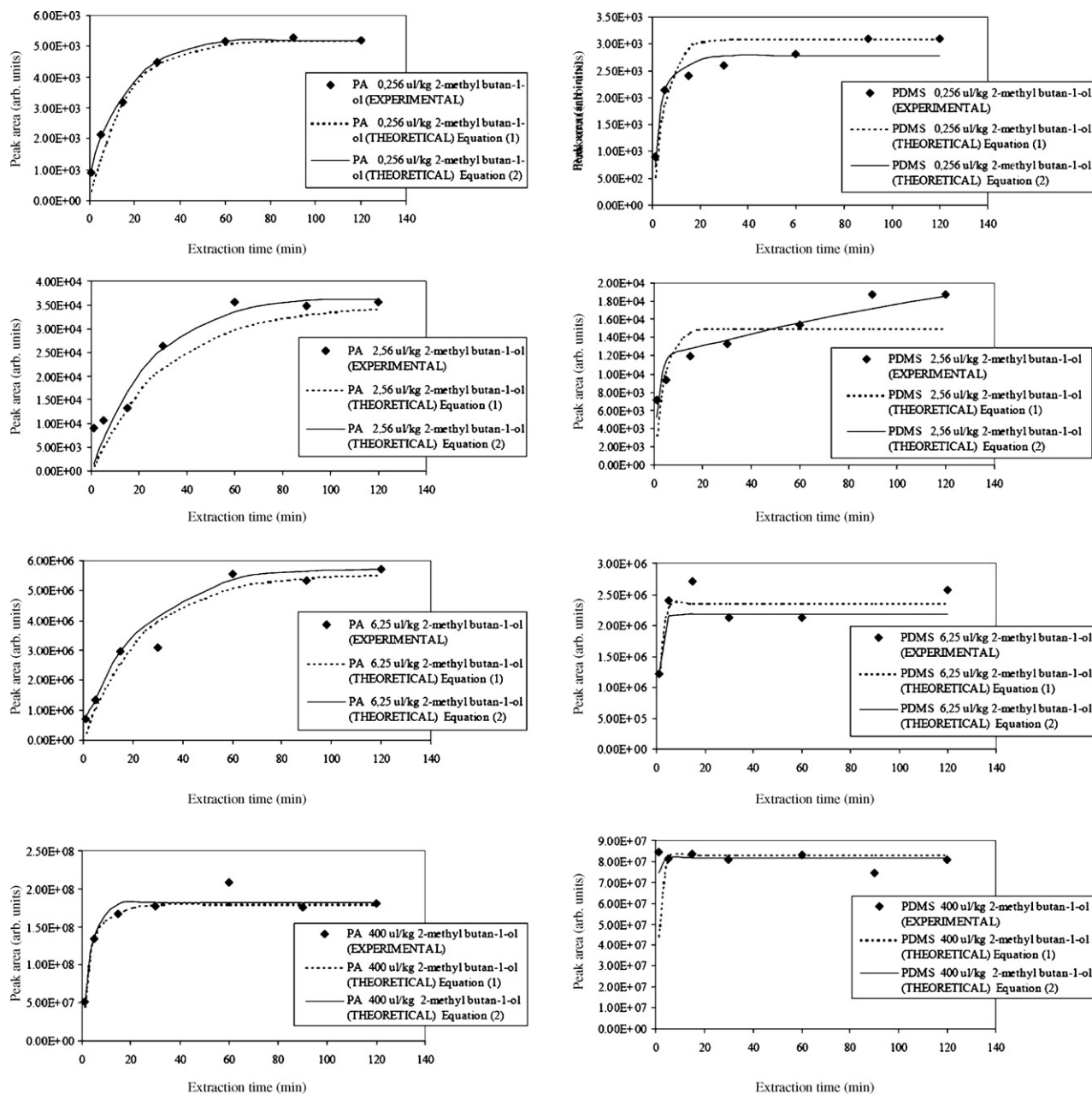
Fig. 1. Absorption kinetic curves. Comparison of experimental data *vs.* theoretical model for 2-methylbutan-1-ol in four different concentrations (0.256 μL/kg, 2.56 μL/kg, 6.25 μL/kg and 400 μL/kg) at 37 °C for the PA and the PDMS fibres.

2.4. Equipment

GC analyses were performed using a GC-Trace Thermo Quest Instruments. For GC analyses, a fused silica DB-Wax column (J&W Scientific, Folsom, USA), 60 m × 0.25 mm i.d. and 1.0 μm film thickness was used. The oven temperature program was as follow: 50 °C (5 min), 2 °C min⁻¹ to 210 °C (10 min). Hydrogen was used as the carrier gas at 100 kPa; the injector temperature and the split flow were set at 260 °C and 30 mL min⁻¹, respectively, after a splitless time of 1 min.

2.5. Data processing

The relative area data of each compound were obtained from the collected chromatograms. The adjustment of the extraction data (for the HS-SPME studies) to the theoretical models described above as Eqs. (1) and (2), was performed through an estimation method by non-linear regression method.

Data were analysed using STATISTICA 6.0 software (StatSoft Inc., Version 6.0, Tulsa, USA). Non-linear estimation user-specified regression was used. The estimation method was the quasi-Newton with a maximum number of iterations of 100. The convergence criterion was set to 0.0001 and the loss function was equal to (observed data – predicted values)².

3. Results and discussion

The volatile compounds chosen for method evaluation were studied with two different SPME fibre coatings and with four different initial concentrations that are comparable to the con-

Table 2
Parameter a_h values calculated according to Eq. (1) for selected compounds in PA fibre at 37 °C using different initial concentrations

Compound	C_0 (µL/kg)	Parameter, a_h (estimated)	Correlation coefficient	Explained variance (%)	Final loss
PA Eq. (1) model: $n/n^\infty = 1 - \exp(-a_h t)$					
2-Ethylfuran	0.256	**0.2003**	0.9587	90.679	0.01718
	2.56	**0.1046**	0.9259	85.729	0.05610
Pent-3-one	0.256	**0.0213**	0.9687	93.819	0.01632
	2.56	**0.0748**	0.9944	99.548	0.00683
Pent-1-en-3-one	0.256	**0.0276**	0.9574	90.817	0.01521
	2.56	**0.0504**	0.9908	98.171	0.00635
Hexanal	0.256	**0.0947**	0.9511	90.459	0.01633
	2.56	**0.1201**	0.9685	93.927	0.02447
4-Methyl-pent-3-en-2-one	0.256	**0.0610**	0.9118	83.134	0.03176
	2.56	**0.0613**	0.9794	94.726	0.02241
	6.25	**0.0665**	0.9601	93.717	0.05509
	400	**0.1573**	0.9746	94.958	0.02166
2-Methylbutan-1-ol	0.256	**0.0620**	0.9685	93.797	0.01431
	2.56	**0.0317**	0.9221	85.027	0.05140
	6.25	**0.0414**	0.9706	94.801	0.04762
	400	**0.2853**	0.9681	93.877	0.03018
Methoxybenzene	0.256	**0.0094**	0.9537	90.956	0.01864
	2.56	**0.0411**	0.9726	94.882	0.02659
	6.25	**0.0912**	0.9656	93.997	0.02575
	400	**0.1900**	0.9505	90.418	0.05919
Hexan-1-ol	0.256	**0.0639**	0.9790	95.852	0.00991
	2.56	**0.0689**	0.9712	94.791	0.02348
	6.25	**0.0638**	0.9683	93.918	0.01927
	400	**0.5292**	0.9679	93.874	0.01956
cis-Hex-3-en-1-ol	0.256	**0.0519**	0.9616	92.461	0.01810
	2.56	**0.0721**	0.9668	93.889	0.01992
	6.25	**0.0754**	0.9999	99.999	0.19901
	400	**0.3774**	0.9621	93.357	0.05625
trans-Hex-2-en-1-ol	0.256	**0.0348**	0.9575	91.682	0.04388
	2.56	**0.0710**	0.9698	93.969	0.01981
	6.25	**0.0789**	0.9729	94.816	0.02480
	400	**0.3495**	0.9957	99.655	0.00842
2-Ethyl-hexan-1-ol	0.256	**0.0262**	0.9736	94.797	0.02069
	2.56	**0.0399**	0.9821	96.613	0.00227
	6.25	**0.0415**	0.9973	99.677	0.00445
	400	**0.2235**	0.9912	99.204	0.00640
trans,trans-Non-2,4-dienal	0.256	**0.0497**	0.9338	87.206	0.02590
	2.56	**0.0270**	0.9535	90.671	0.01638
trans,trans-Dec-2,4-dienal	0.256	**0.0814**	0.9596	91.727	0.04991
	2.56	**0.0354**	0.9582	91.699	0.05290
	6.25	**0.0377**	0.9758	94.817	0.02538
	400	**0.0682**	0.9649	93.669	0.05166

centrations found in olive oils. Their diversified chemical nature and different odorific notes [6] determined their choice. All of these compounds were previously detected in olive oil [7–10]. Table 1 presents the compounds used in this study and it also indicates the concentrations which have been previously measured in olive oil samples and the respective odour perceptions [6]. The analytes chosen intend to represent the broad chemical functionalities of the compounds present in olive oils. An internal standard was used in order to control the retention time.

Prior to the analyses, a temperature study was performed for a time periods from 1 min to 120 min in order to establish the optimal work temperature of the extraction procedure [11]. Three temperatures were studied: 25 °C, 37 °C and 40 °C. At 37 °C and

40 °C the largest amount of compounds was extracted with both fibres (results not shown) [11]. Another concern was to choose a temperature as close as possible that at which the human olfative systems perceives volatile emissions on one hand, and on the other hand to avoid compound degradation that might produce unwanted artefacts. For these reasons 37 °C was chosen as the sampling temperature.

The standard compounds were extracted at six or seven different periods of time and the results of each area *vs.* extraction time were determined. As an example, the absorption curves for 2-methylbutan-1-ol for the concentrations 0.256 µL/kg, 2.56 µL/kg, 6.25 µL/kg and 400 µL/kg are shown in Fig. 1. A sigmoidal-shape curve can be observed which does not depend on the initial concentration, the nature of the coating fibres or the mathematical model

Table 3
Parameter a_h values calculated according to Eq. (1) for selected compounds in PDMS at 37 °C using different initial concentrations

Compound	C_0 (μL/kg)	Parameter, a_h (estimated)	Correlation coefficient	Explained variance (%)	Final loss
PDMS Eq. (1) model: $n/n^\infty = 1 - \exp(-a_h t)$					
2-Ethylfuran	0.256	**0.3127**	0.9981	99.778	0.00501
	2.56	**0.0337**	0.9698	94.051	0.02642
Pent-3-one	0.256	**0.0427**	0.9912	99.101	0.00958
	2.56	**0.0411**	0.9833	96.687	0.00184
Pent-1-en-3-one	0.256	**0.0376**	0.9823	96.489	0.01829
	2.56	**0.2242**	0.9962	99.607	0.00221
Hexanal	0.256	**0.0857**	0.9841	96.915	0.00231
	2.56	**0.0835**	0.9944	99.366	0.00992
4-Methyl-pent-3-en-2-one	0.256	**0.0245**	0.9833	96.687	0.00180
	2.56	**0.2629**	0.9951	99.566	0.00734
	6.25	**0.9898**	0.9764	94.856	0.02873
	400	**0.5240**	0.9993	99.877	0.00157
2-Methylbutan-1-ol	0.256	**0.1886**	0.9983	99.772	0.00441
	2.56	**0.2419**	0.9961	99.714	0.00710
	6.25	**0.7468**	0.9997	99.897	0.00122
	400	**0.7667**	0.9999	99.999	0.01144
Methoxybenzene	0.256	**0.0315**	0.9861	96.799	0.00312
	2.56	**0.2799**	0.9945	99.423	0.00980
	6.25	**0.3732**	0.9994	99.818	0.00411
	400	**0.3483**	0.9798	94.901	0.02391
Hexan-1-ol	0.256	**0.0289**	0.9891	96.988	0.00673
	2.56	**0.3106**	0.9559	91.667	0.04535
	6.25	**0.7631**	0.9845	96.918	0.00522
	400	**0.7316**	0.9584	91.701	0.03990
cis-Hex-3-en-1-ol	0.256	**0.0260**	0.9978	99.267	0.00371
	2.56	**0.5509**	0.9999	99.999	0.05426
	6.25	**0.9401**	0.9992	99.879	0.00248
	400	**0.5509**	0.9751	94.841	0.02866
trans-Hex-2-en-1-ol	0.256	**0.0322**	0.9833	96.855	0.00719
	2.56	**0.9185**	0.9989	99.998	0.00422
	6.25	**0.9193**	0.9996	99.879	0.00310
	400	**0.7284**	0.9581	91.655	0.04901
2-Ethyl-hexan-1-ol	0.256	**0.0971**	0.9959	99.864	0.00371
	2.56	**0.3625**	0.9999	99.999	0.06117
	6.25	**0.3906**	0.9776	94.966	0.01136
	400	**0.4728**	0.9859	96.997	0.00281
trans,trans-Non-2,4-dienal	0.256	**0.0647**	0.9590	91.675	0.04547
	2.56	**0.3603**	0.9999	99.999	0.00131
trans,trans-Dec-2,4-dienal	0.256	**0.0542**	0.9813	96.289	0.01512
	2.56	**0.1133**	0.9966	99.274	0.00282
	6.25	**0.4030**	0.9755	94.899	0.02711
	400	**0.2586**	0.9991	99.884	0.00109

applied. The adjusted curves according to Eqs. (1) and (2) of the model of Ai [4] are shown in the graphs of Fig. 1, for 2-methylbutan-1-ol for both fibres at the concentrations studied. Here the points are raw experimental data and the lines represent the result of the application of the two equations to the experimental data.

The parameters a_h from Eq. (1) and α, c, β, and c_1 from Eq. (2) for all the compounds studied, in PDMS and PA coating fibres, are obtained through exponential regression. Tables 2 and 3 show the values for the a_h parameter, correlation coefficient, explained variance and the loss function for the curves fitted with Eq. (1). The parameters of Eq. (2), α, c, β, and c_1 are listed in Tables 4 and 5, as well as the correlation coefficients, explained variance and the loss function for all fitted curves.

For the selected compounds, the experimental data appears to fit poorly, as expected, to the theoretical model given by Eq. (1).

All the curves could however be satisfactorily described by Eq. (2) and confirm the relevance of the initial period of extraction for the absorption of the olive oil volatiles mainly in PA fibre. Similar results were reported previously by Matich et al. [12] who observed that a two-exponential equation, rather a one-exponential equation, described the experimental data for apple volatiles extracted by SPME.

The values for the a_h parameter for the four different initial concentrations studied are slightly dependent on the initial concentration, as expected [13], especially for the PA fibre.

In Fig. 1 it can be easily perceived how fast the partition equilibrium (between the headspace/polymer interfaces) can be reached,

Table 4
Parameters α, c, β, c_1 values calculated according to Eq. (2) for selected compounds in PA fibre at 37 °C using different initial

Compound	C_0 (μL/kg)	Estimated parameters				Correlation coefficient	Explained variance (%)	Final loss
		α	c	β	c_1			
PA Eq. (2) model: $n/n^\infty = \alpha[1 - \exp(-ct)] + \beta[1 - \exp(-c_1 t)]$								
2-Ethylfuran	0.256	0.8998	0.0085	0.5753	0.4331	0.9996	99.95	0.00092
	2.56	0.5346	0.0894	0.5346	0.0894	0.9948	99.835	0.00441
Pent-3-one	0.256	0.6162	0.0232	0.6163	0.0232	0.9473	89.745	0.06236
	2.56	0.8777	0.0180	0.4186	0.9755	0.9987	97.861	0.00111
Pent-1-en-3-one	0.256	0.9766	0.0102	0.8245	0.0100	0.9913	99.114	0.00779
	2.56	0.8133	0.0988	0.9798	0.0054	0.9999	99.997	0.00011
Hexanal	0.256	0.6407	0.9699	0.9778	0.0052	0.9733	95.644	0.02711
	2.56	0.7769	0.0953	0.8766	0.0091	0.9998	99.960	0.00014
4-Methyl-pent-3-en-2-one	0.256	0.9888	0.0091	0.4657	0.9589	0.9981	99.650	0.00208
	2.56	0.6044	0.0237	0.6044	0.0237	0.9857	97.168	0.01673
	6.25	0.6573	0.0332	0.37822	0.2617	0.97509	95.081	0.03474
	400	0.7798	0.0081	0.8712	0.3866	0.9878	97.921	0.02067
2-Methylbutan-1-ol	0.256	0.9068	0.0401	0.2331	0.9918	0.9988	99.630	0.00148
	2.56	0.5297	0.0396	0.5297	0.0396	0.9693	93.944	0.02704
	6.25	0.2437	0.8876	0.9552	0.0476	0.9982	99.236	0.00283
	400	0.5064	0.2760	0.5064	0.2760	0.9689	93.883	0.02942
Methoxybenzene	0.256	0.3101	0.7898	0.7748	0.0122	0.9997	99.944	0.00023
	2.56	0.5842	0.0307	0.5842	0.0307	0.9439	89.094	0.06708
	6.25	0.4158	0.9661	0.8803	0.0730	0.9794	95.918	0.03102
	400	0.4758	0.2163	0.4758	0.2163	0.9932	98.653	0.00604
Hexan-1-ol	0.256	0.4623	0.0748	0.4623	0.0748	0.9606	92.284	0.01966
	2.56	0.3484	0.5082	0.8578	0.0296	0.9995	99.907	0.00033
	6.25	0.2716	0.9908	0.8527	0.0677	0.9962	99.559	0.00142
	400	0.4922	0.5519	0.4922	0.5519	0.9955	99.738	0.00221
cis-Hex-3-en-1-ol	0.256	0.8938	0.0289	0.2878	0.7679	0.9913	98.266	0.00614
	2.56	0.2259	0.9986	0.8984	0.0311	0.9766	94.078	0.01948
	6.25	0.5018	0.0747	0.5018	0.0747	0.8730	76.216	0.19902
	400	0.5020	0.3736	0.5020	0.3736	0.9317	86.800	0.05527
trans-Hex-2-en-1-ol	0.256	0.5822	0.0257	0.5822	0.0257	0.9700	94.089	0.03119
	2.56	0.1267	0.7637	0.9931	0.0310	0.9709	94.256	0.02623
	6.25	0.5034	0.0776	0.5034	0.0776	0.9001	81.002	0.16214
	400	0.4911	0.3662	0.4911	0.3662	0.9135	83.445	0.06991
2-Ethyl-hexan-1-ol	0.256	0.6386	0.0195	0.6389	0.0195	0.9736	94.788	0.03154
	2.56	0.8587	0.5337	0.8779	0.0034	0.9997	99.913	0.00023
	6.25	0.1956	0.9898	0.8761	0.0397	0.9475	89.775	0.06889
	400	0.4985	0.2256	0.4985	0.2256	0.9328	87.001	0.07414
trans,trans-Non-2,4-dienal	0.256	0.7998	0.0209	0.2311	0.8667	0.9953	98.45	0.00563
	2.56	0.3798	0.0244	0.3798	0.0244	0.9994	99.880	0.00032
trans,trans-Dec-2,4-dienal	0.256	0.5858	0.0129	0.6200	0.2060	0.9621	92.566	0.01750
	2.56	0.6417	0.0220	0.6417	0.0220	0.9847	96.954	0.01949
	6.25	0.6997	0.0344	0.6997	0.0344	0.9961	98.54	0.00314
	400	0.7733	0.0586	0.1872	0.3585	0.9736	94.794	0.03901

for a given compound. In this figure, the ordinate represents the fibre uptake normalized to the equilibrium value. Compared to olive oil headspace/PA interface partition, the parameter a_h at the olive oil headspace/PDMS interface is higher, which means that in the PDMS fibre the partition equilibrium is reached sooner. This is in agreement with the fact that on the PA fibre diffusion coefficients are lower in comparison with the PDMS fibre [14]. Longer extraction times with the PA coating fibre for volatile analytes in the headspace is an expected result. The selection of the fibre that offers the best reproducible results for quantitative purposes, should depend not only on the amount extracted, but also on some other physical/chemical properties such as mass transfer coefficients, equilibrium constants, among others, in order to achieve a linear range behaviour in a non-equilibrium state [4,15]. This work demonstrates that PDMS fibres present for all the compounds studied, lower equilibration times when compared to PA fibres, although PA fibres present a better absorption capacity for compounds with a wide range of functionalities. The initial concentration is crucial for the time profile and the achievement of equilibrium in both fibres. Generally the a_h parameter is higher when the initial concentration is higher, indicating that equilibrium is reached quicker in that situation for both fibres. Since Eq. (1) does not fit as well to the experimental data when compared to Eq. (2), one cannot have any information about the proportionality between the initial concentration and amount extracted. So the biexponential equation (2) was applied to the data.

Table 5
Parameters α, c, β, c_1 values calculated according to Eq. (2) for selected compounds in PDMS fibre at 37 °C using different initial concentrations

Compound	C_0 (μL/kg)	Estimated parameters				Correlation coefficient	Explained variance (%)	Final loss
		α	c	β	c_1			
PDMS Eq. (2) model: $n/n^\infty = \alpha[1 - \exp(-ct)] + \beta[1 - \exp(-c_1 t)]$								
2-Ethylfuran	0.256	**0.6107**	**0.3265**	**0.6107**	**0.3265**	0.9520	91.752	0.00567
	2.56	**0.4215**	**0.7108**	**0.4215**	**0.7108**	0.9894	97.883	0.00941
Pent-3-one	0.256	**0.8939**	**0.0078**	**0.5624**	**0.9778**	0.9654	93.204	0.01904
	2.56	**0.5384**	**0.0353**	**0.5384**	**0.0353**	0.9879	97.597	0.01333
Pent-1-en-3-one	0.256	**0.5780**	**0.0279**	**0.5780**	**0.0279**	0.9950	99.003	0.00523
	2.56	**0.4510**	**0.3209**	**0.4510**	**0.3209**	0.9677	93.312	0.02235
Hexanal	0.256	**0.5975**	**0.0239**	**0.5092**	**0.3247**	0.9992	99.839	0.00032
	2.56	**0.4759**	**0.6125**	**0.5894**	**0.0246**	0.9999	99.991	0.00001
4-Methyl-pent-3-en-2-one	0.256	**0.3514**	**0.9886**	**0.9599**	**0.0011**	0.8919	79.558	0.07828
	2.56	**0.4410**	**0.3978**	**0.4410**	**0.3978**	0.9816	97.427	0.01521
	6.25	**0.6602**	**0.9898**	**0.6602**	**0.9898**	0.9368	87.762	0.00970
	400	**0.4958**	**0.5474**	**0.4958**	**0.5474**	0.7958	63.324	0.00191
2-Methylbutan-1-ol	0.256	**0.4486**	**0.2906**	**0.4486**	**0.2906**	0.9861	97.548	0.01414
	2.56	**0.9998**	**0.0051**	**0.7756**	**0.5926**	0.9916	98.088	0.00619
	6.25	**0.4651**	**0.8052**	**0.4651**	**0.8052**	0.8776	77.019	0.04126
	400	**0.4929**	**0.9798**	**0.4929**	**0.9798**	0.9265	85.836	0.00101
Methoxybenzene	0.256	**0.6215**	**0.9869**	**0.9994**	**0.0013**	0.9793	95.907	0.01221
	2.56	**0.4605**	**0.3680**	**0.4605**	**0.3680**	0.9877	97.568	0.00977
	6.25	**0.4930**	**0.3893**	**0.4930**	**0.3894**	0.9216	84.931	0.05279
	400	**0.4825**	**0.3943**	**0.4825**	**0.3943**	0.9868	97.614	0.01247
Hexan-1-ol	0.256	**0.9899**	**0.0021**	**0.3315**	**0.92357**	0.9756	95.046	0.03832
	2.56	**0.4984**	**0.3250**	**0.4984**	**0.3250**	0.9884	97.721	0.00872
	6.25	**0.5294**	**0.6566**	**0.5294**	**0.6566**	0.9155	83.819	0.04517
	400	**0.5813**	**0.9788**	**0.5813**	**0.9788**	0.7363	54.212	0.02446
cis-Hex-3-en-1-ol	0.256	**0.8898**	**0.0024**	**0.4353**	**0.7689**	0.9231	85.664	0.06423
	2.56	**0.5245**	**0.4418**	**0.5245**	**0.4418**	0.9927	98.058	0.00781
	6.25	**0.4945**	**0.9355**	**0.4945**	**0.9355**	0.9236	85.311	0.02124
	400	**0.4779**	**0.7546**	**0.4779**	**0.7546**	0.9832	97.578	0.01247
trans-Hex-2-en-1-ol	0.256	**0.9899**	**0.0032**	**0.3973**	**0.3177**	0.9616	92.461	0.02358
	2.56	**0.5734**	**0.3859**	**0.5734**	**0.3859**	0.9931	98.107	0.00577
	6.25	**0.4736**	**0.9656**	**0.4736**	**0.9656**	0.8242	67.924	0.04853
	400	**0.4904**	**0.7967**	**0.4904**	**0.7967**	0.9865	97.547	0.01351
2-Ethyl-hexan-1-ol	0.256	**0.4784**	**0.1109**	**0.4784**	**0.1109**	0.9446	89.233	0.01924
	2.56	**0.5413**	**0.2835**	**0.5413**	**0.2835**	0.9922	98.098	0.00712
	6.25	**0.4818**	**0.4189**	**0.4818**	**0.4189**	0.95464	91.133	0.03867
	400	**0.5934**	**0.4728**	**0.5934**	**0.4728**	0.9921	98.203	0.00439
trans,trans-Non-2,4-dienal	0.256	**0.6485**	**0.3395**	**0.8898**	**0.0041**	0.9668	92.742	0.01942
	2.56	**0.5277**	**0.3203**	**0.5277**	**0.3203**	0.9918	98.179	0.00455
trans,trans-Dec-2,4-dienal	0.256	**0.5156**	**0.0508**	**0.5156**	**0.0508**	0.9864	97.311	0.01391
	2.56	**0.4643**	**0.1482**	**0.4643**	**0.1482**	0.9878	97.598	0.01033
	6.25	**0.5219**	**0.3641**	**0.5219**	**0.3641**	0.9557	91.329	0.04179
	400	**0.4911**	**0.3165**	**0.4911**	**0.3165**	0.9869	97.687	0.00733

We found that absorption of olive oil volatiles onto PDMS and PA SPME fibres follow, in a good approximation, the general kinetic equation (2), especially in the case of the PA fibre. In the PDMS fibre the experimental data does not fit well to Eq. (2), suggesting that linearity between initial concentration and extracted amount is not achieved. Thus relative quantification is not possible with the PDMS fibre in a non-equilibrium state. With the PA fibre, a good fit was achieved with Eq. (2), which indicates that there is a linear relationship between the amount of analyte extracted (n), from olive oil headspace, and its initial concentration in the sample matrix (C_0) as a function of sampling time (t). This equation considers the equilibrium disturbance due to fibre introduction into the headspace of the sample, the equilibrium reposition and the variation of the compound concentrations in the sample headspace, which occurs between the disturbance and reposition time periods. For compounds that present c values equal to c_1 values (presenting both adjustment parameters in Eq. (2), which measure how fast the equilibrium is reached in HS-SPME) ($c - c_1$) = 0, meaning that the equilibrium is not disturbed, or the equilibrium reposition takes place immediately. For these compounds it is also verified that for α and β, which measure the variation of the concentration of a particular compound presented in the headspace, due to the equilibrium disturbance, $|\alpha| = |\beta|$. Hence the $a_h = 0$ and the parameter c in Eq. (2) is equal to a_h in Eq. (1).

The PA fibre allows, for the compounds studied, a successful relative quantification at a non-equilibrium state in non-aqueous media. Consequently, in non-aqueous media studies must be conducted to determine which compounds have similar behaviour and only those compounds can be quantified in a non-equilibrium situation with the PA fibre. For all the others, and for quantitative purposes, equilibrium should be reached.

4. Conclusion

The HS-SPME sample preparation technique coupled with GC analysis is well suited for qualitative and relative quantitative analysis of aroma compounds in olive oil. The amount (n) of analyte extracted, from olive oil headspace, might have a linear proportional relation with its initial concentration in the sample matrix (C_0) as a function of sampling time (t), which can be an advantage in the case of routine use. When a given compound in a given sample matrix exhibits this property, quantification can be achieved at non-equilibrium state, which reduces analysis time considerably. In all the other situations equilibrium should be reached for quantitative purposes.

Although it was observed that apolar PDMS-coated fibre is capable of extracting faster the olive oil aroma compounds for routine purposes in comparison with the PA fibre, since equilibrium is reached more quickly, the experimental data obtained with the PDMS fibre did not adjust to both mathematical models used. This indicates that linear proportionality between the initial concentration and amount extracted was not achieved, which does not allow relative quantification in non-equilibrium situations. On the other hand the PA fibre was found to be the adequate fibre to perform relative quantification of aroma compounds in a non-equilibrium state in a non-aqueous sample like olive oil.

References

[1] J. Powers, Current practices and application of descriptive methods, in: J. Piggott (Ed.), Sensory Analysis of Foods, Elsevier Applied Science Publishers, Essex (England), 1984, p. 195.
[2] Z. Zhang, M. Yang, J. Pawliszyn, Anal. Chem. 66 (1994) 844A.
[3] Z. Zhang, J. Pawliszyn, Anal. Chem. 65 (1993) 1843.
[4] J. Ai, Anal. Chem. 69 (1997) 1230.
[5] J. Ai, Quantitation by SPME before reaching a partition equilibrium, in: J. Pawliszyn (Ed.), Applications of Solid Phase Microextraction, RSC, Hertfordshire, UK, 1999, pp. 22–37.
[6] Flavors & Fragrances, Aldrich's Catalog, International Edition, 2000.
[7] S. Vichi, L. Pizzale, L. Conte, S. Buxaderas, E. López-Tamames, J. Agric. Food Chem. 51 (2003) 6572.
[8] S. Vichi, A. Castellote, L. Pizzale, L. Conte, S. Buxaderas, E. López-Tamames, J. Chromatogr. A 983 (2003) 19.
[9] J. Reiners, W. Grosch, J. Agric. Food Chem. 46 (1998) 2754.
[10] M. Morales, R. Aparício, J. Rios, J. Chromatogr. A 668 (1994) 455.
[11] L. Ribeiro, Caracterização do aroma de azeites virgens com atributos positivos e negativos, Ph.D. Thesis Presented to Universidade Nova de Lisboa, Faculdade de Ciências e Tecnologia, Lisboa, Portugal, 2005.
[12] A. Matich, D. Rowan, N. Banks, Anal. Chem. 68 (1996) 4114.
[13] J. Pawliszyn, Solid Phase Microextraction, Theory and Practice, Wiley-VCH, New York, 1997.
[14] L. Ribeiro, A. Costa Freitas, M.D.R. Gomes da Silva, Headspace solid phase microextraction for the characterization of volatile compounds in olive oils, in: Proceedings of the 25th International Symposium on Capillary Chromatography, Riva del Garda, Italy, May, 2002.
[15] D. Roberts, P. Pollien, C. Milo, J. Agric. Food Chem. 48 (2000) 2430.

Comparison of two stationary phases for the separation of five selected polyphenols

A. Rodríguez-Bernaldo de Quirós *, M.A. Lage-Yusty, J. López-Hernández

Analytical Chemistry, Nutrition and Bromatology Department, Pharmacy Faculty, Campus Sur s/n, University of Santiago de Compostela, 15782 Santiago de Compostela (La Coruña), Spain

ABSTRACT

In this study, a conventional TEKNOKROMA, Tr-015605 TRACER EXTRASIL ODS2 ($25\,\mathrm{cm} \times 0.4\,\mathrm{cm}$, i.d. $5\,\mu\mathrm{m}$) column and a new stationary phase TEKNOKROMA, Tr-010065 Mediterranea sea$_{18}$ ($15\,\mathrm{cm} \times 0.4\,\mathrm{cm}$, i.d. $3\,\mu\mathrm{m}$) were compared for the separation of five phenolic compounds.

Sensitivity, performance characteristics, analysis time and method validation were reported for both columns. A better sensitivity and performance were achieved with the novel chromatographic support. In addition the total analysis time was significantly reduced.

The method was applied to the determination of the selected polyphenols in commercial available white wines. LC–MS was used as a confirmatory technique.

© 2008 Elsevier B.V. All rights reserved.

1. Introduction

Polyphenols are important compounds commonly distributed in food plants. In the past years the analysis of these substances has grown due to their beneficial effects on health. Different biological activities such as anti-inflammatory, antimicrobial and cardioprotective which have been attributed to their antioxidant properties have been widely described in the bibliography [1–4].

The technique most commonly used to analyse phenolic compounds is liquid chromatography with diode array detection (DAD) [5–11]; more recently liquid chromatography coupled with mass spectrometry has become an excellent analytical tool to identify and elucidate the structure of the polyphenols and their metabolites [12–14].

In developing a chromatographic method the selection of the stationary phase is a crucial step to achieve a suitable resolution. Latest advances have been addressed to the development of new packings with the aim to obtain chromatographic supports that offer a high level of efficiency and reproducibility [15].

The aim of this study was to compare a conventional TEKNOKROMA, Tr-015605 TRACER EXTRASIL ODS2 ($25\,\mathrm{cm} \times 0.4\,\mathrm{cm}$, i.d. $5\,\mu\mathrm{m}$) column with a new stationary phase, TEKNOKROMA, Tr-010065 Mediterranea sea$_{18}$ ($15\,\mathrm{cm} \times 0.4\,\mathrm{cm}$, i.d. $3\,\mu\mathrm{m}$) for the determination of five selected phenolic compounds present in wines, including, catechin, epicatechin, *trans*-resveratrol, rutin and quercetin.

Sensitivity, performance characteristics, analysis time and method validation were reported for both columns. The proposed method was applied to analyse commercial available white wines.

LC–MS was used as a confirmatory technique.

2. Experimental

2.1. Chemicals and phenolic standard solutions

Acetonitrile, methanol and glacial acetic were provided by Merck (KgaA, Darmstadt, Germany). Water used for all solutions was obtained from a Milli-Q water purification system (Millipore) (Bedford, MA, USA). Standards of catechin, epicatechin, rutin and *trans*-resveratrol were purchased from Sigma–Aldrich (St. Louis, MO, USA) and quercetin was obtained from Fluka BioChemika (Steinheim, Germany).

Stock standard solutions of phenolic compounds were prepared in methanol with concentrations in the range of 0.5–$50\,\mathrm{mg\,L^{-1}}$ and stored at $4\,^\circ\mathrm{C}$ in the dark. Working solutions were prepared by dilution.

* Corresponding author. Tel.: +34 981 598450; fax: +34 981 594912.
E-mail address: anarbq@usc.es (A. Rodríguez-Bernaldo de Quirós).

Table 1
Specifications of the stationary phases

Specifications	TEKNOKROMA ODS2 (25 cm × 0.4 cm i.d., 5 μm)	Mediterranea$_{18}$ (15 cm × 0.4 cm i.d., 3 μm)
Particle size (μm)	5	3
Total carbon content (%)	12	17
Surface area (m^2/g)	200	450
Average pore diameter (Å)	80	80
pH range	2–7	1–12

Table 2
Comparison of system suitability parameters for both stationary phases

	TEKNOKROMA ODS2 (25 cm × 0.4 cm i.d., 5 μm)			Mediterranea$_{18}$ (15 cm × 0.4 cm i.d., 3 μm)		
Analyte	Rt (min)	Width[a] (min)	N[b]	Rt (min)	Width[a] (min)	N[b]
Catechin	6.79 ± 0.2	0.31 ± 0.03	2752	4.04 ± 0.07	0.13 ± 0.02	5986
Epicatechin	9.87 ± 0.2	0.25 ± 0.02	8669	4.90 ± 0.06	0.10 ± 0.005	13205
Rutin	14.79 ± 0.2	0.16 ± 0.002	48781	6.40 ± 0.03	0.08 ± 0.002	31762
Trans-resveratrol	18.01 ± 0.3	0.19 ± 0.002	46284	10.67 ± 0.05	0.11 ± 0.002	49972
Quercetin	20.91 ± 0.3	0.35 ± 0.01	19780	12.51 ± 0.07	0.13 ± 0.002	47688

[a] Peak-width (mean of ten injections).

[b] *N*: number of theoretical plates (mean of ten injections).

Table 3
Parameters of linearity of phenolic compounds studied

Analyte	Range of linearity (mg/L)	TEKNOKROMA ODS2 (25 cm × 0.4 cm i.d., 5 μm)				Mediterranea$_{18}$ (15 cm × 0.4 cm i.d., 3 μm)			
		Slope (±S.D.)	Origin oridinate (±S.D.)	R^2	LOD (μg/mL)	Slope (±S.D.)	Origin oridinate (±S.D.)	R^2	LOD (μg/mL)
Catechin	0.5–50	15.5 ± 0.02	0.18 ± 0.4	0.999996	0.10	15.2 ± 0.008	(−0.03) ± 0.2	0.9999991	0.004
Epicatechin	0.5–50	14.6 ± 0.06	(−1.9) ± 1.4	0.99994	0.10	12.9 ± 0.003	(−0.05) ± 0.07	0.9999998	0.01
Rutin	0.5–50	18.4 ± 0.1	(−3.2) ± 2.6	0.9998	0.03	13.2 ± 0.006	0.3 ± 0.14	0.9999993	0.004
Trans-resveratrol	0.5–50	78.5 ± 0.2	(−5.1) ± 3.8	0.99998	0.02	54.2 ± 0.06	2.7 ± 1.4	0.999996	0.0009
Quercetin	0.5–50	15.2 ± 0.03	1 ± 0.6	0.999990	0.20	23.2 ± 0.03	1.3 ± 0.7	0.999995	0.004

2.2. Samples

Commercial available white wines, (Albariño variety) from Galicia (N.W Spain) were purchased in a local supermarket. The samples were filtered through a 50 μm PTFE membrane filter (Advantec MFS, INC, CA, USA) and directly injected into the chromatograph without previous treatment. The analyses were performed in triplicate.

2.3. Instrumentation

2.3.1. HPLC-UV

HPLC-analysis was performed on a HP1100 system (Hewlett-Packard, CA, USA) equipped with an HP1100 quaternary pump, an HP1100 degassing device, a 20 μL injection loop (Rheodyne, Cotati, CA, USA) an HP1100 UV-detector and HP ChemStation chromatography software (Hewlett Packard, Wallbronn, Germany).

Table 4
Repeatabilites within day and between days (% R.S.D. (*n* = 6)) at three concentrations levels obtained for both stationary phases

Analyte	Concentration (ppm)	TEKNOKROMA ODS2 (25 cm × 0.4 cm i.d., 5 μm)		Mediterranea$_{18}$ (15 cm × 0.4 cm i.d., 3 μm)	
		Intra day %R.S.D. (*n* = 6)	Inter day %R.S.D. (*n* = 6)	Intra day %R.S.D. (*n* = 6)	Inter day %R.S.D. (*n* = 6)
Catechin	0.5	0.9	2	0.5	0.6
	1	1	1	0.7	0.5
	5	0.5	0.9	0.1	0.1
Epicatechin	0.5	2	2	0.9	1
	1	1	1	0.3	0.5
	5	1	2	0.1	0.2
Rutin	0.5	1	1	1	1
	1	0.8	0.9	0.7	0.9
	5	0.6	2	0.1	0.2
Trans-resveratrol	0.5	0.5	0.6	0.4	0.6
	1	0.2	0.3	0.1	0.2
	5	0.3	0.4	0.1	0.1
Quercetin	0.5	1	1	0.4	0.5
	1	0.7	1	0.2	0.3
	5	0.8	1	0.1	0.1

Table 5
Overview of the LC–MS methods applied to the analysis of phenolic compounds in wine samples

Sample	Analyte	Mass spectrometry		Stationary phase	Reference
		MS interface	Ionization mode		
Muscatel sweet wines	Phenolic acids, stilbenes, flavanols	APCI/ESI	Negative/positive	LiChrospher C18 (5 μm, 250 mm × 4 mm i.d.)	[5]
Sicilian red wines	*Trans*-resveratrol, quercetin	ESI	Negative	Luna 18 (5 μm, 250 mm × 2.0 mm, i.d. Phenomenex)	[10]
Red wines from Navarra (Spain)	Nonanthocyanin, phenolic compounds	ESI	Negative	Nova-Pak C18 (4 μm, 300 mm × 3.9 mm. i.d. Millipore)	[22,24]
Red wines from France and South Africa	Phenolic compounds	API-ES	Negative	C18 (5 μm, 250 mm × 4.6 mm, i.d.) (Alltech, Belgium)	[23]
Wines	Phenolic compounds	APCI, API-ES	Positive/negative	Spherisorb ODS2 (3 μm, 250 mm × 4.6 mm, i.d.)	[25]
Red wines	Non-colored, phenolic compounds	ESI-MS/MS	Negative	Zorbax SB-C18 (5 μm, 250 mm × 4.6 mm, i.d.)	[21]
Red and white wines from Italy	Phenolic compounds	API	Negative/positive	Nucleosil ODS (5 μm, 250 mm × 2.1 mm, i.d.)	[26]

2.3.2. HPLC-MS as a confirmatory technique

Liquid chromatography–mass spectrometry analysis was carried out on a 1100 Agilent chromatograph coupled to a Microtof-Bruker spectrometer equipped with an electrospray ionization (ESI) source. The ESI was operated in negative mode. The operating conditions for ESI were: nebulizer gas (N_2), 30 psi; dry gas (N_2) flow, 10 L min^{-1}; and dry gas temperature 325 °C.

2.4. Chromatographic conditions

The chromatographic separation was performed on the stationary phases; TEKNOKROMA, Tr-015605 TRACER EXTRASIL ODS2 (25 cm × 0.4 cm, i.d. 5 μm) and TEKNOKROMA, Tr-010065 Mediterranea sea$_{18}$ (15 cm × 0.4 cm, i.d. 3 μm). The mobile phase was constituted of (water–acetic acid, 99:1, v/v) as solvent A and (water–acetonitrile–acetic acid, 67:32:1, v/v/v) as solvent B.

It was necessary to adjust the gradient elution conditions in order to achieve a suitable separation with each column. With TRACER EXTRASIL ODS2 (25 cm × 0.4 cm, i.d. 5 μm) column; the gradient elution was as follows: 0 min (80%A + 20%B); 4 min (70%A + 30%B); 8 min (60%A + 40%B); 12 min (35%A + 65%B); 16 min (20%A + 80%B); 20 min (5%A + 95%B); 21.8 min (3%A + 97%B) and 25 min (100%B); and with Mediterranea sea$_{18}$ (15 cm × 0.4 cm, i.d.

3 μm) the gradient program employed was: 0 min (80%A + 20%B); 3 min (70%A + 30%B); 6 min (60%A + 40%B); 9 min (35%A + 65%B); 12 min (20%A + 80%B); 15 min (5%A + 95%B) and 18 min (100%B).

The flow rate was 1 mL min^{-1} and the injection volume was 20 μL. The UV detector was set at 280 nm.

2.5. Identification and quantification

The identification of the polyphenols was made by comparison of their retention times with those of pure standards and confirmed by liquid chromatography–mass spectrometry. Quantification was performed on the basis of linear calibration plots of peak area against concentration. Calibration lines were constructed based on five concentration levels of standard solutions within 0.5–50 mg L^{-1} range.

3. Results and discussion

3.1. Comparison of two columns

Parameters such as particle size, surface area and metal content play an important role in the performance chromatographic level. Mediterranea sea$_{18}$ (15 cm × 0.4 cm, i.d. 3 μm) stationary phase is based on perfectly spherical particles of ultra-pure silica with a
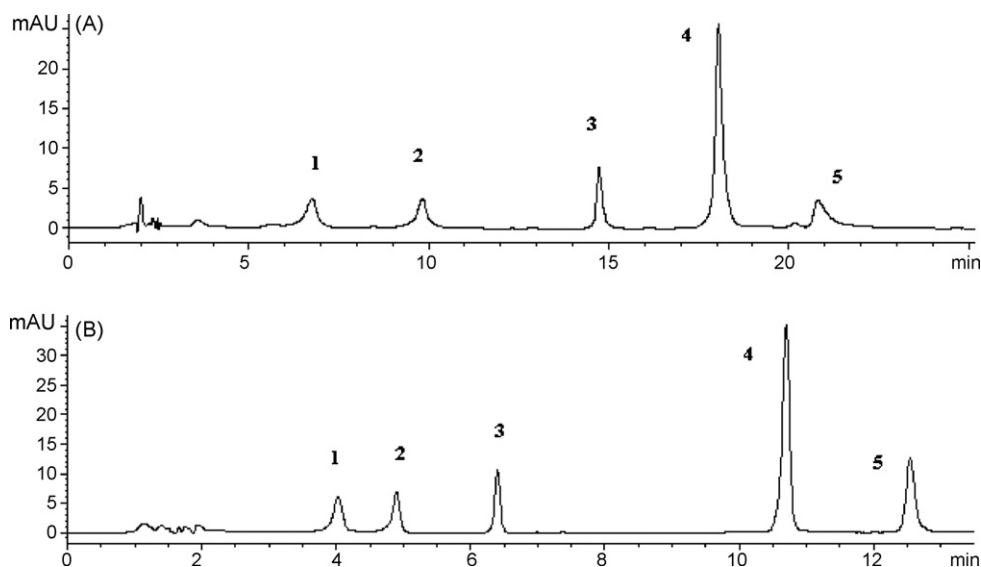

Fig. 1. Chromatogram of a standard solution performed on an ODS2 (A) and Mediterranea sea$_{18}$ (B) column respectively registered under the optimized chromatographic conditions with the HPLC-UV-Vis system. Peaks: (1) catechin; (2) epicatechin; (3) rutin; (4) *trans*-resveratrol; (5) quercetin.
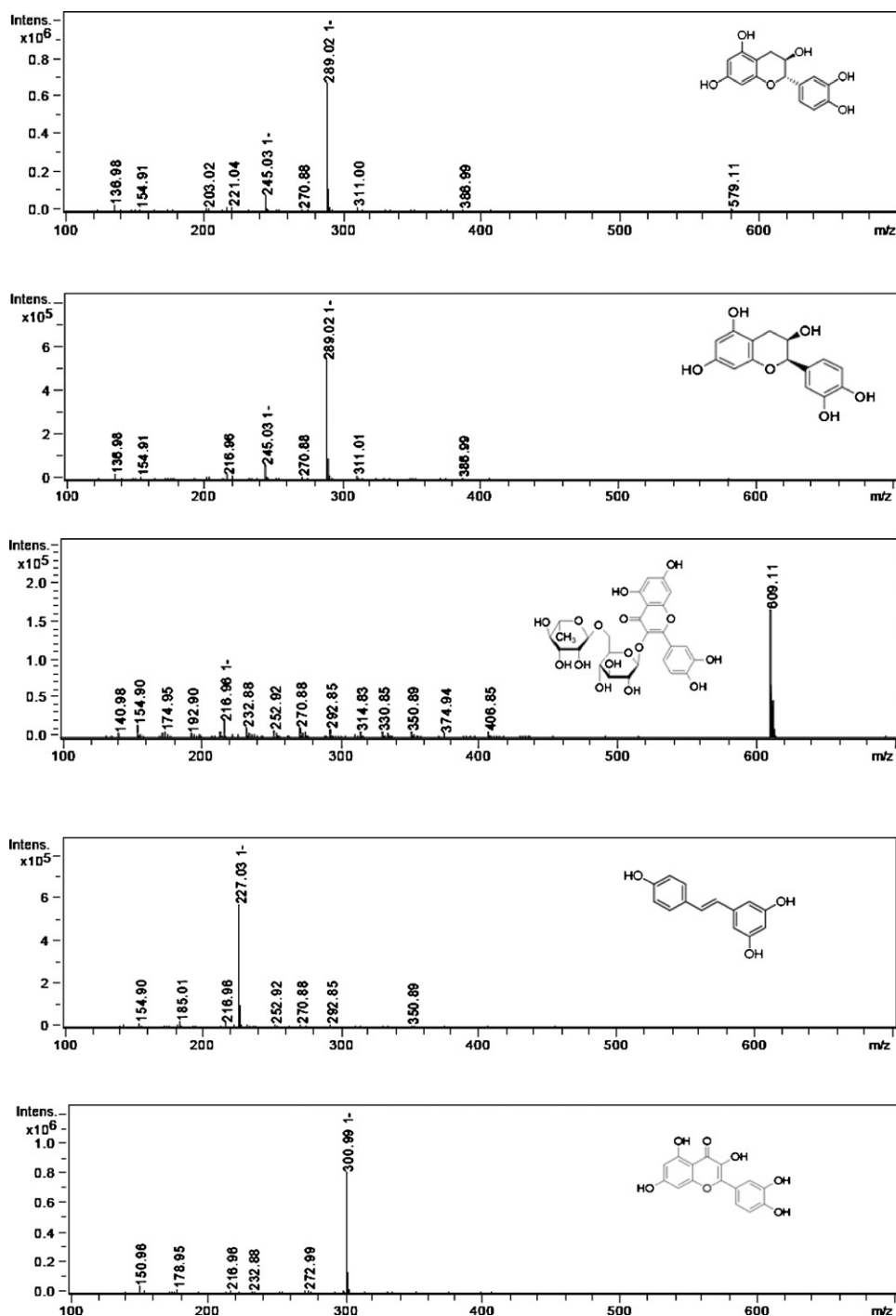
Fig. 2. Mass spectra of catechin, epicatechin, rutin, *trans*-resveratrol and quercetin obtained with ESI-MS in negative-ion mode.

very low metal content. The specifications of both columns are presented in Table 1.

In order to achieve a suitable separation with each column several changes in the gradient elution program were performed; the best chromatographic conditions are described in Section 2. Table 2 summarizes the performance characteristics of the two stationary phases. As can be inferred from the results presented in the table, with the Mediterranea sea$_{18}$ stationary phase the total analysis time is considerably reduced, and on the other hand the chromatographic resolution is significantly improved. Thus, the number of theoretical plates obtained with this column is higher than those

obtained with the conventional ODS2 column for all analytes except for rutin. The total analysis time is diminished almost two times with the novel stationary phase.

Fig. 1 shows chromatograms of a standard solution performed on a Mediterranea sea$_{18}$ and ODS2 column.

3.2. Method validation

The method was validated in terms of linearity, limits of detection, repeatabilities within day and between days and repro-

ducibility. The polyphenol stabilities were evaluated in a previous work [16].

The linearity of the method was evaluated by using a series of polyphenol standards of known concentrations. Calibration curves were constructed using five concentration levels and they were fitted to a linear equation. Each point of the calibration curve is the average of three peak-areas measurements. Parameters of linearity were presented in Table 3. The phenolic compounds studied showed a good linearity, determination coefficients were in all cases greater than 0.9998. Limits of detection (defined as signal three times the height of the noise level) calculated in accordance with American Chemical Society [17] are shown in Table 2. Using the Mediterranea sea$_{18}$ column a very high sensitivity was achieved.

The intra and inter day repeatabilities were determined by analysing six replicates of the standards at three different concentration levels, expressed as the percentage of R.S.D. (%R.S.D. ($n = 6$)), in the same day and in three separated days respectively (Table 4). The method showed good precision; in the case of the Mediterranea sea$_{18}$ column the repeatabilities within a day were lower than 1% except for rutin.

The reproducibility of the method, estimated as the relative standard deviation of six replicate injections (R.S.D. ($n = 6$)) from the same wine sample, was 3% for catechin, epicatechin and rutin and 4% for *trans*-resveratrol and quercetin.

3.3. LC–MS as a confirmatory technique and application to real samples

Identification of polyphenols was based on the comparison of the retention time with an external standard solution and confirmed by LC–MS. The chromatographic conditions used with LC–MS were the same employed with the LC–UV system, and the chromatographic support used was Mediterranea sea$_{18}$ (15 cm × 0.4 cm, i.d. 3 μm).

An overview of the LC–MS methods applied to the analysis of phenolic compounds in wine samples is given in Table 5. Although different MS interfaces, such as APCI and ESI have been used to analyse phenolic compounds, ESI in negative mode seems to be the most suitable tool since exhibit a higher sensitivity [18–23]. Therefore the analyses were performed using ESI source in negative mode. Negative ESI mass spectrum of catechin, epicatechin, rutin, *trans*-resveratrol and quercetin showing the deprotonated molecular ion [M−H]$^{-}$ of m/z 289, 289, 609, 227 and 301, respectively were obtained.

Typical mass spectrum obtained with negative-ion ESI of the polyphenols studied are presented in Fig. 2.

Finally, the method was applied to analyse commercial available white wines. The analyses were performed in triplicate. The mean values found, expressed as mg L^{-1}, were 9.07 ± 0.5; 14.47 ± 0.15; 1.9 ± 0.4; 0.37 ± 0.06; and 3.13 ± 0.15 for catechin, epicatechin, rutin, *trans*-resveratrol and quercetin, respectively. Epicatechin was the predominant compound among flavanols, the values obtained were higher than those described by Fernández-Pachón et al. [27] and by Castellari et al. [9] for Chardonnay, Albana, and Sauvignon varietal white wines. Regarding stilbenes, the concentrations of *trans*-resveratrol found were slightly higher than the values reported by Castellari et al. [9] and with respect to flavonols,

Woraratphoka et al. [28] have detected higher levels of rutin in Italian white wines.

4. Conclusion

In this study two stationary phases were compared for the determination of five selected polyphenols. The new column, Mediterranea sea$_{18}$ (15 cm × 0.4 cm, i.d. 3 μm), offers advantages over the conventional ODS2 stationary phase; the total analysis time is significantly reduced and the chromatographic performance is improved. In addition a very high sensitivity is achieved.

References

[1] J. Burns, P.T. Gardner, J. O'Neil, S. Crawford, I. Morecroft, D.B. McPhail, C. Lister, D. Matthews, M.R. MacLean, M.E.J. Lean, G.D. Duthie, A. Crozier, J. Agric. Food Chem. 48 (2000) 220.
[2] D.M. Golberg, A. Karumanchiri, G.J. Soleas, E. Tsang, Am. J. Enol. Vitic. 50 (1999) 185.
[3] K. Kwang-Seok, S. Ghim, Y. Seu, B. Song, J. Microbiol. Biotechnol. 9 (1999) 691.
[4] P. Bridle, C.F. Timberlake, Food Chem. 58 (1997) 109.
[5] M.N. Bravo, S. Silva, A.V. Coelho, L. Vilas Boas, M.R. Bronze, Anal. Chim. Acta 563 (2006) 84.
[6] A. Peña-Neira, T. Hernández, C. García-Vallejo, I. Estrella, J.A. Suarez, Eur. Food Res. Technol. 210 (2000) 445.
[7] S. Malovaná, F.J. García Montelongo, J.P. Pérez, M.A. Rodríguez-Delgado, Anal. Chim. Acta 428 (2001) 245.
[8] M. López, F. Martínez, C. Del Valle, C. Orte, C. Miró, J. Chromatogr. A 922 (2001) 359.
[9] M. Castellari, E. Sartini, A. Fabiani, G. Arfelli, A. Amati, J. Chromatogr. A 973 (2002) 221.
[10] M. Careri, C. Corradini, L. Elviri, I. Nicoletti, I. Zagnoni, J. Agric. Food. Chem. 51 (2003) 5226.
[11] M.A. Vian, V. Tomao, S. Gallet, P.O. Coulomb, J.M. Lacombe, J. Chromatogr. A 1085 (2005) 224.
[12] T. Puessa, J. Floren, P. Kuldkepp, A. Raal, J. Agric. Food Chem. 54 (2006) 7488.
[13] I. Nicoletti, A. De Rossi, G. Giovinazzo, D. Corradini, J. Agric. Food. Chem. 55 (2007) 3304.
[14] M.L. Mata Bilbao, C. Andrés-Lacueva, O. Jáuregui, R.M. Lamuela-Raventós, Food Chem. 101 (2007) 1742.
[15] Teknokroma Home Page http://www.teknokroma.es/mediterranea/.
[16] A. Rodríguez-Bernaldo de Quirós, J. López-Hernández, P. Ferraces-Casais, M.A. Lage-Yusty, J. Sep. Sci. 30 (2007) 1262.
[17] American Chemical Society (ACS), Subcommittee of Environmental Analytical Chemistry, Anal. Chem. 52 (1980) 2242.
[18] W. Jin, Y.F. Wang, R.L. Ge, H.M. Shi1, C.Q. Jia, P.F. Tu, Rapid Commun. Mass Spectrom. 21 (2007) 2351.
[19] W.M. Stöggl, C.W. Huck, G.K. Bonn, J. Sep. Sci. 27 (2004) 524.
[20] R. Flamini, Mass Spectrom. Rev. 22 (2003) 218.
[21] J. Sun, F. Liang, Y. Bin, P. Li, Ch. Duan, Molecules 12 (2007) 679.
[22] M. Monagas, R. Suárez, C. Gómez-Cordovés, B. Bartolomé, Am. J. Enol. Vitic. 56 (2005) 139.
[23] G. Vanhoenacker, A. De Villiers, K. Lazou, D. De Keukeleire, P. Sandra, Chromatographia 54 (2001) 309.
[24] T. Hernández, I. Estrella, D. Carlavilla, P.J. Martíın-Álvarez, M.V. Moreno-Arribas, Anal. Chim. Acta 563 (2006) 116.
[25] S. Pérez-Magariño, I. Revilla, M.L. González-SanJosé, S. Beltrán, J. Chromatogr. A 847 (1999) 75.
[26] L. Bevilacqua, F. Buiarelli, F. Cocciolli, R. Jasionowska, Annali di Chimica 94 (2004) 679.
[27] M.S. Fernández-Pachón, D. Villaño, A.M. Troncoso, M.C. García-Parrilla, Anal. Chim. Acta 563 (2006) 101.
[28] J. Woraratphoka, K. Intarapichet, K. Indrapichate, Food Chem. 104 (2007) 1485.

Measurement of soil/dust arsenic by gas phase chemiluminescence

Maather F. Sawalha [a], Mrinal K. Sengupta [a], Shin-Ichi Ohira [a], Ademola D. Idowu [b],
Thomas E. Gill [c], Lila Rojo [c], Melanie Barnes [d], Purnendu K. Dasgupta [a,*]

[a] *Department of Chemistry and Biochemistry, University of Texas at Arlington, 700 Planetarium Place, Arlington, TX 76019-0065, United States*
[b] *Department of Chemistry and Biochemistry, Texas Tech University, Lubbock, TX 79409-1061, United States*
[c] *Environmental Science and Engineering Program, University of Texas at El Paso, El Paso, TX 79968-0684, United States*
[d] *Department of Geosciences, Texas Tech University, Lubbock, TX 79409-1053, United States*

ARTICLE INFO

ABSTRACT

A gas phase chemiluminescence (GPCL)-based method for trace measurement of arsenic has been recently described for the measurement of arsenic in water. The principle is based on the reduction of inorganic As to AsH_3 at a controlled pH (the choice of pH governs whether only As(III) or all inorganic As is converted) and the reaction of AsH_3 with O_3 to produce chemiluminescence (Idowu et al., Anal. Chem. 78 (2006) 7088–7097). The same general principle has also been used in postcolumn reaction detection of As, where As species are separated chromatographically, then converted into inorganic As by passing through a UV photochemical reactor followed by AsH_3 generation and CL reaction with ozone (Idowu and Dasgupta, Anal. Chem. 79 (2007) 9197–9204). In the present paper we describe the measurement of As in different soil and dust samples by serial extraction with water, citric acid, sulfuric acid and nitric acid. We also compare parallel measurements for total As by induction coupled plasma mass spectrometry (ICP–MS). As(V) was the only species found in our samples. Because of chloride interference of isobaric $ArCl^+$ ICP–MS analyses could only be carried out by standard addition; these results were highly correlated with direct GPCL and LC–GPCL results ($r^2 = 0.9935$ and 1.0000, respectively). The limit of detection (LOD) in the extracts was 0.36 µg/L by direct GPCL compared to 0.1 µg/L by ICP–MS. In sulfuric acid-based extracts, the LC–GPCL method provided LODs inferior to those previously observed for water-based standards and were 2.6, 1.3, 6.7, and 6.4 µg/L for As(III), As(V), dimethylarsinic acid (DMA) and monomethylarsonic acid (MMA), respectively.

1. Introduction

Arsenic (As) is the 20th most abundant element in the earth's crust. Some forms of As are extremely toxic; As is designated as a group A carcinogen for humans [1–3]. The USEPA has set a maximum contamination level (MCL) of As in drinking water of 10 µg/L [3]; similar limits exist through most of the world. Arsenic contamination in groundwater and thence drinking water has been and continues to be a major concern in eastern India and Bangladesh [4,5]. In many areas in the United States, groundwater contains more than 10 µg/L As [6,7]. Arsenic toxicity and health effects have been extensively discussed and it has been linked to many diseases and disorders [8–16]. Arsenic in water is usually inorganic, present as arsenite (As(III)) or arsenate (As(V)); organic forms such as methylarsenite, methylarsenate, dimethylarsenite and dimethylarsenate also occasionally exist in traces [17]. It has been suggested

[18] that arsenic mutagenicity occurs because of the similarity of the chemistries of arsenic and phosphorus (P). The actual situation is likely to be much more complex. The simplistic mechanism above would not account for why As(III) is much more toxic compared to As(V) and P is exclusively present in biological systems in the +5 oxidation state. Moreover, As(V) toxicity appears to occur via its reduction by reduced glutathione to As(III) [12].

Electrochemical techniques are relatively affordable and highly sensitive. Various electrochemical measurement methods continue to be developed [19–24]; however, few are in practical use. We had developed one ourselves [25], only to discover that in real samples there are too many problems and calibration must be onerously frequent. Atomic spectrometry, typically combined with a front end separation technique, dominates present practice [17,26]. Paradoxically, countries which most need As measurement and speciation can least afford such techniques. At the other extreme, "Field Kits" are available for arsenic detection. These are based on reduction of As to AsH_3 that is then passed through a lead acetate-soaked filter to remove any generated H_2S, and then through a mercuric bromide impregnated filter. The latter turns yellow to brown depending on

* Corresponding author. Tel.: +1 817 272 3171.
E-mail address: dasgupta@uta.edu (P.K. Dasgupta).

the level of As present. The ability of the kits to provide quantitative data at the regulation limit of 10 μg/L is questionable at best and aside from reliability there are other problems related to leakage of arsine from the generators, use of large sample volumes and chemicals, and thence generation of large volumes of waste, some of which includes lead and mercury [27,28]; others have pointed to the valuable information that the kits have nevertheless yielded [29].

Inspired by the original work of Fujiwara et al. [30] and Fraser et al. [31], in the last few years we developed a technique that provides a unique combination of sensitivity and affordability where sub-μg/L LODs can be reached with 2–3 mL samples on equipment costing <US$ 2500. In this technique, inorganic As can be speciated into As(III) and As(V) without chromatographic separation. Aqueous As is reduced by $NaBH_4$ to form AsH_3. This reduction is highly pH dependent—at low pH (<1) both As(III) and As(V) are reduced while at pH 4–7 only As(III) is reduced. The liberated arsine is reacted with ozone generated from ambient air in a reflective enclosure atop a photosensor module (PSM). All liquid handling is conducted by a fully automated syringe pump connected to a multi-port selector valve. Details appear in the original work [32]; As(III) can be determined at pH 4 and the solution can then be strongly acidified and As(V) then determined, or As(III) and total As can be separately determined at pH 4 and pH < 1, respectively, obtaining As(V) by difference. We will henceforth refer to this as the gas phase chemiluminescence (GPCL) method. The GPCL technique has equivalent sensitivity for As(III) and As(V) but does not respond well to organoarsenicals like dimethylarsinic acid (DMA) and monomethylarsonic acid (MMA). Arsenobetaine, which does not form a hydride, does not respond at all.

To speciate arsenic and use the same detection technique, the following strategy was developed [33]: (i) ion exchange chromatographic separation was first conducted using a bicarbonate/carbonate and carbonate/hydroxide eluent; (ii) the column effluent was segmented with nitrogen bubbles to minimize dispersion; (iii) the stream was flowed through a photoreactor (PR) that photodecomposed and oxidized all arsenic species into inorganic As(V); (iv) $NaBH_4$ and acid were added in separate streams continuously; (v) after ~12 s in a flow through reactor the gaseous AsH_3 and H_2/N_2 was separated in a gas liquid separator; and (vi) the AsH_3 entered the GPCL reactor where ozone was simultaneously introduced and the emitted light measured. In the following, this is referred to as the LC–PR–GPCL system.

In the context of ground water, arsenic content of soils is particularly important. In the present paper we establish a scheme of serial soil extraction with increasingly aggressive extractants and analyze these by GPCL as well as LC–PR–GPCL techniques and compare the results with those obtained by induction coupled plasma–mass spectrometry (ICP–MS), considered by many to be the benchmark measurement technique [34–37].

2. Experimental

2.1. Standards and reagents

Stock standards of 50 mg As/L were prepared. Inorganic As(III) and As(V) were prepared from As_2O_3 and $Na_2HAsO_4·7H_2O$ (J. T. Baker), respectively. Solutions of As(III) were prepared in 0.3 M HCl and As(V) solutions were prepared in 1 mM HCl. MMA and DMA standard solutions were prepared from sodium monomethylarsonate sesquihydrate (97.3%, ChemService Inc.) and cacodylic acid (98%, Aldrich), respectively, in water. Lower concentrations were prepared by dilutions with (18.2 MΩ cm) Milli-Q deionized water (DIW). Other reagents used for arsine generation included

1 M sulfuric acid (EMD Chemicals Inc.) and 4% (w/v) $NaBH_4$ (98%, Aldrich) in 0.5 M NaOH (EMD Chemicals) and 1 mM Na_2EDTA (US Biochemicals). Chromatography used a step gradient from 4 mM Na_2CO_3–0.8 mM $NaHCO_3$ (Eluent A) to 60 mM Na_2CO_3–30 mM NaOH (Eluent B). To minimize As(III) oxidation in the chromatographic column under alkaline conditions, the DIW used for eluent preparation was degassed by ultrasonication under vacuum for 25 min prior to use. The ^{115}In isotope (95.7% natural abundance) from indium chloride (Strem Chemicals) was used as an internal standard for ICP–MS measurements; a stock solution of 1000 mg In/L was used.

2.2. Sample extraction

Two different strategies were used. One involved sequential extraction. This was performed by extracting ~0.5 g of the soil sample with 2 mL DIW in a 10 mL capacity centrifuge tube; the mixture was shaken for 1 min, ultrasonicated for 30 min and then centrifuged for 5 min at 2250 rpm. The supernatant was decanted off and labeled Extract 1A. The precipitate was re-suspended in a fresh 2 mL aliquot of DIW, and the process was repeated to obtain Extract 1B. This process was repeated with two sequential extractions with 10 mM citric acid (Fluka, Extracts 2A and 2B), 1 M H_2SO_4 (Extracts 3A and 3B) and 2 M HNO_3 (VWR, Extracts 4A and 4B). Blank extract solutions were analyzed in an identical manner to the sample extracts (including dilution—see below). Blank values were very small but were subtracted as applicable. At least three aliquots of each soil/dust sample were taken and the results reported are in terms of the mean and standard deviations of at least three analyses. The original <2 mL decantate was diluted to 10 mL in a volumetric flask prior to replicate analysis; occasionally, this was further diluted 2× prior to analysis.

Arsenic in six selected samples (~0.4–2 g each) was extracted with 7 mL 1 M H_2SO_4 (shake ~1 min, ultrasonicate 30 min, centrifuge 5 min and decant). A 5-mL aliquot of the supernatant was diluted by DIW to 25 mL. A 5-mL aliquot of this diluted extract was analyzed with and without spiking with a 1 μg/L As(III) standard to attain added levels of 0.0, 5.0, 10.0, and 15.0 μg/L added As in the final solution which was made up to 50 mL. The spiking and calibration standards were made in 20 mM H_2SO_4. The unspiked final diluted extract was analyzed in triplicate by GPCL. Another aliquot of this was brought to near-neutrality by addition of a calculated amount of NaOH and analyzed in triplicate by LC–PR–GPCL. For ICP–MS both unspiked and spiked extracts were analyzed to apply standard addition based quantitation; it was found early on that analysis of unspiked solutions alone do not lead to accurate quantitation. Due to matrix-induced signal suppression, the average recovery of a standard added to a typical sample extract was 85%.

2.3. Analysis methods

Initial screening experiments with LC speciation showed that none of our soil samples contained any As species other than As(V). The direct GPCL method was thus conducted in strong acid medium, which determines total As only. For the GPCL apparatus, see the detailed description in [32]. Briefly, to 3-mL sample delivered to the reactor, 1 mL of 2 M H_2SO_4 was added. Following a syringe wash, 0.5 mL of the $NaBH_4$ reagent is next added at a high speed (1.04 mL/s) to induce rapid mixing. After 60 s, the reactor exit valve is opened to allow the liberated arsine to proceed to the CL cell; the reactor solution is purged simultaneously with 25 cm^3/min of activated carbon filtered air. The PSM was operated at a control voltage of 0.85 V and a secondary amplifier gain of 1250×.

For a detailed description of the LC–PR–GPCL system, see Ref. [33]. For improved separation, in the present work different eluents (see Section 2.1) and chromatographic protocol were used. Each chromatographic cycle was 20 min; Eluent A was used for the first 6 min and switched to Eluent B for the next 8 min before being switched to Eluent A again. Chromatographic conditions are given in detail in Table S1 in supporting information (SI). The PSM was operated with a control voltage of 0.85 V and a secondary amplification of 1000×.

Quantification on an ICP–MS was performed on a single quadrupole instrument of 0.7 amu mass resolution (X-Series II ICP–MS, equipped with a Peltier-cooled nebulizer, Thermo Fisher Scientific). Instrument operating condition and mass calibration was optimized using a manufacturer recommended multi-element standard consisting of a total of 11 elements (As, Ba, Be, Bi, Ce, Co, In, Li, Ni, Pb, U) at a concentration of 10 μg/L each in HCl. As previously stated, samples and standards were spiked with 10 μg/L In; ^{115}In and ^{75}As were monitored. As will be discussed later, because of initial results, the use of both ^{115}In as internal standard and a three-point (+5, +10, +15 μg/L As) standard addition protocol was adopted for As analysis. Operational parameters for the ICP–MS are shown in Table S2 (SI).

Owens Lake bed dust samples were also analyzed by ICP–optical emission spectrometry (ICP–OES) and by established proton-induced X-ray emission (PIXE) analysis methods [38]. The dust sample was further ground to a silt particle size (20–30 μm) and then pelletized to a 2.5-cm diameter disk against a glass surface. PIXE analysis for a thick target was performed on the samples in vacuum using a Van De Graff style accelerator (Elemental Analysis, Inc., Lexington, Kentucky, USA) run at 2.44 MeV. Samples were irradiated using a 5/8-in. collimator for 10–12 min and the X-rays measured by a Si–Li detector. The calculation of the elemental concentrations in PIXE is based on the X-ray intensity yield that is proportional to specific analyte concentrations. These values are determined by a formula based on reference standards, in the present case the NIST SRM 2711, Montana II Soil, which was pelletized and analyzed under the same conditions during the same run. The pre-pulverization of the samples is intended to reduce sample inhomogeneity issues.

Sample analyzed by ICP–OES were first ground in a synthetic corundum mortar and pestle to a size of ≤ 30 μm and digested with HNO_3–H_2O_2 as per EPA Method 3050B [39]. For each batch of samples prepared, method blanks and NIST SRM 2711 were also prepared to determine any impurities in the acids used and to check the sample preparation method. The digest was analyzed using EPA Method 6010B [40] on a Leeman Labs direct reading Echelle grating DRE spectrometer. Instrumental operating conditions are listed in Table S3 (SI).

3. Results and discussion

3.1. Samples

We chose three classes of samples: (a) Soil samples supplied by the United States Geological Survey (Denver, CO) that came from various parts of the United States as noted in Table S4 (SI). As noted, half of these had no deliberate arsenic contamination and half had poultry farm litter applied to them. Roxarsone (3-nitro-4-hydroxyphenylarsonic acid) is widely used as a feed additive in the broiler poultry industry to control coccidial intestinal parasites. Poultry farm litter is often applied to soil; it is known that the As rapidly degrades to the inorganic form [41]. The fate and the mobility of the arsenic is also of interest [42]. (b) Soil samples from fallow lands in Murshidabad district in West Bengal, India, a region known

to have arsenic contamination of groundwater [10], supplied by the School of Environmental Studies (Kolkata, India). (c) Owens Lake bed dust. Owens Lake, in east-central California, once a thriving water body, dried up due to water diversions in the 1930s to accommodate the water needs of the growing city of Los Angeles. Its dry surface is presently one of the most intense sources of dust in the entire Western Hemisphere, as a result of erosion, lack of vegetation, and high winds [43,44]. Storms can generate dust plumes with an aerosol loading of tens of mg/m^3 [45] with peak arsenic concentrations of 0.4 μg/m^3; dust collected in Owens valley measure 10–50 mg/kg As [46]. There is considerable concern over health effects of windblown dust from Owens lake; a "dustcam" continuously broadcasts a live view [47]. Particle size distribution of our samples is given Table S5 and elemental composition determined by PIXE or ICP–OES is given in Table S6.

3.2. Instrument performance and calibration data

3.2.1. Gas phase chemiluminescence methods

The GPCL method provided statistically indistinguishable calibrations for As(III) and As(V). Either peak height or peak area produce essentially the same linear r^2 value (0.9997 vs. 0.9995) for the calibration curve, the simpler peak height based equation was henceforth used for data evaluation (the uncertainties represent 95% confidence limits):

$$\text{Peak height (mV)} = (169.3 \pm 1.1)\,[\text{As, μg/L}] + 91.0 \pm 30.9,$$
$$r^2 = 0.9997 \tag{1}$$

Figs. S1 and S2 in SI show the height and area based calibration plots; uncertainties at each concentration are shown therein as ± 1 S.D. error bars. Fig. S3 (SI) shows output for triplicate analysis of Owens Lake sample OL3. Based on an S/N = 3 criterion, the LOD was 0.36 μg/L. Spike recoveries on sample extracts were quantitative within experimental error. Direct, rather than standard addition based quantitation was thence used.

The LC–PR–GPCL method also produced linear calibration curves and quantitation was based on height:

$$\text{Peak height (mV)} = (5.855 \pm 0.263)\,[\text{As(III), μg/L}] + 22.2 \pm 12.3,$$
$$r^2 = 0.9920 \tag{2}$$

$$\text{Peak height (mV)} = (12.020 \pm 0.210)\,[\text{As(V), μg/L}] + 32.5 \pm 9.7,$$
$$r^2 = 0.9988 \tag{3}$$

$$\text{Peak height (mV)} = (2.339 \pm 0.091)\,[\text{As as DMA, μg/L}] + 1.9 \pm 4.2,$$
$$r^2 = 0.9940 \tag{4}$$

$$\text{Peak height (mV)} = (2.348 \pm 0.062)\,[\text{As as MMA, μg/L}]$$
$$+ 5.7 \pm 2.9, \quad r^2 = 0.9973 \tag{5}$$

MMA was, however, not detected in any of our samples. A detailed calibration plot with uncertainties at each calibration point is shown in Fig. S4 in SI. The (S/N = 3) LODs were 0.26, 0.13, 0.67 and 0.64 ng As for As(III), As(V), DMA and MMA, respectively. A representative chromatogram is shown in Fig. S5. As with direct GPCL, spike recoveries to sample extracts were quantitative and direct, rather than standard addition based quantitation was used.

3.2.2. Induction-coupled plasma mass spectrometry

Any type of mass spectrometry is susceptible to ionization interference that is matrix dependent. Dilution with a stable isotope that occurs only in trace quantities is the ideal solution but this is not possible for arsenic, a monoisotopic element. From early days

of ICP–MS analysis of As, very many different ways of achieving good quantitation have been advocated for different matrices. In measuring As, Sb, Sn, Bi, Se and Te in Steel, the dual use of ^{9}Be and ^{103}Rh was advocated to bracket the ionization potentials of the analytes of interest [48]. Addition of carbon as methanol or ammonium carbonate was found to enhance ^{75}As signals, which the use of ^{121}Sb as internal standard did not adequately compensate for [49]. In electrothermal vaporization (ETV)–ICP–MS analysis of urine, the simultaneous use of standard addition and ^{121}Sb as internal standard was recommended [50]. For whole blood or urine others had recommended ^{69}Ga [51] as an internal standard, yet others have recommended that 1–3% N$_2$ be added to Ar, in which case ^{72}Ge, and especially ^{115}In or ^{130}Te work well as internal standards for urinalysis [52]. Unfortunately, for human urine as a matrix, still more recommendations for internal standards abound, e.g., dilution and use of ^{103}Rh [53], ^{193}Ir [54], etc. In other matrices such as wine (both red and white) ^{115}In has been successfully used [55]. For digested nail samples and an Ar–N$_2$ plasma, ^{130}Te was successfully used [56]. For samples where acid extraction or digestion must be used, varying amounts of acid cause variations in the ^{75}As signal that cannot be compensated for fully by using ^{45}Sc, ^{89}Y or ^{115}In as internal standards; standard addition however leads to satisfactory results [57]. Obviously the recommendations on the best internal standard to use for As analysis are diverse, perhaps even bewildering. We initially tried the use of ^{238}U; this was not very successful, in part because many of our extracts contained this isotope in significant concentrations. Preliminary scans of sample constituents and initial survey led us to settle on ^{115}In. The respective calibration curves were

$$\text{Signal (counts/s)} = (0.983 \pm 0.001)\,[\text{As(III)}\,\mu g/L] + 0.399 \pm 0.038,$$
$$r^2 = 1.0000 \tag{6}$$

$$\text{Signal (counts/s)} = (0.985 \pm 0.050)\,[\text{As(V)},\,\mu g/L] + 3.740 \pm 2.594,$$
$$r^2 = 0.9922 \tag{7}$$

$$\text{Signal (counts/s)} = (0.998 \pm 0.004)\,[\text{As as DMA},\,\mu g/L]$$
$$+\,0.702 \pm 0.182, \quad r^2 = 1.0000 \tag{8}$$

$$\text{Signal (counts/s)} = (0.902 \pm 0.015)\,[\text{As as MMA},\,\mu g/L]$$
$$+\,1.028 \pm 0.394, \quad r^2 = 0.9994 \tag{9}$$

In direct ICP–MS measurement of inorganic As, Narukawa et al. [58] have recently observed that both ICP–OES and ICP–MS measurements produce a slight but discernible (4%) greater sensitivity for As(V) compared to As(III). A similar statistically significant difference between As(III) and As(V) is not apparent in our data. Whether this was because of use of calibration standards in an acidic matrix or the use of a particular internal standard or just simply different instrument/operating conditions is not known. There is clearly lower response with MMA but the purity of this type of a standard cannot be assured. For inorganic As(III) and As(V), we pooled all data and used a single calibration curve. The results with real sample extracts showed however that internal standard counts varied significantly compared to standards (78–99%) and standard addition of As led to recoveries of 85% on the average. Since we could not assure uniform acidity in the extract due to various degrees of neutralization by the sample and resulting different salinities, we chose the standard addition approach for quantitation as recommended by others [57]. We used a three point standard addition approach to assure data quality. Based on a S/N = 3, the LOD was 0.1 μg/L.

3.2.3. Chloride interference in ICP–MS

In high chloride samples in an Argon plasma, variable background and isobaric interference between ^{75}As$^+$ and ^{40}Ar^{35}Cl$^+$ cause problems, this cannot be solved by adding a different As isotope, even if one existed. However, the present samples are not extracted with HCl or NaCl solutions and chloride content of extracts are not particularly high. Matrix interference from chloride that forms ArCl$^+$ was studied and is shown as Fig. S6. The fact that the *y*-intercept (the background signal count at *m/z* 75, presumably due to ArCl$^+$) does not increase systematically with increasing chloride concentration is not obvious in the main plot, this is shown in the inset. In fact even at 100 ppm chloride, the rise in the background counts will only cause a 3% error in the quantitation of 5 μg/L As. But the more important issue and what is obvious in Fig. S6 is that the arsenic calibration slope increases systematically in the presence of chloride. Presumably atomic As is ionized more efficiently by collision with ArCl$^+$. Note that 100 ppm chloride concentration in the final extract (the highest value studied here) is tantamount to a chloride concentration of 5 g/kg when 1 g sample is extracted to produce a final extract volume of 50 mL. Majority of agricultural soil samples (non-brackish soil samples) have extractable chloride levels <2 g/kg [59]. The two Owens Lake dust samples that were used for methods intercomparison did have chloride at the 11–12 g/kg level but only 0.4 g amounts of these samples were used for extraction and extract was diluted to 100 mL. Fig. S7 shows treats the 10-ppb standard as an unknown; a three point standard addition plot as practiced in the present work quantitates the unknown with a relative standard deviation of 8.6% for 0–50 ppm chloride concentration and underestimates the actual concentration by ~11%. The presence pf 100 ppm chloride however leads to a 26% overestimation. These limitations of the ICP–MS measurements should be borne in mind when comparing results.

3.3. Sequential extraction

Different extractants and extraction procedures for arsenic extraction from soil have been described in the literature [39,60–62]. It is not clear that there is any uniquely superior extraction procedure—after all, for geological purposes a total digestion may be most appropriate whereas for the purposes of measuring health hazards of inhaled aerosol the amount that is likely to be readily bioavailable is of the greatest interest. Further, most aggressive oxidative digestion procedures destroy original oxidation state information. Microwave digestion is often used for exhaustive extraction, the USEPA recommends digestion with HNO$_3$–H$_2$O$_2$ [39].

Water, citric acid, sulfuric acid, nitric acid have all been used for extracting As from soil samples. It has been noted that sulfuric acid generally extracts much greater amounts than citric acid [60,63]. Fig. 1 shows the sequential extraction results of the three types of samples; the absolute total amounts of arsenic measured in the samples are shown under each bar (representing the total extracted in extracts A, B, etc., as appropriate). These results were all obtained with GPCL. Owens Lake dust samples consist essentially of re-suspended material that used to constitute a lake. Perhaps it is not surprising therefore that on average half of the arsenic is readily extracted by water. There is very little As that remains after water extraction that is extractable by citric acid. What little is measured in the citric acid extract may well be from the previous extractant in the liquid retained by the sediment. Similarly, there is very little arsenic left that is extractable by nitric acid that was not already extracted by sulfuric acid in these samples. In marked contrast, the fallow soils from Murshidabad examined (WB1–WB5) are rain-washed well drained soils where the water-leachable arsenic has apparently already leached and drained. In fact exclusively for
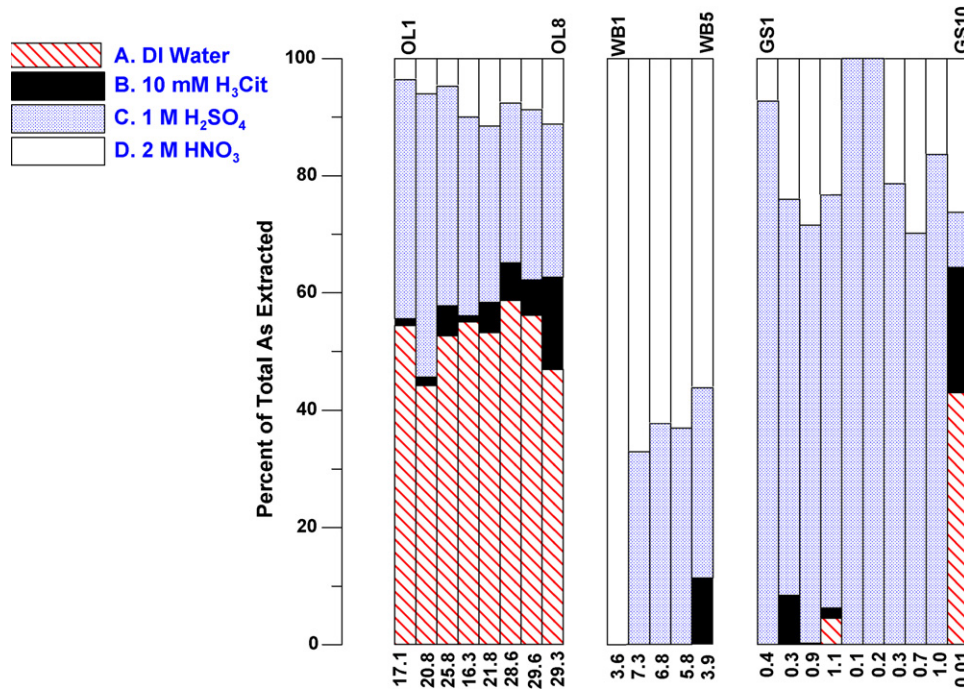
Fig. 1. Fraction As extracted by sequential extraction. Half or more of the As in the Owens lake samples (left group) is water extractable while the soil samples from West Bengal, India (middle group) contain only acid extractable As. The background soil samples from USGS also contain As only in a strong acid-extractable form. The absolute amounts extracted are given in mg/kg below each column. Sample details are given in SI.

WB1, and in general to a major extent for the others, arsenic could be extracted only with the oxidizing acid. The numbers below each bar lists the *total* As extracted. The values for the WB samples are very similar to those reported by Roychowdhury et al. [64] for very similar samples. Note that the Owens Lake samples on the average have 5–6× as much As compared to the samples from WB, India and those have 1–2 orders of magnitude more As than the uncontaminated background soils. Based on the results of repeated extractions with the same extractant (these data are not discussed here), extraction of these samples is likely incomplete and the total As content may be much higher. The arsenic that is extracted comes out most readily in the sulfuric acid fraction. Even in the samples where poultry litter was applied, only As(V) is seen; the same has been observed by others [41,42]. A bar graph depicting the arsenic content (Fig. S8) is given in SI. There is no universal agreement on what the range of arsenic content in typical uncontaminated soil is. While Smedley and Kinniburgh [65] suggest that a range of 1–20 mg/kg is normal for well-aerated uncontaminated soils with limited biological activities, others suggest a much lower "normal" range [66,67].

Despite reasonable efforts at homogenization, small aliquots taken from solid samples are never completely homogeneous. This type of inhomogeneity was particularly apparent in the Owens Lake samples; arsenic concentrations determined in each extract in replicate analysis of the same samples are shown in Fig. S9 in SI. Except for DIW as an extractant with the Owens Lake samples, the amount of arsenic that is extracted by a particular extractant is not necessarily completed in the first extraction; both Figs. S8 and S9 show this.

3.4. Method comparison

A subset of two samples from each class (OL3, OL6; WB4, WB5; GS3, GS6) was chosen for method intercomparison. Initial screening by the LC method showed that As(V) was the only species present

in all the samples. For method intercomparison, the intrinsic variability of the arsenic content due to sample inhomogeneity cannot be allowed to play a role. As such, only a sulfuric acid extract, prepared in a sufficient volume to allow analyses by all three methods (ICP–MS) by three point standard addition was examined.

Fig. 2 shows the result of the two present methods against the ICP–MS data. Because blanks were repeatedly run and the results already adjusted to zero, the regression lines were forced through
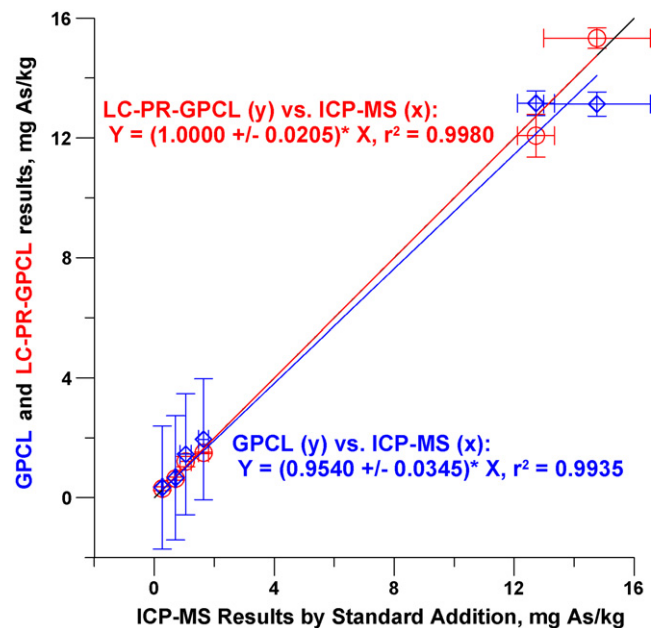

Fig. 2. Regression plots, ICP–MS vs. LC–PR–GPCL (circles) and ICP–MS vs. GPCL (diamonds). Horizontal error bars refer to the ICP–MS measurement, obtained by a three point standard addition method. The 1:1 correspondence line is fully coincidental in this plot with the ICP–MS vs. LC–PR–GPCL regression line.
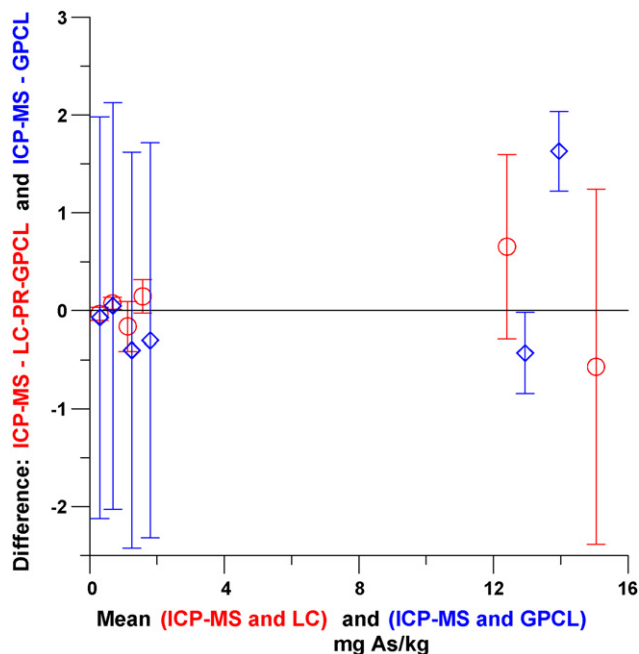
Fig. 3. A difference plot [65] shows no consistent bias for either of the GPCL methods vs. ICP–MS.

Fig. 5. LC–PR–GPCL analysis of a sample extract (sulfuric acid extract, neutralized). Bottom trace is from the unspiked sample (0.37, 0.45 and 0.70 mg/kg As as DMA, As(III) and As(V), in soil, amounting to 41, 51 and 78 μg/L As in the extract, respectively. The extract was then fortified to a level of 50 μg/L DMA and reanalyzed.

the origin. A paired *t*-test cannot take into account standard deviations in the individual measurements which are substantial for the ICP–MS measurements at the high end and for the GPCL measurements at the low end. Still, the ICP–MS and the LC–PR–GPCL methods were indistinguishable at the $p = 0.92$ level while ICP–MS and the GPCL methods were indistinguishable at the $p = 0.82$ level. The linear coefficients of determination are very high and the slopes are indistinguishable from unity for ICP–MS vs. LC–PR–GPCL and nearly so for ICP–MS vs. GPCL. Many believe that a difference plot [68] is of greater help to detect any consistent bias. Such a plot is shown in Fig. 3 and indicates that there is no apparent bias of either method relative to ICP–MS. With soil and dust samples, inherent inhomogeneity is a greater source of uncertainty; this is shown in Fig. 4 for the Owens Lake dust samples where different aliquots were taken for analysis.

All of the above samples showed the presence of As(V) only. Substantial time had generally elapsed between sampling and analysis and the samples were not stored in a manner that would have prevented microbial activity. Previously we had observed organic As species to be present in stagnant surface water samples [33]. We procured a soil sample from a cultivated field and analyzed this as soon as possible. DMA was present in this sample, but not MMA. A LC–PR–GPCL-based chromatogram of this sample, with and without added MMA is shown in Fig. 5. As analyzed, the unspiked sample extract contained 41.1 ± 4.2, 50.8 ± 0.7, 0.0 ± 0.0

Fig. 4. Owens Lake dust sample arsenic content measured in disparate aliquots by GPCL, PIXE and ICP–OES.

and $78.0 \pm 0.7 \,\mu g/L$ As, respectively as DMA, As(III), MMA and As(V). Upon spiking with MMA to a level of $50 \,\mu g/L$ As, reanalysis yielded 42.1 ± 3.3, $48.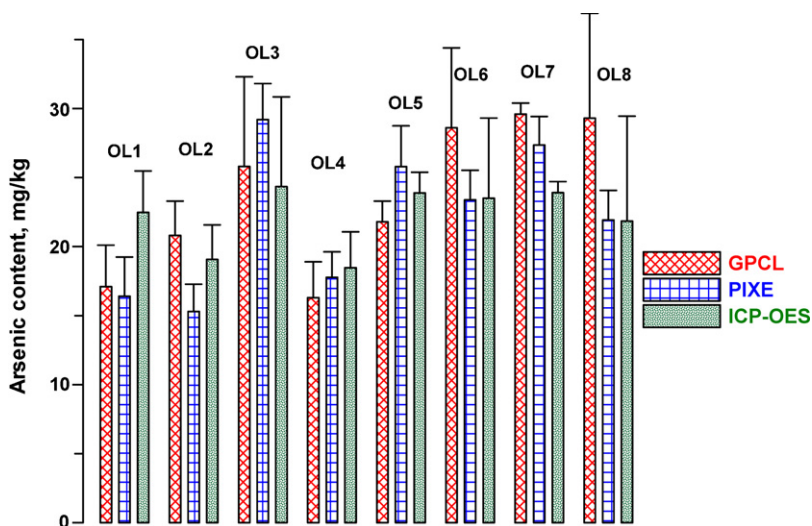3 \pm 1.3$, 51.6 ± 3.3, $78.1 \pm 3.0 \,\mu g/L$ As for the same respective species. The same samples were also analyzed by ICP–MS for total As. The spiked and unspiked samples were respectively measured to contain 172.4 ± 0.3 and $220.0 \pm 1.7 \,\mu g/L$ As (based on an ICP–MS calibration that contained equimolar amounts of all four As species), compared to the chromatographic sum of 169.9 ± 4.4 and $220.1 \pm 5.7 \,\mu g/L$ As. In absolute amounts, the sample contained 0.37 ± 0.04, 0.45 ± 0.01 and $0.70 \pm 0.00 \,\mu g/g$ As abs DMA, As(III) and As(V), respectively, clearly indicating the ability of the method to speciate sub-ppm levels of As in soil.

4. Conclusions

The gas phase chemiluminescence method for arsenic analysis is an inexpensive affordable approach that is not only applicable to water, it is applicable to soil extracts and likely, a variety of other sample types after appropriate extraction. Although the reactor has to be manually washed afterwards, it is interesting to note that because the method intrinsically involves matrix isolation, it is capable of handing mud or sediment samples directly. The GPCL equipment costs ∼1% of that of ICP–MS and can reach an LOD within a factor of 4 of the large, expensive instrument. Unlike ICP–MS, there is no chloride interference issue and there are no needs for internal standards or standard addition based quantitation. At a typical consumption rate for argon of 10+ L/min for a typical ICP-based spectrometer, the operating costs are also two orders of magnitude lower. The GPCL technique can be used equally well with and without a chromatographic front end for speciation. It is ironic that all speciation work on samples from South Asia, where the problem is the most acute, has been carried out in fact outside the affected countries. The GPCL technique can bring affordable speciation to many laboratories. We had previously published a complete parts/vendor list [32] and reiterate herein the offer that we will provide assistance to any nonprofit organization interested un building GPCL analyzers for As.

Acknowledgements

Appendix A. Supplementary data

Supplementary data associated with this article can be found, in the online version, at doi:10.1016/j.talanta.2008.06.037.

References

[1] P.K. Dasgupta, H. Huang, G. Zhang, G.P. Cobb, Talanta 58 (2002) 153–164.
[2] P.B. Tchounwou, A.K. Patlolla, J.A. Centeno, Toxicol. Pathol. 31 (2003) 575–588.
[3] United States Environmental Protection Agency, Arsenic in drinking water. http://www.epa.gov/safewater/arsenic/index.html, 2008 (accessed April 29).
[4] R. Wilson, Chronic arsenic poisoning: history, study and remediation. http://phys4.harvard.edu/(wilson/arsenic/arsenic_project_introduction.html, 2008 (accessed April 29).
[5] School of Environmental Studies, Jadavpur University, Kolkata, India, Groundwater arsenic contamination in Ganga–Meghna–Brahmaputra (GMB) plain (1976–2006). http://www.soesju.org/arsenic/arsenicContents.htm?f=health_effect.html, 2008 (accessed April 29).
[6] A.H. Welch, D.B. Westjohn, D.R. Helsel, R.B. Wanty, Ground Water 38 (2000) 589–604.
[7] S.J. Ryker. Geotimes 46 (11) (2001) 34–36. See also http://water.usgs.gov/nawqa/trace/pubs/geo_v46n11/fig3.html, 2008 (accessed April 29).
[8] C.H.S.J. Chou, C.T. De Rosa, Int. J. Hyg. Environ. Health 206 (2003) 381–386.
[9] K.S. Patel, K. Shrivas, R. Brandt, N. Jakubowski, W. Corns, P. Hoffmann, Environ. Geochem. Health 27 (2005) 131–145.
[10] S.C. Mukherjee, K.C. Saha, S. Pati, R.N. Dutta, M.M. Rahman, M.K. Sengupta, S. Ahamed, D. Lodh, B. Das, M.A. Hossain, B. Nayak, S.K. Palit, I. Kaies, A.K. Barua, K.A. Asad, A. Mukherjee, D. Chakraborti, J. Toxicol. Clin. Toxicol. 43 (2005) 835–848.
[11] S. Kapaj, H. Peterson, K. Liber, P. Bhattacharya, J. Environ. Sci. Health 41A (2006) 2399–2428.
[12] A.D. Kligerman, A.H. Tennant, Toxicol. Appl. Pharmacol. 222 (2007) 281–288.
[13] A. Vahidnia, G.B. Van der Voet, F.A. de Wolf, Hum. Exp. Toxicol. 26 (2007) 823–832.
[14] T.S.Y. Choong, T.G. Chuah, Y. Robiah, F.L.G. Koay, I. Azni, Desalination 217 (2007) 139–166.
[15] D.N.G. Mazumder, Ind. Pediatr. 44 (2007) 925–927.
[16] K.T. Kitchin, K. Wallace, J. Inorg. Biochem. 102 (2008) 532–539.
[17] D.Q. Hung, O. Nekrassova, R.G. Compton, Talanta 64 (2004) 269–277.
[18] M. Patra, N. Bhowmik, B. Bandopadhyay, A. Sharma, Environ. Exp. Bot. 52 (2004) 199–223.
[19] Y. Song, G.M. Swain, Anal. Chim. Acta 593 (2007) 7–12.
[20] J. Vandenhecke, M. Waeles, R.D. Riso, P. LeCorre, Anal. Bioanal. Chem. 388 (2007) 929–937.
[21] S. Laschi, G. Bagni, I. Palchetti, M. Mascini, Anal. Lett. 40 (2007) 3002–3013.
[22] A. Salimi, H. Manikhezri, R. Hallaj, S. Soltanian, Sens. Actuators B 129 (2008) 246–254.
[23] T. Tongesayi, R.B. Smart, Electroanalysis 20 (2008) 434–437.
[24] R. Baron, B. Sljukic, C. Salter, A. Crossley, R.G. Compton, Russ. J. Phys. Chem. A 81 (2007) 1443–1447.
[25] H. Huang, P.K. Dasgupta, Anal. Chim. Acta 380 (1999) 27–37.
[26] E. Terlecka, Environ. Monit. Assess. 107 (2005) 259–284.
[27] M.M. Rahman, D. Mukherjee, M.K. Sengupta, U.K. Chowdhury, D. Lodh, C.R. Chanda, S. Roy, M. Selim, Q. Quamruzzaman, A.H. Milton, S.M. Shahidullah, M.T. Rahman, D. Chakraborti, Environ. Sci. Technol. 36 (2002) 5385–5394.
[28] N.R. Khandaker, Environ. Sci. Technol. 38 (2004) 479A.
[29] A. Van Geen, Z. Cheng, A.A. Seddique, Environ. Sci. Technol. 39 (2005) 299–303.
[30] K. Fujiwara, Y. Watanabe, K. Fuwa, J.D. Winefordner, Anal. Chem. 54 (1982) 125–128.
[31] M.E. Fraser, D.H. Stedman, M.J. Henderson, Anal. Chem. 54 (1982) 1200–1201.
[32] A.D. Idowu, P.K. Dasgupta, Z. Genfa, K. Toda, J.R. Garbarino, Anal. Chem. 78 (2006) 7088–7097.
[33] A.D. Idowu, P.K. Dasgupta, Anal. Chem. 79 (2007) 9197–9204.
[34] United States Environmental Protection Agency, Analytical methods support document for arsenic in drinking water. December 1999. http://www.epa.gov/safewater/arsenic/pdfs/methods.pdf, 2008 (accessed April 29).
[35] C. B'Hymer, J.A. Caruso, J. Chromatogr. A 1045 (2004) 1–13.
[36] P. Niedzielski, M. Siepak, Pol. J. Environ. Stud. 12 (2003) 653–667.
[37] K.T. Suzuki, B.K. Mandal, Y. Ogra, Talanta 58 (2002) 111–119.
[38] J.E. Martin, R. Garcia-Tenorio, M.A. Respaldizada, F.J. Ager, M.F. da Silva, Nucl. Instrum. Methods Phys. Res. B 139 (1998) 175–179.
[39] United States Environmental Protection Agency, Acid digestion of sediments, sludges, and soils. http://www.epa.gov/SW-846/pdfs/3050b.pdf.
[40] United States Environmental Protection Agency, Inductively coupled plasma-atomic emission spectrometry, Method 6010B. http://www.epa.gov/region8/water/biosolids/biosolidsdown/6010b.pdf, 2008 (accessed May 9).
[41] J.R. Garbarino, A.J. Bednar, D.W. Rutherford, R.S. Beyer, R.L. Wershaw, Environ. Sci. Technol. 37 (2003) 1509–1514.
[42] D.W. Rutherford, A.J. Bednar, J.R. Garbarino, R. Needham, K.W. Staver, R.L. Wershaw, Environ. Sci. Technol. 37 (2003) 1515–1520.
[43] T.E. Gill, D.A. Gillette, Geol. Soc. Am. Abstr. Prog. 24 (1991) 432.
[44] M.C. Reheis, J. Geophys. Res. 102 (D22) (1997) 25999–26008.
[45] T.A. Cahill, T.E. Gill, J.S. Reid, E.A. Gearhart, D.A. Gillette, Earth Surf. Proc. Landforms 21 (1996) 621–639.
[46] J.S. Reid, R.G. Flocchini, T.A. Cahill, R.S. Ruth, D.P. Salgado, Atmos. Environ. 28 (1994) 1699–1706.
[47] Great Basin Unified Air Pollution Control District, DustCam at Owens Lake, California. http://www.gbuapcd.org/dustcam.htm.
[48] A.G. Coedo, M.T. Dorado, J. Anal. Atmos. Spectrom. 9 (1994) 1111–1115.
[49] E.H. Larsen, S. Sturup, J. Anal. Atmos. Spectrom. 9 (1994) 1099–1105.
[50] S. Boonen, F. Vanhaecke, L. Moens, R. Dams, Spectrochim. Acta B 51 (1996) 271–278.
[51] D.E. Nixon, T.P. Moyer, Spectrochim. Acta B 51 (1996) 13–25.
[52] C.J. Amarasiriwardena, N. Lupoli, V. Potula, S. Korrick, H. Hu, Analyst 123 (1998) 441–445.
[53] J.H. Wang, E.H. Hansen, B. Gammelgaard, Talanta 55 (2001) 117–126.
[54] W.J. McShane, R.S. Pappas, D. Paschal, J. Anal. Atmos. Spectrom. 22 (2007) 630–635.
[55] S. Wangkarn, S.A. Pergantis, J. Anal. Atmos. Spectrom. 14 (1999) 657–662.

[56] K.L.B. Chen, C.J. Amarasiriwardena, D.C. Christiani, Biol. Trace Elem. Res. 67 (2) (1999) 109–125.

[57] Y. Cai, M. Georgiadis, J.W. Fourqurean, Spectrochim. Acta B 55 (2000) 1411–1422.

[58] T. Narukawa, T. Kurowia, K. Chiba, Talanta 73 (2007) 157–165.

[59] W.A. Norvell, J. Wu, D.G. Hopkins, R.M. Welch, Soil. Sci. Soc. Am. J. 64 (2000) 2162–2168.

[60] S. Saha, K. Ghosh, I. Das, S.K. Sanyal, J. Ind. Chem. Soc. 82 (2005) 364–367.

[61] C.-G. Yuan, B. He, E.-L. Gao, J.-X. Lue, G.B. Jiang, Microchim. Acta 159 (2007) 175–182.

[62] A. Marin, A. Lopez-Gonzalvez, C. Barbas, Anal. Chim. Acta 442 (2001) 305–318.

[63] M.G.M. Alam, S. Tokunaga, J. Environ. Sci. Health A 41 (2006) 631–643.

[64] T. Roychowdhury, T. Uchino, H. Tokunaga, M. Ando, Chemosphere 49 (2002) 605–618.

[65] P.L. Smedley, D.G. Kinniburgh, Appl. Geochem. 17 (2002) 517–568.

[66] M.F. Hossain, Agric. Ecosyst. Environ. 113 (2006) 1–16.

[67] E. Sanz, R. Munoz-Olivas, C. Camara, M.K. Sengupta, S. Ahamed, J. Environ. Sci. Health A 42 (2007) 1695–1705.

[68] K. Linnet, Clin. Chem. 45 (1999) 314–315.

Development and validation of a rapid multiresidue method for pesticide determination using gas chromatography–mass spectrometry: A realistic case in vineyard soils

E. Schreck [a,b,*], F. Geret [a], L. Gontier [b], M. Treilhou [a]

[a] *Laboratoire de Chimie et Biochimie des Interactions, Université de Toulouse, Centre universitaire JF Champollion, Place de Verdun, 81012 Albi, France*
[b] *Institut Français de la Vigne et du Vin-IFV Midi-Pyrénées, V'innopôle, BP 22, 81310 Lisle sur Tarn, France*

A B S T R A C T

A rapid and simultaneous method for residue identification and quantification for seven pesticides in agricultural soils has been developed to study a realistic situation in vineyard. The target compounds are two insecticides, two herbicides and three fungicides, from different chemical families. The procedure is based on a pressurized liquid extraction (PLE) with acetone, before a multiresidue GC–MS analysis. The recovery of PLE is between 53.8 ± 2.4 and $99.9 \pm 4.4\%$ according to pesticide. A limit of detection (LOD) between 1.4 and $4.6\,\mu g\,kg^{-1}$ of dry soil was obtained for five analytes. This procedure for testing soil contamination is sensitive and easy to perform.

© 2008 Elsevier B.V. All rights reserved.

1. Introduction

Pesticides are widely sprayed on agricultural land, especially in wine-growing areas, because of their agronomic applications: chemical weeding, yield damage prevention, pest control against crop destruction, etc. New agricultural practices attempt to reduce the quantities of toxic compounds applied but pesticides are still used in vineyards. They could accumulate in soils and become a real environmental pollution risk [1].

Different mixtures of compounds are typically sprayed on vineyards. However, a cocktail of seven of them is widely used by wine growers (especially in the Gaillac area, south-west France), and potentially present in soil. These pesticides belong to several different chemical families: two herbicides (flazasulfuron: sulfonylurea, and flumioxazin: *N*-phenylimide), two insecticides (chlorpyrifos-ethyl: organophosphate, and λ-cyhalothrin: pyrethroid), and three fungicides (metalaxyl: xylylalanine, folpet: thiophtalimide, and myclobutanil: triazole). So, the aim of this study was to elaborate a rapid and efficient method to determine pesticide accumulation and pollution in Gaillac vineyard.

Sample preparation and compound extraction is one of the most delicate steps in pesticide determination at trace levels in soils. At present, pesticide extraction from soils is mostly done using the Soxhlet technique [2,3], the ultrasonic assisted extraction (UAE) [4] or microwaves-assisted extraction (MAE) [3,5–7]. The non-exhaustive Table 1 shows an overall picture of the different techniques previously used for each compound of this vine cocktail. The extraction procedure changes according to the sample matrices but Table 1 reports also solid–liquid extraction [8] and pressurized liquid extraction (PLE) [9,10] for vine pesticide extraction from soils, sediments, composts or sludges. However, a new study has shown that PLE has better extraction efficiency than MAE or Soxhlet extraction for PAHs and organochlorine pesticides [11]. Moreover, as reported by Ferrell and Vencill [12], PLE was proved to be a highly efficient and repeatable means of extracting flumioxazin from soils.

Table 1 summarizes too the different analytical procedure that have been used for each target compound. These seven vine pesticides have already been studied individually [12,13] or with class-specific methods in different sample matrices. According to the matrix and the analyte, pesticide determination was carried out by different analytical methods such as liquid chromatography–mass spectrometry (LC–MS) or gas chromatography–mass spectrometry (GC–MS) (see references in Table 1). Even if the detection

* Corresponding author at: Laboratoire de Chimie et Biochimie des Interactions, Université de Toulouse, Centre universitaire JF Champollion, Place de Verdun, 81012 Albi, France. Tel.: +33 5 63 48 17 00; fax: +33 5 63 48 64 33.
E-mail address: eva.schreck@univ-jfc.fr (E. Schreck).

Table 1
Reported procedures for pesticide residues determination in different matrices

Pesticide	Extraction Procedure	Analytical Technique	Multiresidue method	Sample, Matrices	Methodological LOD	Ref.
Flazasulfuron	SPE	LC–MS	Multiresidue	Waters	0.005 µg mL^{-1}	[13]
Metalaxyl	SPE	HPLC-UV	Multiresidue with myclobutanil	Groundwaters	0.035 µg mL^{-1}	[14]
	/	GC-NPD	Multiresidue with myclobutanil	Air samples	0.012 µg mL^{-1}	[18]
		HPLC		Air samples	0.012 µg mL^{-1}	
	Ethyl acetate extraction	LC–MS/MS	Multiresidue with clorpyrifos and myclobutanil	Fresh grape samples	10 µg kg^{-1}	[19]
	SPE	GS–MS	Multiresidue	Surface and groundwaters	0.01 µg mL^{-1}	[20]
	SPE	GS–MS	Multiresidue with λ-cyhalothrin	Leafy vegetables	1 µg kg^{-1}	[21]
	Water and methanol extraction	LC–MS/MS	Multiresidue	Tobacco plants	20–40 µg kg^{-1}	[22]
	Solid–liquid extraction	GS–MS	Multiresidue with folpet	Soils	1–4 µg kg^{-1} (soils)	[8]
				Sediments	1–5 µg kg^{-1} (sediments)	
	Ethyl acetate + dispersive SPE	GC-TOF/MS	Multiresidue with chlorpyrifos, myclobutanil and λ-cyhalothrin	Grapes	13 µg kg^{-1}	[23]
		GC X GC-TOF/MS		Grapes	3 µg kg^{-1}	
Chlorpyrifos	Ethyl acetate extraction	LC–ESI-MS/MS	Multiresidue with metalaxyl and myclobutanil	Fresh grape samples	10 µg kg^{-1}	[19]
	PLE	GC–MS	Multiresidue	Composts	30 µg kg^{-1}	[9]
	Ethyl acetate + dispersive SPE	GC-TOF/MS	Multiresidue with metalaxyl, myclobutanil and λ-cyhalothrin	Grapes	6 µg kg^{-1}	[23]
		GC X GC-TOF/MS		Grapes	1 µg kg^{-1}	
	PLE	GC–MS	Multiresidue	Sludges	<62 µg kg^{-1}	[10]
				Agricultural soils	<31 µg kg^{-1}	
Folpet	Solid–liquid extraction	GC–MS	Multiresidue with metalaxyl	Soils	1–4 µg kg^{-1} (soils)	[8]
				Sediments	1–5 µg kg^{-1} (sediments)	
	SPE	HPLC-UV	Multiresidue	Fruit juices	0.5 µg kg^{-1}	[15]
Myclobutanil	/	GC-NPD	Multiresidue with metalaxyl	Air samples	0.006 µg mL^{-1}	[18]
		HPLC		Air samples	0.006 µg mL^{-1}	
	Ethyl acetate extraction	LC–ESI-MS/MS	Multiresidue with metalaxyl and chlorpyrifos	Fresh grape samples	10 µg kg^{-1}	[19]
	Ethyl acetate + dispersive SPE	GC-TOF/MS	Multiresidue with metalaxyl, chlorpyrifos and λ-cyhalothrin	Grapes	10 µg kg^{-1}	[23]
		GC X GC-TOF/MS		Grapes	2.5 µg kg^{-1}	
λ-Cyhalothrin	Combined SPE	GC–MS/MS	/	Vegitable oils	0.3 µg kg^{-1}	[24]
	Ethyl acetate + solid phase dispersion	LC–MS/MS	/	Fruits	0.4–2 µg kg^{-1}	[25]
	SPE	GC–MS	Multiresidue with metalaxyl	Leafy vegetables	2 µg kg^{-1}	[21]
	Ethyl acetate + dispersive SPE	GC-TOF/MS	Multiresidue with metalaxyl, myclobutanil and chlorpyrifos	Grapes	17 µg kg^{-1}	[23]
		GC X GC-TOF/MS		Grapes	3 µg kg^{-1}	
Flumioxazin	SPE-LLE-PLE	GC–MS	/	Soils, waters	Insrumental LOD: 9 ng mL^{-1}	[12]

Note: Non-exhaustive references (Ref.) were obtained from recent analytical abstracts. *Abbreviations*: LOD, limit of detection; GC, gas chromatography; LC, liquid chromatography (ESI: electrospray ionisation); MS, mass spectrometry; SPE, solid-phase extraction; PLE, pressurized liquid extraction; LLE, liquid–liquid extraction; HPLC, high performance liquid chromatography; TOF, time of flight; NPD, nitrogen–phosphorous detector.

limits depended on matrices, GC–MS provided often better results than LC–MS in terms of LOD (limits of detection), except for water and liquid samples [13–15].

Table 1 shows that these seven analytes have never been analysed simultaneously. However, they are lipophilic, volatile and thermally stable (except for flazasulfuron); so they can be determined using the PLE/GC–MS tandem. Moreover, the use of the PLE technique coupled with GC–MS analysis has already been tested with success in soil samples [10,16,17], particularly for organochlorine pesticides.

Thus, the aim of this paper is to focus on an actual case of possible contamination, and then set out a new analytical protocol. We propose a rapid method for the simultaneous determination of seven multi-class analytes from agricultural soils. It is suitable for routine soil analyses from vineyards, often contaminated with this widely used pesticide cocktail.

2. Experimental

2.1. Chemicals and reagents

The standard pesticides were purchased from Promochem (Molsheim, France) (purity ≥ 98%). Syngenta Agro SAS (Saint Cyr l'Ecole, France) supplied two compounds: λ-cyhalothrin and metalaxyl. Standard stock solutions were prepared by dissolving each pesticide in acetone (1 µg µL^{-1}). Reagents and solvents with pesticide analytical grade were obtained from Sigma–Aldrich (St Quentin Fallavier, France).

Table 2
Retention times (RT) and specific selected ions for pesticide identification

Molecule	Use	Molecular weight	RT (min)	Specific fragment ions (m/z)	
				Quantification ion (m/z (% relative abundance))	Qualification ions (m/z (% relative abundance))
Flazasulfuron[a]	Herbicide	407.4	12.23	231.1 (100)	232 (16); 188.1 (16)
Metalaxyl	Fungicide	279.3	13.02	206.1 (87)	160 (100); 132.1 (60)
Chlorpyrifos-ethyl	Insecticide	350.6	13.51	197 (100)	199 (88); 313.9 (83)
Folpet	Fungicide	296.6	14.24	260 (94)	130 (100); 104.1 (72)
Myclobutanil	Fungicide	288.8	14.87	179 (100)	152 (42); 150 (32)
λ-Cyhalothrin	Insecticide	449.9	17.10	181.1 (100)	197.1 (42); 141.2 (33)
Flumioxazin	Herbicide	354.3	20.46	354 (100)	232 (16); 188.2 (15)

Note: The ion extraction in TIC focused on the three characteristic ions. For quantification, the chosen ion is the most representative of the analyte even if its relative abundance was not 100%.

[a] Degradation product.

2.2. Apparatus

The extraction procedure was carried out using an Accelerated Solvent Extraction apparatus: ASE 100 system from Dionex S.A. Corporation (Voisins Le Bretonneux, France) with 66 mL stainless-steel vessels. A Finnigan Polaris Q gas chromatograph-ion trap mass spectrophotometer (Thermo Electron Corporation, Courtaboeuf les Ulis, France) with an RTX-5 (Restek Corporation, Lisses, France) column (30 m × 0.25 mm i.d., 0.25 μm) was used for the quantitative analysis. The mass spectrometer was operated in electron-impact mode (EI-70 eV).

2.3. Soil samples

Agricultural soil samples were collected from an experimental area in a Gaillac vineyard, from the top 40 cm layer. After collection, the samples were immediately frozen in plastic bags at −20 °C until extraction and quantitative analysis. The samples were dried 1 h at 50 °C for dehydration before extraction.

The experiment yield recoveries, linearity and limits of detection (LOD) were determined using an uncontaminated soil (from the same area and with a similar composition) spiked with the target pesticides at known concentrations (concentration range from 1 to 50 μg kg^{-1}).

2.4. Pressurized liquid extraction

Pesticide concentrations in soil samples were determined using pressurized liquid extraction with 100 g being introduced into a 66 mL cell with a piece of cellulose paper in the bottom. Extraction was performed at 10^7 Pa. PLE variables were selected carefully: solvent, temperature and number of cycles were tested in order to improve the soil extraction procedure and after several trials (Section 3.1), acetone was chosen as extraction solvent. Temperature was 100 °C, with 3 cycles per sample, a 60% flush volume, a static time of 3 min and a purge time of 120 s [26,27]. The extract was evaporated to dryness using a rotary evaporator (38–42 °C) and the flask was rinsed three times with dichloromethane. The sample was then concentrated under reduced pressure and re-dissolved with 500 μL of dichloromethane.

2.5. GC–MS analysis

1 μL of the final extract was injected into the GC–MS for a multi-residues detection under temperature gradient.

The instrumental conditions were adapted from Kawata et al. [9]. The injector temperature was 250 °C, in splitless mode. The oven temperature was programmed from 50 °C (hold 1 min) to 280 °C at 15 °C min^{-1} (hold 10 min). Helium (alpha 2 from Air Liquide, France) was used as carrier gas (1 mL min^{-1}). The transfer line and ionisation temperatures were 200 and 250 °C, respectively. The mass spectrometer was calibrated daily.

All the compounds could be identified by their retention time on the chromatogram and their specific ion m/z on the mass spectrum (Table 2). Peak areas were obtained from the chromatogram in total ion current (TIC) with selected ion extraction. Pesticide quantification was based on comparison of the areas in the samples with those of the standards (external standard method).

Extractions and GC/MS analyses were made in triplicate.

3. Results and discussion

3.1. Effect of the PLE variables

Extraction solvent, temperature and number of cycles are important parameters to improve in order to achieve efficient extraction. All the seven pesticides listed were used for evaluating the effect of these variables.

Five different extraction solvents, acetone, hexane, dichloromethane, ethyl acetate and acetonitrile, selected according to their physico-chemical properties (polarity and pesticide solubility efficiency), were evaluated by studying their desorption efficiency.

Table 3 shows the results of the influence of solvent on pesticide extraction recoveries, at a temperature of 100 °C (see below). The choice of solvent for extraction improvement is made by selecting the one with the best desorption efficiency for the largest number of compounds. Hexane is only efficient for two of the multi-class analytes: chlorpyrifos and λ-cyhalothrin, for the other compounds, the recoveries did not exceed 28%. With dichloromethane and ethyl acetate, the recoveries were average. The two most efficient were acetonitrile and especially acetone, which was thus selected as PLE solvent because of its improvement in the extraction methodology and advantages in use. In fact, acetone allows lipophilic compound solubility (>4000 g L^{-1} for several pesticides [28]), it is only weakly toxic (DL 50 = 5800 mg kg^{-1} in the rabbit [29]) and easily eliminated in the environment. Moreover, as one of the cheapest solvents it can be used for routine analyses in the laboratory.

The effect of the extraction temperature on PLE performance for the seven pesticides was evaluated by testing three levels (80, 100 and 120 °C).

Table 4 confirms that 100 °C is the best temperature for optimal pesticide extraction. The recoveries were higher for the seven analytes. A temperature of only 80 °C is not high enough to disrupt the solute-matrix interactions and active sites in soil [9]. However, results show a decrease in efficiency when the temperature is increased to 120 °C, as previously reported by Kawata et al. [9] and Concha-Grana et al. [16] for a temperature of 150 °C. Pesticides are damaged by high temperatures.

Thus, a temperature of 100 °C was recommended for the extraction of the target pesticides.

Table 3
Influence of solvent on pesticide extraction recoveries

	Analytical recovery (%)									
	Acetone		Hexane		Dichloromethane		Ethyl acetate		Acetonitrile	
	Mean (%)	S.D. (%)	Mean (%)	S.D. (%)	Mean (%)	S.D. (%)	Mean (%)	S.D. (%)	Mean (%)	S.D. (%)
Flazasulfuron[a]	68.00	4.65	8.49	4.56	62.08	3.11	59.77	4.26	67.70	2.26
Metalaxyl	99.90	4.40	14.49	3.87	64.36	2.45	81.35	2.71	63.40	3.04
Chlorpyrifos	53.83	2.36	81.36	3.42	41.25	2.85	47.67	2.85	50.46	3.47
Folpet	64.33	4.06	28.01	2.36	42.11	4.08	58.57	3.46	57.51	3.31
Myclobutanil	81.20	0.81	11.59	3.38	77.68	1.99	70.81	2.39	71.56	2.84
λ-Cyhalothrin	87.43	2.97	101.1	5.01	77.82	2.41	84.50	3.01	106.01	6.12
Flumioxazin	96.33	4.91	7.2	3.42	20.9	3.78	31.60	2.97	21.26	3.15

[a] Degradation product.

Table 4
Influence of temperature on pesticide extraction recoveries

	Analytical recovery (%)					
	80 °C		100 °C		120 °C	
	Mean (%)	S.D. (%)	Mean (%)	S.D. (%)	Mean (%)	S.D. (%)
Flazasulfuron[a]	24.33	3.59	68.00	4.65	50.01	4.12
Metalaxyl	55.76	3.86	99.90	4.40	46.92	3.16
Chlorpyrifos	33.55	3.18	53.83	2.36	24.85	3.25
Folpet	35.17	2.16	64.33	4.06	28.86	4.92
Myclobutanil	60.93	2.45	81.20	0.81	48.41	4.67
λ-Cyhalothrin	60.3	4.06	87.43	2.97	55.71	2.83
Flumioxazin	10.24	2.78	96.33	4.91	21.61	4.64

[a] Degradation product.

Table 5
Influence of the number of cycles on pesticide extraction recoveries

	Recovery of each cycle in percentage of the total extractible quantity (%)		
	First extraction cycle	Second extraction cycle	Third extraction cycle
Flazasulfuron[a]	33.9	46	19.2
Metalaxy	79	18.7	2.2
Chlorpyrifos	80.7	16.6	<LOD
Folpet	86.2	12.7	<LOD
Myclobutanil	80.7	18.5	<LOD
λ-Cyhalothrin	84.9	13.9	<LOD
Flumioxazin	81	12.6	<LOD

[a] Degradation product.

The number of extraction cycles was evaluated at a temperature of 100 °C with acetone. The results are given in Table 5. We noticed that two extraction cycles provided a good recovery, and could be sufficient to remove the total pesticide contents extractable by the methodology. However, a third cycle was necessary to improve the extraction of two compounds (metalaxyl and flazasulfuron), so we chose three extraction cycles for this study. Actually, one cycle more did not increase significantly the solvent volume to evaporate and prolong the total extraction time of only a few minutes.

The efficiency and matrix effect during extraction were checked with an inert matrix (celite) spiked with the seven target pesticides. This method helped to detect anomalies due to extraction or instrumental causes (pressure and temperature). All the recoveries were the same as with the contaminated soil (statistical analysis with the non-parametric Kruskal–Wallis test, using the SPSS program (standard version 11.0, SPSS Inc.)).

3.2. Evaluation of the method performance and validation

The target compounds were identified in the soil matrix by their retention time and their mass spectrum. A qualitative chromatogram in total ion current (Fig. 1) shows that the multi-class compounds are simultaneously determined with the multi-residues method.

It is well known that sulfonylureas are generally not very responsive to separation by gas chromatography (GC) because of their extremely low volatility and high thermal instability [30], which explains why the herbicide flazasulfuron has so far only been studied using liquid chromatography [13]. However, this multi-class method allows the reproductive determination of the degradation product of flazasulfuron by GC–MS. The ion tracked in the mass spectrum (Fig. 2) is the thermolyze product, and while this methodology does not give flazasulfuron detection, it is possible to obtain a good idea of flazasulfuron concentration in the soil sample by following its degradation product, which has good linearity (Table 6). The ion 231.1 is chosen because of good sensitivity and selectivity.
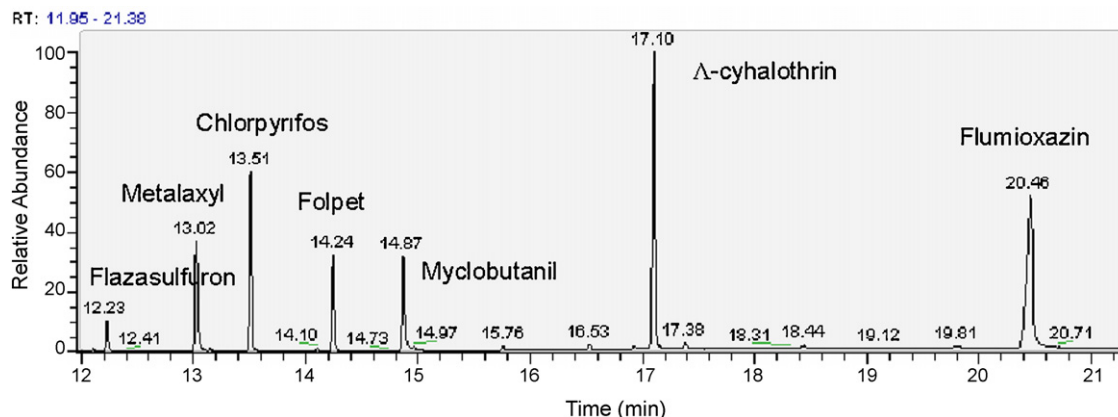
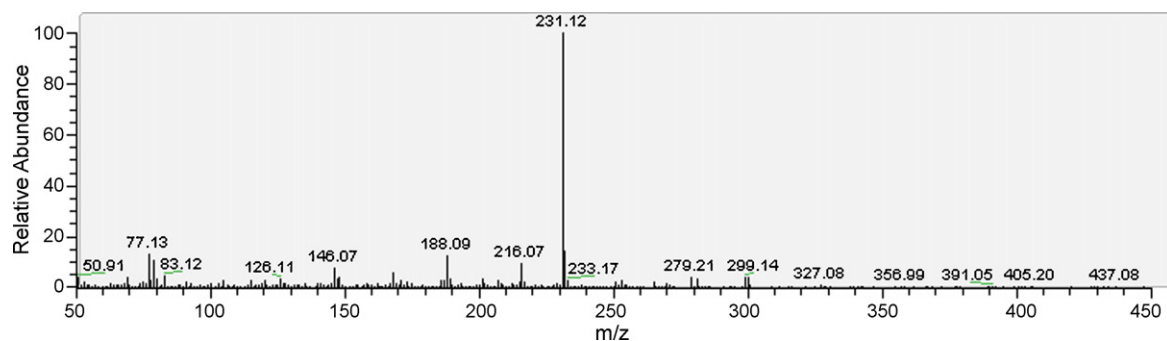**Fig. 1.** A qualitative chromatogram in total ion current (TIC mode).

Fig. 2. Mass spectrum of the thermolyze product of the sulfonylurea herbicide flazasulfuron.

Table 6
Data for calibration curves and quantitative analysis

| | Chromatogram area with ion extraction (3 replicates for each standard solution) | | | | | | | | | | | | | | | | R^2 |
| | 0.00025[a] | | 0.0005[a] | | 0.00075[a] | | 0.001[a] | | 0.0025[a] | | 0.005[a] | | 0.0075[a] | | 0.01[a] | | |
	Area mean	S.D.	Area mean	S.D.	Area mean	S.D.	Area mean	S.D.	Area mean	S.D.	Area mean	S.D.	Area mean	S.D.	Area mean	S.D.	
Flazasulfuron[b]	859	9	1668	67	3104	127	4393	241	11014	443	29350	1175	48672	2092	66770	2874	0.989
Metalaxyl	508	5	1524	52	2260	112	4130	229	8390	328	22093	994	33184	1493	44840	1793	0.995
Chlorpyrifos	435	3	820	8	1235	46	2008	102	5021	204	11643	558	19521	839	27729	1275	0.989
λ-Cyhalothrin	<LOD		<LOD		199	8	807	7	1563	48	4257	178	8424	353	12998	571	0.947
Folpet	<LOD		1890	111	3792	136	5919	239	13025	526	32640	1386	52582	2314	71021	3195	0.993
Myclobutanil	1490	71	2866	114	4887	245	7909	320	18827	753	54254	1807	89645	3852	123017	5658	0.986
Flumioxazin	<LOD		<LOD		276	11	906	9	1864	104	5899	253	10886	468	14018	589	0.972

[a] Concentration $\mu g \, \mu L^{-1}$.
[b] Degradation product.

In order to evaluate performance and quantification for all the target pesticides, spiked samples of soil were used. No target pesticides were detected from these uncontaminated (blank) samples which were then spiked with the cocktail of pesticides at different concentrations (range from 1 to 50 $\mu g \, kg^{-1}$ of soil). The samples were extracted 1 day after spiking and injected in GC–MS to estimate the methodological limits of detection (LOD) and quantification (LOQ). The instrumental LOD and LOQ were determined with pesticide standards in acetone (see concentration range in Table 6). A range of pesticide concentrations (three replicates for each standard solution) allows the linearity of the calibration curve to be checked for each analyte, using peak areas (Table 6). Good response linearity was found for all the pesticides at concentrations within the tested interval (see R^2 in Table 6).

The limits of detection and quantification of the pesticides were experimentally obtained in TIC with ion extractions, on a signal-to-noise basis of 3:1 and 10:1, respectively. Table 7 gives the values of instrumental and methodological limits of detection and quantification. The LODs and LOQs were defined as three times of standard deviation (S.D.) on the basis of three independent determinations. The methodological LOD values are higher than those obtained instrumentally (with standard solutions). In fact, the methodolog-

ical LOD (or LOQ) includes all the procedural steps from sample collection to pesticide detection by mass spectrometry after GC/MS injection. So, the methodological values give an overall picture of extraction recoveries and the potential matrix effect in analyte determination. The matrix effect increases the LOQ and LOD a little, but it is still rather weak.

The methodological LOD (Table 7) are between 1.4 and 4.6 $\mu g \, kg^{-1}$ of dry soil for five compounds (not flumioxazin or folpet). These LOD are in agreement with the bibliography values expressed in Table 1 for metalaxyl in soil and sediments samples [8] and for myclobutanil in grape samples [23], with GC–MS. For λ-cyhalothrin, better values were obtained than those obtained previously in fruits and vegetables [21,23]. An improvement in LOD with the PLE/GC–MS tandem is achieved for chlorpyrifos in soils or composts as compared with previous methods reported in literatures [9,10], Table 1. Thus, this new multiresidue method is sensitive, precise and easy to perform.

4. Application

This method was tested on a series of 54 agricultural soil samples collected from a Gaillac vineyard over a whole season

Table 7
Limit of quantification (LOQ) and limit of detection (LOD) for each compound

| | Instrumental (standard solutions) | | Methodological | |
	LOQ (10:1) ($\mu g/mL^{-1}$)	LOD (3:1) ($\mu g/mL^{-1}$)	LOQ (10:1) ($\mu g/kg^{-1}$)	LOD (3:1) ($\mu g/kg^{-1}$)
Flazasulfuron[a]	0.69	0.25	11.20	3.68
Metalaxyl	0.79	0.25	8.87	3.75
Chlorpyrifos	0.81	0.25	14.01	4.64
Folpet	2.82	1	19.43	7.77
Myclobutanil	1.38	0.5	8.19	3.08
λ-Cyhalothrin	0.75	0.25	3.26	1.43
Flumioxazin	3.06	1	14.57	5.19

[a] Degradation product.

from April to October, covering before, after and during pesticide spreading on the vines. Three sampling sites were located in the vine-growing area and three others in an uncontaminated area (controls). Each sample was divided into three depths, and every depth fraction was analysed in triplicate. We demonstrated that the procedure was very useful for checking pesticide residues in natural soils that had not been spiked artificially. Even if the concentrations were low, pesticide determination was still possible.

No target compounds were detected in blanks. During the pesticide spreading season, six analytes could be easily detected. The folpet was quickly degraded and not detected from the soil samples, as previously reported by Bermudez-Couso et al. [8,28]. The insecticides chlorpyrifos and λ-cyhalothrin were only detected in a very few samples of surface soil (0–5 cm of depth). The concentrations were at the limit of detection for these two pesticides. This observation suggests that chlorpyrifos was retained in soil rather than decomposed, as already noticed by Kawata et al. [9] and Reinecke and Reinecke [31]. Metalaxyl and myclobutanil were the two compounds found the most (as previously shown for fresh fruits like peppers by Martinez-Vidal et al. [32]). The two fungicides could be identified up to 40 cm deep in the soil due to their physico-chemical characteristics (solubility in water), and here their highest concentrations were about $3 \, \mu g \, kg^{-1}$ of dry weight. In surface soil, the values reached a level of $8 \, \mu g \, kg^{-1}$ for myclobutanil and $50 \, \mu g \, kg^{-1}$ for metalaxyl 1 day after pesticide spreading. The herbicides (flumioxazin and flazasulfuron) directly applied on the soil, were identified in surface soil (about $10 \, \mu g \, kg^{-1}$) but also in deeper samples (up to $25 \, \mu g \, kg^{-1}$ wet soil).

5. Conclusion

A new rapid method was proposed in this paper to simultaneously determine seven multi-class pesticides in agricultural soils. This method is sensitive (LOD between 1.4 and $4.6 \, \mu g \, kg^{-1}$ of dry soil for five compounds) and easy to perform (only two steps, complex instrumentation is not required) reducing costs, time and residue loss. The optimum conditions of pressurized liquid extraction and GC/MS detection have been established to improve method selectivity and sensitivity. It is certainly adapted to testing agricultural soil contamination because we investigated a cocktail of pesticides widely sprayed on vines. It has been validated by the study of soil samples from a Gaillac vineyard and could be applied for routine analyses.

References

[1] A.R. Jacobson, S. Dousset, N. Guichard, P. Baveye, F. Andreux, Environ. Pollut. 138 (2005) 250.
[2] J.V. Cizdziel, V.F. Hodge, Microchem. J. 64 (2000) 85.
[3] O.S. Fatoki, R.O. Awofolu, J. Chromatogr. A 983 (2003) 225.
[4] J.P. Bossio, J. Harry, C.A. Kinney, Chemosphere 70 (2008) 858.
[5] E. Fuentes, M.E. Baez, R. Labra, J. Chromatogr. A 1169 (2007) 40.
[6] D.V. Moreno, Z.S. Ferrera, J.J.S. Rodriguez, J. Chromatogr. A 1104 (2006) 11.
[7] C. Padron-Sanz, R. Halko, Z. Sosa-Ferrera, J.J. Santana-Rodriguez, J. Chromatogr. A 1078 (2005) 13.
[8] A. Bermudez-Couso, M. Arias-Estevez, J.C. Novoa-Munoz, E. Lopez-Periago, B. Soto-Gonzalez, J. Simal-Gandar, Water Res. 41 (2007) 4515.
[9] K. Kawata, T. Asada, K. Oikawa, J. Chromatogr. A 1090 (2005) 10.
[10] M.S. Diaz-Cruz, D. Barcelo, J. Chromatogr. A 1132 (2006) 21.
[11] W. Wang, B. Meng, X. Lu, Y. Liu, S. Tao, Anal. Chim. Acta 602 (2007) 211.
[12] J.A. Ferrell, W.K. Vencill, J. AOAC Int. 87 (2004) 56.
[13] E. Ayano, H. Kanazawa, M. Ando, T. Nishimura, Anal. Chim. Acta 507 (2004) 211.
[14] A.A. D'Archivio, M. Fanelli, P. Mazzeo, F. Ruggieri, Talanta 71 (2007) 25.
[15] S. Topuz, G. Ozhan, B. Alpertunga, Food Control 16 (2005) 87.
[16] E. Concha-Grana, M.I. Turnes-Carou, S. Muniategui-Lorenzo, P. Lopez-Mahia, D. Prada-Rodriguez, E. Fernandez-Fernandez, Chemosphere 64 (2006) 588.
[17] A. Hussen, R. Westbom, N. Megersa, L. Mathiasson, E. Bjorklund, J. Chromatogr. A 1152 (2007) 247.
[18] N.G. Tsiropoulos, E.B. Bakeas, V. Raptis, S.S. Batistatou, Anal. Chim. Acta 573 (2006) 209.
[19] P. Venkateswarlu, K.R. Mohan, C.R. Kumar, K. Seshaiah, Food Chem. 105 (2007) 1760.
[20] A. Hildebrandt, M. Guillamon, S. Lacorte, R. Tauler, D. Barcelo, Water Res. 42 (2008) 3315.
[21] R.M. Gonzalez-Rodriguez, R. Rial-Otero, B. Cancho-Grande, J. Simal-Gandara, J. Chromatogr. A 1196 (2008) 100.
[22] B. Mayer-Helm, L. Hofbauer, J. Müller, Talanta 74 (2008) 1184.
[23] K. Banerjee, S.H. Patil, S. Dasgupta, D.P. Oulkar, S.B. Patil, R. Savant, P.G. Adsule, J. Chromatogr. A 1190 (2008) 350.
[24] F.A. Esteve-Turrillas, A. Pastor, M. de la Guardia, Anal. Chim. Acta 553 (2005) 50.
[25] C. Soler, J. Manes, Y. Pico, J. Chromatogr. A 1048 (2004) 41.
[26] E. Conte, R. Milani, G. Morali, F. Abballe, J. Chromatogr. A 765 (1997) 121.
[27] P. Popp, P. Keil, M. Moder, A. Paschke, U. Thuss, J. Chromatogr. A 774 (1997) 203.
[28] Agritox Database, AFSSA France, 2005, www.dive.afssa.fr/agritox/php/fiches.php.
[29] National Institute for Occupational Safety and Health, in: D.V. Sweet (Ed.), Registry of Toxic Effects of Chemical Substances, vol. 1, NIOSH, Cincinnati, OH, 1993, p. 217.
[30] G. Galletti, A. Bonetti, G. Dinelli, J. Chromatogr. A 692 (1995) 27.
[31] S.A. Reinecke, A.J. Reinecke, Ecotox. Environ. Safe. 66 (2007) 92.
[32] J.L. Martinez Vidal, F.J. Arrebola, M. Mateu-Sanchez, J. Chromatogr. A 959 (2002) 203.

Rational design of a colorimetric and ratiometric fluorescent chemosensor based on intramolecular charge transfer (ICT)

Jie Shao[a], Hai Lin[b], Huakuan Lin[a],*

[a] *Department of Chemistry, Nankai University, Tianjin 300071, PR China*
[b] *Key Laboratory of Functional Polymer Materials of Ministry of Education, Nankai University, Tianjin 300071, PR China*

ABSTRACT

A simple colorimetric and ratiometric fluorescent anion sensor 1, 3,6-dichloro-1,8-dinitrocarbazole, was rationally designed and synthesized on basis of the mechanism of intramolecular charge transfer (ICT). In DMSO solutions of 1, the presence of AcO^-, F^- and $H_2PO_4^-$ gave birth to the formation of a 2:1 host-to-guest complex, which was synchronously accompanied by a 'naked-eye' color change from light yellow to purple, a red-shift of the absorption spectrum and a blue-shift of the emission spectrum.

© 2008 Elsevier B.V. All rights reserved.

1. Introduction

Nowadays, development of chemosensors capable of recognizing and sensing anions is rapidly expanding area of interest in supramolecular chemistry because anions play an important role in a wide range of chemical and biological processes [1,2]. For example, fluoride ion is drawing a special attention due to its beneficial (e.g., prevention of dental caries and treatment of osteoporosis) as well as detrimental (e.g., fluorosis) roles [3]. And phosphate is associated with a number of important biomineralization processes such as bone formation as well as pathological processes: the genesis of renal stones [4]. Accordingly, a wide variety of either positively charged or neutral organic anions sensors based on visual (naked-eye), optical (absorption, fluorescence) and electrochemical receptors have been reported to date [5–9].

During the last few years, the fluorescent sensors appear particularly attractive because they offer the potential for high sensitivity at low analyte concentration [10,11]. Most of the reported receptors upon binding with anions exhibit fluorescence intensity changes on a single wavelength [12–14]. However, several factors such as phototransformation, receptor concentration and environmental effects contribute to the fluorescence intensity modulation of a system [15]. The ratiometric fluorescence signaling, which involves the measurement of changes in the ratio of the fluorescence intensities at two different wavelengths, is preferred to the conventional method of monitoring the fluorescence intensity at a single wavelength [16–18]. Therefore, the design of the ratiometric fluorescent sensors is of great current interest [19]. The major challenge to ratiometric fluorescence signaling is developing a system with two emitting states having both the wavelength-dependent and substrate-dependent emission properties [20]. As a general rule, when a fluorophore contains an electron-donating group (often an amino group: anion binding sites) conjugated to an electron-withdrawing group (the change in dipole moment can be quite large), it undergoes intramolecular charge transfer (ICT) from the donor to the acceptor upon excitation by light. The consequent change in dipole moment results in a Stokes shift that depends on the microenvironment of the fluorophore [21,22].

Bearing these in mind, we designed and synthesized the fluorescent sensor 1, 3,6-dichloro-1,8-dinitrocarbazole, which showed ratiometric response towards anions based on the ICT mechanism. The choice of 1 as the ratiometric fluorescent sensor was mainly based on the fact that (1) the NH moiety acted as an anion binding site; (2) two –NO$_2$ groups were an electron-withdrawing group and a chromophore; (3) in this molecule, an electron-donating group (–NH as an anion binding site) was conjugated to an electron-withdrawing group. Accordingly, ratiometric sensing is possible due to altered ground and excited state energetics of the ICT probe upon anion complexation. Just as expected, the sensor 1 could act as

a convenient, colorimetric and ratiometric fluorescent chemosensor for biologically inorganic anions.

2. Experimental

2.1. Apparatus

^{1}H NMR spectra were obtained on a Varian UNITY Plus-400 MHz Spectrometer. ESI-MS was performed with a MARINER apparatus. C, H, N elemental analyses were made on an elementar vario EL. UV–vis spectra were recorded on a Shimadzu UV2450 Spectrophotometer with quartz cuvette (path length = 1 cm) and fluorescent spectra were recorded on a Shimadzu RF-5301PC Spectrophotometer at 298.2 ± 0.1 K and the width of the slits used is 10 nm.

2.2. Chemicals

All reagents for synthesis obtained commercially were used without further purification. In the titration experiments, all the anions were added in the form of tetrabutylammonium (TBA) salts, which were purchased from Sigma–Aldrich Chemical, stored in a vacuum desiccator containing self-indicating silica and dried fully before using. DMSO was dried with CaH_2 and then distilled in reduced pressure.

2.3. General method

All titration experiments were carried out at 298.2 K, unless otherwise mentioned. UV–vis spectra were measured using an UV–vis spectrophotometer, UV2450 (Shimadzu Corp., Kyoto, Japan). A 4.0×10^{-5} M solution of the compound 1 in dried DMSO and solutions of 0.10 M tetrabutylammonium (TBA) salts of the respective anions were prepared in dried DMSO and were stored under a dry atmosphere. These solutions were used for all spectroscopic studies after appropriate dilution. Then, given amount of the solution of 1 was added to the quartz cuvette and the increased amount of anions tested (0.1 M in DMSO-d_6) was added to the solution above-mentioned, whose absorbance/emission spectra was tested immediately.

^{1}H NMR titration experiments were carried out in the DMSO-d_6 solution (TMS as an internal standard). A 1.0×10^{-2} M solution of the compound 1 in DMSO-d_6 was prepared. Then, the increased amount of fluoride anion (1.0 M in DMSO-d_6) was added to the solution above-mentioned and ^{1}H NMR of the host–guest system was tested.

2.4. Synthesis

2.4.1. 3,6-Dichlorocarbazole (2)

The compounds 1 and 2 were synthesized according to the literature [23] (see Scheme 1). To a three-neck, 250 ml round-bottomed flask, carbazole (10 g, 0.06 mol) and CH_2Cl_2 (100 ml) were added and the flask was equipped with a mechanical stirrer and a thermometer. The resulting mixture was cooled to 0 °C and then SO_2Cl_2

(9.6 ml, 0.12 mol) was added dropwise while the solution was being vigorously stirred (*note*: the temperature did not exceed 2 °C). After the addition, the cooling bath was removed and the reaction mixture was stirred for another 4 h at rt. Then, the solid precipitate was filtered off, washed with CH_2Cl_2 and dried to give raw product. The raw 3,6-dichlorocarbazole was suspended in 250 ml of hexane and boiled for 0.5 h. The suspension was filtered, giving pure product (8.35 g, 59%); mp 200–203 °C (lit. 205 °C).

#### 2.4.2. 3,6-Dichloro-1,8-dinitrocarbazole (1)

To a three-neck, 250 ml round-bottomed flask, 3,6-dichlorocarbazole (8.35 g, 35 mmol), acetic acid (28 ml) and acetic anhydride (21 ml) were added and then, the flask was equipped with a magnetic stirrer, a dropping funnel and a thermometer. The solution was cooled to 1 °C and 100% HNO_3 (4.5 ml, 0.11 mol) began to be added dropwise while stirring and the temperature did not exceed 1 °C. Following the addition of 1/8 of the whole volume of HNO_3, the cooling bath was replaced with an oil bath. The mixture was heated to 60 °C and half of HNO_3 was added at this temperature. During the addition of the remaining HNO_3, the reaction mixture was further heated, until it reached to 75 °C. After the addition was completed, the temperature of the solution was elevated to 110 °C for next 10 min. Afterwards, the suspension was filtered while hot and the product was washed with boiling acetic acid (10 ml) and diethyl ether. 8.07 g (70%); mp 281–283 °C (lit. 284 °C); ^{1}H NMR (DMSO-d_6): δ 11.30 (s, 1H, NH), 8.98 (s, 2H, H-4 and H-5), 8.49 (d, 2H, $J_1 = 1.6$, H-2 and H-7); ESI-mass: m/z calcd. for $C_{12}H_5N_3O_4Cl_2$ [M]$^+$: 324.97, found: 324.30; elemental analysis calcd. for $C_{12}H_5N_3O_4Cl_2$: C, 44.20; H, 1.55; N, 12.89; found: C, 44.36; H, 1.61; N, 12.85.

3. Results and discussion

The anions binding ability of the receptor 1 with F$^-$, Cl$^-$, Br$^-$, I$^-$, AcO$^-$ and $H_2PO_4^-$ in DMSO was explored with the naked-eye experiment, the UV–vis absorption, the fluorescence spectrometry and the ^{1}H NMR titration. The anions tested were used as tetrabutylammonium salts to 4.0×10^{-5} M solutions of the host molecule 1 in DMSO.

3.1. Colorimetric signaling and UV–vis spectral titrations

The analyte recognition via hydrogen-bonding interactions could be easily followed by the naked-eye or by monitoring the changes in the UV–vis absorption spectra of the receptor 1. Initially, the qualitative estimation of the affinity of the sensor 1 towards various anions was performed visually (see Fig. 1). Instantaneous color changes were observed from light yellow to purple upon addition of 8 equiv of F$^-$, AcO$^-$ or $H_2PO_4^-$ to DMSO solutions of 1 (4.0×10^{-5} M). Conversely, no detectable color changes was observed even addition of a large excess of Cl$^-$, Br$^-$ and I$^-$ (up to 50 equiv) to the sensor 1. It is noteworthy that, for 1, the naked-eye color changes were fully reversible upon addition of water, which presumably competed with the anions for the binding site [24]. The result indicated that the color changes were most probably
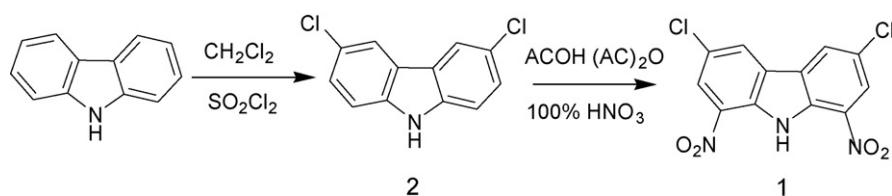
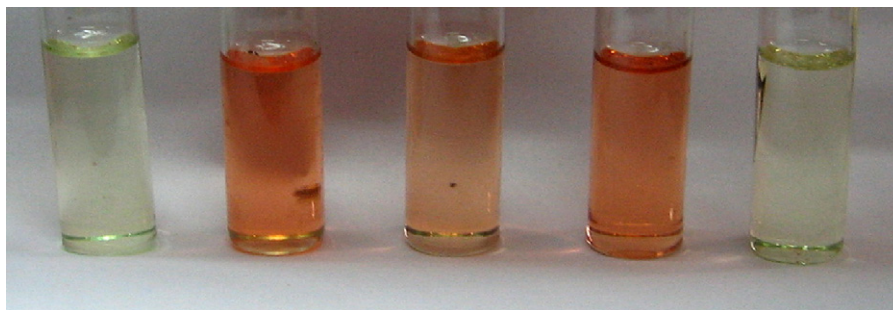**Scheme 1.** General synthetic routes to the target compound 1.

Fig. 1. Color response of the receptor 1 in DMSO (4.0×10^{-5} M) to the addition of anions (from the left to the right: 1 only, 1+ 8 equiv AcO$^-$, 1+ 8 equiv H$_2$PO$_4$$^-$, 1 + 8 equiv F$^-$, 1 + miscellaneous anions including 8 equiv Cl$^-$, 8 equiv Br$^-$ and 8 equiv I$^-$, respectively).

owing to the formation of the new 1 anion complexed species with different electronic properties from that of the receptor 1 and therefore, a new color (purple) was observed.

Fig. 2 showed the family of spectra recorded on titrating a DMSO solution 4.0×10^{-5} M of 1 with a standard DMSO solution of [Bu$_4$N] AcO. Care was taken to avoid the contamination by water during the preparation of the solution and titration. Obviously seen from Fig. 2, the compound 1 was characterized by a broad strong absorption band centered at 370 nm and a weak absorption band centered at 256 nm. As the concentration of AcO$^-$ increased stepwise, the peak at the λ_{max} of 370 nm, the $\pi-\pi^*$ transition of the chromophore, disappeared gradually, the absorption intensity at 256 nm increased and a new band at 510 nm appeared, which was intramolecular charge transfer (ICT) band [25]. At the same time, the color of the sensor solution changed from light yellow to purple. The results obtained demonstrated the H-bond interactions between the host and the anionic guests affected the electronic properties of the chromophore, resulting in a new charge transfer interaction between the electron rich –NH moiety bond anion and the electron deficient –NO$_2$ moiety along with a color change [26]. In addition, there were two well-defined isosbestic points at 306 and 425 nm, respectively, indicating that the stable complex having a certain stoichiometric ratio between the receptor 1 and AcO$^-$ anion formed [27]. A job plot indicated the formation of a 2:1 1-to-F$^-$ complex (see Fig. 3). Similar changes were observed in UV–vis spectra of 1 upon addition of F$^-$ and H$_2$PO$_4$$^-$ ions. Nevertheless, the receptor 1 was insensitive to addition of excess equiv. Cl$^-$, Br$^-$ and I$^-$ ions (see Fig. 4).

Fig. 3. The stoichiometry analysis of complex 1·AcO$^-$ by Job plot analysis.

3.2. Association constants

The 2:1 host–guest interaction was analyzed according to Benesi–Hildebrand equations for spectroscopic UV–vis titration (Eq. (1)) [28]

$$\frac{A_0}{A - A_0} = \left(\frac{\varepsilon_0}{\varepsilon_0 - \varepsilon}\right)^2 \left(\frac{1}{K_B[\text{substrate}]^2} + 1\right) \qquad (1)$$
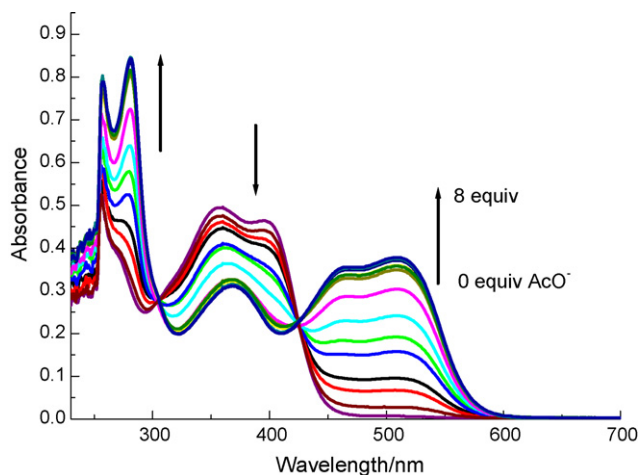

Fig. 2. Evolution of the UV–vis spectrum of the receptor 1 (4.0×10^{-5} M in DMSO) during the titration with tetrabutylammoniun (TBA) AcO$^-$.
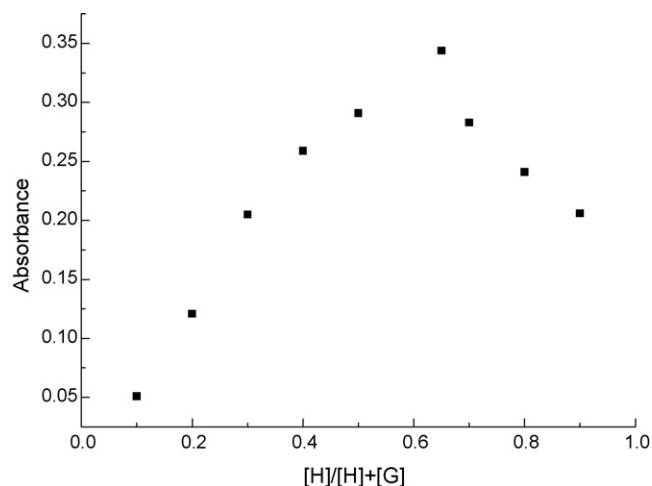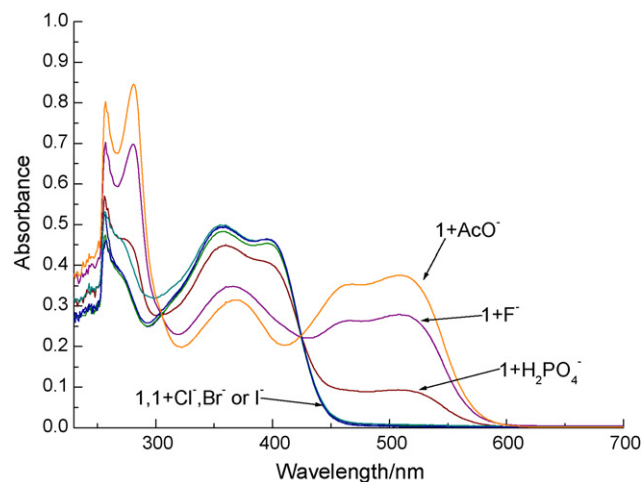

Fig. 4. UV–vis spectral changes of the receptor 1 in DMSO (4.0×10^{-5} M) upon addition of 8 equiv different anions.

Fig. 5. Fluorescent changes of the receptor 1 in DMSO (4.0×10^{-5} M) upon addition of AcO⁻ ions.

Fig. 6. ^{1}H NMR spectra of the receptor 1 in DMSO-d_6 (1×10^{-2} M) upon addition of molar equiv. of F⁻.

A_0 and A are the absorbance of 1 in the absence and presence of the anion analytes, respectively; ε_0 and ε are the corresponding molar absorption coefficients of 1 in the absence and presence of the anion analytes, respectively. [substrate] is the concentration of the titrants and K_B represents the association constant of host–guest complexation. Job plot and Specfit analysis of the titration dada gave substantial association constant values for 2:1 complexes shown in Table 1. The association constants log K_{ass} of the receptor 1 for acetate was calculated to be 8.07 (dependent coefficient: $R^2 = 0.992$). In the case of Cl⁻, Br⁻ and I⁻, the spectral changes were too small to calculate the corresponding association constants. The results unambiguously demonstrated the strong binding ability of 1 for acetate. In addition, with the receptor 1 the strongest complex was formed with AcO⁻. The selectivity for AcO⁻ could be rationalized on the basis of the anionic basicity and the shape complementarity between the host and the anionic guests [29].

3.3. Photophysical properties of 1 upon binding with anions

Fluorescence studies of the interactions of anions with the receptor 1 were also conducted by observing emission spectra with excitation at 354 nm. Just as Fig. 5 showed, the free 1 exhibited one main emission band centered at 510 nm with a shoulder at 400 nm.

The addition of AcO⁻ ions to a solution of 1 (4.0×10^{-5} M) in DMSO resulted in a dramatic decrease in the intensity of the emission band at 510 nm along with an increase in the intensity of the emission band at 400 nm. Such a significant blue-shift (a ∼110-nm emission band shift from 510 to 400 nm) was rarely seen in the ever-reported ICT anion sensors. Interestingly, there is an increasing band around 510 nm observed in the UV–vis absorption spectra of 1 with the addition of AcO⁻. This would indicate that the blue-shift of fluorescence spectra was caused by a change of the charge transfer character of the emissive species [22,30]. When the anion interacted with the binding site, the excited state was more strongly destabilized by the anion than the ground state, and consequently, a blue-shift of the emission spectra was expected. In addition, the presence of F⁻ and H₂PO₄⁻ induced similar changes in fluorescent spectrum with AcO⁻, but addition of excess equiv. Cl⁻, Br⁻ and I⁻ ions had slight effects on fluorescence intensity.

3.4. ^{1}H NMR titrations

To further shed light on the nature of the interactions between 1 and the anions, as an example, ^{1}H NMR spectral changes upon addition of F⁻ as their tetrabutylammonium salts to the

Scheme 2. The proposed host–guest binding mode in solution.

DMSO-d_6 solution of 1 $(1 \times 10^{-2} \, \mathrm{mol \, L^{-1}})$ were investigated. Obviously observed from Fig. 6, the peak at 11.30 ppm, which was assigned to –NH, broadened and exhibited a downfield shift to 13.16 ppm upon addition of different equiv F$^-$ indicating the strong hydrogen-bonding interactions occurred between 1 and F$^-$ ion [31]. The phenyl protons signal exhibited a slight upfield shift which indicated the increase of the electron density on the phenyl ring owing to the through-bond effects. According to the results from UV–vis spectral titration, fluorescent titration and ^{1}H NMR titration, the proposed host–guest binding mode in solution was depicted in Scheme 2. In the complex structure, an anion such as F$^-$ was located on a center of inversion bound by two molecule of 1 *via* N–H···anion hydrogen bonds. In other words, there was the dimer of 3,6-dichloro-1,8-dinitrocarbazole directed by anions through hydrogen-bonding interactions in DMSO solution [32].

4. Conclusion

In summary, we have successfully presented a colorimetric and ratiometric fluorescent anion sensor based on an intramolecular charge transfer mechanism. The obvious blue-shift emission upon addition of anions such as AcO$^-$, F$^-$ and H$_2$PO$_4^-$ to 1 can be observed and it was attributed to the capture of anions by the NH moiety leading to a reduction in conjugation. For practical applications, signal detecting is more effective in the ratiometric sensor 1. Even better is the ratiometric sensor that display distinct color changes for fast and efficient sensing. There is an anion-assisted dimer of the host molecule in DMSO, which is supported by UV–vis spectral titration, fluorescent titration and ^{1}H NMR titration. Particularly, the design strategy and remarkable photophysical properties of the sensor would help to extend the development of fluorescent sensors for biologically inorganic anions.

Acknowledgement

References

[1] V. Amendola, D. Esteban-Gomez, L. Fabbrizzi, M. Licchelli, Acc. Chem. Res. 39 (2006) 343–353.
[2] R. Martinez-Manez, F. Sancenon, Coord. Chem. Rev. 250 (2006) 3081–3093.
[3] J. Shao, M. Yu, H. Lin, H.K. Lin, Spectrochim. Acta: A: Mol. Biomol. Spectrosc 70 (2008) 1217–1221.
[4] F. Grases, J.G. March, Anal. Chim. Acta 229 (1990) 249–254.
[5] C.X. Liu, X.H. Qian, G.Q. Sun, L.W. Zhao, Z. Li, New J. Chem. 32 (2008) 472–476.
[6] M. Zhang, M.Y. Li, F.Y. Li, Y.F. Cheng, J.P. Zhang, T. Yi, C.H. Huang, Dyes Pigments 77 (2008) 408–414.
[7] J. Shao, H. Lin, H.K. Lin, Talanta 75 (2008) 1015–1020.
[8] A. Goel, N. Brennan, N. Brady, P.T.M. Kenny, Biosens. Bioelectron. 22 (2007) 2047–2050.
[9] Y.H. Wang, H. Lin, J. Shao, Z.S. Cai, H.K. Lin, Talanta 74 (2008) 1122–1125.
[10] T. Gunnlaugsson, M. Glynn, G.M. Tocci (née Hussey), P.E. Kruger, F.M. Pfeffer, Coord. Chem. Rev. 250 (2006) 3094–3117.
[11] R. Martinez-Manez, F. Sancenon, Chem. Rev. 103 (2003) 4419–4476.
[12] K. Ghosh, A.R. Sarkar, G. Masanta, Tetrahedron Lett. 48 (2007) 8725–8729.
[13] R. Shen, X.B. Pan, H.F. Wang, J.C. Wu, N. Tang, Inorg. Chem. Commun. 11 (2008) 318–322.
[14] X.F. Yang, S.J. Ye, Q. Bai, X.Q. Wang, J. Fluoresc. 17 (2007) 81–87.
[15] T.Y. Joo, N. Singh, G.W. Lee, D.O. Jang, Tetrahedron Lett. 48 (2007) 8846–8850.
[16] V. Thiagarajan, P. Ramamurthy, D. Thirumalai, V.T. Ramakrishnan, Org. Lett. 7 (2005) 657–660.
[17] E.M. Nolan, S.J. Lippard, J. Am. Chem. Soc. 129 (2007) 5910–5918.
[18] X. Peng, Y. Wu, J. Fan, M. Tian, K. Han, J. Org. Chem. 70 (2005) 10524–10531.
[19] C.L. Chen, Y.H. Chen, C.Y. Chen, S.S. Sun, Org. Lett. 8 (2006) 5053–5056.
[20] Y. Zhang, X. Guo, W. Si, L. Jia, X. Qian, Org. Lett. 10 (2008) 473–476.
[21] K. Rurack, A. Danel, K. Rotkiewicz, D. Grabka, M. Spieles, W. Rettig, Org. Lett. 4 (2002) 4647–4650.
[22] B. Valeur, Molecular Fluorescence: Principles and Applications, Weinheim, New York, 2001, pp. 298–299.
[23] M.J. Chmielewski, M. Charon, J. Jurczak, Org. Lett. 6 (2004) 3501–3504.
[24] J. Shao, H. Lin, H.K. Lin, Spectrochim. Acta: A 70 (2008) 682–685.
[25] J. Shao, H. Lin, M. Yu, H.K. Lin, Talanta 75 (2008) 551–555.
[26] J. Shao, H. Lin, X.F. Shang, H.M. Chen, H.K. Lin, J. Incl. Phenom. Macrocycl. Chem. 59 (2007) 371–375.
[27] Y. Kubo, M. Kato, Y. Yoshihiro Misawa, S. Tokita, Tetrahedron Lett. 45 (2004) 3769–3773.
[28] C.F. Chow, M.H.W. Lam, W.Y. Wong, Inorg. Chem. 43 (2004) 8387–8393.
[29] I.V. Korendovych, M. Cho, P.L. Butler, R.J. Staples, E.V. Rybak-Akimova, Org. Lett. 8 (2006) 3171–3174.
[30] Z. Xu, Y. Xiao, X. Qian, J. Cui, D. Cui, Org. Lett. (2005) 889–892.
[31] M. Bonizzoni, L. Fabbrizzi, A. Taglietti, F. Tiengo, Eur. J. Org. Chem. (2006) 3567–3574.
[32] S.J. Coles, J.G. Frey, P.A. Gale, M.B. Hursthouse, M.E. Light, K. Navakhun, G.L. Thomas, Chem. Commun. (2003) 568–569.

Improved microfluidic chip-based sequential-injection trapped-droplet array liquid–liquid extraction system for determination of aluminium

Hong Shen, Qun Fang*

Institute of Microanalytical Systems, Department of Chemistry, Zhejiang University, Hangzhou, China

ABSTRACT

An improved microfluidic chip-based sequential-injection trapped-droplet array liquid–liquid extraction system with chemiluminescence (CL) detection was developed in this work. Two recess arrays were fabricated on both sides of the extraction channel to produce droplet arrays of organic extractant. A chip integrated monolithic probe was fabricated at the inlet of the extraction channel on the glass chip instead of the capillary probe connected to the microchannel, in order to improve the system stability and reliability. A slotted-vial array system coupled with the monolithic probe was used to sequentially introduce sample and different solvents and reagents into the extraction channel for extraction and CL detection. The performance of the system was demonstrated in the determination of Al^{3+} using Al^{3+}-dihydroxyazobenzene (DHAB) and tributyl phosphate (TBP) extraction system. The operation conditions, including extraction time, concentration and flow rate of the CL reagents, were optimized. Within one analysis cycle of 12 min, an enrichment factor of 85 was obtained in the extraction stage with a sample consumption of 1.8 μL. The consumption of CL reagent, bis(2-carbopentyloxy-3,5,6-trichlorophenyl)oxalate (CPPO), was 120 nL/cycle. The detection limit of the system for Al^{3+} was 1.6×10^{-6} mol/L with a precision of 4.5% (R.S.D., $n = 6$).

© 2008 Elsevier B.V. All rights reserved.

1. Introduction

In recent years, the researches on miniaturized total analysis system (μ-TAS) have made great progress [1–4]. Various microfluidic chip-based analysis systems, including liquid–liquid (L–L) extraction systems, have been developed.

Since 2000, Kitamori's group has reported a series of chip-based L–L extraction systems [5–10] with advantages of extremely low sample and reagent consumption and high extraction efficiency owing to the enhanced interfacing area/volume ratio as well as reduced diffusion distance. These miniaturized L–L extraction systems were applied in the determination of metal ions, such as Fe^{2+} [5], Ni^{2+} [6], Co^{2+} [7–9], Na^+ and K^+ [10]. Kitamura's group [11] also reported a microfluidic chip-based extraction system with a Y-shaped extraction channel using Al^{3+}-dihydroxyazobenzene (DHAB) solution and *n*-butanol as aqueous sample and organic extractant, respectively. A fluorescence microscope was used to monitor the fluorescence intensity of Al^{3+}-DHAB extracted into the *n*-butanol flow to study the effects of extraction time and diffusion distance on the spatially distribution of Al^{3+}-DHAB in the

organic phase both along the flow direction and the channel-width direction. Recently, Bowden et al. reported a microfluidic chip format performing non-aqueous L–L extraction for separation of petroleum composition before GC analysis [12]. In most of these systems, continuous multiphase laminar flow mode was adopted in Y-shaped or ψ-shaped extraction channels, in which higher enrichment factors over 10 were difficult to achieve due to the relatively low aqueous/organic phase ratio under continuous laminar flow mode.

In 2004, we developed a chip-based L–L extraction system based on droplet trapping technique and stopped-flow extraction mode, achieving high enrichment factors of 1000–2000 [13]. Based on this work, recently we developed a chip-based sequential-injection droplet array L–L extraction system [14] with chemiluminescence (CL) detection, in which two droplet arrays of extractant on both sides of the extraction channel were produced using the droplet trapping technique. Compared with the single-droplet system [13], more amount of analyte could be extracted into the organic extractant phase in the droplet arrays, thus the detection sensitivity of the chip system was significantly increased. A fluorescent dye butyl rhodamine B (BRB) was used as a model sample to demonstrate the system performance. However, in a prolonged extraction process, the flow rates of the fluids (especially the aqueous fluids) in the extraction channel tended to decrease with the increase of extraction time, due to the change of microchannel surface property resulted from the dissolving of the epoxy glue at

* Corresponding author at: Institute of Microanalytical Systems, Chemistry Experiment Center, Room 101, Zhejiang University (Zijingang Campus), Hangzhou 310058, China. Tel.: +86 571 88206771; fax: +86 571 88273496.

E-mail address: fangqun@zju.edu.cn (Q. Fang).

the interface of the capillary probe and microchannel by organic solvent.

In the present work, the stability and reliability of the previous chip-based extraction system was improved by using a chip-integrated monolithic probe instead of the fused-silica capillary probe connected with the chip microchannel. The system performance was demonstrated in the determination of Al^{3+} using Al^{3+}-DHAB and tributyl phosphate (TBP) extraction system and CL detection. Such an extraction system for determination of Al^{3+} was employed in several extraction systems with absorbance [15,16] or fluorescence [11,16] detection systems. In this work, we employed the bis(2-carbopentyloxy-3,5,6-trichlorophenyl)oxalate (CPPO) CL reaction system for the detection of Al^{3+}-DHAB after the extraction and preconcentration, which has the advantages of high detection sensitivity and simple structure for detection system without the need of light source. Similar CL system has been used for Al^{3+} detection in conventional analysis systems [17,18], with a sample and reagent consumption in the range 0.1–10 mL. To the best of our knowledge, so far such approach has not been applied in chip-based system.

2. Experimental

2.1. Chemicals and reagents

All chemicals used were of analytical reagent grade unless mentioned otherwise. Demineralized water (18 MΩ cm) was used throughout.

CPPO was obtained from Senjie Chemical Auxiliary Co. (ZiBo, China), and used without further purification. A 3 mg/mL CPPO solution was prepared every 2 days by dissolving 6 mg CPPO in 2 mL acetonitrile in a borosilicate glass flask. NH_4Ac buffer solution (pH 6.3) was prepared by dissolving 25 g NH_4Ac in water, adjusting the pH to 6.3 using 0.1 mol/L HCl, and made up to 100 mL with water. Aqueous stock solution of 1×10^{-3} mol/L Al^{3+} was prepared by dissolving 0.028 g $Al(NO)_3 \cdot 9H_2O$ (Xinjida Chemical Co., Taiyuan, China) in 100 mL NH_4Ac buffer solution. Aqueous stock solution of 1×10^{-3} mol/L DHAB was prepared by dissolving 0.021 g DHAB in 100 mL buffer solution. The stock Al^{3+}-DHAB solution was prepared by mixing 25 mL Al^{3+} solution with 25 mL DHAB solution [11,15]. The series of Al^{3+}-DHAB working solutions in the range of 1×10^{-4} to 1×10^{-6} mol/L were prepared by sequentially diluting the stock solution with the buffer solution. TBP obtained from Xudong Chemical Co. (Beijing, China) was used as extractant. H_2O_2 10% solution was prepared daily by diluting 30% H_2O_2 solution with water.

2.2. Microchip and apparatus

The schematic diagram of the analytical system with microchip is shown in Fig. 1. The microchip was fabricated using a procedure detailed elsewhere [19,20]. An extraction channel ($L8$ cm × $W90$ μm × $D25$ μm) was fabricated through the chip (80 mm × 30 mm). Two recess arrays with a length of 10 mm and 134 recesses ($L100$ μm × $W50$ μm × $D25$ μm) in each array were fabricated on both sides of the extraction channel. At the inlet end of the extraction channel, the chip was ground using an emery drill (Shang Gong International Precision Tool Co., Shanghai, China) into a needle-shaped probe with a tip size of ~200 μm (as shown in Fig. 1) to serve as a sampling probe [21]. At the outlet end of the extraction channel, the chip was ground into a cylinder (5 mm o.d., 10-mm long), which was connected with a Tygon tube (5 mm o.d., 100-cm long).

The slotted-vial array sample presenting system produced by micropipettes with slotted tip and the CL detection system (as
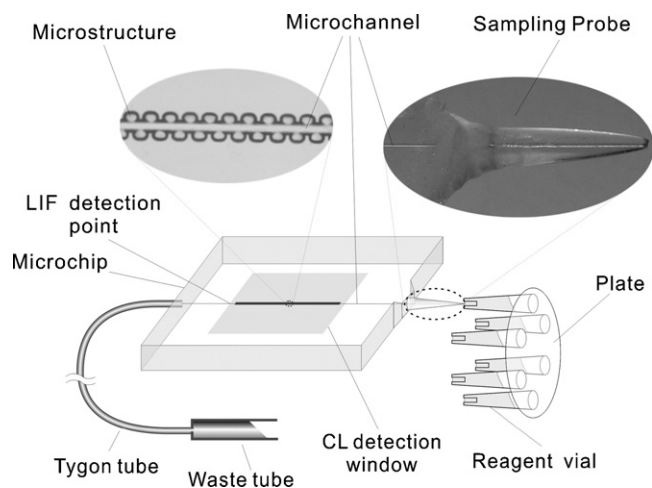
Fig. 1. Schematic diagram of the chip-based sequential-injection trapped-droplet array liquid–liquid extraction system.

shown in Fig. 1) used in this work was similar to those described in the previously reported work [22]. A photomultiplier tube (PMT, CR114, Beijing Hamamatsu Co., Beijing, China) equipped with a luminescence meter (model GD-1, Ruike Electronics, Xian, China) was used for detection of CL light. The PMT window was placed closely beneath the central section of the chip. The chip and PMT were situated within a black light-proof box. The signal was recorded by computer through a data acquisition card (818HG, Advantech Co., Hangzhou, China). For the evaluation of enrichment factor during extraction process, a home-built confocal microscope laser induced fluorescence (LIF) system [13] was used with a detection point as shown in Fig. 1.

2.3. Procedures

The six vials in the sample presenting system were filled with 500 μL of acetonitrile, TBP and aqueous Al^{3+}-DHAB (or DHAB blank) solutions, 10% H_2O_2 solution, water and CPPO acetonitrile solution, respectively. Gravity driven hydrostatic flows used for sequentially introducing sample and reagents into the chip microchannel were generated by lowering the outlet of the waste tube. Operational program of the system is shown in Table 1.

The evaluation for the enrichment factors in different extraction times was performed as described elsewhere [13], except that 1×10^{-5} mol/L Al^{3+}-DHAB aqueous solution was used as sample and TBP as extractant instead.

3. Results and discussion

3.1. System design

In our previously reported chip-based L–L extraction system [14], a fused-silica capillary serving as a probe for sample/reagents introduction was connected to the microchannel on the chip and fixed with epoxy glue. During prolonged analysis processes, the epoxy at the interface of the capillary and microchannel was swelled and dissolved by exposure to the organic solvent for L–L extraction, which may partially block the microchannel and change the channel surface property, resulting in the decrease of flow rate for the fluids in the channel using gravity driving system.

In this work, a monolithic probe [21] was fabricated at the inlet of the extraction channel to avoid the connecting of a capillary with the microchannel and the subsequent use of epoxy glue at the interface. The working stability and reliability were significantly

Table 1
Operational program of the system

Step	Flow rate (μL/min)	Liquid-level difference[a] (cm)	Time (s)	Function
1	0.35	55	20	Rinsing of the microchannel and recesses by CH_3CN
2	0.35	55	20	Displacement of CH_3CN by TBP in extraction channel and recesses.
3	0.18	25	600	Displacement of TBP by Al^{3+}-DHAB solution in extraction channel. Formation of trapped TBP droplet array in recesses. Continuous extraction of Al^{3+}-DHAB from sample solution into TBP droplets
4	0.35	55	20	Displacement of Al^{3+}-DHAB solution from extraction channel by H_2O_2 solution
5	0	0	2	Rinsing of probe tip by water
6	0.35	55	20	Introduction of CPPO acetonitrile solution; mixing of CPPO, H_2O_2 and Al^{3+}-DHAB in the microchannel initiating CL reaction

[a] The liquid-level difference between the sampling probe and the waste tube.

improved due to the good smoothness of the whole extraction channel by the use of monolithic probe. During the experiments over several months, no evident variation on the flow rate of the fluids in extraction channel was observed.

In the previous L–L extraction system [14], for simplifying the operation, the peroxyoxalate reagent CPPO for CL detection was pre-dissolved in the organic extractant before the L–L extraction. However, with such an arrangement, a compromise choice for organic solvent had to be made between the optimized L–L extraction and CL detection conditions, which may result in the discount of the system performance.

In this work, different organic solvents, TBP and acetonitrile, were employed as the extractant and solvent for CPPO, respectively. Therefore, L–L extraction could be performed under optimized conditions as in conventional L–L extraction systems [16]. The versatility of this system was improved by allowing the use of different solvent for extraction and detection. After the L–L extraction and preconcentration process, H_2O_2 aqueous solution and CPPO acetonitrile solution were sequentially introduced into the extraction channel for CL detection (CL reaction equations [23] are shown in Fig. 2).

3.2. Effects of extraction time

In this work, the extraction and preconcentration for Al^{3+} in the extractant droplet array by L–L extraction was carried out before the initiating of the CL reaction, which occupied most of the analysis time. The effects of extraction time in the range of 0–18 min on the enrichment factor of Al^{3+} were studied using 1×10^{-5} mol/L Al^{3+}-DHAB aqueous solution as sample. The results are shown in Fig. 3. The enrichment factors increased with the time up to about 10 min, beyond which the enrichment factors reduced due to the decrease of TBP droplet volume produced by the dissolving of TBP in the continuous aqueous sample flow. Therefore, an extraction time of 10 min was chosen to obtain the highest enrichment factor of 85.
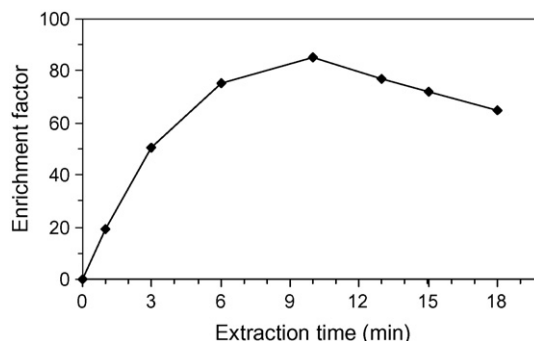
Fig. 3. Effects of extraction time on enrichment factor.

3.3. Effects of H_2O_2 solution concentration

The effects of H_2O_2 solution concentration were studied in the range 5–15%. The results are shown in Fig. 4. H_2O_2 10% solution showed highest CL intensity. In most of the conventional CL reaction systems with CPPO and H_2O_2, the CL intensity usually increases with H_2O_2 concentration. In the present system, the CL intensity decreased with the increase of H_2O_2 concentration in the range higher than 10%. This may be due to the excessive consumption of CPPO in higher H_2O_2 concentration [23] when CPPO solution was mixed with H_2O_2 aqueous solution filled in the extraction channel before reaction with Al^{3+}-DHAB.

3.4. Effects of concentration and flow rate of CPPO acetonitrile solution

In CPPO CL reaction system, a higher CPPO concentration will benefit the increase of the reaction speed and detection sensitivity [24]. However, the increase of CPPO concentration is limited by its solubility in acetonitrile and instability in high concentration. Furthermore, it was observed that the blank solutions with DHAB
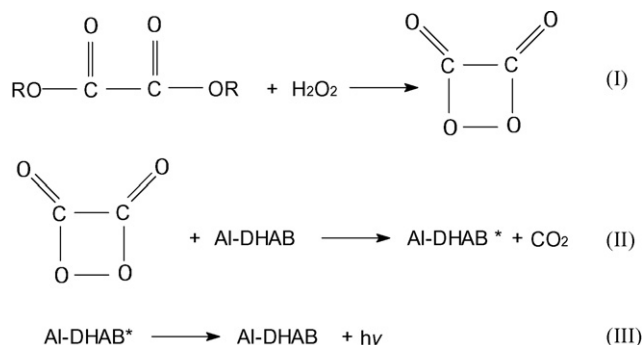
Fig. 2. Equations of CPPO CL reaction.
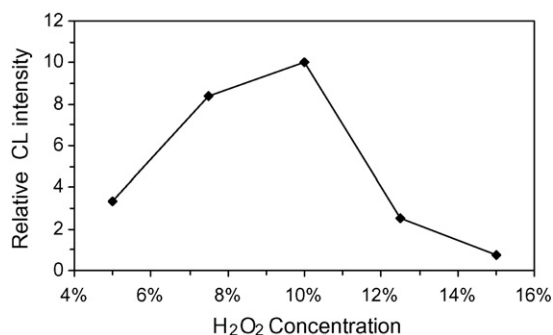
Fig. 4. Effects of H_2O_2 solution concentration.
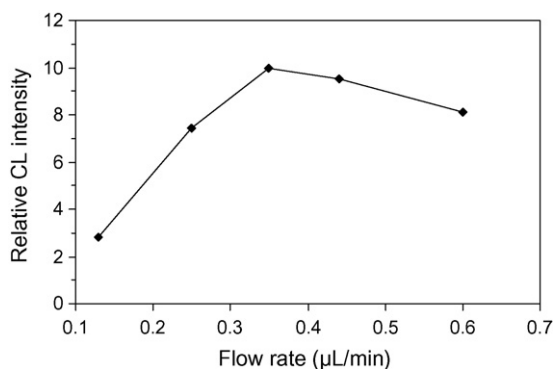
Fig. 5. Effect of flow rate of CPPO acetonitrile solution on CL intensity.
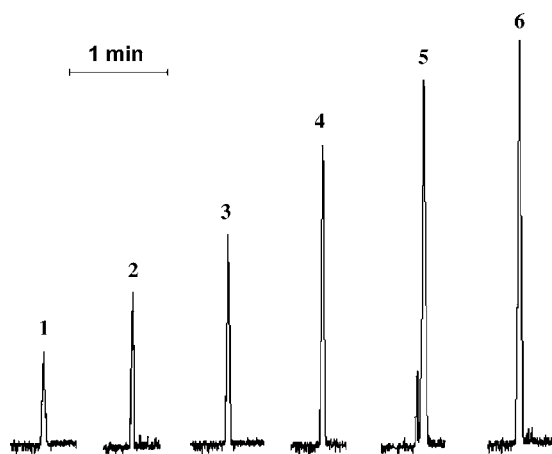
Fig. 6. Typical recordings of sequential determination of DHAB blank solution and 5×10^{-6}, 1.0×10^{-5}, 1.5×10^{-5}, 2.0×10^{-5}, 2.5×10^{-5} mol/L Al^{3+}-DHAB solutions (samples 2, 3, 4, 5 and 6) to show the linear relationship between CL intensity and Al^{3+} concentration.

could also produce a CL signal when mixed with H_2O_2 and CPPO solutions. Such background signals maybe caused by the catalyzing effect of the impurity in CPPO solution on the reaction of H_2O_2 and CPPO, showed increasing trend with the increase of CPPO concentration. Therefore, a medium CPPO concentration of 3 mg/mL was chosen.

The effect of flow rates of CPPO solution on CL intensity was investigated within a range of 0.13–0.60 μL/min. The results are shown in Fig. 5. Flow rate of 0.35 μL/min demonstrated the highest CL intensity, and was adopted in the following experiments.

3.5. Analytical performance

The performance of the system was demonstrated in the determination of Al^{3+} aqueous sample under optimized conditions. The reproducibility of repetitive measurement for a 1.0×10^{-5} mol/L Al^{3+} solution was 4.5% (R.S.D., $n = 6$). A linear response was obtained in the range of 5×10^{-6} to 2.5×10^{-5} mol/L Al^{3+}, with a regression

equation of $I = 3.52 \times 10^6 c + 0.65$ ($r^2 = 0.9926$) (as shown in Fig. 6). The limit of detection for Al^{3+} based on three times the standard deviation of the blank signals was 1.6×10^{-6} mol/L, corresponding to an amount of 2.9×10^{-12} mol Al^{3+}. The total analysis time for one cycle was 12 min, with consumptions for sample and CPPO solution of 1.8 μL and 120 nL, respectively. The volume of the organic phase droplet array trapped in the recesses was ca. 17 nL, estimated from the data of number and size of the recesses.

4. Conclusion

In this work, the stability and reliability of the microfluidic chip-based sequential-injection droplet array L–L extraction system was improved by using a chip integrated monolithic probe coupled with a slotted-vial array liquid-presenting system. The versatility of the system was demonstrated in the determination of Al^{3+} with CL detection using Al^{3+}-DHAB and TBP extraction system and CPPO CL reaction system. In addition to coupling with on-line spectrometric detection approaches, such as fluorescence, absorbance and CL detection, the chip-based droplet array L–L extraction system also provided a potential sample pretreatment platform for gas or liquid chromatography as well as mass spectrometry, by fabricating multi-channel array with droplet array on one chip or increasing the recess number as well as the recess capacity to increase the treated sample amount.

Acknowledgements

References

[1] D.R. Reyes, D. Iossifidis, P.-A. Auroux, A. Manz, Anal. Chem. 74 (2002) 2623.
[2] P.-A. Auroux, D.R. Reyes, D. Iossifidis, A. Manz, Anal. Chem. 74 (2002) 2637.
[3] T. Vilkner, D. Janasek, A. Manz, Anal. Chem. 76 (2004) 3373.
[4] P.S. Dittrich, K. Tachikawa, A. Manz, Anal. Chem. 78 (2006) 3887.
[5] M. Tokeshi, T. Minagawa, T. Kitamori, Anal. Chem. 72 (2000) 1711.
[6] K. Sato, M. Tokeshi, T. Sawada, T. Kitamori, Anal. Sci. 16 (2000) 455.
[7] M. Tokeshi, T. Minagawa, T. Kitamori, J. Chromatogr. A 894 (2000) 19.
[8] T. Minagawa, M. Tokeshi, T. Kitamori, Lab Chip 1 (2001) 72.
[9] A. Hibara, M. Tokeshi, K. Uchiyama, H. Hisamoto, T. Kitamori, Anal. Sci. 17 (2001) 89.
[10] H. Hisamoto, T. Horiuchi, K. Uchiyama, M. Tokeshi, A. Hibara, T. Kitamori, Anal. Chem. 73 (2001) 5551.
[11] H.B. Kim, K. Ueno, M. Chiba, O. Kogi, N. Kitamura, Anal. Sci. 16 (2000) 871.
[12] S.A. Bowden, P.B. Monaghan, R. Wilson, J. Parnella, J.M. Cooper, Lab Chip 6 (2006) 740.
[13] H. Chen, Q. Fang, X.-F. Yin, Z.-L. Fang, Lab Chip 5 (2005) 719.
[14] H. Shen, Q. Fang, Z.-L. Fang, Lab Chip 6 (2006) 1387.
[15] O. Kogi, H.B. Kim, N. Kitamura, Anal. Chim. Acta 418 (2000) 129.
[16] K. Watanabe, H. Yoshizawa, K. Kawagaki, Bunseki Kagaku 30 (1981) 640.
[17] M. Du, W.-C. Huie, Anal. Chim. Acta 443 (2001) 269.
[18] K. Sato, S. Tanaka, Microchem. J. 53 (1996) 93.
[19] X.-F. Yin, H. Shen, Z.-L. Fang, Chin. J. Anal. Chem. 31 (2003) 116.
[20] Z.-J. Jia, Q. Fang, W.-B. Du, Z.-L. Fang, Anal. Chem. 76 (2004) 5597.
[21] Q.-H. He, Q. Fang, W.-B. Du, Z.-L. Fang, Electrophoresis 28 (2007) 2912.
[22] W.-B. Du, Q. Fang, Q.-H. He, Z.-L. Fang, Anal. Chem. 77 (2005) 1330.
[23] K.W. Slgvardson, J.W. Birks, Anal. Chem. 55 (1983) 432.
[24] M.M. Rauhut, B.G. Roberts, A.M. Semsel, J. Am. Chem. Soc. 88 (1966) 3604.

Contents lists available at ScienceDirect

Talanta

Development of a photosystem II-based optical microfluidic sensor for herbicide detection

Dimitrios G. Varsamis [a,*], Eleftherios Touloupakis [b], Pietro Morlacchi [c], Demetrios F. Ghanotakis [b], Maria Teresa Giardi [c], David C. Cullen [a]

[a] Cranfield Health, Cranfield University, Cranfield, Bedfordshire, MK43 0AL, UK
[b] Department of Chemistry, University of Crete, 71003 Voutes-Heraklion, Crete, Greece
[c] Institute of Crystallography, National Research Council (CNR), Via Salaria km 29.300, 00016 Monterotondo Scalo, Rome, Italy

ARTICLE INFO

ABSTRACT

Herbicides are highly toxic for both human and animal health. The increased application of herbicides in agriculture during the last decades has resulted in the contamination of both soil and water. Herbicides, under illumination, can inhibit photosystem II electron transfer. Photosynthetic membranes isolated from higher plants and photosynthetic micro-organisms, immobilized and stabilized, can serve as a biorecognition element for a biosensor. The inhibition of photosystem II causes a reduced photoinduced production of hydrogen peroxide, which can be measured by a chemiluminescence reaction with luminol and the enzyme horseradish peroxidase. In the present work, a compact and portable sensing device that combines the production and detection of hydrogen peroxide in a single flow assay is proposed for herbicide detection.

© 2008 Elsevier B.V. All rights reserved.

1. Introduction

The detection of environmental hazardous chemicals using sensor technology has been rising in demand [1–3]. Chemicals such as herbicides, fungicides and insecticides may exist in harmful levels and pose an environmental threat. Even low levels of contaminants can cause adverse effects on humans, plants, animals and ecosystems. The application of herbicides has increased appreciably during the past few decades, resulting in the massive pollution of water and soil. About 40% of herbicides (derivatives of phenylurea, triazine, diazine and phenolic types) that are currently in use inhibit the light reactions of photosynthesis (photosynthetic herbicides); usually by targeting photosystem II (PSII)-dependent electron flow [4].

At present, the modern methods of herbicide detection are HPLC, GC–MS and bioassays. These methods require expensive equipment, shipment of samples to the laboratories and highly qualified personnel for the analysis [5,6].

Photosystem II is a multisubunit complex located in the thylakoid membranes of algae, cyanobacteria and higher plants. It uses light energy to catalyze a series of electron transfer reactions resulting in the splitting of water into molecular oxygen and protons. Isolated thylakoid membranes produce the superoxide free radical ion and hydrogen peroxide as a product of the dismutation of O_2^- [7]. This reaction is stimulated by autooxidizable electron acceptors of photosystem I and occurs in the presence of the natural electron acceptor system, ferredoxin and NADP, following the reduction of NADP [8].

Triazine, diazines, phenolic and urea herbicides are the ones with the highest effect on chloroplasts. These compounds inhibit photosynthetic process by binding to the D1 protein of photosystem II [9]. Photosynthetic herbicides block electron transport by the displacement of the bound plastoquinone called QB from its binding site on the D1 protein [10]. This protein is an essential part of the PSII reaction centre and together with the homologous protein D2 binds all the prosthetic groups involved in the main PSII electron transfer pathway [11,12].

Immobilized chloroplasts and thylakoids have been used to detect herbicides either by testing inhibition of the Hill reaction, inhibition of DCPIP photoreduction or change in chlorophyll fluorescence [2,13–16]. These observations have initiated interest in

---

developing biological sensors to detect low levels of herbicides in water and soil using PSII.

Magnetic particles have been utilized extensively in diagnostics and other research applications for the capture of biomolecules and cells. Many assays and separations have been adapted to a magnetic bead format to take advantage of the benefits of microspheres and magnetic separation [17–21]. The most reported biosensing configurations based on beads are biosensors and bioreactors integrated into bead injection analytical systems [22–24].

In this study, we describe the production and preliminary characterization of an optical (chemiluminescence) PSII microfluidic sensing device for herbicide monitoring. The proposed detection principle is the chemiluminescence-based monitoring of the concentration of photosynthetically produced H_2O_2, which can be disrupted by herbicides.

The photosystem II complex and the HRP enzyme are immobilized on magnetic beads, which are in turn magnetically entrapped. The sensor unit is able to perform the assays and optically stimulate photosystem II within the unit and detect the HRP-catalyzed chemiluminescence of luminol/hydrogen peroxide. The system combines the production and detection of hydrogen peroxide in a single flow assay by combining all the individual steps in a compact and portable device.

2. Experimental

Polystyrene amino-magnetic beads (5% (w/v); 3.35 μm of diameter) were purchased from Spherotech Inc. (USA). The Carboxyl Terminated Beads (10% (w/v); 3.2 nm of diameter, made of polystyrene copolymer/iron oxide, 55:45) were from Europa Bioproducts (UK). All reagents are of analytical grade and were purchased from Sigma Chemical Co. All buffers were prepared using nanopure water.

2.1. Micro-system principles and design

The detection principle used in this system is chemiluminescence-based monitoring of the concentration of photosynthetically produced H_2O_2, which can be disrupted by herbicides. The sensor unit is able to perform the assays and optically stimulate photosystem II within the unit and detect the enzyme-mediated chemiluminescence of luminol/hydrogen peroxide. The sensor comprises of a short fluidic channel with two "active" regions including: (i) immobilized PSII and (ii) immobilized HRP to catalyze luminol/hydrogen peroxide chemiluminescence. Initial design consists of a flow channel constructed of machined Perspex sandwiching a laser-cut elastomer spacer/flow channel in which regions of appropriate reagents will be magnetically entrapped (Fig. 1).

The sensor consists of: (i) a pump in order to force the sample mixed with luminol through the sensor (after pre-concentration and sample "clean-up" if necessary), i.e. a simple flow-injection arrangement; (ii) a light source and delivery optics to illuminate the PSII region, an Agilent HMLP-C117 "high brightness LED" (peak wavelength 645 nm, with luminous intensity 300 mcd) and (iii) a suitable detector module and collection optics for the detection of chemiluminescence from the hydrogen peroxide detection region, e.g. a photomultiplier tube (PMT) or a staircase avalanche photodiode (SAPD) modules to detect luminescence of luminol at about 431 nm.

2.2. μ-Fluidic system fabrication

The micro-system was manufactured in-house at Cranfield University, following the design and principles described. The
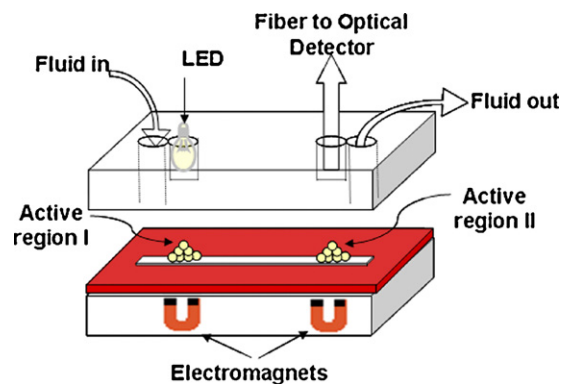
Fig. 1. Schematic representation of the micro-system, with the two Perspex blocks that sandwich the fluidic channel (in red) wide apart. The "active" regions are also shown, with the magnetic beads immobilized into the magnetic field of the magnets. (For interpretation of the references to color in this figure legend, the reader is referred to the web version of the article.)

sandwiching blocks were machined from Perspex (polymethylmethacrylate), while fluidic channels were made from silicon elastomer using a mask as well as black rubber. Each Perspex block has the following dimensions: $H \times W \times L = 20\,mm \times 20\,mm \times 60\,mm$.

The fluidic channel has a height of only 2 mm (for the silicone channel) and 0.3 mm (for the rubber channel). For the rubber fluidic channels, a CO_2 laser was used for cutting the structures, which allowed rapid prototyping of μ-fluidic gaskets/structures, coupled with increased accuracy compared to the silicone ones. Alternative channel structures were used in order to optimize capture and functional activity of HRP-coated magnetic beads. Currently, the fluidic channels are 300 μm thick and 1000 μm wide.

2.3. Particle-based biochemistry

The two "active" regions, PSII and HRP, which are actually non-permanent, are immobilized on magnetic beads, which are in turn immobilized (magnetically) on the "active" regions. The unit was designed taking into consideration all the steps of detection in advance. A protocol of the steps includes the following.

Beads with attached HRP enter the fluidic channel, and are immobilized by magnetic forces on the region II. Beads with attached PSII enter the fluidic channel, and are immobilized by magnetic forces on the region I. A water sample (pre-mixed with luminol) enters the fluidic channel, and is illuminated, on the region I. The sample with H_2O_2 produced by PSII flows towards region II, where the chemiluminescence reaction takes place, and the light produced is, through the optical fiber, detected by the detector. The removal of the magnetic forces and the flow of buffer/water result in the removal of the beads, and the sensor can be used again.

2.4. Luminol chemiluminescence batch H_2O_2

Different concentrations of luminol and HRP were added to 1 ml polystyrene cuvettes, and were placed in the detection region of the spectrophotometer. A sample of Tris–HCl buffer, 10 mM, pH 8.5 with various H_2O_2 concentrations was manually pipetted. To ensure that the crucial first few seconds of the reaction were monitored, the recording of light was started before the addition of the sample, while the ambient light was maintained at the minimum possible.

The chemiluminescence was transduced to an electric signal by a portable SD2000 CCD luminometer (Ocean Optics, Netherlands) or a bench-top VARIAN spectrophotometer. The chemiluminescence intensity profiles were recorded and the maximum intensity was used to plot the graphs.

For samples of thylakoids producing H_2O_2, the procedure was similar. Aliquots of thylakoid membranes were diluted accordingly with Tris–HCl buffer, 10 mM, pH 8.5 and introduced in a glass pipette by aspiration. The glass pipette was then illuminated. Luminol (30 mM), HRP (150 U ml^{-1}) and H_2O_2 (30 μM–3 M) were prepared freshly in Tris–HCl buffer, 10 mM, pH 8.5, and were pipetted in a polystyrene cuvette, that was placed in the appropriate location in or next to the light-reading apparatus. Once the illumination of the glass pipette containing the thylakoids was terminated, its contents were rapidly transferred into the cuvette, to allow instantaneous mixing. The reaction of the H_2O_2, produced by the thylakoids during the illumination, with luminol and the HRP, resulted in the characteristic light which is the product of this reaction. The light-reading apparatus was used to measure the light produced from the very start of this process.

2.5. Immobilization of HRP on magnetic beads

For the immobilization of HRP on the beads, a protocol supplied by Cortex Biochemicals was used (http://www.cortexbiotech.com), with some modifications. One milliliter of MagaBeads-Carboxyl Terminated was washed twice in 10 ml of MES buffer (50 mM, pH 6.1). Volume of particles was adjusted to a 10 mg ml^{-1} concentration. Then a same volume of EDC (100 nM) was added and allowed to react for 15 min at room temperature with continuous mixing. The microsphere particles were washed twice in phosphate–citrate buffer and resuspended in 5 ml of the same buffer. Five milliliters of HRP (1 nM) were added and allowed to react at room temperature for 2 h with constant mixing. The remaining active sites of the MagaBeads were blocked in a solution of 0.03% (w/v) glycine in MES buffer for 30 min at room temperature. The particles were washed four times with 2 ml of MES buffer each time, using a magnet to sediment particles. After a final washing with 2 ml sodium acetate buffer, 0.1 M, pH 4.0, the microspheres were ready to use.

Two types of HRP were used such as HRP-1 (type II, 148 U mg^{-1}) and HRP-2 (type VI, a highly purified and stabilized, 300 U mg^{-1}). EDC (100 nM), HRP (1 nM), glycine (0.03%, w/v) were prepared just before each immobilization assay, in MES buffer, 50 mM, pH 6.1. HRP-1 and HRP-2 were purchased from Sigma Chemical Co.

For the HRP activity assay, one tablet of ABTS was dissolved in 100 ml of 50 mM phosphate–citrate buffer and 25 μl of 30% H_2O_2 was added. One hundred microliters of ABTS–H_2O_2 were added to 100 μl of sample in each well of a white microtitre plate with a clear bottom. Immediately after initiation of the reaction, absorbance at 405 nm was measured every 10 min.

2.6. Flow assay for hydrogen peroxide with HRP immobilized on magnetic beads

The flow system (Fig. 1) consisted of one peristaltic pump, delivering a 10 mM luminol and a H_2O_2 sample pre-mixed at a continuous flow rate of 2.5 ml min^{-1}. Luminol and H_2O_2 were freshly prepared every day in Tris–HCl buffer, 10 mM, pH 8.5. PTFE tubing (0.8 mm i.d.) was used to connect the flow system components. Firstly, the beads (1 mg) were flown in the flow system by a peristaltic pump. A permanent magnet was used to attract the beads as they were flowing, thus immobilizing them in a specific area of the channel, underneath the area "viewed" by the optical fiber (50 μm of diameter, for detection in wavelength: 200–800 nm) (Avantes, Netherlands). The magnet was not moved during the experiment, in order to ensure that the beads were not carried away by the continuing flow. The reaction was initiated once the pre-mixed luminol–H_2O_2 reached the area of the flow channel that was covered with the beads. The chemiluminescence was transduced to an electric signal by a SD2000 portable CCD luminometer (Ocean

Optics, Netherlands). The chemiluminescence intensity profiles were recorded and the maximum intensity was used to plot the graphs.

2.7. Thylakoid membranes isolation protocol

Thylakoid membranes were isolated from fresh spinach leaves (*Spinacea oleracea* L.) using the procedure described by Touloupakis et al. [15]. One hundred grams of leaves were washed with distilled water, dried on filter paper and homogenized in 200 ml of extraction buffer containing 20 mM Tricine, pH 7.8, 300 mM sucrose, 5 mM MgCl$_2$, 1 mM EDTA and 0.2% (w/v) bovine serum albumin (BSA). The homogenate was filtered through six layers of cheesecloth and centrifugated at 7500 × g for 20 min. The pellet was suspended in a buffer containing 50 mM Tricine, pH 7.8, 70 mM sucrose, 5 mM MgCl$_2$ and centrifugated at 7500 × g for 20 min. Finally, the obtained pellet (thylakoid membranes) was resuspended in a buffer containing 50 mM Tricine, pH 7.8, 70 mM sucrose and 5 mM MgCl$_2$. Aliquots at [Chl] = 3 mg ml^{-1} were placed in Eppendorf tubes and kept at −80 °C. The total chlorophyll content was calculated according to Porra [25].

2.8. Immobilization of thylakoid membranes on magnetic, amine polystyrene beads

Five hundred microliters of water suspension of magnetic aminopolystyrene beads (5%, w/v) were washed with 1.0 ml of PBS buffer (KH$_2$PO$_4$ 1.8 mM, KCl 7 mM, NaCl 15 mM, Na$_2$HPO$_4$ 10 mM, pH 7.2) for three times. The pellet was suspended in 1.0 ml of a glutaraldehyde solution (glutaraldehyde dissolved in PBS buffer to a final concentration of 10% (w/v)). The reaction was carried out with continuous mixing at 30 °C for 24 h. The microsphere suspension was washed three times with 1.0 ml of PBS buffer to remove the excess of glutaraldehyde. Pellet was resuspended in 0.5 ml of 15 mM MES, pH 6.5 (wash/coupling buffer). Then, 200 μl of thylakoid membranes ([chlorophyll] = 2.75 mg ml^{-1}) and 300 μl of 15 mM MES, pH 6.5, 70 mM sucrose, 5 mM MgCl$_2$ were added at 4 °C in the dark. To allow the coupling between the thylakoids and glutaraldehyde, the heterogeneous reaction was carried out at 4 °C for 2 h under continuous mixing. Finally, 100 μl of BSA (quenching solution) was added to 400 μl of immobilized thylakoids. The beads were washed three times with 1.0 ml of PBS buffer in order to remove the excess glutaraldehyde.

2.9. Fluorescence efficiency

The stability of the photosynthetic material, before and after immobilization in beads, was tested by measuring changes in fluorescence yield with a 650 nm light every 10 min after a dark period. Under exciting light, the fluorescence yield rapidly rises and then slowly decreases. The F_v/F_m $(F_m − F_0)/F_m$ parameter is the maximum quantum yield of PSII and reflects the potential quantum efficiency of PSII as a sensitive indicator of plant photosynthetic performance [26]. All fluorescence measurements were performed by using the Plant Efficiency Analyser (Hansatech Instruments Ltd., UK) at room temperature.

3. Results and discussion

3.1. Chemiluminescence batch assay for H_2O_2 produced by thylakoid membranes

Luminescent signal is seen with illuminated thylakoid membrane preparations. The signal is proportional to the light intensity
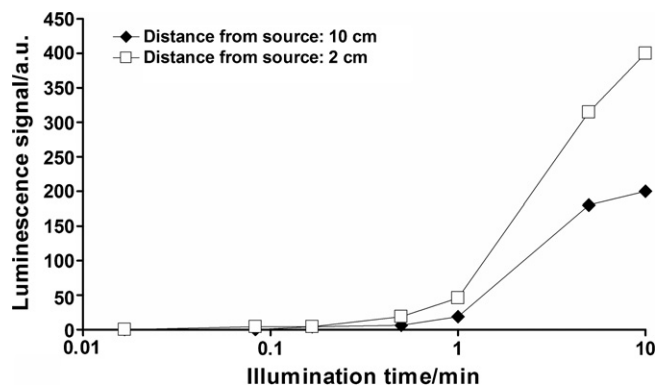
Fig. 2. Light produced by the chemiluminescence reaction of light-induced hydrogen peroxide from thylakoids illuminated for different times and distances. [HRP] = 20 U ml^{-1}, [luminol] = 100 µM, [chlorophyll] = 3.15 mg ml^{-1} with bench-top detector, at pH 8.5.

and duration. The effect of illumination time and distance on luminescence emission is shown in Fig. 2. The same signal is absent in the presence of DCPIP, hydroquinone or catalase, all of which act as either hydrogen peroxide inhibitors or mediators of the electron transport in the photosynthetic cycle. The presence of the latter group of additives means that the electrons never reach the hydrogen peroxide producing complex of the thylakoid, therefore, inhibiting any signal. At the same time, H_2O_2 spiked samples, i.e. thylakoid samples illuminated normally with added known hydrogen peroxide concentrations, give an additive luminescence response, suggesting that the hydrogen peroxide is not consumed by a catalase-type activity in the thylakoid preparation.

Both atrazine and diuron herbicides cause concentration-dependent inhibition of the chemiluminescent signal, and hence the H_2O_2 production by illuminated thylakoids (Fig. 3). The limits of detection (LODs) for these herbicides are: 3.0E−08 for atrazine and 1.0E−08 for diuron. An example of individual luminescence assay for diuron can be seen in Fig. 4.

3.2. Chemiluminescence batch assay for H_2O_2

For the detection of H_2O_2, four concentrations of luminol (10 mM, 1 mM, 100 µM and 50 µM) and four concentrations of HRP (50 U ml^{-1}, 10 U ml^{-1}, 5 U ml^{-1} and 1 U ml^{-1}) were tested in all possible combinations. At higher concentrations of H_2O_2 (mM
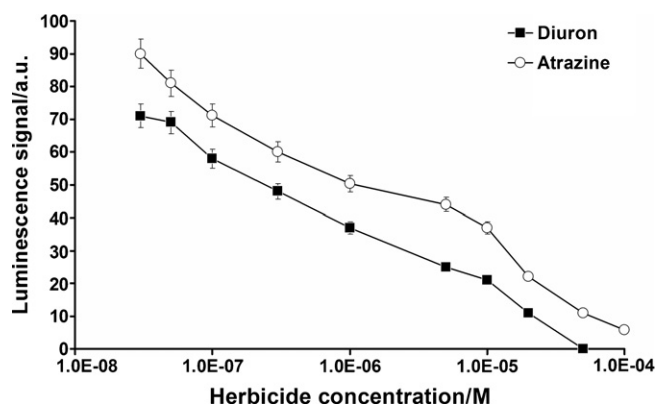
Fig. 3. Light produced by the chemiluminescence reaction of light-induced hydrogen peroxide from illuminated thylakoids in the presence of diuron or atrazine, with [HRP] = 20 U ml^{-1}, [luminol] = 100 µM, [chlorophyll] = 3.15 mg ml^{-1} with bench-top detector, at pH 8.5.
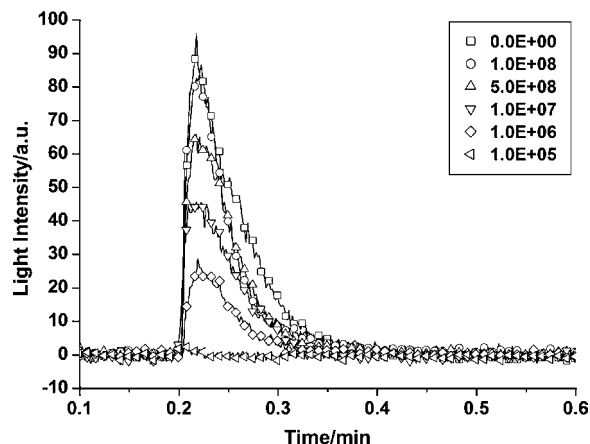
Fig. 4. Light produced by the chemiluminescence reaction of light-induced hydrogen peroxide from illuminated thylakoids in the presence of diuron, with [HRP] = 20 U ml^{-1}, [luminol] = 100 µM, [chlorophyll] = 3.15 mg ml^{-1} with bench-top detector, at pH 8.5.

region), the reaction acts like a typical "glow-type" chemiluminescence reaction expanding over minutes. At concentrations lower than micromolar, the result is typically a flash for less than 1 s. Having identified the peak light production of luminol at 431 nm, measurements of light intensity over time were performed, at a wavelength of 431 ± 20 nm. Such a large "window" was chosen in order to allow the maximum detectable light and, as the reaction is performed in the dark, any light detected would only be from the chemiluminescence reaction.

Calibration curves for all the previously mentioned combinations were plotted, and the LODs were calculated as 5σ values. Calibration curves were obtained for both the maximal light output and the integrated light output (data not shown). Among all the calibrations, the most sensitive detection was in the sample employing luminol 100 µM and HRP 5 U ml^{-1}, with an LOD: 1.34E−06 (data not shown).

3.3. Immobilization of thylakoid membranes on magnetic beads

Thylakoid membranes were immobilized on magnetic beads. Activity of immobilized thylakoid membranes was determined by fluorescence induction analysis. The F_v/F_m parameter represents the maximum quantum yield of PSII. The F_v/F_m parameter of the photosynthetic material, before the immobilization in beads, was 0.7. At 25 °C the observed half-life of thylakoid membranes activity was 53 h (Fig. 5). The data in Fig. 5 represent the average of three experiments with a relative standard devi-
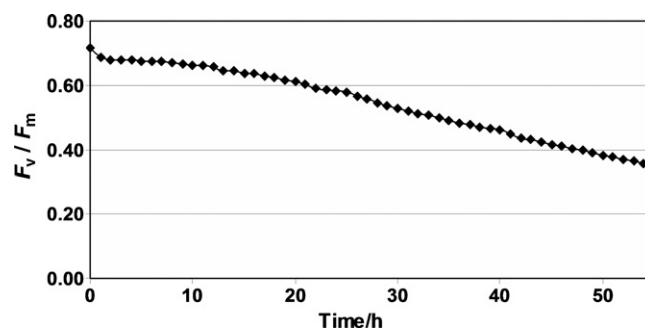
Fig. 5. Fluorescence induction analysis of immobilized thylakoid membranes on magnetic beads. Activity is monitored as F_v/F_m ratio in function of time in storage in the dark at 25 °C.

ation of 6.67. From a chlorophyll calculation it was found that the amount of the immobilized photosynthetic material was $0.3\,\mu g\,(chlorophyll)\,mg^{-1}$ beads.

3.4. Immobilization of HRP on magnetic carboxyl-modified beads

HRP (HRP-1 and HRP-2) were immobilized in active form on magnetic carboxyl-modified beads. The amount necessary to achieve a complete activation of all the carboxyl groups on the beads was 100 nmol of EDC per 1 mg of beads. The optimized immobilization protocol included several washing steps (especially between the EDC and the HRP incubations) and different washing buffers. A step of washing the beads with sodium acetate buffer, 0.1 M, pH 4.0, after the HRP immobilization was included. To evaluate the effect of this, two different routes were taken, one with and one without the sodium acetate buffer washes. It should be noted that, for experimental integrity, the beads that were not washed with sodium acetate were instead washed with MES buffer, which was the buffer used for the washes throughout the experiment, thus bringing the total washes of the two routes to the same number. After the different washing steps, both bead lots were washed three times with the buffer of choice, in this case phosphate–citrate, which was the one favored by the ABTS assay protocol. The beads with the sodium acetate washes had slightly lower HRP activity than the ones washed only with MES. More specific, the rate of activity was lower for the sodium acetate ($0.132\,OD\,min^{-1}$) compared to the MES buffer ($0.150\,OD\,min^{-1}$) although the overall substrate conversion at the end of 10 min of the two bead lots was the same (data not shown). Throughout the immobilization procedure, all the in-between washes were also assayed with ABTS, in order to ensure that the multiple washing steps were actually washing out any excess of unbound HRP, and that the final product did not have any residual free HRP (data not shown).

Initially, an HRP with a lower hemin content and therefore activity was used (HRP-1). This HRP-1 was more prone to deactivation in various environments. A different HRP was then used (HRP-2) which is further purified and chemically stabilized to protect the primary amines and to maintain activity at low pH and higher temperature. Using HRP-1, 1 mg of beads had HRP activity equal to 0.1 purpurogallin units according to the ABTS assay (1 unit will oxidize 1 μmol of ABTS per minute at 25 °C, pH 5.0). With HRP-2, 1 mg of beads had activity equal to 0.375 units. A final alteration of the protocol was the washing out of the excess EDC, before the HRP was incubated with the beads. That was performed by following the protocol suggested by Mueller, whereby the excess unbound EDC would bind to HRP that would otherwise be immobilized to the beads [27]. The results with this alteration showed a dramatic increase in activity; 1 mg of beads had 1.2 units. According to the marked difference in the resulting activities between the two HRPs, as indicated by the ABTS assay, only HRP-2 was used in all the experiments shown either in free-form or immobilized.

The theoretical maximum number of HRP molecules bound to a bead can be calculated assuming a monolayer cubic close packing of HRP on the bead surface. The "monolayer coating" assumption is reasonable since the formation of a multilayer enzyme coating may take place, in fact, as a consequence of protein crosslinking. This requires the activation of the carboxyl groups of the enzyme; with the coating chemistry employed here however, only the carboxyl groups of the beads are activated, minimizing the possibility of a multilayer. In the case of the 3.2 μm of diameter beads, with the spherical diameter of HRP to be 4.6 nm, the theoretical maximum value of 441.67×10^3 HRP molecules per bead is obtained [28]. From further calculations, it was found that the amount needed for a monolayer for 3×10^9 beads, which is the amount of beads in 1 mg, would be 88 μg HRP, which is double the amount sug-
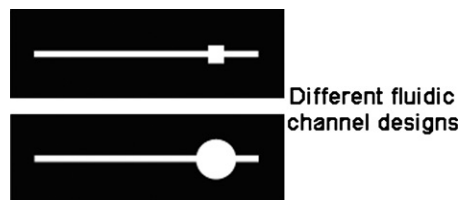
Fig. 6. The rubber channels employed in the experiments. The region used for the entrapment of the magnetic beads is the circular area (channel B) and the rectangular area (channel A).

gested by the protocol and used through the experiments. As for the immobilization experiments only half the amount of HRP was used, thus it can be assumed that only a partial monolayer has been achieved.

Different storage buffers were also tested. The activity of free HRP prepared and stored for 1 week was greatly reduced while the activity of HRP immobilized on beads irrespective of the used buffer as a storage medium remained roughly unchanged. The activity of free HRP prepared and stored for 1 week

3.5. Flow assay for hydrogen peroxide with HRP immobilized on magnetic beads

Beads with immobilized HRP were magnetically entrapped in the fluidic device, in order to perform the H_2O_2 assay with luminol pre-mixed with the sample in flow. The light produced was detected with a portable detector.

Samples of different H_2O_2 and luminol concentrations were premixed just prior to the experiments with a T-mixer. Two different fluidic channels were used for the experiments, as shown in Fig. 6. The circular area of channel B is the area covered by the beads, and attracted by the magnet (area = $200\,mm^2$). For flow channel A, the rectangular area, $16\,mm^2$ covered by beads was smaller. In both cases 1 mg of beads was used, so the only difference was in the spreading of the beads and not the actual amount of HRP.

The light produced by the reaction was measured and the results are shown in Fig. 7. The channel B, allowing the beads to spread over a larger surface area, allowing for more HRP to be employed in the reaction, gave an increased response, as well as a lower LOD of 100 μM, compared to channel A, that had the beads stacked on a smaller area, as the HRP on the beads was not fully used, as a lot of the beads were covered by others, not allowing the luminol–H_2O_2 to reach them. Therefore, the key to the maximization of the possible chemical interaction between the H_2O_2, luminol and HRP lied in the ability to spread out the HRP bound on the beads in a two-dimensional plane.
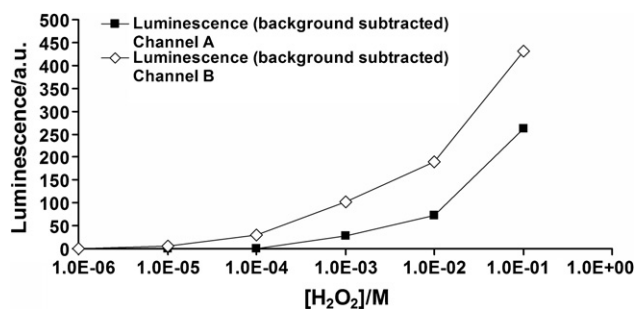
Fig. 7. Light output from different concentrations of H_2O_2. [luminol] = 10 mM at pH 8.5, with buffer 100 mM Tris–HCl. The HRP was immobilized on beads and 1 mg of beads were accommodated in two different channels. In channel A the beads were immobilized on area of $16\,mm^2$, in channel B they employed a surface area of $200\,mm^2$.

4. Conclusions

There is a growing interest for the generation of rapid, inexpensive assays to screen for the presence of herbicides. In this work, we have developed photosystem II-based optical microfluidic sensor for herbicide detection. The sensor is easy to handle and sensitive enough to provide preliminary environmental analysis screening the samples that require more detailed laboratory analyses.

The production of hydrogen peroxide by thylakoid membranes extracted from higher plants was investigated and detected under illumination with concentrations increasing in a time- and light intensity-dependent manner. The presence of herbicides in the thylakoid samples reduces the hydrogen peroxide measured in a concentration-dependent manner.

Thylakoid membranes and HRP were immobilized on magnetic beads, which were in turn magnetically immobilized in the device. The luminol–HRP–H_2O_2 chemiluminescence reaction was investigated in respect to H_2O_2 as the reactant of interest, and a calibration curve was obtained.

The integration of the two-step reaction has been achieved by designing and constructing a microfluidic device, which consists of a flow channel constructed of machined Perspex sandwiching a laser-cut elastomer spacer/flow channel in which regions of appropriate reagents are immobilized.

The sensor unit is able to perform the herbicide assays; optically stimulate photosystem II within the unit and detect the HRP-catalyzed chemiluminescence of luminol/hydrogen peroxide, which can be disrupted by herbicides.

The large number of approved active ingredients in agriculture (approximately 600 chemicals) makes difficult to obtain accurate and actual information on herbicide application in different countries. The real samples are present in a complex mixture containing active ingredients and their metabolites [29]. Our preliminary results indicate that use of real water matrix (control not containing herbicides) does not inhibit PSII activity and in some cases can induce an activation by 5–21% measured as oxygen evolution (data not shown). Therefore, the developed biosensor can be applied in real samples and better reflect the real physiological impact of active compounds because even low concentrations of pollutants affect living organisms by altering physiological processes. A deep study on real samples is in progress and will be presented in a future publication.

Acknowledgments

References

[1] M.T. Giardi, E. Piletska (Eds.), Biotechnological Applications of Photosynthetic Proteins: Biochips, Biosensors and Biodevices, Landes Bioscience Springer, 2006.
[2] M.T. Giardi, L. Guzzella, P. Euzet, R. Rouillon, D. Esposito, Environ. Sci. Technol. 39 (2005) 5378.
[3] J.H. Lee, R.J. Mitchell, B.C. Kim, D.C. Cullen, M.B. Gu, Biosens. Bioelectron. 21 (2005) 500.
[4] C.B. Vicentini, D. Mares, A. Tartari, M. Manfrini, G. Forlani, J. Agric. Food Chem. 52 (2004) 1898.
[5] V. Pacakova, K. Stulik, J. Jiskra, J. Chromatogr. A 754 (1996) 17.
[6] R.J. Bushway, L.B. Perkin, L. Fukal, R.O. Harrison, B.S. Ferguson, Arch. Environ. Contam. Toxicol. 21 (1991) 365.
[7] C. Danna, C. Bartoli, F. Sacco, L. Ingala, G.E. Santa-Marıa, J.J. Guiamet, R.A. Ugalde, Plant Physiol. 132 (2003) 2116.
[8] V. Klimov, G. Ananyev, O. Zastryzhnaya, T. Wydrzynski, G. Renger, Photosynth. Res. 38 (1993) 409.
[9] D.E. Moreland, Z. Naturforsch. 48c (1992) 121.
[10] K. Pfister, K.K. Steinback, G. Gardner, C.J. Arntzen, Proc. Natl. Acad. Sci. U.S.A. 78 (1981) 981.
[11] I.S. Booij-James, W.M. Swegle, M. Edelman, A.K. Mattoo, Plant Physiol. 130 (2002) 2069.
[12] M.T. Giardi, E. Pace, Trends Biotechnol. 23 (2005) 257.
[13] M. Koblitzek, J. Maly, J. Masojidek, J. Komenda, T. Kucera, M.T. Giardi, A.K. Mattoo, R. Pilloton, Biotechnol. Bioeng. 78 (2002) 110.
[14] D. Laberge, R. Rouillon, R. Carpentier, Enzyme Microb. Technol. 26 (2000) 332.
[15] E. Touloupakis, L. Giannoudi, S.A. Piletsky, L. Guzzella, F. Pozzoni, M.T. Giardi, Biosens. Bioelectron. 20 (2005) 1984.
[16] D. Merz, M. Geyer, D.A. Moss, H.J. Ache, Fresen. J. Anal. Chem. 354 (1996) 299.
[17] M. Gijs, Microfluid. Nanofluid. 1 (2004) 22.
[18] R.J.S. Derks, A. Dietzel, R. Wimberger-Friedl, M.W.J. Prins, Microfluid. Nanofluid. 3 (2007) 141.
[19] J.W. Choi, K.W. Oh, J.H. Thomas, W.R. Heineman, H.B. Halsall, J.H. Nevin, A.J. Helmicki, H.T. Henderson, C.H. Ahn, Lab Chip 2 (2002) 27.
[20] C. Elkin, H. Kapur, T. Smith, D. Humphries, M. Pollard, N. Hammon, T. Hawkins, Biotechniques 32 (2002) 1296.
[21] G.P. Hatch, R.E. Stelter, J. Magn. Magn. Mater. 225 (2001) 262.
[22] M. Mayer, J. Ruzicka, Anal. Chem. 68 (1996) 3808.
[23] A. Guënther, U. Bilitewski, Anal. Chim. Acta 300 (1995) 117.
[24] A.R. Varlan, J. Suls, P. Jacobs, W. Sansen, Biosens. Bioelectron. 10 (1995) 15.
[25] R. Porra, J. Photosynth. Res. 73 (2002) 149.
[26] K. Maxwell, G.N. Johnson, J. Exp. Bot. 51 (2000) 659.
[27] S. Mueller, Free Radical Biol. Med. 29 (2000) 410.
[28] T. Deng, G.M. Whitesides, M. Radhakrishnan, G. Zabow, M. Prentiss, Appl. Phys. Lett. 78 (2001) 1775.
[29] L. Guzzella, F. Pozzoni, G. Giuliano, Environ. Pollut. 142 (2006) 344.

Mercury speciation in sea food by flow injection cold vapor atomic absorption spectrometry using selective solid phase extraction

E. Vereda Alonso*, M.T. Siles Cordero, A. García de Torres,
P. Cañada Rudner, J.M. Cano Pavón

Department of Analytical Chemistry, Faculty of Sciences, University of Málaga, E-29071 Málaga, Spain

A B S T R A C T

An on-line inorganic and organomercury species separation, preconcentration and determination system consisting of cold vapor atomic absorption spectrometry (CV-AAS or CV-ETAAS) coupled to a flow injection (FI) method was studied. The inorganic mercury species was retained on a column (i.d., 3 mm; length 3 cm) packed to a height of 0.7 cm with a chelating resin aminopropyl-controlled pore glass (550 Å) functionalized with [1,5-bis (2 pyridyl)-3-sulphophenyl methylene thiocarbonohydrazyde] placed in the injection valve of a simple flow manifold. Methylmercury is not directly determined. Previous oxidation of the organomercurial species permitted the determination of total mercury. The separation of mercury species was obtained by the selective retention of inorganic mercury on the chelating resin. The difference between total and inorganic mercury determined the organomercury content in the sample. The inorganic mercury was removed on-line from the microcolumn with 6% (m/v) thiourea. The mercury cold vapor generation was performed on-line with 0.2% (m/v) sodium tethrahydroborate and 0.05% (m/v) sodium hydroxide as reducing solution. The determination was performed using CV-AAS and CV-ETAAS, both approaches have been used and compared for the speciation of mercury in sea food. A detection limit of 10 and 6 ng l^{-1} was achieved for CV-AAS and CV-ETAAS, respectively. The precision for 10 replicate determinations at the 1 μg l^{-1} Hg level was 3.5% relative standard deviation (R.S.D.), calculated from the peak heights obtained. Both approaches were validated with the use of two certified reference materials and by spiking experiments. By analyzing the two biological certified materials, it was evident that the difference between the total mercury and inorganic mercury corresponds to methylmercury. The concentrations obtained by both techniques were in agreement with the certified values or with differences of the certified values for total Hg^{2+} and CH$_3$Hg$^+$, according to the *t*-test for a 95% confidence level. It is amazing how this very simple method is able to provide very important information on mercury speciation.

© 2008 Elsevier B.V. All rights reserved.

1. Introduction

Mercury is a non-essential toxic element, and is known to affect the central nervous system in a number of ways [1]. Food is a major source of mercury intake, especially in areas where fish and other sea food are the main components of the diet; in particular, marine fish and molluscs either directly or from products fed on these sources are the principal contributors to human uptake. Only 10–15% of inorganic mercury is absorbed by humans and its elimination occurs freely [2,3]. The problem of toxicity associated with inorganic mercury is compounded by methylation reactions. Inorganic mercury is converted by microorganisms and macroalgae to the more toxic organomercury species [4].

Methylmercury constitutes up to 60–90% of the total mercury in fish due to high absorption and low elimination mechanisms [5]. It is therefore clear that total mercury and organomercury, particularly methylmercury, levels in food should be determined and the methods developed should be routine and robust.

Mercury speciation by elemental analytical techniques such as atomic spectrometry requires a separation process prior to detection. The most common way is to couple the separative power of chromatography to the element specific detection offered by atomic spectrometry. There is a large literature on the use of gas chromatography (GC) for separation followed by detection using microwave induced plasma atomic emission spectrometry (MIP-AES) [6–8], inductively coupled plasma mass spectrometry (ICP-MS) [9], atomic fluorescence spectrometry (AFS) [10]. However, these approaches have the disadvantages of requiring a derivatisation step to obtain a volatile derivative. In an attempt to overcome the several drawbacks associated with the GC determi-

* Corresponding author.
E-mail address: eivereda@uma.es (E. Vereda Alonso).

nation of organomercury compounds [11], different authors have resorted to alternative separation procedures. Particularly, liquid chromatography (LC) techniques have been used [12,13]. However, LC methods are significantly less sensitive than GC procedures and this is a great limitation for real samples [14]. A general way-out to this lack of sensitivity of LC hybrid techniques is on-line derivatisation to form a cold vapor of mercury at the exit of the column, $SnCl_2$ and $NaBH_4$ are the most popular reductants for this purpose [15].

Flow injection (FI) on-line preconcentration and separation is a powerful technique for trace mercury determination with enhanced sensitivity and selectivity. Coupling the FI with a mercury-specific detector is a procedure that has been applied to mercury speciation. Tao et al. [16] described a method for the quantification of inorganic and total mercury in biological tissues by CV-AAS in a flow system, with the on-line addition of L-cysteine and cold vapor generation with $SnCl_2$. Cava Montesino et al. [17] suggested a procedure for the on-line speciation of mercury in fish by CV-AFS after converting the organic mercury in inorganic mercury by the on-line addition of an oxidant mixture of $KBr/KBrO_3$. Jian and McLeod [18] described a method for the sequential determination of inorganic mercury and methylmercury in natural waters by CV-AFS after separation/enrichment on a microcolumn of sulphydryl cotton. Sanz et al. [19] have demonstrated the possibility of the selective determination of inorganic mercury and methylmercury by CV-ETAAS with a FI system in which an anion exchange microcolumn is inserted after the injection loop. If hydrochloric acid is used as the carrier solution, the inorganic mercury will be retained by the exchanger (Dowex M-41) while the methylmercury will flow through the resin with negligible retention. On the other hand, numerous analytical methods based on coupling the FI with HPLC have been developed for mercury speciation [20].

The main objective of this work was to develop and validate a reliable method for application to mercury preconcentration and speciation in seafood. Many chelating ion-exchangers have been reported in the literature as being suitable for metal ion separation and preconcentration. Schiff bases, an important class of ligands obtained by condensation of aldehydes with amines, play a significant role in such applications. Our research group, manly interested in sorbents based on Schiff bases has synthesized and studied three new chelating sorbents pertaining to a group of thiocarbonohydrazide. The first one is based on the impregnation of the ion-exchanger DOWEX 1×8–200 with 1,5-bis[(2-pyridyl)-3-sulphopheylmethylene] thiocarbonohydrazide (PSTH). Later, we synthesized and studied a new sorbent based on silica with 1,5-bis(di-2-pyridyl)methylene thiocarbonohydrazide (DPTH) chemically bonded to the surface, by formation of a C=N bond on the polymeric matrix. These resins were applied with very good results, on the determination of total mercury in biological and environmental samples by ICP-AES [21,22]. The principal advantage of DPTH-gel is its very good stability and resistance because chemisorption of chelating molecules on the surface of solid supports provides immobility, mechanical stability and insolubility. Recently, we synthesized [23] a new resin based on aminopropyl-controlled pore glass with PSTH chemically bonded to the surface (PSTH-cpg). In the present work DPTH-gel and PSTH-cpg resins were tested for mercury speciation in seafood. The best results obtained for the separation of inorganic mercury and methylmercury were achieved with the PSTH-cpg resin. On the other hand, the geometry of the glass allows high sample flow rates with low back-pressure facilitating the high sample frequency. The DPTH-gel resin is more susceptible to back-pressure problems and need replacement more frequently. For these reasons, the resin based on controlled pore glass (PSTH-cpg) was chosen for this study

with the aim to develop a fast, sensitive and reproducible method for mercury speciation in biological samples, which can assist to the environmental quality monitoring of this element and in routine control analysis of food from marine origin.

In the present work, a non-chromatographic method for the separation, preconcentration, and determination of mercury species using the PSTH-cpg resin is proposed. Inorganic mercury was found to be quantitatively retained in the resin while organomercurial species were unretained on the resin with the consequent separation of the species (inorganic mercury from organomercury species). Previous oxidation of the organomercurial species to inorganic mercury allowed the determination of total mercury. The organic mercury was calculated as the difference between the total mercury and the inorganic mercury. The determination was performed using CV-AAS and CV-ETAAS coupled with on-line separation and preconcentration methodology. In this study, both approaches have been used and compared for the speciation of mercury in seafood. All variables related to cold vapor generation and detection were studied. Central composite designs (CCDs) [24,25] were used to evaluate the effect of four variables: pH, sample flow rate, eluent concentration and eluent flow rate. This type of design allows the experimental domain to be mapped and optimal values for parameters to be deduced, while reducing the number of experiments compared to a sequential design. Understanding the main factors and their interactions permitted the development of a mathematical model to predict instrumental response.

2. Experimental

2.1. Instrumentation

A PerkinElmer (Überlingen, Germany) Zeeman AAnalyst 800 atomic absorption spectrometer with a longitudinal Zeeman effect background correction system in conjuction with a PerkinElmer FIAS-400 flow injection system and an AS-90 autosampler was used in this study. A PerkinElmer mercury hollow cathode lamp operated at 6–7 mA intensity was used as the radiation source. The mercury absorbance was measured at 253.7 nm with a 0.7 nm spectral band pass. A non-heated quartz cell with a path-length of 165 mm and a diameter of 12 mm or a transversely heated graphite tube with integrated pyrolytic graphite platforms were used as atomizers. The electrothermal atomizers were used with thermal treatment for permanent modifier deposition according to the procedure reported by Moreda Piñeiro et al. [26].

The samples were digested using an Anton Paar (Graz, Austria) Multiwave 3000 microwave oven.

The FI system is shown in Fig. 1, which consists of two peristaltic pumps, a reagent mixing chemifold, an expansion gas–liquid separator and a four way rotary valve; this valve had the minicolumn connected within the sample loop. The minicolumn was a glass tube (3 cm × 3 mm i.d.), packed with the chelating resin to a height of 0.7 cm. At both ends of the minicolumn, polyethylene frits (Omnifit, Cambridge, UK) were fixed to prevent material losses. The minicolumn was initially flushed with 2 M nitric acid; subsequent use of the eluent in each operating cycle was sufficient to make it ready for re-use. Tygon pump tubings were used to deliver sample, reagents and withdraw waste. The reaction coil and connections were made of 0.8 mm i.d. PTFE tubing. The mercury vapor generated in the reactor was transported to the graphite tube through a PTFE transfer line connected to the sampler arm and to a quartz capillary (1.0 mm i.d.) in the other extremity. Argon with a purity of 99.99% was used as the carrier gas for mercury vapor and as the purge and the protective gas for the graphite atomizer.
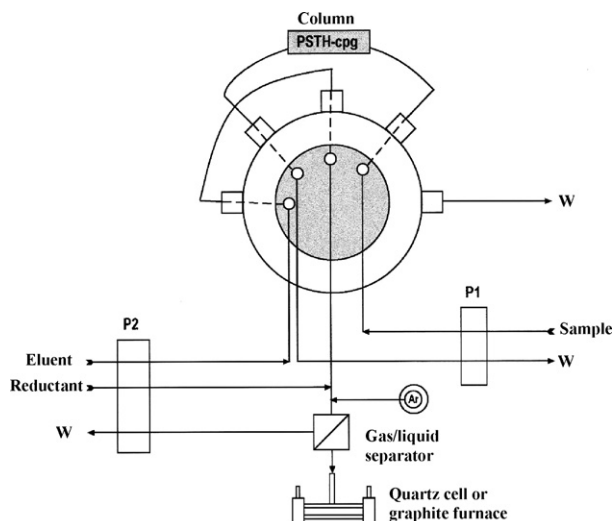
Fig. 1. Schematic diagram of FI system for the preconcentration and separation of mercury: P_1 and P_2, peristaltic pumps; M, mixing coil; Ar, stream of argon and W, waste. For further details see text.

2.2. Reagents

High-purity reagents were employed in all experiments. For the synthesis of PSTH-cpg, the following were used: γ-aminopropyl-controlled pore glass (550 Å) and diglutaric aldehyde were supplied from Fluka (Buchs, Switzerland), thiocarbonohydrazide and 2-benzoilpyridine were purchased from Aldrich Chemie (Steinheim, Germany), and diethyl ether, ethanol, sulphuric acid fuming 30% SO_3 and glacial acetic acid from Merck (Darmstadt, Germany). The synthesis and characterisation of the resin were described by the authors in a previous paper [23]. The structure of PSTH-cpg is shown in Fig. 2.

Standard inorganic mercury solutions were prepared by appropriate dilution of a stock mercury(II) solution (1000 mg l^{-1}; Merck). Stock methylmercury (MeHg) solution (1000 mg l^{-1}) was prepared from methylmercury chloride (Carlo Erba) in ethanol (Merck). Working standard solutions were prepared daily to reduce mercury volatilisation. The MeHg solution was stored away from light at 4 °C to prevent decomposition. A 0.2% (m/v) sodium tetrahydroborate (Fluka Chemie) solution stabilized with 0.05% (m/v) sodium hydroxide (Merck) and stored in a polyethylene flask under refrigeration, was used as the reducing agent. A pH 1 buffer was prepared by mixing 5 ml of 2 M sodium chloride (Merck) and adding 1 M hydrochloric acid (Merck) up to pH 1 and diluting to 100 ml with deionised water. A 6% (m/v) thiourea (Fluka Chemie) solution in 1% (v/v) nitric acid (Merck) was used as eluent. A standard 1.000 μg ml^{-1} Ir(III) solution (PerkinElmer pure, Atomic Absorption Standard) were used to coat the graphite furnace platform.
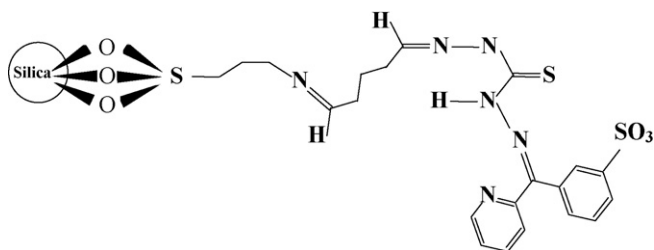
Fig. 2. Structure of PSTH-cpg.

Table 1
Optimum operating conditions for the separation and determination of mercury

FI system	
Internal diameter of coils	0.8 mm
Mixing coil length	100 cm
Sample flow rate	7.2 mL min^{-1}
Elution flow rate	4.6 mL min^{-1}
Reductant flow rate	4.6 mL min^{-1}
Argon carrier flow rate	150 mL min^{-1}

Graphite furnace temperature program

Stage	Parameters			
	Temperature (°C)	Ramp (°C s^{-1})	Hold (s)	Gas flow rate (mL min^{-1})
1	20	1	1	250
2	20	1	1	250
3	1200	0	5	0
4	1500	1	3	250

2.3. Treatment of the graphite tube with a permanent modifier

Pyrolytically coated graphite tubes were pretreated by injecting 50 μl of a 1.000 mg l^{-1} Ir standard solution into the tube, and submitting it to a temperature program based on a work reported by Moreda Piñeiro [26]. Each injection was dried slowly by heating the atomizer at 150 °C with a ramp rate and hold times of 30 and 40 s, respectively. Then a second dried step at 200 °C with a ramp rate and hold times of 20 and 30 s was used. Following this, a reduction step at 2000 °C was applied during 5 s. This procedure was repeated 25 times, resulting in a total mass of 1250 μg of the modifier deposited on the tube graphite wall. A tube treated in this manner can pass through about 500 firing cycles.

2.4. Mercury could vapor generation and preconcentration

The FI manifold used for on-line preconcentration and elution is shown in Fig. 1. Optimum instrumental conditions are given in Table 1. The FI system was operated as follows: during the 2 min sample loading period, valve in the "fill" position, a 7.2 ml min^{-1} flow of sample (standard or blank) at pH 1 is pumped (via pump P_1) through the microcolumn (located in the loop of the valve). The metal is adsorbed on the sorbent minicolumn and the sample matrix sent to waste. During preconcentration, a 4.6 ml min^{-1} flow of eluent (6% thiourea in 1% HNO_3) and reductant (0.2% $NaBH_4$ in 0.05% NaOH) are being aspirated from the containers by the pump P_2 to establish the baseline and the readout for the determination with quartz cell. At the beginning of the 60 s elution stage, the valve position is changed and the sample pump P_1 is stopped. When the valve is in the "inject" position, the eluent passes through the minicolumn. Thus, the accumulated mercury ion is eluted at an elution rate of 4.6 ml min^{-1} and merges with a 4.6 mL min^{-1} flow of reductant in the mixing coil M (length 100 cm, i.d. 0.8 mm), where direct generation of mercury vapor takes place. The gas generated and the solvent are then passed into the gas–liquid separator which provides a separation of gases from liquid. The liquid is drained and the generated mercury vapor is swept into the quartz cell or into the graphite furnace by a stream of argon (150 ml min^{-1}). With this procedure, the FI system and the ETAAS instrument were coupled and operated completely synchronously. The furnace temperature program for mercury determination is shown in Table 1. Peak heights were used for analytical measurements. Quantitation was achieved by the standard addition method.

2.5. Sample preparation

The certified reference materials (CRMs) analysed to determine the accuracy of the proposed procedure were: National Research Council of Canada (NRCC), CRM DOLT-1 Dogfish Liver and TORT-1 Lobster Hepatopancreas. The samples were first dried in accordance with the instructions of the respective analysis certificates, after which an accurately weighed amount of 0.20–1.00 g was subjected to microwave digestion. In order to determine the concentration of total mercury as inorganic mercury the samples were treated as follows: a volume of 2.0 ml of concentrated nitric acid, 2 ml of 30% hydrogen peroxide and 0.5 ml of concentrated hydrochloric acid were added to the weighed amount of sample into a digest vessel, then this vessel was put into the microwave oven to a power of 1400 W for 20 min. At the end of the digestion program the vessels were allowed to cool before removing them from the microwave unit (15 min). Then, the pH of the solutions was adjusted to 1.0 with concentrated NaOH and buffer solution and, finally, the samples were diluted to adequate volume with de-ionised water in a calibrated flask. Samples were analysed, in triplicate, immediately after preparation by introducing them into the manifold described above. Blanks were prepared in parallel. For the determination of inorganic mercury the procedure previously described was followed except for the sample pre-treatment. In this case, a volume of 10 ml of 4.0 M HNO_3 was added (methylmercury was stable up to 4.0 M HNO_3 and degraded at higher concentrations for both evaluated materials, according to Mizanur Rahman and Skip Kingston [27]) to the weighed amount of sample (1.0–2.0 g) and the mixture was subjected to 28 min of microwave irradiation (power 500 W; temperature 45 °C). Then, the samples were placed in a centrifuge tube and sonicated for 5 min. After extraction, the suspension was centrifuged at 3500 rpm for 10 min and the supernatant was taken for further analysis. Blanks were prepared in parallel.

The clam and mussel samples were bought in a market of Málaga, dried at 45 °C in an electric oven for 48 h and powdered, after which an accurately weighed amount of 0.20 g was subjected to microwave digestion. The working conditions of the microwave oven and the preparation of the samples for the analysis were the same that for the certified reference materials.

2.6. Optimization strategy

A rotable uniform central composite design (CCD) [24,25] was used to study the empirical relationship between four controlled factors. The selected factors and their corresponding ranges were determined after preliminary experiments. A mathematical model for a four variable CCD can be described by Eq. (1).

$$Y = \beta_0 + \sum \beta_j x_j + \sum \beta_{jj} x_j^2 + \sum \beta_{jk} x_j x_k \tag{1}$$

where Y is the response of system, x_{jk} is the variable of system and β_0, β_j, β_{jj}, β_{jk} are the regression coefficients for constant, linear, square and interaction terms, respectively.

Regression coefficients are calculated by fitting the value of experimental parameters to the least squares regression line. A quadratic equation or an equation containing only significant terms results. This can then be used to predict the response of the system at given levels of experimental factors. The experimental domain levels appear in Table 2.

The CCD consists of a star design imposed through the centre of a factorial design. The four factor design used in this investigation comprised a 2^4 factorial design (16 experiments), a 2×4 star design (8 experiments) and 2 centre points. The resulting 26 experiments were randomly performed without replication. An α value of 2 was used to ensure rotatability and orthogonality of the design

Table 2
Experimental domain for the CCD experiments

Factor	Levels				
	−2	1	0	+1	+2
A, Eluent concentration (%w/v)	2.0	3.0	4.0	5.0	6.0
B, pH	1.0	2.0	3.0	4.0	5.0
C, Sample flow rate (mL min^{-1})	1.5	3.0	4.5	6.0	7.5
D, Eluent flow rate (mL min^{-1})	2.0	3.0	4.0	5.0	6.0

as calculated by Eq. (2).

$$\alpha = \pm (N_F)^{1/4} = \pm 2.0 \tag{2}$$

where N_F is the number of experiments in factorial portion of design (16).

The experimental data were processed by using the STATGRAPHICS program [28]. For CCD, the significance of the effects was checked by analysis of the variance (ANOVA) and using p-value significance levels. This value represents the probability of the effect of a factor being due solely to random error. Thus, if the p-value is less than 5% the effect of the corresponding factor is significant.

3. Results and discussion

In view of the complex nature of biological samples, selection of the proper chelating resin material for a specific suite of trace elements is most important. In order to establish which was the more adequate column, two supports and two chelating reagents were tested. Silica gel and controlled pore glass (cpg) were investigated as supports and two organic reagents DPTH and PSTH, able to react with the mercury species, were tested. The best reagent/solid support combination for mercury speciation was PSTH-cpg owing to the selective retention of inorganic mercury in this resin and because the geometry of the glass allows high sample flow rates with low back-pressure, facilitating the high sample frequency, while the inherent characteristics of the silica gel beads make this material difficult to manipulate in an on-line system with a microcolumn connected within the sample loop. Thus, this led to tight packing of the microcolumn, resulting in increased flow resistance. The resins based on silica beads, more susceptible to back-pressure problems, needed replacement more frequently. For these reasons PSTH-cpg resin was chosen for this study.

3.1. Optimization of the procedure

To optimize the system, most efforts were focused on the conditions for sample loading and mercury elution from the column, as well as the flow system which was coupled on-line with the preconcentration and separation unit in order to obtain highly sensitive, accurate and reproducible results. For measurements to be useful, it was considered that a relative standard deviation (R.S.D.) of about 5% was acceptable. Peak height was chosen as the figure of merit to be maximised. The chemical and FI variables of the used manifold, which affect the preconcentration and mercury vapor generation were optimized using 5.0 µg l^{-1} Hg(II) standard solution.

Firstly, the trapping time onto the coated graphite tube for mercury cold vapor was investigated; the results obtained showed that a trapping time of 60 s is necessary. On the other hand, the efficiency of trapping mercury cold vapor onto the coated graphite tubes was found to be optimum at room temperature. Thus, an adsorption temperature of 20 °C was selected for further experiments.

To minimize the time needed for quantitative elution the selection of the eluent for the analyte is very important. Strong acids are effective in dissociating complexes and releasing free metal ions. For this reason, hydrochloric acid and nitric acid were tested as
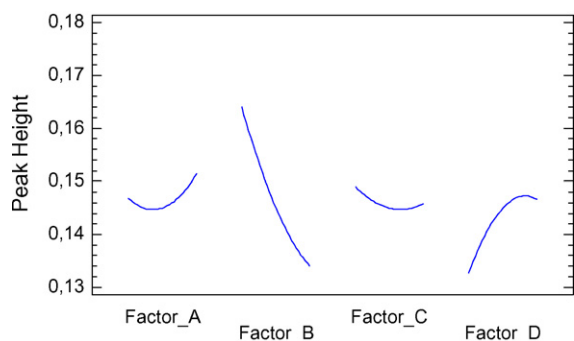
Fig. 3. Graph showing the influence of main effects on the preconcentration of mercury. The lines indicate the magnitude and sign (increase or decrease) of the variation of the peak height with the factor level.

Fig. 4. Response surface obtained from CDC design.

eluents. Ethylene diamine and thiourea were also evaluated as eluent. For this study standard solution of mercury at different pH values were loaded onto the column for 1 min and eluted with the eluents mentioned above at different concentrations. Thiourea was the eluent which offered the best mercury signal, this signal increased as the thiourea concentration increased. Use of the remaining above-mentioned eluents led to transitory signals with elevated dispersion and unacceptable long elution times, which did not permit high sensitivity conditions to be obtained. According to these results, thiourea was selected as the eluent.

The microcolumn dimensions were carefully optimized, very little retention is achieved with a short column (less than 5 mm), maximum efficiency being achieved with a 5.0–7.0 mm column. Considering the high breakthrough capacity of the column, lengths greater than 7.0 mm are not necessary for the proposed system. An increase in resin volume led to an appreciable enlargement of the elution peaks with a consequent decrease in the detection limit. A very small volume of resin could result in saturation of the absorption sites with a decrease in recovery. Also, the effect of the column internal diameter on the elution profile dispersion is widely known [29], 3.0 mm being considered as an acceptable column i.d. Hence, a glass tube microcolumn (3 cm × 3 mm i.d.), packed with the resin to a height of 7 mm, was selected for this study.

NaBH$_4$ was chosen as reductant. The NaBH$_4$ concentration was varied from 0.02 to 0.5% (w/v). The results obtained showed that the peak height remained constant for reductant concentrations equal, or greater than 0.1%. A concentration of 0.2% was used in practice. The influence of mixing coil length was also examined to ensure homogeneous mixing of the sample and NaBH$_4$ solutions. Tubing coils (0.8 mm i.d.) of different lengths (0–200 cm) were tested. The coil length selected here was 100 cm. A coil length above this value is not recommended because the resulting larger back-pressure from the system is less favourable for phase separation.

Once these factors have been fixed, a CCD involving 26 runs was then performed in order to obtain the optimum conditions with the four continuous variables found to be potentially significant for this study. The variables to be optimized were: eluent concentrations (A), pH (B), sample flow rate (C) and eluent flow rate (D). The experimental domain levels for CCD experiments appear in Table 2. The significance of the effects was checked by analysis of the variance (ANOVA) and using p-value significance levels. The ANOVA results produced the graph showing the influence of main effect represented in Fig. 3. These results indicated that the factors A and C were not statistically significant at the 95% confidence level ($p < 0.05$). Neglecting insignificant terms and their associated squares and interactions the results obtained fit the equation:

$$Y = 0.048 - 0.015B + 0.070D - 0.008D^2$$
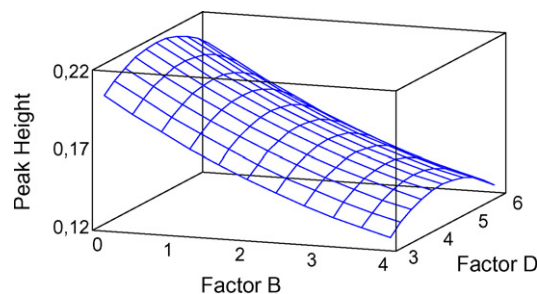
where Y is the peak height. The predicted values by this equation were in accordance with the peak height values obtained experimentally (coefficient of determination $R^2 = 0.989$). The response surface for this equation. is shown in Fig. 4.

As result of these observations, the following working conditions were chosen: $A = 6\%$, $B = 1$, $C = 7.2\,\text{ml min}^{-1}$, $D = 4.6\,\text{ml min}^{-1}$ for latter experiments.

On the other hand, in time-based preconcentration systems the loading time indicates the preconcentration time and affects directly the enrichment factor. Thus, the loading time was investigated in the range between 30 and 540 s using the optimum conditions described above. The absorbance was practically linear up to a 540 s preconcentration time. Although sensitivity increased on increasing the sample loading time, the loading time was set at 120 s in order to achieve high sample frequency with a reasonable sensitivity. Longer loading times can be used for samples with low concentrations of mercury. Also, preliminary tests showed that the sample volume was a not important factor when the mass of analyte arriving at the column was kept constant.

3.2. Selective preconcentration of mercury species

In order to evaluate the separation of the mercury species using the PSTH-cpg resin, the proposed method was separately applied to the determination of inorganic mercury and organomercurial species in synthetic samples at two different concentration levels, viz., 10 and 5 ng l^{-1}. A 100% recovery was obtained for inorganic mercury, while no retention of the organomercurial species on the resin was observed, indicating the total separation of the mercury species. This could be attributed to the double charge of the inorganic ion, which was more strongly retained by the PSTH-cpg column compared to the singly charged species MeHg. Previous oxidation of the organomercurial species to inorganic mercury allowed the determination of total mercury. An estimation of the MeHg content was obtained by difference between the total mercury and the inorganic mercury. Thus, the present methodology appears suitable for distinguishing between inorganic and organic mercury species.

3.3. Analytical performance characteristics

The analytical performance characteristics for both techniques, under the optimum conditions for a 120 s preconcetration time are summarized in Table 3. As can be seen, a lower detection limit (LOD) was obtained for the inorganic mercury determination by CV-ETAAS, as the sensitivity was better for this technique. The LOD was defined as the concentration of analyte giving a signal equivalent to three times the standard deviation of the blank signal plus the net blank intensity. The precision for aqueous standards was evaluated as the relative standard deviation obtained after analysing 10 series of 10 replicates and the enrichment factor (EF) was defined as the ratio of the slopes of the linear section of the calibration

Table 3
Analytical performance of the FI on-line preconcentration method for Hg(II) determination

Parameter	CV-AAS	CV-ETAAS
Sample volume	14.4 ml	14.4 ml
Preconcentration time	120 s	120 s
Sampling frequency	20 h^{-1}	16 h^{-1}
Enrichment factor	28	42
Detection limit	0.01 μg l^{-1}	0.006 μg l^{-1}
Precision (R.S.D., $n = 10$, 1.0 μg l^{-1})	3.4	3.5
Linear range	0.1–30 μg l^{-1}	0.009–1.5 μg l^{-1}
Slope (aqueous Hg^{2+})	0.0954 (μg l^{-1})$^{-1}$	0.1534 (μg l^{-1})$^{-1}$
Correlation coefficient	$R = 0.999$	$R = 0.995$
Slope (standard addition)	0.024–0.048 (μg l^{-1})$^{-1}$	0.036–0.068 (μg l^{-1})$^{-1}$
Correlation coefficient	$R = 0.995$–0.999	$R = 0.997$–0.998

graphs before and after the preconcentration. The LODs obtained were perfectly adequate for the analyzed biological samples, which compares favourably with other values obtained using FI systems coupled on-line to conventional atomic spectrometers [30–32]. On the other hand, the sample loading time is very flexible, allowing the use of different sample volumes according to the concentration level in the sample.

3.4. Interference studies

The effects of representative potential interfering species (at the concentration levels at which they may occur in biological samples after digestion) were tested for their effect upon retention and determination of mercury under the optimum conditions described above, using standard solution of 4 μg l^{-1} Hg(II). The results showed that only few of the elements usually found in biological samples may compete with the Hg(II) during the preconcentration and separation process. Thus, concentration up to at least 5 mg l^{-1} of Ni(II), Al(III), Mn(II), Cd(II), Bi(III), Cr(III), Co(II) and Fe(III), and concentrations up to 4 mg l^{-1} Zn(II), Pb(II) and Cu(II) had no significant effect (less than 5% recovery variation) on the preconcentration and determination of Hg. Commonly encountered matrix components such as alkali elements generally do not form stable complexes and are not retained on the resin. Also, alkaline earth elements such as Ca(II) and Mg(II) were not retained on the column. On the other hand, anions such as PO$_4^{3-}$, NO$_3^-$, SO$_4^{2-}$ and Br$^-$ could be tolerated at concentrations up to at least 5 mg l^{-1}. F$^-$, I$^-$ and citric ions caused small variations to the signal when present at concentrations higher than 3 mg l^{-1}.

3.5. Analytical results

In order to test the accuracy and applicability of the proposed method to the analysis of real samples, two biological reference materials were analysed. The obtained results, as the average of three separate determinations, for total Hg, Hg^{2+} and CH$_3$Hg$^+$ are shown in Table 4. The organic mercury concentration calculated as the difference between the total Hg minus the inorganic mercury agree with the certified methylmercury concentration. This is a confirmation that most of the organic mercury obtained by the difference mentioned is really methylmercury, indicating that the other organic species, where they are detected by the proposed method, are not significant. Also, this is a proof that the obtained value by the proposed procedure, is really the concentration of Hg(II), indicating the total separation of the mercury species. All the determinations were performed by using standard addition for calibration.

Table 4
Results for the determination of total, inorganic mercury and methylmercury in certified reference biological materials by CV-AAS and CV-ETAAS

Samples	Certified/spiked			Determined					
				CV-AAS			CV-ETAAS		
	Total Hg	MeHg	Hg^{2+a}	Total Hg	MeHg[b]	Hg^{2+}	Total Hg	MeHg[b]	Hg^{2+}
TORT-1	0.33 ± 0.06	0.128 ± 0.014	0.202 ± 0.062	0.36 ± 0.01	0.16 ± 0.01	0.20 ± 0.01	0.30 ± 0.01	0.10 ± 0.02	0.20 ± 0.02
DOLT-1	0.225 ± 0.037	0.080 ± 0.011	0.145 ± 0.038	0.22 ± 0.08	0.07 ± 0.08	0.15 ± 0.01	0.21 ± 0.01	0.07 ± 0.02	0.14 ± 0.01
Clams			–	2.15 ± 0.08	2.04 ± 0.08	0.11 ± 0.02	2.16 ± 0.05	2.03 ± 0.05	0.13 ± 0.01
		–	0.80[c]	2.87 ± 0.01	1.99 ± 0.01	0.88 ± 0.01	2.98 ± 0.01	2.61 ± 0.01	0.92 ± 0.01
Mussels		2.0[c]	1.60[c]	3.72 ± 0.02	1.99 ± 0.02	1.73 ± 0.02	3.75 ± 0.02	2.02 ± 0.03	1.73 ± 0.02
		4.0[c]		2.1 ± 0.1	2.0 ± 0.1	0.11 ± 0.02	2.01 ± 0.07	1.9 ± 0.1	0.13 ± 0.01
			–	4.25 ± 0.01	4.14 ± 0.02		4.2 ± 0.1	4.1 ± 0.1	
		–	0.67[c]	6.07 ± 0.01	5.96 ± 0.02	0.08 ± 0.01	6.06 ± 0.02	5.93 ± 0.02	0.08 ± 0.01
		1.2	1.33[c]	1.02 ± 0.04	0.94 ± 0.04	0.75 ± 0.01	0.9 ± 0.2	0.8 ± 0.2	0.74 ± 0.01
		2.4		1.74 ± 0.01	0.99 ± 0.01	1.42 ± 0.01	1.63 ± 0.01	0.89 ± 0.01	1.42 ± 0.01
				2.26 ± 0.01	0.84 ± 0.01	0.08 ± 0.01	2.18 ± 0.01	0.76 ± 0.01	0.08 ± 0.01
				1.02 ± 0.04	0.94 ± 0.04		0.8 ± 0.1	0.7 ± 0.1	
				2.2 ± 0.1	2.1 ± 0.1		2.0 ± 0.1	1.9 ± 0.1	
				3.46 ± 0.04	3.38 ± 0.04		3.13 ± 0.03	3.05 ± 0.03	

Obtained values (average of 3 independient analysis ± the corresponding standard deviation) in μg g^{-1}.
[a] Calculated as the difference between the total Hg minus the Hg as MeHg.
[b] Calculated as the difference between the total Hg minus the inorganic mercury.
[c] Spiked.

In addition, composite samples of mussel tissues and clams were analyzed. The results are presented in Table 4. The samples, previously analyzed, were spiked with Hg(II) at concentrations levels similar than those previously found (see Table 4) and recovery values from 96 to 101% for Hg(II), from 94 to 110% for total mercury and from 98 to 110% for methylmercury were obtained.

4. Conclusions

The FI on-line preconcentration and separation system using PSTH-cpg as a sorbent material allowed the determination of Hg^{2+} and total Hg in biological samples by CV-AAS and CV-ETAAS. The detection limits obtained are adequate for the analyzed samples as the sample loading time can be easily changed in the preconcentration procedure. In addition, the speciation analysis procedure does not use chromatographic techniques, requiring only an atomic absorption instrument with a simple FI system. The use of expensive and sophisticated instruments is also avoided. The high speed, ease of use and automation, selectivity and relative freedom from random contamination by sample handling make this method suitable for mercury speciation in biological samples. The minicolumn has a practically unlimited lifetime without the demand for generation. PSTH-cpg is low cost compared with other chelating sorbents such as Chelex-100 and Muromac A-1.

Acknowledgements

References

[1] Toxicological Profile for Mercury (update), Agency for Toxic Substances and Disease Registry (ATSDR), US. Department of Health and Human Services, Atlanta, GA, 1999, p. 617.
[2] L. Valentino, M.V. Torregrossa, L.J. Saliba, Water Sci. Technol. 32 (1995) 41.
[3] B. Bhattacharya, S.K. Sarkar, Chemosphere 33 (1996) 41.
[4] B.A. Monson, P.L. Brezonik, Biogeochemistry 40 (1998) 147.
[5] L. Ebdon, M.E. Foulkers, S. Le Roux, R. Muñoz-Olivas, Analyst 127 (2002) 1108.
[6] H. Emteborg, D.C. Baxter, W. Frech, Analyst 118 (1993) 1007.
[7] H. Emteborg, D.C. Baxter, M. Sharp, W. Frech, Analyst 120 (1995) 69.
[8] M. Johansson, H. Emteborg, H. Glad, F. Reinholdsson, D.C. Baxter, Fresenius J. Anal. Chem. 351 (1995) 461.
[9] P. Jitaru, H. Goenaga Infante, F.C. Adams, Anal. Chim. Acta 489 (2003) 45.
[10] H.E.L. Armstrong, W.T. Corns, P.B. Stockwell, G. O'Connor, L. Ebdon, E.H. Evans, Anal. Chim. Acta 390 (1999) 245.
[11] R. Cela, R.A. Lorenzo, M.C. Mejuto, N.H. Bollain, M.C. Cassais, A. Botana, E. Rubi, I. Medina, Mikrochim. Acta 109 (1996) 111.
[12] C.F. Harrington, Trends Anal. Chem. 19 (2000) 167.
[13] D.M. Sanchez, R. Martin, R. Morante, J. Marin, M.L. Munuera, Talanta 52 (2000) 671.
[14] J.E. Sanchez Uría, A. Sanz-Medel, Talanta 47 (1998) 509.
[15] G. Tao, S.N. Willie, R. Sturgeon, Analyst 123 (1998) 1215.
[16] G. Tao, S.N. Willie, R.E. Sturgeon, J. Anal. At. Spectrom. 14 (1999) 1929.
[17] P. Cava Montesino, A. Domínguez Vidal, M.L. Cervera, A. Pasto rand, M. de la Guardia, J. Anal. At. Spectrom. 19 (2004) 1390.
[18] W. Jian, C.W. McLeod, Talanta 39 (1992) 1537.
[19] J. Sanz, A. Diego, J.C. Raposo, J.M. Madariaga, J. Larreta, I. Martinez Arkarazo, J. Sep. Sci. 27 (2004) 1202.
[20] L.M. Dong, X.P. Yan, Y. Li, Y. Jiang, S.W. Wang, D.Q. Jian, J. Chromatogr. A 1036 (2004) 119.
[21] P. Cañada Rudner, A. Garcia de Torres, J.M. Cano Pavón, F. Sanchez Rojas, Talanta 46 (1998) 1095.
[22] P. Cañada Rudner, A. García de Torres, J.M. Cano Pavón, E. Rodríguez Castellon, J. Anal. At. Spectrom. 13 (1998) 243.
[23] E. Vereda Alonso, M.T. Siles Cordero, A. García de Torres, J.M. Cano Pavón, Anal. Bioanal. Chem. 385 (2006) 1178.
[24] G. Sado, M.C. Sado, Les Plans d'Expériences, Afnor Techniques, Paris, 1991, p. 100.
[25] J. Goupy, Plans d'Expériences pour Surfaces de Résponse, Dunod, Paris, 1999, p. 253.
[26] J. Moreda Piñeiro, C. Moscoso Pérez, P. López Mahía, S. Muniategui Lorenzo, E. Fernández Fernández, D. Prada Rodríguez, Talanta 53 (2001) 871.
[27] G.M. Mizanur Rahman, H.M. Skip Kingston, J. Anal. At. Spectrom. 20 (2005) 183.
[28] Statgraphics Plus Versión 6.0, Reference Manual, Manugistics, Rockwille, MD, 1992.
[29] Z.L. Fang, Flow Injection Separation and Preconcentration, VCH, Weinheim, 1993.
[30] F. Barbosa Jr., C.D. Palmer, F.J. Krug, P.J. Parsons, J. Anal. At. Spectrom. 19 (2004) 1000.
[31] D. Placido Torres, M. Antunes Vieira, A. Schwing Ribeiro, A.J. Curtius, J. Anal. At. Spectrom. 20 (2005) 289.
[32] V.L. Dressler, E.M. Flores, D. Pozebon, L.E. Kaercher, J. Anal. At. Spectrom. 17 (2002) 790.

Fluorescence sensors for trace monitoring of dissolved ammonia

Kerstin Waich, Torsten Mayr *, Ingo Klimant

Institute of Analytical Chemistry and Radiochemistry, Graz University of Technology, Technikerstr. 4, 8010 Graz, Austria

ARTICLE INFO

ABSTRACT

Even though monitoring of dissolved ammonia is acutely important for environmental studies, fish farms and for industrial surveillance, no system for the performance of online measurements at the concentrations needed exists so far. For many applications it is necessary to detect dissolved ammonia concentrations at sub mg/l-levels, because ammonia is reported to be toxic for aquatic organisms above 25 μg/l. We present new ammonia sensitive materials consisting of fluorescent pH indicators embedded into different cellulose esters. The low pK_a value of the indicators and the high solubility of ammonia in the cellulose polymers lead to detection limits below 1 μg/l and a dynamic range between 5 and 1000 μg/l. Response times at these trace concentration levels are in the order of 20–30 min. The sensors are suitable for fresh and sea water monitoring by an additional silicon layer preventing the interference of protons and salinity. The fluorescent indicators Eosin ethylester and 2′,7′-dichlorofluorescein methylester (DCF) were investigated to achieve sensors with a dynamic range matching the target concentrations. Sensors with improved performance were obtained by employing cellulose ester nanospheres with incorporated Eosin ethylester. The simple sensor design has a high potential to be applied in miniaturized optical measurement system for online ammonia detection.

© 2008 Elsevier B.V. All rights reserved.

1. Introduction

The generation of ammonia is ubiquitous: decomposition of biological waste and sewage by micro-organisms, release of fertilizers, agricultural run-off, excretion by animals and plants, industrial emissions and volcanic activity are quoted as major sources of ammonia in our industrialized environment.

In spite of continual volatilization from the earth's surface, terrestrial exposure is not usually a problem. Ammonia rises rapidly and is destroyed by photolytic reactions.

Aquatic exposure on the other hand raises a severe problem for the underwater habitat, especially in regions of high human habitation and large numbers of farm animals, where most biological waste is released into rivers and oceans. Monitoring waste sides and water quality in natural habitat, but also in fish farms and aquariums is a crucial application for measurements of ammonia dissolved in water since ammonia is known to be toxic for aquatic organisms at concentrations above 25 μg/l [1–4].

Several methods for measurements of dissolved ammonia have been developed. Berthelot reaction, which dates from the 19th century, is still used for water analysis as it allows detecting concentrations of only 10 μg/l of ammonia. Recently, Berthelot reaction has

been integrated into a micro-fluidic system, what makes it applicable for water monitoring [5]. But still, there are disadvantages such as slow kinetics, consumption of reagents and the irreversibility of the reaction itself. One of the most popular ammonia sensors for online measurements is based on a modified pH-electrode. This ammonia selective electrode allows a fast detection of ammonia with a detection limit (LOD) of 30 μg/l, but salinity affects the measurement [6,7].

Various optical methods to measure ammonia based on pH-indicators incorporated into polymer layers have been developed in the last two decades. A wide range of LEDs, photodiodes and optical fibres became available within the last years through the rapid development in semiconductor technology. Thereby the fabrication and miniaturization of devices based on optical principles is easy and cheap [8]. Fluorescence and absorbance techniques have been employed: Bromocresol purple was integrated into a sol–gel to measure in the mg/l-range [9]. Bromophenol blue in silicone gave an LOD of 45 μg/l [10,11]. With rhodamine dyes incorporated into ethyl cellulose, PVC and PVA detection limits of 500 μg/l were reached [12]. The dynamic range of pH-indicator based sensors results chiefly from the pK_a value of the dye. Such sensors respond to gases with basic properties and which are capable of penetrating into the polymer. Simon and coworkers reported of optical NH$_3$ sensors based on pH-indicators combined with specific ionophores for ammonium (such as nonactine) to enhance the selectivity of the membranes. The

* Corresponding author. Tel.: +43 316 873 4324; fax: +43 316 873 4329.
  E-mail address: torsten.mayr@TUGraz.at (T. Mayr).

detection limit of those sensors is 2 ppb of ammonia in nitrogen [13,14].

In this study we use different cellulose esters as matrix polymers, which are capable to interact with ammonia by hydrogen bonding. This capability to interact with the polymer leads to improved diffusion properties and a higher solubility of ammonia in the cellulose esters. The polarity of the polymers varies with the kind of esterification of the polymer (acetate, propionate and butyrate esters) and influences the dynamic range of the membranes in the way the esters allow stronger or weaker interaction between the analyte and the matrix. Nevertheless, the pK_a value of the pH indicator is the parameter, which affects the detection range most. Detection limits of around 50 μg/l and a dynamic range in the mg/l concentration range were obtained using 2,7-dichlorofluorescein (pK_a 4.8) as fluorescent indicator, whereas Eosin (pK_a 3.8) gave detection limits below 1 μg/l and a dynamic range between 5 and 1000 μg/l. The performance of various combinations of dyes and polymers in films and in nanospheres were investigated.

2. Experimental

2.1. Reagents

Unless otherwise noted, materials were obtained from commercial sources and were used without further purification. Cellulose acetate (MW 100,000; CAc), cellulose acetate propionate (15,000; CAcP), cellulose acetate butyrate with 16.5–19% butyrate content (CAcB1) and cellulose acetate butyrate with 44–48% butyrate content (CAcB2) were purchased from Sigma–Aldrich. They were washed with Millipore water and dried in a drying chamber at 80 °C for 48 h to evaporate unreacted acid. Eosin ethylester (E) and Teflon AF was purchased from Sigma–Aldrich, acetone from Merck, 2′,7′-dichlorofluorescein and methyl iodine from Fluka. Silicone (PP2-RG01, 2 part reprographic Silicone) was purchased from ABCR.

2.2. Syntheses

2.2.1. Synthesis of 2′,7′-dichlorofluorescein methylester (DCF)

A mixture of 2′,7′-dichlorofluorescein (600 mg, 1.496 mmol) and methyl iodine (425 mg, 2.992 mmol) were stirred in 5 ml of DMSO and K_2CO_3 solid (435 mg, 3.14 mmol) at room temperature for 24 h. A saturated NaCl solution was added to the reaction. As DCF is well soluble in water the whole mixture, acidified with HCl, was extracted with ethyl acetate. The organic phase was dried with $MgSO_4$ and evaporated to dryness under reduced pressure. The obtained product was further purified by column chromatography (n-hexane:ethyl acetate 1:4; with some ml of methane sulfonic acid, $R_f = 3.5$). Yield: 65% ^{1}H-NMR (δ, 20 °C, DMSO-d_6, 500 MHz): 2.62 (s, 3H, O–CH$_3$), 6.82 (s, 2H, aromat.), 6.90 (s, 2H, $J = 15$ Hz, aromat.), 7.51 (d, 1H, $J = 15$ Hz, aromat.), 7.80 (t, 1H, $J = 15$ Hz, aromat.), 7.90 (t, 1H, $J = 15$ Hz, aromat.), 8.3 (d, 1H, $J = 16$ Hz, aromat.) [15].

2.3. Preparation of the nanospheres

10 ml of acetone containing 100 mg of polymer CAc, CAcP or CAcB2 and 0.14 mg of E were added drop-wise to 50 ml of Millipore water in a round-bottomed flask during ultra sonification. The resulting nanospheres were dialysed for 24 h. After dialyses the nanospheres were dried by lyophilisation.

2.4. Preparation of sensing membranes

2.4.1. Bulk membranes (MB)

Sensing membranes were prepared by spreading cocktails containing cellulose esters (5% (w/w) polymer content) and dye

dissolved in acetone onto polyester films (thickness: 175 μm; Goodfellow, Huntingdon, UK) with a homemade knife coating device to obtain membranes of a calculated thickness of approx. 1 μm for fluorescence and approx. 5 μm for absorption measurements. For the composition of the membranes see Table 1. All cocktails contained additionally 0.6 μmol of methanesulfonic acid. The ammonia sensitive layers were covered with a 5% (w/w) silicone solution in n-hexane to obtain an approx. 1-μm thick silicone layer. For the composition and the thickness of the MBs see Table 1.

2.4.2. Particle membranes (MP)

10 mg of the nanospheres were resuspended in 400 μl of a 2% (w/w) silicone solution in n-hexane containing 1.2 μmol of methanesulfonic acid in an ultrasonic bath. Those cocktails were spread onto polyester films (thickness: 175 μm; Goodfellow, Huntingdon, UK) with a homemade knife coating device to obtain membranes of a calculated thickness of <1 μm (Table 1). The obtained membranes were left for drying for about 20 h at ambient air and then another silicone layer (5% (w/w) silicone in n-hexane), resulting layer thickness: approx. 1 μm was applied.

2.5. Apparatus

2.5.1. Spectral characterization of the sensing membranes

Fluorescence measurements (spectra and intensity vs. time) were performed using a LS 50 B fluorescence spectrometer (PerkinElmer, Wellesley, US). Sensor membranes were mounted in a fluorescence spectrophotometer equipped with a flow-through cell adjusted to 25 °C. Before the measurements the membranes were conditioned with 500 μg/l NH$_3$ in phosphate buffer for membranes containing DCF, 50 μg/l in phosphate buffer for membranes containing E. All measurements were performed at this temperature exposing the membranes to solutions with dissolved ammonia or trimethylamine (TMA).

For absorption spectra sensor membranes were exposed to solutions with dissolved ammonia and investigated with a Cary 50 Bio UV–vis-Spectrometer (Varian, Palo Alto, US).

2.5.2. Characterization of the nanospheres

The average size of the polymer particles was determined by dynamic light scattering (DLS) measurement with Zeta Nanosizer (Malvern Instruments, UK) with particle suspensions containing approx. 1 mg particles per ml water. The software calculates a value called Z–Average size (or cumulant mean), which is an intensity

Table 1
Composition of the sensing membranes

Membrane	Thickness[a] (μm)	Polymer	Dye	Concentration of the dye (mmol/kg)
MB1	1	CAc	E	0.9
MB2	1	CAcP	E	0.9
MB3	1	CAcB1	E	0.9
MB4	1	CAcB2	E	0.9
MB5	1	CAcP (50%), CAcB2 (50%)	E	0.9
MB6	1	CAc	DCF	1.5
MB7	5	CAc	E	3.6
MB8	5	CAc	DCF	6
MP1	1	CAc	E	1
MP2	1	CAcP	E	1
MP3	1	CAcB2	E	1

[a] The method of membrane preparation does not allow regarding the membrane thickness as an exact value. The values we use to indicate the membrane thickness are estimated considering the concentration of the polymer cocktail and the spacer thickness used in the knife coating device.

mean, and the polydispersity index PDI. Particle sizes were measured in water after dialyses.

2.6. Solutions and buffers

Aqueous solutions were prepared from Millipore water. Stock solutions were prepared dissolving ammonium chloride and trimethylammonium hydrochloride in a buffered solution at pH 7. The pH was adjusted using 100 mM sodium phosphate buffer. The amount of free NH_3 and trimethylamine in water is defined by the pH-value of the solution and was calculated by the Henderson–Haselbalch equation. Temperature factors were considered according to Ref. [16].

## 3. Results and discussion

3.1. Choice of dyes

Fluorescence measurements are highly sensitive and easy to perform and were therefore chosen to achieve the demands of trace level detection of dissolved ammonia in μg/l range. Xanthene dyes shown in Scheme 1 were used as pH indicators and incorporated into polymer layers. This class of fluorescent dyes has been mainly employed for pH sensing and for fluorescence imaging [17,18].

The spectral and thermodynamic properties of xanthene dyes are primarily governed by the substitution pattern of the xanthene structure, for instance, emission and absorption characteristics, the quantum yield (QY) and the pK_a values. Generally the substitution at the 2′ and 7′ positions has little effect on the quantum efficiency, whereas substitutions at the 4′ and 5′ positions decrease the quantum yield. Due to this fact the QY of DCF is above 0.9 (pH 9, phosphate buffer), what is in the range of Fluorescein, but the QY of E is around 0.5. The pK_a values of those dyes are determined by the type of halogenation of the 2′, 4′, 5′, 7′-positions. The pK_a value of 2′,7′-dichlorofluorescein is 4.8, whereas Eosin (2′,4′,5′,7′-tetrabromofluorescein, E) has a pK_a value of 3.8 [19–21]. E has the lowest pK_a value of commercially available dyes and is therefore the most promising compound for trace measurements of ammonia.

The sensing scheme employed is based on the acid–base equilibrium between ammonia ($pK_a = 9.24$) and the dye (Eq. (1)). Obviously, the pK_a of the pH indicator determines the dynamic range of the sensor.

$$NH_3(aq) + IndH \leftrightarrow NH_4^+ + Ind^- \tag{1}$$
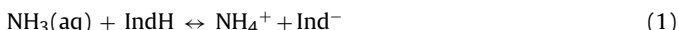
The emission characteristics of xanthenes also strongly depend on species formed by protonation or deprotonation. The presence of ammonia in the sensing layer leads to the deprotonation of the indicator resulting in a rise of the detected fluorescence intensity (Scheme 2). In order to simplify the response to ammonia ethyl- and methylesters of the dyes were used. Thus the protonation of the carboxylic group and formation of the neutral species, a lactone,
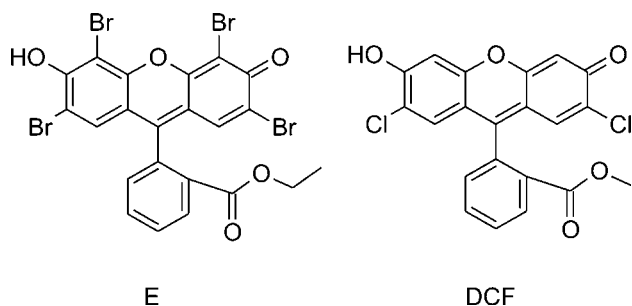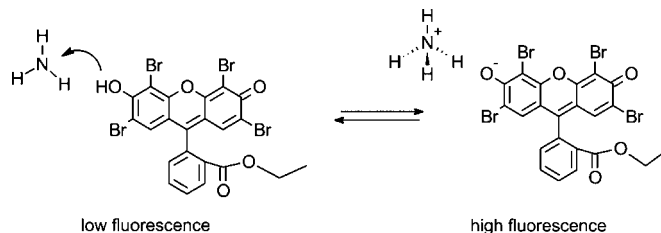
Scheme 2. Sensing scheme of sensors containing Eosin ethylester (E) as pH indicator.

which is colourless and nonfluorescent is prevented [22]. Since the carboxylic and the phenolic group have similar pK_a values the esterification does not influence the magnitude of response towards ammonia [20]. In addition the esters provide an increased solubility in the matrix polymer. This prevents the dye from leaching.

The concentrations of the dyes in the sensing layers (MB and MP) were chosen in an agreement of signal to noise ratio, signal intensities and response times (Tables 1 and 2). Higher concentrations obviously lead to a higher signal and a higher signal to noise ratio, but also to longer response times. The concentrations are in a range where self-quenching of fluorescence is not observed.

3.2. Choice of polymers

Through their hydrophilicity the cellulose esters used in this work constitute a good matrix for xanthene dyes: in hydrophilic environments these dyes possess high quantum yields. Further the matrix is able to stabilize ions resulting from the sensing mechanism (anion of the xanthene dye and the ammonium ion), yielding in a higher sensitivity of the sensor.

The hydrophilicity of the polymers is altered with the nature of the ester (acetyl, propionyl or butyryl), what influences the amount of water absorption. The water absorption over 24 h is up to 7.0% and 2.2% for CAc and CAcB, respectively [23]. Three different adsorbed water species have been reported: hydrate water, liquid water and a rest of water with a structure between the hydrate and the liquid water. Small, hydrophobic pores contain clusters of weakly bonded water, whereas larger, predominantly hydrophilic pores contain liquid water [24,25].

3.3. Sensor assembly

Three techniques for the immobilization of a dye on a solid matrix material are commonly used in optical sensor technology: covalent binding, adsorption and embedding. Physical entrapment was employed, because it is easy and fast. "Cocktails" of the polymer and the dye in acetone were prepared, and spread onto a transparent, inert polyester membrane. The application of methyl- and ethylesters of the dyes and an additional silicone layer assure that

Scheme 1. Eosin ethylester (E), 2′,7′-dichlorofluorescein methylester (DCF).

Table 2
Response times (t_{95}), reversibility and 50% signal change of membranes and particle membranes containing Eosin ethylester (E) as pH-indicator

	t_{95} (min) 25–50 μg/l	Reversibility (min) 50–25 μg/l	50% signal change (μg/l)
MB1	40	35	13
MB2	29	60	32
MB3	22	31	158
MB4	150	166	183
MB5	61	93	158
MP1	22	n. d.	9
MP2	34	38	22
MP3	54	72	80
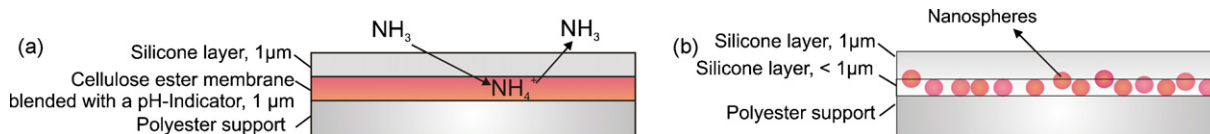
Fig. 1. (a) Sensor assembly using part of a MB. (b) Sensor assembly of a MP. Not to scale.

leaching is prevented and leads to rugged membranes for long time measurements.

Two different sensor layouts are investigated: MB and MP (Fig. 1). Regarding the key limitation – the slow mass transport from the sample to reach the required equilibrium concentration in the sensing membrane – causing long response times in highly dilute samples is, it was tried to produce very thin layers in the two different assemblies [26]. The MB sensors consist of two layers, a sensing layer and a protective layer, which are both around 1-μm thick. The protective layer made from silicon is highly gas-permeable but impermeable for ions preventing the interference of protons and ions (Fig. 1a).

MPs were also prepared by two layers because the first polymer layer containing the nanospheres is very thin (<1 μm) and has to be covered with a protective, second layer of silicone to prevent the nanospheres from poking out of the silicone layer's surface. The over all thickness of the sensor is less than 2 μm.

Traces of methane sulfonic acid were added to the sensor cocktail, because the fluorescent indicators, especially E, are easy to be deprotonated by any basic compound in the sensor cocktail. After conditioning the membranes with ammonia and plain buffer, the sensors were reversible to a certain acid–base equilibrium. This

equilibrium is the baseline for the performed measurements. The concentration of methane sulfonic acid is very low (0.6 μmol/kg polymer in MBs; 1.2 μmol/kg polymer in MPs) and no further influence of the acid on the measurement could be observed.

3.4. Spectral characteristics

The detection of ammonia is carried out by the measurement of the change of fluorescence intensities. As shown in Fig. 2 the protonated and the deprotonated form of all of the dyes have maxima, which differ approx. 60 nm. The difference of the absorption maxima and the more effective absorbance of the deprotonated species result in a high fluorescence intensity change by excitation at an appropriate wavelength. The maxima of the emission spectra do not shift when being deprotonated. Both, absorption and emission maxima of E are shifted 15 nm to higher wavelengths compared to DCF. Because of the Stokes shift of approx. 10 nm the fluorophores were excited at lower wavelengths than their absorption maxima. DCF is exited at 490 nm and fluorescence is detected at 540 nm. E is exited at 510 nm to detect at 560 nm in all measurements, because the polymers used do not significantly influence the maxima of E.
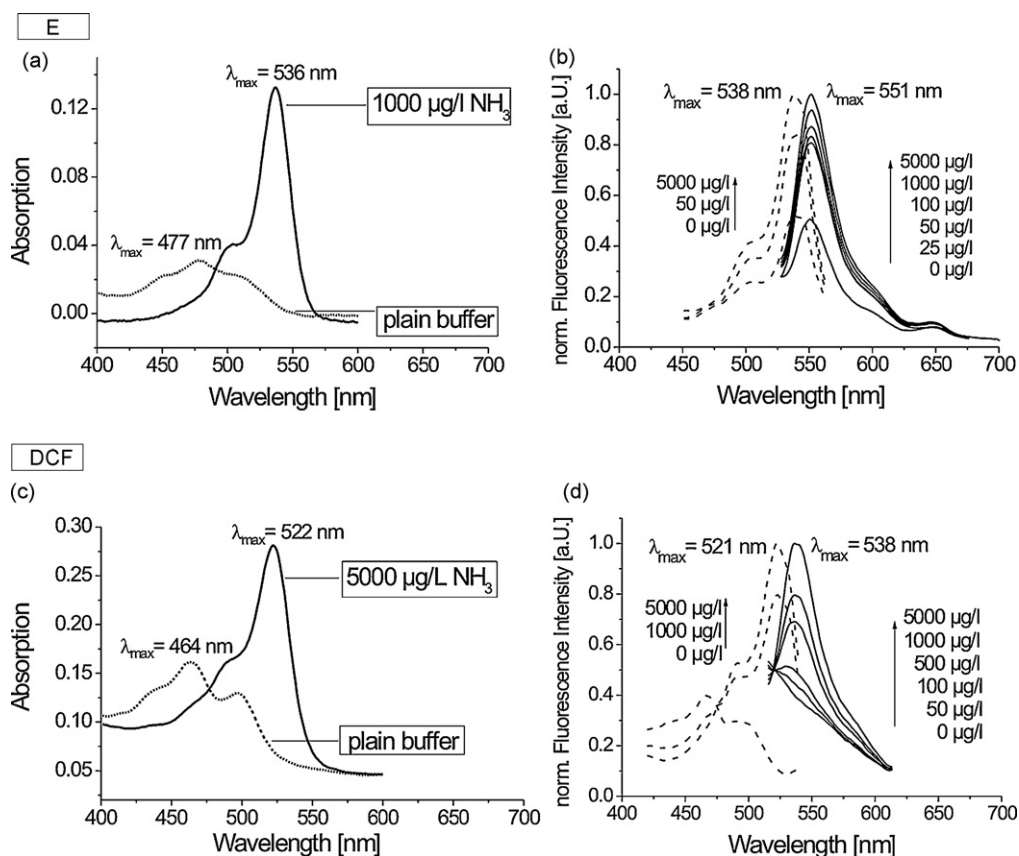
Fig. 2. (a) Absorption spectra of MB7 exposed to plain sodium phosphate buffer and 1000 μg/l of NH$_3$. (b) Excitation (λ_{em} = 580 nm) and emission (λ_{ex} = 505 nm) spectra of MB1 exposed to different concentrations of ammonia. (c) Absorption spectra of MB8 exposed to plain buffer and 5000 μg/l of NH$_3$. (d) Excitation (λ_{em} = 570 nm) and emission (λ_{ex} = 490 nm) spectra of MB6 exposed to different concentrations of ammonia.

Fig. 3. (a) Response curve of MB2 when exposed to different concentrations of dissolved ammonia. (b) Comparison of the calibration curves of MB1–MB5 containing E embedded into different cellulose ester polymers (MB1: –■–, MB2: –●–, MB3: –▼–, MB4: –▲–, MB5: –◆–).

3.5. Response of the membranes to ammonia

The fact that the water uptake of the cellulose esters varies with the type of the ester influences the detection limits and the response times for ammonia of a membrane significantly, even though the same dye is embedded. The response of MBs can be divided into two phases: first a fast signal raise occurs. This response behaviour does not involve the micro-environment of the dye. It happens in the less hydrophobic parts of the cellulose esters, which also contain liquid water and is only limited by the diffusion of the analyte through the silicone and cellulose ester to the dye. After this fast signal raise the highly flexible polymer rearranges when being exposed to the analyte leading to a much lower slope of the response curve. The sensing reaction now only occurs in the more hydrophobic parts of the polymer, where the water is bound to the cellulose esters and the water content is less. A typical response curve of MB2 containing Eosin ethylester is shown in Fig. 3a.

Sensing membranes MB1–MB5 containing Eosin ethylester E as indicator are suitable to measure extremely low ammonia concentrations (see Fig. 3b). MB1 and MB2 show detection limits below 1 µg/l and 50% signal changes of 13 and 32 µg/l, respectively. The 50% signal change is defined by setting the baseline to 0% and the highest ammonia concentration measured to 100%. At the highest concentration of ammonia measured the dye is assumed to be fully deprotonated. MBs containing cellulose butyrate esters (MB3, MB4 and MB5) have a dynamic range at significantly higher ammonia concentrations, because they are more hydrophobic and absorb less water. MB4 contains most butyrate esters. It shows the highest 50% signal change of 183 µg/l of the Eosin containing MBs investigated. Less butyrate esters, as there are in MB3 and MB5,

enhance the response to ammonia concerning the LOD. The 50% signal change is lowered from 183 to 158 µg/l. The response times are also affected significantly by the type of ester: for MB1 and MB2, the response times and the reversible response of 30–60 min when changing from 25 to 50 µg/l are, regarding the low concentrations, in a feasible range. The response times for MB4 are more than 2 h. In the case of MB5 and MB3 the response time is reduced significantly to 60 and 22 min, respectively, for a response to 50 µg/l of ammonia. This illustrates the big influence of the type of cellulose esters on the performance of the sensing materials. The esters are well mixable with each other. The resulting MBs are clear and no texture on their surface was observed. This enables a fine tuning of the dynamic range with the appropriate components (Table 2, Fig. 3).

The application of two different fluorescent pH-indicators yielded in membranes showing different dynamic ranges and LODs. The target concentration for an application in aquatic ecosystem ranges from 5 to 500 µg/l of ammonia. Therefore a signal change of 50% between 30 and 150 µg/l of ammonia is aspired. MB1 is highly sensitive for ammonia. With its dynamic range from 1 to 100 µg/l it is even too sensitive for the target application. Another fluorescent indicator, DCF with a pK_a of 4.8, was investigated and blended into CAc to see if the higher pK_a would result in MBs fitting better to aimed concentrations range.

Even though MB6 responds to ammonia very fast (response times t_{95} of 10–20 min) their LODs of around 50 µg/l are too high as well as the 50% signal change of around 2000 µg/l of ammonia (Fig. 4). As they are embedded into CAc, which is the polymer of the highest affinity and therefore best solubility for ammonia, no improvement of the response is expected by using other polymers.
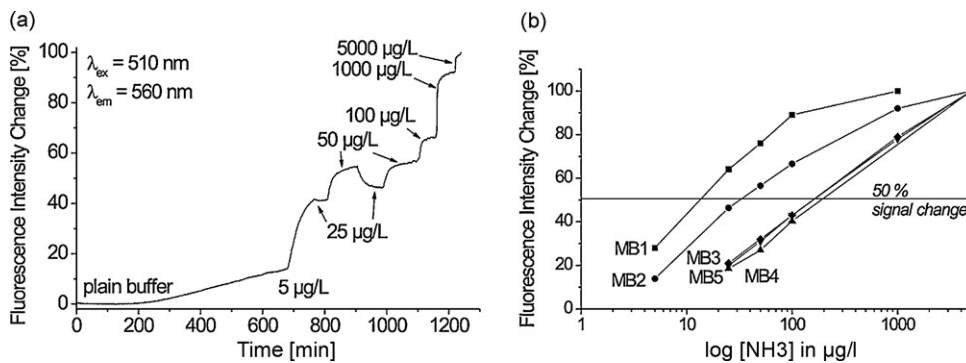
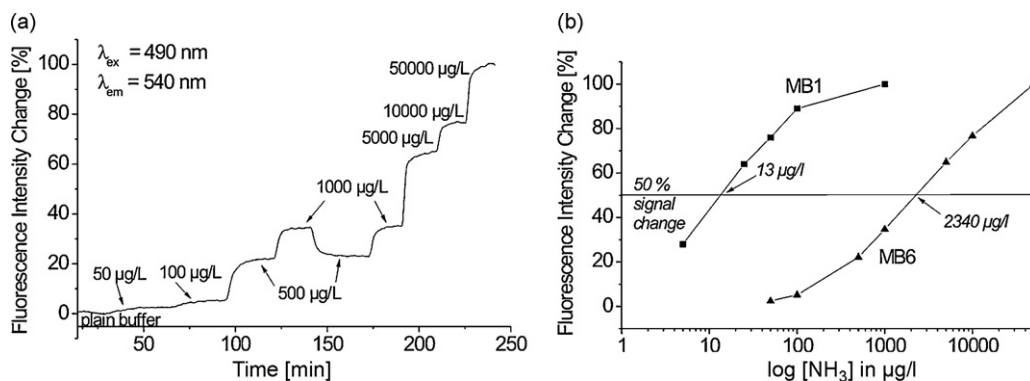

Fig. 4. (a) Response curve of MB6 when exposed to different concentrations of dissolved ammonia. (b) Comparison of the calibration curves of MB1 and MB6 containing different pH indicators embedded into cellulose acetate (MB1: –■–, MB6: –▲–).
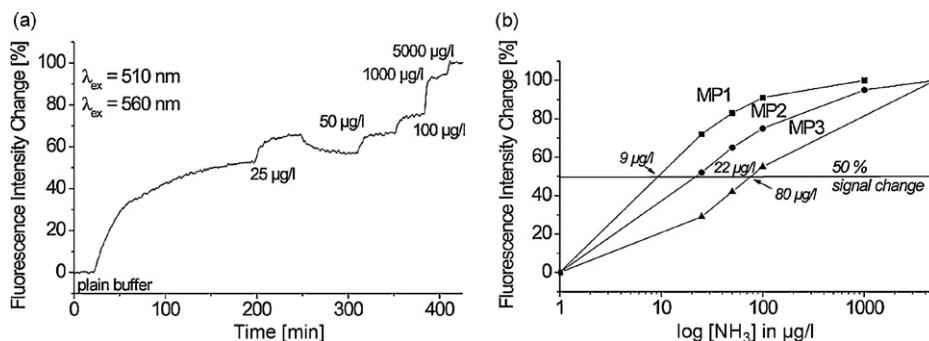
Fig. 5. (a) Response curve of MP2 when exposed to different concentrations of dissolved ammonia. (b) Comparison of the calibration curves of MP1, MP2 and MP3 containing Eosin ethylester (E) embedded into cellulose ester nanospheres (MP1: –■–, MP2: –●–, MP3: –▲–).

3.6. Characteristics of the cellulose ester nanospheres

Another approach for an alternation of the response characteristics was investigated by embedding the dye into nanospheres. Generally small sensors have a higher sensitivity for smaller sample volumes, smaller absolute detection limits, high surface over volume ratio and faster response times [27].

The nanospheres were produced in good yields (∼80%) by precipitation of a dilute acetone–polymer–dye solution in water while being ultrasonificated. Cellulose esters are soluble in acetone and insoluble in water. By changing from one solvent to the other the polymer precipitates forming nanospheres. The nanospheres have a size of around 150 nm and PDIs of 0.091–0.153. Even though PDIs below 0.1 denote a sample to be monodisperse, the size distribution of the obtained particles is sufficient for our application. The fact that the Eosin ethylester is not soluble in water and in *n*-hexane made it possible to produce dyed nanospheres by precipitation and subsequently incorporate them into very thin silicone layers (∼1 μm).

Sensing layers containing nanospheres are more sensitive to ammonia than their corresponding MBs (Fig. 5). The most striking result was obtained with membrane MP3. The 50% signal change and the response time was more than halved, compared to bulk membrane MB4 (Table 2). This behaviour can be explained by the shorter diffusion pathways of ammonia through the cellulose esters. As the surface to volume ratio is higher in the sensing layers containing nanospheres, more dye molecules are quicker accessible than in the membranes. MPs show slightly higher light scattering compared to MBs. This leads to a smaller signal to noise ratio, even though the fluorescence intensity of MPs is in the same range as the fluorescence intensity of MBs.

3.7. Reversibility and interferences

3.7.1. Effect of pH

Protons are the most important interference according to the sensing scheme. All measurements were performed in 100 mM sodium phosphate buffer system of a pH of 7. No interference of protons was observed on going from pH 5 to 8 (see Fig. 6). pH 9 leads to a signal change of 1.5%. In conclusion, the silicone layer adequately hinders protons to pass through to the pH indicator for applications in sea and fresh water.

3.7.2. Reversibility

After screening different materials, MB2 proofed to have the best properties regarding a possible application as warning device for toxic ammonia concentrations in lakes, fish farms, aquariums and in the sea. It has a dynamic range between 5 and 1000 μg/l of ammonia and very short response times of approx. 30 min, even

at concentrations of less than 100 μg/l. In addition the response is reversible and highly reproducible as shown in Fig. 7a.

3.7.3. Response to trimethylamine

TMA is the most common amine in aquatic habitat. It has a pK_a value of 9.76, which is very close to that of ammonia. The acid–base or the ammonium salt–amine equilibrium is shifted by nearly the same magnitude as the ammonium salt–ammonia equilibrium, hence the concentrations of the gaseous compounds are comparable at the same total concentration (ammonium salt plus amine, ammonium salt plus ammonia, respectively) and the same pH. Other potential interferents such as primary and secondary amines will show a response at higher concentration as the target concentration due to their higher pK_a values.

However, the response of the membrane to TMA is in the same order of magnitude as the response to ammonia. It is fast once the sensor is conditioned to TMA and it is reversible. The sensing reaction occurs first in the more hydrophilic parts of the polymer, what leads to a steep response curve. The fact, that the first response is even steeper for trimethylamine than for ammonia shows that TMA diffuses more easily to the hydrophilic parts of the membrane. The odd response curve for the concentration of 25 μg/l is explained by slower rearrangement of the hydrophobic parts of the polymer containing less water when exposed to the bulky amine. The response from 25 to 100 μg/l does not show this behaviour, because the membrane was already conditioned to TMA. The response time for 100 μg/l of TMA (130 min) is about four times longer than t_{95} for 100 μg/l of ammonia (30 min; Fig. 7b).

Trinkel et al. [10] reported that their ammonia sensor was not fully reversible after exposure to amines and that the response to ammonia was altered. This is in contrast to the behaviour of the sensing membranes of our approach. The fact that the sensor performance is not altered after exposure to TMA makes the sensor
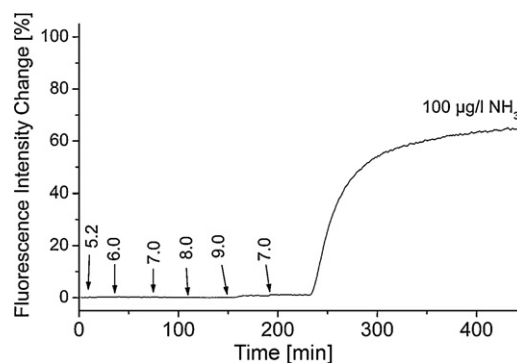
Fig. 6. Effect of pH 5 to pH 9 on MB2.
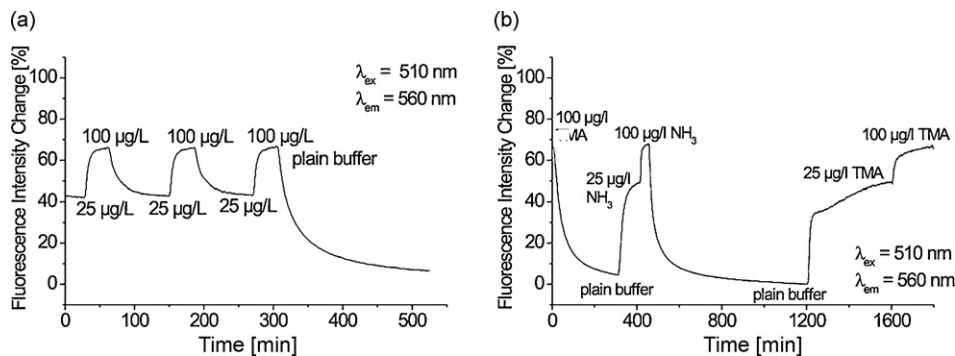
Fig. 7. (a) Reversibility of MB2. (b) Response of MB2 to trimethylamine (TMA).

suitable for the target applications in spite of this interference. It quickly indicates a critical ammonia and amine concentration, what makes it possible to act fast enough to avoid the aquatic life to be effected.

4. Conclusion

New materials for fast detection of ammonia in traces were prepared. Cellulose acetate propionate combined with Eosin ethylester showed ideal response characteristics for an application as warning device for too high ammonia concentrations in lakes, fish farms, aquariums and the sea. The LOD is less than 1 μg/l, it has a dynamic range between 5 and 1000 μg/l and its response times t_{95} are around half-an-hour for concentrations of less than 100 μg/l. Due to the silicone layer which covers the ammonia sensitive layer the sensing membranes show extraordinarily low cross-sensitivity towards pH changes. These properties, the simplicity of the system and the easiness to incorporate the sensing material into a miniaturized optical measurement setup make the material promising for further use: online monitoring of ammonia at these low concentrations was not possible before. In order to improve the signal stability of the sensor further work will be done to develop a suitable referencing system, either by dual wavelength or by dual lifetime referencing [28].

Acknowledgment

References

[1] D.J. Randall, T.K.N. Tsui, Mar. Pollut. Bull. 45 (2002) 17–23.
[2] B. Timmer, W. Olthuis, A. van den Berg, Sens. Actuators B 107 (2005) 666–677.
[3] S. Porello, G. Ferrari, M. Lenzi, E. Persia, Aquaculture 219 (2003) 485–494.
[4] M.H. Riehl, M.B. Cohen, M.A. Arnold, D.W. Murhammer, Biotech. Bioeng. 86 (2004) 852–861.
[5] A. Daridon, M. Sequeira, G. Pennarun-Thomas, H. Dirac, J.P. Krog, P. Gravesen, J. Lichtenberg, D. Dermond, E. Verpoorte, N.F. de Rooij, Sens. Actuators B 76 (2001) 235–243.
[6] R.F. Thomas, R.L. Booth, Environ. Sci. Technol. 7 (1973) 523–526.
[7] M.D. Love, H.L. Pardue, G. Pagan, Anal. Chem. 64 (1992) 1269–1276.
[8] P.A. Lieberzeit, F.L. Dickert, Anal. Bioanal. Chem. 387 (2007) 237–247.
[9] C. Malins, T.M. Butler, B.D. MacCraith, Thin Solid Films 368 (2000) 105–110.
[10] M. Trinkel, W. Trettnak, F. Reininger, R. Benes, P. O'Leary, O.S. Wolfbeis, Anal. Chim. Acta 320 (1996) 235–243.
[11] T. Werner, I. Klimant, O.S. Wolfbeis, Analyst 120 (1995) 1627–1631.
[12] C. Preininger, G.J. Mohr, I. Klimant, O.S. Wolfbeis, Anal. Chim. Acta 334 (1996) 113–123.
[13] S.J. West, S. Ozawa, K. Seiler, S.S.S. Tan, W. Simon, Anal. Chem. 64 (1992) 533–540.
[14] S. Ozawa, P.C. Hauser, K. Seiler, S.S.S. Tan, W.E. Morf, W. Simon, Anal. Chem. 63 (1991) 640–644.
[15] E. Wang, G. Wang, L. Ma, C.M. Stivanello, S. Lam, H. Patel, Anal. Chim. Acta 334 (1996) 139–147.
[16] http://www.edis.ifas.ufl.edu.
[17] S.J. Cope, S. Hibberd, J. Whetstone, R.J. MacRae, C.D. Melia, Pharm. Res. 19 (2002) 1554–1563.
[18] B.M. Weidgans, C. Krause, I. Klimant, O.S. Wolfbeis, Analyst 129 (2004) 645–650.
[19] W.-C. Sun, K.R. Gee, D.H. Klaubert, R.P. Haugland, J. Org. Chem. 62 (1997) 6469–6475.
[20] P. Levillain, D. Fompeydie, Anal. Chem. 57 (1985) 2561–2563.
[21] H.-J. Lin, H. Szmacinski, J.R. Lakowicz, Anal. Biochem. 269 (1999) 162–167.
[22] B. Valeur, Molecular Fluorescence, Wiley-Verlag GmbH, Weinheim, 2001, p. 285.
[23] http://www.goodfellow.com.
[24] W.A.P. Luck, K. Rangsriwatananon, Colloid. Polym. Sci. 275 (1997) 964–971.
[25] D.F. Stamatialis, C.R. Dias, M.N. de Pinho, Biomacromolecules 1 (2000) 564–570.
[26] K. Wygladacz, A. Rau, C. Xu, Y. Qin, E. Bakker, Anal. Chem. 77 (2005) 4706–4712.
[27] R. Kopelman, S. Dourado, SPIE 2836 (1996) 2–11.
[28] T. Mayr, I. Klimant, O.S. Wolfbeis, T. Werner, Anal. Chim. Acta 462 (2002) 1–10.

Characterization of a distributed plasma ionization source (DPIS) for ion mobility spectrometry and mass spectrometry

Melanie J. Waltman [a,b], Prabha Dwivedi [c], Herbert H. Hill Jr [c], William C. Blanchard [d], Robert G. Ewing [a,*]

[a] Pacific Northwest National Laboratory, Richland, WA 99354, USA
[b] Department of Chemistry, New Mexico Tech, Socorro, NM 87801, USA
[c] Department of Chemistry, Washington State University, Pullman, WA 99164, USA
[d] Blanchard & Co. Inc., Phoenix, MD 21131, USA

ABSTRACT

A recently developed atmospheric pressure ionization source, a distributed plasma ionization source (DPIS), was characterized and compared to commonly used atmospheric pressure ionization sources with both mass spectrometry (MS) and ion mobility spectrometry (IMS). The source consisted of two electrodes of different sizes separated by a thin dielectric. Application of a high RF voltage across the electrodes generated plasma in air yielding both positive and negative ions. These reactant ions subsequently ionized the analyte vapors. The reactant ions generated were similar to those created in a conventional point-to-plane corona discharge ion source. The positive reactant ions generated by the source were mass identified as being solvated protons of general formula $(H_2O)_nH^+$ with $(H_2O)_2H^+$ as the most abundant reactant ion. The negative reactant ions produced were mass identified primarily as $CO_3{}^-$, $NO_3{}^-$, $NO_2{}^-$, $O_3{}^-$ and $O_2{}^-$ of various relative intensities. The predominant ion and relative ion ratios varied depending upon source construction and supporting gas flow rates. A few compounds including drugs, explosives and amines were selected to evaluate the new ionization source. The source was operated continuously for 3 months and although surface deterioration was observed visually, the source continued to produce ions at a rate similar that of the initial conditions.

© 2008 Elsevier B.V. All rights reserved.

1. Introduction

Ion mobility spectrometers are widely deployed as field instruments for detection of explosives, chemical weapons and illicit drugs along with other trace analysis applications. Most of the currently available commercial instruments use radioactive isotopes, such as ^{63}Ni, ^3H, and ^{273}Am as ionization sources. Although these ionization sources provide a stable and reliable production of ions, their use results in a variety of safety, environmental and regulatory concerns due to their radioactive nature. Therefore, there have been several investigations into the development of non-radioactive sources for atmospheric pressure chemical ionization (APCI) to be used with ion mobility spectrometry (IMS) and mass spectrometry (MS), including electrospray [1], photoionization [2] and corona discharge [3]. Electrospray ionization requires the use of solvents, pumps, an additional power supply and a heating element

for desolvation of ions produced and is predominantly used for liquid and non-volatile samples [1]. Photoionization requires the use of an extra power supply and a discharge lamp and provides selective ionization. For example alcohols can be ionized with a 10.6 eV discharge lamp [2]. Corona discharge sources require an additional power supply. Of these sources; corona discharge appears to provide the most similar ionization properties to that of ^{63}Ni sources [3].

A primary disadvantage of the corona discharge source for use with IMS is the degradation in performance and eventual failure due to erosion at the discharge point [4,5] (typically the tip of a needle or fine wire). Despite these shortcomings, the desire for a non-radioactive source for IMS has led to the development of corona discharge ionization sources for IMS. For instance, a commercial hand-held IMS with a corona discharge ionization source is currently available from Smiths Detection (Watford, UK) [6]. Positive ionization, with a corona discharge in air at atmospheric pressure, produces ions similar to those produced with a ^{63}Ni source, mainly $H^+ \cdot (H_2O)_n$, with subsequent ionization of analytes involving proton transfer and adduct formation [7]. Negative ions, on the other hand, differ remarkably between corona and ^{63}Ni ionization. The reactant ions produced in a ^{63}Ni source are

* Corresponding author at: Pacific Northwest National Laboratory, Chemical and Biological Sciences, 902 Battelle Boulevard, P.O. Box 999, Richland, WA 99354, USA. Tel.: +1 509 376 3156.

E-mail address: robert.ewing@pnl.gov (R.G. Ewing).

predominantly O_2^- and adducts including $O_2^- \cdot H_2O$ and $O_2^- \cdot CO_2$ as observed in a mass spectrometer. Negative ions observed in a corona discharge were O_2^-, O_3^-, NO_2^-, NO_3^- and CO_3^- along with various adducts of these ions with water and CO_2 [8]. The relative intensities of these ions varied dramatically and appeared to depend upon the configuration of the source used along with the constituents and flow rates of the supporting gas. The predominant ion observed in an APCI mass spectrometer using a point-to-plane discharge source appears at a m/z of 60 and has been confirmed to be CO_3^- through the use of isotopically labeled oxygen, ^{18}O [9]. In an effort to achieve reactant ions in a corona discharge similar to ^{63}Ni, a pulsed corona [3] and a reversed flow continuous corona discharge [8] were explored. Both studies showed a transition to O_2^- reactant ion chemistry postulated due to a reduction in the ozone and NO_x concentrations produced in the discharge region. The identity of the negatively charged reactant ions is critical to the subsequent ionization of analyte vapors. Negative product ions can be formed by interaction of the analyte with the reactant ion via proton abstraction, electron transfer or adduct formation. The nature of the reactant ion and the analyte will determine whether ionization occurs.

This current work describes the development of a different type of corona discharge ionization source that involves placing an RF voltage across two electrodes in contact with and on opposite sides of a dielectric. This source is referred to as a distributed plasma ionization source (DPIS) and preliminary results have been presented previously [12,13]. A recent publication describes another ionization source that also uses an alternating voltage placed across a dielectric material, referred to as a dielectric barrier discharge ionization source (DBDI), that was developed for surface ionization of explosives [10]. Differences in this configuration are that a solid sample was placed on the dielectric surface attached to a flat copper electrode, and the other electrode, a hollow tube with a gas stream directed at the sample surface, was placed a few millimeters away.

In this paper, we discuss the development of the DPIS that involves placing a high-voltage, alternating current across a dielectric to produce plasma. Reactant ions formed in the plasma then ionizes sample vapors that are introduced into the ionization region. The potential advantages of this source over a conventional point-to-plane corona discharge are in the longevity of operation and inherent physical stability obtained by fixing both electrodes to a solid surface. This study involves investigations into various configurations of the source, an analysis of the positive and negative reactant ions produced and subsequent ionization of selected compounds characterized by IMS and MS.

2. Experimental

2.1. Source design

The distributed plasma ion source [11,12] can be of any shape and it simply requires two electrodes of dissimilar size separated by a dielectric. The DPIS used in this study was constructed with a 19 mm × 19 mm microscope slide cover that was 0.018 mm thick (Perfect Parts Company, Baltimore, MD). One side of the slide cover was completely coated with titanium (referred to as the large electrode), while the other side had a 4 mm disk of titanium in the center (referred to as the small electrode). The titanium was sputtered onto the glass cover to an approximate thickness of 1.2 μm (Fig. 1A). Wires were attached to each electrode and connected to a lab built power supply that provided an approximately 6 kV peak to peak RF voltage at a frequency of 100 kHz and was battery powered allowing the source and electronics to float to the desired DC voltage. Application of this RF voltage across the two electrodes sep-
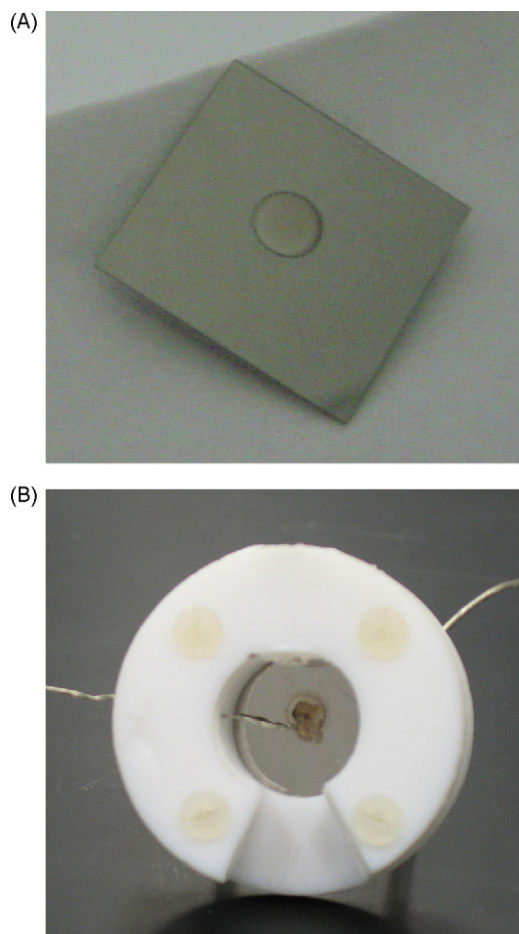
Fig. 1. The distributed plasma ion source, DPIS consisting of a 19 mm × 19 mm microscope slide cover with 1.2 μm thick titanium coating completely covering the bottom side (large electrode) and 4 mm disc on top (small electrode). (A) Is the DPIS shown in an open configuration wires were connected to each electrode and (B) is the enclosed DPIS contained in a Teflon cylinder.

arated by the dielectric caused the production of a plasma that was evident by a blue glow around the outer edge of the small electrode.

The source was operated in two different physical configurations identified as open and enclosed. The open source configuration consisted of only the glass slide cover with wires connected to the electrodes using silver conductive paint (M.G. Chemicals in Toronto, Ont., Canada) and is shown in Fig. 1A. The glass slide was positioned parallel to the interface plate of the mass spectrometer with the small electrode approximately 1 cm in front of and facing the instrument's orifice. For the enclosed source configuration, shown in Fig. 1B, the glass slide cover was placed between a copper washer and a Teflon cylinder 32 mm o.d., 13 mm i.d. and 10 mm thick. The large electrode on the slide cover was placed on the copper washer so the small electrode was in the center of the Teflon cylinder. One wire was attached to the bottom of the copper washer via a metal nut and a second wire was fastened to the small electrode with silver conductive paint. The cylinder, source and copper washer were held together by four nylon screws. A 5 mm hole was placed into the side of the cylinder and an 8 mm wedge (shown on the bottom of the cylinder in Fig. 1) was cut out opposite the hole. The enclosed source was oriented so that the slide cover was perpendicular to the interface plate and the opening of the wedge was 1 cm away from and facing the orifice. Air flow passed through the hole, across the small electrode and through the wedge towards the orifice of the mass spectrometer.

2.2. IMS-QMS

The instrument used in the positive ion study was an ion mobility spectrometer interfaced to a quadrupole mass spectrometer (IMS-QMS) constructed at Washington State University (WSU, Pullman, WA). The basic design of the instrument can be obtained elsewhere [14,15]. IMS operating conditions were as follows: IMS drift tube length: 24.7 cm; drift tube temperature: 200 °C; atmospheric pressure: 690 Torr; drift gas: N_2; drift gas flow rate: ~1000 ml/min; voltage on the target screen 10.48 kV; voltage on the ion gate 8.97 kV; distance between the target screen and the DPIS ~2 cm. The DPIS was floated to a voltage of 14.0 kV.

The IMS was interfaced to a model 150-QC ABB Extrel (Pittsburgh, PA) quadrupole MS (m/z range of 0–4000 amu) via a 40-μm pinhole interface. The output signal from the MS detector (electron multiplier) was further amplified by a Keithley model 427 amplifier (Keithley Instruments, Cleveland, OH) and then sent to either the MS data acquisition system or IMS acquisition system. Merlin software (ABB Extrel, Pittsburgh, PA) was utilized for all mass spectral analysis and mass spectrometer control. For the IMS gating and data acquisition, the electronic controls were built at Washington State University. The data acquisition and IMS gate-control software employed was Labview-based (National Instruments, Austin, TX, PC Card# PCI-M01-16XE-10, Windows 2000) and modified at Washington State University. Ion mobility spectra were obtained in two ways: full scan or single ion monitoring (SIM). In the full scan mode of operation an IMS spectrum of all ions generated is obtained with the MS serving as an ion transfer region between the IMS and the detector. In the SIM mode of operation, an IMS spectrum of preselected ions is obtained with the MS used as an ion filter for ions of specific m/z between the IMS and the detector.

2.3. APCI/MS/MS

The mass spectrometer used to investigate the DPIS in the negative ion mode was a PE Sciex API III triple quadrupole mass spectrometer (Thornhill, Ont., Canada) with a point-to-plane corona discharge ionization source. The corona discharge needle was removed from the factory supplied heated nebulizer APCI source. The DPIS was interfaced to the mass spectrometer by pressing the 5 mm hole in the Teflon housing of the DPIS around the glass tube protruding from the heated nebulizer. Sample flow from the heated nebulizer passed across the surface of the DPIS towards the inlet of the mass spectrometer. The DPIS was floated to −400 VDC below the interface voltage so that anions would move from the source towards the mass spectrometer. Typical interface voltages were between −300 and −600 VDC.

2.4. IMS

The ion mobility spectrometer used in the negative ion study was a Phemto-Chem MMS 160 IMS (PCP Inc., West Palm Beach, FL). Operating conditions were as follows: IMS reaction region: 5 cm; drift tube length: 10 cm; drift tube temperature: 25.6 °C; atmospheric pressure: 646 Torr; drift gas: purified air; drift gas flow rate: 550 ml/min; electric field: 200 V/cm; DPIS floating at 3000 VDC; the DPIS was placed about 2 cm in front of the reaction region.

2.5. Chemicals

UHP Nitrogen (99.999% pure) obtained from Matheson Tri-gas, Albuquerque, NM was used as the plenum gas in the Sciex MS. Purified air obtained from a Zero Air Generator (Puregas, Broomfield, CO) was used as the nebulizer gas for the APCI/MS/MS and for the drift gas in the PCP IMS. In the positive ion investigations, pre-
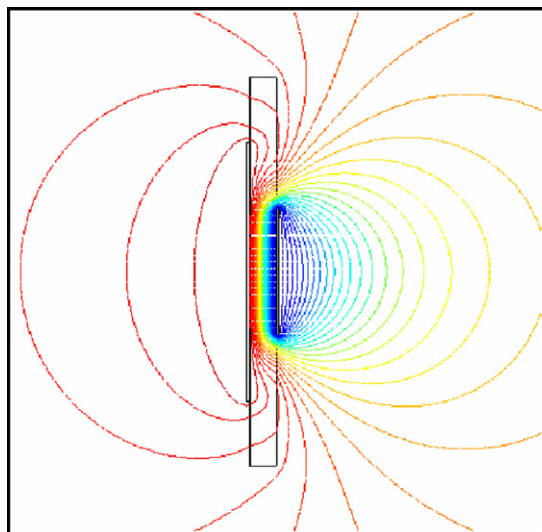
Fig. 2. A side view of the electric field gradient simulation of the DPIS with the large electrode on the left side and the small electrode on the right. Lines show the equipotential voltage contours produced by the source.

heated counter flowing drift gas (N_2; 99.99% pure) at a flow rate of ~900 mL/min was introduced at the end of the IMS drift region after passing through a moisture trap (Aldrich Chemical Co. Inc., Milwaukee, WI, 53201, U.S.A.).

RDX, PETN and NG standards were obtained from Cerilliant (Round Rock, TX) at 1000 μg/mL in acetonitrile and working solutions were diluted in methanol to 1:10 for concentrations of 100 ng/μL. 50 μL (5 μg) of the dilution was added to the heated nebulizer (cold). After the solvent was allowed to evaporate with the temperature off, heat was applied to the nebulizer (to 150 °C) to desorb the explosive. Auxiliary and nebulizer flows were at 500 and 100 mL/min, respectively. Significant quantities of RDX remained and were persistent in the spectra for approximately 10–20 min. Each spectrum was the result of approximately 25 scans (averaged). Caffeine, 2,4-lutidine and methamphetamine were obtained from Aldrich Chemical Co. Inc. (Milwaukee, WI, 53201, U.S.A.) and were classified as ACS reagent grade with ≥99% purity.

3. Results and discussion

3.1. Electric potential modeling

A particle trajectory modeling program, LORENTZ [16], was used to model cross-section of the source configuration. The equipotential voltage lines define field gradient contours within the DPIS and are shown in Fig. 2. Simulation shows that the contours cluster at the interface between the small electrode (right side) and the dielectric, indicating the largest electric field gradient at the edge of the small electrode. This was experimentally observed by a blue glow of the discharge occurring around the edge of the small electrode.

3.2. Physical stability with extended use

Testing was performed to see how prolonged use of the DPIS affected the physical aspects and ion production characteristics of the source. The source was operated continuously for 3 months drawing a current of 40–80 mA using an input voltage of approximately 12 V to power the RF generator. This relates to a power consumption of less than 1 W. Periodically, the source was turned off and photographed under a microscope (Leica, DME, Leica
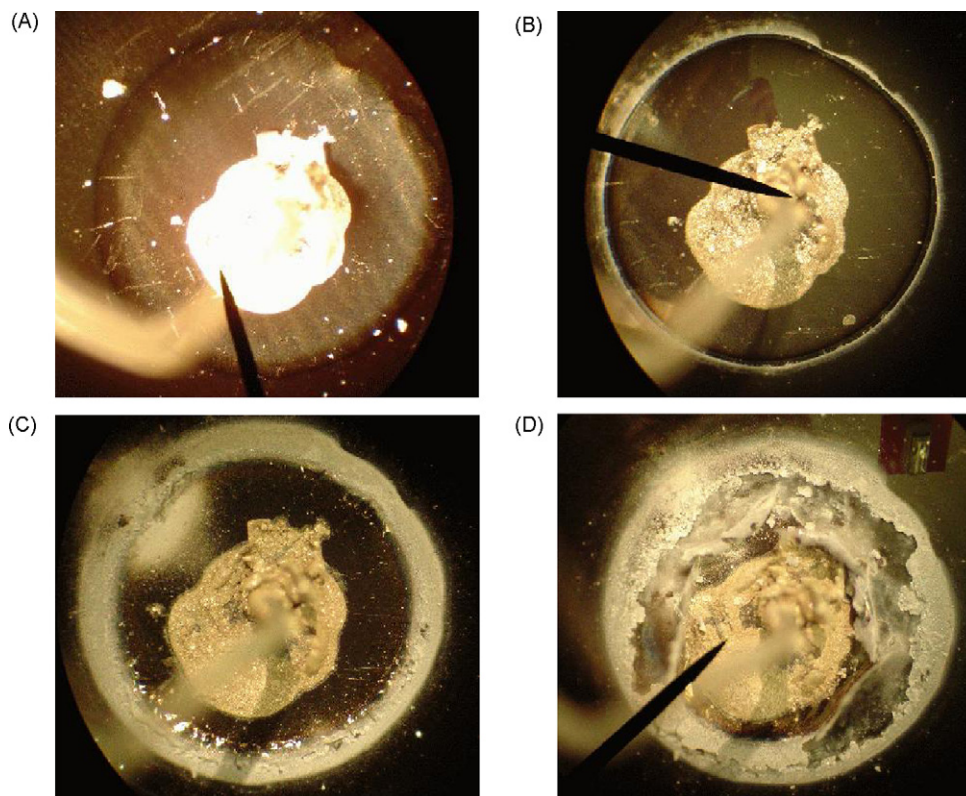
Fig. 3. Magnified images over 33 days of the continuous operation of the DPIS. Photograph of the small electrode (A) prior to use, (B) after 6 days, (C) after 16 days and (D) after 33 days.

Microsystems Inc., Buffalo, NY) with an overall magnification of 40×. Fig. 3 shows the magnified small electrode at 4 intervals encompassing about 1 month of continuous operation: (A) prior to operation, (B) after 6 days, (C) after 16 days, and (D) after 33 days. The small circular electrode, as seen in Fig. 1, mostly fills the square with an attached wire partially visible from the bottom left with a bead of silver paint as seen at the center. After 6 days of continuous operation, surface deterioration became apparent as seen by the ring surrounding the outer edge of the small electrode where the discharge occurs. Fig. 3C is a photograph of the source after 16 days of continuous operation; note that the corrosion had increased as evident by the broader ring. After 33 days significant corrosion over the entire surface of the source was observed; however, the source was still producing ions. The source was operated for an additional 2 months and a blue glow was still visible when the experiment was halted. In all our experience with operating various configurations of the DPIS, whenever a blue glow was observed, subsequent ions were detectable by the mass spectrometer.

3.3. Positive ions in DPIS

Ions generated by the open DPIS were introduced into the IMS-QMS and IMS spectra were acquired by operating the quadrupole mass spectrometer in either single ion mode (SIM) or full scan where the quadrupoles were operated in RF only and passed all ions through to the detector. Each IMS spectrum illustrated was an average of 200 IMS spectra. Background ions produced by the ionization of air were mass identified as $(H_2O)_nH^+$ with m/z 37 ion ($n = 2$) as the most abundant ion. Ion mobility spectra of background ions produced by corona discharge (A) and open DPIS (B) are shown in Fig. 4. Intensity of ions observed by the open DPIS was approximately two-thirds of that observed with corona discharge under

identical experimental conditions with the exception of the physical location of the sources. The DPIS was positioned ∼2 cm away from the target screen of the IMS whereas the corona discharge needle was ∼0.5 cm away from the target screen. The difference in intensities between the sources could be due to the difference in ion transfer efficiency from the source to the spectrometer because
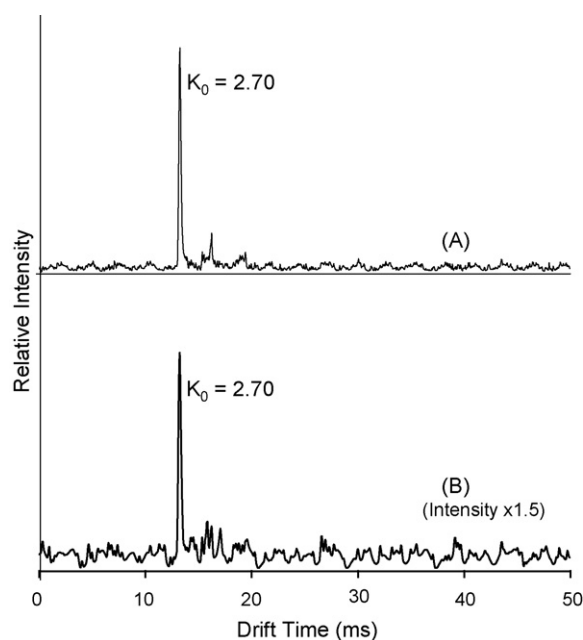
Fig. 4. Ion mobility spectra of positive background ions produced by (A) corona discharge and (B) open DPIS from ionization of ambient air.
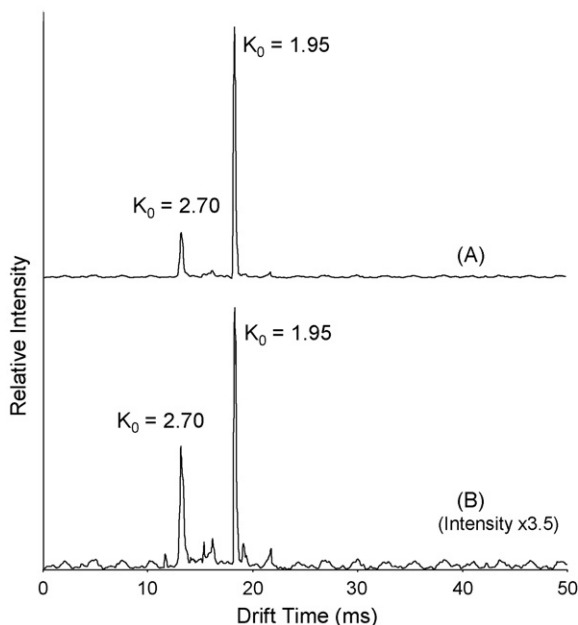
Fig. 5. Ion mobility spectra of 2,4-lutidine produced by (A) corona discharge and (B) open DPIS. IMS peaks of the protonated water reactant ions and protonated monomer ions of the 2,4-lutidine are shown at mobility values of 2.70 and 1.95 $cm^2 V^{-1} s^{-1}$, respectively.

of the relative source-spectrometer distances and/or electric field. The drift time of the positive reactant ions was 13.23 ms with K_0 value of 2.70 $cm^2 V^{-1} s^{-1}$.

Ionization of 2,4-lutidine, caffeine and methamphetamine was achieved by positioning a plastic strip (3 mm wide, 1 mm thickness), on the tip of which each of the analytes were deposited, in the space between the IMS target screen and the ionization source.
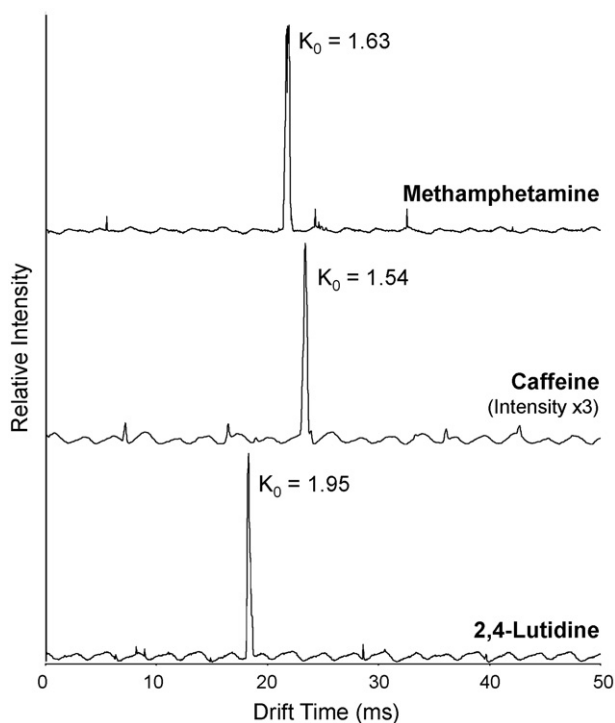
Fig. 6. Single ion monitored (SIM) ion mobility spectra of methamphetamine (m/z 150), caffeine (m/z 195), and 2,4-lutidine (m/z 108) using the open DPIS.
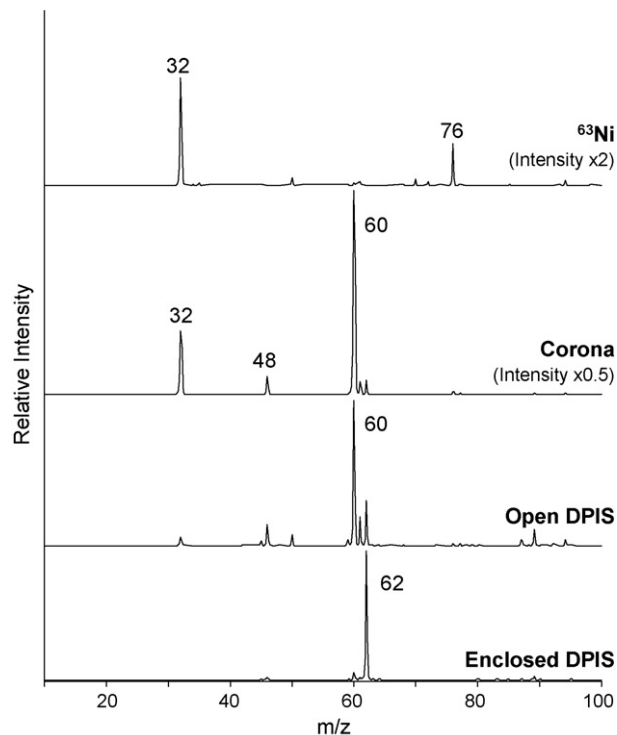
Fig. 7. Mass spectra of negative ions generated in purified air with ^{63}Ni, point-to-plane corona, open DPIS, and enclosed DPIS.

Fig. 5 illustrates the ion mobility spectra of 2,4-lutidine acquired in full scan mode of operation of the IMS-QMS with corona discharge (A) and open DPIS (B). IMS response peaks for reactant ions and protonated 2,4-lutidine monomer (m/z 108) were observed.

Fig. 6 shows the ion mobility spectra of caffeine (mol wt: 194), methamphetamine (mol wt: 149) and lutidine (mol wt: 107) acquired in SIM mode of operation with the IMS-QMS and the open DPIS as the ion source. Dominant ions observed in the IMS for caffeine, methamphetamine and lutidine were the protonated molecular ions of each at m/z values of 195, 150, and 108, respectively. Except for an increase in intensities of the peaks, the analytes ionized by corona discharge were similar to those generated by the open DPIS. The reduced mobility values (K_0) of the analytes were calibrated against the K_0 value of 2,4-lutidine as 1.95 $cm^2 V^{-1} s^{-1}$ and were measured to be: caffeine 1.54 $cm^2 V^{-1} s^{-1}$ and methamphetamine 1.63 $cm^2 V^{-1} s^{-1}$.

3.4. Negative ions in DPIS

Negative ions generated in clean air were investigated with the API III mass spectrometer. The negative reactant ions were created using a variety of ionization sources including a ^{63}Ni foil, the factory installed point-to-plane corona discharge, the open DPIS and the enclosed DPIS. The DPIS and ^{63}Ni ionization sources were all floating at about −400 V below the interface potential. Representative spectra from each source are shown in Fig. 7. The atmospheric pressure ionization of air by ^{63}Ni produced O_2^- and $O_2^- \cdot CO_2$. The conventional corona discharge ionization source produced predominantly CO_3^- in air. The DPIS in an open configuration produced CO_3^- ions similar to those from the corona discharge source. The enclosed DPIS source produced mainly NO_3^- ions.

Increasing flow rates to the corona discharge source of an IMS have been shown previously to shift the reactant ion chemistries to favor the production of O_2^- [8,17]. Ross and Bell [8], using a reversed high flow (100–500 mL/min) in a continuous corona dis-

charge in air at atmospheric pressure, showed that concentrations of O_3^-, CO_3^-, and NO_3^- decreased, and the ions observed were O_2^- and $O_2^-\cdot CO_2$, similar to the reactant ions from a ^{63}Ni source at atmospheric pressure. When the reverse flow rate was reduced to ≤50 mL/min or changed to the forward direction at high flows (250–500 mL/min) CO_3^- was the predominant ion observed. Other ions produced under these conditions included O_3^- and NO_3^-. At lower forward flow rates (50–200 mL/min) NO_3^- became the predominant ion. The shift from O_2^- to CO_3^- to NO_3^- occurs due to the build up of neutrals in the discharge region, including O_3 and NO_x, along with other air contaminants such as CO_2. The formation of CO_3^- may result from a reaction of CO_2 with O_3^-. Subsequent reactions involving NO_x yield the NO_3^- ion. With the DPIS in an open configuration, ozone is produced and the CO_3^- is the predominant ion. The enclosed DPIS allows NO_x to concentrate in the source thus generating NO_3^- as the major reactant ion.

Ion mobility spectra of air obtained using a ^{63}Ni source and an enclosed DPIS are shown in Fig. 8. The reactant ion appearing from the ^{63}Ni source at ambient temperature with a reduced mobility value of 2.17 cm^2 V^{-1} s^{-1} was inferred to be O_2^- [18]. The reactant ion for the DPIS appeared to the right of the peak generated from the ^{63}Ni source under similar conditions. It had a reduced mobility value of 1.98 cm^2 V^{-1} s^{-1} and was believed to be NO_3^- as observed with the Sciex mass spectrometer. Other investigations have shown the nitrate peak appearing to the right of the O_2^- reactant ion [19,20]. In an IMS with an O_2^- mobility value of 2.57 cm^2 V^{-1} s^{-1}, NO_3^- was found at 2.46 cm^2 V^{-1} s^{-1} [19]. Although the mobility values reported do not match those given here, the previous values were measured between 110 and 150 °C, and shifts toward higher mobility could be due to desolvation of the reactant ions. The peak intensity in the spectra from the DPIS is 5–6 times lower than that with ^{63}Ni as ion source. This was due to a loss in ion transmission through the DPIS interface to the IMS and not to lower ion currents being generated. Another interesting note is the lack of other peaks in the spectra. This is believed to result from the relatively high electron affinity and non-reactivity of NO_3^-. The mass spectra of the enclosed DPIS source showed a similar result with NO_3^- as the dominant peak and relatively few minor peaks compared to
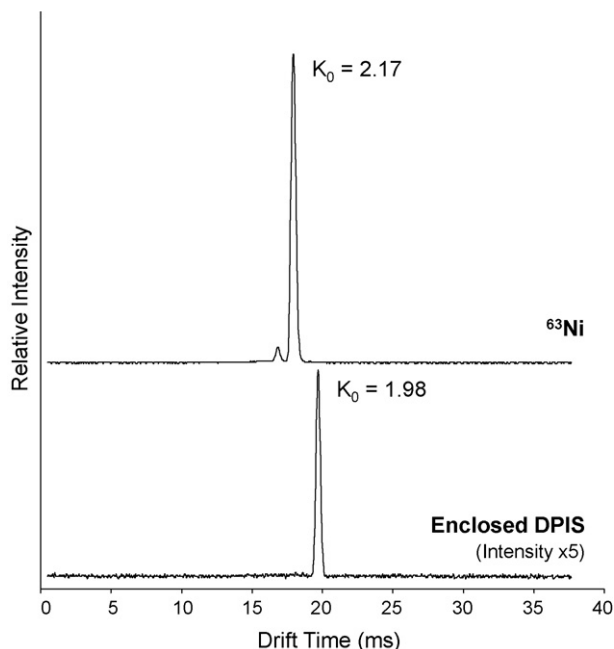
Fig. 8. IMS spectra of negative ions produced by the atmospheric pressure ionization of clean air at ambient temperature with ^{63}Ni and an enclosed DPIS.
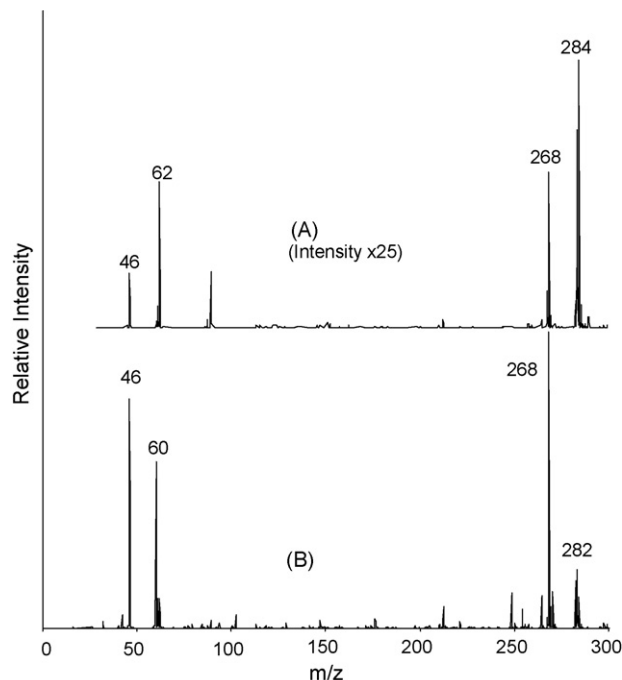
Fig. 9. Mass spectra of RDX (mol wt = 222). Ionization of RDX with the (A) enclosed DPIS and (B) point-to-plane corona discharge.

the other ionization sources. Since negative ionization processes mainly involve electron transfer, proton abstraction or adduct formation between the reactant ion and the analyte, the identity of the reactant ions will impact the ionization of analytes.

One of the major applications of IMS is in the detection of explosives. Commercial ion mobility spectrometers utilize a ^{63}Ni source with a chloride dopant for explosives detection. Under these conditions, RDX ionizes by forming an adduct ion $(RDX\cdot Cl)^-$ with the chloride ion [21]. In the absence of the chloride dopant, RDX ionizes by first producing NO_2^- and at higher concentrations of RDX the $(RDX\cdot NO_2)^-$ adduct is formed [22]. Mass spectrum obtained from the ionization of RDX in the presence of the CO_3^- reactant ion is shown in Fig. 9B. The CO_3^- ion was generated from a corona discharge source. Upon introduction of the RDX (mol wt = 222) to the corona discharge source the NO_2^- is formed along with the most intense peak at m/z of 268 which is the $(RDX\cdot NO_2)^-$ adduct. Small peaks observed at 282, 283 and 284 are likely CO_3^-, HCO_3^- and NO_3^- adducts of RDX, respectively. Fig. 9A is the mass spectra of RDX with an enclosed DPIS source. Upon introduction of RDX, the predominant peak observed at m/z of 284 was the $(RDX\cdot NO_3)^-$ adduct. Low-intensity peaks for NO_2^- and $(RDX\cdot NO_2)^-$ ions were also detected. Despite the "unreactive" nature of the NO_3^- reactant ion that suppressed other ion signal in the background, it provided effective ionization for RDX. Other explosives, such as nitroglycerine and PETN, showed similar ionization properties and were observed to form nitrate adducts as well. Although NO_3^- may not be the optimal reactant ion for all compounds, it does provide further selectivity to the ionization of some explosives.

4. Conclusions

The DPIS is a viable, non-radioactive, ionization source for use with atmospheric pressure ionization mass spectrometry and ion mobility spectrometry. A potential advantage of this ionization source over a standard point-to-plane corona discharge may be in the simplicity and ruggedness of the design. In point to plane

configurations, erosion of the point can cause instability and eventual termination of the corona discharge. Other advantages of the DPIS is that it can be configured to nearly any shape that may be required to interface it to a mass spectrometry or a ion mobility spectrometry, and it requires less power to operate then a corona discharge. The DPIS performed well as an ionization source for both mass spectrometry and ion mobility spectrometry. Positive ions generated appeared similar to those produced by ^{63}Ni. The negative reactant ions produced included CO_3^- and NO_3^- and their relative intensities depended upon source configuration. NO_3^-, although impractical for many applications, appeared effective in the ionization of some explosive compounds.

Acknowledgements

References

[1] D. Wittmer, B.K. Luckenbill, H.H. Hill, Y.H. Chen, Analytical Chemistry 66 (1994) 2348.
[2] S. Sielemann, J.I. Baumbach, H. Schmidt, P. Pilzecker, Analytica Chimica Acta 431 (2001) 293.
[3] C.A. Hill, C.L.P. Thomas, Analyst 128 (2003) 55.
[4] D. Dindosova, J.D. Skalny, Acta Physica Universitatis Comenianae 33 (1992) 77.
[5] H.T. Barnes, A.N. Shaw, J. Zeleny, Proceedings of the Royal Society of London. Series A, Containing Papers of a Mathematical and Physical Character, 82 (1909) 336.
[6] S.J. Taylor, L.J. Piper, J.A. Conner, J. FitzGerald, J.H. Adams, C.S. Harden, D.B. Shoff, D.M. Davis, R.G. Ewing, International Journal for Ion Mobility Spectrometry 1 (1998) 58.
[7] I. Dzidic, D.I. Carroll, R.N. Stillwell, E.C. Horning, Analytical Chemistry 48 (1976) 1763.
[8] S.K. Ross, A.J. Bell, International Journal of Mass Spectrometry 218 (2002) L1.
[9] R.G. Ewing, M.J. Crawford, W.C. Blanchard, Proceedings of the 13th International Conference on Ion Mobility Spectrometry, Gatlinburg, TN, July 2004.
[10] N. Na, C. Zhang, M.X. Zhao, S.C. Zhang, C.D. Yang, X. Fang, X.R. Zhang, Journal of Mass Spectrometry 42 (2007) 1079.
[11] W.C. Blanchard, U.S. Patent 7,157,721 (2007).
[12] R.G. Ewing, W.C. Blanchard, M.J. Crawford, Pittsburg Conference, Orlando, FL, March 2005.
[13] K. Kaplan, H.H. Hill, Gordon Research Conference-Detecting Illicit Substances: Explosives & Drugs Les Diablerets, Switzerland, August 2005.
[14] C. Wu, W.F. Siems, G.R. Asbury, H.H. Hill, Analytical Chemistry 70 (1998) 4929.
[15] G.R. Asbury, H.H. Hill, Journal of Microcolumn Separations 12 (2000) 172.
[16] LORENTZ, supplied by Integrated Engineering Software, Winnipeg, Manitoba, Canada.
[17] W.C. Blanchard, T. Bacon, M.J. Waltman, R.G. Ewing, Proceedings of the 15th International Conference on Ion Mobility Spectrometry, Honolulu, HI, July 2006.
[18] G.E. Spangler, J.P. Carrico, International Journal of Mass Spectrometry and Ion Physics 52 (1983) 267.
[19] G.E. Spangler, J.P. Carrico, D.N. Campbell, Journal of Testing and Evaluation 13 (1985) 234.
[20] R.F. Wernlund, M.J. Cohen, R.C. Kindel, New Concept Symposium and Workshop on Detection and Identification of Explosives, Reston, VA, 1978, p. 185.
[21] G.R. Asbury, J. Klasmeier, H.H. Hill, Talanta 50 (2000) 1291.
[22] S.D. Huang, L. Kolaitis, D.M. Lubman, Applied Spectroscopy 41 (1987) 1371.

Fluorescence resonance energy transfer between acridine orange and rhodamine 6G and its analytical application for vitamin B$_{12}$ with flow-injection laser-induced fluorescence detection

Hao Xu[a], Ying Li[a], Chunmei Liu[a], Qiongshui Wu[b], Yu Zhao[a], Li Lu[a], Hongwu Tang[a,*]

[a] College of Chemistry and Molecular Science, Wuhan University, Wuhan 430072, PR China
[b] School of Electronic Information, Wuhan University, Wuhan 430072, PR China

ARTICLE INFO

ABSTRACT

By coupling flow-injection with laser-induced fluorescence detection, a setup was developed and a novel method combining fluorescence resonance energy transfer (FRET) and flow-injection analysis (FIA) was proposed for the determination of vitamin B$_{12}$ (VB$_{12}$) based on its fluorescence quenching on the system of acridine orange (AO)/rhodamine 6G (R6G). The effective energy transfer could occur between AO and R6G in the dodecyl benzene sodium sulfonate (DBS) while 454 nm argon laser was used as the excitation source, and as a result, the fluorescence emission of R6G has been increased significantly. It was found that the fluorescence of the above system could be sharply diminished by VB$_{12}$. By using the mixed solution AO–R6G–DBS and the same solution containing VB$_{12}$ as the carrier and sample, respectively, a series of negative peaks which could be applied for the quantification of VB$_{12}$ were obtained. The detection limit for VB$_{12}$ was 1.65×10^{-6} mol/L. The linear range for determining VB$_{12}$ was 4×10^{-4} to 2×10^{-6} mol/L (correlation coefficient, $r = 0.9923$). The method was applied to measure VB$_{12}$ injections with satisfactory results.

© 2008 Elsevier B.V. All rights reserved.

1. Introduction

Fluorescence resonance energy transfer (FRET) is the radiationless energy transfer from an excited donor to a suitable ground-state acceptor molecule via through-space resonant dipole coupling [1]. In order to realize FRET effectively, some basic conditions must be satisfied simultaneously: (1) the emission spectrum of donor should have sufficient overlap with absorption spectrum of the acceptor; (2) the donor has certain quantum yield; (3) the distance between the two fluorophores and their relative orientation must be proper [2]. Some studies [3,4] reported the influence of surfactant to the organic fluorophores like rhodamines and AO in the process of FRET to achieve a good FRET effect. FRET and fluorescence quenching have been widely used in biological research and sensing. As it is sensitive to the distance between the donor and the acceptor, typically in a range of 1–10 nm [5], it can be used as a 'spectroscopic ruler' to calculate the nanoscale distance. FRET is also a powerful tool to build sensor [6–8] and study biomacromolecules and their interactions like, protease [9], proteins [10–14] and nucleic acids [15–17].

Vitamin B$_{12}$ (VB$_{12}$), which contains one atom of cobalt, plays a key role in human physiology. The most common method for the quantification of VB$_{12}$ was HPLC/UV–vis [18–21], other methods include: CE [22,23], MECC [24], HPLC–ICP-MS [25] and square wave voltammetry [26]. Liu et al. [27] reported the determination of VB$_{12}$ based on FRET and fluorescence quenching. Song and Hou [28] reported chemiluminescence determination of VB$_{12}$ by a flow-injection method.

To our knowledge, few studies have been focused on the combination of FRET and flow-injection. In this paper, we reported a novel method for the determination of VB$_{12}$ by combining FRET and flow-injection technique using a self-developed setup. The flow-injection system pumped sample to a glass capillary positioned on the microscope stage, and the laser beam was focused on the solution in the capillary, and finally the fluorescence signal was collected by a microscope objective lens. Effective energy transfer can occur between AO and R6G in the presence of dodecyl benzene sodium sulfonate (DBS), and the addition of VB$_{12}$ quenches the fluorescence of the AO–R6G–DBS system. By using the mixed solution AO–R6G–DBS as carrier and the same solution containing VB$_{12}$ as the sample, a series of negative peaks which could be applied for the quantification of VB$_{12}$ were obtained. The proposed method adopts automated sample injection, and fluorimetric detection, based on FRET, thus it has the advantages of high sensitivity, good repro-

* Corresponding author. Tel.: +86 27 68752136; fax: +86 27 68754067.
E-mail address: hwtang@whu.edu.cn (H. Tang).
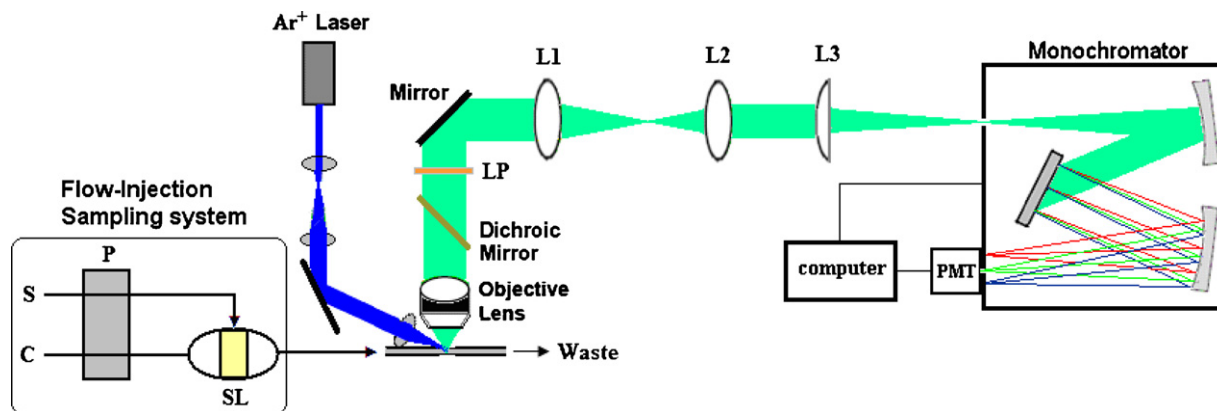
Fig. 1. Schematic diagram of flow-injection laser-induced fluorescence detection system. S, carrier; C, sample; SL, sampling loop; P, peristaltic pump; LP, long pass filter; L1–L3, lenses.

ducibility and the potential to probe biomacromolecules and their interactions promptly.

2. Experimental

2.1. Apparatus

The schematic diagram of the setup is shown in Fig. 1. It contains an IFIS-C set intellect flow-injection sampling system (Xi'an REMEX Analyzes Instrument Co., Ltd.), a research-grade fluorescence microscope (Chongqing Optic-Electro Instrument Company), Argon Laser (Melles Griot American), R928 PMT (Hamamatsu, Japan), a monochromator and some lenses.

The flow-injection instrument pumped the carrier and sample into a glass capillary (500 μm in diameter) positioned on the microscope sample stage. The laser beam was expanded, reflected and focused on the center of the capillary. The fluorescence signal from the solution in the capillary was collected by an objective lens. Through a dichroic mirror and a long pass filter in the vertical route, the signal was reflected out of the microscope and into horizontal route, and was tightly focused on the entrance slit by lenses L1–L3. Finally the fluorescence was detected with a PMT at the exit slit. A negative high voltage of 900 V was supplied to the PMT.

In order to minimize the contribution of R6G fluorescence from the direct excitation of R6G, the FRET measurements were performed with 454 nm laser exciting AO.

Spectrum scanning: monochromator scanning was controlled with a computer and the signal was collected with the PMT and the data were acquired with a 16-bit AD/DA card. The sample was injected consecutively while the fluorescence spectrum was scanned.

Flow-injection sampling: each time 70 μL sample was pumped into the carrier and pushed into the glass capillary, then the sample and the carrier were probed with the laser beam by turns at this position.

2.2. Reagents

Rhodamine 6G (R6G), acridine orange (AO), dodecyl benzene sodium sulfonate, vitamin B_{12}. All chemicals were at least of analytical reagent grade, and doubly deionized water was used throughout the experiment. The VB_{12} injection was obtained from market.

A stock solution of vitamin B_{12} (4×10^{-4} mol/L) was prepared by dissolving 0.0272 g crystalline vitamin B_{12} with carrier to 50 mL in a brown calibrated flask. A series of standard solutions for calibration were prepared freshly from the stock solution before analysis.

2.3. Procedures

(1) 1.0 mL 1×10^{-3} mol/L R6G, 0.76 mL 3.33×10^{-4} mol/L AO, 5.0 mL 1.6×10^{-2} mol/L DBS, and 1.0 mL 1×10^{-4} mol/L VB_{12} were added in some 25 mL volumetric flasks. The mixed solutions were diluted to the final volume with distilled water and shaken thoroughly. The fluorescence spectrum of the solution was recorded when the sample was injected consecutively, and the solutions without VB_{12}, without R6G-VB_{12} and without AO–VB_{12} were recorded at the same time.

(2) By diluting the mixture of 1.0 mL 1×10^{-3} mol/L R6G, 0.76 mL 3.33×10^{-4} mol/L AO, and a quantitative solution of DBS to 25 mL, a series of DBS solutions were prepared. And the carrier was prepared by diluting the mixture of 40.0 mL 1×10^{-3} mol/L R6G, 30.4 mL 3.33×10^{-4} mol/L AO to 1000 mL. The fluorescence intensity of the solution were recorded when samples were injected into the system and pushed through the glass capillary by the carrier.

(3) By diluting the mixture of a quantitative solution of R6G, 0.76 mL 3.33×10^{-4} mol/L AO, 5.0 mL 1.6×10^{-2} mol/L DBS to 25 mL, a series of samples were prepared. The fluorescence intensity of the solution was recorded when the sample was injected consecutively.

(4) 1.0 mL 1×10^{-3} mol/L R6G, 0.76 mL 3.33×10^{-4} mol/L AO, 5.0 mL 1.6×10^{-2} mol/L DBS and a quantitative standard stock solution of VB_{12} (or VB_{12} injection) were added in some 25 mL volu-
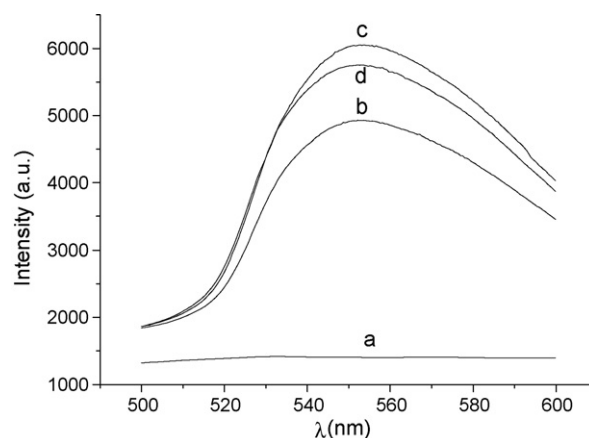
Fig. 2. Fluorescence spectra using 454 nm argon laser (10 mW) as the excitation source. (a) AO; (b) R6G; (c) R6G–AO; (d) R6G–AO–VB_{12} (concentrations of AO, R6G and VB_{12} are 1×10^{-5}, 4×10^{-5} and 4×10^{-6} mol/L, respectively for (a)–(d)).
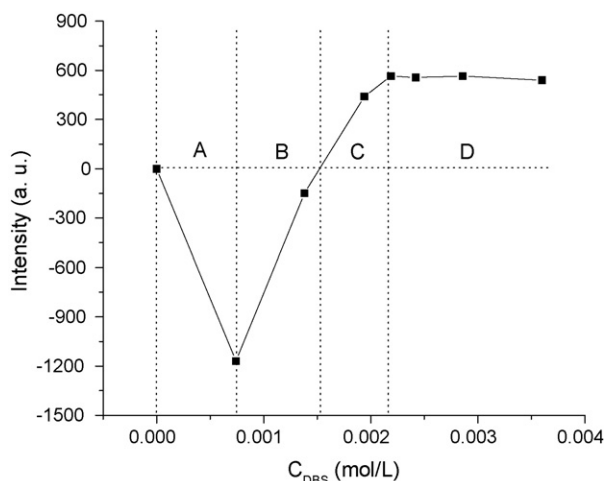
Fig. 3. Effect of DBS concentration on the energy transfer of the system R6G–AO (R6G, 4×10^{-7} mol/L; AO, 1×10^{-7} mol/L).

metric flasks. The mixed solutions were diluted to the final volume with distilled water and shaken thoroughly. The carrier was prepared by diluting the mixture of 40.0 mL 1×10^{-3} mol/L R6G, 30.4 mL 3.33×10^{-4} mol/L AO, 200.0 mL 1.6×10^{-2} mol/L DBS to 1000 mL. The fluorescence intensity of the solution were recorded when samples were injected into the system and pushed through the glass capillary by the carrier.

3. Results and discussion

3.1. Energy transfer among R6G, AO and VB_{12}

The fluorescence emission spectra of R6G under different conditions with 454 nm argon laser probing the system were shown in Fig. 2. The differences of the spectra indicate that the fluorescence intensity of R6G is enhanced in the presence of AO. Although AO only shows low emission, it obviously improves the emission of R6G. However, the fluorescence intensity of the system is diminished when VB_{12} is added into the mixture of R6G–AO. The emission peak of AO (526 nm) is very close to the absorption peak of R6G (532 nm), and the 454 nm argon laser is fit for the maximum absorption of AO (450 nm) and R6G is only slightly excited at this wavelength, therefore the fluorescence energy of AO is absorbed by R6G in the presence of DBS micelles. As a result the intensity at the peak of 560 nm is significantly increased due to the energy transfer. In aqueous solution the maximum absorption peak of VB_{12} (550 nm) matches the emission peak of R6G (560 nm) very well, and DBS micelles allow the dyes and VB_{12} to be close enough to transfer energy. Clearly, the transfer is the direct cause for the fluorescence quenching at 560 nm. Accordingly, the energy transfer between AO/R6G and R6G/VB_{12} could be used to detect VB_{12} in aqueous solution.

3.2. Effect of the DBS concentration

The surfactant keeps the dye molecules in one micelle close enough and suffice for the distance of energy transfer in FRET. The molecules of R6G and AO can be enwrapped in the anion surfactant micelles such as DBS for molecular electric charge. The electropositive dyes could stably live in the electronegative micelles interior. The surfactant concentration markedly affects the energy transfer of the system R6G-AO. As seen from Fig. 3, the fluorescence decreases at low DBS concentration (part A) is due to the fact that micelles is inexistent in low concentration DBS solution

thus the fluorescence is weaken by the simple electrostatic coalescent between anion surfactant and cation dye. In this case, the decrease and blue shift of the emission peak are caused by the dimers formed between DBS anions and R6G cations, and the dimmers of R6G–DBS is a complex salt which owns lower quantum yield than free R6G cation. With the increasing of the DBS concentration, the concentration of R6G–DBS dimer increases to the maximal and the fluorescence emission is weakened to the lowest when DBS concentration reaches 0.00074 mol/L. However, the dimer decomposes due to the electrostatic effort with the increase of DBS concentration because high concentration of DBS anion can build micelles, as a result the R6G cations become monomers and exist in a better micro-environment to emit stronger fluorescence with longer wavelength than in a dimer environment. Therefore, the curve in Fig. 3 shows a dramatic increase (part B) and becomes positive (part C), and finally keeps constant (part D) when DBS concentration is higher enough (more than 0.002 mol/L) to keep constant micelles in this solution, which could make all R6G cations are fully capped by DBS micelles. The curve in Fig. 3 is in good agreement with Yang's report on a similar system [29] which uses sodium lauryl sulfate (SDS) to enhance the fluorescence of Rhodamine 6G
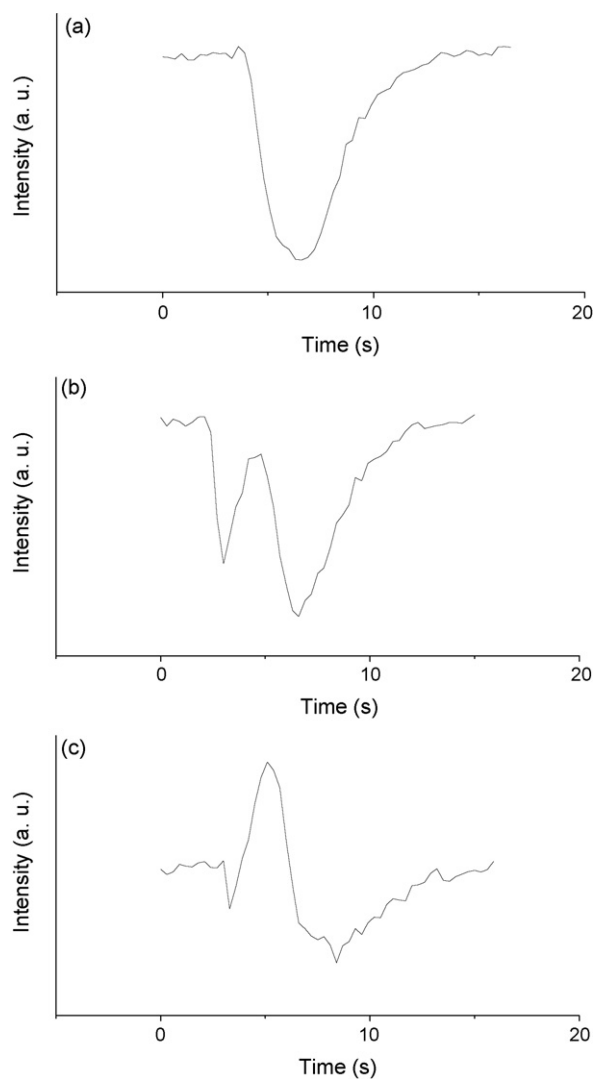
Fig. 4. The single flow-injection units at different DBS concentrations. (a) DBS 0.00074 mol/L; (b) DBS 0.00138 mol/L; (c) DBS 0.00194 mol/L (R6G, 4×10^{-7} mol/L; AO, 1×10^{-7} mol/L).
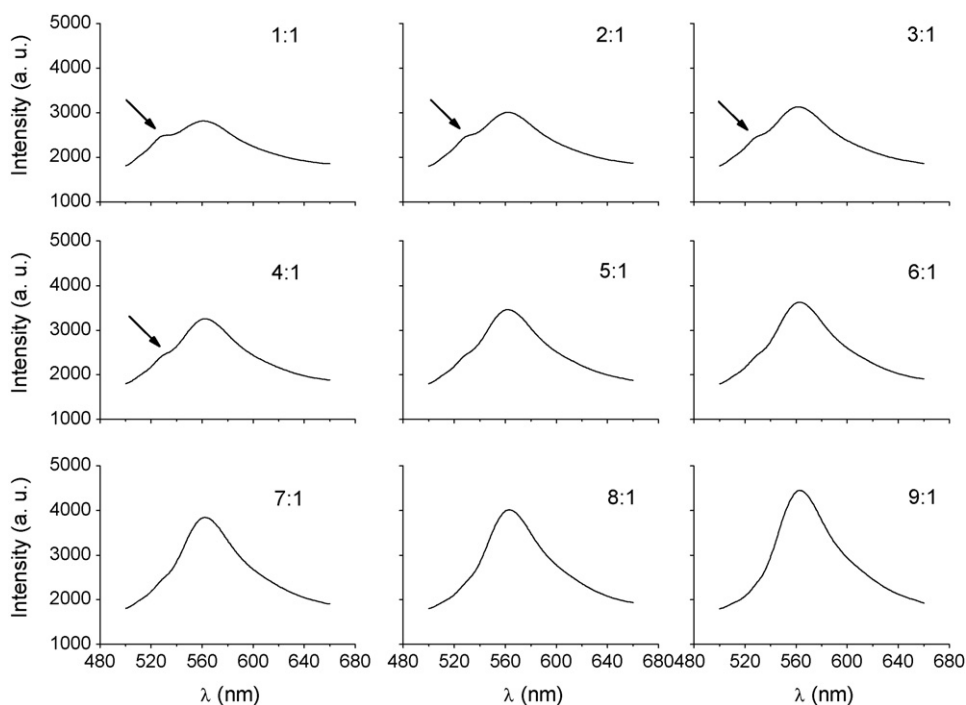
Fig. 5. The fluorescence spectra of AO–R6G–DBS system with increasing ratio of R6G/AO ranging from 1:1 to 9:1.The arrows indicate the 526 nm peak of AO, which disappears when the ratio reaches 4:1.

in water solution. Therefore, 3.2×10^{-3} mol/L DBS was used in the following experiments.

By using the flow-injection method, the time-intensity curves usually exhibit some useful information from the flowing system. Fig. 4 shows three typical single units of the flow-injection cycle of this system. When DBS concentration is the lowest (Fig. 4a), DBS simply weakens the fluorescence and only a single negative peak appears in the curve. While the DBS concentration is increasing, as shown in Fig. 4b, the negative peak is split into two peaks. In other words, there is a positive peak born on the negative peak bottom. With the DBS concentration gradually increasing, the positive peak becomes dominant and the two negative peaks are still perceptible (Fig. 4c). Therefore, the curves b and c precisely reflect the difference between parts B and C/D in Fig. 3.

In the units of the flow-injection cycle of this system, the sample and carrier were excited by laser alternatively, so a series of peaks were obtained. Although they were shifted very quickly during the injection process, sample diffuses to the carrier frontage and backside inevitably, which is termed by lengthways diffuse. In this case, there would be a concentration gradient in the flow. Because DBS plays an important role in the energy transfer process between the two dyes, the fluorescence intensity can be more intense at higher concentration and decrease at lower concentration. If the DBS concentration is more than 0.00074 mol/L (located in part B, part C or part D of Fig. 3), then the DBS concentration gradient caused by lengthways diffuse is from zero to the concentration of original injection, and therefore a positive peak and two negative peaks will be shown in a single unit (Fig. 4b and c) due to the effect of DBS concentration on the energy transfer of the system R6G–AO shown in Fig. 3.

In Fig. 4a, the DBS concentration is in part A of Fig. 3, so only one negative peak appears. In Fig. 4b, the DBS concentration reaches part B, but does not arrive at part C, so the negative peak is split. Interestingly, the strong positive peak exhibited in Fig. 4c is due to a higher DBS concentration (parts C and D in Fig. 3).

It seems that the sample diffuses more easily than delays in the flow, hence its peak is sharper in the front of the concentration gradient than in the back. This explains why in Fig. 4b and c, the negative peaks on the left are smaller and narrower than the right ones.

3.3. Effect of the concentration ratio of AO and R6G

By keeping the concentration of AO constant and increasing R6G concentration, the spectra of this system at different concentration ratios of R6G and AO ranging from 1:1 to 9:1 were investigated. The fluorescence spectra are shown in Fig. 5 and the relative intensity of the same scale is shown to evaluate the spectral changes. The peaks at 526 nm in all the spectra, which are attributed to the maximum emission of AO, decrease with the increase of the concentration of R6G. While the AO peak decreases completely, the efficiency of energy transfer reaches the maximum and most of the energy that AO receives from the laser is absorbed by R6G. When the excited AO molecules return to their ground state, the energy of one AO molecule could transfer to one molecule R6G or directly emit as fluorescence, thereby the energy transfer efficiency is improved when more than one R6G molecules absorb the energy from one AO molecule. Therefore, the peak at 560 nm rises while R6G concentration increases, and simultaneously the peak at 526 nm declines. When the ratio is higher than 4:1, the 526 nm peak disappears, hence the emission of AO is negligible. For this reason, the concentration ratio 4:1 is used as the optimum for energy transfer.

3.4. Quantitative analysis of vitamin B_{12}

3.4.1. The calibration curve and detection limit

In this experiment, the capability of quantitative analysis of VB$_{12}$ based on the R6G/AO FRET system was investigated. The carrier mainly contains R6G and AO, whereas the sample solution is the same as the carrier except that it contains VB$_{12}$.
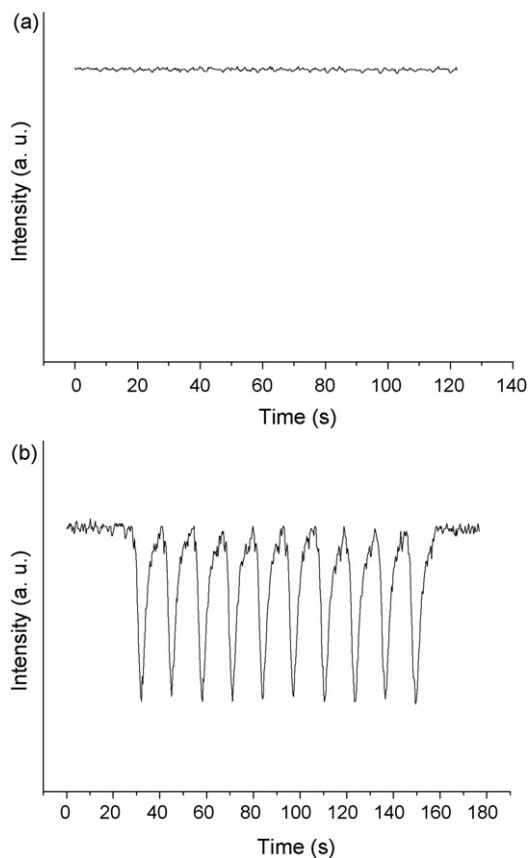
Fig. 6. The reproducibility of quantitative analysis of VB$_{12}$. (a) Baseline exhibiting bright fluorescence background and (b) negative peaks due to the presence of VB$_{12}$.

When the carrier was pumped into the glass capillary and excited with the laser, the fluorescence of R6G is detected by the PMT and the generated aclinic base line exhibits the bright fluorescence signal of R6G/AO FRET (Fig. 6a). Because of the energy transfer between R6G and VB$_{12}$, the fluorescence intensity of R6G declines when the sample is injected into the glass capillary. As shown in Fig. 6b, the concentration of VB$_{12}$ is related to the height of the negative peaks on the baseline of R6G/AO system showing high fluorescence background.

Based on the optimal condition of the energy transferring system, the absolute quenching of fluorescence due to the absorption of a series of VB$_{12}$ standard solutions was detected and the calibration curve for the determination of VB$_{12}$ was obtained. The linear regression equation is $Y = 1439770X + 33.6$, and the correlation coefficient r is 0.9923. In this equation, X and Y represent VB$_{12}$ contents and the absolute fluorescence quenching due to the presence of VB$_{12}$. The linear range of VB$_{12}$ concentration is from 4×10^{-4} to 2×10^{-6} mol/L. For the blank test, the carrier was used as the sample and the detection limit for the proposed method is 1.65×10^{-6} mol/L based on the 3δ criterion.

3.4.2. Effect of foreign substances

When the interference of foreign substances was tested, the R6G–AO–DBS solution was used as the carrier and R6G–AO–DBS solution containing VB$_{12}$ was used as the sample.

The interference of foreign substances such as vitamins and metal salts were tested by analyzing a standard solution of vitamin B$_{12}$ (5.0×10^{-5} mol/L) into which increasing amounts of interfering analytes was added. The tolerable ratios of foreign species with respect to 5.0×10^{-5} mol/L vitamin B$_{12}$ for interference at 5.0% level

Table 1
Results of determination of Vitamin B$_{12}$ in pharmaceutical preparations[a]

Sample	Average ($\times 10^{-4}$ mol/L)[b]	R.S.D. (%)	VB$_{12}$ added ($\times 10^{-6}$ mol/L)	Recovery (%)
Injection 1	2.14	3.39	4.8	99.6
Injection 2	2.16	4.31	8.8	100.1
Injection 3	4.09	4.56	8.8	96.7

[a] The average of five determinations.
[b] The sample of injections were diluted 50 times with R6G–AO–DBS mixed solution when analyzed.

were more than 100 for Cl^-, NO_3^-, Br^-, I^-, SO_4^{2-}, PO_4^{3-}, NH_4^+, Na^+, and K^+, and 10 for vitamin B$_1$, vitamin B$_6$ and vitamin C. Equal amount of Mg^{2+}, Ca^{2+}, Mn^{2+}, Cu^{2+}, Zn^{2+}, Ni^{2+}, Fe^{2+}, Fe^{3+} and other transition metal ions are not tolerable because the mixed solution of R6G–AO–DBS is basic thus hydroxide precipitate may be formed. However, the concentration of these metal ions in biomedical samples is very low and will not seriously affect the results when this method is used.

3.4.3. Analysis of actual sample

Three kinds of VB$_{12}$ injections were detected with this system. 1.0 mL of VB$_{12}$ injection was diluted with R6G–AO–DBS carrier solution to 50 mL in a brown calibrated flask when use. The instruction for the injections indicates that the VB$_{12}$ concentration of all the injections is approximately 3.68×10^{-4} mol/L (500 mg/L). The analytical results are shown in Table 1. The results demonstrate that the proposed method can provide precise data when actual samples are analyzed.

4. Conclusions

By using a self-developed setup of flow-injection laser-induced fluorescence detection, we successfully studied the fluorescence resonance energy transfer between AO and R6G in DBS, and the quenching behavior of VB$_{12}$ on this system in detail. The data show that VB$_{12}$ can be precisely determined based on this system. The method was developed by combining automated sample injection with laser-induced fluorimetric detection, therefore it shows many advantages such as high sensitivity and excellent reproducibility. The results also demonstrate that FRET is a powerful tool to study biomacromolecules and their interactions, and has great potentials for sensitive, precise and prompt quantitative analysis of some important biomolecules when it is employed with flow-injection and laser-induced fluorimetric detection.

Acknowledgement

References

[1] M. Massey, W.R. Algar, U.J. Krull, Anal. Chim. Acta 568 (2006) 181.
[2] S. De, A. Girigoswami, J. Colloid Interface Sci. 271 (2004) 485.
[3] X.W. He, Z.X. Tang, G.Y. Yu, W.L. Yang, G.Z. Zhang, H.M. Shi, Chin. J. Anal. Chem. 22 (1994) 332.
[4] B.S. Liu, H.Y. Sun, Z.C. Liu, Y. Guo, Spectrosc. Spect. Anal. 26 (2006) 2093.
[5] B. Oswald, F. Lehmann, L. Simon, E. Terpetschnig, O.S. Wolfbeis, Anal. Biochem. 280 (2000) 272.
[6] B.R. White, J.A. Holcombe, Talanta (2007) 2015.
[7] H.D. Duong, J. Rhee, Talanta 73 (2007) 899.
[8] M. Suzuki, Y. Husimi, H. Komatsu, K. Suzuki, K.T. Douglas, J. Am. Chem. Soc. 130 (2008) 5720.
[9] Y.Y. Hsu, Y.N. Liu, W.Y. Wang, F.J. Kao, S.H. Kung, Biochem. Biophys. Res. Commun. 353 (2007) 939.
[10] B. Schuler, W.A. Eaton, Curr. Opin. Struct. Biol. 18 (2008) 16.

[11] X. You, A.W. Nguyen, A. Jabaiah, M.A. Sheff, K.S. Thorn, P.S. Daugherty, Proc. Natl. Acad. Sci. U.S.A. 103 (2006) 18458.

[12] Q. Ma, X.G. Su, X.Y. Wang, Y. Wan, C.L. Wang, B. Yang, Q.H. Jin, Talanta 67 (2005) 1029.

[13] G.L. Wang, J.L. Yuan, X.D. Hai, K. Matsumoto, Talanta 70 (2006) 133.

[14] T. Pons, I.L. Medintz, X. Wang, D.S. English, H. Mattoussi, J. Am. Chem. Soc. 128 (2006) 15324.

[15] S. Kalininl, L.B.Å. Johansson, J. Fluoresc. 14 (2004) 681.

[16] M. Sugawa, Y. Arai, A.H. Iwane, Y. Ishii, T. Yanagida, Biosystems 88 (2007) 243.

[17] C.P. Mountford, A.R. Mount, S.A.G. Evans, T.J. Su, P. Dickinson, A.H. Buck, C.J. Campbell, J.G. Terry, J.S. Beattie, A.J. Walton, P. Ghazal, J. Crain, J. Fluoresc. 16 (2006) 839.

[18] W.R. Algar, U.J. Krull, Anal. Chim. Acta 581 (2007) 193.

[19] P. Moreno, V. Salvado, J. Chromatogr. A 870 (2000) 207.

[20] M. Okbamichael, S.A. Sañudo-Wilhelmy, Anal. Chim. Acta 517 (2004) 33.

[21] L. González, G. Yuln, M.G. Volonté, J. Pharm. Biomed. Anal. 20 (1999) 487.

[22] M. Schreiner, E. Razzazi, W. Luf, Nahrung/Food 47 (2003) 243.

[23] L.V. Candioti, J.C. Robles, V.E. Mantovani, H.C. Goicoechea, Talanta 69 (2006) 140.

[24] S. Buskov, P. Møller, H. Sørensen, J.C. Sørensen, S. Sørensen, J. Chromatogr. A 802 (1998) 233.

[25] E.G. Yanes, N.J. Miller-Ihli, Spectrochim. Acta Part B 59 (2004) 891.

[26] S.R. Hernandez, G.G. Ribero, H.C. Goicoechea, Talanta 61 (2003) 743.

[27] B.S. Liu, Z.C. Liu, G. Jing, Anal. Lett. 38 (2005) 1367.

[28] Z.H. Song, S. Hou, Anal. Chim. Acta 488 (2003) 71.

[29] Y.H. He, J. Cheng, H.Y. Zuo, J.G. Yang, Spectrosc. Spect. Anal. 25 (2005) 648.

Sensitive determination of anions in saliva using capillary electrophoresis after transient isotachophoretic preconcentration

Zhongqi Xu[a], Takayuki Doi[a], Andrei R. Timerbaev[b,c], Takeshi Hirokawa[a,*]

[a] *Department of Applied Chemistry, Graduate School of Engineering, Hiroshima University, 1-4-1 Kagamiyama 1, Higashi-hiroshima 739-8527, Japan*
[b] *Vernadsky Institute of Geochemistry and Analytical Chemistry, Russian Academy of Sciences, Kosygin Street 19, 119991 Moscow, Russia*
[c] *Institute of Inorganic Chemistry, University of Vienna, Waehringer Str. 42, A-1090 Vienna, Austria*

A B S T R A C T

A transient isotachophoresis–capillary electrophoresis (tITP–CE) system for the determination of minor inorganic anions in saliva is described. The complete separation and quantification of bromide, iodide, nitrate, nitrite, and thiocyanate has been achieved with only centrifugation and dilution of the saliva sample. In-line tITP preconcentration conditions, created by introduction of the plugs of 5 mM dithionic acid (leading electrolyte) and 10 mM formic acid (terminating electrolyte) before and after the sample zone, respectively, allowed the limits of direct UV absorption detection (at 200 nm) to be up to 50-fold improved as compared with CE without tITP. As a result, nitrate and thiocyanate were still detectable at 4.6 and 3.8 μg l^{-1}, respectively, in 1000 times diluted saliva. The daily variations of anionic concentrations in saliva samples taken from a smoking health volunteer were discussed based on the results of tITP–CE analysis. It was confirmed that the thiocyanate concentration in saliva noticeably increased after smoking. This is apparently the first report on simultaneous quantification of more than four anionic salivary constituents using CE.

© 2008 Elsevier B.V. All rights reserved.

1. Introduction

Biological sample analyses represent an application field where the benefits of capillary electrophoresis (CE) as a tool for inorganic ion analysis increasingly render it the status of the method of choice [1,2]. This is due to the technique's good assets in bioanalytical applications such as conducting multicomponent analyses in a simple, high-speed and cost-efficient way and in a miniaturized format, minor impact of the separation system on the original speciation of analytes, modest requirements on sample clean up, etc. In particular, one can witness a welcome situation when a large proportion of inorganic biofluid constituents are amenable to reliable CE analysis [2]. Of various biological fluids, blood serum and urine undoubtedly dominate the area. On the other hand, analyses of other types of fluids, one of which, saliva, is a matter of concern in the present work, received comparatively limited consideration.

Saliva is the watery secret produced in the mouth of humans which carries a variety of important compounds, including a group of inorganic anions (chloride, phosphate, and bicarbonate are the most abundant constituents). Early CE work on analyses for inorganic anions revised by one of co-authors [1] encom-

passed only a few saliva applications. In recent years, CE with direct UV detection was in most cases applied to the determination of salivary levels of nitrate and nitrite as established indicators of nitric oxide metabolism [3–8] or thiocyanate as a marker of exposure in smokers [4,5]. In order to alleviate the matrix interferences some authors used a sample deproteinization step that involved denaturation of salivary proteins with acetonitrile [5] or sodium hydroxide [6]. Otherwise, a zwitterionic surfactant (i.e. *N*-tetradecyl-*N*,*N*-dimethyl-3-ammonio-1-propanesulfonate) added to the background electrolyte may reduce protein–wall interaction and thus improve analyte resolution, peak symmetry, and reproducibility [4]. However, only prominent salivary anions could be really detected and quantified because of limited detectability of basic CE setup, with limits of detection typically in the (low) micromolar range. An ambitious attempt to resolve this challenge was recently made by the group of Padarauskas [9]. Their method implies derivatization of cyanide into the respective nickel complex, followed by extraction from human saliva into a single microdrop of appropriate solvent placed in the headspace of the sample solution. However, such preconcentration approach is only amenable for volatile analytes.

The goal of the work presented here has been to design a more versatile preconcentration procedure to be in-line incorporated into the CE system for signal enhanced detection for a wider range of salivary anions. In the previous work from this laboratory, meth-

---

* Corresponding author. Fax: +81 82 4247610.
E-mail address: hiro77@hiroshima-u.ac.jp (T. Hirokawa).

ods of enhancement of the analytical performance of CE regarding sensitivity and the number of biologically relevant analytes have been explored [10–12]. The strategy consisted in using transient isotachophoresis (tITP) preconcentration by taking advantage of occurring a high matrix anion or cation that acts as leading ion (so-called sample-induced tITP [13–15]). Particularly, the suitability of the concept has been successfully demonstrated for the enrichment of inorganic anions from serum and urine samples prior to CE analysis [10]. This paper describes a tITP–CE system that affords the simultaneous determination of five anions, including trace bromide and iodide, in saliva. The first part of the work was devoted to exploring and optimizing tITP conditions. A rational combination of externally introduced leading and terminating electrolytes (LE and TE, respectively) was proposed to accommodate the target analytes. The latter part involved demonstrating the figures of merit and utility of the developed method in the analysis of saliva samples. In addition, the results obtained were examined from the viewpoint of daily variations.

2. Experimental

2.1. Chemicals

Hydroxypropylcellulose (HPC) was from Tokyo Kasei (Tokyo, Japan), dithionic acid was the product of Kanto Kagaku (Tokyo, Japan), and 6-aminocaproic acid and formic acid were purchased from Katayama Kagaku (Osaka, Japan). Ultrapure hydrochloric acid (20%, v/v) used for preparation of the running electrolyte was from Tama Chemicals (Kanagawa, Japan). All solutions were prepared in deionized water obtained from a Millipore purification system (Tokyo, Japan). Anion stock solutions ($1.0\,g\,l^{-1}$) of nitrate, nitrite, bromide, iodide, and thiocynate were prepared from sodium salts (analytical grade) in deionized water, and appropriate dilutions were made to the proper concentrations.

2.2. Sample preparation

Saliva samples taken from a health volunteer with smoking habit were collected in the centrifugal filter unit (cat. no. UFC30SV00 from Millipore) and centrifuged at 5000 rpm for 60 min. The filtrated sample (around 2.0 ml) was divided into four portions and stored at $-20\,°C$. Immediately before analysis, the samples were thawed and diluted with deionized water. Oral cleaning was done before every sampling.

2.3. Capillary electrophoresis

CE analyses were performed on a CAPI-3200 instrument (Otsuka Electronics, Osaka, Japan) equipped with a variable wavelength UV detector (set at 200 nm) and a negative power supply, applying a constant voltage of $-30\,kV$ at the injection end of the capillary (migration current around $10\,\mu A$). The temperature of the capillary cartridge was maintained at $25\,°C$. Sample and tITP-supporting electrolytes were injected hydrodynamically at 50 kPa at a specified time. Separations were performed in the 100 cm long, 75 μm i.d. fused-silica capillary, with an effective length of 87.7 cm. Before use, new capillaries were washed with 1 M sodium hydroxide, water, and the separation electrolyte for 10 min. The capillary was flushed with water for 2 min and running electrolyte for 2 min prior to each run. The optimized separation electrolyte consisted of 5 mM HCl with 0.1% (m/v) HPC at pH of 4.4 adjusted with 6-aminocaproic acid. LE (5.0 mM dithionic acid, pH 7.2) and TE (10 mM formic acid, pH 4.4 adjusted with 6-aminocaproic acid) were hydrodynamically (negative pressure) introduced into the capillary before and after the sample injection, respectively. The

identity of the peaks was confirmed using standards added to the sample.

3. Results and discussion

3.1. Optimization of the CE separation

In our previous published work [10], optimal CE separation of a similar selection of biofluid anions was achieved with an acidic chloride-based electrolyte system. A high concentration of sodium chloride (250 mM) was necessary to incorporate in order to match serum or urine matrix salinity, as well as to ensure a certain sample stacking effect and to reduce the electroosmotic flow. In addition, cetyltrimethylammonium chloride was used for selectively decreasing the mobility of iodide. This was essential to have iodide moving well after chloride that served as a leading ion for tITP focusing. Also, the surfactant helped prevent matrix protein adsorption onto the capillary walls.

In contrast, saliva is one of few body fluids that contain no high matrix chloride (typically $\geq 5\,mM$). Therefore, to adapt the above background electrolyte to saliva analyses, the chloride concentration was reduced to 5 mM. However, under such conditions the electroosmotic flow was fairly high to detect highly mobile target anions ($>60 \times 10^{-9}\,m^2\,V^{-1}\,s^{-1}$) within a reasonable time. To suppress it HPC was added to the separation electrolyte. The polymer dynamically coats the capillary wall and hence may also protect it against adsorption of proteins and other matrix constituents (in the same way as the surfactant does). The optimal resolution of the five anions was obtained at pH 4.4, as shown in Fig. 1. Thus, 5 mM HCl with 0.1% (m/v) HPC at pH of 4.4 was used as the separation electrolyte for the rest of this work. The separation voltage was maintained at $-30\,kV$ (which is the highest
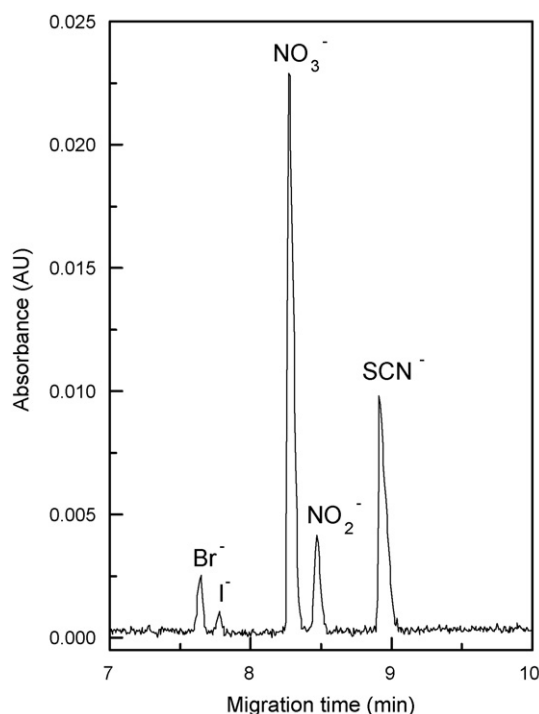
Fig. 1. Electropherogram of a 10-fold diluted saliva sample obtained without tITP preconcentration. Conditions: capillary, fused-silica, 100 cm × 75 μm i.d.; separation electrolyte, 5 mM HCl, 0.1% (m/v) HPC, pH 4.4; sample injection, negative pressure at 50 kPa for 30 s; applied voltage, $-30\,kV$; UV detection at 200 nm. Sampling: 1 h after lunch.

Table 1
Figures of analytical merit

Analyte	Detection limit ($\mu g\, l^{-1}$)	Repeatability (R.S.D., %)[a]		Linear range ($mg\, l^{-1}$)	Correlation coefficient	Average concentration ($mg\, l^{-1}$)[c]
		Migration time	Peak area[b]			
Br^-	3.0	0.28	3.4	0.1–0.5	0.992	5.4 ± 1.4
I^-	5.9	0.28	4.9	0.05–0.5	0.991	0.4 ± 1.0
$NO_3{}^-$	4.6	0.29	1.5	1–10	0.991	19.7 ± 15.8
$NO_2{}^-$	6.4	0.30	2.7	0.5–5	0.962	3.5 ± 5.3
SCN^-	3.8	0.28	1.0	1–10	0.999	44.5 ± 14.8

[a] The saliva was 100-fold diluted ($n = 3$).

[b] Not corrected for migration time.

[c] For 10 samples taken every 2 h in 1 day and monitored after a 10-fold dilution.

value available with the CE instrument employed) where migration times are minimized while baseline noise is not significantly increased.

3.2. Optimization of tITP preconcentration conditions

Inorganic anions in saliva significantly differ in concentrations. Indeed, nitrate, nitrite, and thiocyanate present from mid- to low-$mg\, l^{-1}$ level and thereby can be determined by CE directly [3–8,16,17], without preconcentration other than field-amplified sample stacking. On contrary, bromide and especially iodide occur in saliva in much lower concentrations, and their accurate quantification is only feasible after substantial sample enrichment. As follows from a report by Sádecká and Polonský [18], ITP can work as a preconcentration tool for salivary anions. However, when applied to such analyses in a genuine ITP mode, it suffers from moderate sensitivity (limits of detection ranged 25–127 $\mu g\, l^{-1}$; cf. data of Table 1) and reduced accuracy (because of a specific, stepped character of electropherograms), requires comparatively large sample volumes, and uses less versatile, conductivity detection method. Therefore, in this study the preference was given to ITP, temporarily operating before zone electrophoresis separation (i.e. tITP), followed by UV absorbance detection.

When analyzing high-salinity biological samples, tITP stacking can most straightforwardly be accomplished by exploiting the matrix chloride to play the role of a leading ion [15]. Then, one needs only a suitable slowly migrating anion to be added to the sample or injected as a separate zone so as to accommodate the target anions into the tITP range. However, saliva does not fulfil the condition of sample self-stacking as its chloride (or any other fast anionic component) does not exceed considerably the analyte concentrations.

In order to solve this challenge, an alternative supporting anion whose mobility is greater than that of any sample ions had to be chosen so that the ITP state is created at the initial stage of CE separation. As a matter of fact, there are very few leading-type stackers that satisfy this mobility criterion in the case of inorganic ion analyses, and one of these is dithionite. Its actual mobility depends on the ionic strength and pH and reaches as high as $96.4 \times 10^{-9}\, m^2\, V^{-1}\, s^{-1}$ [19]. Importantly, at a concentration of 5 mM, dithionite has higher mobility than bromide and iodide (as well as the matrix chloride) do, and hence it could be used as leading ion. Taking into account that temporarily ITP focusing is ensured at a sufficiently high molar amount of the stacker [13], the latter was optimized by increasing the loading time at a fixed concentration of dithionite (5 mM), and 10 s was chosen as optimum from the viewpoint of detectability and resolution. Larger loadings did not result in substantially higher peak heights but in a shorter migration of the analytes under CE mode. This may impair the resolution. For instance, the peaks due to bromide and iodide turned out to be overlapped at a 20 s injection time of LE as a consequence of too long ITP time.

Another important consideration for optimization of the tITP performance was the concentration ratio of a stacker (dithionite) to a destacker, i.e., the salivary chloride which can operate against tITP stacking. For efficient focusing, this ratio is known to be large enough [14], and sample dilution affords a means of controlling it. It was found that saliva samples should be diluted at least 10-fold to guarantee electromigrational sharpening effect and in addition, the conditions of field-amplified stacking at the initial stage of separation. Therefore, the following tITP–CE analyses were carried out with ≥100-fold diluted saliva samples.

As the terminating ion to bracket the mobilities of analytes on the low-mobility side, formate was selected as an anion with suitably low mobility ($46 \times 10^{-9}\, m^2\, V^{-1}\, s^{-1}$ at pH 4.4) and not occurring in saliva. In a combination with the highly mobile dithionite, formate was found to work fairly effective to focus isotachophoretically the analyte anions. Since increased amounts of terminator usually lead to higher concentration factors [20], its molar amount was kept reasonably high by loading a 10 mM solution of TE for 30 s. When larger amounts of formate were tried, the peak heights of only nitrate and thiocyanate continue to be markedly increasing but at the expense of enlarged migration
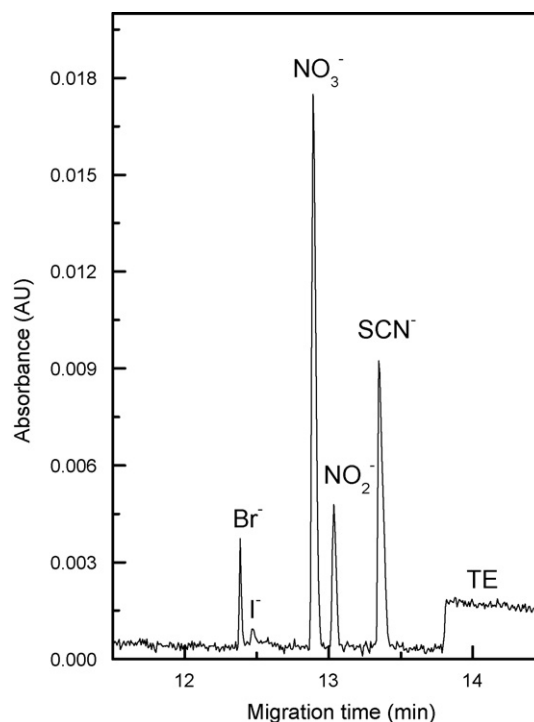
Fig. 2. tITP–CE response of a 100-fold diluted saliva. Conditions: LE, 5 mM dithionic acid, pH 7.2; TE, 10 mM formic acid, pH 4.4; injection time, 10, 30, and 30 s for LE, sample, and TE, respectively. Other conditions are as given in Fig. 1.
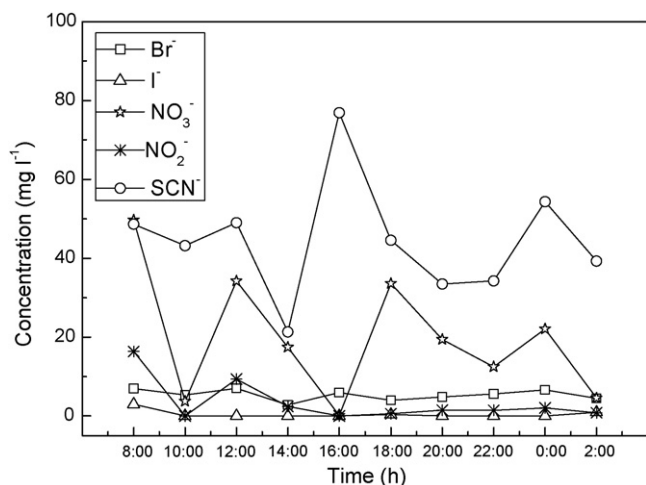
Fig. 3. Time-dependent changes in concentrations of anions monitored by tITP–CE. Conditions are as given in Fig. 2.

times of all anions, and also the stacker appears very close to thiocyanate.

Fig. 2 demonstrates the separation/detection performance for 100-fold diluted saliva under optimized tITP system conditions.

3.3. Limit of detection, calibration range, and precision thresholds

The limits of detection of anions under examination, assessed as three times signal-to-noise ratio, are listed in Table 1. Owing to tITP sample enrichment, the detectability was superior to that of most of previously reported CE methods [3,4,6] and comparable to the data of Tanaka et al. [5]. Notably, none of the mentioned reports takes account of bromide and iodide determination. As a striking result, all anions except for iodide can be detected in saliva yet after 500-fold dilution. Precision measurements performed with a 100-fold diluted saliva sample indicated excellent repeatability of migration time (R.S.D. <0.3%). The R.S.D.s for peak area were below 5% (Table 1). All above demonstrates that tITP–CE is reliable and effective to enhance the determination of inorganic anions in saliva.

3.4. Applicability of the developed method

Five anions were determined in 10-fold diluted saliva samples taken from the smoking volunteer, and the results on concentration variations during 1 day of monitoring are summarized in Fig. 3. The average concentrations of anions are also shown in Table 1. Some preliminary conclusions can be drawn as based on the daily variations of salivary anionic concentrations. First, the nitrate levels are

clearly related to stimulus, tending to increase after having meal. Also obvious is an increase in thiocyanate concentration after smoking. On the other hand, other anions of interest experience virtually no alterations in concentration. In order to elucidate how the salivary analyte concentrations would reflect people's habits, activities, and health conditions, further research is anticipated.

4. Conclusions

A combination of tITP and CE holds great promise for carrying out ionic analyses with the enhanced sensitivity. This is mostly due to its in-line realization (with no necessity to modify conventional CE instrumentation) and the potential of selectively increasing the analyte concentration regardless of the sample conductivity. In this work, these merits of tITP–CE have been shown for the determination of a number of biologically relevant anions in saliva that required an explicit modification of the tITP system. A proper selection of the leading anion and its amount, rather than relying on the major sample component as the transient leader, allowed for a good compromise between the UV detection signals, resolution, and analysis time. Although this system has been demonstrated specifically with inorganic anions, it can be translated to other salivary analytes, which will permit this tITP–CE method to be used in clinical laboratories.

References

[1] A.R. Timerbaev, Analyst 126 (2001) 964–981.
[2] A.R. Timerbaev, J. Sep. Sci. 31 (2008) 2012–2021.
[3] T. Miyado, Y. Tanaka, H. Nagai, S. Takeda, K. Saito, K. Fukushi, Y. Yoshida, S.-I. Wakida, E. Niki, J. Chromatogr. A 1051 (2004) 185–191.
[4] M. Mori, W. Hu, J.S. Fritz, H. Tsue, T. Kaneta, S. Tanaka, Fresen. J. Anal. Chem. 370 (2001) 429–433.
[5] Y. Tanaka, N. Naruishi, H. Fukuya, J. Sakata, K. Saito, S.-I. Wakida, J. Chromatogr. A 1051 (2004) 193–197.
[6] A. Gáspár, P. Juhász, K. Bágyi, J. Chromatogr. A 1065 (2005) 327–331.
[7] M. Mori, Bunseki Kagaku 51 (2002) 197–198.
[8] S. Wakida, T. Miyado, Y. Tanaka, H. Nagai, N. Naruishi, K. Yoshino, K. Matsuoka, Y. Yoshida, E. Niki, Chem. Sens. 22 (2006) 94–96.
[9] S. Jermak, B. Pranaitytė, A. Padarauskas, Electrophoresis 27 (2006) 4538–4544.
[10] T. Hirokawa, M. Yoshioka, H. Okamoto, A.R. Timerbaev, G. Blaschke, J. Chromatogr. B 811 (2004) 165–170.
[11] H. Okamoto, A.R. Timerbaev, T. Hirokawa, J. Sep. Sci. 28 (2005) 522–528.
[12] Z. Huang, A.R. Timerbaev, B.K. Keppler, T. Hirokawa, J. Chromatogr. A 1106 (2006) 75–79.
[13] P. Gebauer, W. Thormann, P. Boček, Electrophoresis 16 (1995) 2039–2050.
[14] P. Gebauer, L. Křivánková, P. Pantůčková, P. Boček, W. Thormann, Electrophoresis 21 (2000) 2797–2808.
[15] A.R. Timerbaev, T. Hirokawa, Electrophoresis 27 (2006) 323–340.
[16] P.K. Dasgupta, L. Bao, Anal. Chem. 65 (1993) 1003–1011.
[17] Z. Glatz, S. Nováková, H. Šterbová, J. Chroamtogr. A 916 (2001) 273–299.
[18] J. Sádecká, J. Polonský, Talanta 59 (2003) 643–649.
[19] T. Hirokawa, M. Nishino, N. Aoki, Y. Kiso, Y. Sawamoto, T. Yagi, J. Akiyama, J. Chromatogr. 271 (1983) D1–D106.
[20] T. Hirokawa, H. Okamoto, N. Ikuta, B. Gaš, Anal. Sci. 17 (2001) i185–i188.

Combined HPLC-CUPRAC (cupric ion reducing antioxidant capacity) assay of parsley, celery leaves, and nettle

Leyla Yıldız, Kevser Sözgen Başkan, Esma Tütem*, Reşat Apak

Istanbul University, Faculty of Engineering, Department of Chemistry, Avcilar 34320, Istanbul, Turkey

ARTICLE INFO

ABSTRACT

This study aims to identify the essential antioxidant compounds present in parsley (*Petroselinum sativum*) and celery (*Apium graveolens*) leaves belonging to the Umbelliferae (Apiaceae) family, and in stinging nettle (*Urtica dioica*) belonging to Urticaceae family, to measure the total antioxidant capacity (TAC) of these compounds with CUPRAC (cupric ion reducing antioxidant capacity) and ABTS spectrophotometric methods, and to correlate the TAC with high performance liquid chromatography (HPLC) findings. The CUPRAC spectrophotometric method of TAC assay using copper(II)-neocuproine (2,9-dimethyl-1,10-phenanthroline) as the chromogenic oxidant was developed in our laboratories. The individual antioxidant constituents of plant extracts were identified and quantified by HPLC on a C18 column using a modified mobile phase of gradient elution comprised of MeOH–0.2% *o*-phosphoric acid and UV detection for polyphenols at 280 nm. The TAC values of HPLC-quantified antioxidant constituents were found, and compared for the first time with those found by CUPRAC. The TAC of HPLC-quantified compounds accounted for a relatively high percentage of the observed CUPRAC capacities of plant extracts, namely 81% of nettle, 60–77% of parsley (in different hydrolyzates of extract and solid sample), and 41–57% of celery leaves (in different hydrolyzates). The CUPRAC total capacities of the 70% MeOH extracts of studied plants (in the units of mmol trolox g^{-1} plant) were in the order: celery leaves > nettle > parsley. The TAC calculated with the aid of HPLC-spectrophotometry did not compensate for 100% of the CUPRAC total capacities, because all flavonoid glycosides subjected to hydrolysis were either not detectable with HPLC, or not converted to the corresponding aglycons (i.e., easily detectable and quantifiable with HPLC) during the hydrolysis step.

1. Introduction

Reactive oxygen species (ROS) that emerge as a result of the respirative cycle of oxidative phosphorylation may attack biological macromolecules like cellular DNA, giving rise to single- and double-strand breaks that may eventually cause cell ageing, cardiovascular diseases, mutagenic changes and cancerous tumor growth. Antioxidants can react with ROS and quench free radicals giving rise to restriction of radicalic chain propagation, eventually preventing tissue damage. When natural antioxidant defences of the organism (of enzymatic, non-enzymatic or dietary origin) are overwhelmed by an excessive generation of reactive oxygen species, a situation of oxidative stress occurs, in which cellular and extracellular macromolecules (proteins, lipids and nucleic acids) can suffer oxidative damage, resulting in tissue injury followed by oxidative stress-originated diseases [1]. Antioxidants, when present at low concentrations in food or organism, can significantly inhibit or retard oxidative degradation reactions [2].

Polyphenols are one of the most diverse classes of phytochemicals widely distributed in plants [3]. Polyphenols are strong antioxidants, and their antioxidant activities are dependent on their structural properties [4–6]. Plant polyphenols are multifunctional, i.e., acting as hydrogen atom donor, singlet oxygen scavenger, and electron donor (reducing agent) [3]. On the other hand, some polyphenols owe their antioxidant properties to their metal chelating abilities, as traces of transition metal ions may catalyze oxidative degradation reactions [7]. Phenolic compounds can be classified into three broad categories of flavonoids, phenolic acids, and phenolic polymers (tannins).

The widest class of plant phenolics, with over 4000 identified species in the leaf, seed, bark, and flower parts of plants, is the flavonoid family having the diphenylpropane (C_6–C_3–C_6) skeleton in which the two aromatic rings (rings A and B) are linked by three carbons cyclized with oxygen (ring C) (Fig. 1). The phenolic hydroxyl groups attached to these rings are largely responsible for the antioxidant activity of the flavonoid. Flavonoids existing

* Corresponding author. Tel.: +90 212 4737034; fax: +90 212 4737180.
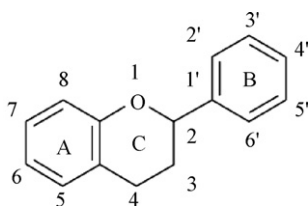*E-mail address:* etutem@istanbul.edu.tr (E. Tütem).

Fig. 1. General flavonoid structure.

in different varieties of plants or even in different parts of the same plant may exhibit significant structural differences [3]. These compounds are present in plants generally as flavonoid glycosides having one or more hydroxyl groups bound to sugars by an acid-labile hemiacetal bond through certain positions (such as the 7-hydroxyl in flavones and isoflavones) [8].

As a part of alternative disease prevention strategies, folk medicinal plants have become important for the preservation of human health. These plants are cheaply available from local markets, and can be consumed in their simple or processed forms for health beneficial purposes. Various parts of medicinal plants, including the roots, leaves, flowers, seeds, berries or bark, depending on the solubility of the active constituents, may comprise a large variety of polyphenolics, namely cinnamic acids, benzoic acids, flavonoids, proanthocyanidins, stilbenes, tannins, coumarins, lignans and lignins. These compounds have many advantageous biological effects, including antioxidant activity [9].

The Umbelliferae family has a large variety of member plants and a wide spreading area. In many laboratories, diverse research studies covering morphology, anatomy, cytology, and plant chemistry are being carried out on this family. This family is very rich in terms of secondary metabolites. Compounds like coumarins, flavonoids, acetylenic compounds, sesquiterpenic lactones, and volatile oils are extracted from various species of the family, and find commercial use in biology and medicine. Certain members of the Umbelliferae family are folk medicinal plants. Angelica species are used as vegetable greens and food ingredients [10]. Species in this family are rich in vitamins (A, B2, C, E) and minerals (copper, zinc, iron, selenium) that may act as immunomodulators. In addition, they contain a wide variety of bioactive phytochemicals like flavonoids and coumarins that show curative, disease preventive and nutritive effects [11].

As a member of Urticaceae family, stinging nettle (*Urtica dioica*) rich in minerals (especially Fe), vitamin C and pro-vitamin A is a medicinal plant and diet food ingredient that finds wide use as hypoglycemic, anti-diabetes, diuretic, anti-inflammatory, anti-rheumatic, and hypotensive agent; it also serves to tackle with circulatory problems, prostate complaints, and skin diseases. Although nettle is essentially consumed as food or food ingredient, its medicinal use covers the use of its leaves as herbal tea [12]. Apak et al. measured the total antioxidant capacity (TAC) of tea bags prepared from stinging nettle (i.e., from a hot water infusion of the dry herb) as 0.18, 0.15, and 0.19 mmol trolox equivalent g^{-1}, using the CUPRAC (cupric ion reducing antioxidant capacity), ABTS, and Folin methods of TAC assay, respectively [13].

Various antioxidant assay methods have been developed for plant antioxidants (vitamins and polyphenolics) that are important for human health [14–21]. In this study, the CUPRAC assay recently developed in our laboratories has been used for the food plants. The chromogenic oxidizing reagent of the CUPRAC assay, bis(neocuproine 2,9-dimethyl-1,10-phenanthroline)copper(II), was previously used for the assay of biologically important reductants [22], cysteine [23], vitamin E [24], vitamin C [25], and proteins [26]. The CUPRAC assay is simple, diversely applicable to both hydrophilic and lipophilic antioxidants, and its reagents are

stable and easily available at low cost [27]. This method has been used for the TAC assay of herbal teas and apricots [13,28], and of human serum [29]. The TAC of food plants subject to this study was comparatively assayed with the CUPRAC and the widely used ABTS [30] methods.

Many research groups dealing with antioxidant chemistry have either used or evaluated the CUPRAC method. In a comprehensive review by Prior et al. [31], the authors classify CUPRAC as one of the electron transfer-based methods, and summarize the superiorities of the CUPRAC method over other antioxidant assays. They state that due to the lower redox potential of the CUPRAC reagent, reducing sugars and citric acid – which are not true antioxidants but oxidizable substrates in other similar assays – are not oxidized with the CUPRAC reagent. Gorinstein et al. [32] state that as an advantage to other electron transfer-based assays as ABTS and Folin, CUPRAC values were acceptable in regard to its realistic pH close to the physiological pH. Gorinstein's research group has used CUPRAC in several occasions: garlic extract, where CUPRAC correlated well with ABTS/TEAC results [32]; kiwifruit [33] and ethylene-treated kiwifruit [34], where CUPRAC gave the highest correlation ($r = 0.97$–0.98) among the tested antioxidant assays with Folin polyphenols content; cereal and pseudocereal methanol extracts [35], where there was again a high correlation ($r = 0.96$) between CUPRAC and Folin. Mazor et al. [36] applied CUPRAC and FRAP simultaneously to a number of –SH compounds, and noted that CUPRAC but not FRAP was capable of quantitating the one thiol-bearing tripeptide glutathione (GSH) in accordance with the 1-e reductant behaviour of GSH. The CUPRAC antioxidant capacity of the methanol and chloroform extracts of the stem and root of Rhubarb (*Rheum ribes*) was linear over a relatively wide concentration range (up to at least 2.0 absorbance units) [37]. Capanoglu et al. [38] stressed that during the processing of tomato fruit to tomato paste, CUPRAC antioxidant capacities were the highest values for lipophilic extracts, indicating that this is a sensitive assay in organic solvents (e.g., CUPRAC values broadly followed the trend of lycopene during processing). The same authors noted that CUPRAC was the best antioxidant assay (among five assays) reflecting the decrease in TAC of lipophilic fraction during tomato processing steps [38].

The antioxidant capacities of plants are generally evaluated in terms of their total phenolic contents [39–43]. The speciation analysis of phenolic compounds [44] and especially their quantification with high performance liquid chromatography (HPLC) [45–47,19] are not abundant in literature due to the low resolution in the separations of flavonoids and phenolic acids [48]. Similar to the studies carried out on food samples, Wojdylo et al. added up the mass quantities of the identified phenolics to give the total phenolic content [45], which would not be correct on a mole-basis. Thus, total phenolic contents calculated on a mass basis in such reports would not enable a true comparison of antioxidant capacities, because each phenolic antioxidant would naturally have a different capacity in the units of equivalents of a standard reference compound such as trolox.

For rapid separation, identification and quantification of individual antioxidants in the selected plants of this study, the nature of stationary and mobile phases of HPLC analysis were optimized using synthetic mixtures of antioxidants; calibration curves were constructed for each antioxidant, and the antioxidant compounds in real mixtures were quantified with the aid of these curves. The HPLC-determined concentration of each antioxidant was multiplied with its TEAC (trolox equivalent antioxidant capacity, defined as the mM trolox equivalent concentration of 1 mM solution of the tested antioxidant) coefficient, and these products were summed up to yield the theoretical TAC value by virtue of the additivity of absorbances of constituents in a mixture. In this regard,

the HPLC analysis results enabled the comparison of individual antioxidant constituents of the studied plants together with their trolox-equivalent antioxidant capacities.

2. Experimental

2.1. Chemical substances

Gallic acid, catechin, hesperidin, isoquercitrin, ABTS (2,2′-azinobis[3-ethylbenzothiazoline-6-sulfonic acid] diammonium salt), quercetin, rosmarinic acid (Fluka), chlorogenic acid, naringenin, hesperetin, rutin, *m*-phosphoric acid (Sigma), caffeic acid, ferulic acid, *p*-coumaric acid, naringin (Aldrich), myricetin (Acros Organics), kaempferol (AppliChem), luteolin, apigenin (Alfa Aesar), ascorbic acid, neocuproine (2,9-dimethyl-1,10-phenanthroline) (Sigma–Aldrich), cupric chloride dihydrate (CuCl$_2$·2H$_2$O), potassium persulfate (K$_2$S$_2$O$_8$), methanol, hydrochloric acid, *o*-phosphoric acid, potassium hydroxide, sodium hydroxide (Merck), ammonium acetate, ethanol, acetone (Riedel-de Haën) were supplied from the indicated sources.

2.2. Instrumentation

A Metrohm Herisau E512 pH-meter was used for pH measurements. The extraction and equilibration operations were made using a Bransonic 221 ultrasonic bath, a HB4 basic KIKA-WERKE water bath, and an Elektro-mag vortex mixer. Plant samples were lyophilized using a Telstar Cryodos freeze-dryer. Spectrophotometric measurements were made with a Cary 1E UV–Vis spectrophotometer (Varian Instruments), and chromatographic separation and identification of plant constituents were performed using a PerkinElmer HPLC system (comprised of Series 200 UV–Vis detector, binary gradient pump, and vacuum degasser). Pure distilled water was used throughout, as obtained from Millipore Simpak1 Synergy 185 ultra-pure water system.

2.3. Reagent and solutions

Gallic acid, catechin, chlorogenic acid, caffeic acid, ferulic acid, *p*-coumaric acid, naringin, naringenin, hesperetin, rutin, isoquercitrin, quercetin, myricetin, and luteolin stock solutions were prepared in MeOH; rosmarinic acid and kaempferol in EtOH; apigenin in 0.2 M ethanolic KOH; hesperidin in 0.05 M methanolic KOH; ascorbic acid in 1% (w/v) *m*-phosphoric acid solution. The antioxidant stock solutions were stable when kept at −20 °C for 1 month.

For the CUPRAC test of TAC, the following solutions were prepared: CuCl$_2$ solution, 1.0×10^{-2} M, prepared by dissolving CuCl$_2$·2H$_2$O in water; ammonium acetate (NH$_4$Ac) buffer at pH 7.0, 1.0 M, prepared from NH$_4$Ac in water; neocuproine (Nc) solution, 7.5×10^{-3} M, prepared daily by dissolving Nc in 96% ethanol. Trolox, 1.0×10^{-3} M, was prepared in 96% ethanol. For the ABTS test of TAC, the chromogenic radical reagent ABTS, at 7.0 mM concentration, was prepared by dissolving this compound in water and adding K$_2$S$_2$O$_8$ to this solution such that the final persulfate concentration in the mixture be 2.45 mM. The resulting ABTS radical cation solution was left to mature at room temperature in the dark for 12–16 h, and then used for ABTS/TEAC assays. The reagent solution was diluted with EtOH at a volume ratio of 1:10 prior to use.

2.4. Preparation of plant samples for analysis

2.4.1. Drying of plants
Fresh parsley, celery leaves, and nettle samples were supplied from the local market, and the leaf parts were freeze-dried at −40 °C

for 8–14 h. All plant samples were kept in the dark at room temperature in stoppered flasks. They were crushed to fine powder in a porcelain mortar prior to analysis.

2.4.2. Extraction of plants
2.4.2.1. Extraction of dried plant materials. As possible solvents for extraction, methanol, ethanol, and acetone at 100, 70, and 50% (v/v) concentrations, and bidistilled water were used for dried parsley leaves; methanol at 70 and 50% and ethanol at 50% for dried celery leaves. Preliminary tests carried out on parsley and celery leaves showed that 70% MeOH gave the highest extraction yield; in addition, methanol had protective power for phenolic antioxidants in subsequent HPLC separations due to its inhibitive effect on phenoloxidase-catalyzed oxidation of phenolics [49]. Thus, nettle was extracted with 70% MeOH. One-gram amount of the dried plant materials was extracted in stoppered flasks placed in an ultrasonic bath first with 15 mL solvent for 45 min, then with added 5 mL solvent for 45 min, and finally with 5 more mL solvent for 15 min, the overall extraction taking 105 min. The plant extracts were first filtered through a filter paper, then through a GF/PET (glass fiber/polyethyleneterephtalate) 1.0/0.45 μm microfilter, and analyzed.

2.4.2.2. Extraction of fresh parsley for vitamin C determination. Finely chopped parsley leaves were extracted in an ultrasonic bath with 1% (w/v) aqueous *m*-phosphoric acid. For this purpose, a 5-g sample was first extracted with 25 mL acid for 45 min, the extract decanted, and extracted for a second time with 25 mL acid for 45 min, the whole extraction taking 90 min [50]. The combined extracts were first filtered through a filter paper, then through a microfilter, and analyzed.

2.4.2.3. Nettle infusion. One-gram amount of the dried nettle was steeped in 50 mL boiling bidistilled water for 5 min. The infusion thus obtained was first filtered through a filter paper, then through a microfilter, and analyzed.

2.4.3. Hydrolysis process for plant materials
2.4.3.1. Hydrolysis of plant extracts. Parsley, celery leaves, and nettle were extracted with 70% MeOH, diluted with water and acidified so as to finally contain 50% methanol and 1.2 M HCl, and hydrolyzed at 80 °C for 4 h [51,52].

2.4.3.2. Hydrolysis of dried plant powders. From dried plant material were taken 0.2 g amounts of samples, and hydrolyzed in a final solution containing 50% MeOH and 1.2 M HCl at 80 °C for 4 h. The hydrolyzates were passed through a microfilter, and analyzed.

2.5. Synthetic antioxidant mixtures

The compositions of synthetic mixtures were regulated to contain the antioxidants most probably existent in the analyzed plant extracts.

2.5.1. Synthetic mixture 1
Prepared to contain in final solution 2.0×10^{-4}, 4.0×10^{-5}, and 1.0×10^{-4} M of *p*-coumaric acid, myricetin, and apigenin, respectively.

2.5.2. Synthetic mixture 2
Prepared to contain in final solution 2.0×10^{-4}, 4.0×10^{-5}, 3.4×10^{-5}, and 1.0×10^{-4} M of chlorogenic acid, myricetin, luteolin, and apigenin, respectively.

2.5.3. Synthetic mixture 3

Prepared to contain in final solution equimolar (2.0×10^{-4} M) concentrations of catechin and chlorogenic acid.

2.6. Methods used in antioxidant assays

2.6.1. Spectrophotometric methods

2.6.1.1. CUPRAC method.
The normal CUPRAC method (CUPRAC$_N$), as described by Apak et al. [27], was applied as follows: A mixture comprised of 1 mL of 1.0×10^{-2} M copper(II) chloride, 1 mL of 1 M ammonium acetate buffer at pH 7.0, and 1 mL of 7.5×10^{-3} M neocuproine solution was prepared, x mL sample solution and $(1 - x)$ mL distilled water were added, and well mixed (total volume: 4.0 mL). This final mixture in a stoppered test tube was let to stand at room temperature for 30 min. At the end of this period, the absorbance at 450 nm was measured against a reagent blank. The 'incubated CUPRAC method' (CUPRAC$_I$), as described by Apak et al. [27], was applied to antioxidant-containing samples by first incubating the mixtures at 50 °C for 20 min, then measuring the absorbance at 450 nm.

This method was applied to the extracts, hydrolyzates of all studied plants, steeped infusions of nettle, and synthetic mixtures. The samples were diluted with 50% MeOH where necessary (i.e., to keep the CUPRAC absorbances within the linear range). The pH of the hydrolyzates was first brought to pH 6 with the addition of NaOH solution, and then analysis was performed.

2.6.1.2. ABTS method.
The ABTS/persulfate method [30] was followed. Briefly, the volumes of $(4 - x)$ mL EtOH and x mL sample solution were taken. The reagent blank was prepared with 4 mL EtOH. One mL amount of 1:10 diluted ABTS radical cation solution was added to each mixture at 15 s intervals, and well mixed (total volume: 5.0 mL). The absorbances of all solutions were recorded at 734 nm against ethanol at the end of 6th min. The absorbance of the reagent blank (A_0) diminished in the presence of antioxidants, the absorbance decrease (ΔA) being proportional to antioxidant concentration.

This method was also applied to the extracts, hydrolyzates of all studied plants, steeped infusions of nettle, and synthetic mixtures. The samples were diluted with 50% MeOH where necessary (i.e., to keep the ABTS absorbance differences within the linear range). Since turbidity was observed in hydrolyzate solutions when the pH was adjusted to pH 6 with NaOH solution addition, samples were directly diluted with 50% MeOH.

2.6.2. HPLC analyses

The analyses were carried out using a Hamilton HxSil C18 (250 mm × 4.6 mm, 5 μm particle size) chromatographic column. Two elution programs were used in the reversed-phase HPLC analyses. For polyphenolic compounds, two different solutions of the mobile phase, i.e., methanol (A) and 0.2% of o-H$_3$PO$_4$ in bidistilled water (B), were used in gradient elution. The following working mode was adopted for gradient elution (the slope being the rate of change of methanol percentage between the indicated time periods):

  8 min 7% (A), slope (0.0);
 8–13 min to 30% (A), slope (−4.0);
13–48 min to 66% (A), slope (1.0);
48–55 min to 75% (A), slope (−4.0).

The detection wavelength was 280 nm and the elution rate was 1 mL min^{-1}. Using the above working mode, the calibration curves and linear equations of peak area *versus* concentration were determined for the phenolic antioxidants of interest. With the aid of these calibration curves, plant extracts in 70% MeOH, hydrolyzates, infusions, and synthetic mixtures were analyzed.

Ascorbic acid determination was performed by using isocratic elution for 8 min, the mobile phase being composed of 7% methanol (A) and 93% bidistilled water containing 0.2% of o-H$_3$PO$_4$ (B). The working wavelength was 215 nm, and flow rate 1 mL min^{-1}. Using this elution mode, the calibration curve and linear equation for ascorbic acid was determined, and ascorbic acid assay was performed in the m-phosphoric acid extract of fresh parsley.

In both applications (of polyphenolics and ascorbic acid assay), the chromatographic column was washed for 10 min with methanol prior to injection, and equilibrated for 10 min with a solvent mixture containing 7% (A) + 93% (B).

3. Results and discussion

3.1. Choice of solvent, molar absorptivities and TEAC coefficients of the tested antioxidants

Although it is not an easy task to select a unique solvent for the analysis of a diverse group of phenolics due to vastly varying chemical structures, and to different conditions in isomerization and hydrolysis, alcoholic extraction (using MeOH or EtOH) has been the usual approach to handling solid samples [53]. A minimum of 70% methanol has been reported to be needed to inactivate polyphenol oxidases, which are widely distributed in plants, and to allow maximum recovery of flavonoids, such as monomeric flavan-3-ols (catechin or epicatechin) [54,55]. A few examples where 70% MeOH as solvent proved to be very effective are extraction of flavones and glycosylated flavanones from orange peel [54], anthocyanins from red and blackcurrant [55], phenolics from *E. purpurea* roots [56], and phenolics from *Echinacea* roots [57]. The extraction efficiency did not change significantly for *Echinacea* spp. when MeOH concentration in the extracting solvent was increased from 70 to 90% [57]. Our extraction yield with 70% MeOH of parsley and celery leaves was highest, confirming literature findings.

The CUPRAC method, using a cupric neocuproine (2,9-dimethyl-1,10-phenanthroline) chelate – abbreviated as (Cu(II)-Nc) – as the chromogenic oxidant, is based on the redox reaction with antioxidants producing the cuprous-neocuproine chelate – abbreviated as (Cu(I)-Nc) – showing maximum light absorption at 450 nm [27]. The reaction equation with n-electron reductant antioxidants can be formulated by:

$$n\text{Cu(Nc)}_2^{2+} + n\text{-e reductant} \rightleftarrows n\text{Cu(Nc)}_2^+$$

$$+\, n\text{-e oxidized product} + n\text{H}^+$$
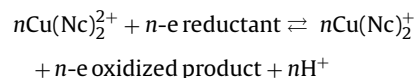
Antioxidant compounds that are expected to be found in the tested plants, namely gallic acid, catechin, chlorogenic acid, caffeic acid, p-coumaric acid, ferulic acid, naringin, naringenin, hesperidin, hesperetin, rutin, myricetin, isoquercitrin, luteolin, kaempferol, apigenin, rosmarinic acid, quercetin and ascorbic acid, were used in standard solutions, and assayed using the normal (at room temperature) and incubated (at 50 °C) CUPRAC methods [27] against trolox as the standard reference compound. The same antioxidant solutions were cross-assayed with ABTS/persulfate as the reference spectrophotometric method. The linear calibration equations of the tested antioxidants (as absorbance in a 1-cm cell *versus* molar concentration) gave the molar absorption coefficient (ε) as the slope (Tables 1 and 2); the linear working ranges over which Beer's law was valid are given in the same tables. The molar absorption coefficient of the tested antioxidant divided by that of trolox under the same conditions gave the trolox equivalent antioxidant capacity, or TEAC coefficient, of that antioxidant (Table 3).

Table 1
The molar absorption coefficients and linear ranges of the tested antioxidants with respect to the CUPRAC method (normal and incubated CUPRAC methods)

Antioxidant	Molar absorption coefficient, ε (L mol^{-1} cm^{-1})		Linear range (mol L^{-1})
	CUPRAC$_N$	CUPRAC$_I$	
Trolox	1.7×10^4	1.9×10^4	2.6×10^{-6}–7.5×10^{-5}
Gallic acid	4.4×10^4	–	1.8×10^{-5}–6.7×10^{-5}
Catechin	5.2×10^4	6.6×10^4	2.0×10^{-6}–1.0×10^{-5}
Chlorogenic acid	4.1×10^4	5.1×10^4	4.0×10^{-6}–2.0×10^{-5}
Caffeic acid	4.8×10^4	5.5×10^4	4.0×10^{-6}–2.0×10^{-5}
p-Coumaric acid	9.2×10^3	1.9×10^4	1.1×10^{-5}–1.5×10^{-4}
Ferulic acid	2.0×10^4	2.3×10^4	4.0×10^{-6}–2.0×10^{-5}
Naringin	3.4×10^2	2.4×10^3	3.0×10^{-4}–4.0×10^{-3}
Hesperidin	1.6×10^4	2.1×10^4	2.6×10^{-6}–7.5×10^{-5}
Rutin	4.3×10^4	4.8×10^4	4.0×10^{-6}–2.0×10^{-5}
Naringenin	–	4.2×10^4	1.0×10^{-5}–5.0×10^{-5}
Hesperetin	1.6×10^4	1.9×10^4	2.6×10^{-6}–7.5×10^{-5}
Quercetin	9.2×10^4	1.0×10^5	2.0×10^{-6}–1.0×10^{-5}
Myricetin	7.1×10^4	8.9×10^4	3.7×10^{-6}–1.3×10^{-5}
Luteolin	4.8×10^4	5.8×10^4	2.3×10^{-6}–2.1×10^{-5}
Kaempferol	2.5×10^4	3.6×10^4	4.9×10^{-6}–4.4×10^{-5}
Apigenin	4.6×10^3	1.5×10^4	1.8×10^{-5}–6.7×10^{-5}
Isoquercitrin	5.2×10^4	6.7×10^4	1.8×10^{-6}–1.7×10^{-5}
Rosmarinic acid	9.4×10^4	1.1×10^5	1.8×10^{-6}–6.7×10^{-6}
Ascorbic acid	1.7×10^4	2.5×10^4	5.6×10^{-6}–6.0×10^{-5}

3.2. HPLC results of the tested antioxidants

Table 4 shows the linear calibration equations of HPLC analysis of the tested antioxidants as chromatographic peak area *versus* concentration. Fig. 2 gives the chromatogram (obtained with the optimized separation scheme for phenolic antioxidants) of a standard mixture composed of 19 antioxidants (phenolics plus ascorbic acid). As the parametric symbols used in the calibration equations given in Table 4, y stands for peak area, c antioxidant molar concentration, and r linear correlation coefficient.

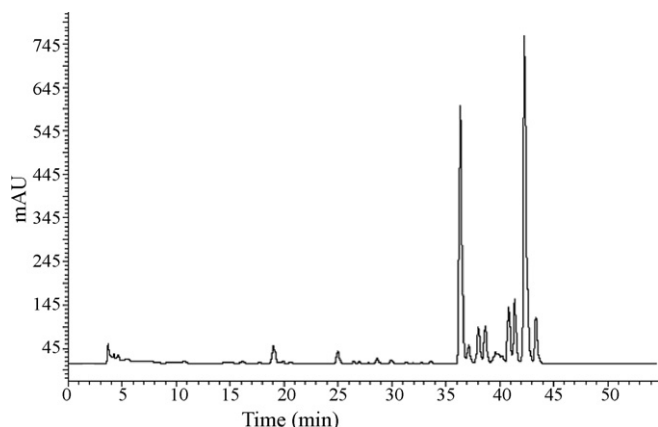In another chromatogram recorded with respect to the optimized (isocratic elution) method (figure not shown), the peak of ascorbic acid emerges at about 3.5 min, and the one before that is due to m-phosphoric acid used in extraction of ascorbic acid. This extractant is useful in preserving ascorbic acid samples during analysis.

Table 2
The molar absorption coefficients and linear ranges of the tested antioxidants with respect to the ABTS/persulfate method

Antioxidant	Molar absorption coefficient, ε (L mol^{-1} cm^{-1})	Linear range (mol L^{-1})
Trolox	2.6×10^4	5.0×10^{-6}–3.0×10^{-5}
Gallic acid	9.1×10^4	2.0×10^{-6}–1.0×10^{-5}
Catechin	8.2×10^4	2.0×10^{-6}–1.0×10^{-5}
Chlorogenic acid	3.2×10^4	4.0×10^{-6}–2.0×10^{-5}
Caffeic acid	3.6×10^4	4.0×10^{-6}–2.0×10^{-5}
p-Coumaric acid	4.2×10^4	4.0×10^{-6}–2.0×10^{-5}
Ferulic acid	5.6×10^4	4.0×10^{-6}–2.0×10^{-5}
Naringin	1.6×10^4	1.0×10^{-5}–5.0×10^{-5}
Hesperidin	3.6×10^4	4.0×10^{-6}–2.0×10^{-5}
Rutin	3.0×10^4	4.0×10^{-6}–2.0×10^{-5}
Naringenin	1.7×10^4	1.0×10^{-5}–5.0×10^{-5}
Hesperetin	2.9×10^4	3.8×10^{-6}–1.9×10^{-5}
Quercetin	8.3×10^4	2.0×10^{-6}–1.0×10^{-5}
Myricetin	8.9×10^4	2.0×10^{-6}–1.0×10^{-5}
Luteolin	2.6×10^4	3.8×10^{-6}–1.9×10^{-5}
Kaempferol	2.3×10^4	8.0×10^{-6}–4.0×10^{-5}
Apigenin	1.7×10^4	1.0×10^{-5}–5.0×10^{-5}
Isoquercitrin	2.6×10^4	6.0×10^{-6}–3.0×10^{-5}
Rosmarinic acid	6.0×10^4	4.0×10^{-6}–2.0×10^{-5}
Ascorbic acid	3.0×10^4	4.0×10^{-6}–2.0×10^{-5}

Table 3
The TEAC coefficients of the tested antioxidants with respect to the CUPRAC and ABTS spectrophotometric methods

Antioxidant	TEAC$_{CUPRAC}$		TEAC$_{ABTS}$
	TEAC$_N$	TEAC$_I$	
Myricetin	4.27	4.79	3.43
Quercetin	5.49	5.57	3.21
Kaempferol	1.47	1.92	0.86
Rutin	2.56	2.56	1.15
Isoquercitrin	3.14	3.60	1.01
Apigenin	0.27	0.82	0.65
Luteolin	2.90	3.14	1.01
Catechin	3.09	3.56	3.14
Naringin	0.02	0.13	0.62
Naringenin	–	2.28	0.64
Hesperidin	0.97	1.11	1.40
Hesperetin	0.99	1.05	1.11
Gallic acid	2.62	–	3.48
Rosmarinic acid	5.65	6.02	2.30
Ferulic acid	1.20	1.23	2.16
p-Coumaric acid	0.55	1.00	1.63
Caffeic acid	2.89	2.96	1.39
Chlorogenic acid	2.47	2.72	1.21
Ascorbic acid	1.00	1.32	1.15

Table 4
HPLC calibration equations of the tested antioxidants

Antioxidant	Linear range (mol L^{-1})	Calibration equation	(r)
Ascorbic acid	1.0×10^{-4}–1.0×10^{-3}	$y = 3.16 \times 10^9 c + 16794$	0.9999
Gallic acid	4.0×10^{-5}–5.0×10^{-4}	$y = 9.04 \times 10^9 c + 73233$	0.9997
Catechin	4.0×10^{-5}–5.0×10^{-4}	$y = 3.79 \times 10^9 c + 4474$	0.9997
Chlorogenic acid	4.0×10^{-5}–5.0×10^{-4}	$y = 9.00 \times 10^9 c + 37950$	0.9996
Caffeic acid	4.0×10^{-5}–5.0×10^{-4}	$y = 9.44 \times 10^9 c + 69934$	0.9999
p-Coumaric acid	4.0×10^{-5}–5.0×10^{-4}	$y = 1.48 \times 10^{10} c + 30571$	0.9999
Ferulic acid	4.0×10^{-5}–5.0×10^{-4}	$y = 1.05 \times 10^{10} c - 24807$	0.9998
Rosmarinic acid	4.0×10^{-5}–5.0×10^{-4}	$y = 9.49 \times 10^9 c + 64341$	0.9995
Naringin	4.0×10^{-5}–5.0×10^{-4}	$y = 1.69 \times 10^{10} c + 9146$	0.9999
Hesperidin	4.0×10^{-5}–5.0×10^{-4}	$y = 1.65 \times 10^{10} c - 44514$	0.9988
Rutin	4.0×10^{-5}–5.0×10^{-4}	$y = 8.79 \times 10^9 c + 3687$	0.9999
Isoquercitrin	4.0×10^{-5}–3.0×10^{-4}	$y = 6.43 \times 10^9 c + 55614$	0.9991
Myricetin	4.0×10^{-5}–5.0×10^{-4}	$y = 5.93 \times 10^9 c - 42007$	0.9996
Naringenin	4.0×10^{-5}–5.0×10^{-4}	$y = 1.47 \times 10^{10} c + 5985$	0.9999
Hesperetin	4.0×10^{-5}–5.0×10^{-4}	$y = 1.43 \times 10^{10} c - 81556$	0.9983
Quercetin	4.0×10^{-5}–5.0×10^{-4}	$y = 9.12 \times 10^9 c + 88516$	0.9989
Luteolin	4.0×10^{-5}–5.0×10^{-4}	$y = 9.02 \times 10^9 c - 79509$	0.9990
Kaempferol	4.0×10^{-5}–5.0×10^{-4}	$y = 7.23 \times 10^9 c - 36137$	0.9996
Apigenin	4.0×10^{-5}–5.0×10^{-4}	$y = 1.04 \times 10^{10} c - 1727$	0.9999

Fig. 2. The chromatogram of a synthetic mixture of antioxidants (phenolics plus ascorbic acid). (1) Ascorbic acid; (2) gallic acid; (3) catechin; (4) chlorogenic acid; (5) epicatechin; (6) caffeic acid; (7) p-coumaric acid; (8) ferulic acid + sinapic acid; (9) naringin; (10) rosmarinic acid; (11) hesperidin; (12) rutin + isoquercitrin; (13) myricetin; (14) naringenin; (15) hesperetin; (16) quercetin; (17) luteolin; (18) kaempferol; (19) apigenin.
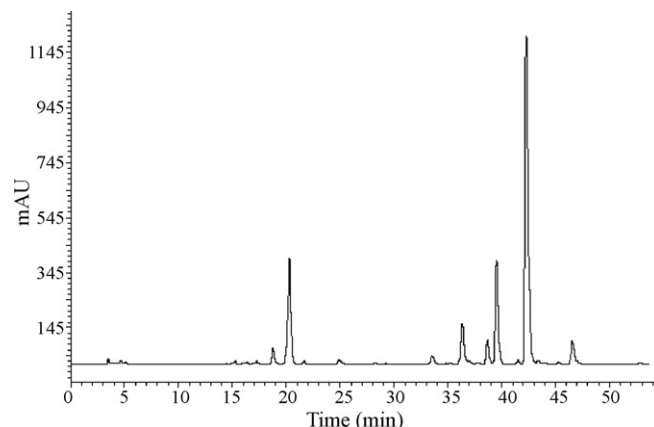
Fig. 3. The chromatogram of 70% methanolic extract of parsley.

3.3. Results of plant analyses

Plant extracts, extract hydrolyzates (prepared for the purpose of identifying complex mixtures containing numerous flavonoid glycosides by converting to the corresponding aglycons), solid plant (dried plant powder) hydrolyzates, and herbal infusions were spectrophotometrically assayed for TAC with CUPRAC (i.e., normal and incubated CUPRAC methods) and ABTS; the individual antioxidants existing in these complex samples were identified and quantified with HPLC. In order to confirm qualitative identification, the change in the peak heights of certain chromatographic bands with fixed retention times were followed with the technique of standard additions. Fig. 3 shows the chromatogram of 70% methanolic extract of parsley, and Fig. 4 gives the chromatogram of the same extract after 4 h hydrolysis. Fig. 5 shows the chromatogram of 70% methanolic extract of celery leaves, and Fig. 6 gives the chromatogram of the same extract after 4 h hydrolysis. Fig. 7 shows the chromatogram of 70% methanolic extract of nettle, and Fig. 8 gives the chromatogram of the dried nettle hydrolyzate after 4 h hydrolysis.

The individual antioxidants of plant samples were determined with the help of calibration curves in HPLC (Table 4). Using the additivity property of TAC in a complex sample, the theoretical total antioxidant capacities of plant samples were calculated by multiplying the concentration with the TEAC value of each identified antioxidant, and summing up the products. Thus, the theoretical TAC of the investigated plant material could be estimated using

Fig. 5. The chromatogram of 70% methanolic extract of celery leaves.
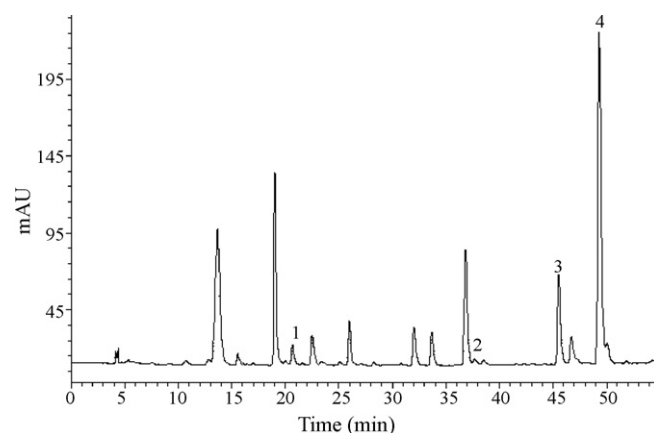
Fig. 6. The chromatogram of 70% methanolic extract of celery leaves after 4 h hydrolysis. (1) Chlorogenic acid; (2) myricetin; (3) luteolin; (4) apigenin.

the equation:

$$\text{TAC}_{\text{theoretical}} = \sum_{i=1}^{n} c_i (\text{TEAC})_i$$

where c_i is the concentration of antioxidant constituent i found with the help of HPLC, and $(\text{TEAC})_i$ is the trolox equivalent antioxidant capacity (TEAC) coefficient of constituent i with respect to a given
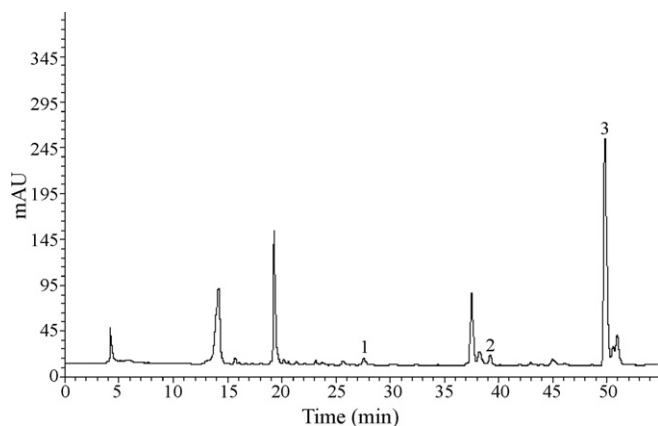

Fig. 4. The chromatogram of 70% methanolic extract of parsley after 4 h hydrolysis. (1) p-Coumaric acid; (2) myricetin; (3) apigenin.
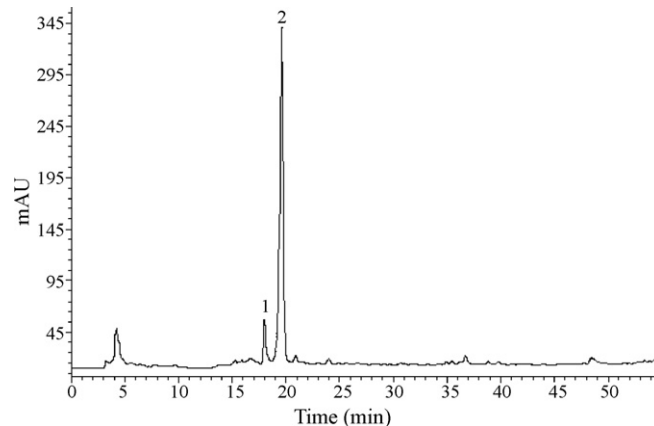

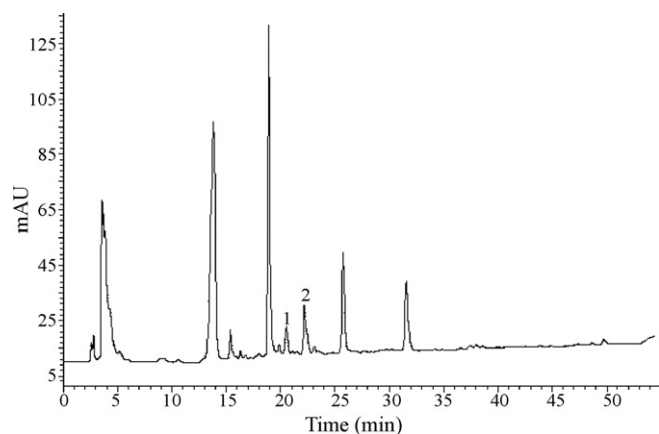Fig. 7. The chromatogram of 70% methanolic extract of nettle. (1) Catechin; (2) chlorogenic acid.

Fig. 8. The chromatogram of the dried nettle hydrolyzate after 4 h hydrolysis. (1) Chlorogenic acid; (2) caffeic acid.

spectrophotometric method (either CUPRAC or ABTS). The theoretical TAC (thus calculated) and experimental TAC (directly measured with a given spectrophotometric method) values were compared in Table 5. In Table 5, due to the lack of complete species identification in the chromatograms of the extracts of parsley and celery leaves, and of information on their exact contributions to the observed TAC, the HPLC-spectrophotometric estimates of TAC were made using the information obtained from their hydrolyzate chromatograms. The HPLC-spectrophotometric calculations for nettle were made based on the identification and quantification of species in the chromatograms of both MeOH extracts and hydrolyzate solutions.

3.4. Results of synthetic mixture analyses

The chromatograms of different possible combinations (i.e., synthetic mixtures at varying concentrations) of antioxidants identified in the tested plants and of a synthetic mixture hydrolyzed for 2 h were recorded (figures not shown). In the chromatogram of the hydrolyzate, it could be clearly seen that, accompanying the large decrease in magnitude of the chlorogenic acid peak, a new peak of caffeic acid (as a constituent of the former) emerged. Additionally, an intense peak at 3 min, and two small peaks at approximately 17 and 29 min appeared. The experimental TAC values of the mixtures (the compositions of which were described in Section 2.5) were spectrophotometrically measured by CUPRAC$_N$, CUPRAC$_I$ and

ABTS assays. The calculated HPLC-spectrophotometric capacities (TAC$_{theoretical}$) of the mixtures, along with experimental TAC results, are tabulated in Table 6.

For synthetic mixtures, the experimental CUPRAC and theoretical HPLC-CUPRAC results for TAC were very close to each other. This finding confirms that if all the antioxidants in a complex mixture were identified and quantified with the help of HPLC techniques, their contribution to the overall capacity could be envisaged, and the experimentally found TAC values (with the use of the spectrophotometric CUPRAC antioxidant assay) could be correctly estimated by theoretically calculating the TAC using the principle of additivity of individual antioxidant capacities (named for the first time in this study as 'HPLC-CUPRAC method' of TAC estimation). On the other hand, if the same comparison was made between the experimental ABTS TAC values and the theoretically found HPLC-ABTS capacities, significant discrepancies were apparent (Table 6), probably showing that there were inherent problems associated with the TAC additivity in the ABTS method of antioxidant assay. The ABTS results were also not coherent with those of CUPRAC. It is known from other studies in the literature that when the colored ABTS radical cation was generated with different mechanisms, the TEAC values of antioxidants varied significantly [30]. Firstly, it is not surprising that turbidity problems were encountered in this work using ABTS at pH 6.0, while the ABTS radical reagent is not stable above pH 6.5, and therefore Cano et al. [58] had to prepare the reagent solution in glycine–HCl buffer at pH 4.5 to preserve its stability at room temperature. It was shown by Cano et al. [58] that the ABTS radical cation is not stable for mixtures containing a ratio of unreacted ABTS-to-ABTS radical cation (i.e., ABTS$_{unreacted}$/ABTS$^{•+}$) less than 50, while for most assays, this critical limit in the ratio cannot be maintained for maximal stability. Due to the above reasons, deviations from additivity of TAC values (of HPLC-analyzed components) of antioxidant mixtures might have arisen both in the literature [59] and in this work, while no problems were encountered in regard to turbidity and additivity of TAC values of mixtures using the CUPRAC method. The data in Table 6 clearly show that the experimental and theoretical TAC values of antioxidants contained in synthetic mixture solutions 1–3 (in trolox equivalent concentrations) were coherent for CUPRAC but not for ABTS.

3.5. Evaluation of common results for synthetic and real mixtures

The percentages of experimental antioxidant capacities of synthetic mixtures and plant extracts as accounted for by

Table 5
The theoretical and experimental TAC (total antioxidant capacity) values of plants in the units of mmol trolox g^{-1} plant

Sample	CUPRAC$_N$	CUPRAC$_I$	ABTS	HPLC-(CUPRAC$_N$)	HPLC-(CUPRAC$_I$)	HPLC-(ABTS)
Parsley						
70% MeOH extn.	0.050	0.079	0.040	–	–	–
70% MeOH extn. 2 h hydrol.	0.056	0.099	0.011	0.043	0.067	0.051
70% MeOH extn. 4 h hydrol.	0.058	0.104	0.012	0.034	0.062	0.049
Solid plant, 2 h hyrol.	0.082	0.166	0.022	0.049	0.074	0.056
Solid plant, 4 h hydrol.	0.093	0.193	0.021	0.035	0.069	0.054
m-Phosphoric acid extn.	0.016	0.023	0.008	0.008	0.011	0.009
Celery leaves						
70% MeOH extn.	0.148	0.180	0.087	–	–	–
70% MeOH extn. 4 h hydrol.	0.141	0.169	0.096	0.068	0.097	0.053
Solid plant, 4 h hydrol.	0.179	0.229	0.133	0.069	0.095	0.049
Nettle						
70% MeOH extn.	0.076	0.097	0.058	0.062	0.069	0.038
70% MeOH extn. 4 h hydrol.	0.077	0.094	0.060	0.043	0.067	0.051
Solid plant, 4 h hydrol.	0.186	0.247	0.170	0.034	0.062	0.049
Steeped infusion	0.050	0.081	0.036	0.049	0.074	0.056
Steeped infusion hydrol.	0.078	0.116	0.027	0.035	0.069	0.054

HPLC-spectrophotometric values represent the theoretically found TAC using the additivity principle; extn.: extraction, hydrol.: hydrolysis.

Table 6
The experimental and theoretical TAC values of synthetic mixture solutions of antioxidants (in the units of mmol trolox equivalents L^{-1})

Sample	$CUPRAC_N$	$CUPRAC_I$	ABTS	HPLC-($CUPRAC_N$)	HPLC-($CUPRAC_I$)	HPLC-(ABTS)
Mixture 1	0.32	0.43	0.33	0.29	0.47	0.54
Mixture 2	0.80	0.90	0.40	0.79	0.92	0.47
Mixture 3	1.29	1.41	0.76	1.19	1.34	0.90
Mixture 3 (2 h hydrol.)	1.32	1.41	0.35	0.18	0.21	0.19

HPLC-spectrophotometric estimates are given in Table 7. The HPLC-CUPRAC method was capable of estimating the following percentages of the experimental CUPRAC capacities of plant samples: 81% of nettle extract, 60–77% of different hydrolyzates of parsley, and 41–57% of different hydrolyzates of celery leaves. The precision of estimation for the proposed method (i.e., 92–108%) was much higher for synthetic mixtures.

This study has identified the essential antioxidant compounds present in parsley, celery leaves, and stinging nettle, measured the total antioxidant capacity of these compounds with CUPRAC and ABTS spectrophotometric methods, and correlated the TAC with HPLC findings. The CUPRAC spectrophotometric method developed in our laboratories was selected for TAC measurement of plant material, because it had low cost, stable and easily available reagents, and was capable of oxidizing both hydrophilic and lipophilic antioxidants relatively rapidly within the protocol time period of the assay. Moreover, the CUPRAC assay results were precise and reproducible, and the TAC of complex mixtures perfectly showed the property of additivity. The CUPRAC assay worked at the realistic pH of 7.0 (close to the physiological pH), thereby measuring the TAC of real samples without exaggeration (e.g., FRAP working at pH 3.6 and Folin at pH 10 either underestimated or overestimated the actual TAC, because phenolic antioxidants were either in molecular acidic form or in totally dissociated conjugate base form, making their oxidation too difficult or too easy, respectively).

Since the basic plant antioxidants comprising numerous flavonoids and phenolic acids exist in plants in the form of their glycosides, esters, or bound to cell walls, their complete identification by HPLC techniques is almost impossible due to the unavailability of the corresponding standards, and therefore these glycosides are generally converted into their aglycons by acid hydrolysis and identified in free forms [48]. As it is known that parsley and celery leaves contain apigenin glycosides, a 4-h hydrolysis was sufficient

for their conversion. On the other hand, the 4-h hydrolysis produced myricetin almost a half of that converted within 2 h. Thus, within this relatively long period of hydrolysis, the literature-reported partial degradation of myricetin [60–62] was confirmed in this study. Moreover, phenolic acids were observed to largely degrade under these hydrolysis conditions [60,62,63]. During the investigations with nettle, the high content of chlorogenic acid in the original plant extract could no longer be found in the hydrolyzate. On the other hand, the presence of caffeic acid in the hydrolyzate in spite of its absence in the original extract hints to the possible conversion of some chlorogenic acid into caffeic acid [64].

In a study in which the contribution of phenolic species to the observed total antioxidant capacity of plum was investigated [59], ten polyphenolic compounds including chlorogenic acid, cyanidin, cyanidin glycosides, peonidin, peonidin-3-glycoside, quercetin, and quercetin glycosides were identified and quantified by HPLC. The HPLC-determined concentrations of individual phenolics multiplied by their ascorbic acid-equivalent capacities with respect to the ABTS method were summed up, and this calculated TAC was found to be smaller than the experimental TAC measured with the ABTS method in the same (ascorbic acid) units. This difference between the calculated and actual values was attributed to matrix variations, and to minor antioxidant constituents contained in the samples such as carotenoids and vitamin C. In this study, HPLC-spectrophotometry combinations were carried out to estimate the theoretical TAC as trolox equivalents of complex samples using the chromatographic standards of the most widely encountered antioxidants. In the hydrolyzates (at 2- and 4-h operations) of synthetic mixtures and plant materials, the pH adjustment to pH 6.0 with the addition of NaOH produced turbidity of ABTS assay samples before the 6th min measurement. Therefore, acidic samples were appropriately diluted without pH adjustment prior to ABTS assay measurement. Looking at the results tabulated in Table 7, there were great discrepancies between the ABTS spectrophotometric measurements (experimental TAC) and HPLC-ABTS estimates (theoretical TAC). On the other hand, there was a harmonical relationship with the analogic CUPRAC results, arising from the validity of the principle of additivity of TAC in CUPRAC.

The two-way ANalysis Of VAriance (ANOVA) comparison by the aid of F-test of the mean-squares of 'between-treatments' (i.e., theoretically expected HPLC-CUPRAC absorbance and experimentally found CUPRAC absorbance of different samples in Table 6) and of residuals [65] for synthetic mixtures 1–3 (excluding the hydrolyzed mixture 3) enabled to conclude that there was no significant difference between treatments. In other words, the experimentally found CUPRAC results and theoretically expected HPLC-CUPRAC calculations were alike at 95% confidence level (using paired comparisons of either $CUPRAC_N$ and HPLC-$CUPRAC_N$ treatment data, or of $CUPRAC_I$ and HPLC-$CUPRAC_I$ treatment data). On the other hand, there was significant difference between samples with respect to concentration of antioxidants (i.e., the residual mean-square was much greater than 'between-sample' mean-square at 95% confidence level). The ANOVA treatment of relatively limited data also showed that the experimental ABTS measurements significantly differed from HPLC-ABTS calculations, probably due to the lack of additivity of TAC values of synthetic mixture components in the

Table 7
The percentages of experimental antioxidant capacities (found by spectrophotometry) of synthetic mixtures and plant extracts as accounted for by HPLC-spectrophotometric estimates

Sample	$CUPRAC_N$ (%)	$CUPRAC_I$ (%)	ABTS (%)
Parsley			
70% MeOH extd. 2 h hydrol.	77	68	>100
70% MeOH extd. 4 h hydrol.	56	60	>100
Solid plant, 2 h hydrol.	60	45	>100
Solid plant, 4 h hydrol.	37	35	>100
m-Phosphoric acid extract	52	46	>100
Celery leaves			
70% MeOH extract hydrol.	48	57	55
50% MeOH extract hydrol.	40	51	46
Solid plant hydrolyzate	39	41	37
Nettle			
70% MeOH extract	81	71	66
70% MeOH extract hydrol.	21	19	14
Solid plant hydrolyzate	9	7	5
Mixture 1	92	108	>100
Mixture 2	98	102	118
Mixture 3	92	95	119
Mixture 3 (2 h hydrol.)	14	15	53

ABTS method under the employed conditions. To summarize the statistical test results, the experimental and computational (theoretical) TAC values of antioxidants contained in synthetic mixture solutions 1–3 (in trolox equivalent concentrations) were coherent for CUPRAC but not for ABTS.

The HPLC-CUPRAC method was capable of estimating the following percentages of the experimental CUPRAC capacities of plant samples: 81% of nettle extract, 60–77% of different hydrolyzates of parsley, and 41–57% of different hydrolyzates of celery leaves. Since the estimation percentages for synthetic mixtures were larger (Table 7), it was obvious that any deviations from ideal estimation in the proposed HPLC-CUPRAC procedure resulted from incomplete identification or conversion of flavonoid glycosides and/or tannin polymers in the tested samples. This argument can be further extended to claim that if all the antioxidants in a complex mixture could be identified and quantified with HPLC, it would be possible to roughly estimate the actual (experimental) TAC of the mixture with the proposed procedure thanks to the validity of the additivity of TAC in the CUPRAC method.

4. Conclusions

This work brings several contributions to food analytical chemistry (specifically antioxidant assays) briefly summarized as: (i) reporting the trolox equivalent antioxidant capacities of several phenolic antioxidants – not assayed previously – with respect to the CUPRAC method; (ii) modifying the mobile phase of gradient elution in HPLC analysis of phenolic antioxidants where resolution in the separation of phenolic acids and flavonoids is not appreciably high; (iii) developing a novel method of estimation of the CUPRAC total antioxidant capacity of antioxidant mixtures and plant extracts utilizing the principle of additivity of the capacities of individual constituents identified and quantified by HPLC. The sum of the products of the concentrations of HPLC-identified antioxidant constituents in plant extracts and their TEAC coefficients (with respect to the CUPRAC method) gave the theoretically calculated TAC values, which accounted for a large percentage of experimental TAC values measured by CUPRAC spectrophotometry. Thus, the 'HPLC-CUPRAC method' is proposed for the first time in this study to give a reliable estimate of the actual antioxidant capacity of plant extracts and hydrolyzates.

The proposed HPLC-CUPRAC method enables a realistic comparison of antioxidant constituents of plant extracts and hydrolyzates by HPLC analysis, and of their calculated TAC values (without performing the actual antioxidant assay) in trolox equivalents. This comparison is certainly more meaningful than that of total phenolic contents made on a mass basis [45]. Since the additivity property of TAC with respect to the proposed method proved to be precisely valid for synthetic mixtures and approximately valid for real mixtures of antioxidants, it becomes feasible to roughly estimate the experimental TAC of complex antioxidant mixtures such as plant extracts and hydrolyzates on the condition that all the antioxidants contained therein be properly identified and quantified by HPLC.

The additivity of TAC with HPLC-CUPRAC is approximately valid for real mixtures of antioxidants, because real mixtures contain flavonoids, their glycosides, their many additional configurational and conformational isomers as well as their oligomers or polymers, and it is almost impossible to find the exactly matching standards for their HPLC analysis. As a result, the chromatographic peaks of certain isomers may easily overlap, and render their precise HPLC estimation and quantification almost impossible. Continuously developing LC/MS/MS techniques for complete characterization of plant polyphenolics face the bottlenecks of insufficiency of data processing and available reference compounds. Thus, we cannot speak of a "one-to-one correspondence" between the experimental CUPRAC and computational HPLC-CUPRAC results of real mixtures, and the proposed methodology of this work may be considered successful if a high percentage of the observed CUPRAC absorbance of a real mixture can be compensated for by a HPLC-CUPRAC computational procedure.

The CUPRAC total capacities of the 70% MeOH extracts of studied plants (in the units of mmol trolox g^{-1} plant) were in the order: celery leaves > nettle > parsley.

References

[1] A. Gönenç, Y. Atak, M.N. Orman, B. Şimşek, Dial. Transplant. 31 (2002) 88.
[2] B. Halliwell, R. Aeschbach, J. Löliger, O.I. Aruoma, Food Chem. Toxicol. 33 (1995) 601.
[3] E. Cadenas, L. Packer, Handbook of Antioxidants, Marcel Dekker, New York/Basel, 2002, ISBN 0-8247-0547-5.
[4] C.A. Rice-Evans, N.J. Miller, G. Paganga, Free Radical Biol. Med. 20 (1996) 933.
[5] C.A. Rice-Evans, N.J. Miller, P.G. Bolwell, P.M. Bramley, J.B. Pridham, Free Radical Res. 22 (1995) 375.
[6] S. Van Acker, D.J. Van-Den Berg, M.N. Tromp, D.H. Griffioen, W.P. Van Bebbekom, W.J.F. Van Der, A. Bast, Free Radical Biol. Med. 20 (1996) 331.
[7] J.A. Brown, H. Khodr, R.C. Hider, C. Rice-Evans, Biochem. J. 330 (1998) 1173.
[8] G. Wallace, S.C. Fry, Int. Rev. Cyt. 151 (1994) 229.
[9] M.P. Kähkonen, A.I. Hopia, H.J. Vuroela, J.P. Rauha, K. Pihlaja, T.S. Kujala, et al., J. Agric. Food Chem. 47 (1999) 3954.
[10] G. İşcan, F. Demirci, N. Kırımer, M. Kürkçüoğlu, K.H.C. Başer, M. Kıvanç, 14. Bitkisel İlaç Hammaddeleri Toplantısı, ISBN 975-94077-2-8, Haziran, 2004.
[11] J.M. Cherng, W. Chiang, L.C. Chiang, Food Chem. 106 (2008) 944.
[12] M. Hojnik, M. Škerget, Ž. Knez, Sep. Purif. Technol. 57 (2007) 37.
[13] R. Apak, K. Güçlü, M. Özyürek, S.E. Karademir, E. Erçağ, Int. J. Food. Sci. Nutr. 57 (2006) 292.
[14] S. Surveswaran, Y. Cai, H. Corke, M. Sun, Food Chem. 102 (2007) 938.
[15] J. Oszmianski, A. Wojdylo, E. Lamer-Zarawska, K. Swiader, Food Chem. 100 (2007) 579.
[16] S. Chun, D.A. Vattem, Y.T. Lin, K. Shetty, Process Biochem. 40 (2005) 809.
[17] G. Toker, M. Aslan, E. Yeşilada, M. Memişoğlu, S. Ito, J. Pharm. Biomed. Anal. 26 (2001) 111.
[18] V. Exarchou, Y.C. Fianegos, T.A. Van Beek, C. Nanos, J. Vervoort, J. Chromatogr. A 1112 (2006) 293.
[19] U. Justesen, P. Knuthsen, Food Chem. 73 (2001) 245.
[20] F.M. Areias, P. Valentão, P.B. Andrade, F. Ferreres, R.M. Seabra, Food Chem. 73 (2001) 307.
[21] S. Karakaya, N.S. El, Food Chem. 66 (1999) 289.
[22] E. Tütem, R. Apak, F. Baykut, Analyst 116 (1991) 89.
[23] E. Tütem, R. Apak, Anal. Chim. Acta 255 (1991) 121.
[24] E. Tütem, R. Apak, E. Günaydı, K. Sözgen, Talanta 44 (1997) 249.
[25] K. Güçlü, K. Sözgen, E. Tütem, M. Özyürek, R. Apak, Talanta 65 (2005) 1226.
[26] K. Sözgen, S. Demirci-Çekiç, E. Tütem, R. Apak, Talanta 68 (2006) 1601.
[27] R. Apak, K. Güçlü, M. Özyürek, S.E. Karademir, J. Agric. Food Chem. 52 (2004) 7970.
[28] K. Güçlü, M. Altun, M. Özyürek, S.E. Karademir, R. Apak, Int. J. Food Sci. Technol. 41 (2006) 76.
[29] R. Apak, K. Güçlü, M. Özyürek, S.E. Karademir, M. Altun, Free Radical Res. 39 (2005) 949.
[30] R. Re, N. Pellegrini, A. Proteggente, A. Pannala, M. Yang, C.A. Rice-Evans, Free Radical Biol. Med. 26 (1999) 1231.
[31] R.L. Prior, X. Wu, K. Schaich, J. Agric. Food Chem. 53 (2005) 4290.
[32] S. Gorinstein, M. Leontowicz, H. Leontowicz, K. Najman, J. Namiesnik, Y.-S. Park, S.-T. Jung, S.-G. Kang, S. Trakhtenberg, Nutr. Res. 26 (2006) 362.
[33] Y.-S. Park, S.-T. Jung, S.-G. Kang, E. Delgado-Licon, E. Katrich, Z. Tashma, S. Trakhtenberg, S. Gorinstein, Plant Foods Hum. Nutr. 61 (2006) 151.
[34] Y.-S. Park, S.-T. Jung, S.-G. Kang, B.G. Heo, P. Arancibia-Avila, F. Toledo, J. Drzewiecki, J. Namiesnik, S. Gorinstein, Food Chem. 107 (2008) 640.
[35] S. Gorinstein, A. Lojek, M. Ciz, E. Pawelzik, E. Delgado-Licon, O.J. Medina, M. Moreno, I.A. Salas, I. Goshev, Int. J. Food Sci. Technol. 43 (2008) 629.
[36] D. Mazor, L. Greenberg, D. Shamir, D. Meyerstein, N. Meyerstein, Biochem. Biophys. Res. Commun. 349 (2006) 1171.

[37] M. Ozturk, F. Aydogmus-Ozturk, M.E. Duru, G. Topcu, Food Chem. 103 (2007) 623.
[38] E. Capanoglu, J. Beekwilder, D. Boyacioglu, R. Hall, R. De Vos, J. Agric. Food Chem. 56 (2008) 964.
[39] V. Katalinic, M. Milos, T. Kulisic, M. Jukic, Food Chem. 94 (2006) 550.
[40] J. Bouayed, K. Piri, H. Rammal, A. Dicko, F. Desor, C. Younos, R. Soulimani, Food Chem. 104 (2007) 364.
[41] K. Tawaha, F.Q. Alali, M. Gharaibeh, M. Mohammad, T. El-Elimat, Food Chem. 104 (2007) 1372.
[42] E.M. Silva, J.N.S. Souza, H. Rogez, J.F. Rees, Y. Larondelle, Food Chem. 101 (2007) 1012.
[43] A. Chanwithheesuk, A. Teerawutgulrag, N. Rakariyatham, Food Chem. 92 (2005) 491.
[44] A.K. Atoui, A. Mansouri, G. Boskou, P. Kefalas, Food Chem. 89 (2005) 27.
[45] A. Wojdylo, J. Oszmiański, R. Czemerys, Food Chem. 105 (2007) 940.
[46] H. Sakakibara, Y. Honda, S. Nakagawa, H. Ashida, K. Kanazawa, J. Agric. Food Chem. 51 (2003) 571.
[47] U. Justesen, P. Knuthsen, T. Leth, J. Chromatogr. A 799 (1998) 101.
[48] C. Hao, Y. Zuo, Y. Deng, J. Chromatogr. A 913 (2001) 387.
[49] C. Proestos, D. Sereli, M. Komaitis, Food Chem. 95 (2006) 44.
[50] J. Singh, A.K. Upadhyay, A. Bahadur, B. Singh, K.P. Singh, M. Rai, Sci. Hortic. 108 (2006) 233.
[51] M.G.L. Hertog, P.C.H. Hollman, M.B. Katan, J. Agric. Food Chem. 40 (1992) 2379.
[52] M.G.L. Hertog, P.C.H. Hollman, D.P. Venema, J. Agric. Food Chem. 40 (1992) 1591.
[53] D. Tura, K. Robards, J. Chromatogr. A 975 (2002) 71.
[54] K. Robards, P.D. Prenzler, G. Tucker, P. Swatsitang, W. Glover, Food Chem. 66 (1999) 401.
[55] R. Chirinos, H. Rogez, D. Campos, R. Pedreschi, Y. Larondelle, Sep. Purif. Technol. 55 (2007) 217.
[56] R. Pomponio, R. Gotti, M. Hudaib, V. Cavrini, J. Chromatogr. A 954 (2002) 239.
[57] F. Pellati, S. Benvenuti, L. Magro, M. Melegari, F. Soragni, J. Pharm. Biomed. Anal. 35 (2004) 289.
[58] A. Cano, J. Hernandez-Ruiz, F. Garcia-Canovas, M. Acosta, M.B. Arnao, Phytochem. Anal. 9 (1998) 196.
[59] O.K. Chun, D.-O. Kim, H.Y. Moon, H.G. Kang, C.Y. Lee, J. Agric. Food Chem. 51 (2003) 7240.
[60] S.H. Häkkinen, S.O. Kärenlampi, I.M. Heionen, H.M. Mykkänen, A.R. Torronen, J. Sci. Food Agric. 77 (1998) 543.
[61] H.M. Merken, G.R. Beecher, J. Agric. Food Chem. 48 (2000) 577.
[62] A.M. Nuutila, K. Kammiovirta, K.-M. Oksman-Caldentey, Food Chem. 76 (2002) 519.
[63] Z. Huang, B. Wang, D.H. Eaves, J.M. Shikany, R.D. Pace, Food Chem. 103 (2007) 1395.
[64] M. Rhodes, L. Wooltorton, Phytochemistry 18 (1976) 929.
[65] J.C. Miller, J.N. Miller, Statistics for Analytical Chemists, 3rd ed., Ellis Horwood and Prentice Hall, New York and London, 1993.

Alumina sol–gel/sonogel-carbon electrode based on acetylcholinesterase for detection of organophosphorus pesticides

Hanane Zejli [a,b,c], José Luis Hidalgo-Hidalgo de Cisneros [b], Ignacio Naranjo-Rodriguez [b], Baohong Liu [d], Khalid Riffi Temsamani [c], Jean-Louis Marty [a,*]

[a] Centre de phytopharmacie, Université de Perpignan-Biomem, Perpignan Cedex, France
[b] Department of Analytical Chemistry, Faculty of Sciences, University of Cádiz, Spain
[c] Equipe de Recherche Bioelectrochemie et Systèmes Interfaciaux, University Abdelmalek Essaadi, Morocco
[d] Department of Chemistry, Fudan University, Shanghai 200433, China

ARTICLE INFO

ABSTRACT

Two new amperometric biosensors based on immobilization of acetylcholinesterase on a sonogel-carbon electrode for detection of organophosphorous compounds are proposed. The electrodes were prepared applying high-energy ultrasounds directly to the precursors. The first biosensor was obtained by simple entrapping acetylcholinesterase in Al_2O_3 sol–gel matrix on the sonogel-carbon. The second biosensor was produced in a sandwich configuration. Its preparation involved adsorption of the enzyme and modification via a polymeric membrane such as polyethylene glycol and the ion-exchanger Nafion. The optimal enzyme loading was found to be 0.7 mIU. Both biosensors showed optimal activity in 0.2 M phosphate buffer, pH 7.0, at an operating potential of 210 mV. The detection limit achieved for chlorpyriphos-ethyl-oxon was 2.5×10^{-10} M at a 10-min incubation time.

© 2008 Elsevier B.V. All rights reserved.

1. Introduction

Organophosphorous pesticides (OPs) have been widely used for decades in agriculture, medicine, industry and even as chemical warfare agents in military practice. Meanwhile, their presence in the environment is very harmful for human health. The methodology optimization study for the detection of OPs is thus quite crucial for analytical researchers especially when the versatility and the cost of the analytical system are taken into account [1–6].

Electrochemistry affords high sensitivity, simple sample treatment, inexpensive instruments, easily operation procedure and it is an ideal analytical technique for in situ analysis. Amperometric biosensors based on the inhibition of acetylcholinesterase enzyme (AChE) using screen printed electrodes (SPE) have shown satisfactory results for real sample analysis [7], in which the acetylcholinesterase activity is employed as an indicator of quantitative measurement of OPs. The relevant reactions are described as follows:

$$\text{acetylthiocholine} + H_2O \xrightarrow{\text{AChE}} \text{thiocholine} + \text{acetic acid} \qquad (1)$$

$$\text{thiocholine} \xrightarrow{\text{anodic oxidation}} \text{dithio-bischoline} + 2H^+ + 2e^- \qquad (2)$$
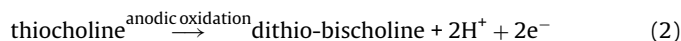
The amperometric response of AChE biosensors, i.e. the anodic oxidation current resulting from the thiocholine (TCH) formed by enzymatic hydrolysis of acetylthiocholine (ATCH), is inversely proportional to the concentration of OPs in the sample.

The employment of sol–gel technology to produce ceramics based bio-sensitive materials [8–13]. This interest is due to inherent advantages such as its relative chemical inertness, simplicity of preparation, negligible swelling in solution, low-temperature encapsulation and high sensitivity; these properties contribute to the effective preservation of the chemical and biological activities of the entrapped molecules. Among these electrodes, the sonogel-carbon electrodes, developed by some of us [14,15], show very favourable electroanalytical properties that facilitate the easy incorporation of numerous receptor molecules, which can notably improve the selectivity and sensitivity of the electrode compared as compared with classical electrodes [16–22].

Methods used for the immobilization of acetylcholinesterase are integral to the success of the sensor. Studies exploring different techniques are of great interest. Several ways of immobilization are being developed at the present. Among these are the immobilization on 3-mercaptopropionic acid SAM gold electrode [23], or on gold nanoparticles embedded in sol–gel film [24]. Immobilization on screen printed electrodes was previously reported [25].

Nevertheless, as far as we know, the immobilization on alumina sol–gel has not been explored. In the present paper, we propose alumina sol–gel for immobilization of AChE; furthermore we have employed a basis not used either with this aim and developed by some of us, the sonogel-carbon electrode. This constitutes the novelty of the paper, and it must be added to the good detection limits attained in the detection of organophosphorous pesticides. The objective proposed for the present studies was to seek new electrochemical biosensors for pesticide determination. The experimental parameters affecting the response of all resulting biosensors are discussed.

2. Materials and methods

2.1. Apparatus and reagents

Methyltrimethoxysilane was purchased from Merck, HCl from Panreac (Barcelona, Spain) and graphite powder (spectroscopic grade RBW) was from SGL Carbon (Ringsdorff, Germany). Acetylcholinesterase was purchased from Sigma (St. Louis, MO, USA); KH_2PO_4 and K_2HPO_4 for phosphate buffer were from Fluka (Buchs, Switzerland). High purity water was obtained by passing twice distilled water through a Mill-Q system (18 mΩ cm^{-1}, Millipore, Bedford, MA). All pesticide compounds tested in this work of analytical grade, and purchased from Sigma. Glass capillary tubes, i.d. 1.15 mm, were used as the bodies for the composite electrodes. Al_2O_3 sol–gel was prepared as described in the literature [26]. Chronoamperometric measurements were performed with an Autolab PGSTAT20 Potentiostat/Galvanostat (Ecochemie, Utrecht, The Netherlands) interfaced with a personal computer using the Autolab software GPES for wave form generation and data acquisition and elaboration. A 600-W model, 20 KHz ultrasonic processor (Misonix Inc., Farmingdale, NY) equipped with a 13-mm titanium tip was used. The ultrasonic processor was inside a closed sound proof chamber during operation.

Electrochemical impedance spectroscopy (EIS) measurements were performed with a Voltalab 10 type PGZ 100 from Radiometer. Scannig electron microscopy (SEM) studies were performed with a JEOL microscope, JSM 5400 type.

All electrochemical experiments were carried out in a cell containing 10 ml of an aerated 0.2 M phosphate buffer solution at pH 7.0 and 22($\pm$1)°C; the three electrodes system consisted of an AChE/Al_2O_3/modified sonogel-carbon, an Ag/AgCl (3 M KCl) and a platinum wire electrodes as working, reference and auxiliary electrodes, respectively. A magnetic stirrer and stirring bar were used to provide continuous convective transport during the measurements.

2.2. Biosensor fabrication

The unmodified sonogel-carbon electrode was prepared as described previously [14,15]. Before modification, the electrodes were polished with emery paper No. 1200 to remove extra composite material, wiped gently with weighing paper, thoroughly washed with deionized water and allowed to dry at room temperature.

The first type of biosensor was obtained by depositing 50 μl of AChE (0.7 mIU in Al_2O_3 sol), onto the sonogel-carbon electrode. The enzymatic membrane was subsequently gelatinized completely in the refrigerator (4°C) for 24 h. All the prepared AChE/Al_2O_3/Sonogel-scarbon biosensors were stored in buffer solution (pH 7.0, 0.2 M) in the refrigerator (4°C) before use.

The second, sandwich configured biosensor was prepared as follows: tyrosinase powder was dissolved in phosphate buffer of pH 7.0; in the first step, 50 μl of this solution (0.7 mIU) were placed onto the surface of an unmodified sonogel-carbon electrode and allowed to adsorb and dry at room temperature. In the second step, 1.5 μl of Nafion solution (0.5% in a mixture of lower-aliphatic alcohols and water) or PEG solution (5% in a mixture of water) were spread on the enzyme film. The resulting biosensors were stored for a minimum of 8 h to dry in a refrigerator at 4°C. All biosensors were washed carefully with buffer solution before and after each manipulation, and were stored by immersing in a phosphate buffer solution of pH 7.0 at 4°C when not in use.

3. Results and discussion

3.1. Cyclic voltammetric studies

The electrochemical behaviour of the proposed AChE/Al_2O_3/sonogel-carbon biosensor versus acetythiocholine was examined. Fig. 1 shows the cyclic voltammogram of the sensor in phosphate buffer (pH 7.0) at a scan rate of 100 mV s^{-1}. No response was observed in absence of acetylthiocholine, whereas in presence of the substrate an anodic wave was clearly observed; this wave corresponds to the oxidation of the thiocholine released from acetylthiocholine via enzymatic hydrolysis.

3.2. Enzyme loading and pH studies

The influence of enzyme loading in the Al_2O_3 sol–gel matrix was studied and the responses of the biosensors in presence of a 1-mM substrate concentration are shown in Fig. 2. As can be seen, the response of the biosensor increases with the increasing amount of the enzyme, first rapidly and then slowly; in all cases the stability of the response was quite good. For a loading of 0.7 mIU of the enzyme, the current intensity was almost as good as for 1.5 mIU. Thus, AChE loading was set at 0.7 mIU for subsequent studies to conserve the enzyme while retaining comparable sensitivity.

The pH dependence of the enzyme electrode over the range 6.0–9.6 in 0.2 M phosphate buffer in the presence of 100 mM substrate is illustrated in Fig. 3. The resulting profile indicated maximum sensitivity of the enzyme electrode at pH 7.0, corresponding to the optimum pH for the reaction between the enzyme and the substrate. For AChE sensors, the matrix pH must be kept below 9 to allow for the requisite chemical hydrolysis to occur [27]. Thus, all experiments, including inhibition studies, were performed at pH 7.0.
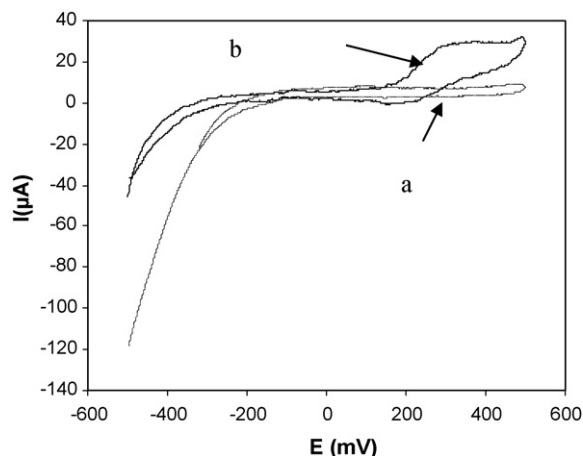

Fig. 1. Cyclic voltammograms of AChE/Al_2O_3/sonogel-carbon electrode in 0.2 M phosphate buffer, pH 7.0, (a) without acetylthiocholine and (b) with 1 mM acetylthiocholine.
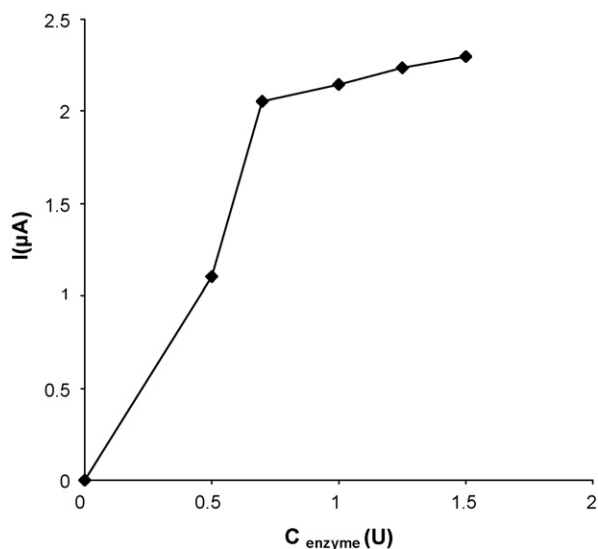
Fig. 2. Effect of enzyme loading into sol–gel matrix on the response of biosensor system, 0.2 M phosphate buffer, pH 7.0, applied potential 210 mV.

3.3. Reproducibility and stability of the enzyme electrodes

At a concentration of 1 mM acetylthiocholine, the Al_2O_3/sol–gel biosensors showed a signal of 2.02 μA and a quite good reproducibility. Electrodes prepared in the same batch demonstrated a standard deviation of 1.4% ($n = 11$). When the enzyme electrode was stored in the refrigerator at 4 °C between measurements, it retained 98% of initial current response after 20 assays. If the current response was measured once a day, after the intermittent use over a 50-day period, it retained 50% of its initial current response. In the same 50-day period we can use these sensors for more than 100 assays.

These results demonstrate that sol–gel film is very efficient for retaining the activity of acetylcholinesterase with a good long-term stability. This is attributed to the fact that the method provides a mild immobilization process. Specifically, the method does not involve any additive that results in chemical modification and fouling of the enzyme molecules. This allows the enzyme to maintain its activity to a large extent. Also, the sol–gel contains numer-
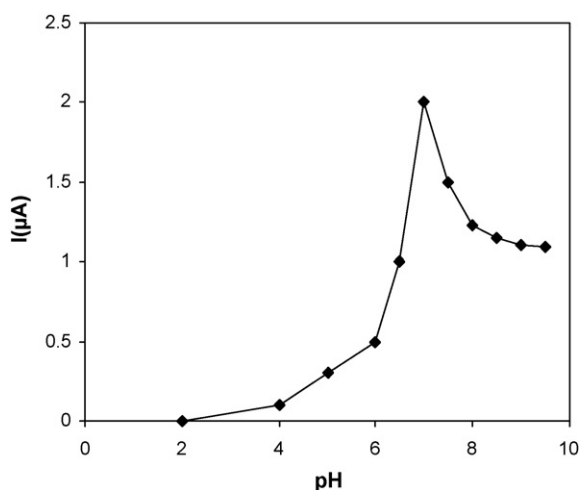
Fig. 3. Effect of pH on the enzyme response for a substrate concentration of 1 mM, 0.2 M phosphate buffer, pH 7.0, applied potential 210 mV.
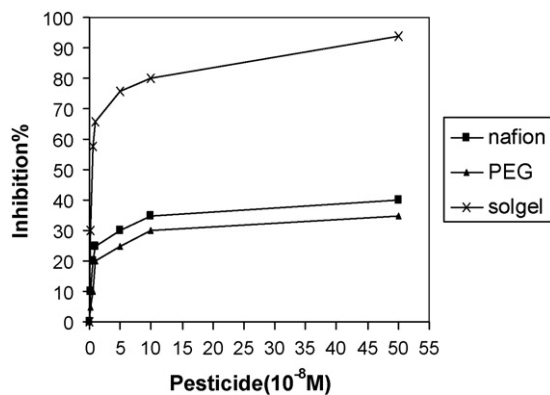
Fig. 4. Inhibition curves of AChE by Chlorpyrifos-ethyl-oxon after 10 min incubation. Measurement conditions: 0.2 M phosphate buffer, pH 7.0, applied potential: 210 mV, 1 mM acetythiocholine substrate concentration.

ous hydroxyl groups which can form strong hydrogen bonds with acetylcholinesterase and sol–gel cages for enzyme loading.

3.4. Detection of pesticides

It is well known that numerous pesticides can be determined using the signal inhibition that they cause in several (bio)sensors. AChE sensors have been used to carry out inhibition studies with three pesticides: Paraoxon, dichlorvos, and chlorpyriphos-ethyl-oxon. In order to obtain a lower-detection limit, an incubation time of 10 min was selected for inhibition measurements. The detection limit was calculated as the concentration of pesticide resulting in 20% inhibition [27]. Inhibition curves for chlorpyriphos-ethyl-oxon with immobilized AChE by two methods are presented in Fig. 4. The greatest inhibition was obtained with alumina sol–gel and may be attributed to the microenvironment surrounding the enzyme, because in the sol–gel. This may be due to the microenvironment encaging the enzyme. The sol–gel pores or cages are easily accessed by the substrate pesticide in the buffered electrolyte solution, whereas the PEG and Nafion membranes operate as diffusion barriers which impose kinetic limitation and restrict access to the active sites of the enzyme, thus affecting the detection limit and the sensitivity of these sensors.

Our results, presented in Table 1, are comparable or better than AChE screen-printed electrodes described in the literature [28–32]. In all these previous cases, the enzyme was immobilized by glutaraldehyde, PVA, silica sol–gel or metal-chelate affinity and a considerable enzyme amount was loaded on each screen. Fig. 5 shows the inhibition of the three pesticides with AChE immobilized in the same matrix (alumina sol–gel) employing an incubation time of 10 min. The higher inhibition is obtained for chlorpyriphos-ethyl-oxon.

3.5. EIS measurements

In order to confirm the presence of enzyme onto the surface of sonogel, EIS measurements were performed. The impedance spectra were collected at 210 mV (vs. SCE) in a frequency range

Table 1
Comparison between the three pesticides, 0.2 M phosphate buffer, pH 7.0, applied potential: 210 mV, 1 mM acetylthiocholine

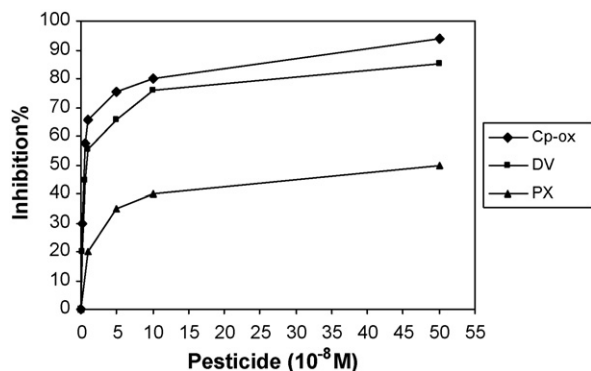| Pesticide	Limit of detection
Paraoxon (M)	7.5×10^{-9}
Dichlorvos (M)	5.0×10^{-10}
Chlorpyrifos-ethyl-oxon (M)	2.5×10^{-10}

Fig. 5. Inhibition curve of AChE immobilized in Al_2O_3 sol–gel matrix by paraoxon (Px), dichlorvos (DV) and chlorpyriphos-ethyl-oxon (Cp-ox), 10 min incubation. Measurement conditions: 0.2 M phosphate buffer, pH 7.0, applied potential: 210 mV, 1 mM acetylthiocholine substrate concentration.

from 100 kHz to 10 MHz with AC amplitude of 5 mV. Fig. 6A shows the Nyquist plot for the AChE-free modified sonogel-carbon electrode. If we use the Randles equivalent circuit model, the calculated (Voltamaster 4.0 software) charge transfer resistance R_{ct} and the double layer capacitance C_d are successively: 50 kΩ cm^2 and 6 μF cm^{-2}, respectively.

On the other hand, Fig. 6B also exhibits an arc-like Nyquist plot for the AChE/Al_2O_3/sonogel-carbon electrode system. The electrical parameters calculated were: R_{ct} = 38 kΩ cm^2 and C_d = 41.8 μF cm^{-2}. It appears clearly from these data that the capacitance at the interface increases when the AChE onto the sonogel-carbon electrode. The observed decrease of the charge transfer resistance means also that AChE/Al_2O_3/sonogel-carbon system favours the electron transfer reaction at the electrode surface.
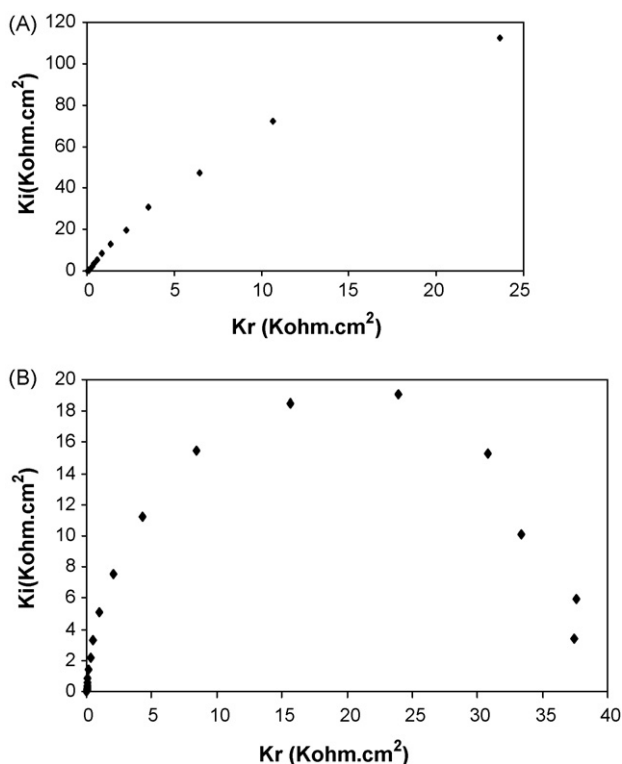
Fig. 6. Nyquist plot for (A) Al_2O_3/sonogel-carbon electrode and (B) AChE/Al_2O_3/sonogel-carbon electrode.
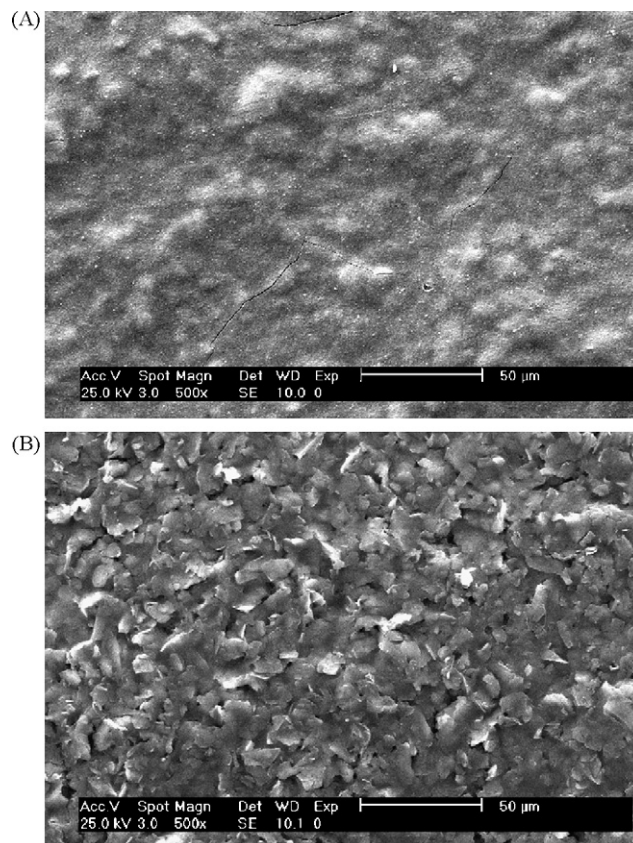
Fig. 7. Scanning electron micrograph of (A) Al_2O_3 sol–gel/sonogel-carbon electrode and (B) AChE/Al_2O_3 sol–gel/sonogel-carbon electrode, obtained at 25.0 kV with a 500× zoom.

3.6. SEM measurements

The results of morphological studies conducted on Al_2O_3/sonogel-carbon and AChE/Al_2O_3/sonogel-carbon are shown in Fig. 7A and B. The SEM of Al_2O_3/sonogel-carbon indicates that the film is uniform. The SEM of AChE/Al_2O_3/sonogel-carbon shows granular (porous) structure which confirms the presence of enzyme.

4. Conclusion

A new procedure to successfully immobilize acetylcholinesterase on a sonogel-carbon electrode is proposed. The enzyme is easily immobilized on the electrode surface employing Al_2O_3 and a simple sol–gel technology which requires minimal preparation time. The enzyme is well immobilized in sol–gel matrix, retains satisfactory enzymatic catalytic activities and the carbon provides the electric conductivity. The present study demonstrates that this simple encapsulation procedure for the development of electrochemical biosensors is highly sensitive to the pesticide studied. The developed biosensor showed quite stable and good responses towards substrate and inhibitors and could be applied to monitoring of other organophosphorous compounds.

Acknowledgement

References

[1] M. Fernandez, Y. Pico, S. Girotti, J. Manes, J. Agric. Food Chem. 49 (2001) 3540.
[2] A. Cappiello, G. Famiglini, P. Palma, F. Mangani, Anal. Chem. 74 (2002) 3547.
[3] P.M. Eline, H.M. Win, G.S. Peter, Environ. Sci. Technol. 29 (1995) 553.
[4] J.K. Lee, K.C. Ahn, D.W. Stoutamine, S.J. Gee, B.D. Hammock, J. Agric. Food Chem. 51 (2003) 3695.
[5] Y.J. Kim, Y.A. Cho, H.S. Lee, Y.T. Lee, B.D. Hammock, Anal. Chim. Acta 475 (2003) 65.
[6] K.R. Rogers, Y. Wang, A. Mulchandani, P. Mulchandani, W. Chen, Biotechnol. Prog. 15 (1999) 517.
[7] A.N. Ivanov, G.A. Evtugyn, R.E. Gyuresanyi, K. Toth, H.C. Budnikov, Anal. Chim. Acta 404 (2000) 55.
[8] M.D. Tsionsky, G.A. Rivas, Electroanalysis 12 (2000) 1159.
[9] L. Rabinovich, O. Lev, Electroanalysis 13 (2001) 265.
[10] J. Wang, Anal. Chim. Acta 399 (1999) 21.
[11] M.M. Collinson, A.R. Howells, Anal. Chem. 72 (2000) 702A.
[12] W. Jin, J.D. Bernnan, Anal. Chim. Acta 461 (2000) 1.
[13] L. He, C.S. Toh, Anal. Chim. Acta 556 (2006) 1.
[14] M.M. Cordero-Rando, J.L. Hidalgo-Hidalgo de Cisneros, E. Blanco, I. Naranjo-Rodríguez, Anal. Chem. 74 (2002) 2423.
[15] J.L. Hidalgo-Hidalgo de Cisneros, M.M. Cordero-Rando, I. Naranjo-Rodríguez, E. Blanco, L. Esquivias, Patent P200100556, Spain (March 2001).
[16] M.M. Cordero-Rando, I. Naranjo-Rodríguez, J.M. Palacios-Santander, L.M. Cubillana-Aguilera, J.L. Hidalgo-Hidalgo de Cisneros, Electronalysis 17 (2005) 806.
[17] H. Zejli, P. Sharrock, J.L. Hidalgo-Hidalgo de Cisneros, I. Naranjo Rodríguez, K.R. Temsamani, Talanta 68 (2005) 79.
[18] H. Zejli, P. Sharrock, J.L. Hidalgo-Hidalgo de Cisneros, I. Naranjo Rodríguez, K.R. Temsamani, Anal. Lett. 39 (2006) 1053.
[19] M. El Kaoutit, I. Naranjo-Rodriguez, K.R. Temsamani, J.L. Hidalgo-Hidalgo de Cisneros, Biosens. Bioelectron. 22 (2007) 2958.
[20] M. El Kaoutit, I. Naranjo-Rodriguez, K.R. Temsamani, M. Domínguez de la Vega, J.L. Hidalgo-Hidalgo de Cisneros, J. Agric. Food Chem. 55 (2007) 8011.
[21] M. El Kaoutit, I. Naranjo-Rodriguez, K.R. Temsamani, M. Domínguez de la Vega, J.L. Hidalgo-Hidalgo de Cisneros, J. Sol-Gel. Sci. Tech. 45 (2008) 57.
[22] H. Zejli, J.L. Hidalgo-Hidalgo de Cisneros, I. Naranjo-Rodriguez, B. Liu, K.R. Temsamani, J.L. Marty, Anal. Chim. Acta 612 (2008) 198.
[23] V.A. Pedrosa, J. Caetano, S.A.S. Machado, R.S. Freire, M. Bertotti, Electroanalysis 23 (2007) 130.
[24] D. Du, S. Chen, J. Cai, A. Zhang, Biosens. Bioelectron. 19 (2007) 1415.
[25] B. Bucur, S. Andreescu, J.L. Marty, Anal. Lett. 37 (2004) 1571.
[26] Z.J. Liu, B.H. Liu, J.L. Kong, J.Q. Deng, Anal. Chem. 72 (2000) 4707.
[27] S. Andreescu, A. Avramescu, C. Bala, V. Magearu, J.L. Marty, Anal. Bioanal. Chem. 374 (2002) 39.
[28] Y.G. Li, Y.X. Zhou, J.H. Jiang, L.R. Ma, Anal. Chim. Acta 382 (1999) 277.
[29] L. Hart, W.A. Collier, D. Janssen, Biosens. Bioelectron. 7 (1997) 645.
[30] M. Albareda-Sirvent, A. Merkoci, S. Alegret, Anal. Chim. (2001) 442.
[31] S. Andreescu, L. Barthelmebs, J.L. Marty, Anal. Chim. Acta 171 (2002) 180.
[32] G.S. Nunes, G. Jeanty, J.L. Marty, Anal. Chim. Acta 523 (2004) 107.

Sensitive voltammetric determination of rutin at an ionic liquid modified carbon paste electrode

Ya Zhang [a,b], Jianbin Zheng [a,*]

[a] *Institute of Analytical Science/Shaanxi Provincial Key Lab of Electroanalytical Chemistry, Northwest University, Xi'an, Shaanxi 710069, China*
[b] *Department of Chemistry and Chemical Engineering, Yulin College, Yulin, Shaanxi 719000, China*

ARTICLE INFO

ABSTRACT

An ionic liquid modified carbon paste electrode (IL/CPE) had been fabricated by using hydrophilic ionic liquid 1-amyl-3-methylimidazolium bromide ([AMIM]Br) as a modifier. The IL/CPE was characterized by scanning electron microscope and voltammetry. Electrochemical behavior of rutin at the IL/CPE had been investigated in pH 3.29 Britton–Robinson (B–R) buffer solution by cyclic voltammetry (CV) and square wave voltammetry (SWV). The experimental results suggested that the modified electrode exhibited an electrocatalytic activity toward the redox of rutin. The electron transfer coefficient (α) and the standard rate constant (k_s) of rutin at the modified electrode were calculated. Under the selected conditions, the reduction peak current was linearly dependent on the concentration of rutin in the range of 4.0×10^{-8} to 1.0×10^{-5} mol L^{-1} ($r = 0.9998$), with a detection limit of 1.0×10^{-8} mol L^{-1} (S/N = 3). The relative standard deviation (R.S.D.) for six times successful determination of 8.0×10^{-7} mol L^{-1} rutin was 1.2%. The proposed method was applied to determine rutin in tablet and urine sample. In addition, the IL/CPE exhibited a distinct advantage of simple preparation, surface renewal, good reproducibility and good stability.

© 2008 Elsevier B.V. All rights reserved.

1. Introduction

Ionic liquids (ILs) are ionic compounds consisting of organic cations and various kinds of anions, which are liquids at ambient or even far below ambient temperature. ILs have many specific physicochemical properties such as high chemical and thermal stability, good ionic conductivity, negligible vapor pressure and wider electrochemical windows [1,2]. They have been widely used in the field of electrochemistry [3], organic synthesis [4], material science [5], liquid–liquid extraction processes [6,7] and biocatalysis [8–10]. There are a lot of reports on the use of ILs for electrode preparation. Some of them are concerned with deposition of ionic liquid on electrode surface during the oxidation of neutral organic liquid microdroplets [11]. Others are concerned with using composite material such as Nafion–IL composite film [12], gel containing ILs and multiwalled carbon nanotubes [3], polymer/ILs [13] or molecular films of ILs [14,15] to fabricate modified electrode. The electrochemistry of small molecules such as nitrite, nitric oxide, uric acid, chlorpromazine and dopamine had been investigated on the IL composite film modified electrode [3,16–18]. A carbon composite electrode by using hydrophobic RTILs as a new binder was fabricated by

Makeli et al. [19], which provided a remarkable increase in the rate of electron transfer and decreased the overpotentials of some organic substances. The electrooxidation processes of some phenolic compounds were further investigated on this kind of IL modified electrode [20–22]. Sun et al. also demonstrated that carbon ionic liquid electrode had some specific characteristics and the direct electrochemistry of Hb was successfully studied on the surface of carbon ionic liquid electrode [23,24]. To our knowledge, there was no report about the fabrication of chemical modified carbon paste electrode by using hydrophilic ionic liquid [AMIM]Br as a modifier.

Rutin is a kind of flavonoid glycoside, called as vitamin P. Rutin has been shown to act as a scavenger of various oxidizing species, i.e. superoxide anion ($O_2{}^-$), hydroxyl radical and peroxyl radicals. As a result of these biological effects, its several pharmacological activities have been widely exploited including antibacterial, antiinflammatory, antitumor, antiallergic, antiviral and antiprotozoal properties [25–28]. Hence, the quantification of rutin is of considerable interest. Some analytical methods, including capillary electrophoresis [29], adsorptive stripping voltammetry [30], chemiluminescence [31], HPLC [32], sequential injection analysis [33], spectrophotometry [34] and sensor [28,35] have been applied to determine rutin.

In the present work, an IL/CPE had been fabricated by using [AMIM]Br as a modifier. The IL/CPE was characterized by scanning electron microscopy and voltammetry. The electrochemical behavior of rutin at the IL/CPE was investigated in detail by CV and SWV.

---

* Corresponding author. Tel.: +86 29 88302077; fax: +86 29 88303448.
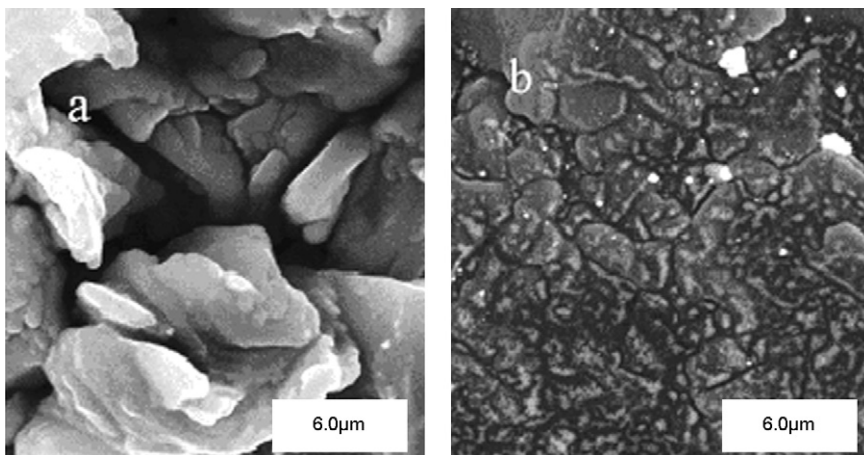*E-mail address:* Zhengjb@nwu.edu.cn (J. Zheng).

Fig. 1. SEM images of (a) CPE and (b) IL/CPE.

The α and the k_s of rutin at the modified electrode were calculated. In addition, a novel method for the determination of rutin with simple, sensitive and rapid characteristics was developed.

2. Experimental

2.1. Reagents and solution

Amyl bromide (Shanghai Shiyan Reagent Corporation, Shanghai, China) and ethyl acetate (Tianjin Chemical Reagent Corporation, Tianjin, China) were of analytical reagent grade. The purity of 1-methylimidazole was 99% (w/w%, Kaile Chemical Reagent Factory, Zhejiang, China). High purity graphite powder (Shanghai Carbon Plant, Shanghai, China) and paraffin liquid (AR, Kermel Center of Chemical Reagent, Tianjin, China) were used without further treatment. All other chemicals were analytical grade. Ionic liquid [AMIM]Br was prepared following the procedures described in literature [36].

All solutions were prepared with ultrapure water obtained from a Milli-Q water purification system. B–R buffer solutions with various pH values were used as supporting electrolytes. Rutin was purchased from Sigma and a 5.0×10^{-4} mol L^{-1} stock solution was dissolved in 10% (v/v) ethanol and prepared in pH 3.29 B–R buffer solution. Other solutions were prepared from the stock solution by appropriated dilutions with the same buffer solution.

2.2. Apparatus

CV and SWV experiments were performed on a CHI660A electrochemical workstation (Shanghai Chenhua Co., China) controlled by a microcomputer with CHI660 software. A three-electrode system was used, where a saturated calomel electrode (SCE) served as the reference electrode, a platinum wire electrode served as the auxiliary electrode and an IL/CPE or a CPE served as the working electrode. All the following potentials reported in this work were versus the SCE. DL-180 ultrasonic apparatus (Haitian Electronic Apparatus Company, Zhejiang, China) was applied in ultrasonic experiment. The surface morphologies of the prepared electrodes were observed through SEM on JEOL JSM-6700F at an accelerating voltage of 20 kV.

2.3. Electrode preparation

Firstly, a mixture of [AMIM]Br and paraffin liquid in varying volume ratio (v/v) was ultrasonically dispersed for 5 min, then 0.5 mL of the mixture was mixed by hand with 1.0 g graphite powder to form a homogeneous carbon paste. This ionic liquid modified carbon paste was tightly packed into a cavity (3.0 mm diameter) of a PVC tube and the electrical contact was established via a copper steel handle. The resulting electrode was recorded as IL/CPE. The preparation process of CPE was similar to that of the IL/CPE but a replacement of the mixture with paraffin liquid. Prior to use, the surface of the well-prepared electrode was smoothed with a weighing paper.

3. Results and discussion

3.1. Characterization of the IL/CPE

Fig. 1 compared the morphological features of CPE and the IL/CPE using SEM. The CPE was characterized by a surface formed by irregularly shaped flakes of graphite that were isolated and each layer could be clearly distinguished (Fig. 1a). The SEM image of IL/CPE became more uniform and no separated carbon layers could be observed, showing the good adherence of [AMIM]Br to graphite due to its high viscosity (Fig. 1b).

Potassium ferricyanide was selected as a probe to evaluate the performance of the CPE and the IL/CPE. Fig. 2 showed electrochemical responses of the CPE and the IL/CPE in 6.0×10^{-4} mol L^{-1} K$_3$[Fe(CN)$_6$] + 0.1 mol L^{-1} KCl solution, respectively. At the CPE, the peak-to-peak potential separation (ΔE_p) was 0.240 V, correspond-

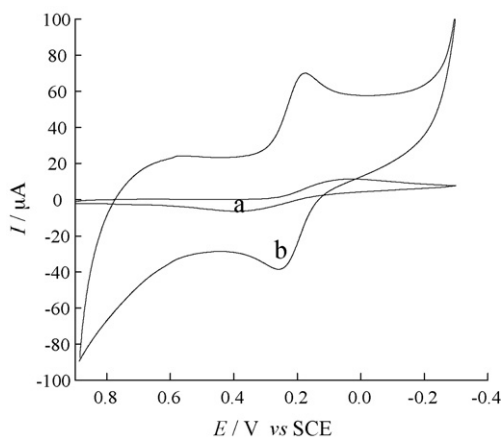**Fig. 2.** CV curves of (a) CPE and (b) IL/CPE in 6.0×10^{-4} mol L^{-1} K$_3$[Fe(CN)$_6$] +0.1 mol L^{-1} KCl solution, scan rate 0.1 V s^{-1}.
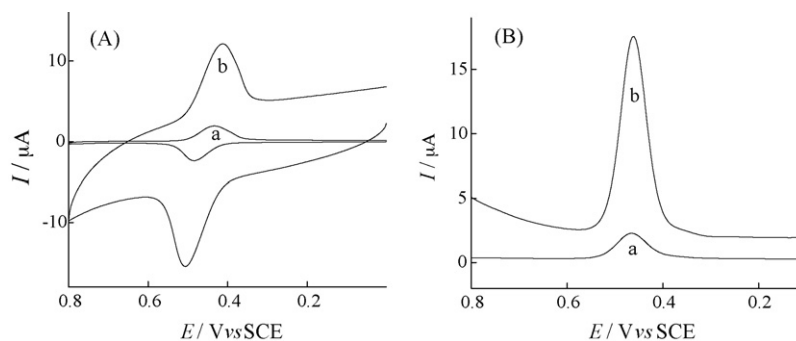
Fig. 3. CV (A) and SWV (B) curves of 5.0×10^{-6} mol L^{-1} rutin in pH 3.29 B–R buffer solution at (a) CPE and (b) IL/CPE. In (A) scan rate 0.15 V s^{-1} and in (B) amplitude 0.035 V, frequency 15 Hz, quiet time 120 s.

ing to an irreversible electron transfer process (Fig. 2a). While at the IL/CPE, the ΔE_p was decreased to 0.082 V, indicating a quasi-reversible electron transfer process. Furthermore, the peak currents of K_3 [Fe(CN)$_6$] at the IL/CPE were much bigger than that at the CPE. Above experimental results showed the superiority of IL/CPE to CPE in terms of improving reversibility and enhancing sensitivity. All these were attributed to the use of ILs as a modifier. Therefore, ILs played an important role in improving the electrochemical performance of the IL/CPE.

3.2. Voltammetric behavior of rutin at the IL/CPE

Fig. 3 showed electrochemical responses of an IL/CPE and a CPE in 5.0×10^{-6} mol L^{-1} rutin + B–R solution (pH 3.29), respectively.

At the CPE and the IL/CPE, rutin showed a pair of redox peaks (Fig. 3A), with oxidation peak potential (E_{pa}) of 0.502 V and reduction peak potential (E_{pc}) of 0.447 V. However, the peak current of rutin at the IL/CPE was much larger than that at the CPE, it was about 9.1 times of that at the CPE by SWV (Fig. 3B). Thus, the modified electrode exhibited an electrocatalytic activity toward the redox of rutin. This result further testified the superiority of IL/CPE to CPE, indicating the use of ILs as a modifier facilitated the electron transfer between rutin and electrode.

3.3. Influence of rutin concentration and potential scan rate

The changes of the peak current with the variety of rutin concentration were investigated by CV. Fig. 4 exhibited the effect of the concentration of rutin on I_{pc}/c, showing that I_{pc}/c was reduced rapidly with the increase of rutin concentration, and then gradually tended to the stable value. This confirmed that the electrode process was transferred from adsorption-controlled mode to diffusion-controlled mode [37].
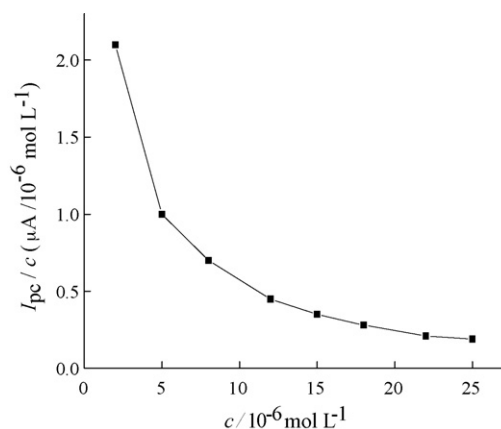

Fig. 4. Effect of the concentration of rutin on I_{pc}/c in 0.1 mol L^{-1} B–R buffer solution (pH 3.29) at scan rate of 0.15 V s^{-1} and quiet time of 120 s.

The influence of potential scan rate (v) on I_p of 5.0×10^{-6} mol L^{-1} rutin at the IL/CPE was studied by CV at various sweep rates. As shown in Fig. 5A, the peak currents of rutin grow with the increasing of scan rates and there are good linear relationships between the peak currents and v (Fig. 5B). The regression equation is $I_{pc} = 0.931 + 45.23v$ (I_{pc}: μA, v: V s^{-1}, $r = 0.9981$); $I_{pa} = -0.649 - 53.41v$ (I_{pa}: μA, v: V s^{-1}, $r = 0.9994$), indicating the redox process of 5.0×10^{-6} mol L^{-1} rutin at the IL/CPE was adsorption-controlled. A further evidence of the adsorption of rutin at the surface of the IL/CPE is the restraint effect of surfactant on the peak current because competitive adsorption would happen at the surface of electrode [38]. In 0.1 mol L^{-1} B–R (pH 3.29) solution containing 5.0×10^{-6} mol L^{-1} rutin, a small quantity of polyvinyl alcohol, diphenylguanidine, sodium dodecyl sulfonate, hexadecyl

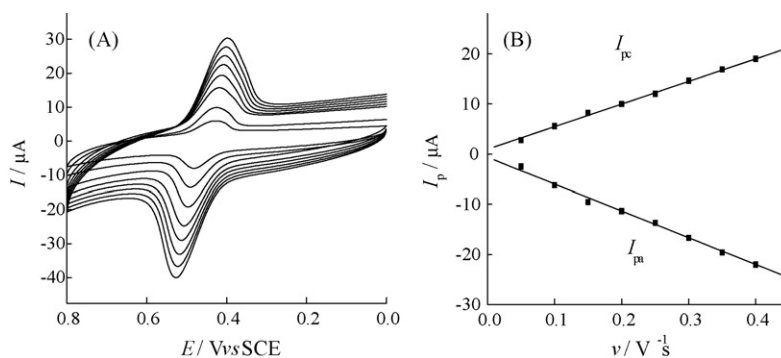**Fig. 5.** CV curves (A) and linear relationship of I_p vs. v (B) of 5.0×10^{-6} mol L^{-1} rutin in pH 3.29 B–R buffer solution at IL/CEP. Scan rate (inner to outer): 0.05, 0.10, 0.15, 0.20, 0.25, 0.30, 0.35, 0.40 V s^{-1}.
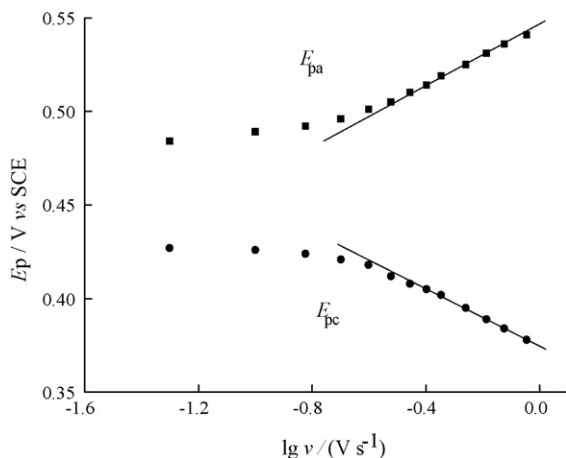
Fig. 6. Relationship between E_p and logarithm of potential scan rate.

pyridine bromide, cetyl trimethyl ammonium bromide, were added into the solution, respectively. As expected for an adsorption-controlled process, all these surfactants decreased the peak current of rutin in different degree. According to the above results, it could be deduced reasonably that rutin was firstly adsorbed on the surface of the electrode and then the electrode reaction was followed.

The influence of v on the peak potentials of rutin was also investigated. With the increase of v the oxidation peak potential was positively shifted and the reduction peak potential was negatively shifted, indicating that the redox reversibility of rutin was impaired. According to above results, the electron transfer kinetics of rutin at the IL/CEP can be obtained by using the approach developed by Laviron [39], when the ΔE_p is higher than 0.200 V/n, the relationship between the peak potential E_p and the scan rate can be expressed in Eq. (1):

$$E_p = f(\lg \upsilon) \tag{1}$$

Fig. 6 provided the variations of peak potentials with the logarithm of the scan rate at the IL/CEP.

At higher scan rates, the peak potentials and log v show linear relationships with the slope of -0.05086 for cathodic peak and 0.07012 for anodic peak, respectively. The number of electrons involved in the electrode reaction of rutin was 2 [40,41]. For cathode peak, the slope value is $-2.3RT/\alpha nF$, and for anode peak, the slope value is $2.3RT/(1-\alpha)nF$. So the electron transfer coefficient α was calculated to be 0.46. And k_s, the electron transfer rate constant of reaction, is expressed in Eq. (2):

$$\lg \; k_s = \alpha \; \lg(1-\alpha) + (1-\alpha)\lg \; \alpha - \lg\left(\frac{RT}{nFv}\right) - \left(\frac{\alpha(1-\alpha)nF\Delta E_p}{2.3RT}\right) \tag{2}$$

where α is the electron transfer coefficient, n is the number of electrons involved in the reaction and ΔE_p is the peak-to-peak potential separation. The resulting value of k_s is 3.5 (R.S.D. 1.8%).

3.4. Influence of the ratio of IL and paraffin liquid

As mentioned above, [AMIM]Br is a hydrophilic ionic liquid, it cannot be directly used as a binder. However, the mixture of [AMIM]Br and liquid paraffin with appropriate ratio could be used as binder. The volume ratio (v/v) of [AMIM]Br/liquid paraffin showed obvious influence on the stability and sensitivity of the modified electrode. When enhancing the ratio from 1/6 to 2/3, the peak current of rutin increased and peak shape unchanged. When the ratio exceeded 2/3, the peak current tended to be unstable and

the background current remarkably increased. In a same rutin solution the maximum and steadiest current was observed at the ratio of 2/3. So, the volume ratio of [AMIM]Br/paraffin was fixed at 2/3 in this work.

3.5. Influence of supporting electrolyte and pH

The types of supporting electrolytes played a key role in the voltammetric responses of rutin. The current responses of 8.0×10^{-6} mol L^{-1} rutin were estimated in different supporting electrolytes such as Na$_2$HPO$_4$–KH$_2$PO$_4$, NaAc–HAc, sodium citrate–HCl, tartaric acid–sodium tartrate and B–R buffer solution. The results showed that higher peak current and better peak shape could be obtained in B–R buffer solution. Therefore, B–R buffer solution was adopted.

The effect of pH of B–R buffer solution, which ranged from 3.29 to 9.06, on the response of 8.0×10^{-6} mol L^{-1} rutin was investigated. The reduction peak potential of rutin was found to be dependent on pH and linear shifted to negative potential with the increase of pH. The linear relationship between E_{pc} and the pH was $E_{pc} = 0.61 - 0.051$ pH ($r = 0.9982$), a slope of -0.051 V/pH for rutin reduction indicating that the number of electrons and protons involved in the reaction mechanisms was the same. Thus, the electrode process of rutin reduction was a two-electrons with two-protons process. It was also found that the I_{pc} of rutin decreased gradually with the increase of pH value. This further indicated that proton took part in the electrochemical reaction of rutin. Therefore, pH 3.29 was chosen for the determination of rutin.

3.6. Influence of accumulation time, potential and SWV parameters

For consideration of the adsorption of rutin on the IL/CPE surface, SWV technique coupled with accumulation procedure was used for study. With an increase in accumulation time, the peak current increased. When accumulation time was above 120 s, peak current achieved a maximum value. So 120 s was chosen as the accumulation time. The accumulation potential had little effect on the peak current of 8.0×10^{-6} mol L^{-1} rutin in the range from 1.1 to +0.8 V. To reduce scanning time, 0.8 V was selected as the accumulation potential.

The influence of the square wave parameters such as amplitude and frequency on the I_{pc} was also investigated. The peak current increased with the increasing of square wave amplitude from 0.005 to 0.075 V or square wave frequency in the range of 5–55 Hz, but the peak potential shifted to less negative values and the peak changed unshapely. So 0.035 V was chosen as the optimum amplitude and 15 Hz was chosen as the optimum frequency.

4. Determination of rutin

4.1. Calibration curves, stability and repeatability

Fig. 7 presented SWV curves of six different concentrations of rutin at IL/CPE under the optimum conditions.

A linear relationship could be established between I_{pc} and the concentration of rutin in the range of 4.0×10^{-8} to 1.0×10^{-5} mol L^{-1}. The linear regression equation was $I_{pc} = 3.251 \times 10^6$ $c + 0.0733$, $r = 0.9984$, where I_{pc} was the reduction peak current in μA and c was the rutin concentration in mol L^{-1}, the detection limit of rutin was found to be 1.0×10^{-8} mol L^{-1} (S/N = 3).

To estimate the stability of the proposed electrode, the R.S.D. of six times successful measurement the peak current of 8.0×10^{-7} mol L^{-1} rutin at an IL/CPE was calculated to be 1.2%, which demonstrated the good stability of the proposed electrode.

Table 1
Comparison of different modified electrodes for rutin determination

Electrode	Line range (mol L^{-1})	Detection limit (mol L^{-1})	Reference
MWNTs/β–CD/GCE	4.0×10^{-7} to 1.0×10^{-3}	2.0×10^{-7}	[28]
gilo/Chi/epichlorohydrin/GCE	3.4×10^{-7} to 7.2×10^{-6}	2.0×10^{-8}	[35]
SWNTs/Au	2.0×10^{-8} to 5.0×10^{-6}	1.0×10^{-8}	[42]
MCNTPE	1.0×10^{-7} to 1.0×10^{-5}	4.0×10^{-8}	[41]
IL/CPE	4.0×10^{-8} to 1.0×10^{-5}	1.0×10^{-8}	This paper

MWNTs: multi-walled carbon nanotubes; β–CD: β-cyclodextrin; Chi: chitosan; SWNTs: single-walled carbon nanotubes; MCNTPE: multi-wall carbon nanotubes paste electrode.

Table 2
Determination of rutin in tablets[a] and urine sample by SWV

Sample	Content[b] (mg/tablet)	Added in tablet sample (10^{-1} mg L^{-1})	Found in tablet sample (10^{-1} mg L^{-1})	Average recovery (%)	Added in urine sample (10^{-6} mol L^{-1})	Found in urine sample (10^{-6} mol L^{-1})	Average recovery (%)
1	19.6 ± 0.2	1.22	1.18 ± 0.04	96.7	0.50	0.48 ± 0.01	96.0
2	20.4 ± 0.4	2.46	2.52 ± 0.06	102.4	1.20	1.18 ± 0.03	98.3
3	19.3 ± 0.3	3.64	3.59 ± 0.08	98.6	1.50	1.48 ± 0.05	98.7
4	20.5 ± 0.5	4.86	4.72 ± 0.11	97.1	3.50	3.52 ± 0.09	100.6
5	19.8 ± 0.4	6.10	6.29 ± 0.13	103.1	5.00	5.11 ± 0.12	102.2

[a] Label amount: 20 mg/tablet.
[b] Mean value ± standard deviation ($n = 5$).

The electrode-to-electrode reproducibility of the SWV method was examined on six IL/CPEs constructed individually; the R.S.D. of the six average peak current of 8.0×10^{-7} mol L^{-1} rutin was calculated to be 2.7%.

The proposed IL/CPE for rutin determination was compared with other kinds of modified electrode and the results were listed in Table 1. It can be seen that this method can provide comparable linear range and detection limit with a simple electrode preparation procedure.

4.2. Interferences study

In some cases, the interference of foreign compounds can be overcome by using the reduction peak for determination. The effects of inorganic ions and organic compounds commonly existed in pharmaceuticals and biological samples on the determination of 8.0×10^{-7} mol L^{-1} rutin was studied. The tolerance limit was defined as the concentration ratio of additive/rutin causing less than ±5.0% relative error. The tolerance limit of additives to 8.0×10^{-7} mol L^{-1} rutin was 150 times for citrate, carbonate, ascor-

bic acid, saccharose, glucose, fructose, 100 times of Ca^{2+}, Fe^{3+}, Cu^{2+}, Na^+, K^+, $CO_3{}^{2-}$, $PO_4{}^{3-}$, Cl^-, $NO_3{}^-$, 50-fold of lactic acid, urea, thein, glucose, starch, sucrose, 5 times for dopamine and 3 times for epinephrine.

4.3. Determination of rutin in rutin tablets and urine samples

Ten rutin tablets (label amount: 20 mg/tablet) were weighed then grinded to a fine powder and mixed adequately. The sample solutions were prepared by accurately weighing a certain amount of the powder and dissolving it in ethanol with the aid of ultrasonic agitation and then diluted with buffer solution. The determination of rutin was conducted by the proposed method. As shown in Table 2, the results obtained by the proposed method were in good agreement with label amount. The recovery of the proposed method was also conducted to evaluate the accuracy of the method, and the results were also listed in Table 2. From Table 2, the recovery of five independent experiments varied from 96.7 to 103.1%, demonstrating the accuracy of the proposed method.

As a preliminary evaluation of the validity of the proposed electrode, the recovery of rutin in urine samples was testified. Varying amounts of rutin standard solutions were added to the diluted (50-fold) urine samples and the results were also listed in Table 2. The recovery results showed that the IL/CPE could be used for the determination of rutin in urine samples.

5. Conclusion

An IL/CPE, using hydrophilic [AMIM]Br as modifier, had been fabricated and characterized by SEM and voltammetry. The electrochemical behavior of rutin at the modified electrode was investigated in pH 3.29 B–R buffer solution. Compared with its response at CPE, the electrochemical sensitivity of rutin at the proposed electrode was improved dramatically, revealing some advantages of IL/CPE over CPE such as high conductivity and fast electron transfer. Under the optimized conditions, a sensitive and simple method for the determination of rutin was established and it had been successfully applied to the determination of rutin in tablets and urine samples. In addition, the modified electrode exhibited a distinct advantage of simple preparation, surface renewal, good reproducibility and good stability.
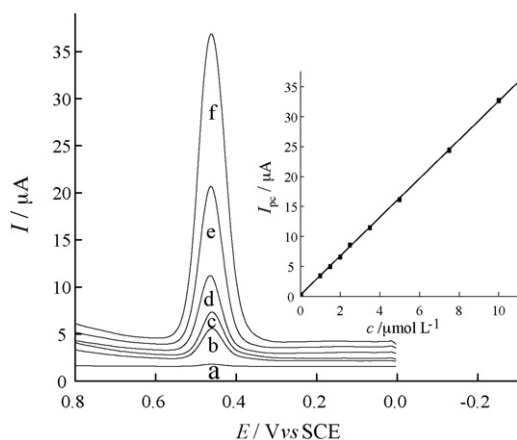

Fig. 7. SWV curves of different concentrations of rutin in pH 3.29 B–R buffer solution at IL/CPE: (a) 4; (b) 100; (c) 150; (d) 250; (e) 500; (f) 1000×10^{-8} mol L^{-1}. Amplitude 0.035 V, frequency 15 Hz and accumulation time 120 s. *Insert*: curves of I_p vs. rutin concentration.

Acknowledgments

References

[1] M.C. Buzzeo, C. Hardace, R.G. Compton, Anal. Chem. 76 (2004) 4583.
[2] Z. Li, H. Liu, Y. Liu, P. He, H. Li, J.H. Li, Langmuir 20 (2004) 10260.
[3] Z. Zhao, Y. Gao, D. Zhan, H. Liu, O. Zhao, Y. Kou, Y. Shao, M. Li, Q. Zhuang, Z. Zhu, Talanta 66 (2005) 51.
[4] K.S. Kim, D. Demberelnyamba, H. Lee, Langmuir 20 (2004) 556.
[5] Y. Zhou, M. Antonietti, J. Am. Chem. Soc. 125 (2003) 1490.
[6] K. Shimojo, M. Goto, Anal. Chem. 76 (2004) 5039.
[7] H. Luo, S. Dai, P.V. Bonnesen, A.C. Brchanan, J.D. Holbrey, N.J. Bridges, R.D. Rogers, Anal. Chem. 76 (2004) 3078.
[8] M.B. Turner, S.K. Spear, J.D. Holbrey, R.D. Rogers, Biomacromolecules 5 (2004) 1379.
[9] J.A. Laszlo, D.L. Compton, J. Mol. Catal. B: Enzyme 18 (2002) 109.
[10] H. Huang, N.F. Hu, Y.H. Zeng, G. Zhou, Anal. Biochem. 308 (2002) 141.
[11] F. Marken, R.D. Webster, S.D. Bull, S.G. Davies, J. Electroanal. Chem. 437 (1997) 209.
[12] H.J. Chen, Y.L. Wang, Y. Liu, Y.Z. Wang, L. Qi, S.J. Dong, Electrochem. Commun. 9 (2007) 469.
[13] X.B. Lu, J.Q. Hu, X. Yao, Z.P. Wang, J.H. Li, Biomacromolecules 7 (2006) 975.
[14] J.D. Wadhawan, U. Schröder, A. Neudeck, S.J. Wilkins, R.G. Compton, F. Marken, C.S. Consorti, R.F. de Souza, J. Dupont, J. Electroanal. Chem. 493 (2000) 75.
[15] P. Yu, Y.Q. Lin, L. Xiang, L. Su, J. Zhang, L.Q. Mao, Langmuir 21 (2005) 9000.
[16] H. Liu, P. He, Z. Li, C. Sun, L.J. Shi, Y. Liu, G.Y. Zhu, J.H. Li, Electrochem. Commun. 7 (2005) 1357.
[17] C.M. Li, J.F. Zang, D.P. Zhan, W. Chen, C.Q. Sun, A.L. Teo, Y.T. Chua, V.S. Lee, S.M. Moochhala, Electroanalysis 18 (2006) 713.
[18] Q.P. Yan, F.Q. Zhao, G.Z. Li, B.Z. Zeng, Electroanalysis 18 (2006) 1075.
[19] N. Maleki, A. Safavi, F. Tajabadi, Anal. Chem. 78 (2006) 3820.
[20] A. Safavi, N. Maleki, O. Moradlou, F. Tajabadi, Anal. Biochem. 359 (2006) 224.
[21] A. Safavi, N. Maleki, F. Tajabadi, Analyst 132 (2007) 54.
[22] Y. Zhang, J.B. Zheng, Electrochim. Acta 52 (2007) 7210.
[23] W. Sun, D.D. Wang, R.F. Gao, K. Jiao, Electrochem. Commun. 9 (2007) 1159.
[24] W. Sun, R.F. Gao, K. Jiao, J. Phys. Chem. B 35 (2007) 567.
[25] R.M. Gene, C. Cartana, T. Adzet, E. Marin, T. Panella, S. Canigueral, Planta Med. 62 (1996) 232.
[26] R. Ramanathan, W.P. Das, C.H. Tan, Int. J. Oncol. 3 (1993) 115.
[27] A. Hasan, I. Ahmad, Fetoterapia 67 (1996) 182.
[28] J.L. He, Y. Yang, X. Yang, Y.L. Liu, Z.H. Liu, G.L. Shen, R.Q. Yu, Sens. Actuators B 114 (2006) 94.
[29] G. Chen, J.X. Zhang, J.N. Ye, J. Chromatogr. A 923 (2001) 255.
[30] G.J. Volikakis, C.E. Efstathiou, Talanta 51 (2000) 775.
[31] Z.H. Song, S. Hou, Talanta 57 (2002) 59.
[32] K. Ishii, T. Furuta, Y. Kasuya, J. Chromatogr. B 759 (2001) 161.
[33] Z. Legnerova, D. Satinsky, P. Solich, Anal. Chim. Acta 497 (2003) 165.
[34] H.N.A. Hassan, B.N. Barsoum, I.H.I. Habib, J. Pharm. Biomed. Anal. 20 (1999) 315.
[35] I.R.W.Z. de Oliveira, S.C. Fernandes, I.C. Vieira, J. Pharm. Biomed. Anal. 41 (2006) 366.
[36] J.G. Huddleston, A.E. Visser, W.M. Reichert, H.D. Willauer, G.A. Broker, R.D. Rogers, Green Chem. 3 (2001) 156.
[37] Y.H. Zeng, Y.L. Zhou, Chin. J. Ana1. Chem. 27 (1999) 832.
[38] A.P. dos Reis, C.R.T. Tarley, N. Maniasso, L.T. Kubota, Talanta 67 (2005) 829.
[39] E. Laviron, J. Electroanal. Chem. 101 (1979) 19.
[40] I.R.W. Zwirtes de Oliveira, S.C. Fernandes, I.C. Vieira, J. Pharm. Biomed. Anal. 41 (2006) 366.
[41] X.Q. Lin, J.B. He, Z.G. Zha, Sens. Actuators B 119 (2006) 608.
[42] B.Z. Zeng, S.H. Wei, F. Xiao, F.Q. Zhao, Sens. Actuators B 115 (2006) 240.

Amperometric sulfite sensor based on multiwalled carbon nanotubes/ferrocene-branched chitosan composites

Hong Zhou, Weiwei Yang, Changqing Sun[*]

College of Chemistry, Jilin University, Changchun 130012, PR China

ABSTRACT

A novel amperometric sensor for the determination of sulfite was fabricated based on multiwalled carbon nanotubes (MWCNTs)/ferrocene-branched chitosan (CHIT-Fc) composites-covered glassy carbon electrode (GCE). The electrochemical behavior of the sensor was investigated in detail by cyclic voltammetry. The apparent surface electron transfer rate constant (K_s) and charge transfer coefficient (α) of the CHIT-Fc/MWCNTs/GCE were also determined by cyclic voltammetry, which were about $1.93\,cm\,s^{-1}$ and 0.42, respectively. The sensor displayed good electrocatalytic activity towards the oxidation of sulfite. The peak potential for the oxidation of sulfite was lowered by at least 330 mV compared with that obtained at CHIT/MWCNTs/GCE. In optimal conditions, linear range spans the concentration of sulfite from 5 μM to 1.5 mM and the detection limit was 2.8 μM at a signal-to-noise ratio of 3. The proposed method was used for the determination of sulfite in boiler water. In addition, the sensor has good stability and reproducibility.

© 2008 Elsevier B.V. All rights reserved.

1. Introduction

As is known, sulfite is a typical example of sulfur oxoanions. The main interest in sulfite lies in its reducing properties. Along with ascorbate, they are well established and play an important part in the anti-oxidant defence. Generally, sulfite is widely used as an additive in food and beverages to prevent oxidation and bacterial growth and to control enzymatic reactions during production and storage. Despite these great advantages, the sulfite content in food and beverages should be strictly limited due to its potential toxicity and harmful effects towards hypersensitive people [1]. Therefore, it is important to develop a rapid, reliable and sensitive detection method for determination of sulfite for food and beverages industry in order to control product quality. In the past decade, the reported analytical methods for sulfite determination include mainly spectrophotometry [2,3], chromatography [4,5], electrochemical methods [6–14] and biosensors [15–17].

Carbon nanotubes (CNTs) have been intensively investigated since Iijima's discovery [18] due to their unique electrical, mechanical and structural properties. As electrode materials, one promising application of carbon nanotubes involves their use in the construction of biosensors and chemical sensors. CNTs represent a new kind of carbon-based material and are superior to other kinds of carbon materials commonly used in electrochemistry, such as glassy car-

bon, graphite and diamond, mainly in the special structural features and unique electronic properties [19]. Such potential applications would greatly benefit from the ability that the CNTs exhibit a high ability to promote some type of the electron transfer reactions between electroactive species and electrodes, minimize fouling of electrode surfaces, enhance electrocatalytic activity, and facilitate the immobilization of molecules such as enzymes or antibodies on their surface with a view to developing biosensors [20]. Recent electrochemical studies revealed that the unique properties of the CNTs make them very promising in electrochemical application, for example, for protein electrochemistry [21–24], development of novel electrochemical sensors and biosensors [25–29].

Chitosan is a linear β-1,4-linked polysaccharide (similar to cellulose) that is obtained by the partial deacetylation of chitin [30]. Because chitosan containing abundant amino groups with pK_a 6.3 is soluble in slightly acidic solution due to the protonation and insoluble in solution above pH 6.3 for the deprotonation, it exhibits robust film-forming ability. In addition, chitosan displays nontoxicity, biocompatibility, cheapness and a susceptibility to chemical modification. Because of its desirable properties, chitosan has been widely used as an immobilization matrix for biosensors and bioreactors. Recently, our research group has successfully synthesized ferrocene-branched chitosan derivatives (CHIT-Fc) and reagentless enzyme-based biosensors had been fabricated by the redox polymer [31].

The redox polymers have been used for mediated electron transfer in biosensors since they were reported by Heller's and Calvo's groups [32,33]. Recently, Gorski and Schmicltke reported

* Corresponding author.
E-mail address: sunchq@mail.jlu.edu.cn (C. Sun).

a new electrode system that utilized synergy between carbon nanotubes and redox mediators, and their results suggested that the integration of redox and carbon nanotubes in a polymeric matrix was able to provide a remarkable synergistic augmentation of sensor performance [27,29,34]. In the present work, a novel amperometric sulfite sensor was prepared by using multiwalled carbon nanotubes/ferrocene-branched chitosan composites-covered glassy carbon electrode. The integration of CHIT-Fc and MWCNTs for the development of electrochemical sulfite sensor has not been explored thus far. The electrochemical behavior and electrocatalytic activity towards the oxidation of sulfite for the sensor were studied in detail. Due to the excellent electrocatalytic ability of CHIT-Fc and the unique physiochemical properties of MWCNTs and especially the synergistic augmentation of MWCNTs and CHIT-Fc, the sensor showed very good performance characteristics towards electrocatalytic determination of sulfite.

2. Experimental

2.1. Apparatus

Electrochemical measurements were performed with a CHI 660A electrochemical workstation (CH Instruments, USA). Three-electrode systems were employed in this study. A platinum wire and a saturated calomel electrode (SCE) were used as auxiliary and reference electrode, respectively. All potentials were referred to the latter. CHIT-Fc/MWCNTs composites electrode employed as working electrode was prepared in our laboratory according to the procedure described below. A magnetic Teflon stirrer provided the convective transport during the amperometric measurements. All the experiments were performed at room temperature.

2.2. Reagents

Sodium sulfite was obtained from Changchun Reagent Co. Ltd. (Changchun, China). Chitosan with a degree of deacetylation of 92% was purchased from Sanland-chem International Inc. (Xiamen, China). Sodium cyanoborohydride ($NaCNBH_3$, 98%) and ferrocenecarboxaldehyde (Fc-CHO, 98%) were obtained from Acros and Fluka, respectively.

Multiwall carbon nanotubes (MWCNTs, diameter: 10–20 nm, average length: 1–2 μm, purity: ≥95%) were purchased from Shenzhen Nanotech. Port. Co. Ltd. (Shenzhen, China). Before use, the MWCNTs were treated with mixed acid according to a method already described [35] and the oxidized MWCNTs (MWCNTs-COOH) were formed.

Ferrocene-branched chitosan (CHIT-Fc) was prepared according to the method described in the literature [31]. All other reagents were of analytical grade and used without further purification. All aqueous solutions were prepared with doubly distilled water. The solutions containing sulfite bubbled with ultrapure N_2 and kept under the nitrogen atmosphere during the electrochemical experiments.

2.3. Sensor preparation

Firstly, a GCE (3 mm-diameter) was polished with emery paper followed by polishing it with alumina (1.0, 0.5, and 0.3 μm), and then thoroughly washed with twice-distilled water, sonicated in ethanol, washed again with twice-distilled water and ethanol, and finally dried in nitrogen at room temperature.

0.5 mg CHIT-Fc was dissolved in 0.5 ml 0.1 M acetic acid and 0.5 mg oxidized MWCNTs was dispersed in 0.1 M acetic acid with ultrasonication for 15 min, respectively.

The CHIT-Fc/MWCNTs composites were prepared by mixing above two solutions by sonicating the mixture for 30 min. Then a 6 μl aliquot of this solution was cast on the surface of cleaned GC electrode, dried at room temperature for 2 h. The obtained electrode, the CHIT-Fc/MWCNTs/GCE, dipped into 0.1 M (pH 7.0) phosphate buffer solution (PBS) for 5 min, was ready for use. The composition of the layer of the electrode was 3 μg CHIT-Fc and 3 μg MWCNTs, respectively. The fabricated method of different composition of the layer of electrodes was similar to that above. In the comparing test, fabrication process of the sensor was similar to that of CHIT-Fc/MWCNTs/GCE by substituting MWCNTs with graphite.

3. Results and discussion

3.1. Electrochemical behavior of the CHIT-Fc/MWCNTs/GCE

To investigate whether MWCNTs on GCE could provide a remarkable synergistic augmentation of the sensor performance, cyclic voltammetry (CV) was performed with the different kinds of electrodes in 0.1 M PBS (pH 8.0). Fig. 1 shows cyclic voltammograms (CVs) at a CHIT-Fc/GCE and the CHIT-Fc/MWCNTs/GCE, respectively. In the initial comparing experiment, at the GCE modified with CHIT-Fc film alone, a pair of well-defined redox peaks corresponding to the oxidation and reduction of the CHIT-Fc were observed at +0.32 and +0.26 V vs. SCE, respectively (Fig. 1(a)). The formal potential ($E^{\circ\prime}$) of +0.29 V was calculated from the average value of the anodic and cathodic peak potentials and the peak-to-peak separation (ΔE_p) was 60 mV at a scan rate of 0.05 V s^{-1}. Obviously this is a one-electron redox reaction of CHIT-Fc$^+$/CHIT-Fc.

For the case of CHIT-Fc/MWCNTs composites-coated GCE modified with the same redox polymer, although no change in the shape and peak potentials of CV was observed, yet there was an obvious increase in the redox peak currents (Fig. 1(b)–(d)). This suggests that in the case of the electrode with the CHIT-Fc alone, not all of redox centers were in electrical communication with the electrode surface and that the MWCNTs increased efficiency in mediating electron transfer for the CHIT-Fc/MWCNTs composites-coated GCE.

Inset of Fig. 1 shows the relationship between oxidation peak currents and the amounts of MWCNTs in the composites film. As can be seen that the oxidation peak current response increased linearly with the amounts of MWCNTs and maximum oxidation
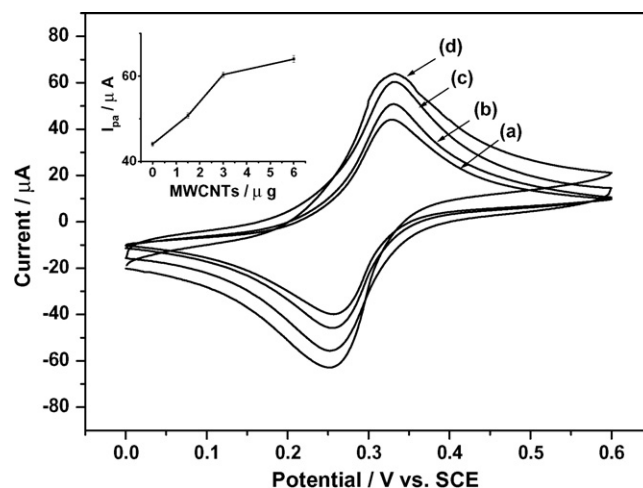

Fig. 1. Cyclic voltammograms of GCE modified with different composite film. (a) 3 μg CHIT-Fc; (b) 3 μg CHIT-Fc and 1.5 μg MWCNTs; (c) 3 μg CHIT-Fc and 3 μg MWC-NTs; (d) 3 μg CHIT-Fc and 6 μg MWCNTs. Conditions: 0.1 M PBS (pH 8.0); scan rate: 50 mV s^{-1}. Inset shows the relationship between oxidation peak currents (I_{pa}) and the amounts of MWCNTs in the composite film.
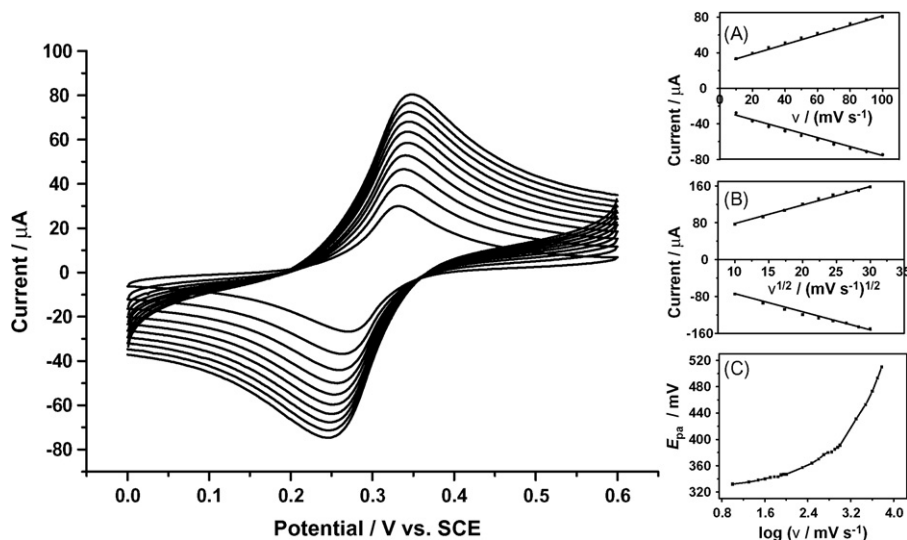
Fig. 2. Cyclic voltammograms of the CHIT-Fc/MWCNTs/GCE in 0.1 M PBS (pH 8.0) at scan rates (from inner to outer) 10, 20, 30, 40, 50, 60, 70, 80, 90 and 100 mV s^{-1}, respectively. Inset A: plot of I_p *vs.* υ. Inset B: I_p *vs.* $\upsilon^{1/2}$. Inset C: E_{pa} *vs.* log υ.

current was obtained at 3 μg of MWCNTs. At higher amounts of MWCNTs, the plot of oxidation peak currents *vs.* plot of amounts of MWCNTs deviated from linearity. Therefore, 3 μg of MWCNTs was chosen as the optimum amount of MWCNTs in the composites for all following electrochemical experiments.

Fig. 2 shows the cyclic voltammograms of CHIT-Fc/MWCNTs/ GCE at different scan rates in potential range of 0.00–0.60 V in 0.1 M PBS (pH 8.0). As shown in the inset A of Fig. 2, the oxidation peak currents increased linearly with the scan rate between 10 and 100 mV s^{-1} as expected for a surface-controlled electrode process. At higher sweep rates, the plot of oxidation peak currents *vs.* scan rate plot deviated from linearity and the oxidation peak currents became proportional to the square root of the scan rate (inset B of Fig. 2), showing a diffusion controlled process. At higher sweep rates, the oxidation peak potentials (E_{pa}) were proportional to the logarithm of the scan rate (inset C of Fig. 2) and the slop of the $\partial E_{pa}/\partial \log \upsilon$ was about 140.0 mV. According to Lavirou's theory [36], when $\Delta E_p > 200$ mV, using the equation $E_p = k - 2.303(RT/\alpha nF) \log \upsilon$ and one electron transferred for CHIT-Fc$^+$/CHIT-Fc redox couple, charge transfer coefficient, $\alpha = 0.42$, was obtained. Introducing this α value in the following equation:

$$\log K_s = \alpha \log(1 - \alpha) + (1 - \alpha) \log \alpha - \log\left(\frac{RT}{nF\upsilon}\right) - \frac{\alpha(1-\alpha)nF\Delta E_p}{2.303RT}$$

An apparent surface electron transfer rate constant, $K_s = 1.93$ cm s^{-1}, was estimated. For the case of the electrode with the CHIT-Fc alone, the obtained K_s was 0.63 cm s^{-1} by similar method (date not shown here). The above results also show that the integration of CHIT-Fc and MWCNTs can provide a remarkable synergistic augmentation of sensor performance.

3.2. Electrocatalytic oxidation of sulfite at CHIT-Fc/MWCNTs/GCE

The electrocatalytic oxidation of sulfite by water-soluble ferrocene derivatives in homogeneous solution has been reported [13]. Here, we take sulfite as an example of sulfur oxoanions and investigated its electrocatalytic oxidation through the CHIT-Fc/MWCNTs/GCE. At CHIT/MWCNTs/GCE a little response was obtained in the range from 0.00 to 0.90 V (vs. SCE) in 0.1 M PBS (pH 8.0) containing 2 mM sulfite, as shown in Fig. 3, curve (a) and (b). However, the catalytic oxidation of sulfite at the CHIT-Fc/MWCNTs/GCE can be seen clearly in Fig. 3, curve (c) and (d).

Adding sulfite to the cell produced a dramatic change in the cyclic voltammogram with an increase in anodic current and decrease in cathodic current, which indicated that the electrocatalytic oxidation of sulfite occurred at the modified electrode. The oxidation peak potential of sulfite at the modified electrode was negatively shifted about 330 mV compared with that at CHIT/MWCNTs/GCE. This suggests that CHIT-Fc/MWCNTs composites exhibit high electrocatalytic activity towards sulfite.

The effect of buffer solution pH on the electrocatalytic activity of CHIT-Fc/MWCNTs composites towards sulfite was investigated. The experimental results show that the catalytic currents increase and the peak potentials were negatively shifted as pH increase in 2.0–10.0 pH range and maximum growth of catalytic current occurred at pH 8.0, as shown in Fig. 4. The catalytic response increased with pH and reached a platform at pH larger than 8.0. Therefore, an optimum pH for the electrocatalytic system of 8.0 was selected.

Fig. 5 shows the cyclic voltammograms of 2 mM sulfite at the CHIT-Fc/MWCNTS/GCE in 0.1 M PBS (pH 8.0) at different scan rates in potential range 0.0–0.6 V. The oxidation peak currents were proportional to the square root of the scan rate (inset (A) of Fig. 5). This result indicates that the reaction system was controlled by
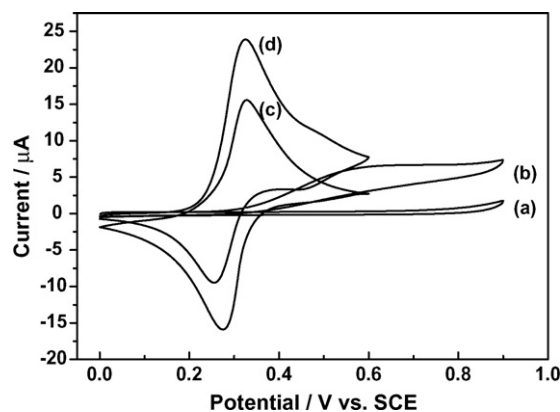

Fig. 3. Cyclic voltammograms in 0.1 M PBS (pH 8.0) at scan rate of 5 mV s^{-1}: CHIT/MWCNTs/GCE in buffer solution containing no sulfite (a) and containing 2 mM sulfite (b); CHIT-Fc/MWCNTs/GCE in buffer solution containing no sulfite (c) and containing 2 mM sulfite (d).
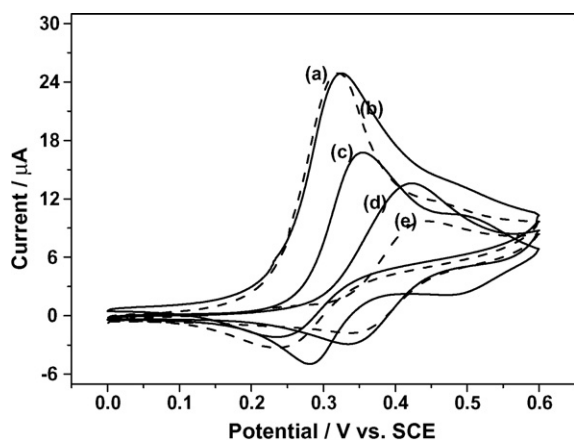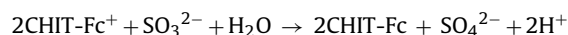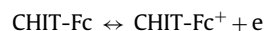
Fig. 4. Cyclic voltammograms of the CHIT-Fc/MWCNTs/GCE in the presence of 2 mM sulfite in 0.1 M PBS at various pH: (a) 2, (b) 4 and (c) 6, (d) 8, (e) 10. Scan rate: 5 mV s^{-1}.

sulfite diffusion. It can also be noted in Fig. 5 that by increasing the scan rate the peak potential for the catalytic oxidation of sulfite shifted to more positive values, suggesting a kinetic limitation in the reaction system. Based on the above results, the catalytic process (EC catalytic mechanism) could be expressed as follows:

$$CHIT\text{-}Fc \leftrightarrow CHIT\text{-}Fc^+ + e$$

$$2CHIT\text{-}Fc^+ + SO_3^{2-} + H_2O \rightarrow 2CHIT\text{-}Fc + SO_4^{2-} + 2H^+$$

For information on the rate-determining step, a Tafel plot was obtained from the linear relationship observed for E_{pa} vs. log υ (inset (B) of Fig. 5) by using the following equation [37].

$$E_p = \frac{(b \log \upsilon)}{2} + constant$$

On the basis of the above equation, the slop of E_p vs. log υ is $b/2$, where b is the Tafel slop. Thus $b = 2 \times \partial E_p / \partial \log \upsilon = 139.6$ mV. The result is close to that obtained from ferrocenemonocarboxylic acid used as a homogeneous mediator to catalyze the electrooxidation of sulfite [13].
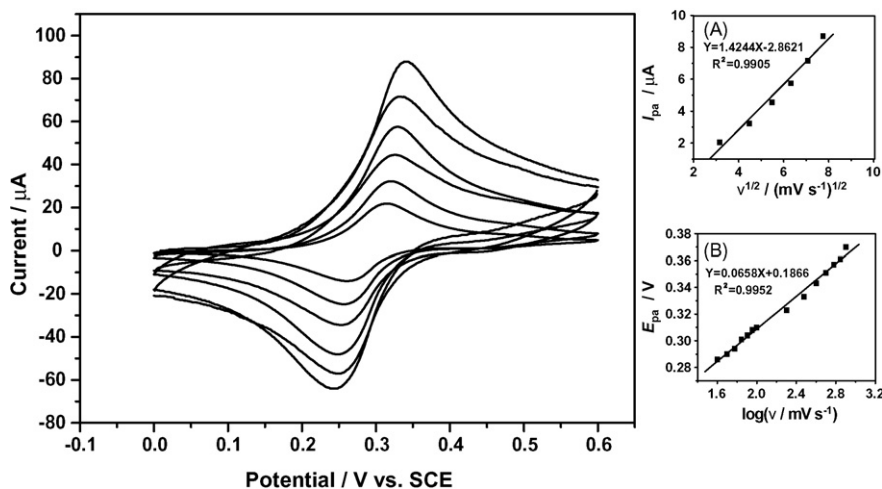
3.3. Amperometric determination of sulfite at the CHIT-Fc/MWCNTs/GCE

Firstly, in order to optimize the working potential, the dependence of the sulfite response on the applied potential was studied by the amperometry over the potential range from +0.20 to +0.45 V. The current response was measured as a function of applied potential on exposure to 0.1 mM sulfite in a stirring 0.1 M PBS (pH 8.0). At the CHIT-Fc/MWCNTs/GCE, the current response increased with the increase in potential and the optimal value was observed at +0.35 V (data not shown here). Therefore, a potential of +0.35 V was selected for constant potential amperometry to study the amperometric response of the sensor on sulfite.

Fig. 6 displays the typical steady-state catalytic current-time response of the CHIT-Fc/MWCNTs/GCE with successive injection of sulfite at an applied potential of +0.35 V. As shown during the successive additions of 0.15 mM (Fig. 6(A), high concentration section) and 0.02 mM (Fig. 6(B), low concentration section) of sulfite, a well-defined response was observed, respectively. And from Fig. 6 it can be seen that the time required to reach 95% of the steady-state current was less than 10 s after the addition of sulfite, which showed that the current response of the sensor was rapid. The insets in Fig. 6(A) and (B) illustrate the calibration curves of the sensor under the optimal experimental conditions. The linear range spanned the concentration of sulfite from 5 μM to 1.5 mM. In the linear range, the sensor had a high sensitivity of 13.08 μA mM^{-1}. The detection limit of the sensor was determined to be 2.8 μM at a signal-to-noise ratio of 3. Obviously, the analytical performance parameters of the proposed sensor are better than that obtained by water-soluble ferrocene derivatives in homogeneous solution [13]. High sensitivity can be attributed to the synergistic augmentation of MWCNTs and CHIT-Fc towards sulfite response. In the past decade, the detection limit, linear concentration range and sensitivity of other related modified electrodes for sulfite detection have been reported in Table 1.

In order to demonstrate the electrocatalytic oxidation of sulfite in a real sample, the determination of sulfite in boiler-water samples was carried out by the standard addition method. The results obtained were compared with those come from a standard iodometric method [38] and were shown to be in good agreement, as shown in Table 2.

In addition, interference of coexisting species come from boiler-water samples was studied. The experimental results showed that

Fig. 5. Cyclic voltammograms of the CHIT-Fc/MWCNTs/GCE in 0.1 M PBS (pH 8.0) containing 2 mM sulfite at scan rates (from inner to outer) 10, 20, 30, 40, 50 and 60 mV s^{-1}, respectively. Inset A: I_{pa} vs. $\upsilon^{1/2}$. Inset B: E_{pa} vs. log υ.

Table 1
The comparison of the performance of present sensor and others reported in the literatures for sulfite detection

| No.	Type of film modified electrode	Linear range	Sensitivity	Detection limit	Ref.
1	NiPCNF/Al	4×10^{-6} to 2×10^{-4} M		3×10^{-6} M	[10]
2	CoPCNF/GCE	5×10^{-6} to 1×10^{-4} M		3×10^{-6} M	[13]
3	Fe/CCE	0.73–95.42 mg/l		0.59 mg/l	[14]
4	In situ plated copper modified gold ultramicroelectrode arrays	20–500 μM	0.35 nA/μM	6 μM	[15]
5	Fc/CPE	8.7×10^{-5} to 1.1×10^{-2} M		5.3×10^{-6} M	[16]
6	PB/GCE	0.0–4.0 mM	2.18 μA/mM	80 μM	[17]
7	NiPPIX/GCE	~9.0 μg/ml		0.15 μg/ml	[18]
8	NiPCNF/CCEs	2 μM–2.0 mM	13.5 nA/μM	0.5 μM	[20]
9	Sulfite oxidase	0.01–1.0 mM			[21]
10	Sulfite oxidase	0.04–5.9 mM		4.0 ppm	[22]
11	Sulfite oxidase	0.2–1.8 mM		0.2 mM	[23]
12	CHIT-Fc/MWCNTs/GCE	5.0 μM–1.5 mM	13.08 μA/mM	2.8 μM	This work
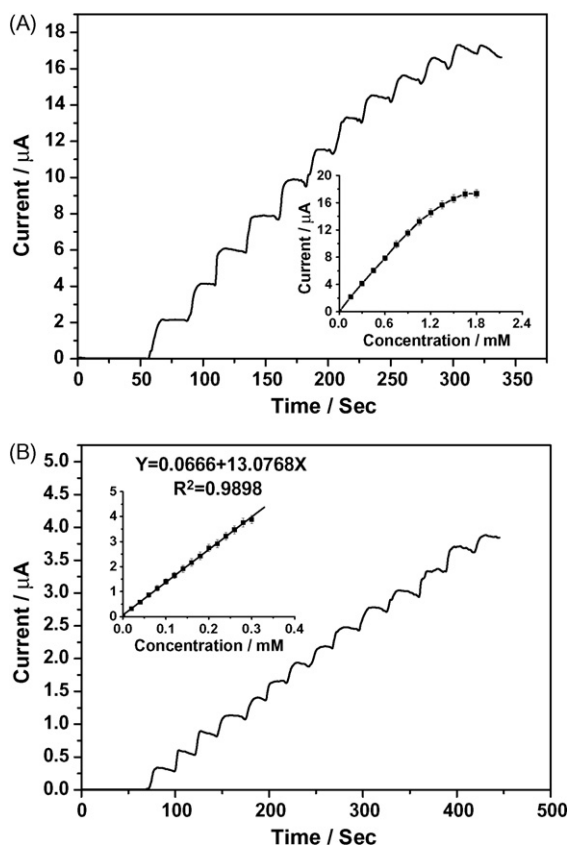
Fig. 6. An amperometric response at the CHIT-Fc/MWCNTs/GCE for successive addition of (A) 0.15 mM and (B) 0.02 mM sulfite. Conditions: 0.1 M PBS (pH 8.0); applied potential: 0.35 V (*vs.* SCE). Insets show the relationship between catalytic currents and sulfite concentrations.

a 600-fold excess of Ca^{2+}, Mg^{2+}, Ba^{2+}, PO_4^{3-}, NO_3^-, CO_3^{2-} and Cl^- did not interfere in the determination of sulfite.

The stability of the CHIT-Fc/MWCNTs/GCE was investigated. In the potential range from 0.00 to 0.60 V at a scan rate of 50 mV s^{-1} and in pH 8.0 0.1 M PBS, after about 50 scanning cycles the redox currents decreased about 3.0%. When the sensor was stored in

Table 2
The results of determination of boiler-water sample

Sample number	Concentration of sulfite (mg/l)	
	Proposed method	Iodometric method
1	10.3	9.7
2	16.3	15.8
3	20.9	19.8

atmosphere, the current response remained almost unchanged for at least a month. In addition, after 30 days the sensor remained 95% of its initial response to electrocatalytic oxidation of sulfite. The good stability of the CHIT-Fc/MWCNTs/GCE can be attributed primarily to electrostatic interaction between MWCNTs contained negative charges and CHIT-Fc contained positive charges, and robust film-forming ability of CHIT-Fc. The sensor has good repeatability. The relative standard deviation (R.S.D.) is 6.7% for seven determination of 30 μM sulfite in 0.1 M PBS (pH 8.0).

4. Conclusions

In this work, we developed a novel way to fabricate amperometric sulfite sensor by CHIT-Fc/MWCNTs composites-covered GCE. The CHIT-Fc and MWCNTs composites showed obvious synergistic augmentation of the sensor performance compared with that obtained by CHIT-Fc alone. The sensor showed good electrocatalytic activity for the oxidation of sulfite in 0.1 M PBS (pH 8.0). Because of electrostatic interaction between MWCNTs and CHIT-Fc and robust film-forming ability of the latter, the sensor also exhibited very good reproducibility and stability. The above results suggest that the proposed sensor can be used as amperometric sensor for the determination of sulfite.

References

[1] E. Dinckaya, M.K. Sezgintürk, E. Akyilmaz, F.N. Ertas, Food Chem. 101 (2007) 1540.
[2] I.V. Pulyayeva, N.L. Yegorova, L.P. Experianova, A.B. Blank, Anal. Chim. Acta 357 (1997) 239.
[3] S.S.M. Hassan, M.S.A. Hamza, A.H.K. Mohamed, Anal. Chim. Acta 570 (2006) 232.
[4] Y. Zuo, H. Chen, Talanta 59 (2003) 875.
[5] G.A. Perfetti, G.W. Diachenko, J. AOAC Int. 86 (2003) 544.
[6] M.H. Pournaghi-Azar, M. Hydarpour, H. Dastangoo, Anal. Chim. Acta 497 (2003) 133–141.
[7] M.H. Pouranghi-Azar, R.E. Sabzi, Electroanalysis 16 (2004) 860.
[8] D.R. Shankaran, K.I. Iimura, T. Kato, Electroanalysis 16 (2004) 556.
[9] O. Ordeig, C.E. Banks, F.J.d. Campo, F.X. Muñoz, J. Davis, R.G. Compton, Electroanalysis 18 (2006) 247.
[10] J.B. Raoof, R. Ojani, H. Karimi-Maleh, Int. J. Electrochem. Sci. 2 (2007) 257.
[11] T. García, E. Casero, E. Lorenzo, F. Pariente, Sens. Actuators B 106 (2005) 803.
[12] R. Carballo, V.C. DalÎOrto, A.L. Balbo, I. Rezzano, Sens. Actuators B 88 (2003) 155.
[13] Z.N. Gao, J.F. Ma, W.Y. Liu, Appl. Organomet. Chem. 19 (2005) 1149.
[14] A. Salimi, K. Abdi, G.R. Khayatiyan, Electrochim. Acta 49 (2004) 413.
[15] M. Zhao, D.B. Hibbert, J.J. Gooding, Anal. Chim. Acta 556 (2006) 195.
[16] A.K. Abass, J.P. Hart, D. Cowell, Sens. Actuators B 62 (2000) 148.
[17] M.K. Sezgintürk, E. Dinckaya, Talanta 65 (2005) 998.
[18] S. Iijima, Nature 354 (1991) 56.

[19] G.A. Rivas, M.D. Rubianes, M.C. Rodríguez, N.F. Ferreyra, G.L. Luque, M.L. Pedano, S.A. Miscoria, C. Parrado, Talanta 74 (2007) 291.
[20] M. Valcárcel, S. Cárdenas, B.M. Simonet, Anal. Chem. 79 (2007) 4788.
[21] J.X. Wang, M.X. Li, Z.J. Shi, N.Q. Li, Z.N. Gu, Anal. Chem. 74 (2002) 1993.
[22] J.C. Cai, J. Chen, Anal. Biochem. 325 (2004) 285.
[23] G. Zhao, L. Zhang, X. Wei, Z. Yang, Electrochem. Commun. 5 (2003) 825.
[24] J.A. Guiseppi-Elie, C. Lei, R. Baughman, Nanotechnology 13 (2002) 559.
[25] J. Wang, M. Musameh, Anal. Chem. 75 (2003) 2075.
[26] L. Qian, X. Yang, Talanta 68 (2006) 721.
[27] M. Zhang, W. Gorski, Anal. Chem. 77 (2005) 3960.
[28] Y. Liu, J. Lei, H. Ju, Talanta 74 (2008) 965.
[29] M. Zhang, W. Gorski, J. Am. Chem. Soc. 127 (2005) 2058.
[30] H. Yi, L. Wu, W.E. Bentley, R. Ghodssi, G.W. Rubloff, J.N. Culver, G.F. Payne, Biomacromolecules 6 (2005) 2881.
[31] W. Yang, H. Zhou, C. Sun, Macromol. Rapid Commun. 28 (2007) 265.
[32] A. Heller, Acc. Chem. Res. 23 (1990) 128.
[33] J. Hodak, R. Etchenique, E.J. Calvo, Langmuir 13 (1997) 2708.
[34] P.P. Joshi, S.A. Merchant, Y. Wang, D.W. Schmidtke, Anal. Chem. 77 (2005) 3183.
[35] M. Zhang, Y. Yan, K. Gong, L. Mao, Z. Guo, Y. Chen, Langmuir 20 (2004) 8781.
[36] E. Laviron, J. Electroanal. Chem. 52 (1974) 355.
[37] J.A. Harrison, Z.A. Khan, J. Electroanal. Chem. 28 (1970) 131.
[38] Chinese Institute of Boiler Water Treatment, Water Quality for Industrial Boilers, Chinese Standard Publishing Company, Beijing, 2004.